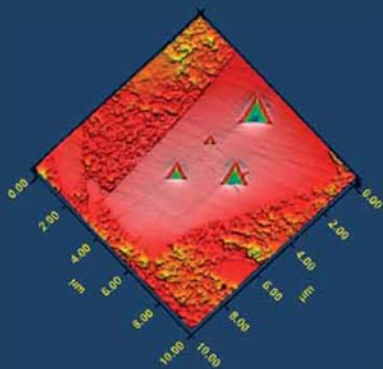


E.E. Gdoutos  
*Editor*

# Experimental Analysis of Nano and Engineering Materials and Structures

*Proceedings of the 13th International Conference on Experimental  
Mechanics, Alexandroupolis, Greece, July 1-6, 2007*



Springer

EXPERIMENTAL ANALYSIS OF NANO AND ENGINEERING MATERIALS  
AND STRUCTURES

# Experimental Analysis of Nano and Engineering Materials and Structures

Proceedings of the 13th International Conference  
on Experimental Mechanics, Alexandroupolis,  
Greece, July 1–6, 2007

Edited by

E.E. GDOUTOS

*Democritus University of Thrace,  
Xanthi, Greece*



Springer

A C.I.P. Catalogue record for this book is available from the Library of Congress.

ISBN 978-1-4020-6238-4 (HB)

ISBN 978-1-4020-6239-1 (e-book)

---

Published by Springer,  
P.O. Box 17, 3300 AA Dordrecht, The Netherlands.

*www.springer.com*

Cover picture

**Ceramic Matrix Composite:** The high resolution of the in-situ imaging and accuracy of indent positioning allows individual indents applied at increasing loads to be applied on a particle within this composite matrix. This study enabled the mode of failure to be identified for each particle and the maximum load before catastrophic failure to be determined. Courtesy of Hysitron Inc., Minneapolis, Minnesota, USA

*Printed on acid-free paper*

All Rights Reserved

© 2007 Springer

No part of this work may be reproduced, stored in a retrieval system, or transmitted in any form or by any means, electronic, mechanical, photocopying, microfilming, recording or otherwise, without written permission from the Publisher, with the exception of any material supplied specifically for the purpose of being entered and executed on a computer system, for exclusive use by the purchaser of the work.

# Contents

Editor's Preface .....	xxxv
Organizing Committees .....	xxxvii
ICEM13 TRACKS .....	xxxix
ICEM13 SPECIAL SYMPOSIA/SESSIONS.....	xli

## A. INVITED PAPERS

Modern Photoelasticity for Residual Stress Measurement in Glass .....	3
<i>Hillar Aben, Johan Anton and Andrei Errapart</i>	
Thermoelastic Stress Analysis of Vascular Devices .....	5
<i>J.M. Dulieu-Barton, J. Eaton-Evans, E.G. Little and I.A. Brown</i>	
Micro/Nano Speckle Method with Applications to Material, Tissue Engineering and Heart Mechanics .....	7
<i>Fu-Pen Chiang</i>	
In-Situ Electron Microscopy Testing of Nanostructures.....	9
<i>Horacio D. Espinosa</i>	
Air Blast Loading of Cellular Media .....	11
<i>George A. Gazonas and Joseph A. Main</i>	
Importance of Full-Field Measurement Techniques for Better Models in Solid Mechanics .....	13
<i>Michel Grediac</i>	
Recent Developments and Applications of Photomechanics Methods for Microelectronics Product Development.....	15
<i>Bongtae Han</i>	
A Tentative Analysis of the Status of Speckle Interferometry in Experimental Mechanics .....	17
<i>Pierre Jacquot</i>	
On the Characterisation of Cellular Materials Used in Sandwich Construction.....	19
<i>R.A.W. Mines</i>	
Three-Dimensional Displacement Analysis by Windowed Phase-Shifting Digital Holographic Interferometry .....	21
<i>Yoshiharu Morimoto, Toru Matui and Motoharu Fujigaki</i>	
ONR Solid Mechanics Research Program Overview .....	23
<i>Yapa D. S. Rajapakse</i>	
Large-Deformation Constitutive Theories for Structural Composites: Rate Dependent Concepts and Effect of Microstructure.....	25
<i>Kenneth Reifsnider and Liqun Xing</i>	
Experimental Mechanics at the Nanometric Level.....	27
<i>Cesar A. Sciammarella</i>	
Mechanical Property Measurement at the Micro/Nano Scale .....	29
<i>W. N. Sharpe, Jr</i>	
Characterisation and Assessment of Failure and Fatigue Phenomena in Sandwich Structures Induced by Localized Effects.....	31

*Ole Thybo Thomsen*

## B. TRACKS

<b>1T3. Nanocomposites .....</b>	<b>35</b>
Metal-Polymer-Ceramic Nano/Composite Material.....	35
<i>M.V. Kireitseu and L.V. Bochkareva</i>	
Characterization of a New Titanium Dioxide-Polymer Composite Material for Electronic Packaging Applications .....	37
<i>Barish Dantal, Anil Saigal and Michael Zimmerman</i>	
Forming of Fullerene-Dispersed Aluminum Composite by Compression Shearing Method .....	39
<i>Noboru Nakayama and Hiroyuku Takeishi</i>	
Study of the Mechanical Properties of Cellulose/ ZRO <sub>2</sub> .NH <sub>2</sub> O Composites .....	41
<i>Daniella Regina Mulinari and Maria Lúcia Caetano Pinto da Silva</i>	
Thermo-Mechanical Characterization of Epoxy/Silica Nanocomposites .....	43
<i>M.S. Konsta-Gdoutos, I.M. Daniel, Z. Metaxa and J. Cho</i>	
<b>1T6. Nanostuctured Materials .....</b>	<b>45</b>
Global Mechanical Behavior of a Nanostructured Multilayered Composite Material Produced by Smat and Co-Rolling.....	45
<i>L. Waltz, T. Roland, D. Retraint, A. Roos, P. Olier and J. Lu</i>	
Preparation of High Molecular Weight Poly(vinyl Carbazole) Web by Electrospinning .....	47
<i>Won Seok Lyoo, Ki Bum Lee, Young Jae Lee and Hee Sam Kim</i>	
Preparation of Hydrophilic Antioxidant-Loaded Poly(vinyl Alcohol) Nanoweb by Electrospinning and its Wound Healing Effect .....	49
<i>Sung Jun Lee, Se Geun Lee, Hoyoung Kim, Jae Ryong Kim, Cha Young, Sun Gil Kim and Won Seok Lyoo</i>	
Tensile Strength of Surface Nanostructured Copper.....	51
<i>H. L. Chan and J. Lu</i>	
Some Considerations about the Formulation of Constitutive Equations of Organic Materials: Industrial View and Needs .....	53
<i>A. Martinet, François Moussy and Florian Trioux</i>	
<b>1T7. Thin Films .....</b>	<b>55</b>
Cohesive Properties of Molten Particle Deposited Onto Substrate by a Free Fall .....	55
<i>Masayuki Arai, Hirotada Toyama and Yasuo Ochi</i>	
Evaluation of Wear Resistance of Sputtered Amorphous SiCN Film and Measurement of Delamination Strength of Film by Micro Edge-indent Method.....	57
<i>Masahiko Kato, Jinhua Zheng, Seiji Takezoe and Keijiro Nakasa</i>	
Preparing of Diamond in the Presence of CH <sub>4</sub> -H <sub>2</sub> in a Cold Plasma Produced by a Magnetron .....	59
<i>Maryam Habibi, Mahmood Ghoranneviss and Reza Naranji</i>	
High Temperature Behavior of Al Thin Film .....	61
<i>C.-S. Oh, J.-S. Bae, S.-H. Choa and H.-J. Lee</i>	
Bauschinger Effect in Thin Metal Films on Compliant Substrates .....	63

*J.P.M. Hoefnagels and J.J. Vlassak*

<b>2T3. Applications .....</b>	<b>65</b>
Practical Problems of Modal analysis of Aero Engine Blades .....	65
<i>Strain Posavljak</i>	
Optical Techniques for Relief Study of Mona Lisa's Wooden Support .....	67
<i>Fabrice Brémand, Pascal Doumalin, Jean-Christophe Dupré, Franck Hesser and Valéry Valle</i>	
Residual Stress and Deformation Induced by Laser Shock Peening on Titanium Alloys.....	69
<i>Christophe Cellard, Pierre Osmond, Delphine Reintant, Emmanuelle Rouhaud, Sébastien Remy and Ana Viguera-Sancho</i>	
Development and Application of Biaxial Compression Test Device for Metallic Materials.....	71
<i>Ichiro Shimizu</i>	
Measurement of Residual Stresses in Large Engineering Components .....	73
<i>F. Hosseinzadeh, D.J. Smith and C.E. Truman</i>	
Measurement of Interaction Forces between Wheel and Rail on an Extreme Train Wheelset.....	75
<i>R.A. Cláudio, J. Duarte Silva, A.J. Valido and P.J. Moita</i>	
Monitoring and Diagnosis of Drill Wear and the Thermodynamic Phenomenas of Material Removal by Drilling of Stainless Steels.....	77
<i>Jozef Jurko</i>	
Modeling Prosperities Drives Elements of Cars after Heat Treatment Processes by Means Neural Networks.....	79
<i>Michal Szota and Jozef Jasiski</i>	
The Mechanical Strength of Intestinal Anastomoses in Hypothyroid Rats .....	81
<i>S.K. Kourkoulis, K.A. Ekmektzoglou, S.-A. Papanicolopoulos, G.C. Zografos, I.A. Dontas, T. Xanthos and D.N. Perrea</i>	
The Anterior Cruciate Ligament of the Knee Joint under Mechanical Constraints.....	83
<i>S.K. Kourkoulis and E. Gogossi</i>	
<b>2T4. Applied Photoelasticity .....</b>	<b>85</b>
Digital Photoelastic Evaluation of Isochromatic Fringe Order in a 3D Model of Complex Rocket Motor Strap-on Joint .....	85
<i>K. Ashokan, K. Ramesh, S.A. Pillai and Jeby Philip</i>	
Smoothing of Digital Photoelastic Data Using Robust Outlier Algorithm.....	87
<i>M. Ramji and K. Ramesh</i>	
3D Photoelasticity and Digital Volume Correlation Applied to 3D Mechanical Studies	89
<i>A. Germaneau, P. Doumalin and J.C. Dupré</i>	
Stress Separation by Means of Phase Shifting in Photoelasticity .....	91
<i>Dongsheng Zhang, Yongsheng Han and Dwayne Arola</i>	
Linear and Non-Linear Algorithms of Photoelastic Tomography .....	93
<i>Hillar Aben and Andrei Errapart</i>	
Generalized Onion-Peeling Method in Integrated Photoelasticity of Axisymmetric Problems.....	95
<i>Johan Anton and Andrei Errapart</i>	

<b>2T6. Composite Materials .....</b>	<b>97</b>
Mechanical Properties of Oil Palm Fibre Reinforced Epoxy for Building Short Span Bridge.....	97
<i>Mimi Azlina Abu Bakar, Valliyappan D. Natarajan, Anizah Kalam and Nor Hayati Kudiran</i>	
Research on the Shear Behaviour of Plain Fabric Prepreg at Lateral Compaction Stage.....	99
<i>Lin Guochang, Wang Youshan and Du Xingwen</i>	
Mechanical Behavior of Soil – Geotextile Composites: Effect of Soil Type .....	101
<i>A.I. Droudakis and I.N. Markou</i>	
An Experimental Investigation and Finite Element Analysis of Composite Energy Absorption Systems .....	103
<i>Hakim S. Sultan</i>	
Experimental Determination of Fiber Mat Permeability of Chopped Fiberglass Mats	105
<i>Hossein Golestanian</i>	
Mechanical Properties of Particle Filled Polymers .....	107
<i>O.A. Stapountzi, M. Charalambides and J.G. Williams</i>	
Mechanical and Thermal Properties of Acrylic Hydrazide Cured Epoxy; In- Situ Polymerization .....	109
<i>R. P. Yadav, P. C. Gope and P. L. Sah</i>	
Artificial Neural Network Model for Prediction of Fatigue Lives of Composites Materials.....	111
<i>Sanjay Mathur, Prakash Chandra Gope and J. K. Sharma</i>	
Process and Health Monitoring Using Fiber Bragg Grating Distributed Sensor for Vacuum Infusion Process.....	113
<i>Soohyun Eum, Kazuro Kageyama, Hideaki Murayama, Kiyoshi Uzawa, Isamu Osawa, Makoto Kanai and Hiroataka Igawa</i>	
Using DCB and Pull-Out Tests for Experimental Investigation of Rib-Skin Interface Fracture Toughness of Stiffened Composite Shell.....	115
<i>A. Korjakins, O. Ozolins and D. Pizele</i>	
Experimental Tests of Fatigue Induced Delamination in GFRP and CFRP Laminates.....	117
<i>D. Tumino, G. Catalanotti, F. Cappello and B. Zuccarello</i>	
Composte Sandwch Structures; Experimental Evaluation and Finite Element Analysis of Mechancial Propertes.....	119
<i>S. B. Bozkurt, F. E. Sezgin, O. O. Egilmez, E. Aktas and M. Tanoglu</i>	
Some New Strength Criteria for FRP Test Methods Substantiation.....	121
<i>Alexandre N.Polilov and Nikolay A.Tatous</i>	
Composite Repair Technology and its Application .....	123
<i>Kuo-Wei Wu</i>	
Some Influences on the Fatigue Behaviour of Short-Glasfiber-Reinforced Polymers	125
<i>Ch. Guster, G. Pinter, W. Eichlseder and R.W. Lang</i>	
Theoretical Research on the Influence of the Interface Wood-Adhesive on the Stiffness of the Composite Panels Made of Wood Lamellas .....	127
<i>Camelia Boieriu, Ioan Curtu, Dumitru Lica, Mariana Stanciu and Adrian Popoi</i>	



Residual Internal Stresses Determined Experimentally in Hollow Composite Laminates .....	129
<i>Horatiu Teodorescu, Sorin Vlase, Dorin Rosu and Mihai Ulea</i>	
Quasi-Static Compression of Carbon Fibre Square Honeycombs .....	131
<i>B.P. Russell, V.S. Deshpande and N.A. Fleck</i>	
Notch Root Opening Displacement Versus Damage for Particulate MMC's .....	133
<i>V. Kytopoulos, Ch. Riga and S.K. Kourkoulis</i>	
<b>2T7. Damage Assessment .....</b>	<b>135</b>
Fatigue Properties of 2024-T3 Aluminium Specimens Reinforced with Composite Patches .....	135
<i>M.L. Pastor, X. Balandraud, J.L. Robert and M. Grédiac</i>	
Experimental Investigation of Dynamic Damage Evolution for PP/PA Polymer Blends Under High Strain Rates .....	137
<i>Zi-Jian Sun and Li-Li Wang</i>	
Evaluation of Damage and Plastic Properties by Microindentation and Inverse Method .....	139
<i>Bruno Guelorget, Manuel François and Jian Lu</i>	
Acoustic Emission in Adhesively Bonded Joints Composed of Pultruded Adherends	141
<i>Till Vallée, Andreas J. Brunner and Thomas Keller</i>	
Impedance-Based Technique and Guided Wave Method for Damage Assessment with Using Smart Materials .....	143
<i>Yong Hong, Gao-Ping Wang, Dong-Pyo Hong and Young-Moon Kim</i>	
Strain Evaluation in the Neck of a Tensile Test Specimen by ESPI Strain Rate Measurement.....	145
<i>Bruno Guelorget, Manuel Francois and Guillaume Montay</i>	
Evaluation of Hardening of Plastically Deformed Steels .....	147
<i>P. Yasniy, V. Hlado, P. Maruschak and D. Baran</i>	
Experimental Characterization of Ductile Damage using Nanoindentation.....	149
<i>C.C. Tasan, J.M.P. Hoefnagels, R.H.J. Peerlings and M.G.D. Geers</i>	
Mechanisms of Plasticity and Fracture in Crystals, Polymers Under Low/Shock-Wave Stresses .....	151
<i>Valery P. Kisel</i>	
Failure Surfaces in Ductile Non Linear Elastic Materials .....	153
<i>N.P. Andrianopoulos, V.M. Manolopoulos and V.C. Boulougouris</i>	
<b>2T8. Dynamic Systems.....</b>	<b>155</b>
Comparison of Vibration Response Spectrum with Linear and Reverse-Miso Frequency Response Functions for Non-Linear Cushioning Systems.....	155
<i>Michael A. Sek, Anthony Parker and Vincent Rouillard</i>	
The Non-Linear Characteristics of Cushioning Materials .....	157
<i>Anthony Parker, Michael A. Sek and Vincent Rouillard</i>	
Modal Control of Vibrations of a Machine Structure by Using Electromagnetic Exciters.....	159
<i>Tetsuo Sato</i>	
High Strain Rate Behaviour of Aluminium Alloys Using Split Hopkinson Bar (SHB) Testing .....	161

<i>G. I. Mylonas, G. N. Labeas and Sp. G. Pantelakis</i>	
Experimental Investigations of the Dynamics of PLC Bands in Al3%mg .....	163
<i>Leobaldo Casarotto, Rainer Tutsch, Hanno Dierke and Hartmut Neuhäuser</i>	
One-to-One Resonance Phenomenon on a Nonlinear Quadrangle Cantilever Beam..	165
<i>Myoung-Gu Kim</i>	
<b>2T9. Fiber Optic Sensors .....</b>	<b>167</b>
Effects of Leading and Trailing Edge of Current Pulse on AE Wave.....	167
<i>Yoshiaki Akematsu, Atsutoshi Hirao, Kazuro Kageyama, Naotake Mohri and Hideaki Murayama</i>	
High Precision Operation of Fiber Bragg Grating Sensor with Intensity-Modulated Light Source .....	169
<i>N. Takahashi, H. Yokosuka, K. Inamoto and S. Tanaka</i>	
Creep Measurement of Optical Fiber with a Double Interferometer System .....	171
<i>Zhihong Xu and Fahard Ansari</i>	
<b>2T10. Fracture and Fatigue.....</b>	<b>173</b>
A Guideline for Fatigue Testing of Components .....	173
<i>Mehrdad Zoroufi and Ali Fatemi</i>	
New Equipment for Liquid Metal Embrittlement Characterisation for Vertical Axis Testing Machines .....	175
<i>J. Carpio, J.A. Alvarez, J.A. Casado and F. Gutierrez-Solana</i>	
Experimental Random Signals in Industrial Conditions and Applications by Computer Analysis.....	177
<i>M. Kopecky</i>	
Measurement and Identification Techniques for Cracks: Application in Cyclic Fatigue.....	179
<i>Julien Réthoré, Stéphane Roux and François Hild</i>	
Impact of Machining Parameters on Fatigue Behaviour of 15%SiCP- Reinforced Aluminium Matrix Composites .....	181
<i>Ali Mkaddem, Patrick Ghidossi, Samuel Crequy and Mohamed El Mansori</i>	
The Effect of Machining on the Surface Integrity .....	183
<i>Ataollah Javidi, Ulfried Rieger and Wilfried Eichlseder</i>	
Evaluation of KI-V Relation in Ceramics by Using DT Technique (Crack Length Measurement by Using Compliance Method) .....	185
<i>Hitoo Tokunaga, Kiyohiko Ikeda, Koichi Kaizu and Hiroyuki Kinoshita</i>	
Experimental Study of the Out-of-Plane Displacement Fields for Different Crack Propagation Velocities.....	187
<i>S. Hédan, V. Valle and M. Cottton</i>	
Experimental Study on the Influence of the Shape and the Size of the Specimen on Compression Behaviour of High Strength Concrete.....	189
<i>J. R. Del Viso, J. R. Carmona and G. Ruiz</i>	
Specimen Geometry and Material Property Uncertainty Model for Probabilistic Fatigue Life Predictions .....	191
<i>Prakash Chandra Gope, Sandeep Bhatt and Mohit Pant</i>	
Photoelastic Studies of Mixed Mode Stress Intensity Factors Under Biaxial Loading Condition.....	193

<i>Vinay Kumar Singh and Prakash Chandra Gope</i>	
Fracture Strains at Holes in High-Strength Steel, a Comparison of Techniques for Hole-Cutting .....	195
<i>J. Eman and K. G. Sundin</i>	
Characterization of Concrete in Mixed Mode Fracture Under Confined Conditions..	197
<i>Oscar I. Montenegro, D. Sfer and I. Carol</i>	
V-Notched Specimen Under Mixed-Mode Fracture .....	199
<i>N. Recho, J. Li and D. Leguillon</i>	
Genetic Programming in Modelling of Fatigue Life of Composite Materials.....	201
<i>Anastasios P. Vassilopoulos, Efstratios F. Georgopoulos, Thomas Keller</i>	
Fatigue Behaviour of Adhesively Bonded Pultruded GFRP .....	203
<i>Ye Zhang, Anastasios P. Vassilopoulos and Thomas Keller</i>	
Upper Tail of Material Strength Distribution and Strength Prediction of Bonded Joints Composed of Pultruded Adherends .....	205
<i>Till Vallée, Thomas Keller and Gilles Fourestey</i>	
Crack Propagation in Naval Aluminum Panels .....	207
<i>Konstantinos P. Galanis and Vassilios J. Papazoglou</i>	
Cracked Brazilian Tests of Lamellar Tial .....	209
<i>Gunes Uzer, Fu-Pen Chiang and Andrew H. Rosenberger</i>	
Influence of Concrete's Mineralogical Components on Fracture Compressive and Tractive .....	211
<i>M.P. Morales Alfaro and F.A.I. Darwish</i>	
Opening and Mixed Mode Fatigue Crack Growth Simulation Under Random Loading .....	213
<i>P. C. Gope, S. P. Sharma and B. Kumar</i>	
Numerical Study of Fatigue Behavior of Spot Welded Joints .....	215
<i>M. Zehsaz and S. Hasanifard</i>	
The Identification of a Hidden Long-Term Plastic Damage Stage During Splitting Tensile Loading of Concrete .....	217
<i>Zacharias G. Pandermarakis and Anastasia B. Sotiropoulou</i>	
The Relationship Between Creep Rupture Life and Microstructure of Aged P92 Weldment .....	219
<i>B. J. Kim and B. S. Lim</i>	
Numerical Simulation of Combined Effects of Heat Treatment and Crack Length on Tensile Panels Integrity .....	221
<i>M. Kiric and A. Sedmak</i>	
Characterization of the Fracture Behaviour of Elastomers Under Complex Loading Conditions .....	223
<i>Z. Major, K. Lederer and R.W. Lang</i>	
Experimental and Numerical Determination of the Local S-N Curve of Shot-Peened Steel Gears .....	225
<i>G. Olmi, M. Comandini and A. Freddi</i>	
Effect of Hydrogen Environment on Non-Propagation and Propagation of Fatigue Crack in a Type 304 Austenitic Stainless Steel .....	227
<i>H. Matsunoa, Y. Aoki, Y. Odab and H. Noguchic</i>	
Fatigue Behaviour of Scratch Damaged Shot Peened Specimens at Elevated Temperature .....	229

<i>R.A. Cláudio, C.M. Branco and J. Byrne</i> Instable Crack Propagation at High Temperature .....	231
<i>Nicolas Tardif, Michel Coret and Alain Combescure</i> Driving Forces Formulations During Crack Damage Interactions in a Brittle Material .....	233
<i>M. Chabaat, M. Touati and S. Djouder</i> Cohesive Laws of Ductile Adhesives: an Experimental Study .....	235
<i>A. Nokkentved, P. Brondsted and O.T. Thomsen</i> A Study on Stress Intensity Factor of Outer Surface Crack along the Direction of the Axis of Double Column Composed Dissimilar Material under Torsion Load .....	237
<i>Syuutei Sasaki and Tsutomu Ezumi</i> Fatigue Fracture Mechanism in Ultralong of Cemented Carbide WC-Co.....	239
<i>Manabu Yasuoka</i> Experimental Investigation into the Fatigue of Welded Stiffened 350WT Steel Plates Using Neutron Diffraction Method.....	241
<i>B.K.C. Yuen, F. Taheri and M. Gharghour</i> Importance of Standardization for Fatigue Testing and Fatigue Data Analysis in Very High Cycle Regime .....	243
<i>Tatsuo Sakai</i> Fatigue Strength of 7050 T7451 Aluminum Alloy: Coating Effects.....	245
<i>Herman Jacobus Cornelis Voorwald, José André Marin de Camargo and Maria Odila Hilário Cioffi</i> Fatigue on NC2/RTM6 Composites.....	247
<i>Maria Odila Hilário Cioffi, Herman Jacobus Cornelis Voorwald, Mirabel Cerqueira Rezende and Luigi Ambrosio</i> Evaluation on the Fatigue Strength of Ti-6Al-4V with WC 10Co-4Cr Deposited by HVOF .....	249
<i>Midori Yoshikawa Pitanga Costa, Maria Odila Hilário Cioffi and Herman Jacobus Cornelis Voorwald</i> Mechanics Behavior of Sisal Fabric .....	251
<i>Andressa Cecilia Milanese, Maria Odila Hilário Cioffi and Herman Jacobus Cornelis Voorwald</i> Test Conditions Effect on the Fracture Toughness of Hollow Glass Micro-Spheres Filled Composites .....	253
<i>C. Capela, J.D. Costa and J.A.M. Ferreira</i> Crack Growth Behavior in the Interface of Repair Welded 1Cr-0.5Mo Steel .....	255
<i>Un Bong Baek, Kee Bong Yoon, Hea Moo Lee</i> Modeling of Fatigue in a Low-Carbon Roller-Quenched Tempered Steel .....	257
<i>D. Angelova and R. Yordanova</i> Effect of Corrosion Environment Activity on Fatigue in a Low-Carbon Steel .....	259
<i>A. Davidkov and D. Angelova</i> Monitoring of the Construction Materials' Alarm States are Caused by Both Fatigue and Embrittlement by Liquid Metals .....	261
<i>S.Kh. Shamirzaev, E.D. Mukhamediev and G. Yu. Shamirzaeva</i> Evaluation of Residual Stresses During Fatigue Test in a FSW Joint .....	263
<i>S. Pasta and A.P. Reynolds</i> Calibration for Machine Deformation for High Temperature Fracture Testing.....	265
<i>S.K. Ray and G. Sasikala</i>	

Mixed Mode Fracture Toughness of an Adhesive Bonded Joint .....	267
<i>M. Alfano, F. Furgiuele, C. Maletta</i>	
The Relationship Between Creep Rupture Life and Microstructure of Aged P92 Steel.....	269
<i>B.J. Kim and B.S. Lim</i>	
Study the Caustics, Isochromatic and Isopachic Fringes at a Bi-Material Interface Crack-Tip .....	271
<i>G.A. Papadopoulos</i>	
<b>2T11. Hybrid Techniques .....</b>	<b>273</b>
Methods for Measuring Biaxial Deformation on Rubber and Polypropylene Specimens .....	273
<i>Ch. Feichter, Z. Major and R.W. Lang</i>	
Hybrid Testing of Historic Materials .....	275
<i>M. Drdácký, O. Jiroušek, Z. Slížková, J. Valach and D. Vavřík</i>	
Determination of Parameters of Local Approach to Ductile Fracture of Steel Using Combined Experimental-Numerical Procedure .....	277
<i>M. Rakin, M. Zrilic, N. Gubeljak, Z. Cvijovic, A. Sedmak</i>	
Computer Simulation and Experiments to Evaluate Digital Image Correlation Methods.....	279
<i>Sven Bossuyt, Sam Coppieters, David Lecompte, Hugo Sol and John Vantomme</i>	
<b>2T12. Impact Mechanics.....</b>	<b>281</b>
Analysis of Inertia Effect on a Three Point Bend Specimen Loaded by the Hopkinson Pressure Bar.....	281
<i>Xiaoxin Zhang, Gonzalo Ruiz and Rena C. Yu</i>	
Size and Strain Rate Effects on the Fracture of Reinforced Concrete .....	283
<i>Gonzalo Ruiz, Xiaoxin Zhang and Rena C. Yu</i>	
Modelling and Experimental Investigation of a Composite Cushion Under Impact Loading .....	285
<i>Michael A. Sek, Vincent Rouillard and Manuel Garcia-Romeu</i>	
Concurrent Bending and Localized Impact on Sandwich Panels .....	287
<i>Jorgen A. Kepler and Peter H. Bull</i>	
Discussions on Standardization of Hopkinson Bars Technique.....	289
<i>L.M. Yang, Li Song and Li-Li Wang</i>	
Identification of Strain-Rate Sensitivity Parameters of Steels with an Inverse Method .....	291
<i>Lorenzo Peroni, Marco Peroni and Giovanni Belingardi</i>	
Experimental Parameter Identification for Material Models Including Deformation Induced Volume Dilatation for Thermoplastic Materials.....	293
<i>F. Huberth</i>	
Experimental Analysis of the Shock Enhancement of a Cellular Structure Under Impact Loading .....	295
<i>S. Patoffatto, I. Elnasri, H. Zhao and Y. Girard</i>	
Compression Testing by Means of Charpy Pendulum.....	297
<i>V. Mentl and J. Dzugan</i>	

Detection and Quantification of Impact Loads in Fibre Reinforced Polymers.....	299
<i>Ch. R. Koenig, D.H.Mueller, O. Focke and M. Calomfirescu</i>	
Visualization of Mercury Cavitation Bubble Collapse .....	301
<i>Mstoshi Futakawa, Takashi Naoe and Nobuatsu Tanaka</i>	
<b>2T13. Inverse Problems .....</b>	<b>303</b>
Three-Dimensional Strain Field Identification Using Speckle-Less Images of X-Ray CT.....	303
<i>Shoji Kuzukami, Osamu Kuwazuru and Nobuhiro Yoshikawa</i>	
Full-Field Stress Measurement from Strain and Load Data.....	305
<i>Giovanni B. Broggiato and Luca Cortese</i>	
Identification of Orthotropic Material Behaviour Using the Error in Constitutive Equation .....	307
<i>T. Merzouki, H. Chalal and F. Meraghni</i>	
Adjustment of the Boundary Conditions in a Finite Element Model of a Plate Suspended with Springs by an Inverse Method.....	309
<i>E. Euler</i>	
Permeability Identification of a Stereolithography Specimen Using an Inverse Method .....	311
<i>Gerd Morren, Hugo Sol, Bart Verleye and Stepan Lomov</i>	
<b>2T17. Numerical Solutions .....</b>	<b>313</b>
Measuring Soft Tissue Properties Using Digital Image Correlation and Finite Element Modelling.....	313
<i>S.L. Evans, C.A. Holt, H. Ozturk, K. Saidi and N.G. Shrive</i>	
Strain Characteristics of Materials Fracture Under Low-Cycle Plastic Deformation..	315
<i>A. Khromov, D. Fedorchenko, E. Kocherov and A. Bukhanko</i>	
Formability Analysis of Magnesium Alloy at Elevated Temperature with Experimental and Numerical Method.....	317
<i>Lin Wang, L.C. Chan and T.C. Lee</i>	
FEM Analysis of the Creep Behaviour of Steel Pipes under Thermal Gradients.....	319
<i>F. Vakili-Tahami, F. Talati, A.H. Sorkhabi and O. Arashnia</i>	
<b>2T18. Optical Methods .....</b>	<b>321</b>
Development of the Advanced Moiré Methods with High Resolution Microscopy at FML.....	321
<i>Huimin Xie, Satoshi Kishimoto, Yanjie Li, Bing Pan, Zhanwei Liu, Haixia Shang and Fulong Dai</i>	
In-Situ Non-Destructive Evaluation of Concrete Structures Using Shearography .....	323
<i>Y.Y. Hung, L. Liu, Y.H. Huang and Edward C.Y. Yiu</i>	
Measurement of Thermal Stress in COB Packaging Structures .....	325
<i>Xiao-Yuan He and Fanxiu Chen</i>	
Surface Roughness Measurement of a Semi-Conductor Wafer Using Laser Scattering Technique.....	327
<i>C.J. Tay, S.H. Wang and C. Quan</i>	
A 20 KiloHertz Optical Strain Gage .....	329
<i>W. N. Sharpe, Jr</i>	

An Application of Microscopic Digital Image Correlation to Dental Materials .....	331
<i>Dongsheng Zhang, Miao Luo, Dwayne Arola and Ahmad Nazari</i>	
Active Interferometric System for MEMS/MOEMS Measurement .....	333
<i>Jacek Kacperski and Malgorzata Kujawinska</i>	
Applicability of Time Average Stochastic Moire for Cryptographic Applications .....	335
<i>Minvydas Ragulskis</i>	
Tomographic Reconstruction of 3D Ultrasound Fields Measured Using Laser Vibrometry .....	337
<i>Kourosh Tatar, Erik Olsson and Fredrik Forsberg</i>	
Experimental Detection of one Dimensional Grout Spread Using Image Processing Active Contour Model .....	339
<i>A. Ait Alaiwa, N. Saiyouri and P.-Y. Hicher</i>	
Digital Holographic Method Used to Detect an Object's Deformation.....	341
<i>Wen-Wen Liu, Xiao-Yuan He and Xin Kang</i>	
Application of Wavelet Transform in the Image Analysis of Soil Microstructure .....	343
<i>Wang Wei, Sun Qiu, Hu Xin, Hong Baoning and He Xiaoyuan</i>	
Image and Complex Correlation Near Discontinuities .....	345
<i>Mikael Sjudahl</i>	
Estimation of Digital Image Correlation (DIC) Performances .....	347
<i>Laurent Robert</i>	
Visible, Infrared and Incoherent Light Transport Optical Techniques for In-Situ Material Testing .....	349
<i>N. Renault, S. Andre, C. Baravian and C. Cunat</i>	
Evaluation of Shrinkage Stresses and Elastic Properties in a Thin Coating on a Strip-Like Substrate.....	351
<i>D.A. Chelubeev, R.V. Goldstein, V.M. Kozintsev, A.V. Podlesnyh and A.L. Popov</i>	
Full-Field Strain Rate Measurement by White-Light Speckle Image Correlation .....	353
<i>Giovanni B. Broggiato, Leobaldo Casarotto and Zaccaria Del Prete</i>	
Radiographic Observation of Strain Field and Consequent Damage Zone Evolution.	355
<i>D. Vavrik, T. Holy, J. Jakubek, M. Jakubek and J. Valach</i>	
Strain Measurement in the Adhesive Layer of a Bonded Joint Using High Magnification Moire Interferometry.....	357
<i>P.D. Ruiz, F. Jumbo, J.M. Huntley, I.A. Ashcroft and G.M. Swallowe</i>	
Wooden Surface Investigation: an Optical Approach Based on Shadow Moiré .....	359
<i>L. D'Acquisto, A. La Pica, A.M. Siddiolo</i>	
Shearographic Detection of Delaminations in Sandwich Structures: Investigation on Various Excitation Modes .....	361
<i>G. Kalogiannakis, B. Sarens, D. Van Hemelrijck and C. Glorieux</i>	
Observation of Fundamental Variables of Optical techniques in the Nanometric Range .....	363
<i>Cesar A. Sciammarella and Luciano Lamberti</i>	
Processing of a Hrtm Image Pattern to Analyze an Edge Dislocation.....	365
<i>Federico M. Sciammarella, Cesar A. Sciammarella and Luciano Lamberti</i>	
AN Approach to Errors Introduced in the Mesh-Free Full-Field Strain Measurement Method .....	367
<i>A.P. Iliopoulos and N.P. Andrianopoulos</i>	

New Improvements in Shearography Techniques .....	369
<i>Hernani M. Lopes, Mario A. Vaz, Rui M. Guedes and J.F. Silva Gomes</i>	
<b>2T19. Research in Progress .....</b>	<b>371</b>
Dynamic Deformation Evaluation by Electro Motive Force .....	371
<i>Tetsuo Kumazawa and Noboru Nakayama</i>	
Modern Situation in Photoacoustic and Thermoelastic Stress Analysis in Application to the Problem of Mechanical Stress Measurements .....	373
<i>K.L. Muratkov and A.L. Glazov</i>	
Derivation of Uniaxial Stress-Strain Curves for Cast Iron from Samples Tested in Flexure .....	375
<i>D.A. Jesson, H. Mohebbi, H.M.S. Belmonte, M.J. Mulheron and P.A. Smith</i>	
<b>2T20. Smart Materials and Structures .....</b>	<b>377</b>
Electromechanical Response of Large Strain Ferroelectric Actuators .....	377
<i>Doron Shilo, Amir Mendelovich and Haika Drezner</i>	
Testing System For Ferromagnetic Shape Memory Micro-Actuators .....	379
<i>Y. Ganor, D. Shilo, J. Messier, T.W. Shield and R.D. James</i>	
Buckling Control of Glass/Epoxy Composite Columns with PZT Actuators .....	381
<i>R. Mini, C. Lakshmana Rao and S.M. Sivakumar</i>	
Enhancement of Buckling Load of Thin Plates Using Piezoelectric Actuators .....	383
<i>R. Indira Priyadarshini, C. Lakshmana Rao and S.M. Siva Kumar</i>	
Investigation of Twin-Wall Structure at the Nanometer Scale Using Atomic Force Microscopy.....	385
<i>Doron Shilo, Guruswami Ravichandran and Kaushik Bhattacharya</i>	
Design Construction and Testing of a Smart Actuated Helicopter Blade .....	387
<i>J. Monreal, G. Giannopoulos, F. Santafe, J. Vantomme, F. Buyschaert and P. Hendrick</i>	
Multiaxial One Way Shape Memory Effect and Superelasticity .....	389
<i>Karine Taillard, Sylvain Calloch, Shabnam Arbab Chirani and Christian LExcellent</i>	
<b>2T21. Speckle Interferometry .....</b>	<b>391</b>
Stress Distribution Measurement of Welding Part by Electronic Speckle Pattern Interferometry .....	391
<i>Hyun-Chul Jung, Ho-Sub Chang, Ki-Soo Kang, Sang-Kyu Baek and Koung-Suk Kim</i>	
Small Strain Test System for Optical Strain Measurement Systems .....	393
<i>R. Steinberger, M. Jerabek, Z. Major and R.W. Lang</i>	
Determination of the Stress Intensity Factor by Means of the ESPI Technique .....	395
<i>A. Cirello and A. Pasta</i>	
Strain Localization Analysis by a Combination of the ESPI with a Bulge Test .....	397
<i>Guillaume Montay, Bruno Guelorget, Ignacio Lira, Marie Tournex, Manuel François and Cristián Vial-Edwards</i>	
Residual Strain and Stress Analysis by Speckle Interferometry Combined with the Drill of a Groove .....	399
<i>Afaf Maras , Guillaume Montay , Olivier Sicot, Emmanuelle Rouhaud</i>	



---

*and Manuel François*

Full-Field Vibration Measurement by Time-Average Speckle Interferometry and by Doppler Vibrometry – A Comparison..... 401  
*A. Moreau, D. Borza, I. Nistea and M. Arghir*

Optical Configurations for ESPI..... 403  
*Amalia Martínez, J.A. Rayasa and R. Corderob*

Reduction of Pseudo Vibrations in Rotational Measurements, Using Sensor Arrays 405  
*M.L. Jakobsen and S.G. Hanson*

**2T24. Structural Integrity and Health Monitoring..... 407**

Characteristics of Operational Displacement and Curvature Shapes and their Effect on Curvature Based Damage Detection Algorithms ..... 407  
*Colin P. Ratcliffe and Roger M. Crane*

Biomimetic Guided Structural Health Monitoring for Civil Aircraft ..... 409  
*Eddie O'Brien*

In-Situ Health Monitoring of Objects Consisting of Visco-Elastic Materials. .... 411  
*Karl-Hans Laermann*

Experimental Safety Evaluation of Roofs..... 413  
*Marc Gutermann and Klaus Steffens*

Determinaion of Location and Size of a Through-Thickness Part-Width Crack in Cantilever Beams ..... 415  
*L. Kannappan, K. Shankar and A.G. Sreenatha*

Monitoring Life Expenditure of Power Station Engineering Plant..... 417  
*Andrew Morris1, John Dear, Miltiadis Kourmpetis, Alexander Fergusson and Amit Puri*

Condition Monitoring of Induction Motors for Vertical Pumps with the Current and Vibration Signature Analysis. .... 419  
*Young-Shin Lee and Yeon-Whan Kim*

Unbiased Experimental Reflection Method for the Ultrasonic Characterization of Materials..... 421  
*D. A. Sotiropoulos*

Fatigue Crack Detection by Acoustic Emission Monitoring in the Course of Laboratory Strength Test..... 423  
*Jiri Behal*

Residual Stress Measurement Using a Miniaturised Deep Hole Drilling Method ..... 425  
*X. Ficquet, D. J. Smith and C. E. Truman*

**2T25. Structural Testing..... 427**

Neutron Diffraction Performance Based on Multiple Reflection Monochromator for High-Resolution Neutron Radiography..... 427  
*Pavel Mikula and Miroslav Vrana*

A Modified Three Point Bend Specimen..... 429  
*Kjell Eriksson*

Experimental Studies on Wrinkling Behaviors of Gossamer Space Structures..... 431  
*Changguo Wang and Xingwen Du*

A Momentum Transfer Measurement Experiment Between Contacting Bodies in the Presence of Adhesion Under Near-Zero Gravity Conditions ..... 433

<i>M. Benedetti, D. Bortoluzzi and M. De Cecco</i>	
On Field Measurement of Forces and Deformations at the Rear Part of a Motorcycle and Structural Optimization .....	435
<i>G. Olmi, A. Freddi and D. Croccolo</i>	
Ballistic Impact Facility - Considerations and Experiences .....	437
<i>Peter H. Bull and Jørgen A. Kepler</i>	
Measurement of Moment Redistribution Effects in Reinforced Concrete Beams.....	439
<i>R.H. Scott, R.T. Whittle and A.R. Azizi</i>	
Mechanical Property Measurement of Flexible Multi-Layered Materials Using Postbuckling Behavior .....	441
<i>Atsumi Ohtsuki</i>	
Friction Coefficients Definition in Compression-Fit Couplings Applying the Doe Method .....	443
<i>Dario Croccolo, Rossano Cuppini and Nicolò Vincenzi</i>	
Residual Stresses of Welded Structures and Their Effect on the Dynamic Behaviour	445
<i>Joeran Ritzke, Peter Nikolay, Andreas Hanke and Guenther Schlottmann</i>	
An Experimental Technique to Evaluate the Strength of Adhesive Bonds in Multiaxial Loading .....	447
<i>Lorenzo Peroni and Massimiliano Avalle</i>	
Study of the Substitution of Limestone Filler with Pozzolanic Additives in Mortars.	449
<i>M. Katsioti, D. Gkanis, P. Pipilikaki, A. Sakellariou, A. Papathanasiou, Ch. Teas and E. Haniotakis</i>	
A Testing Technique of Confined Compression for Concrete at High Rates of Strain	451
<i>P. Forquin, F. Gatuingt and G. Gary</i>	
A Wavelet-Based System for Structural Health Monitoring of Aeronautic Structures	453
<i>I. Dimino and V. Quaranta</i>	
<b>2T26. Thermal Problems .....</b>	<b>455</b>
Homogeneous Administration of Experiments in Material Science for Configuration, Monitoring and Analysis .....	455
<i>Ferdinand Ferber, Thorsten Hampel, Franz-Barthold Gockel, Thorsten Pawlak and Rolf Mahnken</i>	
Material Simulation and Damage Analysis at Thermal Shock Conditions .....	457
<i>Franz-Barthold Gockel and Rolf Mahnken</i>	
Grids Reformation for Effective Strain Measurement of Forming Titanium Tailor- Welded Blanks at Elevated Temperatures.....	459
<i>C. P. Lai, L.C. Chan and C.L. Chow</i>	
Experimental Study of Optimal Process Parameters for Deformation Welding of Dissimilar Metals .....	461
<i>T.F. Kong, L.C. Chan and T.C. Lee</i>	
Mechanical Behaviour of UDIMET 720Li Superalloy.....	463
<i>S. Chiozzi, V. Dattoma and R. Nobile</i>	
Solid Phase Change Observation Using Digital Image Correlation .....	465
<i>S. Valance, M. Coret, J. Réthoré and R. de Borst</i>	
Effects of Applied Stress on the Shape Memory Behaviour of NiTi Wires .....	467
<i>A. Falvo, F. Furgiele and C. Maletta</i>	

---

Study on Micro-Damage of Al Alloy Welded Joint in Aerospace Thermal Cycling Condition.....	469
<i>Cheng Jina, Jitai Niub and Shiyu He</i>	
<b>2T27. Time Dependent Materials .....</b>	<b>471</b>
Development of a Compression Tool for Polymeric Materials .....	471
<i>M. Jerabek, R. Steinberger and Z. Major</i>	
Application of Full-Field Strain and Temperature Measurement and Analysis for Polymer Testing .....	473
<i>Z. Major, R. Steinberger, Ch. Feichter, M.Jerabek and R.W. Lang</i>	
Assessing Lifetime of Polyolefins for Water and Gas Distribution Systems.....	475
<i>James Atteck, John Dear, Jean-Louis Costa, Aurélien Carin and Jean-Pierre Michel</i>	
<b>2T28. Transducers and Sensors .....</b>	<b>477</b>
Experimental Calibration of Computational Constants for Hole drilling Method.....	477
<i>O.Weinberg, J.Václavík, J.Jankovec, P.Jaroš and S.Holý</i>	
Methods for Sitting Posture Evaluation: Static Posture and Applications.....	479
<i>S. Scena and R. Steindler</i>	
Correct Prediction of the Vibration Behavior of the High Power Ultrasonic Transducers by FEM Simulation .....	481
<i>Abbas Pak and Amir Abdullah</i>	
The Influence of the Insertion Torque on the Pull-Out Force of Pedicle Screws .....	483
<i>P. Chatzistergos, E. Magnissalis and S.K. Kourkoulis</i>	

## C. SPECIAL SYMPOSIA/SESSIONS

### 2. Experimental Characterization and Multiscale Modeling of Building

<b>Materials .....</b>	<b>487</b>
Specific Fracture Energy Determination of Dam Concrete by Large-Scale Size Effect Tests.....	487
<i>Amirreze Ghaemmaghami and Mohsen Ghaemian</i>	
Autogenous and Isothermal Restrained Shrinkage of Hydrating Cement Pastes - Experimental Study.....	489
<i>Arnaud Pertue, Pierre Mounanga, Abdelhafid Khelidj and Denis Fournol</i>	
Exploring the Mechanical Design of Wood at the Micro- and Nanoscale.....	491
<i>I. Burgert</i>	
Wood Adhesive Bondlines by Nanoindentation .....	493
<i>Johannes Konnerth, Andreas Jäger, Josef Eberhardsteiner, Ulrich Müller and Wolfgang Gindl</i>	
3D Shape Measurement at Different Length Scales Using Speckle and Gap Effect...	495
<i>Fu-Pen Chiang and Gunes Uzer</i>	
Indentation Hardness and Yield Stress Correlations in Polymers.....	497
<i>Thomas Koch and Sabine Seidler</i>	
Advanced Test Methods for Experimental Characterization of Asphalt Concrete .....	499
<i>Ronald Blab, Michael Wistuba, Markus Spiegl and Karl Kappl</i>	
Autogenous Shrinkage and Creep of Early-Age Cement-Based Materials: Multiscale Modeling with Experimental Identification and Verification .....	501
<i>Christian Pichler and Roman Lackner</i>	
Finer-Scale Extraction of Viscoelastic Properties from Materials Exhibiting Elastic, Viscous, and Plastic Material Behavior .....	503
<i>Andreas Jager, Christian Pichler, Thomas Niederkofler and Roman Lackner</i>	
Ultrasonic Characterization of Porous Biomaterials Across Different Frequencies....	505
<i>Christoph Kohlhauser, Christian Hellmich, Chiara Vitale-Brovarone, Aldo Boccaccini, Dirk Godlinski and Josef Eberhardsteiner</i>	

### 3. Experimental Analysis of Mechanical Properties in Advanced Materials .....

Examination of the Optimal Frequency of the Cyclic Load in the Inverse Analyses of the Heat Conduction of Infrared Thermography.....	507
<i>Kenji Machidaa, Shohei Miyagawab and Koich Hayafunec</i>	
Formation Behavior of Shape Recovery Force in TiNi Fiber Reinforced Smart Composite .....	509
<i>Keitaro Yamashita and Akira Shimamoto</i>	
Effects of Biaxial Stress Condition for Fatigue Properties of Titanium .....	511
<i>Yasumi Itoh, Akira Shimamoto, Do Yeon Hwang, Tetsuya Nemoto and Hiroyuki Matuura</i>	
An Application of Image-Processing to Stress Measurement by Copper Plating Foil (On the Effect of Frequency, Stress Ratio and Stress Waveform).....	513
<i>Masakatsu Sugiura, Ryuji Ozeki and Masaichiro Seika</i>	
Fabrication of Cu Nanowire at the Intended Position by Utilizing Stress Migration ..	515
<i>F. Yamaya, N. Settsu and M. Saka</i>	

Numerical and Experimental Study of Bending Behavior of Thin Walled Beams Filled with Metallic Foams .....	517
<i>Gustavo José Cazzola, Francisco Aparicio Izquierdo and Teresa Vicente Corral</i>	
Evaluation of Off-Axis Wood Compression Strength.....	519
<i>Nilson Tadeu Mascia, Elias Antonio Nicolas and Rodrigo Todeschini</i>	
Mechanical Characteristics of Spectacles .....	521
<i>H. Kaneko, S. Kakunai, M. Morita and J. Nishimura</i>	
Rupture of Bottleneck Seal of Liquid Packaging Bags.....	523
<i>Akira Shimamoto, Hiroyuki Aoki and Katsunori Futase</i>	
Crack Inhibition Effect of TiNi Fiber Reinforced CFRP Composite.....	525
<i>Doyeon Hwang and Akira Shimamoto</i>	
Damage Inspection and Evaluation in the Whole View Field Using Laser.....	527
<i>Akira Kato and Tin Aung Moe</i>	
Behaviors of Young's Modulus by Constriction of Reinforced Smart TiNi-Fiber Composite .....	529
<i>Teruko Aoki and Akira Shimamoto</i>	
Evaluation of Mixed-Mode Thermal Stress Intensity Factor at Various Temperatures .....	531
<i>Masahiro Suetsugu, Kouichi Sekino, Takashi Nishinohara and Koji Shimizu</i>	
Stress Analysis of an Unpressurized Elastomeric O-Ring Seal into a Groove by Photoelastic Experimental Hybrid Method.....	533
<i>J. Nam, J. Hawong, O.-S. Kwon, S. Han and G. Kwon</i>	
Evaluation in Skin by Hierarchical Separation Viscoelasticity Measurement by Rheometer .....	535
<i>Tetsuya Nemoto, Zenzo Isogai, Kazuharu Koide, Yasumi Itoh, Hroyuki Matsuura and Akira Shimamoto</i>	
<b>4. Plasticity, Fracture and Fatigue at the Micro and Nano Scales .....</b>	<b>537</b>
A New Method for Investigating the Mechanical Properties of Twin Walls.....	537
<i>Haika Drezner and Doron Shilo</i>	
Opto - Mechanical Reliability Studies of AlN Driven Cantilevers.....	539
<i>A. Andrei, K. Krupa, L. Nieradko, C. Gorecki, L. Hirsinger, P. Delobelle, J. Kacperski and M. Jozwik</i>	
Instabilities in Nanostructured Materials .....	541
<i>K.T. Ramesh, S.P. Joshi and B.E. Schuster</i>	
Use of Instrumented Microindentation to Determine the Global Mechanical Behavior of Nanocrystallised Copper Samples .....	543
<i>L. Waltz, B. Guelorget, D. Reiraint, A. Roos and J. Lu</i>	
Fatigue Characteristics of Nano-Structured Tool Steel Under Load Variation by Ultrasonic Cold Forging Treatment .....	545
<i>Chang-Min Suh, Gil-Ho Song, Min-Ho Kim and Young-Shik Pyoun</i>	
<b>5. Mission Synthesis .....</b>	<b>547</b>
Gaussian Decomposition of Non-Stationary Random Vehicle Vibrations .....	547
<i>Vincent Rouillard</i>	

On the Statistical Distribution of Segment Lengths of Road Vehicles Non-Stationary Vibrations .....	549
<i>Vincent Rouillard</i>	
The Statistical Distribution of the Root Mean Square of Road Vehicle Vibration .....	551
<i>M.A. Garcia-Romeu-Martinez and V. Rouillard</i>	
<b>6. Optical Methods for 3-D Displacement Field Measurement .....</b>	<b>553</b>
Full 3D Strain Measurement by Digital Volume Correlation from X-Ray Computed and Optical Scanning Tomographic Images.....	553
<i>A. Germaneau, P. Doumalin and J.C. Dupré</i>	
Crack Tip Growth Measurement Using Digital Image Correlation.....	555
<i>Phillip L. Reu, Brendan R. Rogillio and Gerald W. Wellman</i>	
Study on Defromation of a Micro Beam Using Interferometry.....	557
<i>W. Sun, X.-Y. He, M. Li and Y. Fu</i>	
3D Surface Elastic-Plastic Strain Mapping in Hemming, Bending, and Indentation Tests .....	559
<i>Wei Tong</i>	
Projected Fringe Pattern Analysis by the Fourier Method: Application to Vibration Studies.....	561
<i>R. Rodriguez-Vera, C. Meneses-Fabian, J.A. Rayas, and F. Mendoza-Santoyo</i>	
<b>7. Fracture and Fatigue of Piezoelectric Ceramics .....</b>	<b>563</b>
Antiplane Problem of Crack Arrest for a Cracked Piezoelectric Plate .....	563
<i>R.R. Bhargava and Namita Saxena</i>	
Electric-Field Induced Fatigue Crack Growth in Ferroelectric Single Crystals .....	565
<i>F. Fang, W. Yang, F.C. Zhang and R.H. Wen</i>	
Integrity of Piezo-Composite Beams Under High Cyclic Electro-Mechanical Loads – Experimental Results.....	567
<i>Lucy Ederly-Azulay and Haim Abramovich</i>	
M-Integral for Piezoelectric Ceramics Using the Exact Boundary Conditions on Crack Surfaces .....	569
<i>Yael Motola and Leslie Banks-Sills</i>	
Failure PZT Thin Films in MEMS.....	571
<i>D.F. Bahr, D.J. Morris, M.C. Robinson, A.L. Olson, C.D. Richards and R.F. Richards</i>	
Charge-Free Zone Model for Failure of Conductive Cracks in Piezoelectric Ceramics under Electrical and/or Mechanical Loading .....	573
<i>Tong-Yi Zhang</i>	
Fracture Mechanics for Electroactive Materials .....	575
<i>Robert M. McMeeking</i>	
Fracture in Piezoelectric Ceramics and PZT/Electrode Interfaces .....	577
<i>H. Jelitto, F. Felten, G.A. Schneider, C. Häusler and H. Balke</i>	
<b>8. Digital Holography.....</b>	<b>579</b>
Vibration Phase Based Ordering of Vibration Patterns Acquired with a Shearing Speckle Interferometer and Pulsed Illumination.....	579
<i>Peter A.A.M. Somers and Nandini Bhattacharya</i>	

Recent Developments of Speckle Pattern Interferometer for Bone Strain Measurement.....	581
<i>L.X. Yang and H. Yokota</i>	
Investigation of the Thermal Deformation of Electronic Packages with Electronic Speckle Pattern Interferometry .....	583
<i>Hans Reinhard Schubach</i>	
One-Shot Digital Holography Using Polarization Imaging with a Pixelated Micro-Retarder Array.....	585
<i>S. Yoneyama, N. Mizuhara, K. Tabata, T. Nomura and H. Kikuta</i>	
Explosive Embossing of Holographic Structures: Computational Simulation of Procedural Influences to the Reconstructed Hologram.....	587
<i>T. Scholz, A. Kraft, E. Reithmeier and G. Helferich</i>	
Contouring of Diffused Objects by Using Digital Holography .....	589
<i>Chandra Shakher, Dalip Singh Mehta, Md. Mossaraf Hossain and Gyanendra Sheoran</i>	
Nonlinear Bulk Elastic Waves in Layered Solid Waveguides .....	591
<i>I.V. Semenova, G.V. Dreiden and A.M. Samsonov</i>	
Effects of Window Size on Accuracy and Spatial Resolution in Windowed Phase-Shifting Digital Holographic Interferometry .....	593
<i>Yoshiharu Morimoto, Toru Matui, Motoharu Fujigaki and Norikazu Kawagishi</i>	
Identification of Specimen Position and Orientation Using Standard Deviation of Intensity in Phase-Shifting Digital Holography.....	595
<i>Motoharu Fujigaki, Youhei Ashimura, Toru Matui and Yoshiharu Morimoto</i>	
Reflection Hologram Interferometry as Unique Tool in the Course of Residual Stresses Determination.....	597
<i>V.S. Pisarev and V.V. Balalov</i>	
Compensation Speckle Pattern Interferometry in Material Testing Techniques.....	599
<i>I.N. Odintsev and V.S. Pisarev</i>	
Fast Transforms for Digital Holography.....	601
<i>L. Yaroslavsky</i>	
Null Test in Speckle Light by Comparative Digital Holography.....	603
<i>Wolfgang Osten, Giancarlo Pedrini, Xavier Schwab and Thorsten Baumbach</i>	
3D Pulsed Digital Holography for the Simultaneous Acquisition of Vibration Displacements .....	605
<i>Fernando Mendoza Santoyo , Carlos Perez Lopez , Tonatiuh Saucedo and Ramon Rodriguez Vera</i>	
Digital Holographic Interferometers Cameras for Remote Monitoring and Measurements of Mechanical Parts .....	607
<i>Aneta Michalkiewicz and Malgorzata Kujawska</i>	
3-D Micro-Structure Measurement Method Based on Shadow Moiré using Scanning.....	609
<i>Yasuhiko Arai and Shunsuke Yokozeki</i>	
Measurement of Surface Shape and Positions by Phase-Shifting Digital Holography	611
<i>I. Yamaguchi, T. Ida and M. Yokota</i>	
Terahertz Digital Holography .....	613
<i>Yan Zhang and Weihui Zhou</i>	

The Three-Dimensional Displacement Measurement of Sandwich Circular Plates with a Single Fully-Potted Insert Using Electronic Speckle Pattern Interferometry ...	615
<i>Song-Jeng Huang and Hung-Jen Yeh</i>	
<b>9. Mechanics of MEMS.....</b>	<b>617</b>
Mechanical Characteristics Determination of Materials and Covers by Means of Micro- and Nano- STM-Hardness Meter with Semi-Conductor Diamond Pyramids .	617
<i>V.A. Andruschenko, A.A. Bondarenko, V.N. Nikitenko and V.V.Meleshko</i>	
A New Instrument for Tensile Testings of Thin Free Standing Films at High Strain Rates.....	619
<i>Eran Ben-David, David Elata, Daniel Rittel, and Doron Shilo</i>	
Nanocharacterization of Gold/ Gold Contact Surface Failure in MEMS contact switches.....	621
<i>M. Al-Haik, H. Sumali, S. Trinkle and J.M. Redmond</i>	
Measuring Natural Frequency and Non-Linear Damping on Oscillating Micro Plates.....	623
<i>Hartono Sumali</i>	
Biologically Inspired Mechanics of Wavy Surface Adhesion .....	625
<i>Pradeep R. Guduru</i>	
Embedded Sensors in Rubber and Other Polymer Components.....	627
<i>Keith Harmeyer, Michael A. Holland and Gary Krutz</i>	
<b>10. Measurement of Residual Stress and Strain in Composite Processing and Service Life.....</b>	<b>629</b>
Evaluation of Finite Element Based Correction of Layer Removal During XRD measurements for Geometries and Stress Distributions of Interest in Aircraft Engines.....	629
<i>Yogesh K. Potdar, Karthick Chandraseker, Robert McClain, Mike Hartle, Paul Domas and Rohinton Irani</i>	
Stress Analysis of Laser Marked Low Carbon Steel .....	631
<i>Z. Kalincsak, L. Balogh, L. Borbas and J. Takacs</i>	
Investigation of Residual Stresses Development in a Single Fibre Composite with FBG Sensor.....	633
<i>F. Colpo, D. Karalekas and J. Botsis</i>	
Validation Specimen for Contour Method Extension to Multiple Residual Stress Components .....	635
<i>P. Pagliaroa, M.B. Primeb, B. Zuccarelloa, B. Clausenb and T.R. Watkinse</i>	
Development and Uncertainty Analysis of a Sonic Controlled Drilling Unit on Residual Stresses Measurement by the Hole Drilling Method .....	637
<i>A. Albertazzi Jr, M.R. Viotti and W.A. Kapp</i>	
Strain and Temperature Discrimination and Measurement Using Superimposed Fiber Bragg Grating Sensor .....	639
<i>M. Demirel, L. Robert, J. Molimard, A. Vautrin and J.-J. Orteu</i>	
Monitoring of LRI Process by Optical Fibre Bragg Gratings.....	641
<i>S. Vacher, J. Molimard, A. Vautrin, H. Gagnaire and P. Henrat</i>	
Extention of the Grid Method to Large Displacements .....	643
<i>J. Molimard, K. Zhani, C. Desrayaud and M. Darrieulat</i>	



<b>12. Time-Dependent Behavior .....</b>	<b>645</b>
Time-Dependent Behavior of Ropes Under Impact Loading .....	645
<i>A. Nikonov, M. Udov, B. Zupani, U. Florjani, B.S. von Bernstorff and I. Emri</i>	
Material Properties of Mixtures .....	647
<i>Samo Kralj</i>	
Colloidal Emulsions .....	649
<i>Gennady Maksimochkin, Sergey Pasechnik, Mitja Slavinec, Milan Svetec and Samo Kralj</i>	
 <b>14. Photoelasticity and its Applications.....</b>	 <b>651</b>
An Automated Phase Unwrapping Algorithm for Isoclinic Parameter in Phase-Shifting Photoelasticity .....	651
<i>Pichet Pinit and Eisaku Umezaki</i>	
Phase Unwrapping for Absolute Fringe Order in Photoelasticity.....	653
<i>Pichet Pinit, Yudai Nomura and Eisaku Umezaki</i>	
A New Automated Measuring Instrument for Minute Photoelasticity .....	655
<i>Kenji Gomi, Kensuke Ichinose and Yasushi Niitsu</i>	
Effect of UV Illumination Wavelengths on Stress and Temperature in Curing Process of UV Curing Resin .....	657
<i>Eisaku Umezaki and Masahito Abe</i>	
Measurement of Stress and Temperature in Curing Process of Epoxy Adhesives .....	659
<i>Eisaku Umezaki and Kazuya Iwanaga</i>	
 <b>15. Identification of Mechanical Constitutive Equations .....</b>	 <b>661</b>
Identification of Strain-Rate Sensitivity with the Virtual Fields Method .....	661
<i>Stéphane Avril, Fabrice Pierron, Junhui Yan and Michael A. Sutton</i>	
Identification of 3-D Heterogeneous Modulus Distribution with the Virtual Fields Method .....	663
<i>Stéphane Avila, Jonathan M. Huntleyb, Fabrice Pierrona and Derek D. Steeleb</i>	
Identification from Multi-Physics Full-Field Measurements at the Micrometer Scale: the Electro-Elastic Coupling .....	665
<i>F. Amiot, F. Hild, F. Kanoufi and J.P. Roger</i>	
Determination of the Elongational Properties of Polymers using a Mixed Numerical-Experimental Method .....	667
<i>L. Robert, S. Hmida-Maamar, V. Velay and F. Schmidt</i>	
Thermomechanical Behaviour Prediction of Glass Wool by using Full-Field Measurements .....	669
<i>Jean-Francois Witz, Stéphane Roux and François Hild</i>	
Modeling of Adsorption-Induced Mechanical Loading on Microcantilevers using Full-Field Measurements .....	671
<i>Nicolas Garraud, Fabien Amiot, François Hild, Jean Paul Roger</i>	
On the Image Correlation Measurement of Displacement Fields with Strong Strain Gradients or Discontinuities .....	673
<i>Wei Tong and Hang Yao</i>	
Identification of the Local Stiffness Reduction of Damaged Composite Plates Using Full-Field Measurements.....	675

<i>J.-H. Kim, F. Pierron and M. Wisnom</i>	
An Attempt to Identify Hill's Yield Criterion Parameters using Strain Field Measured by DIC Technique .....	677
<i>H. Haddadi and S. Belhabib</i>	
<b>16. Impact Behaviour of Composite Materials and Structures .....</b>	<b>679</b>
Effect of Aluminum Foam and Foam Density on the Energy Absorption Capacity of 3D "S" Space Frames .....	679
<i>Roselita Fragoudakis and Anil Saigal</i>	
High Strain-Rate Compressive Characteristics of a Unidirectional Carbon/Epoxy Laminated Composite: Effect of Loading Directions .....	681
<i>T. Yokoyama, K. Nakai and T. Odamura</i>	
Determination of Vertical Characteristics of Rail Vehicle Suspensions by Drop Test on the Track .....	683
<i>J. Chvojan, R. Mayer, P. Polach and J. Vaclavik</i>	
Dynamic Effects on Mechanical Characteristics of Composite Plates Submitted to Impact Tests .....	685
<i>G. Belingardi, M.P. Cavatorta and D.S. Paolino</i>	
A Method to Measure Crack Opening Displacement of Fast Propagating Crack in Araldite B .....	687
<i>Shinichi Suzuki and Kazuya Iwanaga</i>	
<b>17. Fiber Reinforced Polymer Applications .....</b>	<b>689</b>
Experimental Investigation of the Static Behaviour of a Hole Drilled Steel Plate Reinforced with a Composite Patch .....	689
<i>Nicholas G. Tsouvalis and Lazaros S. Mirisiotis</i>	
Italian Design Guidelines for the Structural Strengthening with FRP Materials .....	691
<i>Luigi Ascione and Luciano Feo</i>	
Laboratory Tests and Mechanical Models for the Validation of FRP Reinforcement of Masonry Structures .....	693
<i>Alessandro Baratta, Ileana Corbi and Ottavia Corbi</i>	
Adhesion Problems between FRP Reinforcement and Masonry Support in Existing Building Strengthening .....	695
<i>Silvia Briccoli Bati, Luisa Rovero and Ugo Tonietti</i>	
Quality Control and Monitoring of FRP Applications to Masonry Structures .....	697
<i>Renato S. Olivito and Francesca A. Zuccarello</i>	
Experimental Investigation on Debonding between Masonry and FRP .....	699
<i>Christian Carloni, Kolluru V. Subramaniam and Lucio Nobile</i>	
FRP Width Effect on Shear Debonding from Concrete .....	701
<i>Kolluru V. Subramaniam, Christian Carloni and Lucio Nobile</i>	
Advanced Composites for Retrofit of Historical Masonry Structures: Dynamic Tests and Comparative Assessment .....	703
<i>Gaetano Manfredi and Andrea Prota</i>	
<b>18. Advances in Speckle Interferometry .....</b>	<b>705</b>
Applications of the Empirical Mode Decomposition Method in Speckle Metrology .....	705
<i>Maria B. Bernini, Gustavo E. Galizzi, Alejandro Federico</i>	

<i>and Guillermo H. Kaufmann</i>	
Flaw Detection Enhancement in Lockin Temporal Speckle Interferometry using Thermal Waves.....	707
<i>A.E. Dolinko and G.H. Kaufmann</i>	
The Spatial Structures of Pseudophase Singularities in the Analytic Signal Representation of a Speckle Pattern and their Application to Biological Kinematic Analysis.....	709
<i>Wei Wang, Yu Qiao, Reika Ishijima, Tomoaki Yokozeki, Daigo Honda, Akihiro Matsuda, Steen G. Hanson and Mitsuo Takeda</i>	
A New Family of Speckle Interferometers .....	711
<i>Luigi Bruno, Andrea Poggialini and Orlando Russo</i>	
Analysis of DSPI Fringe Patterns Issued from Transitory Mechanical Loadings .....	713
<i>V. Valle, E. Robin and F. Brémand</i>	
Multifunctional Encoding System for Assessment of Movable Cultural Heritage .....	715
<i>V. Tornari, E. Bernikola, W. Osten, R.M. Grooves, G. Marc, G.M. Hustinx, E Kouloumpi and S. Hackney</i>	
Identification of Some Acoustic Noise Sources in Cars by Speckle Interferometry ...	717
<i>Dan Borza</i>	
Phase Extraction in Dynamic Speckle Interferometry by Empirical Mode Decomposition .....	719
<i>Antonio Baldia, Sébastien Equisb and Pierre Jacquotb</i>	
Analytic Processing of Experimental Data by a B-Spline Fitting .....	721
<i>Luigi Bruno</i>	
ESPI-Measurement of Strain Components on a CFRP-Reinforced Bending Beam....	723
<i>Erwin Hack and Ann Schumacher</i>	
<b>19. Mechanical and Thermomechanical Properties of Smart Materials and Structures .....</b>	<b>725</b>
Martensite and Reverse Transformation During Two-Direction Simple Shear of NITI SMA.....	725
<i>S.P. Gadaj, W.K. Nowacki, E.A. Pieczynska and J. Luckner</i>	
Transformation Induced Effects in TiNi Shape Memory Alloy Subjected to Tension	727
<i>E.A. Pieczynska, S.P. Gadaj, W.K. Nowacki and H. Tobushi</i>	
From Thermomechanical Heat Source Reconstruction to the Validation of Mechanical Behavior's Laws.....	729
<i>N. Renault, S. Andre and C. Cunat</i>	
The Influence of Temperature and Pre-Aging on the Low Cycle Fatigue Behaviour of Nickel Coatings (Ni 200/201).....	731
<i>Hubert Koberl, Heinz Leitner and Wilfried Eichlseder</i>	
Geometric Scale Effect in Dynamic Tension Tests, a Numerical Analysis .....	733
<i>R. Cheriguene, A. Rusinek, R. Zaera and J.R. Klepaczko</i>	
Effect of a Quasi-Static Prestrain on Subsequent Dynamic Tensile Curves.....	735
<i>L. Durrenberger, A. Rusinek, A. Molinari and D. Cornette</i>	
Self-Healing of a Single Fiber-Reinforced Polymer Matrix Composite.....	737
<i>Eyassu Woldeesenbet and Rochelle Williams</i>	
Monitoring and Analysis of Damage Development in Pipelines due to Exploitation Loadings.....	739

*Zbigniew L. Kowalewski, Tadeusz Skibiski, Jacek Szelazek  
and Sawomir Mackiewicz*

<b>22. Sandwich Structures and Core Materials.....</b>	<b>741</b>
Experimental Investigation of Stress Concentrations Caused by Inserts in Sandwich Panels .....	741
<i>Nicholas G. Tsouvalis and Maria J. Kollarini</i>	
On the Progressive Collapse of Micro Lattice Structures .....	743
<i>R.A.W. Mines, S. McKown, W. Cantwell, W. Brooks and C.J. Sutcliffe</i>	
Quasi-Static Testing of New Peel Stopper Design for Sandwich Structures .....	745
<i>J. Jakobsen, E. Bozhevolnaya and O.T. Thomsen</i>	
Optimization of Surface Damping Treatments for Vibration Control of Marine Structure .....	747
<i>Ramji Koona, Ganesh Kumar. PVS and S. Ranganath</i>	
Measuring Mixed Mode Cohesive Laws for Interfaces in Sandwich Structures.....	749
<i>Christian Lundsgaard-Larsen, Christian Berggreen and Bent F. Sørensen</i>	
Testing of Sandwich Core Materials and Sandwich Panels Subjected to Slamming Loads.....	751
<i>Carl-Johan Lindholm</i>	
Assessment of Hygrothermal Ageing and Damage in Sandwich Foam using TSA....	753
<i>E. Lembessis, J.M. Dulieu-Barton, R.A. Shenoi</i>	
Aluminum/Foam Sandwich Beams in Three-Point Bending.....	755
<i>E.E. Gdoutos and D.A. Zacharopoulos</i>	
Researching the Processes Leading to the Failure of Composite Sandwich Structures .....	757
<i>Alexander Fergusson, Amit Puri, John Dear and Andrew Morris</i>	
Impact Energy Absorption in Novel, Lightweight Sandwich Panels with Metallic Fibre Cores.....	759
<i>J. Dean, P.M. Brown and T.W. Clyne</i>	
Dynamic Modulus of Syntactic Foam Core - A Non Destructive Approach .....	761
<i>Eyassu Woldesenbet and Phani Mylavarapu</i>	
Thermal and Mechanical Response of Sandwich Panels in Fire .....	763
<i>P.A. Cutter, R.A. Shenoi and H. Phillips</i>	
Tensile and Flexural Properties of Solid-State Microcellular ABS Panels.....	765
<i>Krishna Nadella and Vipin Kumar</i>	
Mixed Problem for Free Radial Vibrations of a Closed Spherical Sandwich Shell ....	767
<i>V. Polyakov and R. Chatys</i>	
Finite Element for Sandwich Panels Based on Analytical Solution of Constitutive Equations.....	769
<i>Markus Linke and Hans-Gunther Reimerdes</i>	
Impact Damage in Sandwich Composite Structures from GAS Gun Tests .....	771
<i>Nathalie Toso-Pentecote and Alastair Johnson</i>	
Effects of Missing Cells on the Compressive Behavior of Closed-Cell Al Foam .....	773
<i>I. Jeon, Y. Yamada, T. Yamada, K. Katou, T. Sonoda and T. Asahina</i>	
Failure Behaviour Investigation of Metallic Open Lattice Cellular Structures .....	775
<i>G.N. Labeas and M.M. Sunaric</i>	

<b>24. Experimental Buckling and Postbuckling of Lightweight Structures .....</b>	<b>777</b>
Smart Meshing of Imperfect Structures for the Improved Prediction of Buckling and Postbuckling Behaviour .....	777
<i>Carol A. Featherston</i>	
Cyclic Buckling Tests of CFRP Boxes under Compression and Torsion .....	779
<i>Chiara Bisagni and Potito Cordisco</i>	
Floor Dynamics for Truss System with Light Gauge Steel and Concrete .....	781
<i>S.E. Lee</i>	
Local Buckling and Postbuckling Behaviour of Thin-Walled Shells (Test Data & Theory) .....	783
<i>G.D. Gavrylenko</i>	
Initial Skin Buckling and Mode-Jumping in Integrally Stiffened Metallic Panels .....	785
<i>Adrian Murphy, Damian Quinn and Mark Price</i>	
Buckling Design Optimisation of Fibre Reinforced Polymer Shells using Lower Bound Post-Buckling Capacities .....	787
<i>Hongtao Wang and James G. A. Croll</i>	
<b>25. Impact/Crash and Other Dynamic Test Applications for Metallic Materials 789</b>	
Metallurgical Reasons of Scattering of Toughness in the Welded Joints of the Construction Steels .....	789
<i>E. Bayraktar, D. Kaplan and J.P. Chevalier</i>	
Study of a Substitution Test for Explosion Tests on Submarines Hulls.....	791
<i>Thierry Millot and Aude Menegazzi</i>	
High Strain Rate Reloading Compression testing of a Closed-Cell Aluminum Foam.....	793
<i>Alper Tasdemircia, Mustafa Gdena and Ian W. Hallb</i>	
Quasi-Static Axial Crushing Behavior of Aluminum Closed Cell Foam-Filled Multi-Packed Aluminum and Composite/Aluminum Hybrid Tubes .....	795
<i>Mustafa Guden, Halit Kavi and Sinan Yuksel</i>	
Calibration of Ductile Fracture Properties of Two Cast Aluminum Alloys .....	797
<i>Hiroyuki Mae, Xiaoqing Teng, Yuanli Bai and Tomasz Wierzbicki</i>	
State of the Art of Impact Tensile Test (ITT): Its Historical Development as a Simulated Crash Test of Industrial Materials .....	799
<i>E. Bayraktar, D. Kaplan and M. Grumbach</i>	
Experimental and Numerical Analysis of Circular Tube Systems under Quasi-Static and Dynamic Loading. ....	801
<i>Edmund Morris, A.G. Olabi, M.S.J. Hashmi and M.D. Gilchrist</i>	
3D Mechanical Analysis of Axially Loaded CFRP Confined Concrete Columns .....	803
<i>Youliang Chen, Ping Zheng, Jing Ni, Lequn Chang and Feng Yang</i>	
Conception and Construction of an Impact Machine (100kJ) for Frontal and Skew Shocks .....	805
<i>Etienne Pecquet, Jrme Tchuindjang and Serge Cescotto</i>	
<b>26. Application of Joining Techniques for Industrial Materials .....</b>	<b>807</b>
Influence of Precipitation on the Grain Growth During the Welding of Interstitial Free (IFS) Steels.....	807
<i>E. Bayraktar, D. Kaplan and J.P. Chevalier</i>	

Analysis of Mechanical Behaviour of Spotweld and FSW Metallic Assemblies under Quasi-Static and Dynamic Loadings.....	809
<i>J. Fabis, S. Blanchard, B. Langrand and E. Markiewicz</i>	
Testing and Modeling of Moisture Diffusion into Aluminum Particle Filled Epoxy Adhesive.....	811
<i>Ramazan Kahraman and Mamdouh Al-Harathi</i>	
Joining and Mechanical Strength of Self-Piercing Riveted Structure – Numerical Modeling and Experimental Validation .....	813
<i>S. Fayolle, P.O. Bouchard and K. Mocellin</i>	
A Comparative Study on Laser Welded Joints: Mechanical and Metallurgical Aspects.....	815
<i>E. Bayraktar, D. Kaplan and B.S. Yilbas</i>	
Carburization Behavior of Haynes-214 in Ethane-Hydrogen Gas Mixtures .....	817
<i>I.M. Allam</i>	
<b>27. Bio-compatible and Bio-Composite Materials .....</b>	<b>819</b>
Isothermal Crystallization Kinetics of Poly(3-Hydroxybutyrate)/Layered Double Hydroxide Nanocomposites.....	819
<i>Tzong-Ming Wu, Sung-Fu Hsu and Chien-Shiun Liao</i>	
Thermal Properties of Silk/Poly(Lactic Acid) Bio-Composite.....	821
<i>Hoi-Yan Cheung and Kin-Tak Lau</i>	
Crystallization Kinetics and Thermal Behavior of PCL/Multi-Walled Carbon Nanotubes Composites.....	823
<i>Erh-Chiang Chen and Tzong-Ming Wu</i>	
Preparation and Characterization of New Biodegradable Materials: Poly(Lactic Acid)/Layered Double Hydroxides Nanocomposites.....	825
<i>Ming-Feng Chiang and Tzong-Ming Wu</i>	
Isothermal Crystallization Kinetics of Poly(Lactic Acid)/Montmorillonite Nanocomposites.....	827
<i>Mei-Jan Chu and Tzong-Ming Wu</i>	
Synthesis and Characterization of Sol Gel Derived Silicon Substituted Porous Hydroxyapatite Scaffolds - Effect of Silicon Level on the in Vitro Biocompatibility of Si-HAP .....	829
<i>A. Balamurugan, J.H.G. Rocha, S. Kannan, A. Rebelo, J.M.G. Ventura and J.M.F. Ferreira</i>	
Designing Intelligent Polymeric Scaffolds for Tissue Engineering: Blending and Co-Electrospinning Synthetic and Natural Polymers .....	831
<i>P.I. Lelkes, M. Li, A. Perets, M.J. Mondrinos, Y. Guo, X. Chen, A.G. MacDiarmid, F.K. Ko, C.M. Finck and Y. Wei</i>	
<b>29. Transport Phenomena in Experimental Mechanics .....</b>	<b>833</b>
The Evaluation of Grain Boundary Diffusion Coefficient of Iron Ions in Wustite ....	833
<i>Yasushi Sasaki, Manabu Iguch and Mitsutaka Hin</i>	
Wet Etching Rate in the Cavity of Printed Circuit Board.....	835
<i>K. Matsumoto, D. Takahashi, K. Matsumura, T. Suzuki and S. Taniguchi</i>	
Experimental Determination of Preform Permeability Variation with Porosity for Woven Fiberglass and Carbon Mats .....	837

<i>Hossein Golestanian</i>	
Swirling Jet Mixing of a Bath Covered with a Top Slag Layer .....	839
<i>M. Iguchi, Y. Sasaki, D. Iguchi and T. Ohmi</i>	
Dissolution Behavior of Elements in Steelmaking Slag into Seawater .....	841
<i>Takahiro Miki and Mitsutaka Hino</i>	
<b>31. Thermal Methods for Stress and Damage Analysis.....</b>	<b>843</b>
Experimental Study of the Stress Relief in Patched Aluminium Specimens.....	843
<i>Marie-Pierre Moutrille, Xavier Balandraud and Michel Grédiac</i>	
Stress Separation using Thermoelastic Data.....	845
<i>Eann A. Patterson and Robert E. Rowlands</i>	
Evidence of Viscoelastic and Elasto-Plastic Dissipation in Metals by Measurements of the Thermal Energy Release in Cyclic Tensile Tests .....	847
<i>F. Maquin and F. Pierron</i>	
Thermoelastic Investigation of Crack Paths .....	849
<i>R.A. Tomlinson, J.R. Yates and M. Zanganeh</i>	
A New Motion Compensation Technique for Infrared Stress Measurement using Digital Image Correlation .....	851
<i>Takahide Sakagami, Naoki Yamaguchi and Shiro Kubo</i>	
Thermoelastic Investigation of Damage Evolution in Small Stainless Steel Pipework .....	853
<i>S. Quinn, P.J. Tatum, J.M. Dulieu-Barton and J. Eaton-Evans</i>	
Combining Thermoelastic and Stress Function Data to Evaluate Individual Stresses Around a Near-Edge Hole.....	855
<i>S.-J. Lin, S. Quinn, D.R. Matthys, I.M. Kincaid, B.R. Boyce and R.E. Rowlands</i>	
Thermoelastic Stress Analysis of Sandwich Structures with Core Junctions .....	857
<i>M. Johannes, J. M. Dulieu-Barton, E. Bozhevolnaya and O.T. Thomsen</i>	
Progress in the Development of a Thermoelastic Gauge for Stress Separation.....	859
<i>P. Stanley, T. S. Phan and J.M. Dulieu-Barton</i>	
Thermoelastic Stress Analysis by Means of a Standard Thermocamera and a 2D-FFT Based Lock-In Technique .....	861
<i>G. Pitarresi, L. D'Acquisto, F. Lo Nigro and A.M. Siddiolo</i>	
Energy Analysis of Steel Subjected to High Cycle Fatigue.....	863
<i>A. Chrysochoos, B. Berthel, A. Galtier, F. Latourte, S. Pagano and B. Wattrisse</i>	
The Effect of Crack-Tip Interactions on the Curve-Fitting of Mixed-Mode Isopachics.....	865
<i>G. Isaac, A. Spencer, K. Worden and J. M. Dulieu-Barton</i>	
A Novel Experimental Procedure for Stress Separation on Composite Components .....	867
<i>D. Modugno, G. Vitale, U. Galietti and C. Pappalettere</i>	
Combined Thermoelastic and Thermographic Data for the Evaluation of Crack Growth in Industrial Components.....	869
<i>F. Carofiglio, U. Galietti, D. Modugno and C.Pappalettere</i>	
Thermomechanical Analysis of the Yield Behaviour of a Semicrystalline Polymer....	871
<i>Jean-Michel Muracciole, Bertrand Wattrisse and André Chrysochoos</i>	

Thermal Effects in Viscoelastic Materials .....	873
<i>A. Hussain, R. J. Greene and R. A. Tomlinson</i>	
Thermoelastic Stress Analysis of Inhomogenous Composite Materials.....	875
<i>R.K. Fruhmanna, J.M. Dulieu-Bartonb and S. Quinn</i>	
<b>32. Novel Applications of Experimental Mechanics .....</b>	<b>877</b>
Optimization of the FSW Process for Aluminum Alloys AA5083 by the Grey-Based Taguchi Method .....	877
<i>Thaiping Chen, Chi-Hui Chien, Wei-Bang Lin and Yuh J. Chao</i>	
The Effects of Different Cranial Size on Mechanical Properties of Cranial Suture in Rat and Same-Aged Mice .....	879
<i>Chi-Hui Chien, Yii-Der Wu and Yuh J. Chao</i>	
Validation of Mechanical Properties of Single Crystal Silicon By Atomic-level Numerical Model .....	881
<i>Chun-Te Lin, Chan-Yen Chou and Kuo Ning Chiang</i>	
Strain Measurement of Nickel Thin Film by a Digital Image Correlation Method.....	883
<i>Shun-Fa Hwang, Jhih-Te Horn and Hou-Jiun Wang</i>	
The Effects of Internal Stressrs in BGA Ni Layer on the Strength of Sn/Ag/Cu Solder Joint .....	885
<i>Chi-Hui Chien, Chi-Chao Tseng and Thaiping Chen</i>	
Novel Applications of Experimental Mechanics on the Design of Ultrasonic Horns .	887
<i>Wei-Chung Wang, Ying-Huang Tsai and Chun-Yao Ni</i>	
The Out-of-Plane Strains Measurement in Sandwich Plates with Single Fully-Potted Insert by using Digital Speckle Pattern Shearography.....	889
<i>Song-Jeng Huang and Yu-Tan Lin</i>	
An Experimental Study on the Elastic-Plastic Fracture in a Ductile Material under Mixed Mode Loading .....	891
<i>Perng-Fei Luo and Ching-Hsiung Wang</i>	
Mechanical Characterization of KMPRTM by Nano-Indentation for MEMS Applications .....	893
<i>Kuang-Shun Ou, Hong-Yi Yan and Kuo-Shen Chen</i>	
Mechanical Properties Measurement of PECVD Silicon Nitride after Rapid Thermal Annealing Using Nanoindentation Technique.....	895
<i>Hong-Yi Yan, Kuang-Shun Ou and Kuo-Shen Chen</i>	
Novel Phase Unwrapping Algorithm for Retrieving ESPI Map with Real Physical Discontinuity.....	897
<i>M.J. Huang and J.K. Liou</i>	
Wavelength Shift Determination using a Common-Path Interferometer.....	899
<i>Shyh-Tsong Lin and Cheng-Chung Chang</i>	
On the Thermal Dissipation of the Board-Level Electronic Packaging.....	901
<i>Hsien-Chie Cheng, Wen-Hwa Chen and Hwa-Fa Cheng</i>	
Use of Digital Image Correlation Technique to Measure Dental Composite Shrinkage .....	903
<i>Shu-Fen Chuang, Terry Yuan-Fang Chen and Chih-Han Chang</i>	
The Flexible 3-Dimensional Load Measurement Sensor using the Elastic Sphere .....	905
<i>Noboru Nakayama, Jianhui Qiu, Tetsuo Kumazawa and Kenji Torii</i>	



In-Plane Residual Stress Analysis Combining Hole-Drilling and Moiré Interferometry .....	907
<i>J.N. Aoh, C.Y. Huang and J.Y. Lee</i>	
The Development and Application of Magnetophotoelasticity .....	909
<i>A. Conway, R. Tomlinson and G. Jewell</i>	
Determining Individual Stresses Around a Near-Edge Hole Subjected to an Offset Load Using Thermoelasticity .....	911
<i>S.-J. Lin, D.R. Matthys, S. Quinn, J.P. Davidson, B.R. Boyce and R.E. Rowlands</i>	
A New Heterodyne Polariscope for Sequential Measurements of Multi-Parameter in a Multiple-Order Waveplate .....	913
<i>Yu-Tsan Jeng and Yu-Lung Lo</i>	
Measurements for the Optical Parameters of Linear Birefringence Materials by Using Thermal Light Polarization-Sensitive Optical Coherence Tomography .....	915
<i>Yu-Lung Lo, Chia-Chi Liao, and Cheng-Yen Yeh</i>	
Full-Field Mapping of the Stress-Induced Birefringence on the Internal Interfaces using a Polarized Low Coherence Light Interference Microscope .....	917
<i>Jenq-Shyong Chen and Yung-Kuo Huang</i>	
Diffractionmeter with a Mobile X-Ray Tube-Detector System .....	919
<i>B.S. Roshchin, V.E. Asadchikov, A.V. Buzmakov, I.V. Kozhevnikov and R.A. Senin</i>	
<b>33. Modern Practice in Acoustic Emission .....</b>	<b>921</b>
Wavelet Based Feature Extraction for Acoustic Emission .....	921
<i>J. Hensman and K. Worden</i>	
Embedded PVDF Sensors for Impact and AE Detection in Composite Structures .....	923
<i>C. Caneva, I.M. De Rosa and F. Sarasini</i>	
Advanced Location and Characterisation of Damage in Complex Metallic Structures Using Acoustic Emission .....	925
<i>Rhys Pullin, Karen M. Holford, Sam L. Evans and Matthew Baxter</i>	
Current Practice and Applications of Acoustic Emission .....	927
<i>K.M. Holford and R. Pullin</i>	
Signal Processing and Pattern Recognition of AE Signatures .....	929
<i>Athanasios A. Anastasopoulos</i>	
<b>35. Biaxial Testing .....</b>	<b>931</b>
Inverse Method for Parameter Determination of Biaxially Loaded Cruciform Composite Specimens .....	931
<i>A. Smits, D. Lecompte, D. Van Hemelrijck, H. Sol and W. Van Paepegem</i>	
A Review of Biaxial Test Methods for Composites .....	933
<i>A. Smits, C. Ramault, A. Makris, D. Van Hemelrijck, A. Clarke, C. Williamson, M. Gower, R. Shaw, R. Mera, E. Lamkanfi and W. Van Paepegem</i>	
Plastic Material Model Identification using DIC on Biaxial Tensile Test .....	935
<i>D. Lecompte, S. Cooreman, H. Sol, J. Vantomme, D. Van Hemelrijck and A.M Habraken</i>	
Development of a Cruciform Specimen Geometry for the Characterisation of Biaxial Material Performance for Fibre Reinforced Plastics .....	937

<i>M. Gower, R. Shaw and R. Mera</i>	
Investigation Into the Failure of Open Holes in CFRP Laminates under Biaxial Loading Conditions.....	939
<i>C. Williamson and J. Thatcher</i>	
Application of Ultrasonic Phased Array for Nondestructive Detection of Damage in Biaxial Cruciform .....	941
<i>E. Lamkanfi, A. Smits, W. Van Paepegem and D. Van Hemelrijck</i>	
<b>36. Residual Stress Measurements by Hole Drilling Techniques .....</b>	<b>943</b>
On the Residual Stress Field in the Aluminum Alloy FSW Joints .....	943
<i>V. Dattoma, M. De Giorgi and R. Nobile</i>	
Fine Increment Hole-Drilling Method for Residual Stress Measurement, Proposal of a Calibrating Apparatus .....	945
<i>E. Valentini, M. Benedetti, V. Fontanari, M. Beghini, L. Bertini and C. Santus</i>	
Residual Stress on Titanium Alloy Welded Joints .....	947
<i>Caterina Casavola and Carmine Pappalettere</i>	
<b>37. Mechanical Behaviour and Failure of Natural Building Stones.....</b>	<b>949</b>
Restoring Marble Fragments: The Pull-Out Problem .....	949
<i>S.K. Kourkoulis, I. Vayas, A. Marinelli and S.-A. Papanicolopoulos</i>	
Transversely Isotropic Natural Building Stones under Three-Point Bending.....	951
<i>S.K. Kourkoulis</i>	
The Brazilian Disc with a Central Notch: A Numerical and Experimental Study.....	953
<i>S.K. Kourkoulis and A.D. Levantis</i>	
The Influence of the Flutes on the Mechanical Behaviour of the Ancient Greek Columns .....	955
<i>S.K. Kourkoulis, K.E. Moupagitsoglou and N.L. Ninis</i>	
The Size-Effect for Natural Building Stones .....	957
<i>S.K. Kourkoulis, E. Ganniari-Papageorgiou and N.L. Ninis</i>	
Evaluation of Accelerated Weathering Effects on the Surface of two Coloured Sicilian Building Stones.....	959
<i>Rizzo Giovanni, Ercoli Laura and Megna Bartolomeo</i>	
The Bond Mechanism in Stone or Brick to Grout Interfaces.....	961
<i>Elizabeth Vintzileou and Chryssi-Elpida Adami</i>	
Mechanical Strength and Water Content of Porous Limestones.....	963
<i>Kevin Beck, Hamidreza Adib-Ramezani and Muzahim Al-Mukhtar</i>	
Crystallization Pressure and Salt Distribution in Tuffeau Limestone.....	965
<i>Thua-Tri Van, Kevin Beck, Xavier Brunetaud and Muzahim Al-Mukhtar</i>	
Analysis and Interpretation of the Structural Failures of the Orthostate Blocks of the Northern Wall of the Athens Parthenon.....	967
<i>Eleni-Eva Toumbakari</i>	
Compaction Bands in Oedometric Tests on High Porosity Soft Rocks .....	969
<i>Riccardo Castellanza, Eleni Gerolymatou and Roberto Nova</i>	

## **Editor's Preface**

This volume contains two-page abstracts of the 482 papers presented at the "13th International Conference on Experimental Mechanics," (ICEM13) held in Alexandroupolis, Greece, July 1-6, 2007. The accompanying CD attached at the back cover of the book contains the full length papers.

The abstracts of the fifteen plenary lectures are included in the beginning of the book. The remaining 467 abstracts are arranged in 23 tracks and 28 special symposia/sessions with 225 and 242 abstracts, respectively. The papers of the tracks have been contributed from open call, while the papers of the symposia/sessions have been solicited by the respective organizers.

Started in 1959, the International Conference on Experimental Mechanics (ICEM) takes place every four years in a European country. Its scope is to promote world-wide cooperation among scientists and engineers concerned with experimental mechanics of solids and structures. ICEM13 was under the auspices of the European Association for Experimental Mechanics (EURASEM) and was sponsored by the Society for Experimental Mechanics (SEM), the British Society for Stain Measurement (BSSM), the German Society for Experimental Mechanics (GESA), the French Society of Mechanics (AFM), the Italian Society for the Analysis of Stresses (AIAS), the Japanese Society for Experimental Mechanics (JSEM), the Japanese Society of Materials Science (JSMS), and the European Structural Integrity Society (ESIS). ICEM13 focused in all aspects of experimental mechanics with emphasis to nanostructured materials and nanostructures and micro and nanoelectromechanical systems (MEMS and NEMS). The technical program of ICEM13 was the product of hard work and devotion of more than 100 world leading experts to whom I am greatly indebted. The success of ICEM13 relied solely on the dedication and titanic work of the members of the Scientific Advisory Board, the pillars of ICEM13. As chairman of ICEM13 I am honored to have them on the Board and have worked closely with them for a successful conference.

Experimental methods have been successful to increase the knowledge of physical phenomena, to further the understanding of the behavior of materials, structures and systems; and to provide the necessary physical basis and verification for analytical and computational approaches to the development of engineering solutions.

More than five hundred participants attended ICEM13, while more than four hundred fifty papers were presented. The participants of ICEM13 came from 53 countries. Roughly speaking 50% came from Europe, 10% from the Americas, 27% from the Far East and 13% from other countries. I am happy and proud to have welcomed in Alexandroupolis well-known experts who came to discuss problems related to the analysis and prevention of failure in structures. The tranquility and peacefulness of this small town provided an ideal environment for a group of scientists and engineers to gather and interact on a personal basis. Presentation of technical papers alone is not enough for effective scientific communication. It is the healthy exchange of ideas and scientific knowledge, formal and informal discussions, together with the plenary and

contributed papers that make a fruitful and successful meeting. Informal discussions, personal acquaintance and friendship play an important role.

I am proud to have hosted ICEM13 in the beautiful town of Alexandroupolis, site of the Democritus University of Thrace and I am pleased to have welcomed colleagues, friends, and old and new acquaintances.

I very sincerely thank the authors who have contributed to this volume, the symposia/sessions organizers for their hard work and dedication and the referees who reviewed the quality of the submitted contributions. Our sponsors' support, given in various forms, is gratefully acknowledged. The tireless effort of the members of the Organizing Committee as well as of other numerous individuals, and people behind the scenes is appreciated. I am deeply indebted to the senior students of the Department of Electrical and Computer Engineering of the Democritus University of Thrace Messrs. N. Tsiantoulas and S. Siailis for their hard work and dedication in the preparation of the ICEM13 website in a timely and efficient manner and the organization of the conference, and for their efforts in helping me compile this volume. Finally, a special word of thanks goes to Mrs. Nathalie Jacobs of Springer for the nice appearance of this book and her kind and continuous collaboration and support.

January 2007

Emmanuel E. Gdoutos

Xanthi, Greece

Editor

## ORGANIZING COMMITTEES

### Scientific Advisory Board

Emmanuel E. Gdoutos (Chair)

Janice Barton (Vice-Chair)

Peter Stanley (Honorary Chair)

Aben, H. (Estonia), Ajovalasit, A. (Italy), Albertazzi, G.A. Jr (Brazil), Andrianopoulos, N. (Greece), Angelova, D. (Bulgaria), Arakawa, K. (Japan), Asundi, A. (Singapore), Atzori, B. (Italy), Balthazar, J.M. (Brazil), Banks-Sills, L. (Israel), Belingardi, G. (Italy), Blinc, R. (Slovenia), Borbas, L. (Hungary), Burguete, R. (UK), Cardon, A. (Belgium), Carne, T. (USA), Chen, T. (Taiwan), Chiang, F-P. (USA), Chona, R. (USA), Chrysochoos, A. (France), Conti, C. (Belgium), Daniel, I. M. (USA), Eberhardsteiner, J. (Austria), Emri, I. (Slovenia), Espinosa, H. (USA), Featherston, C. (UK), Freire, J. (Brazil), Giacomini, J. (UK), Galietti, U. (Italy), Gilchrist, M. (Ireland), Goldar, D. (India), Grediac, M. (France), Gungor, S. (UK), Holford, K. (UK), Hu, X. (Australia), Huang, Z. (UK), Hung, M. (Hong-Kong), Huntley, J. (UK), Iguchi, M. (Japan), Iliescu, N. (Romania), Inaudi, D. (Switzerland), Inman, D.J. (USA), Jacquot, P. (Switzerland), Johnson, A. (Germany), Jones, J. (UK), Kato, A. (Japan), Konsta-Gdoutos, M. (Greece), Kourkoulis, S. (Greece), Kujawinska, M. (Poland), Kunnemeyer, R. (New Zealand), Larkin, A. (Russia), Laermann, K. H. (Germany), Lau, A. (Hong-Kong), Lord, J. (UK), Machida, K. (Japan), Mines, B. (UK), Morimoto, H. (Japan), Moy, S. (UK), Nobile, L. (Italy), O' Brien, E. (UK), Orr, J. (UK), Orteu, J. J. (France), Papadopoulos, G. (Greece), Papakaliatakis, G. (Greece), Pappalettere, C. (Italy), Patterson, E. (USA), Pieczyska, E. (Poland), Pierron, F. (France), Pluvinage, G. (France), Poggialini, A. (Italy), Pryputniewicz, R. (USA), Ramesh, K. (India), Ravi-Chandar, K. (USA), Rodriguez-Vera, R. (Mexico), Sainov, V. (Bulgaria), Sciammarella, C. (Italy), Shankar, K. (Australia), Shimamoto, A. (Japan), Shukla, A. (USA), Sirisoonthorn, S. (Thailand), Sjodahl, M. (Sweden), Stang, B. (Denmark), Stupnicki, J. (Poland), Su, X. (China), Suhling, J. (USA), Sumali, A. (USA), Takashi, M. (Japan), Tanner, L. (UK), Tay, C.J. (Singapore), Toyooka, S. (Japan), Trendafilova, I. (UK), Truman, C. (UK), Ulea, M. (Romania), Umezaki, E. (Japan), Van Hemelrijck, D. (Belgium), Vantomme, J. (Belgium), Vautrin, A. (France), Walker, C. (UK), Wang, W.-C. (Taiwan), Warrior, N. (UK), Whelan, C. (Italy), Widjaja, J. (Thailand), Worden, K. (UK), Xiaoping, W. (China), Xie, H. (China), Yokoyama, T. (Japan), Yoneyama, S. (Japan), Zacha-roopoulos, D. (Greece).

**LOCAL ORGANIZING COMMITTEE**

Emmanuel E. Gdoutos (Chair)

M.S. Konsta-Gdoutos, S. Sails, N. Tsiantoulas

## ICEM13 TRACKS

### B: TRACKS

- 1T3. Nanocomposites
- 1T6. Nanostuctured Materials
- 1T7. Thin Films
- 2T3. Applications
- 2T4. Applied Photoelasticity
- 2T6. Composite Materials
- 2T7. Damage Assessment
- 2T8. Dynamic Systems
- 2T9. Fiber Optic Sensors
- 2T10. Fracture and Fatigue
- 2T11. Hybrid Techniques
- 2T12. Impact Mechanics
- 2T13. Inverse Problems
- 2T17. Numerical Solutions
- 2T18. Optical Methods
- 2T19. Research in Progress
- 2T20. Smart Materials and Structures
- 2T21. Speckle Interferometry
- 2T24. Structural Integrity and Health Monitoring
- 2T25. Structural Testing
- 2T26. Thermal Problems
- 2T27. Time Dependent Materials
- 2T28. Transducers and Sensors

## ICEM13 SPECIAL SYMPOSIA/SESSIONS

### C: SPECIAL SYMPOSIA/SESSIONS

2. Experimental Characterization and Multiscale Modeling of Building Materials (Organized by Josef Eberhardsteiner and Roman Lackner)
3. Experimental Analysis of Mechanical Properties in Advanced Materials (Organized by A. Shimamoto)
4. Plasticity, Fracture and Fatigue at the Micro and Nano Scales (Organized by Horacio D. Espinosa and Emmanuel Gdoutos)
5. Mission Synthesis - Simulation of the Random Loadings Acting on Engineering Structures (Organized by Joseph A. Giacomini and Vincent Rouillard)
6. Optical Methods for 3-D Displacement Field Measurement (Organized by Jean-Jose Orteu and Rainer Tutsch)
7. Fracture and Fatigue of Piezoelectric Ceramics (Organized by Leslie Banks-Sills)
8. Digital Holography, Exploring Possibility of Using Digital Holography for Experimental Mechanics (Organized by Yoshiharu Morimoto and Satoru Yoneyama)
9. Mechanics of MEMS (Organized by Hartono Sumali)
10. Measurement of Residual Stress and Strain in Composite Processing and Service Life (Organized by Alain Vautrin and John Botsis)
12. Time-Dependent Behavior of Multifunctional Nanostructured Polymers and Nanocomposite Materials (Organized by Igor Emri and Urska Florjancic)
14. Photoelasticity and its Applications (Organized by Eisaku Umezaki)
15. Identification of Mechanical Constitutive Equations from Kinematic Full-Field Measurements (Organized by Fabrice Pierron, Per Stahle and Michel Grediac)
16. Impact Behaviour of Composite Materials and Structures (Organized by Takashi Yokoyama)
17. Fiber Reinforced Polymer Applications for Repair and Strengthening Existing Structures (Organized by Lucio Nobile and Alessandro Baratta)
18. Advances in Speckle Interferometry (Organized by Pierre Slengen, Kay Gastering and Pierre Jacquot)
19. Mechanical and Thermomechanical Properties of Smart Materials and Structures (Organized by Elzbieta A Pieczyska)
22. Sandwich Structures and Core Materials (Organized by Ole Thybo Thomsen and Robert Mines)
24. Experimental Buckling and Postbuckling of Lightweight Structures (Organized by Carol Featherston)



25. Impact/Crash and Other Dynamic Test Applications for Metallic Materials (Organized by Emin Bayraktar, Bekir Sami Yilbas, Genevieve Inglebert and Jean-Pierre Chevalier)
26. Application of Joining Techniques for Industrial Materials in Automotive, Aeronautic-Aerospace, Marine and Pipelines Industries (Organized by Emin Bayraktar, Bekir Sami Yilbas, Genevieve Inglebert and Jean-Pierre Chevalier)
27. Bio-Compatible and Bio-Composite Materials (Organized by Alan Kin-Tak Lau)
29. Transport Phenomena in Experimental Mechanics (Organized by Manabu Iguchi and Yasushi Sasaki)
31. Thermal Methods for Stress and Damage Analysis (Organized by Janice Barton and Umberto Galietti)
32. Novel Applications of Experimental Mechanics (Organized by Wei-Chung Wang, Terry Yuan-Fang Chen and Yu-Lung Lo)
33. Modern Practice in Acoustic Emission (Organized by Karen M. Holford)
35. Biaxial Testing (Organized by D. Van Hemelrijck)
36. Residual Stress Measurements by Hole Drilling Techniques (Organized by Carmine Pappalettere)
37. Mechanical Behaviour and Failure of Natural Building Stones (Organized by Stavros K. Kourkoulis)

# **A. INVITED PAPERS**

## MODERN PHOTOELASTICITY FOR RESIDUAL STRESS MEASUREMENT IN GLASS

Hillar Aben, Johan Anton and Andrei Errapart  
 GlasStress Ltd.  
 21, Akadeemia tee, 12618 Tallinn  
 aben@glasstress.com

Residual stress is one of the important indicators of the quality of any glass product. The paper gives a review of the methods, which are nowadays used in glass industry for measuring residual stress both in architectural and automotive glass panels and in hollow glassware.

### Stress measurement in architectural and automotive glass panels

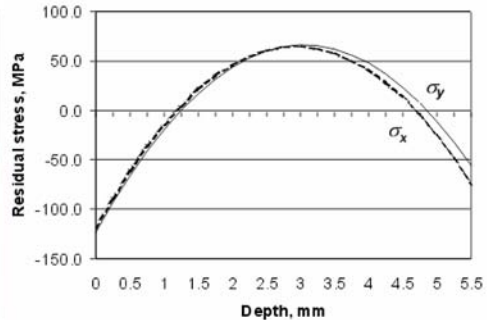
Since in the case of glass panels most important is the surface stress, nowadays the most popular technology by the assessment of the residual stress in architectural and automotive glass panels is differential refractometry or the mirage method [1]. Most popular device for the surface stress measurement is GASP, manufactured by Strainoptic Technologies, Inc [2].

The mirage method, used in GASP, can be applied if the gradient of the refractive index of the glass near the surface is very high. This condition is fulfilled on the tin side of the float glass. At the other surface of the float glass the gradient of the refractive index is not high enough and the device GASP can not be applied.

A universal photoelastic method for 3D stress measurement is the scattered light method [1]. The scattered light method permits determination of the stress profile through the thickness of the panel [3, 4]. Figure 1a shows a portable scattered light polariscope SCALP-03, manufactured by GlasStress Ltd. In Fig. 1b profile of the stress in a tempered glass panel is shown. Measurement of the stress profile at a point takes 10 sec.



(a)



(b)

FIGURE 1. (a) Portable scattered light polariscope SCALP-03; (b) stress profile in a tempered glass panel.

### Stress measurement in hollow glassware

In hollow glassware stresses are measured with integrated photoelasticity [1] (Fig. 2) Figure 3 illustrates stress measurement in a tempered tumbler. Integrated photoelasticity is actually

photoelastic tomography. In the axisymmetric case it is sufficient to pass polarized light through the specimen only in one direction. In the case of the general 3D stress measurement, tomographic photoelastic measurements are to be carried out in a section of the specimen for many different directions [5].

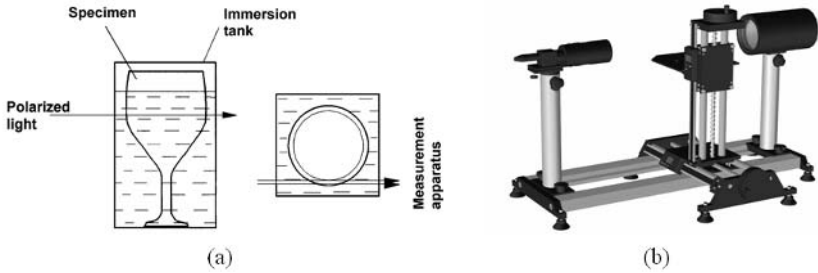


FIGURE 2. (a) Experimental set-up in integrated photoelasticity; (b) polariscope AP-06C.

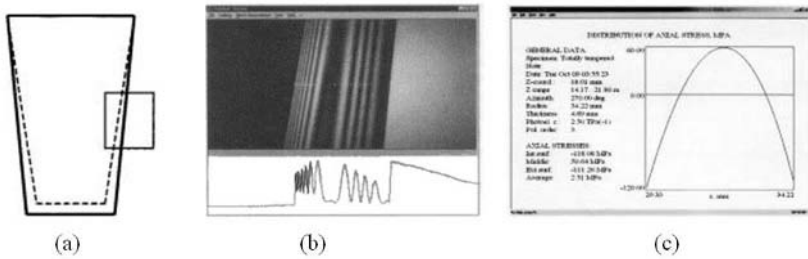


FIGURE 3. Geometry of a tempered tumbler (a), physical and digitized fringe patterns (b), and axial stress distribution in the wall (c).

Contemporary photoelastic technology permits highly automated and quick residual stress measurement in a large variety of glass products. This technology is practically applied in many glass companies.

## References

1. Aben, H and Guillemet, C. *Photoelasticity of Glass*, Springer, Berlin, 1993.
2. Redner, A.S. and Bhat, G.K. In *Proceedings of Glass Processing Days*, Tampere, 1999, 169-171.
3. Hundhammer, I., Lenhart, A. and Pontasch, D. *Glass Sci. Technol.*, vol. **75**, 236-262, 2002.
4. Lochegnies, P., Romero, E, Anton, J., Errapart, A. and Aben, H. In *Proceedings of Glass Processing Days*, Tampere, 2005, 88-91.
5. Aben, H., Errapart, A., Ainola, L. and Anton, *Opt. Eng.*, vol. **44**, 093601, 2005.

## THERMOELASTIC STRESS ANALYSIS OF VASCULAR DEVICES

J.M. Dulieu-Barton<sup>1,a</sup>, J. Eaton-Evans<sup>2,b</sup>, E.G. Little<sup>2,c</sup> and I.A. Brown<sup>3,d</sup>

<sup>1</sup>School of Engineering Sciences, University of Southampton, UK.

<sup>2</sup>Department of Mechanical and Aeronautical Engineering, University of Limerick, Ireland.

<sup>a</sup>janice@ship.soton.ac.uk, <sup>b</sup>James.Eaton-Evans@ul.ie, <sup>c</sup>Edward.Little@ul.ie, <sup>d</sup>Ian.Brown@ul.ie

The research described in this plenary paper deals with the application of experimental techniques to medical devices used in the treatment of vascular disease. Vascular disease is a medical condition where fatty material narrows the artery. It is reported that over 4 million deaths can be attributed to the disease each year in Europe alone. Vascular disease can occur at locations throughout the arterial network. A blockage located in the carotid artery can cause what is known as a stroke, or if located in one of coronary arteries may lead to a heart attack. A major advance in the treatment of the disease was made when the Percutaneous Transluminal Coronary Angioplasty (PTCA) was introduced by Gruntzig in 1977. The procedure offered a non-invasive, cost effective and rapid treatment for cardiovascular disease and was soon adapted to treat diseased vessels elsewhere in the body. During a typical procedure access to the vascular system is gained via the femoral artery at the groin. From this point a cardiologist uses endovascular techniques to navigate a catheter, with a polymer balloon deflated and tightly wrapped around its tip, through the artery network to the site of the blockage. The balloon is positioned across the blockage and is momentarily inflated. As the balloon inflates it exerts a radial force on the accumulated atherosclerotic plaque material, displacing it and thereby restoring patency to the vessel. Angioplasty balloons are used at locations throughout the arterial network and therefore range in size depending on the intended site of operation. They are typically constructed from rigid polymeric materials and are designed to exhibit low compliance at inflation high pressures; the balloon material is anisotropic. Fig. 1 shows a commercially available balloon. Studies have found the incidence of restenosis post angioplasty to be as high as 30 - 50%. To combat this a fine mesh, metallic, cylindrical component known as an intravascular stent may be implanted as a follow up procedure to the angioplasty. The device is permanently implanted and acts as a scaffold within the artery (see Fig. 2). Two principal categories of stents exist: balloon expandable and self-expanding. The former are plastically deformed into position using an angioplasty balloon and are typically constructed from a stainless steel alloy. The latter, self-expanding stents (see Fig. 2) are deployed from the tip of a catheter and expand elastically into position, to provide support to the vessel wall. Self-expanding stents are constructed from a NiTi alloy commonly known as Nitinol. Nitinol is classed as a superelastic material as it can elastically recover strains in excess of 8% via a stress induced (reversible) transformation from a parent austenite microstructure to a martensitic phase. The stress-strain curve follows a non-linear path with significant thermal variations occurring as the material undergoes the phase change.

Thermoelastic Stress Analysis (TSA) [1] is a non-contacting technique that provides full field stress information and can record high-resolution measurements from small structures. The work presented in this paper summarises the application of TSA to angioplasty balloons and Nitinol vascular stents carried out at the University of Southampton [2-6] and identifies the significant challenges in apply the technique to such devices. The use of high resolution optics is described along with a calibration methodology that allows quantitative stress measurements to be taken from the balloon structure. The paper then describes new work that assesses the effect of geometrical variations on balloon performance. Typical data from a balloon is shown in Figure 3. A brief account of a study undertaken to characterise the thermoelastic response from Nitinol is

also included and it is demonstrated that thermoelastic data can be obtained from a stent at high resolutions (see Figure 4). Further work on stents conducted at body temperature is described.

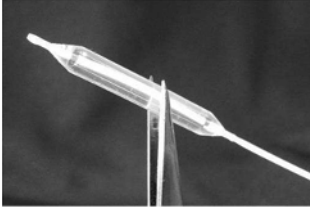


Figure 1 Angioplasty balloon

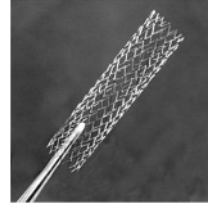


Figure 2 Nitinol self expanding stent

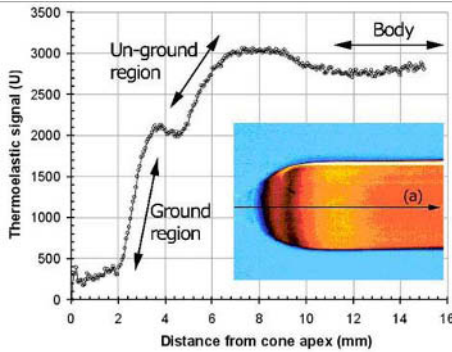


Figure 3 TSA image of balloon loaded under internal pressure and plot of signal along line (a)

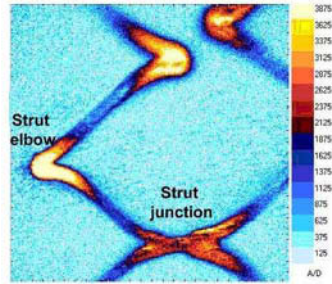


Figure 4 High resolution image of stent under radial loading

## References

1. Dulieu-Barton, J.M. and Stanley, P., *J. of Strain Analysis*, vol. **33**, 93-104, 1998.
2. Eaton-Evans, J. E., Dulieu-Barton, J. M., Little, E. G. and Brown, I. A., *Applied Mechanics and Materials*, vols. **3-4**, 47-52, 2005.
3. Eaton-Evans, J. E., Dulieu-Barton, J. M., Little, E. G. and Brown I. A., *Applied Mechanics and Materials*, vols **5-6**, 63-70, 2006.
4. Eaton-Evans, J., Dulieu-Barton, J. M., Little, E. and Brown, I., *Proc. of the IMechE Part H, J. of Eng. In Med.*, vol. **220**, 425-438, 2006.
5. Eaton-Evans, J., Dulieu-Barton, J. M., Little, E. G. and Brown I. A., *J. of ASTM International*, vol. **3**, 1-12, 2006.
6. Eaton-Evans, J., Dulieu-Barton, J. M., Little, E. G. and Brown I. A., *J. of Strain Analysis*, vol. **41**, 481- 495, 2006.

## MICRO/NANO SPECKLE METHOD WITH APPLICATIONS TO MATERIAL, TISSUE ENGINEERING AND HEART MECHANICS

Fu-Pen Chiang  
 SUNY Distinguished Professor & Chair  
 Dept. of Mechanical Engineering  
 Stony Brook University  
 Stony Brook, NY 11794-2300  
 Fu-Pen.Chiang@sunysb.edu

Using a random speckle pattern as a quantitative transducer for displacement and deformation measurement constitutes a major milestone in the advancement of experimental mechanics techniques. Heretofore, displacement or strain transducers or gages utilize regular patterns as the measurement base. It is the dimensional changes of these bases that are converted into displacement/strain information. The speckle method, on the other hand, uses a random array of particles (either physical or virtual) as displacement transducers. The displacement information of a cluster of random particles is obtained either through correlation calculations with its neighbors or a Fourier transform processing scheme. It is the latter approach that will be discussed in this paper.

First a random speckle pattern is created either on the surface or in the interior of the specimen. A digital photographic process is used to record the speckle pattern before and after the deformation of the specimen. A specially designed software called CASI (Computer Aided Speckle Interferometry) is employed to process thus obtained specklegrams.

As shown in Fig. 1, the digital speckle images are divided into subimages with  $32 \times 32$  pixels, for example. Then a FFT (Fast Fourier Transforms) is applied to the corresponding pair of subimages. The result is multiplied by a numerical filter and a second FFT is applied afterwards. The final result is a delta function situated at a point in the second transform plane. And the position vector of this delta function is nothing but the displacement vector represented by the cluster of speckles. By going through every subimages this way, the deformation field of the entire specimen plane can be obtained. Appropriate displacement-strain relations are then used to calculate the strain distribution.

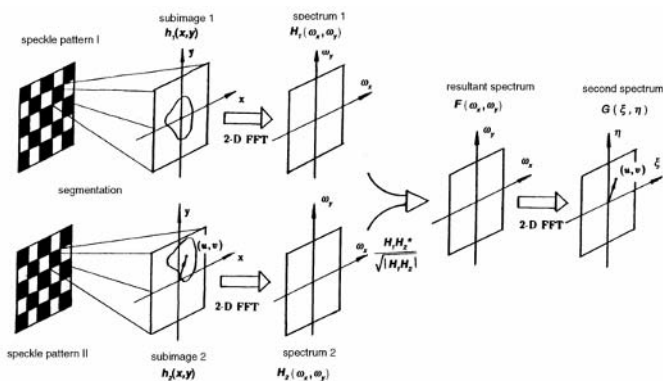


FIGURE 1. Processing of speckle patterns

We have applied this technique to various topics such as the residual plastic strain distribution at a crack tip within a small region of about  $40\ \mu\text{m} \times 50\ \mu\text{m}$  after various cyclic loadings (as shown in Fig. 2), the thermal differential strain ( $T = 86\ ^\circ\text{C}$ ) at the interfaces of an electronic package, the mechanical properties of SU-8 (a MEMS material), the mechanical properties of normal and cancerous artificial skins, the effect of regional ischemia on the pumping efficiencies of an animal heart, both in vitro and in vivo, etc. Potential applications of the advanced electron speckle photography technique to nanotechnology will also be discussed.

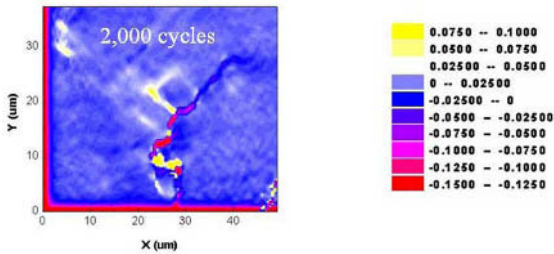


FIGURE 2. Residual plastic shear strain field  $\epsilon_{xy}$  surrounding an extending fatigue crack in a steel specimen as obtained by SIEM

## Reference

1. Chiang, F. P. *Optical Engineering*, vol. **42**(5), 1288-1292, 2003



## IN-SITU ELECTRON MICROSCOPY TESTING OF NANOSTRUCTURES

Horacio D. Espinosa  
 Department of Mechanical Engineering, Northwestern University  
 Evanston, IL 60208-3111, USA  
 espinosa@northwestern.edu

Over the past decade, there has been a major thrust to reduce the size of electronic and electromechanical systems to the nanometer scale by fabricating devices out of thin films, carbon nanotubes (CNTs) and nanowires (NWs). In these applications, a thorough understanding of material mechanical, electrical and thermal properties as well as device performance and reliability requires the development of novel experimental approaches. In this plenary lecture, two such experimental methodologies will be introduced and discussed. The first addresses the development of MEMS devices for *in-situ* electron microscopy mechanical testing of thin films and one dimensional (1-D) nanostructures [1, 2]. The second experimental methodology addresses the *in-situ* SEM testing of NEMS to assess device electro-mechanical performance (pull-in voltage, I-V curves, and time response) and reliability [3].

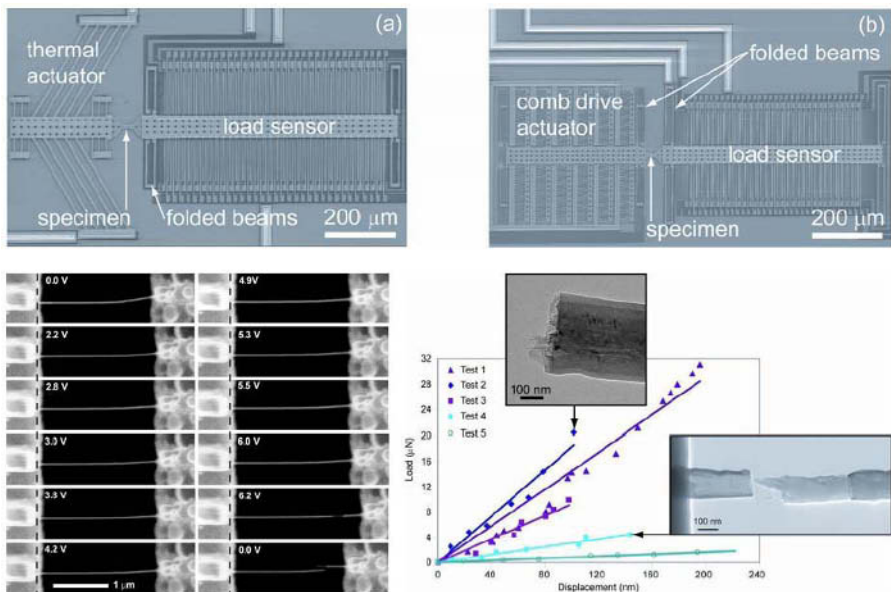


FIGURE 1. (a) Displacement-controlled and (b) force-controlled MEMS-based n-MTS. (c) Sequential SEM images showing the tensile testing of a multi-walled CNT using the n-MTS. (d) Load-displacement data obtained using the n-MTS on MWNTs exposed to varying types and degrees of radiation. Irradiation dose decreases with the test number [2].

The design, microfabrication, and operation of a MEMS-based nanoscale material testing system (n-MTS) will be presented. Results obtained from *in-situ* SEM and TEM tensile testing of

NWs and CNTs will be discussed. Specifically, tensile tests of NWs confirm predictions that material strength increases as its scale decreases. Tensile tests of multi-walled CNTs exposed to varying types and degrees of radiation reveal a stiffening effect that occurs with irradiation. This is attributed to radiation-induced crosslinking between concentric shells of the multi-walled CNTs to improve load sharing.

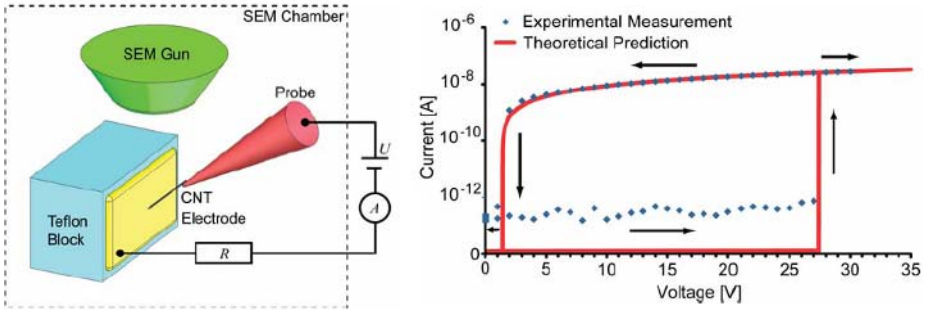


FIGURE 2. Left: Schematic of the experimental setup for in-situ SEM testing of nanotube cantilever devices. Right: Comparison of experimentally-measured and theoretically-predicted current-voltage behavior of the nanotube cantilever devices [3].

A carbon nanotube NEMS bistable switch with feedback control, developed in our lab, will be used to demonstrate methods of *in-situ* SEM testing (Fig. 2). This example will also be used to highlight present and future research challenges. Experimental results showing good agreement with theoretical predictions of current-voltage behavior will be discussed. Experimentally-observed failure modes will also be discussed. These failure modes, which may be common to other nanotube-based NEMS, are a current topic of interest as they preclude production of reliable, large-scale arrays of these devices.

## References

1. Zhu, Y., and Espinosa, H. D., PNAS, vol. **102**, 14503-14508, 2005.
2. Espinosa, H.D., Zhu Y., Moldovan N., JMEMS, in press, 2007.
3. Ke, C.-H. and Espinosa, H. D., *Small*, vol. **2**, 1484-1489, 2006.

## AIR BLAST LOADING OF CELLULAR MEDIA

George A. Gazonas and Joseph A. Main

U.S. Army Research Laboratory, Weapons and Materials Research Directorate,  
Aberdeen Proving Ground, Maryland, 21005-5069, U.S.A.  
National Institute of Standards and Technology  
100 Bureau Drive, Mail Stop 8611, Gaithersburg, Maryland, 20899-8611, U.S.A.  
gazonas@arl.army.mil, joseph.main@nist.gov

Much of the early literature on shock and wave propagation in porous media is found in the geophysical literature, but Riemann [1] was the first to describe how a compressional wave transforms into a shock wave. A century later, shock and particle velocity measurements in solids enabled McQueen et al. [2] to develop Hugoniot for minerals thought to comprise the earth's interior. This naturally led to the study of shock-induced phase transformations in minerals as the possible cause of the major body-wave velocity discontinuities in the Earth. The interest in shock wave loading of porous geologic media accelerated with the advent of underground nuclear testing (e.g. at the Nevada test site [3]), and concurrent computational modeling of such events [4]. Studies of shock and wave propagation in porous and permeable sedimentary media [5] ensued during the era of oil exploration. Today, the wide-spread use of porous materials such as cellular foams and honeycombs in structural applications is attributed to their capacity to absorb energy, particularly at low impact velocities. Surprisingly, however, the use of porous crushable materials subjected to air blast pressure loading has, in many instances, led to the enhancement rather than mitigation of blast effects [6, 7, 8].

In order to gain a better understanding of the mechanics of shock wave propagation in cellular media, an analytical model [9] will be presented that investigates the influence of mass distribution on the uniaxial crushing of cellular material sandwiched between rigid layers. This model is also applicable to the crushing of cellular media in "blast pendulum" experiments. In the analytical model, the cellular core is modeled as a continuum using a rigid, perfectly-plastic, locking idealization. The front and back faces are modeled as rigid masses, with pressure loading applied to the front face, and unrestrained motion of the back face. Predictions of this analytical model show excellent agreement with explicit finite element computations [9, 10]. The model is designed to investigate the influence of the mass distribution between the core and the faces on the system response. An increase in the mass fraction in the front face is found to increase the impulse required for complete crushing of the cellular core but also produces an undesirable increase in back-face accelerations. Optimal mass distributions are found that maximize the impulse capacity while limiting the back-face accelerations to a specified level [9].

Finally, this paper will extend previous work [9], to include a class of cellular media that exhibits a continuously nonhomogeneous plateau yield stress distribution. The plateau yield stress magnitude could be graded by spatially varying the relative density of the foam. This will influence the microphysical failure mechanisms, either through buckling, plastic yielding, or crushing of the cell walls [11]. Several concepts are also discussed for possibly mitigating the effects of the transmitted shock wave in light of recent advances in related fields [12, 13].

**References**

1. Riemann, B., Über die Fortpflanzung ebener Luftwellen von endlicher Schwingweite. *Abhandl der Göttinger Ges der Wiss*, vol **8**, 43, 1860.
2. McQueen, R.G., Marsh, S.P., and Fritz, J.N., Hugoniot equation of state of twelve rocks. *J. Geophys. Res.*, vol. 72, 4999-5036, 1967.
3. Borg, I.Y., Some shock effects in granodiorite to 270 kilobars at the Piledriver site. In *Flow and Fracture of Rocks, Geophysical Monograph 16*, American Geophysical Union, Washington, 293-311, 1972.
4. *Ground Motion Models and Computer Techniques*, Systems, Science and Software, DNA Report No. 3SR-1071, 1972.
5. Bloom, F., Constitutive models for wave propagation in soils, *Transactions of the ASME*, vol. **59**, 146-175, 2006.
6. Seitz, M.W., and Skews, B.W., Effect of compressible foam properties on pressure amplification during shock wave impact. *Shock Waves*, vol. **15**, 177-197, 2006.
7. Hanssen, A.G., Enstock, L., and Langseth, M., Close-range blast loading of aluminum foam panels. *Int. J. of Impact Eng.*, vol. **27**, 593-618, 2002.
8. Xue, Z., and Hutchinson, J.W., A comparative study of impulse-resistant metal sandwich plates. *Int. J. of Impact Eng.*, vol. **30**, 1283-1305, 2004.
9. Main, J.A., and Gazonas, G.A., Uniaxial crushing of sandwich plates under air blast: influence of mass distribution. *Int. J. of Solids and Struct.*, in review, 2006.
10. AUTODYN<sup>®</sup> Explicit Software for Nonlinear Dynamics, User Manual Version 6.0, Century Dynamics Inc., 2005.
11. Ben-Dor, G., Mazor, G., Igra, O., Sorek, S., and Onodera, H., Shock wave interaction with cellular materials, Part II: open cell foams; experimental and numerical results. *Shock Waves*, vol. **3**, 167-179, 1994.
12. Thamburaj, P., Santare, M.H., and Gazonas, G.A., The effect of graded strength on damage propagation in continuously nonhomogeneous materials. *J. Eng. Mats. Technol.*, vol. **125**, 412-417, 2003.
13. Gazonas, G.A., Weile, D.S., Wildman, R., and Mohan, A., Genetic algorithm optimization of phononic bandgap structures. *Int. J. of Solids and Struct.*, vol. **43**, 5851-5866, 2006.

## IMPORTANCE OF FULL-FIELD MEASUREMENT TECHNIQUES FOR BETTER MODELS IN SOLID MECHANICS

Michel Grediac

Laboratoire de Mécanique et Ingénieries  
Université Blaise Pascal. Institut Français de Mécanique Avancée  
Campus de Clermont-Ferrand. Les Cézeaux  
BP 265, 63175 Aubière Cedex, France  
Michel.Grediac@univ-bpclermont.fr

During the two last decades, the improvements in image processing with microcomputers and the advances in camera technology have caused non contact measurement techniques such as digital image correlation, moiré interferometry, speckle, grid method or infrared thermography to become more and more popular in the experimental mechanics community [1]. This is clearly illustrated by the increasing number of recent papers in which such techniques are used to improve the knowledge in the mechanical behaviour of materials and structures.

The aim of this presentation is to give an overview of the use of full-field measurement techniques in experimental solid mechanics. A keyword and a guideline are proposed for this purpose.

Full-field measurement techniques enable to detect and to quantify heterogeneities in displacement, strain or temperature fields. "Heterogeneity" can therefore be regarded as a common keyword of all studies involving these techniques.

It is then proposed to use the link between full-field measurement techniques and modelling to classify recent papers published in the literature in this area. Such techniques can be used at different stages, for instance:

- to observe and to discover some local phenomena. For instance, full-field measurement techniques enable to detect very local strain gradients or displacement discontinuities such as cracks [2]. This information is very relevant and useful to construct more reliable constitutive equations of materials;
- to perform unbiased mechanical tests, for instance by detecting some unexpected heterogeneities due ill-controlled boundary conditions. Most of the data collected during classical tests such as tensile tests are processed under the assumption of homogeneous strain fields. In the case of tensile test, full-field measurement techniques enable to detect the effect of misaligned grips. In the case of shear test, strain heterogeneities which take place near to the free boundaries of the specimen as well as possible parasitic bending of the supports can be detected and quantified with such techniques [3]. This leads to the determination of more reliable parameters used to feed constitutive models of materials;
- to verify the validity of some assumptions under which numerous models describing the mechanical response of structures are constructed. In thick beam bending problems for instance, an assumption is made concerning the displacement and shear strain distributions through the thickness. Various theories are deduced from this assumption such as the first or higher order theories. The latter corresponds to an enrichment of the functions describing the through-thickness displacement field. In the case of higher theories, a warping of the cross section occurs. This warping can be detected using full field measurement techniques, thus validating such theories [4].

- to compare experimental displacement or strain fields to their numerical counterparts to validate models [5]. The final goal in mechanics of structure is mainly to correctly compute the stress/strain/displacement fields within the structures. Full-field measurement techniques can be used to capture displacement fields on the external surface of tested structures and therefore to verify whether numerical or analytical models are correct or not;
- to process heterogeneous strain field using mixed experimental/numerical strategies in order to simultaneously extract an important number of parameters governing constitutive equations. Usual testing procedures are based on mechanical tests which are supposed to give rise to homogeneous stress/strain fields. In this case, measuring the strain at one point is sufficient and one can establish a direct link between loading and measured strain. With such an approach, only a reduced number of constitutive equations can be identified. On the other hand, heterogeneous strain fields often involve a much greater number of constitutive parameters. Capturing such fields and extracting constitutive parameters is an issue since no direct link generally exists between measured strain and unknown parameters. Specific identification strategies among which the virtual fields method [6] have been recently developed for this purpose.

This classification along with some relevant examples will be presented throughout the paper and the importance of full-field measurement techniques for the construction of better models in solid mechanics will be underlined. A special emphasis will also be given to the last section dealing with the processing of full-field measurements to identify parameters governing constitutive equations.

## References

1. Grédiac M., *Composites Part A*, vol. **35**, 751-761, 2004.
2. Toussaint E., Destrebecq J.-F. and Grédiac M., *Cement and Concrete Composites*, vol. **27**, 399-411, 2005.
3. Grédiac M. and Dufort L., *Experimental Mechanics*, vol. **42**, 186-193, 2002.
4. Dufort L., Grédiac M. and Surrel, Y., *Composite Structures*, vol. **51**, 37-47, 2001.
5. Mathias, J.D., Balandraud, X. and Grédiac M., *Composites Part A*, vol. **37**, 177-190, 2006.
6. Grédiac M., Toussaint E. and Pierron.F., *International Journal of Solids and Structures*, vol. **39**, 2691-2705, 2002.

## RECENT DEVELOPMENTS AND APPLICATIONS OF PHOTOMECHANICS METHODS FOR MICROELECTRONICS PRODUCT DEVELOPMENT

Bongtae Han  
Mechanical Engineering Department  
University of Maryland  
College Park, MD 20742  
bthan@eng.umd.edu

The traditional role of mechanical analysis in electronic packaging had been reliability assessment of microelectronic and photonic devices at the final stage of development. The shrinking product development cycle time, however, has changed the role of mechanical analysis from a problem solving (passive) mode to a predictive (active) mode, where the mechanical analysis is performed for (1) design optimization and (2) reliability prediction of a new technology product at its conceptual stage of development. This dependency of product development on mechanical analysis has fostered increasing activity in mechanical experimentation, both for specific studies and for guidance of numerical modeling.

As the components and structures involved in high-end devices are made smaller, the thermal gradient increases and the strain concentrations become more serious. Numerical analyses have been used extensively to estimate stresses and strains in device structures. Although one can model almost any kind of device for complex loading and boundary conditions, simplifications and uncertainties are inevitable. The models and results usually require verification by other means. Accordingly, advanced experimental techniques are in high demand to provide accurate solutions for deformation studies of microelectronic and photonic devices.

In recent decades, numerous optical methods for deformation measurements have matured and emerged as important engineering tools. With these methods, the data are received as whole-field fringe patterns representing contour maps of equal displacements. Recently, several methods have been applied to microelectronic and photonic product development [1,2]. They include moiré interferometry, microscopic moiré interferometry, Twyman/Green interferometry, far infrared Fizeau interferometry and shadow moiré. The first two provide contour maps of in-plane displacement fields for stress/strain analyses, and the next three map out-of-plane displacement fields for warpage analyses.

Figure 1 illustrates an example of moiré interferometry. The specimen is a flip-chip plastic ball grid array (FC-PBGA) package assembly. In the assembly, a silicon chip was first attached to an organic substrate through tiny solder bumps. This subassembly was then surface-mounted to a typical FR-4 printed circuit board (PCB) through larger solder ball arrays to form a final assembly. A specimen grating was replicated at 82°C using a high temperature curing epoxy and the fringes were recorded at room temperature ( $\Delta T = -60^\circ\text{C}$ ). The difference of the coefficient of thermal expansion (CTE) between the substrate and the PCB caused the deformations in the solder balls.

An example of out-of-plane displacement measurement technique is shown in Fig. 2. The warpage of a PBGA package is attributed to a large mismatch of CTE between the chip and substrate. As mentioned earlier, electrical and mechanical connections are made by solder balls between the substrate and a PCB in the subsequent assembly process. If the bottom side of the substrate warps significantly at the solder reflow temperature, as illustrated in Fig. 2, it yields an uneven height of solder interconnections, which could cause premature failure of the assembly. Figure 2 shows the shadow moiré fringes on the bottom surface of the package after processed by

the *phase shifting technique*. Detailed knowledge of this out-of-plane deformation is essential to optimize design and process parameters for reliable assemblies.

This paper presents recent developments of the methods as tools for product development of microelectronic and photonic devices and illustrates selected applications for design evaluation, failure analysis, and verification of numerical modeling.

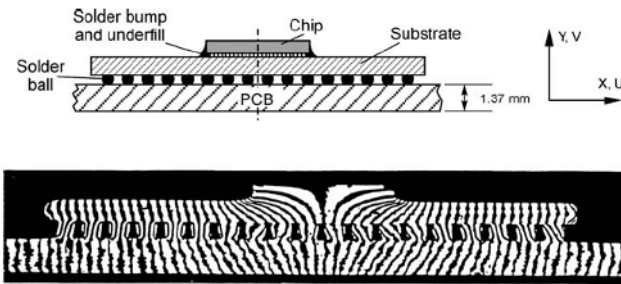


FIGURE 1. U displacement fields of a FC-PBGA package assembly documented by moiré interferometry. The deformation was induced by thermal loading of  $\Delta T = -60^\circ\text{C}$ .

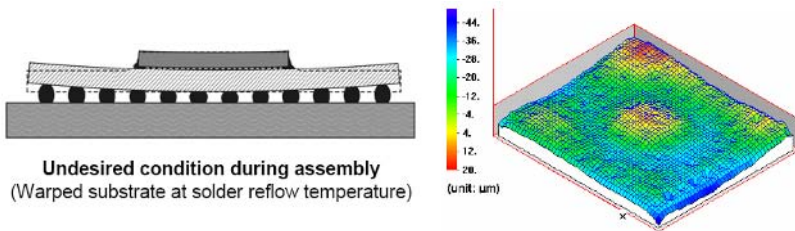


FIGURE 2. Warpage of the bottom surface of a plastic ball grid array package at the solder reflow temperature.

## References

1. Han, B., *J. Thermal Stresses*, vol. **19**, 583-613, 2003.
2. Han, B., 14. Characterization of Stresses and Strains in Microelectronic and Photonic Devices Using Photomechanics Methods, *Micro-and Optoelectronic Materials and Structures: Physics, Mechanics, Design, Reliability, and Packaging*, Y. C. Lee and A. Suhr, ed., Springer, NY, 2006.



## A TENTATIVE ANALYSIS OF THE STATUS OF SPECKLE INTERFEROMETRY IN EXPERIMENTAL MECHANICS

Pierre Jacquot

Nanophotonics and Metrology Laboratory, Swiss Federal Institute of Technology Lausanne  
EPFL-STI-NAM, Station 11, CH-1015 Lausanne, Switzerland  
pierre.jacquot@epfl.ch

The paths followed by a new technique before being widely accepted are generally not straightforward. Speckle interferometry (SI) certainly does not escape the rule.

As far as I remember, the articles by Leendertz, [1], and Butters, [2], aroused a considerable interest in the early 70s among the holographic interferometry (HI) community. Scientists working in the field of optical metrology were astonished to discover that the direct recording of a 2-beam interference pattern between a reference and a speckle wave carries in itself the phase information of the speckle wave, without the need to reconstruct its 3D complex amplitude as in holography – a step absolutely obvious nowadays. This was the birth of SI. Though most of the first recordings were made with very high spatial resolution emulsions – the same as in holography – the new paradigm, in practice, was clearly leading the way for low spatial resolution media. Indeed, video cameras soon became a standard, and the name ESPI, for Electronic Speckle Pattern Interferometry, was coined. The choice of low spatial resolution – by no means a necessity but widely adopted for evident reasons of convenience – produced at first two opposite outcomes: a rapid acceptance of the new method, due to its simplicity and the availability of photoelectric imagers and analogue processing electronics, by someone, and, on the contrary, a rejection by others, belonging mostly to the HI circles, who didn't accept the heavily speckled aspect of SI fringes, see Figs. 1 and 2.

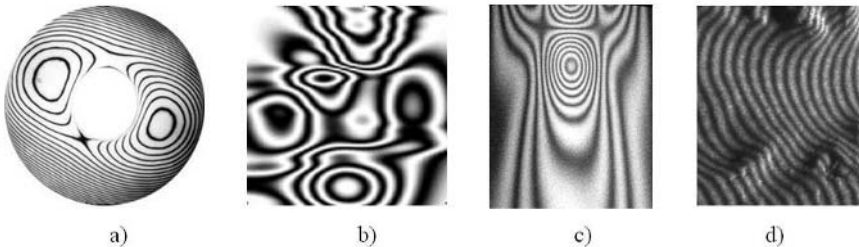


FIGURE 1. Examples of fringe patterns. a) classical Fizeau fringes of a computer hard disc; b) MATLAB “peaks” function depicted as a classical fringe pattern; c) HI fringes of a cylinder locally heated; d) contouring using coherent fringe projection on a cast of pathological scar.

These figures give a dramatic idea of the fundamental differences in quality between SI and HI interference patterns, the latter being quite similar to classical fringes. Moreover, researchers in HI were thinking, rightly or wrongly, that the theory of SI was completely contained in the theory of HI, as developed for example by Schumann [3].

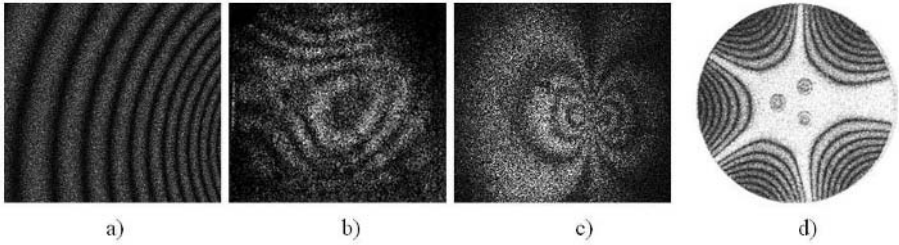


FIGURE 2. Examples of SI fringe patterns. a) simulated ideal SI correlation fringes; b) out-of-plane fringes of a  $2.8 \times 4 \text{ m}^2$  plaster wall; c) shearing SI fringes of the same wall locally heated; d) out-of-plane Bessel-type fringes of a disc vibrating at a resonance frequency of 1.9 kHz.

However, this nascent antagonism between a “noble” and a “poor man” technique didn’t develop any further, simply because high spatial resolution media ceased progressively to be commercially available. Comprehensible for the silver halide and dichromated emulsions, the stop in production, amazingly, touched even the efficient thermoplastic plates and films, and the photorefractive materials never really broke through. Exit HI and long live SI! At the same time, the rapid growth of digital image processing, both in hardware and software, more propitious to SI than to HI, gave a second lift to the former. Fig. 3 shows the result of the processing of SI correlation fringes using phase shifting and adapted filtering techniques. The demonstration was made that high quality phase maps could be obtained by SI.

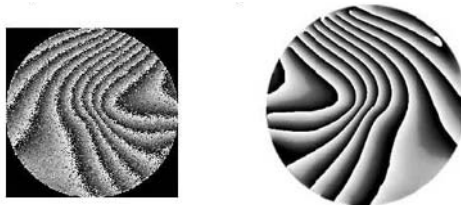


FIGURE 3. Examples of SI phase maps. Left: rough result of a 5-image phase stepping algorithm; right: the same map after linear filtering.

Interestingly, in the last few years, HI is reappearing on the constantly evolving optical metrology scene, under the label “*digital holography*”. Some variants of digital SI and HI are in fact very close to each other, looping the loop.

Besides such chronological markers, the contribution attempts to analyse the role of speckle interferometry in experimental mechanics from a scientific point of view, mainly inspired by the paper [4] and the references therein.

## References

1. Leendertz, J.A., *J. Phys. E: Sci. Instrum.*, vol. **3**, 214-218, 1970.
2. Butters, J.N., Leendertz, J.A., *Opt. Laser Technol.*, vol. **3**, 26-30, 1971.
3. Schumann, W., Dubas, M., *Holographic Interferometry*, Springer-Verlag, Berlin, 1979.
4. Jacquot, P., In *Proceedings of SPIE*, vol. **6252**, V. Sainov et al. Eds., 2005, 1S 1-12.

## ON THE CHARACTERISATION OF CELLULAR MATERIALS USED IN SANDWICH CONSTRUCTION

R.A.W. Mines  
Department of Engineering  
University of Liverpool, Brownlow Street  
Liverpool, L69 3GH, UK  
r.mines@liv.ac.uk

The paper gives an overview of issues relating to the characterisation of the progressive collapse of core cellular materials used in sandwich construction. The specific structural application addressed is foreign object impact, and in this case the core cellular material is subject to multi axial stresses, progressive collapse and possible rupture.

Crushable foams have been used for many years as core materials. Possible foam materials are based on polymers (e.g. Divinycell, Rohacell), metals (e.g. Alporas) and graphite. It has been shown that the mechanical properties of cellular materials, e.g. elastic behaviour, uniaxial crush and densification, are dependent on the cell geometry, on the cell size (foam density) and on the parent material.

For example, truncated octahedral shell structures have been proposed to characterise elastic and collapse behaviour of Rohacell foam [1]. Mills and Zhu [2] develop this truncated octahedral approach to model a single cell with edges and faces. Typically, cell edges contain 40% of the material in a closed cell foam. Additional complexity comes from the variation of cell size in foams.

These (and other) cellular models have been developed and validated for simple loading cases, e.g. elastic behaviour and uniaxial crush. However, a feature of foam behaviour during the progressive collapse of a sandwich beam or the perforation of a sandwich panel is multi axial crush. This can be simulated using finite element analysis and continuum models, in which not only deviatoric deformation is taken into account but also hydrostatic effects [3]. However, such models require extensive experimental data as input, e.g. hydrostatic compression and even hydrostatic tension data [4, 5].

One of the disadvantages of the continuum modelling approach for crushable foams is the occurrence of strain softening in some foams, e.g. Rohacell. This gives rise to strain localisation, which means that strains are discontinuous through a volume being crushed [6].

Other issues relating to the characterisation of foams are as follows. Metallic foams (e.g. Alporas) have large cell size that can make a continuum analysis inappropriate for cores with small relative dimension. Also, such foams have variable cell size by up to a factor of five, which means that there are large property variations through a core volume [7, 8].

It is perhaps worth noting here the direct approach of taking a computed X ray tomography picture of the full depth of the foam and inputting the geometry into a finite element analysis [9]. This is a useful approach for small blocks of material but it is still problematic for the non linear behaviour of large scale structures. Also, the approach does not give transparent understanding of micro structural effects.

Another driver for micro mechanical models is the development of manufacturing procedures for lattice structures. These include conventional manufacturing techniques [10] as well as more advanced manufacturing techniques [11]. In the latter, the rapid prototyping selective laser melting technique allows the realisation of metallic open cellular lattice structures at the micro meter scale

[11,12]. This manufacturing technique allows the tailoring of lattice structure and even the realisation of graded structures.

The paper identifies possible modelling approaches, and associated experiment study, required to develop micro mechanical models and hence progress our understanding of the use of cellular materials as optimal cores in sandwich construction.

## References

1. Chen, C.P., Lakes, R.S., *Cellular Polymers*, **14** (3), 186-202, 1995
2. Mills, N.J., Zhu, H.X., *J. Mech Phys Sol*, **47**, 669-695, 1999
3. Deshpande, V.S., Fleck, N.A., *J. Mech Phys Sol*, **48**, 1253-1283, 2000
4. Mines, R.A.W., Alias, A., *Composites Part A*, **33**, 11-26, 2002
5. Li, Q.M., Mines, R.A.W., Birch, R.S., *Int J Sol Struct*, **37**, 6321-6341, 2000
6. Li, Q.M., Mines, R.A.W., *Strain*, **38**, 132-140, 2002
7. McKown, S., Mines, R.A.W., *Journal of Applied Mechanics and Materials*, **1-2**, 211-216, 2004
8. McKown, S., Mines, R.A.W., Impact behaviour of metal foam cored sandwich beams, In *ECF16* (Ed. E.E. Gdoutos), Paper No. **254**, 2006
9. Youssef, S., Maire, E., Gaertner, R., *Acta Materialia*, **53**, 719-730, 2005
10. Wadley, H.N.G., Fleck, N.A., Evans, A.G., *Composites Science and Technology*, **63**, 2331-2343, 2003
11. Santorinaios, M., Brooks, W., Sutcliffe, C.J., Mines, R.A.W., *WIT Transactions on the Built Environment*, **85**, 481-490, 2006
12. Mines, R.A.W., McKown S., Cantwell W., Brooks W., Sutcliffe C.J., On the progressive collapse of micro lattice structures, In *ICEM13* (Ed. E.E. Gdoutos), Paper No. **158**, 2007

## THREE-DIMENSIONAL DISPLACEMENT ANALYSIS BY WINDOWED PHASE-SHIFTING DIGITAL HOLOGRAPHIC INTERFEROMETRY

Yoshiharu Morimoto, Toru Matui and Motoharu Fujigaki

Faculty of Systems Engineering, Wakayama University

Sakaedani, Wakayama 640-8510, Japan

morimoto@wakayama-u.ac.jp, matui@sys.wakayama-u.ac.jp, fujigaki@sys.wakayama-u.ac.jp

Digital holography is useful to reconstruct three-dimensional shapes of objects. The reconstruction process of the objects is fast and accurate because the reconstruction is performed by computer calculation without developing photographic plate. Phase-shifting digital holographic interferometry is possible to measure shape and displacement of objects quantitatively. The authors developed windowed phase-shifting digital holographic interferometry (WPSDHI) which provides very accurate results by decreasing the effect of speckle noise.

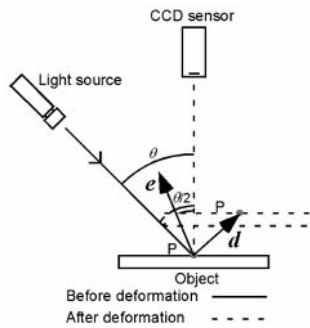


FIGURE 1. Positional relationship between light source, object and observation point

In order to measure three-dimensional displacement components, three-directional-illumination method or three-directional-observation method is usually employed. It is important for accurate analysis to measure the three-dimensional information simultaneously. In this paper, a simultaneous three-directional illumination method is proposed (Figs 1 and 2). To miniaturize the equipment for practical use, a spherical beam is used. However, if the spherical wave is used, incident angles are different for each point and then each point has different sensitivity vectors. The incident angle for each point on objects is determined by the three-dimensional positions of the point and the point source of light. It is, however, difficult to measure it accurately. The authors propose a calibration method with a reference flat plane. The reference plane is installed on a XYZ piezo stage which is movable in three axis directions with very small amount. The reference plane is moved in three directions with very small amount. By calculating the each phase difference between before and after deformation using the digital holography, the parameter can be obtained for relational expression of displacement and phase difference. Tabulation of parameters for each point helps to measure the displacement and strain in high speed from the phase difference of the specimen. Displacement and strain measurement using spherical wave can be realized with this calibration method. Experimental results of deformation measurement using this method are shown.

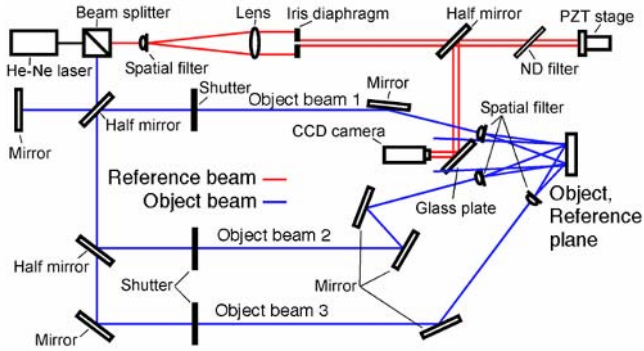


FIGURE 2. Optical setup for three-directional displacement analysis

## References

1. U. Schnars and W. Jüptner, *Digital Holography*, Springer, 2005.
2. I. Yamaguchi and T. Zhang, "Phase-shifting digital holography", *Opt. Lett.*, vol. **22**(16), pp.1268-1270, 1997.
3. Morimoto, Y., Nomura, T., Fujigaki, M. Yoneyama S. and Takahashi, I., Deformation Measurement by Phase-shifting Digital Holography, *Experimental Mechanics*, vol. **45**(1), 65-70, 2005.
4. Fujigaki, M., Matui, T., Morimoto, Y., Kita, T., Nakatani, M. and Kitagawa, A., Development of Real-Time Displacement Measurement System Using Phase-Shifting Digital Holography, *Proceedings of the 5th International Conference on Mechanics of Time Dependent Materials (MTDM05)*, 160-163, 2005.
5. Morimoto, Y., Matui, T., Fujigaki, M. and Kawagishi, N., Effect of Weight in Averaging of Phases on Accuracy in Windowed Digital Holographic Interferometry for Pico-meter Displacement Measurement, *Proc. of SPIE*, vol. **6049**, 60490D (CD-ROM), 2005.

## ONR SOLID MECHANICS RESEARCH PROGRAM OVERVIEW

Yapa D. S. Rajapakse  
Program Manager, Solid Mechanics  
Office of Naval Research (ONR 332)  
Arlington, VA 22203-1995, U.S.A.  
rajapay@onr.navy.mil

Naval structures operate in severe environments, and are designed to withstand complex multi-axial loading conditions, including highly dynamic loadings. The effective design of these structures requires an understanding of the deformation and failure characteristics of structural materials, and the ability to predict and control their performance characteristics.

The Solid Mechanics Research Program at the Office of Naval Research provides the scientific basis for the effective design of affordable Naval structures. Today, the major focus is on mechanics of marine composite materials and composite sandwich structures. The program deals with understanding and modeling the physical processes involved in the response of glass-fiber and carbon-fiber reinforced composite materials and composite sandwich structures to static, cyclic, and dynamic, multi-axial loading conditions, in severe environments (sea water, moisture, temperature extremes, and hydrostatic pressure).

An overview will be provided of this Navy-unique research program, with a discussion of its objectives, research issues, recent accomplishments, and future directions. Topics discussed will include: effect of sea water on marine composites, and composite sandwich structures; long-term durability of marine composites; size effects in failure of composite sandwich structures; fatigue behaviour of woven and knitted fabric composites; impact damage in sandwich structures; effect of impact damage on fatigue; strain rate effects in marine composites; dynamic fracture of interfaces; dynamic interaction effects in multiple delaminations; fatigue of foam core used in sandwich structures; and concepts for mitigating impact damage in sandwich structures.

Research is also conducted into methods for the enhancement of mechanical/physical properties and for the introduction of multi-functionality to composite structures, through the use of nanoparticles. Topics will include experimental techniques for the visualization of nanoparticle dispersion, buckling of single-walled carbon nanotubes, and thermoplastic/carbon nanotube films for strain sensing.

Future directions of research in mechanics of marine composites and sandwich structures will be discussed, including shock and blast effects on composite structures, experimental investigations of blast effects, progressive damage modeling, high strain rate effects in core materials, effects of transverse core compressibility, and concepts for blast resistance.

### References

1. *Proceedings of Analysis and Design Against Local Effects in Sandwich Structures*, Office of Naval Research (ONR) Solid Mechanics Program - Marine Composites and Sandwich Structures, edited by Y. Rajapakse, University of Maryland, March 2004.

## LARGE-DEFORMATION CONSTITUTIVE THEORIES FOR STRUCTURAL COMPOSITES: RATE DEPENDENT CONCEPTS AND EFFECT OF MICROSTRUCTURE

Kenneth Reifsnider and Liqun Xing  
Department of Mechanical Engineering  
University of Connecticut, Storrs, CT 06269, U.S.A.  
Reifsnider@enr.uconn.edu

Continuous-fiber reinforced structural composite materials are typically classified as “brittle,” with strains to break in the principal fiber directions of only a percent or so. However, fiber architectures and material choices provide “ductility” that is highly dependent on microstructure. Woven glass-reinforced polymer systems, for example, with strains to break on the order of 20 percent for uniaxial loading in off-axis directions are now in common use in a variety of applications, including Naval structures. An example of such behaviour for three different strain rates is shown in Fig. 1.

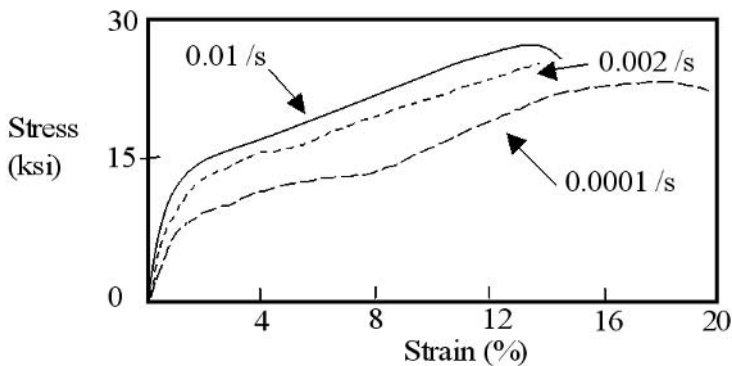


FIGURE 1. Stress-strain response of woven-glass reinforced vinyl ester for uniaxial loading at 45 degrees to the fiber axis, at three different strain rates.

In some situations, the off-axis “ductility” can be exploited to greatly improve performance. One of those situations is blast loading, in which out-of-plane, high-rate loading is applied in a fairly localized area. The present paper will address this class of material response.

In this study, a plain-weave vinyl ester composite material was selected and a number of different strain rate and temperature tensile tests of off-axis coupon specimens were conducted. Comparison of composite nonlinear behavior under different strain rate and temperatures indicated that there was a strain rate–temperature relationship that could be used to relate them. The paper will begin with experimental characterization methods and analysis methods for rate-dependent, large deformation response of anisotropic materials. The approach will be a generalization and refinement of earlier work by the authors, their colleagues, and others[1-4]. In the present case the previous work will be expanded to include large strains, up to about 20 percent. The principal thrust of that effort will be to include progressive damage up to the point of rupture into



constitutive equations that can be used in commercial codes for implementation in structures. An example of model predictions compared to observed response is shown in Fig. 2.

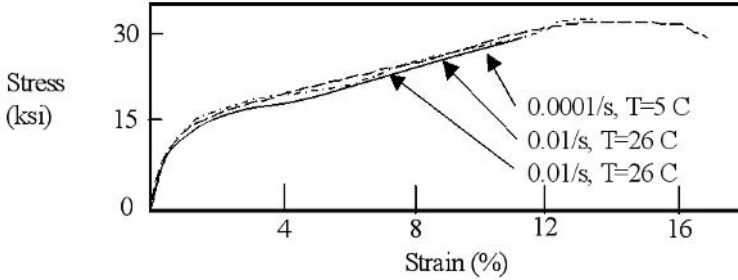


FIGURE 2. Validation of 30° specimen test data at different strain rate and temperature.

The representations of that response will then be discussed in terms of the microstructure of the materials involved. Strength concepts will be introduced, and related to the microstructure. It will be shown that strain to break can be estimated from a fundamental knowledge of the manufacturing details of the composite material. Special attention will be given to constructing strength concepts and criteria that are rate dependent. A Monkman-Grant concept will be generalized to yield a strength concept that reduces all strength parameters for an anisotropic material to a single material constant, for all directions of loading and all strain rates.

Finally, implementation of such an approach for large strain analysis of structures which have nonuniform strain will be discussed, using commercial codes such as ABAQUS. Comparisons between experimental predictions of structural failure modes and structural strength and observations will be presented.

## References

1. Tamuzs, V.m, Dzelzitis, K. and Reifsnider, K.L., Applied Composite Materials, vol. **11**, no.5, 259-279, 2004
2. Tamuzs, V.m, Dzelzitis, K. and Reifsnider, K.L., Applied Composite Materials, vol. **11**, no.5, 281-293, 2004
3. Ogihara, S. and Reifsnider, K.L., Applied Composite Materials, vol. **9**, 249-263, 2002
4. Sun C.T. and Chen, J.L., Composite Materials, vol. **23**, 1009-11020, 1989

---

## EXPERIMENTAL MECHANICS AT THE NANOMETRIC LEVEL

Cesar A. Sciammarella  
Dipartimento di Ingegneria Meccanica e Gestionale  
Politecnico di Bari, Bari, 70126, Italy  
csciamma@poliba.it  
Department of Mechanical, Materials and Aerospace Engineering  
Illinois Institute of Technology, Chicago (IL), 60616 - USA  
sciammarella@iit.edu

Recent advances in the science and technology have originated the need of developing new tools to make observations at the molecular level. Nano-sciences and technology provide a great challenge to experimental mechanics and at the same time extend the horizons of the discipline to new grounds and novel problems.

Of the different disciplines that are required to meet the challenges presented by nano-sciences and technology, optics is a tool that seems particularly adapted for this task. However, classical optics puts a limit to the possibility of making measurements beyond half of the wavelength of light: that is, a couple of hundreds of nanometers at best. However, this quantity is not good enough to perform studies in the nanometric range.

Recent developments in the field of optics have brought back some features of light that have been known for at least half of a century. The limit of Rayleigh that has been thought for long time insurmountable has been proven valid only for certain types of illumination techniques. In the late 1940's, Toraldo di Francia started both experimentally and theoretically to work towards getting beyond the Rayleigh limit. Today, his predictions have come to be a reality.

Quite independently on these developments, in the area of data analysis began the exploration to overcome the classical limit in optics by numerical means. On the mathematical basis of two fundamental theorems, methods have been developed in the spatial domain and frequency domain that have proven that effective to get information beyond the classical limit. The combined use of the new developments in optics and in numerical methods of data analysis give us the confidence that in the near future optical information will be gathered and analyzed within the range that previously was thought only reachable by the electron microscope.

## MECHANICAL PROPERTY MEASUREMENT AT THE MICRO/NANO SCALE

W. N. Sharpe, Jr.  
Department of Mechanical Engineering  
Johns Hopkins University  
Baltimore, Maryland 21218, USA  
sharpe@jhu.edu

There are three main challenges in measuring the mechanical properties of specimens with minimum dimensions on the order of microns or less – preparation and handling, force application and measurement, and strain measurement. This is a brief overview of the various test methods with emphasis on tensile testing because it produces a uniform stress and strain field, which enables unambiguous property measurements.

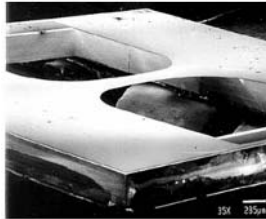


FIGURE 1. Wide, thin tensile specimen. The gage cross-section is 3.5 by 600  $\mu\text{m}$ .

A wide and robust tensile specimen is shown in Fig. 1 from Sharpe et al. [1]. The polysilicon film is 3.5  $\mu\text{m}$  thick in this case, although aluminium films 60 nm thick have been tested. The silicon die supporting the film is one cm square and is etched out from the back to release the gage section. After the wide grip ends have been glued into a small test machine, the two side support strips are cut to leave a free-standing tensile specimen. The test machine consists of a movable grip supported by an air bearing and a 100-gram force load cell mounted on a piezoelectric actuator.

Sharpe et al. [2] have tested smaller polysilicon specimens (50  $\mu\text{m}$  wide); several of these can be produced on a single die by photolithography and etching from the front. One end of the specimen remains fixed to the die, and the other end has a large paddle that is released from the silicon die and gripped by gluing a small silicon carbide fiber to it. The die is glued into the test machine and specimens tested in sequence.

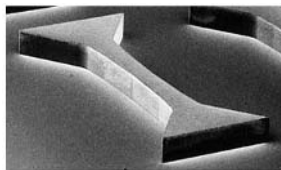


FIGURE 2. Large, thick tensile specimen. The gage cross-section is 200 by 200  $\mu\text{m}$ .

Fig. 2 from Sharpe et al. [3] shows a larger specimen that can be handled separately. It is nickel electroplated into a photoresist mold on a silicon substrate, which is then removed. The cross-section of the gage section is  $200 \times 200 \mu\text{m}$ , and the wedge-shaped ends fit into inserts in the grips of a test machine that has a larger load cell.

Strain can be measured directly on these specimens by either laser interferometry or digital imaging. In the first case, reflective markers must be placed on the specimen surface and illuminated with a laser. The resulting interference fringes move as the specimen is strained and can be monitored to enable real-time measurements. The markers are either gold lines deposited as the last step in the specimen manufacture [1, 2] or indentations by a diamond indenter [3]. Digital imaging requires no surface preparation unless it is exceptionally smooth, but requires post-processing to generate the strains. The images can either be optical as in Long et al. [4] or from an atomic force microscope scan as in Chasiotis et al. [5]. Poisson's ratio can be determined by either of these methods. A different tensile test is conducted by Espinosa et al. [6] who use a nanoindenter to push down the center of gold tensile strips fastened at each. Strain is measured by optical interferometry to determine the displacement along the specimen length.

There are several indirect tests that have advantages although they may not provide the complete set of mechanical properties that the tensile test does. These will be discussed and referenced in the paper. The bulge test provides an important measure of residual stress in a deposited film as well as Young's modulus; Poisson's ratio can be obtained by using two different shapes of the diaphragm. Bending tests of cantilever beams are particularly amenable to MEMS materials; modulus can be inferred from overall displacement, which can be relatively large. Fracture strengths of very small single crystal silicon cantilevers have been measured using a nanoindenter for force measurement. Young's modulus has been measured by exciting a cantilever-based structure to resonance. Nanoindentation can be used to determine the modulus and strength of thin films.

A fruitful area of research is the use of MEMS-based structures to measure the properties of nano-sized specimens. One example is the use of two small cantilevers to measure the stress-strain curve of carbon nanotubes by Yu et al. [7]. Each cantilever has a very sharp tip to which one end of the nanotube can be attracted and then 'welded' with a focused ion beam. One cantilever is attached to a fixed grip, and the other is moved with a translation stage. This is done inside a SEM and the end displacements of the cantilevers are measured to provide both force and overall elongation. Haque and Saif [8] fabricate a complete 'test machine' to include a very thin and small specimen of a different material. It too is actuated in a SEM to determine force and overall displacement.

## References

1. Sharpe, W. N., Jr., Yuan, B., and Edwards, R. L., *J. MEMS*, vol. **6**, 193-199, 1997.
2. Sharpe, W. N., Jr., Turner, K. T., and Edwards, R. L., *Exp. Mech.*, vol. **39**, 162-170, 1999.
3. Sharpe, W. N., Jr., LaVan, D. A. and Edwards R. L., *Proceedings Transducers '97*, Chicago, IL, 1997, 607-610.
4. Long, G. S., et al., *ASTM Special Technical Publication*, **1413**, 262-277, 2001.
5. Chasiotis, I., et al., *Thin Solid Films*, in press, available online, 2006.
6. Espinosa, H. D., Prorok, B. C., and Peng, B., *J. Mech. Phys. Solids*, vol. **52**, 667-689, 2004.
7. Yu, M-F. et al., *Science*, vol. **287**, 637-640, 2000.
8. Haque, M. A. and Saif, M. T. A., *Proc. National Acad. Science*, Vol. **101**, 6335-6340, 2004.

## CHARACTERISATION AND ASSESSMENT OF FAILURE AND FATIGUE PHENOMENA IN SANDWICH STRUCTURES INDUCED BY LOCALIZED EFFECTS

Ole Thybo Thomsen

Department of Mechanical Engineering, Aalborg University  
Pontoppidanstraede 101, DK-9220 Aalborg East, Denmark  
ott@ime.aau.dk

Sandwich structures are notoriously sensitive to failure by the application of concentrated loads, at points or lines of support, and due to localized bending effects induced in the vicinity of points of geometric and material discontinuities. The reason for this is that localized shearing and bending effects induce severe through-thickness shear and normal stresses. These through-thickness stress components can be of significant magnitude, and may, in many cases, exceed the allowable stresses in the core material (as well as in) especially close to the interfaces between the core and the face sheets.

In addition, localized bending effects may induce in-plane stress concentrations in the face sheets, which, depending on the loading situation and the boundary conditions, may exceed the “globally” induced stresses, and thereby seriously endanger the structural integrity. The majority of failures in sandwich structures, due to either static overloading or under fatigue loading conditions, are caused by localized effects as described above.

The objective of the presentation is to provide an overview of the mechanical effects, which determine the occurrence and severity of localized bending effects in sandwich structures, and, in addition, to provide a survey of the available structural sandwich models, with special emphasis on their ability to describe local bending effects.

The presentation includes a brief survey of the various structural models, including classical, “first-order shear”, “high-order” and continuum mechanics based models. Moreover, the paper will focus on and address the experimental characterisation and assessment of local effects in sandwich structures based on realistic engineering practice examples including ply-drop effects in sandwich structures, junctions between sandwich panels of different curvature, sandwich panels with core materials of different stiffness (core junctions) and sandwich panels with rigid inserts (Figs 1 and 2). The issue of failure and fatigue of such sandwich structures subjected to out-of-plane and in-plane loads is discussed in some detail, with the inclusion of recent theoretical and experimental results.

### References

1. Thomsen, O.T., Rits, W., Eaton, D.C.G., Dupont, O. and Queekers, P., *Composites Science and Technology*, vol. **56**, 423-431, 1996.
2. Lyckegaard, A., Bozhevolnaya, E. and Thomsen, O.T., *Composites Part B: Engineering*, vol. **35**, Issues 6-8, Pages 629-637, 2004.
3. Bozhevolnaya, E., Lyckegaard, A. and Thomsen, O.T., 2005, *Applied Composite Materials*, vol. **12**, 135-147, 2005.
4. Bozhevolnaya, E. and Thomsen, O.T., *Composite Structures*, vol. **70**, 517-527, 2005.
5. Bozhevolnaya, E. and Thomsen, O.T., *Composite Structures*, vol. **70**, 528-539, 2005.

- 6. Thomsen, O.T., Bozhevolnaya, E. and Lyckegaard, A., *Composites Part A: Applied Science and Manufacturing*, vol. 36, 1397-1411, 2005.

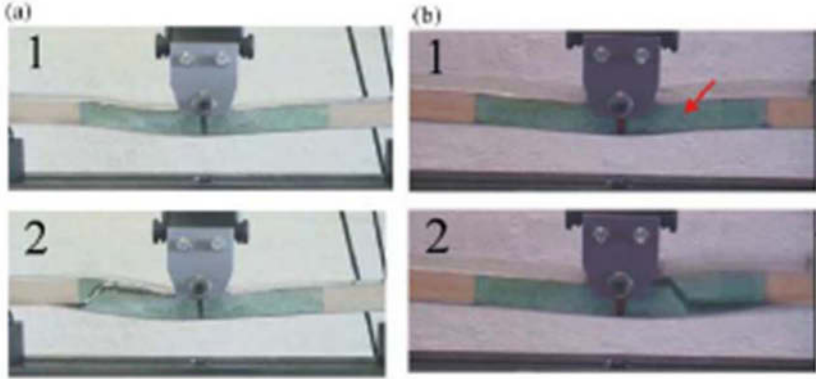


FIGURE 1. Crack initiation and final rupture in sandwich beams under quasi static loading. (a) conventional butt junction, (b) reinforced butt junction.

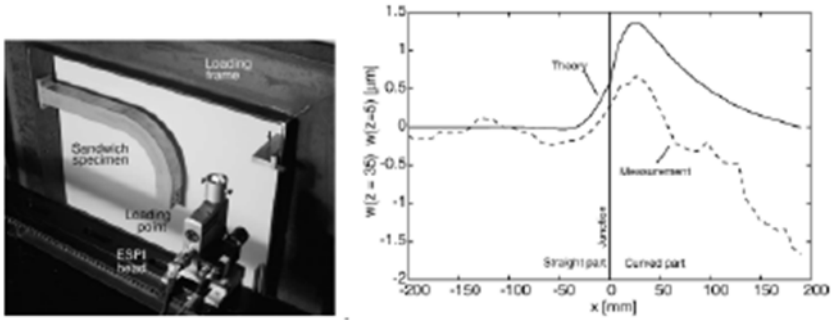


FIGURE 2. Local bending effects in terms of change of sandwich panel thickness at junction between straight and curved sandwich panel measured using Electronic Speckle Pattern Interferometry (ESPI).

## **B. TRACKS**

## METAL-POLYMER-CERAMIC NANO/COMPOSITE MATERIAL

M.V. Kireitseu and L.V. Bochkareva  
 KROTO Nanotechnology Research Institute/the University of Sheffield  
 Mappin Street, Sheffield S1 3JD, the United Kingdom  
 m.kireitseu@shef.ac.uk  
 United Institute of Informatics Problems NAS of Belarus,  
 Filatova str. 7 – 28, Minsk 220026, Belarus  
 l\_silver@rambler.ru

Constrained layer damping (CLD) design concept is based on polymeric layer, which is deposited in confined space between adjacent layers of other materials: metals or ceramics [1]. Aluminum, aluminum oxide particles and polyamide granular particle powders have been respectively used for CLD design. Aluminum alloy powders have granules size of 50-80  $\mu\text{m}$ , 94% Al, 4%Cu and 2% Si.  $\text{Al}_2\text{O}_3$  particle mixtures were prepared by mixing 98 wt.% aluminum oxide powder with particle diameter of 50 m, purity of 99.7% and 2 wt.% aluminum oxide nanopowder with diameter 40-47 nm and specific surface area of 40-45  $\text{m}^2/\text{g}$  supplied by Sigma-Aldrich Europe Ltd. The materials were dried for 2-3 hours in vacuum.

Thermal flame spraying of coating structures were applied as a candidate manufacturing technology for advanced CNT-reinforced sandwich materials. The technology has a benefit of particle management and manufacturing possibilities for nano to mesoscale-structured materials in many applications, including multilayer metal-ceramics-polymer coatings [2]. In comparison with plasma spraying the technology, it offers significant cost benefits and functional properties.

The overall processing sequence for the sprayed nanostructured coatings is layer by layer design of sandwich illustrated in Fig. 1. Heating gas was butane and distance of spraying was 120-130 mm. Available powders of the materials were mixed and reconstituted into sprayable size agglomerates onto metal substrate of vibrating beam. Deposited coating layers have some amount of carbon nanotubes and increased amount of closed pores for the benefits of acoustic noise adsorption and structural vibration damping.

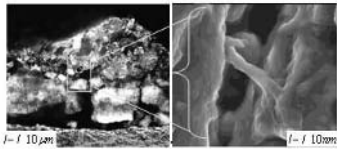
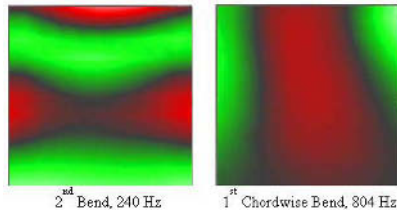


FIGURE 1. Layer-by-layer design of CLD sandwich.

The use of thermal spraying technology permitted an efficient integration of multidisciplinary engineering efforts to produce finely structured damping metal-polymer-ceramics sandwiched coating that is unique in microstructure, superior in properties and readily technology transferable into an industry. Manufacturing design concepts for the coating materials are a viable perspective for damping members in transportation (aerospace, automotive).



In Fig. 2 it is seen the first modes of the metal-ceramics coated plate, as viewed by vibrometry. Nodal lines are not always apparent and in few images, the node lines appear as thin almost white bands. For example, in the first torsion image in Fig. 2, the shape is twisting about the center line running vertically through the plate (which appears in white in the image). If the left half is displaced above the plane, the right half is below. This displacement is not evident from the image; the image only shows that the areas nearest the center line (in green) have the same magnitude of velocity, and the areas of the plate in the free corners (in red) have equivalent velocity magnitudes. In each modal point, an increase of damping level is achieved due to coating design. When area of specimen coverage is about 80% of total area, increased damping levels were achieved in the frequency range (table 1). This effect can be explained by a non-linear contact between surfaces of damping structure and the plates. Thus, an optimal stress-strain relation should be achieved in the selected design. For any given sample, damping is not a constant at all frequencies, nor is it a linear function of frequency.



2<sup>nd</sup> Bend, 240 Hz    1<sup>st</sup> Chordwise Bend, 804 Hz

FIGURE 2: Modes 5 through 6, metal-ceramics coated plate, viewed by holography.

TABLE 1. Comparison of damping factor and coverage area.

Modes	Coverage area				
	0%	40%	60%	80%	100%
1-2	0,2	0,38	0,34	0,32	0,33
3-4	0,21	0,32	0,42	0,49	0,43
5-6	0,18	0,31	0,42	0,45	0,32
7-8	0,23	0,33	0,29	0,33	0,24
9-10	0,17	0,21	0,24	0,27	0,19

## References

1. Kireitseu, M.V., *Int.-I J. Applied Mech. and Eng.*, vol. **8**(2), 250-271, 2003.
2. Kireitseu, M.V., *ASM J. Thermal Spray Technology*, vol. **12** (4), 586-596, 2003.

## CHARACTERIZATION OF A NEW TITANIUM DIOXIDE-POLYMER COMPOSITE MATERIAL FOR ELECTRONIC PACKAGING APPLICATIONS

Barish Dantal, Anil Saigal and Michael Zimmerman

Mechanical Engineering Department, Tufts University, Medford, MA 02155, U.S.A.

barish.dantal@tufts.edu, anil.saigal@tufts.edu, mzimmerman@qlpkg.com

Titanium dioxide ( $\text{TiO}_2$ ) is a versatile filler material used in polymer based applications. The most common application is in the form of white pigment. However, titanium dioxide brings more to the polymer industry than just white, bright opacity. Titanium dioxide is a photo-responsive material - its value is in its interaction with light. Unlike colored pigments that provide opacity by absorbing visible light, titanium dioxide and other white pigments provide opacity by scattering light. This scattering is possible because the white pigment can bend light. If there is enough pigment in the system, all light striking the surface, except for the small amount absorbed by the polymer or pigment, will be scattered outward, and the system will appear opaque and white. Light scattering is accomplished by refraction and diffraction of light as it passes through or near pigment particles [1].

$\text{TiO}_2$ -polymer composite materials are being developed for new applications such as Liquid Crystal Display (LCD), Light Emitting Diode (LED) etc. Refractivity of the composite material is a function of dispersion of titanium dioxide particles. In order to characterize the particle size distribution on the surface of the molded part, Scanning Electron Microscope (SEM) and Atomic Force Microscope (AFM) are used for imaging. Image analysis method has been developed using Matlab® software based on AFM and SEM images.

Fig. 1 shows a SEM image while Fig. 2 shows the image after image processing of a  $\text{TiO}_2$  - Polymer composite.

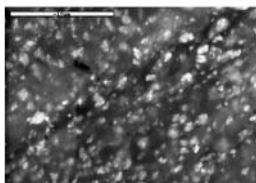


FIGURE 1. Scanning Electron Micrograph of a  $\text{TiO}_2$ -Polymer composite.

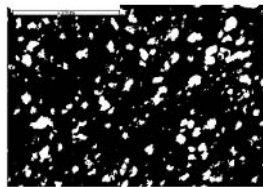


FIGURE 2. Image after image processing using Matlab.

Although there are many types of software available in the market to do similar tasks, understanding of the features used to achieve final goal is essential before the use of particular software.

Matlab image analysis approach is developed based on sieving technique. In sieving technique, disks of known pixel radius are passed through the image in increasing order and then intensity of the remaining field of the image is calculated. Minima and maxima of the intensity are calculated by taking derivative of the intensity curve. Key features used in Matlab are strel (Van den Boomgard and Van Balen [2] and Adams [3]), graythresh, bwlabel (Haralick [4]), regionprops etc.

Statistical information acquired from Matlab® involves Particle Size Distribution (PSD), Number of Particles, Mean Area, Median Area, and Standard Deviation of the particles. Figures 3 and 4 show the distribution of particles achieved before Matlab programming and particle size distribution after Matlab image processing, respectively.

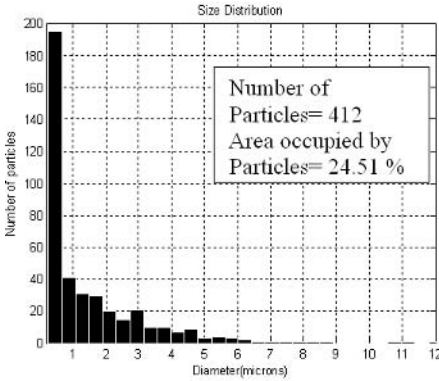


FIGURE 3. Particle Size Distribution obtained before Matlab image processing.

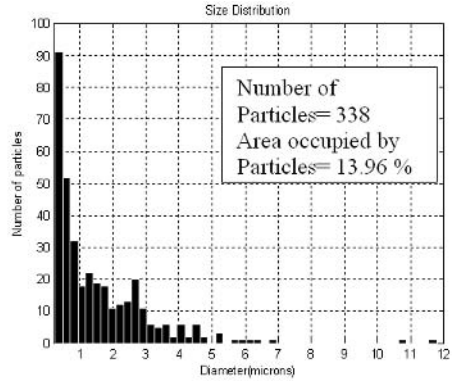


FIGURE 4. Particle Size Distribution obtained after Matlab image processing.

Results accomplished with this method are helpful in analyzing regions with single particle and regions with agglomeration. These two regions are important for determining the percentage reflectivity of the material.

## References

1. Polymer Light and Science of TiO<sub>2</sub> particle, DuPont Literature, 2006.
2. Van den Boomgard, R. and Van Balen, R., "Methods for Fast Morphological Image Transforms Using Bitmapped Images," Computer Vision, Graphics, and Image Processing: Graphical Models and Image Processing, vol. **54**, no. 3, 252-254, May 1992.
3. Adams, R., "Radial Decomposition of Discs and Spheres," Computer Vision, Graphics, and Image Processing: Graphical Models and Image Processing, vol. **55**, no. 5, 325-332, September 1993.
4. Haralick, R.M. and Shapiro, L.G., Computer and Robot Vision, Volume I, Addison-Wesley, 28-48, 1992.

## FORMING OF FULLERENE-DISPERSED ALUMINUM COMPOSITE BY COMPRESSION SHEARING METHOD

Noboru Nakayama and Hiroyuku Takeishi  
Akita Prefectural University,  
84-4 Tsuchiya-Ebinokuti, Yurihonjyo, Akita/ 015-0055, Japan  
nakayama@akita-pu.ac.jp  
Chiba Institute of Technology  
2-17-1 Tsudanuma, Narashino, Chiba/ 275-8588, Japan  
takeishi.hiroyuku@it-chiba.ac.jp

The fullerene (C60 or C70 etc.) or cluster diamond (CD or GCD) exhibit lubrication characteristics that can not be matched by conventional materials. Therefore, it is likely that the fullerene or cluster diamond will be utilized as solid lubricants in a variety of applications. In recent years, composite materials containing cluster diamond (CD or GCD) uniformly dispersed in a metal matrix have been examined as ultra-high performance solid lubricating materials with superior lubricating properties [1]-[2]. However, since the composite materials were fabricated by powder metallurgy method (the hot press or dynamic compaction method), the materials contained many pores and exhibited low mechanical properties [3]. As a result, the composite material is not capable of producing enhanced lubricating properties.

A new solidification method concept has been developed that employs compression shearing [4]. Using this method, the grain size of the fabricated material is on a nano meter scale, and the strength of the specimen is improved. When the compression shearing process is applied to powdered aluminum under room temperature and atmospheric conditions, a thin plate specimen consisting of ultra fine crystal grains with preferred orientation can be obtained. Conventional methods are not capable of obtaining such a specimen under room temperature.

In this paper, fullerene-dispersed aluminum composites were fabricated by the compression shearing method. The mechanical properties, friction coefficient and microstructures of the compacted powders were investigated.

Figure 1 shows a schematic drawing of the setup for the compression shearing method. The powders were filled on the lower-plate, and the upper plate is loaded on the lower plate with holding powders between their surfaces, and it sets in equipment. Shear stress was applied to the powders by moving the lower steel plate to the direction of an axial compression presser. The compressive load  $P$  was generated by rotating an upside screw using a lever rod. The compressive load  $P$  given to the sample was determined from the value of this strain gauge.

The shear stress applied to the compacted powder was calculated to be 500 MPa for the compacted powder with a compacted area of 400 mm<sup>2</sup> (20mm × 20 mm). The moving distances  $L$  of the lower steel plate was 5 mm. The moving speed of the lower plate was maintained at around 0.1 mm/s. This forming procedure can be carried out under room temperature and in the air without heating.

The matrix consisted of a rapid-solidified Al-Si-Cu-Mg alloy powder with an average particle size of 41.4 μm. On the surface of each grain, a hard and stable oxide layer of 5 micrometer thickness was naturally generated. The amounts of fullerene were 0 - 30% volume fraction. The entire procedure was carried out in an Ar atmosphere using a glove box. The enclosed powders were mechanically mixed at 500 rpm for four hours by the ball-milling method.

To examine the friction properties, friction measurements were carried out by the pin-on-disk method in air. For these measurements, the pin was made of stainless steel (SUS304) and had a head spherical surface of 4 mm in diameter. Friction tests were conducted using a test load of 0.2 N at a sliding speed of 1.7 mm/s. The friction test was conducted in air.

Figure 2 shows the friction coefficient of Al-Si-Cu-Mg composites containing various volume fractions of fullerene. The addition of 1 vol. % fullerene to Al-Si-Cu-Mg improved the friction coefficient. The average friction coefficients of Al-Si-Cu-Mg, the 1 vol. % fullerene sample, and the 15 vol. % fullerene sample were found to be 1.00, 0.94 and 0.33, respectively. Compared with the Al-Si-Cu-Mg results, these values account for a reduction of 6% and 67%, respectively.

This result suggests that the Al-Si-Cu-Mg/fullerene composite has excellent solid-lubricating properties.

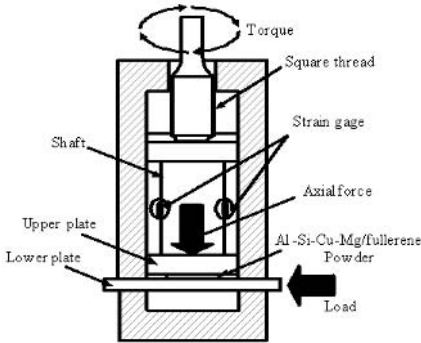


FIGURE 1. Schematic diagram of compression sharing device

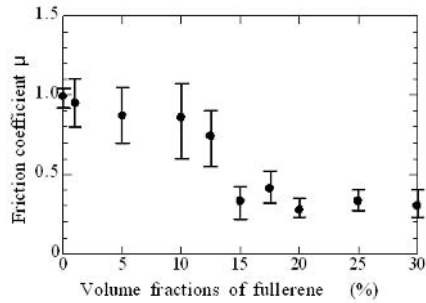


FIGURE 2. Effect of volume fraction of fullerene on friction properties

## References

1. N. Nakayama *et al.*, *Adv. Technol. Plasticity*. 1321-1326, 1999.
2. N. Nakayama *et al.*, *Surface Modification Technologies XVIII*, pp. 203-207, 2006.
3. K. Hanada *et al.*, *New Diamond and Frontier Carbon Technology*, vol. **13**, no. 3, 133-142, 2003.
4. N. Nakayama *et al.*, *The 7th China-Japan Joint Conference on Composites*, 206-214, 2006.

## STUDY OF THE MECHANICAL PROPERTIES OF CELLULOSE/ $ZrO_2.nH_2O$ COMPOSITES

Daniella Regina Mulinari and Maria Lúcia Caetano Pinto da Silva

Fatigue and Aeronautic Materials Research Group, Department of Materials and Technology  
State University of São Paulo – UNESP. Av. Ariberto Pereira da Cunha, 333 CEP 12516-410  
Guaratinguetá/SP-Brazil

News Materials Group, Department of Chemical Engineering- /EEL/USP.  
Rodovia Lorena-Itajubá, Km 74,5 CEP 12600-000 Lorena/ SP-Brazil  
danimulinari@dequi.faequil.br

The cellulose obtained of the natural fibre used as reinforced in the composites materials have found an increasing number of applications in recent years[1-3]. Car manufacturers have shown special interest in these materials. Advantages of natural fibres over the traditional counter- parts include: relatively low cost, low weight, less damage to processing equipment, improved surface finish of moulded parts, good mechanical properties. Another important advantage of natural fibres is the relatively abundant in nature and, therefore, can be obtained from renewable resources, and been also recycled.

Polymer is relatively inert because hydrous groups, which are responsible for the majority of the reactions with organic and inorganic reagents, are involved in inter and intramolecular hydrogen bonding [2]. In the recent years, procedures for the preparation of metal oxide- coated cellulose fibers, Cell/  $M_xO_y$ , have been described. According to the nature metal oxide can be applied as  $ZrO_2$  for retention and analysis of Cr(VI) [4].

The experimental methodology of the fiber- coating process is depend on the cellulose application: as fiber or as membrane. As fiber form, the treatment of cellulose with a precursor reagent can be made in aqueous or non- aqueous solvent. To prepare the membranes, cellulose acetate is normally used due to the high solubility characteristic in most of the common organic solvents such as acetone [5].

The cellulose/  $ZrO_2.nH_2O$  composite processed by an oxide precursor reagent dissolved in an aqueous solvent presented an adequated incorporation of the oxide on the cellulose surface. The Table 1 shows the results of the analyses specific superficial area .

TABLE 1. Surface area measurements.

Material	Surface area ( $m^2.g^{-1}$ )
Cellulose	0.6
$ZrO_2.nH_2O$	253.7
Cellulose / $ZrO_2.nH_2O$	36.1

The Fig. 1 shows the incorporation  $ZrO_2.nH_2O$  on the surface of the fibres cellulose by scanning electron microscopy (SEM) .

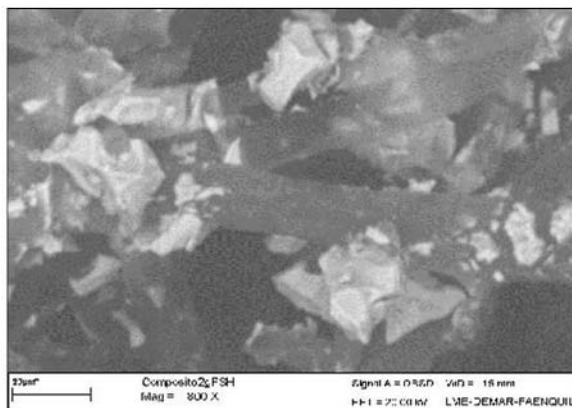


FIGURE 1. Micrographs of the Cellulose /ZrO<sub>2</sub>.nH<sub>2</sub>O Composite.

Since materials have presented excellent mechanical properties, should be used as structural applications [6].

## References

1. Idicula, M., Boudenne, A., Umadevi, L., Ibos, L., Candau, Y., Thomas, S., *Composites Science and Technology*, vol. **66**, 2719-2725, 2006.
2. Ma, X., Yu, J., Kennedy, J. F., *Carbohydrate Polymers*, vol. **62**, 19-24, 2005.
3. Torres, F. G., Diaz, R. M., *Polymers and Polymer Composites*, vol. **12** (8) 705-718, 2004.
4. Gushikem, Y., Toledo, E. A. (1999) in: *Polymer Interfaces and Emulsions* 509-510.
5. Mulinari, D. R., Silva, G. L. J. P. , Silva, M. L. C. P. , *Química Nova*, vol. **29** (3) 496-500, 2006.
6. Uesaka, T., Ogata, N., Nakane, k., Shimizu, k., Ogihara T., *Journal of Applied Polymer Science*, vol. **83**(8) 1750-1758, 2001.

## THERMO-MECHANICAL CHARACTERIZATION OF EPOXY/SILICA NANOCOMPOSITES

M.S. Konsta-Gdoutos<sup>a</sup>, I.M. Daniel<sup>b</sup>, Z. Metaxa<sup>a</sup> and J. Cho<sup>b</sup>

<sup>a</sup>School of Engineering, Department of Civil Engineering, Democritus University of Thrace  
12 Vas. Sofias, GR-671 00, Xanthi, Greece

<sup>b</sup>McCormick School of Engineering and Applied Science, Civil and Environmental Engineering  
and Mechanical Engineering, Northwestern University  
2137 Tech Drive, Evanston, IL 60208, USA  
mkonsta@civil.duth.gr, z-metaxa@northwestern.edu  
imdaniel@northwestern.edu, jm-cho@northwestern.edu

Composite materials consisting of organic polymer and inorganic nanoparticles are expected to present superior thermal and mechanical properties i.e. high modulus and strength and good performance at elevated temperatures [1, 2]. Research on the mechanical properties of stiff particulate-filled polymeric materials show that their mechanical behavior is a result of a complex combination of the properties of the constituent phases [3]. The principal relevant parameters are the properties of the matrix (resin system), the particle size and shape, and particle content [4, 5]. Particles of micron level dimensions produce an increase in toughness; however, they also increase the viscosity of the epoxy resin thus reducing the ease of processing. Addition of nanoparticles in epoxy resins has been shown to further increase the toughness of the nanocomposite without significantly increasing the viscosity of the epoxy matrix [6-9]. Another important parameter that can significantly alter the properties of the nanocomposites is the filler aspect ratio. Because of their high surface area to volume ratio, nanofillers have been found to have a high reinforcing efficiency even at very low concentrations [10].

In this work, nanocomposite materials consisting of an epoxy matrix and various concentrations of silica nanoparticles were processed and characterized thermomechanically. Samples were prepared with silica concentrations of up to 20 wt%. The epoxy resin system used was obtained by mixing stoichiometric amounts of a commercial difunctional liquid epoxy monomer, diglycidyl ether of bisphenol-A (DGEBA), with a solid aromatic amine, diaminodiphenyl sulphone (DDS), hardener. The curing agent was added to the epoxy resin at the temperature at which the resin has low viscosity. Colloidal silica dispersed in 30 wt % isopropanol was used as the nanoparticle filler. The nanosilica particles had a mean particle size of about 8 nm.

For the characterization of the viscoelastic properties of the epoxy silica nanocomposites, dynamic mechanical tests were carried out using a dynamic mechanical analyzer (DMA 2980 from TA Instruments, USA). The tests were performed on prismatic samples (80x7.5x2.5 mm<sup>3</sup>) loaded under dual cantilever mode. The scanning temperature mode was in the range from room temperature to 250 °C, at a heating rate of 3 °C /min and with an oscillating frequency of 1.0 Hz. The storage and loss moduli of both the neat epoxy and silica/epoxy specimens were determined. The glass transition temperature (T<sub>g</sub>) was determined from the peak of the tanδ curve.

Tensile tests were conducted to measure the variation of the elastic modulus, tensile strength and the ultimate strain as a function of the silica content of the nanocomposite. The tests were carried out at room temperature on an Instron 8500 servohydraulic machine at a cross head rate of 0.13 mm/min. The fracture surfaces of the tensile specimens were examined using a Hitachi S4500 FE SEM.



The resin system (epoxy plus hardener) selected generated a strong high modulus system with a high glass transition temperature (T<sub>g</sub>). Addition of nanosilica particles did not significantly affect the measured glass transition temperature. The modulus of the nanocomposites was found to increase with increasing silica content.

## References

1. Ragosta, G., Abbatea, M., Mustoa, P., Scarinzia, G., Mascia, L, *Polymer*, vol. **46**, 10506, 2005.
2. Miyagawa, H., Foo, K.H, Daniel, I.M., Drzal, L.T., *J Appl Polym Sci*, vol. **96**, 281-287, 2005
3. Harismendy, I., et al., *Polymer*, vol. **38**, 5573, 1997.
4. Nakamura, Y.; Yamaguchi, M.; Okubo, M.; Matsumoto, T. *Polymer*, vol. **32** (12), 2221-2229, 1991.
5. Koh, S., Kim, J., Mai, Y., *Polymer*, vol. **34**, 3446, 1993.
6. Nakamura, Y.; Yamaguchi, M.; Okubo, M.; Matsumoto, T., *J Appl Polym Sci*, vol. **45**, 1281, 1992.
7. Yasmin, A., Luo, J.J., Abot, J.L., Daniel, I.M., *Comp Sci Tech*, vol. **66**, 2415-2422, 2006.
8. Kinloch, A.J., Taylor A.C., Lee J.H., Sprenger, S., Eger C., Egan D., *J Adhes*, vol. **79** (8-9), 867-873, 2003.
9. Kinloch, A.J., Mohammed, R.D., Taylor, A.C., Eger, C., Sprenger S., Egan, D., *J Mater Sci*, vol. **40** (18), 5083-5086, 2005.
10. Nakamura, Y.; Yamaguchi, M.; Okubo, M.; Matsumoto, T. *Polymer*, vol. **32** (16) 2976-2979, 1991.

## GLOBAL MECHANICAL BEHAVIOR OF A NANOSTRUCTURED MULTILAYERED COMPOSITE MATERIAL PRODUCED BY SMAT AND CO-ROLLING

L. Waltz<sup>a</sup>, T. Roland<sup>a</sup>, D. Retraint<sup>a</sup>, A. Roos<sup>b</sup>, P. Olier<sup>c</sup> and J. Lu<sup>d</sup>

<sup>a</sup> LASMIS, University of Technology of Troyes, 10000 Troyes, France

<sup>b</sup> ONERA DMSE/LCME, 29 Avenue de la Division Leclerc,  
BP72 F-92322 Châtillon cedex, France

<sup>c</sup> CEA-Saclay, 91191 Gif sur Yvette cedex, France

<sup>d</sup> Department of Mechanical Engineering, Hong Kong Polytechnic University,  
Hung Hom Kowloon, Hong Kong  
delphine.retraint@utt.fr

Nowadays, 316L austenitic stainless steel is a widely used engineering material in a large number of applications. In spite of its excellent corrosion and formability characteristics, this material has a low mechanical strength. In recent years, many studies relating to nanocrystallisation by severe plastic deformation processes have been carried out. Tao *et al.* [1], Liu *et al.* [2], Roland *et al.* [3] and Chen *et al.* [4] have shown that a recently developed Surface Mechanical Attrition Treatment (SMAT) technique, applied to pure metals or alloys may induce a grain refinement in the top surface layer down to the nanometer scale, arising from severe plastic deformation at high strain rate. From the mechanical point of view, one of the effects of this treatment is a considerable enhancement of strength and surface hardness. As shown for a 316L stainless steel [3] [4], a 1mm thick tensile sample treated by SMAT on both sides for 15 minutes with 3 mm diameter shots reaches a yield strength as high as 525 MPa and exhibits approximately a microhardness of 4,5 GPa in the top surface layer, owing to the presence of the nanocrystalline region.



FIGURE 1. Photograph of the SMAT machine.

The aim of the present work is to produce a nanostructured multilayer composite with high mechanical properties by assembling three 316L surface nanostructured stainless steel plates using the co-rolling process. The SMA-treatment is first used to generate nanocrystalline layers on the elementary plates, so that their mechanical properties are improved (Fig. 1). They are then assembled through co-rolling. A composite structure alternating nanostructured layers of high strength with more ductile layers is thus obtained. As a consequence, the material exhibits a global high strength and conserves a good ductility. In order to quantify the influence of different experimental parameters, such as shot diameter, reduction ratio, rolling temperature and number of SMATed sides, several tests were carried out. To follow the evolution of the microhardness through the section of samples, and consequently the evolution of the average grain size,

nanoindentation experiments and microscopy observations have been carried out. In parallel, tensile tests were performed to show the correlation between the microstructure evolution (Table 1) and the global mechanical response.

TABLE 1. Chemical composition of the 316L stainless steel samples.

Elements	C	Si	Mn	P	S	Cr	Mo	Ni	N	Cu	B	Co
Mass %	0.025	0.38	1.33	0.027	0.002	16.70	2.09	10.20	0.030	0.40	0.0006	0.07

## References

1. Tao, N.R., Sui, M.L., LU, J, and LU, K, *Acta Metallurgica*, vol. **11**, 443-440, 1999.
2. Liu, G., Lu, J., and LU, K., *Materials Science and Engineering*, vol. **A 286**, 91-95, 2000.
3. Roland, T., Reintant, D., Lu, K., Lu, J., *Materials Science Forum*, edited by Trans Tech Publications, Switzerland, 2005, 625-630.
4. Chen, X.H., Lu, J., Lu, L., Lu K., *Scripta Materialia*, vol. **52**, 1039-1044, 2005.

## PREPARATION OF HIGH MOLECULAR WEIGHT POLY(VINYL CARBAZOLE) WEB BY ELECTROSPINNING

Won Seok Lyoo<sup>1</sup>, Ki Bum Lee<sup>1</sup>, Young Jae Lee<sup>1</sup> and Hee Sam Kim<sup>2</sup>

<sup>1</sup>Division of Advanced Organic Materials, School of Textiles,  
Yeungnam University, Gyeongsan, Korea

<sup>2</sup>Department of Knit Design, Korea Textile & Fashion Polytechnic,  
Daegu 704-901, Korea  
wslyoo@yu.ac.kr

High molecular weight poly(N-vinyl carbazole) (PVCz) nanoweb were prepared by electrospinning technique. To investigate the effects of type of solvents on the spinnability and the morphology of electrospun PVCz, PVCz solutions were prepared by dissolving PVCz in chloroform and 1,1,2,2-tetrachloroethane (TCE) and were spun at various electrospinning conditions. The spinnability of PVCz in TCE was better than those in THF and in chloroform, which was ascribed to the difference in solution properties. Bead-fiber morphology was observed when the concentration was low concentration, but fine fibers were obtained when the concentration was high concentration.

To prepare fine and even PVCz webs, we performed a series of experiments varying processing parameters, like solvents and its tip to the collector distance (TCD), applied voltage, and concentration. Fig. 1 shows SEM micrographs of the webs electrospun from 3%, 5% and 10% PVCz solutions in the chloroform at 25 kV when the TCD was 15 cm. The electrospun fibers exhibited bead-onto-fiber when the concentration was 3%, but more fibrous shapes were obtained at 5% and 10%. In THF, bead was obtained at 3% and at 5%, and fiber was obtained at 10%.

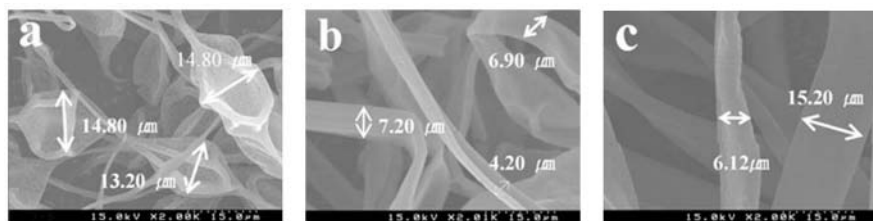


FIGURE 1. SEM photographs of PVCz webs electrospun at various solution concentrations: (a), 3%; (b), 5%; (c), 10%. The solvent, applied voltage and TCD were chloroform, 25 kV, 15 cm, respectively.

Fig. 2 shows SEM micrographs of the fine fibers electrospun from 10%, 15% and 18% PVCz solutions in the TCE solvent at 20 kV when the TCD was 40 cm. The spinnability of PVCz was better and the diameters of nanofiber were in TCE than chloroform and THF. All PVCz fibers prepared at high concentrations were not cylindrical but planer.

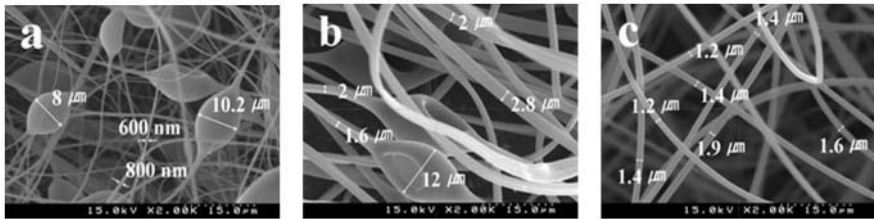


FIGURE 2. SEM photographs of PVCz webs electrospun at various concentrations: (a), 10%; (b), 15%; (c), 18%. The solvent, applied voltages and TCD were TCE, 20 kV, 40 cm, respectively.

At relatively lower concentration, bead and bead-onto-fiber were found with respect to the kinds of applied solvents and fiber was found at relatively higher concentration. Raising the applied voltage and increasing the TCD tend to produce smaller diameters of the electrospun fibers.

### Acknowledgements

This work was supported by grant No. RTI04-01-04 from the Regional Technology Innovation Program of the Ministry of Commerce, Industry, and Energy (MOCIE).

### References

1. Lee, J.S., Lyoo, W.S., Noh, S.K., Kim, J.H., Lee, J.W., Ghim, H.D., Lee, J.Y., *J. Appl. Polym. Sci.*, vol. **89**, 2391, 2003.
2. Li, W.J., Laurencin, C.T., Caterson, E.J., Tuan, R.S., Ko, F.K., *J. Biomed. Mater. Res*, vol. **60**, 613, 2002.
3. Sanders, E.H., Koefkorn, R., Bowlin, G.L., Simpson, D.G., Wnek, G.E., *Macromolecules*, vol. **36**, 3803, 2003.

## PREPARATION OF HYDROPHILIC ANTIOXIDANT-LOADED POLY(VINYL ALCOHOL) NANOWEB BY ELECTROSPINNING AND ITS WOUND HEALING EFFECT

Sung Jun Lee,<sup>1</sup> Se Geun Lee,<sup>1</sup> Hoyoung Kim,<sup>1</sup> Jae Ryong Kim,<sup>2</sup> Cha Young,<sup>2</sup> Sun Gil Kim<sup>3</sup>  
and Won Seok Lyoo<sup>3\*</sup>

<sup>1</sup>Advanced Nano Material Research Team, Daegu Gyeongbuk Institute of Science & Technology, Daegu, Korea

<sup>2</sup>Biochemistry & Molecular Biology, College of Medicine, Yeungnam University, Gyeongsan, Korea

<sup>3</sup>Division of Advanced Organic Materials, School of Textiles, Yeungnam University, Gyeongsan, Korea  
wslyoo@yu.ac.kr

Poly(vinyl alcohol) (PVA) has been used as a material for electrospinning due to its good properties in forming membranes and fibers. [1,2] Beside, it has attracted particular attention because of its inherent low toxicity, good biocompatibility, and desirable physical properties. [3] In this study, at first, electrospinning was utilized to fabricate a PVA nanoweb with antioxidant which has been used to prevent apoptosis in neuronal cells for wound dressing application. Also, PVA nanoweb with various contents of antioxidant were characterized. In the end, the wound healing effect of antioxidant-loaded PVA nanoweb was examined using male Sprague-Dawley rats with excisional wounds.

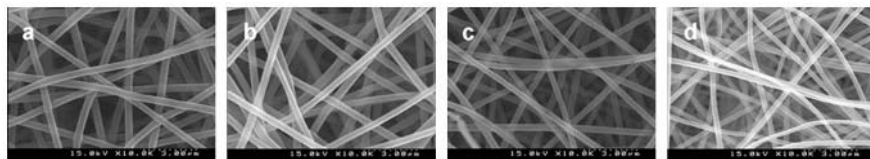


FIGURE 1. SEM photographs of electrospun PVA nanoweb containing different amounts of antioxidant: a, 0 wt.%; b, 0.5 wt.%; c, 1 wt.%; d, 2 wt.%.

Fig. 1 showed the SEM micrographs of PVA nanoweb with different amount of antioxidant prepared by electrospinning. As the content of antioxidant was increased, the fiber diameter became smaller. Generally, the addition of polar substances such as salts, acids, and alkalis enhanced the dielectric properties of spinning solution and resulted in a good spinnability. [4] In this study, the morphology variation according to antioxidant contents which is polar owing to its carboxylic acid, thiol, and amide bond was caused by the increased dielectricity of PVA solution. High dielectricity of PVA solution enlarged the charge density on the surface of the ejected polymer jet. The increased charge density imposed greater elongation and thinning forces on the jet as it travels through the electric field, resulting in smaller diameter fibers. Furthermore, all PVA nanofibers had an even and uniform surface structure and no insoluble antioxidant were detected either on the surface or outside of the fibers. That is to say, antioxidant was perfectly included in the fibers.

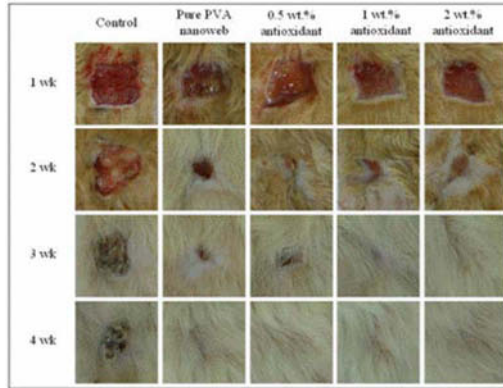


FIGURE 2. The effect of antioxidant-loaded PVA nanoweb on cutaneous wound healing in rats.

To examine the effect of PVA nanoweb with the antioxidant on cutaneous wound healing in rats, we determined the wound size from 0 week to 4 week of the healing process in PVA nanoweb with and without antioxidant. As shown in Fig. 2, there was a trend toward an enhancement of wound closure in antioxidant-loaded PVA nanoweb compared to control and pure PVA nanoweb. In addition, wound size was significantly lesser in pure PVA nanoweb compared to control throughout the 2 week study period.

### Acknowledgements

This work was supported by grant No. RTI04-01-04 from the Regional Technology Innovation Program of the Ministry of Commerce, Industry, and Energy (MOCIE).

### References

1. Koski, A., Yim, K., Shivkumar, S., *Mater. Lett.*, vol. **58**, 493, 2004.
2. Lee, J. S., Choi, K., Chim, H. D., Kim, S. S., Chun, D. H., Kim, H. Y., Lyoo, W. S., *J. Appl. Polym. Sci.*, vol. **93**, 1638, 2004.
3. Briscoe, B., Luckham, P., Whu, S., *Polymer*, vol. **41**, 3851, 2000.
4. Zong, X. H., Kim, K., Fand, D. F., Ran, S. F., Hsiao, B. S., Chu, B., *Polymer*, vol. **43**, 4403, 2002.

## TENSILE STRENGTH OF SURFACE NANOSTRUCTURED COPPER

H. L. Chan and J. Lu  
The Hong Kong Polytechnic University  
Hung Hom, Kowloon, Hong Kong  
Iris.chanhl@polyu.edu.hk

Various research topics arises from Nanostructured (NS) metals and their usage are increasing gain moments in the field of materials research regardless of structure, properties or the development of the process for bulk forms for applications. The reduction of grains size could have quite significant implications on the properties of the bulk material. Increasing the strength and hardness were some of the well known enhanced properties that can be obtained for metals with grains of nano-scale. However, only a few techniques, such as electrodeposition and Surface Mechanical Attrition Treatment (SMAT) could produce nanostructured materials with sufficient thermal stability to allow the fabrication in bulk form [1].

Having the advantages of producing 3-D bulk material on the surface of the complex shape samples without porosity, contamination and other defects, and low cost, SMAT is a new approach to nanostructure processing. It was made good use of spheres frequency displacement generator to hit the surface of the samples to obtain nanostructured surface. It is also clear that the processing history had a significant effect on mechanical properties of nanostructured materials. Although it is a newly developed technology, it is already well known for providing the surface layer with high strength, in the case of stainless steel, 3 times higher than the original materials. Thus, after this SMAT, the surface mechanical, tribological, chemical and corrosion properties of the bulk materials could subsequently be enhanced [2].

In this newly study, copper had been put on test to see the effect of SMAT on it and its mechanical properties, mainly strength and hardness. Copper after electrodeposition had been first studied. Electrodeposited Copper had the well-known improvement on the strength compared with the bulk hard copper. After SMAT, although the ductility had dropped, the yield strength is further enhanced up to 50% (350MPa) to obtain a stronger materials. This is similar in the hardness test. The hardness of the electrodeposited Copper had further improved up to 35% after SMAT. Since the parameters of the electrodeposition affects the properties of the materials we get, rooms for improvement could be expected.

In the paper, a more detailed experimental results will be presented as well as the experimental setup.

### References

1. Han, B. Q., Lavernia, E. J. and Mohamed, F. A., *Rev. Adv. Mater. Sci.*, vol. **9**, 1 – 16, 2005
2. Lu, J. and Lu, K., *Comprehensive structural integrity*, Oxford, San Diego, California, United States of America, 2003



## **SOME CONSIDERATIONS ABOUT THE FORMULATION OF CONSTITUTIVE EQUATIONS OF ORGANIC MATERIALS: INDUSTRIAL VIEW AND NEEDS**

A. Martinet, François Moussy and Florian Trioux  
Renault- Technocentre  
TCR LAB 035 – 1, Avenue du Golf -78288 Guyancourt Cedex – France  
francois.moussy@renault.com

The car industry must challenge several conflicting requirements. Among them are “weight reduction” and “safety increase for passengers and pedestrians”. One way to reach these goals is the introduction of organic materials for the manufacturing of automotive structures. To be able to realize robust and reliable structures with these rather new materials, accurate dimensioning calculations have to be performed.

For steels such simulations are operative since 20 years and more, even being in constant development : Constitutive Equations and associated identification test procedures are well defined. The introduction of aluminium, as an alternative to steel was also quite easy to managed, aluminium being as steel a metallic material. For organic materials, the problem is completely different. The micro-mechanisms of deformation are much more complex and less known than for metallic materials ; the variability of the concerned materials is large ( uncharged materials, fibers reinforced materials... ) ; the mechanical behaviour of these materials is complex : viscosity, anisotropy, temperature dependence, heterogeneity...

Industrial partners are today simply looking for the most appropriate Constitutive Equations. The existing ones are proposed by Research Laboratories, Materials Suppliers, Software Companies and Car Manufacturers. There is a need for a synthesis and a better comprehension of the behaviour of these organic materials.

This presentation is devoted to an elementary description of some key points linked to the mechanical behaviour of organic materials ; it presents some guidelines to define the most appropriate Constitutive Equations. The development of the arguments will be realized by setting up a comparison of the existing and well established know how on metallic materials (mechanical testing and model of the mechanical behaviour) with the actual developments in the field of organic materials.

The basic mechanical test remains the uni-axial tensile test. The mechanical analysis of this test is presented. Attention has to be brought on volume changes which can be important : up to 60 %... The elastic properties are difficult to quantify. The Young Modulus has to be defined as an initial one. This Modulus is strongly dependent on the strain rate : up to 50 % variation over the range of strain rates corresponding to classical crash situations. During the tensile test, strain gradients often occur rapidly : after 5-8 % ; how to analyze the tests data after strain localization ? These procedures are indispensable to be established to reach Constitutive Equations valid for large deformations up to 80 %.

The uniaxial tensile test is probably not sufficient to characterize organic materials at least for two reasons :

- strain localization in tension ;
- due to the volume variation, the mechanical behaviour of organic materials should be dependent of the first invariant of the stress tensor . First results issued from shearing tests will be presented.

Today only simple Constitutive Equations are used for numerical simulation of crash, even for steels... Before being used by Engineering Departments, the Constitutive Equations need to be validated. The classical method consists to perform a numerical simulation of crash on an elementary structure (demonstrator) defined to be more complex than the elementary mechanical tests used for the identification but sufficiently simple to be crashed and analyzed properly under “laboratory conditions”. For organic materials, the situation is more complex than for metallic materials. Specific validation methodologies are presented and discussed. More than one demonstrator is needed to cover the different loading paths occurring in a real crash.

The first conclusions summarizing the actual knowledge present :

- the Constitutive Equations which seem the most promising to describe the mechanical behaviour of organic materials ;
- the needs of industrial actors : which developments are they waiting for ;
- methodologies to identify and validate the Constitutive Equations ;
- the possible strategies to use available Constitutive Equations describing only some loading paths, for applications to real crash situations.

Some industrial examples will be presented.

## COHESIVE PROPERTIES OF MOLTEN PARTICLE DEPOSITED ONTO SUBSTRATE BY A FREE FALL

Masayuki Arai<sup>1</sup>, Hirotada Toyama<sup>2</sup> and Yasuo Ochi<sup>2</sup>

<sup>1</sup> Central Research Institute of Electric Power Industry  
2-11-1, Iwado-Kitta, Komae-shi, Tokyo, 201-8511, Japan  
marai@criepi.denken.or.jp

<sup>2</sup> University of Electro-communication  
1-5-1, Chohfugaoka, Chohfu-shi, Tokyo, 182-8585, Japan

In plasma spraying processes, a lot of molten particles are impinged continuously onto the substrate due to a high-power plasma flow, and form a thin coating layer. Thus, particle size, velocity, melting temperature and substrate temperature as the process parameter affect on mechanical properties of the coating deposited consequentially on the target. Interests in this research field are mainly addressed on a flattening formation mechanism of flying particles. Madejski [1], who is pioneer in this area, has modelled deposition process that particle spreads on the substrate, and then showed the simplified formula for the flattening ratio, which is given by;

$$\xi = \frac{D}{d} = f(Re) \quad (1)$$

where  $D$  is diameter of the flattening and  $d$  is diameter of molten particle, respectively. He has proposed that the flattening ratio varies simply with Reynolds number  $Re$  as a physical parameter characterizing the flying particle motion. Clyne [2] has analysed numerically about a rapid solidification process for particle spreading on the substrate in consideration with heat exchange at the contact boundary between the particle and the substrate. Zhang [3] has modelled the molten particle spreading and solidification process, which accounts for simultaneous effect of surface tension, solidification of metal and thermal contact resistance at the contact boundary. He has obtained an analytic solution for the flattening ratio as function of Reynolds, Weber, Prandtl and Jakob numbers. Matejicek et al. [4] have measured residual stress in the surface of the single flattening particle by using X-ray diffraction method, and indicated that the residual stress reduces with increasing the substrate temperature.

In this study, the cohesion properties for molten metallic particle dropped onto the substrate were examined based on a free fall experimental procedure, which could simply simulate a particle deposition process. The material used for dropping onto the substrate is a wire-type Sn60%Pb and the substrate is Type 304 stainless steel, which is a polished plate shape. All tests were performed by using a free fall-type deposition device (see Fig. 1). As a drop condition, the substrate was heated at constant temperature 373K, 393K and 413K, and kinetic energy  $K_d$  in the molten particle was varied by changing a free fall distance from 500mm to 1500mm and molten particle mass. After dropping tests, flattening shape of solidified particle on the substrate was examined quantitatively and also the peeling tests were done.

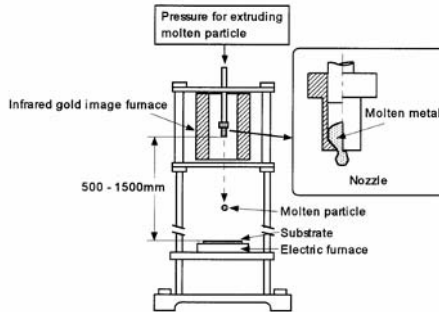


FIGURE 1. Schematic illustration of free fall -type deposition device

As a typical flattening shape of the particle solidified on the substrate, the particle spread to approximately several millimeter by dropping on the substrate, and it had a crown-like shape.

Fig. 2 shows variation of cohesion strength of deposited flattening particle with flattening ratio. It was found that cohesion strength of the single particle deposited on the substrate increases with flattening ratio in independence of substrate temperature and particle kinetic energy. We can recommend from this result that a higher substrate temperature or particle velocity lead formation of more flattening particle deposition on the substrate and also the flattening brings to increase the cohesion strength of the particle.

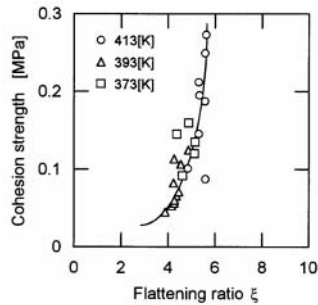


FIGURE 2. Variation of cohesion strength of deposited particle on the substrate with flattening ratio

## References

1. Madejski, J., *Int. J. Heat Transfer*, vol. **19**, 1975, 1009-1013
2. Clyne, T.W., *Metallurgical Tran. B*, vol. **15B**, 1984, 369-381
3. Zhang, H., *Int. J. Heat Transfer*, vol. **42**, 1999, 2499-2508
4. Matejicek, J., Sampath, S., *Acta Mater.*, vol. **49**, 2001, 1993-1999

## EVALUATION OF WEAR RESISTANCE OF SPUTTERED AMORPHOUS SiC FILM AND MEASUREMENT OF DELAMINATION STRENGTH OF FILM BY MICRO EDGE-INDENT METHOD

Masahiko Kato, Jinhua Zheng, Seiji Takezoe and Keiji Nakasa  
Hiroshima Univ., Kagamiyama, Higashi-Hiroshima, 739-8527, Japan  
kato@mec.hiroshima-u.ac.jp

SiC and SiCN films were deposited on titanium and tool steel substrates in an RF magnetron sputtering apparatus with a SiC target and a mixture of argon and nitrogen gas under various substrate heating temperatures and nitrogen gas flow rates. A micro edge-indent method was newly proposed to evaluate delamination energy of the thin films. The delamination energy is defined as follows[1]:

$$E_d = \frac{\int_0^{\delta_0} P dh - \int_0^{\delta_0 - B_1} P' dh}{S} \times \frac{2\theta}{2\pi}, \quad \theta = \tan^{-1} \frac{S}{x^2}, \quad (1)$$

where,  $B_1$  is the film thickness,  $S$  is the delamination area,  $x$  is the distance from edge to the indentation point,  $\delta_0$  is the displacement of the indenter at delamination, and  $P'$  is the load measured during the micro edge-indent test only on substrate.

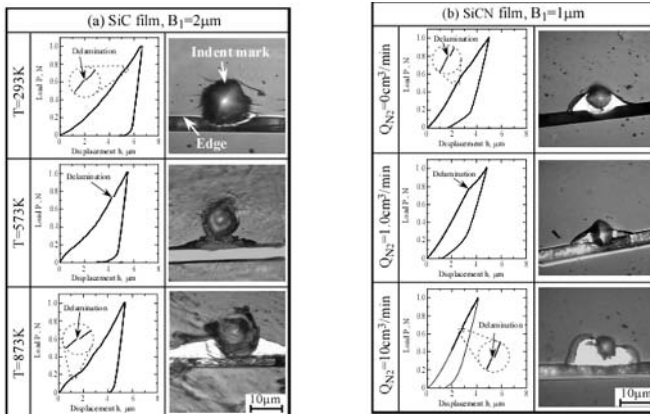


FIGURE 1. Load-displacement curves and optical micrographs of (a)SiC and (b)SiCN films after micro edge-indent tests.

Figure 1 shows load-displacement curves obtained by the micro edge-indent method and optical micrographs of (a)SiC and (b)SiCN films after the micro edge-indent test. Triangular shaped delamination of the films occurs between the indent point and the edge. The load increases with increase in the displacement, and discrete increase in the displacement due to the film delamination is observed.

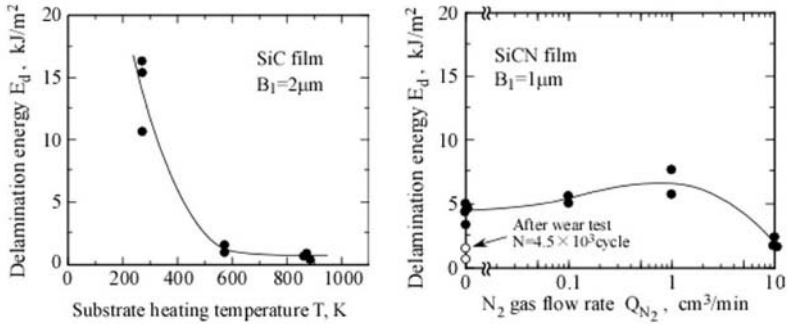


FIGURE 2. Delamination energy of (a)SiC and (b)SiCN films.

Figure 2(a) shows the relationship between substrate heating temperature  $T$  and delamination energy  $E_d$  of the SiC film. The maximum delamination energy is obtained when the substrate is not heated, and the  $E_d$  decreases with increasing  $T$ . The relationship between  $N_2$  gas flow rate  $Q_{N_2}$  and delamination energy  $E_d$  of the SiCN film is shown in Fig. 2(b). The  $E_d$  increases with increasing  $Q_{N_2}$  and reaches a maximum value at  $Q_{N_2} = 1 \text{ cm}^3/\text{min}$ .

Pin-on-disk type wear tests of the films were carried out under a pin load of 2.94N and a sliding velocity of 0.1m/s. The result shows that delamination of the films occurs when the number of rotation cycles reaches a critical number of rotation cycles. The wear delamination cycles of the SiC film decrease with increasing substrate heating temperature, and those of the SiCN film decrease with increasing nitrogen gas flow rate. The delamination cycles of the films almost correspond with the delamination energy before the wear tests.

In order to investigate the repeating damage accumulated at the interface of the SiC film during the wear test, the micro edge-indent test is applied on the wear scar at  $N = 4.5 \times 10^3$  cycles. The result is shown in Fig. 2(b) as an open circle symbol. The remarkable decrease in  $E_d$  is observed after the wear test.

From our research, it can be concluded that the micro edge-indent test is effective to evaluate the delamination energy of thin films.

## References

1. K.Nakasa, M.Kato, D.Zhang, K.Tasaka, J. Soc.Materials Science Japan, vol. 47, 413-419, 1998.

## PREPARING OF DIAMOND IN THE PRESENCE OF CH<sub>4</sub>-H<sub>2</sub> IN A COLD PLASMA PRODUCED BY A MAGNETRON

Maryam Habibi<sup>1</sup>, Mahmood Ghoranneviss<sup>1</sup> and Reza Naranji<sup>2</sup>

<sup>1</sup>Plasma Physics Research Center, Science & Research Branch, I.A.University, P.O.Box 14665-678, Tehran, Iran.

<sup>2</sup>I.A.University, Ardabil Branch, Ardabil, Iran.  
m\_habibi\_pprc@yahoo.com

In this paper we have prepared diamond by depositing the mixture of CH<sub>4</sub> and H<sub>2</sub> (%98 H<sub>2</sub> and %2 CH<sub>4</sub>) on silicon substrate in a cold plasma produced by a DC magnetron.(Fig. 1)

The percentage of the mixture is %98 H<sub>2</sub> and %2 CH<sub>4</sub> at the pressure of  $5 \times 10^{-3}$  Torr. Different pressures and different exposure times have been examined and different analyser such as,Raman Spectrum ,XRD and SEM have been used to investigate the results (Fig. 2).

details will be discuss in the full paper.

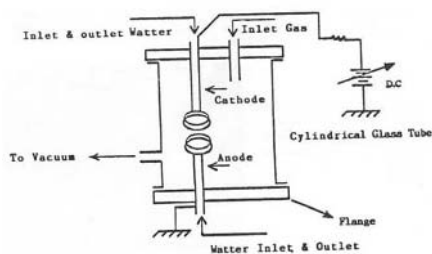


FIGURE 1. -Schematic diagram of Dc Magnetron Sputtering apparatus.

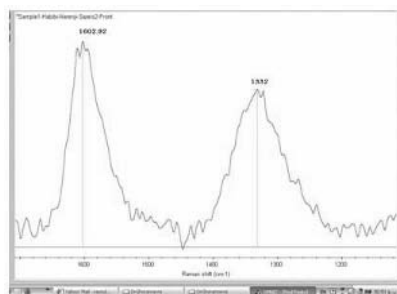


FIGURE 2. - Raman Spectrum obtion from coating DLC on silicon substrate.

---

**References**

1. S.Matsumoto, Y.Sato, M.Kamo and N.Setaka: *J.Appl.Phys.*, vol. **21** (1982) 483.
2. M.Kamo, Y.Sato, S.Matsumoto and N.Setaka: *J.Cryst.Growth*, vol. **62** (1983) 642.
3. S.Matsumoto: *J.Mater.Sci.Lett.*, vol. **4** (1985) 600.
4. A.Sawabe and T.Inuzuka: *Appl.Phys.Lett.*, vol. **46** (1985) 146.
5. K.Suzuki, A.sawabe, H.Yasuda and T.Inuzuka: *Appl.Phys.Lett.*, vol. **50** (1987) 728.
6. R. C. Devries, *Annu. Rev. Mater. Sci.*, vol. **17**, 167 (1987).
7. R. Messier, A. R. Badzian, T. Badzian, K. E. Spear, P. Bachmann, and R. Roy, *Thin Solid Films*, vol. **153**, 1 (1987).
8. R. Roy, *Nature (London)*, vol. **325**, 17 (1987).
9. J. C. Angus and C. C. Hayman, *Science*, vol. **241**, 913 (1988).
10. K. Suzuki, A. Sawabe and T.Inuzuka: *Appl.Phys. Lett.*, vol. **53** (1988) 1818.
11. F. G. Celi, P. E. Pehrsson, H.-t. Wang and J. E. Butler: *Appl. Phys. Lett.*, vol. **52** (1988) 2043.
12. F. G. Celii and J. E. Butler: *Appl. Phys. Lett.*, vol. **54** (1989) 1013.
13. K. E. Spear, *J. Am. Ceram. Soc.*, vol. **72**, 171 (1989).
14. J. C. Angus, F. A. Buck, M. Sunkara, T. F. Groth, C. C. Hayman, and R. Gat, *MRS Bull. October*, vol. **38** (1989).
15. W. A. Yarbrough and R. Messier, *Science*, vol. **247**, 688 (1990).
16. J. C. Angus, "History and Current Status of Diamond Growth at Metastable Conditions," *Proc. Of the 1<sup>st</sup> Int. Symp. On Diamond and Diamond-Like Films, The Electrochem. Soc., Pennington, New Jersey*, 1989, J. P. Dismukes, A. J. Purdes, K. E. Spear, B. S. Meyerson, K. V. Ravi, T. D. Moustakas, and M. Yoder, eds. (1989), P. 1.



## HIGH TEMPERATURE BEHAVIOR OF AL THIN FILM

C.-S. Oh<sup>1</sup>, J.-S. Bae<sup>2</sup>, S.-H. Choa<sup>3</sup> and H.-J. Lee<sup>4</sup>

Kumoh National Institute of Technology, 1 Yangho-dong, Gumi-si, Gyeongbuk, 730-701, Korea  
 Samsung Advanced Institute of Technology  
 Korea Institute of Machinery & Materials

<sup>1</sup> ocs@kumoh.ac.kr, <sup>2</sup> naco1025@kumoh.ac.kr, <sup>3</sup> shchoa@samsung.com, <sup>4</sup> hjlee@kimm.re.kr

Mechanical properties of thin films play a crucial role in the reliable design of the small-scale systems used in MEMS/NEMS and semiconductor industries. As the applications of thin film become more demanding, there is a need for accurate characterization of thermal and mechanical properties of the materials that are used in the devices. The aluminium (Al) film is widely used in many components because of its high electrical conductivity and low cost compared with some noble metals like gold, silver or platinum. The principal goal of this investigation is to extract two important thermo-physical properties, coefficient of thermal expansion (CTE) and creep behaviour, of a sputtered Al film by adopting a direct strain measurement technique while heating in a furnace.

We have developed techniques and procedures to directly measure the thermal strain in Al tensile specimens at high temperatures. This enables the measurement of both the CTE and the creep behavior at temperatures as high as 300 °C. A specimen has the shape shown in Fig. 1 and are heated directly in a homemade furnace. The specimen is 530 nm thick and 5 mm wide at its center. There are two Cr markers in the middle of a specimen for the interferometric strain measurement. The more detailed descriptions regarding the strain measurement are given in [1]. The test procedures including a novel specimen releasing technique and the entire test setup incorporating a homemade miniature furnace are firstly introduced by Oh *et al.* [2, 3]. The test setup is shown in the right side of Fig. 1. The system has three features. First of all, the thermal strain can be measured directly, accurately, and precisely without contact. Secondly, the test procedures can be applied in both tensile and fatigue tests in addition to the current high temperature test. Finally, the strain measurement technique is applicable without any modifications for not only thin films but also bulk materials.

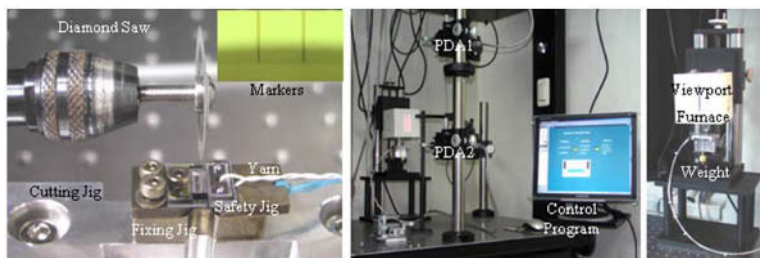


FIGURE 1. Specimen preparation procedure and high temperature test setup.

The thermal strain is recorded continuously while raising the temperature at the rate of 1 °C / min. Temperature is measured with a T-type thermocouple attached closely to a specimen. It is

proved that this heating rate is slow enough to exclude any thermal inertia effect. The thermal strains of Al film for the predefined temperature profile, room temperature (RT) to 200 °C and then return to the RT, are measured and one of them is shown in Fig. 2. There are three important matters to consider at this point. Firstly, the thermal strain shows very linear behavior up to 160 °C upon heating and from 175 °C upon cooling. The CTE values are calculated with the linear data only and evaluated as 27.9 and 24.9  $\mu\epsilon/^\circ\text{C}$  on heating and cooling, respectively. The reason of this difference is not clear right now but we're working on this. Secondly, the CTE of Al film is a little higher than that of bulk material. It is assumed that this difference can be originated from the microstructural differences. A transmission electron micrograph is shown in Fig. 3 for the reference. Finally, the material becomes nonlinear, deforms plastically, after 160 °C at a rather modest applied stress of 74 MPa. This is the evidence of creep.

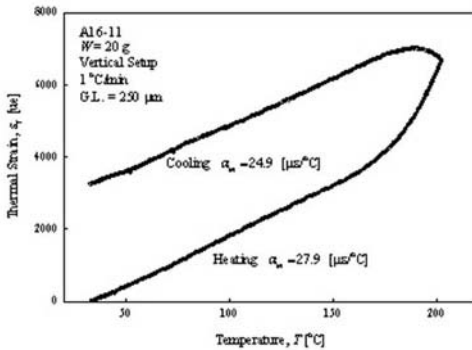


FIGURE 2. Thermal strain of Al film.

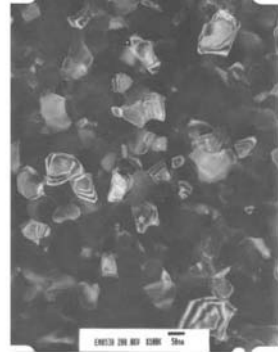


FIGURE 3. A TEM micrograph.

The direct strain measurement under direct heating in a furnace is the first ever obtained for this thin film material. The test methods have been established, initial results obtained, and a comprehensive study of this important aspect of thin film material behavior is under way. This approach is a logical extension of previous work [4] and is an important contribution to material testing at the micro-scale.

## References

1. Sharpe Jr., W.N., *An Interferometric Strain/Displacement Measurement System*, NASA Technical Memorandum 101638, 1989.
2. Oh, C.-S., Lee, C.-S., Choa, S.-H. and Lee, H.-J., In *SEM Annual Conference*, St. Louis, 2006 (presentation only).
3. Oh, C.-S., Lee, C.-S., Choa, S.-H. and Lee, H.-J., *Key Engng. Mat'ls*, vol. **326-328**, 2006.
4. Oh, C.-S., Sharpe Jr., W.N., *Sens. & Acts. Physical A*, vol. **112**, 66-73, 2004.

## BAUSCHINGER EFFECT IN THIN METAL FILMS ON COMPLIANT SUBSTRATES

J.P.M. Hoefnagels and J.J. Vlassak

Eindhoven University of Technology, Department of Mechanical Engineering, PO Box 513,  
5600MB, Eindhoven, The Netherlands

Division of Engineering and Applied Sciences, Harvard University, 29 Oxford Street, Cambridge,  
MA 02138-2901, USA

j.p.m.hoefnagels@tue.nl

Flexible electronic devices such as flexible displays and solar cells draw more and more attention from the industry. In these devices, the functionality is delivered by small-scale structures consisting of thin metal lines and other materials that are integrated on a compliant (e.g. polymer) substrate to make the device flexible. A major concern is reliability, since the small-scale structures with features on the order of micrometers or below are highly fragile, however, they are subjected to large thermo-mechanical loads during manufacturing and use. Although a growing literature exists on rupture and buckling of thin metal films on polymer substrates, see for instance Hutchinson and Suo [1], many mechanical issues of flexible electronics have not been studied in depth. In this project, one such issue, the Bauschinger effect of thin metal films bonded to a compliant substrate, will be studied in more detail, because the Bauschinger effect appears to be a particularly important issue in flexible electronics applications where the device is subjected to multiple strain cycles.

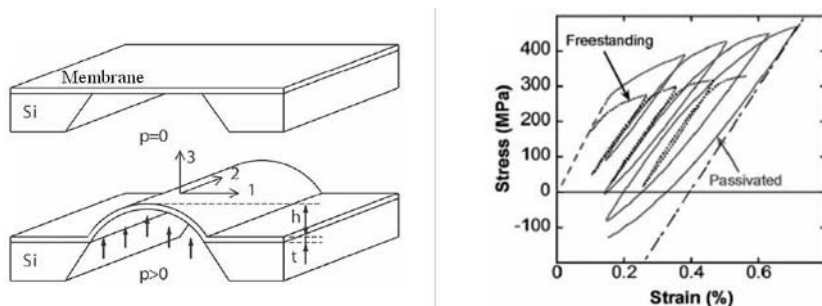


FIGURE 1. (a) Schematic of the plane-strain bulge test to determine the stress-strain curves of thin membrane, where the membrane may be a single material layer or a stack of multiple material layers. (b) Stress-strain curves of a freestanding 0.6  $\mu\text{m}$  Cu film and the same Cu film passivated by a hard SiN film. Both figures taken from Ref. [2].

We will study the effect of weak interfaces experimentally by means of the plane-strain bulge test technique, which was developed within the Vlassak group at Harvard University, see e.g. Ref. [3]. In this technique, rectangular micromachined membranes fabricated out of the material of interest are deflected by applying a pressure to the membrane, see Fig. 1(a). The stress-strain curve of the membrane material is readily determined from the deflection,  $h$ , of the membrane. Previously, this technique has been used to measure stress-strain curves of metal films as thin as

100 nm [4]. It should be noted that the membrane does not need to be a single material layer, but can in fact be any multi-layer stack of thin material films.

Xiang and Vlassak used a double-layer stack consisting of a sputter deposited Cu thin film adhered on a hard SiN film to alternately drive the Cu film in tension and compression [2], see Fig 1(b). They observed that the Cu film exhibit an unusual Bauschinger effect with reverse flow already occurring on unloading. This behavior was explained by the built-up of a dislocation density at the Cu-SiN interface that was assumed to be impenetrable to dislocation movement, i.e. the interface was said to be 'fully passivated'. On the other hand, the freestanding Cu thin film, showed little or no reverse flows when the film is fully unloaded, see Fig. 1(b).

While the effect on plasticity in metallic films with a free surface versus films with a strong interface on a hard and stiff substrate may be understood, it is unclear what is the effect of a weak interface or an interface with a soft layer, as is often the case in flexible electronics. For instance, plastic deformation in the thin film may trigger debonding of the interface, thereby allowing strain localization. Moreover, most free metal surfaces develop a native oxide which may also prevent dislocation movement to a certain degree, therefore, a highly compliant interface may reveal mechanical behavior closer to a truly unpassivated surface than a free metal surface with native oxide.

To test these hypotheses, in the present research, a range of three-layer membranes consisting of SiN/polymer/Cu and SiN/Cu/polymer stacks have been manufactured for testing in the bulge test apparatus. The SiN layer is always present in the stack to be able to drive the Cu layer into compression, while a range of polymer films with different hardness applied by a spin coating process is added to create a set of Cu interfaces with varying compliance. Particular care has been taken to assure that the Cu film at the Cu-polymer interface is not oxidized. The bulge tests are scheduled to be executed in the upcoming months and the resulting stress-strain curves of a Cu film adhered to compliant substrates will be compared to the stress-strain curves of (the same) Cu film in a freestanding and fully-passivated configuration. Emphasis will be on differences in the Bauschinger effect and in the flow stress [see Fig. 1(b)], while the evolution of the microstructure may be measured with transmission electron microscopy. The results promise to yield new and detailed insight into the plasticity of thin metal films found in flexible electronics applications and will be used to formulate an (extended) model of the dislocation dynamics at (weak) interfaces.

## References

1. Hutchinson, J.W. and Suo, Z., *Advances in Applied Mechanics*, vol. **29**, 63-191, 1991.
2. Xiang, Y. and Vlassak, J.J., *Scripta Materialia*, vol. **53**, 177-182, 2005.
3. Xiang, Y., Chen, X., and Vlassak, J.J., *Journal of Materials Research*, vol. **20**, 2360-2370, 2005.
4. Xiang, Y., Li, T., Suo, Z., and Vlassak, J.J., *Applied Physics Letters*, vol. **87**, 161910, 2005.

## PRACTICAL PROBLEMS OF MODAL ANALYSIS OF AERO ENGINE BLADES

Strain Posavljak  
“ORAO” a.d.

Sabackih djaka bb, 76300 Bijeljina, Bosnia and Herzegovina  
oraoi@rstel.net

For some of the aero engine blades, overhaul technology requires testing of their modal shapes and eigenfrequencies. Arrangement of blades on disk according to eigenfrequencies can be the first reason. The second reason can be fatigue control or endurance testing which is carried out on the shaker. In order to help operator on the shaker in searching of eigenfrequencies, it is good to use The Finite Element Method (FEM). For example, modal shapes and eigenfrequencies of blade marked with B1 (Fig. 1), with satisfying deviation, were obtained using FEM and using shaker supported by technique known as technique of “sand figures” [Posavljak S., View on Problems of Development and Exploitation of Aero Engine Disks and Blades (in Serbian), Proceedings of The 5th International Conference DQM-2002, Belgrade, Serbia, 26-27 June 2002, 373-379].

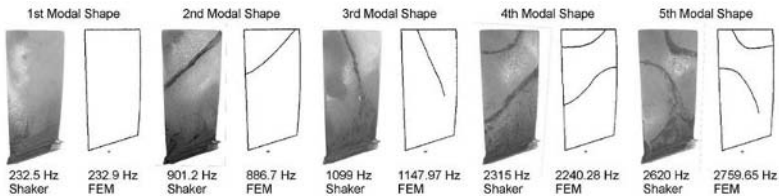


FIGURE 1. Modal shapes and eigenfrequencies of blade marked with B1

Fatigue control of aero engine blades is procedure consisted in looking for an answer on the question, can the blade endure defined number of cycles on defined stress level. It is usually that fatigue control is performed on the level of the first bending shape of oscillating and eigenfrequency  $f$  in Hz which belongs to it. Defined number of cycles  $N$  in that case can be controlled by measuring of time  $t$  in minutes

$$t = \frac{N}{f \cdot 60} \quad (1)$$

Defined stress level can be controlled by perimeter  $D$  which presents blade top oscillating range. For blade marked with B2, defined stress level  $\sigma = \pm 480$  MPa was controlled by perimeter  $D = 2.2$  mm determined on the following way [Posavljak S., Endurance of Aero Engine Blades, Journal of Mechanical Engineering Design, vol. 8, No 1, 23-28, 2004 (Yugoslav Society for Machine Elements and Design)]. Two blades of type B2 was taken. The first bending shapes of oscillating were provoked by shaker equipped with strobe lamp and measuring microscope. Using Wheatstone's quarter bridge formed of HBM strain gages LY41 1.5/350, with nominal resistance 350  $\Omega$  and factor  $K = 1.92$ , dependency  $D$  of voltage measuring signal  $U_M$  was determined. Quarter bridge was being supplied by direct current of voltage  $U_S = 5$  V via amplifier RM4220. Voltage measuring signal was conducted via the same amplifier to oscilloscope HP54501A. Complete measuring chain, quarter bridge – amplifier – oscilloscope is presented in Fig. 2a. Dependence  $D$  of  $U_M$ , according to Fig. 2b., is given in form of empirical expression

$$D = 0.3838 U_M \quad (2)$$

For stress level  $\sigma = \pm 480$  MPa and modulus of elasticity  $E = 2 \cdot 10^5$  MPa, corresponding strain level  $\varepsilon = \pm 2400 \mu\text{D}$  ( $1 \mu\text{D} = 1 \mu\text{m/m}$ ) was determined by expression

$$\varepsilon = \frac{\sigma}{E \cdot 10^{-6}} \quad (3)$$

Using shunt calibration according to [Hofman K., *An Introduction to Measurement using Strain Gages*, Hotinger Baldwin Messtechnik GmbH, Darmstadt, 1989.], measuring voltage signal for strain  $\varepsilon = -2400 \mu\text{D}$  amounted  $U_M = 5.867$  V. For that value of  $U_M$ , using (2), approximate value of perimeter  $D = 2.2$  mm was obtained.

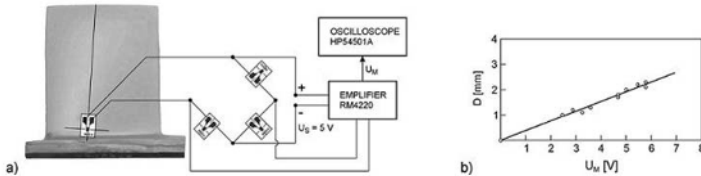


FIGURE 2. Measuring chain (a) and dependence  $D$  of  $U_M$  of blades type B2

Fractures of aero engine blades in many cases are result of their oscillating. In Fig. 3a it can be seen blade B3 fractured during exploitation. Fracture distance from root section is 40 mm. In the purpose of investigation of fracture reasons, modal analysis was realized. It is shown that fracture is result of fatigue on the third bending shape of oscillating with eigen frequency  $f = 10692.92$  Hz. Distance of expected fracture from root section according to Fig. 3b, determined by FEM, amounts 39.1 mm and has good coincidence with real fracture position.

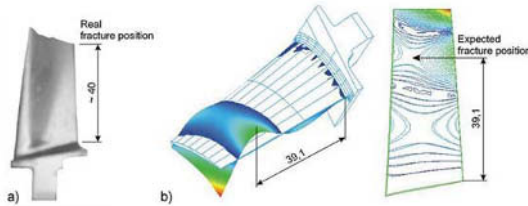


FIGURE 3. Real (a) and expected fracture position (b) of blade B3

## References

1. Posavljak S., *View on Problems of Development and Exploitation of Aero Engine Disks and Blades (in Serbian)*, Proceedings of The 5th International Conference DQM-2002, Belgrade, Serbia, 26-27 June 2002, 373-379
2. Posavljak S., *Endurance of Aero Engine Blades*, Journal of Mechanical Engineering Design, vol. 8, No 1, 23-28, 2004 (Yugoslav Society for Machine Elements and Design)
3. Hofman K., *An Introduction to Measurement using Strain Gages*, Hotinger Baldwin Messtechnik GmbH, Darmstadt, 1989.

## OPTICAL TECHNIQUES FOR RELIEF STUDY OF MONA LISA'S WOODEN SUPPORT

Fabrice Brémand, Pascal Doumalin, Jean-Christophe Dupré, Franck Hesser and Valéry Valle  
Laboratoire de Mécanique des Solides, CNRS, UMR 6610, Université de Poitiers  
SP2MI Bd M. et P. Curie, Téléport 2, BP 30179, 86962 Futuroscope Chasseneuil cedex, France  
jean-christophe.dupre@lms.univ-poitiers.fr

We present in this paper an original application of the use of optical methods for the study of the famous painting: Mona Lisa. Several laboratories [1] have participated to the study of this painting to evaluate the degradation risk, especially in relation with the existing crack and to optimise the conservation conditions, regarding both the humidity regulation and the design of the frame. Mona Lisa is painting on a poplar support, so the aim of our study, is to obtain a whole field 3D profile of the panel on front and back face of Mona Lisa [2]. Furthermore, these values allow us to understand the mechanical impact by the frame in which the panel is maintained attached and are used to describe the hygromechanical behaviour of the wooden painting by many measurements realized during several hours. These experimental data have been used to realize a numerical model of the panel, and also to validate the numerical simulations of the mechanical behavior of the panel [1, 3].

The difficulties of this study are different than the classical ones in laboratory. In fact, there exist a large number of unknown factors like brightness and contrast of the painting and the room's lighting in the Louvre museum. The measurement technique must have a low lightening of the painting and a minimum apparatus. The dimension of the studied zone is relatively large  $800 \times 600 \text{ mm}^2$  with an accuracy of several  $1/100 \text{ mm}$ . So, two techniques have been chosen: shadow moiré and projection moiré [4][5]. The first technique is the more precise but more complicated to put into practice (specially the use of a reference grating put on the front of the specimen). It is generally used to study the behavior of materials under mechanical stresses, but also for determining the form of small objects. The second technique, is less sensitive, but easier to execute, and may be used for large objects. After one test realized at the C2RMF (Centre de Recherche et de Restauration des Musées de France) laboratory on a painting of the same period, the shadow moiré has been chosen. It is more accurate but especially less sensitive to the dark tints, changes of contrast and color of the picture, or its luster.

The device is constituted by a large grating with a pitch of 1 line/mm mounted on translation stages in order to impose a phase shift of the moiré fringes (Fig. 1). The images are recorded by a numerical CCD camera. A phase shifting technique [6] based on 8 recorded images is used.

Just a few seconds are necessary to obtain the images, which made it possible to perform multiple measurements and to witness change, even fast change, over time. Reliefs were obtained with an average precision of  $5/100$  of a millimeter over a surface of  $518 \times 770 \text{ mm}$ , and a resolution of the order of  $600 \times 900$  points (Fig. 2). During the day of tests, we have observed the deformations of the panel. A contraction of the order of  $3/10$  of a millimeter was detected early on in the center right part of the panel. This deformation may originate in changes in the wood's behavior in response to atmospheric conditions of humidity and temperature, which are not the same in the room as in the case. The greatest distortion was observed on removal from the frame ( $\pm 1 \text{ mm}$ ) (Fig. 3), the deformation and curvatures are at their greatest at the level of the crack and also in the lower part of the panel. This is an indication that these two zones are more strongly affected by forces of flexion and are critical areas calling for careful monitoring. In the future, it

might be possible to test the picture through the glass of its case. If so, it would be possible to establish a procedure to check the panel frequently without handling it or even opening the case.



FIGURE 1. Experimental device

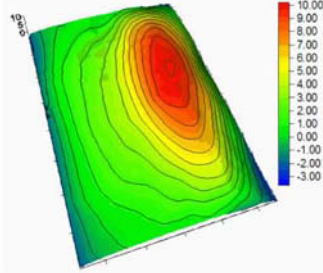


FIGURE 2: Measured relief (mm) on the front face

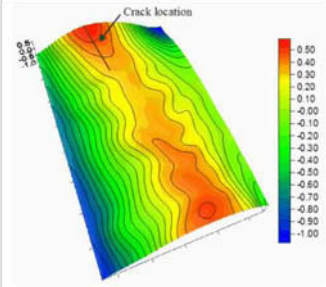


FIGURE 3 : out of plane deformation after remove the panel from the frame

## Acknowledgments

We thank Jean-Pierre Mohen, Michel Menu and Bruno Mottin (C2RMF, UMR 171), Cécille Scallierez and Vincent Pomarède, Curators in the Louvre Museum for supporting the research work.

## References

1. J.P Mohen, M. Menu, B. Mottin, "Mona Lisa, Inside the Painting", Abrams, New York, september 2006.
2. F. Brémand, P. Doumalin, F. Hesser, J.C. Dupré, V. Valle, "Measuring the relief of the panel support without contact", "Mona Lisa, Inside the Painting", J.P Mohen, M. Menu, B. Mottin, Abrams, New York, September 2006.
3. J. Gril, E. Ravaud, L. Uzielli, J.C. Dupré, P. Perré, D. Jaunard et P. Mandron, "Mona Lisa saved by Griffith theory: assessing the crack propagation risk in the wooden support of a panel painting", Integrated Approach to Wood Structure, Behaviour and Applications ESWM and COST Action E35 meeting; Florence (Italy), 14-17 mai 2006
4. C. Brèque, J.C. Dupré, F. Brémand, "Calibration of a system of projection moiré for relief measuring application to biomechanics". Optics and Laser in Engineering, vol. **41**, no 2, p. 241-260, February 2004.
5. Mauvoisin G., Brémand F., Lagarde A. (1994). 3D shape reconstruction by phase shifting shadow moiré, Applied Optics vol. **33**, no 11, pp 2163-2169, 1994
6. Morimoto, Y. and Imamoto, Y. (1994) Error causes and error reduction in fringe pattern analysis by phase shifting method using Fourier transform, Experimental Mechanics, vol. **34**, pp. 379-384



## RESIDUAL STRESS AND DEFORMATION INDUCED BY LASER SHOCK PEENING ON TITANIUM ALLOYS

Christophe Cellard, Pierre Osmond, Delphine Reiraunt, Emmanuelle Rouhaud, Sébastien Remy and Ana Viguera-Sancho

Université de Technologie de Troyes (UTT), SNECMA Evry - Corbeil  
 Université de Technologie de Troyes, 12 Rue Marie Curie BP 2060 10010 TROYES Cedex  
 SNECMA Evry – Corbeil, Route Henry Auguste Desbrières BP 81 91003 EVRY Cedex  
 christophe.cellard@utt.fr, pierre.osmond.2006@utt.fr, delphine.reiraunt@utt.fr,  
 emmanuelle.rouhaud@utt.fr, sebastien.remy@utt.fr, ana.viguerasancho@sncema.fr

During operation, a turbojet can swallow foreign objects (birds, fragments, etc.). The damage induced by these objects is known as FOD (Foreign Object Damage), and can lead to the cracking of the fan blades. In order to reduce the costs of maintenance, engine manufacturers try to find a way to increase the fatigue life, after FOD, of the fan blades by introducing compressive residual stresses in some areas with a specific surface treatment : laser shock peening (LSP). [1]

The aim of this study is to point out the effects of this new treatment. The following results were carried out on square-shaped samples of Ti-6Al-4V alloy (TA6V) and Ti-5Al-2Sn-2Zr-4Cr-4Mo alloy (Ti17).

A first task has been carried out on the determination of the surface residual stresses on laser shock peened samples, by X Ray diffraction and by the crack compliance method (Fig. 1) [2].

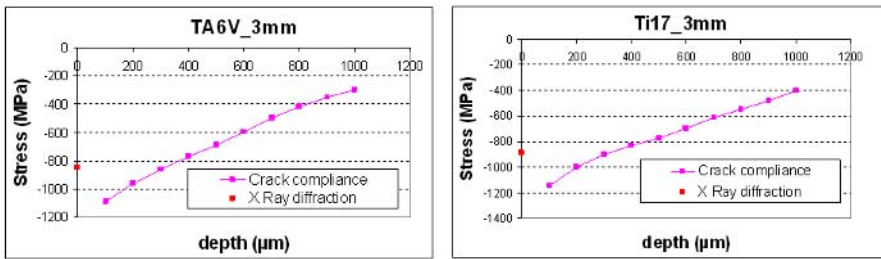


FIGURE 1. Comparative of measures : X Ray diffraction and crack compliance

A second task was dedicated to the determination of the global shape of the samples. Those one have been measured with two methods, a coordinate measuring machine and laser triangulation.

From the knowledge of the residual stress profile, the curvature can be calculated [3]. The following method is applied :

- Introduction of the residual stress profile, in Zebulon, obtained when the sample is constrained. (1)

$$\sigma_{constrained} = \varepsilon_p \frac{E}{1 - \nu} \quad (1)$$

$$\text{with } \varepsilon_p = \frac{1-\nu}{E} \sigma - (A.z + B)$$

A, B : terms relative to the curvature and the elongation of the specimen respectively.

- Relaxation of the boundary conditions and elastic readjustment of the specimen.

It is then compared to the one obtained by laser triangulation on the Ti17 sample with 3mm compression (Fig. 2). The same approach is done for the residual stress profile (Fig. 3).

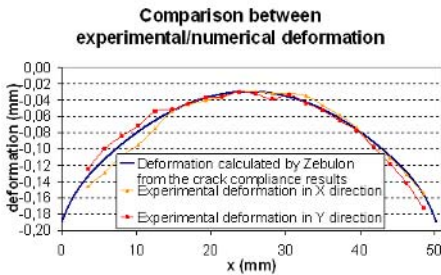


**FIGURE 2. Comparison between experimental/numerical deformation**

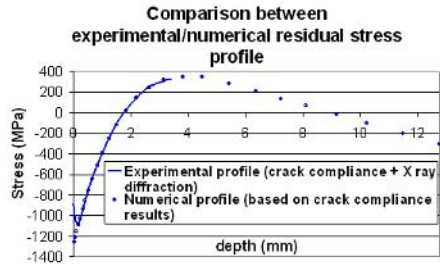


**FIGURE 3. Comparison between experimental/numerical residual stress profile**

As a conclusion, we can say that this study pointed out that the laser shock peening generates deeper and more compressive residual stresses than shot peening, which is a great asset for fatigue life. However, it produces a small deformation on the 12.75mm thickness specimens. That is why a detailed study should be carried out to determine the effects on thin pieces like fan blades.

### Acknowledgements:

The present study was sponsored by SNECMA (Safran group)

### References

1. R. Fabbro, P. Peyre, *Le principe du choc laser et ses applications au traitement des matériaux*, Souder – 1998 – Septembre – no 5
2. W. Cheng, I. Finnie, *Measurement of residual stress distributions near the toe of an attachment welded on a plate using the crack compliance method*, Engineering Fracture Mechanics, Volume 46, Issue 1, September 1993, p. 79-91
3. M. Francois, F. Cochenec, E. Rouhaud, J.L. Chaboche, L. Roucoules, *From residual stresses to the curvature of shot-peened plates*, to be published

## DEVELOPMENT AND APPLICATION OF BIAXIAL COMPRESSION TEST DEVICE FOR METALLIC MATERIALS

Ichiro Shimizu

Graduate School of Natural Science and Technology, Okayama University

3-1-1, Tsushima-naka, Okayama 700-8530, Japan

shimizu@mech.okayama-u.ac.jp

The multiaxial testing methods have been used to investigate the mechanical behavior of engineering materials, especially for evaluating yield surfaces and forming limits. Most of the methods employed are a biaxial tension test and a bulge test for sheet material in small strain range, e.g. by Green *et al.* [1] and by Azrin and Backofen [2], and a torsion test with tension or internal pressure for tube type material, e.g. by Takahashi *et al.* [3] and by Hecker [4]. However, the multiaxial testing under compressive stress condition for bulk material has been scarcely performed, though such a condition often appears in metal forming processes, e.g. forging, extrusion, etc. In addition, the compressive stress condition permits the deformation to large strain range, which is effective for evaluation of plastic behavior of metallic materials.

In order to achieve the biaxial compression test with an arbitrary strain path, a biaxial compression test device was newly developed in the present study. Fig. 1 shows the developed mechanism of the biaxial compression as well as the manufactured test device. A specimen of rectangular block shape is placed in the center and its surfaces are contacting with four dies. Each die is attached to a linear slide unit, which enable the die movement during compression. The compression of the specimen in  $y$  direction is performed by dies 1 and 3. At the same time, dies 2 and 4 are forced to move in  $y$  direction, so that they do not obstruct the compression. The compression of the specimen in  $x$  direction is performed by dies 2 and 4, with the movement of dies 1 and 3 in  $x$  direction. It is possible to perform these compressions simultaneously, so that the arbitrary strain path can be achieved. The abrupt strain path change is also possible without unloading, which is another advantage for the investigation of plastic behavior.

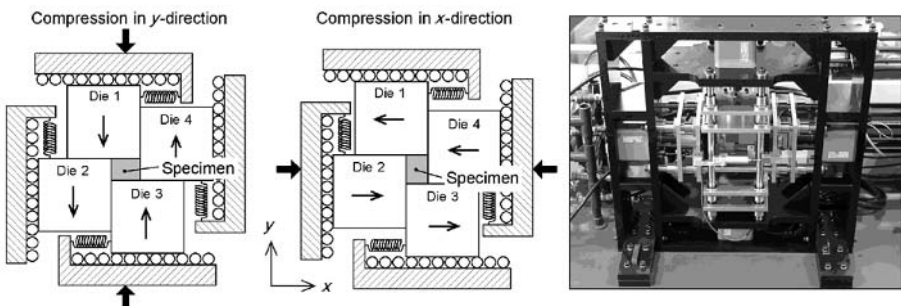


FIGURE 1. Mechanism for biaxial compression with an arbitrary strain path and a photo of the newly developed biaxial compression test device.

As one of the applications of this new device for the study on the mechanical behavior of metallic materials, sequential biaxial compression tests with an abrupt path change were performed

on industrial pure aluminum (fcc structure) and titanium (hcp structure). Fig. 2(a) shows the applied strain paths in the test, by the plane strain compression in  $x$  direction followed by that in  $y$  direction. The switch of the strain path is performed without unloading, when the  $x$  strain by the first compression becomes the predetermined value  $\varepsilon_{x0}$ . Fig. 2(b) and (c) show the equivalent stress-equivalent plastic strain curves of the aluminum and the titanium, respectively, with the various values of  $\varepsilon_{x0}$ . The equivalent stress of the aluminum rapidly increases and then it gradually decreases just after the strain path. Meanwhile, the equivalent stress of the titanium once decreases and then gradually increases with the path change. Such specific phenomena are closely related to both the anisotropy evolution and the latent hardening effect. The latter was studied earlier on the single crystalline metals, e.g. by Franciosi *et al.* [5] by uniaxial tension followed by tension, and later on the polycrystalline metals, e.g. by Stout *et al.* [6] by rolling followed by plane strain compression. For the investigation of latent hardening effect, the sequential biaxial compressions with the newly developed device is quite effective because the macroscopic stress condition is uniform during deformation. The difference of such transient stress variations between the aluminum and the titanium also has important informations for crystal plasticity. This difference is supposed to be caused by the different crystal structures, because the slip systems in titanium is limited and twin deformation must occur when the compression is performed to the specific direction with regard to the crystal orientation. The influence of such microscopic phenomena on the plastic behavior is also investigated by microscopic approaches.

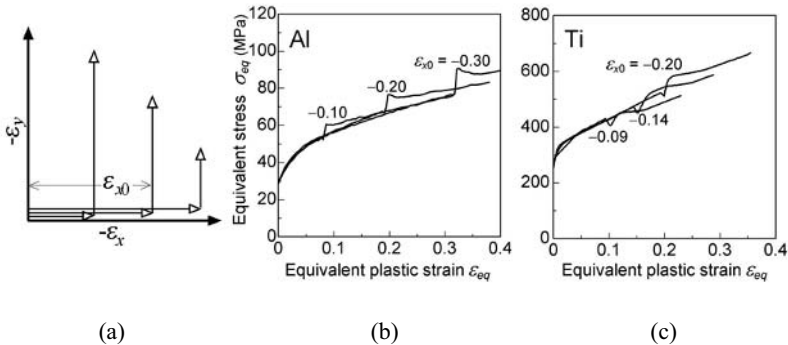


FIGURE 2. Applied strain path with an abrupt path change and equivalent stress - equivalent plastic strain curves for pure aluminum and titanium.

## References

- Green, D. E., Neale, K. W., MacEwen, S. R., Makinde, A. and Perrin, R., *Int. J. Plasticity*, vol. **20**, 1677-1706, 2004.
- Azrin, M. and Backofen, W. A., *Metall. Trans.*, vol. **1**, 2857-2861, 1970.
- Takahashi, H., Fujiwara, K. and Nakagawa, T., *Int. J. Plasticity*, vol. **14**, 489-509, 1998.
- Hecker, S. S., *Acta Mechanica*, vol. **13**, 69-86, 1972.
- Franciosi, P., Berveiller, M. and Zaoui, A., *Acta Metall.*, vol. **28**, 273-283, 1980.
- Stout, M. G., Martin, P. L., Helling, D. E. and Canova, G. R., *Int. J. Plasticity*, vol. **1**, 163-174, 1985.

## MEASUREMENT OF RESIDUAL STRESSES IN LARGE ENGINEERING COMPONENTS

F. Hosseinzadeh, D.J. Smith and C.E. Truman  
 Solid Mechanics Group, Department of Mechanical Engineering  
 University of Bristol, UK, BS8 1TR  
 David.Smith@Bristol.ac.uk

Residual stresses play an important role in the strength and life of the components in service. Furthermore, full knowledge of the residual stress field through the whole component is crucial to understanding how residual stresses impact on failure [1]. In the present investigation through thickness residual stress measurements are carried out using the deep hole drilling technique in large components used in the steel rolling industry.

Residual stresses are introduced into the steel rolling mill components during their manufacture, subsequent heat or mechanical treatments and also machining. Also, these initial residual stress fields redistribute under different operating loadings such as rotation, thermal or mechanical loadings. Although there is a wide range of residual stress measurement methods few can penetrate greater than about 30mm inside large components. One technique is the deep hole drilling method that has been able to measure residual up to depths of about 400mm, adapted to measure residual stresses through very thick components [1, 2]. Deep hole drilling technique is mainly based on diametric strain measurement of a reference hole. Firstly a reference hole is drilled through the thickness of the component followed by diameter measurement of the hole. Consequently a column of material including reference hole is extracted from the specimen. The core is coaxial with the reference hole and is assumed to be stress free. After trepanning the reference hole diameter is remeasured and the variation in hole diameter through depth is applied to determine residual stresses through the thickness. Deep hole drilling procedures are shown in Figure 1 and the analysis of converting strains to stresses can be found in [2].

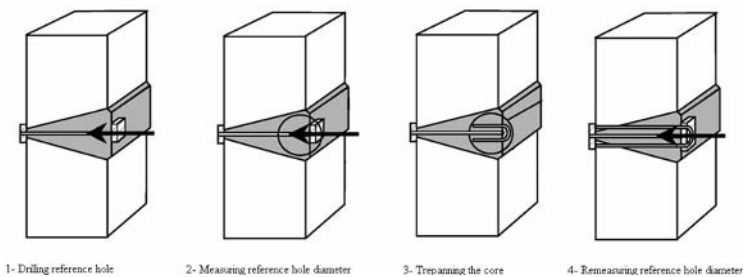


FIGURE 1. Deep hole drilling procedures.

Residual stresses were measured in samples used in large rolls under severe cooling/heating load cycles, rotation and mechanical contact with extremely hot stocks used in rolling mills. Geometry of the specimens and deep hole drilling directions are shown in Figure 2. Two different sets of measurements were carried out. The first one is a horizontal universal roll assembly consisting of a roll shaft onto which a spheroidal graphite iron sleeve was shrink-fitted, the

external diameter of the sleeve was 854 mm. A series of sleeves for vertical rolls were also measured at different stages of their manufacture, as-cast, machined, and then with a bearing fitted. (Figure2).

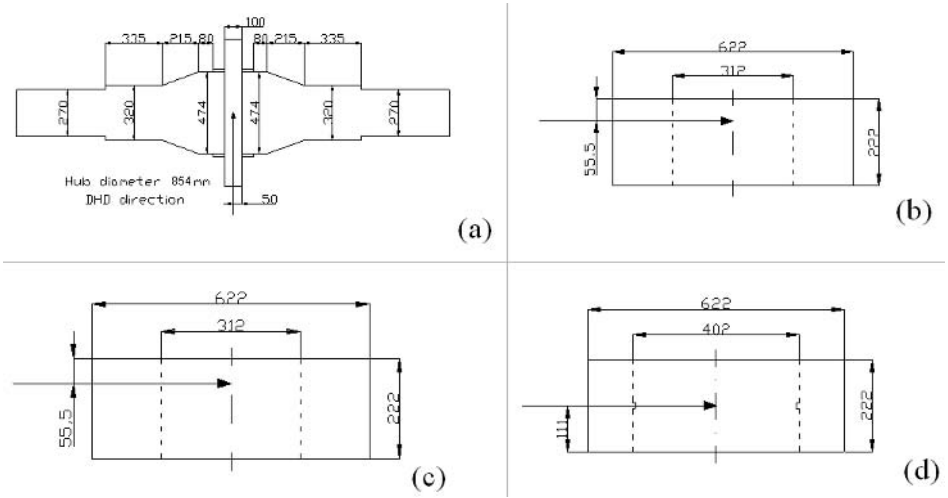


FIGURE 2. Specimens geometry and the direction of deep hole drilling method ((a). universal roll, (b) unmachined sleeve,(c) machined sleeve, (d) machined sleeve with a bearing fitted).

The contributions of the different operation and manufacturing processes are discussed. In particular redistribution of residual stress fields have been investigated at the different stages: before and after machining the components, after assemblage and followed by use in service.

## References

1. Withers, P.J., Bhadeshia, K.H.D.H , Materials Science and Technology, vol. 17, 355-365, 2001
2. E.K. Kingston, D. Stefanescu, A.H. Mahmoudi, C.E. Truman and D.J. Smith, "Novel applications of the deep-hole drilling technique for measuring through-thickness residual stress distributions", Journal of ASTM International, April 2006, vol. 3, no. 4, Paper ID JAI12568

## MEASUREMENT OF INTERACTION FORCES BETWEEN WHEEL AND RAIL ON AN EXTREME TRAIN WHEELSET

R.A. Cláudio, J. Duarte Silva, A.J. Valido and P.J. Moita  
Department of Mechanical Engineering, Escola Superior de Tecnologia de Setúbal,  
Polytechnic Institute of Setúbal, 2910-761 Setúbal, Portugal  
rclaudio@est.ips.pt; jsilva@est.ips.pt; avalido@est.ips.pt; pmoita@est.ips.pt

During the last few years the development of software and hardware has provided large improvements in terms of computational simulation including dynamic analysis. Particularly, with respect to the study of railway vehicles it is possible to have a quite accurate prediction of the vehicle dynamic behaviour, under any running conditions. By this way it is possible to put on market a new train technology in a shorter period of time, reducing to a minimum the number of necessary prototypes, having consequent effects on final costs. However, to validate a new train, computational simulations are not enough, being necessary experimental tests, in real conditions, to ensure the vehicle safety and reliability.

The UIC 518 Code [1] covers all the provisions dealing with on-line running tests for acceptance of railway vehicles from the point of view of dynamic behaviour in connection with safety, track fatigue and running behaviour for international traffic acceptance purposes. The vehicle type, the track quality, the loading conditions, the atmospheric conditions and the quantities to be measured are parameters that have to be considered in these tests. The code also defines the statistical treatment of the calculated quantities in order to verify if they are inside safe limits [1].

Two of the most important quantities to be measured are the lateral and vertical wheel/rail interaction forces on each wheel of a wheelset. According to the terminology defined by [1], they are designated by  $Y$  and  $Q$ , respectively. Dealing with the measurement of  $Y$  and  $Q$  forces, same works have been presented, Joly [2] and Silva *et al.* [3].

The measurement of the wheel/rail interaction forces can be done by a direct method or an indirect method, Silva *et al.* [3]. Using an indirect method the interaction forces can be easily obtained by measuring the forces transmitted by the suspension to the car body. Establishing the dynamic equilibrium it is possible to determine the vertical force on each wheel of the same wheelset, and the sum of the lateral forces produced by both wheels. However, using this method it is not possible to determine the lateral force in each wheel (only the sum) and lacks in accuracy since it depends on many characteristics of the suspension elements. The direct method provides a solution to many of these problems but involves direct instrumentation of the wheelset that in many cases can be quite an involving process. In some situations the real wheelset is replaced by a specific one designed exclusively for the force measurement.

This paper presents a methodology to measure directly the lateral and vertical wheel/rail interaction forces in each wheel, independently. The principle is based on a hybrid technique that relates the strains measured on the faces of a wheel using strain gages, with the corresponding values of strain calculated by the Finite Element Method (FEM) considering unitary lateral and vertical forces. Several whetstone full bridges were used to combine different signals obtained from specific strain gages, whose location was determined according to the results of the FEM analysis, in order to have signals that are proportional only to the applied lateral or vertical forces. This methodology was validated statically in a testing facility by simulating several combinations of the forces and different contact points between wheel and rail, on a complete wheelset as well as on a bogie, Cláudio [4].

In real conditions, the forces were measured on an extreme wheelset of a passenger's train, running at high speed. Telemetry equipment was used to transmit the strain gages signals measured in the wheel to the train car body where a data logger was installed. Various curves showing the variation of lateral and vertical forces measured on the instrumented wheelset under several load conditions are presented. As an example, Fig. 1 shows all the forces measured in the front wheelset when the train is running at 97,5Km/h, describing a curve with 550m radius.

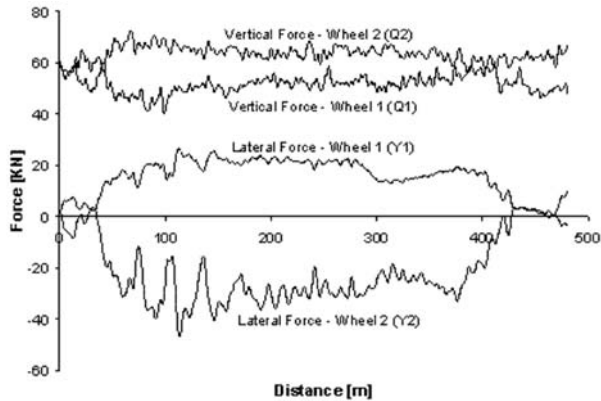


FIGURE 1. Forces measured on an unloaded passengers train.  
Front wheelset; Speed 97,5km/h; Curve Radius 550m.

## References

1. International Union of Railways, "Testing and acceptance of railway vehicles from the point of view of dynamic behaviour, safety, track fatigue and running behaviour", UIC code 518, 2<sup>nd</sup> Edition, 1999
2. Joly, Roland, *Essais de Dynamique Ferroviaire, Extrait de la revue générale des chemins de fer*, Juillet-Août, 1975
3. Silva, J.M., Silva, J.D., Figueiras, L., Marques, J.D., Pereira, A., *Mecânica Experimental*, No. 6, 99-108, 2001
4. Cláudio, R., *Proceedings of the 2as Jornadas Politécnicas de Engenharia Mecânica, Automóvel, Organização e Gestão Industrial, Energia e Ambiente*, Escola Superior de Tecnologia de Setúbal, 2002.



## MONITORING AND DIAGNOSIS OF DRILL WEAR AND THE THERMODYNAMIC PHENOMENAS OF MATERIAL REMOVAL BY DRILLING OF STAINLESS STEELS

Jozef Jurko

Technical University in Košice, Faculty of Production Technology seat in Prešov  
Štúrova 31, 080 01, Prešov, Slovakia  
jurko.jozef@fvt.sk

The paper described the phenomenas, which influencing on the twist drill of chisel cutting edge. Research and development of the phenomenas its very important for the next problem solution by drilling. The cutting part of twist drill is frequently the tool wear (for example fracture of cutting part) in the tool peak point and by chisel cutting edge. This is problems is very important and use for very difficult the machinability materials (for example stainless steels Cr18Ni8). The results of experimental verifying of the tools for the tool life of twist drill in practice. This paper investigates the performance of a cutting tool embedded with a heat pipe on reducing cutting temperature and wear in machining. The temperature of a tool plays an important role in thermal distortion and the machined part's dimensional accuracy, as well as the tool life in machining. A new embedded heat pipe technology has been developed to effectively remove the heat generated at the tool–chip interface in machining, thereby, reducing tool wear and prolonging tool life. In particular, the technique can effectively minimize pollution and contamination of the environment caused by cutting fluids, and the health problems of skin exposure and particulate inhalation in manufacturing. The finite element analysis simulations show that the temperature near the cutting edge drops significantly with an embedded heat pipe during machining. Temperature measurements at several locations on the cutting tool insert agree with the simulation results both with and without the heat pipe. Experiments were carried out to characterize the temperature distributions when performing turning experiments using a cutting tool installed with an embedded heat pipe. The paper described the experimental results of research works number 01/3173/06. There is no single universally accepted definition of tool life. The life needs to be specified with regard to the process aims. A common way of quantifying the end of a tool life is to put a limit on the maximum acceptable flank wear,  $VB$  or  $VB_{max}$ . Typical figures are by table 1:

TABLE 1. Evalue of the Tool Wear “VB “

HSS tools, roughing	1.5 mm
HSS tools, finishing	0.75 mm
Carbide tools	0.7 mm
Ceramic tools	0.6 mm

The problems of machinability materials be connected with tool life (tips of wear), cutting forces and energy, quality of machined surface and chip formation. At present is more works, which orientated on the experimental measurements the system parameters on the quality influence. Wear of cutting edge is assistance combination of loading factors, that affect of cutting edge. Metal cutting of difficult materials (for example stainless steel) have a differents cutting phenomenas in cutting zone (Figure 1).

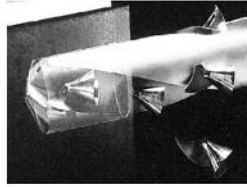


FIGURE 1. The Cutting Zone by drilling.

Technological system is obtained four elements: Machine – Tool – Fixture – Object. For cutting process is very important interaction between Tool and Object, and past elementary definition is interaction Cutting edge – Workpiece Surface.

The base condition for characteristic energy of elements system is defined

$$U_t + U_{ch} + U_o = U_s \quad (1)$$

$$U_t = U_{t,c} + U_{t,0} \quad (2)$$

$$U_{ch} = U_{ch,c} + U_{ch,0} \quad (3)$$

$$U_o = U_{o,c} + U_{o,0} \quad (4)$$

where:  $U_t$  – energy of tool,  $U_{ch}$  – energy of chip,  $U_o$  – energy of object (workpiece)  $U_{t,0}$  – energy of tool base,  $U_{ch,0}$  – energy of chip is equal  $U_{o,0}$ ,  $U_{o,0}$  – energy of object, (workpiece) base,  $U_{t,c}$  – energy of tool in cut,  $U_{ch,c}$  – energy of chip is cut,  $U_{o,c}$  – energy of object, (workpiece) in cut

The energy  $U_{ch,0}$  is equal  $U_{o,0}$  because the non start cutting proces. The result for cutting is machined surface. On the surface has the energy cut influence. Because the different of cut energy, is the cutting conditions influence and the input energy. The change of energy  $U_{o,0}$  have the main influence energy  $U_{ch}$  and energy  $U_t$ . The energy  $U_t$  is distributed for different technological methods the number of cutting edge (Figure 2).



FIGURE 2. The Screw Drill Wear.

a) optimal the cutting conditions, b) non-optimal the cutting conditions

## MODELING PROSPERITIES DRIVES ELEMENTS OF CARS AFTER HEAT TREATMENT PROCESSES BY MEANS NEURAL NETWORKS

Michał Szota and Józef Jasicki  
Czestochowa University of Technology,  
Faculty of Materials Processing Technology and Applied Physics,  
Materials Engineering Institute,  
Biomaterials and Surface Layer Research Institute,  
Av. Armii Krajowej 19, 42-200 Czestochowa, Poland  
mszota@mim.pcz.czest.pl

This paper presents neural network model used for designing the properties drive elements of cars after heat treatment processes in fluidized bed. These processes are very complicated and difficult as multi-parameters [1,2] changes are non linear and car drive elements structure is non homogeneous. This fact and lack of mathematical algorithms [3-7] describing these processes makes modeling this properties by traditional numerical methods difficult or even impossible. In this case it is possible to try using artificial neural network

The research are divided into three stages:

- using special computer system to obtain training data set,
- designing and building neural network structure,
- minimizing model structure, training and testing error.

At present different techniques are used in the thermo chemical treatment. One of this is heat treatment in fluidized bed. This is characterized by high coefficient heat and mass transfer. These techniques are very often used in researching institutes and small industrial plant [8-11].

The neural network structure is designed and prepared by choosing input and output parameters of process. The method of learning and testing neural network, the way of limiting nets structure and minimizing learning and testing error are discussed.

Theoretically the problem of choosing neural structure is restricted to approximation of multi-variable function for given vector  $x_n$  [3]. The case discussed in this paper concerns multi-dimensional input vector and continuous activation function. Building that kind of neural network model is defined by Komogorow statement [12]. He proved that in order to obtain k-dimensional output vector  $y_k$  for n-dimensional input vector  $x_n$  and continuous activation function, using one hidden layer neural network built of  $2n+1$  neurons is sufficient.

Such prepared neural network model, after putting expected values of assumed hardness curve in output layer, can give answers to a lot of questions about running carbonizing process in fluidized bed. The neural network model can be used to build control system capable of on-line controlling running processes and supporting engineering decision in real time.

The information obtained in this way can be used in practice by engineering designed running carbonizing process and property of final products. This research will be continued to complex solve this subject and applied it in Industrial plant. The final solution will be special computer system, which will be connected in real time [13] with heat medium and gas distribution station. This connection and special work application make to possible to add new data in training and testing data. Connection of this system with heat treatment control system makes to possible on-line control running process [14-15] and support engineering decision in real time.

This paper presents different conception to obtain assumed properties of materials after processes in fluidized bed. The specially prepared neural networks model could be a help for engineering decisions and may be used in designing processes in fluidized bed as well as in controlling changes of this process.

## References

1. J. Jasinski, Oddziaływanie złoza fluidalnego na procesy nasycania dyfuzyjnego warstwy wierzchniej stali, Wydawnictwo WIPMiFS, Częstochowa 2003
2. J. Jasinski, L. Jeziorski, M. Kubara, Carbonitriding of steel In fluidized beds, Heat Treatment of Metals, vol. 12, no 2, 1988
3. S. Osowski, Sieci neuronowe do przetwarzania informacji, Oficyna Wydaw. Politechniki Warszawskiej, Warszawa 2003
4. L. Rutkowski Sieci neuronowe i neurokomputery, Wydawnictwo Politechniki Częstochowskiej, Częstochowa, 1996
5. J. Trzaska, L.A. Dobrzański, Application of neural networks for designing the chemical composition of steel with the assumed hardness after cooling from the austenitising temperature, Journal of Materials Processing Technology 164-165, 2005
6. W. Sitek, L.A. Dobrzański, Application of genetic method in materials' design, Journal of Materials Processing Technology 164-165, 2005
7. L.A. Dobrzański, M. Kowalski, J. Madejski, Methodology of the mechanical properties prediction for the metallurgical products from the engineering steels Using the Artificial Intelligence methods, Journal of Materials Processing Technology 164-165, 2005
8. Z. Rogalski, Obróbka cieplna fluidalna – stan techniki, część 1, Inżynieria Powierzchni nr 2, Warszawa 2000
9. T. Babul, A. Nakonieczny, Z. Obuchowicz, D. Orzechowski, J. Jasinski, L. Jeziorski, T. Fraczek, R. Torbus, Przemysłowe zastosowanie wizualizacji i sterowania komputerowego piecami do obróbki cieplnej i cieplno-chemicznej, Inżynieria Materiałowa, nr 5, 2002
10. J. Jasinski, L. Jeziorski, T. Fraczek, R. Torbus, P. Chrzstek, T. Babul, A. Nakonieczny, Z. Obuchowicz, Komputerowy system sterowania i wizualizacji procesami F-A/O-D w wersji laboratoryjnej, Inżynieria Materiałowa, nr 5, 2002
11. J. Jasinski, System wizualizacji i sterowania procesów obróbki cieplno-chemicznej w wersji laboratoryjnej, Biuletyn Automatyki ASTOR, Automatyka, Sterowanie i Organizacja Produkcji, Kraków 2004
12. S. Haykin, Neural networks, a comprehensive foundation, Macmillan College Publishing Company, New York, 1994
13. Joon-Sik Son, Duk-Man Lee, Ill-Soo Kim, Seung-Gap Choi, A study on on-line learning neural networks for prediction for rolling force in hot-rolling mill, Journal of Materials Processing Technology, 164-165, 2005
14. Sviatlicznyj D., Pietrzyk M., On-line Model of Thermal Roll Profile during Hot Rolling, Metall. Foundry Eng., vol. 1, 27, 2001
15. J. Kusiak, Pietrzyk M., Sviatlicznyj D., Application of artificial neural network in on-line control of hot flat rolling processes, Int. Journal Engineering Simulation, vol. 1, 3, 2000

## THE MECHANICAL STRENGTH OF INTESTINAL ANASTOMOSES IN HYPOTHYROID RATS

S.K. Kourkoulis<sup>1</sup>, K.A. Ekmektzoglou<sup>2</sup>, S.-A. Papanicolopoulos<sup>1</sup>, G.C. Zografos<sup>3</sup>, I.A. Dontas<sup>2</sup>, T. Xanthos<sup>(2)</sup> and D.N. Perrea<sup>(2)</sup>

<sup>1</sup> Laboratory of Testing and Materials, Dept. of Mechanics, Nat. Tech. Univ. of Athens, 5 Heroes of Polytechnion Avenue, 15773 Zografou Campus, Athens, Greece

<sup>2</sup> Dept. of Experimental Surgery and Surgical Research «N.S. Christeas», Univ. of Athens, Medical School, 15B Agiou Thoma Street, 11527 Athens, Greece

<sup>3</sup> 1<sup>st</sup> University Department of General Surgery, Athens School of Medicine, “Hippocratico” General Hospital of Athens, 114 Vasilissis Sofias Avenue, 11527 Athens, Greece  
stakkour@central.ntua.gr

Intestinal wound healing is an essential process for surgical reconstruction of the digestive tract. Compromised healing - a multifactorial process - is considered a life-threatening complication, leading to prolonged hospitalization, decreased quality of life and increased medical costs [1]. Parameters for anastomotic repair and adhesion formation are mechanical, biochemical or histological, with the measurement of choice being mostly mechanical, biochemical or both.

In this paper the mechanical behaviour of intestinal anastomoses in hypothyroid rats is studied. More specifically the response of the anastomoses to a directly applied uniaxial tensile load is explored and the respective tensile strength is determined. Thirty male Wistar rats, divided into two groups, were used. Group 1 (n=15) consisted of control rats, namely healthy animals, while group 2 consisted of hypothyroid rats (n=15). A colonic segment, 1 cm of length, 5 cm distal to the ileocecal junction was transected and re-anastomosed end-to-end. To obtain the test specimen, the animals were sacrificed on the 5th post-operative day (the crucial time point upon which anastomotic failure is mostly recognized in clinical practice). An 8 cm segment of the colon with the anastomosis in the middle was resected. For comparison reasons a number of additional tests was carried out with healthy animals that were not subjected to anastomosis (Group 3).

The experiments were carried out from September 4 to September 29, 2006 from 09.00 to 13.00, with no time interval between sampling and processing. The most difficult problem to be solved, as it always happens in experiments with biological materials, was the proper support and alignment of the specimens on the loading frame. For this purpose a special system was designed in order to achieve the fastest and safest procedure for mounting the specimens to the grips of the loading device, consisting of a pair of light metallic pins of cylindrical cross-section with rounded heads. Attention was paid to avoid restricting as much as possible the rotational degrees of freedom of the specimen making thus possible both the self-alignment and the “un-twisting” of the intestine during tension, without external limitations and therefore without the development of parasitic tensions and disfigurements. A detailed description of the gripping system can be found in [2]. An extremely accurate load cell of capacity 5 and sensitivity of 10<sup>-3</sup> was used, attached to a stiff electromechanical loading frame. The displacement-control function mode was preferred since for the specific specimens the strain is difficult to be defined and measured rendering the strain-control function mode inapplicable. A relatively low loading speed was selected, and thus the experiments are considered as quasi-static ones. The results of the successful tests are included in Table 1. Characteristic plots for the three groups of specimens are shown in Fig. 1.

Concerning the overall appearance of the load-versus-time plots it is to be mentioned that they are characterized by three distinct regions, for almost all tests carried out. The dominant one is a

linear or almost linear portion interrupted by a number of abrupt load drops due to “un-twisting” or unfolding of the specimens. This linear portion could provide an indicative modulus of elasticity assumed that the displacement rate is properly recorded. Prior to this linear portion, an upwards curved region appears (not consistently) corresponding to a preliminary loading phase, namely the one before the complete alignment of the specimens. Finally, after the peak load the curves start decreasing rapidly up to the complete fracture of the specimens. The average value of the tensile strength for the healthy animals without anastomosis (group 3) was found equal to  $F_{cr,normal} = 2.05 \pm 0.53$  N, in very good agreement with the results obtained by Ekmektzoglou et al. [2] from a similar series of tests. On a comparative basis it could be said that the scattering of the results appears to be rather significant. The anastomotic operation for the healthy animals yields failure loads decreased by about 45% in comparison to the intact specimens. In case of the hypothyroid rats the anastomotic operation becomes even more difficult and the respective strength is about 60% lower compared to that of the normal group.

TABLE 1: The statistical data for the anastomotic strength (in N) for the three groups tested.

Group	1 (Control)	2 (Hypothyroid)	3 (Normal)
Mean	1.15	0.88	2.05
Sd	0.41	0.33	0.53
Median	1.03	0.78	2.15
Min	0.67	0.39	1.28
Max	1.75	1.42	2.62

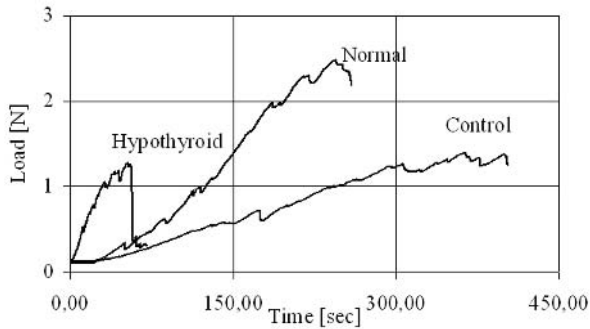


FIGURE 1: Characteristic load-vs.-time plots for the three groups tested.

## References

1. Ekmektzoglou K.A., Zografos G.C., *World J Gastroenterol*, vol. **12**, 2721-2729, 2006.
2. Ekmektzoglou K.A., Zografos G.C., Kourkoulis S.K., Dontas I.A., Giannopoulos P.K., Marinou K.A., Poulakou M.V., Perrea D.N., *World J Gastroenterol*, vol. **12**, 5668-5673, 2006.

## THE ANTERIOR CRUCIATE LIGAMENT OF THE KNEE JOINT UNDER MECHANICAL CONSTRAINTS

S.K. Kourkoulis and E. Gogossi

Department of Mechanics, National Technical University of Athens

Zografou Campus, Athens, Greece

stakkour@central.ntua.gr

The human knee joint is a complicated structure consisting of several parts interacting with each other in order to provide motion and stability. The major ligaments of the knee are the medial and lateral collateral ones (MCL, LCL) and the anterior and posterior cruciate ones (ACL, PCL) (Fig. 1a). The research studies on the knee joint aim to clarify the aetiology of injuries and to improve the medical treatment. In this context it is crucial to understand the function of each constituent part of the joint. ACL, which restrains the forward motion of tibia, is the most vulnerable component of the knee joint and attracts increased biomechanical attention. Unfortunately experimental studies are prohibitively complicated: cadaveric, animal or synthetic specimens do not display the in-vivo behaviour of the human ligament and it is difficult to impose realistic boundary conditions. As a result numerical methods are employed since they are advantageous for parametric analyses and accurate simulation of the boundary conditions combined with low cost.

In this study, the behaviour of the ACL under mechanical constraints is examined. No difference between the material behaviour of the ligament body and its insertion is assumed. The time dependence of the material properties (viscoelasticity, creep, relaxation) was neglected due to the high ratio between the viscoelastic time constant of the material and the loading time of interest in this study. Therefore a transversely isotropic hyper-elastic model was developed including the effect of a family of fibres, as it is commonly adopted for the ligaments: ACL is considered as a homogeneous hyper-elastic matrix in which densely distributed fibres are embedded. The incompressible fibres were assumed to be described by a free-energy function  $F$  of the form [1]:

$$\lambda \frac{\partial F}{\partial \lambda} = 0, \lambda < 1, \quad \lambda \frac{\partial F}{\partial \lambda} = C_3 (e^{C_4(\lambda-1)} - 1), \lambda < \lambda^*, \quad \lambda \frac{\partial F}{\partial \lambda} = C_5 \lambda + C_6, \lambda > \lambda^* \quad (1)$$

where  $\lambda$  is the stretch,  $\lambda^*$  the stretch at which collagen fibers start to be straightened changing the energy function from exponential to linear.  $C_3$  scales the exponential stress,  $C_4$  is related to the rate of collagen uncrimping and  $C_5$  is the elastic modulus of the straightened collagen fibers. The  $\sigma$ - $\varepsilon$  curve of the fibers was approximated by a two-parameter Mooney Rivlin model (Fig.1b):

$$\sigma(\varepsilon) = 777.15 \left( 1 + \varepsilon - \frac{1}{(1 + \varepsilon)^2} \right) - 760.87 \left( 1 - \frac{1}{(1 + \varepsilon)^3} \right) \quad (2)$$

Finally it was assumed that a Neo-Hookean model describes the strain-energy, of the matrix:

$$\Psi = \frac{1}{2D} \ln(J)^2 + C_1(I_1 - 3) \quad (3)$$

where  $J$  is the Jacobean of the deformation gradient,  $I_1$  is the first invariant of the modified Cauchy-Green tensor,  $C_1$  is the Neo-Hookean constant and  $D$  is the inverse of the bulk modulus.

The model was designed in ‘‘Solid Works’’ based on the measurements by Hirokawa et al. [2]. Fibers were embedded within the ligament in three different directions. When the knee is fully extended the ACL is stretched and twisted about 46° around its longitudinal axis. According to

existing studies ACL reaches the length of 29.35 mm when it is bounded in the knee. In order to model full extension one can either first rotate the ligament around its longitudinal axis and then stretch it or vice versa. The results for these two cases are not identical due to the assumed non-linear behavior of the ligament. It seems that the second case gives more realistic results, which are plotted in Figs. 2(a,b). Concerning the density of the fibers two different patterns were used. Comparing the results it is concluded that the more densely packed fibers yield lower stress concentrations, obviously because they share the loads in a more uniform manner. However, it seems that the distribution of the fibers is not uniform but rather they tend to condense in groups.

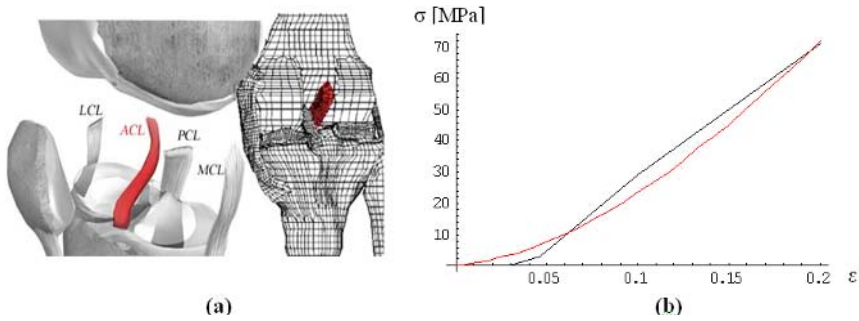


FIGURE 1. (a) The knee joint. (b) Weiss' assumption (black line) and the two-parameter Mooney-Rivlin fit (red line) for the simulation of the mechanical behaviour of the fibers.

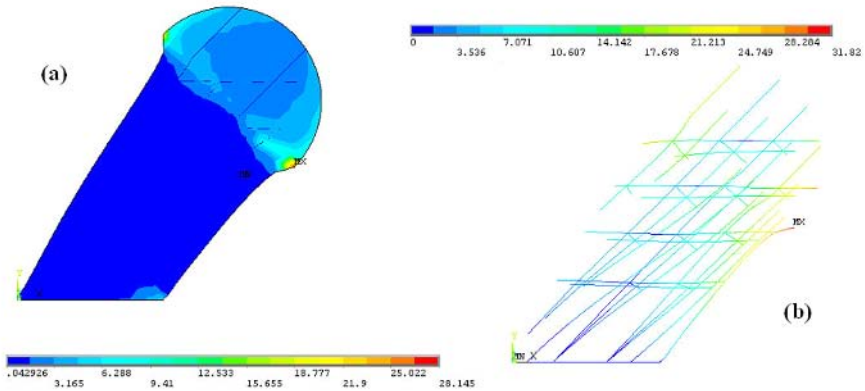


FIGURE 2: (a) The distribution of the equivalent von Mises stress within the ligament in full extension. (b) The total displacement of the ligament fibers in full extension.

References

1. Weiss, J. A., Gardiner, J. C., *Journal of Orthopaedic Research*, vol. **21**, 1098-1106, 2003.
2. Hirokawa, S., Tsuruno, R., *J. of Biomechanics*, vol. **33**, 1069-1077, 2000.



## DIGITAL PHOTOELASTIC EVALUATION OF ISOCHROMATIC FRINGE ORDER IN A 3D MODEL OF COMPLEX ROCKET MOTOR STRAP-ON JOINT

K. Ashokan<sup>1</sup>, K. Ramesh<sup>1</sup>, S.A. Pillai<sup>2</sup> and Jeby Philip<sup>2</sup>

<sup>1</sup>Department of Applied Mechanics, Indian Institute of Technology Madras,  
Chennai 600 036, India.

<sup>2</sup>Experimental Mechanics Division, Vikram Sarabhai Space Centre,  
Trivandrum 695 022, India.

ukashokan@iitm.ac.in, s\_annamala@vssc.gov.in, kramesh@iitm.ac.in

Digital Photoelasticity is a whole field technique, which provides the information on magnitude of difference in principal stresses (isochromatics) and direction (isoclinics) of principal stresses at every pixel in the image domain based on intensity processing [1]. Phase shifting techniques which are commonly used for quantitative estimation in digital photoelasticity give only a wrapped isochromatic phase map. This has to be unwrapped for obtaining the absolute phase values. One of the main issues in wrapped isochromatic phasemap is interpretation of the sign of the fractional retardation calculated. This is referred to as ambiguity in isochromatic phasemap. Depending on the problem one may have several zones where there may be ambiguity and these zones are labelled as ambiguous zones. The reason for ambiguous zones is due to the fact that isoclinic angle evaluated is not uniformly representing either  $\sigma_1$  or  $\sigma_2$  direction over the whole domain of the model [1]. For effective phase unwrapping, the isochromatic phasemap should be corrected for ambiguity. Identification and correction of ambiguity is not simple. There are different classes of ambiguous zones [2] and each of the available ambiguity removal methods can resolve ambiguity for only a certain class of problems. In cases involving complex geometries and loading one has to select appropriately, a combination of these algorithms for removing the ambiguity in the whole domain of the model.

Phase unwrapping is a process which involves adding integer multiples of  $2\pi$  to the wrapped phase values in order to get absolute phase data. This process is normally carried out by successive comparisons of the neighbourhood pixels. Among the unwrapping algorithms available, quality guided path following algorithm [3] is one which is autonomous in nature and unwraps the phase data by using the quality map. For effective unwrapping of isochromatic phase map in complex models having cut outs and physical discontinuity, the different regions within the problem domain are delimited and then each region is unwrapped separately [4]. In domain delimiting, the regions outside the boundary are masked out, thereby making the unwrapping algorithm to work within the chosen model domain.

In this paper, the details of photoelastic analysis carried out on a slice cut from a stress frozen 3D model of a complex rocket motor joint is discussed. Dark field isochromatics of the slice cut from the model is shown in Fig. 1. The phasemap generated using the six step phase shifting arrangement [5] with monochromatic light source is shown in Fig. 2a. One of the ways, the presence of ambiguous zones can be identified is by comparing the dark field isochromatics with the phasemap. The point here is that the general nature of the fringe field in a dark field image needs to be mimicked by the phasemap. With this view in mind, one can identify several regions of ambiguity in the model which are shown in Fig. 2a. These are corrected using various combinations of the ambiguity removal methodologies and one of the ambiguous zones corrected (zone 6) is shown in Fig. 2b for illustration. After the isochromatic phase map of the whole domain is corrected for ambiguity, it is unwrapped by quality guided unwrapping algorithm using the concept of domain delimiting. The unwrapped fringe order is then plotted as a color image for the

whole domain of the model using Matlab. For simple problems the methodology for digital photoelasticity is straightforward. However for complex problems, the issue of resolving the ambiguity in the sign of fractional fringe order cannot be ignored, which is brought out by this example problem.



FIGURE 1. Dark field isochromatics captured using monochromatic light source

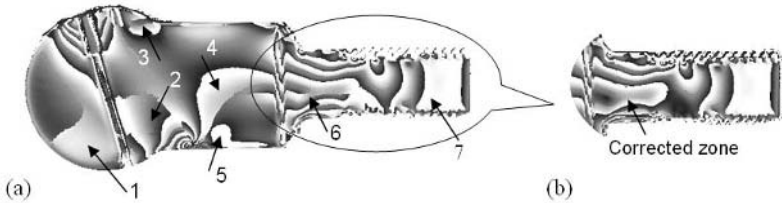


FIGURE 2. (a) Phasemap containing several ambiguous zones (b) Phasemap corrected for ambiguity in zone 6

## References

1. Ramesh, K., *Digital Photoelasticity: Advanced Techniques and Applications*, Springer-Verlag, Berlin, Germany, 2000.
2. Prashant, P. L., Madhu, K. R. and Ramesh, K., In *Proceedings of SPIE*, vol. **5852**, 2005, 192-197.
3. Dennis, C. Ghiglia and Mark, D. Pritt, *Two-Dimensional Phase Unwrapping: Theory, Algorithms and Software*, Wiley-Inter Science Publication, 1998.
4. Ashokan, K., Ramji, M., Raja Guruprasath, R. and Ramesh, K., Proc. *Int. Conf. on Exp. Mech.*, Lotte Hotel, Jeju Island, Korea, 26<sup>th</sup> - 29<sup>th</sup> September, 2006.
5. Ajovalasit, A., Barone, S. and Petrucci, G., *J. Strain Analysis for Engg. Des.*, vol. **33**(3), 207-16, 1998.

## SMOOTHING OF DIGITAL PHOTOELASTIC DATA USING ROBUST OUTLIER ALGORITHM

M. Ramji and K. Ramesh

Department of Applied Mechanics, IIT Madras, Chennai 600 036, India.

ramji\_mano@iitm.ac.in, kramesh@iitm.ac.in

Photoelasticity is an optical technique for experimental stress analysis. It is widely used for 2-D and 3-D analysis of components for getting the information of principal stress difference (isochromatics) and principal stress direction (isoclinics) at every point in the domain. With the advent of digital computers, recording of images as intensity data became easier and a separate branch of photoelasticity namely *digital photoelasticity* came into existence [1]. In digital photoelasticity intensity information of the captured image is used for evaluating the isoclinic and isochromatic parameters. Thus, in principle one gets values of isoclinic ( $\theta$ ) and isochromatic ( $N$ ) for the whole-field in the form of phase map [1]. Phase shifting / polarization stepping techniques are widely used in digital photoelasticity for getting the phase maps [1]. But these phase maps are wrapped and has to be unwrapped for getting continuous phase values. Both isoclinic and isochromatic phase maps have interdependence and this interaction affect their evaluation. For stress separation studies, one requires both isochromatics and isoclinics accurately free of any kinks in the domain.

Mathematically, isoclinic values are undefined at isochromatic skeletons [2]. This is termed as isochromatic-isoclinic interaction in the case of isoclinic phase map. The isochromatic-isoclinic interaction increases with increased load and this is a major source of error in evaluating the isoclinic parameter [2]. Multiple wavelength approach [1], multiple load approach [1] and interpolation [3] have been used in reducing noise occurring in isoclinic phase map due to these interactions. Since, a large quantum of data is available, one could reduce the noise due to isochromatic-isoclinic interaction by developing appropriate methods for data smoothing. Recently, Ramji & Ramesh proposed a polynomial based smoothing of isoclinic data [2]. The polynomial fitting is a global smoothing technique which in principle can alter the trend of experimental isoclinic data in some zones.

In this paper, smoothing algorithm is developed for handling both simply and multiply connected models. The smoothing is done using the outlier algorithm which comes under the class of local regression techniques. The smoothing procedure is termed local because each smoothed value is determined by the neighbouring data points defined within a span. The span defines a window of neighbouring points to be included in the smoothing calculation for each data point. The data points lying outside the trend are omitted and a local curve fitting is done by least squares analysis. For smoothing, the information of isoclinic data row by row within the model domain is required. Usually the phase data is stored as an array and from this the retrieval of sequence of pixel coordinate values row by row within the model boundary is required for implementing the smoothing algorithm. A new data extraction technique has been evolved for implementing the smoothing algorithm. Application of this smoothing algorithm to isoclinic and isochromatic data is demonstrated.

Isoclinic phase map for the problem of a ring under diametral compression (only one-quarter) is shown in Fig.1a. The phase map is obtained using Brown & Sullivan algorithm [4] with monochromatic light source. One could see a semblance of isochromatic fringes in the phase map. This is actually noise due to isochromatic-isoclinic interaction. Figure 1d shows the binary representation of the isoclinic plot in steps of  $10^\circ$  obtained experimentally. The binary

representation has clearly brought out more forcefully the bad impact of noise due to isochromatic – isoclinic interaction on the isoclinic phase map. Figure 1b is the isoclinic phase map obtained after smoothing. One can notice that a semblance of isochromatic fringes seen in Fig. 1a is not seen here. After applying the smoothing algorithm as mentioned above, there is total improvement in the binary isoclinic plot of Fig. 1e when compared to Fig. 1d. The smoothed isoclinic plots look similar to the plot obtained using analytical solution (Figs. 1c & 1f). The experimentally calculated theta (raw & smoothed) is compared with the theta calculated theoretically for a line at  $y/R = 0.80$  in Fig. 2. The results obtained by the smoothing algorithm do not have undulations and compare well with the theory.

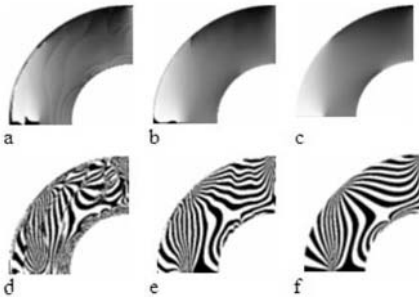


FIGURE 1

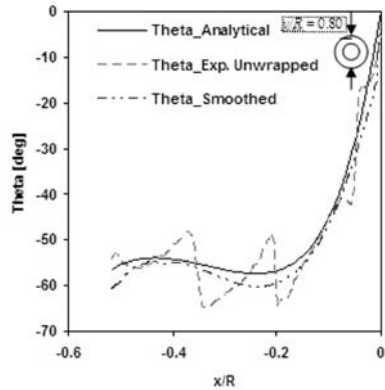


FIGURE 2

FIGURE 1. Isoclinic plot for the problem of a ring under diametral compression obtained using Brown & Sullivan algorithm (raw & smoothed) compared with the theta obtained analytically; grey level plot for - (a) raw unwrapped theta (b) smoothed theta (c) theta obtained analytically; binary isoclinic plots in steps of 10 (d) raw unwrapped theta (e) smoothed theta (f) theta obtained using analytical solution.

FIGURE 2. Comparison of smoothed theta with experimentally unwrapped and analytically obtained theta along a line ( $y/R = 0.80$ ) for the problem of a ring under diametral compression

## References

1. Ramesh, K., *Digital Photoelasticity: Advanced Techniques and Applications*, Springer-Verlag, Berlin, Germany, 2000.
2. Ramji, M. and Ramesh, K., In *CD Proceedings of the International Conference on Optics and Optoelectronics*, Instruments Research & Development Establishment, Dehradun, India, 2005.
3. Wang, Z. F. and Patterson, E. A., *Opt. and Lasers in Engg.*, vol. **22**, 91-104, 1995.
4. Brown, G. M. and Sullivan, J. L., *Exp. Mech.*, vol. **30**(2), 135-144, 1990.

## 3D PHOTOELASTICITY AND DIGITAL VOLUME CORRELATION APPLIED TO 3D MECHANICAL STUDIES

A. Germaneau, P. Doumalin and J.C. Dupré

Laboratoire de Mécanique des Solides, CNRS, UMR 6610, Université de Poitiers  
SP2MI Bd Marie et Pierre Curie, Téléport 2, 86960 Futuroscope Chasseneuil, France  
germaneau@lms.univ-poitiers.fr, doumalin@lms.univ-poitiers.fr, dupre@lms.univ-poitiers.fr

Generally in mechanics, 3D problems can be analysed from simulations by finite elements and the results can be compared with the measurements obtained on the surface of the specimen. However, in the case of structures with complex geometries or specific loads, it can be necessary to determine experimentally the 3D strain field to validate the numerical approach in the whole volume. We present two techniques we have developed to observe 3D mechanical effects at the core of a specimen: the scattered light photoelasticity and the optical scanning tomography coupled to Digital Volume Correlation (DVC). The aim of this work is to determine the limitations, advantages and drawbacks of both methods and allows us to choose the well-adapted technique at each study.

### 3D scattered light photoelasticity by optical slicing

This technique uses the birefringence phenomenon of transparent materials [1,2]. Its principle is to isolate a slice of the studied photoelastic model between two plane laser beams (Fig. 1). The optical setup is constituted by a laser source, a separator device giving both beams, a convergent lens and a cylindrical lens. In the direction perpendicular to the two illuminated sections, we observe a speckle pattern due to the interferences of light beams of each section. The possibility of interference depends on the birefringence of the isolated slice. To observe the isoclinic and isochromatic fringes within the specimen, we have to calculate a correlation factor by a statistical analysis between three images corresponding to the speckle pattern for one plane alone, the second plane alone and both planes together. From the expressions of the scattered light, we can write an equation of the correlation factor which is similar to the one usually used for the illumination obtained by the analysis of an identical slice between two parallel polarizers. So, we can determine the 3D stress or strain state on successive slices within the specimen.

### Digital Volume Correlation and optical scanning tomography

DVC [3,4] is the extension in 3D of DIC [5] generally used for the determination of 2D strain fields. DVC needs volume images containing a 3D distribution of grey levels. Recently, we have developed a technique allowing to record volume images by optical slicing of a transparent material [6]. To obtain a random distribution of the grey levels within the volume image, we use the scattered light phenomenon involved by some particles included in the specimen. A plane laser beam scans the specimen and 2D images of the scattered light are successively recorded at each position of the beam in order to constitute a volume (Fig. 2). The optical setup is similar to the one used for the scattered light photoelasticity technique except the use of only one plane laser beam (Fig. 1). DVC gives the discrete displacement field between two states on several volume subsets by assuming a 3D material transformation. From the determination of 3D displacement, we calculate the full Green-Lagrange tensor.

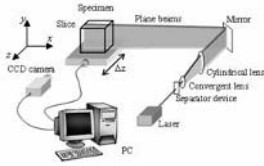


FIGURE 1: Optical setup



FIGURE 2: Volume image reconstruction

## Experiments

In order to compare the fields of applications and the performances of both methods we have performed a located compression test with a spherical indentation model. A fringe pattern obtained by 3D scattered light photoelasticity is presented in Fig. 3 and the strain component along the loading axis given by DVC is shown Fig. 4. We have calculated the principal secondary strain difference in the two cases. This first comparison show that DVC seems to be better adapted for large strains than photoelasticity which is limited by a too large number of fringes near the contact zone. Nevertheless photoelasticity gives better results for small strains, DVC being limited by a strain uncertainty of about 0.1%.

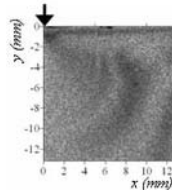
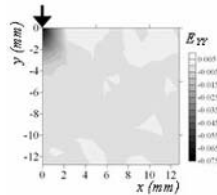


FIGURE 3: Isochromatic and isoclinic fringes on a slide inside the specimen

FIGURE 4:  $E_{YY}$  Green-Lagrange component on a slide inside the specimen

## References

1. Dupré, J.C. and Lagarde, A., *Exp. Mech.*, vol. **37**, 393-397, 1997.
2. Zenina, A., Dupré, J.C. and Lagarde, A., *Eur. J. Mech. A/Solids*, vol. **18**, 633-640, 1999.
3. Bay, B.K., Smith, T.S., Fyrhie, D.P. and Saad, M., *Exp. Mech.*, vol. **39**, 217-226, 1999.
4. Verhulp, E., Van Rietbergen, B. and Huiskes, R., *J. of Biomech.*, vol. **37**, 1313-1320, 2004.
5. Bruck, H.A., Mc Neill, S.R., Sutton, M.A. and Peters, W.H., *Exp. Mech.*, vol. **29**, 261-267, 1989.
6. Germaneau, A., Doumalin, P. and Dupré, J.C., In *Proceedings of Photomechanics 2006*, edited by M. Grédiac and J. Huntley, Clermont-Ferrand, France, 2006.

## STRESS SEPARATION BY MEANS OF PHASE SHIFTING IN PHOTOELASTICITY

Dongsheng Zhang<sup>1</sup>, Yongsheng Han<sup>2</sup> and Dwayne Arola<sup>3</sup>

<sup>1</sup>Department of Mechanics, Shanghai University,  
Shanghai, 200444, PR China  
donzhang@staff.shu.edu.cn

<sup>2</sup>Shanghai Institute of Applied Mathematics and Mechanics,  
Shanghai, 200072, PR China  
yongshenghan998@hotmail.com

<sup>3</sup>Department of Mechanical Engineering, University of Maryland Baltimore County,  
Baltimore, MD 21250  
darola@umbc.edu

Photoelasticity has served as a valuable experimental method for performing stress analysis for decades. Since its inception, it has been applied in solving a tremendous number of engineering problems. This paper presents an automatic approach for the evaluation of isochromatics and isoclinics in photoelasticity using complimentary phase shifting. The phase map of the isoclinics is obtained from 4 images acquired in the plane polarizer arrangement by rotating the polarizer and analyzer simultaneously, as shown in Fig. 1(a). Ambiguity exists due to the isoclinic phase values are wrapped in a range of  $(0, \pi/2)$ , which indicate the angle made by either  $\sigma_1$  or  $\sigma_2$  with horizontal axis. We present a novel method to extend the range of isoclinic phase value to  $(-\pi/2, \pi/2)$ , which represent the orientation of  $\sigma_1$  only, as shown in Fig. 1(b). In circular polariscope, phase shifting can be applied to isochromatic fringe patterns if the orientation of  $\sigma_1$  is given analogous to Tardy compensation. Phase maps for the isochromatics are then achieved at 8 specifically selected discrete orientations through sequential analyzer rotations. With the knowledge of  $\sigma_1$  orientation, a whole-field description of the phase values of the isochromatics is then constructed, as shown in Fig. 2(a). The absolute phase value of isochromatics can be obtained through an unweighted least-squares phase unwrapping processing, as shown in Fig. 2(b). Sophisticated software has been developed for automatic photoelastic data processing from image acquirement to stress analysis. In an effort to validate the process and illustrate application, an example of the proposed method is presented using a plate loaded in diametrical compression. Stress components at three horizontal sections of the circular plate are calculated with the shear stress differential method (Fig. 3). Results show good agreement with the theoretical solution and the method is easy to conduct and applicable to engineering problems.

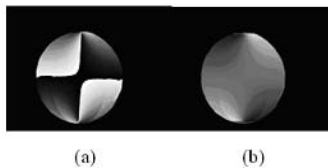


FIGURE 1. isoclinic phase map before and after phase extension

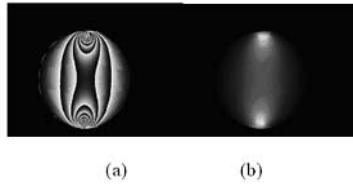


FIGURE 2. isochromatic phase map before and after unwrapping processing

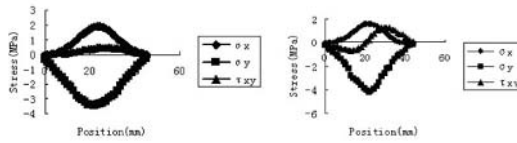


FIGURE 3. Distribution of stress components at different sections

## References

1. Chen, T.Y., *Optics and Lasers in Engineering*, vol. **31**, no 5, 325-338, 1999.
2. Yoneyama, S., Morimoto, Y., Kawamura, M., *Measurement Science and Technology*, vol. **16**, no 6, 1329-1334, 2005.
3. Asundi, A., *Experimental Techniques*, vol. **17**, no 1, 19-23, 1993.
4. Ramesh, K., *Digital Photoelasticity-Advanced Techniques and Applications*, Springer, 2000, pp. 152-153



## LINEAR AND NON-LINEAR ALGORITHMS OF PHOTOELASTIC TOMOGRAPHY

Hillar Aben and Andrei Errapart  
Institute of Cybernetics, Tallinn University of Technology  
21 Akadeemia tee, 12618 Tallinn, Estonia  
aben@ioc.ee, andreie@ioc.ee

Photoelastic tomography in linear approximation is based on the formulas [1]

$$\Delta \cos 2\varphi = C \int (\sigma_x - \sigma_y) dy, \quad \Delta \sin 2\varphi = 2C \int \tau_{xz} dy, \quad (1)$$

where  $\Delta$  is optical retardation,  $\varphi$  is the parameter of the isoclinic,  $C$  is the photoelastic constant and  $y$  is the direction of light propagation. It has been shown that if tomographic photoelastic measurements have been carried out by rotating the specimen around the  $z$  axis, distribution of  $\sigma_z$  can be determined either by solving a Poisson equation [2] or using the Radon inversion [3]. Several examples of application of photoelastic tomography are described in [3].

Equations (1) are valid if birefringence is weak or rotation of the principal stress axes on the light rays is small. Often these assumptions are not valid and photoelastic tomography is based on the non-linear relationships of integrated photoelasticity [4]. For building an iterative solution method we use differential evolution [5], a kind of genetic algorithms.

As an example, let us consider residual stress measurement in the lower part of the stem of a wine glass (Fig. 1a). Figure 1b shows fringe pattern in a light-field circular polariscope. In section A–A optical retardation is about half the wavelength. It means that Eqs. (1) are not valid if rotation of the principal axes is present.

In Fig. 1c measurement data  $\Delta^m \cos 2\varphi^m$  and  $\Delta^m \sin 2\varphi^m$  in section A–A are shown with solid lines. Let us mention that here  $\varphi^m$  denotes azimuth of the characteristic direction and  $\Delta^m$  is characteristic optical retardation [4]. Using linear approximation of photoelastic tomography, distribution of the stress  $\sigma_r^1$ ,  $\sigma_z^1$ , and  $\sigma_\theta^1$  were determined (Fig. 2a). On the basis of the values of  $\sigma_r^1$ ,  $\sigma_z^1$  and  $\sigma_\theta^1$  “theoretical” values of  $\Delta^c$  and  $\varphi^c$  can be calculated;  $\Delta^c \cos 2\varphi^c$  and  $\Delta^c \sin 2\varphi^c$  are shown in Fig. 1c by dashed lines. Considerable difference of measured and calculated data, especially of  $\Delta \cos 2\varphi$ , shows that linear approximation does not give reliable results in this case.

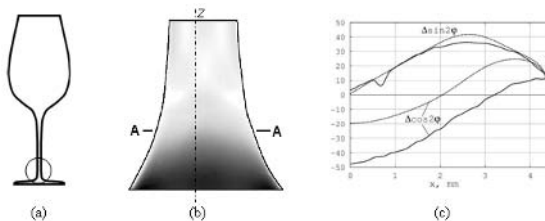


FIGURE 1. (a) geometry of the wine glass; (b) fringe pattern of the lower part of the stem in a light-field circular polariscope; (c) comparison of the measured (—) and calculated with linear approximation (---) data.

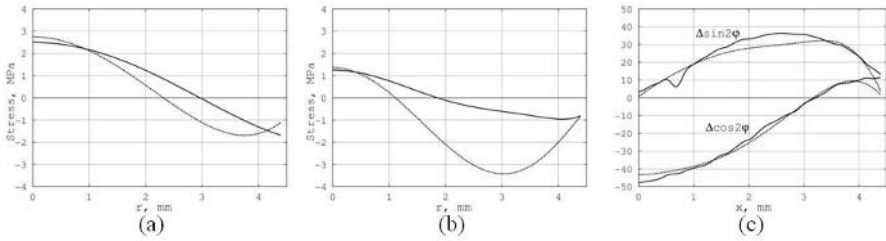


FIGURE 2. (a) stress in section A–A obtained with linear algorithm; (b) the same obtained with non-linear algorithm; (c) comparison of the measured data (—), and that calculated on the basis of the non-linear algorithm (---).

To determine the stresses that best correspond to the measurement data, the following algorithm was used. First, adding to the linearized solution for the stress field random errors, a population of 100 stress fields was generated. For every member of the population “theoretical” measurement data were calculated for many light rays on which photoelastic measurements were carried out. Penalty function

$$F = \frac{1}{n} \sum_{i=1}^n \left[ (\Delta_i^c \cos 2\varphi_i^c - \Delta_i^m \cos 2\varphi_i^m)^2 + (\Delta_i^c \sin 2\varphi_i^c - \Delta_i^m \sin 2\varphi_i^m)^2 \right] \quad (2)$$

was calculated for every member of the population.

Differential evolution algorithm [5] was used to generate new populations of the stress field so that  $F$  finally reaches the minimum. Figure 2b shows stress components obtained with the non-linear algorithm. Calculated on their basis theoretical data correspond rather well to the real measurement data (Fig. 2c).

Non-linear formulation of the algorithm widens considerably the domain of application of photoelastic tomography.

## References

1. Aben, H. and Guillemet, C., *Photoelasticity of Glass*, Springer, Berlin, 1993.
2. Sharafutdinov, V., *Integral Geometry of Tensor Fields*, VSP, Utrecht, 1994.
3. Aben, H., Errapart, A., Ainola, L. and Anton, J., *Opt. Eng.*, vol. **44**, 2005.
4. Aben, H., *Integrated Photoelasticity*, McGraw-Hill, New York, 1979.
5. Price, K.V., Storn, R.M. and Lampinen, J. A., *Differential Evolution, a Practical Approach to Global Optimisation*, Springer, Berlin, 2005.

## GENERALIZED ONION-PEELING METHOD IN INTEGRATED PHOTOELASTICITY OF AXISYMMETRIC PROBLEMS

Johan Anton and Andrei Errapart  
Institute of Cybernetics, Tallinn University of Technology  
21, Akadeemia tee, 12618 Tallinn, Estonia  
{johan,andreie}@ioc.ee

By measuring residual stress in axisymmetric glass articles, stress distribution is usually described with polynomials [1]. In case of cylinders, axial stress distribution can be measured also using a discrete algorithm, named “onion-peeling” [2]. In this method, the cylinder is considered as consisting of a number of concentric cylindrical rings (Fig. 1), in each of which the axial stress  $\sigma_z$  may be considered constant. Axial stress in the first ring  $\sigma_z^{(1)}$  is determined through

$$\sigma_z^{(1)} = \frac{\Delta_1}{2C y_{11}}, \quad (1)$$

where  $\Delta_1$  is optical retardation on the ray, which is tangent to the middle surface of the first ring and  $y_{11}$  is half of the path length of the ray 1 in the ring 1;  $C$  is photoelastic constant.

In an arbitrary ring  $j$  the axial stress is calculated as

$$\sigma_z^{(j)} = \frac{\Delta_j - 2C \sum_{i=1}^{j-1} y_{ji} \sigma_z^{(i)}}{2C y_{jj}}, \quad (2)$$

where  $y_{ji}$  is half of the path length of the ray  $j$  on ring  $i$ .

This version of the onion-peeling method can be used only if stress gradient in the direction of the  $z$  axis is absent. Otherwise optical retardation depends also on the stress components  $\sigma_r$ ,  $\sigma_\theta$  and  $\tau_{rz}$ . The onion-peeling method is generalized as follows.

In case of weak birefringence, basic equations of integrated photoelasticity are [1]:

$$V_1 = \Delta \cos 2\varphi = C \int (\sigma_z - \sigma_x) dy, \quad V_2 = \Delta \sin 2\varphi = 2C \int \tau_{zx} dy. \quad (3)$$

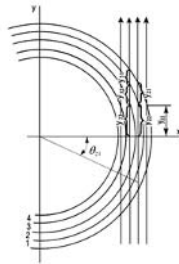


FIGURE 1. Discrete representation of an axisymmetric specimen.

Here  $\varphi$  is the parameter of the isoclinic and  $\Delta$  is integral optical retardation.

On the basis of the second Eq. (3), distribution of  $\tau_{zx}$  can be determined using Eqs. (1) and (2).

Using a macrostatic equilibrium condition [1], the following equation can be derived:

$$\int \sigma_z dy = \frac{1}{2C} \int \frac{dV_2}{dz} dx + \frac{1}{C} V_1. \tag{4}$$

Equation (4) permits calculation of the distribution of  $\sigma_z$  with the classical onion-peeling procedure. Stress components  $\sigma_r$  and  $\sigma_\theta$  can be determined using the equilibrium equation and the generalized sum rule[3].

Figure 2a shows geometry of a CRT glass bulb. Stresses in a section  $z = 1$  mm of the neck tube were determined both with the onion-peeling method and by using polynomial approximation with different number of terms in the polynomial (Fig. 2b).

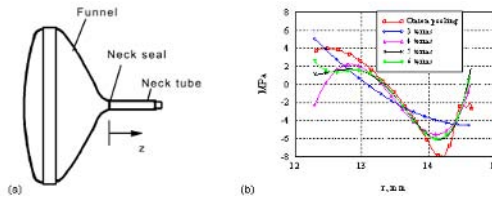


FIGURE 2. (a) geometry of the CRT glass bulb; (b) axial stress distribution, determined with the onion-peeling method and with polynomial approximation using different number of terms.

It can be seen that at the internal surface the stress depends very strongly on the number of terms in the polynomial and the onion-peeling method gives more reliable results. At the external surface measurement errors influence strongly the results of the onion-peeling method. Here polynomial approximation gives more reliable results.

In case of arbitrary birefringence, Eqs. (3) are not valid and stress analysis must be based on the measurement of the characteristic directions and characteristic optical retardation [4]. In this paper a generalized onion-peeling method for the case of arbitrary birefringence is elaborated for residual stress measurement in axisymmetric glass articles.

Application of new onion-peeling algorithms is demonstrated by residual stress measurement in various glass articles.

**References**

1. Aben, H. and Guillemet, C. *Photoelasticity of Glass*, Springer, Berlin, 1993.
2. Drucker, D.C. and Woodward, W.B. *J. Appl. Phys.*, vol. **25**, 510-512, 1954.
3. Aben, H., Ainola, L. and Anton, J. *Opt. Lasers Eng.*, vol. **33**, 49-64, 2000.
4. Aben, H. *Integrated Photoelasticity*, McGraw-Hill, New York, 1979.

## MECHANICAL PROPERTIES OF OIL PALM FIBRE REINFORCED EPOXY FOR BUILDING SHORT SPAN BRIDGE

Mimi Azlina Abu Bakar, Valliyappan D. Natarajan, Anizah Kalam and Nor Hayati Kudiran  
Faculty of Mechanical Engineering  
Universiti Teknologi MARA (UiTM),  
40450 Shah Alam, Selangor, Malaysia.  
mimi\_azlina@yahoo.com or mimi932@salam.uitm.edu.my

Oil palm industries generate at least 30 million tonnes of lignocellulosic biomass annually in the form of oil palm trunks (OPT), empty fruit bunches (EFB), oil palm fronds (OPF) and palm pressed fibres (PPF). At present, the biomass is either left to rot in the plantations to provide organic nutrients to the oil palm trees (mulching) or used as solid fuel in the boilers to generate steam and electricity at the mills. An oil palm plantation produces about 55 tonnes ha<sup>-1</sup> yr<sup>-1</sup> of total dry matter in the form of fibrous biomass as compared to only about 5.5 tonnes ha<sup>-1</sup> yr<sup>-1</sup> of palm oil and palm kernel oil.<sup>1</sup> The fibrous biomass is yet to be commercially exploited. Technology development in the industry is still focused on process development and improvement rather than creating and inventing newer products for value-added application. The need for materials not harmful to the body but having appropriate properties has increased due to a lack of resources and increasing environmental pollution. Thus, composites prepared from recycled materials are actively being sought after.<sup>2</sup> Many synthetic polymeric materials are produced by combining with various reinforcing fillers to improve their mechanical properties and obtain the desired properties. Among these reinforcing fillers, active research is under way concerning the use of lignocellulosic materials, which are among the most environmentally friendly agrowastes, as a substitute for synthetic materials.<sup>3</sup> Lignocellulosic materials offer many environmental benefits when used as reinforcing fillers for plastics, including their making the final product lightweight, decreasing the erosion of the manufacturing machinery, low cost, biodegradability, and absence of production of residue or toxic by-products when burnt.<sup>4</sup>

In Malaysia, the construction of early roads and bridges was a necessity to facilitate the movements of peoples and goods. There are now more than 10,000 bridges in Malaysia of various sizes and forms, out of which approximately 2,500 are located on federal roads. The early bridges were mainly made of steel in the form of trusses, arches and beams, which was a subsequent product out of the 18<sup>th</sup> century Industrial Age in England. Concrete and steel have been replaced by other materials such as FRP, GFRP and others fibre polymer materials<sup>5</sup>. This offers a good opportunity for fibre reinforced polymer composites to be used for maintenance of old bridge structures. Oil palm empty fruit bunch (OPEFB) fibre and oil palm frond fibre mat (OPF FM), which are studied in this research, also contribute positively to waste management solutions in the oil palm mill or plantation. Investigation of mechanical properties have been done experimentally for five samples which two composite samples were fabricated using OPEFB fibre which differs in their fibre mass fraction, one is 10% and the other one is 20%. The other composite sample was fabricated using OPF fibre mat (OPF FM). A controlled sample is made of homogeneous epoxy, which is the matrix itself; a mixing of epoxy and hardener by a mass fraction of 2 to 1, which means two parts of epoxy mixed with one part of hardener. Table 1 below shows the list of samples.

Table 1. Composite samples.

Types of fibre as filler in composite	Fibre mass fraction
OPEFB fibre	0%
OPEFB fibre	10%
OPEFB fibre	20%
OPF fibre mat (OPF FM)	-

This paper presents the tensile, flexural and impact properties of indigenous natural fibres composite materials namely, OPEFB and OPF FM in epoxy as the matrix. The tensile strength of composites made from OPEFB appreciates 35% as compared the homogeneous epoxy. Although the average flexural strength for both of the composites is less than the homogeneous epoxy, the flexural modulus of the OPEFB composite increased up to 62%. The presence of OPEFB fibre and OPF FM improved the impact strength of the homogeneous epoxy as much as 40%. Based on these results, we have simulated the use of the composites, which we term *semi-structural-members*, namely the column and beam to build short span bridge (SSB). Results of the FEM analysis indicated that the 10% OPEFB composite would be able support about 200 kg load with a maximum deflection of 0.05 mm and 0.2 mm for the 5-m and 7-m span SSB, respectively using the T-beam configuration. This outcome, when compared to the strain at failure, indicates the potential use of OPEFB to build moderate load supporting structures but also in reducing the cost of SSB for usage in the rural areas as well as in recreational spots in the urban areas.

## References

1. Wan Hasamudin and Rosnah Mat Soom. *Road Making Using Oil Palm Fiber*. MPOB Information Series, ISSN 1511-7871, 2002.
2. Yang H-S, Kim H-J, Son J, Park HJ, Lee BJ, Hwang TS. *Rice-husk filled polypropylene composites; mechanical and morphological study*. Compos Struct, vol. **63** (3), 305–12, 2004
3. Hattotuwa G, Premalal B, Ismail H, Baharin A. *Comparison of the mechanical properties of rice husk powder filled polypropylene composites with talc filled polypropylene composites*. Polym Testing, vol. **21** (7), 833–9, 2002
4. Han-Seung Yang, Hyun-Joong Kim, Hee-Jun Park, Bum-Jae Lee, Taek-Sung Hwang. *Water absorption behavior and mechanical properties of lignocellulosic filler–polyolefin biocomposites*, 2005
5. A. Kriker, G. Debicki, A. Bali, M.M. Khenferand M. Chabannet. *Mechanical properties of date palm fibres and concrete reinforced with date palm fibres in hot-dry climate*.

## RESEARCH ON THE SHEAR BEHAVIOUR OF PLAIN FABRIC PREPREG AT LATERAL COMPACTION STAGE

Lin Guochang, Wang Youshan and Du Xingwen  
 Center for Composite Materials, Harbin Institute of Technology  
 Box 3011, Harbin Institute of Technology, No. 2, Yi-kuang Street,  
 Harbin HeiLongjiang, China, 150001  
 Lingc@hit.edu.cn

The shear behaviour of plain fabric prepreg can be divided into two different stages. The first stage is before the fabric lock-up, the angle between the yarns decreases with the increase of the shear angle and the adjacent yarns become close until fabric lock-up. After fabric lock-up, which is call compaction stage, the adjacent yarns compact each other which results in a rapid increase in the shearing force. McGuinness[1], Spencer[2], Harrison[3] have established different constitutive equations to describe the rheological behaviors of fabric prepreg at first stage. But those constitutive equations can not describe the shear behaviors at the compaction stage, so this paper will focus on the shear behavior at the second stage by using the picture frame test. During the research, a unit cell of fabric prepreg is selected (see Fig. 1) and supposes that there are only two forces in the cell to resist external fore deformation. One is the friction force between the yarn intercross, and the other is the lateral compaction force. On the basis of the moment balance, the relationship between the load and shear angle was deduced.

This paper assumes that there is a very thin resin layer between the intercrosses of yarns, so the friction force is regarded as shear force of the resin when the yarns rotate at the intercross. Usually, the shear rate is very low in the picture frame test, so the Newton fluid is chose to describe the rheology behaviour of the resin between the intercrosses. The Eq. (1) is the friction moment

$$M_F = \frac{\eta_m \dot{\gamma} w_0^4}{16dL \sin(\theta)} I \quad (1)$$

During the solution of compaction moment, a uniformly distributed force along the yarns is assumed to represent the lateral compaction force between adjacent yarns. In order to get this compaction force, a constitutive model is set up for prepreg yarn, which was considered as transversely isotropic material. Because of the existence of the resin in the yarns, the axial stress and transverse stress is the function of the strain ratio, and the stiffness matrix is formed by tow viscosity coefficients and the transverse one is predicted. In the picture frame test, the yarn did not extend so the compaction force is equal the result of transverse stress multiply lateral contact area of yarn. The lateral compaction shear moment was predicted as

$$F_C = \sigma_{TT} S t_y = \eta_T \frac{S^2 \dot{\gamma}}{2w_0} t_y \sin(\gamma) \quad (2)$$

External force moment of the cell is obtained by analysis of picture frame test

$$M_p = 2 \frac{FS^2}{L} \cos(\gamma) \quad (3)$$

Eq. (4) is the load-shear angle model for plain fabric prepreg at compaction stage and the Fig. 2 is the predicted result and experimental result.

$$F = \eta_T \frac{\pi t_y S L \dot{\gamma}}{16 w_0 \cos(\gamma)} \sin^2(\gamma) + \frac{\eta_m \dot{\gamma} w_0^4}{8 d S^2 \sin(\theta) \cos(\gamma)} I \quad (4)$$

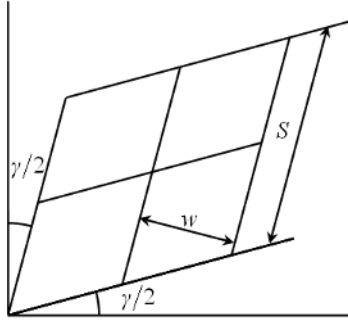


FIGURE 1. The unit cell of a prepreg plain weave fabric at the locking angle

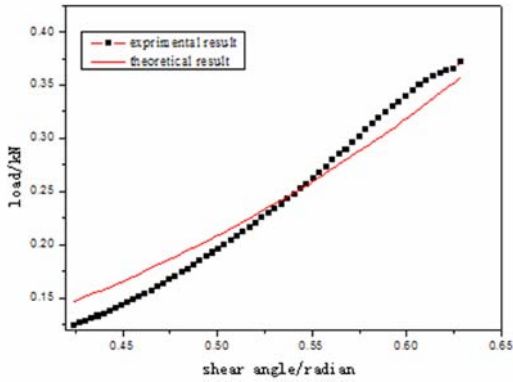


FIGURE 2. Curve of the shear angle to load

## References

1. McGuinness, G.B., Ó Brádaigh, C.M.. *J Non-Newtonian Fluid Mech*, vol. **73**, 1-28, 1997
2. Spencer, A.J.M. *Composites: Part A*, vol. **31**, 1311-1321, 2000
3. Harrison, P., Clifford, M.J., Long, A.C. *Composites: Part A*, vol. **35**, 915-931, 2004



## MECHANICAL BEHAVIOR OF SOIL – GEOTEXTILE COMPOSITES: EFFECT OF SOIL TYPE

A.I. Droudakis and I.N. Markou

Department of Civil Engineering, Democritus University of Thrace, Greece  
12 Vas. Sofias str., GR-671 00 Xanthi, Greece  
imarkou@civil.duth.gr

Geotextile reinforced soil is used in a large number of applications because of its cost and engineering effectiveness. Free draining granular materials, e.g. sands, are specified as backfill material for reinforced soil structures. However, difficulties are encountered when the available quantity of such materials is insufficient. Therefore, the investigation of the mechanical behavior of reinforced cohesive soils of low plasticity became necessary. Toward this end, triaxial compression tests were conducted in order to compare the mechanical behavior of a granular and a cohesive soil both reinforced with geotextiles and the observed results are reported herein.

For the purposes of this investigation, dry and dense Ottawa 20-30 clean sand and a fine-grained, cohesive silty soil of low plasticity were tested. Three non-woven (designated as NP, TB and TTS) and two woven (designated as HS and SG) geotextiles of various types were used for soil reinforcement. The cylindrical specimens for triaxial compression testing contained 5 horizontal layers of geotextile and had diameter and overall height equal to 50 mm and 105 mm, respectively. Fine-grained soil specimens were compacted using energy comparable to that of Standard Proctor compaction test, with water content equal to 19%. The triaxial compression tests were conducted under undrained conditions, with cell pressures,  $\sigma_3$ , ranging from 10 kPa to 600 kPa and at a constant axial displacement rate of 0.57 %/min.

The axial strain at failure of reinforced soil,  $\epsilon_{fr}$ , the axial strain ratio,  $\epsilon_{fr}/\epsilon_{fu}$ , defined as the ratio of the axial strains at failure of reinforced and unreinforced soil for the same cell pressure and the strength ratio,  $S_R$ , defined as the ratio of the maximum deviator stresses of reinforced and unreinforced soil for the same cell pressure, are used for the quantification of the deformability and strength of reinforced soils. The  $\epsilon_{fr}$ ,  $\epsilon_{fr}/\epsilon_{fu}$  and  $S_R$  values obtained are presented in Table 1. It can be seen that unreinforced fine-grained soil presents higher values of axial strain at failure than unreinforced sand. For this reason, the values of  $\epsilon_{fr}/\epsilon_{fu}$  ratio of fine-grained soil are lower than the ones of sand, although reinforced fine-grained soil presents higher values of axial strain at failure than reinforced sand. Therefore, it is concluded that the effect of reinforcement on the axial strain at failure is greater in sand than in fine-grained soil.

Shown in Fig. 1a are typical failure envelopes of unreinforced and reinforced sand and fine-grained soil. It can be observed that triaxial compression tests yielded bilinear envelopes for reinforced sand in agreement with the observations of Gray and Al-Refeai [1]. Reinforced fine-grained soil also presents bilinear failure envelope. Curved and bilinear failure envelopes were reported by Athanasopoulos [2] for reinforced fine-grained soil, indicating a continuous transition from drained to undrained behavior as normal stress is increased. Strength ratio values obtained are shown in Fig. 1b. The  $S_R$  values range from 2.17 to 4.62 and from 0.94 to 1.84 for reinforced sand and fine-grained soil, respectively. It is evident that the reinforcement effect on strength is greater in sand than in fine-grained soil. Reported SR values by Ingold [3] and Fabian and Fourie [4] for clays reinforced with geotextiles, are generally lower than 2 and, therefore, are in good agreement with the values presented herein. Strength ratios of sand decrease as cell pressure increases and strength ratios of fine-grained soil attain to maximum values for cell pressures between 50 and 100

kPa (Fig. 1b). This difference in behavior is justified by the positions of failure envelopes of reinforced soils relative to those of unreinforced soils (Fig. 1a).

TABLE 1. Values of axial strain at failure and axial strain ratio.

Soil	$\sigma_3 /$ kPa	Unreinforced	TB		NP		TTS		HS		SG	
		$\epsilon_{fu} / \%$	$\epsilon_{fr} / \%$	$\epsilon_{fr} / \epsilon_{fu}$	$\epsilon_{fr} / \%$	$\epsilon_{fr} / \epsilon_{fu}$	$\epsilon_{fr} / \%$	$\epsilon_{fr} / \epsilon_{fu}$	$\epsilon_{fr} / \%$	$\epsilon_{fr} / \epsilon_{fu}$	$\epsilon_{fr} / \%$	$\epsilon_{fr} / \epsilon_{fu}$
Sand	50	2.36	2.35	0.99	5.75	2.44	5.40	2.29	2.36	1.00	3.54	1.50
	100	3.27	4.25	1.30	8.73	2.67	6.34	1.94	3.30	1.01	4.01	1.23
	200	1.67	4.69	2.81	8.02	4.80	11.03	6.60	3.77	2.26	4.46	2.67
Fine-grained	25	8.12	13.21	1.63	19.28	2.37	20.00	2.46	9.29	1.14	10.89	1.34
	50	15.02	11.79	0.78	19.73	1.31	19.71	1.31	19.76	1.32	19.56	1.30
	100	19.29	16.27	0.84	19.51	1.01	19.71	1.02	20.00	1.04	19.33	1.00
	200	17.72	18.66	1.05	19.06	1.08	17.07	0.96	15.95	0.90	18.00	1.02

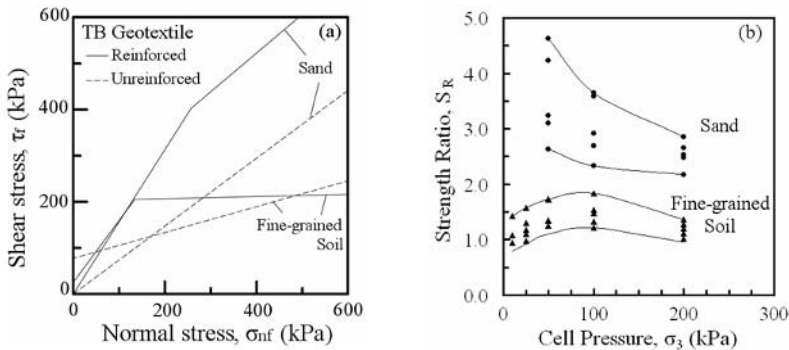


FIGURE 1. Strength of reinforced soils: (a) failure envelopes, (b) strength ratio values.

**References**

1. Gray, D.H and Al-Refeai, T., *J. Geotech. Engineering*, vol. **112**, 804-820, 1986.
2. Athanasopoulos, G.A., *Geotextiles and Geomembranes*, vol. **14**, 619-644, 1996.
3. Ingold, T.S., *J. Geotech. Engineering*, vol. **109**, 738-744, 1983.
4. Fabian, K. and Fourie, A., *Geotextiles and Geomembranes*, vol. **4**, 53-63, 1986.

## AN EXPERIMENTAL INVESTIGATION AND FINITE ELEMENT ANALYSIS OF COMPOSITE ENERGY ABSORPTION SYSTEMS

Hakim S. Sultan

Mechanical and Manufacturing Engineering Department, Faculty of Engineering, University Putra Malaysia, 43400 UPM, Serdang, Selangor, Malaysia  
hakimss@hotmail.com

Polymer matrix fiber-reinforced composite materials offer many advantages over conventional materials for structural applications, particularly where weight is an important aspect of the design. Recent work has shown that structures made from these materials are capable of absorbing large amounts of energy in a controlled manner. The specific energy absorption coefficient of polymer matrix composites in tubular form is much greater than for conventional metallic materials. Thus, composites are candidate materials for applications in transport where lightweight structures are required which provide a measure of protection in overload impact situations. Work on the axial compression of axisymmetric tubes, to be used in energy absorbing applications, has been extended to cones.

In this paper, experimental and finite element results for the composite conical shell subjected to quasi static axial loading and slipping solid steel cone into composite cone are discussed. The effects of semi-vertex angle of conical shell on the crushing behaviour and energy absorption capabilities were investigated for woven roving glass/epoxy subjected to quasi-static loading are presented and discussed. The semi-vertex angles of the cone used were 4, 8, 12, 16 and 20 degrees. The cone height and bottom diameter were kept constant for all cases as 100 mm and 76.2 mm, respectively. Experimental and finite element simulation was designed to predict the load-displacement curves, deformation histories and energy absorption capability throughout the E-glass fibre fabricated. Detailed discussion on the effects of semi-vertex angle on the crushing behaviour of conical shells and energy absorption capability are discussed. The effect of semi-vertex angle of conical composite tube on load carrying capacity; in which the specimen composed of one part with same thicknesses from woven roving glass/epoxy composite laminate and tested under quasi-static axial load and slipping solid steel cone into composite cone. The results are presented in terms of above-defined parameters, such as specific energy absorption, volumetric energy absorption, crush force efficiency, initial failure indicator, strain efficiency and failure modes. Details of these crashworthiness parameters are presented and discussed. From these tests it is seen that the force-displacement behaviour shows a polynomial relationship prior to the first crush initiation, The results demonstrated that at first crush stage the energy is dissipated in the form of friction and crazing and the conical responded in an elastic manner, while the post crush stage is dominated by tearing failure mechanisms. The experimental work was designed to predict the load-displacement curves, deformation histories and energy absorption capability throughout the E-glass fiber fabricated and semi-vertex angles. The relations between load and displacement for the composite cones and then calculate the crashworthiness parameters and energy absorption capabilities are presented. An encouraging agreement was obtained between the experimental results of composite conical shell and the numerical predictions.

### Keywords:

Conical Shell, semi-vertex angle, energy absorption

## EXPERIMENTAL DETERMINATION OF FIBER MAT PERMEABILITY OF CHOPPED FIBERGLASS MATS

Hossein Golestanian

Mechanical Engineering Department, University of Shahrekord  
Shahrekord, Kilometer 2 of Saman Rd., Iran  
golestanian@eng.sku.ac.ir

This paper presents the results of experimental investigation on fiber bed permeability variation with porosity and injection pressure. Flow measurement experiments were designed to measure fiber mat permeability for chopped fiberglass preforms with various fiber volume fractions. These experiments were performed using a rectangular mold cavity. Several layers of chopped fiberglass mats were used as reinforcement and RL 440 epoxy resin as the working fluid in the experiments. The effects of porosity and injection pressure on fiber bed permeability are investigated. Resin flow in the chopped fiberglass mats was very closely circular, suggesting an isotropic permeability tensor. Still, the analysis was performed based on an anisotropic preform permeability. The results indicate a nonlinear permeability increase with fiber bed porosity (Fig. 1). In Fig. 1 the permeability values in the maximum and minimum flow directions are plotted versus preform porosity. Close values of  $K_1$  and  $K_2$  suggests isotropic preform permeability. Note also that permeability increases sharply as porosity increases from 0.8 to 0.84. This suggests that, at high porosity values, resin flows more easily into the preform since more voids are present within the mats inside the mold cavity. The effects of injection pressure on permeability indicate a lower limit where the flow becomes too slow, thus resulting in an inaccurate permeability determination. On the other hand, if the injection pressure is set too high, resin rushes into the fiber preform. This results in an unreal high permeability determination for the fiber preform. The results of this investigation could be employed in the process/product optimization in an RTM process.

Preform permeability is an important process parameter in composite part manufacturing methods, such as in Resin Transfer Molding (RTM). In RTM resin is injected into an enclosed mold containing previously positioned reinforcement preforms. This process can be employed to manufacture large and complicated composite parts such as fiberglass boats, swimming pools, bathtubs, and parts in automotive and aircraft industries [1, 2]. The reinforcement is composed of several layers of fiber mats laid inside a two-piece mold. The mold is closed and resin is injected into the mold through one or multiple injection ports to impregnate the fibers of the preform. Injection times vary from several minutes to several hours depending on the size of the part, fiber volume fraction, fiber type, resin viscosity, and injection pressure. The integrity of the finished part in RTM depends on the selection of the preform, surface treatment of fibers, design of the mold, the choice of resin, filling parameters, and the resin cure conditions. Mold design is a highly labor intensive and complex operation [3]. Proper mold filling requires proper positioning of the inlets and outlets, close monitoring of mold temperature and injection pressure, and selection of optimum resin flow rate into the mold. Thus, fiber bed permeability must be determined experimentally for each fiber type and volume fraction prior to the actual manufacturing. Theoretically, preform permeability should depend only on the fiber type and fiber volume fraction [2, 4]. However, in the actual injection cycles pressure plays an important role too.

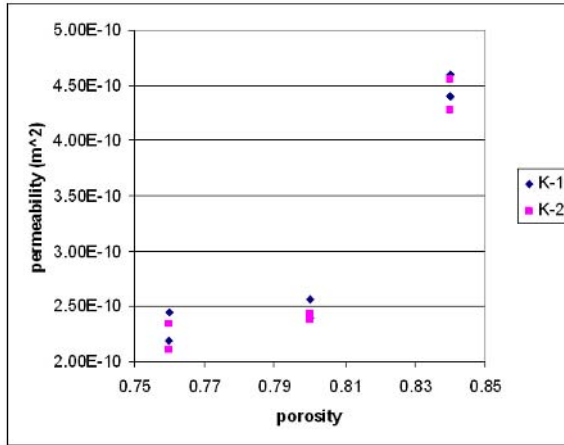


FIGURE 1. Permeability variation of chopped fiberglass mats with porosity.

## References

1. Richardson, T., *Composites, A Design Guide*, Industrial Press Inc., New York, 1987.
2. Golestanian, H., "Modeling of Process Induced Residual Stresses and Resin Flow Behavior in Resin Transfer Molded Composites with Woven Fiber Mats," Ph.D. thesis, University of Missouri-Columbia, MO, 1997.
3. Golestanian, H. and El-Gizawy Sherif, A., *J. Polymer Composites*, vol. **19**, no. 4, 395-407, 1998.
4. Sawley, M.L., Cleary, P.W., and HA, Joseph, *In Proceedings of the Second International Conference on CFD in the Minerals and Process Industries*, Melbourne, Australia, 1999, 473-478.

## MECHANICAL PROPERTIES OF PARTICLE FILLED POLYMERS

O.A. Stapountzi, M. Charalambides and J.G. Williams  
Imperial College London  
Exhibition Road, London, SW7 2AZ, United Kingdom  
olga.stapountzi@imperial.ac.uk

Particle filled polymer composites continue to replace other engineering materials in structural and architectural applications. Apart from the cost reduction, the addition of particles to polymers has been proved to be an effective way to control their thermal, optical, and aesthetic properties. However, improvements of the mechanical properties have not generally been established [1], [2]. The scope of the current research is to assess the mechanical behaviour of particle filled solid surface composites (made of poly-methyl methacrylate matrix filled with alumina trihydrate micro-particles) and to identify the key mechanisms affecting their performance. A series of mechanical tests were performed including static fracture and flexural investigations.

Slow rate fracture toughness tests were carried out in an effort to characterise the resistance of the composites to brittle failure in the presence of a natural crack. The fracture performance of the materials was assessed via the determination of fracture toughness at crack initiation. Testing was conducted according to the ISO standard [3] for determining fracture toughness ( $K_{IC}$  and  $G_{IC}$ ) for plastics. The slow rate fracture tests showed that the addition of fillers improved the fracture properties, e.g. fracture toughness.

Three-point flexural tests were also performed as a practical way to categorize the materials with respect to their flexural modulus. The flexural behaviour of the composites was assessed as a function of temperature (0 - 90 °C) and filler volume fraction (29 % vol. – 49 % vol.). The tests were carried out in conjunction with method (I) - procedure (A) of the ASTM D790M-93 standards for plastics [4]. The variation of the elastic modulus showed a gradual decrease with temperature and an approximately linear increase with particle volume fraction. The results were compared to the predictions of theoretical models derived for composites with dispersed fillers. Broad theories such as the rule of mixtures [5] were initially adopted, although the use of material specific models was necessary for more accurate predictions. The Einstein [6] and Mori-Tanaka [7] predictions followed the experimental results only for lower filler loadings. The Guth [8] prediction overestimated the composite modulus by an approximate factor of 1.4. The correlation between the Kerner [9] analytical prediction and the experimental data was satisfactory only at lower temperatures and mainly for loadings below 40 % vol. The Halpin-Tsai [10] theoretical curves fitted well with the experimental data, Fig. 1. The shape factors incorporated into the analysis were determined empirically by fitting the Halpin-Tsai curves to the experimental data for the range of temperatures. Thus, the shape factors were constant for each set of volume fractions but changed with temperature.

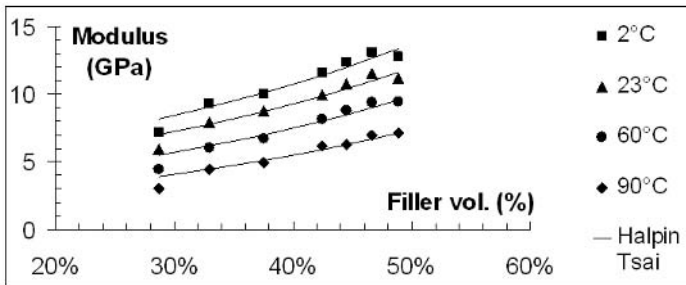


FIGURE 1. Halpin-Tsai theoretical predictions and comparison with experimental data (points denote experimental values and lines denote Halpin-Tsai predictions).

Microscopy was used to examine the structure-property relationships of the materials. The optical study provided an indication of the dispersion of filler particles in the polymer matrix as well as an approximation of the particle size distribution. The microscopy results confirmed the amounts of filler stated by the manufacturer. A considerable percentage, 2.5 to 3 % vol. was found to be the contribution of voids. Scanning electron microscopy (SEM) revealed that the alumina trihydrate particles resemble aggregates of tabular and prismatic crystals, with sizes varying from around 1.5  $\mu\text{m}$  up to 50  $\mu\text{m}$ .

It was concluded that the properties of particulate filled composites depend strongly on the interaction between constituent phases, the interaction between particles, as well as the size and shape of the fillers. Supplementary testing, including impact tests, and the development of a concise methodology for the theoretical explanation of the observed phenomena are planned in future work.

## References

1. Obakponovwe, O. and Williams, J.G., *J. Mater. Science*, vol. **41**, 437- 443, 2006
2. Ferreira, J.M., Costa, J.D. and Capela, C., *Theor. Appl. Fract. Mechanics*, vol. **26** 105–116, 1997
3. ISO 13586, *Plastics - Determination of Fracture Toughness (GIC and KIC)*, 2000
4. ASTM D790M-93, *Annual Book of ASTM Standard, American Society for Testing and Materials*, 1993
5. Ahmed, S. and Jones, F.R., *J. Mater. Science*, vol. **25**, 4933, 1990
6. Einstein, A., *Ann Phys*, vol. **19**, 289, 1906
7. Tandon, G.P. and Weng, G.J., *Polymer Composites*, vol. **5**, 327, 1984
8. Guth, E., *J. Appl. Phys.*, vol. **16**, 20, 1945
9. Kerner, E. M., *Proc. Phys. Soc.*, vol. **69**, 808, 1956
10. Halpin, J.C. and Kardos, J.L., *Polymer Eng Science*, vol. **16**, 344, 1976

## MECHANICAL AND THERMAL PROPERTIES OF ACRYLIC HYDRAZIDE CURED EPOXY; IN- SITU POLYMERIZATION

R. P. Yadav, P. C. Gope and P. L. Sah

Department of Mechanical Engineering, College of Technology, G. B. Pant University of Agriculture & Technology, Pantnagar-263145, Utranchal, India  
pcgope@rediffmail.com

Polymeric composite materials are of versatile scientific and technological significance due to their enhanced mechanical and thermal properties. In the recent year these composite materials have reflected the importance as high performance materials and multidisciplinary concept of material science. Recent advances in space and other technologies have produced a continuous and growing need for such composite materials that could withstand under prolong wear, compression and exposure to high temperature without loss in their transparency.

In the present investigation a series of acrylic hydrazide cured epoxy were synthesized at varying concentration of acrylic hydrazide ranging from 11.5:1 to 6.14:1 (ER: CA, v/v %) through benzoyl peroxide initiated in-situ polymerization method. Synthetic process was carried out in two steps. In the first step acrylic hydrazide was synthesized that was used subsequently as a curing agent to a commercially available epoxy (CY230). In order to evaluate the mechanical and thermal performance of acrylic hydrazide another set of epoxy composites was synthesized with commercially available curing agent HY951. The properties of epoxy resin synthesized with acrylic hydrazide and that of HY951 were studied and compared in terms of density, wear, compression strength, tensile strength, hardness, impact strength, material fringe value, thermal analysis, etc. Some of the results are shown in Figs 1 & 2.

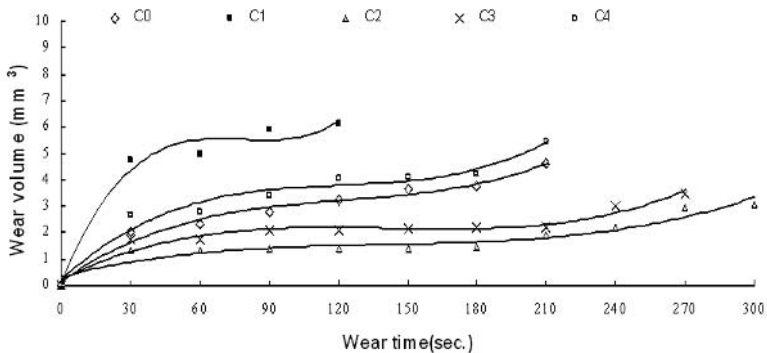


FIGURE 1. Wear variation for HY 951 and AH cured Epoxy composites (Speed= 232 rpm, load = 53.09 N) (C<sub>0</sub>-HY 951 cured, C<sub>4</sub>: 14% AH cured epoxy)



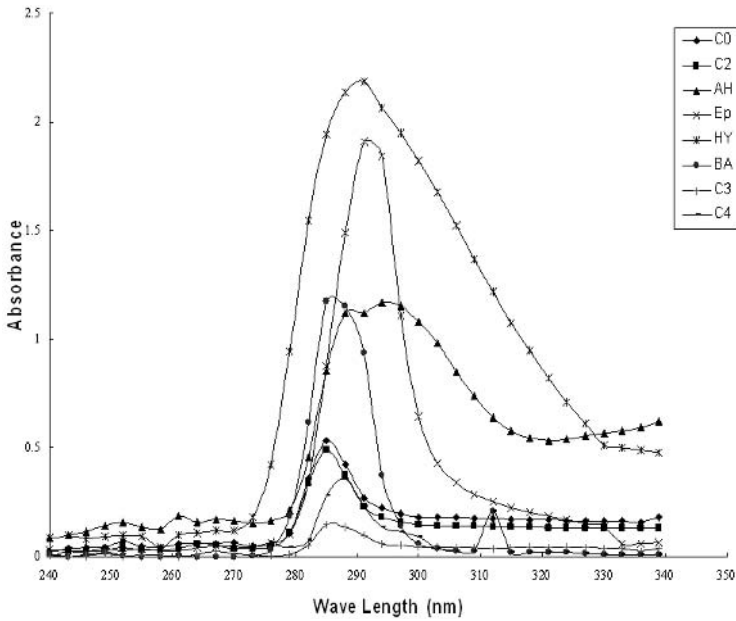


FIGURE 2. UV-vis spectrum of HY 951, AH, Epoxy, Bisphenal – A related composites

Thermo-oxidative stability of composite was evaluated through simultaneously TG-DTA-DTG performed over Perkin Elemer (Pyris Diamond) in static air 200 ml per minute at heating rate of the 10oC per minute up to 600oC using alumina as reference. A UV-vis spectrum of the sample was also recorded over Genesis 10 UV thermo-sopic UV-visible spectrometer in chloroform. FTIR spectra were recorded on Perkin Elemer spectrophotometer for spectral characterization. In present investigation it has been observed that density of AH cured epoxy composite is higher compared to hardener HY951 cured epoxy composite at same concentration of curing agent. It is observed that acrylic hydrazide cured epoxy 9:1 & 7.33:1 (epoxy: acrylic hydrazide, v/v %) have lower wear rate compared to hardener HY951 cured epoxy. Mechanical and thermal property of the developed composite is found to be superior compared to composite made from commercially available hardener HY951 cured epoxy CY230. It is found that composite developed with acrylic hydrazide cured epoxy CY230 of ratio 9:1 & 7.33:1 have higher tensile strength, compressive strength, impact strength and hardness compared to HY951 cured epoxy composite. With reference to its material fringe value, it can also be used as photo-elastic material.

For spectral characterization UV-VIS spectra and FTIR tests were conducted to study the stabilization of the developed composites. DTA-DTG-TG tests were conducted to study the thermal properties of the composites. Results are compared with HY951 cured epoxy composite. Properties are found to be superior than the composite made from HY951 cured CY230.

## References

1. Devi K. A.; Nair C.P.R. and Ninan K.N.. Journal of Polymers and Polymer Composites. vol. **11**. pp. 551-558, 2003.
2. Lin, J.S. Journal of Polymers and Polymer Composites. vol. **10**. pp. 607-618, 2002.

## ARTIFICIAL NEURAL NETWORK MODEL FOR PREDICTION OF FATIGUE LIVES OF COMPOSITES MATERIALS

Sanjay Mathur<sup>2</sup>, Prakash Chandra Gope<sup>1</sup> and J. K. Sharma<sup>1</sup>

<sup>1</sup>Department of Mechanical Engineering,

<sup>2</sup>Department of Electronics & Communication Engineering,  
College of Technology, G B Pant University of Agriculture & Technology,  
Pantnagar-263145, Udham Singh Nagar, Uttaranchal, India  
pcgope@rediffmail.com

The application of composites as engineering materials has become state of art and fatigue is one of the most complicated problems for fiber composites. The life prediction of a newly developed material is costly and time consuming. A potential solution to this problem is offered by artificial neural networks (ANNs).

In the present study an ANN model is developed for fatigue life prediction of carbon fibre reinforced plastics (CRPF) IM7/977, HTA/913, T800/5245, T800/924 with [(±45,0)2]S lay up and HTA/919 with [(±45,90,0)2]S lay up and glass fibre composites G/913, G913/913, G913/920, G913/SiC, G913/PE, G913/G laminates. The ANN data base contain more than three hundred fatigue lives over a range of different stress ratios of 10 to -3.33. Different monotonic, fatigue and statistical properties have been taken as input parameter. The inputs to ANN model are lay up, volume fraction, monotonic properties such as tensile modulus, tensile strength, compression strength, failure strain, applied load parameters such as stress ratio, maximum stress, minimum stress, probability of failure and statistical parameters of fatigue life. The output of the ANN is logarithmic value of fatigue life cycles. The architecture selected has two hidden layers with 18 and 6 units each. The learning rate coefficient is optimised as 0.9 and momentum factor as 0.3.

The predicted of fatigue life by ANN are compared with experimental results. The percentage error in more than 94 percent cases is found to be less than 10 percent (Fig. 1). The present studies have shown that fatigue life of composite material is sensitive to many parameters such as material composition, monotonic properties, applied load, fatigue properties etc.

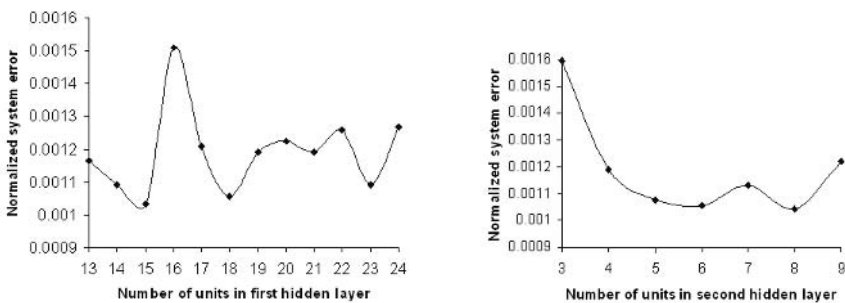
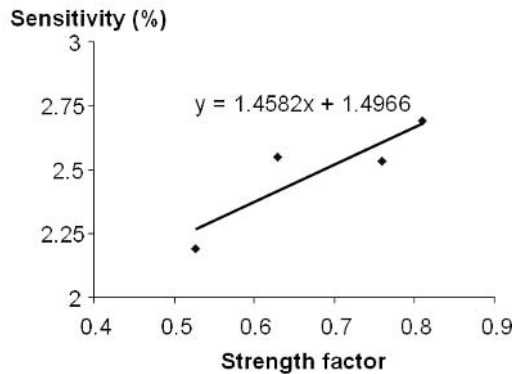
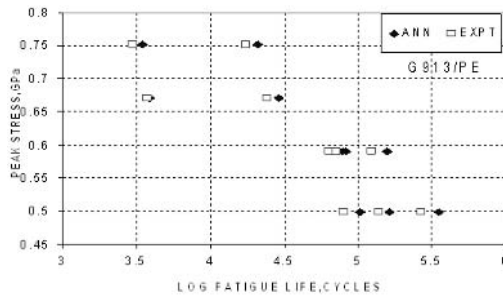
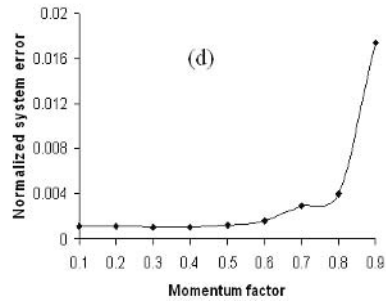
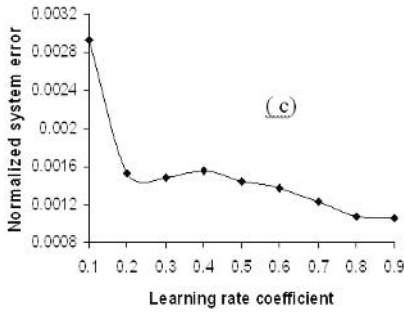


FIGURE 1. Variation of normalized error with number of nodes in (a) First ( b) Second hidden layer



The above figures shows some of the results on the optimization of momentum and learning rate factors, predicated and experimental fatigue life of glass fiber composites and the sensitivity of strength factor on fatigue life. Similar studies have been carried out for all materials mentioned in the present investigation. The limitation of the ANN method and sensitivity analysis of different factors on fatigue life has also been addressed.

**References**

1. Al-Assaf, Y., El Kadi, H., 2002 Energy-based fatigue life prediction of fiber glass/epoxy composite using modular neural networks, Composite Structures, vol. 57, pp. 85-89.

## PROCESS AND HEALTH MONITORING USING FIBER BRAGG GRATING DISTRIBUTED SENSOR FOR VACUUM INFUSION PROCESS

Soohyun Eum<sup>1</sup>, Kazuro Kageyama<sup>1</sup>, Hideaki Murayama<sup>1</sup>, Kiyoshi Uzawa<sup>1</sup>, Isamu Osawa<sup>1</sup>, Makoto Kanai<sup>1</sup> and Hiroataka Igawa<sup>2</sup>

<sup>1</sup> Dept. of Environmental and Ocean Engineering, the University of Tokyo  
7-3-1 Hongo Bunkyo Tokyo, 113-8656, Japan

<sup>2</sup> Japan Aerospace Exploration Agency  
6-13-1 Osawa, Mitaka-shi, Tokyo, 181-0015 Japan  
eum@giso.t.u-tokyo.ac.jp

Vacuum infusion process (VIP) has been accepted for composites industry over last decade due to low fabrication cost and applicability to complex and large composite structures. Vacuum is used as the driving force to impregnate preform with resin [1]. VIP has been applied to automotive, aerospace, boat, and various industrial fields widely. Process control and the quality assurance of composites structure are required. Especially resin flow is very important factor in VIP because resin should be impregnated into a preform perfectly without dry spot before starting gelation of resin. Residual stress is generated due to shrinkage of matrix in thermosetting resin during cure. These will be causes of delamination [3] and lower dimensional stability in composite structures. Therefore, control of the manufacturing processes is needed through resin flow monitoring and cure monitoring.

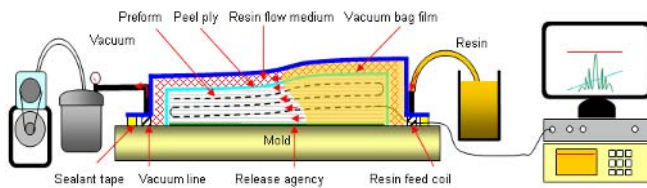


FIGURE 1. Resin flow front monitoring with OFDR and long gauge FBGs

Optical frequency domain reflectometry (OFDR) and fiber Bragg grating (FBG) sensor were employed for process and health monitoring. Especially a long gauge FBG (about 100mm) which are 10 times longer than an ordinary one was employed for a distributed sensing. The released pressure due to the volume of resin can be detected along a long gauge FBG with a high spatial resolution by OFDR as shown in Fig. 1. FBG is able to use for cure monitoring and structural health monitoring without change or modification of sensor after infusing resin. Long gauge FBGs were embedded in GFRP laminates. In this study, we intended to detect the gradient of pressure between impregnated part and unimpregnated one. We could get the wavelength shifts due to pressure changes along the gauge length of FBG as performing short-time Fourier transformation (STFT) for signal acquired from FBG [3]. Therefore, we could know the resin flow front with the gradient of compressive strain of FBG as shown in Fig. 2. Embedded FBGs also could measure the shrinkage of matrix. After cure, three point bending test was conducted with the laminate in order to prove an ability of health monitoring.

In this study, we could conduct process and health monitoring for VIP by using OFDR and long gauge FBGs. We could measure resin flow front with the changes of pressure. Shrinkage of resin was also detected by long gauge FBGs. The ability of health monitoring was proved by three point bending test with same optical fiber sensors which were used for resin flow and cure monitoring in VIP.

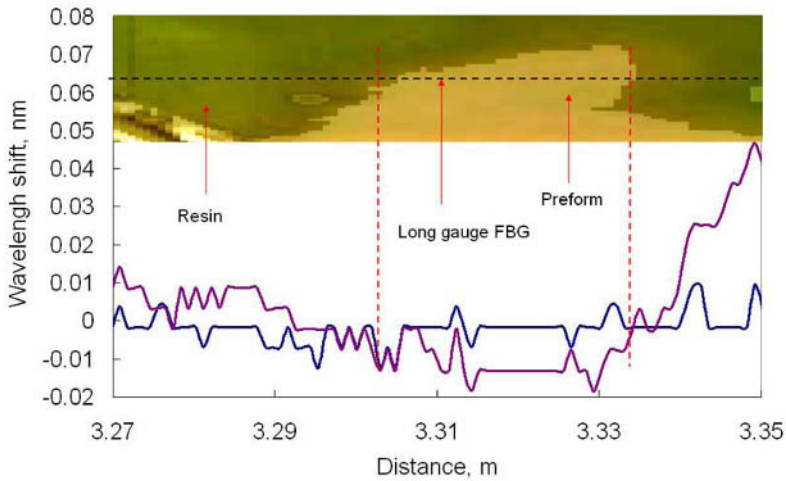


FIGURE 2. Result of resin flow monitoring

## References

1. J. Dai, D. Pellaton, and H.T. Hahn, *Polymer composites*, vol. **24**, no. 6, pp. 672-685, 2003.
2. J.A. Ramos, N. Pagani, C.C. Riccardi, J. Borrajo, S.N. Goyanes, I. Mondragon, *Polymer*, vol. **46**, pp. 3323-3328, 2005.
3. H. Igawa, H. Murayama, T. Kasai, I. Yamaguchi, K. Kageyama, and K. Ohta., *Proc. of SPIE*, vol. **5855**, pp.547-550, 2005.

## USING DCB AND PULL-OUT TESTS FOR EXPERIMENTAL INVESTIGATION OF RIB-SKIN INTERFACE FRACTURE TOUGHNESS OF STIFFENED COMPOSITE SHELL

A. Korjakins, O. Ozolins and D. Pizele

Riga Technical University

Institute of Materials and Structures, Kalku str. 1, Riga, LV 1658, Latvia

aleks@latnet.lv, olgerts@bf.rtu.lv, polmaterials@gmail.com

With the increased emphasis on reducing the cost of manufacturing composite structures, secondary bonding or co-curing is an attractive option to eliminate the need for mechanically fastening subassemblies. Many composite components in aerospace structures consist of flat or curved panels with co-cured frames and stiffeners. Out-of plane loading such as internal pressure in a composite fuselage or out-of-plane deformations in a compression loaded post-buckled panel may cause the frame or stiffener to debond from the panel [1].

In polymer matrix composites, progressive type failures are often observed where catastrophic failure is generally preceded by constituent level damage accumulation. A number of research efforts propose progressive failure algorithms aimed at capturing the progressive failure process from initial to final failure [2]. The possibility to accurately predict damage and progressive failure in structures produced from composite materials is important task in the design of lightweight structures.

The interlaminar delamination fracture toughness of composite rib stiffened shell elements made from carbon/epoxy material has been investigated. DCB tests and pull-out tests has been fulfilled for this aim. Specimens were manufactured from CFRP in the form of the co-cured rib stiffened multilayered shell. All tests have been performed on the universal testing system Zwick Z100. The width of skin of the specimens was  $b = 100 \pm 0.5$  mm, the width of glued rib was  $60 \pm 0.5$  mm and panel length  $L = 76 \pm 0.5$  mm. The thickness of skin of the specimens was 1 mm and thickness of the rib 3 mm. Glued thickness of the rib changes from 1.5 mm near the rib to 0.5 mm at the tip. The loading rate during the test was 2.0 mm/min. The limit load  $P_c$  and critical displacement  $\delta$  (deflection) at mid-span of the specimen were measures at the moment of the crack extension.

The control of crack expansion and form of crack has been fulfilled using ultrasound techniques. Knowledge of experimentally observed failure mechanisms is needed to determine the constituent ultimate strength from the micromechanics based volume averaged stress values.

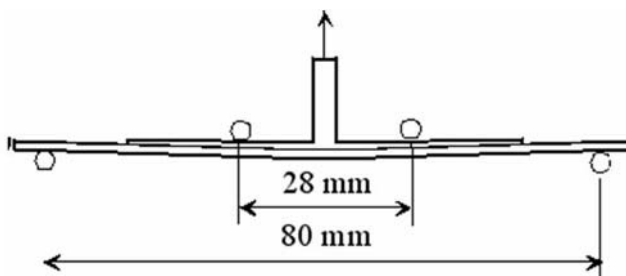


FIGURE 1. Stiffened shell pull-off boundary conditions

Pull-out test results of co-cured joints were analyzed in different temperatures to understand the failure mode and strength of attaching frames and bulkheads to the fuselage skin. The boundary conditions are shown in Fig. 1. The differential scanning calorimetry analysis have been made for the investigation of materials of skin and rib. These definitions of glass transition temperature allowed make a choice of the testing temperatures of composite specimens. Five levels of temperatures have been chosen for investigations: 20°, 50 °, 100 °, 170 ° and 250 ° C.

The E-modulus of CFRP has been defined at the same temperature levels using laser non-contact extensometer OptiXtens. The fiber bridging was not observed in the specimens. This can be explained by the using of pre-preg manufacturing technology. The fracture of specimens has been caused by complex stress conditions between layers at the place of rib curvature. DCB tests was performed in order to obtain the mode I delamination fracture toughness at the interface of the present laminated composite material. By using experimental investigation of specimens the form of fracture in the zone of joining between rib and skin has been obtained. The obtained results can be used for numerical analysis of the specimens and whole structures for prediction of damage and progressive failure.

## References

1. Minguet P. J., Fedro M. J., Brien T. K. O., Martin R. H., Ilcewicz L. B., Awerbuch J. and Wang A., In Proceedings, Fourth NASA/DoD Advanced Composite Technology Conference, Salt Lake City, UT, June 1993, 58-65
2. Key C. T., Garnich M. R. and Hansen A. C., Composite Structures, vol. **65**, 357-366, 2004

## EXPERIMENTAL TESTS OF FATIGUE INDUCED DELAMINATION IN GFRP AND CFRP LAMINATES

D. Tumino, G. Catalanotti, F. Cappello and B. Zuccarello  
 Dipartimento di Meccanica, Università degli Studi di Palermo  
 Viale delle Scienze 90128 – Palermo, Italy  
 tumino@dima.unipa.it

This work deals with the experimental analysis of the delamination phenomena in various composite materials under different loading conditions. Quasi-static and fatigue tests are performed on specimens made of glass-fibre reinforced plastic (GFRP) and carbon-fibre reinforced plastic (CFRP). In particular, under both quasi-static and fatigue loading, single fracture modes I and II (using standard DCB and ENF test configurations) and mixed modes I+II (using the MMB test configuration) with several mode mixtures, have been analysed. Further experiments of delamination growth with mode mixture that varies with the crack length, will be performed.

### Experimental results

In this section only preliminary results obtained from experiments on GFRP composite are reported. In details, such tests have been carried out by using specimens cut-off from a composite laminate  $[0_{12}]$  obtained by a hand lay-up process and made of glass-epoxy layers with a fibre volume fraction  $V_f=0.26$ . The starter crack has been obtained by inserting in the stacking sequence a thin strip of Mylar®. The elastic properties of the composite material have been determined by standard tensile and shear tests (see table 1).

TABLE 1. Material properties.

Material	$E_L$ [GPa]	$E_T$ [GPa]	$\nu_{LT}$	$G_{LT}$ [GPa]
E-glass/Epoxy	21	6	0.28	1.6

The average dimensions of the specimens used for the tests are: width  $B=20$  mm, half-thickness  $h=2.4$  mm, mid-span length  $l=55$  mm. In order to observe the actual crack length during the delamination tests, a white paint has been sprayed on one side of each specimen and marks are drawn at regular intervals. The crack length has been monitored by optical observation carried out through high-resolution digital images.

From quasi-static tests performed under displacement control, the critical values for the Strain Energy Release Rates (SERR) have been obtained. Fig. 1 shows the released energy  $G$  computed by using the modified beam theory [1] versus the crack length  $a$ , for DCB (Fig. 1a) and ENF (Fig. 1b) tests. In details, the resistance curve depicted in figure 1a shows that fibre bridging plays an important role during the delaminations process under mode I, as observed also in [2] for CFRP laminates. The resistance of the material, determined by considering the peak in the force-displacement curve, is  $G_{IC}=1.2$  N/mm. Fig. 1b shows the resistance curve obtained for mode II; from this figure it is possible to observe how the energy rises up to a critical value which corresponds to the unstable crack propagation and then the crack suddenly grows to 60 mm. The critical value of the SERR in mode II is then calculated as  $G_{IIC}=3.5$  N/mm.



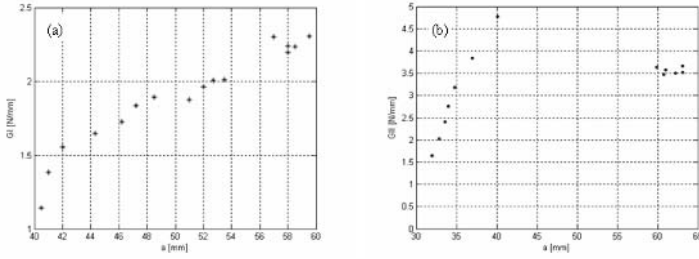


FIGURE 1. Resistance curve for mode I (a) and mode II (b).

Fatigue tests have been performed under force control with a servo-hydraulic machine at a frequency of 2 Hz and with a load ratio  $R=P_{min}/P_{max}=0.1$ . In Fig. 2a the curve of the crack length versus the number of cycles in mode I and in mode II is depicted. In figure 2b and 2c the crack growth rate versus SERR, in a log-log diagram, is reported for both fracture modes. By fitting properly the experimental results with a power law, the Paris curve of the material can be described by the following expression:

$$\frac{da}{dN} = B(G)^m \tag{1}$$

where  $m=0.38$  for fracture mode I, whereas  $m=0.55$  for mode II. These values are smaller than those reported in literature [3]; although further tests are necessary to explain correctly this difference, most likely it can be due to the particular manufacturing process (hand lay-up) and to the small value of the fibre volume fraction ( $V_f=0.26$ ).

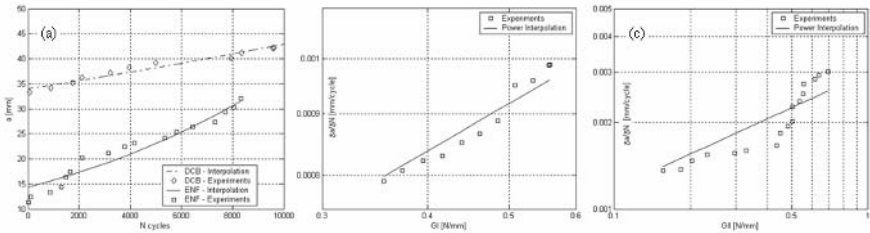


FIGURE 2. Fatigue tests: crack length vs. cycles (a), Paris curve for mode I (b) and mode II (c).

A detailed campaign of tests in mixed mode condition is the actual object of the research activity both for GFRP and CFRP.

**References**

1. Reeder, J.R., Crews J.H., Nasa TM 102777, 1991.
2. Gregory, J.R., Spearing, S.M., Composites: Part A, vol. 36, 665-674, 2005.
3. Kenane, M., Benzeggagh M.L., Composites Science & Technology, vol. 27, 597-605, 1997.

## COMPOSITE SANDWICH STRUCTURES; EXPERIMENTAL EVALUATION AND FINITE ELEMENT ANALYSIS OF MECHANICAL PROPERTIES

S. B. Bozkurt<sup>1</sup>, F. E. Sezgin<sup>1</sup>, O. O. Egilmez<sup>2</sup>, E. Aktas<sup>2</sup> and M. Tanoglu<sup>1</sup>  
Izmir Institute of Technology

<sup>1</sup> Mechanical Engineering Department

<sup>2</sup> Civil Engineering Department

Gülbağçe Campus, 35437 Urla, Izmir, Turkey

baharbozkurt@iyte.edu.tr, fatmasezgin@iyte.edu.tr, ozguregilmez@iyte.edu.tr,  
enginaktas@iyte.edu.tr, metintanoglu@iyte.edu.tr

Sandwich composite structures have been applied in aerospace applications and civil infrastructures due to their extremely low weight, high flexural stiffness, high transverse shear stiffness and corrosion resistance, Shivakumar and Chen [1]. Two thin stiff facesheets and a thick lightweight core between them have been in general, the components of the sandwich structures. The facesheets carry the bending loads where the core material carries the shear loads, Borsellino *et al.* and Mamalis *et al.* [2-3]. The mechanical properties of the sandwich structures and their components have great importance in terms of industrial applications, Cantwell *et al.* and Vuure *et al.* [4-5]. The main objective of this present work is to improve the understanding of the failure mechanisms of these types of structures.

In this study, polypropylene based honeycomb core and glass fiber reinforced polymer (GFRP) facesheets have been fabricated by hand lay up technique with various core thicknesses. GFRP laminates were fabricated by using non-crimp glass fibers and epoxy matrix. After post-curing treatment, the laminated sandwich structures were cut into test specimens based on the related standards. Core thickness variation is the main parameter for each test in order to understand the mechanical behaviour of the sandwich structures. Flatwise compression (FC), edgewise compression (EC), three point bending and double cantilever beam (DCB) tests have been applied on these specimens.

The sandwich structures are also being analyzed by means of three dimensional finite element analytical (FEA) models. The test data is evaluated by ANSYS software in order to make predictions about the mechanical behaviors of the sandwich structures. The mechanical test results of each component are being used as input data in the finite element analysis in ANSYS software in order to accurately model the sandwich structures. Linear elastic material properties is being utilized and the failure criteria that need to be specified in the FEA model will be obtained from the failure modes observed for each component of the sandwich structure. The experimental data will be verified with numerical results.

### References

1. Shivakumar, K., Chen, H., *Journal of Sandwich Structures and Materials*, vol. **7**, 77-90, 2005
2. Borsellino, C., Calabrese, L., Valenza, A., *Composite Science and Technology*, vol. **64**, 1709-1715, 2004
3. Mamalis, A. G., Manolacos, D. E., Ioannidis, M. B., Papapostolou, P. D., *Composite Structures* vol. **71**, 246-257, 2005
4. Cantwell, W. J., Scudamore, R., Ratcliffe, J., Davies, P., *Composite Science and Technology* vol. **59**, 2079-2085, 1999

5. Vuure, A. W. van, Pflug, J., Ivens, J. A., Verpoest, I., *Composite Science and Technology* vol. **60**, 1263-1276, 2000
6. Ural, A., Zehnder, A. T., Ingrassia, A.R., *Engineering Fracture Mechanics* vol. **70**, 93-103, 2003

## SOME NEW STRENGTH CRITERIA FOR FRP TEST METHODS SUBSTANTIATION

Alexandre N.Polilov and Nikolay A.Tatous  
Mechanical Engineering Research Institute named by A.A.Blagonravov,  
Russian Academy of Sciences  
4, Malyi Kharitonievsky per, Moscow, Russia, 101990  
polilov@imash.ru

The four well-known test methods for FRP (fiber-reinforced-plastics) are analyzed in this report and using new simple fracture criteria it's possible to understand the experimental data more correctly.

### 1. The linear criterion of composite beam delamination

For short-beam-bending test which is used usually for interlaminar strength determination we proposed the linear criterion

$$\sigma_x + m \cdot \tau_{xy} = c \quad 1.1$$

where  $m, c$  are the experimentally determined constants. This criterion gives the following relation between critical load  $P = 1.33\tau_0 t h$  and length to height ratio  $l/h$  in a good accordance to experimental data (Fig. 1), in contrast to traditional maximum stress criteria:

$$\tau_0 = \frac{c \cdot m}{m^2 + (l/h)^2} \quad 1.2$$

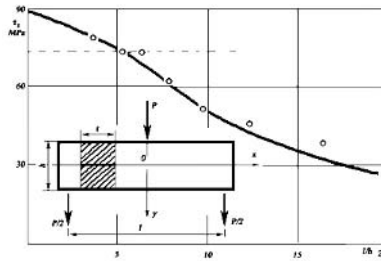


FIGURE 1. The scheme of loading and the  $\tau_0 - l/h$  dependence.

### 2. Strength criteria for monolayer and the optimum angle of misalignment

Linear fracture criteria for fiber rupture  $\sigma_{n1} + m_1 \tau_{n1} = \sigma(0)$  and fiber-matrix interface splitting  $\sigma_{n2} + m_2 \tau_{n2} = \sigma(90)$  for off-axis tension of unidirectional FRP make it possible to determine the optimum small angle of misalignment  $\alpha^* \approx \arctg[\sigma(90)/m_2 \sigma(0)]$ , and the composite material with this misalignment angle has near the same strength as the strength of unidirectional frp, but the splitting resistance is much more.

(where  $m_1, m_2$ , - material parameters  $\sigma(0), \sigma(90)$  – strengths along and across the fibers)

### 3. Strength criterion for couple pair of layers $\pm\varphi$

For symmetric balanced pairs of layers the new criterion was proposed and it explains rather well the experimental results for biaxial tension of composite tube with lay-up structure  $(\pm\varphi)$ . In  $\sigma_\theta - \sigma_z$  plane (Fig. 2) this criterion has the form of two straight lines 1 (and 2)

$|\sigma_z / tg \varphi - \sigma_\theta / ctg \varphi| = \sigma(45)$  and the set of experimental points may be approximated also by ellipse (3.1), where,  $\sigma_\theta$ ,  $\sigma_z$  - uni-axial strengths for tubes with (0), and ( $\pm 45$ ) wound structure, correspondly.

$$\sigma_z^2 tg^2 \varphi + \sigma_\theta^2 ctg^2 \varphi - \sigma_z \sigma_\theta \left( 2 - \sigma(45)^2 (1 + tg^2 \varphi)^2 ctg^2 \varphi / \sigma(0)^2 \right) = \sigma(45) \quad 3.1$$

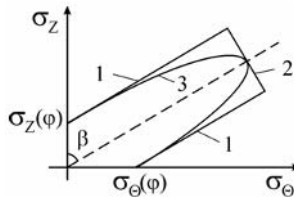


FIGURE 2. Limit surfaces in stress space for ( $\pm\varphi$ ) tube under biaxial loading  $\sigma_\theta$ ,  $\sigma_z$ .

#### 4. “Chinese lantern” mode of composite tubes failure under compression

The fracture of composite unidirectional tubes and rods may have three main modes:

- a local microwave buckling at a critical stress  $\sigma_c$ , not depending on the length of tube.
- Euler-type macro-buckling of a tube at the critical stress, depending on the length  $l$ :

$$\sigma_E = \pi^2 ER^2 / 2l^2 \quad 4.1$$

- “Chinese lantern” mode of a tube fracture with multiply splitting and buckling of originated strips. It’s necessary to calculate the critical stress  $\sigma_{cl}$  numerically, but for thin-walled tubes we can receive the formula,  $a$  – the angle of circle segment:

$$\sigma_{cl} \cong 1,2 \left( \gamma^4 E^5 / R^2 l^2 \right)^{1/9} \text{ for } \alpha^* = 3,21 \left( \gamma^4 / ER^5 \right)^{1/9} \quad 4.2$$

The condition of simultaneous start of all fracture modes gives us the optimum sizes  $l$ ,  $R$  of composite tube structure.  $R_0 = 1,01 E \gamma / \sigma_{cl}^2$ ;  $l_0 = 2,24 E^{3/2} \gamma / \sigma_{cl}^{5/2}$

#### References

1. Rabotnov Yu.N., Kogaev V.P., Polilov A.N. and Strekalov V.B. (1983). Interlaminar Strength Criterion for CFRP under Cyclic Loadings. Mechanics of Composite Materials (Translated from Russian, Consultants Bureau, New York), vol. **18**, 6, 652-656.
2. Rabotnov Yu.N. and Polilov A.N. (1977) Strength Criteria for Fibre-Reinforced Plastics. Fracture 1977, ICF 4, Waterloo, Canada, June 1977. In: Advances in research of the strength and fracture of materials. Pergamon Press, New York, USA, vol. **3B**, part YII, Non-metals, 1059-1065.
3. Polilov A.N. The scheme of strength estimation for symmetric reinforced composite tubes under plane stress state. Mechanics of Composite Materials, 1980, vol. **2**, pp. 221-226.
4. Polilov A.N., Rabotnov Yu.N. On composite tubes fracture with a mode like “Chinese Lantern”. Mechanics of Composite Materials, 1983, vol. **3**, pp. 548-550.

## COMPOSITE REPAIR TECHNOLOGY AND ITS APPLICATION

Kuo-Wei Wu  
Aeronautical Systems Research Division (ASRD/CSIST)  
P.O. Box 90008-11-12 Taichung, Taiwan, R.O.C  
wukuowei23@yahoo.com.tw

With the characteristics of high specific strength and modulus, fiber-reinforced composites have been applied for aircraft structures. Due to the manufacturing anomalies, mishandling and environment damage, those structures would be damaged and affect their performance. For restoring the damaged composite structures, we need to develop a useful and easy repair method. The requirements of composite structure are the restoration of strength and stiffness, the aerodynamics smooth, the least weight growth, environment compatibility, durability and accessibility.

Composite structure repair technology must organize non-destructive inspection (NDI) engineer, structure design & analysis engineers, material and manufacturing engineers. The whole repair procedures include damaged area NDI, assessment of residual strength, repair design, repair processing and NDI etc.

In the study, the strength of bolted and bonded repair was evaluated by the specimen test. The test results of single-lap shear strength of Al 6061-T6 specimen bolted by AD62 blind fastener and those of 1581 glass fiber prepreg specimen bonded by film adhesive FM73 were shown in tables 1 and 2, respectively. Obviously, it shows that the bonded strength was better than the bolted strength.

Then, the bonded flush co-cured patch method was applied to the damaged composite sandwich structure. The repair processes include the NDI inspection and assessment of damaged area, repair analysis and design, treatment of damaged area, replacement of core, bonded flush co-cured patch and the inspection of repaired area. The repair approaches for the composite sandwich structures are fully developed. The repaired structure was shown Fig. 1.

TABLE 1. The test results of single-lap shear strength of Al 6061-T6 specimen bolted by AD62 blind fastener.

Specimen no.	1	2	3	Mean value
Strength (ksi)	0.781	0.747	0.755	0.761

TABLE 2. The test results of single-lap shear strength of 1581 glass fiber prepreg specimen bonded by film adhesive FM73

Specimen no.	1	2	3	4	Mean value
Strength (ksi)	0.789	0.994	0.900	0.970	0.913



FIGURE 1. The repaired composite sandwich structure

### References

1. M.M. Schwartz, Composite Materials Handbook Chapter 7, McGraw-Hill Book Company, New York N.Y. 1984.
2. M.C.Y. Niu, "Composite Airframe Structures", Conmilit Press Ltd., Hongkong, 1992.
3. A.A. Baker and R. Jones, "Bonded Repair of Aircraft Structures", Chapter 1, Martinus Nijhoff Publishers, Dordrech, Netherlands, 1988.
4. R.H. Stone, "Development of Repair Procedures for Graphite/Epoxy Structures on Comercial Transports", in "Composite Repairs SAMPE MONOGRAPH, No.1", 1985.
5. J.D. Labor and S.H. Myhre, "Large Area Composite Structure Repair", AFFDL-TR-79-3040, March, 1979.
6. J.E. Robson, F.L. Matthews and A.J. Kinloch, J. of Reinforced Plastics and Composites, vol. **11**, Jul., 1992.

## SOME INFLUENCES ON THE FATIGUE BEHAVIOUR OF SHORT-GLASFIBER-REINFORCED POLYMERS

Ch. Guster<sup>1,2</sup>, G. Pinter<sup>3</sup>, W. Eichlseder<sup>1</sup> and R.W. Lang<sup>2,3</sup>

<sup>1</sup> Chair of Mechanical Engineering, University of Leoben,  
Franz-Josef-Straße 18, 8700 Leoben, Austria

<sup>2</sup> Polymer Competence Center Leoben GmbH,  
Parkstraße 11, 8700 Leoben, Austria

<sup>3</sup> Institute of Material Science and Testing of Plastics, University of Leoben,  
Franz-Josef-Straße 18, 8700 Leoben, Austria  
Christoph.Guster@mu-leoben.at

Because of the importance of lightweight constructions and the reduction of production time and costs, nowadays other materials more and more substitute components, which are made so far of metals. The usage of short-glasfiber-reinforced plastics instead of metals seems self-evident in many cases because of their high specific strength and the favourable manufacturing processes.

The available material-data of this material group from datasheets are mostly static values like tensile strength, yield strength and fracture elongation. For the dimensioning of parts having regard to geometry, loading conditions and material behaviour, static material data are not sufficient. For the dimensioning of dynamically loaded components concerning the fatigue life time, the knowledge of the local S/N-curve is necessary. These local S/N-curves are essentially influenced by component specific effects such as fiber orientation, type of loading, size, stress ratio, stress gradient, temperature, production process and many more. Hence, these effects on material behaviour have to be analysed.

One of the main aims of a big research project in our group is the generation of a comprehensive database which is necessary for the applicability of fatigue life calculation with local S/N-curves. In this work the effect of fiber orientation and concentration as well as stress ratio on the fatigue behaviour of two materials was investigated.

The parameters fiber-orientation and –concentration influence the material behavior of short fiber reinforced polymers essentially. The orientation of the fibers in injection molded components is affected by complex flowing conditions. Injection molded fiber reinforced thermoplastic-plates for example have a layer composition, as shown in Fig. 1 ([1, 2]). For determination of an average orientation factor experimental methods as well as flowing simulations are used. A comparison of both methods will be shown in the final paper. For detection of S/N-curves with different average fiber orientations, different test-specimens and two different materials were tested. So it was possible to assign S/N-curves to fiber-orientation factors.

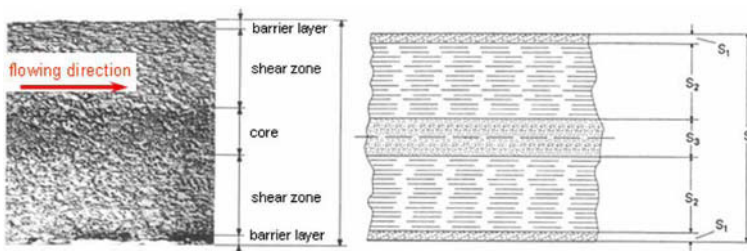


FIGURE 1. Schematic fiber orientation in an injection molded plate



Another parameter which influences the cyclical material behaviour significantly is the stress ratio. To determine this effect, the specimens were tested under tension/tension ( $R=0,1$ ), compression/compression ( $R=10$ ) and tension/compression ( $R=-1$ ). All tests were performed stress controlled with a servo-hydraulic test rig at room temperature. Results of these cyclic tests are S/N-curves as shown in Fig. 2.

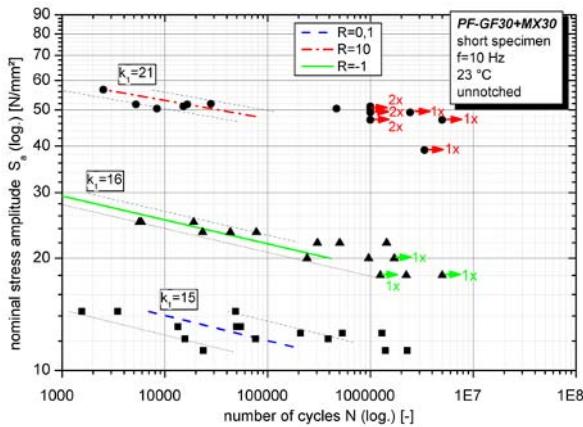


FIGURE 2. Influence of stress ratio on fatigue strength at finite life

## References

1. Menges, G. and Geisbüsch, P., *Die Glasfaserorientierung und ihr Einfluss auf die mechanischen Eigenschaften thermoplastischer Spritzgießteile – Eine Abschätzmethode*, *Colloid Polymer Science*, vol. **260**, 73-81, 1982
2. Johannaber, F., Michaeli, W., *Handbuch Spritzgießen*, Carl-Hanser Verlag, 2004.

## THEORETICAL RESEARCH ON THE INFLUENCE OF THE INTERFACE WOOD-ADHESIVE ON THE STIFFNESS OF THE COMPOSITE PANELS MADE OF WOOD LAMELLAS

Camelia Boieriu, Ioan Curtu, Dumitru Lica, Mariana Stanciu and Adrian Popoi  
 “Transylvania” University of Brasov  
 500036 Brasov, B-dul Eroilor 29, Romania  
 cboieriu@unitbv.ro

The paper presents the results of the FEM (*Finite Element Method*) analysis applied to the anisotropic-orthotropic panels made of lamellas of hardwood (beech and maple wood) considered to be subjected to a static load. The research follows the influence of the interface wood - adhesive on the stiffness of the panels, for different lamella width.

The lignin - cellulose based panels presented in this paper are composite panels made of small sized wood lamellas of hardwood species with the structures presented in Fig. 1. The lamellas are finger-jointed on the length and edge-jointed on the width. In each panel the basic material is the beech wood and it is mixed with maple wood. In order to compare the results, a standard panel made only of beech lamellas has been tested together with the composite panels [1].

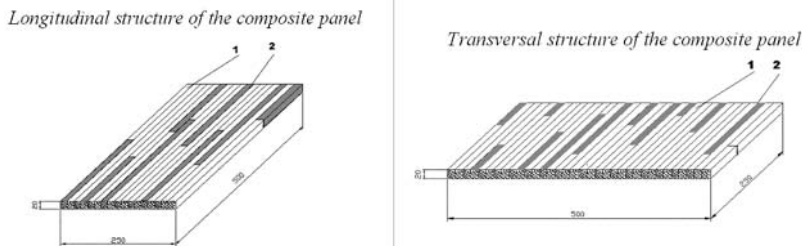


FIGURE 1. The real structure of the composite panels. 1-beech wood, 2-beech wood (for standard panel) or maple wood (for composite panel).

The theoretical model (used for FEM analysis) is shown in Fig. 2.

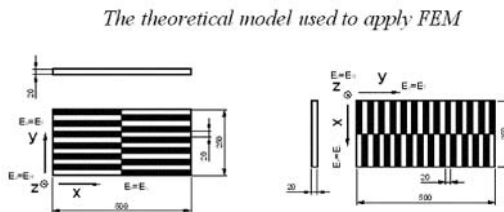


FIGURE 2. The theoretical model of the panels used for FEM analysis.

The theoretical research is applied in order to determine the bending strength of the panels loaded with a uniformly distributed load as shown in Fig. 3. The Finite Element Method used for this purpose was applied for different sizes of lamella width in order to determine the dependence between the width size and the panel deflection. In the same time the method was applied both to the longitudinal and to the transversal structure [2].

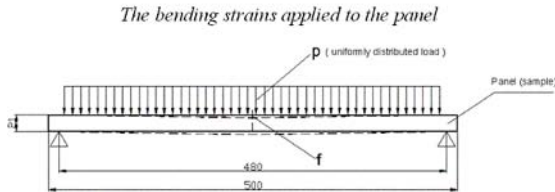


FIGURE 3. The theoretical model of the panels used for FEM analysis.

First the FEM analyse has been performed without considering the adhesive layer, as shown in Fig. 4. The obtained results were not quiet accurate. The second determination using FEM analyse and considering the existence of the adhesive layer has shown the tendency of increasing the stiffness with the increasing of the lamella width [3].

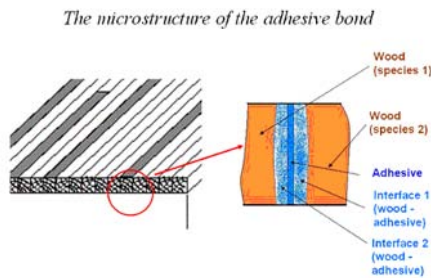


FIGURE 4. The wood-adhesive interface.

The obtained results have been compared with the experimental results. The experimental research has confirmed the results of the theoretical analysis [4].

## References

1. Boieriu, C., *Contributii la studiul panourilor reconstituite, decorative, din lemn masiv de foioase, folosite in decoratiuni interioare si mobilier*, Ph D Thesis, 2006
2. *SR ISO 7170/96- Mobilier. Corpuri de depozitare. Determinarea rezistentei si durabilitatii*, 7-9.
3. Curtu, I., Ghelmeziu, N., *Mecanica lemnului si materialelor pe baza de lemn*, Editura Tehnica Bucuresti, 1984, 11-12.
4. Boieriu, C., Lica, D., Curtu, I., In *Proceedings of the 9th International Research/Expert Conference TMT 2005 Antalya*, 26-30 September, 2005, 1133-1136, ISBN 9958-617-28-5.

## RESIDUAL INTERNAL STRESSES DETERMINED EXPERIMENTALLY IN HOLLOW COMPOSITE LAMINATES

Horatiu Teodorescu, Sorin Vlase, Dorin Rosu and Mihai Ulea  
Transilvania University of Brasov, Romania, Department of Mechanical Engineering  
29, Eroilor Blvd., 500036-Brasov, Romania  
hteodorescu@yahoo.com, svlase@unitbv.ro, compozitebv@yahoo.com, ulea@unitbv.ro

The paper presents an experimental destructive method to determine residual internal stresses introduced in hollow polymer matrix composite structures during their manufacturing process. According to this method the shape variations of a hollow structure resulted from the destructive process will be considered as a measure of residual internal stresses. The distribution of residual internal stresses along the length of the specimens is presented.

A trustworthy and complete calculus to determine residual internal stresses introduced in hollow polymer matrix composite structures during their manufacturing process is very difficult to accomplish. The mathematical description must consider various factors of influence and material values which depend on temperature and time. Therefore, experimental methods to determine residual internal stresses are still used. These methods are divided in destructive and non-destructive ones. All destructive methods to determine residual internal stresses are based on the determination of shape changes of a composite structure, changes caused by the balance state disturbance. This balance state is disturbed since the forces flux included at the inner of the composite structure is interrupted by the destructive process. Structure's shape changes (strains) resulted from the destructive process will be interpreted as a measure of residual internal stresses. Determining the composite structure's shape changes, the values of these internal stresses can be computed. The most known destructive methods to measure residual internal stresses introduced in the manufacturing process of a composite hollow structure are presented by Elfinger *et al.* [1].

Regarding the experimental determination of residual internal stresses introduced in the manufacturing process of a composite hollow structure, a method partial similar to that described by Aleong and Munro [2] has been used. The experiments were accomplished on specimens made at COMPOZITE Ltd. Brasov. The tubes material used during tests is a compound based on glass-fabric reinforced polyester resin. The tube wall structure was manufactured very accurate in the fabric winding process. Fabric strips used in the winding process were cut in length and at 45° from the production direction. Rings have been cut from the left end, from middle and from the right end of the specimens used in tests. In principle, the method of determination residual internal stresses consists in the disturbance of rings' balance state by cutting them on the generator, on radial direction and to determine the external surface strains resulted from the cutting process, see Scharr and Funck [3]. Regarding the specimens made in the fabric winding process, the highest residual internal stresses take form on circumferential direction. The axial residual internal stresses may be neglected since they are insignificant in comparison with the circumferential ones and does not act on main stress direction.

A cutting method of the fabric strips used in the winding process is presented by Teodorescu [4]. The maximum value of the internal stresses distribution can be found in the outer surface ply of the ring, value which decreases in neutral fiber direction, Tzeng and Pipes [5]. In case of ring's radial cut, the balance state of residual internal stresses is disturbed, stresses become free and deform the ring. A ring's widening means the existence in the ring before cutting, of tensile (compression) residual internal stresses at the inner (outer) surface of the ring. A decrease of ring

diameter after the cutting process signify the initial existence of compression (tensile) residual internal stresses at the inner (outer) surface of the ring.

Because of small differences regarding the diameters ratio ( $d_o/d_i \approx 1$ ), the residual internal stresses at the inner of a hollow specimen present close values with those existent of its outer surface since a symmetric distribution of stresses occurs. A method to compute the stresses existent at the outer surface of the ring, is the string measure method, Willems [6]. According to this method, the residual internal stresses can be computed after, beforehand, the string length, formed as a result of its radial cut, has been measured.

As a result of experimental determinations of residual internal stresses introduced in specimens manufacturing process, the following conclusions can be drawn: the maximum value of residual internal stresses can be found in the outer plies of the tube specimens; the residual internal stresses decrease in neutral fiber direction; there were no differences between the residual internal stresses determined in left, middle and right rings of the specimens.

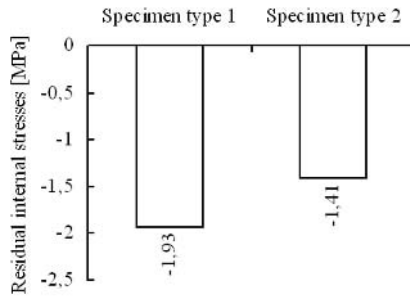


FIGURE 1. Distributions of residual internal stresses introduced in the manufacturing process of two types of tube specimens

## References

1. Elfinger, F., Peiter, A., Theiner, W., and Stücker, E., *Verfahren zur Messung von Eigenspannungen*, VDI-Bericht no. 439, 1982.
2. Aleong, C., Munro, M., *Experimental Techniques*, 55 – 58, 1991.
3. Scharr, G., Funck, R., *Messtechnische Briefe*, vol. 30, 11 – 14, 1994.
4. Teodorescu, H., *The increase of loading capability of hollow composite structures by introduction supplementary internal stresses*, PhD thesis, 2001.
5. Tzeng, J., Pipes, R., *Composites Manufacturing*, vol. 3, no. 4, 273 – 279, 1992.
6. Willems, G.: *Einfl. der Verarb. Par. auf die Baut. beim Thermopl*, IVW-Bericht 93-25, 1993.

## QUASI-STATIC COMPRESSION OF CARBON FIBRE SQUARE HONEYCOMBS

B.P. Russell, V.S. Deshpande and N.A. Fleck  
 University of Cambridge, Engineering Department  
 Trumpington Street, Cambridge CB2 1PZ, United Kingdom  
 bpr23@eng.cam.ac.uk

The superiority of metallic square honeycomb cores over competing metallic topological designs for uses as structural elements in sandwich panels has been established by research done by Cote et al. (2004) [1].

Composite square honeycomb cores have the potential to achieve much higher specific strengths than those of their metallic counterparts. Carbon fibre honeycomb cores constructed from woven fibre materials have reached peak strengths of over twice that attained by metallic cores. A route for fabricating these core structures has been developed, using a micro-milling technique.

A combined experimental, analytical and numerical modelling study was performed. The compressive response (out of plane) of the honeycombs was measured and the failure modes captured and determined. X-ray tomography has been used to capture the internal structure of the specimens, and hence the failure modes of these structures, Fig. 1. Parameters investigated are the relative density, cell aspect ratio, fibre weave orientation and the number of cells.

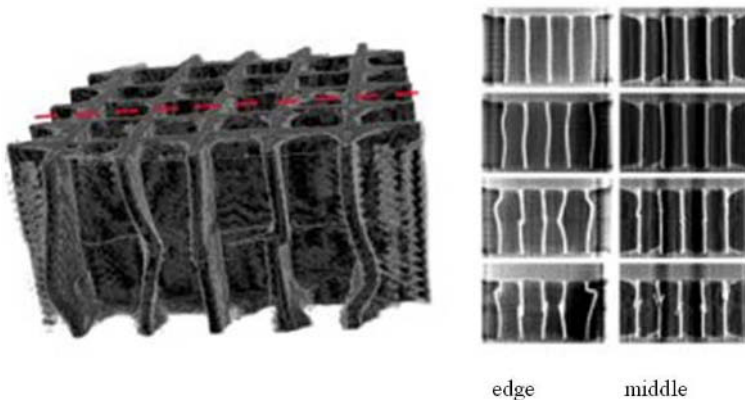


FIGURE 1. Sections taken through a carbon fibre honeycomb using x-ray tomography, showing a microbuckle running across the width of the specimen.

### References

1. Cote, F.; Deshpande, V.S.; Fleck, N.A.; Evans, A.G.; The out-of-plane compressive behavior of metallic honeycombs. *Materials Science and Engineering A*, vol. **380**, n 1-2, Aug 25, 2004, p 272-280

## NOTCH ROOT OPENING DISPLACEMENT VERSUS DAMAGE FOR PARTICULATE MMC'S

V. Kytopoulos, Ch. Riga and S.K. Kourkoulis

Department of Mechanics, National Technical University of Athens  
5, Heroes of Polytechnion Avenue, Zografou Campus, Athens, Greece  
stakkour@central.ntua.gr

The object of the study is the quantification of the Notch Root Opening Displacement (NROD) and of the extent of the damage zone developed around a pre-existing notch, in an effort to define a relationship between these two quantities that could be used as failure criterion for modern particulate metal matrix composites (MMC's). The study is carried out experimentally with the aid of a complex including a Scanning Electron Microscope (SEM) and an Electron Probe Microanalyser (X-ray EPMA) measuring system. The on-load, i.e. the 'dynamic' NROD-experiments, were possible by means of a special servo-stepping motorized tensile stage attached inside the chamber of a S4-10 Cambridge Stereoscan Electron Microscope. The in-situ SEM 'dynamic' NROD-data collections were performed by a TV-frame grabber-video processor system at a given magnification of about 133x. In this way it was possible to 'catch-up' the critical (ultimate) NROD of the notch just before the final cracking of the specimen. The direct measurements of the NRODs were carried out on the photographs taken by means of a magnifying digital-optical 'x-y'-micropositioner, leading thus to an effective working magnification of about 2400x.

The quantification of the dimensions of the damage zone was achieved by means of the X-ray electron probe microanalysis technique, a new semi-quantitative experimental approach for measuring the local damage distribution [1]. The method is based on the fact that during the inelastic scattering of the beam electrons in a solid specimen, two kinds of X-rays are generated: continuous X-rays and characteristic X-rays. Depending on the critical excitation energy, certain characteristic X-rays are generated over a substantial material volume fraction of the interaction of the electron beam with the solid. In order to predict the depth of X-ray production (penetration), the electron penetration range also called electron range, must be known. Based on experimental results concerning the X-ray production and electron range, the following mass-range equation for X-ray production has been introduced [2]:

$$\rho R_x = 0.064 \left( E_0^{1.7} - E_c^{1.7} \right) = \text{const.} \quad (1)$$

In Eq.(1) is the mass density of the solid,  $R_x$  is the measure of the depth of X-ray generation (in  $\mu\text{m}$ ),  $E_0$  is the operating voltage on the SEM (in KV) and  $E_c$  is the critical excitation energy (in KV) for a given characteristic X-ray wavelength for the element in the solid. From the above statements one can expect variations of the detected X-rays due to changes in the actual local mass density of the real solid. The electron probe of the SEM can be easily chosen so as to have optimal spatial resolution. In this manner one can detect local or very localized variations in the X-ray signal and the corresponding changes in the local mass density which are connected with changes in the micro-cracking field. For this purpose the technique of the electron probe microanalysis (EPMA) was used with the aid of a WDX-210 microspec unit, attached to the SEM [3].

In this context an operational *local damage distribution function*,  $D(x)$ , is introduced as:

$$D(x) = 1 - \frac{\tilde{I}(x)}{\tilde{I}_0} \quad (2)$$

where  $\tilde{I}(x)$  is the X-ray intensity from the damaged field and  $\tilde{I}_0$  is the X-ray intensity from the undamaged one. In the same manner, an operational total damage degree,  $\bar{D}$ , is introduced as:

$$\bar{D} = \int_0^{x_d} D(x) dx \quad (3)$$

where  $x_d$  is the corresponding process zone length.

The materials used were the BP 8090 Al-Li metal matrix composite which is reinforced with 17% per volume of fine SiC particles of dimension  $\sim 0.3 \times 10^{-6}$  m [4] and the respective alloy. The material after machining was subjected to heat treatment at 550 oC for 90 min and, then, oil quenched according to the manufacturer's instructions. The mechanical behaviour of the material in its heated form is proved to be adequately described by an equation of the form [4]:

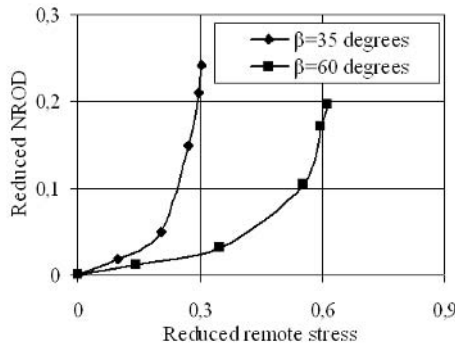


FIGURE 1: The reduced NROD versus the remotely applied reduced stress.

$$\bar{\sigma} = \begin{cases} E \bar{\varepsilon}, & \bar{\sigma} \leq \sigma_y \\ a + b \ln \varepsilon, & \bar{\sigma} \geq \sigma_y \end{cases} \quad (4)$$

In Eq.(4) and represent the stress and strain, respectively, while the overbar is used to denote the equivalent quantities according to the von Mises criterion.  $E$  denotes the elasticity modulus and  $\sigma_y$  is the yield stress. Finally  $a$ ,  $b$  are constants defined numerically from the experimental data [4].

For the needs of the study, a series of uniaxial tension tests were carried out with Single Edge Notched (SEN) specimens. In each specimen an initial notch of length  $o$  and inclination was machined using a diamond disk of thickness 300  $\mu\text{m}$ . The analysis of the results revealed an exponential increase of the NROD with increasing load as it is shown in Fig. 1. A similar behaviour is exhibited by the damage parameter as obtained by Eqs. (2,3). Thus after suitable calibration a relationship between NOD and damage is obtained yielding an easy-to-use failure criterion for the case of pre-notched MMCs.

## References

1. Kytopoulos, V.N., Papadopoulos, G.A. and Sadowski, T., *J. Mat. Sci.*, vol. **41**, 2121, 2006.
2. Rice, R.W., *J. Mat. Sci.*, vol. **19**, 895, 1984.
3. Goldstein, J. I. and Yakowits, H. (editors), *Practical Scanning Electron Microscopy-Electron Probe and Ion Microprobe Analysis*, Plenum Press, New York and London, 1976.
4. Saragas, S., Kourkoulis, S. K. and Andrianopoulos, N. P., *Int. J. Fracture*, vol. **79**, 179, 1996.



## FATIGUE PROPERTIES OF 2024-T3 ALUMINIUM SPECIMENS REINFORCED WITH COMPOSITE PATCHES

M.L. Pastor, X. Balandraud, J.L. Robert and M. Grédiac  
Laboratoire de Mécanique et Ingénieries (LaMI)  
Université Blaise Pascal  
Institut Français de Mécanique Avancée  
IUT de Montluçon, Av. A. Briand BP. 2235  
03100 Montluçon - France  
pastor@moniut.univ-bpclermont.fr

The maintenance of aeronautic components is an important issue for military aircrafts. Fatigue damage generates crack initiation and growth which reduce the aircraft lifetime. For about thirty years, composite patches have been widely used to repair aeronautic structures [1]. An alternative to repair is to reinforce components before appearance of cracks. Such composite patches are bonded around the highly loaded zones, such as fuselage skins [2]. They enable to avoid or to delay the initiation and growth of fatigue cracks by decreasing the stress levels existing in the critical parts of structural components. From the fatigue point of view, a low decrease of the stress level in the considered zone may significantly increase the residual lifetime of the structure. It is therefore necessary to characterize the beneficial effect of composite patches in terms of extension of the aluminium substrate lifetime and to test small structures reinforced by a composite patch to validate the software developed to predict structures lifetime extension. This software is based on the use of cumulative damage models and multiaxial fatigue criteria. The aim of this work is to evaluate the actual lifetime increase of some aluminium specimens reinforced by composite patch and subjected to different loadings.

The specimens are made of aluminium 2024-T3 reinforced with prepreg system 914 T300 (epoxy/carbon composite) bonded on both sides. They have been cut by water jet and then milled. In some cases, the composite patches have also been milled simultaneously with the aluminium specimen (specimen b).

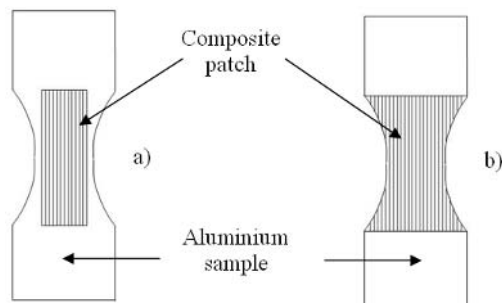


FIGURE 1. Two types of reinforced aluminium specimens

The first part of the study aims at evaluating the influence of the composite patch milling upon the lifetime results. Two types of reinforced specimens (see Figure 1) are tested with the same

maximum uniaxial tensile load (11 500N). For this load level, the observations carried out during fatigue tests and the comparison with the aluminium fatigue data indicate that fracture occurs first in the aluminium substrate. The adhesive fails straightaway afterwards under shear stress.

Table 1 sums up the experimental data. Milling the composite patches strongly affects the lifetime of the aluminium specimen. It is 40% lower than the one obtained for specimen (a) which patch is not milled. In both cases, the life extension of the specimen is important: the mean life ratio of specimens (a) and (b) are equal to 11 and 7 respectively with respect to the mean life of specimens without any patch.

TABLE 1. Lifetime results for the two kinds of reinforced specimens  
(loading ratio  $R=0$ , maximum force  $F_{\max} = 11\ 500\ \text{N}$ ).

	Mean fatigue life (cycles)	Standard deviation (cycles)
Specimen without any patch	41 000	4 400
Specimen (a)	452 700	134 700
Specimen (b)	292 100	35 700

The second part of the study investigates the behaviour of the patched specimens in case of higher load levels. As a shear stress concentration exists in the adhesive [3] and because of the ultimate shear stress of the adhesive, this latter should fail before the crack initiation within aluminium substrate. As a consequence the life extension of the specimen will depend on this phenomenon.

In the third part of the study, some fatigue tests are performed on small structures reinforced by composite patches and to verify the good agreement between the experimental lifetimes observed during the fatigue tests with the predicted lifetimes given by the fatigue assessment software developed in this study.

These three issues about the lifetime extension of the specimens and the validation of the software will be discussed in the presentation.

## References

1. Backer, A.A., *Composite Structures*, vol. 2, 153-164, 1984.
2. Mathias, J.D., Balandraud, X., Grediac, M., *Composites Part A: Applied Science and Manufacturing*, vol. 37, 177-190, 2006.
3. Mathias, J.D., Grediac, M., Balandraud, X., *International Journal of Solids and Structures (IJSS)*, In Press, Corrected Proof, Available online 28 February 2006.

## EXPERIMENTAL INVESTIGATION OF DYNAMIC DAMAGE EVOLUTION FOR PP/PA POLYMER BLENDS UNDER HIGH STRAIN RATES

Zi-Jian Sun and Li-Li Wang

Mechanics and Materials Science Research Center, Faculty of Engineering, Ningbo University  
818 Fenghua Road, Ningbo, Zhejiang, 315211, China  
sunzijian@msn.com, llwangch@nbu.edu.cn

The dynamic response of structures and materials to high strain-rate loading is of great interest in a variety of civilian and military applications. As well recognized, the main differences between the dynamic response of structures under high strain rates and the static response are attributed to two dynamic effects: the inertia effect (wave effect) and the strain rate effect. The former is studied by wave propagation in various forms, either explicitly or implicitly, and the latter has promoted the studies on all kinds of rate-dependent constitutive relations and failure criteria.

The difficulty lies in that the wave effects and the strain-rate effects are usually coupled. In fact, without knowing the dynamic constitutive relation of material the wave propagation can not be analyzed, since the constitutive relation of material is always one of governing equations of the problem. On the other hand, for studying dynamic constitutive relations and failure criteria of materials at high strain rates, the wave propagation either in testing facilities or in specimens should be taken into consideration.

Moreover, if the deformation is large enough, then a deformation process of material is usually accompanied with an evolution of internal damage, which will finally lead to dynamic failure of material. The complexity lies in that the deformation process and the damage evolution process are also coupled or interactively related. Because, on the one hand, the damage evolution is usually dependent on stress/strain; while on the other hand, the damage evolution will in turn influence the stress/strain response of material. Thus, the experimental study on the dynamic evolution of damage under impact loading, and consequently on the dynamic constitutive relation of materials taking account of the dynamic damage evolution, has become one of research frontiers in the new century.

For two kinds of polypropylene-polyamide (PP/PA) polymer blends which are compatibilized with two different compatibilizers, the dynamic evolution law of internal damage and the associated non-linear rate-dependent constitutive relation are investigated in the authors' laboratory under a wide range of strain rate from  $10^{-4} \text{ s}^{-1}$  up to  $10^3 \text{ s}^{-1}$ , by using both the INSTRON Servo-hydraulic Testing Machine and the Split Hopkinson Pressure Bar (SHPB).

Since any internal damage following a deformation process, in whatever form, is not easy to be measured directly and described quantitatively in macroscopic level particularly at high strain rates, the change of elastic modulus of the specimen experienced a certain dynamic deformation is firstly measured to approximately characterize the macro-damage  $D=1-E_D/E_0$ , where  $E_D$  is the elastic modulus of the damaged material and  $E_0$  the initial elastic modulus of the undamaged material. In practice, the final strain of each specimen is controlled respectively in the experiments under different strain rates. Considering that the accurate and reliable determination of the dynamic unloading elastic modulus of specimen during a SHPB test is still an unsolved problem, the moduli of specimens after impacted test were then statically measured. The experimental results show that for both PP/PA polymer blends the damage  $D$  begins to grow only after a threshold strain  $\varepsilon_{th}$  ( $4\% < \varepsilon_{th} < 6\%$ ) is reached, and then it increases with both stain and strain rates,  $D=D(\varepsilon, \dot{\varepsilon})$ .

The above investigation is based on the assumption that a linear elastic deformation stage exists in the initial loading process and the unloading process, such as for an elastic material or an elastic-plastic material with elastic unloading character. However, for polymers or polymer blends which are known as visco-elastic materials, strictly speaking, the elastic modulus in the sense of elasticity does not exist. So a further study on  $D=D(\varepsilon, \dot{\varepsilon})$  for visco-elastic material is required from another approach based on visco-elasticity. Thus, the damage-modified visco-elastic constitutive response at high strain rate is identified for both polymers blends mentioned respectively, by combining the SHPB technique with the BP neural network technique, without any pre-assumption of constitutive model. In practice, based on the SHPB experimental data which are used as appropriate input/output of BP neural network, both the dynamic constitutive response of undamaged material (when  $\varepsilon < \varepsilon_{th}$ ), and the dynamic constitutive response taking account of damage evolution (when  $\varepsilon > \varepsilon_{th}$ ), are determined. Then, by comparing those two sets of results, the influence of the dynamic damage evolution on the dynamic constitutive behavior for the polymer blends tested can be obtained. In other words, the dynamic rate-dependent law of damage evolution and the dynamic damage-modified constitutive relation can be finally obtained.

The results obtained for the polymer blends compatibilized with two different compatibilizers are compared, and it is found that the damage evolution in the polymer blend compatibilized with PP-g-MAH (polypropylene grafted with maleic anhydride) is quicker than the polymer blend compatibilized with TPE-g (thermoplastic elastomer grafted with maleic anhydride) in high strain rates, so the latter is recommended for using in the impact loading condition.

## References

1. Kolsky, H., *Stress Waves in Solids*, Clarendon Press, Oxford, 1953.
2. Wang Li-li, *Foundations of Stress Waves*. National Defense Industry Press, Beijing, China 2005.
3. Wang Li-li, Jiang Zhao-biao and Chen Jiang-ying, In *IUTAM Symposium on Rheology of Bodies with Defects*, edited by Ren Wang, Kluwer Academic Publishers, Dordrecht, 1999, 167-178.
4. Kolsky, H., *Proc. Phys. Soc.*, vol. **B62**, 676, 1949.
5. Kachanov, L.M., *IVZ. Akad. Nauk., U.S.S.R., Otd Tech Nauk*, vol. **8**, 26-31, 1958.
6. Xu Ming-qiao and Wang Li-li, *Mechanics of Materials*, vol. **38**, no.1-2, 68-75, 2006.
7. Lippmann, R.P., *IEEE ASSP Mag.*, 4-22, 1987.

## EVALUATION OF DAMAGE AND PLASTIC PROPERTIES BY MICROINDENTATION AND INVERSE METHOD

Bruno Guelorget<sup>a</sup>, Manuel François<sup>a</sup> and Jian Lu<sup>b</sup>

<sup>a</sup>Université de technologie de Troyes, ICD-CNRS FRE 2848, LASMIS, 12 rue Marie Curie,  
B.P. 2060, 10010 Troyes Cedex, France

<sup>b</sup>Department of Mechanical Engineering, Hong Kong Polytechnic University,  
Hung Hom Kowloon, Hong Kong  
bruno.guelorget@utt.fr, manuel.francois@utt.fr, Jian.Lu@inet.polyu.edu.hk

Local determination of Young's modulus and hardness is performed through microindentation on a longitudinal section of a semi-hard copper sheet, which was broken in a tensile machine.

(i) the shorter the distance between the measured point and the fracture, the higher the hardness;  
(ii) local variations of Young's modulus in the neighbouring of the fracture gives access to local damage variations. Using an inverse method, yield stress and strain hardening coefficient are evaluated in the localized neck.

For Lemaitre and Chaboche, damage can be evaluated through Young's modulus variations [1]. In case of damage, the measured Young's modulus  $E'$  is lower than  $E$  the nominal one:

$$E' = (1 - D) E \quad (1)$$

Indentation tests have already been used to identify damage law of a tensile test specimen [2, 3], but it was based on microhardness measurement associated with a phenomenological model assuming that, in case of no damage, microhardness is proportional to the flow stress with a shift in strain, induced by the hardness indentation.

In the present paper, damage is deduced from Young's modulus variations determined by microindentation. The specimen was cut in a 0.8 mm thick semi-hard copper sheet which was first tested by a tensile machine till fracture along direction  $x$ . The specimen was then cut and polished on the section  $((x,z)$  plane, with  $z$  normal to the sheet surface). Indents were performed with a Berkovich tip, on the  $(x,z)$  section, at different distances from the fracture. Variations of Young's modulus  $E$  and hardness  $H$  were measured versus the distance  $d$  to the fracture. Results are reported in Fig. 1, where error bars are equal to +/- one standard deviation, estimated on 4 to 6 indents (except for  $d = 20$  and  $100 \mu\text{m}$ , only 2 measures). For comparison, data obtained (5 tests average) in undamaged zone (called "E bulk" and "H bulk") are plotted in Fig. 1 at an arbitrary distance to the fracture equal to  $40\,000 \mu\text{m}$ . Damage was evaluated through Eq. 1 and can be estimated up to 60 % ( $E = 53 \text{ GPa}$  for  $d = 10 \mu\text{m}$  and  $E = 140,3 \text{ GPa}$  for  $d = 600 \mu\text{m}$ ). Due to work hardening, the shorter the distance between the measured point and the fracture, the higher the hardness [4, 5]

An inverse method [6] was applied to evaluate the yield stress  $\sigma_y$  and the strain hardening coefficient  $n$  from 820 nm deep indents performed with a spherical tip (radius =  $10 \mu\text{m}$ ). Results are plotted in Fig. 2-3. Values called "Ref." were obtained by a tensile test experiment. For the moment, the extracted values for  $\sigma_y$  and  $n$  are more to be considered as orders of magnitude than as exact values, nevertheless the tendencies are interesting. If for  $n$ , no clear tendency can be drawn (Fig. 2);  $\sigma_y$  increases when decreasing  $d$  (for  $d$  between  $30 \mu\text{m}$  and  $2 \text{ mm}$ ), probably due to the strain hardening (Fig. 3). But for  $d = 10 \mu\text{m}$ , the extracted  $\sigma_y$  value begins to go down. This can be attributed to the effect of the strong damage.

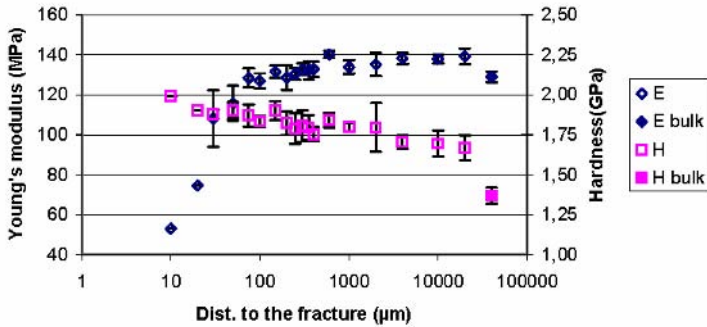


FIGURE 1. Young's modulus and hardness versus distance to the fracture.

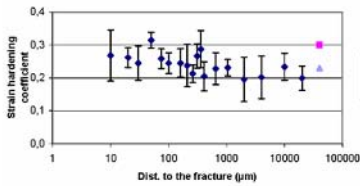


FIGURE 2. Strain hardening coefficient versus distance to the fracture.

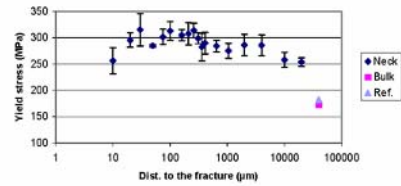


FIGURE 3. Yield stress versus distance to the fracture.

## References

1. Lemaitre, J. and Chaboche, J.-L., *Mechanics of Solid Materials*, 3<sup>rd</sup> ed., Cambridge University Press, Cambridge, UK, 2000.
2. Arnold, G., Hubert, O., Dutko, M. and Billardon, R., *Int. J. Forming Process.*, vol. **5**, 163-173, 2002.
3. Mkaddem, A., Gassara, F. and Hambli, R., *J. Mater. Process. Technol.*, vol. **178**, 111-118, 2006.
4. Cotterell, M., Schambergerova, J., Zielgelheim, J. and Janovec, J., *J. Mater. Process. Technol.*, vol. **124**, 293-296, 2002.
5. Guelorget, B., François, M. and Lu, J., *Mater. Lett.*, in press.
6. Cao, Y.P. and Lu, J., *Acta Mater.*, vol. **52**, 4023-4032, 2004.

## ACOUSTIC EMISSION IN ADHESIVELY BONDED JOINTS COMPOSED OF PULTRUDED ADHERENDS

Till Vallée<sup>1</sup>, Andreas J. Brunner<sup>2</sup> and Thomas Keller<sup>1</sup>

<sup>1</sup> Composite Construction Laboratory (CCLab), and <sup>2</sup> Swiss Federal Laboratories for Materials Testing and Research (EMPA)

<sup>1</sup> EPFL, BP2225, Station 16, CH-1015 Lausanne, Switzerland, and

<sup>2</sup> Überlandstrasse 129, CH-8600 Dübendorf, Switzerland

till.vallee@epfl.ch, andreas.brunner@empa.ch, thomas.keller@epfl.ch

Previous experiments related to the strength of adhesively bonded joints composed of glass fiber reinforced polymer (GFRP) pultruded adherends (Vallée et al. [1-3]) indicated that, even using enhanced mathematical methods on the basis of a fully linear mechanical model, a gap of around 10% between predicted and experimentally gathered joint strengths remain.

One reason invoked in [3] were i) possible damages occurring by microscopic defect accumulation (micro-cracks or cavitation) and/or ii) a possible non-linear behaviour of the GFRP material at higher stresses, beyond those that could be reached by testing samples of a size of 40mmx40mm.

Regarding assumption i), even though the authors did not notice any visible cracking up to failure when inspecting the lateral faces of the bonded splice, which certainly does not exclude microscopic damages to have occurred before failure. Such small damages, which are almost impossible to detect, especially considering that the explosive failure of the bonded joint does not allow any post-failure inspection, lead to a localized softening of the composite material.

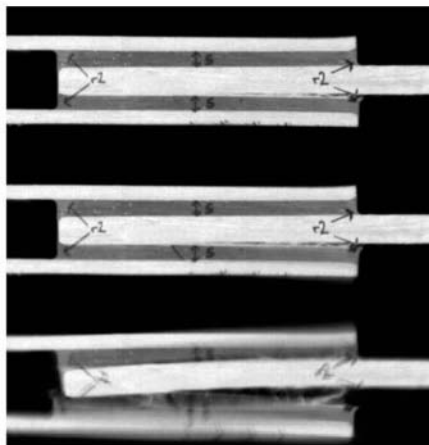


FIGURE 1. *Typical brittle and explosive failure of a bonded joints composed of pultruded adherends (filmed at 2000 fps)*

Acoustic Emission (AE) is a non-destructive test method capable of detecting microscopic damage types in composites (see, e.g., Bohse [4]). In the frame of the investigation presented here, this technique was used to record AE signals during tensile loading up to failure, in a series of nine adhesively bonded double-lap joints composed of pultruded adherends. The AE behaviour was analysed with respect to the load levels and the relation between AE signals and type of damage mechanisms investigated.

In the present investigation, acoustic sensors have been fixed on the adhesively bonded joints, close to the location of failure, to monitor the acoustic emissions over the whole loading process, up to failure. This data has then been analyzed in relation with the load-displacement data to identify micro-damages. These observations have then been refined by looking at the time-frequency spectra to identify typical damage mechanisms leading to the failure of the joint.

Based on the results obtained by AE, a refined Finite Elements Analysis was performed which included the stress redistribution due to micromechanical damage that improved the quality of the joint strength predictions.

## References

1. Vallée, T., Correia, J.R. and Keller, T., *Composites Science and Technology*, vol. **66**, no. 13, 1903-1914, 2006
2. Vallée, T., Correia, J.R. and Keller, T., *Composites Science and Technology*, vol. **66**, no. 13, 1915-1930, 2006
3. Vallée, T., Keller, T., Fourestey, G., Fournier, B. and Correia, J.R., *Composites Science and Technology*, submitted for publication
4. Bohse, J., *Composites Science and Technology*, vol. **60**, no. 8, 1213-1226, 2000



## IMPEDANCE-BASED TECHNIQUE AND GUIDED WAVE METHOD FOR DAMAGE ASSESSMENT WITH USING SMART MATERIALS

Yong Hong<sup>1,a</sup>, Gao-Ping Wang<sup>1,b</sup>, Dong-Pyo Hong<sup>2,c</sup> and Young-Moon Kim<sup>3,d</sup>

<sup>1</sup> Department of Precision Mechanical Engineering, Chonbuk National University Jeonju  
Jeonbuk 561-756 South Korea

<sup>2</sup> Department of Precision Mechanical Engineering, The Research Center of Industrial  
Technology, Chonbuk National University Jeonju Jeonbuk 561-756 South Korea.

<sup>3</sup> Department of Arcitectural Engineering, Chonbuk National University Jeonju Jeonbuk 561-756  
South Korea.

ahongyong@chonbuk.ac.kr, bgpwang@chonbuk.ac.kr, chongdp@chonbuk.ac.kr,  
dkym@chonbuk.ac.kr

The paper mainly presents an impedance-based technique and also a guided wave method to detect and localize the same incipient damages in structures, respectively. The impedance-based technique utilizes the direct and converse electro-mechanical impedance properties of bonded piezoceramic (PZT) patches which serve as actuator-sensors. The interaction between a PZT and its host structure can be described by using a simple 1-D vibration model. A longitudinal wave is applied to the structure by the special arrangement of the PZT pairs, Park *et al.* [1]. The guided wave method needs high-frequency wave propagation for achieving the necessary time and space resolution to detect and localize the incipient damages instead of the electro-impedance obtained by the efficient impedance analyzer. To check the time-of-flight of the wave the damage is localized. Results of several experiments presented show high sensitivity and reliability of the guided wave method, Giurgiutiu *et al.* [2]. Based on the electro-impedance based technique and the guided wave method, a large number of experiments are conducted. Additionally, the applications of the wavelet transform to detect incipient damages are also presented by means of several simulated examples. The numerical method requires only the response of the damaged structure. When the suitable wavelet is selected, the ability of wavelet to detect and localize the damages is verified.

In the high frequency range, the electro-impedance-based technique with PZT is very sensitive for evaluation of the incipient and small damage, such as the bolt loosening, small cracks and holes. Fig. 1 shows that specimen 1 is the aluminum plate of 1000mm length, 25mm width and 2mm thickness with twenty-five 4mm diameter holes. The holes are fastened with using twenty-five 4mm diameter bolts and nuts with gaskets. Two pairs of PZT1, 1" and PZT2, 2" are bonded to the two ends of the plate, as shown in Fig. 1. To simulate the damage, one bolt is loosened from 3 N.m to 1 N.m and then 0 N.m at a randomly desired location while all the rest are maintained in a tightly screwed position by 3 N.m torques. Simultaneously, the bolt is loosened from 3 N.m to 1 N.m and 0 N.m separately to simulate the extent of bolt loosening at the specific location. Fig. 2 shows that the specimen 2 is the aluminum plate of 490mm length, 25mm width and 2mm thickness with a hole. The pair of PZT 3, 3" is located at the right end of the plate. To simulate the damage, the diameter of the hole varies from 3mm, to 6mm and then 9mm, respectively. Fig. 3 shows the specimen 3 that has the same specification as specimen 2. However, the damage is simulated as a crack with different length, i. e. 3, 6, 9, 12, 15, 21, 22mm, respectively. For each step, with respect to the specimens 1, 2 and 3, the admittance of the healthy and damaged conditions are measured by using the impedance analyzer HP4192A, respectively. Therefore several indices are presented to assess the different simulated damages, such as RMSD (Root Mean Square Deviation), Cov (Covariance), and CC (Correlation Coefficient), etc.

For the specimens 2 and 3, the guided wave method is also presented by using the HP Oscilloscope and the HP Function Generator. The guided wave method needs high-frequency wave propagation for achieving the necessary time and space resolution to detect and localize the incipient damages. To check the time-of-flight of the wave, the damage is localized. The results of the guided wave method with respect to the specimens 2 and 3 are compared with those obtained by the electro-impedance based technique. Additionally, the applications of numerical simulation of the wavelet transform to detect the hole and crack in the specimens 2 and 3 are discussed. The simulation results show strongly the consistency of the localization of the damage.

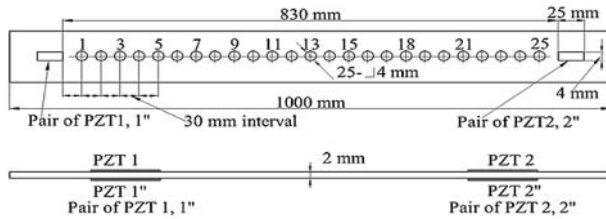


FIGURE 1. Specimen 1 with a simulated damage of the bolt loosening

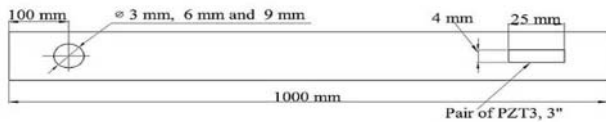


FIGURE 2. Specimen 2 with a simulated damage of a hole

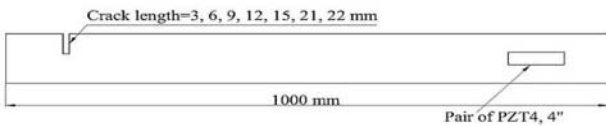


FIGURE 3. Specimen 3 with a simulated damage of a crack.

## References

1. Park, G., Sohn, H., Farrar, R., Inman, D. J., *Overview of piezoelectric impedance-based health monitoring and path forward*, The Shock and Vibration Digest, vol. **35**, 451-463, 2003.
2. Tseng, K. K-H, Naidu, AS.K., *Non-parametric Damage Detection and Characterization Using Smart Piezoceramic Material*, Smart Materials and Structures, vol. **11**, 317-329, 2002.

## STRAIN EVALUATION IN THE NECK OF A TENSILE TEST SPECIMEN BY ESPI STRAIN RATE MEASUREMENT

Bruno Guelorget, Manuel Francois and Guillaume Montay  
 Universite de technologie de Troyes, ICD-CNRS FRE 2848, LASMIS, 12 rue Marie Curie,  
 B.P. 2060, 10010 Troyes Cedex, France  
 bruno.guelorget@utt.fr, manuel.francois@utt.fr, guillaume.montay@utt.fr

In-plane ESPI strain rate measurement during a tensile test is used to determine plastic strain in a semi-hard copper sheet specimen during the localization process in the neck. The width of the localization zone is deduced at several steps of the experiment.

An in-plane ESPI set-up [1] was used to measure strain rate on a 0.8 mm thick semi-hard copper sheet specimen during a tensile test [2, 3]. The strain rate between two points  $A$  and  $B$  is [3]:

$$\dot{\varepsilon}_{AB} = \frac{\varepsilon_{AB}}{\Delta t} = \frac{1}{\Delta t} \frac{u_{AB}}{l_{AB}} = \frac{1}{\Delta t} \frac{N_{AB} \cdot s}{k(x_B - x_A)}, \quad (1)$$

where  $\varepsilon_{AB}$  is the average strain,  $\Delta t$  is the time elapsed between the two pictures,  $u_{AB}$  is the relative displacement,  $l_{AB}$  is the distance,  $N_{AB}$  is the number of interfringes,  $s$  is the sensitivity,  $k$  is the scaling factor,  $x_A$  and  $x_B$  the coordinates of the fringes. Strain rates were measured in three different zones (Fig. 1) during the test, results are plotted on Fig. 2. Applying Eq. 1, strain rate can be extracted along line 314 (Fig. 1), results are gathered on Fig. 3.

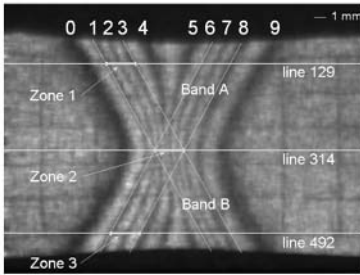


FIGURE 1. Fringe pattern just before fracture.

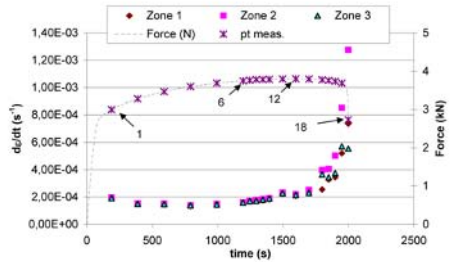


FIGURE 2. Strain rates and tensile force versus time.

In order to be able to determine accurately the width of the strain rate peaks of Fig. 3, the curves were fitted with Lorentz functions (Fig. 4), which can be written:

$$f(x) = A \left/ \left( 1 + \frac{(x - x_0)^2}{B^2} \right) \right., \quad (2)$$

where  $A$  is the maximum of  $f$  and  $B$  the peak width. In the case of Fig. 4, the integral width is equal to 4 mm, that is 5 times larger than the sheet thickness (0.8 mm) and from 3 to 5 times larger

than the shear band. Consequently, the zone where strains are localizing is much larger than the shear band, even if it is decreasing during the experiment.

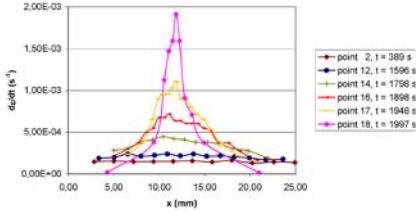


FIGURE 3. Time evolution of the strain rate along line 314.

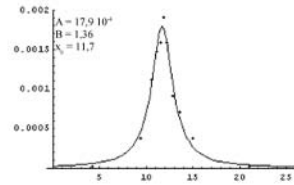


FIGURE 4. Fitting by a Lorentz function of one peak of Fig. 3.

Moreover, an evaluation of the total strain can be deduced by integrating the strain rate curve of Fig. 2. Values are plotted on Fig. 5 and compared with those found with a classic white light grid method. The advantage of the integration method is its capability to determine the strain when the grid's method cannot any more.

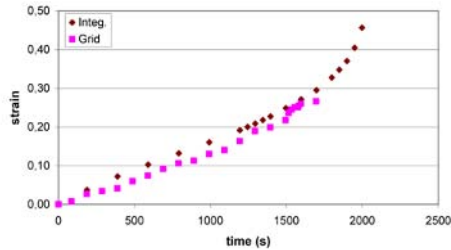


FIGURE 5. Comparison of strains determined by grid or integration method.

## References

1. Jones, R. and Wykes C., Holographic and Speckle Interferometry, 2nd ed., Cambridge University Press, Cambridge, UK, 1989.
2. Toyooka, S. and Gong, X.L, Jap. J. Appl. Phys., vol. **34**, L1666-L1668.
3. Guelorget, B., Francois, M., Vial-Edwards, C., Montay, G., Daniel, L. and Lu, J., Mater. Sci. Eng. A, vol. **415**, 234-241, 2006.

## EVALUATION OF HARDENING OF PLASTICALLY DEFORMED STEELS

P. Yasniy<sup>1</sup>, V. Hlado<sup>2</sup>, P. Maruschak<sup>3</sup> and D. Baran<sup>4</sup>

<sup>1</sup>-Professor, Head of Department of Material Sciences, <sup>2,3</sup>- Senior Researchers,

<sup>4</sup>-Junior research assistant

<sup>1,2,3,4</sup>- Ternopil Ivan Pul'uj State Technical University, Ruska 56 str., Ternopil, Ukraine

<sup>2</sup>-Labmat@tu.edu.te.ua

The aim of this paper is to study the effect of the tensile plastic deformation on the microstructure parameters of the 15Kh13MF and 25Kh1M1F steels, and to establish the relationship between the material hardness, microhardness and the dislocation density and plastic strain. The above steels are used for manufacturing bimetallic rolls of billet continuous casting machines [1].

Specimens (5×6×30 mm) were cut out from a bimetallic roll band along the axial direction and subjected to uniaxial tension loading at a temperature of +600<sup>0</sup> corresponding to the temperature of the roll surface at the area of contact with the slab billet. Tests were performed on a servo-hydraulic machine of the type STM-100 equipped with an IBM computer.

After fracture of specimens, the hardness and microhardness were measured, and the microstructure was studied depending on the specimen necking  $\tilde{\psi}$ . The hardness was measured on a Super Rockwell hardness meter at an indentation load of 150 N. The microhardness was measured on a PTM-3-type device at an indentation load of 0.1 N. The specimen microstructure was studied on a transmission electron microscope TEM-125K using the thin-foil method. Objects for the microstructure study were cut out from the necks of the failed specimens. The dislocation density was measured within the low-angle boundaries and subboundaries from the analysis results for the azimuthal disorientation of the microdiffraction pattern reflections [2]. For each of the points, 25-30 measurements of the hardness and microhardness were made.

Steel 15Kh13MF belongs to steels of the ferrite-martensite class. The microstructure of steel 15Kh13MF is a lath dislocation martensite which contains a high percentage of ferrite, massive inclusions, carbide precipitates and dispersed precipitations. A high crack growth resistance of steel 15Kh13MF is caused by the presence of dislocation boundaries of the lath martensite, a considerable dislocation density in laths, the pinning of dislocations due to the atoms of alloyed elements and dispersed precipitations, the locking of dislocation migration by inclusions.

Steel 25Kh1M1F belongs to steels of the pearlitic class. Electron-microscopic studies revealed the presence of the structurally free ferrite, pearlitic colonies that are located in different parts of ferritic and pearlitic grains. Cementite plates in pearlite have various shapes and dimensions. By evaluating the dispersion of cementite plates, the structure can be classified as a sorbite.

Electron-microscopic studies of the specimens of steel 15Kh13MF after tensile deformation revealed the changes in the morphology of the dislocation structure, in particular, both the fragmentation of laths of the martensite and the out-of-parallelism of dislocation subboundaries increases and the distance between them decreases. It was also revealed the increase in the angle of disorientation between the structure subboundaries and laths of the dislocation martensite as compared to the initial state of the material. At high plastic strains, the formation of microcracks and pores that are primarily nucleated near the "massive" inclusions was observed. A great number of reflections and their blur on microdiffraction patterns of microcrack regions are indicative of the decrease in the distance between the low-angle boundaries and a continuous disorientation.

The study of the microstructure of steel 25Kh1M1F after tensile deformation revealed the formation of a great number of separate dislocations in the ferrite, decrease of the distance between the subboundaries of the ferrite structure, the formation of a cellular dislocation structure, whereas at high plastic strains, the formation of a fragmented structure was revealed. In pearlite areas of this steel, the break-down of the cementite plates into separate fragments was observed.

The quantitative analysis of the dislocation density shows that with increasing actual necking of the specimens of steels 15Kh13MF and 25Kh1M1F the dislocation density within the low-angle boundaries increases according to linear relationships. The dislocation density in steel 15Kh13MF increases more intensely, which is due to a high energy intensity of the deformation caused by distinctions in the transformations of dislocation substructures.

The linear dependences of variation in the hardness and microhardness on the actual necking of the specimens of steels 15Kh13MF and 25Kh1M1F were obtained. The hardness and microhardness of the above steels increase with increasing plastic strain. In this case, steel 15Kh13MF is hardened more intensely, which is caused by more intense increase in the dislocation density in this steel. The increase of the microhardness due to strain hardening can be explained mainly by two reasons: the formation of the intragranular substructure that fulfils the role of additional barriers and the increase in the disorientation of the boundaries of the structure components existing in the initial state of the material [3].

Based on the obtained experimental data, the correlation relationship was established between the dislocation density within the low-angle boundaries and the hardness and microhardness of the 15Kh13MF and 25Kh1M1F steels plastically deformed in tension.

## References

1. Adamov I.V. and Khyt'ko. Durability of rolls with two-layer cast sleeves in slab CCM. *Metallugicheskaya i gornorudnaya promyshlennost*, vol. 3, 31-33 (2001).
2. Novikov I.I. Defects in the Crystalline Structure of Metals, *Metallurgiya*, Moscow, 232 p. (1983).
3. Koneva N.A. and Kozlov E.V. Physical nature of the stage character of plastic deformation. *Izv.VUZov. Fizika*, vol. 2, 89-108 (1990).

## EXPERIMENTAL CHARACTERIZATION OF DUCTILE DAMAGE USING NANOINDENTATION

C.C. Tasan<sup>1,2</sup>, J.M.P. Hoefnagels<sup>2</sup>, R.H.J. Peerlings<sup>2</sup> and M.G.D. Geers<sup>2</sup>

<sup>1</sup>The Netherlands Institute for Metals Research (NIMR),  
PO Box 5008, 2600GA, Delft, The Netherlands

<sup>2</sup>Eindhoven University of Technology, Department of Mechanical Engineering,  
PO Box 513, 5600MB, Eindhoven, The Netherlands  
c.tasan@tue.nl

In most types of sheet metal forming processes, such as drawing, stretching and bending operations, necking is the primary limiting factor in defining safe forming regions. However, it is also observed that, material failure can occur without any significant neck formation especially for non-traditional materials with relatively low formability, such as some aluminum alloys and high strength steels, [1]. The mechanisms of such failures are not very clearly identified but it is believed that internal damage is an important parameter in these occurrences (Fig. 1).

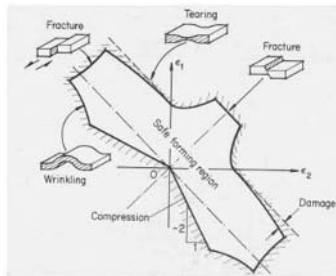


FIGURE 1. Safe forming regions as defined by Marciniak [2]

The micromechanisms that are responsible for damage formation and evolution are relatively well understood. Based on this understanding and on phenomenologies, continuum damage models have been proposed in the literature and implemented forming simulations. [3] However, these models require damage growth relations and parameters for which experimental identification is required.

Several methods have been examined during the past decades for this purpose; both direct measurement of the crack area and also indirect measurement through other material properties such as variation of density, propagation of ultrasonic waves, change in electrical resistance, stiffness, hardness, acoustic emission etc. [4]

Among these methods, microindentation analysis appears to be the most promising [5]. It has been established experimentally and theoretically that hardness is related linearly to yield stress. So following Lemaitre's [3] approach one can quantify damage comparing the microhardness of the damaged material,  $H$ , with the microhardness of the undamaged material,  $H'$ , by using the following formula:

$$D = 1 - \frac{H}{H'} \quad (1)$$

The main objective of this work is to assess the potential and limitations of this method use this method to characterize different alloys.

For this purpose, tensile tests were conducted with interstitial free and dual phase steel specimens. The local strains at the surface were measured using an image correlation software (Figure 2) and nanoindentation tests were carried out along the specimen surface. Specimen surface preparation prior to the nanoindentation experiments was done with great care: surface roughness was measured with confocal microscopy, the amount of material removal was monitored via SEM analysis and the amount of hardening due to specimen preparation itself has also been taken into account. Nanoindentation experiments were carried out also in the Continuous Stiffness Measurement (CSM) mode, therefore the variation of hardness with the depth of indentation is also measured.

Obtained quantitative results are compared with the results obtained in SEM analysis of the same specimens. It is seen that the nanoindentation method is an effective method in quantitative ductile damage measurement.

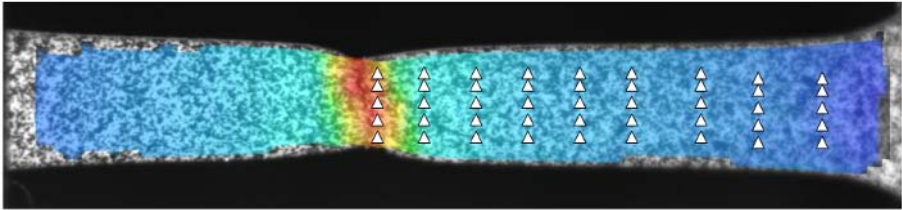


FIGURE 2. Mises strain measurement of a tensile test specimen with image correlation. Indent locations are also shown on the specimen

## References

1. Hooputra, H., Gese, H., Dell, H., Werner, H., *Int. Jour. of Crash*, vol. **9**, p.449-463, 2004
2. Marciniak, Z., *The mechanics of Sheet Metal Forming*, Arnold, London, 1992
3. Mediavilla, J., Peerlings, R.H.J and Geers, M.G.D, *Engng. Fracture Mech.*, vol. **73** (7), 895 – 916, 2006
4. Lemaitre, J., *A Course on Damage Mechanics*, Springer-Verlag, Berlin, 1996
5. Mkaddem, A., Gassaea F., Hambli, R., *Journal of Materials Processing Technology*, vol. **178**, 111-118, 2006



## MECHANISMS OF PLASTICITY AND FRACTURE IN CRYSTALS, POLYMERS UNDER LOW/SHOCK-WAVE STRESSES

Valery P. Kisel  
 Institute of Solid State Physics,  
 142432 Chernogolovka, Moscow district, Russian Federation  
 kisel@issp.ac.ru

The effect of applied compressive/extension stresses,  $s$  ( $s = 0.6S$  to  $95S$ , where  $S$  is the resolved shear stress) and stress rates ( $10$  to  $10^6$  MPa/sec) on dislocation dynamics was investigated in pure NaCl and InSb single crystals in the temperature range  $T = 4 \cdot 10^{-3}$  to  $0.945 T_{\text{melt}}$ ,  $T_{\text{melt}}$  is the melting point. The general damping character of dislocation unpinning, motion and multiplication (work hardening of crystals, WH) under creep and interrupted loadings manifests in the ultimate mean path lengths of individual dislocations (UMPID). Having covered a certain UMPID determined by crystal prehistory and test parameters, the dislocations exposed to successive exhausting multiplication and then fracture thus forming point defects, slip lines, slip bands, subgrains, grain boundaries, nano- and microcracks, macrocracks in series in all the materials [1-2].

The first important finding of this work is the fact that the dependences of the UMPID versus creep, impulse, impact and shock wave stresses, temperature and impurity concentration are topologically similar to the conventional macroscopic strain-stress WH curves for the same crystals and test parameters. As for microscopic stresses for dislocation motion and multiplication the concentration dependences of flow stresses under fixed strains or fracture stresses at low and ultra-low temperatures and strain rates [2-4] are similar to the same dependences of impact/shock wave stresses and stress rates at normal and elevated temperatures [4-6]. The climb, dislocation cross-slip and athermal bowing mechanisms are confirmed by the same so-called "memory effect" at low (Figs 23-24 in [7]) and ultra-high ( $s \sim 48S$ , [8]) stresses and stress rates, because dislocation dipoles-debris are left in the wake of expanded dislocation loops along the whole deformation WH curve. This means that the same micromechanisms govern the dislocations and macroscopic flow up to the flow stresses in nanostructured (NSC) and fractured crystals.

The second important finding is that the micro-/macro-WH varies nonmonotonously to crystal softening according to the pulse length of the unloading (restore) time, and these V-formed dependences are the same for micro-/macroscopic flow up to the extremely high values in NSC crystals [9] and fractured oriented polymers [10]. The last fact and the similarity of the other features of deformation and fracture of crystals and polymers at various length scales corroborate the universality of the mechanisms of plastic flow and fracture in crystals and polymers due to the same elemental slips. The third finding of this work is the same quasi-linear correlation between the starting stresses for dislocation motion,  $S_{st}$ , multiplication,  $S_m$ , and for the initiation of micro-,  $S_f$ , and macrofracture,  $SF$ , in NaCl and KCl-KBr single crystals (this work), polycrystal-line ice, metal alloys and YBCO ceramics (literature data). It is worth stressing that in the low range of stresses (low WH, pure crystals or high temperatures) the crystals fractured in so-called "ductile" mode irrespective of test conditions where dislocations demonstrated noticeable cross-slip, wavy glide, while at higher WH stresses dislocation slip lines were straightened, cross-slips were frequent and small, and their fracture mode was only 'brittle'. These findings clearly evidence for the key role of dislocation double cross-slip, climb and retardation thus forming various dislocation structures during deformation modes. When the deformation modes had been exhausted the beginning of fracture modes (the nano-/microcrack initiation, their spreading and coagulation into macrocracks) followed. This means that the atomic-size cracks are the cores of dislo-

cations, and they stop and unite one after another into nanosize cracks with the help of their close spacing and cross-slip events at higher WH stages of plastic flow. In all tests new flaws originated at much higher stresses from the parent cracks that had initiated earlier, as well as the new-formed flaws at new sites due to the stopped plastic zones around the tips of previous flaws or new sources of dislocation multiplication (due to concentrated local stresses) in the crystal bulk

The proposed chain of events clearly demonstrates that the mechanisms of plasticity and fracture have the same origin as a sequential chain of the WH deformation modes in crystals, the very beginning of which is demonstrated in the work [1]. It is the above scaling of the parameters of deformation stresses and fracture just with the dislocation multiplication one that points to the crucial role of dislocation double cross-slip and climb mechanisms in all these processes irrespective of other experimental conditions. Moreover, it is clear that the scaling of microfracture and macrofracture stresses with each other and with the flow stresses strictly confirms the crucial and inevitably key role of precursor and intermittent plasticity in nucleation, multiplication and coagulation of initial atomic-size cracks into nano-cracks and so on. It is the applied stress and stress rate that synchronize the successively lengthening of dislocation paths, slip lines and bands, cell walls and bands, etc., thus promoting the initiation and sequential spreading of the waves of plastic modes under various kinds of deformation [1]. The increase of the deformation stress and stress rate raises the production of point defects and their clusters due to cross-slip-jog dragging, reduces the dislocation spacing in deformation structures, activates the numerous new sources of dislocation nucleation and multiplication. The above chain of events initiates closer lay-out of cracks and nano-/micro-macrocleavage transitions between them, thus forming the special structures of fracture surfaces (the spacing, sizes, and the form of microcracks coagulated into the larger rupture structures, microcleavage steps, dimples and microvoids on fracture surfaces) up to the sample explosion with the dust fragments at very high stress rates and stresses. The practical art of cleavage for various crystals clearly proves that it is the parameters of dislocation cross-slip in precursor plasticity favors fracture propagation and damage. It is well known that the crystals which are extremely hardened with high impurity content, irradiation dose, very low temperature of cleavage are cleaved much easier than the very plastic (soft) ones. Second, fast cleavage macrocracks are usually produced with extremely sharp chisel and with very rapid and strong blow struck on the chisel (with high stress rate and stress) which has to be along the cleavage planes. Only in these cases the preceding deformation is extremely hardened and localized, the dislocation bands are straight, dense and very narrow (the lowest cross-slip heights and feebly marked climb of dislocations - the so-called 'brittle' fracture mode). But in the case of the soft crystals or very slow, weak and non-crystallographic attacks with blunt chisel at the struck surface these opposite actions lead to much larger areas of crystal deformation zones with all the signs of the crystal softening near the contact points. Here the dislocations are prompt to higher rare cross-slips which make the dislocation slip bands to be wide and diffuse. So, these heavily deformed places have a high density of diffuse microcracks and micropores, which color dense 'milk' due to their intensive day-light scattering. The spacing of these cracks/pores is so large that they rarely unite into macrocracks with rare dislocation cross-slips and hardly form the fracture surfaces. All the above statements are valid for the polymers and all other types of matter [2].

## References

1. V.P. Kisel. *Physica Status Solidi (a)*, 1995, vol. **149**, No 1, pp 61-68.
2. V.P. Kisel. In: "Mechanisms and mechanics of damage and failure" (ECF-11), Eds. J.Petit et al., EMAS, Warley, UK, 1996, vol.1, pp.145-150. Abstracts of the V Int. Conf. on the Fundamentals of Fracture (ICCF-V), Aug.18-21,1997, NIST, Gaithersburg, Maryland, USA, pp 28-29.
3. N.S. Kissel and V.P. Kisel, *Mater.Sci. Engn.A*, 2001, vol. **309-310**, pp 97-101.
4. A.K. Mukherjee, W.G. Fergusson, et al. *J. Appl. Phys.*, 1966, vol. **37**, No 10, pp 3707-3713.
5. V.P. Kisel. *J. Phys. (Paris)*, 1985, vol. **46**, Suppl. No 12, pp C10-(529-532).
6. S.V. Razorenov, G.I. Kanel' et al. *Fiz. Metal. Metallovedenie*, 2003, vol. **95**, No 1, pp 91-96
7. J.J. Gilman, W.G. Johnson. *Solid State Physics*, 1962, vol. **13**, pp 147-222.
8. E.V. Darinskaja, A.A. Urusovskaja, et al., *Fiz. tverd. Tela*, 1982, vol. **24**, No 3, pp 940-941
9. R.Z. Valiev, I.V. Aleksandrov, *Doklady Acad. Nauk*, 2001, vol. **380**, No 1, pp 34-37.
10. V.R. Regel, F.I. Slutsker, E.T. Tomashevskii. *Kineticheskaja priroda prochnosti tverdykh tel*, Moscow, Nauka, 1974, 560 pp (in Russian).

## FAILURE SURFACES IN DUCTILE NON LINEAR ELASTIC MATERIALS

N.P. Andrianopoulos, V.M. Manolopoulos and V.C. Boulougouris  
 Department of Mechanics, Faculty of Applied Sciences  
 National Technical University of Athens, GR-157 73, Greece  
 nandrian@central.ntua.gr

It is interesting to note that the oldest failure criterion, that is the Coulomb one, covers from a physical point of view all possible specific criteria in the realm of Continuum Mechanics. This conclusion is based on the generality of its description (*proper combination of shear and normal stresses*) and on the fact that it reflects both discrete and geometrically permissible modes of failure activated during loading, i.e. slip caused by shear and cleavage caused by normal stresses. Consequently, the pressure dependence of failure surfaces, emerging from the as above '*proper combination*', is inherent property of materials. It is clearly true in case of the so called Coulomb or Prager materials but there is no qualitative argument to exclude any type of them, e.g. ductile materials.

In the present study the failure behaviour of brittle non linear elastic isotropic materials is presented in a way imitating Coulomb's approach, by means of the T-criterion of failure [1]. In this criterion, stresses are replaced by the respective elastic strain energy densities, being independent from post-yield strains. So, elastic strain energy densities, distortional  $T_D$  for slip and dilatational  $T_V$  for cleavage failure, are introduced. Apparently, both quantities act independently from each other, but an inherent 'communication' is established between them as far as the development of total strains controls their elastic parts through constitutive equations of the type:

$$K_s = K_s(I_1, J_2'), \quad G_s = G_s(I_1, J_2') \quad (1)$$

Thus, by incorporating the general form of constitutive equations for non linear elastic, isotropic materials, it is concluded that failure surfaces are unique (loading path independent) when the secant shear modulus,  $G_s$ , depends only on the second deviatoric strain invariant,  $J_2'$ , and the secant bulk modulus  $K_s$ , of the material depends only on the first strain,  $I_1$ , invariant, respectively, i.e. when distortion does not depend on dilatational strain energy density and dilatation does not depend on distortional strain energy density. In this case and according to the present approach, non linear elastic behaviour of materials leads to pressure dependent failure surfaces only by the mere assumption that failure occurs when either the distortional or dilatational strain energy densities take a critical value. This conclusion fits well with the observation that materials exposing pressure dependent failure behaviour, such as soils, rocks, concrete etc. present a high order elastic non linear behaviour.

The study is based on the principle of conservation of the total strain energy density  $T$  or, equivalently, on the path-independence of this quantity. In other words, it is asked for a vector field  $T [T_V(I_1, J_2'), T_D(I_1, J_2')]$  to satisfy the condition:

$$\oint_{\gamma} T_V dI_1 + T_D dJ_2' = T [I_1 K_s(I_1, J_2'), 2G_s(I_1, J_2')] = 0, \quad \gamma = \gamma(I_1, J_2'), \quad (2)$$

along a path  $\gamma$ .

In the general case, when  $G_s$ , and  $K_s$ , depend on both  $J_2'$  and  $I_1$ , failure surfaces are not unique. Various non linear elastic constitutive equations, especially those of higher order, result to a great variety of failure surfaces, through the simple mechanism described by the T-criterion, a finding

which may be of technological interest (Fig. 1). This may lead to improved strength of materials through the selection of a proper sequence of loading/stretching paths. Here, the study is focused in the behaviour of ductile materials and experimental evidence indicates promising agreement with the theoretical predictions.

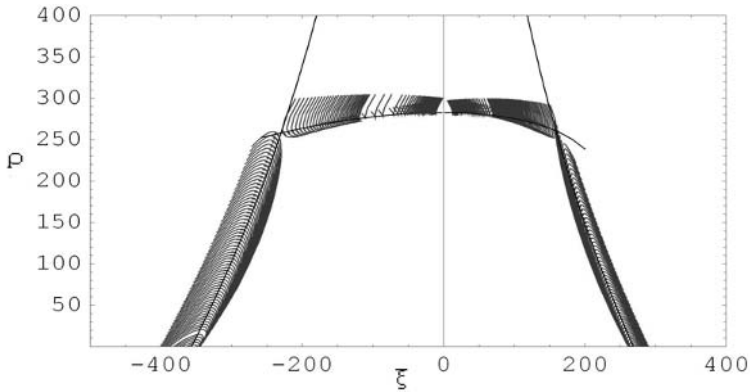


FIGURE 1. Dependence of failure surfaces on loading/stretching paths. Continuous lines correspond to ‘basic’ failure, obtained with straight loading paths. Small lines in both sides of the basic failure lines are obtained with kinked loading paths. Haig – Westergaard coordinates system ( $\xi$ ,  $\rho$ ) is used.

## References

1. I. N. P. Andrianopoulos, Metalforming Limit Diagrams According to the T-criterion, *J. Mat. Proc. Technology*, vol. **39**, 213-226, 1993

## COMPARISON OF VIBRATION RESPONSE SPECTRUM WITH LINEAR AND REVERSE-MISO FREQUENCY RESPONSE FUNCTIONS FOR NON-LINEAR CUSHIONING SYSTEMS

Michael A. Sek, Anthony Parker and Vincent Rouillard  
Victoria University, Melbourne, Australia

PO Box 14428 MCMC, Melbourne 8001, Australia

michael.sek@vu.edu.au, anthony.parker@research.vu.edu.au, vincent.rouillard@vu.edu.au

There are two main characteristics of cushioning materials, such as expanded polystyrene (EPS), that are required to design a robust protection of critical element against environmental hazards: the attenuation of shocks as a function of the static load and the vibration transmissibility. The effect of a shock on a hypothetical critical element is judged by a Shock Response Spectrum (SRS). The Frequency Response Function (FRF) performs similar function in relation to vibrations. This paper is concerned with the latter. Cushioning materials are generally non-linear and, together with the interacting mass, form a non-linear dynamic system. Parker *et al.* [1,2], who used the Reverse MISO method (Bendat [3]), have shown that a typical linear Frequency Response Function is not able to adequately characterise the vibration transmissibility of cushioning materials, in contrast to the R-MISO method. However, the R-MISO technique results in more than one FRF term, which creates ambiguity in relation to the effect of transmitted vibration on the critical element (Fig. 2). This paper proposes to resolve it, by analogy to the SRS, through a numerical calculation of the Vibration Response Spectrum (VRS) for a hypothetical critical element, using either experimental cushion response data or synthesised via R-MISO FRFs, as the excitation of the critical element. Values of the VRS are defined as the ratio of acceleration rms of critical element to the rms of its excitation (Fig. 2), although other descriptors of critical element's exertion can also be considered. Since the cushion system is non-linear, the excitation of the critical element will generally be non-Gaussian (Fig. 1). A chosen hypothetical critical element can be linear or, if its characteristics can be determined in advance, non-linear. In this paper experimental data of vibration transmissibility for broadband excitation (5-100Hz) is used to calculate the linear and the R-MISO non-linear FRFs. The measured cushion response signal is then used in a numerical SDOF model with an arbitrary damping ratio (0.05 in this case) to predict the response of critical element. The results for the EPS, subjected to the static load associated with the optimum shock attenuation (5.2 kPa), are shown as an example of results.

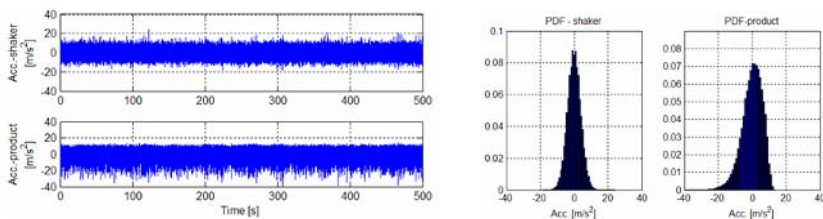


FIGURE 1. Broadband excitation and cushion response and the corresponding PDF.

Fig. 2 illustrates that linear components of FRFs, either linear H1 or R-MISO, do not correctly explain the location of frequency of maximum VRS, and that the contribution of the R-MISO higher terms makes it clearer.

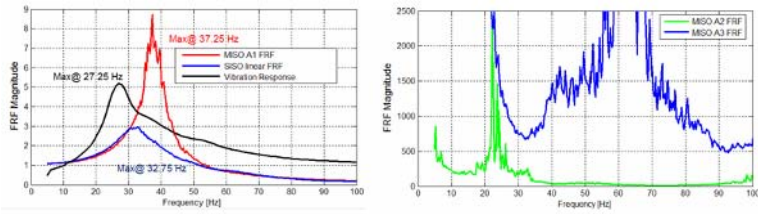


FIGURE 2. Comparison of the VRS with various terms of FRFs (max VRS at 27.25Hz).

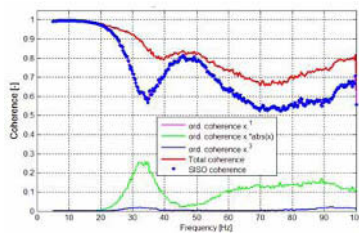


FIGURE 3. Improvement of the Total Coherence in the R-MISO results.

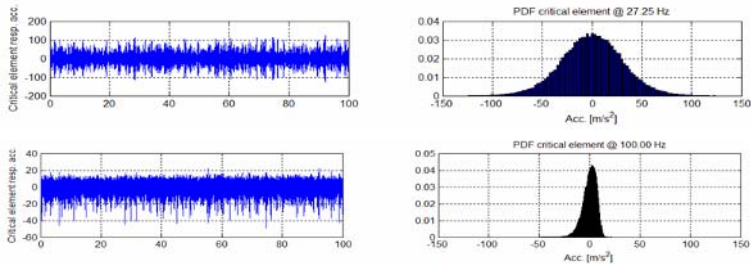


FIGURE 4. Response of the critical element at 27.25 Hz (max VRS) and at 100 Hz.

Fig. 4 illustrates a near-Gaussian PDF for the critical element in the vicinity of maximum VRS. At higher frequencies the PDF shape gradually departs from the Gaussian.

**References**

1. Parker A., Rouillard V. and Sek M., In *Proceedings of the 4th Australasian Congress on Applied Mechanics*, edited by M.Xie, Melbourne, Australia, 2005, 739 - 744.
2. Parker A., Rouillard V. and Sek M. In *Proceedings of the Society for Experimental Mechanics Annual Conference on Experimental and Applied Mechanics*, Portland OR, 2005, 46.
3. Bendat, J.S., *Nonlinear Systems Techniques and Applications*, John Wiley & Sons, New York NY, 1998.

## THE NON-LINEAR CHARACTERISTICS OF CUSHIONING MATERIALS

Anthony Parker, Michael A. Sek and Vincent Rouillard  
Victoria University, Melbourne, Australia

PO Box 14428 MCMC, Melbourne 8001, Australia

anthony.parker@research.vu.edu.au, michael.sek@vu.edu.au, vincent.rouillard@vu.edu.au

Much of the mechanical damage to packages or products in shipment can be attributed to shocks and vibrations encountered during transportation. These vibrations, which are generally random in nature, can cause the shipment, or critical elements within, to resonate. This has the potential for damage to or failure of the product due to the repetitive application of stresses. It is therefore imperative that the design of protective cushioning systems takes into account the resonant frequencies of critical elements within the product. Conventionally, this is achieved by the measurement of the linear Frequency Response Function (FRF) or transmissibility of the product/cushion system. However, commonly used cushioning materials can exhibit strong non-linear behaviour. This non-linear behaviour is exacerbated when the cushioning system is placed under high static loads. Large static loads are often a result of attempts to minimise the environmental impact (as well as the associated economical benefits) of packaging materials by reducing the amount of cushioning material used. Non-linear behaviour can have significant implications for the design and optimisation of protective packaging systems, especially when trying to evaluate the transmissibility of the system.

This paper describes the application of a non-linear identification technique to investigate the dynamic characteristics of cushioning materials and reveals that non-linear effects must be taken into account in order to obtain true estimates of the system transmissibility and natural frequencies. Packaging systems include several discrete mechanical components, which are often non-linear. This non-linearity adds to the challenge of describing and predicting the behaviour of such systems.[2] Conventional spectral analysis techniques assume that the system adheres to the additive and homogeneous properties of the excitation function [1]

The technique developed in this paper is based on the Reverse Multiple Input Single Output (R-MISO) algorithm introduced by Bendat and Piersol [3]. The principal concept of the reverse non-linear dynamic analysis method is as follows: An extensive class of single degree of freedom (SDOF) non-linear systems, can be described by the non-linear differential equation of motion:

$$m\ddot{u}(t) + c\dot{u}(t) + ku(t) + p(u, \dot{u}, t) = F(t) \quad (1)$$

Where  $F(t)$  is the force input and  $u(t)$  is the displacement output while  $m$ ,  $c$  and  $k$  are the system mass, viscous (linear) damping and stiffness coefficients respectively.  $p(u, \dot{u}, t)$  is the general non-linear damping-restoring term [3]. The linear SDOF case occurs when  $p(u, \dot{u}, t)$  is zero. Analysing such a system in the usual (forward) way results in an excitation - response diagram with feedback, this feedback term complicates the analysis, usually resulting in a time consuming iterative solution process that is prone to serious errors [4]. If the system is analysed with the reverse method, with the displacement output  $u(t)$  as the reverse mathematical input  $x(t)$  and the force input  $F(t)$  as the reverse mathematical output  $y(t)$ :

$$m\ddot{x}(t) + c\dot{x}(t) + kx(t) + p(x, \dot{x}, t) = y(t) \quad (2)$$

The system can be represented as an excitation - response system without feedback. This concept can be extended to a multiple input system to yield the Reverse-MISO technique.

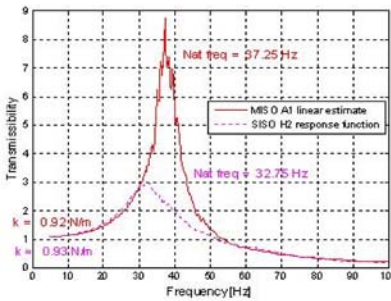


Figure 1 Linear Frequency Response Function for an expanded polystyrene sample

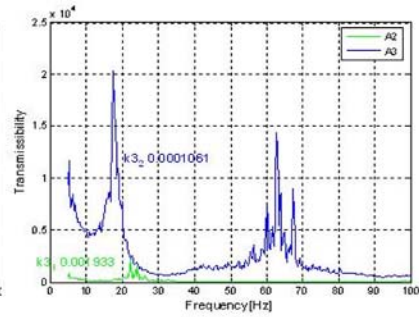


Figure 2 Non-linear Frequency Response Function for an expanded polystyrene sample

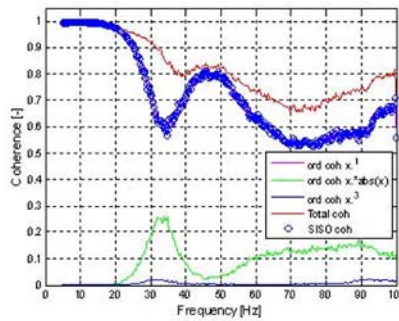


Figure 3 Ordinary coherence functions for an expanded polystyrene sample

Figs 1-3 are the results of the R-MISO analysis of an expanded polystyrene cushion sample that was subjected to broadband excitation between 5-100 Hz @ 0.40g rms using the inputs  $x$ ,  $x^*|x|$ ,  $x^3$ . It can be seen from Fig. 1 there is a significant difference in the transmissibility estimate. In Fig. 2 the Non-linear Frequency Response Functions show there is a contribution from the R-MISO higher terms. Fig. 3 is the total coherence plot for the sample, note the contribution to the coherence by the  $x^*|x|$  input. The results confirm the contribution of the non-linear behaviour and show that a consideration of the effects is necessary.

## References

1. Bendat, J.S. *Nonlinear system analysis and identification from random data*. John Wiley & Sons, New York, NY, 1990.
2. Schetzen, M. *The Volterra & Wiener theories of nonlinear systems*. Wiley-Interscience, New York, NY, 1980.
3. Bendat, J.S. and Piersol, A.G., *Spectral analysis of nonlinear systems involving square law operations*. Journal of Sound and Vibration, vol. **81** (2), 199 - 213, 1982.
4. Bendat, J.S., Piersol, A.G., *Engineering applications of correlation and spectral analysis*. Second Edition, John Wiley & Sons, New York, NY, 1993.



## MODAL CONTROL OF VIBRATIONS OF A MACHINE STRUCTURE BY USING ELECTROMAGNETIC EXCITERS

Tetsuo Sato

Experimental Study and Computer Simulation

Tokyo Metropolitan College of Industrial Technology

17-1, Minami-Senju 8-chome, Arakawa-ku, 116-0003, Tokyo, Japan

tsato@kouku-k.ac.jp

The present study aims to apply the modal control technique[1],[2] which has been served for a class of linear distributed parameter controls to multi-degree of freedom vibratory mechanical systems[3]. By the design procedure for lumped parameter modal control systems, the active vibration controls of machine tools, during machining operations, are to be realized.

The simple L-shaped beam structure mounted with two electromagnetic exciters (which work as dampers) is expressed by the vibratory model taking eventually four natural modes into account. The electromagnetic exciters[4] have developed to serve as vibration dampers which could suppress harmful chattering phenomena of machine tools. The exciters are small, that is, 117(H)×117(W)×69(D) mm of the size, and are lightweight, that is, 2.4 kg of the mass. These are easy to install for machine structures and are easy to maintain in operation.

The basic experimental studies have attempted to verify how the control systems work for the vibrations induced in the machine structure by means of the frequency responses using random disturbance forces in kind[5].

In advance to the computer simulation, the root loci of the closed loop systems for the vibration control have been investigated to clarify the effects of both the time constant  $T$  (msec) stemmed from the impedance of the exciting coils of exciters and the feedback loop gain  $K$ . Assuming a controlled system with the single mode, the root loci of the characteristic roots of the closed loop system with the acceleration feedback are depicted as to parameters  $T$  and  $K$ . For fifteen combinations of the conditions of the computation, a pair of the best sets of the values, that is, ( $K=4.1$ ,  $T=5$  msec) and ( $K=10$ ,  $T=10$  msec) is attained in the view point of the vibratory decrements, and it is seen that the performance of control is effected remarkably by the value of  $T$ .

To estimate the parameters quantitatively, the computer simulation, MATLAB Simulink, for the present modal control system (Fig. 1) has been carried out[6]. In the simulation, the feedback compensator  $A(s)$  is located in the feedback loop in the modal domain, and has such transfer functions as  $\lambda_1(s)$ ,  $\lambda_2(s)$ ,  $\lambda_3(s)$  and  $\lambda_4(s)$  in its diagonals. In addition to the case of the root locus, the PID compensators are implemented for two exciters in the simulating system, and they have the relative displacement signals,  $w_1-w_3$  and  $w_2-w_4$ , as the inputs which are detected by the optical reflex-type detectors built-in the exciters.

Two compensators must be able to *stabilize* the system bearing the vibration of which amplitude happens unfortunately to be *in large*, because the real system is different from the present model and it possesses the nonlinearity due to the operating principle of electromagnetic exciters.

### Concluding Remarks

- The present modal control is *the primary study* for the class of multi-degree of freedom vibratory system as the plan.

- The electromagnetic exciters which are small size and are lightweight are adopted for the active vibration controls.
- Although not expected in advance, the computer simulation results in success for modal control system of all 4 natural modes by using 2 exciters (dampers).

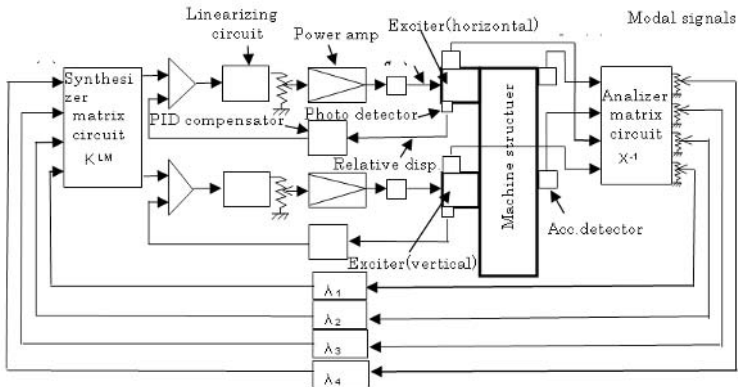


FIGURE 1. Schematic of modal control system by using electromagnetic exciters.

## References

1. Gould, L. A., et al, *IEEE Trans.*, AC-11, vol. 4, 729-739, 1966.
2. Takahashi, Y., et al, *Control and Dynamic System*, Addison-Wesley, 1970.
3. Sato, T., Printing paper, Graduate School of Tokyo Metr. Univ., Mar. 1976, (In Japanese)
4. Sato, T., *Memoirs of Tokyo Metr. College of Aeronautical Engng*, vol. 17, 45-52, 1980.
5. Sato, T., *Prep. of JSME*, 011-2, 171-172, Sept., 2001, (In Japanese)
6. Sato, T., *Prep. of JSME*, 06-1, 455-456, Sept., 2006, (In Japanese)

## HIGH STRAIN RATE BEHAVIOUR OF ALUMINIUM ALLOYS USING SPLIT HOPKINSON BAR (SHB) TESTING

G. I. Mylonas, G. N. Labeas and Sp. G. Pantelakis  
 Laboratory of Technology and Strength of Materials (LTSM)  
 Department of Mechanical Engineering and Aeronautics  
 University of Patras, Panepistimioupoli, Rion GR-265 00, Greece  
 gmylonas@mech.upatras.gr, labeas@mech.upatras.gr, pantelak@mech.upatras.gr

In certain engineering materials processes (e.g. machining) the material is required to operate in high temperature conditions where at the same time deformation occurs in a very small period of time. In such cases the material's mechanical behaviour can differ significantly from the behaviour obtained by conventional quasi – static tension or compression tests. Hence, experimental data is required that can describe the material's behaviour under high strain rate (SR) and high temperature conditions.

In order to investigate materials behaviour at high SR, several testing methods have been developed over the last years. The most widely used technique for high SR testing is the Split Hopkinson pressure Bar test (SHB). The SR that can be studied by the use of a SHB technique, are in the order of  $100 - 10000 \text{ sec}^{-1}$ . A classic arrangement of a SHB apparatus, presented in Fig. 1, consists of a striker bar, an input and an output bar and a specimen located between the input and output bar.

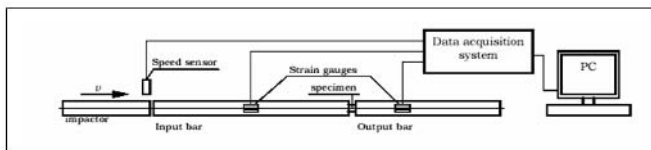


FIGURE 1. Classic SHB apparatus arrangement

During the experiment the striker bar impacts the input bar and produces a strain pulse (Fig. 2) to the system that is recorded by the strain gauges and is used to derive the material's properties. Analytically, by the impact, a compressive wave (incident) is created at the incident bar, which is travelling along the bar towards the specimen; when this compressive wave reaches the incident bar / specimen interface, a part of it is reflected back as a tensile wave, while the rest travels through the specimen and transmitted to the output bar as a compressive wave.

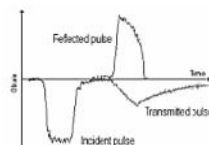


FIGURE 2. Recorded strain pulses

In order to obtain the material's characteristics the tensile reflected and the compressive transmitted waves are utilized. The three equations used to derive the strain rate (Equ. 1) and the stress (Eq. 2) – strain (Eq. 3) characteristics of the material, out of the above mentioned recorded pulses, are the following:

$$\frac{d\varepsilon_s(t)}{dt} = -2 \cdot \frac{C_i}{L_s} \cdot \varepsilon_i(t) \quad (1)$$

$$\sigma_s(t) = E_o \cdot \frac{A_0}{A_s} \cdot \varepsilon_o(t) \quad (2)$$

$$\varepsilon_s(t) = -2 \cdot \frac{C_i}{L_s} \cdot \int_0^t \varepsilon_i(t) \cdot dt \quad (3)$$

In the work the stress – strain response of a new 7 series, aircraft aluminium alloy under high SR compression loading has been studied for strain levels up to  $3000 \text{ Sec}^{-1}$  at room temperature (RT). In Fig. 3 the stress – strain curves for SR 1650, 2400 and  $3000 \text{ Sec}^{-1}$  are displayed alongside with a tensile quasi – static, stress – strain material response. The Young's modulus, yield stress and ultimate stress obtained by SHB tests for the different SR were compared against the respective values from the tensile test. The comparison indicated that the increase of strain rate is accompanied by an increase in yield strength of the material, as it was expected.

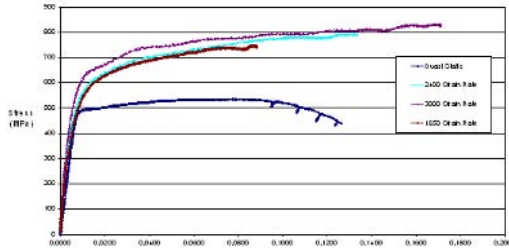


FIGURE 3. Stress – strain curves for 7 series Al at high SR in RT

## References

1. Kuhn, H., Medlin, D., *ASM Handbook Volume 08: Mechanical Testing and Evaluation*, ASM International, USA

## EXPERIMENTAL INVESTIGATIONS OF THE DYNAMICS OF PLC BANDS IN AL3%MG

Leobaldo Casarotto, Rainer Tutsch, Hanno Dierke and Hartmut Neuhäuser  
Institut für Produktionsmesstechnik, Technische Universität Braunschweig  
Schleinitzstrasse 20, 38106, Braunschweig, Germany

Institut für Physik der Kondensierten Materien, Technische Universität Braunschweig  
Mendelsohnstrasse 3, 38106, Braunschweig, Germany

l.casarotto@tu-braunschweig.de, r.tutsch@tu-braunschweig.de, h.dierke@tu-braunschweig.de,  
h.neuhaeuser@tu-braunschweig.de

The Portevin-Le Châtelier (PLC) effect is an undesired behaviour of ductile alloys consisting in a regime of unstable plastic deformation. A relevant feature of this phenomenon is the repetitive concentration of the strain in narrow regions, referred to as PLC bands, that resemble incipient neckings. Depending on the loading conditions and on material factors, three different kinds of band behaviour are traditionally distinguished in tensile tests: type A, a band moving with a constant velocity as a regular and continuous propagation along the specimen; type B, a series of stationary bands that emerge one beside the other at regular intervals in time and in space; type C, stationary bands that emerge with a regular frequency but disordered in space, Hähner *et al.* [1]. Whereas this is a well established classification, the way in which a single band actually emerges is still an open question, but only in the last years a few investigations could start to deal with this aspect, Tong *et al.* [2] and Jang *et al.* [3].

The aim of the present work is the presentation of an experimental setup for the investigation of the dynamics of band emergence. The system consists of a high speed camera that frames a small area on the surface of a tensile specimen in order to acquire sequences of images with a high temporal and lateral resolution. The camera is triggered by means of an optical extensometer that frames the entire specimen and detects in real time the position of the bands. Each image sequence is successively processed with a digital image correlation technique in order to calculate the steps of strain distribution during the formation of the band. The setup couples than a global observation of the phenomenon with an accurate measurement of the band characteristics.

This system was employed to investigate the PLC effect in a series of tensile tests on an Al3%Mg alloy and permitted to achieve a new insight in the dynamics of band formation. It could be observed that bands are local shear deformations along the direction of the maximum shear stress and that type B and C bands, which are stationary and isolated, emerge with an extremely rapid strain burst that initiates on one side of the specimen and then moves rapidly to the other side in the mentioned direction. The duration of this process is around 5ms and some phases of this evolution can be seen in Fig. 1.

In a type A band the strain is concentrated in a propagation front whose movement has been described until now as regular and continuous. Resolved in small temporal intervals, however, the movement reveals a more complex progression mechanism: the front consists of a series of narrow bands close to each other that move across the specimen as single type B-C bands. When a new band enters the group, the front advances one step as schematically illustrated in Fig. 2. This mechanism accounts also for a periodical variation of the angle formed by the band with the specimen axis as the number of bands in the group is alternatively larger on the enter side or on the exit side.

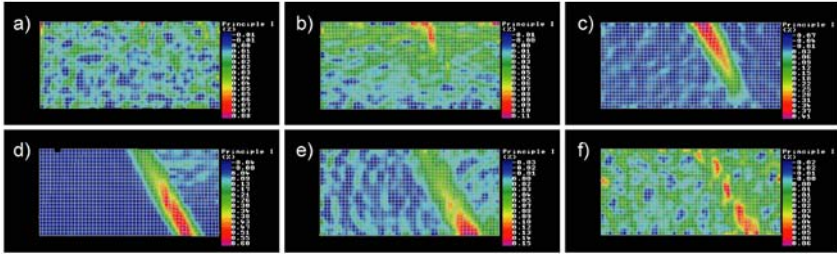


FIGURE 1. The emergence of a type C band in a sequence of six strain maps (specimen axis in longitudinal direction; framed area:  $8 \times 4 \text{ mm}^2$ ; time interval between two steps: 1.1ms).

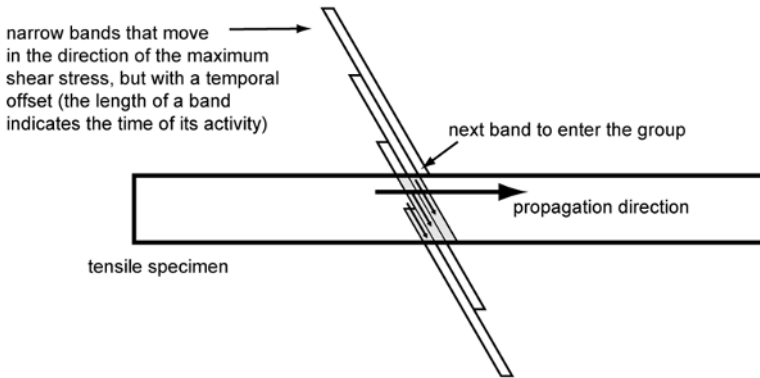


FIGURE 2. Interpretative model of the type A propagation as a succession of narrow bands moving in the direction of the maximum shear stress.

## References

1. Hähner, P., Ziegenbein, A., Rizzi, E. and Neuhäuser, H., *Phys. Rev. B*, vol. **65**, 134109, 2002
2. Tong, W., Zhang, N. and Hector, L.G., *Scripta Materialia*, vol. **53**, 87-92, 2005
3. Jiang, Z., Zhang, Q., Jiang, H., Chen, Z. and Wu, X., *Mat. Sci. Eng. A*, vol. **403**, 154-164, 2005

## ONE-TO-ONE RESONANCE PHENOMENON ON A NONLINEAR QUADRANGLE CANTILEVER BEAM

Myoung-Gu Kim

Inha University Mechanical Engineering

IasmeLab(2N374B) Department of Mechanical Engineering, Inha University,  
253, Yonghyun-Dong, Nam-Ku, Incheon city, South Korea.

mgkim21@hotmail.com

The response of a cantilever beam with non-linear characteristics of one-to-one resonant excitation was investigated both experimentally and theoretically and the results from those two cases were compared and analyzed. In analysis of the motion of a beam, Crespo da Silva's motion equations of beams and method of analysis was used. In the experimental investigation, we applied the experimental variables found in the first, second and third mode of a cantilever beam to the theoretical equations and performed the theoretical analysis. The characteristics of the first mode of a cantilever beam with one-to-one resonant excitation obtained both in experiment and theory was almost same as each another quantitatively. However, there was a slight difference between the experiment and the theory qualitatively. (Figs 1 and 2). It seems to be a cause that the experiment showed lower response characteristics than the theory because of the damping effects in the system. It can be seen that in the first mode the response of one-to-one resonant excitation was affected more by the effects of non-linear spring than by the effects of non-linear inertia.

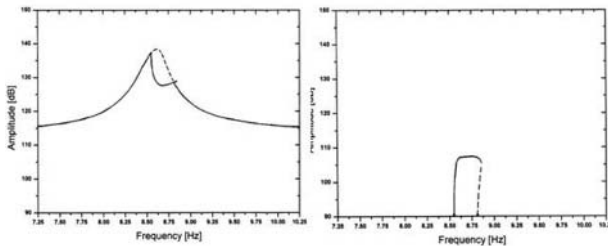


FIGURE 1. The analytical amplitude frequency response of the 1st mode for  $\varepsilon^3 f^* = 0.0466$ ,  $(e^* = 0.61 \text{ mm})$ ,  $e^2 c_2 = 0.0625$ ,  $\varepsilon^2 \Delta_2 = 0.05$  (in-plane and out-of-plane)

In the second mode, the experiment and the theory showed almost the same results. In this mode, the effects of both the non-linear inertia and the non-linear spring together are well seen. Thus, the out-of-plane motion over the in-plane motion is seen more remarkably in this mode than in any other modes. In the third mode, the results from both experiment and the theory are very different and the responses are different from each other both qualitatively and quantitatively. Thus, the third mode shows that the effect of the non-linear inertia is more remarkable than the effect of the non-linear spring. Therefore, it is considered that the theoretical equations for the higher mode than the third need correction in non-linear characteristics of response.

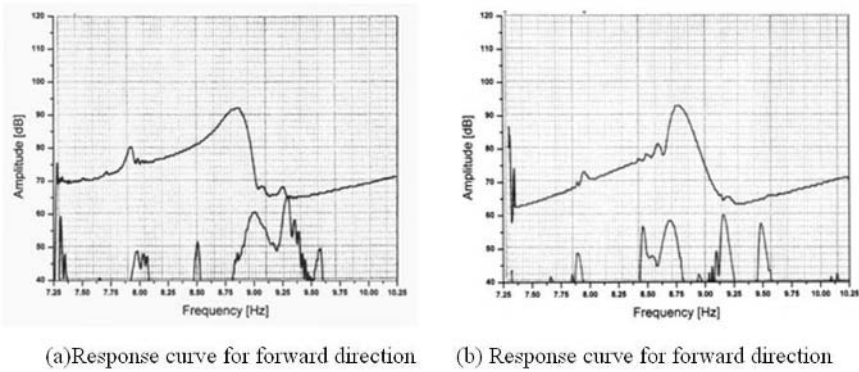


FIGURE 2. Frequency response curve for forward direction on the 1st mode (in-plane and out of plane response curve)

## References

1. Haight, E. C., and King, W. W., *Stability of non-linear oscillations of an elastic rod*, Journal of the Acoustical Society of America, vol. **52**, pp. 899-911, 1971.
2. Zaretzky, C. L., and Crespo da Silva, M. R. M., *Experimental investigation of non-linear modal coupling in the response of cantilever beams*, Journal of Sound and Vibration, vol. **174**, pp. 145-167, 1994.
3. Zavodney, L. D., and Navfeh, A. H., *The nonlinear response of a slender beam carrying a lumped mass to a principal parametric excitation: theory and experiment*, International Journal of Nonlinear Mechanics, vol. **24**, pp. 105-125, 1989.



## EFFECTS OF LEADING AND TRAILING EDGE OF CURRENT PULSE ON AE WAVE

Yoshiaki Akematsu<sup>1</sup>, Atsutoshi Hirao<sup>2</sup>, Kazuro Kageyama<sup>1</sup>, Naotake Mohri<sup>2</sup>  
and Hideaki Murayama<sup>1</sup>

<sup>1</sup> Department of Environmental and Ocean Engineering, The University of Tokyo

<sup>2</sup> Department of Precision Engineering, The University of Tokyo  
7-3-1, Hongo, Bunkyo-ku, Tokyo, 113-8654 Japan  
akematsu@giso.t.u-tokyo.ac.jp

In this study, the mechanism of pressure occurrence in Electrical discharge machining (EDM) was investigated by Acoustic emission (AE) technique. AE wave was detected by optical fiber vibration sensor during single pulse discharge. This paper describes some experimental results on AE wave characteristics during single pulse discharge. The generation factor and propagation characteristic of AE wave were investigated. Numerical analysis by using finite element method (FEM) was adapted on the assumption that the AE wave was only depending on a force. In order to investigate the effect of current behavior on AE propagation, the numerical analysis result using the FEM and the experimental result along with the single pulse discharge were compared.

Figure 1 shows the experimental setup. The electrical discharges were made to fall on thin plate. In order to make several s discharge duration, condenser circuit was applied. The current flowing through the anode is monitored with a current probe. The applied voltage was 100V which is defined by the charging voltage of the capacitor. Discharge interval time was controlled several 10ms by 1M resistance. Optical fiber vibration sensor was bonded on the thin plate. The optical fiber sensor was located at the center of the thin plate so as avoid the effect of reflection of elastic wave. AE wave which was detected by optical fiber vibration sensor was changed to volt signal by heterodyne interferometer [1-3]. Data acquisition and analysis were carried out with 10MHz sampling rate.

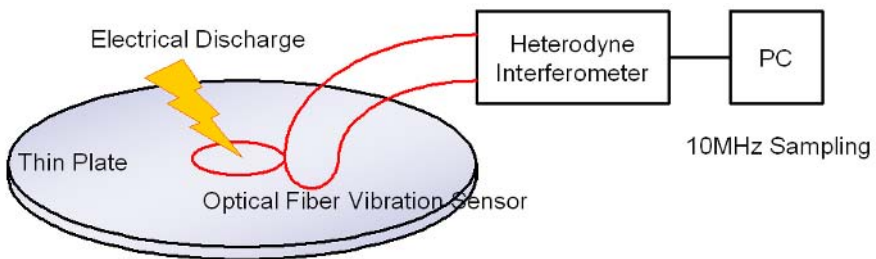


FIGURE 1. Experimental setup.

Based on the assumption that the AE wave was only depending on a force, the numerical analysis result using the FEM [4] and the experimental result along with the single pulse discharge were compared.

Figure 2 show the results of comparing with FEM result and experimental one when plate thickness was 1mm. Electrical discharge and input force duration was 1s. It is found that the

behavior of detected waveform and simulated one is almost the same. It was considered that the pressure was occurred on the leading and trailing edge of current pulse, respectively.

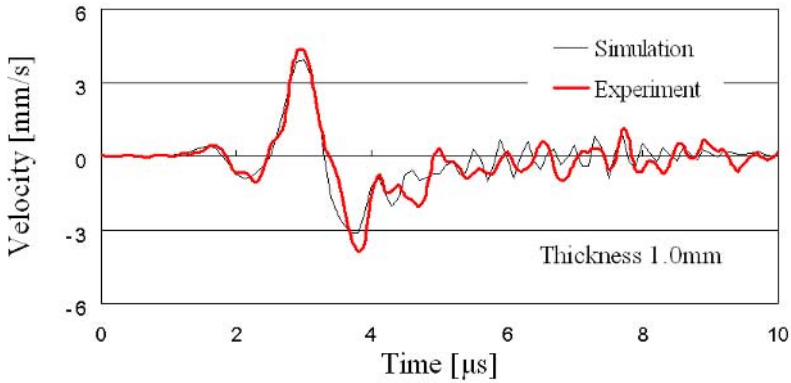


FIGURE 2. Comparison with FEM result and experimental one

In order to investigate the effect on the leading and trailing edge of current pulse, rectangular current pulse was made by transistor circuit. As the results, burst AE wave was detected on the leading and trailing edge of current pulse, respectively. It was considered that the factor of AE wave occurrence during electrical discharge was mainly discharge current.

## References

1. Kazuro Kageyama et al., IEEE J. Lightwave technology, vol. **24** (4), 1768-1775, 2006
2. Kazuro Kageyama et al., Smart Materials and Structures, vol. **14**, S52-S59, 2005
3. Yoshiaki Akematsu et al., J. J. Soc. Precision Engineering, vol. **72**(6), 804-808, 2006
4. Yoshiaki Akematsu et al., SPIE 11th Annual Symposium Nondestructive Evaluation for Health Monitoring and Diagnostics, San Diego, 2006, vol. 6179, 617900

## HIGH PRECISION OPERATION OF FIBER BRAGG GRATING SENSOR WITH INTENSITY-MODULATED LIGHT SOURCE

Nobuaki Takahashi, Hiroki Yokosuka, Kiyoyuki Inamoto and Satoshi Tanaka  
 Department of Communications Engineering, National Defense Academy  
 1-10-20 Hashirimizu, Yokosuka, Kanagawa 239-8686 Japan  
 tak@nda.ac.jp, yokosuka@nda.ac.jp, g44005@nda.ac.jp and satoshi@nda.ac.jp

Among dynamic strain sensor systems using an optical fiber as a sensing element [1], a FBG (fiber Bragg grating) sensor in the intensity modulation scheme is known to be simple in structure, stable in operation, and wide in dynamic range and frequency response while allowing us to observe in a rather direct manner a waveform, i.e., amplitude and phase of a signal in real time [2]. When one wants to observe clearly a waveform of a small signal, however, various noises deteriorate the signal and make it difficult to observe the waveform, which results in increase of ambiguity especially in determining phase of the signal.

In this paper, therefore, we propose a new method to clarify a FBG sensor signal for precise measurement by reducing noises involved in the system. The principle is based on the envelope detection in demodulating amplitude-modulated signals. Although the principle is applicable to measurement of either mechanical vibration or sound pressure, we here demonstrate it in the case of vibration measurement and present its results.

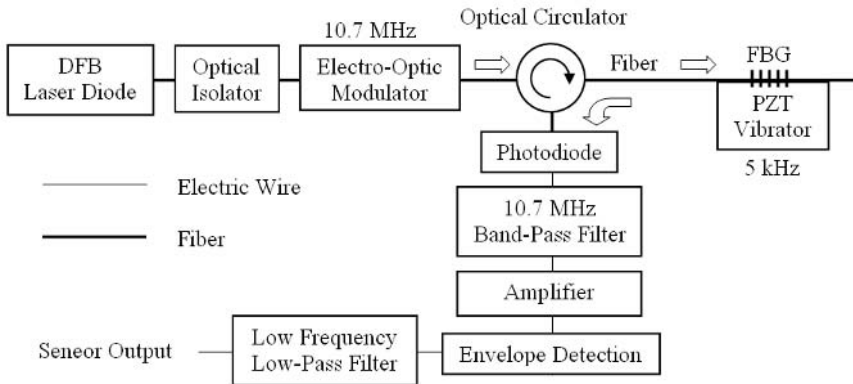
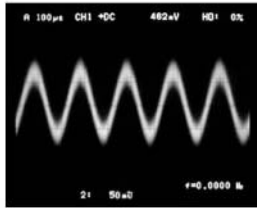
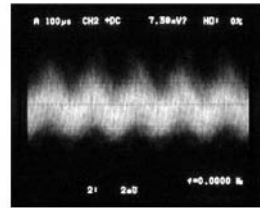


FIGURE 1. Experimental Setup.

Figure 1 shows the experimental setup for the proposed vibration sensor. The laser output is intensity modulated at 10.7 MHz by an EO (electro-optic) modulator and incident on a FBG sensing element. When the light is reflected back from the FBG, it is again intensity modulated by dynamic strain caused by vibration. The optical detection by a photodiode generates photocurrent that consists of a dc component and 10.7 MHz component whose envelope is modulated by 5 kHz mechanical vibration applied to the FBG. Passing through a band-pass filter, an amplifier, an envelope detection circuit and a low-pass filter, output signal of the sensor is obtained.



(b) With Envelope Detection



(a) Without Envelope Detection

FIGURE 2. Experimental Results.

Figure 2a and b show the experimental results obtained with and without using the EO modulation and envelope detection technique, respectively. It is seen from the figures that the proposed method provides us with a clear and stable signal output though the output signal is indistinct and its phase is ambiguous without it. Dependence of the sensor on the vibration amplitude is also measured and the linearity of the sensor is confirmed even in the proposed configuration.

In conclusion, EO modulation of source light and envelope detection of the signal are utilized for precise operation of a FBG vibration sensor. It is successfully demonstrated that the proposed method allows us to observe the signal much unambiguously compared to the case without it. The sensor still works with linearity. The operation frequency range of the sensor is limited by the bandwidth of the 10.7 MHz band-pass filter but much wider than that of the sensor using the lock-in detection, with which the frequency range is limited to about 1 kHz [3]. Although we demonstrated the principle in FBG vibration sensing, it should also be possible to apply the same principle to measurement of other dynamic parameter such as sound pressure in water [4].

## References

1. Kersey, A.D., Davis, M.A., Patrick, H. J., LeBlanc, M., Koo, K.P., Askins, C.G., Putnam, M.A. and Friebele, E.J., *J. Lightwave Technol.*, vol. **15**, 1442-1463, 1997.
2. Takahashi, N., Thongnum, W., Ogawa, T., Tanaka, S. and Takahashi, S., *Opt. Rev.*, vol. **10**, 106-110, 2003.
3. Yokosuka, H., Tanaka, S. and Takahashi, N. In *Proceedings of the 17<sup>th</sup> International Conference on Optical Fiber Sensors*, edited by M. Voet, R. Willsch, W. Ecke, J. Jones, B. Culshaw, Proceedings of SPIE Vol. 5855, Washington, 2005, 731-734.
4. Takahashi, N., Yoshimura, K., Takahashi, S. and Imamura, K. *Ultrasonics*, vol. **38**, 581-585, 2000.

## CREEP MEASUREMENT OF OPTICAL FIBER WITH A DOUBLE INTERFEROMETER SYSTEM

Zhihong Xu and Fahard Ansari

<sup>1</sup>Science School, Nanjing University of Science & Technology

<sup>2</sup>Civil & Material Engineering Department, University of Illinois at Chicago  
Chicago, Illinois, U.S.A.

<sup>1</sup>xuzh@mail.njust.edu.cn, <sup>2</sup>Ansari@mail.uic.edu

The creep of the optical fibres were tested under static and cyclic loading were studied in this paper. In static load creep test, the specimens are hanged vertically and divided into two groups. The two groups are loaded with weights of 3N and 5N respectively. The gauge length of the specimens is 0.5m. A specimen free of load is measured at same time to provide the reference to compensate the influence of the temperature. The creep deformation of the fibers is measured for every 24 hours (one day). The elongations of the fiber via the time are shown in Figure 1.

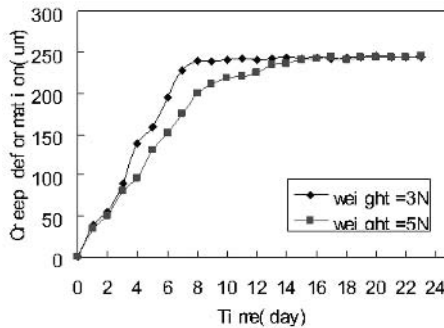


FIGURE 1. Creep of the optical fiber under static load

In this test a high-speed step motor is employed to drive the moving of the stage. The specimens are stretched cyclically as the stage goes back and forward. The position resolution of the stage is  $1\mu\text{m}$  and the loading frequency is 2Hz. The mean strain level was 0.5% in group 1 and 0.75 % in group 2, and the strain oscillation amplitude was 0.25%. For each 10000 cycles the specimen is removed from the stage and the length difference is measured by interferometer at stress free condition. The tests are done in room temperature and humidity. Fig. 2 shows the elongation of two groups of optical fibers after they are released from cyclic load. It can be seen that the limitation of the elongation of the optical fiber was about 250mm/m ( $250\mu\epsilon$ ). The elongation of the fiber length is relatively larger at the beginning. As the increase of the cycle number the length of the fiber tends to stable. This phenomenal is similar to that with static load.

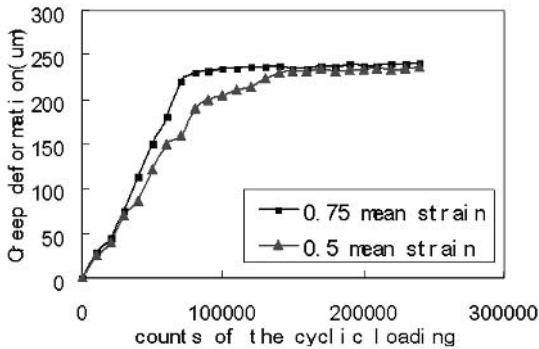


FIGURE 2. The creep of optical fibers under cyclic loading

Because of the inconsistent deformability of the coating and the silica core (including the core and cladding) in production process, there are residual stresses in the optical fiber. The residual deformation of the core and cladding was released as the fiber undergoes cyclic loading or loaded for a period time, the coating creeps and the residual stress is released. With the cycle number or loading time increase, the coating creeps, residual stress gets smaller and smaller. The effect of the coating gets weaker and weaker and the silica core determines the material properties of the optical fiber, the silica core is a typical brittle material and no creep deformation in it.

## References

1. Ph.M.Nellen, P.Mauron, A.Frank, U.Sennhauser, K.Bohnert, P.Pequignot, P.Bodor, H.Brandle, *Sensors and Actuator*, vol. **103**, 364-376, 2003
2. Zhihong Xu, F.Ansari, vol. **5758**, 390-404, 2005
3. Ansari, F., *cement and concrete composites*, vol. **19**, 1-10, 1997
4. S.T. Shiue, Y.K. Tu, *J. Appl. Phys.*, vol. **86**, 4085-4090, 1999
5. S.T. Shiue, H. Ouyang, *J. Appl. Phys.*, vol. **90**, 5759-5762, 2001
6. Li,TC,Wang, A, Murphy,K., and Calus, R., *Optics letters.*, vol. **20**, 785-787, 1995
7. Y. Zhao, F. Ansari, *Appl. Opt.*, vol. **40**, 3176-3181, 2001

## A GUIDELINE FOR FATIGUE TESTING OF COMPONENTS

Mehrdad Zoroufi and Ali Fatemi

Department of Mechanical Engineering,

Iran University of Science and Technology, Tehran, Iran

Department of Mechanical, Industrial and Manufacturing Engineering,

The University of Toledo, Toledo, Ohio, USA

mzoroufi@iust.ac.ir, afatemi@utnet.utoledo.edu

Material properties, loading, geometry and manufacturing processes are considered as the major elements in fatigue design problems. The effect of geometry has always been one of the challenging issues for designers to face with. The methodologies to transfer material properties obtained from specimen fatigue tests to fatigue behavior of real components, where neither a nominal stress nor a notch factor could be defined, have not been completely accurate or reliable. Therefore, direct component testing, though time consuming and expensive, is often a necessity in fatigue design. Contrary to specimen testing, which numerous standards have been developed for, component testing is more a matter of designer's practice. Various parameters such as simulation of the actual service condition, collecting useful data, and correspondence of the test results to analytical predictions determine the correctness and applicability of the conducted test. Based on previous studies regarding fatigue testing of components [1-9], this article intends to provide a step-by-step guideline to conduct fatigue testing, with a focus on automotive parts. Essential pre-test, during-the-test, and post-test details are discussed. The guideline is implemented on sample steering knuckles and connecting rods as example parts, and the challenges and shortcomings for each test are investigated.

A flowchart of the developed guideline is illustrated in Fig. 1. This guideline is implemented to two types of automotive parts from different manufacturing processes and representing different service categories; forged steel and cast aluminum steering knuckles that are safety-critical suspension components subject to large-amplitude fluctuations of load and forged steel and powder-metal connecting rods that are engine components subject to constant-amplitude loads. The emphasis of this work is on elaborating the importance of performing the accurate test by following a comprehensive guideline that precisely incorporates all the necessary experimental details. Service identification, analytical evaluation, numerical simulation, test apparatus preparation, and test monitoring are among the major steps pursued in detail for the variety of components and service conditions. Finite element simulation of the component in real-life service is recommended as a main tool to predict the critical locations as well as to configure the proper fixtures and constraints in the test arrangement. Load-control tests are found to be sufficient testing modes if accompanied by strain measurements to guarantee the accuracy of the test. The test progress should be monitored for changes in displacement amplitude to detect crack initiation, growth rate and failure. The results of this work will help component designers in both design and optimization stages to limit the number of component tests by obtaining reliable fatigue performance data for in-service or to-be-designed components.

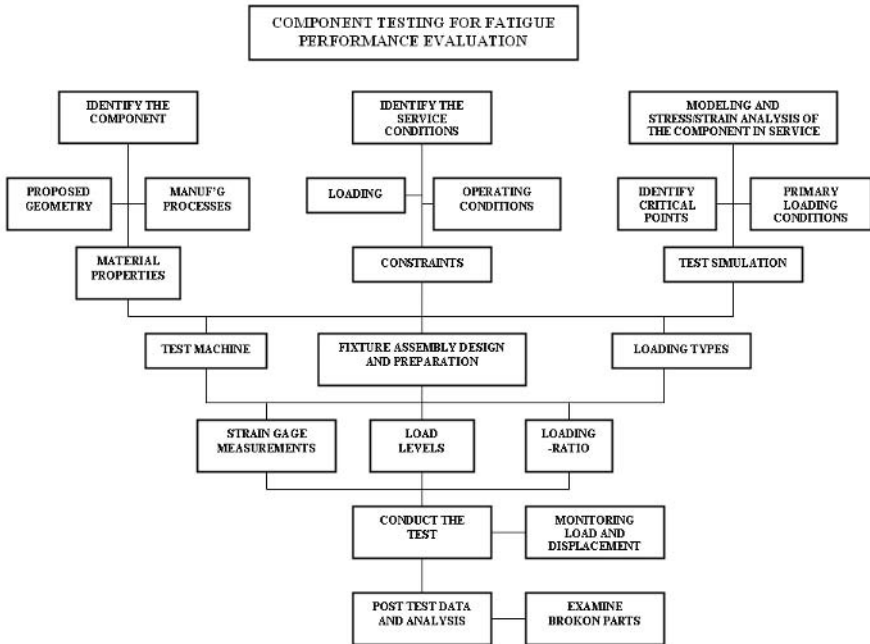


FIGURE 1. Flowchart for fatigue component testing.

## References

1. Beretta, S., Blarasin, A., Endo, M., Giunti, T., and Murakami, Y., *International Journal of Fatigue*, vol. **19**, no. 4, 319-333, 1997.
2. Berger, C., Eulitz, K.G., Heuler, P., Kotte, K.L., Naundorf, H., Schuetz, W., Sonsino, C. M., Wimmer A., and Zenner, H., *International Journal of Fatigue*, vol. **24**, 603-625, 2002.
3. Chu, C.C., *International Journal of Fatigue*, vol. **19** (supp. no. **1**), S325-S330, 1997.
4. Firat, M. and Kocabicak, U., *Engineering Failure Analysis*, vol. **11**, 655-674, 2004.
5. Heuler, P. and Birk, O., *Fatigue & Fracture of Engineering Materials & Structures*, vol. **25**, 1135-1148, 2002.
6. Lee, Y.L., Raymond, M.N., and Villaire, M.A., *Journal of Testing and Evaluation*, vol. **23**, 354-363, 1995.
7. Savaidis, G., *Material wissenschaft und Werkstoff technik*, vol. **32**, no. 4, 362-368, 2001.
8. Zoroufi, M. and Fatemi, A., *SAE Technical Paper No. 2004-01-0628*, Society of Automotive Engineers, 2004.
9. Taylor, D., Bologna, P., and Bel Knani, K., *International Journal of Fatigue*, vol. **22**, 735-742, 2000.



## NEW EQUIPMENT FOR LIQUID METAL EMBRITTLEMENT CHARACTERISATION FOR VERTICAL AXIS TESTING MACHINES

J. Carpio, J.A. Alvarez, J.A. Casado and F. Gutierrez-Solana  
Division de Ciencia e Ingenieria de los Materiales. E.T.S.I. de Caminos, Canales y Puertos.  
Universidad de Cantabria  
Avenida de los Castros, s/n. 39005 Santander, Spain  
uc27128@alumnos.unican.es

This text shows the design, validation and working of new experimental equipment. This set-up allows the performance of mechanical test with vertical axis universal testing machines when the specimens have to be horizontally immersed in aggressive liquids.

A practical implementation to determine liquid metal embrittlement is showed in this paper. The design, validation process and the results obtained with the equipment for J tests using CT specimens immersed in liquid Zn at 450°C are explained in detail.

The set-up consists of two inclined arms, jointed at the top with the universal testing machine and at the bottom with two other horizontal arms attached to the specimen, as represented in Fig. 1. The parts of the set-up are made of heat resistant steel.



FIGURE 1. Experimental set-up for testing in liquid Zn.

The set-up is placed on the upper part of a furnace designed for the maintenance of liquid Zn at 450°C. Furnace and set-up are put under the actuator of a vertical universal testing machine, as shown in Fig. 2.



FIGURE 2. Experimental set-up under the universal testing machine.

The experimental set-up can be used with fracture toughness specimens, such as CT or DCB, and with tensile test specimens. For the specific device of Fig. 2 the load transmission was measured, and a factor of 0,96 was to be applied to compensate the friction effect. This value was obtained in the validation stage, which consisted of the performance of air tensile tests in a vertical loading machine on the same material with the experimental set-up (specimen horizontally tested) and without it (specimen vertically tested).

The results obtained in the characterisation of liquid metal embrittlement during the galvanization of structural steel can be observed Fig. 3.

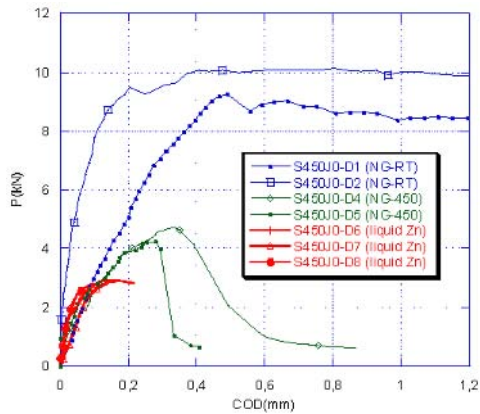


FIGURE 3.  $J_I$  tests of the EN10025 S450J0 structural steel in air at room temperature, in air at 450°C and in liquid Zn with the experimental set-up explained in this paper.

## EXPERIMENTAL RANDOM SIGNALS IN INDUSTRIAL CONDITIONS AND APPLICATIONS BY COMPUTER ANALYSIS

M. Kopecky

Dept. of Physical Material Engineering

Faculty of Industrial Technologies,

AD University of Trencin , SK-020 01 Puchov, Slovak Republic

mirkopecky@inmail.sk

The paper focused on the service loads and cumulative damage analysis. The description of the service load contains: the examples of statistical analysis of random stress process, stress spectrum and stress program.

This work presents a method of determining of structural parts random loading distribution, [1], [3]. The methods described in this paper are the ways to reach the solution goals by means of a characteristic curve of strength reliability with the maximum use of computer technology. The results of its application would be presented to mobile facility elements.

A motorcycle running along a road is subjected to two vertically imposed displacements, one at each wheel. The description of the road surface must be complete enough to describe adequately the displacement imposed at each wheel at least in statistical terms and the correlation between the two displacements.

In some mobile machinery and equipment, or their elements are the problems of fatigue. The problem of fatigue strength and service-life, [2], as the most important phenomena of strength reliability under those conditions, is connected more or less with a certain degree of uncertainty.

The basic elements of the fatigue life evaluation,[3] , [2], are reviewed in Fig 1. and 2. The results of its application would be presented to mobile facility elements. The basic elements of the fatigue life evaluation,[3], are reviewed in Fig. 1.

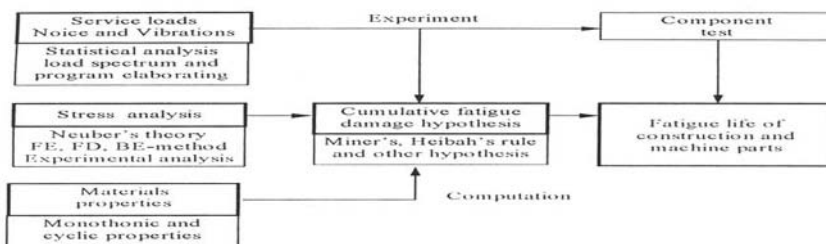


FIGURE 1. Basic elements of the fatigue design process

The result of analysis give us the possibility of estimation of complex character service load and enable on this base the choice of suitable counts cycle method for block-load spectrum determining, mentioned in schematic diagram.

**Key words:** Dynamic Failure, Fatigue, Non Linear Dynamic Systems, Numerical Method and Validation.

### **Acknowledgments**

The author expressed his thanks to Slovak Agency for Research and Science for its support of this work (grant 1/2081/05).

### **References**

1. Kopecky M. , Experimental-numerical method of random analysis. In: 9<sup>th</sup> Inter. Conf. on Experimental Mechanics, vol.3, pp. 1006-1012, Copenhagen, Denmark , 1990.
2. Kopecky M. and Vavro J. , A fatigue curve as a random element. In: 5<sup>th</sup> Polish - Slovak Scientific Conference on "Computer Simulation in Machine Design", Wierzba, Poland, pp.79-82, ISBN 83-912190-3-8, 2000.
3. Szala J. , Fatigue fracture of parts of structures as a vibration effect. In: 16<sup>th</sup> Symposium on "Vibration in physical system", Poznan-Blazejewko, Poland pp. 40- 49, 1996.

## MEASUREMENT AND IDENTIFICATION TECHNIQUES FOR CRACKS: APPLICATION IN CYCLIC FATIGUE

Julien Réthoré, Stéphane Roux and François Hild  
LMT-Cachan, ENS Cachan / CNRS-UMR 8535 / Université Paris 6  
61 avenue du Président Wilson, F-94235 Cachan Cedex, France  
{rethore,roux,hild}@lmt.ens-cachan.fr

One of the commonly encountered mechanical failures is fracture dominated. It usually occurs before large scale yielding. In many materials, small scale yielding arises in the vicinity of the crack tip. Therefore, the classical elastic solutions [1] are only first order idealizations of the practical situation. Elastic-Plastic Fracture Mechanics (EPFM) aims at analyzing more complex situations for which plasticity needs to be accounted for with global quantities.

Different quantities are introduced to describe cracks in a small scale yielding regime. The crack opening displacement was proposed as a fracture parameter to analyze propagation under quasi-static [2] and cyclic [3] loading conditions. However, the critical values of crack opening displacements were not always easy to evaluate. Rice [4] considered the potential energy changes induced by crack growth in a non-linear elastic material. This author proposed to use a path-independent contour integral, the  $J$ -integral. It can be used to predict the inception of crack propagation. The so-called HRR fields [5,6] were also introduced to describe more locally the stress and strain fields in non-linear elastic materials.

With the development of full-field measurement techniques, some of the aspects discussed above can be assessed experimentally without having to use numerical simulations. Under these circumstances, the measurable quantities are usually displacement fields [7]. Among various techniques, Digital Image Correlation (DIC) allows one to estimate full displacement fields based on a series of digital images of the surface of a specimen subjected to a specific loading history. Recent advances have been achieved through a novel formulation that enables one to decompose the searched displacement field onto a suited library of such fields. The latter are either finite element shape functions [8], which open the way to a further identification step, or enriched fields such as analytic displacement fields for cracks [9].

A multiscale approach has been proposed to avoid spurious local minima, and to provide a robust and accurate displacement measurement. The uncertainty that is reached lies typically in the range  $10^{-2}$  to  $10^{-3}$  pixel size for displacements. The interest of this experimental tool is that it provides full kinematic fields. For cracked samples or structures, it thus gives access to a wealth of data that are exploited to estimate mechanical properties. A first route is given by post-processing measured displacements. Two options are followed. First, by using a standard least squares technique, stress intensity factors and crack tip locations are determined by using a known displacement basis [10]. Second, an integral interaction formulation gives also access to stress intensity factors [11,12]. By choosing suitable test functions, the minimization of a scalar product with respect to measurement noise yields the optimal basis to extract stress intensity factors [13]. An alternative route consists in using the displacement basis directly at the measurement stage. Therefore there is no decoupling between the measurement and identification stages. It is referred to as *integrated* Digital Image Correlation (or I-DIC) [9].

A cracked steel sample (CCT geometry) subjected to a fatigue test is analyzed. A far field microscope provides pictures such that the physical size of one pixel is about one micrometer. Consequently, displacement fluctuations on the order of tens of nanometers are measurable. The history of stress intensity factors during loading/unloading cycles is analyzed. In particular, non-

linear crack closure is observed and effective stress intensity factor ranges are determined. Last, the three identification techniques are compared.

## References

1. Kanninen, M. F. and Popelar, C. H., *Advanced Fracture Mechanics*, Oxford University Press, Oxford (UK), 1985.
2. Wells, A. A. In *Proc. Crack Propagation Symp.*, Cranfield, UK, 1961, 210-230.
3. Rice, J. R. In *Proc. Fatigue crack propagation*, STP 415, ASTM, Philadelphia, 1967, 247-309.
4. Rice, J. R., *ASME J. Appl. Mech.*, vol. **35**, 379-386, 1968.
5. Hutchinson, J. W., *J. Mech. Phys. Solids*, vol. **16**, 18-31, 1968.
6. Rice, J. R. and Rosengren, G. F., *J. Mech. Phys. Solids*, vol. **16**, 1-12, 1968.
7. Rastogi, P. K. (Edt.), *Photomechanics*, Springer, Berlin, Germany, 2000.
8. Besnard, G., Hild, F. and Roux, S., *Exp. Mech.*, 2006, in press.
9. Hild, F. and Roux, S., *C.R. Mecanique*, vol. **334**, 8-12, 2006.
10. Roux, S. and Hild, F., *Int. J. Fract.*, 2006, in press.
11. Hellen, T. K., *Int. J. Num. Meth. Eng.*, vol. **9**, 187 - 207, 1975.
12. Réthoré, J., Gravouil, A., Morestin, F. and Combescure, A., *Int. J. Fract.*, vol. **132**, 65-79, 2005.
13. Réthoré, J., Roux, S. and Hild, F., 2006, submitted for publication.

## IMPACT OF MACHINING PARAMETERS ON FATIGUE BEHAVIOUR OF 15%SiC<sub>p</sub>- REINFORCED ALUMINIUM MATRIX COMPOSITES

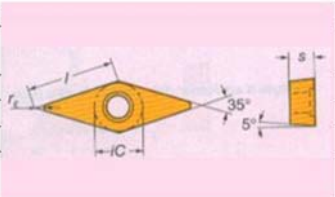
Ali Mkaddem, Patrick Ghidossi, Samuel Crequy and Mohamed El Mansori  
Ecole Nationale Supérieure d'Arts et Métiers, LMPF(EA4106)  
Rue saint dominique BP 508 – 51006 Châlons-en-Champagne, France  
ali.mkaddem@chalons.ensam.fr

Nowadays, high quality product becomes more and more required. Particulates reinforced composites have been established as competitive materials for naval, automotive and aerospace manufactory. However, the fatigue behaviour of such materials is so complex and diverse that much more investigations still required for completing knowledge in these fields. Metal matrix composites (MMC) have been increasingly used for critical structural applications in industrial sectors.

The proposed paper aims to investigate the impact of the machining conditions on the machinability and fatigue variance of silicon carbide (SiC) particulates reinforced aluminium metal matrix. An experimental approach has been conducted through a design of experiment including three machining speeds and two feed rates. The surface quality of machined specimen is studied through different roughness inspections which lead to make interaction between the machining factors and the finish surfaces.

Uncoated tungsten carbide tools with the specifications of table 1 are used for turning operations. Their morphology has been discussed in order to give some explanation after their use.

TABLE 1. Uncoated carbide tool specifications.

Tool material and grade		Uncoated tungsten carbide tool (WC)
Specification		VCGX 16-04-04-AL-H10
Clearance angle (°)		5
Cutting edge angle (°)		35
Nose radius $r_n$ (mm)		0.4
Diameter $\varnothing$ (mm)		15.875
Tool width $s$ (mm)		4.76
Length edge $l$ (mm)	9.525	

Firstly, tensile test has been conducted for characterising considered material under quasi-static conditions. Linear and non linear zones of stress-strain curve were discussed and required parameters for both regions were deduced from experimental data in the first stage of the work. Then, the fatigue life of the considered composite is studied under two stress amplitudes, using four-point reversed loads and bending machine as can be seen in Fig. 1. Different experiences have been performed at room temperature up to failure in order to investigate the behaviour of material in each case of chosen domain.

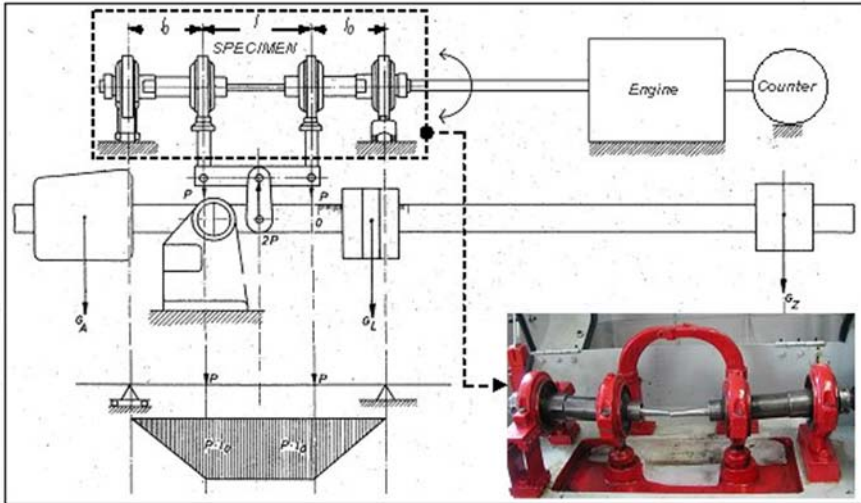


FIGURE 1. Four-point bending machine for fatigue tests.

Finally, the influence of adhesion phenomenon on cutter flank is discussed for the uncoated carbide tool used in processing composite material and fatigue life of specimens under stress-controlled conditions is presented for different parameter ranges.

## References

1. Tjong, S.C., Wang, S. and Mai, Y.W., *Materials Sciences and Engineering*, vol. **A358**, 99-106, 2003.
2. Dermakar, S., *Techniques de l'Ingénieur*, chap. **M250**, 1-16, 1990.
3. Kalam, A., Sahari, B.B., Khalid, Y.A. and Wong, S.V., *Composites Structures*, vol. **71**, 34-44, 2005.
4. Mao, H. and Mahadevan, S., *Composite Structures*, vol. **58**, 405-410, 2002.



## THE EFFECT OF MACHINING ON THE SURFACE INTEGRITY

Ataollah Javidi, Ulfried Rieger and Wilfried Eichlseder  
 University of Leoben, Leoben, Austria  
 ataollah.javidi@mu-leoben.at, ulfried.rieger@stud.unileoben.ac.at,  
 wilfried.eichlseder@mu-leoben.at

Steel components often have to be machined after heat treatment in order to obtain the correct shape as well as the required surface finish. Hard turning allows manufacturers to simplify their processes and still achieve the desired surface finish quality [1]. Surface integrity involves study and control of two factors, surface roughness and surface metallurgy. The study of surface metallurgy entails the investigation of the possible alteration in the surface layers after machining such as plastic deformation and residual stress distribution. The residual stresses that can be found in a mechanical component are mainly generated in the final steps of the machining process. The level of the generated residual stresses depends on the machined material and on the process parameters used [2]. The effects of residual stress may be either beneficial or detrimental, depending upon the sign, magnitude and distribution of the stress, all of which can be critical to performance and have to be considered in the design of a component [3]. In this study the residual stresses were measured using the blind hole drilling method in axial and circumferential directions. The goal of this work is to identify a relationship between surface integrity, turning process parameters and fatigue behavior of components. Figure 1 shows the geometry of the round specimens studied in this work.

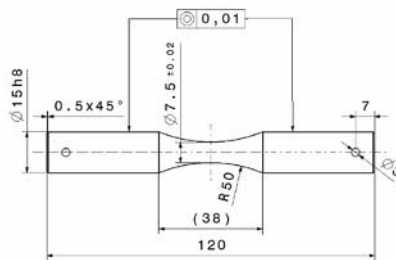


FIGURE 1. Specimens for rotating bending test.

Steel bars of the type 34CrNiMo6 were used in this investigation. The mechanical properties of this steel are given in Table 1.

TABLE 1. Mechanical properties.

Material	$R_e / \text{N}\cdot\text{mm}^{-2}$	$R_m / \text{N}\cdot\text{mm}^{-2}$	$A_5 / \%$
34CrNiMo6	1085	1100	17.0

The residual stresses were measured using the blind hole drilling method [4]. Figure 2 shows the residual stress distribution in machined surface by means of this method.

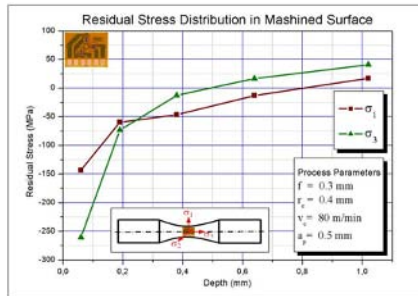


FIGURE 2. Residual stress distribution in machined surface.

Results show that residual stresses on the surface of a turned component are mainly influenced by the feed rate and by the nose radius of the tool. Increasing the feed rate tends to increase the compressive residual stresses. An increase in the nose radius leads to a decrease in compressive residual stresses (Figure 3).

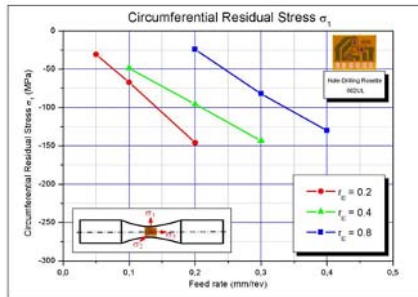


FIGURE 3. Residual stress vs. feed rate for different nose radii.

## References

1. Vernon, A. and Özel, T., *Factors affecting surface roughness in finish hard turning*, Department of Industrial and Systems Engineering, Report No. 03-104, 2003.
2. Dahlman, P., Gunnberg, F. and Jacobson, J., *Journal of Materials Processing Technology*, vol. **147**, 181-184, 2004.
3. Grant, P.V., Lord, J.D. and Whitehead, P.S., *The Measurement of Residual Stresses by the Incremental Hole Drilling Technique*, NPL, Teddington, United Kingdom, 2002.
4. Schajer, G.S., *J. Eng. Mat. Tech.*, vol. **110**, 338-343, 1988.

## EVALUATION OF $K_I$ -V RELATION IN CERAMICS BY USING DT TECHNIQUE (CRACK LENGTH MEASUREMENT BY USING COMPLIANCE METHOD)

Hitoo Tokunaga<sup>1</sup>, Kiyohiko Ikeda<sup>2</sup>, Koichi Kaizu<sup>2</sup>, and Hiroyuki Kinoshita<sup>2</sup>

<sup>1</sup> Ube National College of Technology, Ube-shi, 755-8555, Japan,

<sup>2</sup> Faculty of Engineering, University of Miyazaki, Miyazaki, 889-2192, Japan  
tokunaga@ube-k.ac.jp

Double torsion (DT) technique has been widely used as crack growth test for brittle materials. The technique is known to be convenient for that the applied stress intensity factor,  $K_I$ , is independent of the crack length, specimen and loading geometries are simple, and the slow crack growth data can be obtained using the load relaxation method. However it is difficult to obtain accurate data by the relaxation method because of extraneous relaxations by thermal expansion and the lack of stiffness in test devices. So, in this study, the new method to estimate the crack growth of ceramics will be suggested by combining a compliance method with a grid pattern film method[1].

At first, we describe about the new method. It is known that the specimen compliance is linear with the crack length [2]. So, it is possible to predict the crack length from the displacement of loading point. In order to obtain the compliance, the loading point displacement  $\Delta$  is measured by a laser displacement meter as shown in Fig. 1(a). On the other hand, the crack length  $a$  is measured by using grid pattern metal film deposited on the tensile stress side of DT specimen as shown in Fig.1(b). In the grid pattern metal film technique the crack length can be detected from stair like responses of electric resistance by cutting the grids with crack growth. On the basis of above measurements, the relative crack length  $a/L$  is expressed as a function of compliance  $\Delta/P$  as follows: [3]

$$a/L = b_0 + b_1 \cdot U + b_2 \cdot U^2 + b_3 \cdot U^3 + b_4 \cdot U^4 + b_5 \cdot U^5 \quad (1)$$

$$U = \left( \sqrt{\frac{BE\Delta}{P}} + 1 \right)^{-1} \quad (2)$$

where  $a$  is the crack length,  $E$  Young's modulus,  $\Delta$  loading point displacement and  $b_0, b_1, \dots, b_5$  are regression coefficients. By using the above equations, the crack length could be determined without doing the direct measurements of the crack length and detaching the specimen from the instrument under crack growth test.

Next, an experiment to examine the validity of the suggested measurement method was performed by using soda lime glass. Figure 2 shows the relationship between loading time  $t$  and crack length  $a$  obtained from DT crack growth test under a constant stress rate. As shown in this figure, it is confirmed that the crack length can be continuously detected over a wide range of crack growth rate by using the suggested method. Furthermore, Figure 3 shows the log-log plots of  $K_I$ - $da/dt$  relation obtained by using crack growth data shown in Fig. 2. The  $K_I$ - $da/dt$  relation plotted in log-log paper exhibits the linear relationship. The obtained  $K_I$  and slow crack growth rate are 0.4 to 0.6 MPam<sup>1/2</sup>, and  $10^{-7}$ - $10^{-4}$  m/s, respectively. The crack growth parameter,  $n$ , determined from the slope of  $K_I$ - $da/dt$  relation is about 13. These results are in good agreement with the results reported by Wiederhorn[4].

As a result, it was found that the crack length in slow crack growth in ceramics can be detected with high accuracy by using the suggested method. Therefore,  $K_I$ - $da/dt$  relation can be evaluated over a broad range of crack growth rate from a single experiment. Furthermore, since the method is based on the simple measurement system, it is considered that the method has a good availability for  $K_I$ - $da/dt$  evaluation in ceramics.

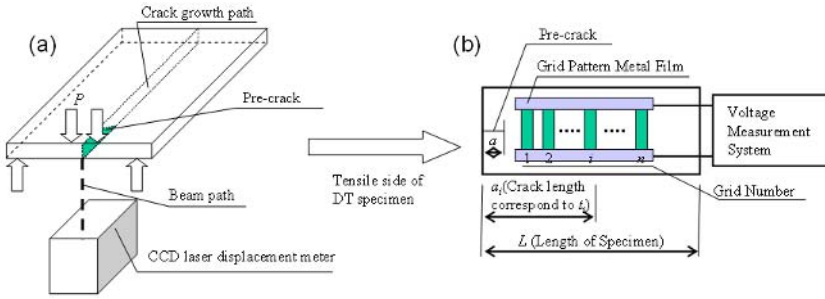


FIGURE 1. Schematic diagram of the crack length measurement system

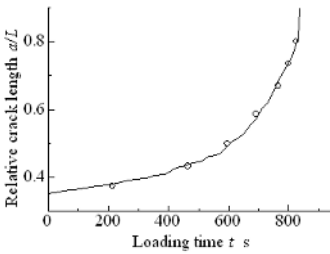


Fig.2 Relationships between loading time and relative crack length

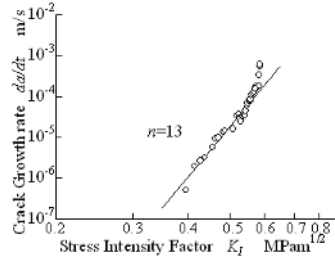


Fig.3 Relationships between stress intensity factor and crack growth rate

**References**

1. Deng, G., Tokunaga, H., et al., *JSME Series C*, vol. **72**, 997-1002, 2006 (in Japanese)
2. Evans, A.G., *Journ. of Materials Sci.*, vol. **7**, 1137-1146, 1972
3. Saxena, A. and Hudak J.Jr., *Int. Journ. of Fracture*, vol. **14**, 453-468, 1978
4. Wiederhorn, S. M., *J. Am. Ceram. Soc.*, vol. **50**, 407-414, 1967

## EXPERIMENTAL STUDY OF THE OUT-OF-PLANE DISPLACEMENT FIELDS FOR DIFFERENT CRACK PROPAGATION VELOCITIES

S. Hédan, V. Valle and M. Cottron

Université de Poitiers, Laboratoire de mécanique des Solides, UMR 6610, Poitiers, France  
 hedan@lms.univ-poitiers.fr, valle@lms.univ-poitiers.fr, cottron@lms.univ-poitiers.fr

The fundamental aim of this study is to determine the influence of crack propagation speed on the out-of-plane displacement fields in the neighbourhood of a crack tip (i.e. on the size of the 3D effects zone). As the crack propagation is a complex process that involves the deformation mechanisms, the out-of-plane displacement measurement gives pertinent information about the 3D effects. We propose in this paper, to analyse the out-of-plane displacements fields for different crack velocities in brittle materials.

For investigations, we use the interferometric method. The optical device includes a laser source, a Michelson interferometer [3, 4] and an ultra high-speed CCD camera. To take into account the crack velocity, we dispose of a maximum frame rate of 1Mfps. The crack velocity is connected to the fracture energy. The experimental tests have been carried out for a SEN (Single Edge Notch) specimen of PMMA material. The crack propagation is initiated by adding a dynamic energy given by the impact of a cutter on the initial crack. The obtained interferograms are analysed with a new phase extraction method entitled MPC [5, 6]. This analysis, which has been specially developed for dynamic studies, gives the out-of-plane displacement field with an accuracy of about 10 nm. The measured out-of-plane displacement are compared with the theoretical expression of Westergaard (i.e. 2D solution) (eq.1) [1] and the Humbert three-dimensional expression (i.e. 3D solution) (eq.2) [2]. In these formulations the cylindrical coordinates ( $R=r/h$ ,  $\theta$ ,  $z$ ) are centred on the crack tip.

$$U_{th}(R, \theta) = -\frac{\nu K_{Id} \sqrt{h}}{E} \cos\left(\frac{\theta}{2}\right) \frac{1}{\sqrt{2\pi R}} + cte \quad \text{with } cte = 0 \quad (1)$$

and the Humbert's formulation i.e. 3D solution [2].

$$U_{3D}(R, \theta) = -\frac{\nu K_{Id} \sqrt{h}}{E} \left[ \frac{c_2 e^{-c_1 R}}{1 + \sqrt{c_1 R}} + (1 - e^{-c_3 R}) \right] \cos\left(\frac{\theta}{2}\right) \frac{1}{\sqrt{2\pi R}} \quad (2)$$

where  $h$ ,  $\nu$ ,  $E$  and  $K_{Id}$  are respectively the thickness, the Poisson's ratio, the Young's modulus and the dynamic stress intensity factor

In our tests, to modify the crack velocity, it is necessary to change the static loading intensity. We made some tests with different loading values and we present some of these tests. For a better comparison, we extracted results from the measured displacement field for only 5 values of  $\theta$  ( $-90^\circ$ ,  $-45^\circ$ ,  $0^\circ$ ,  $45^\circ$ ,  $90^\circ$ ). On the following example (Fig. 1), the analytical and experimental results are presented as a function of  $R$ , for three instants of crack propagation ( $a=38.1$ ,  $40.2$  and  $42.3$  mm) and with a crack velocity of 210 m/s. 2D and 3D solutions are plotted with  $K_{Id}$  respectively equal to 3.50, 3.56, 3.61, 3.66, 3.71 and 3.76 MPa $\sqrt{m}$  according to the crack tip position during the dynamic event. In relation with the experimental data (Fig. 1), the 3D solution coefficients  $c_1$ ,  $c_2$  and  $c_3$  are respectively estimated equal to 1.1, 0.38 and 0.5. We can notice that these coefficients are constant during the crack propagation for a given loading value.

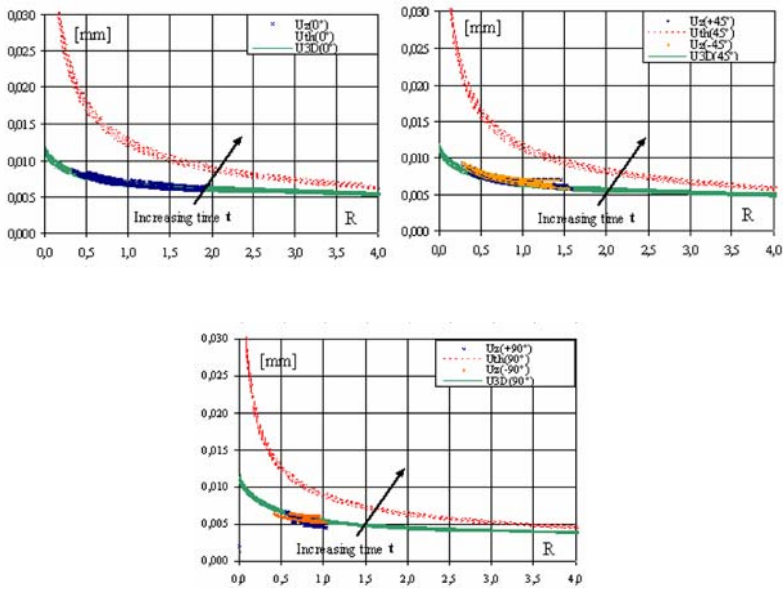


FIGURE 1. Field of theoretical and experimental displacements at  $t = 16, 20, 24, 28, 32$  and  $36 \mu\text{s}$ .

We observe on Fig. 1 that the experimental data give values smaller than those calculated with the 2D solution. This phenomenon was already observed in static by Humbert and is directly connected to the presence of 3D effects. Another remark can be made, concerning the R limit value where the 2D solution is not valid anymore. In static, this 3D limit is equal to  $R=0.5$  [7], but in dynamic, it seems to be higher. We can estimate this limit to  $3 < R < 4$ . In the end of this paper we present the evolution of the 3D limit in function of the crack velocity.

## References

1. Westergaard H.M, *J. of Applied Mechanics*, vol **6**, 49-53, 1939.
2. Humbert L., Valle V. and Cottron M., *Int. J. Solids and Struct.*, vol **37**, 5493-5504, 2000.
3. Pfaff, R. D., Washabaugh, P. D. and Knauss, W. G., *Int. J. Solids and Struct.*, **32**, vol 939-955, 1995.
4. Born M. and Wolf E., *Principles of Optics*, 6<sup>th</sup> ed. Pergamon Press, New York, 1980.
5. Robin E. and Valle V., *J. of Applied Optics*, vol **43**, 4355-4361, 2004.
6. Robin E., Valle V. and Brémand F., *J. of Applied Optics*, vol **44**, 7261-7269, 2005.
7. Rosakis A. J. and Ravi-Chandar K., *Int. J. of Solids and Struct.*, vol **22**, 121 - 134, 1986.

## EXPERIMENTAL STUDY ON THE INFLUENCE OF THE SHAPE AND THE SIZE OF THE SPECIMEN ON COMPRESSION BEHAVIOUR OF HIGH STRENGTH CONCRETE

J. R. Del Viso, J. R. Carmona and G. Ruiz  
Camilo José Cela s/n, 13071 Ciudad Real, Spain.  
Javier.RdelViso@uclm.es

In this paper we investigate the mechanical behavior of high-strength concrete (around 100 MPa) in compression and tested in strain-control. We are particularly interested in the influence of the shape and the size of the specimens on the compressive strength,  $f_c$ , of the material.

In a previous study [1] we managed to get ductile compressive tests by using small cylinders and by controlling the strain instead of the load. The experiments were tested at four strain rates since the purpose of the research was to check the sensitivity of the whole stress-strain curve to the speed at which the specimen is loaded. Here we address the problem of the effects of the size and the shape of the specimens on their mechanical behavior. We use cylinders and cubes of different sizes: the dimensions of the cylinders are 75 x 150, 100 x 200 and 150 x 300 mm (diameter x height); the edges of the cubes are 33, 50, 66 and 100 mm long. The plane sides of the cylinders and all the cubes were polished to avoid local imperfections and to minimize friction against the loading platens. The standard properties of the material are given in Table 1. By 'standard' we mean properties obtained according to well-established procedures, i.e., procedures devised for normal strength concrete. Please, notice that the characteristic length,  $l_{ch}$ , of this concrete is roughly 150 mm, closely half the  $l_{ch}$  of normal concrete. This means that, from a Fracture Mechanics standpoint, we expect that high-strength concrete (HSC) is more brittle than NSC for the same specimen size [1-4].

Cylinders and cubes were tested in strain control at a rate that was kept constant throughout the experimental program. Figure 1a shows some of the curves obtained. The abscissa is the average strain, i.e. the displacement between the top and bottom plane surfaces over the height of the specimen. It is clear that the post-peak behavior of the cubes is milder than that of the cylinders [1, 3, 4], which results in a strong energy consumption after the peak. This is consistent with the observation of the crack pattern (Fig. 2): the extent of micro-cracking throughout the specimen is denser in the cubes than in the cylinders. Indeed, a main inclined fracture surface is nucleated in cylinders, whereas in cubes we find that the lateral sides get spalled and that there is a dense columnar cracking in the bulk of the specimen. Figure 1b compares the compressive strength,  $\sigma_c$ , obtained for the various specimens tested. The size effect in the cubes is quite strong, although it looks that the biggest cube is close to the behavior expected for the infinite size. By contrast, the average  $\sigma_c$  obtained from cylinders is roughly constant and approximately 10% lower than the horizontal asymptote for the cubes. According to our results and having in mind that cubes do not need capping nor polishing of their edges to be tested, the optimum specimen for HSC would be a cube whose edge be commensurate to the internal characteristic length of the material, approximately 150mm.

TABLE 1. Material properties.

$f_c$ (MPa)	$f_t$ (MPa)	$E_c$ (GPa)	$G_f$ (N/m)	$l_{ch}$ (mm)
94.2	5.4	36.1	119.0	147.3

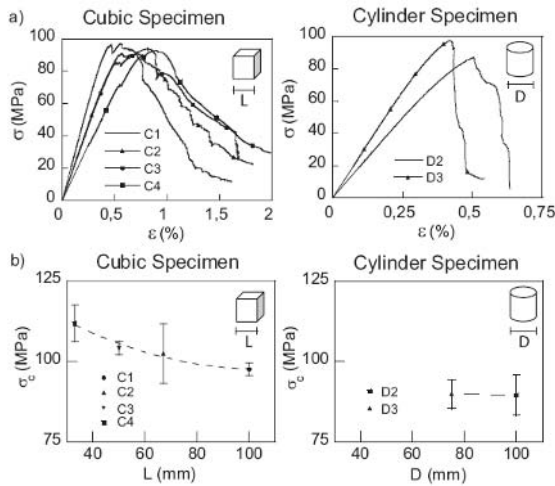


FIGURE 1. a) Stress-strain curves; b) Compressive strength versus size of the specimens.

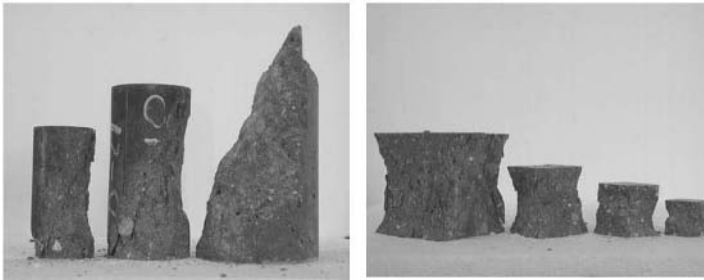


FIGURE 2. Cylinders and cubes after being tested. (See pdf)

## References

1. G. Ruiz, del Viso J. R., Carmona J. R., *Characterization of the ductility and of the mechanical behaviour at various strain-rates of high-strength concrete (over 100 MPa)*, 6<sup>th</sup> Int. Conference Fracture Mechanics of Concrete and Concrete Structures (FraMCoS-6) Catania (Italy). Submitted.
2. Jose Umberto A. Borges, Kolluru V. Subramaniam, W. Jason Weiss, Surendra P. Shah and Túlio N. Bittencourt, *Length Effect on Ductility of Concrete in Uniaxial and Flexural Compression*, ACI Structural Journal, vol. **101**, No. 6, November-December 2004.
3. Shah, S. P., Swartz, S. E., and Ouyang, C. *Fracture Mechanics of Concrete*. Wiley, New York, 1995.
4. Jansen, D.C., and Shah, S.P., 1997, "Effect of Length on Compressive Strain Softening of Concrete," Journal of Engineering Mechanics, ASCE, vol. **123**, no. 1, pp. 25-35.



## **SPECIMEN GEOMETRY AND MATERIAL PROPERTY UNCERTAINTY MODEL FOR PROBABILISTIC FATIGUE LIFE PREDICTIONS**

Prakash Chandra Gope, Sandeep Bhatt and Mohit Pant

Mechanical Engineering Department, College of Technology, G B Pant University of Agriculture  
& Technology, Pantnagar-263145, India  
pcgope@rediffmail.com

The present paper describes an analytical model derived from energy theorem which is coupled with the uncertainty associated with material properties and geometrical parameter to estimate fatigue life and crack growth at different level of probability and confidence level.

The analysis of cracks within structure is an important application if the damage tolerance and durability of structures and components are to be predicted. As part of the engineering design process, engineers have to assess not only how well the design satisfies the performance requirements but also how durable the product will be over its life cycle. Often cracks cannot be avoided in structures; however the fatigue life of the structure depends on the location and size of these cracks. In order to predict the fatigue life for any component, crack growth study needs to be performed.

Fatigue life is related to and is affected to a great extent with the uncertainties in both the material properties and the specimen or component geometrical parameters. The intent of the work is to contribute to the fundamental understanding of fatigue life and its relation with these uncertainties. Fatigue life data exhibits wide scattered results due to inherent microstructural inhomogeneity in the material properties even if the test specimens are taken from the same lot and tested under same loading condition. As the fatigue testing is time consuming and costly, setting up of an analytical method for prediction of fatigue life is necessary.

The different monotonic material properties such as yield strength, modulus of elasticity; fracture properties such as critical stress intensity factor, threshold and crack opening stress intensity factors, loading parameters and geometry parameters such as specimen or component width, thickness, length, crack aspect ratio etc. have been considered in the model. These parameters are treated as random variable and assuming normally distributed, the associated uncertainty in these parameters are incorporated in the crack growth model. The assumptions of these variables are also verified from the simulated results. Crack growth model is derived from the energy theorem. In the present work an approximate analytical model derived from the energy theorem and probabilistic nature of material properties and specimen geometry parameters are combined and correlated to determine the associated error in the predicted fatigue life. The Error in estimating the fatigue life is derived from the expected values of fatigue life. The prediction is based on minimization of the error. The model can also be used to predict the fatigue life or crack growth at different level of probability and confidence. Hence it can be used to draw P-S-N curve. Some of the predicted results are shown in Figs 1 and 2. A substantial amount of published data has been presented to validate the proposed model for predicting S-N curve as well as fatigue crack growth of steel, aluminum alloys, copper alloys and titanium alloys. Some of are 4340, 304 steel, 0.26 % Carbon steel, different aluminum alloys, titanium alloys etc. Different test geometry such as CT specimen, SEN specimen geometry etc has also been taken to find out the acceptability of the model.

Table 1. Some mechanical & geometrical parameters of 7075-T6 al alloy

Parameters	Modulus ( GPa)	YS (MPa)	$K_{IC}$ $MPa\sqrt{m}$	$K_{th}$ $MPa\sqrt{m}$	$K_{op}$ $MPa\sqrt{m}$	Aspect ratio	W (mm)
Mean values	68.9	540	30	1.7	*	0.2	50
Co-eff. of var (%)	6.8	5.8	5.9	5.9	5.3	3.2	4.9

The model was used to study the crack growth also. The model was also verified with the ASTM procedure described in its standard E 739-91. It is found that present model can be used successfully to find out the S-N curve at different probability and confidence level only from the monotonic and fracture properties of the material.

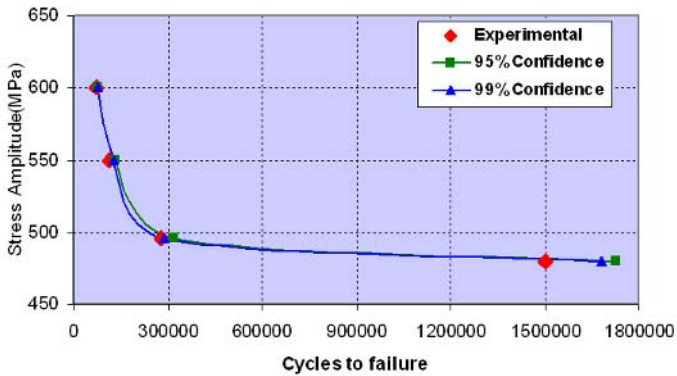


FIGURE 1. S-N curve for Ti-6Al-4V alloy at 50 % probability of failure

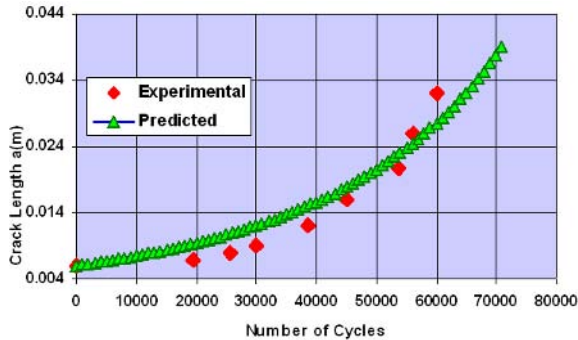


FIGURE 2. Crack growth curve for 7075 Al alloy (R=0)

**References**

1. Ramsamooj D. V., and Shugar, T. A., *International J. Fatigue*, S287-S300, 2001
2. Gope P. C , *Journal of Engg. Materials and Technology, ASME Trans*, 2002
3. Gope P. C, *International Journal of Fatigue*, vol. **18** (8), 745, 1999

## PHOTOELASTIC STUDIES OF MIXED MODE STRESS INTENSITY FACTORS UNDER BIAxIAL LOADING CONDITION

Vinay Kumar Singh and Prakash Chandra Gope  
Department of Mechanical Engineering, College of Technology,  
G. B. Pant University of Agriculture & Technology, Pantnagar-263145, India  
pcgope@rediffmail.com

The effect of biaxial load factor, crack inclination angle and aspect ratio on stress intensity factors  $K_I$ ,  $K_{II}$  and constant stress term,  $\sigma_{ox}$  is investigated. The theory of determining the stress intensity factors using photo elastic method is formulated taking three stress terms. Three-parameter method of fracture analysis for determining the mixed mode stress intensity factors under biaxial loading conditions from photo-elastic isochromatic fringe data is used. A special biaxial test rig is designed and fabricated for loading the specimen biaxially. A simplified and accurate method is proposed to collect the data from isochromatic fringes. Taking specimen geometry and boundary conditions into account, regression models are developed for estimation of fracture parameters. Experimental results are compared with theoretical results.

Many authors have shown the application of photo-elasticity in the study of fracture mechanics. Most of the studies for evaluating mixed mode stress intensity factor are for uniaxial loading. Experimental study of the effect of biaxial load factor and specimen geometry on mixed mode stress field parameters  $K_I$ ,  $K_{II}$  and  $\sigma_{ox}$  is very limited. This paper deals with the study of the effect of biaxial factor on stress intensity factors.

A biaxial test rig was designed, fabricated and calibrated with standards and shown in Figure 1. The material used in the present casting is 100 parts by weight of Araldite CY-230 and 9 parts by weight of hardener HY-951. Square pieces of 100 mm×100 mm×2.55 mm size were cut from a cast plate. Mechanical slits were made at the center of the plate at required angle of inclination with respect to vertical loading axis by the method described in the literature. The final crack lengths taken are 12, 16 and 20 mm and crack inclination angles are 0, 30, 45 and 60°. Specimen was subjected to both horizontal and vertical loads. The biaxial load factor was varied from 1.0 to 2.0 in a step of 0.2. A special technique has been developed for data collection. Collected data on the basis of presented method shows that the standard deviation and coefficient of variation from 10 observations from the identical test conditions are less than 0.035 and 0.007, respectively. Starting from complex stress functions near an inclined crack under biaxial loading condition, N-K relation have been derived taking into consideration of the non-singular (three) stress terms. The relations have been solved to study the effect of crack angle, load biaxiality and aspect ratio on the stress intensity factors and T stress.



## FRACTURE STRAINS AT HOLES IN HIGH-STRENGTH STEEL, A COMPARISON OF TECHNIQUES FOR HOLE-CUTTING

J. Eman and K. G. Sundin  
Solid Mechanics, Luleå University of Technology  
LTU, SE-97187 Luleå, Sweden  
kgsundin@ltu.se

Sheet metal is often used as a raw-material from which structural parts are fabricated through pressing operations. This is the case for example in the vehicle industry where the entire structure of a car is made from sheet material. In many modern cars, crash-protecting parts are made from ultra-high strength steel and such parts are often press-hardened to a tensile strength of 1500 MPa or more in a process with simultaneous forming and quenching. Holes in these parts are sometimes necessary for practical reasons and the fracture criteria used in the design process must be relevant also for such cases.

The ductility of the material is fully utilized in the deformation of the part during the crash process. In modeling and simulation it is therefore important to describe correctly the behavior of the material up to the onset of fracture. The process of hole-making and the technique used will influence the material behavior close to the boundary through heat effects, micro-cracks and so on. Therefore the fracture criterion used for the homogeneous material may be erroneous for the material influenced by a hole. This work presents the result of an experimental investigation of the deformation field close to holes in sheet specimens just before the onset of fracture. In Fig. 1 the principle of the specimen and the evaluated strain field are sketched.

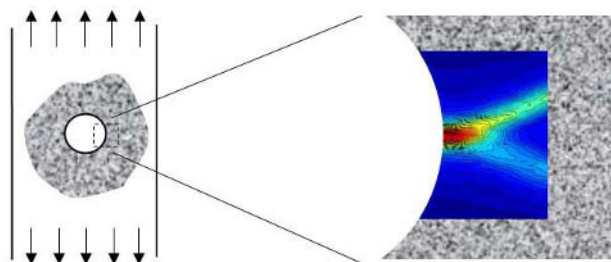


FIGURE 1. Tensile hole-specimen with speckled area for strain monitoring and plot of experimentally obtained strain-field at onset of fracture.

Digital speckle correlation is used to monitor the deformation. The basic principle is that a sequence of digital photographs of white-light speckles is recorded during tensile loading of the specimen and the in-plane deformation field is obtained from the changes in speckle pattern by correlation of sub-areas. Strains are then calculated from measured displacements. Recent reviews and evaluations of the method can be found in Tong [1], Schreier and Sutton [2] and Hild and Roux [3] and some examples of its application in Kajberg and Lindkvist [4], Quinta da Fonseca *et al* [5], Wattrisse *et al* [6] and Brunet and Morstin [7].

The tested material is a boron-steel called Boron 02. It has a small content of boron (30ppm) which makes the material suitable for the press-hardening (or hot stamping) process where the hot blank (900 °C) is formed, fixed and quenched between cooled tools. In this case flat tools are used to produce flat sheet material for specimens. Abrasive water cutting is used to cut specimens from the hardened sheets with thickness 1.2 and 2.4 mm respectively. Holes in the specimens are produced with the following methods; 1) Punching before heating, 2) Punching after quenching, 3) Laser cutting after quenching. The width of the specimens is 40 mm and the diameter of the holes is 4 and 8 mm respectively.

From the evaluated strain fields in the sequence of frames taken during loading to fracture, the evolution of the plastic localization and the necking process is investigated and quantified. For example, the maximum equivalent strain in the specimen just before fracture is monitored and the difference in strain level between the techniques for hole-making is documented. These results are also compared with results from specimens without holes that are designed so that fracture emanates from the central part. Hence, fracture behavior at holes and the effect of edges are compared to fracture behavior at an inner point in the sheet material through experimental observations of the developing plastic strain field.

## References

1. Tong, W., *Strain*, vol. **41**, 167-175, 2005.
2. Schreier, H.W. and Sutton, M.A., *Experimental Mechanics*, vol. **42**, 303-310, 2002.
3. Hild, F. and Roux, S., P.A., *Strain*, vol. **42**, 167-175, 2006.
4. Kajberg, J. and Lindkvist, G., *Int. J. Solids and Structures*, vol. **41**, 3439-3459, 2004
5. Quinta da Fonseca, J., Mummery, P.M. and Withers, P.J., *J. Microscopy*, vol. **218**, 9-21, 2004.
6. Wattrisse, B., Chrysochoos, A., Muracciole, J.-M. and Némot-Gaillard, M., *Experimental Mechanics*, vol. **41**, 29-39, 2001.
7. Brunet, M. and Morestin, F., *J. Mater. Process. Technol.*, vol. **112**, 214-226, 2001.

## CHARACTERIZATION OF CONCRETE IN MIXED MODE FRACTURE UNDER CONFINED CONDITIONS

Oscar I. Montenegro<sup>1</sup>, D. Sfer<sup>2</sup> and I. Carol<sup>1</sup>

<sup>1</sup> ETSECCPB (School of Civil Engineering)-UPC (Technical Univ. of Catalonia).  
Jordi Girona 1-3, Campus Nord – Edif. D-2, E-08034 Barcelona, Spain

<sup>2</sup> Universidad Nacional de Tucumán – Instituto de Estructuras.

Avenida Roca 1800, 4000 – Tucumán - Argentina

oscar.montenegro@upc.edu, dsfer@herrera.unt.edu.ar, ignacio.carol@upc.edu

Although considerable research has been devoted to concrete fracture in recent years, cracking and fracture under confined conditions remain largely unstudied. From the theoretical/numerical viewpoint, some models have been proposed which advocate for the asymptotic mixed mode (mode IIa) with a second fracture energy independent and significantly higher than the traditional mode I energy [1,2]. In 1990, the Group of Mechanics of Materials of the School of Civil Engineering at UPC Barcelona (ETSECCPB-UPC), introduced the concept of asymptotic shear-compression mixed mode, or *mode IIa*, for frictional materials such as concrete, consisting of a shear (mode II) crack developing under very high compression level across the fracture plane, such that all dilatancy would be suppressed and the crack would become sensibly straight, cutting through heterogeneities such as aggregates and matrix (Carol and Prat [1], Carol et al. [2]).

In conventional concrete, the strength of aggregates is larger than that of the mortar, and the interface between them represents the weakest part of the composite. Thus, the proposed mode IIa cracking would be in contrast to the traditional cracking mode observed in mode I, in which the cracks normally exhibit a winding path following aggregate–mortar interfaces (Fig. 1).

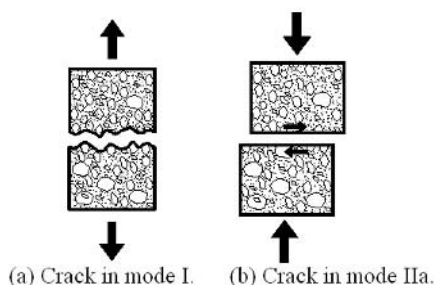


FIGURE 1. Paths of cracks.(a) Crack in mode I.(b) Crack in mode IIa.

Since first proposed, the model based on the new mode IIa, has been implemented in a FE code by means of the so-called "zero-thickness interface elements", and has been used quite successfully in a number of numerical studies. However, experimental validation was a pending task. Attempts to reproduce shear compression cracks can be found in the concrete literature, for instance with notched beams subject to transversal compression. However, in most cases the crack has the tendency to deviate from the prescribed fracture plane and results are not useful for the purpose.

In this paper, some recent experimental work developed at ETSECCPB-UPC is described.

The specimens employed are similar to those proposed by Luong [3,4], short cylinders with coaxial cylindrical notches from top and bottom faces leaving an also cylindrical ligament (Fig. 2.a). They are loaded vertically on the outer (top) and inner (bottom) parts of the circular faces, originally with no confinement. In the setup developed, this specimen is introduced in the large-capacity triaxial cell, protected with membranes and subject to different levels of confining pressure prior to vertical loading (Fig. 2.b).

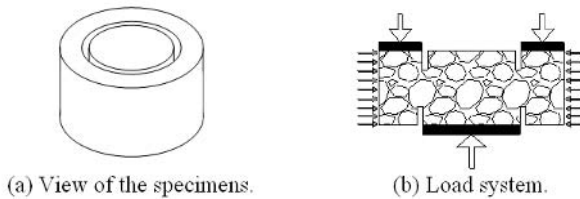


FIGURE 2. Fracture mixed mode tests.

Special measuring devices have been also developed to operate inside the pressure chamber. The preliminary results obtained look very promising, with load-displacement and load-dilatancy curves that exhibit the expected trends. Post-mortem observation of specimens also shows the predicted features regarding fracture plane, aggregate fracture, etc. On-going work is aimed at solving remaining experimental details and then evaluating the associated fracture energy under "mode IIa".

## References

1. Carol and Prat, Multicrack model based on the theory of multisurface plasticity and two fracture energies. In *COMPLAS4. CIMNE (UPC)*, edited by E. Oñate et al. eds, Barcelona, 1583-1594, 1995.
2. Carol, Prat and Lopez, Normal/shear cracking model: Application to discrete crack analysis. *Journal of Engineering Mechanics*. vol. **123**, No.8, 765-773, 1997.
3. Luong, M.P., Tensile and shear strength of concrete and rock. *Engineering Fracture Mechanics*, vol. **35**, N°1/2/3, 127-135, 1990.
4. Luong, M.P., Fracture testing of concrete and rock materials. *Nuclear Engineering and Design*, vol. **133**, 83-95, 1992.



## V-NOTCHED SPECIMEN UNDER MIXED-MODE FRACTURE

N. Recho<sup>2</sup>, J. Li<sup>1</sup> and D. Leguillon<sup>3</sup>

<sup>1</sup>LPMTM, CNRS UPR 9001, University of Paris XIII, Villetaneuse, France.

<sup>2</sup>LMM, University of Paris VI, France and LaMI, University Blaise Pascal, Clermont-II, France.

<sup>3</sup>LMM, University of Paris VI, France.

li@lpmtm.univ-paris13.fr, recho@lmm.jussieu.fr, dol@ccr.jussieu.fr

A general methodology to study the crack nucleation and propagation initiated from a V-notch was established under mixed-mode static loading on the basis of a criterion involving both strength and toughness of the material and developed in recent studies of one of the authors [1]. In order to predict the critical load and the path corresponding to the onset and growth of a crack, a series of experiments on V-notched specimens under mixed-mode loading have been performed on CTS (Compact-Tension-Shear) PMMA specimens under mixed mode-loadings, using a device initially developed by Richard [2], see Figs 1 and 2. The effect of the loading angle on the crack direction angle is analyzed. On the basis of these experimental results, a crack nucleation model is proposed.

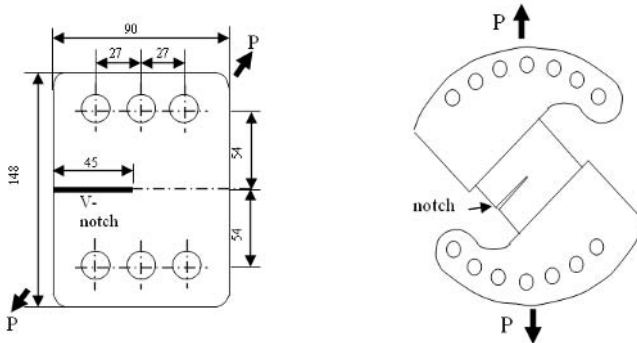


FIGURE 1. Specimens and loading device (*Dimensions in mm*)

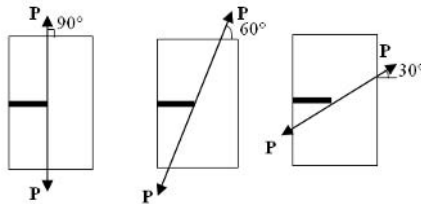


FIGURE 2. Loading angles  $\beta$

All specimens are made of PMMA (Young's modulus  $E = 3300\text{MPa}$ , ultimate strength

$\sigma_f$  76 MPa, elongation to rupture  $\epsilon_c$  5%). The specimens are 10mm thick. Specimens are machined with five different V-notch angles ( $30^\circ$ ,  $60^\circ$ ,  $90^\circ$ ,  $120^\circ$ , and  $160^\circ$ ).

The tests are conducted on a machine MTS-810 (Material Test System) at room temperature. The CTS specimens are tested with four loading angles  $90^\circ$ ,  $60^\circ$ ,  $30^\circ$  and  $0^\circ$  with respect to the notch bisector. They make it possible to introduce mixed modes I and II. The  $90^\circ$  case corresponds to a pure mode I test. Two or three specimens are used for each loading condition. Each test is carried out under monotonic quasi-static loadings (2mm/minute) until the appearance of a crack. Following, a total unloading occurs. The re-loading is performed on the specimen containing the crack until the final failure. Two kinds of crack surfaces are visible, the first one corresponds to the initiation phase while the second is associated with the brittle crack growth. The second step allows calculating the critical energy release rate from the measure of the load to rupture and from a finite element simulation.

Figure 3 shows an example of specimens after the crack extension. The developed methodology is compared to the experimental results. It enables us to compare experiments and prediction of the crack angle according to the notch and loading angles. Moreover, there is an agreement between experiments and predictions to show an increase of the critical load at crack onset with the angle of loading  $\beta$  as a consequence of the increasing role played by the mode II.

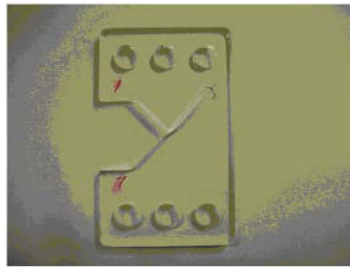


FIGURE 3. test  $\alpha=90^\circ$ ,  $\beta=30^\circ$

## References

1. Leguillon, D., "Strength or toughness? A criterion for crack onset at a notch", *European J. Mech. A/Solids*, vol. **21** pp.61-72, 2002.
2. Richard, H.A., and Benitz, K., "A loading device for the creation of mixed mode in fracture mechanics". *Int. J. Fracture*, vol. **22**: R55. 1983.

## GENETIC PROGRAMMING IN MODELLING OF FATIGUE LIFE OF COMPOSITE MATERIALS

Anastasios P. Vassilopoulos<sup>1</sup>, Efstratios F. Georgopoulos<sup>2</sup>, Thomas Keller<sup>1</sup>

<sup>1</sup> Composite Construction Laboratory (CCLab), School of Architecture Civil and Environmental Engineering, Swiss Federal Institute of Technology, EPFL, Station 16, CH-1015 Lausanne, Switzerland

<sup>2</sup> Technological Educational Institute of Kalamata, GR-241 00 Kalamata, Greece  
anastasios.vassilopoulos@epfl.ch, sfg@teikal.gr, thomas.keller@epfl.ch

In the current paper a novel method that uses a Genetic Programming tool is proposed for modelling fatigue life of multidirectional laminates made of GFRP composite materials and tested under constant amplitude loading patterns.

The main benefit of this novel modelling tool is that only a small portion, in the range of 40%-50%, of the experimental data is needed for the production of a model. Thus, expensive tests for determination of S-N curves could be significantly reduced without noteworthy loss of accuracy. Another asset of the proposed method is that it generates mathematical models and it is not a “black box” technique like, for example, artificial neural networks [1-2].

Genetic Programming [3-4] is an evolutionary method that works by emulating natural evolution, as introduced by Darwin, in order to produce a model structure that optimizes (minimizes or maximizes) some fitness measure (Mean Square Error, for example). Genetic Programming uses a population of models, which are represented in tree form, and evolves it through many generations towards finding some solution. The Genetic Programming method for the production of a model works briefly as follows [3]:

- An initial population (generation 0) of models is generated in random; every model (structure and parameters) of this initial population is produced randomly. The models usually are represented as trees like the one in Fig. 1. If this tree representation is been turned clockwise it can be viewed as a conventional system block diagram. Each tree is of variable length, as it is constructed of nodes and represents one candidate model. The nodes can be terminal nodes (called also leafs) placed at the end of a branch signifying an input or a constant, or non-terminal nodes representing functions performing some action on their terminal nodes (see Fig. 1).
- The performance of each model in the population is evaluated by simulating the corresponding model and calculating some fitness measure like Mean Square Error, Mean Relative Error etc. that define the quality of the model with respect to the experimental data.
- A new population of models is created, using certain selection schemes (like proportional selection, tournament selection, rank based selection, etc.) and evolutionary operators like crossover and mutation.
- Then the algorithm proceeds with the evaluation of this new population (go to step 2) and so on. After some number of generations the algorithm converges at a near-optimum for the problem model.

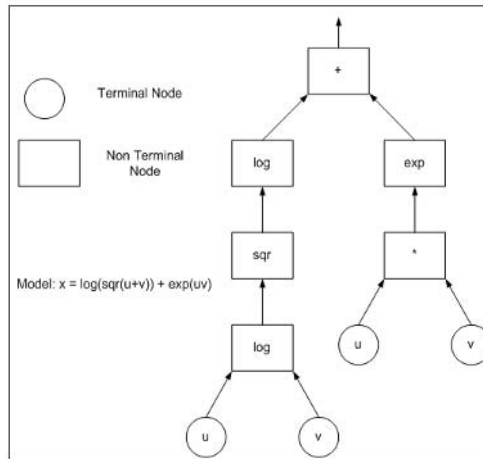


FIGURE 1: A tree representation of a simple model

The Genetic Programming method has been applied using experimental data from two different (in nature) material systems and it has been proved that fatigue life of both can be efficiently modelled using a much smaller set of experimental data compared to that needed for the determination of stress- or strain-life curves (S-N or -N curves) by the conventional way.

Modelling efficiency of the models produced by the Genetic Programming tool is satisfactory for both material systems, irrespective of the test conditions, i.e., R-ratio, that defines the developed stress state on the coupon. Tension-Tension, Compression-Compression and even Tension-Compression loading patterns were investigated and modelling accuracy of the proposed method was validated. Because of its simplicity and flexibility, this technique seems to be very promising for application on other engineering problems as well.

## References

1. Vassilopoulos, A.P., Georgopoulos, E.F. and Dionyssopoulos V, *Adv. Compos Lett*, vol. **15** (2), 43-51, 2006
2. Vassilopoulos, A.P., Georgopoulos, E.F. and Dionyssopoulos V, *Int. J. Fatigue*, in press, doi:10.1016/j.physletb.2003.10.071
3. Banzhaf W.P., Nordin P, Keller R.E., and Francone F.D., *Genetic programming: An introduction*, Kaufmann, San Mateo, CA, 1998
4. Koza J.R., *Genetic programming: on the programming of computers by means of natural selection*, MIT Press, Cambridge, MA, 1992

## FATIGUE BEHAVIOUR OF ADHESIVELY BONDED PULTRUDED GFRP

Ye Zhang, Anastasios P. Vassilopoulos and Thomas Keller

Composite Construction Laboratory (CCLab), School of Architecture Civil and Environmental Engineering, Swiss Federal Institute of Technology, EPFL, Station 16, CH-1015 Lausanne, Switzerland  
 ye.zhang@epfl.ch, anastasios.vassilopoulos@epfl.ch, thomas.keller@epfl.ch

Adhesively bonded FRP joints have been successfully used in aerospace and automotive structures and a lot of knowledge about their fatigue behaviour has already been obtained. During the last years, adhesively bonded joints are also used in the civil infrastructure sector [1-2] in order to replace welding or bolted connections and overpass their problems.

The fatigue behaviour of adhesive joints is influenced by many factors, such as, joint geometry, environmental ageing, loading patterns, type of adhesive etc. The aim of this on-going work is mainly to investigate the fatigue behaviour of adhesively bonded pultruded GFRP materials, under various environmental conditions, and to provide certain practical guidelines for structural engineers.

In this work, adhesively bonded joints composed of pultruded GFRP laminates, including double lap joints (DLJ) and step lap joints (SLJ), were experimentally investigated under different environmental conditions. Having as basis the ultimate tensile stress (UTS) of the coupons, constant amplitude fatigue tests, under tension-tension,  $R=0.1$ , loading were realized. Tests at four different stress levels were conducted for each type of joints, DLJ and SLJ, in order to determine the S-N curve. Each S-N curve were determined using 12 coupons, three at each one of the four selected stress levels, at 45%, 55%, 65%, 80% of UTS. Stress level selection was performing in order to have representative experimental data in the region between  $10^2$  and  $10^7$  cycles. After an exploratory study it was shown that the frequency is not affecting fatigue life, if in the range between 2-10 Hz. This effect has also been reported elsewhere [3] for a different epoxy adhesive. However, in order to test as closer as possible to real loading conditions, it was decided to perform tests at a constant frequency of 2 Hz, for all stress level. The only exception was the lower stress level, at 45% of UTS where, due to time limitations (10 million cycles were anticipated) it was decided to perform the tests at a frequency of 10 Hz.

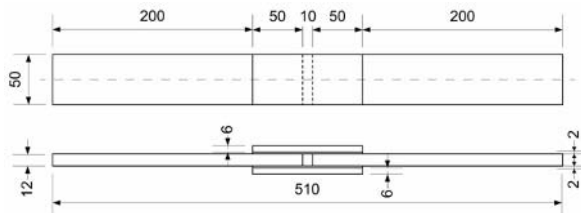


FIGURE 1. Double lap joint configuration

Double lap joints geometry is schematically depicted in Fig. 1. The overlap length of 100 mm, the bonded length of  $4 \times 50$  mm and the thickness of the configuration and the adhesive layer are significant design parameters.

Similar geometrical characteristics for step lap joint configuration are presented in Fig. 2.

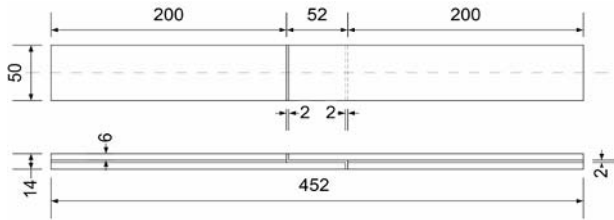


FIGURE 2. Step lap joint configuration

Several measurements were performed during fatigue tests. Along with applied load and grip displacement, per cycle, strain at predetermined points was recorded by using strain gauges. Failure of coupons was driven by a crack that was initiated and propagated in certain area. Thus, crack propagation gauges were glued at the side faces of the coupons, to monitor the crack initiation and propagation during the cyclic loading. Based on results from crack propagation gauges, the crack propagation rate  $da/dN$ , was plotted against the maximum strain energy release rate,  $G_{\max}$  to describe the fatigue behaviour of the adhesively bonded joints. The crack initiation process was obvious for both types of joints. The second phase of damage evolution, crack propagation was also identified. However, the final failure was very brittle.

Fatigue behaviour of two different types of adhesive joints, that are widely used in infrastructure constructions is modelled using two different approaches, fracture mechanics and stress-life, or stress based approach. Based on these experimental data a theoretical model for fatigue life prediction of adhesive joints under different environmental conditions and for several geometrical configurations is under development. First experimental results have already been collected and analysed. Two S-N curves, one for each type of joints have been determined experimentally. During these tests crack initiation and propagation measurements were also performed. The basis for the theoretical models has also been set. In this first phase of the work, comparisons between theoretical predictions and experimental data are very promising.

## References

1. Keller T. and Zhou A., *Compos Part A-Appl S*, vol. **17**, 1119-1130, 2006
2. Keller T. and Gurtler H., *Compos Struct*, vol. **74**, 202-212, 2006
3. Crocombe A.D. and Richardson G., *Int. J Adhes Adhes*, vol. **19**, 19-27, 1999

## UPPER TAIL OF MATERIAL STRENGTH DISTRIBUTION AND STRENGTH PREDICTION OF BONDED JOINTS COMPOSED OF PULTRUDED ADHERENDS

Till Vallée<sup>1</sup>, Thomas Keller<sup>1</sup> and Gilles Fourestey<sup>2</sup>

<sup>1</sup> Composite Construction Laboratory (CCLab) and

<sup>2</sup> Chair of Modelling and Scientific Computing (CMCS)

EPFL, CH-1015 Lausanne, Switzerland.

till.vallee@epfl.ch, thomas.keller@epfl.ch

The strength prediction of adhesively bonded joints composed of glass fiber reinforced polymer (GFRP) pultruded adherends, due to huge stress concentrations at the ends of the overlaps, cannot be done using a simple stress based approach.

Based on a previously developed probabilistic strength prediction method for such joints [1,2], where it was found that a two-parameter Weibull probabilistic distribution was not able to model accurately the upper tail of the cumulative distribution function (pdf) of the material strength, different improved probabilistic distributions were compared to enhance the quality of predictions, see Fig. 1.

For a 2P Weibull, it has been shown, using the Bootstrap technique [3], that the inaccuracy in the prediction does not result of an inappropriate estimation of the statistical parameters. It is per se not able to model accurately the upper tail of the experimental data.

It has also been shown that taking into account the flattening of the pdf at the upper tail greatly enhances the quality of the predictions. A 2-fold and 3-fold pdf, as well as a Grafted pdf, slightly enhanced the quality of the predictions.

The best predictions were obtained by using a General Lambda Distribution (GLD), a family of four-parameter distributions known for their high flexibility [4], where the resulting strengths diverged (at average) by less than 8.5% compared to experimental values.

The quality of the pdf resulting of the GLD was then compared to a pdf resulting from a Genetic Algorithm, search procedures that use the mechanics of natural selection and natural genetics, which was fitted to match the experimental strength. It has been independently found that both pdf compare well, see Fig. 2, giving more confidence to the GLD results.

The paper also addressed potential reasons for the relatively large deviation of the best-adapted pdf from the linear form assumed by the 2P Weibull. Two major reasons were invoked: i) possible damages occurring by micro-cracks or cavitation and/or ii) a possible non-linear behavior of the FRP material at higher stresses, beyond those that it was possible to reach by testing the 40x40mm samples.

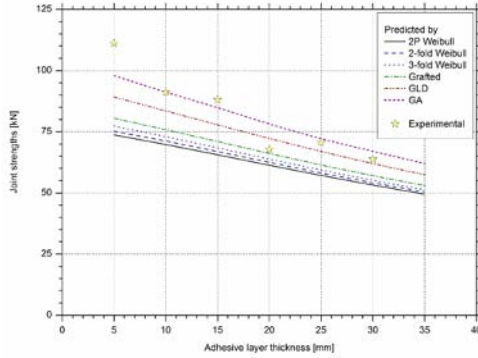


FIGURE 1. – Joint strength predictions using different statistical methods

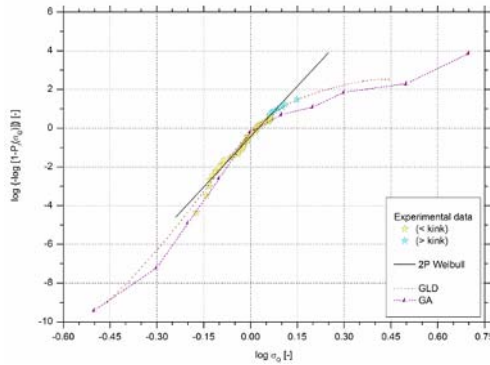


FIGURE 2 – GLD and GA pdf compared to experimental data

**References**

1. T. Vallée, J. R. Correia and T. Keller, Probabilistic strength prediction for double lap joints composed of pultruded GFRP profiles part I: Experimental and numerical investigations, *Composites Science and Technology*, Volume 66, Issue 13, October 2006: 1903–1914.
2. T. Vallée, J. R. Correia and Thomas Keller, Probabilistic strength prediction for double lap joints composed of pultruded GFRP profiles - Part II: Strength prediction, *Composites Science and Technology*, Volume 66, Issue 13, October 2006: 1915–1930.
3. Efron, B., Bootstrap methods: Another look at the jackknife, *Ann. Statist.*, vol. 7, 1979:1–26.
4. Biggerelle, M. and Najjar, D., Fournier, B. and Rupin, N. and Iost, A., Application of Lambda Distributions and Bootstrap analysis to the prediction of fatigue lifetime and confidence intervals, *International Journal of Fatigue*, vol. 28, 2005:223–236.



## CRACK PROPAGATION IN NAVAL ALUMINUM PANELS

Konstantinos P. Galanis and Vassilios J. Papazoglou  
National Technical University of Athens  
School of Naval Architecture and Marine Engineering  
Shipbuilding Technology Laboratory  
9, Heroon Polytechniou Ave., GR-157 73 Zografou Athens, Greece  
galanis@naval.ntua.gr, papazog@deslab.ntua.gr

A ship structure can be regarded as a complex assemblage of continuous stiffened plates. The most common mode of failure of such plates is fracture. Crack propagation and arrest in naval aluminum panels, however, has not been an area of in-depth research. As a consequence, the increased use of aluminum in the shipbuilding industry is highly dependent on the understanding of the fracture mechanics that govern naval aluminum panels, given that the vessels operate in extreme environmental and functional conditions that may lead to the loss of the entire structure.

The crack arrest phenomena in cylindrical containers and pipes have been extensively studied in relation to the pressure vessel technology, e.g. Freund et al. [1] and Zhuang and O'Donoghue [2]. Similar analyses, though, are not readily available for the case of the tearing fracture mode in plates, in which case the mechanics of the crack arrest process must be well understood. For example, the webs or girders in the Advanced Double Hull (ADH) structure seem to offer a formidable obstacle for a propagating crack in the transverse direction.

Tearing fracture in stiffened plates was considered up to now to be arrested for a while at the foot of the stiffener, and then be re-initiated on the other side of the stiffener; eventually the longitudinal stiffener would fracture as well. A test on a quarter model of splitting damage of a longitudinally stiffened, double hull, which was performed by Rodd [3], gives only a glimpse on this important phenomenon. It is still unknown, however, what aspect of the design (strength of the fillet weld, relative thickness of the bare plate and stiffener, height of the stiffener or hull separation) will stop the crack, re-direct it or overcome the obstacle, Fig. 1. Recently, Paik and Thayamballi [4] have performed some work on the estimation of the strength of cracked aluminium unstiffened plates.



FIGURE 1. A conceptual sketch of the crack arrestor. Stopping the crack (left), redirecting (center), and passing through (right)

As a first step and in order to map the crack path in naval panels, a series of experimental tests and numerical analyses were performed based on the standard Compact Tension (CT) specimen. For this case, the aluminium alloy grade 1561 (relevant to AlMgMnZr based on ISO 209-1) of 4 mm thickness was selected which has a density of  $2.65 \cdot 10^3$  kg/m<sup>3</sup> and yield stress of 190 MPa. The CT specimens were tested by varying several parameters, such as the structural configurations,

the geometries of the specimen and the crack tip, the displacement rate, the stiffener type and configuration (extruded and welded) and the crack length, Fig. 2. Additionally, several uniaxial tests of “dogbone” specimens were performed to verify the material properties, to examine the failure mode of the naval aluminium and for calibrating the numerical simulations.



FIGURE 2. Unstiffened (left) and I-type welded (middle) and T-type extruded (right) CT specimens tested under varied displacement rate

It was observed that when the crack propagates perpendicular to the loading direction its direction is strongly dependent on the presence of the stiffener, the stiffening configuration, type of stiffener and the material behind the stiffener. There was no crack propagation through the stiffener in the case of extruded specimens. On the other hand and under similar conditions, the crack propagated through the stiffener when it was welded on the plate. The displacement rate and the crack tip geometry seem not to significantly affect crack initiation and propagation. Four evolution phases were noticed: (a) crack initiation and propagation up to the web of the stiffener, (b) crack propagation through the foundation of the stiffener, (c) crack propagation on the stiffener, and (d) crack link-up and propagation at the plate behind the stiffener, with parallel propagation on the web of the stiffener. The results of these experiments is expected to lead to the creation of a fracture test database on continuous aluminium panels and the formulation of appropriate criteria for cracked aluminium panels in order to extend the service of marine vehicles and structures.

## References

1. Freund, L.B. and Parks, D.M., *Journal of Pressure Vessel Technology, Transactions of ASME*, vol. **101**, 51-58, 1979.
2. Zhuang, Z. and O'Donoghue, P. E., *International Journal of Fracture*, vol. **101**, 269-290, 2000.
3. Rodd, J.L., Phillips, M. P. and Anderson, E.D., In *Proceedings of The Advanced Double Hull (ADH) Technical Symposium*, Paper No.2, Gaithersburg, MD, 1994.
4. Paik K.P. and Thayamballi A.K., *Ultimate Limit State Design of Steel-Plated Structures*, John Wiley & Sons Ltd., The Atrium, Southern Gate, Chichester, England, 2003.

## CRACKED BRAZILIAN TESTS OF LAMELLAR TiAl

Gunes Uzer<sup>1</sup>, Fu-Pen Chiang<sup>1</sup> and Andrew H. Rosenberger<sup>2</sup>

<sup>1</sup>Dept. of Mechanical Engineering, Stony Brook University  
Stony Brook, NY 11794-2300, U.S.A.

<sup>2</sup>Weight-Patterson Air Force Base, AFRL/MLLN, Ohio 45433-7817, U.S.A.  
guzer@ic.sunysb.edu

A disc specimen containing a center-crack and subjected to a compressive load has also been used frequently for mixed mode fracture tests in brittle materials since first introduced [1]. This is often called the cracked Brazilian disc specimen. Brazilian disc specimen containing a center-crack and subjected to a compressive load has also been used frequently for fracture tests in brittle materials e.g. [2-8]. Brazilian tests are performed for the purpose of investigating the mixed mode crack propagation characteristics in lamellar TiAl with the grain size of  $\sim 450\mu\text{m}$ . Circular disks of about 1mm in thickness and 3.5mm to 9mm in diameter are manufactured. Slits of 0.15mm in width are cut into the central part of the disks with length being 1/3 of the diameter. A multi-scale speckle method [9] is employed to measure the full field strain distributions at both macro and micro scales. Specimens with different slot orientations are tested in order to control the crack initiation. Crack orientations have chosen according to work done by Fett. *et al*[10]. Micro scale tests are performed inside the chamber of Hitachi S2460-N scanning electron microscope. Results indicate that the highest strain occurs at the point where the surface of the straight line edge of the slot meets the curved edge, regardless of the slot orientation. The crack propagation speed slows down when the crack approaches a grain boundary. It then either stops or jumps to the next grain depending on the grain orientation. A technique is proposed to evaluate the mode mixity from two representative displacement vectors on either side of the crack, an example can be seen in Fig. 1. The aim of this paper is an effort to understand the crack propagation behavior of TiAl under different loading modes.

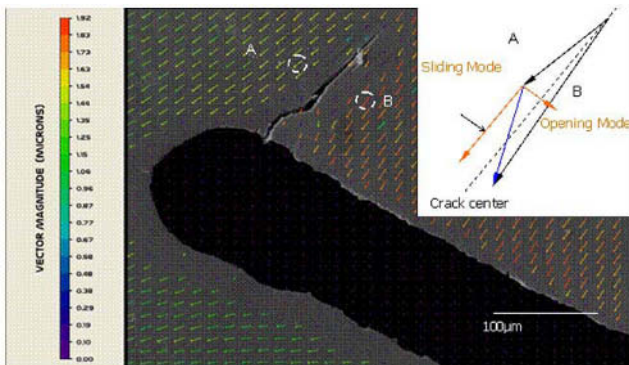


FIGURE 1. Evaluation of mode mixity on CBD specimen.

The aim of this paper is an effort to understand the crack propagation behavior of TiAl under different loading modes.

---

**References**

1. Awaji, H., Sato, S., *J. Engng. Mater. Technol.*, vol. **100**, 175-182, 1978
2. Atkinson, C., Smelser, R.E., Sanchez, *Int. J. Fract.*, vol. **18**, 279-291, 1982
3. Shetty, D.K., Rosen, A.R., Duckworth, W.H., *Engng. Fract. Mech.*, vol. **26(6)**, 825–840, 1987.
4. Liu C., Huang Y., Stout, M.G., *Acta. Mater.*, vol. **46(16)**, 5647-5661, 1998
5. Krishnan, GR *et al.*, *Int. J. Rock Mech. Min. Sci.*, vol. **35(6)**, 695-710, 1998
6. Khan, K., Al-Shayea N.A., *Mech. Rock Engng.*, vol. **33(3)**, 179–206, 2000
7. Scherre, S.S. *et al*, *J. Biomed. Mater. Res. (Appl Biomater)*, vol. **53**, 362–370, 2000
8. Chang, S.H., Lee, C.I., Jeon, S., *Engng. Geology* vol. **66**, 79–97, 2002
9. Chiang, F.P., *Optical Engineering*, vol. **42(5)**, 1288-1292, 2003.
10. Fett, T., *Engng Fract Mech* vol. **68**, 1119–1136, 2001

## **INFLUENCE OF CONCRETE'S MINERALOGICAL COMPONENTS ON FRACTURE COMPRESSIVE AND TRACTIVE**

M.P. Morales Alfaro and F.A.I. Darwish  
Universidade Federal Fluminense RJ  
Rua Passo da Pátria 156-3 andar – Sala 365 - bloco “D” São Domingos –  
Niterói - RJ Brasil – CEP 24210-020  
pattiwasi@hotmail.com or fadarwish@civil.uff.br

### **INTRODUCTION**

Diverse specialties as Geology and of Engineering, as Chemistry and Civil, are responsible for the election of materials to produce, prepare and use of the construction's materials. However, the isolated knowledge between who manufactures and who construe leads, in general, to control its quality alone for its mechanical behavior without the knowledge of that this external properties must it the mineralogical components of the matrix that conforms them.

### **PROBLEM'S STORY**

Few researches about the mineralogical influence of components of concrete on the mechanical properties, didn't could explain many mechanical behaviors. Generated in this way one controversy since 1964 in relation the effect of the reason water/cement in the tenacity to the fracture of concrete.

According to Dos Santos (1998, p.16) [1]:

"As well as Petersson (1980), one concludes that the value of the relation water/cement inversely influences of proportional form the tenacity to the fracture of the concrete, or either, when the relation is increased water/cement the tenacity to the fracture diminishes, this conclusion opposes the position of LOTT and KESLER (1964)".

### **OBJECTIVE**

The objective of this research is to determine if the mineralogy of the components of the concrete has significantly influences in the formation of the surfaces of fracture when submitting it in compression, traction for compression and in special to the direct traction for the displayed in the item above.

### **MATERIALS AND EXPERIMENTAL TECHNIQUES**

Were used cement Portland V-ARI-RS for high initial resistance, course aggregate had been triturated and were from three geologic origins with Tnom. max. ½ inch, m.f 7.6 and the same granulometry. Fine aggregate had m.f 2.43. The tests were did in cylindrical concretes with 6x12 inches except the high strength concrete were did in 4x8 inches, the test in tenacity used "short rod" cylindrical specimen.

TABLE 1: Level of the resistance's concretes studied

	Standard Concrete	Mediums Resistance	High StrengthConcrete
water/cement = 0.50	24 MPa	40 MPa	-
water/cement = 0.60	20 MPa	30 MPa	-
water/cement = 0.36	-	-	100 MPa
slump	5 – 6 inches	5 – 6 inches	3 inches

## RESULTS AND ANALYSIS

TABLE 2 – Properties mechanics of the concretes

MECHAN- ICALS PROPRIETIES	Standard Concrete w/ course aggregate w/c =0.5:			Medium Concrete w/ course aggregate w/c =0.5:			High strength Con- crete w/course aggre- gate w/c =0.36:		
	White	Black	Gray	White	Black	Gray	White	Black	Gray
R. Compressive (MPa)	26,0	26,6	26,2	46,4	41,9	40,0	90,8	91,5	90,3
R. Traction by compressive (MPa)	3,43	3,40	3,27	5,49	5,31	5,03	11,54	9,33	9,42
Traction direct (MPa/√m)	0,98	0,96	0,96	1,08	1,09	1,02	>2,02	>1,97	>1,9 4

The results gotten in this work about the influence of the reason water-cement in the tenacity to the fracture in the concrete standard had revealed essentially independent of the type of course aggregate and the reason water-cement in virtue of the predominance of the effect of pores, humidity and the low cement content of the mixture. For the concrete of medium resistance, the tenacity increases with the increase of the reason water-cement. Being kept invariable the cement contents the increase of the tenacity of the concrete with the increase of the reason water-cement can be attributed to the performance of the pores as energy spendthrifts during the process of consistent fracture with observed in the concrete standard. The superiority of the tenacity of the concrete of medium resistance in relation to the concrete standard is attributed to the biggest cement content. In relation to the tenacity of the concrete of high performance a value of 2 MPa√m was gotten around as minimum limit with a relation water-cement of 0,36. Comparing with the gotten results of the tenacity for concrete the standard and of average resistance, this high value was gotten with a reduction of the reason water-cement even so with similar cement content of this last one is not possible such which had comparison, the one that in the concrete of high performance was used microsilica and additive superfluidificante. The effect of these additives tends to eliminate the porosity and transition zones are filled in almost its totality, making with that the interface aggregate-mortar is very resistant and the rupture mechanism in general goes to be given by breaking of aggregates different of the mechanism of rupture of the concrete standard and medium resistance.

## REFERENCES

1. Santos, A.C, Sousa, J.L.A.O., Bittencourt, T.N. "Determinação Experimental da Tenacidade ao Fraturamento do Concreto com Corpos de Prova do tipo "short rod", BT/PEF/9807, Boletim Técnico da Escola Politécnica da Universidade da São Paulo, (1998, p16).

## OPENING AND MIXED MODE FATIGUE CRACK GROWTH SIMULATION UNDER RANDOM LOADING

P. C. Gope<sup>1</sup>, S. P. Sharma<sup>2</sup> and B. Kumar<sup>2</sup>

<sup>1</sup>. Mechanical Engineering Department, College of Technology,  
G. B. Pant University of Agriculture & Technology, Pantnagar-263145, India  
pcgope@rediffmail.com

<sup>2</sup>. Mechanical Engineering Department, National Institute of Technology,  
Jamshedpur-831014, India

A model for the crack growth analysis under mixed mode random loading that includes the loading sequence effect is presented. The model was applied to the analysis of the crack growth life under different random loading on the sheets of two different aluminum alloys, 2024-T3 and 2199-T851. Analyses were carried out on the simulated loading histories obtained from different spectral densities of the nominal stress and various loading history lengths for each case. The crack growth predictions based on the presented model are found to be reasonable with the experimental results.

Engineering structures and component contains crack of varying size, shape, and orientation. The randomly oriented crack produces mixed mode loading. In the mixed mode loading condition a crack will propagate in a non-self similar manner. Most of the crack growth rate equations proposed for mixed mode loading is based on either strain energy density approach or stress intensity factor approach.

A closure parameter based on strain energy density factor has been introduced in the present crack growth model. The statistical nature of the damage produced due to crack advancement is interrelated with the strain energy based closure parameter. In the present paper a model for the estimation of crack opening stress intensity factor for random loading based on the constant amplitude test results under mixed mode (mode I &II) conditions is presented. A new closure parameter based on the strain energy density factor has been defined and incorporated in the crack growth model. An algorithm is developed and presented for the estimation and analysis of the fatigue life under spectrum loading. The generation of the spectrum loading is also included in the algorithm.

The crack growth predictions based on the presented model are found to be reasonable with the experimental results. The different type of random loading has been considered for mixed mode fatigue crack growth studies. Cycle-by-cycle simulation of crack growth from specified crack length has been carried out. The average ratio and standard deviation estimated from the results of present method are 1.118 and 0.259 compared to the values 0.846 and 0.213 obtained from JC model. It is seen that crack opening stress intensity factor is highly influenced by the selection of threshold value of over load. An iterative method has been presented to optimize the threshold value of over load to obtain fatigue life within acceptable error. The influence of bandwidth, history length and loading angle (crack position) on results obtained was analyzed by comparing the various statistical parameters of lives produced by each group of the loading history. The effect of loading history length, bandwidth, peak stress etc on probability distribution, mean life, etc has been studied and presented.

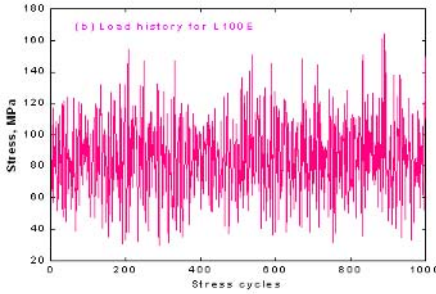


Fig. 1 Loading history

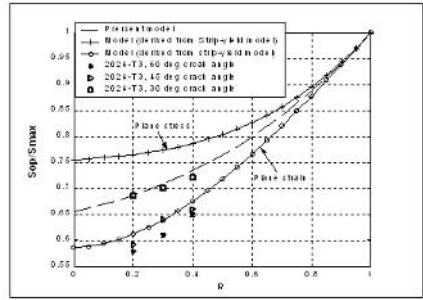


Fig. 2 Comparisons of prediction of Opening stress with extended N Newman's equation and Expt data

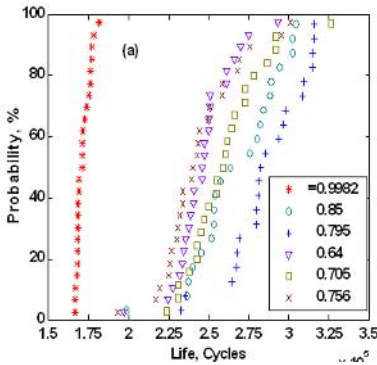


FIGURE 3. Probability distribution of Fatigue life for  $\alpha = 3^0$  and for different band width

TABLE 1. Comparison of the test and predicted life of 2219-T851 Al

Load	$a_f$ (mm)	$a_f$ (mm)	Test	Present
M81	4.06	13.0	115700	179875
M82	3.81	35.4	58585	59957
M83	3.81	23.3	18612	15000
M84	4.00	55.9	268908	329850
M85	3.87	32.8	36397	35314
M88	3.81	45.8	380443	357101
M89	3.81	38.4	164738	184149
M90	3.81	51.6	218151	331834
M91	3.81	36.1	65627	78269
M92	3.81	29.5	22187	18315

The history length to be used is a decisive element in making a test or simulation of crack growth process under random loading. The use of too short histories and their repetition until failure may produce non conservative results and provide much longer lives than those obtained with longer loading histories, which will be closer to facts. In estimating fatigue lives under random loading it is required to generate or test with different representative random loading histories and to determine the life distribution.

**References**

1. Sih, G.C., and Barthelemy, B.M., Engineering Fracture Mechanics, vol. 13, 439-451, 1980.
2. P. C. Gope, S.P. Sharma, and B. Kumar, Journal of Institution of Engr (India), vol. 85, 2004.
3. Gope P. C., Sharma S. P., Kumar, B., Second International Conference on Theoretical, Applied, Computational and Experimental Mechanics, (ICTACEM), Paper No 37 I.I.T, Kharagpur, Dec. 2001.
4. Dominguez J., Zapatero J., and Moreno B., Engng Fracture Mechanics, vol. 62, 351-369, 1999.



## NUMERICAL STUDY OF FATIGUE BEHAVIOR OF SPOT WELDED JOINTS

M. Zehsaz and S. Hasanifard

Faculty of Mechanical Engineering, University of Tabriz, Tabriz, Iran  
zehsaz@tabrizu.ac.ir, hasanifard@tabrizu.ac.ir

In the present paper, complete investigation about the fatigue behaviour of spot welded joints will be carried out in details.

There are a number of parameters that affect the fatigue life of spot welded joints which can be summarized as follows:

1. Residual stress is one of the most important parameters which influence the fatigue life of the spot welds. The electrical force and the rigorous temperature gradient produce the residual stresses during the welding process. In the regions close to the spot welds due to the temperature gradient and relatively high electrode force, the plastic strain components exist, while in the regions far from the nugget, stresses and strains are mainly in elastic range. Therefore, the residual stresses remain on the joint after the electrode removal and reaching the temperature distribution to the steady-state condition. Residual stress is a non-linear and complicated phenomenon that its measurement is very costly.
2. The gap effect between sheets in three dimensional finite element analyses which is very considerable for mono spot-welded tensile-shear. Due to expansion and shrinkage of the aluminum alloy when cooling down to the room temperature, a gap is generated between two sheets. The gap distance between sheets and the residual stresses near the root of nugget have been calculated using an axi-symmetric model of the electrodes and sheets (Fig. 1) and ANSYS Parametric Design Language (APDL).

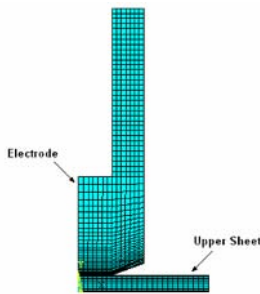


FIGURE 1. Axisymmetric meshed model of electrodes and sheets

Then the two sheets with the calculated gap from previous analysis have been simulated again in Ansys-FEM code using three dimensional model to study the effect of residual stresses and the gap between sheets (Fig. 2).

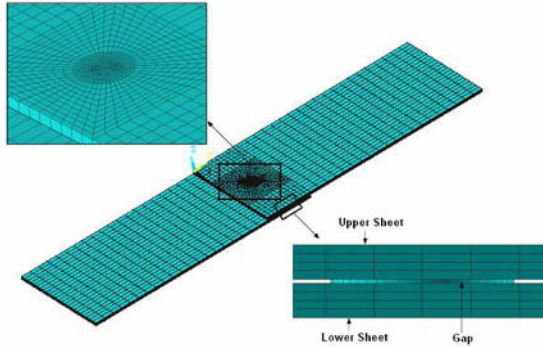


FIGURE 2. Three dimensional meshed model of specimens

The Morrow equation has been used to predict the fatigue life of spot welded joints:

$$\frac{\Delta \varepsilon}{2} = \frac{\sigma_f - \sigma_m}{E} (2N_f)^b + \varepsilon_f (2N_f)^c \quad (1)$$

In this equation  $\Delta \varepsilon$  is the total strain amplitude,  $\sigma_f$  is fatigue strength coefficient,  $\sigma_m$  is the mean stress,  $\varepsilon_f$  is fatigue ductility coefficient,  $b$  is fatigue strength exponent,  $c$  is fatigue ductility exponent and  $N_f$  is the number of cycles.

The results from the transient analysis show that the relatively high value tensile residual stresses remain in the sheet joint at the areas near the nugget and HAZ. The results also indicate that the welding residual stresses influence on the fatigue life of the joint, therefore, the differences between the fatigue life durations, with and without considering the welding residual stresses, increase with decreasing the applied cyclic load.

## References

1. Adib, H., Gilgert, J., Pluvinage, G., *Fatigue life duration prediction for welded spots by volumetric method*, International Journal of Fatigue, vol. **26**, 2004, 81-94.
2. M. Zehsaz and S. Hasanifard, *Investigating Gap Effects in Fatigue Life of Spot Welded Joints*, 16<sup>th</sup> European Conference of Fracture, edited by E.E. Gdoutos, Alexandroupolis, Greece, 2006.
3. X. Long and Sanjeev K. Khanna, Residual stresses in spot welded new generation aluminium alloys Part B- finite element simulation of residual stresses in a spot weld in 5754 aluminium alloy, Science and Technology of Welding and Joining, vol. **10**, no. 1, 2005.
4. A. De, *Finite element modelling of resistance spot welding of aluminium with spherical tip electrodes*, Science and Technology of Welding and Joining, vol. **7**, no. 2, 2002.
5. Jamil A. Khan, Lijun Xu, Yuh-Jin Chao, Kirkland broach, *Numerical Simulation of Resistance Spot Welding Process*, Numerical Heat Transfer, Part A, vol. **37**, 2000, 425-446.

## THE IDENTIFICATION OF A HIDDEN LONG-TERM PLASTIC DAMAGE STAGE DURING SPLITTING TENSILE LOADING OF CONCRETE

Zacharias G. Pandermarakis and Anastasia B. Sotiropoulou  
 Department of Civil and Structural Engineering Technology Teachers  
 School of Pedagogical and Technological Education (ASPETE)  
 “Irene” Train Station, Athens – Greece  
 z.g.panderma@gmail.com, dmitsop@tee.gr

A very deep hidden -until now- feature of a long-term localize plastic damage stage in a known semi-brittle material as un-reinforced concrete is, was observed under carefully prepared carried out splitting tensile tests (1,2). The identification of this unknown but also uncommon response of typical concretes was ought to the modification and suitably adaptation of the standard splitting tensile test in order to make easier its investigation, preserving parallel the character of the test and also of the concrete.

These specific results, even though not-expected, were repeatedly verified in our laboratory also for various concrete specimens with different compositions and prepared conditions. The most characteristic feature of this behaviour is the appearance of a typical yielding point at approximately 300 to 500 s ( $\times 10^{-6}$ ) strain (fig.1a), in a moment where normally a tensile fracture point would be observed. This point is followed by a long-term yielding-like flowing in a load to direct measured transverse strain diagram. This almost horizontal variation of load continues until macroscopically fracture of concrete cylinder specimens take place at strains where varied from 1000 to 4500 is. This means that we observe, in an un-reinforced concrete, strains that are almost 300 to 1000% higher than the expected ones from the relative bibliography. And all these for a severe loading state where intensive tension stresses are generated.

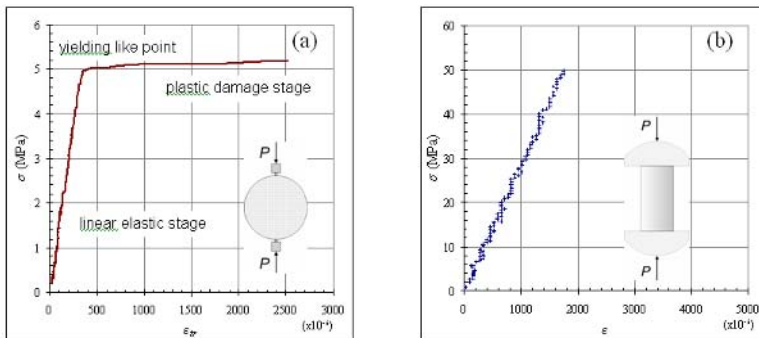


FIGURE 1. Stress – strain curve after tensile splitting test (a) and unconstrained compression (b) of a common concrete.

The rectangular plane region of cylinder concrete specimen, which is responded for the above behavior, is localized along the vertical diameter of its bases in the same place where the traces of fracture plane will be appeared after the total failure. From this set of experiments it is evident that the energetic and important role of this fracture surface isn't limited to the simple initiation,

propagation and finally the appearance of fracture cracks at the end of the test but an intensive plastic damage is grown inside this region, through the formation of a fracture process zone (3,4). The gradually growing of this zone (Fig. 2) is the reason for the inelastic behavior of the semi-brittle concrete which appeared in Fig. 1.

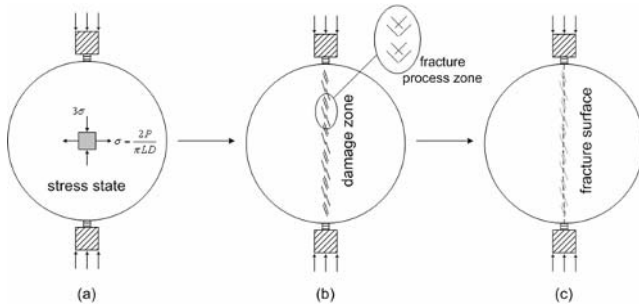


FIGURE 2. a) stress state condition –at the centre of the specimen- under splitting tensile loading where an almost linear elastic stage is appeared, b) the formation of a damage zone along a vertical plane in the early almost pure plastic damage stage, and c) the formation of a fracture surface after the crack propagation at the end of the almost pure plastic damage stage

The modifications in the planning of the common splitting tensile test, which were helped to the identification of this plastic damage stage, concerned differentiations in the size of the used aggregates and prepared specimens, concerned additional aiming measured quantities using suitably positioned strain gauges and also carefully prepared test in order to minimize all the secondary effect which could alter markedly the final results.

The present work consist a part of research program with code number MIS86473-14096/5/8/04 in the framework of “Archimedes I”, and is co-financed by the European Social Fund and National Resources from the EPEAEK II Program.

## References

1. European Standard: EN 12390.06: “Testing hardened concrete-Part6: Tensile splitting strength of test specimens”, Oct. 2000
2. Rocco C., Guinea G.V., Planas J. and Elices M., *Cem. Concr. Res.*, vol. **31**, 73-82, 2001
3. Markeset G. and Hillerborg A., *Cem. Concr. Res.*, vol. **25**, 702-708, 1995
4. Bazant Z.P. and Jirasek M., *J. Eng. Mech.*, vol. **128** (11), 1119-1149, 2002

## THE RELATIONSHIP BETWEEN CREEP RUPTURE LIFE AND MICROSTRUCTURE OF AGED P92 WELDMENT

B. J. Kim and B. S. Lim

School of Mechanical Engineering, Sungkyunkwan University  
300, Cheoncheon-dong, Jangan-gu, Suwon, gyeonggi-do 440-746, Korea  
kultra@skku.edu and bslim@skku.edu

As the static loading period of a power plant increases, high temperature components such as main steam pipe and header are degraded and their creep lives are reduced. Generally, material degradation is influenced by nucleation, growth and coalescence of cavity, and precipitates formed during the long operating period of power plants. Creep strength and life of material are closely related with the microstructural characteristics. Components used under creep condition for long time are unable to maintain the stability of microstructure and experience degradation of material [1]. From this viewpoint, it is necessary for safety and residual life estimation of power plant to investigate creep properties of specimens prepared from the material cut directly from the operating service components. Small punch test has been developed as an useful method to estimate mechanical properties because of its miniaturized specimen size [2]. In this study, small punch creep tests were carried out to investigate the effect of aging time on creep properties using P92 steel weldment aged for 0~12100 hrs at 600°C. Microhardness measurement and microstructure observation of both base and weld metals were performed to analyze their effects on creep strength and rupture life. The coarsening behavior of martensite lath with aging time was investigated by TEM (Transmission electron microscope) and SEM (Scanning electron microscope) to examine the effect of microstructural change for the minimum creep rate. Also, the area fractions of precipitates and cavities were analyzed to investigate the relationship between creep rupture life and aging time. The chemical composition of P92 (9Cr2W) steel used in this experiment is shown in Table 1.

TABLE 1. Chemical composition of P92 steel and welding electrode(wt%)

	C	Si	Mn	P	S	Ni	Cr	Fe
Base metal	0.1	0.22	0.48	0.017	0.006	0.18	9.11	Bal.
*GTAW	0.10	0.36	0.44	0.012	0.005	0.72	8.89	Bal.
**SMAW	0.11	0.22	0.54	0.014	0.005	0.59	8.50	Bal.
	Mo	W	Cu	V	Nb	B	N	Al
Base metal	0.47	1.75	-	0.18	0.056	0.002	0.041	0.01
GTAW	0.41	1.75	-	0.23	0.069	-	0.052	-
SMAW	0.50	1.45	0.06	0.20	0.02	0.002	0.041	-

\* Gas Tungsten Arc Welding(1~4pass), \*\* Shielded Metal Arc Welding(5 and beyond)

Fig. 1 shows the small punch test apparatus used in this study. Fig. 2 shows the comparison results of base metal and weld metal for displacement rate versus applied load for '0 hr' aged P92 steel. The minimum displacement rate of weld metal was lower than that of base metal. Specimens aged up to 12100hrs were employed in this study. In the main paper, detailed analysis and discussions will be carried out on the experimental results of hardness, microstructural evolution, area fraction of precipitates and cavities as well as displacement rates of weld and base metal.

Finally, a phenomenological equation will be produced for the estimation of the residual life of P92 steel exposed to high temperature operating conditions.

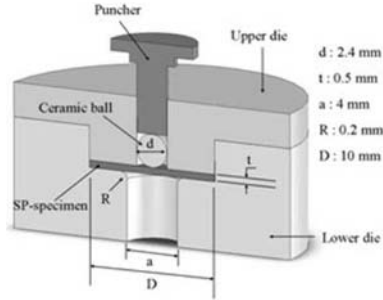


FIGURE 1. Schematic illustration of SP test apparatus.

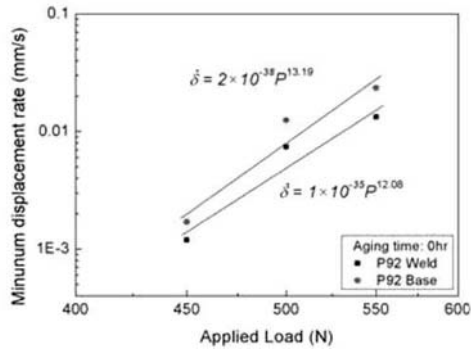


FIGURE 2. Displacement rate vs. applied load

**References**

1. X. Jia and Y. Dai, *J. Nucl. Mater.*, vol. **323**, 360-367, 2003
2. J. S. Cheon and I. S. Kim, *J. Nucl. Mater.*, vol. **278**, 96-101, 2000

## NUMERICAL SIMULATION OF COMBINED EFFECTS OF HEAT TREATMENT AND CRACK LENGTH ON TENSILE PANELS INTEGRITY

M. Kiric and A. Sedmak

The Innovation Center of the Faculty of Mechanical Engineering  
Kraljice Marije 16, Belgrade, Republic of Serbia and Montenegro  
mkiric@mas.bg.ac.yu

This paper describes numerical modelling of the post weld heat treatment (PWHT) effects as well crack length impact on integrity of modelled members subjected to tension load. Residual stresses (RS) influence considerably welded components of power plants integrity when combined with thermal cycling, mechanical stresses and some corrosion mechanisms, like intergranular stress corrosion cracking in austenitic steel pipes, Mirzae-Sisan et al. [1] and Adziew et al. [2]. Their numerical analysis is an appropriate approach, particularly where experimental research work is expensive and mathematical solution is complicated.

Numerical analysis of flat experimental specimens, reviewed in the first part of the paper, is based on consideration of influences of primary and secondary stresses on strain intensity factor (SIF). Two principal flaw directions are assumed - parallel and perpendicular to the weld direction and that RS acts in the same direction as the external load. It is considered an overmatched weld in the first case and an undermatched weld in the latter arrangement.

The behaviour of real panels (specimens) is 3D, but relatively thin specimens are considered with the plane stress conditions, typical for structures of small thickness. Plane strain occurs in thick specimens and it is dominant in the middle of the specimen.

It is assumed surface cracks, because they are common in many structural components. Accurate stress analysis of these surface-cracked components are needed for reliable prediction of their crack-growth rates and fracture strengths. However, because of the complexities of such problems, exact solutions are not available. Thus it is used the superposition of primary and secondary stress effects according to Newman and Raju [3]. SIF is calculated from a 3D FE analysis for semielliptical surface cracks in finite elastic plates subjected to tension and bending loads.

$$K_I^P = (P_m + H_{NR} P_b) \sqrt{\pi c / Q} F, \text{ kN} / \text{m}^{3/2} \quad (1)$$

$$K_I^S = (S_m + H_{NR} S_b) \sqrt{\pi c / Q} F, \text{ kN} / \text{m}^{3/2} \quad (2)$$

where  $c$  is the surface crack depth,  $Q$  is the shape factor for elliptical crack,  $P_m$  and  $P_b$  are primary membrane and bending stress respectively,  $S_m$  and  $S_b$  are corresponding secondary stresses and  $F$  and  $H_{NR}$  are constants. The resulting SIF is given by

$$K_r = \frac{K_I}{K_{Ic}} = \frac{K_I^P + K_I^S}{K_{Ic}}, \text{ kN} / \text{m}^{3/2} \quad (3)$$

In the second part of the paper, it is applied the approach of Harrison, Loosemore and Milne, which allows to interpolate between linear elastic fracture for one extreme of failure and large-scale plastic yielding or collapse at the other extreme, known as failure assessment curve (FAC) or R-6 curve. For a thin panel of width  $2W$  containing a central through-thickness crack, the stress ratio  $S_r$ , calculated for the failure assessment diagram (FAD) is according to PD 6493 given by

$$S_r = \sigma_n / \sigma_0 \quad (4)$$

where  $\sigma$  and  $\sigma_0$  are uniform remote stress and flow stress (effective yield stress) respectively. For points indicating tensile load values, ratio  $S_r$  corresponds to the stress from the load  $\sigma_n^I$

$$S_r = \sigma_n^I / \sigma_n \quad (5)$$

It is devised FAD with FAC for different crack lengths calculated using EPRI approach with

$$S_r = P / P_0 \quad (6)$$

where  $P$  is load per unit thickness and  $P_0$  is the limit load.

In the third part of the paper the failure prediction is given for a set of load and RS values. It is defined the boundary in the load - RS plane as the locus of predicted failure points, so that on one side of the boundary the panel is safe from failure and on the other side failure occurs. The analysis is performed for panels made of the HSLA steel T.StE 460 (with  $\sigma_y = 460$  MPa and  $\sigma_0 = 542,5$  MPa) and made of the A 533B low alloy ferritic steel ( $\sigma_y = 414$  MPa and  $\sigma_0 = 484$  MPa). The results are compared with data from literature, Adziew [4].

## References

1. Mirzae-Sisan, A., Truman C.E., Smith D.J., In *Proceedings of the Sixtinth European Conference of fracture*, edited by E.E. Gdoutos, Springer, Dordrecht, 2006, 1305-1306.
2. Adziew G., Sedmak A., Adziew T., Ibid 1, 1043-1044.
3. Newman J.C., Raju I.S., *Analysis of Surface Cracks in Finite Plates Under Tension or Bending Loads*, NASA, Technical Paper No. 1578, 1979.
4. Adziew T., In *Proceedings of the 6th ML[ML: Eksploatacijske prsline u posudama pod pritiskom i rezervoarima* (in serbian), edited by S. Sedmak, TMF, Evropski centar za mir i razvoj, and GOSA, Belgrade 1994, 127 - 148.



## CHARACTERIZATION OF THE FRACTURE BEHAVIOUR OF ELASTOMERS UNDER COMPLEX LOADING CONDITIONS

Z. Major<sup>2</sup>, K. Lederer<sup>1</sup> and R.W. Lang<sup>1,2</sup>

<sup>1</sup> Polymer Competence Center Leoben GmbH

<sup>2</sup> Institute of Materials Science and Testing of Plastics

University of Leoben, Leoben, Austria

zoltan.major@notes.unileoben.ac.at

In engineering applications elastomers are frequently exposed to complex combinations of mechanical loads (monotonic, static, intermittent and cyclic loads) superimposed by various environmental effects. A better understanding of the material resistance against crack initiation and propagation becomes of increasing practical importance which can be illustrated by the example of the rapid decompression failure behavior of pressurized seals for oilfield applications. A phenomenon termed rapid gas decompression (ED) damage occurs if elastomer seals exposed to high gas pressure fail upon the sudden release of the gas pressure in a brittle manner. As to the characterization of the explosive decompression failure behaviour of pressurized elastomer seals, our research program deal with (1) the instrumented autoclave tests of pressurized O-rings, (2) the bulk deformation behaviour of elastomers under highly confined conditions, (3) crack initiation and crack growth under high deformation rates, and (4) the pressure and temperature dependent gas permeability of various elastomers using various types of gases.

In the first part of the study pressurization/depressurization experiments were performed in an autoclave on component level using O-rings made from two rubber types (HNBR and FKM). The main focus was given to develop instrumented experiments, where the pressure and temperature change of the chamber and the expansion of the O-rings were continuously measured and recorded. Both free and constrained O-rings were investigated and the complex thermo-mechanical response of the elastomer materials was recorded and analyzed. The change of the test parameters and the behaviour of the O-ring are shown in Fig. 1 during an instrumented ED test;

In the second part of the study fracture tests were run on two servohydraulic test systems (MTS 831.59 Polymer Test System and MTS 858 Axial-Torsional Test System). A pure shear specimen configuration with a faint waist in the mid-section (FWPS specimen) and with thicknesses of 2 mm and a cylindrical specimen configuration with 14 mm nominal diameter were used in this study. Both single parameter critical tearing energy values and the crack growth resistance of various elastomer types under monotonic test conditions were determined over a wide loading rate range and the results are analysed based on the crack growth kinetics (da/dt-T curves are shown in Fig. 2). In addition, to gain more insight into the real material behavior under complex loading conditions full field strain and temperature measurements were performed both in the near crack tip and in the far field in the specimen ligament and subsequently analyzed.

The FWPS specimens revealed stable, in-plane crack growth in these monotonic tests and the various stages of the crack growth from the crack initiation in a highly blunted crack tip to the final unstable crack growth were analyzed. Moreover, a material grade dependent increase of both the near crack tip and far-field specimen temperature was observed using this specimen configuration. The cracked round bar specimens revealed a more unstable crack growth for all materials investigated which is associated with the higher degree of triaxiality. Finally, significant differences were observed regarding the fracture behaviour and the test parameter dependence between the elastomer types investigated.

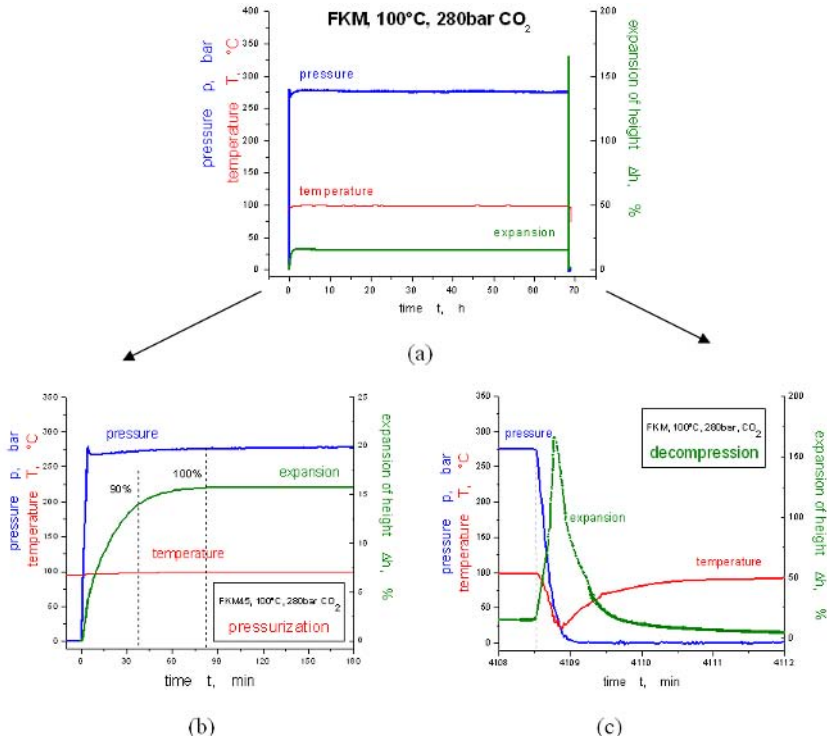


FIGURE 1. The change of the test parameters and the O-ring during an instrumented ED test; (a) the complete test sequence, (b) pressurization phase and (c) decompression phase.

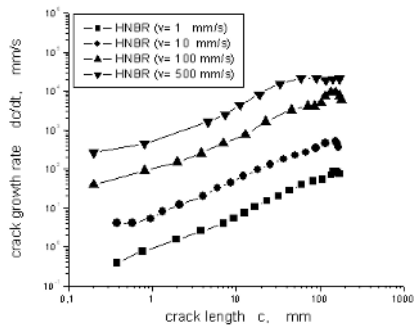


FIGURE 2. Loading rate dependence of crack growth kinetics.

## EXPERIMENTAL AND NUMERICAL DETERMINATION OF THE LOCAL S-N CURVE OF SHOT-PEENED STEEL GEARS

G. Olmi, M. Comandini and A. Freddi

DIEM – Department of Mechanical Engineering – Engineering Faculty – University of Bologna  
Viale del Risorgimento, 2 – 40136 Bologna – Italy  
giorgio.olmi@mail.ing.unibo.it, matteo.comandini@mail.ing.unibo.it

Mechanical design of components can be performed according to different criteria, aiming to prevent unexpected failures and to maintain structure weight at low values. When loads are strongly variable with sporadic peaks in intensities, “safe life” criterion is applied. In particular this criterion prevents failures in components expressively designed for a limited number of load cycles and according to very strict weight specifics. A typical application of this methodology is on competition cars, where many components must be designed for a life limited to the only race duration. The use of such criterion is often expensive, since it requires the knowledge of local Wöhler S-N curve. The purpose of this paper is to determine, by experimental and numerical methods, the S-N curve at the tooth root of a gear in the transmission of a Formula1 competition car. This component (Fig. 1) is carburized, hardened and shot-peened with peen diameter of 0.3 mm (S110) and shot operating pressure of 4 bar. Parameters of the analysed spur gear are modulus, 4 mm, pressure angle, 20°, face width, 5.5 mm, number of teeth, 22; moreover a correction (correction factor = 0.96) is applied. Fatigue tests for the evaluation of the fatigue limit and the determination of the S-N curve were performed on a Rumul resonant machine (Fig. 2), able to work at a frequency of 108 Hz. A device had to be used to correctly refer the gear to the testing machine, in order to reproduce work load distribution, as described by Olmi *et al.* in [1]. Such device is able to apply a bending fatigue load just to a couple of teeth: on any gear five couples of teeth can be tested.

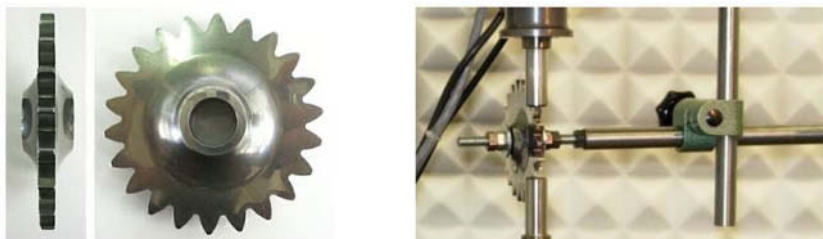


FIGURE 1. A photo of one of the tested gears FIGURE 2. Experimental installation

The fatigue limit was firstly investigated, by the application of the Staircase method described by Dixon in [2]. Six nominal tests were conducted for the determination of dynamic strength. A FEM analysis was performed for the conversion of the fatigue limit for the applied load into a local fatigue strength (1355 MPa) at the tooth root. The S-N curve (for finite life) was determined by operating tests at five equally spaced load levels, with three replications for each. This procedure was performed in accordance to ISO 12107 [3] and the S-N curve was elaborated at the 88% confidence level.

Obtaining an S-N curve for a specific component is an expensive and long procedure. For this reason several authors suggested methodologies for the numerical calculation of the local S-N curves. Eichlseder in [4] presents a general approach applicable to components of whatever shape, however, to the authors' knowledge, it was never applied to peened components. Firstly the shot-peening process was numerically simulated. Explicit time integration is very efficient in solving the problem for highly dynamic and non linear conditions. The peens were modelled as bodies considered infinitely rigid in comparison to the stiffness of the target material [5]. The results of simulations were validated by comparing them to experimental stress distributions. They were derived by X-ray diffractometry (Fig. 3) for three peening treatments with peen diameter of 0.3 mm (S110) and shot pressure ranging from 3.5 to 4.5 bar.

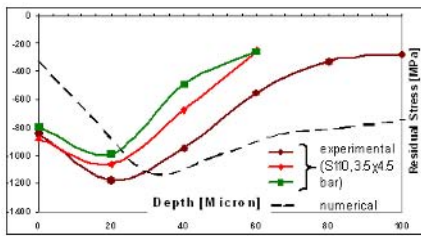


FIGURE 3. Residual stress distributions derived by diffractometry and by FEM

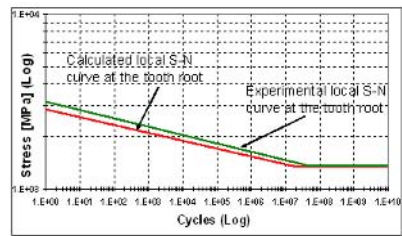


FIGURE 4. Local S-N curves by experimentation and numerical calculation

Stresses at the tooth root were investigated by FEM, by simulating bending fatigue loads acting on a tooth couple. Total state of stress was calculated as the sum of stresses due to external loads and of residual stress. Eichlseder proposed that the local S-N curve of a component at the most critical location can be achieved by the knowledge of the relative stress gradient at that location and by data related to specimens (of the same material) fatigue performance in basic load condition. Thus from the total stress distribution (considering both external loads and residual stress due to shot-peening) the relative stress gradient,  $\chi = (1/\sigma_{max}) \cdot (d\sigma/dx)$ , was calculated ( $38 \text{ mm}^{-1}$ ). The local fatigue strength  $\sigma_f$ , the slope  $k$  of the S-N curve and the number of cycles at the fatigue limit  $N_D$  were calculated as functions of  $\chi$  [4]. Fig. 4 shows in a Log-Log diagram a comparison between experimentally and numerically derived curves. Good accordance testifies that this methodology can be applied to quantify fatigue performance improvement due to peening treatment.

## References

1. Olmi, G., Freddi, A., In *Proceedings of the 5<sup>th</sup> ICCSM*, edited by Croatian Society of Mechanics, Trogir, 2006
2. Dixon, W.J., Massey, F.J.Jr., *Introduction to Statistical Analysis*, McGraw-Hill, U.S., 1983
3. ISO12107, *Metallic materials-Fatigue testing-Statistical planning and analysis of data*, 2003
4. Eichlseder, W., *Computers & Structures*, vol. **80**, 2109-2113, 2002
5. M. Guagliano, *Journal of Materials Processing Technology*, vol. **110**, 277-286, 2001.

## EFFECT OF HYDROGEN ENVIRONMENT ON NON-PROPAGATION AND PROPAGATION OF FATIGUE CRACK IN A TYPE 304 AUSTENITIC STAINLESS STEEL

H. Matsuno<sup>a</sup>, Y. Aoki, Y. Oda<sup>b</sup> and H. Noguchi<sup>c</sup>

<sup>a</sup>Graduate school of Kyushu University, <sup>b,c</sup>Kyushu University  
744, Moto-oka, Nishi-ku, Fukuoka, 819-0395, Japan

ate206325@s.kyushu-u.ac.jp, boda@mech.kyushu-u.ac.jp, cnogu@mech.kyushu-u.ac.jp

Hydrogen energy is expected to solve both the lack of fossil fuel resources and carbon dioxide emission. In order to develop the hydrogen society, it is urgent matter to establish the strength evaluation method for the components exposed to hydrogen in machines and structures, such as fuel-cell vehicles and infrastructures, because hydrogen has been reported to degrade the strength of materials [1,2]. Our previous study as in Fig. 1, on a type 304 austenitic stainless steel which is a candidate for use in hydrogen environment shows that the fatigue crack growth rate under the hydrogen gas environment is higher than that under air atmosphere in the range of high growth rate.

In this study, the effect of hydrogen environment on the fatigue limit and the crack growth rate in the range of low growth rate are discussed. The material used here is JIS SUS304 stainless steel solution-treated, which is the same material as used in Fig. 1. Fig. 2 shows the shape and dimensions of a specimen. Bending fatigue tests were carried out on a specimen with small twin holes. Testing environments were 0.18MPa (in absolute pressure) hydrogen gas, inert gases; argon or nitrogen at the same pressure as hydrogen, and in air at 313K. Fatigue process was in-situ observed using a scanning laser microscope.

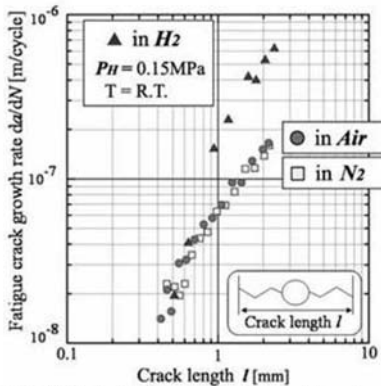


FIGURE 1. Fatigue crack growth rate at  $\Delta\varepsilon=0.45\%$  ( $\Delta\varepsilon$  denotes the total strain range)

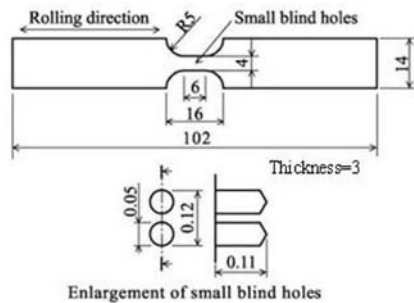


FIGURE 2. Shape and dimensions (in mm) of a specimen

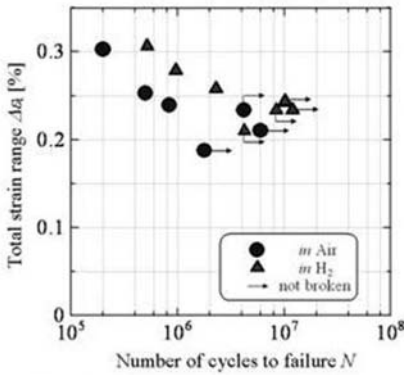


FIGURE 3.  $\Delta\varepsilon_f$ - $N_f$  diagram  
( $P_H=0.18\text{MPa}$ ,  $T=313\text{K}$ )

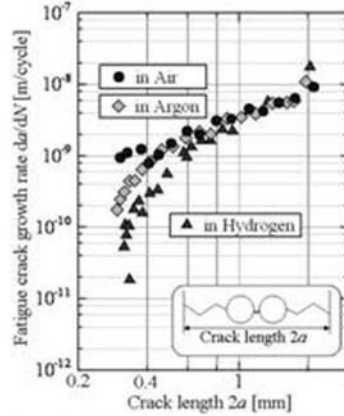


FIGURE 4. Fatigue crack growth rate at  
 $\Delta\varepsilon_f=0.28\%$  ( $P_H=0.18\text{MPa}$ ,  $T=313\text{K}$ )

Fig. 3 shows  $\Delta\varepsilon_f$ - $N_f$  diagram. The fatigue limit is not sufficiently different in hydrogen and in air and the fatigue lives in hydrogen is longer than in air. At the strain level of fatigue limit in each environment a crack emanated from twin holes stops after propagation to some length. If hydrogen environment enhances crack growth the fatigue limit may fall and fatigue lives may shorten, but the facts are contrary to those. The reason was discussed on the basis of crack closure factors; such as plasticity, oxidation, debris, and asperity. In order to further discuss, fatigue crack growth tests in the range of extremely low growth rate were added. Fig. 4 shows the fatigue crack growth rate at  $\Delta\varepsilon_f=0.28\%$  in hydrogen, in argon, and in air. The fatigue crack growth rate less than  $10^{-9}$  m/cycle in hydrogen is lower than that in argon and in air. This result and retardation of fatigue crack initiation due to the absence of oxygen and water vapor [3] explain the longer fatigue lives under the hydrogen than under air in Fig. 3. In order to clarify the behavior of the fatigue limit and crack growth rate in the range of low growth rate, another factors; amount of transformation martensite and crack opening stress were measured by the X-ray diffraction and by the observation of a crack opening during one loading cycle with a scanning laser microscope, respectively. Within the limits of this experiment, plasticity- and transformation-induced closure seems to play important roles in hydrogen environment.

Hydrogen environment has both acceleration and deceleration factors for fatigue crack growth. It seems that the effect of hydrogen environment appear as a summation of effects due to these factors, in a different manner in the different stage of crack growth or in the different environmental condition; such as, pressure and temperature.

## References

1. *Hydrogen effects in metals*, edited by I. M. Bernstein and Anthony W. Thompson, The Metallurgical Society of AIME, 1980.
2. *Special issue on recent advances in the engineering aspects of hydrogen embrittlement*, Engineering Fracture Mechanics, 1988, 68 – 10.
3. Aoki, Y., et, al, *Int. J Fracture*, vol. **133**, 277-288, 2005

## FATIGUE BEHAVIOUR OF SCRATCH DAMAGED SHOT PEENED SPECIMENS AT ELEVATED TEMPERATURE

R.A. Cláudio<sup>1</sup>, C.M. Branco<sup>1</sup> and J. Byrne<sup>2</sup>

<sup>1</sup> Department of Mechanical Engineering, Escola Superior de Tecnologia de Setúbal  
Department of Mechanical Engineering, Instituto Superior Técnico  
Campus do IPS, Estefanilha, 2910-761 Setúbal  
Av. Rovisco Pais, 1049-001 Lisboa, Portugal

<sup>2</sup> Department of Mechanical and Design Engineering, University of Portsmouth  
Portsmouth, Hants PO1 3DJ, United Kingdom  
rclaudio@est.ips.pt; cmbranco@ist.utl.pt; jim.byrne@port.ac.uk

It is clearly shown that surface condition has a strong effect on fatigue life. 80 – 90% of total high cycle fatigue life is taken up by crack nucleation/initiation at the surface. Shot peening is a quite successful surface treatment process for extending the service life of a large number of components. The benefit is created by the compressive stress field at the surface and a limited effect of cold work, which has advantages in reducing the likelihood of crack formation, Webster *et al.* [1]. However shot peening only introduces a very thin layer of compressive residual stress, in the order of hundreds of micrometres. Below the compressive layer near the surface is an elastic region in a tension state to achieve equilibrium and not cold worked, which may have a detrimental effect on fatigue life if a scratch created in the treated surface is bigger than the compressive layer, Burgess *et al.* [2]. Little information is available about the influence of small scratches on a shot peened surface and how it will affect the fatigue life of a component.

Several experimental tests and some FE (finite element) work was made in order to evaluate the effect of different scratches in a shot peened surface at elevated temperature in RR1000 powder metallurgy nickel base superalloy. The geometry studied is representative of a critical feature of a gas turbine aero engine compressor disc with an elastic stress concentration factor  $K_t = 1.32$  due to a curvature radius of 4.5 mm. Several specimens were tested in the conditions as machined and shot peened (110H 6-8A 100%). In some specimens, a scratch was created with a cutting tool in the curvature of the specimen ( $R=4.5\text{mm}$ ) after the shot peening treatment. The scratch was 3 mm long with a  $90^\circ$  V groove with a root radius of  $50\ \mu\text{m}$  and two different depth sizes,  $50\ \mu\text{m}$  and  $100\ \mu\text{m}$ . These sizes lie within the peak of compressive residual stress and within the end of the compressive layer respectively. The experimental tests were made at high temperature,  $650^\circ\text{C}$ , in a servo hydraulic testing machine with a trapezoidal loading waveform 1-1-1-1s and load ratio of  $R=0.1$ . Crack propagation rate was measured with a DC potential drop system developed for these tests with calibration curves obtained by numerical methods and corrected by beach marking, Cláudio [3].

A discussion is presented about the fatigue behaviour by comparing all the six situations studied, as machined, for shot peened conditions both with and without the  $50\ \mu\text{m}$  and  $100\ \mu\text{m}$  scratches sizes. Fig. 1 shows some of the results obtained presenting the S/N curves for all groups of specimens tested experimentally. The influence of shot peening on crack propagation and crack shape was also evaluated experimentally.

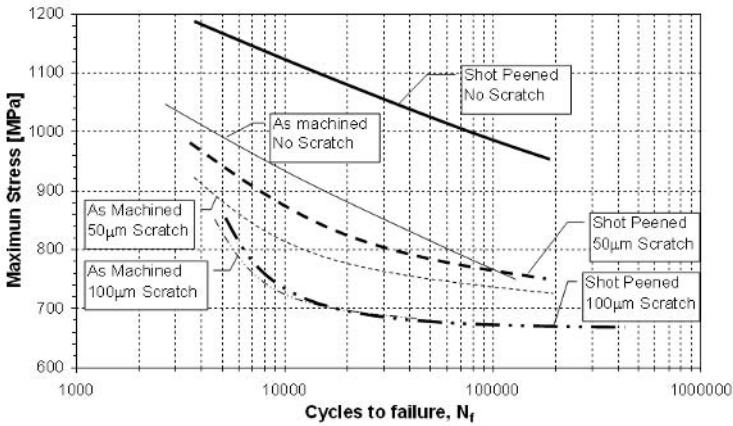


FIGURE 1. S/N curves obtained experimentally.

To complement this work several FE analyses are presented showing the stress distribution evolution in front of the scratch as the number of cycles increase. These results were used to prove the experimental ones and to understand the scratch damaging effect of shot peening. It was concluded that shot peening has a remarkable effect on fatigue life at high temperature for the geometry without scratches. With scratches, the benefit of shot peening is drastically reduced. For the 100  $\mu\text{m}$  depth the shot peening benefit almost disappears, however for the 50  $\mu\text{m}$  depth an improvement in cyclic life compared with the as-machined condition is found. A small benefit of shot peening can also be noticed for long crack propagation, where the compressive layer at the surface creates a tunnelling effect, decreasing overall crack propagation rate slightly. According to the numerical results, for scratched geometries shot peening seems to have a limited effect on crack initiation.

## References

1. Webster, P. S. and Cunningham, T. P., *Shot Peening: Techniques and Applications*, Ed. by Marsh, K.J. London, EMAS, 1993.
2. Burgess A., Byrne J. and Penny J., *Fatigue 2002 - Proceedings of the Eighth International Fatigue Congress*, Stockholm, Sweden, 2002.
3. Cláudio, R. A., *Fatigue Behaviour and Structural Integrity of Scratch Damaged Shot Peened Surfaces at Elevated Temperature*, PhD Thesis - University of Portsmouth, 2005.



## INSTABLE CRACK PROPAGATION AT HIGH TEMPERATURE

Nicolas Tardif<sup>1,2</sup>, Michel Coret<sup>2</sup> and Alain Combescure<sup>2</sup>

<sup>1</sup> IRSN DSR SAGR, BP 17, 92262 Fontenay-aux-Roses, France

<sup>2</sup> LaMCoS, UMR 5514, INSA de Lyon, 20 av, Albert Einstein,  
F69621 Villeurbanne Cedex France

{nicolas.tardif, michel.coret, alain.combescure}@insa-lyon.fr

This paper presents high temperature (900°C or 1000°C) tensile tests on precracked flat 16MND5 test piece with a rectangular section. Cohesive zone model has been used to simulate the crack propagation into a very ductile material.

The context of these tests is the study of the rupture of a nuclear reactor submitted to an accidental mechanical and thermal loading due to the reactor core melting during an uncontrolled nuclear reaction [1]. The test purpose is the incipient crack threshold and propagation crack speed characterization.

The 16MND5 test piece has a 4 x 25 mm effective area at the 5 mm length notch. The mechanical loading is applied by a Schenck tensile testing machine which is controlled in force. The thermal loading is applied by an inductor heating. We first imposed a slope in temperature until the aimed one (900°C or 1000°C) and then a slope in stress until rupture. Force and displacement are recorded. An infrared camera and thermocouples are used to measure the temperature distribution. Finally, two methods are used to obtain the crack propagation speed. A high speed numerical camera (1000 f/s) allows us to find the position of the crack tip (Fig. 1). Moreover, we apply a constant electric current in the test piece and we measure the voltage on both side of the crack during the propagation. The voltage evolution is correlated to the crack tip position.



FIGURE 1. Numerical images of crack propagation (16MND5, 900°C)

To simulate the test, we model the crack by a cohesive zone (Fig. 2). An elastic damageable behaviour law from Hinte [2,3] is used for the cohesive elements. The 16MND5 behaviour is elastoplastic with kinematic hardening [4]. First, we are interested in the Hinte parameters adjustment and then, in the plastic parameters influence on the crack propagation. The propagation speed comes from two phenomenons. The snap-back instability governed by the ratio of the matrix and the interface stiffness tends to accelerate the propagation [5,6]. On the opposite, plastic dissipation in the matrix tends to reduce the propagation speed.

Finally simulations are compared to the experimental results.

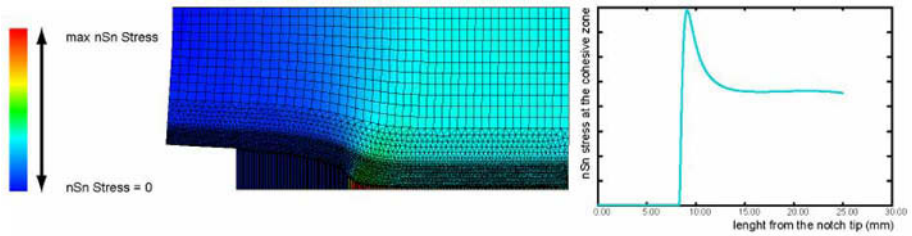


FIGURE 2. Simulated stress field of the propagation by a Hinte cohesive model

## References

1. Altstadt E et al, *Modelling of in-vessel retention after relocation of corium into the lower plenum*, SARNET-Corium, Report No. WP 10-2, 2005
2. Allix O et al, Identification and forecast of delamination in composite laminates by an interlaminar interface model, *Composites Science and Technology*, vol. **58**, 671-678, 1998
3. Corigliano A, Allix O, Some aspects of interlaminar degradation in composites, *Comput. Methods Appl. Mech Engrg*, vol. **185**, 203-224, 2000
4. Nicolas L., RUPATHER - Traction à haute température, CEA, Report No. DMT 96-381, 1996
5. Gao Y F, Bower A F, A simple technique for avoiding convergence problems in finite element simulations of crack nucleation and growth on cohesive interfaces, *Modelling and Simulation in Materials Science and Engineering*, vol. **12**, 453-463, 2004
6. Lorentz E, Badel P, A new path-following constraint for strain-softening finite element simulations, *International Journal for Numerical Methods in Engineering*, vol. **60**, 499-526, 2004

## DRIVING FORCES FORMULATIONS DURING CRACK DAMAGE INTERACTIONS IN A BRITTLE MATERIAL

M. Chabaat, M. Touati and S. Djouder

Dept. of Constructions, Civil Engineering Faculté, University of Sciences and Technology Houari Boumediene. B.P. 32 El Alia, Bab Ezzouar, 16111 Algiers, Algeria.  
mchabaat2002@yahoo.com.

In this study, expressions for translation (J), isotrope expansion (M), distorsion (N) and interactions effects representing the active parts of crack driving forces known as energy release rates are formulated in a purely theoretical context. It is shown throughout this research that these elementary movements correspond to the active parts of crack driving forces occuring during the interaction of the Damage Zone (DZ) or the so-called Fracture Process Zone (FPZ) with a main crack. On the basis of a stress field obtained by the use of a Semi-Empirical Approach (SEA), which relies on the Green's functions, these driving forces corresponding to the mentioned degrees of freedom are derived within the framework of the plane problem of elastostatics.

In the last decade, sufficient experimental data has been collected, evidencing that in most cases, a severely damage zone, which often precedes the crack itself, surrounds a propagating crack. This zone can reveal itself as microcrackings in ceramics and polymers [1], as slip lines or shear bands in metals [2], and as crazing in amorphous polymers [3].

Consider a two dimensional, linear elastic solid containing an edge crack of length  $l$  and an adjacent layer of microcracks as shown in Fig. 1.

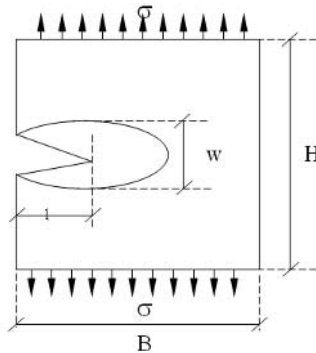


FIGURE 1. Size dimensions of the proposed model

Herein, an approach based on the representation of displacement discontinuities by means of the Green's function theory is used. The result can be obtained using the experimental measurements of the crack opening displacement and thus avoiding the difficulties of analytical solutions. In this case, the displacement field  $\tilde{U}(\tilde{x})$  at a point  $\tilde{x}$  generated by a discontinuity at point  $\tilde{x}'$  can be represented for a plane problem as

$$\tilde{U}^d = \int_{\Omega} \tilde{b}(\tilde{x}') \Phi(\tilde{x}, \tilde{x}') d\tilde{x}' \tag{1}$$

where  $\tilde{b}(\tilde{x}')$  is the discontinuity displacement,  $\Phi(\tilde{x}, \tilde{x}')$  is the second Green's tensor. This second Green's tensor for a plane stress problem is given as follows [4]:

$$\Phi(\tilde{x}, \tilde{x}') = \frac{(1 + \nu)}{4\pi R^2} \left\{ (1 - \nu) \left[ \tilde{n}_{\tilde{x}'} \cdot \tilde{R} - \tilde{R} \cdot \tilde{n}_{\tilde{x}'} - \tilde{n}_{\tilde{x}'} \cdot \tilde{R} \cdot \tilde{E} \right] - 2 \frac{\tilde{n}_{\tilde{x}'} \cdot \tilde{R}}{R^2} \cdot \tilde{R} \cdot \tilde{R} \right\} \tag{2}$$

Since the work  $W$  done by an applied force  $F$  at the grips ( $x_2 = h$ ) is given by;

$$W = F \cdot U_{\text{Total}} = U_I + U_{DZ} \tag{3}$$

then, the total energy release rate  $A_1$  takes the following form:

$$A_1 = - \frac{1}{2t} \frac{\partial P}{\partial L} = \frac{1}{2t} F \cdot \frac{\partial U_{\text{Total}}}{\partial L} \tag{4}$$

Carrying out this procedure, expressions for active parts of crack driving forces  $J$ ,  $M$  and  $N$  can be derived from Eq. (4) as:

$$A_1 = \frac{F}{E t} \hat{\phi}_{22} \frac{\partial \hat{\phi}_2}{\partial L} + \frac{F}{E t} \hat{\phi}_{2q} \hat{c}_j \frac{\partial V_{\hat{c}_j}}{\partial L} + \frac{F}{E t} \hat{\phi}_{2q} V_{\hat{c}_j} \frac{\partial \hat{c}_j}{\partial L} \tag{5}$$

Finally, one can obtain;

$$A_1 = \left[ J_I + M \partial_L \ell + \tilde{N} \partial_L \tilde{d} \right] + \Gamma \partial_L t \tag{6}$$

where  $J_I$ ,  $M$  and  $N$  correspond to the translational, the isotropic expansional and the distorsional energy of the active zone, respectively. Here,  $\Gamma$  is the change in concentration (flaws and new crazes) and interaction effects (time dependency).

In this study, formulation of the different driving forces representing the active parts of the damage are obtained in a purely theoretical context proving that the expenditure of energy into various modes of crack propagation meaning the translational motion of the crack with the process zone unchanging on one hand and the expansion as well as the distorsion of the DZ on the other hand. These latest constitute an important percentage of the total energy release rate.

**References**

1. T. Takemori, *Polymer Eng. Sci.*, vol. **22**, 937-945, 1982.
2. J. Botsis, A. Chudnovsky, A. Moet, *Internat. Jour. of Fracture*, vol. **33**, 263-284, 1987.
3. M. Chabaat, *International Journal of Fracture*, vol. **37**, 47-54, 1988.
4. A. Chudnovsky, A. Dolgopolsky, M. Kachanov, *Intern. Jour. of Fracture*, vol. **23**, 1-21, 1987.

## COHESIVE LAWS OF DUCTILE ADHESIVES: AN EXPERIMENTAL STUDY

A. Nokkentved<sup>1</sup>, P. Brondsted<sup>1</sup> and O.T. Thomsen<sup>2</sup>

<sup>1</sup> Riso National Laboratory, Materials Research Department  
DK-4000 Roskilde, Denmark

<sup>2</sup> Department of Mechanical Engineering, Aalborg University  
DK-9220 Aalborg East, Denmark

alexandros.noekkentved@risoe.dk, povl.brondsted@risoe.dk, ott@ime.aau.dk

The evolution of adhesive bonding technology and its current knowledge base was made possible by the rapid growth of adhesive applications in a great variety of industries in the past few decades. Adhesive joints are found today in the electronic, automobile, aerospace, wind turbine and shipbuilding industries. While the description of their elastic properties required for the prediction of deformation is well established, predicting failure evolution is more difficult, thus creating a great need for development of tools that predict failure evolution. Such failure analysis tools must excel in predicting initiation, size and propagation of the crack within the adhesive layer, while taking into consideration the bonds asymmetry, anisotropy and thickness variations. Such analysis can be achieved by the use of the cohesive law approach.

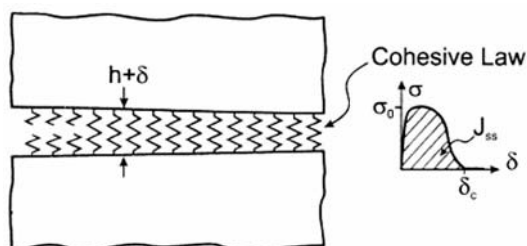


FIGURE 1. The whole adhesive joint is modelled by the separation-traction law.

The fracture process zone is characterised by a traction-separation law, a cohesive law, Sorensen [1], see Fig 1. The behaviour of "ductile" fracture and strength prediction requires modelling of the failure process zone. This can be done with fracture mechanics and a study of the local crack opening and propagation. The cohesive law establish a relationship between,  $\sigma$ , the stress across the failure process zone and its stretch,  $\delta$ , during a monotonic increase in  $\delta$ , Sorensen and Jacobsen [2]. The cohesive law can be taken as a basic fracture property and this offers the advantage that its shape can be predicted by micromechanical models, [2] and Bao and Suo [3]. The cohesive laws are determined experimentally. This method is used in this work in order to derive the cohesive law from measurements taken on the J-integral and the end-opening. In order to determine the J-integral directly from the specimen's geometry and load level, a stable crack growth is needed so that the entire  $\sigma(\delta)$ - $\delta$  curve can be determined. The double cantilever beam (DSB) loaded with pure bending moments fulfils these demands, Suo, Bao, Fan and Wang [4].

In this paper, cohesive laws for two different ductile epoxy polymers were investigated, M300- and M420 Plexus. Epoxy polymer joints with different mechanical properties and geometries are considered in order to study the effect of plasticity within the bond of ductile adhesives, since this

can enhance their fracture toughness. The J-integral can be established by a general approach and experimental measurements. Cohesive laws are obtained for pure mode I fracture of double cantilever beam (DCB) specimens. A pre-crack made by a thin teflon film is imbedded in all the specimens during manufacturing. During the experiments the load and the end-opening is measured. Retrieving the cohesive law is done by differentiating J in respect to the opening of the pre-crack tip. The "trend" of the cohesive laws where found to be quite different for the two adhesive systems and for their different thicknesses. A dramatic decrease of the maximum cohesive stresses was shown with the increase of specimen thickness for the M300 Plexus adhesive. However, the M420 Plexus adhesive's maximum cohesive stresses seem to have little dependency on specimen thickness, suggesting that the M300 Plexus adhesive might be notch sensitive. An increase of  $J_{ss}$  with larger adhesive thicknesses is also observed for both M300- and M420 Plexus adhesives suggest that for those specimens an additional toughening happens due to plasticity, Tvergaard and Hutchinson [5].

The objective of the project is to establish and demonstrate methods for modelling the mechanical behaviour of adhesively bonded joints in polymer matrix composite materials. Fracture mechanics will assist to establish the relevant framework for their mechanical performance. The main results from this study are expected to be part in a set of recommendations regarding production parameters, design, inspection and control of adhesively bonded joints.

## References

1. Sorensen, B.F., "Cohesive law and notch sensitivity of adhesive joints", *Acta Materialia*, vol. **50**, 1053-1061, 2002.
2. Sorensen, B.F., and Jacobsen, T.K., "Large-scale bridging in composites: R-curves and bridging laws", *Composites Part A*, vol. **29A**, 1443-1451, 1998.
3. Bao, G. and Suo, Z., "Remarks on crack-bridging concepts", *Appl. Mech. Rev.*, vol. **45**, 355-361, 1992.
4. Suo, Z., Bao, G., Fan, B. and Wang, T.C., "Orthotropy rescaling and implications for fracture in composites", *International Journal of Solids and Structures*, vol. **28**(2), 235-248, 1991.
5. Tvergaard, V., Hutchinson, J.W., "Toughness of an interface along a thin ductile layer joining elastic solids", *Philosophical Magazine A*, vol. **70**, 641-656, 1994.

## A STUDY ON STRESS INTENSITY FACTOR OF OUTER SURFACE CRACK ALONG THE DIRECTION OF THE AXIS OF DOUBLE COLUMN COMPOSED DISSIMILAR MATERIAL UNDER TORSION LOAD

Syuutei Sasaki and Tsutomu Ezumi

<sup>1</sup> Graduate School, Department of Engineering, Shibaura Institute of Technology, 3-7-5 Toyosu, Koto-ku, Tokyo, 108-8548 Japan

<sup>2</sup> Department of Engineering, Shibaura Institute of Technology, 3-7-5 Toyosu, Koto-ku, Tokyo, 108-8548 Japan

m603102@sic.shibaura-it.ac.jp, ezumi@sic.shibaura-it.ac.jp

This study is the purpose to obtain the stress intensity factor of the double column that is made of the dissimilar material by the experiment. The authors used the model made of the epoxy resin like the test specimen, this is changed the rigidity that these specimen are made to change the curing agency for the epoxy resin. In the case of changing the compounding ratio of the hardner, the rigidity changes. This is applied and experimented by the caustics method and the stress frozen method of the photo elasticity method.

### Introduction

The homogeneous of an internal defect and the material are often contained, avoided, and in these materials also which is a new important problem without the carefully thinking. [1] The double columnar produced with epoxy resin is modeled when a three-dimensional surface crack exists on the interfacial vicinity of a double column which consists of the dissimilar material, and the experiment analysis by the stress frozen method of the photo elasticity method is done. [2][3]

This research is assumed the case where a double column which axially had the crack acts a static load, evaluated the three-dimensional surface crack when stress intensity factor  $K_I$ ,  $K_{II}$  and  $K_{III}$  existed at the same time single according to the stress intensity factor, and elucidated the transformation style of crack up-to-date. It was compared with the rigidity and the joint boundary radius etc. of the material examine the influence which causes for the transformation style in the crack point as a result. A double columnar was modeled by the epoxy resin when a three-dimensional crack existed in interfacial of the surface of a double column which consisted of the dissimilar kind material, the stress frozen method of the photo elasticity method was applied to the caustics method, and the experiment analysis was done for the obtaining the  $K$  value.

The method of calculating stress intensity factor  $K_I$ ,  $K_{II}$ , in the photo elasticity method, and  $K_{III}$  is which uses the common method in general from expression of (1)(2)and(3).

$$\frac{K_{II}}{K_I} = \frac{2}{3} (\cot 2\theta_m \pm \sqrt{\cot^2 2\theta_m + \frac{3}{4}}) \quad \dots \quad (1)$$

$$\left. \begin{aligned} K_I &= \frac{N_m (2\pi r_m)^{1/2}}{\alpha [(\sin\theta_m + 2A \cos\theta_m)^2 + A^2 \sin^2 \theta_m]^{1/2}} \\ K_{II} &= \frac{AN_m (2\pi r_m)^{1/2}}{\alpha [(\sin\theta_m + 2A \cos\theta_m)^2 + A^2 \sin^2 \theta_m]^{1/2}} \end{aligned} \right\} \quad \dots \quad (2)$$

$$K_{III} = 0.5986 \frac{\sigma Y \max^{3/2}}{Z_o A^{1/2}} \quad \dots \quad (3)$$

### Test specimen and experiment method

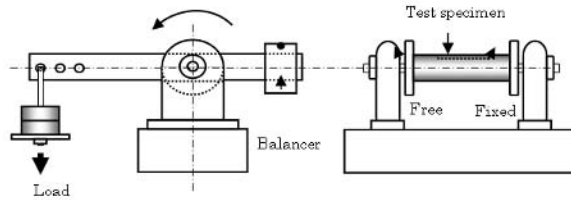


FIGURE 1. Static torsion tester (The load : 2.12N)

The test specimen was made by using epoxy resin to see the influence for the  $K$  value of an interfacial position like the column of outside diameter  $D = 50$  mm, length  $L = 20$  mm, joint boundary radius  $R_{in} = 25$  mm, 30mm, 35mm, and 40mm, and the crack was inserted width  $W = 0.15$  mm, depth  $D = 5$  mm, and length  $L = 100$  mm in the direction of the axis with the miller cutter of 0.15mm in the thickness of the blade. Modulus of longitudinal elasticity of these specimen are  $E$  (GPa) 3.93, 4.06, 4.13 and 4.25. The modulus of transverse elasticity  $G$  (GPa) 1.45, 1.48, 1.51 and 1.55. Fig. 1 is the torsion test machine for the test specimen. The left side moves by the load, and the right side is fixed by the bolt.

## Conclusions

In this research, a double column which is composed by the dissimilar material that was made of the epoxy resin was produced, the surface axially crack was inserted on the surface of the specimen, the static torsion load was put, and it was experimented. The influence which caused it for the crack point was examined, therefore the following knowledge was obtained by the diameter ratio of inside and outside compared with the horizontal elasticity coefficient using the optical elasticity method together with the caustics methods.

- The influence of the value of  $K_I$  by the change compared with the modulus of longitudinal elasticity is large in a double column which has the surface axially crack, and the value of  $K_{II}$  has understood the influence by the change compared with the modulus of longitudinal elasticity is small.
- $K_{III}$  is large, and is small in both ends. The tendency as which any type was the same was shown. In a double column which has the surface axially crack, it has been understood the value of  $K_I$  is to be able to control by putting the material with a different elasticity rate internally.
- The influence of the value of  $K_I$  and  $K_{II}$  by changing  $R_{in}/R_{out}$  compared with an inside and outside radius is large in a double column which has the surface axially crack, and it has been understood that the influence on  $K_{III}$  is small.

## Reference

1. Hisashi Shibuya and Akihiro Otomo, *Twist of double cylinder which has Akihiro one outer toroidal crack*, Japan Society of Mechanical Engineers **A**, 59-567, 2510-2516, 1993
2. Shibuya Hisashi Inoue, Kishimoto Kikuo, and Takashi Okamura, *Twist of this mind double cylinder which has and outer toroidal crack*, Japan Society of Mechanical Engineers **A**, 63-615, 2351-2358, 1997
3. Hisashi Someya and Akihiro Ootomo, *Twist of double cylinder which has outer toroidal crack*, Japan Society Of Mechanical Engineers Thesis Collection **A**, 590-56, 2510-2516, 1993



## FATIGUE FRACTURE MECHANISM IN ULTRALONG OF CEMENTED CARBIDE WC-CO

Manabu Yasuoka

1-1-1 Fujikoshi Honmachi Toyama, Japan

yasuokag@nachi-fujikoshi.co.jp

Rotating bending fatigue test was carried out using the cement carbide WC-Co in ultra-long life. A carbide metal WC has many defects on the boundary. A crack initiates from these defect, and propagates along the boundary. Fatigue limit does not exist. Because the brittleness materials like glass, ceramics obeys to the weakest link. The boundary slips easily, and is weak to sharing force. The fatigue crack propagation rate ( $da/dN$ ) cannot calculate. But, fracture toughness  $K_{IC}$  can calculate from relationship Fractal dimension or Hurst number (localized wavelets transformation) and yield area. Yield area of fracture in ultralong  $N_f=2.05 \times 10^7$  broad. Origin of fracture is surface defects. When  $K_{IC} > K_{max}$  in surface stands up, the crack in the plane stress propagate. The fatigue strength of WC cemented carbide is obeyed to weakest link model of defects. Because, even if it supposes that it was worked the cyclic stress over the fatigue strength, the fatigue fracture did not always happen. If  $K_{max}/K_{IC} = \text{const.}$  stands up, a small crack is equivalent to a small defect, and fracture of material is induced by initiated crack. By the fractal dimension analysis, the phenomenon of fracture mechanisms will be clear. Namely, the fracture happens simultaneously with crack initiation. Crack initiation and developing spread and then, generally, the rate-determining fracture process the course of the last failure. It is clarified by the crack progressing curve to the steady growth of the crack. The  $da/dN$ - $K$ th figure understood with the one which shows the characteristic of the material respectively. However, in to draw out from the material, which was destroyed by extracting the material, specialization matters which show each characteristic and being shown, the rate determining process is complete. Therefore, it aimed at the forming of a plastic region as the characteristic of the fracture surface, and the this research computed the distribution of destruction toughness value  $K_{IC}$  from inside to the surface and showed As following conclusion from them. This cemented  $W_C$  metal being formed under a hot and high pressure has the characteristic of the excellent material in the fatigue strength. And, morphology of powder is smaller as much as it, adhesion power is stronger. Those fracture modes are internal origin. When the plastic-region isn't clear, it decides most of the area by the fractal dimension and it finds  $K_{IC}$  value from them and compares with the  $K_{max}$  value. Fracture of used material in experiment shows that occurred straightly from internal to surface as  $K_{max}/K_{IC}$  is constant value.

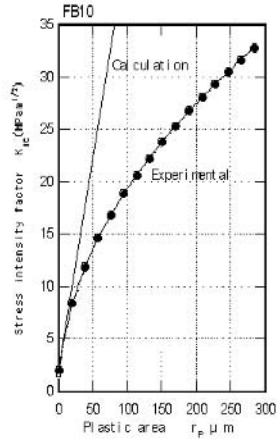


FIGURE 1. Relationship between fracture toughness  $K_{IC}$  and plastic zone  $w_p$

## EXPERIMENTAL INVESTIGATION INTO THE FATIGUE OF WELDED STIFFENED 350WT STEEL PLATES USING NEUTRON DIFFRACTION METHOD

B.K.C. Yuen<sup>1</sup>, F. Taheri<sup>1</sup> and M. Gharghourim<sup>2</sup>

<sup>1</sup>Department of Civil and Resource Engineering, Dalhousie University  
1360 Barrington Street, Halifax, NS, Canada, B3J 1Z1

<sup>2</sup>Canadian Neutron Beam Centre, Chalk River Laboratories  
Building 459, Stn. 18, Chalk River, ON, Canada, K0J 1J0  
Brian.Yuen@dal.ca, Farid.taheri@dal.ca and gharghourim@aecl.ca

Stiffened plates are widely used in aircraft, ships and civil infrastructures. They offer light weight and high strength and stiffness. In ship structures, they are often used in areas where the amount of fatigue loading is the greatest. The survey of the literature has shown that there has been a large volume of research to address fatigue crack growth in stiffened plates in aircraft structures; however, most of the studies have considered aluminium panels that have been either riveted or adhesive bonded stiffeners. It has been observed that investigations on welded steel stiffened plates, often found in ship structures, are much scarce [1, 2]. The heating and cooling resulting from the welding of such stiffeners to the parent plate induces a complex three-dimensional state of residual stresses in the structure. Moreover, despite the fact that the distribution of such residual stresses is recognized to have considerable influence on the fatigue crack growth rates of welded stiffened panels, the fatigue behaviour of such structures, especially as a result of such residual stress states, is not well understood. There is also a paucity of test data in characterizing the fatigue response of such structures.

This study focuses on evaluation of the residual stresses in 350 WT steel stiffened plates using the neutron diffraction strain-scanning technique. Typical test specimen is shown in Fig. 1. In the present investigation, the principal strains directions were assumed to follow the symmetry axes of the specimen: transverse ( $x$ ), longitudinal ( $y$ ) and normal ( $z$ ) as shown in Figure 1. The wavelength of the neutron beam was chosen to be approximately  $1.5 \text{ \AA}$  by rotating the germanium crystal in the monochromator to the (115) diffraction plane. The detector was then driven to the appropriate angle  $2\theta$ , such that strains were measured on the (211) plane of the specimen, which is the recommended diffraction plane for ferritic steel

Typical results are shown in Fig. 2. The neutron diffraction measurements indicated that in general the residual stresses were tensile near the welded stiffeners and compressive between the stiffeners and ahead of the starter notch tip. Fatigue testing indicated that the fatigue crack growth rates of the stiffened plates were in general lower than that of a corresponding unstiffened plate, especially near the notch tip where compressive residual stresses existed. The longitudinal component of the residual stress conceivably had the most influence on the fatigue life of the stiffened plate as it was in the direction of the fatigue loading

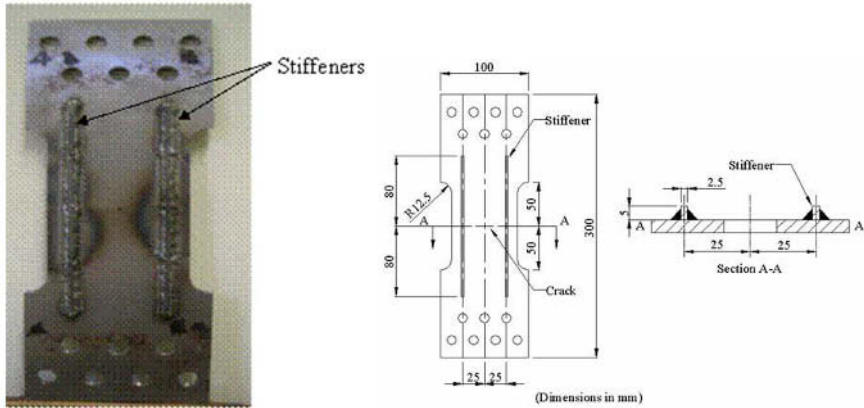


FIGURE 1. The stiffened plate specimen and its dimensions.

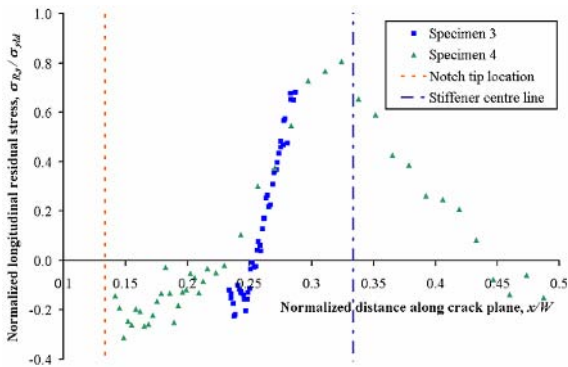


FIGURE 2. The measured longitudinal residual stresses.

## References

1. Nussbaumer, A.C., Fisher, J.W. and Dexter, R.J., *Journal of Structural Engineering*, vol. **125**, 1232-1238, 1999.
2. Dexter, R.J., Pilarski, P.J. and Mahmoud, H.N., *International Journal of Fatigue*, vol. **25**, 1169-1174, 2003.

## IMPORTANCE OF STANDARDIZATION FOR FATIGUE TESTING AND FATIGUE DATA ANALYSIS IN VERY HIGH CYCLE REGIME

Tatsuo Sakai

Department of Mechanical Engineering,  
College of Science and Engineering, Ritsumeikan University  
1-1-1 Nojihigashi, Kusatsu, Shiga, 525-8577, Japan  
sakai@se.ritsumei.ac.jp

Mechanical structures are usually fabricated by using various kinds of metallic materials as the structural components. The structural steels indicate the distinct fatigue limit in the  $S-N$  property, in which the  $S-N$  curve becomes horizontal and no fatigue fracture occurs at the stress levels lower than this critical level. Thus, mechanical components have been designed to operate well at stress levels lower than the fatigue limit measured at  $10^7$  cycles. However, during the last decade, several unexpected failures have been reported even for structural components made of ferrous metals, which were assumed to have a distinct fatigue limit. In recent years, economic and environmental considerations have increased the need to safely extend the service life of mechanical structures such as energy conversion and transportation systems beyond their design life. From this trend, the fatigue behavior of structural materials in the very high cycle regime of  $10^9$ - $10^{10}$  cycles has become an important subject of research all over the world. In this background, some international conferences were organized and hot discussions were made on a wide variety of the fatigue characteristics of those structural materials[1-3].

Based on the recent researches performed by many researchers, some metallic materials such as high strength steels and case-hardened steels have a characteristic fatigue property in the very high cycle regime to indicate the duplex  $S-N$  property consisting of the respective  $S-N$  curves for surface-induced fracture and interior inclusion-induced fracture[4]. In the latter case, fish-eye is usually observed on the fracture surface and an inclusion is found at the center of the fish-eye[5]. In addition, it is noted that a characteristic area having the fine granular morphology is formed around the inclusion at the crack initiation site[5]. Such characteristic fatigue behaviors depend upon the kind of metallic materials, the loading types, the loading frequency, the testing temperature and environments and so on. From this point of view, what is the standard fatigue property common to the different testing conditions, and, what is the individual fatigue property peculiar to each testing condition. In some cases, only the S-N data are obtained as the fundamental design data for the actual mechanical products in the fatigue tests. In such a case, fracture surfaces are not usually observed by means of an SEM. Even if the fracture surface was observed by SEM, the central portion of the fish-eye was not usually observed at very high magnification. Thus, existence of inclusion at the crack origin is not always confirmed and the formation of the fine granular area(FGA) around the inclusion is not always investigated in the fractography.

In the above circumstances for the fatigue testing method and the testing procedure, some kinds of standardizations should be established in order to clarify the true aspect of the fatigue characteristics of metallic materials in the very high cycle regime. Loading types in the fatigue tests are axial loading, plane bending, rotating bending, torsion and some other special loading. The type of fatigue testing machine is also in the wide variety such as electro-hydraulic servo type testing machine, piezo-electric ultrasonic fatigue testing machine and many other special types including some multi-type testing machines which can perform fatigue tests for many specimens simultaneously. Thus, fatigue tests in the very high cycle regime were carried out following the

individual testing machine and procedure depending on the respective researchers. It is difficult to compare directly those fatigue test results with one another. We have another important subject in the present research area. Namely, how can we analyze the fatigue test data obtained in the very high cycle regime[6]? How can we determine the  $S-N$  curve from the numerical data providing pairs of stress level and fatigue life ( $\sigma_a$  versus  $N_f$ )? How can we separate the failed specimens into the surface-induced fracture and the interior inclusion-induced fracture? Thus, the concrete procedure to analyze the fatigue test data is an important subject which should be established as a standard method from the global viewpoint.

In the author's opinion, the conventional standardized procedure for the fatigue tests in the usual life region less than  $10^7$  cycles should be referred and some original procedures should be added in order to perform the long life fatigue tests. For example, it takes 200 days to perform the fatigue test toward  $10^9$  cycles at the frequency of 50Hz. Thus, the long-term stability of the testing machine is important article in the fatigue tests. On the other hand, the ultrasonic fatigue testing machine can give us the high cycle fatigue property within a short period as reported by many researchers. However, the temperature elevation of the specimen introduces a difficulty in the ultrasonic fatigue testing. In order to overcome this difficulty, several kinds of special techniques to keep usual temperature were developed and reported by many researchers. But, effects of the frequency and the cooling technique are still unsolved clearly. Thus, some standard testing procedures should be established, even if the ultrasonic testing method was applied in the fatigue tests.

In conclusion, some standard fatigue testing methods should be selected and the concrete testing procedures should be specified for the respective testing machines. There are many fundamental fatigue test data other than  $S-N$  data, such as chemical compositions, heat treatment conditions, specimen type and dimensions, surface finishing and relative mechanical properties, should be measured and recorded for every fatigue test. What kinds of relative data should be recorded as the fundamental fatigue data? This is also another important articles in the standardization of the fatigue test and the data analysis in the present area[7]. In this lecture, typical articles required to the standardization in the very high cycle fatigue tests are indicated for the sake of convenience to facilitate the applicability of the fatigue test data.

## References

1. Organized by C. Bathias, *EUROMECH382 "Fatigue Life in The Gigacycle Regime"*, Paris, 1998.
2. Organized by S. Stanzl-Tcshegg and H. Mayer, "*Fatigue in the Very High Cycle Regime*", Vienna, 2001.
3. Organized by T. Sakai and Y. Ochi, "*The 3rd Int. Conf. Very High Cycle Fatigue(VHCF-3)*", Kyoto/Kusatsu, 2004.
4. T. Sakai, M. Takeda, K. Shiozawa, Y. Ochi, M Nakajima, T. Nakamura and N. Oguma, *Proc. 7<sup>th</sup> International Fatigue Congress*, vol. **1**, 573-578, 1999.
5. T. Sakai, Y. Sato and N. Oguma, *Fat. Fract. Engng. Mater. Struct.*, vol. **25**, 765-773, 2002.
6. T. Sakai, Y. Sato, Y. Nagano, M. Takeda and N. Oguma, *International Journal of Fatigue*, vol. **28**, 1547-1554, 2006.
7. T. Sakai, A. Sugeta, H. Nakayasu and I. Nishikawa, *Proc. ICOSSAR2005*, CD-ROM, 2005.

## FATIGUE STRENGTH OF 7050 T7451 ALUMINUM ALLOY: COATING EFFECTS

Herman Jacobus Cornelis Voorwald, José André Marin de Camargo

and Maria Odila Hilário Cioffi

Fatigue and Aeronautic Materials Research Group, Department of Materials and Technology  
State University of São Paulo – UNESP. Av. Ariberto Pereira da Cunha, 333 CEP 13516-410  
Guaratinguetá/SP-Brazil  
cioffi@feg.unesp.br

For landing gear, considering the potential to support all the structure and cyclic loading during landing, the most important criteria design is high strength and fatigue resistance [1,2]. Aluminum alloys have been the best choice for commercial aircraft with a much more rapid insertion due to lower manufacturing costs, low replacing risk and the use of an existing production infrastructure. The 7xxx series are predominating alloys when strength is the primary requirement [3,4].

A well known and used surface impact treatment to improve the fatigue strength of components subjected to variable amplitude loading, is shot peening [5]. A compressive residual stress field is created which retards or eliminates the nucleation and propagation of fatigue cracks. The present study evaluates a tungsten carbide cobalt (WC-Co) coating applied by the high velocity oxy-fuel (HVOF) process, used to replace anodizing.

This research evaluates a tungsten carbide-cobalt (WC-Co) coating applied by the high velocity oxy-fuel (HVOF) process, used to replace anodizing. S-N curves for axial fatigue tests were obtained for base material 7050 T 7451 aluminum alloy and base material with anodic films grown by sulphuric acid anodizing, chromic acid anodizing and hard anodizing. To compare with previous experimental results, three groups of specimens were prepared and tested in axial fatigue to obtain S-N curves: base material, base material WC-17%Co coated by HVOF.

The influence on axial fatigue strength of anodic films grown on the aluminum alloy is to degrade the stress life performance of the base material. The sulphuric acid and hard anodizing showed the strongest effect. The WC-17%Co thermal spray coatings improved the axial fatigue strength of Al 7050 T 7451 alloy.

Tensile residual stress at interface coating/substrate (+ 130MPa), which increased to + 170MPa at 0,05 mm from interface, were induced by the WC-17% thermal spray coating process. A reduction in the axial fatigue life of shot peened coated specimens in comparison to Al 7050 T7451, WC-17%Co thermal spray coated, was observed. Tensile residual internal stresses were obtained at interface coating/substrate (+ 190MPa) and inside base material (+130MPa at 0,10mm and + 100MPa at 0,15mm).

The results of the axial fatigue tests for the base material and specimens with WC –17% Co thermal spray coated, are shown in Fig. 1.

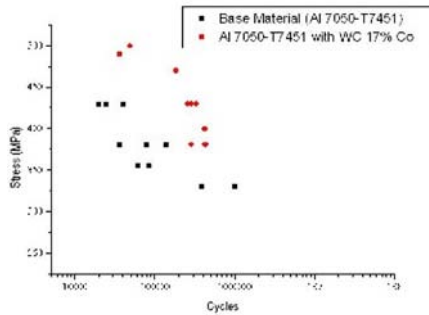


FIGURE 1. Axial fatigue life of base material and WC – 17% Co thermal spray- coated specimens an Al 7050 T7451 alloy substrate.

## References

1. Nascimento, M.P., Souza, R.C., Miguel, I.M., Pigatin, W.L. and Voorwald, H.J.C. Effects of tungsten carbide thermal spray coating by HP/HVOF and hard chromium electroplating on AISI 4340 high strength steel. *Surf. Coat. Tech.*, vol. **138**, 2-3, 113-124, 2001.
2. Torres, M. A. S. and Voorwald, H. J. C. An evaluation of shot peening, residual stress and stress relaxation on the fatigue life of AISI 4340 steel. *Int. Jour.Fatigue*, vol. **24**, pp. 877-886, 2002.
3. Williams. J. C. and Starke Jr., E.A. progress in structural materials for aerospace systems. *Acta Materialia*, vol. **51**, 5775-5799, 2003.
4. Starke Jr., E. A. and Staley, J.T. Application of modern aluminium alloys to aircraft. *Progress in aerospace Science*, vol. **32**, 131 – 172, 1995.
5. Nascimento, M. P., Souza, R. C., Pigatin, W. L. and Voorwald, H. J. C. Effects of surface treatments on the fatigue strength of AISI 4340 aeronautical steel. *Int. Jour.Fatigue*, vol. **23**, 607 – 618, 2001.



## FATIGUE ON NC2/RTM6 COMPOSITES

Maria Odila Hilário Cioffi<sup>a</sup>, Herman Jacobus Cornelis Voorwald<sup>a</sup>, Mirabel Cerqueira Rezende<sup>b</sup>  
and Luigi Ambrosio<sup>c</sup>

<sup>a</sup>Fatigue and Aeronautic Materials Research Group, Department of Materials and Technology  
State University of São Paulo – UNESP. Av. Ariberto Pereira da Cunha, 333 CEP 13516-410  
Guaratinguetá/SP, Brazil

<sup>b</sup>AMR/IAE/CTA Praça Marechal Eduardo Gomes, 50 Campus do CTA - Vila das Acácias 12228-  
901 São José dos Campos, SP

<sup>c</sup>Institute of Composite and Biomedical Materials, IMCB-CNR, Piazzale Tecchio 80 - 80125  
Napoli, Italy  
cioffi@feg.unesp.br

The improvement of composites materials in the infrastructure and engineering areas in the last years is excellent. Consequently, technological challenges as sophisticated test methods and accurate tools development are generated. Also environmental considerations, which correspond to the mechanical requirements to application of these materials, are fundamental [1].

The RTM process is one of more efficient techniques to produce advanced fibers reinforcing polymeric matrix composites [2]. It is associated to an effective low cost technology to produce great scale composites components. It was developed as an economic method of high quality composites to produce more complex components than that obtained from the traditional methods [3], present excellent controlling of mechanical properties and shorter cycle of process [4].

The NCF/RTM6 composite processed by RTM, shows potential as aeronautical material. The Fig. 1a shows the NC2/RTM6 composites laminate processed by RTM and the figure 1b shows the impregnation map from ultra-son analysis. The material was produced and provided by Hexcel composites.

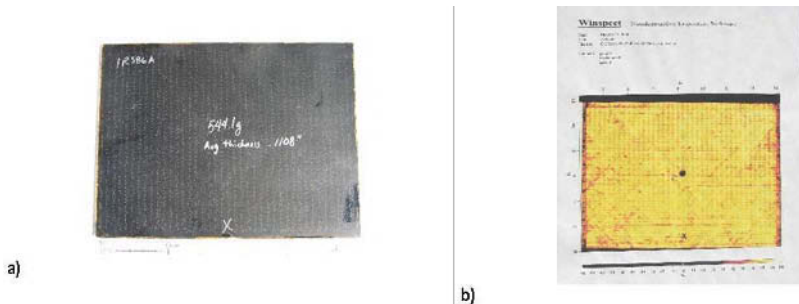


FIGURE 1. NC2/RTM6 Composite a) Laminate; b) Impregnation map

The fatigue phenomenon in composites reinforced with fiber is very complex and the behaviour of these heterogeneous materials is quite different from metals, for example.

Fatigue failure analysis was performed using the stress intensity factor and minimum and maximum applied load ( $\Delta K$ ), from which is dependent the energy dissipation while  $K_{max}$  controls the fracture velocity. The stress ratio,  $R = \left( \frac{K_{min}}{K_{max}} \right)$ , confers significance to the  $K$  data. The material strength in relationship to the dimension of crack is determined as the growing velocity by

load cycle  $dc/dN$ . For an intermediate  $DK$ , the growing velocity follows the Paris-Erdogan equation [5, 6].

$$\frac{d_c}{dN} \equiv \beta(\Delta K)^n$$

For axial tests using a INSTRON 8801, a sinusoidal load of 10 Hz frequency and load ratio  $R_a=0.1$  was applied in the NCF/RTM6 composite specimens, which were done according to ASTM D3039, indicated in Fig. 2.

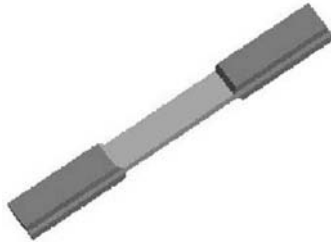


FIGURE 2. Typical axial fatigue specimens.

Data obtained from axial fatigue tests are presented in the SxN curve indicated in Fig. 3

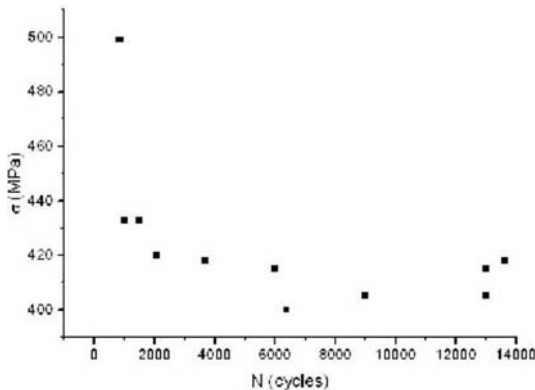


FIGURE 3. Fatigue tests SxN curve of NC2/RTM6 composites.

## References

1. Macbagonluri, F., Garcia, K., Hayes, M., Verghese, K. N. E., Lesko, J. J., *Int. J. Fatigue.*, vol. **22**, 53-64, 2000
2. Antonucci, V., Giordano, M., Nicolais, L., Di Vita, G. *Polymer Eng. Science*, vol. **40** (12) 2471-2481, 2000
3. Hillermeier, R. W., Seferis, J.C. *Composites: part A*. 32 721-729, 2001.
4. Luo, J., Liang, Z., Wang, B. *Composites: part A*. 32 877-888, 2001.
5. Hull, D., Clyne, T. W. (1996) in: *An Introduction to Composite Material. Cambridge Solid State Science Series* 1-8.
6. ASTM STP 675. (1979) Fatigue Mechanisms. Jeffrey T. Fong, editor, 762-779.

## EVALUATION ON THE FATIGUE STRENGTH OF TI-6AL-4V WITH WC 10CO-4CR DEPOSITED BY HVOF

Midori Yoshikawa Pitanga Costa, Maria Odila Hilário Cioffi  
and Herman Jacobus Cornelis Voorwald

Fatigue and Aeronautic Materials Research Group, Department of Materials and Technology  
State University os São Paulo – UNESP. Av. Ariberto Pereira da Cunha, 333 CEP 13516-410  
Guaratinguetá/SP-Brazil  
midori@feg.unesp.br

Titanium alloys is a widely used material for structural components because this alloy characteristics as low density, nearly 50% of steel density, high strength which provide high weight/strength ratio. The weight savings and high corrosion resistance make titanium attractive for application in landing gears [1,2].

However, titanium has a poor tribological behaviour. Straffelini and Molinari explain that titanium alloys have low sliding wear resistance because of their low resistance to plastic shearing and low protection exerted by the surface oxides [3].

Surface coatings are a usual alternative to improve wear resistance of mechanical components. HVOF Thermally sprayed coatings with excellent wear resistance properties have been used in aerospace, oil and paper industries. Considering safe and security of landing gear components, fatigue strength of Ti-6Al-4V coated was evaluated [4,5].

The aim of this paper is investigate the microstructure of WC-10%Co-4%Cr deposited by HVOF in Ti-6Al-4V substrate by scanning electron microscopy and analyse its influence in fatigue behaviour of Ti-6Al-4V coated.

The fatigue experimental tests were performed on axial fatigue test specimens prepared according to standard ASTM E 466. Typical dimensions of the specimen used for fatigue axial tests are shown in Fig. 1.

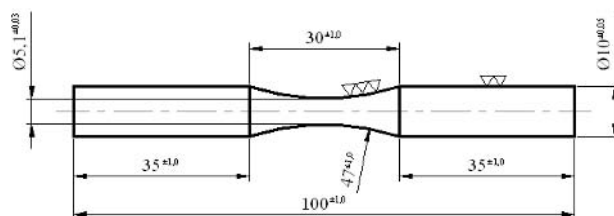


FIGURE 1. Axial fatigue testing specimens

Figure 2 shows the influence of WC10%Co-4%Cr on the fatigue strength of Ti-6Al-4V. It is possible to observe reduction in the fatigue strength due to the HVOF coating, in comparison to base material. The Results shows that fatigue strength of Ti-6Al-4V coated reduce from 950 MPa to 400 MPa.

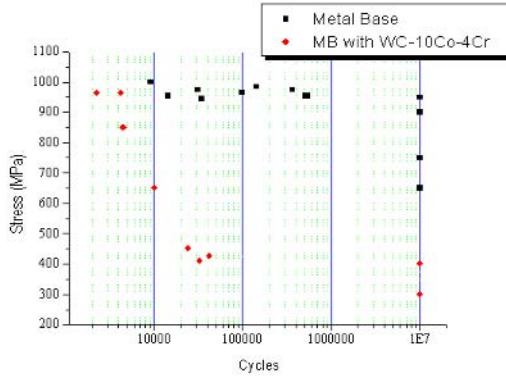


FIGURE 2. SN curve for Ti-6Al-4V coated with WC-10%Co-4%Cr

Figure 3 shows a surface polished of Ti-6Al-4V coated with WC-10%Co-4%Cr which present a micro crack inside of coating.

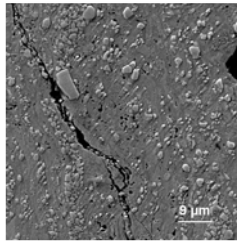


FIGURE 3. Microstructure of Ti-6Al-4V coated with WC-10%Co-4%Cr

## References

1. Boyer, R.R., *Materials Science Forum*, vol. **426**, 643-648, 2003.
2. Williams, J. C., *Mat. Sci. and Engineering A*, vol. **263**, 107-111, 1999.
3. Straffelini, G. and Molinari, A., *Wear*, vol. **236**, 328-338, 1999.
4. Voorwald, H.J.C., Souza, R.C., Pigatin, W.L. and Cioffi, M.O.H., *Surf. & Coat. Tech.*, vol. **190**, 155-164, 2005.
5. Toma, D., Brandl, W. and Marginean, G., *Surf. & Coat. Tech.*, vol. **138**, 149-158, 2001.

## MECHANICS BEHAVIOR OF SISAL FABRIC

Andressa Cecília Milanese, Maria Odila Hilário Cioffi and Herman Jacobus Cornelis Voorwald  
Fatigue and Aeronautic Materials Research Group, Department of Materials and Technology  
State University of São Paulo – UNESP. Av. Dr. Ariberto Pereira da Cunha, 333 CEP 12516-410  
Guaratinguetá/SP-Brazil  
pos06001@feg.unesp.br

Natural fibers as reinforce material presents innumerable advantages, such as: low specific mass; low superficial consuming in equipment as extrusions; easy handle; biodegradability and renewable resource; insulator thermal, electric and acoustic; aesthetic aspects; non-toxic; beyond low cost [1,2]. In the automobile industry is considered as a great potential to apply in the internal covering area of cars, bus and trucks; in the civil construction to reinforce cement; as textile material, characterizing a market in expansion [2]. The raw material from renewed resources is of great interest to the research area, due to the replacement possibility fibers originated from petrochemical derivatives, which should contribute to the environmental control.

Natural fibers as curauá [2], coconut [3], sisal [3], rami, bagasse of sugar-cane [4], jute and pineapple have been used as reinforcement material. Sisal fibers are extracted from *Agave sisalana perrine* leaves, monocotyledon classified originated from Mexico. Each leaf of sisal provides 4% in weight of staple fibers and 96% in weight of residues [5]. Brazil has a great production of sisal and export for the entire world, with a yearly production of 119.000 tons. Is also responsible for 56% of the worldwide production, which is approximately 204.000 tons [6]. The main producers states are Bahia - 93.5%, Paraíba - 3.5% and Rio Grande do Norte - 3%, the semiarid region [7]. Commercially the products of sisal are found mainly as ropes, wires and fabrics. The sisal fabric used in the specimens has the form plain weave [8] and shown in Fig. 1.



FIGURE 1. Form of sisal fabric: plain weave.

The sisal fabric specimens are tested *in natural* and thermal treated at 60°C for 48h. Specimens have been confectioned in agreement to the ASTM D3039 [9], indicated in Fig. 2.

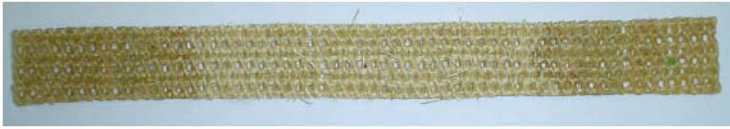


FIGURE 2. Sisal fabric specimen.

Tensile tests data indicated in Table 1, shows for *in natura* specimens a tensile strength 50% greater than thermal treated specimens. Also the tensile tests provide a located rupture of one or few fibers and the load was transferred to the unbroken fibers.

TABLE 1. Results of strength.

Properties	In natura	Thermal treated
Average maximum load / KN	1,570	1,012
Average displacement at break / mm/mm	0,060	0,061
Average area /mm <sup>2</sup>	68,16	66,71
Average tensile strength / MPa	23,06	15,13
Standard deviation	2,99	1,98

In this research, sisal fibers will be submitted to the fatigue test and the scanning electron microscopic will be conducted.

## References

1. Carvalho, R. F.; Calil Júnior, C., In: *Encontro Brasileiro de Madeiras e em Estruturas de Madeira*, Uberlândia, Minas Gerais, Brasil, 2002, Cd-rom.
2. Mothé, C. G.; Araujo, C. R. de, *Polímeros*, vol. **14**, no.4, 274-278, 2004.
3. Silva, R. V; Spinelli, D.; Bose Filho, W. W.; Claro Neto, S.; Chierice, G. O.; Tarpani, J. R., *Composites Science and Technology*, vol. **66**, no.10, 1328-1335, 2006.
4. Mulinari, D. R.; Silva, G. L. J. P.; Silva, M. L. C. P., *Química Nova*, vol. **29**, no.3, 496-500, 2006.
5. Mattoso, L. H. C.; Ferreira, F. C.; Curvelo, A. A. S., In: *International Symposium On Lignocellulosics-Plastics Composites*, UNESP, São Paulo, Brasil, 1996, 241-266.
6. [http://www.apexbrasil.com.br/noticia\\_detalhe.aspx?idnot=265](http://www.apexbrasil.com.br/noticia_detalhe.aspx?idnot=265). Accessible: Sept. 28<sup>th</sup> 2006.
7. <http://www.cnpa.embrapa.br/produtos/sisal/index.html>. Accessible: September 28<sup>th</sup> 2006.
8. Gay, Daniel; Hoa, S. V.; Tsai, S. W., *Composite Materials: Design and Applications*, CRC Press, Paris, France, 1997.
9. American Society for Testing and Materials. *ASTM D 3039-00*: Standard Test Method for Tensile Properties of Polymer Matrix Composite Materials, 2000.

## TEST CONDITIONS EFFECT ON THE FRACTURE TOUGHNESS OF HOLLOW GLASS MICRO-SPHERES FILLED COMPOSITES

C. Capela<sup>1</sup>, J.D. Costa<sup>2</sup> and J.A.M. Ferreira<sup>2</sup>

<sup>1</sup> Polytechnic Institute of Leiria, Mechanical Engineering Department  
Morro do Lena - Alto Vieiro, 2400-901 Leiria, Portugal

<sup>2</sup> University of Coimbra, Mechanical Engineering Department, ICEMS  
Polo II da Univ. de Coimbra, Pinhal de Marrocos, 3030, Coimbra, Portugal  
ccapela@estg.ipleiria.pt, josé.domingos@dem.uc.pt, martins.ferreira@dem.uc.pt

Low-density sheet moulding compounds based in hollow glass micro-spheres are being increasing used namely in automotive industry where can present advantages compared with traditional metal, such as: lower weight, less expensive for low volume production in consequence of lower tool costs, no corrosion effects, a more design freedom, etc. These materials are usually classified as syntactic foams if the filler content is relatively high. Syntactic foams are potential good materials for applications where impact loads occurs once they are able to reduce impact force [1,2]. The addition of hollow micro-spheres trends to reduce the Young modulus and ultimate strength [2,3] and even the specific values are only increased in terms of impact force and marginally in flexural modulus for high volume fractions of micro-spheres [2].

The main objective of current work was to study the effects of load rate and humidity (in the case immersing the specimens in water for periods until seventy days) on the flexural mechanical properties and particularly on the fracture toughness  $K_{IC}$ .

Hollow micro-spheres Verre ScotchitTM-K20 manufactured by 3M with particles size of 33.5  $\mu$ m were used. The resins used for binding micro-spheres, consist of epoxy 520 with hardener 523 and polyester Hetron 92 FR supplied by Ashland Chemical Hispania. Rectangular parallelepiped specimens were cut from the moulded plates with volume fraction of 28% and machined for the dimensions of 65x12x6 mm for flexural and mode I fracture toughness tests.

The tests were performed using an Instron universal testing machine, equipped with computer controller and recorder system according to ASTM D790-98 and ASTM D5045-96, for flexural properties and mode I fracture toughness, respectively.

A batch of specimens was immersed in water at 20 °C until seventy days. The water absorption was quantified in order to relate it with the obtained mechanical properties. Fracture toughness  $K_{IC}$ , flexural stiffness modulus and ultimate strength were obtained as function of the load rate and the immersed time. The parameters studied show a slight effect and in some cases negligible on mechanical properties. Figures 1 and 2 present the results of the toughness  $K_{IC}$  against the water immersion time and the load rate, respectively, confirming the slight effect of these parameters.

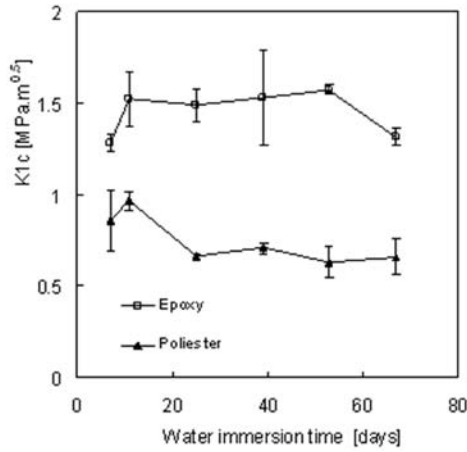


FIGURE 1. Influence of the time of water immersion on the  $K_{IC}$ .

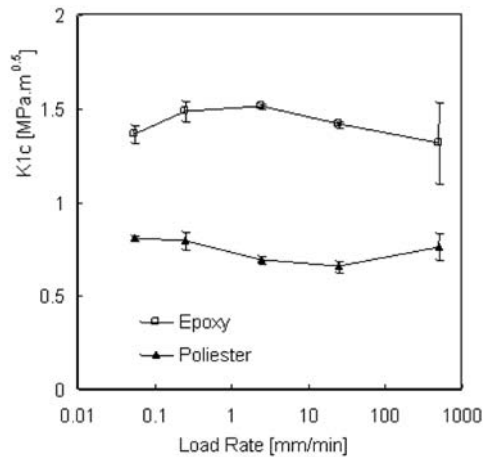


FIGURE 2. Influence of the load rate on the  $K_{IC}$ .

## References

1. Kim, H.S., Oh, H.H., *J. Appl. Polym. Sci.*, vol. **76**, 1324-1328, 2000.
2. Kim, H.S., Khamis, M.A., *Composites Part A: Appl. Sci. and Manuf.*, vol. **32**, 1311-1317, 2001.
3. Black, P.A., *Fatigue of TIG-Welds*, ABC Co., Report No. R-231, 1993. Oldenbo, M., Fernberg, S.P., Berglund, L.A., *Composites Part A: Appl. Sci. and Manuf.*, vol. **34**, 875-885, 2003.



## CRACK GROWTH BEHAVIOR IN THE INTERFACE OF REPAIR WELDED 1Cr-0.5MO STEEL

Un Bong Baek, Kee Bong Yoon, Hea Moo Lee  
 Korea Research Institute of Standards and Science  
 1 Doryong-Dong, Yuseong-Gu, Daejeon 305-340, Korea  
 ubbaek@kriss.re.kr

Considerable amount of creep-fatigue crack growth (CFCG) data with characterizing fracture parameter  $C^*$  or  $C_t$  have been generated for the last 25 years. On the contrary similar efforts for weld interface crack started only a few years ago. In this article the CFCG behavior of 1Cr-0.5Mo steel particularly for weld interface cracks is intensively studied by experimental methods.

In order to measure high temperature material properties involved in CFCG study of the weld interface crack, tensile and creep properties were measured for each part of the weld metal, the heat affected zone(HAZ) and the parent metal of 1Cr-0.5Mo steel at 538 °C. HAZ metal was obtained by a simulated heat treatment[1]. Results showed that the order of tensile strength is weld>HAZ>parent both at 24 °C and at 538 °C. Creep resistance was also the highest for weld metal and lowest for parent metal. Creep rupture life curves were obtained and converted to Monkman-Grant relation [2] which is useful for life assessment.

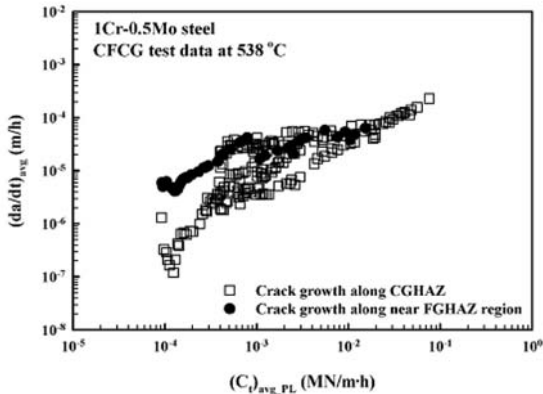


FIGURE 1. Creep fatigue crack growth rates related with considering crack tip plasticity

With use of the data obtained from the above study, high temperature crack growth behavior was investigated. Creep-fatigue crack growth behavior was experimentally measured particularly when a crack was located in the heat affected region of 1Cr-0.5Mo steel. Load hold times of the tests for trapezoidal fatigue waveshapes were varied among 0, 30, 300 and 3,600 seconds. Time-dependent crack growth rates were characterized by the  $C_t$  estimated with the equation proposed by the previous finite element analysis work. It was concluded that the  $C_t$  values calculated from the properties of parent metal were quite comparable to the accurate  $C_t$  values calculated from both of weld and parent metals. Scatter of data was claimed due to the difference of exact location of the

cracks in HAZ. By metallographic observation, it was revealed that the cracks have a tendency to change their path from the original location eventually to the relatively soft HAZ (ie, near-fine grained HAZ region). The crack tends to grow along the fine grained HAZ regardless of the initial position of the crack tip. The reason of this crack growth trend was discussed based on creep properties of the HAZ. Creep-fatigue crack growth law of the studied case is suggested in terms of  $(da/dt)_{avg}$  vs.  $(C_t)_{avg}$  for residual life assessment.

$$\left(\frac{da}{dt}\right)_{avg} = 7.05 \times 10^{-4} (C_t)_{avg}^{0.519} \quad (1)$$

## References

1. M. S. Shamms "Metallographic methods for predicting the remanent life erritic coarse-grained weld heat affected zones subject to creep cavitation", *Int. Conf. on Life Assessment and Extension*, Hauge, Netherlands, 1315 June, 1988.
2. Dobe, F. and Milicka, K., 1976, "The relation between minimum creep rate and time to fracture," *Metal Science*, vol. **10**, pp. 382384.
3. A. Saxena and B. Gieseke. "Transients in elevated temperature crack growth." *In Proceedings of MECAMET-International Seminar on High Temperature Fracture Mechanisms and Mechanics*, Dourdan, France, pp. 1936., 1987
4. B. Gieseke. and A. Saxena. "Correlation of creep-fatigue crack growth rates using crack tip parameters." *Proceedings of the Seventh International Conference of Fracture: ICF-7*, pp. 189196, Pergamon Press, 1989.

## MODELING OF FATIGUE IN A LOW-CARBON ROLLER-QUENCHED TEMPERED STEEL

D. Angelova and R. Yordanova

Donka Angelova – Professor and Rozina Yordanova – Assistant Professor in the University of Chemical Technology and Metallurgy-Sofia, 8 Kl. Ohridski Blvd., 1756 Sofia, Bulgaria  
 dona\_ang@techno-link.com, rozi.yordanova@abv.bg

A low-carbon roller-quenched tempered steel, *RQT501*, used for offshore applications was subjected to tension-tension loading at a stress ratio  $R = 0.1$  using a servo-electric fatigue rig with a load capacity of 100 *kN*. Tests were performed in load control at stress levels of 396, 470 and 516 *MPa* within a 0.6M *NaCl* environment [1], and at 520, 522 and 525 *MPa* in air [2]. A sinusoidal waveform was used at frequencies 0.2, 0.5, 1 and 10 *Hz*. Pit and short crack initiation and growth were monitored by surface replication of the specimen and their diameters and lengths – measured with the help of an image-analysis system.

The three distinct regimes  $da/dN - a$  describing the fatigue behaviour of *RQT501* – those of microstructurally short cracks  $a_{sh}$ , physically small cracks  $a_{phs}$  and long cracks  $a_l$  – are modeled by parabolic-linear system of equations M, shown in Eqs. (1), Figs. 1, 2 and Tabl. 1:

$$M: \begin{cases} \left(\frac{da}{dN}\right)_{sh} = A_1 a^2 + A_2 a + A_3, a \in [a_0, d_1]; & \left(\frac{da}{dN}\right)_{phs} = B_1 a^2 + B_2 a + B_3, a \in [d_1, d_2]; & \left(\frac{da}{dN}\right)_l \\ = C_1 a^{C_2}, a \geq d_2 \end{cases} \quad (1)$$

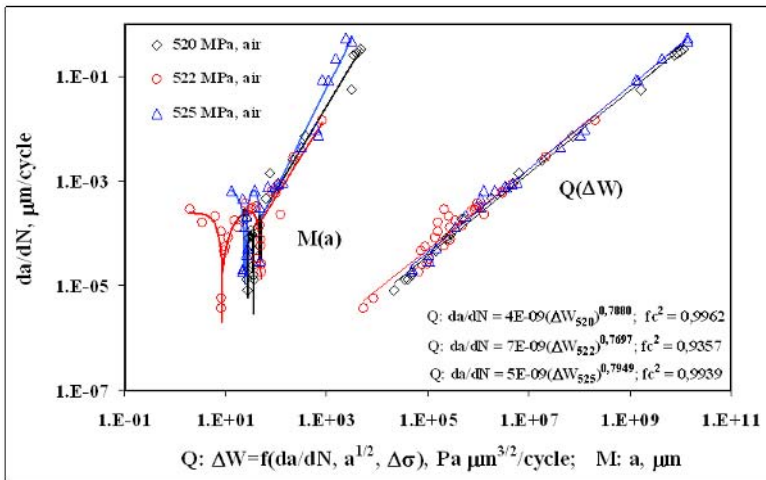


FIGURE 1. Short fatigue crack *in-air* data presentations – conventional M and alternative Q

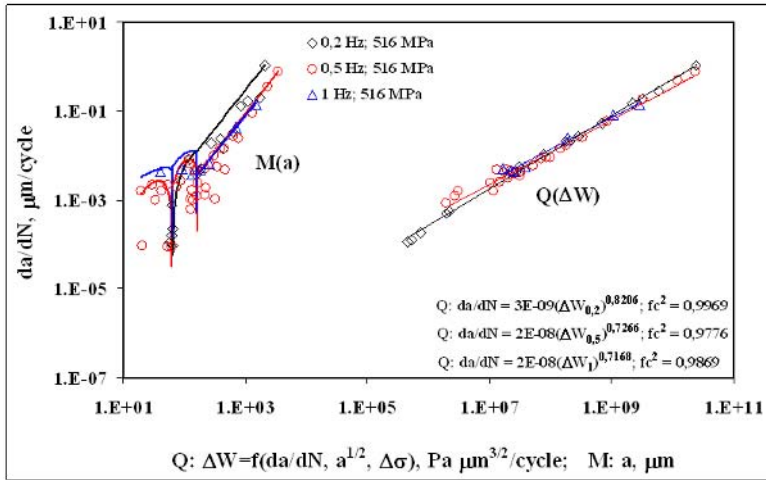


FIGURE 2. Short fatigue crack corrosion data presentations – conventional M and alternative Q

TABLE 1. Coefficients in Fatigue Model from Equations (1) under different test conditions

Steel RQT501	Short crack			Physically small crack			Long crack	
	A <sub>1</sub>	A <sub>2</sub>	A <sub>3</sub>	B <sub>1</sub>	B <sub>2</sub>	B <sub>3</sub>	C <sub>1</sub>	C <sub>2</sub>
$\sigma$ MPa	Air, f = 10 Hz							
520	-2,6.10 <sup>-5</sup>	12,3.10 <sup>-4</sup>	-14,2.10 <sup>-3</sup>	-5,2.10 <sup>-6</sup>	3,3.10 <sup>-4</sup>	-5.10 <sup>-3</sup>	4.10 <sup>-7</sup>	1.6057
522	-4,5.10 <sup>-6</sup>	12,3.10 <sup>-6</sup>	24,5.10 <sup>-5</sup>	-6.10 <sup>-7</sup>	3,5.10 <sup>-5</sup>	-2,3.10 <sup>-4</sup>	4.10 <sup>-7</sup>	1.5516
525	-3,1.10 <sup>-6</sup>	5.10 <sup>-5</sup>	54,8.10 <sup>-5</sup>	-4,5.10 <sup>-6</sup>	3,3.10 <sup>-4</sup>	-5,3.10 <sup>-3</sup>	1,2.10 <sup>-7</sup>	1.9028
f / Hz	3,5% NaCl, $\Delta\sigma = 516$ MPa							
0.2	-	-	-	-3,9.10 <sup>-7</sup>	2,2.10 <sup>-4</sup>	-1,3.10 <sup>-2</sup>	1,7.10 <sup>-6</sup>	1,7410
0.5	-3,9.10 <sup>-6</sup>	2,9.10 <sup>-4</sup>	-29,6.10 <sup>-4</sup>	-1,9.10 <sup>-6</sup>	4,6.10 <sup>-4</sup>	-2.10 <sup>-2</sup>	5,5.10 <sup>-7</sup>	1,7355
1	-2,1.10 <sup>-6</sup>	2,1.10 <sup>-4</sup>	-1,1.10 <sup>-4</sup>	-1,4.10 <sup>-6</sup>	3,7.10 <sup>-4</sup>	-1,3.10 <sup>-2</sup>	6,6.10 <sup>-7</sup>	1,6881

An alternative presentation of the same fatigue data reveals a linear behaviour of a newly-involved energy fatigue-function  $\Delta W$ , expressed as a line corresponding to a given stress range at very high correlation coefficients  $f_c$  [3]. This enables us to model and predict fatigue behaviour in a simpler and more precise way.

**References**

1. Angelova, D., and Akid R., *Fat. & Fract. of Eng. Mat. & Struct.*, vol. **21**, 771-779, 1998.
2. Hu, H., *Fatigue and Corrosion Fatigue Crack Growth Resistance of RQT501*, PhD Thesis, Sheffield University, 1997.
3. Angelova, D., “An alternative approach to conventional data-presentation of fatigue”, In *Proceedings of ECF16*, edited by E. E. Gdoutos, July 2006, Alexandroupolis, Greece.

## EFFECT OF CORROSION ENVIRONMENT ACTIVITY ON FATIGUE IN A LOW-CARBON STEEL

A. Davidkov and D. Angelova

Aleksander Davidkov – Research Fellow, Institute of Metals Science, Bulgarian Academy of Sciences, 67, Shipchenski Prohod, 1574 Sofia, Bulgaria, e-mail: alda14042001@yahoo.com

Donka Angelova – Professor, University of Chemical Technology and Metallurgy-Sofia (UCTM), 8 Kl. Ohridski, 1756 Sofia, Bulgaria  
dona\_ang@techno-link.com

The corrosion fatigue crack propagation behavior of a low-carbon low-alloyed construction steel was investigated under testing frequencies  $f=6,6\text{Hz}$  and  $f=11\text{Hz}$  and stress ranges  $\Delta\sigma=580$  and  $\Delta\sigma=620$  MPa at rotating bending (RB) conditions. The applied loading scheme was symmetric (loading ratio  $R = -1$ ) and the specimens were subjected to corrosion fatigue tests in a 0,35% and 3,5% NaCl water solution.

A table model **Fatigue Rotating Bending Machine**, FATROBEM-2004 with a corrosion cell for environment assisted short fatigue crack growth investigations was designed, constructed, assembled and put in operation in the Laboratory of Plastic Deformation at UCTM-Sofia. The principal scheme of FATROBEM-2004 is shown in Fig. 1 and:

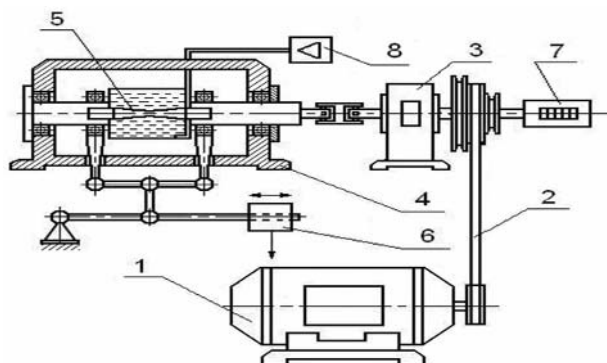


FIGURE 1. Scheme of FATROBEM-2004 fatigue machine: electric engine 1, driving belt 2, ball-bearing unit 3, testing box 4, specimen 5, device for loading 6, counter 7, device for circulation and aeration of corrosion agent 8.

The employed stress ranges  $\Delta\sigma$  and the corresponding registered fatigue lifetimes  $N_f$  are shown in Tabl. 1. Both previously introduced, a parabolic-linear model  $M$  and an alternative linear fatigue energy-function  $\Delta W$  for describing short fatigue crack growth behaviour in-air [1, 2] are adapted for corrosion environment in the present study, Fig. 2. Figure 2 includes all 8 sets of data from Tabl.1 presented in two ways by: the parabolic-linear family  $M$ ; and the linear family  $\Delta W$  expressed analytically through 8 line-equations in log-log scale, showing very high correlation coefficients  $f_c$ .

TABLE 1. Experimental conditions and fatigue lifetimes

Rotation-bending, R=-1, NaCl solution environment				
Specimen	Stress range/ Mpa	Frequency/ Hz	Concentration NaCl %	Lifetime cycles
1	620	11	0,35	110330
2	580	11	0,35	212300
3	580	6,6	0,35	74250
4	620	6,6	0,35	72380
5	580	6,6	3,5	80740
6	580	11	3,5	30360
7	620	6,6	3,5	41800
8	620	11	3,5	16600

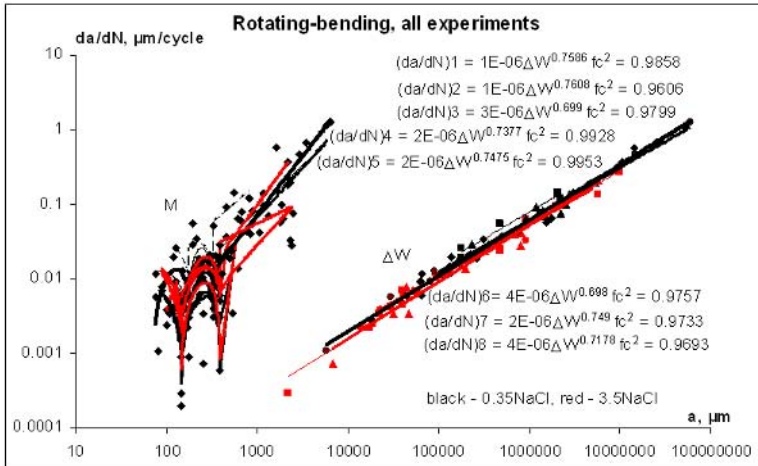


FIGURE 2. Different fatigue data presentations: conventional, M and new,  $\Delta W$

In order to estimate the applicability of the adapted model M and energy-function  $\Delta W$  for aggressive environment uses, a comparison was made between the fatigue lifetimes calculated by the models and those registered experimentally, which showed a good agreement.

**References**

1. Angelova, D., Davidkov A., “Different analytical presentations of rotation-bending fatigue”, In *Proceedings of ECF16*, edited by E. E. Gdoutos, July 2006, Alexandroupolis, Greece.
2. Angelova, D., “An alternative approach to conventional data-presentation of fatigue” In *Proceedings of ECF16*, edited by E. E. Gdoutos, July 2006, Alexandroupolis, Greece.

## MONITORING OF THE CONSTRUCTION MATERIALS' ALARM STATES ARE CAUSED BY BOTH FATIGUE AND EMBRITTELEMENT BY LIQUID METALS

S.Kh. Shamirzaev, E.D. Mukhamediev and G. Yu. Shamirzaeva  
Physical-Technical Institute of AS of Uzbekistan  
G. Mavlyanova 2-b, Tashkent ,700084, Uzbekistan  
shamir@uzsci.net

It is known , that some construction material (CM) from Aluminum Alloy (AA) or steel being wetted by lick of liquid metal such as Ga or Hg, under imposed a fatigue loads became very brittle and reduce to zero their lifetime. In [1] we have represented the sensitive elements of the fatigue gages. In [1-3] we have examined three questions: 1) what kind of the rheological structures are formed in the space of a real material? 2) Is there a general law transforming this structure? 3) Is there any difference in the reaction of a construction material (CM) under fast and slow loads?

In this paper we represent the framework of the new experimental method for estimating the effective output parameters of CMs and their changes under imposed fatigue deformation. The output data of CMs depend on the micro - structures they are possessed of. For example, effective internal friction –  $Q_{eff}^{-1}$  of the CM are formed as a sum of micro – structures internal friction –  $Q_k^{-1}$  with fit statistics -  $g_k$  [1-2].

Damages accumulated at the initial stage of fatigue process change local parameters of the CM [2,3]. The micro – structures are irreversible changed if sufficiently high deformation is imposed on CM. This process become more intensive and more intricate under wetted by liquid metals. As a number of cycles increases CMs' micro – structures eventually begin to make evolution. As a result the alarm state of CM arises.

A sample of an Aluminum Alloy was selected as a pattern of CM. There is not a common law permits one in advance to determine both what kind of micro - structures and how many of micro - structures will be simultaneously belong to CM after the number cycles of loads. To accomplish these ends the new experimental techniques of  $g_k$  and  $Q_k^{-1}$  measurement was developed. The Internal friction ( $Q^{-1}$ ) of CMs is very sensitive to cracking processes.  $Q^{-1}(N; \varepsilon)$  depends on both the number -  $N$  of imposed acoustic cycles and the value -  $\varepsilon$  of the amplitude of imposed acoustic deformation.  $Q^{-1}(N; \varepsilon)$  is the reciprocal of the merit factor (or - **Q factor**). **Q factor** shows the capability of homogeneous material to absorb the acoustic energy :  $Q = W / \Delta W$ , here  $W$  - the full acoustic energy which the material possess ;  $\Delta W$  – the absorbed energy. The greater is  $Q$  of the homogeneous material, the less energy is absorbed by each micro-region of a tested sample.

But CMs are heterogeneous materials for which the greater is the effective merit factor -  $Q_{eff}$ , the more energy can be absorbed by selected micro-regions of a tested sample. At the same time there are some micro-regions, which have negligibly small probability to absorb the acoustic energy. Each micro-regions will be able to contribute to the  $Q_{eff}$  accordance with statistic  $q_k$  [3]:

$$Q_{eff}(N; \varepsilon, m) = \sum_{k=1}^L [q_k * Q_k(N; \varepsilon, m)]; \sum_{k=1}^L q_k = 1; (k = 1, 2, 3, \dots, L)$$

Series  $q_k$  &  $Q_k$  represent the micro – structures of CMs [2,3].  $Q_k(N; \varepsilon, m)$  - is the merit factor (related with the internal friction  $Q_k^{-1}$ ) of a  $k$ -th micro-region and depends on the amplitude -  $\varepsilon$

and degree of asymmetry -  $m$  of the imposed regular cyclic deformation.  $L$  is a number of micro-regions. For example, if  $L=2$ , and  $q_1 \rightarrow 0$  (but  $Q_1 \rightarrow \infty$  so that  $[q_1 * Q_1] \rightarrow Q_{eff} \gg 1$ ) and  $q_2 = 1 - q_1$ , respectively, then the equality  $Q_{eff} = q_1 * Q_1 + (1 - q_1) * Q_2$  leads to  $Q_2 = W_2 / \Delta W_2 \approx 1$ . As a result the part of full acoustic energy  $W_2 = W - W_1$  is absorbed by the second region of tested sample. So micro-crack arises in the space of CM.

In this paper we find a number of micro-regions -  $L$  and series  $q_k$  &  $Q_k$  from the experimental data like as the internal friction  $Q_{eff}^{-1}(N; \varepsilon)$  versus -  $N$  and -  $\varepsilon$ .

The ways of realization. After imposed a limit number cycles of fatigue deformation, that change the CMs micro - structure, the fast cycle of deformation with selected value of amplitude is imposed on the specimen [2]. The curve  $Q_{eff}^{-1} - \varepsilon$  ( $Q_{eff}^{-1}$  - effective internal friction of CM and  $\varepsilon$  - value of imposed deformation), that was automatically recorded within this fast cycle of deformation, permits one to bring out the forthcoming structures of CM and its features, that will take place at the near future cycles of imposed deformation [3]. So the monitoring of CMs alarm states will be made. For the sake of convenience, assume that

$$Q_k(\varepsilon; m, N) = \begin{cases} G * N & \text{if } N_{k-1} \leq N \leq N_k \\ \\ G * N_k & \text{if } N_k \leq N \end{cases}$$

$$Q_{eff}^{-1}(max) = M_g(m), \text{ and } Z_k = Q_k / M_g(m), (k = 1, 2, 3, \dots, L). \quad (1)$$

$Z_k$  and  $q_k$  can be found from experimental data like as the internal friction  $Q_{eff}^{-1}(N; \varepsilon)$  versus -  $N$  and -  $\varepsilon$  and formula (1). This model also admits control of the structure mutations in AA and FE within one fast cycle of an imposed deformation  $\varepsilon$ . High level of computer engineering was used by us for study the effect of the cracking processes, caused by liquid metals, on the amplitude-dependent internal friction  $Q^{-1}(\varepsilon)$ . We are using the two-component oscillator (ZrTiPb-19 piezoceramics and the aluminum alloy sample wetted by liquid gallium with rigidly installed on it the fatigue element), having an eigen-frequency of about 20 kHz, for study the effect of the oscillation amplitude and micro-cracking processes on the amplitude-dependent internal friction  $Q^{-1}(N; \varepsilon)$ .

Results of paper. The new software as well as automated equipment for monitoring of the construction materials' alarm states was represented. The analysis of both the new materials' micro - structures and existing materials' micro - structures by novel methods was made.

## Reference

1. Shamirzaev S. *Published by The Iron and Steel Institute of Japan Proceedings of the 7th International conference, STEEL ROLLING'98, November, 9-11, 1998, Makuhari, Chibo, Japan, pp. 844-849.*
2. Shamirzaev S., *International Journal of Fatigue*, vol. **24**, pp.777-782, 2002
3. Shamirzaev S., *Solid State Sciences*, vol. **6**, pp. 1125-1129, 2004



## EVALUATION OF RESIDUAL STRESSES DURING FATIGUE TEST IN A FSW JOINT

S. Pasta and A.P. Reynolds

<sup>a</sup> Dipartimento di Meccanica, Università di Palermo, 90128 Palermo, Italy.

<sup>b</sup> Department of Mechanical Engineering, University of South Carolina, Columbia, 29208 USA.

<sup>a</sup> spasta@dima.unipa.it, <sup>b</sup> apr@sc.edu

At present, friction stir welding (FSW) represents one of the most interesting techniques in the field of welding. The process has been implemented in industrial practice for joining aluminium alloys, while the welding of the titanium alloy and the steels is still primarily in a developmental stage.

The thermo-mechanical action of the tool causes a residual stress field in the FSW joint. Although, the peak temperatures of the process are relatively low; residual stresses similar to the traditional welding technique may develop in the FSW joint. Moreover, the restraints of clamps, which are used for fixing the plates during the process, impede the relief of the heated zones that causes longitudinal and transversal residual stresses.

The fatigue crack growth behaviour in FSW joints was investigated by several authors [1-4] and most of them [1, 3-4] have shown through experimental tests that the residual stresses play a predominant role on the fatigue crack growth rate as compared to the effects of microstructure and hardness changes. Therefore, an accurate method has to be adopted for measurement of the residual stress field in order to evaluate the influence of the same residual stresses on the fatigue crack growth behaviour of FSW joints.

Several experimental techniques can be used to evaluate the residual stress field developing in FS welded joints. The non-destructive techniques of X-rays and neutrons have enabled the determination of the longitudinal and transverse residual stress profiles. The destructive cut compliance method described by Prime [5] is widely used to provide the through-thickness residual stress intensity factor of a supposed crack front. Subsequently, the residual stress profile can be analytically extrapolated by the knowledge of the residual stress intensity factor,  $K_{res}$ . Similarly, the hole drilling method provides the residual stress distribution by means of incremental hole-drilling steps and numerical routines. Nevertheless, both these techniques require the knowledge of the influence functions which depend from the cut depth, the strain gage location and the geometry of the investigated body. Moreover, it has been recently illustrated that the innovative techniques of the contour method described by Prime *et al.* [6] and the on-line crack-compliance method [7] combined with the adjusted compliance ratio [8,9], ACR, can be used to measure the residual stress field in FSW joints.

In this paper, an application of the ACR method and of the on-line crack-compliance technique is shown for a FSW joint in titanium alloy. The on-line crack-compliance is used to obtain the residual stress intensity factor in real time from a fatigue crack growth test. Thus, the post-processing ACR methodology is adopted to separate the closure and residual stress effects from the fatigue crack growth rate data. The on-line crack-compliance method is similar to the cut compliance method. This technique uses the load-displacement curve directly provided during the fatigue test, so that a specific test for the determination of the residual stresses is avoided. Moreover, the practical application of this methodology does not require the knowledge of the influence functions; only a sufficient signal stability and linearity of displacement need to compute the residual stress intensity factor. At the same way, on the basis of ratio of displacement, the ACR

methodology provides the effective stress intensity factor range,  $\Delta K_{eff}$ , taking into account the crack closure effects, below the opening load, caused by the mating broken faces along the crack wake. The FTA, Fracture Technology Associates, software is used to perform the fatigue test in  $K$ -control and to provide the  $K_{res}$  profile. Specimen compliance was measured continuously in order to calculate the crack length and to provide feedback to the fatigue test software. The fatigue tests were carried out on a Ti-6Al-4V titanium alloy sheet which is friction stir welded at the University of South Carolina.

## References

1. Pasta, S., Reynolds, A.P. and Fratini, L. *Italian Association for the Analysis of Stresses*, Ancona, Italy, 2006.
2. Dalle Donne, C., Biallas, G. Ghidini, T. and Raimbeaux, G., *Second International Symposium on FSW*, Gothenburg, Sweden, 2000.
3. John, R., Jata K.V. and Sadanada, K., *Int J Fatigue*, vol. **25**, 939-948, 2003.
4. Bassu, G. and Irving, P.E., *Int J Fatigue*, vol. **25**, 77-88, 2003.
5. Prime, M.B., *Applied Mechanics Reviews*, vol. **52**, 75-96, 1999.
6. Pagliaro, P., Prime, M.B. and Zuccarello, B. *Italian Association for the Analysis of Stresses*, Ancona, Italy, 2006.
7. Lados, D.A. and Apelian, D., *Metall and Matls Trans*, vol. **37A**, 133-145, 2006
8. Donald, J.K., Bray, G.H., and Bush, R.W., *29<sup>th</sup> National Symposium on Fatigue and Fracture Mechanics*, ASTM STP 1332, edited by T.L. Panontin, S.D. Sheppard, American Society for Testing and Materials 1998, 674-695.
9. Zonker, H.R., Bray, G.H., George, K. and Garratt, M.D., *34<sup>th</sup> National Symposium on Fatigue and Fracture Mechanics*, ASTM STP 1461, edited by S.R. Daniewicz, J.C. Newman, K.H. Schwalbe, American Society for Testing and Materials 2005.

## CALIBRATION FOR MACHINE DEFORMATION FOR HIGH TEMPERATURE FRACTURE TESTING

S.K. Ray and G. Sasikala  
 Materials Technology Division, Indira Gandhi Centre for Atomic Research  
 Kalpakkam 603 102, India  
 gsasi@igcar.gov.in

A procedure has been developed for calibrating the non-linear elastic machine deformation and demonstrated for evaluating  $J$  at 653 K and 803 K for a modified 9Cr-1Mo steel. The calibration procedure involves determining the non-linear elastic relation between machine deformation  $x_m$  and load ( $P$ ), from the  $P$ - $x_t$  data for a blank specimen with known elastic compliance  $C$  (as measured at the loading pins) deforming in the elastic regime, using the relation

$$x_m(P) = x_t - C \cdot P \quad (1)$$

Elastic compliance of the specimen was computed using two-dimensional elastic boundary element method (BEM) were carried out for one symmetric half of the specimen using the BEM code of Portela and Aliabadi [1] marginally modified for the present application. Calibration testing consists of three steps: (i) blank specimen is ramped at the chosen constant stroke rate to the desired load level, (ii) actuator motion is arrested for a period sufficient to complete any load relaxations and (iii) specimen is ramped down to zero load at the same actuator speed. The calibration and fracture tests were carried out in a servohydraulic universal testing machine using the same testing assembly and constant actuator speed of 0.1 mm/min. For the fracture tests with pre-cracked specimens, the load line displacement was measured using a double cantilever type LLD gage. Data for three unloads (for better confidence) above a small cut off load (because of strong curvilinearity in  $P$ - $x_t$  data at low  $P$ ) were least-square fit to the empirical functional form:

$$x_t = \delta_i + C \cdot P + x_m(P) = \delta_i + C \cdot P + \sum_j q_j \cdot P^{r_j} \quad (2)$$

where  $\delta_i$  is the zero-offset for  $i$ -th unload, and  $q_j$ ,  $r_j$  are fitting constants., data (determined by trial and error) were used for the least square fit. The error of fit beyond the cut-off load was essentially within  $\pm 2\mu\text{m}$  for 653 K and  $\pm 4\mu\text{m}$  for 803 K, quite comparable to typical resolutions for high temperature LLD gages. The  $x_m(P)$  equation is used for inferring  $x_{sp}$  from the  $x_t$  data for a fracture test. Since for fracture tests, the early  $P$  - inferred  $x_{sp}$  data are linear well beyond the cut off load, these can be easily back-extrapolated to  $P=0$  to correct the inferred  $x_{sp}$  data to ensure  $x_{sp}=0$  for  $P=0$ .

The agreement between the measured and inferred  $x_{sp}$  was better than the 1% for all the tests at 653 and 803 K. Fig. 1 shows a region of slippage of the LLD gage resulting in a backward displacement at 803 K, beyond this point, the measured  $x_{sp}$  continuously increased and eventually exceeded the inferred  $x_{sp}$ . This suggests that beyond some critical rotation in the specimen, the free arm of the gage started sliding down the flat surface. This actually shows that inferred  $x_{sp}$ , rather than  $x_{sp}$  measured by the specific specimen-extensometer configuration used here, should be more reliable. Also, even for large displacements, unlike measured  $x_{sp}$ , inferred  $x_{sp}$  does not require to be corrected for the LLD measurement line progressively shifting away from loading line (cf. the rotation correction, Section A2.4.4 in [2]).

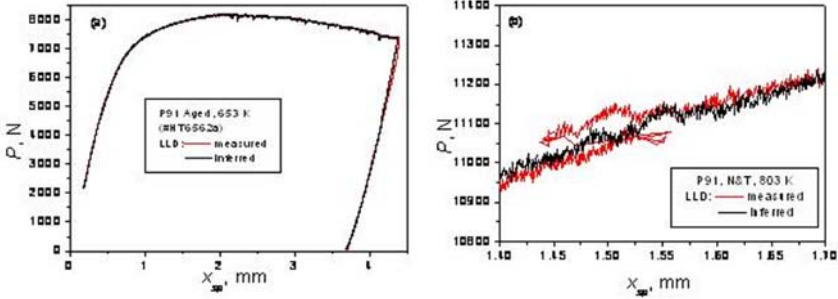


FIGURE 1. (a) Typical plots of  $P$  versus  $x_{sp}$ , for tests at 653 K (b) magnified view of a region corresponding to a slippage of the LLD gage resulting in a backward displacement for 803 K.

The nominal  $J$  (without crack growth correction) resistance ( $J_{nom}$ - $R$ ) curves for 653 K computed using inferred and measured  $x_{sp}$  are presented in Fig. 2. Data for both NT and aged conditions are included in these plots and are not distinguished. It is clear that using inferred  $x_{sp}$  results in considerably less scatter compared to when using measured  $x_{sp}$  reflected in the fact that the constants of fit of the  $J$ - $\Delta a$  relation,  $J = C \Delta a^n$ ,  $C$  and  $n$  are better determined (indicated in these figures). Also, conservative estimate of  $J_{0.2}$  ( $\sim 290 \text{ kJ.m}^{-2}$ ) is obtained using inferred  $x_{sp}$  compared to using measured  $x_{sp}$  ( $\sim 330 \text{ kJ.m}^{-2}$ ). The same conclusion was reached for 803 K too. Similar conclusions were drawn for single specimen normalization method for  $J$  estimation (cf. A15, ASTM E1820); these results are not presented here.

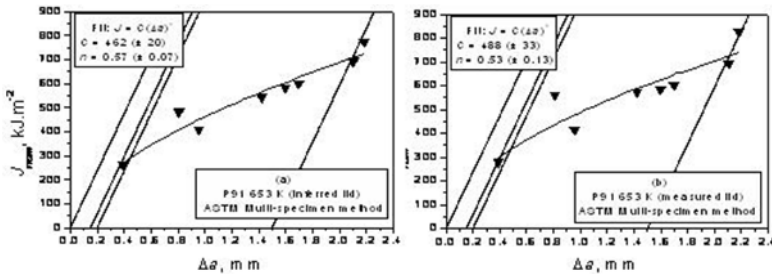


FIGURE 2. Results of multiple-specimen analysis of fracture test data for 653 K following ASTM E1820-01 prescriptions (a) inferred LLD and (b) measured LLD.

**References**

1. Portela, A. and Aliabadi, M.H., *Crack Growth Analysis using Boundary Elements*, Computational Mechanics Publications, Southampton, 1993.
2. Standard Test Method for Measurement of Fracture Toughness, ASTM E 1820-01, August 2001, American Society for Testing of Materials (ASTM), Philadelphia.

**MIXED MODE FRACTURE TOUGHNESS OF AN ADHESIVE BONDED JOINT**

M. Alfano, F. Furgiuele, C. Maletta

Department of Mechanical Engineering, University of Calabria  
Via Ponte Pietro Bucci, Cubo 44C, Rende (CS), Italy  
alfano@unical.it, furgiuele@unical.it, carmine.maletta@unical.it

The use of adhesive bonded joints is constantly increasing owing to the advantages that they offer with respect to the traditional methods of joining, *e.g.*, fewer sources of stress concentration, improved stress distribution, weight and cost reduction, ability to join dissimilar materials, etc. [1]. However, adhesive joints contain defects and they do appear in the manufacturing cycle or in service condition. The most common type of defect occurs at the interface and is represented by voids and contamination of substrates surfaces by foreign objects. Joint strength is affected by crack location and crack path [2-4] and, as a result, a knowledge of the interfacial toughness become of critical concern in design calculations. A great research effort has been made in this field in the last decades and different specimens type have been employed: Brazil nut specimen [5], symmetric and asymmetric double cantilever beam [6-7], end notch and mixed mode flexure [8].

The purpose of the present paper is to investigate the interfacial fracture resistance of Al/Epoxy joints using a Cracked Lap Shear (CLS) specimen loaded in four point bending. Procedures for specimens' fabrication are those reported in [10]. In particular, substrates are aluminium 6061-T6 alloy while the resin is Loctite Hysol<sup>®</sup> 3422 A&B (Henkel-Germany), a two component, medium viscosity and fast curing industrial grade epoxy adhesive. Initial cracking is achieved simply introducing a thin Teflon tape at the Al/Epoxy interface, in such a way is possible to reproduce those cracks that are likely to be encountered in service condition. Two bond line thicknesses have been investigated, 0.25 and 0.5 mm respectively, while the mode mixity of the applied load has been controlled varying the relative thickness of the substrates.

Fracture toughness has been pointed out in terms of the critical energy release rate and of the phase angle of the complex stress intensity factor. As the adhesive layer thickness is much smaller than the other in plane length, the phase angle is determined using the universal relation proposed by Suo *et al* [11], *i.e.* adding up to the phase angle of the homogeneous base specimen (obtained neglecting the presence of the adhesive layer) a correction term that accounts for the elastic moduli mismatch.

Experimental results have shown an interfacial stick-slip fracture confirming the general finding that an adhesive bonded joint subject to mixed mode load fails at the interface. However, after each test, substrates have been completely separated using a wedge, *i.e.* in mode I loading condition: the resulting fracture was cohesive in layer (Fig. 1). As the crack path is dictated by the mode mixedness of the applied loads, this change in failure mechanism could be considered as a proof of the good quality bond achieved during fabrication. In addition, optical micrographs of fracture surfaces provided clear evidence of markings associated with initial growth and crack arrest associated with the fast unstable crack propagation process. In particular, these were essentially featureless, suggesting that a brittle fracture occurred. This is usual for epoxy resin tested at room temperature [12].

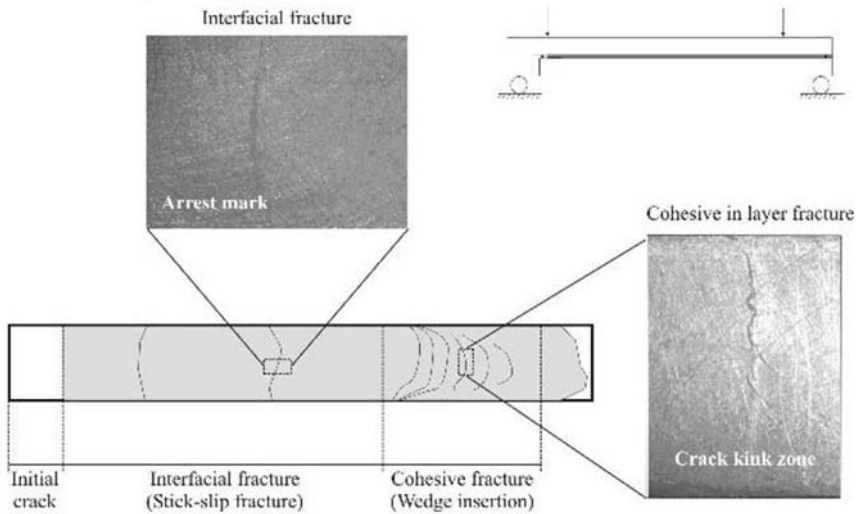


FIGURE 1. Fracture surfaces.

## References

1. Kinloch, A.J., *Adhesion and Adhesives, Science and Technology*, Chapman & Hall, London, UK, 1986
2. Chai, H, *Engineering Fracture Mechanics*, vol. **24**, p. 413, 1986.
3. Chai, H, *International Journal of Fracture*, vol. **32**, p. 211, 1987.
4. Akisanya, A.R., Fleck N.A., *International Journal of Fracture*, vol. **58**, p. 93, 1992.
5. Wang, J.-S., Suo, Z., *Acta Metallurgica et Materialia*, vol. **38**, p. 1279, 1990.
6. Thouless, M.D., *Scripta Metallurgica et Materialia*, vol. **26**, p. 949, 1992.
7. Duer, R., Katevatis, D., Kinloch, A.J., Williams, J.G., *International Journal of Fracture*, vol. **75**, p.157, 1996.
8. Pavartareddy, H., Dillard, D.A., *International Journal of Fracture*, vol. **96**, p. 215, 1999.
9. Chen, B., Dillard, D.D., Dillard, J.G., Clark, R.L., *International Journal of Fracture*, vol. **114**, p. 167, 2002.
10. Alfano, M., Furgiuele, F., Maletta, C., *Key Engineering Materials*, vol. **325**, p. 149, 2006
11. Suo, Z., Hutchinson, J.W., *Material Science & Engineering A*, vol. **107**, p. 135, 1989
12. Shi, X.Q., Zhang, X.R., Pang, J.H.L., *International Journal of Adhesion and Adhesives*, vol. **26**, p. 250, 2006.

## THE RELATIONSHIP BETWEEN CREEP RUPTURE LIFE AND MICROSTRUCTURE OF AGED P92 STEEL

B.J. Kim and B.S. Lim

School of Mechanical Engineering, Sungkyunkwan University  
300, Cheoncheon-dong, Jangan-gu, Suwon, gyeonggi-do 440-746, Korea

kultra@skku.edu and bslim@skku.edu

As the static loading period of a power plant increases, high temperature components such as main steam pipe and header are degraded and their creep lives are reduced. Generally, material degradation is influenced by nucleation, growth and coalescence of cavity, and precipitates formed during the long operating period of power plants. Creep strength and life of material are closely related with the microstructural characteristics. Components used under creep condition for long time are unable to maintain the stability of microstructure and experience degradation of material [1]. From this viewpoint, it is necessary for safety and residual life estimation of power plant to investigate creep properties of specimens prepared from the material cut directly from the operating service components. Small punch test has been developed as an useful method to estimate mechanical properties because of its miniaturized specimen size [2]. In this study, small punch creep tests were carried out to investigate the effect of aging time on creep properties using P92 steel aged for 0~12100 hrs at 600°C. Microhardness measurement and microstructure observation of base metal was performed to analyze their effects on creep strength and rupture life. The coarsening behaviour and chemical composition of precipitates with aging time were investigated by SEM (Scanning electron microscope) to examine the effect of microstructural change for the creep rupture life. Also, the area fractions of precipitates were analyzed to investigate the relationship between creep rupture life and aging time. The chemical composition of P92 (9Cr2W) steel used in this experiment is shown in Table 1.

TABLE 1. Chemical composition of P92 steel(wt%)

	C	Si	Mn	P	S	Ni	Cr	Fe
Base metal	0.1	0.22	0.48	0.017	0.006	0.18	9.11	Bal.
	Mo	W	Cu	V	Nb	B	N	Al
Base metal	0.47	1.75	-	0.18	0.056	0.002	0.041	0.01

Fig. 1 shows the small punch test apparatus used in this study. Specimens aged up to 12100hrs were employed in this study. In the main paper, detailed analysis and discussions will be carried out on the experimental results of hardness, microstructural evolution, area fraction of precipitates and cavities as well as displacement rates of base metal.

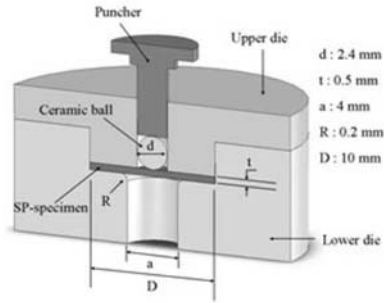


FIGURE 1. Schematic illustration of SP test apparatus.

## References

1. X. Jia and Y. Dai, *J. Nucl. Mater.*, vol. **323**, 360-367, 2003
2. J. S. Cheon and I. S. Kim, *J. Nucl. Mater.*, vol. **278**, 96-101, 2000



## STUDY THE CAUSTICS, ISOCHROMATIC AND ISOPACHIC FRINGES AT A BI-MATERIAL INTERFACE CRACK-TIP

G.A. Papadopoulos

Department of Engineering Science, Section of Mechanics, National Technical University of Athens, GR-157 73, Zografou campus, Athens, Greece.  
gpap@central.ntua.gr

The shape of crack-tip caustics, isochromatic and isopachic fringes, at a bi-material interface under static load, are studied. When the crack-tip, which is perpendicular to interface, is at the interface of the bi-material, the caustics, the isochromatic and the isopachic fringes depend on the properties of the two materials. Thus, the caustics, the isochromatic and the isopachic fringes are divided into two branches. The size of the two branches mainly depends on the elastic modulus and the Poisson's ratio of the two materials. From the caustics, the stress intensity factor  $K_I$  can be calculated while, from the comparison of the isochromatic and the isopachic fringes, the principal stresses  $\sigma_1, \sigma_2$  can be calculated.

In this work an attempt to study the shape of crack-tip caustics, isochromatic and isopachic fringes at a bi-material interface and the evaluation of the principal stresses is made.

Two plates of moduli  $E_1$  and  $E_2$  and Poisson's ratios  $\nu_1$  and  $\nu_2$  are perfectly bonded along their common interface (Figure 1). In plate (1) there is a crack perpendicular to the interface. The crack-tip is exactly at the interface of the two plates.

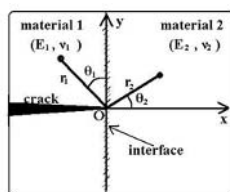


FIGURE 1. Geometry of bi-material plate.

The Airy stress function  $X(r, \theta)$  for this problem, used by Zak and Williams (1963), is

$$X(r, \theta) = r^{\lambda+1} F(\theta) \quad (1)$$

$$\text{with } F(\theta) = \alpha \sin(\lambda + 1)\theta + b \cos(\lambda + 1)\theta + c \sin(\lambda - 1)\theta + d \cos(\lambda - 1)\theta \quad (2)$$

where  $\alpha, b, c, d$  are constants and  $\lambda$  takes values between 0 and 1, which is depended on the ratio  $E_{12}=E_1/E_2$  of the two plates moduli.

From the stress function (1) the polar stresses at the crack-tip are taken

$$\sigma_r = (\lambda + 1) r^{\lambda-1} F(\theta) + r^{\lambda-1} F''(\theta) \quad (3)$$

$$\sigma_\theta = \lambda(\lambda + 1) r^{\lambda-1} F(\theta) \quad (4)$$

$$\tau_{r\theta} = -\lambda r^{\lambda-1} F'(\theta) \quad (5)$$

**1. Theory of caustics**

The parametric equations of the caustics (r) and (t) ((r) is the caustic which is formed by the reflected light rays from the rear face of the plate and (t) is the caustic which is formed by the transmitted light rays through the plate) are obtained (Fig. 2)

$$X_{r,t} = \lambda_m r_{01,2} \left\{ \cos \theta_{1,2} - \frac{1}{(\lambda - 2)\sqrt{c_2^2 + d_2^2}} [c_2 \sin(\lambda - 2)\theta_{1,2} + d_2 \cos(\lambda - 2)\theta_{1,2}] \right\} \quad (6)$$

$$Y_{r,t} = \lambda_m r_{01,2} \left\{ \sin \theta_{1,2} - \frac{1}{(\lambda - 2)\sqrt{c_2^2 + d_2^2}} [c_2 \cos(\lambda - 2)\theta_{1,2} - d_2 \sin(\lambda - 2)\theta_{1,2}] \right\} \quad (7)$$

**2. Theory of photoelasticity**

Isochromatic fringes are loci of points with the same value for the difference of the principal stresses or the maximum shear stress. The isochromatic fringes are plotted by the relation (Fig. 3)

$$r = \left\{ \frac{1}{\left[ [(1 - \lambda^2)F(\theta) + F''(\theta)]^2 + 4\lambda^2(F'(\theta))^2 \right]^{1/2}} \frac{N_c(f_c)_{1,2}}{t} \right\}^{\frac{1}{\lambda-1}} \quad (8)$$

**3. Theory of isopachic fringes**

Isopachics fringes are loci of points with the same value for the sum of the principal stresses. The isopachic fringes are plotted by the relation (Fig. 4)

$$r = \left\{ \frac{1}{(\lambda + 1)^2 F(\theta) + F''(\theta)} \frac{N_p(f_p)_{1,2}}{t} \right\}^{\frac{1}{\lambda-1}} \quad (9)$$

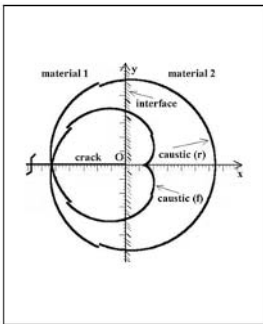


Figure 2

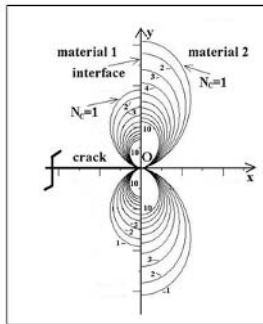


Figure 3

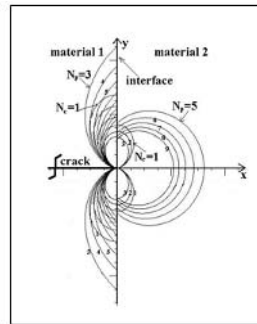


Figure 4

## METHODS FOR MEASURING BIAXIAL DEFORMATION ON RUBBER AND POLYPROPYLENE SPECIMENS

Ch. Feichter<sup>1</sup>, Z. Major<sup>2</sup> and R.W. Lang<sup>1,2</sup>

<sup>1</sup> Polymer Competence Center Leoben GmbH, Parkstraße 11, A-8700 Leoben

<sup>2</sup> Institute of Materials Science and Testing of Plastics, University of Leoben,  
Franz-Josef-Straße 13, A-8700 Leoben, Austria  
feichter@pccl.at

Biaxial measurements are very often used in order to characterize the material behaviour in more constrained conditions than in the usual tensile tests. For rubbers this is necessary for the determination of hyperelastic material laws (Ogden [1]). But also for detailed material characterization of polypropylene this loading condition is utilized. There exist several loading methodologies for applying biaxial load. The basis of the method used in this paper is the inflation of a thin material sheet to a bubble with the help of pressurized air (Reuge, [2]). This method demands for exact pressure measurement and for a determination of the strain distribution around the pole of the resulting bubble (Bergamnn [3]). Figure 1 shows the utilized testing system in the standard configuration.

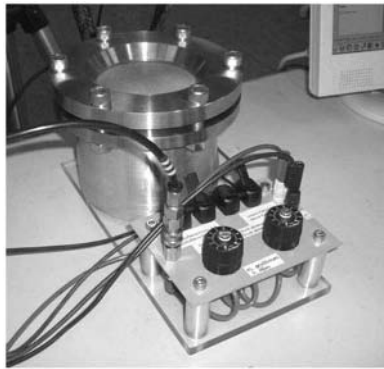


FIGURE 1. Biaxial testing system in the standard configuration.

The true strain is exported from the strain analysis system, the resulting true stress is calculated using Equation 1.

$$\sigma = \frac{\Delta p \cdot r_B \cdot \lambda^2}{2 \cdot t_0} \quad (1)$$

In this Equation  $\Delta p$  is the pressure that inflates the bubble,  $r_B$  is the bubble radius,  $\lambda$  is the extension ratio ( $\lambda = 1 + \varepsilon$ ) measured with the full-field strain analysis system and  $t_0$  is the initial thickness of the specimen.

This methodology is a well-known approach for analysis of the deformed bubble. However, it would be more comfortable if the measurement of the deformation would be possible without a full-field strain analysis system, that demands for a complicated preparation of the test-piece. For that reason a second volume was put on the testing system. This second volume has a second pressure sensor in it, that allows for calculation of the bubble volume and furthermore, for the radius of the resulting bubble used in data analysis. Figure 2 shows the testing system with the second volume.

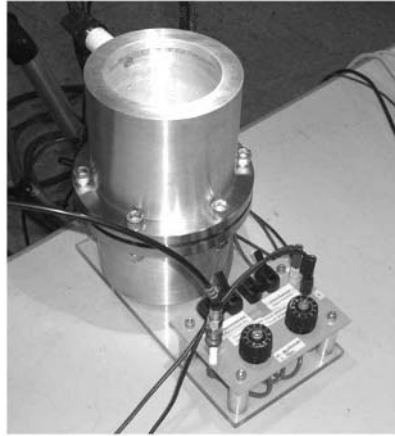


FIGURE 2. Biaxial testing system with second volumen.

With these approaches different rubber types and polypropylene have been tested in both ways. The results are presented along with the calculation method and compared to each other. Especially the rubbers exhibit a small difference between the more sophisticated method with full-field strain measurement and the simplified method with the pressure measurement on the upper volume, therefore the method is a very useful tool if quick results are necessary.

## References

1. R. W. Ogden, *Rubber Chemistry and Technology*, vol. **59**, 361-383 (1986).
2. N. Reuge, F. M. Schmidt, Y. Le Maout, M. Rachikand F. Abbé, *Polymer Engineering and Science*, vol. **41**, 522-531 (2001).
3. D. Bergmannand R. Ritter. in *Proc. SPIE - Optical Inspection and Micromesurements*; C. Gorecki, Ed., 1996, p. 212-223.

## HYBRID TESTING OF HISTORIC MATERIALS

M. Drdáký, O. Jiroušek, Z. Slížková, J. Valach and D. Vavřík  
 Institute of Theoretical and Applied Mechanics of the Czech Academy of Sciences  
 190 00 Praha 9, Prosecká 76, Czech Republic  
 drdacky@itam.cas.cz, jirousek@itam.cas.cz, slizkova@itam.cas.cz,  
 valach@itam.cas.cz, vavrik@itam.cas.cz

The paper describes hybrid approaches to testing of mechanical properties of historic materials which are mostly available in very small amounts and bulks unsuitable for standard testing procedures and techniques. Three case studies are presented. In all three, simple mechanical testing procedures were combined with special optical measurements and tailored software tools.

For research into behaviour of lime mortars with natural fibres, which is quite frequent historic material in almost all European countries, we need to know mechanical characteristics of natural fibres. They are usually very short, of irregular cross section, with a quite high thickness to length ratio. For their testing a simple loading frame has been constructed and during the loading changes of position of contrast marks on the fibres were optically recorded using microscopy. As contrast marks some colour nonhomogeneities have been selected and their position evaluated by special software written in Matlab 6.1. Measurement mark and its surrounding of about 45 x 45 pixels were adopted as a mask in the first loading step. In the next loading step the position with the least difference between the new record and the mask. When the mark was found the mask as well as the mark positions were actualized and the procedure continued. The measurement accuracy reaches the level of one picture pixel, the measurement distance oscillated around 900 pixels which gives accuracy in the length measurement of about 0,11%. Because the measured values oscillated in limits of one pixel around the actual value, the measured load-deformation diagrams can be considered reliable. The measured mechanical characteristics are shown in Table 1.

TABLE 1. Measured properties of natural fibres

Fibres or fibrous particles	Abbrev	Legth (mm)	Equivalent diameter (m)	Tensile strength (MPa)	Modulus of elasticity (GPa)	Elongation at failure (%)	Moisture (%)
goat's hair	Ko	12	30-100	110-230	6,2-7,7	2-29	negligible
horse hair	Ku	12	50-140	110-200	3,9-5,1	4,5-32	negligible

In the second case, very flat small historic mortar samples had to be tested for measurements of their modulus of elasticity. Surface deformations of the specimens during compression tests were measured using a high-resolution CCD camera and stored in bitmap format without compression. The exact time of exposure was recorded together with the image. The deformation was then calculated using the texture on the specimen's surface as a natural marker. After several pre-processing techniques based on thresholding, four distinct markers were chosen to calculate their time-dependent positions by identification of the centre of gravity of each of the markers using

moments of inertia of pixels weighted by their intensity values. This enables to attain sub-pixel accuracy of the position measurement.

Last example describes tests of detection of changes of subtle material characteristics – the thermal and moisture expansion of sandstone – due to treatment using different products based on ethylsilicates. Again only small samples were available, taken from the original medieval structure of the Prague St.Vitus Cathedral. Changes of length of small sandstone plates (15 x 40 x 3 mm) were measured during their cooling from a preheated state into the ambient temperature of the laboratory in the case of thermal dilatation study or during their drying from saturated state into natural moisture content corresponding to the laboratory temperature and relative humidity. In both measurements the specimens were placed in a special rig and optical system. During the thermal dilatation tests the changes of temperature were recorded using Thermocamera AGA. The optical system contained a mirror which inclined in accordance with specimen length variations and reflected a focused laser beam on a screen. The movement of the laser beam spot on the screen was recorded with one pixel resolution in a digital camera.

In the evaluation procedure, the data from image analysis must be connected with data from cooling (or drying) records. This connection was done using developed software tools by means of time synchronization. The position of the laser spot on the screen was determined as the center of gravity of light points weighted by their intensity. The temperature change (cooling) was recorded in intervals of 10 seconds during ten minutes. From the thermograms the average temperature of the specimen was calculated, (during cooling a temperature gradient of several degrees was observed in the inclined specimen), and synchronized with the deformation measurements.

The presented cases are illustrated by photographs of experimental setups, graphical representation of measured characteristics and a description of other comparative tests, necessary for evaluation of measured characteristics or effects of different material modifications.

## DETERMINATION OF PARAMETERS OF LOCAL APPROACH TO DUCTILE FRACTURE OF STEEL USING COMBINED EXPERIMENTAL-NUMERICAL PROCEDURE

M. Rakin<sup>1</sup>, M. Zrilic<sup>1</sup>, N. Gubeljak<sup>2</sup>, Z. Cvijovic<sup>1</sup>, A. Sedmak<sup>3</sup>

<sup>1</sup>Faculty of Technology and Metallurgy, Karnegijeva 4, University of Belgrade, 11000 Belgrade, Serbia

<sup>2</sup>Faculty of Mechanical Engineering, Smetanova 17, University of Maribor, SI2000 Maribor, Slovenia

<sup>3</sup>Faculty of Mechanical Engineering, Kraljice Marije 16, University of Belgrade, 11000 Belgrade, Serbia

marko@tmf.bg.ac.yu, misa@tmf.bg.ac.yu, nenad.gubeljak@uni-mb.si,  
zocvij@tmf.bg.ac.yu, asedmak@mas.bg.ac.yu

In this paper, two examples of combined experimental-numerical procedure of local approach to fracture mechanics have been presented. In first example, the level of fracture of steel in exploitation - pressurised steamline at elevated temperature - has been determined using uncoupled Rice-Tracey [1] model of local approach.

To enable the application of post-processing calculation according to the model applied, good agreement between experimentally and numerically obtained tensile curves is obligatory. Round tensile specimens with notch were used, where notch size was varied in order to attain different stress triaxiality, according to [2]. By comparison of numerically calculated values for critical void growth ratio  $(R/R_0)_c$  for new (virgin) and old (used) steel, the level of damage of steel from exploitation was determined, for details see [3].

In second example, an analysis of ductile fracture initiation of low-alloy steel on two geometries has been presented: smooth round specimen and precracked CT specimen. Coupled method of local approach was used, according to the Gurson-Tvergaard-Nedleeman (GTN), [4, 5] model. For determination of critical values of model parameters corresponding to ductile fracture initiation, a simple procedure has been applied based on combination of experimental and numerical results. The details about the procedure can be found in [6, 7].

To determine experimental value of J-integral corresponding to onset of crack growth,  $J_i$  final stretch zone width was measured, according to [8]. Numerically,  $J_i$  was determined according to the criterion

$$f \geq f_c \quad (1)$$

where  $f$  denotes actual value of void volume fraction in front of the crack tip and  $f_c$  is its critical value determined using combined experimental-numerical procedure on a smooth specimen.

Having in mind the effect of finite element (FE) size in micromechanical analysis, the relation between this quantity and microstructure of tested steel has been analyzed. A series of measurements of microstructural quantities was conducted using light microscopy. It has been concluded that the computation with FE size approximating to the mean free path  $l$  between non-metallic inclusions in steel gives the results in accordance with the experimental ones.

The second example was based on recommendations given within the scope of the European round-robin research, the details can be found in [Brocks]. In both examples, numerical

calculations using FE method were made using the academic license of the Abaqus programme (www.hks.com).

### Acknowledgments

The authors acknowledge gratitude to Serbian Ministry of Science and Environmental Protection for funding this work under the project numbers OI1793 and OI144027.

### References

1. Rice J.R. and Tracey D.M., *J. Mech. Phys. Solids*, vol. **17**, 201-217, 1969
2. ESIS P6-98, *Procedure to Measure and Calculate Material Parameters for the Local Approach to Fracture Using Notched Tensile Specimens*, European Structural Integrity Society Publication, 1998.
3. Zrilic M., *The Application of Local Approach to Residual Life Assessment of Equipment Components at Elevated Temperatures*, Ph.D. Thesis (in Serbian), Faculty of Technology and Metallurgy, Belgrade, 2004.
4. Gurson A.L., *J. Eng. Mat. Technology*, vol. **99**, 2-15, 1977
5. Tvergaard V. and Needleman A., *Acta Metallurgica*, vol. **32**, 157-169, 1984
6. Bernauer G. and Brocks W., *Numerical Round Robin on Micro-Mechanical Models - Results*, ESIS TC8, GKSS Research Center, Geesthacht, Germany, 2000.
7. Rakin M., Cvijovic Z., Grabulov V. and Sedmak A., *Engng. Fract. Mechanics*, vol. **71**, 813-827, 2004
8. ESIS P2-92, *Procedure for Determining the Fracture Behaviour of Materials*, European Structural Integrity Society Publication, 1992.



## COMPUTER SIMULATION AND EXPERIMENTS TO EVALUATE DIGITAL IMAGE CORRELATION METHODS

Sven Bossuyt<sup>1</sup>, Sam Coppeters<sup>1</sup>, David Lecompte<sup>2</sup>, Hugo Sol<sup>1</sup> and John Vantomme<sup>2</sup>

<sup>1</sup> Department of Mechanics of Materials and Constructions, Vrije Universiteit Brussel  
Pleinlaan 2, B-1050 Brussels, Belgium.

<sup>2</sup> Department of Materials and Constructions, Royal Military Academy  
Avenue de la Renaissance 30, B-1000 Brussels, Belgium.  
sven.bossuyt@vub.ac.be, scoppiet@vub.ac.be, hugo.sol@vub.ac.be,  
david.lecompte@rma.ac.be, john.vantomme@rma.ac.be

Digital image correlation is an optical-numerical full field displacement measurement technique, which is more and more widely used in experimental mechanics[1-3]. The technique is based on a numerical comparison of digitized images taken at different stages of deformation of an object. In principle, any imaging technique can be used, provided that the deformed image can be predicted starting from the undeformed image and the displacement field. The digital image correlation technique then consists of numerically searching the space of all possible displacement fields, to find the displacement field which gives the best correlation of the predicted image with the actual image of the deformed state.

Mathematically, this technique should be successful if the correlation is a monotonically decreasing function of the difference between the actual and hypothetical displacement fields. In practice, the technique works rather well, but unless the natural texture of the object image provides satisfactory results, patterned coatings —e.g., a random pattern of speckles easily created by spray painting— must be applied to obtain images with high contrast and fine detail, without self-similarity. Rules of thumb have been given for evaluating the quality of a given pattern, and quantitative analysis is the subject of ongoing research [4]. It would be useful to be able to synthesize a pattern, if the imaging conditions are known beforehand, that would provide optimal performance for digital image correlation under those conditions. However, the digital image correlation method can incorporate various tricks and strategies to decrease computation time or compensate for deficiencies in the images such as effects caused by lighting variations. The effectiveness of these tricks will again depend on the pattern, so the optimal pattern depends on the algorithms and parameters used for digital image correlation.

This paper presents the evaluation of a series of patterns for digital image correlation, both experimentally and by means of computer simulation at various levels of detail for the image creation process, illustrated in Fig. 1.

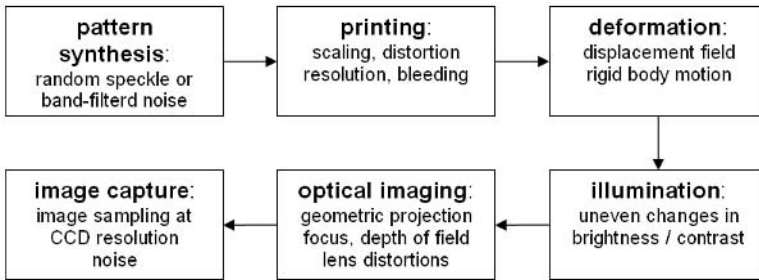


FIGURE 1. modular simulation of image creation process in digital image correlation method

Comparison of the experiments with the simulations reveals that omission or idealized treatment of the imaging system from the simulation significantly alters some aspects of the digital image correlation results. This leads to erroneous conclusions with respect to optimal patterns and algorithm choices. On the other hand, idealized treatment or exaggerated aberrations of the imaging system in the simulations provide useful insights regarding limitations and possible improvements of the digital image correlation method.

## References

1. Sutton M.A. et al, *Image Vision Comput.*, vol. **1**, 133-139, 1983.
2. Asundi A. and North H., *Opt. Lasers Eng.*, vol. **29**, 159-169, 1998.
3. Knauss W.G., Chasiotis I. and Huang Y., *Mech. Mater.*, vol. **35**, 217-231, 2003.
4. Lecompte D. et al, *Opt. Lasers Eng.*, vol. **44**, 1132-1145, 2006.

## ANALYSIS OF INERTIA EFFECT ON A THREE POINT BEND SPECIMEN LOADED BY THE HOPKINSON PRESSURE BAR

Xiaoxin Zhang<sup>1,2</sup>, Gonzalo Ruiz<sup>2</sup> and Rena C. Yu<sup>2</sup>

<sup>1</sup>College of Mechanical and Electrical Engineering, Harbin Engineering University, Harbin 150001, P.R. China.

<sup>2</sup> ETSI Caminos, C. y P., Universidad de Castilla-La Mancha, 13071 Ciudad Real, Spain.  
zhangxiaoxinhrb@gmail.com, Gonzalo.Ruiz@uclm.es, rena@uclm.es

In the paper, the inertia effect was analyzed using dynamic finite element method to a three point specimen loaded by the Hopkinson pressure bar. The schematic diagram of the experimental apparatus is shown in Fig. 1. The nominal load (the external load) applied on the specimen was measured by the strain gauges mounted at the center of the Hopkinson pressure bar; the crack initiation time was determined using strain gauge method.

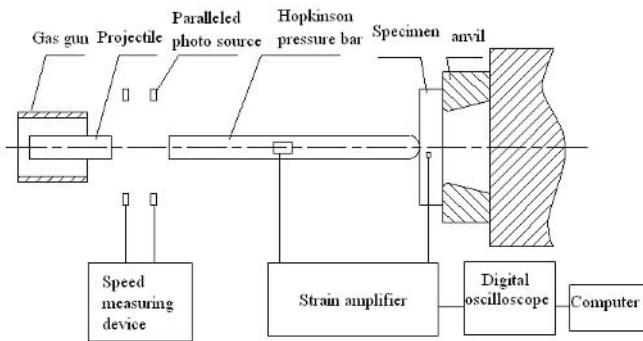


FIGURE 1. Experimental apparatus and its recording system.

The material used is a low alloy steel, and the mechanical properties are shown in Table 1. The relationship between the dynamic yield strength  $\sigma_{yd}$  of the material with the strain rate  $\dot{\epsilon}$  is shown in Equation 1.

$$\sigma_{yd} = 480 \left[ 1 + \left( \frac{\dot{\epsilon}}{64560.7} \right)^{0.275} \right] \quad (1)$$

Charpy impact fatigue-precracked specimens were used in this experiment. As shown in Fig. 2, only one half of the specimen and one support (anvil) were modelled due to symmetry. The mesh of the specimen and support consisted of 627 nodes and 217 eight-node isoparametric elements in total. Using the contact wizard in ANSYS we conducted a contact analysis between the specimen and the support. The specimen is assumed to be under plane strain condition. The material model of the specimen follows Equation 1 under dynamic loading conditions, and the material of the anvil follows the linear elastic behaviour.

TABLE 1. Mechanical properties of the steel

Yield Strength / MPa	Ultimate trenchth / MPa	Area reduction	Elongation	Poisson's Ratio	Density / kgm <sup>-3</sup>	Modulus / GPa
480	600	77%	30%	0.3	7800	210

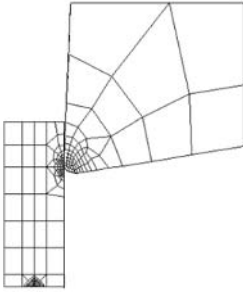


FIGURE 2. Schematic diagram of finite element mesh

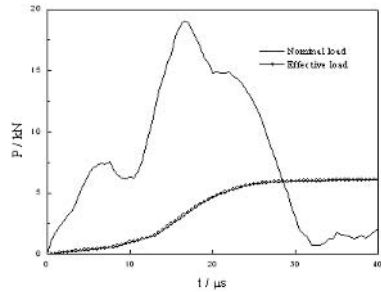


FIGURE 3. Comparison of the nominal load and the effective load as a function of time

The effective displacement of the specimen loading point was calculated using the dynamic finite element method by applying the nominal load (the external load). By prescribing this effective displacement, the effective load was again determined numerically. Fig. 3 shows the comparison of the nominal load and the effective load as a function of time. A considerable difference between the nominal load and the effective load is found. It is clear that the effective load is much less than the nominal load. This indicated that most of the nominal load is used to maintain the balance with the inertia force during loading and only a small portion of the nominal load (the effective load) is actually used to deform and fracture the specimen. Hence, the energy exhausted in crack initiation derives purely from the effective load.

Furthermore, the distribution of strain rate around the crack tip of the specimen was found to be not uniform and changed with the time. The order of average strain rate at the crack tip is about 10<sup>3</sup>/s.

**References**

1. Kobayashi, T., Engineering Fracture Mechanics, vol. 19, 49-65, 1984
2. Liu, Y. N. and Zhou, H. J., Engineering Fracture Mechanics, vol. 48, 299-304, 1994

## SIZE AND STRAIN RATE EFFECTS ON THE FRACTURE OF REINFORCED CONCRETE

Gonzalo Ruiz<sup>1</sup>, Xiaoxin Zhang<sup>1,2</sup> and Rena C. Yu<sup>1</sup>

<sup>1</sup> ETSI Caminos, C. y P., Universidad de Castilla-La Mancha, 13071 Ciudad Real, Spain.

<sup>2</sup> College of Mechanical and Electrical Engineering, Harbin Engineering University, Harbin 150001, P.R. China.

Gonzalo.Ruiz@uclm.es, zhangxiaoxinhrb@gmail.com, rena@uclm.es

This paper presents very recent results of an experimental program aimed at disclosing size and strain rate effects on the fracture behavior of reinforced concrete beams. Thirty-six reinforced beams made of two micro-concretes (material A and material B), of three sizes (75mm, 150mm and 300mm in depth), were tested under four strain rates ( $1.05 \times 10^{-5}/s$ ,  $1.25 \times 10^{-3}/s$ ,  $1.25 \times 10^{-2}/s$  and  $3.75 \times 10^{-2}/s$ ).

The schematic diagram of the beams was shown in Fig. 1. We used the constant reinforcement ratio ( $\rho = 0.15\%$ ) and the same thickness ( $B=50$  mm) for all the specimens. The rebar was kept in the same relative position in the beams.

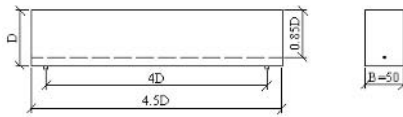


FIGURE 1. Schematic diagram of the beams.

Table 1 shows the characteristic mechanical parameters of the micro-concrete determined in the various characterization and control tests. Where  $f_c$ ,  $f_t$ ,  $E_c$ ,  $G_F$  and  $l_{ch}$  are the compressive strength, tensile strength, elastic modulus, fracture energy and Hillerborg's characteristic length, respectively.

TABLE 1 Micro-concrete characteristics

		$f_c$ / MPa	$f_t$ / MPa	$E_c$ / GPa	$G_F$ / N·m-1	$l_{ch}$ / mm
Material A	Mean	40.37	4.83	29.57	51.70	65.53
Material B	Mean	28.43	3.74	29.64	49.48	104.85

The mechanical properties of the steel are as follows. The elastic modulus is 133.2GPa, the standard yield strength at the strain of 0.2% is 434.1 MPa, the ultimate strength is 465.1MPa, and the ultimate strain is 0.9%. The bond strength  $\tau_c$  is  $7.00 \pm 0.79$  MPa for material A, and  $5.34 \pm 0.80$  MPa for material B.

Fig. 2 shows the effect of loading rate on the peak load ( $P_{max}$ ) for each size. As it is clear from the figure, the measured values of the peak load suffer scattering, which could be explained by the fact that the specimens were cast from different batches of reinforced micro-concrete.

Nevertheless, some general trends can still be observed: (1) the peak loads increase with increasing strain rate; (2) the rate dependence of the peak load is stronger for larger specimens than for smaller ones.

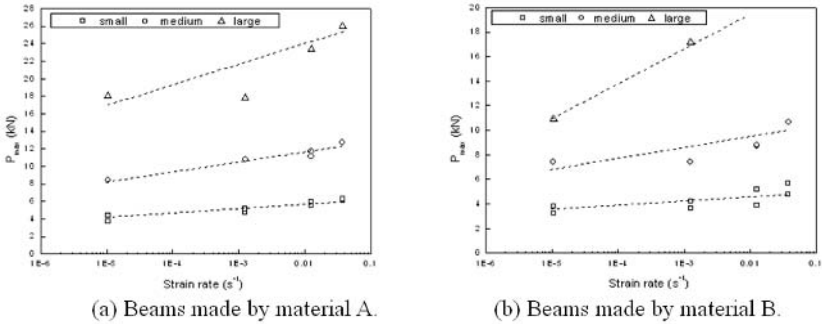


FIGURE 2. Effect of loading rate and specimen size on the peak load.

Fig. 3 represents the mean cracking load of all the kinds of beams tested versus their corresponding beam depth under various strain rates; both are expressed in dimensionless form: the load level by means of the nominal strength divided by the concrete tensile strength ( $\sigma_{Nmax} / f_t = 3 P_{max} S / (2 BD^2 f_t)$ ) and the size by the Hillerborg's brittleness number. For beams made by material A ( $l_{ch}$  is 65.53 mm) and material B ( $l_{ch}$  is 104.85 mm), size effect is only shown under the strain rate  $1.05 \times 10^{-5} / s$ , while it is inconspicuous to the higher strain rates. The apparent absence of size effect at higher strain rates is explained numerically. The growth of the peak load due to the growing CMOD rate might have compensated its decrease due to size effect.

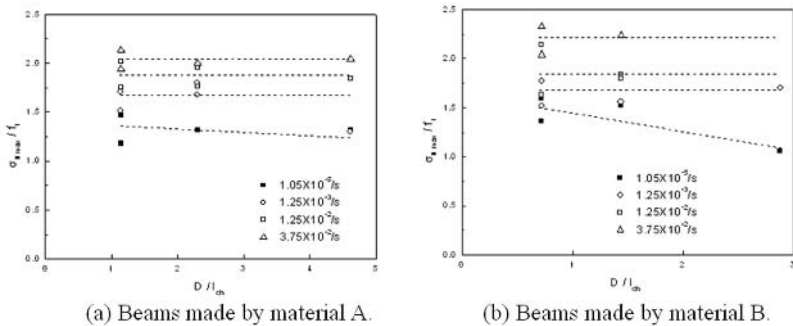


FIGURE 3. Non-dimensional cracking strength versus their corresponding depth under various strain rates.

References

1. Ruiz, G., Elices, M., Planas, J., Materials and Structures, vol. 31, 683-691, 1998
2. Pandolfi, A., Ortiz, M., Engineering with Computers, vol. 18 (2), 148-159, 2002

## MODELLING AND EXPERIMENTAL INVESTIGATION OF A COMPOSITE CUSHION UNDER IMPACT LOADING

Michael A. Sek<sup>1</sup>, Vincent Rouillard<sup>1</sup> and Manuel Garcia-Romeu<sup>2</sup>

<sup>1</sup>Victoria University, Melbourne, Australia

PO Box 14428 MCMC, Melbourne 8001, Australia

<sup>2</sup>ITENE®, Instituto Tecnológico del Envase, Embalaje y Transporte

Poligono D'Obradors, C/Soguers, 2

46110 Godella – Valencia, Spain

michael.sek@vu.edu.au, vincent.rouillard@vu.edu.au, mgarciaromeu@itene.com

The behaviour of corrugated fibreboard composite cushion comprising laminations with differing pre-compression strain under impact loading is modelled and then investigated numerically and experimentally with the assistance of a high-speed video camera. Similar configurations were investigated, only experimentally, by Sek *et al.*[1], Sek and Rouillard [2] who showed an improvement in cushion performance. For the purpose of this study a Simulink library of discrete dynamic elements and s-functions was developed (Fig. 1) and used to conduct virtual experiments. As an example, the compression characteristics of a simulated single corrugated layer is shown in Fig. 1.

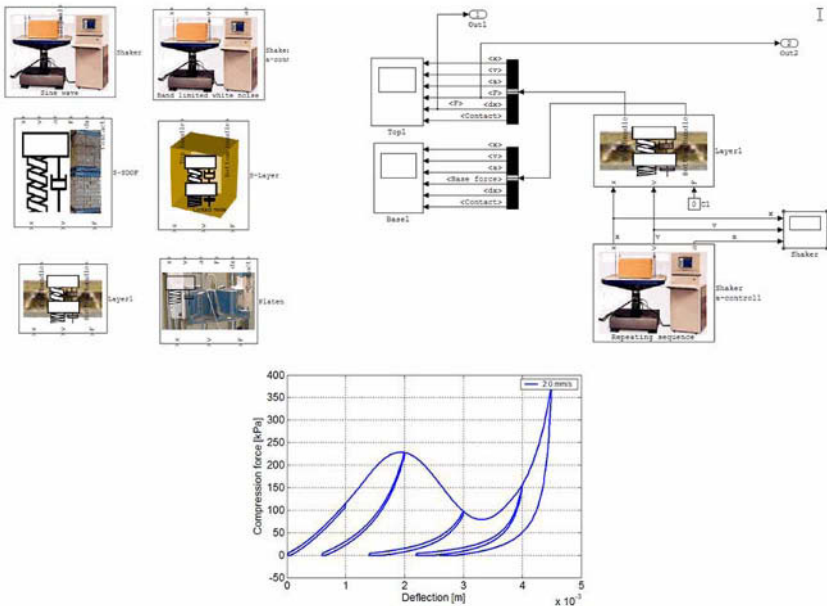


FIGURE 1. Library of discrete dynamic elements and the model of progressive compression.

Multi-layer samples were then assembled and subjected to impacts by a platen falling on the sample from various drop heights. Fig. 2 illustrates results (initial velocity of 2.4m/s at 5mm

before the contact) obtained for a laminated sample comprising five pre-compressed layers and three smaller sacrificial virgin crumple layers. Dynamic forces within the sample vary rapidly, particularly in the period when one layer is collapsing, which lasts a fraction of millisecond (Fig. 3). When crumple layers are not used, the shock is significantly more severe - acceleration of the platen is almost three times higher.

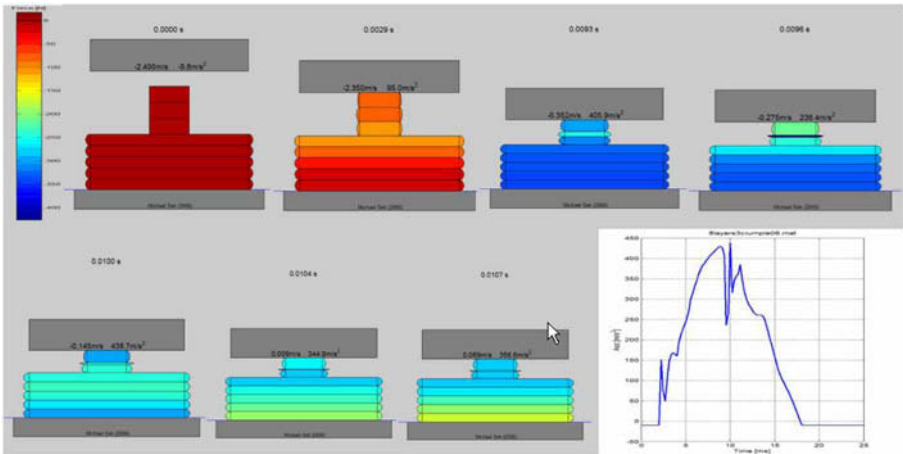


FIGURE 2. Results of simulation of an impact involving a collapse of crumple layer.

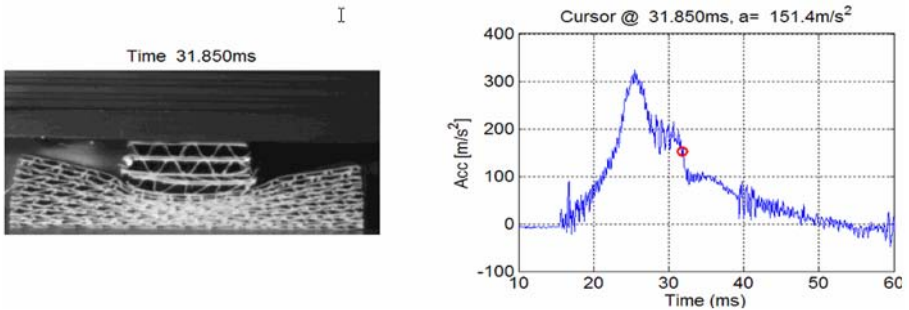


FIGURE 3. Shock pulse synchronised with a frame (filmed and sampled 20,000 per second).

**References**

1. Sek M., Rouillard V., Crawford S., and Tarash H. In *Proceedings of the 21st IAPRI Symposium on Packaging*, ITENE, Valencia, Spain, 2003.
2. Sek M. and Rouillard V. In *Proceedings of 4th International Conference on Advances in Experimental Mechanics - Applied Mechanics and Materials*, edited by J. Barton, Southampton UK, 2005, **3-4**, 383-388.



## CONCURRENT BENDING AND LOCALIZED IMPACT ON SANDWICH PANELS

Jorgen A. Kepler and Peter H. Bull  
Aalborg University, Department of Mechanical Engineering  
Pontoppidanstraede 101, DK-9220 Aalborg East, Denmark  
jk@ime.aau.dk

The paper describes impact/bending testing of sandwich panels with 10 mm foam core and FRP face-sheets, with emphasis on test procedures, registration of results and description of the specialized test equipment developed. The sandwich panels were subjected to a cylindrical bending load of varying magnitude, while impacted at approximately 500 m/s. The impactor body was a steel sphere, diameter 10mm, with a mass of approximately 4g. The energy absorption and damage morphology of preloaded panels were compared with similar data for impact on specimens without preload. A high-speed camera was used for qualitative registration of panel response.

Sandwich panels consists of two stiff, thin face-sheets separated by and glued to the surfaces of a lightweight core plate. A bending moment is carried primarily by membrane stresses in the face sheets, while shear loads are transferred as transverse shear stress in the core material. This structural layout may be employed to produce panels with a particularly good ratio between stiffness/strength and mass for a bending load (in much the same way as an I-profile steel beam). Some complications may arise, however; sandwich structures are sensitive to imperfections in load application, in particular in the form of concentrated loads, and as “fully stressed” structures, there is little reserve capacity once one structural component has failed. Furthermore, the multitude of damage modes make prediction of damage morphology a complex matter.

The subject of localized, penetrating impact on sandwich structures has been the focus of considerable attention in recent years. Typically, the primary topics of interest has been energy absorption and mechanical properties after impact (residual stiffness/strength). While these matters may be addressed separately, they do not necessarily give any fair indication of what happens when a stressed sandwich panel is penetrated. In particular, the risk of sudden catastrophic deterioration (defined as complete or near-complete loss of structural integrity) initiated by a localized impact is worth investigating.

Simultaneous localized impact and structural preload has been investigated for pressurized tubes (airplanes, oil pipes etc.), see e.g. [1] by Rosenberg *et al.*, and monolithic composite structures under such load combinations has received increasing attention in recent years (for some recent advances, see e.g. [2] by Mikkor *et al.* and [3] by Khalili *et al.*) whereas similar combined loading on sandwich structures has apparently been largely neglected.

In [4], Malekzadeh *et al.* describes a model for predicting the contact force and panel response when subjecting an in-plane prestressed sandwich panel to low velocity, nonpenetrating impact. It was, among other things, demonstrated that the peak contact force would increase and the deflection decrease with increasing tensile preload. These tendencies were qualitatively identical to those described by Khalili *et al.* in [3]. However, the matter of structural response and possible catastrophic failure following penetrating impact is not addressed.

A series of tests are described, where a panel under cylindrical bending is penetrated by a spherical impactor. Figure 1 shows the bending rig with a sandwich panel specimen inserted.

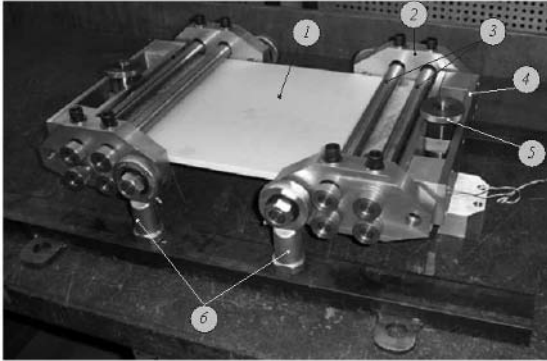


FIGURE 1. Bending rig with specimen, laid out on table for clarity. The parts are:

- 1: Test specimen, 2: Moment yoke, 3: Clamp bars
- 4: Load yoke, 5: Load screw, 6: Yoke supports

For the impact tests, the bending rig is fitted to a rigid steel frame, permitting transverse, penetrating impact by a steel sphere propelled by a compressed-air gun. Entry and exit velocities are measured, thus providing data for loss of impactor momentum and kinetic energy.

### References

1. Rosenberg, Z., Mironi, J., Cohen, A. and Levy, P., *International Journal of Impact Engineering*, vol. **15**, p. 827-831, 1994
2. Mikkor, K. M., Thomson, R. S., Herszberg, I., Weller, T. and Mouritz, A. P., *Composite Structures*, vol. **75**, p. 501-513, 2006
3. Khalili, S. M. R., Mittal, R. K. and Mohammad Panah, N., *Composite Structures*, vol. **77**, p. 263-268, 2007
4. Malekzadeh, K., Khalili, M. R. and Mittal, R. K., *Journal of Sandwich Structures and Materials*, vol. **8**, p. 157-181, 2006

## DISCUSSIONS ON STANDARDIZATION OF HOPKINSON BARS TECHNIQUE

L.M. Yang, Li Song and Li-Li Wang  
Mechanics and Materials Science Research Center Ningbo University  
Ningbo, Zhejiang, 315211, P. R. China  
yangliming@nbu.edu.cn, songli@nbu.edu.cn, llwangch@nbu.edu.cn

It is well known that the constitutive behaviour of most materials exhibits rate sensitivity and that the rate dependent (tensile/compressive) properties of such materials should be experimentally studied. The Split Hopkinson Bar (SHB) technique has been successfully applied to investigate the visco-elastic and visco-plastic behaviour of plastics and metals under high strain rates. Recently, it has widely been used to study the dynamic behaviour of materials, such as rubbers, composites, foams and concretes. Then, it often happens that the measured data by SHB in one laboratory are different from those in another laboratory. Even in the same laboratory, sometimes, the SHB measured data by one person are different from those by another one. The cause to produce the difference, as revealed by our experiments and the related theoretical analysis, is mainly attributed to that there are some important factors which do affect the accuracy of data measured in SHB tests, and that researchers sometimes ignore the basic assumptions in SHB technique.

For obtaining the reliable and comparable data measured from SHB tests, a standardization of SHB technique must be set up. According to our experimental results and numerical analysis, the standardization should include the following contents:

- **The duration of incident pulse.** In an SHB test, if the duration of incident pulse  $T$  is longer than the actual loading duration  $T_l$  experienced by specimen until fracture, the remaining part at the tail of incident pulse ( $T - T_l$ ) does not affect the experimental results. The specimen is loaded by the front part of incident pulse with duration  $T_l$  only. Thus, the duration of incident pulse in an SHB test is actually defined to be  $T_l$ . To reduce the transverse inertial effect which produces the dispersion of the incident pulse, the following condition must be satisfied:  $\alpha = (CT_l)/r \gg 1$ , where  $C$  is the elastic wave velocity and  $r$  is the radius of bars. The minimum value of  $\alpha$  should be standardized.
- **One dimensional condition.** The stress state in the specimen tested should be of one dimension, which requires to reduce the friction effects between specimen and bars. The contact surfaces between specimen and bars should be well lubricated and the geometry of specimen should satisfy some relationship e.g.  $h \geq r$ , where  $h$  is the thickness of the specimen. The thicker the specimen is, the less the friction effect on the one dimensional stress state is. However, the thicker the specimen is, the longer time needed to reach stress uniform in specimen is.
- **Stress uniform in SHB testing.** In SHB testing, a basic assumption is that the stress distribution in the specimen is uniform or dynamic equilibrium, during testing. This assumption may not hold when the specimen is excessively brittle, because the specimen fails during initial loading before stress equilibrium is established, particularly when the wave speed in the specimen is comparatively slow. Conditions necessary for attaining uniformity of stress distribution within a specimen have been highlighted previously. A finite time  $t_b$  is required for stress within a specimen to equilibrate and it has been found that  $t_b$  is dependent on the shape of the incident pulse and the material properties of bar and specimen. It should also be noted that reliability of data measured from SHB testing is

affected by  $t_b$ . Before attainment of stress equilibrium in a specimen, the data obtained cannot be used because the analysis assumes that stress is uniform in the specimen. Hence, the time  $t_b$  is an inherent limitation in SHB tests. An estimation of  $t_b$  serves to distinguish which mechanical properties of material can be measured by an SHB and which ones are not suitable for determination using SHB techniques. Furthermore, information on how  $t_b$  can be reduced is important in obtaining reliable measurable data.

- **The method to calculate stress, strain and strain rate based on the measured data.** The experience on the experimental data treatment tells us that the calculated stress-strain curves of the specimen, based on incident, reflection and transmission waves recorded, are very sensitively dependent on the selection of beginning points of the three waves. Thus, the method to determine the wave beginning points should be identical.
- **The qualification of the bars.** For SHPB, the straightness of bars should be standardized and the situation of contacting surfaces between bars and specimen is also required. The bars are also action as transducer to measure stress and strain of specimen through measuring the strain waves propagating in the bars. The rising edge of incident wave could be very steep, where the dispersion is serious in the beginning stage of incident wave generated by an impact. After propagating some distance, the dispersion of the incident wave is not as serious as that in the beginning stage. Thus, the location of strain gages on the bars should also need to be confined.
- **Fixture system used in SHTB.** For SHTB, a fixture system is often used to connect specimen and bars. The fixture system affects the stress wave propagation in bars and specimen, which results in that the time  $t_b$  increases with increasing the length of fixture system. Thus, the size of the fixtures system must be identical. The stiffness of the fixture system will affect the measuring accuracy of strain in specimen. So, its stiffness should be standardized. Furthermore, the connection of fixture system to bars and specimen is also needed to be standardized.

### **Acknowledgement:**

The authors acknowledge the financial support from the National Natural Science Foundation of China (No. 10672083)

## IDENTIFICATION OF STRAIN-RATE SENSITIVITY PARAMETERS OF STEELS WITH AN INVERSE METHOD

Lorenzo Peroni, Marco Peroni and Giovanni Belingardi  
 Dipartimento di Meccanica, Politecnico di Torino  
 Corso Duca degli Abruzzi 24, 10129 Torino, Italy  
 lorenzo.peroni@polito.it

Since the second half of the past century, research in the automotive industry focused on vehicle performance, environmental compatibility, and safety improvement. Increasing interest about passive safety and the ever stricter regulations, both in the US and EU, pushed towards more reliable models of the vehicle behaviour and, to achieve this, to a deeper insight into material behaviour. For what concerns crash simulations, one of the most critical uncertainty relates to the influence of the loading speed on the material mechanical properties. This influence can be accounted by means of the strain-rate sensitivity that is substantial for most materials. Strain-rate sensitivity of low-carbon steels, such as the deep-drawing steels of most automotive body, is very well known.

Aim of the present work is to show a combined experimental and numerical technique, based on an inverse approach, to determine strain-rate sensitivity parameters of steels. This technique is based on the numerical simulations, by means of a finite element explicit code, of experimental tensile tests. The tests are conducted at different speeds, from quasi-static loading conditions with a general purpose hydraulic testing machine, to high speed, with a Hopkinson Tensile Bar. This latter device is able to induce strain-rates of the order of magnitude of some thousand of  $s^{-1}$ . Each test, independently by the used test rig, substantially gives a load-stroke curve.

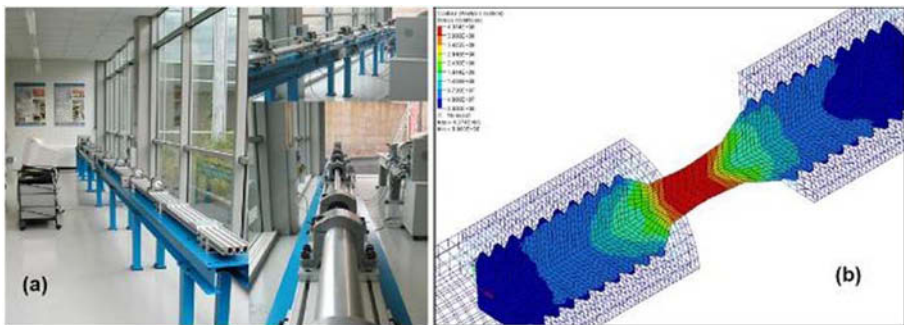


FIGURE 1. Hopkinson Bar (a) at the II Faculty of Engineering of Politecnico di Torino (Vercelli site); (b) numerical model of a cylindrical specimen.

Usually stress-strain relations are obtained, analytically, from these experimental data: however the particular geometry and small dimension of the specimen used in dynamic tensile tests introduces some error essentially due to the triaxiality of the stress and strain fields.

To avoid this problem, and improve the correctness of the results, a series of simulations (LS-Dyna) in the same conditions of experimental tests are performed, changing material strain and strain-rate law parameters in each run by means of an optimization strategy (Hyperstudy).

The parameters that give the minimum error, i.e. giving the best fit of the numerical result to the experimental one, are the identified parameters for the material.

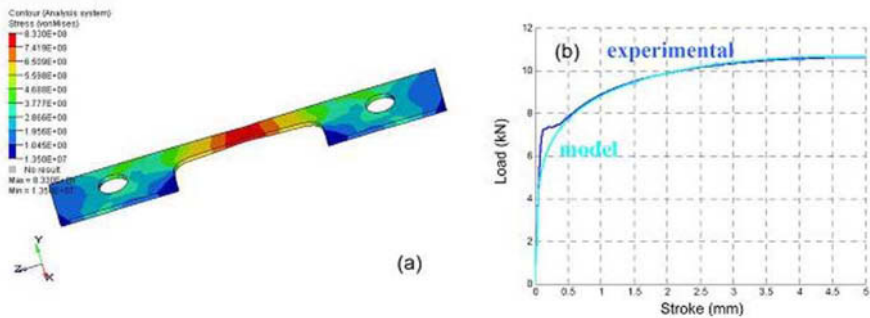


FIGURE 2. (a) numerical model of a sheet specimen, (b) comparison between experimental data and optimized numerical model

## References

1. Peroni L., In Proceedings of ICEM12- 12<sup>th</sup> International Conference on Experimental Mechanics, 2004 Politecnico di Bari, Italy, 188-189.
2. Bragov A. M., Lomunov A. K., *Int. J. Impact Engineering*; vol. **16**; No 2; 1995; p. 321-330.
3. Hauser E. F., *Experimental Mechanics*; vol. **6**; 1966; pp 395-402.
4. Gong J. C., Malvern L. E., Jenkins D. A., *Journal of Engineering Materials and Technology*; September 1990; pp. 232-235
5. Tyas A. and A.J. Watson, *International Journal of Impact Engineering*, 25, 2001, pp. 87-101.
6. Nicholas T., Bless S. J., *High strain rate-tension testing*, *ASM Metals Handbook*; vol. **8**; 1985.
7. Staab G. H., Gilat A., *Experimental Mechanics*; 1991; pp. 232-235.
8. Jones N., *Structural Impact*, Cambridge University Press, Cambridge, 1989.
9. Johnson W., *Impact strength of materials*; Edward Arnold; 1972; Londra.
10. Regazzoni G., Johnson J. N., Follansbee P.S, *Journal of Applied Mechanics*; 1986; pp. 519-528.

## EXPERIMENTAL PARAMETER IDENTIFICATION FOR MATERIAL MODELS INCLUDING DEFORMATION INDUCED VOLUME DILATATION FOR THERMOPLASTIC MATERIALS

F. Huberth  
 Fraunhofer EMI  
 Eckerstrasse 4, 79104 Fribourg, Germany  
 frank.huberth@emi.fraunhofer.de

Simulation of structures made from thermoplastic materials under crash loads including large deformations and failure is still a challenge for most existing numerical tools [1]. To model the complex mechanical behaviour of thermoplastic materials new models have been developed. To reproduce the mechanical behaviour in the simulation, model parameters for each material have to be identified by experimental testing.

The investigation of the strain rate dependency is done by tensile tests at different loading speeds. The material behaviour under shear and compression needs additional testing. The limits of these different setups for the material characterisation are investigated. For tensile tests the stress calculation is significantly influenced by the cross section. For standard testing different assumption are made. A measurement of the cross section during the tests helps to determine the true stress developing.

An experimental set-up will be shown that allows for measuring changes in volume and cross section (Fig. 1). The impact of volume dilatation on numerical results will be explained applying the LS-DYNA SAMP-1 model [2].

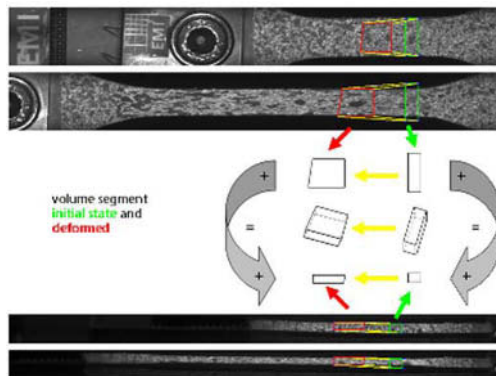


FIGURE 1. Segment volume and cross section measurement during tensile tests by picture analysis for two perpendicular perspectives.

The sample is camera observed from two directions during the deformation process. From the pictures taken, the deformation of defined segment surfaces on the sample is measured by the use of texture analysis. Using the segments, the change in cross section and volume are calculated.

In Fig. 2 a segment volume evaluation under tensile loading by the use of 2D-picture analysis is shown related to the tensile strain.

Based on the measurement, the plastic Poisson ratios for a PC-ABS-blend and a PA-ABS-blend are derived. The plastic Poisson ratios describe the correlation between strain in loading direction and the transversal strains.

Furthermore, the cross sectional area of the sample is measured to allow for a true stress calculation. Fig. 3 shows the different stress strain curves depending on the stress calculation. Assuming constant volume, the highest stresses are calculated using the true cross section. A significantly reduced stress level is found using volume dilatation.

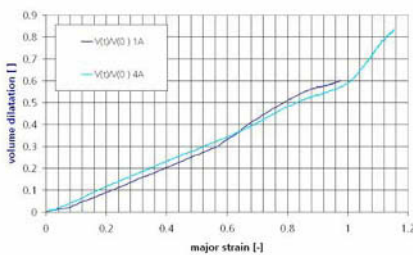


FIGURE 2. Volume evaluation for a PA-ABS-blend for 2 experiments.

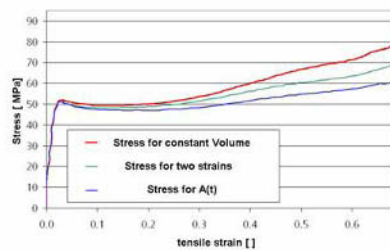


FIGURE 3. Stress-strain curves for different approaches of stress calculation.

The plastic Poisson ratio can be treated by the LS-DYNA SAMP-1 model. By this value or curve a dilatation under tensile loading is taken into account.

To show the practical application in comparison to simple material models and experimental data, results of different loading cases are discussed.

A flat plate is clamped around the edge and loaded by a spherical impactor like in a dynamic cupping test. For this loading case failure strains occur, that are three times higher than that determined in uniaxial tensile tests. This indicates an influence of a multi axial stress-strain state. The model parameters can be fitted until the experimental results of the cupping tests are reproduced.

The limits of experimental testing for parameter identification are shown. A focus was put on the volume dilatation during loading and the iterative optimisation of model parameters.

## References

1. Junginger, M.: "Charakterisierung und Modellierung unverstärkter thermoplastischer Kunststoffe zur numerischen Simulation von Crashvorgängen", Schriftenreihe Forschungsergebnisse aus der Kurzzeitdynamik, Heft Nr. 3, Freiburg/Brsg. 2004, ISBN 3-8167-6339-1 Fraunhofer IRB Verlag]
2. Kolling, S., Haufe, A., Feucht M., DuBois, P.: "SAMP: A Semi-Analytical Model for Polymers", crashMAT 2006, 4. Freiburger Workshop zum Werkstoff- und Strukturverhalten bei Crashvorgängen, Freiburg 2006



## EXPERIMENTAL ANALYSIS OF THE SHOCK ENHANCEMENT OF A CELLULAR STRUCTURE UNDER IMPACT LOADING

S. Pattofatto<sup>1</sup>, I. Elnasri<sup>1</sup>, H. Zhao<sup>1</sup> and Y. Girard<sup>2</sup>

<sup>1</sup> Laboratoire de Mécanique et Technologie  
ENS-Cachan/CNRS-UMR8535/Université Paris 6  
61, avenue du président Wilson, 94235 Cachan cedex, France

<sup>2</sup> EADS- CCR Suresnes, 12 bis rue Pasteur  
92152 Suresnes cedex, France  
stephane.pattofatto@lmt.ens-cachan.fr

This study is part of a research program on the analysis of the impact behavior of metallic cellular materials (honeycomb, foam, hollow sphere agglomerate) used in the energy absorption design of aeronautical applications (Zhao [1]).

In previous studies, the dynamic compression behaviour of honeycombs and aluminium foams (Zhao *et al.* [2, 3]) has been presented. In this study, the shock enhancement of an impacted aluminium foam is investigated using a specific dynamic image correlation method.

Crushing experiments are performed on an Alporas foam using a large diameter (60 mm) nylon Hopkinson bar. The impact velocities (47 m/s and 56 m/s) are chosen lower and above the critical velocity corresponding to the occurrence, into the specimen, of a shock front propagation. This phenomenon can be predicted by classical models, such as the RPRL model proposed by Reid and Peng [4].

In order to validate this model, an optical measurement of the strain field into the specimen is used. A high speed camera captures 20 000 images/s and the displacement and strain field during testing are obtained by a special image correlation calculation program (Correli<sup>LMT</sup>) (see Roux *et al.* [5]). This strain field measurement shows that at high strain rate a shock discontinuity propagates as depicted in Fig. 1. From this measurement, one can measure the shock front velocity. For example, an impact velocity of 56 m/s gives a shock front velocity measured at 87 m/s.

Based on these results, a modified model is proposed because the RPRL model relies on parameters that cannot be accurately determined (the rigid locking strain for example). In this improved model, the analytical solution is given in the case of a linear locking and numerical solution is given if the whole hardening curve of the foam is taken into account. The prediction of the shock front velocity is therefore compared to RPRL model and measurements. Satisfactory agreement between improved theory and the optical shock front speed is presented.

Finally, numerical analysis using Ls-Dyna explicit code with a macroscopic homogeneous phenomenological material law (crushable foam) is finally presented. It shows that such a simple model can reproduce essential feature of shock enhancement.

### References

1. Zhao, H., *Cellular materials under impact loading*, IFTR-AMAS Edition, Warsaw, Poland. ISSN 1642-0578, 2004.
2. Zhao H. et Abdennadher S., *Int. J. Solids & Structs.* vol. **41**, 6677-6697, 2004.
3. Zhao H., Nasri I. et Abdennadher S., *Int. J. Mech. Sci.*, vol. **47**, 757-774, 2005.
4. Reid, S. R., Peng, C., *Int. J. Impact Engng.* vol. **19**, 531-570, 1997.

5. Roux, S., Hild, F., Pagano, S., *European J. Mechanics A/Solids*. vol. **24**, 442-451, 2005.

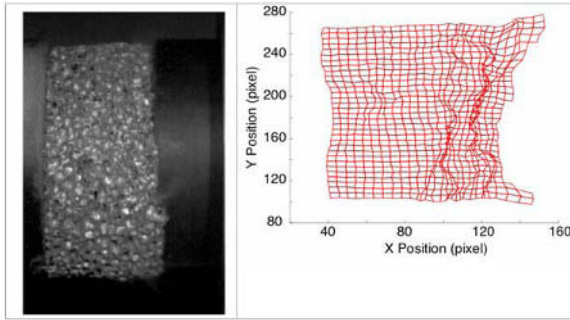


FIGURE 1. One captured image and the corresponding calculated deformed mesh ( $t=0.5\text{ms}$ ).

## COMPRESSION TESTING BY MEANS OF CHARPY PENDULUM

V. Mentl and J. Dzugan

<sup>1</sup>Skoda Research Ltd., <sup>2</sup>COMTES FHT

316 00 Tylova 1/57, CZ-316 00 Plzen, Czech Republic

vaclav.mentl@skoda.cz

Mathematical modelling and virtual testing of components and structures represent a useful and economical tool for design and safety assessment. The so called basic mechanical properties which can be found in material standards are not relevant in cases where the real service conditions differ from those applied during testing. Thus e.g. mechanical behaviour at higher strain rates can be interesting for the car components when the simulation of crash situations is used during structure development.

The dynamic compression tests are usually performed by means of drop towers, high speed hydraulic testing machines or Hopkinson bar method. At the Mechanical Testing Laboratory of the SKODA Research Inst., in Pilsen, Czech Republic, an instrumentation of Charpy pendulum testing machine was used to perform dynamic compression tests. A new striking tup was designed and calibrated. At the same time, a new software was developed which makes it possible to evaluate the test force-deformation record.

The correctness of the instrumentation and software was verified by comparison of measured and evaluated values of energies and deformations. A very good good agreement was obtained.

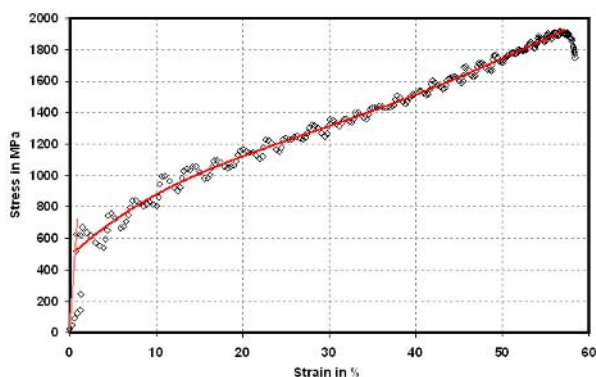


FIGURE 1. Example of compression test record of a steel sample

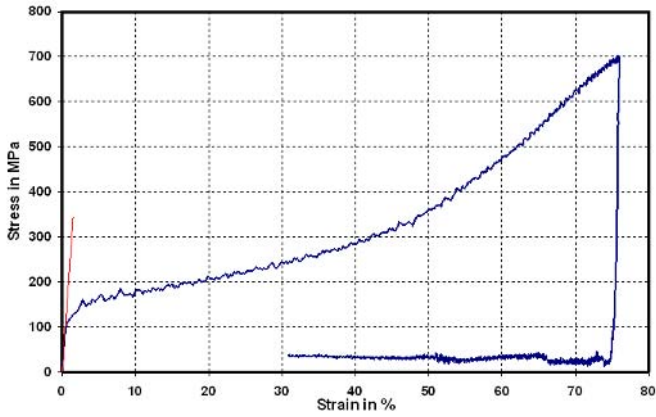


FIGURE 2. Example of compression test record of an Alluminium sample

Examples of two records for steel and Al-alloy are in Figs. 1. and 2. An international round-robin within the frames of ESIS TC5-Subcommittee on “Mechanical testing at intermediate strain rates” is realised at present.

## DETECTION AND QUANTIFICATION OF IMPACT LOADS IN FIBRE REINFORCED PLOYMERS

Ch. R. Koenig<sup>1</sup>, D.H.Mueller<sup>1</sup>, O. Focke<sup>2</sup> and M. Calomfirescu<sup>3</sup>  
<sup>1</sup>BIK – University of Bremen, <sup>2</sup>BIAS Bremen, <sup>3</sup>Faserinstitut Bremen  
 Badgasteiner Str. 1, 28359 Bremen, Germany  
 chkoenig@uni-bremen.de

Reinforced composites are mainly used when high accelerations take place. The reinforced composites offer a high potential to reduce the kinetic energy. As a consequence these parts have a higher risk of being exposed to impact loads. Sudden structural failure of fibre-reinforced polymers caused by impact is an important factor in product development for the aircraft industry. Therefore it is necessary to obtain knowledge of the mechanisms and of the material loading during and shortly after an impact load.

An impact test device was developed at the University of Bremen. The time variable, the dynamic material properties, stress and strain conditions in composite plates have been measured using photoelastic technique, strain gauges and holographic interferometry (Fig. 1) [1,2].

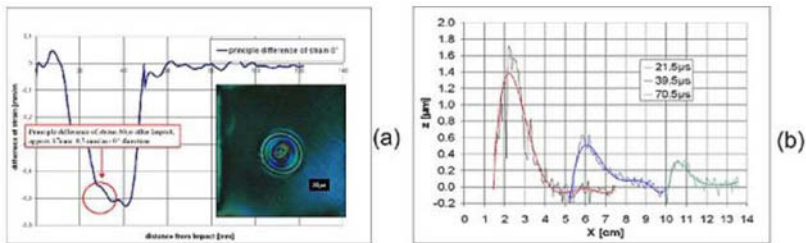


FIGURE 1. (a) The principle difference in strain with the photoelastic coating 30 $\mu\text{s}$  after the Impact and (b) the displacement of the surface with the holographic interferometry

The distribution of stresses and / or strains in a two-dimensional composite specimen subjected to an impact load is difficult to solve mathematically. Therefore a Finite Element Model was developed. This Model was validated with the results of the experiments (Fig. 2) [1].

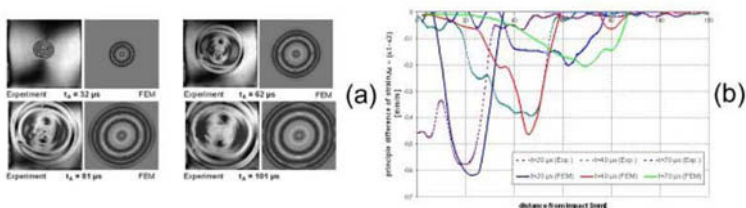


FIGURE 2. (a) qualitative validation, (b) quantitative validation of the FE Simulation

This knowledge of the flexural wave propagation in FRP and the potentiality to describe them in a finite element simulation is a valid attempt for an 'impact load monitoring' to detect, reconstruct and evaluate the feasibility of possible damages of even barely visible impact loads in FRP materials.

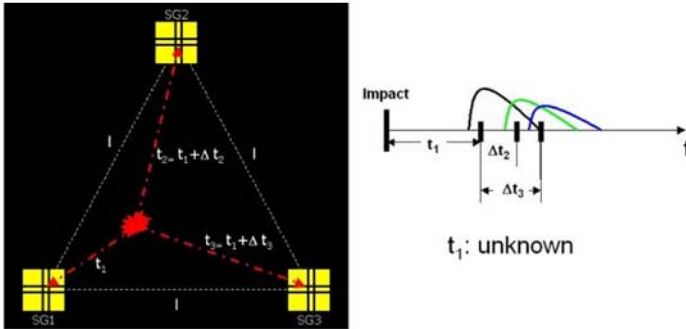


FIGURE 3. The experimental set up to detect an impact load in a FRP Specimen. The time  $t_1$  is unknown,  $\Delta t_2$  and  $\Delta t_3$  are measured.

Fig. 3 shows the experimental set up. If times  $\Delta t_2$  and  $\Delta t_3$  are measured the impact point can be determined easily within isotropic materials. Because of the anisotropic characteristic of the FRP specimen, the stiffness - and therewith the velocity - and the damping coefficient is changing with the angle. So the location of the impact is calculated recursive with the developed Finite Element Model. Finally it was investigated if any kind of damage caused by an impact leads to changes in the characteristically shape of the flexural wave. These different changes in the shape of the flexural wave can classify the nature of the damage.

### Acknowledgement

This work was supported by the German Research Foundation (DFG).

### References

1. Koenig, C.R., Mueller, D.H. et al.: *Visualization and Simulation of Flexural Wave Propagation within Fibre-Reinforced Polymers*, SEM Annual Conference, St. Louis, USA, 2006
2. Koenig, C.R., Mueller, D.H. et al.: *Fibre-reinforced Polymers under Impact load*, *Key Engeneering Materials*, vols 326-328 (2006), pp 1563 - 1568, Trans Tech Publications LTD, Switzerland, 2006.

## VISUALIZATION OF MERCURY CAVITATION BUBBLE COLLAPSE

Msatoshi Futakawa<sup>1</sup>, Takashi Naoe<sup>1</sup> and Nobuatsu Tanaka<sup>2</sup>

<sup>1</sup> Japan Atomic Energy Agency, Tokai-mura, Naka-gun, Ibaraki-ken, Japan, 319-1195

<sup>2</sup> Ibaraki Univ., Hitachi-shi, Ibaraki-ken, Japan, 316-8511  
futakawa.masatoshi@jaea.go.jp

Innovative researches will be performed at Materials & Life Science Experimental Facility in J-PARC, in which a mercury target system will be installed in an MW-class pulse spallation neutron source. Proton beams will be injected into mercury target to induce the spallation reaction. At the moment the intense proton beam hits the target, pressure waves are generated in the mercury because of the abrupt heat deposition[1]. The pressure waves interact with the target vessel leading to negative pressure that may cause cavitation along the vessel wall. Localized impacts by micro-jets and /or shock waves which are caused by cavitation bubble collapse impose pitting damage on the vessel wall. Fig. 1 shows micrographs of the pitting damage caused by mechanically creating the pressure waves in mercury. Such pitting damage is a crucial issue for high power mercury targets.

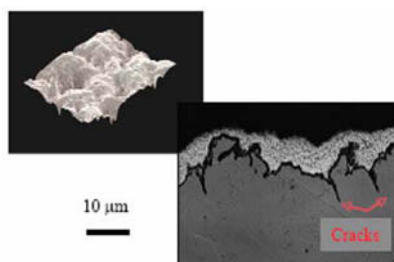


FIGURE 1. Micrographs taken by a laser microscope: The pitting damage was observed after  $10^6$  pulses whose amplitude is equivalent to the pressure pulse induced by MW-class proton beam injection. Cracks were propagated under the bottom of pits.

The visualization of mercury cavitation-bubble collapse behavior was carried out by using a high-speed video camera, and also simulated numerically (Fig. 2). In the experiment, the pressure wave was generated in mercury by using electric magnetic force instead of proton beam injection because of avoiding radiation hazard. The micro-jet and shock waves were observed clearly at the mercury micro-bubble collapse. Localized impact was quantitatively estimated through comparison between numerical simulation and experiment and the velocity was to be ca. 200m/s. The shock wave speed was confirmed to be 1480 m/s. Through the visualization and simulation on the mercury cavitation-bubble collapse behavior, the mechanism of pitting damage is discussed.

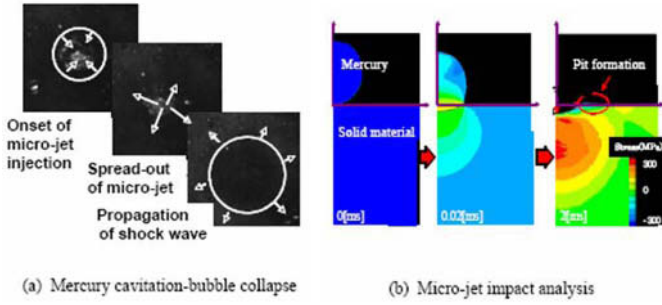


FIGURE 2. Micro-jet impact analysis with impact velocity (ca 200m/s) estimated from observing bubble collapse behavior describes well the pit formation.

## References

1. Futakawa, M., Naoe, T., Tsai, C.C., Kogawa, H., Ishikura, S., Ikeda, Y., Soyama, H., Date, H., *J. Nucl. Mat.*, vol. **343**, 70-80, 2005.



## THREE-DIMENSIONAL STRAIN FIELD IDENTIFICATION USING SPECKLE-LESS IMAGES OF X-RAY CT

Shoji Kuzukami<sup>1</sup>, Osamu Kuwazuru<sup>2</sup> and Nobuhiro Yoshikawa<sup>2</sup>

<sup>1</sup>Graduate Student, The University of Tokyo

<sup>2</sup>Institute of Industrial Science, The University of Tokyo  
4-6-1 Komaba, Meguro-ku, Tokyo, 153-8505, Japan  
kuzukami@telu.iis.u-tokyo.ac.jp

A non-invasive identification method of a three-dimensional strain field within a biological soft tissue is presented. The diagnosis by medical image data as X-ray CT has been limited within a static observation of an abnormal organ. A deformation of organ seems observable by utilizing time series of such images. The exact identification of deformation in terms of displacement and strain induces a new methodology of diagnosis with the characterization of the soft tissue in the framework of solid mechanics related with fractures. We extend the full field digital image correlation[1][2], which has been developed in the two-dimensional problems with speckled images, to full-volume one so as to identify three-dimensional displacement and strain field with speckle-less cross-sectional images of X-ray CT.

Two sets of three-dimensional image data are constituted from multiple cross-section viewings by X-ray CT operated with small intervals for the reference and deformed configurations of a body. We assume the displacement function is successfully described by tri-cubic B-spline[3] function with unknown coefficients in the identification domain. The reference image data is transformed to a virtually deformed image data by a tentative displacement field calculated from the displacement function with tentative coefficients. Under the assumption that the intensity at the same material point is identical both for the reference and deformed images, the intensity difference between the virtually and actually deformed image data is minimized through the displacement identification process by revising the coefficients.

The measurement error is easily included in X-ray CT image intensity, and it violates the hypothesis that the identical material point has the identical intensity even after deformation. The identification problem naturally becomes indeterminate in dealing with the soft tissue, where the modification of displacement field less affects the intensity difference, since large portion of the image data is speckle-less. A constraint from the viewpoint of solid mechanics is introduced to cope with the measurement error and the speckle-less image. The soft tissue is moist in general. The incompressibility constraint associated with water is plausible for the constraint imposed on the identification. The penalty function method with an adequate value of penalty coefficient is employed where an incompressibility constraint is evaluated at the sparse sample points. The modified objective function is minimized with respect to the unknown coefficients by successively solving the linearized equations constructed in line with the Levenberg-Marquardt Method[4]. A modified parallel conjugate gradient method solves the linearized equations with a high parallel efficiency.

The displacement gradient tensor is calculated straightforward as continuous polynomial functions by the identified B-spline basis displacement function. The Green-Lagrange strain field  $\mathbf{E}$  is consecutively evaluated as a continuous function from the gradient tensor.

To demonstrate the validity of the proposed method, we identify the displacement and strain fields in an experimental specimen under compressive load. Figure 1 shows the specimen by the iso-volume visualization of X-ray CT intensity, where a half of image data set is omitted to reveal

a cross section view. Figure 2 indicates the Green-Lagrange strain tensor  $E_{11}$ ,  $E_{22}$  and  $E_{33}$  for a quarter of identification domain by the iso-volume visualization.

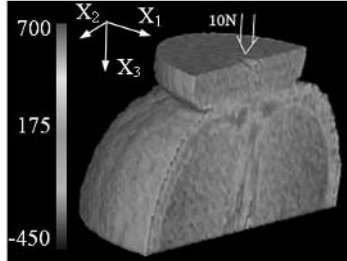


FIGURE 1. Deformed Image Data.

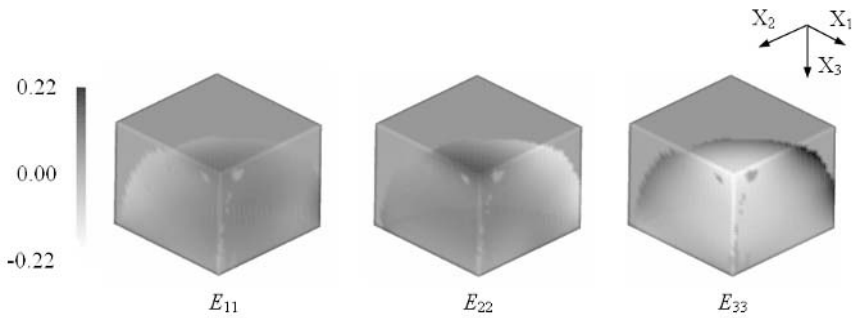


FIGURE 2. Identified Strain Field.

## References

1. Cheng, P., Sutton, M. A., Schreier, H. W. and McNeil, S. R., *Experimental Mechanics*, vol. **42**(3), 344-352, 2002.
2. Peters, W. H. and Ranson, W. F., *Optical Engineering*, vol. **21**(3), 427-431, 1981.
3. de Boor, C., *A Practical Guide to Splines*, Springer-Verlag, New York, U.S.A., 2001.
4. Press, W. H., Flannery, B. P. Teukolsky, S. A. and Vetterling, W. T., *Numerical Recipes, The Art of Scientific Computing*, Cambridge University Press, Cambridge, U.K., 1966.

## FULL-FIELD STRESS MEASUREMENT FROM STRAIN AND LOAD DATA

Giovanni B. Broggiato and Luca Cortese

University of Rome “La Sapienza” – Mechanics and Aeronautics Department

Via Eudossiana, 18 – 00184 Rome, Italy

giovanni.broggiato@uniroma1.it, luca.cortese@uniroma1.it

In experimental mechanics, the possibility of tracking on component surfaces the full-field stress and strain states during deformation, always stimulated the research and the study of new measurement techniques. This information, then, can be utilized for many purposes such as formability limits determination, quantification of stress intensification factors, material characterization and so on. Concerning the last topic, an interesting application could be a direct identification of the elasto-plastic material response up to high deformation. It is well known, in fact, that with traditional measurement devices it is possible to retrieve the true equivalent stress versus true equivalent strain data from tensile tests up to the onset of necking, where localization starts to occur. On the contrary, the acquisition of the whole local stress-strain field would allow the overcoming of this limitation.

This work aims to show how from the knowledge of a tensile test full-field strain and global data it will be possible to retrieve complete material elasto-plastic behaviour as well as the full-stress field. Nowadays many methods have been developed which successfully allow to determinate the local strain field. The one that has been mostly improved in the last few years, is based on the numerical correlation of white light speckle images [1]. With this technique, once optimised [2], is it possible to retrieve the full-field strain state during deformation with good accuracy, and almost in real-time. Fig. 1 shows the method results when applied on a tensile test on rectangular section test specimen. The snapshot refers to a post-necking moment of the test itself. Strain map is visualized.

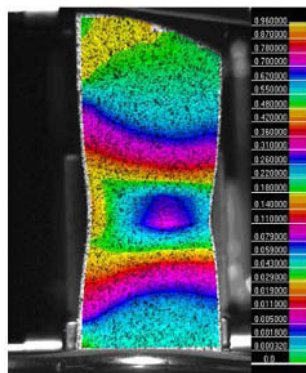


FIGURE 1 Strain field on a tensile test rectangular cross-section specimen.

Provided the true stress – true strain material response and the full-field strain evolution, the following Prandtl-Reuss’s formulas [3] describe stress-strain tensor relations, expressed in a rate form, which allow full-stress field updating:

$$\varepsilon_{kk}^{el} = \frac{\dot{\sigma}_H}{K} \quad (1)$$

$$\dot{\varepsilon}_{ij}^{pl} = \frac{3\dot{\varepsilon}_{eq}^{pl}}{2\sigma_Y^2} \sigma'_{ij} \quad (2)$$

where  $\varepsilon_{ij}^{el}$  and  $\varepsilon_{ij}^{pl}$  are the elastic and plastic strain tensors,  $\sigma_{ij}^{pl}$  the deviatoric stress tensor  $\varepsilon_{eq}^{pl}$  the equivalent plastic strain,  $\sigma_Y = \sigma_Y(\varepsilon_{eq}^{pl})$  the current yield stress,  $\sigma_H$  the hydrostatic stress and  $K$  the bulk modulus. Elastic shape change can be neglected.

This operation doesn't take much computing time so that, if strain information is available in real-time, stress determination will be in real-time as well. A further step will be undertaken. If full-strain field is acquired synchronously with global tensile load data, equivalent stress vs equivalent strain curve can be identified along with full-stress field. This curve can be expressed parametrically as a linear combination of exponential functions in the pre-necking regime:

$$\sigma_Y = \sum_{i=1}^n A_i (1 - e^{-b_i \varepsilon_{eq}^{pl}}) \quad (3)$$

The number of fitting functions  $n$  will depend on the kind of investigated material. In the post-necking regime a linear combination of a tangent and a power law extrapolation will be tried as stated in [4]:

$$\sigma_Y = \sigma_u \left[ w (1 + \varepsilon - \varepsilon_u) + (1 - w) \left( \frac{\varepsilon - \varepsilon_u}{\varepsilon_u - \varepsilon_u} \right) \right] \quad (4)$$

where  $\sigma_u$  and  $\varepsilon_u$  are relative to the onset of necking conditions. Only the additional parameter  $w$  is required. The corresponding, now parameter dependent, stress field is subsequently retrieved.

For some arbitrary specimen cross sections, then, local axial stresses are summed up to give global axial loads. An error function, intended as the difference between experimental and (parameter dependent) computed global load data can be minimized by means of an optimisation algorithm. The outcome of this procedure will be the unknown fitting parameter set. A step-by-step minimization is repeated during deformation starting from last obtained parameters so that optimisation results can be improved further on. Doing so, the material constitutive law and stress-field can be concurrently built up.

## References

1. Broggiato, G.B., In *Proceedings of ICEM12 - 12th International Conference on Experimental Mechanics*, Bari (Italy), 2004.
2. Broggiato, G.B., Cortese, L. and Santucci G., In *Proceedings of XXXV AIAS Conference (in Italian)*, 2006, Ancona (Italy).
3. Khan, A. S. and Huang, S., *Continuum Theory of Plasticity*, John Wiley & Sons, 1995.
4. Y. Ling, *AMP Journal of Technology*, vol. 5 (1996) 37-48.

## IDENTIFICATION OF ORTHOTROPIC MATERIAL BEHAVIOUR USING THE ERROR IN CONSTITUTIVE EQUATION

T. Merzouki, H. Chalal and F. Meraghni

E.N.S.A.M. Laboratoire de Physique et Mécanique des Matériaux

4 Rue Augustin Fresnel, 57078 METZ CEDEX 3, France

tarek.merzouki@metz.ensam.fr, hocine.chalal@metz.ensam.fr, fodil.meraghni@metz.ensam.fr

The aim of this work is to allow the simultaneous identification of the mechanical parameter governing an orthotropic behaviour law from one single specimen. The chosen mechanical test is a non-standard geometry used in a latest works Meuwissen *et al.* [1] as shown in Fig. 1. It was shown that this test is appropriate for giving rise to heterogeneous stress/strain fields from which the whole set of material parameters are involved. The identification procedure consists in a processing of the strain fields and minimising a cost function constructed from a fundamental variational principle, namely the error in constitutive equation proposed by Bonnet *et al.* [2]. The inverse problem is optimised using the regularised Levenberg-Marquardt algorithm. To illustrate the pertinence and the numerical stability of the procedure, the identification is performed on data provided by finite element simulations ABAQUS [3]. In this work, numerical aspects inherent to the identification procedure sensitivity in terms of accuracy and stability were investigated. A systematic error due to a shift image and white Gaussian noise (random) were added to strain values provided by FE computations to simulate an experimental errors. Only the last one is presented in this abstract. Several identifications with different guess values of the parameters are performed. Identified values are reported in table 1. For each case of the initial values, all behaviour parameters ( $Q_{ij}$ ) were identified with a high accuracy and stability even from noisy strain fields. The experimental implementation of the method is currently on-going and will be presented in the final paper.

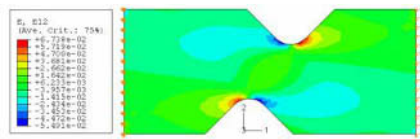


FIGURE 1. Geometry of the non-standard test used in [1]

TABLE 1. Identified stiffness from noisy strain fields.

Noise amplitude: $5 \cdot 10^{-4}$	$Q_{xx}$	$Q_{yy}$	$Q_{xy}$	$Q_{ss}$
Reference (GPa)	25.93	10.37	3.112	4.00
Test 1				
Initial values (GPa)	50.00	25.00	1.50	5.30
Identified (GPa)	25.90	10.03	3.135	3.99
Coeff. of variation (%)	0.11	0.49	0.54	0.12
Test 2				
Initial values (GPa)	12.00	7.00	4.50	2.50
Identified (GPa)	25.90	10.03	3.135	3.99
Coeff. of variation (%)	0.11	0.49	0.54	0.12
Test 3				
Guess values (GPa)	42.00	5.00	5.80	1.50
Identified (GPa)	25.90	10.03	3.135	3.99
Coeff. of variation (%)	0.11	0.49	0.54	0.12

### Reference

1. Meuwissen, M., Oomens, C., Baaijens, F., Petterson, R., and Janssen, J., *J. Mat. Pro. Tech.*, vol. **75**, 204-211, 1998
2. Bonnet, M. and Constantinescu, A., *Inverse Problem*, vol. **21**, 2005.
3. HKS Inc. *ABAQUS theory and users manuals*, version 6.5.1, 2005.

## ADJUSTMENT OF THE BOUNDARY CONDITIONS IN A FINITE ELEMENT MODEL OF A PLATE SUSPENDED WITH SPRINGS BY AN INVERSE METHOD

E. Euler  
Vrije Universiteit Brussel  
Pleinlaan 2, 1050 Brussel, Belgium  
dvhemelr@vub.ac.be

The aim of this study is to determine the material properties of composite structures in function of temperature. Identification of material properties using vibration-based mixed numerical experimental techniques [MNETs] often takes a freely suspended rectangular plate as test configuration [1]. However, in a remote-controlled furnace, contactless acoustic excitations are used and the vibration amplitude is registered contactless with a laser beam or camera. In this configuration, a plate with a free-free suspension is difficult to position in a stable way. An alternative in such cases is the suspension of the specimen using steel helical extension springs. Figure 1 shows a possible suspension configuration. The mass, stiffness and damping of the suspension springs influences the structural vibration. Material identification by using vibration-based mixed numerical experimental techniques [MNETs] can only be successfully applied if the mathematical model – which is solved using the finite element method – is appropriate [1, 2]. The mathematical model is appropriate if it represents mass, stiffness and damping properties of the physical test setup in sufficient detail.



FIGURE 1. possible suspension configuration

Consequently, relevant properties of the suspension system must be determined in order to start the material identification procedure. This paper describes an inverse method to identify the mass, stiffness and damping properties of the suspension system. This information is used to adapt the boundary conditions in the mathematical model.

The presented method can be described as follows. First the material identification procedure is applied to a plate specimen at room temperature with free – free boundary condition [1]. A mathematical model of the plate specimen is developed. The material properties in this model are the above identified material properties. The mathematical model is complemented with local mass and stiffness elements to model the suspension system. An initial value for axial spring stiffness is provided by the manufacturer of the helical extension springs. An initial mass value can be derived by reasoning. At this stage, a sensitivity analysis is carried out to verify if rigid body modes of the system can be used to identify the spring stiffness and/or mass influence. If not, helical extension springs with other properties must be used to suspend the physical plate specimen.

If correct helical springs are chosen, the translational rigid body frequency of the suspended system can be used to identify the axial spring stiffness. The rotational rigid body modes of the suspended system are used to identify the exact location of the spring elements in the mathematical model. Fig. 2 shows the experimentally measured rigid body modes of the system pictured in Fig. 1.

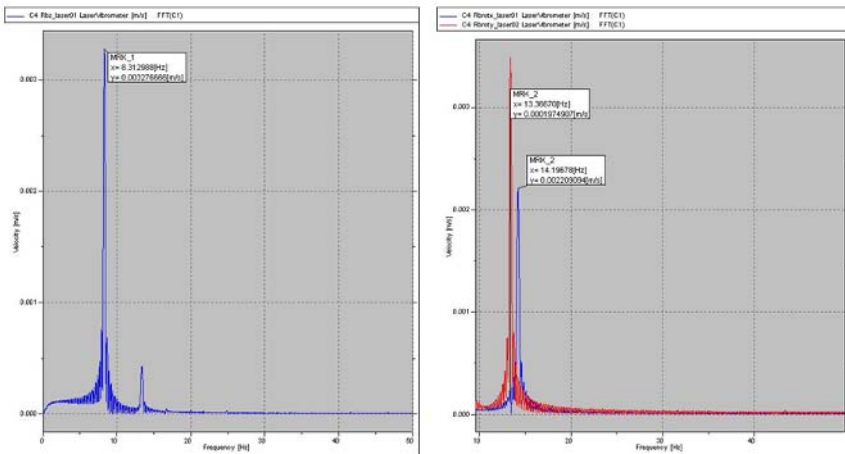


FIGURE 2. (left) translational rigid body mode of the system, (right) two rotational rigid body modes of the system

Next the relevant resonant frequencies of the suspended plate specimen are experimentally measured. These experimentally obtained values are compared with the frequencies of the mathematical model. The spring masses are modified in such a way as the difference between experimental and numerical frequencies becomes minimal. At this stage a mathematical model is obtained which reflect the vibratory behavior of the suspended plate system. It is our intent to apply the same approach to determine damping properties of the suspension system as well.

Finally, the mathematical model can be used to start an identification procedure to determine the material properties of the plate specimen in function of temperature.

**Keywords:** inverse methods, FEA, orthotropic material properties, composite materials, modal data, boundary conditions

## Reference

1. H. Sol. *Identification of anisotropic plate rigidities using free vibration data*. PhD thesis, Vrije Universiteit Brussel, Brussels, Belgium, 1986.
2. H.Sol and C.W.J. Oomens. *Material identification using mixed numerical-experimental methods*. Kluwer Academic Publishers, Kerkrade, The Netherlands, 1<sup>st</sup> edition, 1997.



## PERMEABILITY IDENTIFICATION OF A STEREO LITHOGRAPHY SPECIMEN USING AN INVERSE METHOD

Gerd Morren<sup>1</sup>, Hugo Sol<sup>1</sup>, Bart Verleye<sup>2</sup> and Stepan Lomov<sup>3</sup>

<sup>1</sup>Department of Mechanics of Material and Construction, Vrije Universiteit Brussel, Pleinlaan 2, B-1050 Brussel, Belgium

<sup>2</sup>Department of Computer Science, Katholieke Universiteit Leuven, Celestijnenlaan 200A, B-3001, Leuven, Belgium

<sup>3</sup>Department of Metallurgy and Materials Engineering, Katholieke Universiteit Leuven, Kasteelpark Arenberg 44, B-3001, Leuven, Belgium  
gmorren@vub.ac.be, hugos@vub.ac.be, Bart.Verleye@cs.kuleuven.be,  
Stepan.Lomov@mtm.kuleuven.be

The simulation of a resin flow through a porous medium by FE-models has become a very important aspect for the design of a high-performance RTM produced composite part. The key parameters to perform RTM flow simulations are the permeability values of the fibre reinforcement. The measurement of this material parameter is still not standardized and thus many different set-ups have been proposed. This paper presents an inverse method, or a so-called mixed numerical/experimental method, for the identification of the permeability values.

In this iterative inverse technique an experimental observation on a highly automated central injection rig, called “PIERS set-up” (Fig. 1) [1], is compared with a computed observation using a numerical model that simulates exactly the same experiment. In this model the permeability values will appear as parameters which will be iteratively tuned in such a way that the computed observation matches the experiment.



FIGURE 1. PIERS (Permeability Identification using Electrical Resistance Sensors) set-up.

The core of the numerical model, called RTMtimes, is based on the orthotropic radial in-plane flow model in elliptical coordinates developed by Adams et al. [2 - 4]. It was validated by comparing it with a commercial FE program (PAM-RTM [5]) that allows the flow simulation

through porous media. The small relative errors demonstrate that the analytical computation gives the same accurate results as the FE simulation, for the considered test rig.

A major problem in comparing different permeability identification methods has always been the fact that there exists no reliable reference material on which a comparative permeability measurement can be performed. Therefore, a solid epoxy test specimen (Fig. 2) that can be used as a reference sample has recently been developed by Morren et al. [6] and was produced with a stereolithography (SL) technique. Moreover, this SL specimen has a simple and geometrically correctly known unit cell, which allows a correct import of the geometry into numerical flow simulation software (such as FlowTex [7]) for the numerical prediction of the permeability.

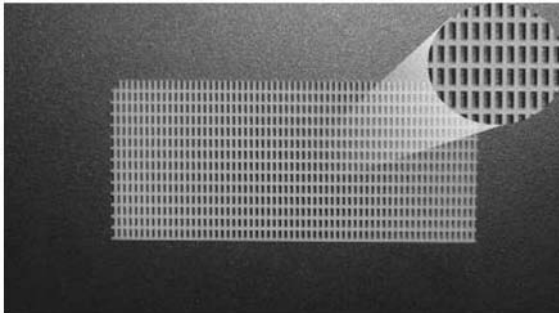


FIGURE 2. The SL specimen.

Consequently, the SL specimen allows an objective comparison of different permeability identification methods and an experimental validation of the flow simulation software.

## References

1. Hoes, K., *Development of a new sensor-based set-up for experimental permeability identification of fibrous media*, Ph.D. thesis, Department Mechanics of Materials and Constructions, Free University of Brussels, March 2003
2. Adams, K. L., Miller, B. and Rebenfeld, L., *Polymer Engineering and Science*, vol. **26**, 1434-1441, 1986
3. Adams, K. L. and Rebenfeld, L., *Textile Research Journal*, vol. **57**, p. 647-654, 1987
4. Adams, K. L., Russel, W. B. and Rebenfeld, L., *Int. J. Multiphase Flow*, vol. **14**, No.2, 203-215, 1988
5. Trochu, F., Gauvin, R. and Gao, D.M., *Advances in Polymer Technology*, vol. **12**, No. 4, 329-342, 1993
6. Morren, G. et al., *Stereolithography specimen to calibrate permeability measurements for RTM flow simulations*, accepted by *Advanced Composites Letters*
7. Verleye, B. et al., *In Proceedings of the 17th IMACS conference*, edited by Borne, P. et al., CD, Paris, 2005, pp. 1-06

## MEASURING SOFT TISSUE PROPERTIES USING DIGITAL IMAGE CORRELATION AND FINITE ELEMENT MODELLING

S.L. Evans, C.A. Holt, H. Ozturk, K. Saidi and N.G. Shrive  
School of Engineering, Cardiff University  
The Parade, Cardiff CF24 3AA, United Kingdom  
EvansSL6@cf.ac.uk

An understanding of the mechanical properties of skin and other soft tissues is valuable for many applications, for example in planning surgical procedures or in designing equipment that must interface with the body such as orthopaedic implants, seating or razors. Similarly, the ability to characterise the properties of soft tissues is valuable in many areas of medicine and biology, for example in evaluating the effects of drug treatments or the progression of a disease. However, the properties of soft tissues, and particularly those of skin, are complex and not amenable to conventional engineering analysis. The properties are highly dependent on the environment and should ideally be measured *in situ* in a living subject. Because of these two problems, conventional test methods are rarely appropriate or adequate in testing soft tissues, and new techniques are required.

The general problem in characterising the properties of a material is to find a function  $f$  which relates the stresses and strains at a point within the material:-

$$\{\sigma\} = f(\{\epsilon\}) \quad (1)$$

When testing homogenous, linearly elastic materials such as metals, the form of the function  $f$  is well known and provides a linear relationship between the stress and strain. It is then possible to separate the calculation of the applied stresses from the measurement of the resulting strains, and also to calculate properties such as the modulus from the average deformation over an area of the specimen, since the deformation may be assumed to be homogenous. When testing materials which obey more complex, as yet unknown constitutive functions, this approach is not possible. Instead it is necessary to assume an approximate form of the constitutive function  $f$ , to measure the strain under some known load, and to use a finite element model in which the various constitutive parameters are iteratively optimized until the numerical results match as closely as possible the results of the experiment. Alternatively, in some cases other numerical procedures such as the virtual fields method may be used [1], but this is difficult for soft tissues because of the very complex and highly nonlinear constitutive models that are required.

Various experimental designs have been used, such as indentation testing [2]. Typically a load is applied and the resulting displacement at the loading point is measured. This provides only a limited amount of data and it is necessary to use the whole load- displacement curve to find parameters that correctly predict the nonlinear elastic behaviour of the material. However, the acquisition of the load- displacement curve takes some time, during which some viscoelastic deformation occurs, and so it is difficult to separate the nonlinear elastic and viscoelastic behaviour of the material. Additionally, some material parameters may have little effect on the overall displacement at the load point and so cannot be accurately optimized.

The use of full field displacement measurements offers some significant advantages in this type of testing. Non- contact techniques such as digital image correlation are well suited to *in vivo* measurements in living subjects, and the measurement of the whole strain field provides a wealth of information which allows much more accurate determination of the material parameters. When the displacement at a single point is measured, it is necessary to use the whole load- displacement

curve to investigate nonlinear elastic behaviour, but if the full strain field is measured, information is available for a range of stresses and strains for a single load point. The additional information from different points on the load- displacement curve can then be used to determine the viscoelastic properties of the material.

A further advantage is that the large amount of data acquired for the full strain field allows the definition of multiple material parameter sets for different regions without using multiple tests. For example, the properties of scar tissue and the adjoining healthy tissue can be determined from a single test in which a load is applied somewhere in the general region of the scar. Conventional tensile tests would require multiple samples to be cut out from each region and tested in isolation. This has obvious applications in clinical experiments. Another advantage in the context of clinical testing is that since full field displacement data is recorded, it is not always necessary to precisely control the boundary conditions during the test. For example, a piece of skin could be tested by applying a point load, and this could be linked to a finite element model where the boundary of the region of interest was constrained by prescribed displacements derived from the experimental displacement data.

## References

1. Grediac, M., *Applied Mechanics and Materials*, vols 3-4, 9-14, 2005.
2. Lu, X. L., Miller, C., Guo, X. E. and Mow, V. C., *Journal of Biomechanics*, vol. 39, S25, 2006.

## STRAIN CHARACTERISTICS OF MATERIALS FRACTURE UNDER LOW-CYCLE PLASTIC DEFORMATION

A. Khromov, D. Fedorchenko<sup>1</sup>, E. Kocherov<sup>2</sup> and A. Bukhanko<sup>3</sup>  
 Samara State Aerospace University named after S.P. Korolyov  
 34, Moskovskoe shosse, Samara, SU-443086, Russia

<sup>1</sup> Kuznetsov Samara Research und Engineering complex

<sup>2</sup>Samara Machine – Building Design Bureau

<sup>3</sup> Institute of Machining and Metallurgy FEB RAS  
 1, Metallurgov Str., Komsomolsk-on-Amur, 681005, Russia  
 Khromov@smr.ru, Bukhanko@imim.ru

Plastic fracture of materials under quasistatic deformation processes is characterized by deformation and energy fracture criteria. At the same time such criteria are tightly bound among themselves as any process of plastic deformation is connected with energy dissipation. The basic problem will consist in separation of the deformation and energy parameters independent from each other which characterizes tendency of the material to fracture. Principles of the theory development of rigid-plastic body excluding nonuniqueness of plastic flow developed by authors are incorporated in the basis of the suggested approach. These principles are based on sequential application of nonequilibrium thermodynamics principles [1-3].

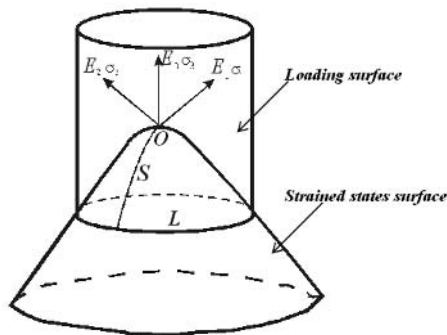


FIGURE 1. Surfaces of loading and strained states

Moreover the loading surface connected with level lines of the strained states surface (Fig. 1) is introduced on the basis of the hardening incompressible body theory.

The strained states surface in space of the principal strains of Almansi tensor  $E_{ij} = \frac{1}{2}(\delta_{ij} - x_{k,i}^0 x_{k,j}^0)$ , ( $i, j = 1, 2, 3$ ) is described by the equation

$$(1 - 2E_1)(1 - 2E_2)(1 - 2E_3) = 1 \quad (1)$$

The loading surface connected with level lines of the surface (1) is defined by the equation

$$2x^3 - 6xy^2 - 3\sqrt{2}Hx^2 - 3\sqrt{2}Hy^2 + 2\sqrt{2}H^3 - 6\sqrt{6} = 0 \quad (2)$$

where  $x = -\frac{1}{\sqrt{2}h'}(\sigma_1 - \sigma_2)$ ,  $y = -\frac{1}{\sqrt{3}}x - \frac{2}{\sqrt{6}h'}(\sigma_2 - \sigma_3)$ ,  $H = -\frac{2}{\sqrt{3}}(E_1 + E_2 + E_3) + \sqrt{3}$ ,  $h'$  is defined for the concrete structural material by the hardening curve received on the basis of uniaxial stress-strain test of the material.

The given loading surface at small deformations coincides with the Mises plasticity condition. The fracture condition is defined by line  $L$  on the strained states surface (1)

$$L: \begin{cases} E_1 + E_2 + E_3 = h(D) \\ (1 - 2E_1)(1 - 2E_2)(1 - 2E_3) = 1 \end{cases} \quad (3)$$

It is postulated: *the material fracture occurs if deformation process (line  $S$ ) intersects line  $L$ .*

Line  $L$  possesses the following properties:

- under any simple deformation process (principal directions of velocity strain tensor and stress tensor coincide) under deformation it is observed same energy dissipation  $D_0$  from strainless state (point ) before intersection line  $L$ ;
- under other deformation process for achievement of line  $L$  it is required greater energy dissipation  $D_1$  ( $D_1 > D_0$ ).

Initial position of line  $L$  is defined from fracture experiment under single simple deformation (for example, uniaxial fracture of the cylindrical sample).

Under complicated deformation processes line  $L$  approaches to strainless state (point ) according to function  $h(D)$  from (3) which should be defined experimentally. For example, from experiments about cyclic plastic deformations with the subsequent finishing the sample before fracture

## References

1. Kozlova, O.V., and Khromov, A.I., *Doklady Physics.*, vol. **47**, No. 7, 548-551, 2002.
2. Khromov, A.I., Bukhanko, A.A. and Stepanov, S.L., *Doklady Physics.*, vol. **51**, No. 4, 223-226, 2006.
3. Khromov, A.I., Bukhanko, A.A., Kozlova, O.V., and Stepanov, S.L., *J. Applied Mechanics and Technical Physics.*, vol. **47**, No. 2, 274-281, 2006.

## FORMABILITY ANALYSIS OF MAGNESIUM ALLOY AT ELEVATED TEMPERATURE WITH EXPERIMENTAL AND NUMERICAL METHOD

Lin Wang<sup>1</sup>, L.C. Chan<sup>2</sup> and T.C. Lee<sup>3</sup>

Department of Industrial System Engineering, The Hong Kong Polytechnic University  
Hong Kong

mflwang@inet.polyu.edu.hk<sup>1</sup>, mftclee@inet.polyu.edu.hk<sup>2</sup>, mflcchan@inet.polyu.edu.hk<sup>3</sup>

Magnesium alloys (such as ASTM-AZ31, ASTM-AZ60, ASTM-AZ61, ASTM-AZ91 etc.), have been readily adopted in the manufacturing industry for their light weight, highly specific strength and stiffness, good damping characteristics, excellent machinability, and castability. The adoption of magnesium alloy sheets has been driven primarily by the automotive industry in an effort to increase vehicle fuel efficiency. Weight reduction of vehicles is one of the major means available to improve automotive fuel efficiency. Magnesium alloys are lighter than aluminum alloys and have a greater tensile strength than steels. More recently, portable electronic appliance manufacturers have shown strong interest in implementing press-formed magnesium alloy sheet metal parts into their products [1].

However, the low ductility resulting from the hexagonal close-packed microstructure of most magnesium alloys suffocates their applications in the sheet metal forming operation. In order to achieve an optimal property of magnesium alloys for sheet forming, an intensive study of complicated isothermal treatment has to be carried out. At the elevated temperatures, the material ductility has a great improvement represented by the raised uniaxial tensile curves and Forming Limiting Curves (FLC). Standard test method (ASTM E2218) is adopted for determining FLC of Magnesium alloy sheets AZ31 at temperature 200°C, 250°C and 300°C. A closed loop temperature control system is tailor made for this forming test. The various widths specimens with laser marked grids are suitable for determining FLC curves at high temperatures. Experimental FLCs are delineated in the principle strain space. The lowest point of FLC, which strain ratio is zero, increases with the temperature. Tensile testing at different elevated temperatures is also compared when rolling direction is considered. The rolling direction has a great impact on the tensile curve which indicates a strong material anisotropy.

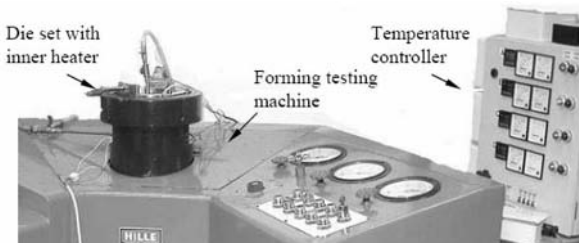


FIGURE 1. Hille forming testing machine with closed loop temperature controller.

On the other hand, numerical analysis is another effective tool that can be used to construct the FLC. Therefore, Swift model and Vertex theory are put into use individually to predict the Forming Limiting Diagram (FLD). Swift model and vertex theory with different yield criteria, e.g.

Hill 48 [2], and Hill 90 [3], are developed and proposed to compare with experimental result. Therefore, a more suitable theoretical FLC is constructed for the magnesium alloy sheet at an elevated temperature.

Limit strains are calculated at different strain ratios by Swift model and Hill 48 yield criterion.

$$\begin{aligned}\varepsilon_1^* &= \frac{(1+r_0-r_0\alpha) \cdot [1+r_0+\alpha^2 \cdot (r_0/r_{90})(1+r_{90})-2\alpha r_0]}{(1+r_0-r_0\alpha)^2 + \alpha \cdot (\alpha \frac{r_0(1+r_{90})}{r_{90}} - r_0)^2} * n \\ \varepsilon_2^* &= \frac{(1+r_0-r_0\alpha) \cdot [\alpha + \alpha r_0 - \alpha^2 r_0 + \alpha \cdot (r_0/r_{90})(1+r_{90}) - r_0]}{(1+r_0-r_0\alpha)^2 + \alpha \cdot (\alpha \frac{r_0(1+r_{90})}{r_{90}} - r_0)^2} * n\end{aligned}\quad (1)$$

In this paper, a novel testing method for FLC of magnesium alloy sheets at elevated temperatures is proposed. The experimental result reveals the great impact of temperature on this material. The isothermal forming process should be developed indispensably due to the greatly improvement of ductility at a high temperature.

The numerical calculated FLCs vary with the use of yield criterion. Swift model is limited to the right side of FLD, while Vertex theory can cover both sides. Vertex theory accompanying with Hill 90 and Hill 93 yield criteria is more accordant with the experimental result.

## References

1. Kainer, K. U., *Magnesium alloys and technologies*, Geesthacht : Wiley-VCH, 2003.
2. Hill, R., *A theory of the yielding and plastic flow of anisotropic metals*. In *Proceeding of Royal Social London A*, 1948, 281-297
3. Hill, R., *J. Mech. Phys. Solids*, vol. **38**, 405-417, 1990.
4. Swift, H.W., *J. Mech. Phys. Solids*, vol. **1**, 1-16, 1952.
5. Stören, S. and Rice, J.R., *J. Mech. Phys. Solids*, , vol. **23**, 421-441, 1975.



## FEM ANALYSIS OF THE CREEP BEHAVIOUR OF STEEL PIPES UNDER THERMAL GRADIENTS

F. Vakili-Tahami, F. Talati, A.H. Sorkhabi\* and O. Arashnia  
 Department of Mechanical Engineering, University of Tabriz, Iran  
 \*Amirsorkhabi@gmail.com

In this paper the creep behaviour of ex-service 21/4Cr 1Mo steel pipes carrying super-heat steam has been studied at the presence of through-wall temperature gradient. The creep behaviour of the pipe has been studied at steady state using uncoupled thermo-mechanical Finite Element method; and, the results have been obtained in two different categories: one with constant pipe-wall temperature which is the average temperature; and, the other at the presence of through-wall temperature gradient. Then the results have been compared and it has been shown that the existing thermal stresses caused by through-wall temperature gradient combined with the mechanical stresses due to the internal pressure have significant effect on the creep behaviour of the pipe. In addition, the exponential dependence of the creep strain rate to temperature also plays a major role in this case. It has been shown that the creep analysis at constant-temperature to study the behaviour of the pressure vessels or pipes will produce erroneous results and to predict their actual behaviour accurately, it is strongly recommended to take into account the effect of the through-wall temperature gradient.

### Method

In this study a 21/4Cr 1Mo steel pipe with the inner diameter of 50 mm and 25 mm wall thickness has been selected which carries super-heat steam with at 550°C at 9 MPa. The Fourier's thermal conductivity and heat flux equations which are in the form of axi-symmetric partial differential equations have solved using FEM method to obtain the through-wall temperature distribution. These data have been used as input data to carry out the thermo-mechanical analysis to calculate the initial thermal stresses; and then, the creep strain and stress redistribution have been calculated using Norton power-law. The most common relationship which describes the uni-axial creep strain rate,  $\dot{\epsilon}$ , as a function of stress,  $\sigma$ , absolute temperature,  $T$ , and time,  $t$ , is:

$$\dot{\epsilon} = M \sigma^n \exp(-Q/\mathfrak{R}T) t^m \quad (1)$$

where  $M$ ,  $n$ ,  $Q$  and  $m$  are material dependent parameters and  $\mathfrak{R}$  is universal gas constant. The values of stress exponent,  $n$ , and the activation energy,  $Q$ , are sensitive to the dominant creep mechanism. The procedure to generalise the uni-axial creep behaviour to multi-axial state has been formulated by Odqvist. The multi-axial creep strain rates can be written in terms of the stress deviator tensor,  $s_{ij}$  ( $=\sigma_{ij}-1/3\sigma_{kk}\delta_{ij}$ ), as follows:

$$\dot{\epsilon}_{ij} = \frac{3}{2} \frac{s_{ij}}{\sigma_e} \dot{\epsilon}_e \quad (2)$$

where  $\sigma_e$  ( $=\sqrt{3s_{ij}s_{ij}/2}$ ); and,  $\dot{\epsilon}_e$  ( $=\sqrt{2\dot{\epsilon}_{ij}\dot{\epsilon}_{ij}/3}$ ) are effective stress and effective creep strain rate respectively. The effective strain rate,  $\dot{\epsilon}_e$ , can be obtained by the extension of equation (1) to the multi-axial stress-state:

$$\dot{\epsilon}_e = K \sigma_e^n t^m \quad (3)$$

Substitution of equation (3) into equation (2) gives the generalised form of the power law formulation for the multi-axial stress-state:

$$\dot{\varepsilon}_{ij} = \frac{3}{2} K \sigma_e^{n-1} s_{ij} t^m \exp(-Q/\Re T) \quad (4)$$

## Conclusion

The redistribution of stresses due to creep in a super-heat steam steel pipe at the presence of the through-wall temperature gradient was modelled and compared to the results predicted at the constant temperature. The cases modelled included thermal variation across the wall of the pipe. It has been shown that the stress evolution obtained in these two cases are different; and, more complex interactions were noted as a result of coupled thermal variation of creep rates and thermally induced stresses.

The results also show that the effect of thermal gradient on thick walled pressure vessels or pipes is significant. In industrial applications such as power plants or petro-chemical processing systems, high thermal gradients exist even in steady-state operations; and, therefore, thermally induced stresses exist in addition to the mechanical stresses due to the internal pressure. The creep response of the pipe-wall depends on the local stress, temperature, and previous creep history. The combination of the altered initial stress-state due to the thermal stresses and the altered creep response caused by through-wall temperature gradient leads to different pattern of stress redistribution and creep strain rate through time.

## Some of the References

1. Timoshenko, S., Goodier, J., Theory of Elasticity. New York: McGraw Hill; 1951. p. 413.
2. Evans, R., Wilshire, B., Creep of Metals and Alloys. London: Institute of Metals; 1985.
3. Parker, J., Prediction of Creep Deformation and Failure for 1/2Cr-1/4V and 2-1/4Cr-1Mo Steels. ASME J Pressure Vessel Technol 1985;107:279-84.
4. Snowden, K., Merhtens, E., Analysis of Creep Data for Remaining Life Estimation. Proceeding of the Remaining Life Assessment on High Temperature Plant in Australia, Lucas Heights; 1990.
5. Law, M. , Payten, W., Snowden, K., Modelling Creep of Pressure Vessels with Thermal Gradients Using Theta Projection Data, International Journal of Pressure Vessels and Piping 79 ;2002. 847-851.
6. Vakili-Tahami, F., Hayhurst, D. R. , Prediction of Creep Damage Evolution in Pressurised Welded Ferritic Steel Pipework Made Using DAMAGE XX, Internal Research Report DMM.01, Dept. Mech. Aerospace and Manufacturing Engineering, UMIST,2001.
7. Vakili-Tahami, F., Hayhurst, D. R and Wong, M.T., High-Temperature Creep Rupture of Low Alloy Ferritic Steel Butt-Welded Pipes Subjected to Combined Internal Pressure and End Loadings, Phil. Trans. R. Soc. A; 2005; 363, 2629-2661.
8. Vakili-Tahami , F., Hasanifard, S., The Temperature Gradient Effect on The Creep Behaviour of Structures, 16th European Conference of Fracture, Alexandroupolis, Greece, 2006.

## DEVELOPMENT OF THE ADVANCED MOIRÉ METHODS WITH HIGH RESOLUTION MICROSCOPY AT FML

Huimin Xie<sup>1</sup>, Satoshi Kishimoto<sup>2</sup>, Yanjie Li<sup>1</sup>, Bing Pan<sup>1</sup>, Zhanwei Liu<sup>3</sup>, Haixia Shang<sup>1</sup>  
and Fulong Dai<sup>1</sup>

<sup>1</sup>FML, Dept of Engineering Mechanics, Tsinghua University Beijing China 100084

<sup>2</sup>National Institute for Materials Science, Tsukuba 305-0047, Japan

<sup>3</sup>Department of Mechanics, School of Science, Beijing Institute of Technology,  
Beijing, 100081, China

xiehm@mail.tsinghua.edu.cn

The mechanical behaviours of engineering materials in micro/nanoscale range have aroused general concern in recent years. To understand the rule of these behaviours, the experimental technique with high sensitivity and spatial resolution are required. However, most of the existing methods cannot meet such requirements.

Some novel micro/nano-moiré methods have been developed recently at failure mechanics lab. (FML), Tsinghua University, China. This paper offers an introduction of these new methods, which can be realized under the focus ion beam (FIB), atomic force microscope (AFM), scanning tunnelling microscope (STM), laser scanning confocal microscope (LSCM) as well as the transmission electron microscope (TEM). These micro/nano-moiré methods are able to offer quantitative analysis to micro/nano-deformation of the sample surface. The measurement principles and experimental techniques of these methods are described in detail. Some applications of these methods are given. The successful experimental results demonstrate the feasibility of these methods and also verify that the methods can offer a high sensitivity for displacement measurement with micro/nano-meter spatial resolution, and it will find a wide application in micro/nano-mechanics research.

In the AFM nano-moiré measurement, the moiré patterns are formed by interfering between the probe scanning line of AFM and the specimen grating.

Suppose the spatial frequency of the atomic lattice of the standard specimen in the  $y$  direction is  $f_s$ , i.e. the specimen grating pitch is  $p_s$ . The frequency of the master grating  $f_m$  can be defined as

$$f_m = \frac{1}{p_m} = \frac{N}{L} \quad (1)$$

where  $N$  is the number of scanning lines and  $L$  is the length of scanning area.

When there are  $x$  orders of moiré fringes in scanning area ( $x$  is integer, and  $x \geq 2$ ), the scanning area length can be decided as:

$$L = p_s [N \pm (x - 1)] \quad (2)$$

The real displacement and normal strain incurred by the load in the  $y$ -axis direction can be calculated:

$$v_y = v_y^1 - v_y^0 = (X' - X)p_s \quad (3)$$

$$\varepsilon_y = \varepsilon_y^1 - \varepsilon_y^0 = \frac{P_s}{s^1} - \frac{P_s}{s_0} \quad (4)$$

Where  $X'$  and  $X$  are the order of moiré pattern before and after the deformation,  $s^1$  and  $s_0$  are the spacing between two adjacent moiré fringes before and after the deformation.

A regular lattice of mica is captured by AFM and shown in Fig. 1.

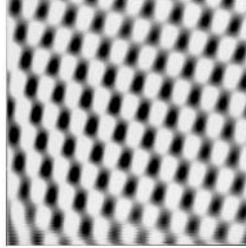


FIGURE 1. Lattice of Mica (4nm × 4nm)

Moiré fringes can be used to find microscopic defects of crystal lattices, dislocation, bond failure, and stack faults, which are very important in nano-mechanics and material science. Twin crystal structure can also be found using moiré fringe. Fig. 2 illustrates the AFM nano-moiré pattern formed by lattice of mica near twin crystal and scanning lines of AFM with parameters at  $N=128L=79nm$ .

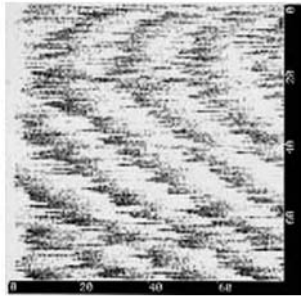


FIGURE 2. Fringe pattern near twin crystal

## References

1. Kishimoto S, Egashira M, Shinya N, *Opt. Eng.*, vol. **32**, 522-526, 1993
2. Dai FL, Xing YM, *ACTA MECHANICA SINICA*, vol. **15**, 283-288, 1999
3. Xie HM, Kishimoto S, Asundi A, Chai GB and Norio SY, *Nanotechnology*, vol. **1**, 24-29, 2001

## IN-SITU NON-DESTRUCTIVE EVALUATION OF CONCRETE STRUCTURES USING SHEAROGRAPHY

Y.Y. Hung, L. Liu, Y.H. Huang<sup>1</sup> and Edward C.Y. Yiu  
Department of MEEM, City University of Hong Kong, Hong Kong  
<sup>1</sup>50008128@student.cityu.edu.hk

Building and construction is important industry concerning life safety. Contrary to its importance, the testing techniques used in this industry are relatively out-of-date. For example, the accessing of strength of aged concrete still relied heavily on the traditional core test, which is laborious, time consuming and destructive. Convenient non-destructive testing methods including rebound hammer, ultrasonic pulse velocity and pull-out test have been proposed for decades but not yet used widely due to the low reliability of these techniques. With more and more buildings in the world are aging, the need for aged building evaluation has come to an unprecedented level.

Optical techniques such as shearography, digital image correlation, moiré, holography, and fringe projection have gained rapid recognition in this few decades. The main advantages of these techniques lie in being full-field, non-destructive, and non-radioactive. During testing, data acquisition, retrieval, analysis and interpretation can be achieved extremely fast with digital image processing techniques. Moreover, the invention of optical fibre for light transmission allows inspection of areas non-accessible by conventional methods, further making optical techniques more flexible for industrial applications.

Holography and high sensitivity moiré have been applied to concrete structures assessing; however, a main limitation of these techniques is their stringent requirement for environmental stability (e.g., test sample, substrate vibration and air fluctuation) during testing. Shearography, which had been invented by the first author of this paper, overcomes this problem and has been adopted for aircraft tire inspection as well as in various industrial sectors for in-situ inspection. Shearography is also a technique that yields direct strain- or surface slope- related results, making it an excellent tool for full-field flaw detection and stress/strain measurements.

Digital image correlation is another optical technique which requires less stability (since it is not a laser interferometry technique) and has great potential for use in industrial environment. This technique utilizes the object surface feature as an information carrier and cross-correlates two images captured before and after a deformation to obtain a full-field deformation of the object under testing. In the last two decades, digital image correlation has been applied to many fields in experimental mechanics.

In this study, we explore the feasibility of using optical techniques for concrete properties evaluation. To obtain the concrete elasticity modulus, digital image correlation is used as an optical strain gauge. When a concrete sample is loading, the concrete strain is obtained by digital image correlation in real-time and the stress-strain curve is plotted. The concrete elasticity modulus is then determined from the curve. This optical strain gauge has several advantages over traditional mechanical or electronic strain gauge including being ultra fast, simple setup, non-contact and no laborious sensor adhesion. Furthermore, the optical setup is adaptive for testing of various sample sizes without change the measurement unit. Experiments conducted confirm that the method is reliable and accurate.

Another important problem is in-situ determination of concrete elasticity modulus since core testing is always a damage to the concrete structure and time consuming. With this aim, laser shearography is explored to measure the concrete deformation in the field environment when

loading in the direction normal to the concrete surface. The deformation magnitude is related to the concrete elasticity modulus, Poisson's rate and the loading force, thus by measuring the deformation and the loading force, the concrete elasticity modulus is readily determined. Concrete yield strength is also determined by an in-situ micro-damage impact experiment. By using a hammer or a metal ball to impinge the concrete surface, the surface undergoes a small permanent deformation which is related to the concrete yield strength. Again shearography and digital image correlation are used to determine this permanent deformation and the yield strength is determined.

**Key words:** shearography, digital image correlation, laser interferometry, concrete inspection, elasticity modulus, yield strength, in-situ measurement

## MEASUREMENT OF THERMAL STRESS IN COB PACKAGING STRUCTURES

Xiao-Yuan He and Fanxiu Chen

Department of Engineering Mechanics, Southeast University,

Si Pai Lou 2#, Nanjing JS 210096, P.R.China

Key Laboratory of MEMS of Ministry of Education, Southeast University,

Si Pai Lou 2#, Nanjing JS 210096, P.R.China

mmhxy@seu.edu.cn, cfxcfx@seu.edu.cn

Packaging techniques is widely used in micro electro mechanical systems (MEMS). But it produce a set of failure modes due to the mechanical nature of MEMS. Although the challenges of MEMS packaging has been known for some time, little published research has been achieved to compile data and work towards meeting these challenges. Experimental data for sensors, which exploit piezoresistivity, shows that packaging affects the output of the device<sup>[1]</sup>. It is therefore important to investigate the stresses arising from the packaging process.

In the modern optical metrology, a variety of techniques have been applied to the deformation measurement due to the advantages of automatic, non-contact, full field and real time. The digital speckle correlation method, introduced by Peters and Ranson<sup>[2]</sup>, has found valuable and widespread use in many research and engineering applications<sup>[3-5]</sup>. In this paper, digital speckle correlation method is used to measure the thermomechanical coupling effect in COB packaging structures<sup>[6-7]</sup>. The correlation function used in this paper is defined as below and the setup of experiment is shown in Fig. 1.

$$c = \frac{\sum \sum [f(x, y) - \bar{f}] * [g(x + u, y + v) - \bar{g}]}{\left\{ \sum [f(x, y) - \bar{f}]^2 * \sum [g(x + u, y + v) - \bar{g}]^2 \right\}^{1/2}} \quad (1)$$

The CCD camera is applied to capture the speckle patterns of CMOS chip when the application of the temperature field is changed. Analyzing the speckle patterns by using the DSCM, the in-plane deformation of the CMOS chip is obtained. And based on the trigonometrical theory, the out-plane displacement can be obtained. Then the elasticity thermal stress of the chip is evaluated when the application of the temperature field is repeated.

In this paper, finite element analysis(FEA) is used to estimate the packaging stress that occurs at different temperature field. And the results from the FEA showed agreement with the experiment data. And they are both agree well with the theoretical results. The experiment results are proved that DSCM can successfully be applied to the analysis of the thermomechanical coupling effect. The experiment results provide a availability consult to the design of MEMS apparatus.

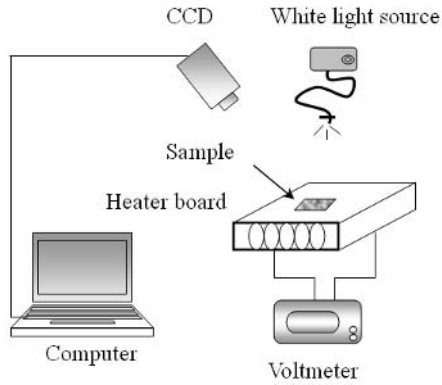


FIGURE 1. Experimental setup

## References

1. Nysaether JB, Larsen A, Liverod B, *et al. Micromech Microeng*, vol. **8**, 168-171,1998.
2. Peter W H, Ranson W F. *Opt Eng*, vol. **21**, 427-431, 1982.
3. Dongsheng Zhang. *Journal of Biomedical Optics*, vol. **9**, 691-699, 2004.
4. Wang Yu; Cuitiño, Alberto M. *International Journal of Solids and Structures*, vol. **39**, 3777-3796, 2002.
5. Jun Zhang, Guanchang Jin, Shaopeng Ma, *et al. Optics & Laser Technology*, vol. **35**, 533-542, 2003.
6. Wen Yujun, Basaran Cemal. *Mechanics of Materials*, vol. **36**, 369-385, 2004.
7. Tsai Ming-Yi, *et al. Electronics Packaging Manufacturing*, vol. **28**, 328-337, 2005.



## SURFACE ROUGHNESS MEASUREMENT OF A SEMI-CONDUCTOR WAFER USING LASER SCATTERING TECHNIQUE

C.J. Tay, S.H. Wang and C. Quan

Department of Mechanical Engineering, National University of Singapore  
9 Engineering Drive 1, Singapore 117576  
mpetaycj@nus.edu.sg

Light scattering is a non-contact technique which can be used for characterizing the topography of smooth reflecting surfaces. A technique which incorporates an integrated laser scattering model for surface roughness measurement of a semi-conductor wafer has been developed. The technique employs a He-Ne laser and incorporates various optical components (Fig. 1) to record surface roughness in the nanometer range with a high degree of accuracy. Theory of the technique and the experimental program are described. The results obtained show excellent agreement with method using the atomic force microscope with only minor discrepancy. This is a significant improvement over the conventional stylus methods. In addition, unlike previous laser scattering method which uses a spherical arrangement to record diffused light, the proposed technique detects reflected light normal to the test surface and hence resulting in a simpler and more stable optical arrangement. Using the proposed optical arrangement, accurate and repeatable measurement of a semi-conductor wafer roughness of in the nanometer range can be readily obtained.

**Keywords:** surface roughness, light scattering, non-contact measurement, integrated laser scattering.

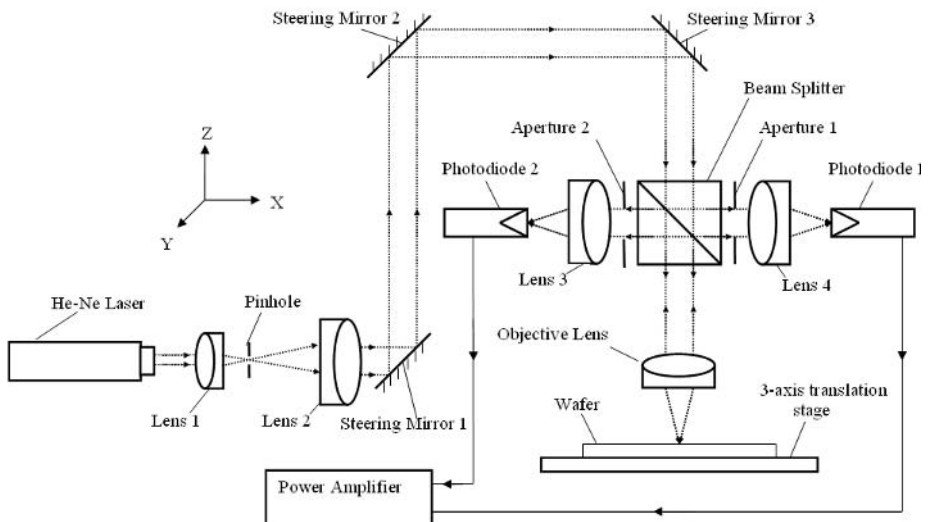


FIGURE 1.

## A 20 KILOHERTZ OPTICAL STRAIN GAGE

W. N. Sharpe, Jr.  
 Department of Mechanical Engineering  
 Johns Hopkins University  
 Baltimore, Maryland, 21218, USA  
 sharpe@jhu.edu

The endurance limit for steels is traditionally taken at one million cycles, but modern machinery such as gas turbines and high-speed train wheels can expect lifetimes of one billion cycles or more. Further, microdevices such as digital light projection mirrors and RF switches operate at high frequencies and last for long times. It is possible, in both cases, to cycle test specimens at 20 KHz and produce one billion cycles in 14 hours or so. However, force and strain measurement are difficult.

Research at the University of Michigan uses an ultrasonic generator coupled to a variable cross-section 'horn' with a test specimen at the end, which is excited to resonance at 20 KHz. The specimen has an hourglass shape, and the vibrating system produces a node and maximum strain at its center. The specimen can be heated to 1000°C by an RF coil around it. The specimen initially has two foil strain gages mounted on it, and these are used to correlate strain with power levels of the ultrasonic generator at low strains. Tests are run at higher power levels, but the strain gages do not survive. There is a need for an accurate strain measurement, and DARPA (Defense Advanced Research Projects Agency) has sponsored the development of an optical system at Johns Hopkins to be installed on the Michigan test machine.

Strain measurement by laser-based interferometry was introduced by the author almost 40 years ago [1] and has been used for various studies requiring a short gage length. Two tiny reflective markers are placed on a specimen to serve as gage points. These can be lines applied via photolithography or Vickers microhardness indentations. When they are illuminated with a laser, the light diffracts from each one and overlaps to produce fringe patterns. As the markers move due to strain, the fringes move proportionally. The phenomenon is simply Young's two-slit interference experiment, but in reflection. Fringe motion can be recorded with photodiode arrays to provide real-time direct strain values for quasistatic testing; procedures are described in Sharpe [2]. In that case, the positions of the fringe minimums on the arrays are tracked and converted to strain. The equation relating strain to fringe movement is

$$\varepsilon = \Delta m \lambda / d_0 \sin \alpha_0 \quad (1)$$

where the distance between the markers is  $d_0$ , the laser wavelength is  $\lambda$ ,  $\alpha_0$  is the angle between the incident laser beam and the diode array, and  $\Delta m$  is the relative fringe shift.

The photodiode arrays are much too slow for dynamic measurement, but the intensity of a fringe pattern can be measured at high frequencies. The intensity of an interference fringe pattern,  $I$ , is

$$I = I_0 \cos^2 (\pi d \sin \alpha / \lambda) \quad (2)$$

where  $I_0$  is the maximum intensity, which is taken as constant here – in reality it varies because of the diffraction. The equation can be rewritten as

$$I = I_0 \cos^2 (Kd) \quad (3)$$

with  $K$  as a constant. It can then be inverted to relate strain to the change in measured intensity  $\Delta I$  as

$$\varepsilon = \cos^{-1}(\Delta I/I_0)^{1/2} / K d_0 \quad (4)$$

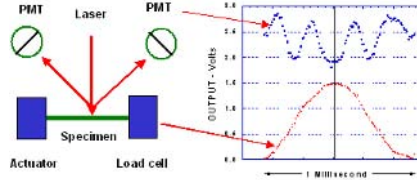


FIGURE 1. Schematic of the dynamic setup with fringe and load signals.

For dynamic strain measurement, the photodiodes are replaced with photomultiplier tubes (PMT) covered with a slit that is narrower than the spacing between fringes. The setup is shown schematically in Fig. 1 from Sharpe and Bagdahn [3] for cyclic loading where the force signal and one intensity signal are plotted. The fringe signal is a mirror image about the peak load.

The arrangement for 20 KHz testing uses two photomultiplier tubes, a 20-mw diode laser, and a data acquisition board sampling at 20 MHz on each of four channels. A program in Agilent VEE takes 200 data points from the two PMTs over a 50 microsecond period and converts them into strain. Acquisition, computation, storage, and display take less than one second. The system is set up to take measurements periodically; it is not practical to record and store each cycle. Details of the experimental setup as well as calibration and test results will be presented.

## References

1. Sharpe, W. N., Jr., *Exp. Mech.*, vol. **8**, 164-170, 1968.
2. Sharpe, W. N., Jr., NASA Technical Memorandum 101638, 1989.
3. Sharpe, W. N., Jr. and Bagdahn, J., *FATIGUE 2002 – Proceedings of the Eighth International Fatigue Congress*, Stockholm, 2002, 2197-2212.

## AN APPLICATION OF MICROSCOPIC DIGITAL IMAGE CORRELATION TO DENTAL MATERIALS

Dongsheng Zhang, Miao Luo, Dwayne Arola and Ahmad Nazari

Department of Mechanics, Shanghai University,  
Shanghai, 200444, PR China

Department of Mechanical Engineering, University of Maryland Baltimore County,  
Baltimore, MD 21250, U.S.A.

donzhang@staff.shu.edu.cn, luomiao82@hotmail.com, darola@umbc.edu, anazari1@umbc.edu

The mechanical properties of the human tooth have been of interest for many decades. While the strength and elastic modulus of these tissues have been examined in detail, comparatively few studies have been carried out on their fatigue and fracture behavior due to limitations posed by the small volume of available tissue, and consequent difficulties in applying standardized techniques to potentially hydrated and very small specimens. Although indentation fracture test eliminates the size constraints, a recent review has addressed the shortcomings of indentation fracture tests, particularly in regards to the load dependence. In this paper, fracture behavior of human dentin is studied by means of stable crack growth. Miniature compact tension (CT) specimens were machined from human teeth, as shown in Fig. 1. A portable motorized loading frame combined with a microscopic imaging system has been developed to document load and displacement field while the specimen is stressed, as shown in Fig. 2. Digital Image Correlation (DIC) was adopted to examine the mechanisms of crack growth resistance and near-tip displacement distribution for cracks in human dentin that are subjected to opening mode loads. According to the unique geometry of the dentin CT specimen (Fig. 1), the stress intensity distribution with crack growth could not be estimated using relationships provided by ASTM standards E399 or E647. Therefore, numerical models were developed to determine the stress intensity distribution as a function of crack length, opening load and specimen geometry. The distribution in  $K_I$  with crack extension for the CT specimens as described in Figure 2(a) is given by

$$K_I = \frac{P}{B^* \sqrt{W}} \left( \frac{B^* + 1}{B + 1} \right)^{\frac{1}{2}} (0.131 + 0.320 \alpha + 0.211 \alpha^2) \quad [\text{MPa}\cdot\text{m}^{0.5}] \quad (1.4 \leq a \leq 3.0)$$

where  $P$  is the opening load (in Newtons),  $\alpha$  is the ratio of  $a$  to  $W$  (Fig. 1) and the quantities  $B^*$  and  $B$  are the ligament thickness and nominal specimen thickness, respectively. Examples of specimens chosen from two different age groups (18age35 and age50) are given. The crack opening displacement (COD) curves are resulted from analyzing the displacement field of CT specimen under tension (Fig. 3 and Fig. 4)), and tendency of crack growth resistance curves ( $R$ -curves) are estimated from identifying the location of the crack tip and the equation presented above. By combining the benefits of microscopic DIC with unique approaches for preparing and loading specimens, a detailed and reliable understanding of dentin fracture is possible.

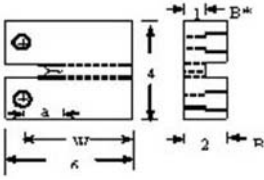


FIGURE 1. CT specimen



FIGURE 2. test system

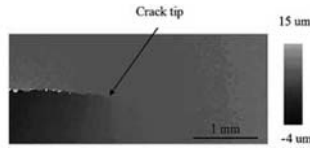


FIGURE 3. displacement field near the crack tip

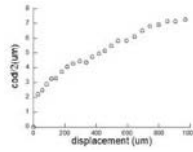


FIGURE 4. COD profile at crack tip

**References**

1. Quinn G.D., in Proceedings of the 30th International Conference on Advanced Ceramics and Composites, Cocoa Beach FL, January, 2006.
2. Zhang D, Luo M, and Arola D., Opt Eng. 2006, vol. **45**(3): 033605(1-9).
3. Zhang D and Arola D., J Biomed Opt. 2004, vol. **9**(4): 691-699.

## ACTIVE INTERFEROMETRIC SYSTEM FOR MEMS/MOEMS MEASUREMENT

Jacek Kacperski and Malgorzata Kujawinska  
Institute of Micromechanics and Photonics, Warsaw Univ. of Technology,  
8 Sw. A. Boboli St., 02-525 Warsaw, Poland  
j.kacperski@mchtr.pw.edu.pl, m.kujawinska@mchtr.pw.edu.pl

Micro-Electro-Mechanical Systems are nowadays frequently used in many fields of industry. The number of their applications increases and their functions became more responsible. Therefore precise knowledge about their static (shape, deformations, stresses) and dynamic (resonance frequencies, amplitude and phase of vibration) properties is necessary. Reliability or fatigue tests or other long term examinations are also becomes important in point of view their applications and the economic reasons. Due to fragility of MEMS parts and small sizes non-contact and high sensitive measurement method is required. Two-beam laser interferometry is one of the most popular testing methods of microelements. Such method implemented in Twyman-Green interferometer allows for full-field shape determination and out-of-plane displacement measurement, Salbut *et al.* [1]. However the elements under test may bring additional challenges: their surfaces may have complicated shape or large shape gradients which restrict their testing by means of interferometer with flat reference mirror – fringes in the interferogram may be too dense to be distinguished by CCD camera. To overcome such problems an active reference element may be used in an interferometer setup. “Active” means that it can manipulate of the reference beam in order to introduce phase shift or tilt and influence the wavefront shape of the reference beam to make it similar to the wavefront shape of the object beam.

In this paper we propose to use LCOS (Liquid Crystal On Silicon), Wang *et al.* [2], – phase, reflective SLM as active reference element. The control of this element is very easy i.e. X VGA image or video signal is generated by computer graphic card and directly input to the LCOS driver. 2-D phase information can be directly written to the phase-only device, at high accuracy and with video speed. The reference wavefront modifications are obtained by introducing to the LCOS driver Phase Correction Maps (PCM; which are grey-level bitmaps) representing computer generated or experimentally determined phase distribution. Introduced phase shift is proportional to intensity values in PCM.

LCOS may be used as an interferogram phase shifter (when TPS algorithm of interferogram analysis is used) or to introduce linear or circular spatial carrier, Kacperski *et al.* [3], (to allow the use of FT algorithm) what is useful for dynamic tests because shape or displacement can be measured on the basis of one interferogram only. Using experimentally determined PCM initial shape of the object under test can be compensated or systematic error can be removed. The object wavefront compensation and spatial carrier frequency introduction or phase shifting may be performed simultaneously. Thanks to it out-of-plane displacement measurements are simplified because displacement of the specimen may be observed and measured directly (no subtraction of two measured states of the object under test is needed). The compensation of object wavefront increase also measurement range of the interferometer what may be convenient for measurement of highly deformed elements. Moreover it is possible to visualize Bessel fringes in interferogram of vibrating object under test in live mode.

The application of the LCOS in Twyman-Green interferometer for microelements testing was possible after some modifications of the interferometer and performing calibration procedures that are described in this paper. Opto-mechanical modifications require placing a laser beam expander

into the reference arm of the interferometer in order to adjust size of the LCOS active area to the actual field of view of the microscope. Simply: nowadays LCOS pixel size and in consequence matrix size is too big for matching to CCD without additional optics. Calibration procedures concern the determination of the SLM (Spatial Light Modulator) characteristic (determination of the relation between the grey levels and output phase modifications). Moreover aberrations of the beam expander and nonflatness of the LCOS reflective surface introduces the systematic error to the measurement results which should be calculated and subtracted if the real shape of the object under test is supposed to be determined.

The usefulness of the system is shown at the examples of active microelements (micromembranes and microbeams with piezoelectric layer) testing in static and dynamic work modes. Errors and measurement uncertainty of the system are analyzed.

Adaptiveness of the interferometric system introduced by application of LCOS SLM as a reference element is a very useful property which increases functionality of two beam interferometer, simplifies measurement procedures and extends measurement range and class of objects possible to analyse. In other words proposed methodology is convenient for experimental mechanics tests.

## References

1. L. Salbut, J. Kacperski, A. Styk, M. Jozwik, H. Urey, C. Gorecki, A. Jacobelli, T. Dean, "Interferometric methods for static and dynamic characterizations of micromembranes designed for sensing functions", in *Optical Micro- and Nanometrology in Manufacturing Technology*, edited by C. Gorecki and A. K. Asundi, Proc. SPIE 5458, 2004, 287-298
2. X. Wang, B. Wang, J. Pouch, F. Miranda, J. E Anderson, P. J Bos, "Performance evaluation of a liquid-crystal-on-silicon spatial light modulator", *Opt. Eng.* vol. **43**, 2769-2774, 2004
3. J. Kacperski, M. Kujawinska, J. Krezel, "Modified linear and circular carrier frequency Fourier transform method applied for studies of vibrating microelements", in *Optical Micro- and Nanometrology in Manufacturing Technology*, edited by C. Gorecki and A. K. Asundi, Proc. SPIE 5458, 2004, 287-298

## APPLICABILITY OF TIME AVERAGE STOCHASTIC MOIRE FOR CRYPTOGRAPHIC APPLICATIONS

Minvydas Ragulskis  
Kaunas University of Technology  
Studentu 50-222, LT-51368, Kaunas, Lithuania  
minvydas.ragulskis@ktu.lt

An algorithm for the construction of Hash function [1] based on optical time average moiré experimental technique is proposed in this paper. Algebraic structures of greyscale colour intensity functions and time average operators are constructed. Properties of time average operators and effects of digital image representation are explored. The fact that the inverse problem of identification of the original greyscale colour intensity function from its time averaged image is an ill-posed problem and is computationally infeasible helps to construct an efficient algorithm for the construction of one-way Hash function applicable in cryptographic algorithms.

Inverse problems involving time average geometric moiré [2] are characterized by the fact that the information of interest (e.g. the distribution of greyscale colour intensity on the surface of a non-deformable body) is not directly available. The imaging device (the camera) provides measurements of a transformation of this information in the process of time averaging while the body performs complex chaotic in-plane motion. In practice, these measurements are both incomplete (sampling) and inaccurate (statistical noise). This means that one must give up recovering the exact image. Indeed, aiming for full recovery of the information usually results in unstable solutions due to the fact that the reconstructed image is very sensitive to inevitable measurement error. Otherwise expressed, slightly different data would have produced a significantly different image. In order to cope with these difficulties, the reconstructed image is usually defined as the solution of an optimization problem. Solution of the inverse problem from the time average image is known is computationally infeasible and that fact is the object of this study.

It is quite natural that time averaged greyscale colour intensity distribution is calculated exploiting digital computational techniques. That leads to an immediate contradiction. From the definition of time average operator it is clear that any time averaged greyscale function is a continuous function if the object is not stationary. But if the formation of digital images is considered in terms of pixels, it is clear that only greyscale functions with finite discontinuities at inter-pixel boundaries can be visualised.

Moreover, calculation of the definite integral in the process of time averaging is replaced with calculation of the limit sum. It can be noted that the step size of the limit sum is an important physical parameter. If the oscillations would be harmonic, time step equal to  $\pi$  would produce double exposure (stroboscopic) geometric moiré image. Naturally, the time step should be small for time average images. The relationship between the time step and the number of correctly reconstructed fringes is explicitly presented in [3]. The time step (the number of discrete time moments in one half of the period of oscillation) can be one of the control (input) parameters of the hash function.

Many engineering problems are based on the reconstruction of parameters of time average operators. A typical example is presented in [3] where both the original greyscale function and its time averaged image are known. Then the amplitude (and the direction of oscillations in a two-dimensional problem) can be determined solving an approximate optimisation problem.



Solution of the inverse problem when the greyscale function must be determined from its time averaged image is a much more complex problem. If the time averaging is performed experimentally, the problem is unsolvable due to extreme sensitivity to the inevitable measurement errors; only optimisation techniques can be used for approximating of the original image. Even if time averaging is performed using computational techniques, it is an ill-posed inverse problem and is practically unsolvable even if  $s$  is known.

Several considerations can be taken into account when constructing the cryptographic Hash function based on time average moiré. It is possible to eliminate even the theoretical possibility of reconstruction of the greyscale colour invariant in the original static image. Stretching of the time averaged greyscale intensity scale to min-max colour range would eliminate even this possibility.

One may also exploit the feature that sequential time averaging operation is not multiplicative (the proof is provided in the paper). Double (sequential) time averaging can be applied what can be considered as a next step of algorithmic safety.

The algorithm for construction of the Hash function comprises three main parts:

- a) Acquisition of input data: the secret function (greyscale colour intensities at appropriate pixels) and a discrete scalar time series (particularly it can be simplified to a harmonic series);
- b) Production of the intermediate result - time averaged greyscale intensities at appropriate pixels;
- c) Delivery of output data: time averaged greyscale function stretched to min-max intensity levels.

It can be noted that the proposed algorithm has a strong physical motivation. The observation window in realistic physical experiments is finite and the areas of the analysed body covered by the background colour are far away from the observation window. Then it is natural to expect that the time averaged image will be grey. That is clearly demonstrated by experimental investigations where natural stochastic greyscale structure of the surface serves as a stochastic geometric moiré grating for time average analysis

## References

1. Bicakci, K., Tsudik, G. and Tung, B., *Computer Networks*, vol. **43**, 339-349, 2003.
2. Ragulskis, M., Maskeliunas, R. and Saunoriene, L., *Experimental Techniques*, vol. **29**(6), 41-45, 2005.
3. Ragulskis, M., Palevicius, A. and Ragulskis, L., *Int. J. of Numerical Methods in Engg.*, vol. **56**(11), 1647-59, 2003.

## TOMOGRAPHIC RECONSTRUCTION OF 3D ULTRASOUND FIELDS MEASURED USING LASER VIBROMETRY

Kourosh Tatar, Erik Olsson and Fredrik Forsberg  
Luleå University of Technology  
Div. of Experimental Mechanics  
971 87 Luleå, Sweden  
kourosh.tatar@ltu.se

A method for obtaining the amplitude and phase distribution of an ultrasound field in air, using laser vibrometry and computed tomography, is described.

Radiating ultrasound transducers causes pressure variations in the air, which lead to refractive index changes, which in turn can be recorded by the use of interferometric instruments like the laser vibrometer. This point measuring method for the measurement and visualization of sound fields was proposed by Zipser *et al.* [1, 2]. In order to measure the whole sound field, the laser beam is scanned over the area of interest. With this technique, the absolute phase of the field is obtained directly from the measurements while the amplitude needs some calculations using the Gladstone Dale equation [3]. Moreover, the obtained result using laser vibrometry for sound measurements is an integral of the sound field along the laser light path. The projection effects due to this integral were studied by Olsson and Tatar [4]. In this paper however, the projection property of the measurement method is taken into advantage. Tomographic 3D reconstruction of the sound field is obtained using several projections taken at different angles. The phase and the amplitude distributions of an ultrasound field due to several transducers, emitting at a frequency of 40 kHz, positioned both symmetrically and non-symmetrically are reconstructed.

The ultrasound transducers were situated in a special made holder fixed on a rotation stage. The projections were captured at equiangular steps of 5 degrees. The full three-dimensional ultrasound field was reconstructed from the projection data using a cone-beam computed tomography algorithm. This algorithm is in its turn based on a three-dimensional filtered back projection algorithm. The projection data measured by the laser vibrometer is first filtered, using a ramp-filter, and then back projected along the scanning direction. Finally, when this procedure has been carried out for all scanning angles the full three-dimensional ultrasound distribution has been reconstructed.

Fig. 1 shows the real part of a reconstructed sound distribution emitted from the three ultrasound transducers positioned along a straight line, parallel with the x-axis at  $y=70$  mm. The sound propagates along the z-direction. The middle transducer seems to be phase shifted compared to the outer positioned transducers. This phase shift is due to a small difference in position levels, along the z-direction, between the transducers. The spatial resolution limit is a quarter of the ultrasound wavelength (about 2 mm) which corresponds to an upper frequency resolution of 170 kHz in air.

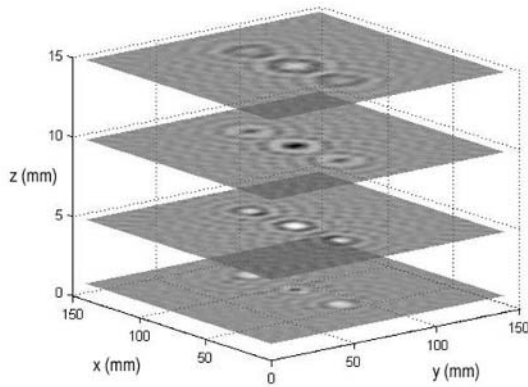


FIGURE 1. The real part of the reconstructed ultrasound field.

## References

1. Zipser L, Lindner S und Behrendt R Anordnung zur Messung und visuellen Darstellung von Schalldruckfeldern, Patent DE 10 057 922 vom 23.11.2000.
2. Zipser L and Lindner S, In *Proceedings of the 17th Int. Congress on Acoustics*, Rome 2001 24-25.
3. Vest C M *Holographic Interferometry*, Wiley, New York, 1979.
4. Olsson, E and Tatar, K. *Measurement science and technology*, vol. **17**, 2843-2851, 2006.

## EXPERIMENTAL DETECTION OF ONE DIMENSIONAL GROUT SPREAD USING IMAGE PROCESSING ACTIVE CONTOUR MODEL

A. Ait Alaiwa, N. Saiyouri and P.-Y. Hicher  
 Institut de recherche en Génie civil et Mécanique (GeM) UMR CNRS 6183  
 Ecole Centrale de Nantes, BP 92101, 44321 Nantes cedex 3, France  
 abdelghafour.ait-alaiwa@ec-nantes.fr

The use of ultrafine cement-based grout has been gaining importance for soil grouting over the last few years. Laboratory experiments were conducted to examine the spread of grout injection through porous media under saturation conditions. During grouting, a suspension of cement particles is injected through Loire sand column under constant flow rate to fill up their void spaces. All grout injection was performed utilizing automated monitoring and recording equipment, facilitating evaluation of field data (Fig. 1). Unlike water, grouts are usually viscous and behave as non-Newtonian fluid. Therefore, the equations describing the grout flow are more complicated and the solutions are quite difficult to obtain. To improve this study, it is necessary to follow grout propagation evolution with a complementary technique to validate the modelling developed for this use.



FIGURE 1. Grout propagation in saturated Loire Sand column at different instants.

In this paper, image processing algorithm model is proposed for analyzing the one-dimensional grouting process. The model is based on active contour also known as “deformable model” approach (Kass *et al.* [1]). Geometrically, a contour  $\mathbf{v}$  is a parametric curve embedded in the image plane. The initial shape of the contour subject to an image is given by the functional

$$E(\mathbf{v}) = S(\mathbf{v}) + P(\mathbf{v}) \quad (1)$$

The functional can be viewed as a representation of the energy of the contour and the final shape of the contour corresponds to the minimum of this energy.

While it is natural to view energy minimization as a static problem, a potent approach to computing the local minima of a functional such as (1) is to construct a dynamical system that is

governed by the functional and allow the system to evolve to equilibrium. The system may be constructed by applying the principles of Lagrangian mechanics. This leads to dynamic deformable models that unify the description of shape and motion, making it possible to quantify not just static shape, but also shape evolution through time (Chan and L.A. Vese [2], Xu and Prince [3]). The first term in (1)

$$S(\mathbf{v}) = \int_0^1 w_1(s) \left| \frac{\partial \mathbf{v}}{\partial s} \right|^2 + w_2(s) \left| \frac{\partial^2 \mathbf{v}}{\partial s^2} \right| ds \quad (2)$$

is the internal deformation energy. It characterizes the deformation of a stretchy, flexible contour. Two parameter functions govern the simulated characteristics of the contour:  $w_1(s)$  controls the “tension” of the contour while  $w_2(s)$  controls its “rigidity”. The second term in (1) couples the active contour to the image.

Traditionally, the last term in (1)

$$P(\mathbf{v}) = \int_0^1 P(\mathbf{v}(s)) ds \quad (3)$$

denotes a scalar potential function defined on the image plane. To apply active contour to images, external potentials are designed to coincide with intensity extrema, edges, and other image features of interest.

For grout injection tests, this algorithm can provide grout front progression. Parametric studies have been carried out to investigate the effects of various factors on the accuracy of the detection model. The results showed that the model is efficient both for binary and grey scale images. Further development will compute colour images.

## References

1. M. Kass, A. Witkin, and D. Terzopoulos. Snakes: Active Contour Models. *International Journal of Computer Vision*, pages 321-331, 1987.
2. Chan and L.A. Vese. Active Contours Without Edges. *IEEE Transactions on Image Processing*, 10(2): 266-277, 2001.
3. C. Xu and J. L. Prince, “Snakes, Shapes, and Gradient Vector Flow”, *IEEE Transactions on Image Processing*, 7(3), pp. 359-369, March 1998.

## DIGITAL HOLOGRAPHIC METHOD USED TO DETECT AN OBJECT'S DEFORMATION

Wen-Wen Liu, Xiao-Yuan He and Xin Kang  
Department of Engineering Mechanics of Southeast University  
Nanjing 210096, Jiangsu, China  
Liuww22@163.com

The structure deformation measurement is always to be the important problem of the field of the structure engineering. The traditional way of structure deformation measurement is not exact enough, and it is complex. While the optical measurement method has many good qualities such as high precision, simple facilities, changeable optical line, no damage to the measured object, no special treatment to the surface of the measured object and so on. It has been abroad used in macroscopical fields and microcosmic fields, especially in wisp deformation measurement. Thus we tried measuring small structure deformation using the digital holography interferometry which is in the field of the optical measurement.

Optical holography was proposed by Gabor in 1948. Along with the appearance and improvement of CCD and the improvement of computer technology, digital holography was proposed by Goodman in 1970s. It is a combination of traditional holography and modern electronic technology. Due to its all-digital experimental procedure, digital holography can be easily performed and transmitted with modern information technologies. Its procedure involves no chemical processing, so digital holography is much more convenient and speedy than traditional holography. Further more, it can simultaneously obtain both the intensity and profile information of a specimen with only one exposure, so it is much favorable for many practical applications. Owing to all these outstanding advantages, digital holography is regarded as a great progress in the development of modern optical measurement in mechanics and has been broadly studied.

Significant progress has been made in digital holography since it was proposed in 1994. It has proved to be a powerful tool for scientific researches and has found many applications in profile measurement, deformation measurement, aberration compensation, defect detection and neural network et al. However, almost all these researches were intended to demonstrate how to replace traditional holography with digital holography. Only few attempts at studying the characteristics of digital holography have been reported, and all research works are seriously restricted to the domains that originally belong to traditional holography. Digital holography is badly hindered from its further development.

In order to make full use of digital holography, we must study all its basic characteristics systematically and detailedly, and combine it with other information processing technologies. Only to do this, can we fundamentally solve the problem which digital hologram is confronted with.

This thesis involves the following research works.

1. The traditional optical holography and most of basic characteristics of digital holography including the resolving power, record scope, and the separate condition of reconstructed images are studied theoretically.
2. The CCD device used for hologram acquisition and reconstruction is detailedly studied by analyzing its influence on digital holography.
3. The hologram acquisition and reconstruction is simulated by computer. The phase-shifting technology for eliminating zero-order diffraction images and twin-images is studied.

4. A novel application of digital holography, an interferometric method for deformation measurement is introduced and experimented in this thesis. Fig. 1 shows the experimental setup. And the images is dealt with using my program, and the deformation of the small structure is obtained. At the same time, the future of the digital holograph is expected.

**Key words:** Optical Measurement; Digital Holography; Digital Image Processing; Fast Fourier Transform; Deformation Measurement.

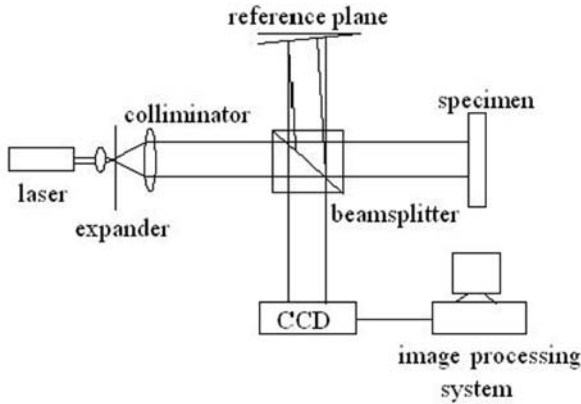


FIGURE 1. Experimental Setup

## References

1. Griffin, D.W., J. Opt.Lett., vol. **26**, 140-141, 2001
2. Giancarlo Pedrini, Upatieks, J., J. Optics Communications, vol. **7**, 257-262, 1999
3. Matsushima, D., J. Opt. Soc.Am., vol. **20**, 1755-1761, 2003
4. Yann, F., Bahram, J., J. Opt.Lett., vol. **26**, 1478-1480, 2001

## APPLICATION OF WAVELET TRANSFORM IN THE IMAGE ANALYSIS OF SOIL MICROSTRUCTURE

Wang Wei<sup>1,a</sup>, Sun Qiu<sup>2,b</sup>, Hu Xin<sup>2,c</sup>, Hong Baoning<sup>2,d</sup> and He Xiaoyuan<sup>1,e</sup>

<sup>1</sup>Department of Engineering Mechanics, Southeast University  
2 Sipailou Street, Nanjing, JS210096, P R China

<sup>2</sup>Research Institute of Geotechnical Engineering, Hohai University,  
1 Xikang Road, Nanjing, JS210098, P R China

<sup>a</sup>ww117@seu.edu.cn, <sup>b</sup>sunqiucn@yahoo.com.cn,

<sup>c</sup>moyuan@126.com, <sup>d</sup>hongbaoning24@sohu.com, <sup>e</sup>mmhxy@seu.edu.cn

Along with the rapid development of computer vision, image analysis technique was proposed to investigate engineering materials, such as soil [1-3]. First, the acquisition images methods were described by the computer-assistant tracking system. Fig. 1 shows the experiment system, whose main principle was digital image correlation technology. Then the problem of the parametrical characterization of soil microstructure was presented: geometry parameters and morphology parameters. To obtain these precise parameters would depend on the quality of images. On account of the concavo-convex feature of soil particles, the depth of field of the long work distance telecentric microscope lens had resulted in some blurred parts and clear ones existed in the same image. However, the greys of blurred parts of the image were changed smoothly. At the same time, the greys of clear ones were changed acutely. The greys of images were very like the frequencies of signals. So the wavelet transform was taken into account to improve the quality of such images. Based on the multi-resolution analysis of wavelet transform, the frequencies of signals were divided in different scales. In regard to the image transformed by the wavelet technology, the parts changed acutely of the image, that is the clear ones, were reserved. While, the parts changed smoothly of the image, that is the blurred ones, were abandoned. Therefore, the series images were acquired by auto-adjusting the control table of the computer-assistant tracking system under the same loading. Using the statistical characteristic of wavelet coefficient, the better quality images under the same condition were obtained by the fusion of series images. The experiment results show the method is valid and can improve the precision of the extraction parameters.

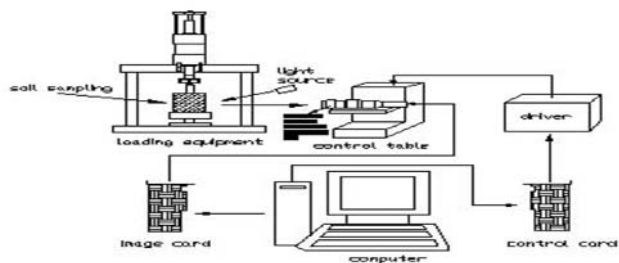


FIGURE 1. Configuration of the computer-assistant tracking system



**References**

1. Yue, Zhong Qi; Morin, and Isabelle. *Journal of Civil Engineering*, vol. **23**, 480-489, 1996
2. Coster, M. and Chermant, J.-L. *Cement and Concrete Composites*, vol. **23**, 133-151, 2001
3. Moore C. A. and Donaldson C. F. *Journal of Geotechnique*, vol. **45**, 105-116, 1995
4. He X. Y, Kang X., Quan C., Tay C. J., Wang S. H. and Shang H. M.. *Proceedings of SPIE*, vol. **4537**, 63-68, 2002

## IMAGE AND COMPLEX CORRELATION NEAR DISCONTINUITIES

Mikael Sjødahl  
Dept. Applied Physics and Mechanical Eng.  
SE-971 87 Lulea, Sweden  
mikael.sjodahl@ltu.se

Digital Image Correlation [1-3], also known as Digital or Electronic Speckle Photography [4-6], has since it was introduced about 20 years ago grown to become one of the most versatile and widespread experimental techniques in experimental full field strain analysis. The procedure is well known. Two, at least, images are acquired of the surface of an object undergoing deformation. One of the images is treated as a reference and the relative deformation field between two states of deformation is calculated using a sub-block correlation approach. For the accuracy and reliability of the technique it is important to have a high-contrast broad banded random pattern present in the image of the object, see Sjødahl [6], without violating the sampling condition. Recently the concept of Digital Complex Correlation was introduced in experimental mechanics by Svanbro [7] as an extension of Digital Image Correlation. The procedure is in many respects the same as in traditional image correlation, but instead of intensity images complex amplitude images from a speckle interferometry experiment are used as input to the correlation wherefore additional information about the interferometric phase change between the two images is obtained from the phase at the correlation peak.

Since finite sub-blocks are used in the analysis the image correlation procedure clearly runs into problems close to edges and discontinuous jumps in the deformation field. The problem is illustrated in Fig. 1. The figure below shows the results from correlating two images with a vertical crack in the second image with the sub-block positioned at four different positions relative the crack. When the sub-block is positioned such that nothing of the crack is present in the sub-block a high-quality correlation peak is obtained at the position representing the deformation of the sub-block. When the sub-block is gradually slid across the crack it is seen how energy is transported from the first peak into the new peak at the position representing the deformation on the other side of the crack. It is also seen that the energy balance between these two peaks corresponds to the number of pixels on either side of the crack. Two consequences of this behaviour of the correlation surface, both troublesome, can be identified. If the relative displacement is larger than the average speckle size two separate correlation peaks will appear, but only one will be chosen as the correct one. This will result in a susceptibility to the positioning of the sub-block, and as a consequence a small change in sub-block position may result in a large change in detected displacement. If the relative displacement is smaller than the average speckle size the correlation peak will be distorted and systematic errors appear. This presentation will go through a few approaches to cope with discontinuities in image and complex correlation and illustrate with a few examples.

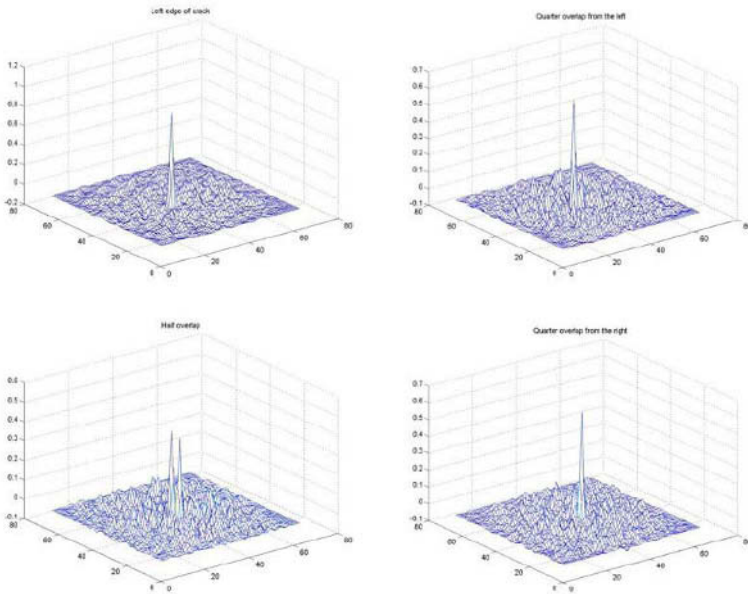


FIGURE 1. Change of the correlation surface as the sub-block is slid over the crack in steps of a quarter sub-block going from the upper left to the lower right image.

## References

1. M. A. Sutton, W. J. Wolters, W. H. Peters, W. F. Ranson and S. R. McNeill, *Image and Vision Computing*, vol. **1**, 133-139, 1983.
2. H. A. Bruck, S. R. McNeill, M. A. Sutton and W. H. Peters, *Exp. Mech.*, vol. **29**, 261-267, 1989.
3. F. Hild and S. Roux, *Strain*, vol. **42**, 69-80, 2006.
4. M. Sjodahl and L. R. Benckert, *Appl. Opt.*, vol. **32**, 2278-2284, 1993.
5. M. Sjodahl, *Appl. Opt.*, vol. **33**, 6667-6673, 1994.
6. M. Sjodahl, *Appl. Opt.*, vol. **36**, 2875-2885, 1997.
7. A. Svanbro, *Appl. Opt.*, vol. **45**, 2006 (in press).

## ESTIMATION OF DIGITAL IMAGE CORRELATION (DIC) PERFORMANCES

Laurent Robert

Workgroup “Metrology” of CNRS research network 2519<sup>a</sup> “MCIMS”,

<sup>a</sup><http://www.ifma.fr/lami/gdr2519/>

CROMeP, Ecole des Mines d’Albi-Carmaux, 81013 ALBI Cedex 9, France

laurent.robert@enstima.fr

Optical full-field measurement techniques are promising tools for experimental analyses of materials and structures. While they are widely used, they still suffer from the lack of a complete metrological characterisation. The collaborative work carried out by the workgroup “Metrology” of CNRS research network 2519 aims at contributing to a systematic approach to these questions [1].

DIC techniques are among the most popular optical methods, because of the availability of commercial packages, price and apparent simplicity. An important element of the measurement procedure is the image analysis software package supposed to provide an apparent 2D displacement field that maps a so-called “reference image” to a “deformed image”. Quantitative evaluations of the performances of DIC measurements are usually limited to situations with homogeneous mechanical transformations, namely, uniform translation, in plane rotations, out of plane rigid body motions, which result in apparent affine transformations of the image [2]. Very few works [2–4] address situations with spatially fluctuating displacement fields, which need to be investigated for a quantitative assessment of the spatial resolution of such techniques. Since it is experimentally difficult to generate non uniform deformation fields, it is necessary to perform the analysis on simulated images. In Ref. [3] quadratic displacement fields have been considered; the present approach extends the analysis to plane sinusoidal displacements, with varying spatial frequencies. The RMS errors of the displacements obtained with various DIC softwares are evaluated as functions of the spatial frequency and the amplitude, for various correlation window sizes and DIC formulations.

Two sets of synthetic speckle pattern images have been generated. Deformed images are obtained assuming a plane sinusoidal displacement  $u_x(X, Y) = \alpha p \sin(2\pi X / p)$  where  $p$  is the period in pixels and  $2\pi\alpha$  is the amplitude of the displacement gradient  $u_{x,x}$ . Each generated set contains one reference 1024 x 1024 pixel image and 42 deformed images obtained with  $\alpha \in \{0.1, 0.05, 0.02, 0.01, 0.005, 0.001\}$  and  $p \in \{10, 20, 30, 60, 130, 260, 510\}$  pixels. Images have been processed with various DIC packages, including 7D (P. Vacher, Univ. Savoie), Aramis 2D (S. Mistou, ENIT), Correla (J.C. Dupré/F. Brémand, Univ. Poitiers), Correli (F. Hild, ENS Cachan), CorrelManuV (M. Bornert, EP), KelKins (B. Wattrisse, Univ. Montpellier) and Vic-2D (L. Robert/J.J. Orteu, EMAC). Square correlation windows (subset) of different sizes  $f$  have been used, from 9 to 64 pixels. Displacements have been evaluated at all positions of a regular square grid in the initial image, with a separation such that subsets at adjacent positions do not overlap (i.e., statistical independence of the corresponding errors). Differences between the evaluated and prescribed displacements along  $x$  are analysed statistically in terms of RMS errors. As a general point of view, it is shown that the RMS error is described as  $\sigma_u = \text{function}(p, \alpha, r, \Phi, f, \dots)$  where  $r$  characterises the speckle size,  $\Phi$  (the local transformation in the subset assumed by the DIC algorithm) and  $f$  are relative to the main DIC packages options.

Preliminary results show that the overall RMS error is mainly controlled by the first order difference between the real transformation and the local transformation  $\Phi$  of the subset. Limiting

situations are, on the one hand, displacements varying at low spatial frequencies for which the classical error observed for rigid motions is recovered, and on the other hand, displacement fields with small periods (lower than the subset size  $f$ ), for which the RMS error is equal to the RMS of the displacement itself, and the DIC evaluation being almost zero (Fig. 1). The transition between these two regimes depends on  $f$  and  $\Phi$ : an asymptotic regime is obtained faster if  $f$  is smaller and  $\Phi$  is of higher degree. When  $\Phi$  is assumed to be a rigid (resp. affine) transformation, the asymptotic error is proportional to the first (resp. second) derivative of  $u_X$  (see Fig. 1). Moreover, this error is independent of  $f$  but increases with  $r$  in the case of a rigid transformation  $\Phi$ , or increases with  $f$  in the case of an affine transformation  $\Phi$  for sufficiently large  $f$  and strains. For small subsets and small strains, the asymptotic error decreases with  $f$  as it is observed for pure translation. For  $\Phi$  of high order (e.g., quadratic), it is shown that the asymptotic error is independent of  $p$  and  $\alpha$  (and not governed by the third derivative of  $u_X$ , second order phenomenon). Additional investigations, including the analysis of the transition, influence of the speckle geometry and of image noise, are the subject of ongoing collaborative work and will be addressed during the presentation.

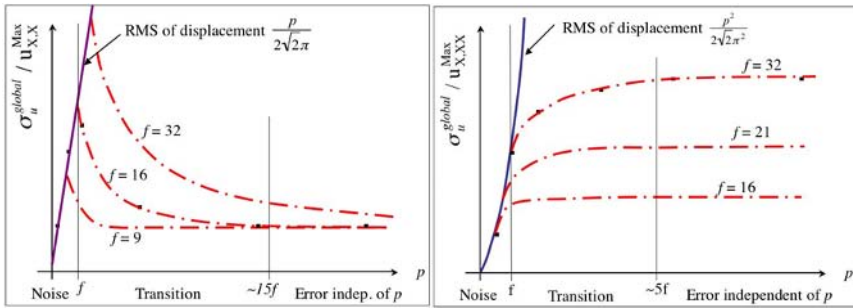


FIGURE 1. Schematic observation of the regimes for the RMS error. Two cases are presented:  $\Phi =$  rigid transformation (RMS error normalised by the first derivative of  $u_X$ , left) and  $\Phi =$  affine transformation (RMS error normalised by the second derivative of  $u_X$ , right).

## References

1. Bornert, M., in Photomechanics 2006, Clermont-Ferrand, France, 2006.
2. Wattrisse, B., Chrysochoos, A., Muracciole, J.-M and Némoz-Gaillard, M., *Exp. Mech.*, vol. **41**, 29-39, 2000.
3. Schreier, H. W. and Sutton, M. A., *Exp. Mech.*, vol. **42**, 303-310, 2002.
4. Lecompte, D., Smits, A., Bossuyt, S., Sol, H., Vantomme, J., Van Hemelrijck, D. and Habraken, A.M., *Opt. Laser Eng.*, vol. **44**, 1132–1145, 2006.

## VISIBLE, INFRARED AND INCOHERENT LIGHT TRANSPORT OPTICAL TECHNIQUES FOR IN SITU MATERIAL TESTING

N. Renault, S. Andre, C. Baravian and C. Cunat

LEMMA – UMR CNRS 7563

2, av. de la forêt de Haye – BP160

F-54504 VANDOEUVRE Cedex

Norbert.Renault@ensem.inpl-nancy.fr , Stephane.Andre@ensem.inpl-nancy.fr

Three experimental non intrusive techniques are used simultaneously for the metrological monitoring of the deformation of a material in a tensile load machine. The first technique is a video-extensometer (Videotraction®) based on ink spots tracing. The image treatment is fast enough to allow an active control of the machine. It furnishes the true stress-true strain curves for a given specimen according to a desired loading path. An infrared camera is placed on the opposite side of the sample and records some picture of the temperature field evolution during the whole experiment. Thanks to a numerical technique developed for solving the inverse problem of heat source reconstruction, it is possible to get the dissipated power versus strain curve. This brings a new information, of thermodynamic nature, reflecting the thermal activity of the internal mechanisms of deformation. Finally, on the same side of the sample, a third optical technique is used. This technique applies to turbid samples (neither absorbent nor completely transparent to visible light). A laser impact the sample on a very small spot (50  $\mu\text{m}$ ). An incoherent steady-light transport (ISLT) occurs within the turbid sample. Thanks to a high resolution camera, the backward scattering image (10  $\text{mm}^2$ ) is analysed through a theoretical modelling of incoherent light transport in disordered materials. It allows to follow the concentration of the scattering objects as well as their anisotropy during the experiment thus yielding additional information about what happens in the microstructure of the sample during the test.

These techniques are all three very simple to use and offer the advantage of being compatible each one with the other. They bring simultaneously the metrological information of engineer type i.e. the evolution of macroscopic variables along with two other informations relative to the microscopic processes operating in the matter. An example is given here on HDPE to illustrate the potentiality of this combination of tools.

Fig. 1 gives the stress-strain curve obtained on a HDPE sample of 2 mm thickness. After necking, the material flows with relatively small efforts before it experiences a hardening phase. Plotted on the same figure, one can see the behavior of the reconstructed heat power that affects the process during the experiment. This power is the sum of three components : the thermoelastic coupling (a thermodynamic coupling between macroscopic variables), the thermomechanical couplings (a thermodynamic coupling between macroscopic and 'internal' variables usually referred to as stored cold-work) and the heat that is dissipated in an irreversible manner that results from the couplings between internal variables themselves.

Fig. 2 gives the stress-strain curve plotted along with the measured parameters brought by an incoherent light scattering transport theory in disordered systems i.e. a parameter that reflects the concentration of scattering particles and their anisotropy. HDPE is a polymer that has a whitish colour for such thickness. During a tensile test, the deformation is accompanied with a strong whitening of the matter. It is the result of the crazing phenomena. Voids are created during the deformation process that will change the intensity of the scattering process of an incident laser. This optical phenomena can be detected by human eyes but it can be quantified thanks to an image analysis based on theoretical modelling of the physical processes involved.

These three optical techniques will be described in the full paper and the nature of the informations they brought will be discussed further.

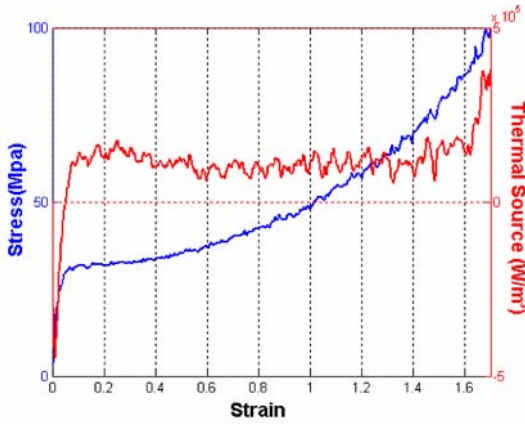


FIGURE 1. True stress-strain curve and evolution of the involved calorific power during a tensile test at rate  $\dot{\epsilon} = 10^{-2} s^{-1}$

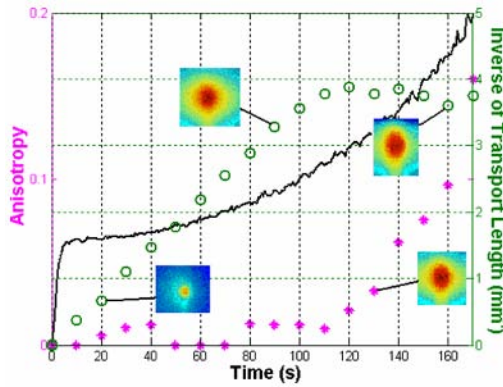


FIGURE 2. True stress-strain curve and evolution of the micro-structural parameters yield from ISLT technique during a tensile test at rate  $\dot{\epsilon} = 10^{-2} s^{-1}$

## EVALUATION OF SHRINKAGE STRESSES AND ELASTIC PROPERTIES IN A THIN COATING ON A STRIP-LIKE SUBSTRATE

D.A. Chelubeev, R.V. Goldstein, V.M. Kozintsev, A.V. Podlesnyh and A.L. Popov  
 Laboratory on Mechanics of Strength and Fracture of Materials and Structures, Institute for  
 Problems in Mechanics of the Russian Academy of Sciences,  
 119526, prosp. Vernadskogo 101-1, Moscow, Russia  
 goldst@ipmnet.ru

Theoretical and experimental models of deformation of a strip-like substrate from solidifying a coating are considered. On the basis of these models, the algorithm for evaluation of shrinkage stresses in a coating and its elastic properties is suggested. Similar studies for the case of equal elastic properties of a coating and a substrate have been fulfilled starting from the classical paper by Stoney [1]. The method suggested in the present paper is applicable for the cases of coinciding and different elastic properties of materials of the coating and substrate. Moreover, these elastic properties can be in advance unknown.

Let on a strip-like substrate of length  $l$  and rectangular cross-section of thickness  $b$  and width  $h$  a coating of width  $\delta \ll h$  was deposited. We consider, that the substrate is hinge supported at edges  $x=0, l$  (Fig. 1).

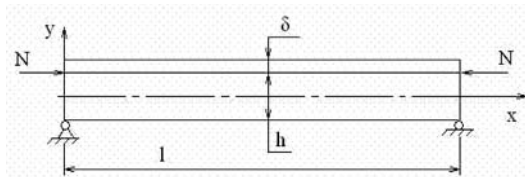


FIGURE 1. The calculated scheme for evaluation of shrinkage stresses in a coating.

Coating shrinkage occurs after the film solidifying. It leads to generation of stresses in a substrate and coating and to substrate bending.

At first the substrate and coating in the free disconnected state are considered as two independent strips of length  $l$  and  $l_0$ . Having accepted, that  $l > l_0$ , lengthening  $\Delta l = l - l_0$  is determined  $\Delta l = N l_0 / (E_2 F)$ , where  $F = b \delta$  is the area of cross-section,  $E_2$  is the elastic modulus of a coating,  $N$  is the force which is necessary for coating stretching on size  $\Delta l$ . Force  $N$  is considered enclosed to the substrate edges, as it is shown in Fig. 1.

The appropriate bending moment equals  $M = Nh/2$ . On the other hand, longitudinal force can be expressed through a stress in a coating ( $N = \sigma F$ ) and the bending moment - through the maximal deflection of the hinge supported strip  $w_{max}$ , bent by the edge moment  $M = 8EJ w_{max} / l^2$ , where  $E$  is the elastic modulus of the substrate material,  $J$  is the moment of inertia of the substrate section.

Hence, having measured the maximal deflection of the strip, we can determine residual stresses in the coating by the formula  $\sigma = 4Eh^2 w_{max} / (3l^2 \delta)$ .

If it is impossible to consider the coating being thin or its elastic characteristics exceed similar characteristics of the substrate it is necessary to consider the additional factors influencing the value of shrinkage stresses.



Evaluation of the basic elastic characteristic of a coating - its elastic modulus - also can be made experimentally by interferometric measuring a substrate deflection under the action of known loading. For instance, from the maximal deflection  $w_{max}$  of a cantilever beam under the action of the transverse force  $P$  on the free edge the stiffness of the substrate  $EJ=Pl^3/(3 w_{max})$  is determined.

In some cases one can not observe the whole beam part from the clamping to the point of force application. Denote by  $l_1$  and  $l_2$  the distances from the clamping point to the boundaries of the observable interval, while the difference of displacements of these points [ $w(l_1) - w(l_2)$ ] will be denoted by  $d$ . Then from the equation of an elastic line we obtain

$$EJ = \frac{P(3l(l_2^2 - l_1^2) - (l_2^3 - l_1^3))}{6d}$$

Evaluation of the elastic modulus of a coating material was made by comparing the stiffness values of samples with and without coating. This possibility is illustrated in Fig. 2 where interferograms of a bend of the samples with (top strip) and without the coating by the same force are given. The difference of band numbers characterizes a difference in the maximal deflections.

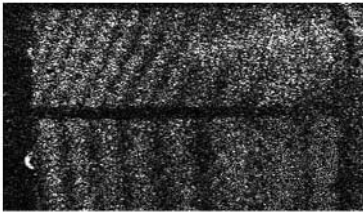


FIGURE 2. Interferograms of a bend of samples with (above) and without coating.

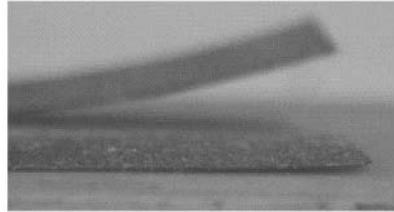


FIGURE 3. Steel and cardboard strips after the bend made by the sprayed paint.

In Fig. 3 steel and cardboard strips are shown after the bend made by the solidifying of sprayed aerosol double acrylic concentrated metallic paint, put on these strips on the one side. The sizes and elastic characteristics of strips, as well as the measured sizes of their maximal deflections under the action of shrinkage stresses and values of these stresses are given below.

TABLE 1. The characteristics of substrates and shrinkage stresses in coating.

Material	Sizes / mm	$w_{max}$ / mm	E / GPa	$E_2$ / GPa	Shrinkage stresses / Pa
Steel	$30 \times 6 \times 0,15$	0,55	200	24	2,8
Cardboard	$17,5 \times 8 \times 0,1$	3	2,5	24	1,3

Thus, the described method enables to evaluate shrinkage stresses at coating solidifying as well as unknown elastic characteristics of the coating and substrate. Values of these characteristics are determined experimentally by measuring the substrate form changing. In the case of coating with unknown history of solidifying the problem on shrinkage stresses evaluation is similar to the problem on evaluation of residual stresses, for example, in a welded joints by drilling of blind holes. In this case it may be rational to evaluate the shrinkage stresses in coating by means of scratch-test.

The study was supported by the Russian Foundation for the Basic Research (Projects 06-08-01017 and 05-01-08017).

**References**

1. Stoney, G.G. Proc. Royal Society, London. Ser. A. vol. **82**, p. 172–175, 1909.

## FULL-FIELD STRAIN RATE MEASUREMENT BY WHITE-LIGHT SPECKLE IMAGE CORRELATION

Giovanni B. Broggiato<sup>1</sup>, Leobaldo Casarotto<sup>2</sup> and Zaccaria Del Prete<sup>1</sup>

<sup>1</sup> Mechanics and Aeronautics Department – University of Rome “La Sapienza”  
Via Eudossina, 18 – 00184 Rome, Italy

<sup>2</sup> IPROM, Institut für Produktionsmeßtechnik – Technische Universität Braunschweig  
Schleinitzstraße 20 – D-38106 Braunschweig, Germany

giovanni.broggiato@uniroma1.it, l.casarotto@tu-braunschweig.de, zaccaria.delprete@uniroma1.it

Experimental techniques based on numerical correlation of white light speckle images have recently reached considerable results in full-field strain measurement. These improvements have been facilitated and allowed by the continuous growth, in quality and capabilities, of digital cameras and computers. In addition, the present inexpensiveness of these instrumentations is making these methods more and more popular in experimental mechanics, even when it comes to acquire image sequences of fast events.

The aim of the present paper is to show a numerical procedure able to process sequences of digital images and return a full-field evaluation of the strain rate as a color map of the measured field overlapped to the specimen picture.

The research objective is focused to study the plastic behavior of metals and, in particular, to highlight any transient phenomena that may occur during yielding and strain hardening phases on the thin sheets used in sheet metal forming. A typical example for such phenomena is the Portevin-Le Châtelier effect, a repetitive yielding of alloys in regime of plastic deformation. The strain rate is an important parameter for the theoretical modelling of the strain avalanches but until now it could only be measured in a couple of points [1] or be estimated on the basis of some boundary conditions [2]. The measurement of the strain rate distribution inside a region of local deformation would offer a novel approach for the description of the phenomenon.

### Background

One of the most effective methods to obtain a full-field strain evaluation correlating white-light speckle images is the so-called “global approach” [3, 4]. It consists in dividing a speckle field into sub-images likewise a plane area is meshed to perform a structural analysis by the finite element method. Each image element is joined to its neighborhoods on its vertex nodes so that it cannot freely change its shape during the correlation process but it must always accomplish a congruency constrain assuring spatial continuity to the displacement field.

The aim of a global correlation algorithm is to find the warping function that maps the mesh nodes from the undeformed to the deformed image so that each element contains exactly the same pattern on both pictures. This problem can be mathematically posed as a nonlinear least squares minimization of the difference between the element contents in the two configurations. The solution of this problem represents the displacements of the nodes that occurred because of the deformation and permits the calculation of the strain distribution, which can be displayed by means of a color map as visible in Fig. 1.

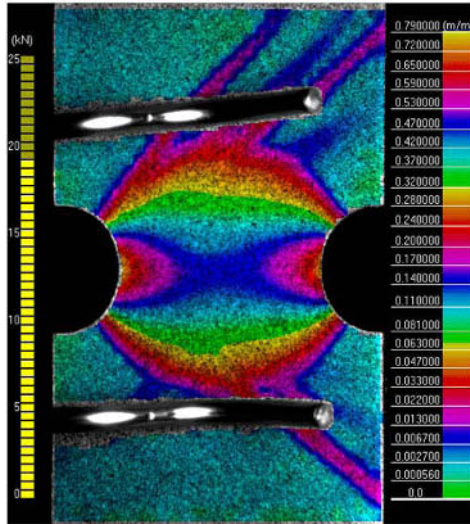


FIGURE 1. The field of equivalent strain computed on a notched specimen and shown on the specimen itself.

### Strain-rate computation

The present paper shows how the concept of global approach used to correlate each image all together, can be extent over the time axis to obtain a better description of strain evolution and, consequently, a correct evaluation of strain-rate field.

The implementation of this correlation procedure enhancement has required the use of time-dependent shape functions and has implied a further growth of the amount of data to process simultaneously. Besides, a special care has been put on strain and strain-rate computation by the use of Cauchy-Green theory for large strain representation.

### References

1. Thevenet, D., Milha-Touati, M. and Zeghloul A., *Mat. Sci. Eng. A*, vol. **291**, 110-117, 2000
2. Rizzi, E. and Hähner, P., *Int. Jour. Plast.*, vol. **20**, 121-165, 2004
3. Gao, Z., Wang, Y., Gioia, G. and Cuitiño, A. M., *Proceedings of SEM Annual Conference and Exposition*, Milwaukee (Wisconsin-USA), 2002.
4. Broggiato, G.B., *Proceedings of ICEM12 - 12th International Conference on Experimental Mechanics*, Bari (Italy), 2004.

## RADIOGRAPHIC OBSERVATION OF STRAIN FIELD AND CONSEQUENT DAMAGE ZONE EVOLUTION

D. Vavrik<sup>1,2</sup>, T. Holy<sup>2</sup>, J. Jakubek<sup>2</sup>, M. Jakubek<sup>2</sup> and J. Valach<sup>1</sup>

<sup>1</sup>Institute of Theoretical and Applied Mechanics of the Czech Academy of Sciences, Prosecka 76, Prague 9, Czech Republic, E-mail: vavrik@itam.cas.cz

<sup>2</sup>Institute of Experimental and Applied Physics of the Czech Technical University in Prague, Horská 3a/22, 128 00, Prague 2, Czech Republic

This work reports on results of the radiographic observation of 3D displacement/strain field and consequent damage evolution during loading of specimens with recognizable inner structure. Assuming flat geometry of the loaded specimen, the in-plane deformation is evaluated from radiographs using the image correlation technique. The related out-of plane displacement field is measured thanks to an accurate ‘radiograph intensity to material thickness’ calibration. The resultant 3D displacement field is determined using actual and reference radiograph.

Failures in ductile materials and composites precede intensive internal material damage evolution. Not only the onset and existence of damage but also its quantification and time evolution have to be determined for material science research. An experimental method called “X-Ray Dynamic Defectoscopy (XRDD)”, Vavrik *et al.* [1], is successfully used for this purpose, see Fig. 1 for illustration.

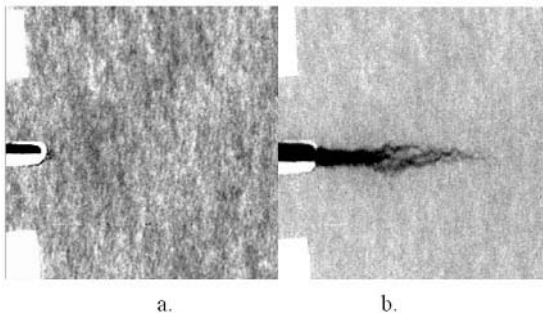


FIGURE 1. Time development of damage zone at stress concentrator tip as imaged by XRDD. Real dimension of each subfigure is 5x5 mm. Stress concentrator tip is on left. Inner structure of the material is visible in the subfigure a.

Using the image correlation technique for measurement of the in-plane strain field based on radiograph evaluation is quite known for materials with distinct inner structure such as reinforced composites, Russel [2]. However this approach is applicable also for metals where the grain structure becomes recognizable in radiographs, as will be presented

Regarding to the scale of the grain structure and damage zone to be observed, a radiographic spatial resolution of micrometric scale is required. The principal requirements to be fulfilled in order to achieve high spatial resolution in X-ray imaging are a “point” source X-ray beam, a highly efficient X-ray detector with large dynamic range and the beam hardening correction. We

employed an X-ray tungsten microfocus tube with focal spot of 5  $\mu\text{m}$  and divergent cone “point source” beam which enable a magnification up to the micrometer scale in spatial resolution. As X-ray detector we used the single X-ray photon counting digital pixelated Medipix-2 device, see [3]. The so called beam hardening effect arises as a significant source of X-ray image distortion, which can be eliminated by the “Direct thickness calibration method” [1]. A map of thickness values substituting radiograph intensities is obtained by this method. The direct thickness calibration technique improves significantly the transmission roentgenogram quality regardless of the object material and thickness variations.

For the purpose of XRDD and 3D displacement field measurements, a new transferable 25 kg and highly stiff loading device was developed. This device is equipped with four stepper engines ensuring the symmetrical loading of specimens with stable position of the observed area in the X-ray beam. Grips displacement is realized by the screws rotation using stepper motors with harmonic transmission. The resultant transmission ratio is extremely high and allows for precise and very slow loading. The loading force is recorded by two load cells while grip displacement is measured by two extensometers. The loading force capacity of the device is 100 kN and weights only 25 kg with dimensions 377x343x190 mm. These parameters allow to fix the loading equipment onto a PC controlled motorized stage during measurements. Furthermore, it is possible to place the loading frame together with the motorized stage into a fully shielded case, making X-ray radiographic transmission observation easily accessible.

Work carried out within the framework of the CERN Medipix Collaboration

## References

1. Vavrik, D., Holy, T., Jakubek, J., Jakubek, M., Bryscejn, J., Tichy, V., Vykydal, Z., Valach, J.: Radiographic observation of damage zone evolution in high ductile specimen, In *Proceedings of the 16th European Conference of Fracture*, edited by E. Gdoutos, Alexandropolis, Greece, Springer, 2006
2. S. S. Russell and M. A. Sutton, *Experimental Mechanics*, vol. **29**, 237-240, 1989
3. Medipix collaboration: <http://www.cern.ch/MEDIPIX/>

## STRAIN MEASUREMENT IN THE ADHESIVE LAYER OF A BONDED JOINT USING HIGH MAGNIFICATION MOIRÉ INTERFEROMETRY

P.D. Ruiz<sup>a</sup>, F. Jumbo<sup>a</sup>, J.M. Huntley<sup>a</sup>, I.A. Ashcroft<sup>a</sup> and G.M. Swallowe<sup>b</sup>

<sup>a</sup> Wolfson School of Mechanical and Manufacturing Engineering, Loughborough University, Loughborough, LE11 3TU, United Kingdom

<sup>b</sup> Physics Department, Loughborough University, Loughborough, LE11 3TU, United Kingdom, p.d.ruiz@lboro.ac.uk, g.m.swallowe@lboro.ac.uk

Adhesive bonding is acknowledged as superior to riveting in terms of structural efficiency because of the weight penalty of introducing a mechanical fastener and the improved stress distribution and rigidity of the bonded joint. However, the adoption of adhesively bonded joints in structural applications has been inhibited by the lack of trusted design codes. The complexity of the stress distributions in bonded joints has led to their analysis using the finite element (FE) method (Harris *et al.* [1]), the predictions of which have to be experimentally verified (Tsai and Morton [2-4]). In the current paper we use high magnification moiré interferometry (HMMI) to measure surface strains within the narrow ( $\sim 200 \mu\text{m}$ ) adhesive layer in the fillet region of the joints, and compare the experimental measurements with FE simulations. The strain distribution in this region of the joints is of key importance because it is there where the crack initiates in the case of failure. We also implemented significant improvements in MI instrumentation over previously reported systems, including automated analysis of the interferograms by phase shifting techniques, and the construction of an interferometer with reduced sensitivity to environmental disturbances.

The interferometer is shown schematically in Fig. 1 and uses a single optical fibre to deliver a light beam that is first collimated by lens  $L_1$  and then diffracted by a crossed-lines transmission grating beam splitter  $G$  ( $1200 \text{ lines mm}^{-1}$ ). This produces a pair of collimated beams in the  $xz$  plane and another pair in the  $yz$  plane. Four mirrors ( $M_x, M_y$ ) steer the beams coming from the grating beam splitter towards the sample  $S$ , which has a reflection crossed-lines diffraction grating ( $600 \text{ lines mm}^{-1}$ ) replicated onto its surface. The sample grating is imaged with a high-speed camera  $C$  and a long working distance microscope objective lens  $L_2$ . Quantitative displacement fields were obtained across the replicated grating from the optical phase change measured between the reference and loaded states of the sample. Temporal phase shifting was implemented by translating  $G$  with a PZT transducer on its plane and along an axis at 45 degrees to the  $x$  axis. A phase shift of  $\pi/2$  between the +1 and -1 diffracted orders in the  $xz$  or  $yz$  planes is introduced when the grating  $G$  moves a distance  $g/8$  (with  $g$  the grating pitch) along an axis at 45 degrees to the  $x$ -axis. In this way, the system is insensitive to vibrations affecting the delivery optical fibre. Wrapped phase maps representing the in-plane displacement components  $u$  and  $v$  were unwrapped and then differentiated to give the engineering shear strain  $\varepsilon_{xy} = \partial u / \partial y + \partial v / \partial x$ .

Aluminium/Aluminium (Al/Al) and Aluminium/Carbon Fibre Reinforced Composite (Al/CFRP) double-lap joints (DLJ) were manufactured using unclad 7075 T6 aluminium alloy and uniaxial CFRP adherends bonded with FM73M adhesive (Cytec Ltd) as shown in Fig. 2.

Figure 3 shows the engineering shear strain obtained on the adhesive layer in the fillet region of an Al/Al DLJ. The field of view studied is denoted FOV on Figure 2. The region of strain concentration visible close to the (0,0) position has been predicted with a three-dimensional FE model and corresponds to the region where cracks initiate.

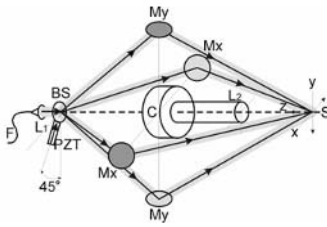
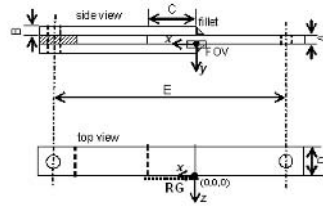


FIGURE 1. Moiré Interferometer.



DLJ	A (mm)	B (mm)	C (mm)	D (mm)	E (mm)
Al/Al	3.0	3.0	25.0	25.0	250.0
CFRP-Al	4.2	2.0	12.5	25.0	150.0

FIGURE 2. Adhesively bonded DLJ.

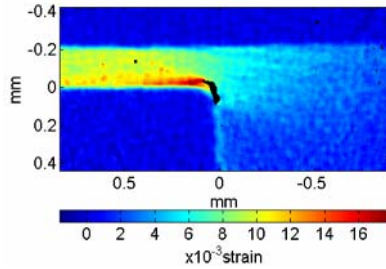


FIGURE 3. Engineering shear strain obtained for an Al/Al DLJ under a tensile load of 7kN, in the field of view indicated in Fig. 2.

**References**

1. Harris, J.A. and R.D. Adams, Int. J. Adhesion & Adhesives, 1984, vol. 4: p. 65-78.
2. Tsai, M.Y. and J. Morton, J. Strain Analysis, 1994, vol. 29(2): p. 137-145.
3. Tsai, M.Y. and J. Morton, Mechanics of Materials, 1995, vol. 20(3): p. 183-194.
4. Tsai, M.Y. and J. Morton, Composite Structures, 1995, vol. 32(1-4): p. 123-131.

## WOODEN SURFACE INVESTIGATION: AN OPTICAL APPROACH BASED ON SHADOW MOIRÉ

L. D'Acquisto<sup>a</sup>, A. La Pica<sup>b</sup>, A.M. Siddiolo<sup>a</sup>

<sup>a</sup> Dipartimento di Meccanica, Università degli Studi di Palermo <sup>b</sup> Dipartimento di Ricerche Energetiche ed Ambientali, Università degli Studi di Palermo

Viale delle Scienze, 90128 Palermo, Italy

dacquisto@dima.unipa.it; lapica@unipa.it; siddiolo@dima.unipa.it

The interest in the mechanical behaviour of wood is a very important task due to the increasing role played by wood structures in modern architecture as well as its applicability in restoration of ancient buildings. The behaviour of wooden surfaces experiencing variable humidity conditions is of great importance both with concern to performances of wooden building's structures and to ensure correct restoration and conservation of art works like wooden sculptures and panel paintings [1]. In literature there are only a few studies dealing with the influence of moisture on the physical properties of wood [1,2]. The characterization of wooden behaviour related to changes in the humidity level could make easier restoration and preservation of wooden artefacts. In the last years, the increasing development of technology allowed the application of non contact whole-field measurement techniques. These techniques could play a fundamental role in the analysis of the mechanical behaviour of materials such as plastic and wood. Among these techniques: Digital Image Correlation, Structured Light, Electronic Speckle Pattern Interferometry (ESPI) [3]. Recently some real-time 3D wood panel surface measurement using laser triangulation [4] and light shadow scanning [5] have been proposed.

The goal of the present study is to investigate the applicability of a shadow moiré technique [6] combined with an *ad-hoc* image processing procedure based on the use of the 2D Fast Fourier Transform (2D-FFT) capable to measure shape along wooden surfaces. The measurement of wooden surfaces undergoing hygrometric variations is performed to characterise the different behaviour of wooden species.

The optical shadow moiré system adopted in the present investigation includes: a monochrome light source (SUWTECH laser,  $\lambda=532$  nm e  $P=105$  mW), moiré grids on glass plate (Graticules mod. SAG4), a Dalsa DS-21-02M30 digital camera with frame grabber microEnable-III, a Nikkor AF lens (focal length 60 mm). A *quasi*-standard lay-out was set-up (the grid was tilted in order to introduce a carrier fringe pattern). A proper climatic chamber was realized in order to test wooden samples undergoing hygrometric variations. The chamber had to fulfil some requisites: a transparent wall and a mechanical system inside to allow a precise tilting of the grid. An ultrasonic humidifier was chosen to vary the moisture content of the air inside the chamber and probes were installed to measure humidity and temperature. Several wooden samples were realized ( $83 \times 83 \times 20$  mm<sup>3</sup>) made by Swedish pine, pitch pine, red fir, oak and chestnut. The models were closed inside the chamber and undergone to variable humidity,  $H$  ( $T=24$  °C). In particular, from an initial state characterized by  $H=55\%$ , the samples were located inside the chamber for 24 hours at  $H=85\%$  (humidification phase). During the first 12 hours, shape variations of the models were monitored. Afterwards, the models underwent to a dehumidification phase ( $T=24$  °C and  $H=55\%$ ) for 12 hours and the wooden surface shape was measured at a definite rate. Two parameters were chosen to be representative of the current surface characteristics: the volume difference  $\Delta V$  (a scalar quantity), that indicates the amount of volume variation, and the centroid of the volume difference  $\mathbf{G}_{\Delta V}$  (a vector quantity), that provides information regarding the direction towards which the surface is deforming (Fig. 1a-b).



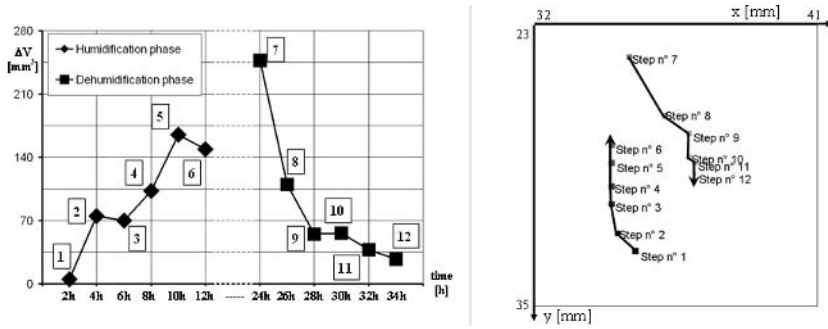


FIGURE 1. Oak experiment. a)  $\Delta V$  parameter plot; b)  $G_{\Delta V}$  parameter plot.

Preliminary experimental investigations have proven the capabilities of the optical approach in object to monitor wooden surface variations during hygrometric changes. Results showed how differently various wood species behave; all the species studied act similarly in response to a step-wise increase in humidity and almost all of them are not in equilibrium with the external environment at the end of the humidification phase (24 hours). On the contrary, the wooden species behave quite differently when undergone to a step-wise decrease in moisture content and most of them gain a stable surface configuration after just 12 hours. A new campaign of experiments is currently being carried on varying the duration of the humidification and dehumidification phases, monitoring at a higher rate the surface shape nearby the step-wise humidity change and including more wooden species.

## References

1. Dionisi Vici, P., Mazzanti, P., Uzielli, L., *J Cult Heritage*, vol. **7** (1), 37-48, 2006
2. Siau, J.F., *Wood: influence of moisture on physical properties*, Department of Wood Science and Forest Products, Virginia Polytechnic Institute, 1995
3. Schirripa Spagnolo, G., Ambrosini D. and Guattari G., *J. Opt.*, vol. **28**, 99–106, 1997
4. Ramoser H., Cambrini L., Rötzer H., In *Proceedings of SPIE, Machine Vision Applications in Industrial Inspection XIV*, vol. **6070**, 103-111, 2006
5. Sandak J., Tanaka C., *Journal of Wood Science*, vol. **51** (3), 270-273, 2005
6. D'Acquisto L., Fratini L., Siddiolo A.M., *Meas Sc Tech*, vol. **13** (4), 613-622, 2002

## SHEAROGRAPHIC DETECTION OF DELAMINATIONS IN SANDWICH STRUCTURES: INVESTIGATION ON VARIOUS EXCITATION MODES

G. Kalogiannakis<sup>1,2</sup>, B. Sarens<sup>1</sup>, D. Van Hemelrijck<sup>2</sup> and C. Glorieux<sup>1</sup>

<sup>1</sup>Laboratory of Acoustics and Thermal Physics, Katholieke Universiteit Leuven, Celestijnenlaan 200D, B3001 Heverlee, Belgium

<sup>2</sup>Department of Mechanics of Materials and Constructions, Vrije Universiteit Brussel, Pleinlaan 2, Building Kb, 1050 Brussels, Belgium

Georgios.Kalogiannakis@fys.kuleuven.be, Bart.Sarens@fys.kuleuven.be, Christ.Glorieux@fys.kuleuven.be, dvhemelr@vub.ac.be

Delaminations are a common problem that occurs between the core and the skins of sandwich structures. Such defects may originate either from malfunctions in the manufacturing process leading to a reduced adhesion strength or from certain types of load like impacts during the operation. This study was focused on the detection of such defects with the increasingly popular shearography technique (Butters and Leendertz [1]).

Shearography is based on the speckle effect, which occurs when coherent light is scattered on a rough surface. Rays from different positions on the sample surface interfere randomly in space to create a granular kind of image, with distinct intensity fluctuations called speckles. In shearography, two images of the same area on the object are simultaneously recorded laterally sheared with one another (Fig. 1). Images are recorded before and after the excitation and their difference results in a fringe pattern, which is associated with the full strain field.

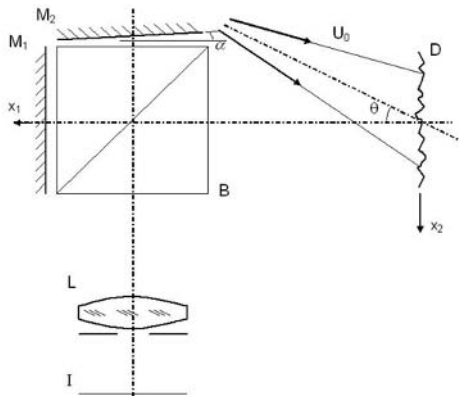


FIGURE 1. The principle of shearography.

Different excitation schemes exist, which operate in static or dynamic mode and allow the visualization of a subsurface delamination (Steinchen and Yang [2]). Vacuum and thermal excitations present more or less the same advantages with the second technique being more flexible in terms of space limitations as vacuum excitation depends on the size of the chamber or hood, which are used to perform the test. Dynamic thermal excitation or excitation with a shaker

allows to investigate the possibility of obtaining higher contrast using the nonlinear response of the defected area (Solodov et al. [3]).

In the framework of this study, we used thermal excitation by means of a powerful diode laser to apply uniform heating in static as well as dynamic mode (Fig. 2). The latter was implemented by means of an acousto-optic modulator placed in front of the diaphragm, which was used to select the 0th diffraction order. The shearography system is perfectly suited to probe the increased deformation over the delamination. In a second approach, we used a piezo-shaker to vibrate the object under investigation and essentially open and close the underlying delamination. Both of these techniques offer enhanced signal-to-noise ratio. Nonlinear approaches were further applied to enhance the contrast.

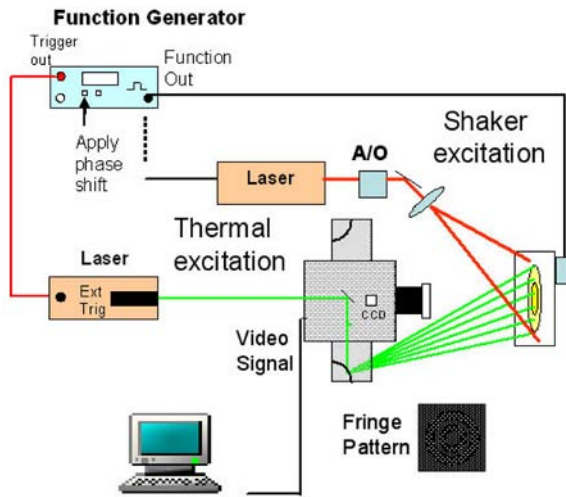


FIGURE 2. Experimental setup.

## References

1. Butters J.N. and Leendertz, J.A., *Opt. Laser Tech.*, vol. **3**, 26-30, 1971.
2. Steinchen W. and Yang L., *Digital Shearography*, SPIE, Washington, USA, 2003.
3. Solodov I.Yu., Krohn N., Busse G., *Ultrasonics*, vol. **40**, 621-625, 2002

## OBSERVATION OF FUNDAMENTAL VARIABLES OF OPTICAL TECHNIQUES IN THE NANOMETRIC RANGE

Cesar A. Sciammarella and Luciano Lamberti  
Dipartimento di Ingegneria Meccanica e Gestionale  
Politecnico di Bari, Bari, 70126 - ITALY  
Department of Mechanical, Materials and Aerospace Engineering  
Illinois Institute of Technology, Chicago IL, 60616 - USA  
csciamma@poliba.it, sciammarella@iit.edu

For a long while the so called Rayleigh limit posed severe constraints to the application of optical techniques beyond the range of  $\lambda/2$  of the wavelength of light. In 1952, Toraldo di Francia [1] pointed out that the Rayleigh limit came from historical period in which the existence of evanescent fields was not known. On the basis of the possibility of taking advantage of evanescent fields, he postulated the possibility of going beyond the Rayleigh limit practically within the limitation posed by energy one can go to much smaller fractions of the wavelength of light. In the present paper this argument is pursued both on the theoretical ground and experimental results showing the possibility of reaching  $1/20$  of the wavelength of light, the limit for eyes from the energy and the availability of sensors with enough spatial resolution. Examples of particle dimensions, analysis of the phase of grating patterns and moiré patterns (Fig. 1) are provided. The properties of the speckle fields are investigated by carrying out a statistical analysis of the experimental data.

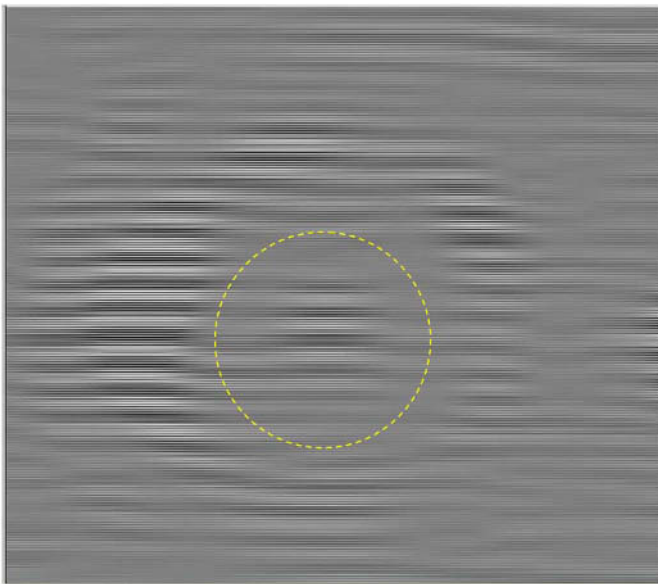


FIGURE 1. Moiré pattern produced by the presence of a spherical particle on a system of lines with 30.9 nm pitch

**References**

1. Toraldo di Francia, G., Super-gain antennas and optical resolving power. *Nuovo Cimento*, vol. **9**, 426-438, 1952
2. Mugnai, D., Ranfagni, A. and Ruggeri, R., Beyond the diffraction limit: super-resolving pupils. *Journal of Applied Physics*, vol. **95**, 2217-2222, 2004.

## PROCESSING OF A HRTEM IMAGE PATTERN TO ANALYZE AN EDGE DISLOCATION

Federico M. Sciammarella, Cesar A. Sciammarella and Luciano Lamberti  
Department of Mechanical, Materials and Aerospace Engineering  
Illinois Institute of Technology, Chicago IL, 60616 - USA  
Dipartimento di Ingegneria Meccanica e Gestionale  
Politecnico di Bari, Bari, 70126 - ITALY  
sciammarella@iit.edu, csciamma@poliba.it

Dislocations were introduced in the theory of Elasticity to evaluate the possibility of multiple values in displacement fields. The initial work was done by Volterra [1] in the 1900's who came with the basic types of dislocations that currently are used in theoretical elasticity. The argument was further elaborated by Love [2] in the 1920's. In the 1930's, dislocations re-appeared as an argument to explain the actual behavior of crystals upon deformations compared to theoretical results coming from crystalline structures [3-5]. In the 1960's, using X-rays dislocations were visualized by reconstructing X-ray diffraction patterns. However, no efforts were made to numerically or analytically evaluate the observed patterns.

In the present paper, an evaluation of the core of the dislocation is analyzed utilizing the tools of optical techniques that provide displacement and strain information (Fig. 1). Tentative explanations are given to the meaning of the obtained strain fields.

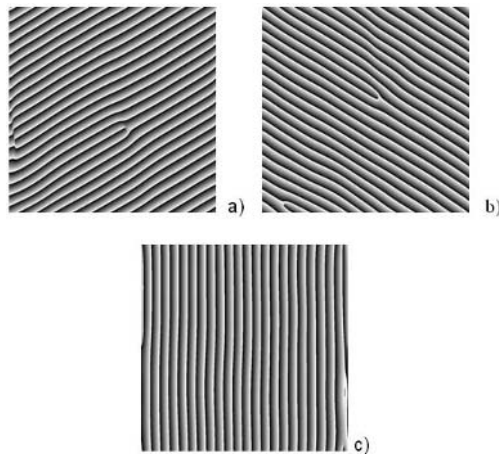


FIGURE 1. Phases of the harmonics that modulate the structure of the crystal: a)  $-60^\circ$ , b)  $+60^\circ$  and c) vertical systems

**References**

1. Volterra, *V. Ann Ec. Norm.*, vol. **24**, 1907, 401
2. Love, A.E.H. *A treatise on the mathematical theory of elasticity*, Cambridge, UK, 1927.
3. Taylor, G.I. *Proc. Roy. Soc. of London*, vol. **A145**, 1934, 362
4. Orowan, E., *Z. Phys*, vol. **89**, 1934, 634
5. Polanyi M.Z., *Z. Phys*, vol. **89**, 1934, 660

## AN APPROACH TO ERRORS INTRODUCED IN THE MESH-FREE FULL-FIELD STRAIN MEASUREMENT METHOD

A.P. Iliopoulos and N.P. Andrianopoulos  
Department of Mechanics, Faculty of Applied Sciences  
National Technical University of Athens, GR-157 73, Greece  
nandrian@central.ntua.gr

One major advantage of digital imaging is that one can measure the placement of a sampled spot in sub-pixel accuracy. This means that if the set-up has a field capable of sampling  $X$  length units per pixel, the location of any gray-level spot can be measured with accuracy of  $X/N$ , where  $N$  is a number mainly depending on the color depth, beyond the overall quality of the imaging set-up [1, 2]. The present work refers to the errors imposed by the recently introduced full-field strain measurement method [3]. Beyond systematic errors of the digital camera, the method itself is not an error-free procedure.

A not so obvious source of errors is the sub-spot displacement of each spot-center. It is assumed that the center is invariant relative to the spot boundaries. This is not exactly true in the case of large gradient of deformation. We analytically derive those errors and define the limits where it is kept in affordably low values. A solution to eliminate this systematic error is, also, proposed.

The last important source of errors is that of the mesh-free interpolation. This arises from the limited order of approximation to the field function. In general a  $k^{\text{th}}$  order approximation results in a  $(k+1)^{\text{th}}$  order of error. Because of the higher order of continuity, compared to an element discretization like this used in FEM, the interpolation error is smaller. Numerical examples are presented for both the interpolated function and its derivatives.

Finally, numerical and experimental examples are presented here to demonstrate the accuracy in various realistic applications. An example is presented in Figs 1 and 2.

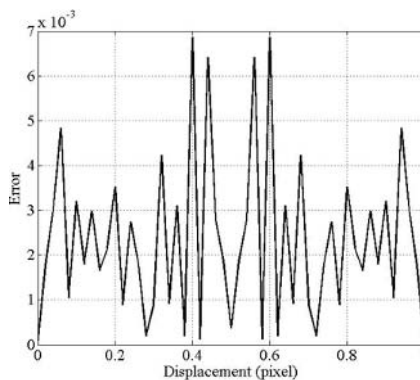


FIGURE 1. Error in displacement for a simulated simple displacement of a surface



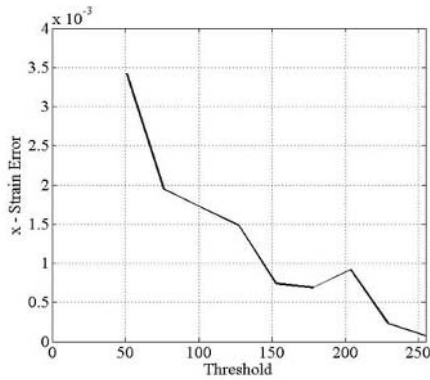


FIGURE 2. Error in strain for a simulated uniform tension of a surface

### References

1. Sevenhuijsen, P.J., The photonical pure grid method., *Opt. lasers in Eng.*, vol. **18**, 173-194, 1992
2. Schreier, H. W., Sutton, M. A., Systematic Errors in Digital Image correlation Due to Under-matched Subset Shape Functions, *Exp. Mech.*, vol. **42**(3), 303-310, 2002
3. Andrianopoulos N. P., Iliopoulos A. P., Displacements Measurement in Irregularly Bounded Plates Using Mesh Free Methods, *16th European Conference of Fracture*, Alexandroupolis, Greece, July 3-7, 2006

## NEW IMPROVEMENTS IN SHEAROGRAPHY TECHNIQUES

Hernani M. Lopes<sup>1</sup>, Mario A. Vaz<sup>2</sup>, Rui M. Guedes<sup>2</sup> and J.F. Silva Gomes<sup>2</sup>

<sup>1</sup> ESTIG - Polytechnique Institute of Braganca, Cp. St Apolonia, Apr. 134 - 5301-857 Braganca

<sup>2</sup> Faculty of Engineering, University of Porto, R Dr Roberto Frias, 4200-465 Porto, Portugal  
gmavaz@fe.up.pt

Shearography is a non-contact full field technique used in the assessment of spatial gradient of displacements through a preset direction, Hung and Taylor [1]. The optical set-up can be based on a Michelson interferometer scheme, for static or quasi-static measurements, and on the Mach-Zehnder interferometer if dynamic measurements have to be performed, Santos *et al* [2]. In both set-ups a speckle pattern, obtained from a rough surface, is laterally shifted to create the interference and the light used for the interferometer arms have a common path between the object and the set-up. So, this interferometric technique can be used with low coherence lasers and is almost insensitive to rigid body motion. The fringe patterns obtained with shearography result from the interference between two speckled wave fronts and have lower contrast that the ones obtained with specular reference interferometers.

Compact set-ups can be designed which can be used to perform measurements in industrial environments. Image processing techniques can be associated to shearography to improve data analysis and increase the measurement resolution. Phase calculation algorithms, based on temporal or spatial phase shift, are already available and the same stands for phase filtering and unwrapping. New image processing routines were developed to deal with shearography noisy patterns and extract the important information and this technique became an important tool in Non-destructive inspection (NDI) of structures.

The shearography is shown to be a very effective way of measuring the first spatial derivate of the displacements and avoids error propagation through the used of numerical methods. Recent developments in image analysis tools for processing noisy images allowed the assessment of the displacement by integration or the following derivatives by image differentiation, as can be seen in Fig. 1.

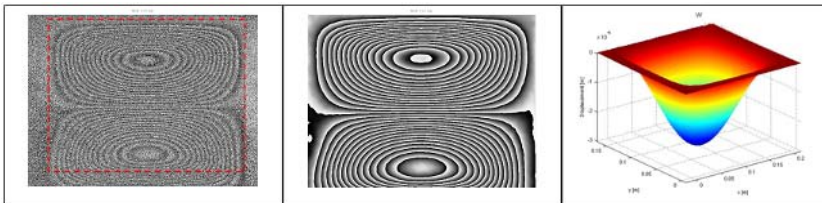


FIGURE 1. Phase-map obtained with shearography, filtered phase and the displacement field

In this work two set-ups for continuous and pulsed illumination measurements with shearography were constructed and tested. All the necessary software for image analysis was implemented and used with experimental data. Several filtering and smoothing algorithms were also tested to obtain data differentiation with good signal to noise ratios, Lopes *et al* [3][4]. Using an extra mirror in the original Michelson set-up was possible to obtain up to the third derivative.

The results obtained with optical and numerical differentiation were compared with the analytical solution as is shown in Fig. 2. The experimental data was obtained by measuring the out of plane displacement gradient of a rectangular composite plate clamped in its entire border and submitted to a uniform pressure.

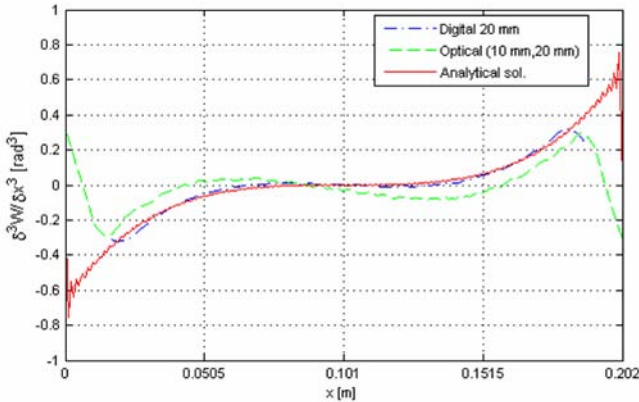


FIGURE 2. Comparison between the analytical solution and the numerical and optical differentiation, for the third displacement derivative.

## References

1. Hung, Y., Taylor, C., A tool for measurement of derivatives of surface displacement. Proc Photo-opt Instrum Eng (SPIE), vol. **41**, 169 – 175, 1973
2. Santos, F., Vaz, M.A.P., Monteiro, J., “A new set-up for pulsed digital shearography applied to defect detection in composite structures”, Optics and Lasers in Engineering, vol. **42**, 131-140, 2004
3. Lopes, H.M., Guedes, R.M., Vaz, M.A.P., *An improved mixed numerical-experimental method for stress field calculation*, Optics & Lasers Technology, vol. **39**, 1066-1073, 2007.
4. Lopes, H.M., Guedes, R.M., Vaz, M.A.P., *Techniques for numerical differentiation of experimental noisy data*, Proc. Of 5<sup>th</sup> Intern. Conf. on Mechanics and Materials in Design, Ed. J F Silva Gomes & S A Meguid, Edicoes INEGI, 27 – 28, Porto, 2006

## DYNAMIC DEFORMATION EVALUATION BY ELECTRO MOTIVE FORCE

Tetsuo Kumazawa and Noboru Nakayama

Department of Machine Intelligence and Systems Engineering, Akita Prefectural University, 84-4  
Tsuchiya-Ebinokuchi, Yurihonjyo, Akita, 015-0055, Japan  
Kumazawa@akita-pu.ac.jp

An electromotive force (Emf) was generated during metal deformation and measured with a thermocouple. Both the Emf–strain curve and stress–strain curve were obtained simultaneously in a tension test [1]. The Emf curve was correlated with the stress curve which depends on thermal change, i.e., strain energy. Therefore, this method was applied to a dynamic and an impact deformation test. Both Emf and strain were measured in a vibration test of a steel plate at first. Secondly, an impact test using a Hopkinson-Bar was conducted. Finally, the Emf data in the dynamic and impact loading range were reported.

### Measurement method of electromotive force in bending vibration

The Emf measurement method in bending vibration is shown in Fig. 1. The thermocouple used was a combination of copper (Cu) and con. (constantan, NiCu alloy). Both the copper and con. wires were 60 cm long with a 0.1mm diameter. This material combination was selected because it is a large Emf generation coupling material at room temperature [2]. These wires were bonded separately on a steel narrow plate, one end of which was fixed in a rigid block. The separation distance of the two wires was 2mm. Both ends of the thermocouple were kept at 0°C by immersing in an ice-filled vessel. A dummy thermocouple was placed near the test plate for the purpose of compensating for the Emf caused by room temperature and electric noises. The compensated Emf was amplified, displayed on the oscilloscope and recorded on a personal computer. A strain gauge was mounted at the same position as the thermocouple on the plate. The strain generated was also amplified and recorded.

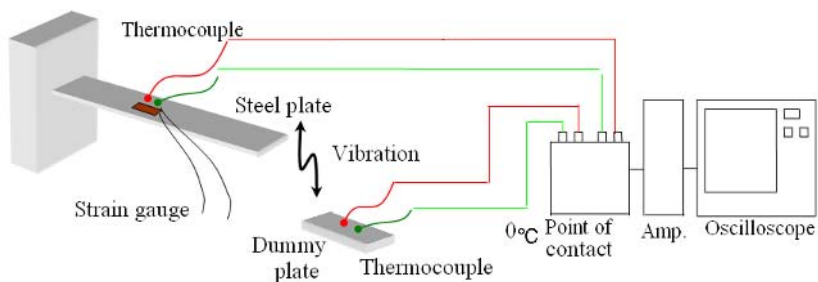


FIGURE 1. Arrangement of electromotive force measurement by thermocouples measurement at tension

### Electromotive force and strain in bending vibration

The steel plate was bent at first and unloaded suddenly, which caused vibration. The plate surface was tensioned and compressed alternatively by the vibration. Both Emf and strain were recorded, while the plate vibration was being dampened and this is shown in Fig. 2. It was clear that the Emf was generated during the dynamic deformation and could be detected as a strain pattern. The Emf increased when the strain decreased and vice versa. The Emf value was proportional to the strain, even though the data showed a small fraction value in Fig. 3 and were expressed as follows:

$$\text{Emf} / \varepsilon \cong -(0,005) (\text{mV})100(\mu\varepsilon)$$

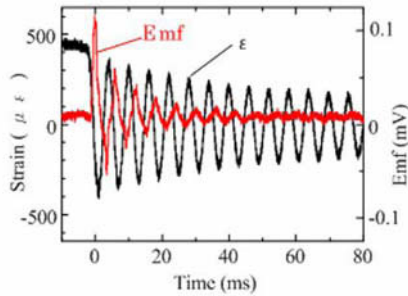


FIGURE 2. Strain and Emf curves at repeating of tension-compression loading

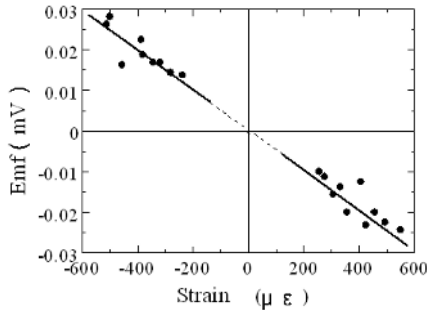


FIGURE 3. Relationship between elastic strain and Emf

Furthermore, the Emf was investigated in the stress wave propagation by using a Hopkinson-Bar. The Emf pattern was measured as a strain pattern obtained by the strain-gauge method.

### References

1. Tetsuo Kumazawa and Noboru Nakayama, *Advances in Experimental Mechanics*, MacGraw-Hill, Milano, pp. 611-612, 2004.
2. Scientific Tables, Maruzen Co., Ltd., Tokyo, 2002.

## MODERN SITUATION IN PHOTOACOUSTIC AND THERMOELASTIC STRESS ANALYSIS IN APPLICATION TO THE PROBLEM OF MECHANICAL STRESS MEASUREMENTS

K.L. Muratkov and A.L. Glazov  
Physical-Technical Institute of RAS  
194021, St.Petersburg, Russia  
klm.holo@mail.ioffe.ru

The performance of any component to a great extent is determined by residual stress, resulting from virtually all manufacturing processes. Therefore the problem of residual stress detection and measurement is urgent in modern engineering, mechanics and material physics. A good deal of effort has been undertaken in developing different methods for the residual stress detection. Optical, ultrasonic, magnetic methods, Raman spectroscopy, X-ray and neutron diffraction are effectively applied for detection of residual stresses in many cases. Thermoelastic stress analysis (TSA) is also now a well-known experimental technique (Pitarresi and Patterson [1]) providing information on the surface stress fields in structures. Two common systems based on TSA are developed at present. Stress pattern analysis by measurement of thermal emission (SPATE) has a single detector, while DELTATHERM<sup>®</sup> systems have a staring array of detectors. These techniques have been already implemented effectively for the residual stress detection. It was experimentally demonstrated that mechanical stresses modify the thermal emission signal. Hole drilling and compliance methods are also actively investigated at present for residual stress detection. Recently holographic or speckle interferometry in conjunction the hole-drilling method has attracted serious attention for solution of this problem. Unfortunately, as a rule many of these methods have limited fields of application. For example, Raman spectroscopy is mainly used in science and technology of semiconductors for which the phonon lines have a relatively simple structure and their shifts with stress are well known. SPATE, DELTATHERM<sup>®</sup> and holographic interferometry are of more general applicability, but have comparatively low spatial resolution.

From this viewpoint photoacoustic (PA) methods are attractive for modern diagnostics and imaging of the near surface structures. The PA methods have micrometer resolution, are non-destructive and appeared to be useful for detection of cracks and voids, delaminations and possible second phase material inclusions in the near surface layer of objects. Nevertheless, applications of the PA method for residual stress detection are not widely accepted yet. This situation, in our opinion, is primarily due to the lack of in-depth systematic studies of the PA effect in solids with residual stress including direct connection between residual stress and the PA signal. Accounting this fact we have performed systematical experimental and theoretical investigation of the PA effect in stressed solids (Muratkov *et al* [2-5]).

The main purpose of this work is to compare theoretical foundations of TSA and PA stress analysis.

To consider the theoretical foundation of the PA approach to the problem of residual stress detection we use the modern theory of thermoelasticity of elastic solids. By introducing in the explicit form the thermoelastic parameter in the system of thermoelastic equations instead of the coefficient of linear expansion one can get

$$\nabla^2 T - \frac{1}{\kappa} \dot{T} - T_0 \frac{3\lambda + 2\mu}{\lambda_T} \rho C_\epsilon K_\epsilon \operatorname{div} \dot{u} = - \frac{Q}{\lambda_T} \quad 1a$$

$$\rho \ddot{\bar{u}} = \mu \nabla^2 \bar{u} + (\lambda + \mu) \text{grad div } \bar{u} - (3\lambda + 2\mu) \rho C_\varepsilon K_\varepsilon \text{grad} T \quad 1b$$

where  $T$  is the temperature of the body,  $T_0$  is the environmental temperature,  $\bar{u}$  denotes deformations of the body,  $Q$  is the heat produced in the body by external sources,  $\lambda$  and  $\mu$  are Lamé's elastic constants,  $\lambda_T$  and  $\kappa$  are thermal conductivity and diffusivity,  $\rho$  and  $C_\varepsilon$  are the density and specific heat of the body, respectively; the ratio  $K_\varepsilon = \alpha_T / \rho C_\varepsilon$  is the thermoelastic parameter of the material and  $\alpha_T$  is the coefficient of linear expansion.

The system of Eqs.(1a) and (1b) involves the so called thermoelastic parameter which depends on stress [1]. Using this system, a comparative analysis of TSA and PA techniques was performed. It is shown that both the PA and TSA use the same dependence of the thermoelastic parameter on stress and, thus, have very close physical foundations.

Another important purpose of the work is to gather the most important recent experimental results demonstrating modern situation in the field of PA detection and imaging of residual stresses. The work presents some new experimental results in this field demonstrating the influence of external stresses on PA images of Vickers indented ceramics and metals including nanonickel and nanocopper. The influence of machining stresses on PA images of ceramics is also demonstrated. The presented results show some possible PA microscopy applications for residual stress detection.

It is shown also that advantage of the PA microscopy over modern TSA techniques consists first of all in a higher spatial resolution (up to a micrometer scale).

This work was partially supported by Russian Foundation for Basic Research under Grant No.06-02-17148.

## References

1. Pitarresi, G. and Patterson, E.A., *J. Strain Analysis*, vol. **38**, 405-417, 2003
2. Muratikov, K.L. *et al*, *Tech. Phys. Lett.*, vol. **23**, 3, 188-190, 1997
3. Muratikov, K.L. *et al*, *J. Appl. Phys.*, vol. **88**, 5, 2948-2955, 2000
4. Muratikov, K.L. *et al*, *Rev. Sci. Instrum.* vol. **74**, 7, 3531-3535, 2003
5. Muratikov, K.L. and Glazov, A.L., *Mat. Sci. Forum*, vols. **524-525**, 471-476, 2006

## DERIVATION OF UNIAXIAL STRESS-STRAIN CURVES FOR CAST IRON FROM SAMPLES TESTED IN FLEXURE

D.A. Jesson<sup>1</sup>, H. Mohebbi<sup>1</sup>, H.M.S. Belmonte<sup>2</sup>, M.J. Mulheron<sup>1</sup> and P.A. Smith<sup>1</sup>

<sup>1</sup>School of Engineering, University of Surrey, Guildford, Surrey, GU2 7XH, United Kingdom

<sup>2</sup>Thames Water Plc.

d.jesson@surrey.ac.uk

Cast iron is a material that still has significant usage in the water industry. Although cast iron pipes, both distribution and trunk mains, are being phased out, a significant portion of current pipe networks are still comprised of the aging cast iron infrastructure that can be 50 to 150 years old. The cast iron pipes display a range of microstructures which, unsurprisingly, is related to their manufacturing process (pit cast and spun cast). Since it is prohibitively expensive, time consuming and too disruptive to replace this infrastructure in one programme of work, it is necessary to understand the properties of the remaining pipes so that replacement work can be focused in the first instance on areas of critical importance (Rajani and Makar [1]).

Previous work has examined several aspects of the in-service conditions of distribution cast iron water pipes (Atkinson *et al* [2] and Belmonte *et al* [3]).

In the current research, Weibull methods have been used to assess the condition of mains water pipes from three locations in the London area. This has been linked to a study of the microstructure of the pipes. Further, a method developed by Crocombe *et al* [4] has been applied to test data derived from four-point bend (4PB) tests of cast iron samples. This method allows uniaxial stress-strain curves to be derived from strain measurements taken during the 4PB test. In this method the stress is considered in incremental quantities, such that the maximum stress is equal to the maximum stress of the previous increment, which will now be observed at a distance  $\omega$  from the surface plus the stress observed between  $\omega$  and the surface. Both tension and compression curves can be derived using equations 1 and 2 in which a typographical error in the original paper has been corrected.

$$\sigma_{t(i)} = \frac{M_i - M_{i-1} \left[ 1 - \frac{\omega_{t(i)} + \omega_{c(i)}}{t} \right]^2 - \sigma_{t(i-1)} \omega_{t(i)} \left[ \frac{t}{2} - \frac{\omega_{t(i)}}{3} - \frac{\omega_{c(i)}}{6} \right] + \sigma_{t(i-1)} \frac{\omega_{c(i)}^2}{6}}{\frac{\omega_{t(i)}}{2} \left[ t - \frac{\omega_{t(i)} + \omega_{c(i)}}{3} \right]} \quad (1)$$

$$\sigma_{c(i)} = \frac{-1}{\omega_{c(i)}} \left[ \sigma_{t(i-1)} \omega_{t(i)} + \sigma_{c(i-1)} \omega_{c(i)} + \sigma_{t(i)} \omega_{t(i)} \right] \quad (2)$$

Where  $\sigma$  is a stress,  $M$  a bending moment,  $t$  the thickness of the specimen and  $\omega$  is a region of undefined material. The subscripts  $t$  and  $c$  refer to tension and compression respectively, whilst  $i$  relates to the current increment.

Fig. 1 compares the raw data taken from the tension and compression faces of the strain-gauged specimen with the tension and compression data derived from equations 1 and 2. Each data point of the derived curves is the result of averaging ten data points prior to the calculations. This is a necessary step since otherwise the curve oscillates over a significant range. This provides a balance between smoothing, whilst still allowing for a realistic interpretation of the data. As might be expected there is a difference between the experimental flexure stress-strain curves and



the derived uniaxial stress-strain curves which is consistent with the movement of the neutral-axis which occurs in materials with differing properties in tension and compression. Further, the uniaxial stress-strain curves are consistent with data reported for cast irons by Walton and Opar [5].

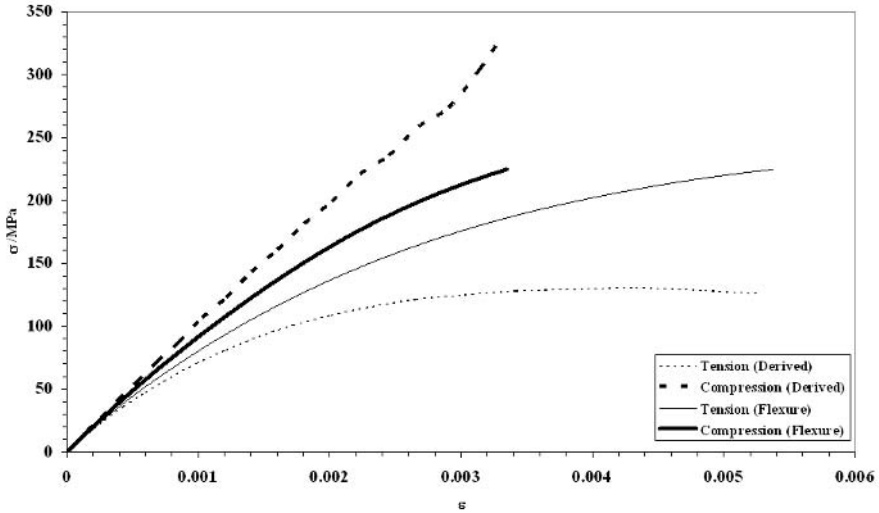


FIGURE 1. Stress-strain data for a specimen tested in four point bending, compared with derived uniaxial data.

## References

1. Rajani, B. and Makar, J., "A methodology to estimate remaining service life of grey cast iron water mains", *Canadian Journal of Civil Engineering*, Vol. **27** [2000], 1259-1272.
2. Atkinson, K., Whiter, J.T., Smith, P.A. and Mulheron, M., "Failure of small diameter water pipes", *Urban Water*, Vol. **4** [2002], 263-271.
3. Belmonte, H., Mulheron, M. and Smith, P.A., *Evaluation of a failure hypothesis for small diameter cast iron water distribution pipes*, [2004], Thames Water Plc.
4. Crocombe, A.D., Richardson, G. and Smith, P.A., "Measuring Hydro-Static Dependent Constitutive Behaviour of Adhesives Using a Bend Specimen", *Journal of Adhesion*, Vol. **42** [1993], 209-223.
5. Walton, C.F., *Iron castings handbook : covering data on Gray, Malleable, Ductile, White, Alloy and compacted graphite irons*. [1981]: Iron Castings Society Inc.

## ELECTROMECHANICAL RESPONSE OF LARGE STRAIN FERROELECTRIC ACTUATORS

Doron Shilo, Amir Mendelovich and Haika Drezner  
Department of Mechanical Engineering, Israel Institute of Technology  
Department of Mechanical Engineering, Technion, Haifa 32000, Israel  
shilo@tx.technion.ac.il

One of the desired properties of actuators is large actuation strains, which also correlates to a large amount of work per volume. This property becomes especially important in Micro Electro Mechanical Systems (MEMS) where small devices are required to produce relatively large strokes (displacements). The existing mechanisms for electromechanical actuation, such as those based on electrostatic interaction or piezoelectric response, are limited to small actuation strains (up to 0.15% in the piezoelectric materials) and hence recent years have seen a variety of attempts at achieving larger strain actuation. One such attempt considered the 90° domain switching in single crystals of BaTiO<sub>3</sub> has recently been experimentally demonstrated by Burcsu *et al.* [1].

Burcsu *et al.* [1] obtained up to 0.9% strain in (001)BaTiO<sub>3</sub> single crystals which were subjected to constant uniaxial compression load and cyclic electric field. Since at room temperature BaTiO<sub>3</sub> is spontaneously polarized in the <100> directions, at zero applied voltage the applied stress forces the polarization to be in-plane (e.g., the [010] direction). As the voltage is increased, the electric field tries to align the polarization along the out-of-plane direction (i.e. the [001] direction), but this is resisted by the stress. There is an exchange of stability at a critical voltage and the polarization switches to [001]. The strain which is accompanied to the described process can be up to 1.1% in BaTiO<sub>3</sub> and up to 6.5% in PbTiO<sub>3</sub>. Finally, as the voltage is decreased, the polarization reverts back to in plane, recovering the strain. Thus, cyclic actuation is obtained.

Before implementing the 90° domain switching in real actuators two questions must be answered-

- 1 What is the frequency limit for this actuation process (the previous experiments were done at very low frequencies)?
- 2 Is it possible to significantly diminish the reported fatigue (a decrease of actuation strains with time of operation) and mechanical damage?

In order to answer these questions we developed an experimental setup which allows performing dynamic experiments at high frequencies and avoid two of the main sources for fatigue and mechanical damage in Burcsu's experiment. In our setup (Fig. 1), the in-plane polarization is reverted by a uniaxial tensile stress instead of the compressive stress at Burcsu's experiment. This loading geometry avoids the friction forces at the crystal surfaces, which were found to cause a significant mechanical damage in previous experiments (Shilo *et al.* [2]).

The overall dimensions of the actuator in Fig. 1 are about 25 mm and hence it allows performing dynamic experiments with frequencies of up to 100 kHz. Moreover, its small dimensions allow mounting it under a vibrometer for measuring the displacements and under a polarized optical microscope for *in-situ* visualization of domain switching. The constant load is applied by a pair of small permanent magnets and hence the response time is determined by the speed of light.

Fig. 2 shows a typical curve of the strains as a function of electric field (butterfly curve).

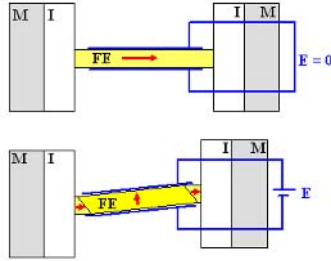


FIGURE 1. Illustration of the experimental setup. A ferroelectric single crystal (indicated by 'FE') is subjected to cyclic electric field and constant tensile load applied by a pair of magnets (indicated by 'M'). The ferroelectric crystal is connected to the magnets through insulating plates (indicated by 'I') to prevent short-circuiting. The polarization is indicated by arrows.

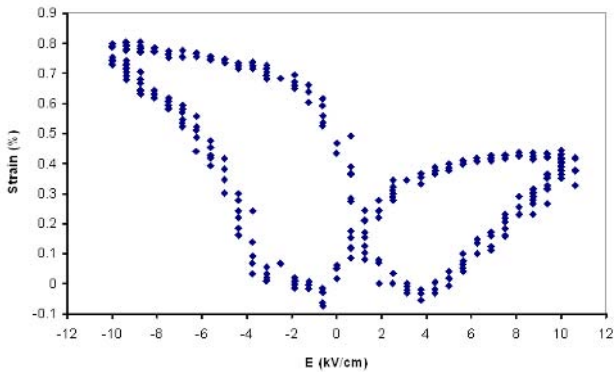


FIGURE 2. A Typical experimental result.

## References

1. Burcu, E., Ravichandran, G., Bhattacharya, K., *Appl. Phys. Lett.*, vol. 77, 1698–1700, 2000.
2. Shilo, D., Burcu, E., Ravichandran, G., Bhattacharya, K., *Int. J. Solids and Structures* (In Press).

## TESTING SYSTEM FOR FERROMAGNETIC SHAPE MEMORY MICRO-ACTUATORS

Y. Ganor<sup>1</sup>, D. Shilo<sup>1</sup>, J. Messier<sup>2</sup>, T.W. Shield<sup>2</sup> and R.D. James<sup>2</sup>

<sup>1</sup> Department of Mechanical Engineering, Israel Institute of Technology – IIT, Technion, Haifa 32000, Israel

<sup>2</sup> Department of Aerospace Engineering and Mechanics, University of Minnesota, Minneapolis, Minnesota 55455, U.S.A.  
yanivg@tx.technion.ac.il

Materials that alter their physical properties in response to environmental changes are classified as active materials. These materials are commonly applied as actuation devices in micro-electro mechanical systems. Many of these systems require an application of large strokes by a small component, which means large actuation strains. However, existing active materials are either limited to very small strains, as piezoelectric and magnetostrictive materials, or to a slow response, as shape memory alloys. Therefore, materials that can provide significantly increased strain levels and fast response times are of great interest. The concept of combining properties of ferromagnetism with those of reversible martensitic transformation led to a new class of active materials known as ferromagnetic shape-memory (FSM) alloys (James and Wuttig [1]). It was theorized that a mobile microstructure of martensite could be rearranged by applying a magnetic field, and reset by applying a stress or a field in a different direction. FSM alloys combine the large strain capability of ordinary shape memory alloys with the quick actuation possible using magnetic fields (Shield [2]). FSM alloys are therefore very promising for actuation applications at both large and small scales, and embody a new mechanism for converting electromagnetic to mechanical energy. However, to date, micro FSM alloy devices are not yet available in spite of their great potential in aerospace and medical instruments.

The present study focuses on a new experimental system developed to explore the magneto-mechanical characteristics of micro-scale ferromagnetic shape memory actuators. It combines an alternating magnetic field generator (AMFG) (Fig. 1a) and a mechanical apparatus (Fig. 2a). The AMFG generates spatially-changing dynamic magnetic field with amplitude of approximately 1Tesla. The field alternates between two orthogonal directions in a manner that was designed to facilitate variant switching, yet prevent nucleation of 180° magnetization domains, which cause energy loss without strain production. The mechanical apparatus maintains a constant mechanical load with a sensitivity of less than 1 $\mu$ N by means of a cantilever beam. The specimen displacement is optically monitored with a resolution of approximately 0.1 $\mu$ m. Further, the specimen temperature is controlled and the surface is observed microscopically.

Additionally, to analyze the experimental results, an analytical model utilizing the Karush-Kuhn-Tucker (KKT) theorem for quadratic programming was developed. A suitable micro-magnetic energy functional which includes the effects of applied magnetic fields and mechanical loads is minimized from within a constrained space of possible deformations and magnetizations. The solution describes the evolution of the net magnetizations in the magnetic fields and stress volume. As typical of quadratic programming problems, the nature of the solution changes at critical values of the applied fields and stresses. It shows that the solution moves from multi-variant to single variant states at certain field and stress combinations determined by the material constants. The results can help to design and predict the behavior of FSM actuators.

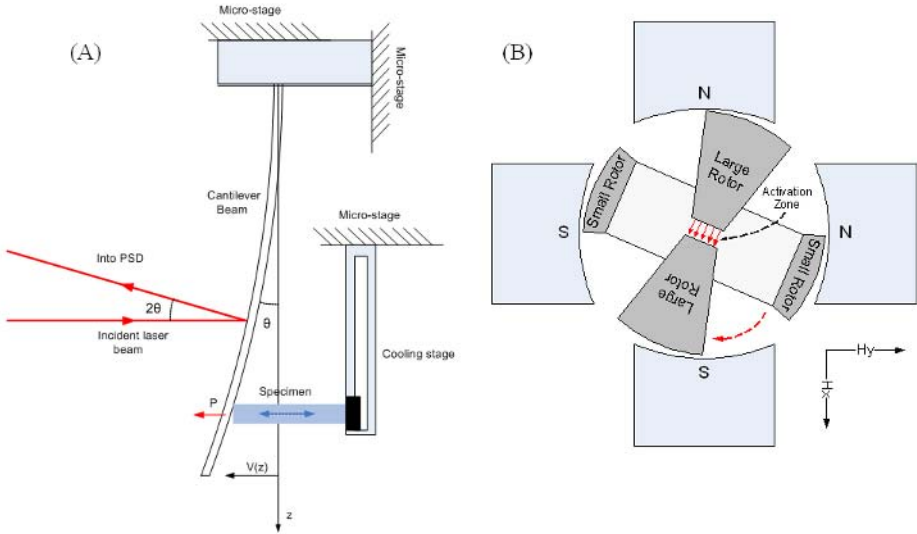


FIGURE 1. (A) Schematic close-up view of the mechanical testing system positioned perpendicularly to the activation zone. (B) The Alternating Magnetic Field Generator (AMFG) generates magnetic field that alternates between two orthogonal directions  $H_x$ ,  $H_y$ .

Preliminary experiments were performed using  $\text{Ni}_2\text{MnGa}$  specimens with typical cross section of  $200\text{m} \times 200\text{m}$ . The results were in agreement with the theoretical simulations and showed feasibility towards their implementation as micro-mechanical devices.

## References

1. James R.D. and Wuttig M., *Philosophical magazine A*, vol. **77**(5), 1273-1299, 1998
2. Shield T.W., *Rev. Sci. Instrum.*, vol. **74**(9), 4077-4088, 2003

## BUCKLING CONTROL OF GLASS/EPOXY COMPOSITE COLUMNS WITH PZT ACTUATORS

R. Mini<sup>a</sup>, C. Lakshmana Rao<sup>a,b</sup> and S.M. Sivakumar<sup>a,b</sup>

<sup>a</sup> Department of Civil Engineering, IIT Madras, Chennai 600 036. India

<sup>b</sup> Department of Applied Mechanics, IIT Madras, Chennai 600 036. India  
miniremanan@yahoo.co.in, lakshman@iitm.ac.in, mssiva@iitm.ac.in

The buckling of compressively-loaded members is one of the most important factors limiting the overall strength and stability of a structure. In many cases, especially in aerospace applications, it may be more beneficial and sometimes absolutely necessary to resort to active methods to enhance the buckling load of slender structures. Active control can increase the load carrying capacity of a structure and piezoelectric materials are good actuators to provide this active control. In literature, Thomas Bailey and James E. Hubbard [1] have reported that distributed piezoelectric polymers bonded on the surface of the structure can be used to control the vibration of a cantilever beam. Mini *et.al* [2] have demonstrated a 11% increase in the load carrying capacity of aluminium column strips by the application of 100V to the piezoceramic actuator. An exact theoretical analysis of their experiments was carried out introducing an equivalent imperfection to the column and it gave the same results. Thomson and Loughlan [3] have carried out experiments on composite column strips fabricated from commercially available carbon-epoxy pre-impregnated sheets and have demonstrated that an increase in load carrying capability of the order of about 20% to 37% is possible in slender columns. Rao and Singh [4] have proposed an enhancement of buckling load of a column by introducing a follower force paradigm and have shown that there is theoretically a possibility of increasing the buckling load by a factor of up to 3.5 in the case of a uniform cantilever column.

This paper describes an experimental investigation into the effect of piezoelectric force on active control of glass/epoxy composite columns under an axial-compressive loading. The tests were conducted on three column specimens. The glass fibre used was E-glass WRM (Woven Roving Mat) of aerial density density 610gsm. The composites consisting of 4 plies were prepared by hand lay-up technique. LY556 Araldite was used as the epoxy matrix and HY951 as the corresponding hardener. After fabrication of columns, piezoceramic actuators were surface bonded at their mid-heights. Sensing was carried out using a pair of strain gauges which were connected in half bridge circuit to a strain gauge amplifier. Tests were conducted using a single PZT and also using two PZT's on both sides of the column. Experiments were initially conducted for four different voltages, 50, 100, 150 and 200 and the load strain plots were obtained for each case. The voltage was supplied by a high voltage DC supply. The experiments were conducted on the experimental setup which was specifically developed for this investigation. The loading frame is shown in Fig. 1. The column was placed in between the platforms of the loading frame such that it simulated hinged supports. A novel way of smoothly increasing the applied compressive load was adopted. The load was applied by allowing water to flow through a small tube, into a container which was placed on the loading platform.

The experiments were also conducted with active control on composite columns. In active control, the signal from the strain gauges was transmitted to the controller. The controller was implemented using a programmable computer equipped with analogue-to-digital and digital-to-analogue interface cards that allows it to sense and respond to the column motion in real time. When the controller detects out of plane deformations, it determines the appropriate voltage required to counteract the bending motion. A simple proportional control strategy was adopted for

the closed loop control. The command voltage was sent to a high voltage amplifier to provide the voltage necessary to drive the piezoelectric actuators surface bonded to the member. The test procedure is outlined and load strain plots, obtained with and without control are presented. It is shown that the buckling of the column can be postponed beyond the first critical load by means of feedback using piezoelectric actuators and strain gauge sensors. The columns with active control are shown to clearly demonstrate an increase in axial compressive load carrying capacity compared to those without control. The experimental results were closely matching with the theoretical predictions.

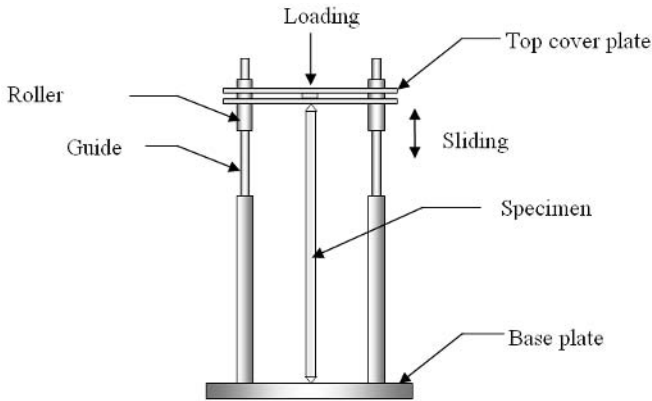


FIGURE 1. Experimental setup

## References

1. Bailey, and J. E. Hubbard, Distributed Piezoelectric-Polymer Active Vibration Control of a Cantilever Beam, *Journal of Guidance, Control, and Dynamics*, vol. **8**, 605-611, 1985.
2. R. Mini, R.P. Indira, S.M. Sivakumar and C. Lakshmana Rao, Buckling Control of Rectangular Columns with PZT Actuators, In *Proceedings of the Fourth International Conference on Smart Materials, Structures and Systems*, edited by R.V Krishnan, Ramesh Sundaram and G. M. Kamath, Precision Fototype Services, Bangalore, 2005, SA156 – SA162.
3. S. P. Thompson, and J. Loughlan, The Active Buckling Control of Some Composite Column Strips Using Piezoelectric Actuators, *Composite Structures*, vol. **32**, 59-67, 1995.
4. G. Venkateswara Rao, and A. Gajbir Singh, A Smart Structures Concept for the Buckling Load Enhancement of Columns, *Smart Materials and Structures*, vol. **10**, 843-845, 2001.

## ENHANCEMENT OF BUCKLING LOAD OF THIN PLATES USING PIEZOELECTRIC ACTUATORS

R. Indira Priyadarshini<sup>a</sup>, C. Lakshmana Rao<sup>ab</sup> and S.M. Siva Kumar<sup>ab</sup>

a) Department of Applied Mechanics, IIT-Madras, Chennai-600 036. India

b) Department of Civil Engineering IIT-Madras, Chennai-600 036. India

priyadarshini@iitm.ac.in, lakshman@iitm.ac.in, mssiva@iitm.ac.in

Thin plates which are used in most aeronautical and aircraft structures are often subjected to form failures called buckling. Certain passive techniques such as adding stiffeners increase the buckling load, as well increases the weight of the system. Aesthetic considerations and limited availability of space and weight restrict the use of stiffeners. Hence it is necessary to resort to certain active control techniques such as usage of smart materials to control the deflections under operation. Several researchers have used PZT actuators for vibration control of columns. Bailey and Hubbard [1] used Distributed piezoelectric-polymer (PVDF) films as actuators for vibration control of columns. Thompson and Loughlan [2] have experimentally shown that PZT actuators enhance the buckling load of a composite column by 37%. Mini et al [4] have conducted experiments on aluminum columns and found increase in the initial buckling load by 11%.

From the experience gained by the column experiments, an attempt is made to look at the effect of PZT actuators on buckling load of two dimensional structures such as plates Experiments have been conducted on a rectangular aluminum plate of size length 0.5m, width 0.3m and thickness 0.001m with two edges simply supported and other two opposite edges free. The initial buckling load of this plate is compared with the numerical analysis. Unlike columns, plate have post buckling strength the initial buckling load and the failure load are different, so a plate can be loaded beyond the initial buckling load. According to the initial mode shape of the plate, the location and the shape of the PZT actuators is optimized. The initial mode shape looks like a half sine wave, so the PZT patches are chosen to be rectangular and the location of the PZT patches is optimized.

The experiment setup is exclusively designed and fabricated for loading slender structures. The plate is held in between the two platforms such that the loading edges simulated hinged support. The top platform is allowed to slide in the loading direction. Water is drawn from the source to the container on the loading platform. A load cell is placed at the bottom of the plate to measure the load that is applied on the plate. Maximum displacement is observed at the center of the plate, so the strain gauges are pasted on either sides of the plate where the maximum displacement is observed. The four leads of the strain gauge are connected to half bridge circuit of the strain gauge amplifier where the bending strain is measured. The measured strain is interfaced to the computer with Analog to Digital converter card (ADC). Counteracting force on the plate is applied through actuating PZT patches with appropriate gain factor. This counteracting force acts in such a way that it reduces the bending strain. Initially open loop experiments are carried out, to analyze the effect of voltage on the plate. The control voltage was supplied by a high voltage dc source separately. Experiments are conducted by applying 100, 200 and 300 voltages to the PZT patches. The voltages are first applied to the PZT patches and then allowed to stabilize, later load is applied on the plate.



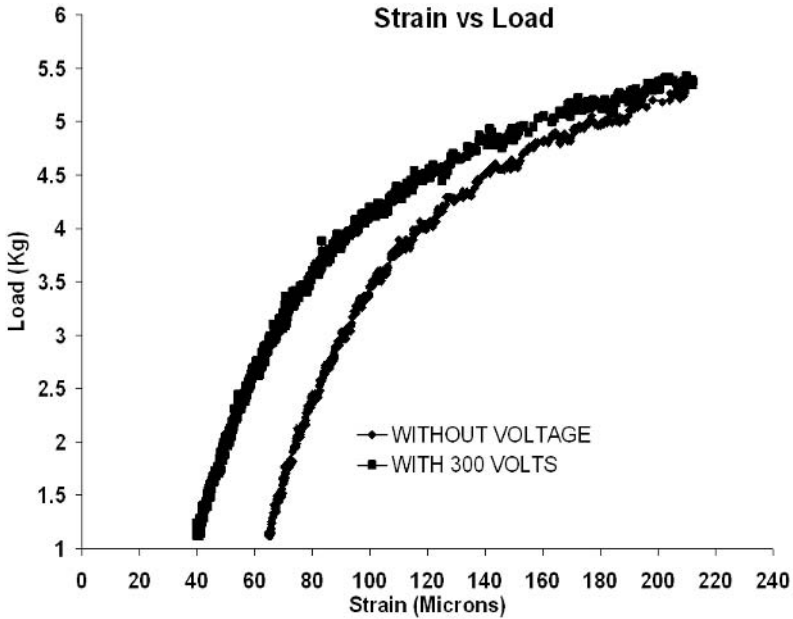


FIGURE.1 Graph showing the affect of voltage on the plate

Experiments are initially conducted on the plate without supplying voltage to PZT patches later 300 volts is applied on the PZT patches. The variation of strain with respect to loading is as shown in the graph. Fig. 1 clearly demonstrates the ability of passively actuated PZT, in enhancing the buckling characteristics of a plate.

## References

1. T. Bailey, and J. E. Hubbard, "Distributed piezoelectric-polymer active vibration control of a cantilever beam", *Journal of Guidance, Control, and Dynamics*, vol. 8(5), pp. 605-611, 1985.
2. S. P. Thompson, and J. Loughlan, "The active buckling control of some composite column strips using piezoelectric actuators", *Composite Structures*, pp. 59-67, 1995.
3. S. P. Timoshenko, and J. M. Gere, "Theory of Elastic Stability", McGraw-Hill, New York, 1961.
4. R.Mini, R.P.Indira, C.Lakshmana Rao, S.M.Sivakumar,"Buckling Control of Rectangular Columns with PZT Actuators", *International Conference on Smart Materials Structures and Systems* July 28-30-2005.

## INVESTIGATION OF TWIN-WALL STRUCTURE AT THE NANOMETER SCALE USING ATOMIC FORCE MICROSCOPY

Doron Shilo<sup>1</sup>, Guruswami Ravichandran<sup>2</sup> and Kaushik Bhattacharya<sup>2</sup>

<sup>1</sup>) Department of Mechanical Engineering, Israel Institute of Technology – IIT  
Technion, Haifa 32000, Israel

<sup>2</sup>) Division of Engineering and Applied Science, California Institute of Technology  
Pasadena, California 91125, U.S.A.  
shilo@tx.technion.ac.il

The structure of twin-walls and their interaction with defects has important implications for the behavior of a variety of materials including ferroelectric, ferroelastic, and co-elastic crystals. One unique characteristic of such crystals is that their physical properties as well as their macroscopic response to electrical, mechanical, and optical loads are strongly related to their microstructural twin patterns. These, in turn, are governed by the atomistic and mesoscale structure of twin-walls and their interaction with other crystal defects.

The structural parameter that determines most of the properties of twin walls is their thickness, which relates to the region around the wall in which the strains (and polarization in ferroelectrics) are changed from the values of one twin variant to the values of another. The wall thickness is directly related to the energy of the wall and its measurement can serve for the evaluation of the later (see e.g. Salje [1]). Moreover, it was shown by Lee *et al.* [2] that the wall thickness is also related to the activation energy for twin wall motion and hence it determines the mobility of twin walls.

Despite the important role of twin walls, their structure and properties are still ambiguous as they can be quite narrow, in the nanometer scale, in many materials of interest. Many experimental techniques are capable of imaging twin patterns, but it is much more difficult to image the twin walls with an accuracy that allows studying their structure. We present a new method for investigating the structure of twin-walls with nanometer-scale resolution.

In this method (Shilo *et al.* [3]), the surface topography measured using atomic force microscopy (AFM) is compared with theoretical solutions of the displacement field, and this allows for the determination of the twin-wall thickness and other structural features. For example, a typical AFM image, which was taken from a vicinity of a twin wall, and its best-fit simulation, are shown in Fig. 1. Moreover, analysis of both complete area images and individual line-scan profiles provides essential information about local mechanisms of twin-wall broadening, which cannot be obtained by other experimental methods.

The method is demonstrated in the ferroelectric crystal  $\text{PbTiO}_3$  and the shape memory alloy  $\text{CuAlNi}$ . Both materials exhibit twin-wall thickness of few nanometers. Further, it is shown that accumulation of point defects in  $\text{PbTiO}_3$  is responsible for significant broadening of the twin-walls. Such defects are of interest because they contribute to the twin-wall kinetics and hysteresis.

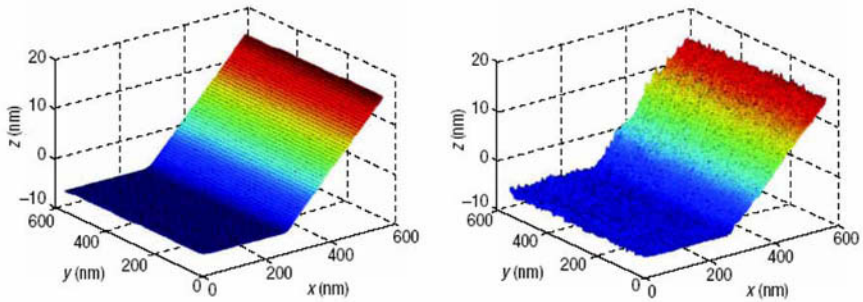


FIGURE 1. AFM image (a) and its best-fit simulation (b) taken from a vicinity of an individual twin wall in a  $\text{PbTiO}_3$  crystal.

## References

1. Salje, E. K. H., *Phase Transition in Ferroelastic and Co-Elastic Crystals*, Cambridge University Press, Cambridge, UK, 1990.
2. Lee, W. T. et al., *Phys. Rev. B*, vol **73**, 214110, 2006.
3. Shilo, D., Ravichandran, G. and Bhattacharya, K., *Nature Mater.*, vol. **3**, 453-457, 2004.

## DESIGN CONSTRUCTION AND TESTING OF A SMART ACTUATED HELICOPTER BLADE

J. Monreal<sup>1</sup>, G. Giannopoulos<sup>1</sup>, F. Santafe<sup>1</sup>, J. Vantomme<sup>1</sup>, F. Buyschaert<sup>1</sup> and P. Hendrick<sup>2</sup>

<sup>1</sup> Royal Military Academy, Civil and Materials Engineering Department,  
Av. de la Renaissance 30, B-1000, Brussels, Belgium

<sup>2</sup> ULB, Service of Fluid Mechanics, Av. F.D. Roosevelt, 50, B-1050 Brussels, Belgium  
javier.monreal@rma.ac.be, giorgos.giannopoulos@rma.ac.be

Researchers have only recently addressed the issue of using smart materials and especially piezoelectrics for (aero)mechanical applications. The inherent drawback of piezoelectrics, is that they only provide small displacements, resulting in the undeserved negligence of their potential use in aeronautical structures. Fortunately, nowadays a number of technologies, using smart structures, have been developed coping partially with this difficulty. But in spite of this progress, there is still a significant amount of challenges to face.

Helicopters constitute one of the aeronautical domains that could benefit a lot from the use of smart materials. Hereby, rotor and blade design can profit most of this technology since the application of smart materials can improve aerodynamic performance as well as reduce noise and vibration. Most of the research done on using piezoelectrics in helicopter blades is focused on the IBC (Independent Blade Control) technique. An example of this work is the one of Büter et al. [1]. In this work the blade tip is equipped with an internal piezoelectric actuator that actuates in twisting the blade tip due to the tension torsion coupling of this part of the blade. The aim of this design is to reduce vibrational and noise problems. Analogous works have been performed by Bernhard et al. [2], [3] and Chen et al. [4]. The same problems are addressed, using similar techniques as long as the actuation of the edge of the helicopter blade (active part) is concerned. It is very important to mention here that all these approaches could not produce adequate blade twisting, which could be used to obtain collective and cyclic control of the helicopter, to eventually get rid of the heavy blade control mechanism that is part of the rotor. It is clear that piezoelectrics might reduce the overall weight of the aircraft. Especially small helicopters would benefit from this gain in weight.

In this direction the work of Barrett et al. [5] had to offer some innovative aspects. Based on existing technology developed by Barrett [6], [7], high blade twist angles were achieved. This type of piezoelectric actuator was used for the cyclic control of a small helicopter blade, while the collective control was performed using another mechanism. The approach showed clearly that piezoelectric actuators can be used for displacements that exceed those needed for vibration and noise suppression. This study proved also that it is possible to reduce the amount of moving parts a helicopter rotor needs in order to be functional, by the intelligent use of piezoelectric actuators.

The work done in the RMA departs from piezoelectric actuators, developed on existing technology. They are used for cyclic and collective pitch control of a helicopter blade, planned to be used on a small UAV helicopter. It is obvious that this approach aims on the construction of a totally smart actuated helicopter blade. As a consequence the construction of a solid hub without moving parts is possible. The radius of this blade, being about 0.8 m, makes the issue of piezoelectric actuation even more demanding. However, one expects to profit from the weight decrease a piezoelectric rotor incorporates such that the payload can be increased or allowing a very small helicopter platform to lift off.

The aim of the research work presented here is initially not to optimize aerodynamic rotor and blade performance, but to focus more on the smart actuation mechanism. However, the airfoil selection is of critical importance. In order to reduce the torsion load, exerted on the piezoelectric actuators, a symmetric airfoil seems to be a good choice. A good compromise between high lift, low pitching moment and high drag divergence Mach number performance is found to be the NACA 0012 airfoil. One can still improve performances using camber and with the use of an evolutive profile, though, this would complicate blade construction. Moreover, such a profile should be selected carefully in order not to increase piezoelectric actuator load. Therefore, the selection of the NACA 0012 airfoil for the rotor blades seems to be the most interesting at this time.

The paper deals with the conceptual design, the analysis as well as the experimental results of a 0.8 m radius adaptive helicopter blade. The innovative aspects are the high radius, giving it the possibility to carry high (pay)loads and most importantly, its full control (cyclic and collective pitch control) through a smart actuation mechanism. Aerodynamic tests are carried out in a wind tunnel in order to check the performance of the actuators and their validity to command the cyclic and collective pitch angle of the helicopter blade under aerodynamic loads. Control issues were examined as well in order to cancel parasitic vibrations induced by aerodynamic loads. Thus, the design proposed here is in fact pushing further the operational envelope of smart actuated helicopter blades in terms of radius and pitch control.

## References

1. Andreas Büter, Elmar Breitbach, *Adaptive Blade Twist-Calculations and experimental results*, Aerospace Science Technology, vol. 4, 2000, pp. 309-319
2. Andreas P. F. Bernhard, Inderjit Chopra, *Development and Hover Testing of a Smart Trailing Edge Flap with a Piezo-Induced Bending-Torsion Coupled Actuator*, American Helicopter Society National Technical Specialist's Meeting on Rotocraft Structures, Williamsburg, Virginia, October 30-November 2, 1995, pp. 107-137
3. Andreas P.F. Bernhard, Inderjit Chopra, *Development of a smart moving blade tip activated by a piezo-induced bending-torsion coupled beam*, SPIE proceedings, vol. 2717, pp. 63-79
4. Peter C. Chen, Inderjit Chopra, *Induced Strain Actuation of composite beams and rotor blades with embedded piezoceramic elements*, Smart Materials and Structures, vol. 5, 1996, pp. 35-48
5. Ron Barrett, Phillip Frye and Michael Schliesman, *Design, Construction and Characterization of a flightworthy piezoelectric solid state adaptive rotor*, Smart Materials and Structures, vol. 7, 1998, pp. 422-431
6. Ron Barrett, *Aeroservoelastic DAP missile fin development*, Smart Materials and Structures, vol. 2, 1993, pp. 55-65
7. Ron Barrett, *Active plate and wing research using EDAP elements*, Smart Materials and Structures, vol. 1, 1992, pp. 214-226

## MULTIAXIAL ONE WAY SHAPE MEMORY EFFECT AND SUPERELASTICITY

Karine Taillard<sup>a</sup>, Sylvain Calloch<sup>b</sup>, Shabnam Arbab Chirani<sup>c</sup> and Christian LExcellent<sup>d</sup>

<sup>a</sup>LMT Cachan 61 avenue du Président Wilson 94235 Cachan cedex, France

<sup>b</sup>LMSN Brest, France

<sup>c</sup>LI2 Brest, France

<sup>d</sup>LMARC Besançon, France

Karine.Taillard@lmt.ens-cachan.fr

The specific behaviour of Shape Memory Alloys (SMA) is due to a solid-solid transformation called martensitic transformation [1]. This reversible transformation consists mainly in a shear without volume change and is activated either by stress or temperature. This partition between austenite (high temperature phase) and martensite (low temperature phase) is responsible for the specific properties of SMA: the superelastic behaviour (isothermal) and the one way shape memory effect (non-isothermal).

The superelastic effect is obtained for fully austenitic SMA: loaded up to 5% strain, a sample recovers its initial shape after unloading with a hysteretic loop. The one way shape memory effect is obtained when a martensitic SMA, which is apparently plastically deformed, recovers its initial shape by simple heating.

Superelasticity and one way shape memory effect are useful for several three-dimensional applications. Despite all these phenomena are well known and modelled for one-dimensional mechanical solicitations, the 3D behaviour, and especially the one way shape memory effect, remains quite unexplored (Tokuda *et al.* [2]). Actually the development of complex 3D applications requires time consuming iterations and expensive prototypes. Predictive phenomenological models are consequently crucial objectives for the design and dimensioning of such SMA structures.

Therefore, we perform several multi axial proportional and non-proportional, isothermal and non-isothermal tests. This database is then used to build a phenomenological model within the framework of irreversible processes.

### Experimental procedure

The first part concerns the experimental procedure. We perform tension-compression-torsion tests on a hydraulic testing machine. Linear and rotary actuators apply the displacements which are measured. Force and couple are measured by the load cell. The samples are thin tubes of Ni-Ti and Cu-Al-Be so that the stress field can be considered homogenous. Rosette type strain gages glued on the samples are used to determine axial and shear strain. The device also includes a thermal chamber used for heating and cooling. An electrical resistance measurement is used during some of the tests to determine the volume fraction of martensite using the resistance difference of austenite and martensite.

### Results

Then, in the second part, observations and comments are developed about the results. The existence of an equivalent stress, able to describe the yield stress surface for both superelasticity and one way shape memory effect is discussed (Fig. 1)

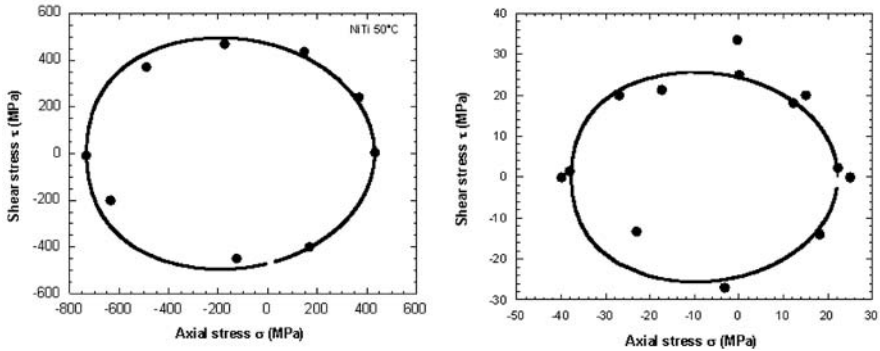


FIGURE 1. Yield surfaces for superelasticity (left) and for one way shape memory effect (right): experimental and modelled

Meanwhile, the existence of a linear relation (1), proposed by Bouvet *et al.* [3], between the volume fraction of oriented martensite and the equivalent transformation strain is also validated (Taillard *et al.* [4]).

$$\varepsilon_{eq}^{tr} = \gamma \cdot Z_{\sigma} \quad (1)$$

### Phenomenological model

Finally the phenomenological model is presented. It is based on two yield surfaces evolution, and uses normality rule [3]. Internal variables are: the transformation strain tensor and the volume fraction of thermally induced martensite. The main difference with other models, like Helm and Haupt [5] for instance, is the shape of the yield stress surfaces and the choice for the norm of the transformation strain.

The so obtained model is able to describe anisothermal, proportional and non proportional behaviour of SMA.

### References

1. Patoor, E. and Berveiller, M., *Technologie des Alliages à Mémoire de Forme*, Hermès, 1994.
2. Tokuda, M., Sittner, P., Takakura, M. and Ye, M., *Mat. Sc. Res. Int.*, vol. **1**, 260–265, 1995.
3. Bouvet, C., Calloch, S. and Lexcellent, C., *Eur. J. of Mech. A/Solids*, vol. **23**, 37–61, 2004.
4. Taillard, K., Arbab Chirani, S., Calloch, S. and Lexcellent, C., *Mech. Mat.*, submitted, 2006.
5. Helm, D. and Haupt, P., *Int. J. Sol. Struct.*, vol. **40**, 827–849, 2003.

## STRESS DISTRIBUTION MEASUREMENT OF WELDING PART BY ELECTRONIC SPECKLE PATTERN INTERFEROMETRY

Hyun-Chul Jung<sup>1,a</sup>, Ho-Sub Chang<sup>1,b</sup>, Ki-Soo Kang<sup>2</sup>, Sang-Kyu Baek<sup>3</sup> and Koung-Suk Kim<sup>4</sup>

<sup>1</sup> LARC, Chosun University, <sup>2</sup> KRIS, <sup>3</sup> Graduate School, Chosun University, and <sup>4</sup> Dept. of Mechanical Design Engineering

<sup>1</sup> 375 Seosuk-Dong, Dong-Gu, Gwangju, 501-759, Korea,

<sup>2</sup> P.O.Box 102, Yuseong, Daejeon, 305-600, Korea,

<sup>3</sup> 375 Seosuk-Dong, Dong-Gu, Gwangju, 501-759, Korea,

<sup>4</sup> 375 Seosuk-Dong, Dong-Gu, Gwangju, 501-759, Korea

<sup>1,a</sup> yonggary@ieee.org, <sup>1,b</sup> hschang@chosun.ac.kr, <sup>2</sup> kskang@kriss.re.kr,

<sup>3</sup> baek0408@hanmail.net, <sup>4</sup> gskim@chosun.ac.kr

The welding which is one of material joining methods plays an important role for development of the modern industry. The welding has several advantages such as high joint effect, high airtightness, and reduction of the materials being used. Nowadays, the applying or loading condition of the plates which are used for various mechanical structures becomes various. For applying the plates to the industrial field, its characteristics by tensile or compressive testing should be measured. Especially, the stress distribution at the welding part must be measured. During welding process, the thermal damage causes several types of defect including porosity, crack, insertion of impurities. A crack at the welding part results from these defects so that the mechanical structures could be destructive. In this paper, the butt welded S30400(STS304 in KS) specimen is prepared and the stress distribution at the welding part is measured by electronic speckle pattern interferometry (ESPI).

ESPI is one of the optical metrology methods using speckle effect. An interference fringe in the ESPI system has a phase information respect to the displacement of the object. Interference fringes in ESPI are observed by a process of video signal subtraction. Finally, if this phase information is obtained, the displacement of an object could be estimated by Eq. (1).

$$\Delta\phi = \left( \frac{4\pi}{\lambda} \right) d_x \sin\theta \quad (1)$$

where,  $\Delta\phi$  is the phase difference between displacement of an object and laser beam,  $\lambda$  is wavelength of laser beam,  $d_x$  is the displacement of an object in  $x$  direction, and  $\theta$  is the illumination angle of a laser beam.

For measuring phase difference, the 4-step phase shifting method is introduced. A mirror causes the phase difference between object beam and reference beam is set on the PZT actuator. If an image is stored in the frame grabber when the phase variation with  $\pi/2$ ,  $\pi$ ,  $3\pi/2$ ,  $2\pi$  on the reference beam is introduced,  $\Delta\phi$  can be quantitatively obtained by Eq. (2).

$$\phi = \tan^{-1} \left( \frac{I_4 - I_2}{I_1 - I_3} \right) \quad (2)$$



In this study, butt welded S30400 stainless steel plate is used as specimen. Its material properties are shown in Table 1. Over-all length, thickness, and width of a specimen is 100 mm, 0.5 mm, and 20 mm, respectively and length and width of the reduced section is 32 mm and 5 mm..

TABLE 1. Material properties.

Material	Modulus / GPa	Density / kg·m <sup>-3</sup>	Poisson's Ratio
S30400	206	7800	0.29

A phase map of interference fringe pattern is obtained by ESPI system (with Nd:YAG laser whose wavelength is 532 nm). When the tensile force difference is increased, the number of the interference fringe is increased. However, the number of the interference fringe at the welding part is less than that of other parts. Fig. 1 shows the result of the deformation profile at the centre line of a specimen. The relative deformation to the pixel is shown in Fig. 1(a), and strain for unit length to the pixel is shown in Fig. 1(b). In the Fig. 1(b), it shows that the strain of the part A and C is almost same and that of the part B is lower than other parts relatively. Therefore, if the cross section area is constant and the loading force is same, the stress at the welding part is lower than the basic material parts because of the residual stress.

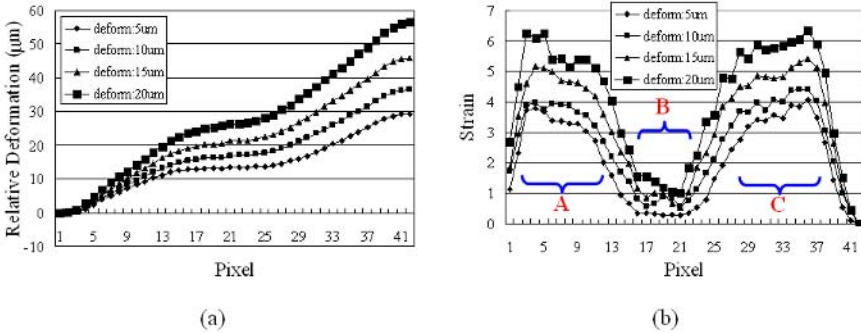


FIGURE 1. Deformation profile at the centre line of a specimen. (a) Relative deformation to the pixel and (b) strain for unit pixel to the pixel.

**References**

1. Lancaster, J.F., *Metallurgy of welding*, 3rd Ed., Unwin Hyman, 1980.
2. Masubuchi, K., *International Series on Materials Science and Technology*, vol. 33, 1-10, 1980.
3. Kang, Y.J., Lee, J.S., Park, N.K., and Kwon, Y.K., *International Journal of the Korean Society of Precision Engineering*, vol. 19, no. 12, 20-26, 2002.
4. *Designation: A370-05, Annual Book of ASTM Standards 2006*, vol. 01-03, 87-133, 2006.

## SMALL STRAIN TEST SYSTEM FOR OPTICAL STRAIN MEASUREMENT SYSTEMS

R. Steinberger<sup>1</sup>, M. Jerabek<sup>1</sup>, Z. Major<sup>2</sup> and R.W. Lang<sup>1,2</sup>

1) Polymer Competence Center Leoben GmbH, Parkstrasse 11, 8700 Leoben, Austria

2) Institute of Materials Science and Testing of Plastics, University of Leoben, Franz-Josef-Strasse 18, 8700 Leoben, Austria  
steinberger@pccl.at

The major goal of the work presented is to develop test methodologies for small strain measurement tasks. The implementation is especially driven by the potential of novel optical strain field measurement systems, a pattern correlation system and an electronic speckle pattern interferometer (ESPI). The high sensitivity especially of the ESPI system, capable to resolve displacements down to 50 nm poses requirements on the loading system in terms of displacement resolution, vibration isolation and rigidity of the loading frame. These requirements can be fulfilled best in a custom loading system.

In this paper the development and implementation a loading system complying the needs for the ESPI strain measurement and pattern correlation systems and designed for various loading conditions, such as tension and compression tests under monotonic, creep and relaxation conditions is presented. Example results and test methods are provided and discussed.

The loading frame was designed with various features in order to meet the requirements of the ESPI measurement system. These are: perfect alignment of the moving grips, symmetric displacement on the specimen with two moving cross heads, high resolution in the displacement control, flexible programming of the displacement control for the various load cases such as monotonic, creep or relaxation testing.

The two moveable crossheads are driven by a precision positioning actuator each. A LVDT and a load cell are provide specimen deformation and load information and can also be used for closed loop control of the cross head displacements. Photos of the loading frame are shown in Figure 1.

Example results on small strain creep and relaxation tests of polypropylene will be presented. The developed testing system presented is a multi-axial small strain loading and measurement system, especially designed for the high resolution strain field measurement systems, the pattern correlation and EPSI systems. Small strain measurements on a specimen level encompass tests where e.g. the limits of the linear visco-elastic range shall be identified or the time dependent behaviour in the linear visco-elastic regime is to be analyzed. The ESPI for example acts as a high resolution longitudinal and transverse strain sensor. With notched specimens, also local strain information in multi-axial stress-strain situations of materials can be analyzed. But the loading system can also be used independently from the strain field measurement systems like a standard universal testing system for low loads and displacements. Further applications are e.g. tension tests of polymer films using a conventional video extensometer; strain measurement under microscopic conditions with local strain analysis.

The creep and relaxation test results generated with the developed measurement system shall help in the fundamental analysis of the time dependence of polymers, and thus shall help in the understanding of the material behaviour and the development of material laws, as needed e.g. for simulation. The possibility to combine this system with the microscopic pattern correlation system has potential for in-situ microstructure investigations. The applicability of the ESPI system not

only on specimens but also on curved surfaces allows the investigation of the strain fields on complex parts and components e.g. for localization of critical strain concentrations or for comparison with simulation results.

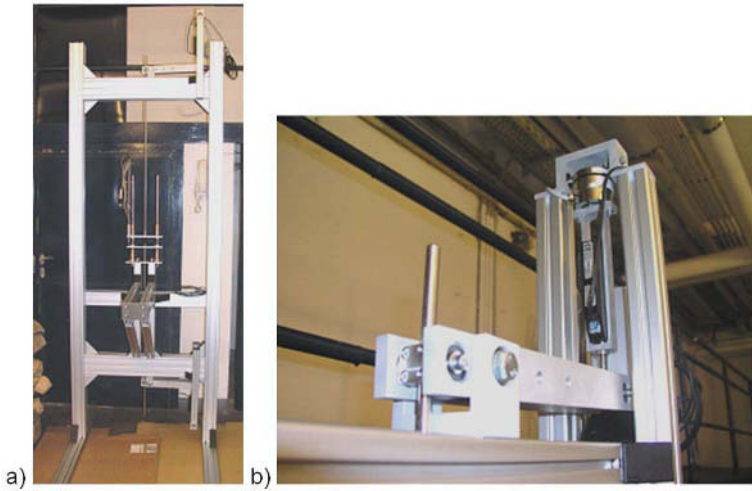


FIGURE 1. Photos of the small strain loading frame: (a) full loading frame with the alignment cage in the center, and (b) one of the two loading cantilevers with the precision actuator and load cell.

## DETERMINATION OF THE STRESS INTENSITY FACTOR BY MEANS OF THE ESPI TECHNIQUE

A. Cirello and A. Pasta  
Mechanical Department, University of Palermo  
Viale delle Scienze 90128 Palermo, Sicily, Italy  
cirello@dima.unipa.it, pasta@dima.unipa.it

The experimental determination of stress intensity factors by means of non-destructive techniques is a research topic of actual interest. In fact there are many applications, where a reliable and accurate experimental procedure is needed to evaluate numerical or theoretical models about the behaviour of cracked or notched structures.

The non-destructive techniques nowadays available, usually need preliminary calibration procedures performed by applying the techniques their application upon standard materials and specimen which have a well known stress-strain behaviour [1].

This paper presents an application of a technique for the determination of the stress intensity factor by means of phase shifting ESPI. The procedure is performed on single edge cracked homogeneous specimens loaded in four points bending. A software for the complete analysis of the experimental fringes has been developed and used, allowing the simple and accurate determination of the stress intensity factor.

### The implemented technique

Various experimental techniques based on speckle interferometry have been implemented and are suitable for the determination of the stress intensity factor. In this paper a “phase stepping speckle interferometry” has been implemented [2], offering high sensitivity together with a high contrast of the acquired fringes, this last being a fundamental feature for performing accurate automatic elaboration analyses.

The optical setup used has a  $0.3\pm 0.6$  m in plane displacement sensitivity while the influence of out of plane displacement is negligible. A specific software has been developed to assist in the setup configuration, acquisition and post-processing of images.

Fig. 1a shows the phase fringes corresponding to the in-plane displacement parallel to the crack. It is important to note that the image is characterized by a high level of noise (left area in the figure) that has been filtered using an iterative version of the mean filter proposed by Ghiglia [3], which improves the image quality without affecting the phase discontinuities. The stress intensity factor has been evaluated by means of an iterative Newton-Rapson algorithm [4], that allows the calculation of the SIF by means of a large number of measured displacement point values.

The algorithm allows the evaluation of the stress intensity factors by mean of a least square fitting of the analytical displacement expression over a large number of measured points [4, 5]. This method presents a low sensitivity to high frequency noise and allows the evaluation of the unknown factors with low percentage of errors. The evaluation points chosen for the fitting algorithm are taken along several radial lines that starts near the crack tip as showed in Fig 1 a).

Fig. 1b shows the  $K_I$  calculated with the proposed method vs  $K_I$  calculated analytically [5]. It is important to note that the error in the experimental values decreases with increasing load value due to a better signal to noise ratio of the analyzed points [6,7]. The maximum value of this error has been 18.8% for the first point while for all other points this error is negligible ( $< 1.7\%$ ).

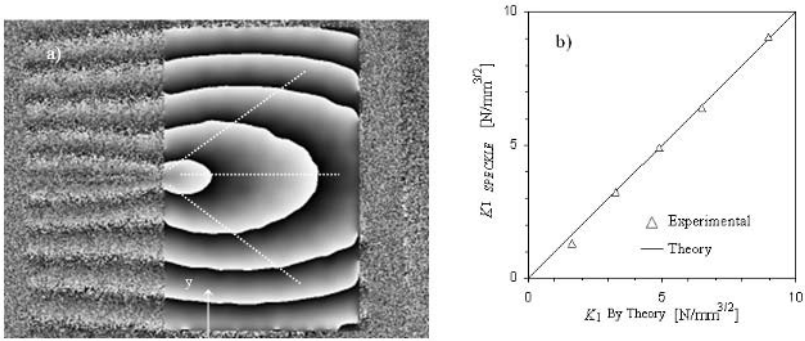


FIGURE 1. a)  $v$  displacement fringe pattern; b)  $u$  displacement after filter application.

## References

1. E. Patterson, M. Whelan, E. Hack, T. Siebert, R. Burguete and Q. Saleem: "Standard Test for the Evaluation of Optical Strain Measurement Systems", International Conference on Advances in Experimental Mechanics, 6-8 September 2005, University of Southampton, UK.
2. Cloud G.L. "optical method of engineering analysis". Cambridge University press.
3. Ghiglia C. D., Pritt, D. M., "Two dimensional phase unwrapping Theory algorithms and software" Wiley interscience 1998.
4. Baker, D.B., Sanford, R.J., Chona, R., "Determining K and related Stress-field parameter from displacement field", Experimental Mechanics, vol. **25** (12), 399-407 1985.
5. A. Cirello, A. Pasta, "Crack growth in bimaterial joints with crack perpendicular to interface under various stress condition" International Conference on Fatigue Crack Paths (FCP Parma 2003).
6. A. J. Moore, J. R. Tyler: "Phase stepped ESPI and moiré interferometry for measuring stress-intensity factor and J-integral" Experimental Mechanics, vol. **35** (4), 306-314 (1995).
7. A. Shterenlikht et All: "Mixed mode ( $K_{I} + K_{II}$ ) stress intensity factor measurement by electronic Speckle pattern interferometry and image correlation" International Applied Mechanics and Materials, vol. **1-2**, 107-112 (2004).

## STRAIN LOCALIZATION ANALYSIS BY A COMBINATION OF THE ESPI WITH A BULGE TEST

Guillaume Montay<sup>1</sup>, Bruno Guelorget<sup>1</sup>, Ignacio Lira<sup>2</sup>, Marie Tourneix<sup>1</sup>, Manuel François<sup>1</sup>  
and Cristián Vial-Edwards<sup>2</sup>

<sup>1</sup>Université de Technologie de Troyes,  
Laboratoire des Systèmes Mécaniques et d'Ingénierie Simultanée  
(ICD/LASMIS FRE CNRS 2848)

12 rue Marie Curie, BP 2060, 10010 Troyes, France

<sup>2</sup>Pontificia Universidad Católica de Chile, Department of Mechanical and Metallurgical  
Engineering, Vicuña Mackenna 4860, Santiago, Chile  
montay@utt.fr

The problem of strain localization is important in sheet metal forming, as it determines the forming limit diagram of the material. To analyze this process, engineers use a variety of tests. One of them is the bulge test. In it, an initially flat specimen is placed between a matrix and a blank holder, and hydraulic pressure is applied on one of its surfaces. An approximately equi-biaxial strain loading path is obtained [1,2].

The aim of this study is to detect the localization of plastic strain (diffuse and localized necking) during the bulge test combined with a common speckle interferometer. This paper describes an original technique to detect the localization using the strain rate at different positions on the sample.

A classical speckle interferometer [3] with in-plane sensitivity is placed over the specimen to measure the strain rate during the bulging. The LASER beam is divided into two beams by the beam splitter. The two beams produce speckle patterns in the reference state and in a subsequent state. The fringe pattern is obtained by a pixel to pixel subtraction of the two speckle patterns, Fig. 1.

The difference pixel by pixel of this two images create an image of fringe patterns. Total strains between the initial flat state and the current state were found from white light images of a square grid impressed on the specimen. The grid sizes in the  $x$  and  $y$  directions,  $L_x$  and  $L_y$ , were measured at different positions and at different load stages.

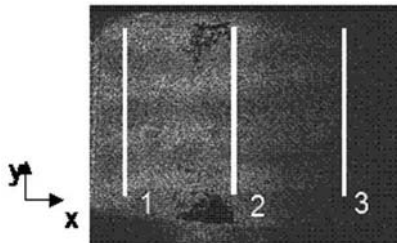


FIGURE 1. Images of fringes patterns

Fig. 2 presents the strain rate for the three positions on the sample, this positions are  $x=2.5$  mm (on the left of the image fringe patterns),  $x= 16.75$  mm (at the centre of the plate which is the position of the fracture) and  $x=31$  mm (on the right of the image).

The strain rate is also represented for several increment of strain. Knowing the strain rate as a function of the time and the total strain as a function of the time, we present the strain rate as function of the total strain which is an important information for the engineer [4].

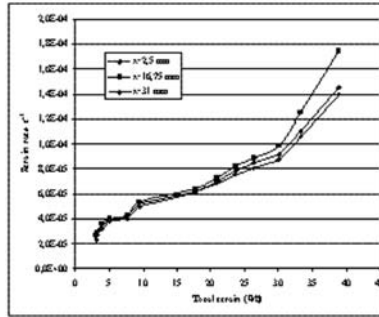


FIGURE 2. Strain rate as a function of the total strain

It can be seen from Fig. 3 that the heterogeneity in strain rate increases slowly to a maximum of 7% at about 48% in strain and then decreases slightly until a strain of 59% after which it increases dramatically until the final fracture.

This change of the deformation mode of the specimen is a way to determine the onset of the localization of strain. However, a criterion to quantify the onset of strain localization is to use this sharp change in the deformation mode. In this case, a 59% strain may indicate an instability point.

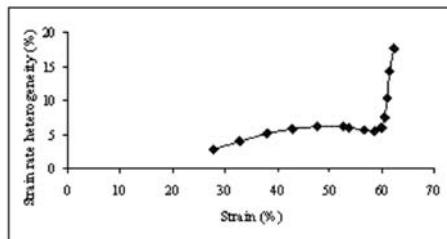


FIGURE 3. Strain rate heterogeneity as a function of the strain.

## References

1. Atkinson, M., In International Journal of Mechanical Sciences, vol. **39**, 761-769, 1997
2. Gutscher G., Wu H.C., Ngaile G., Altan T, In Journal of Materials Processing Technology vol. **146**, 1-7, 2004
3. Cloud G. Optical methods of engineering analysis. Cambridge University Press, New York, 1995.
4. Montay, G.; Francois, M.; Tourneix, M.; Guelorget, B.; Vial-Edwards, C.; Lira, I., In Optics and Lasers in Engineering, vol. **45**, 222-228, 2007

## RESIDUAL STRAIN AND STRESS ANALYSIS BY SPECKLE INTERFEROMETRY COMBINED WITH THE DRILL OF A GROOVE

Afaf Maras , Guillaume Montay , Olivier Sicot, Emmanuelle Rouhaud and Manuel François  
Université de Technologie de Troyes (UTT)  
Institut Charles Delaunay, LASMIS, FRE CNRS 2848  
12, rue Marie Curie, BP 2060, 10010 Troyes, France  
montay@utt.fr, maras@utt.fr

A new method for residual stresses determination combining Electronic Speckle Pattern Interferometry (ESPI) with the machining of a groove. The internal stress field is perturbed as the depth of the groove is increased incrementally [1]. The structure finds a new equilibrium state generating displacements which are measured using ESPI. This method was tested on an aluminium alloy plate treated locally by ultrasonic shot-peening. The investigation of the images obtained with the phase shifting technique and fringe patterns makes it possible to analyze, simultaneously, the stress profile along two directions: along the depth of the structure, and along the groove direction.

The method proposed allows analyzing the stress profile, in 2D, along two directions. It is based on the principle of stress relaxation during a machining operation. The structure is mechanically disturbed by machining an incremental groove of 2 mm width. The structure finds a new equilibrium creating, on the surface, displacements or deformations. This field is measured using Speckle interferometry.

The test specimen was a rectangular plate made of aluminium alloy AlCu4Mg (AU4G) which was treated by ultrasonic shot-peening to produce a band with compressive residual stresses like shown in Fig. 1.

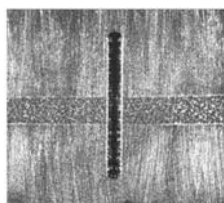


FIGURE 1. Photograph of the groove and of the shot peened band. The sensitivity vector of the interferometer is in the plane of the surface and perpendicular to the groove.

The machining of the groove is performed by a small milling machine with variable rotation speed. The groove was machined incrementally, like in the incremental hole-drilling method, to determine the profile of residual stress along the depth and along the groove. The displacement generated by the stress relaxation is measured by Speckle interferometry [2].

The exploitation of the images obtained by phase shifting, Fig. 2 allows to determine, for each increment, the displacement field on all the surface of the tested specimen.



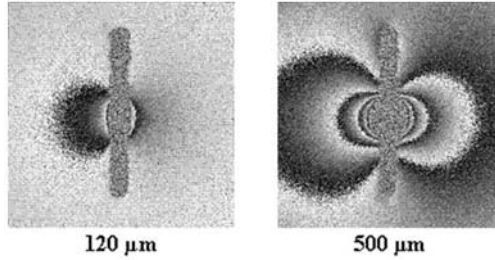


FIGURE 2. Phase distribution obtained for 2 increments

Fig. 2 shows the wrapped phase distribution. The number of fringes increases with the bored depth. This is due to the increase in stress relaxation as the machining gets deeper. It can be seen that the fringe is different than fringe obtained with hole-drilling technique. For each increment displacement data along different lines are extracted.

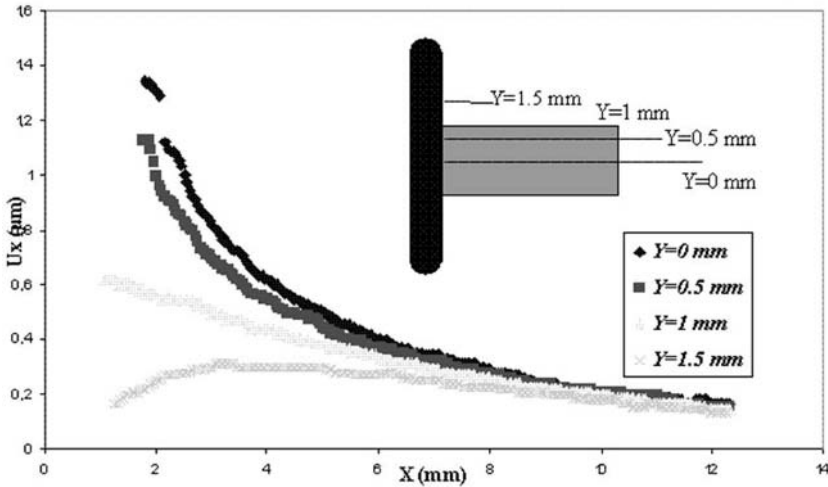


FIGURE 3. Displacement along lines perpendicular to the groove for a machined depth of 500μm

Fig. 3 shows curves of the x component of displacements along 4 lines perpendicular to the groove for a machined depth of 500μm. The first line is taken at y=0, in the center of the shot peened band. Obviously, it exhibits displacements that are larger than for y=1.5 mm, away from the strongly stressed shot-peened band.

**References**

- 1. Lu J., Handbook of measurement of residual stresses. SEM, edited by Jian Lu,1996.
- 2. Cloud G., Optical methods of engineering analysis. Cambridge University Press, New York, 1995.

## FULL-FIELD VIBRATION MEASUREMENT BY TIME-AVERAGE SPECKLE INTERFEROMETRY AND BY DOPPLER VIBROMETRY – A COMPARISON

Aurélien Moreau<sup>1</sup>, Dan Borza<sup>1</sup>, Ioana Nistea<sup>1</sup> and Mariana Arghir<sup>2</sup>

<sup>1</sup>Institut National des Sciences Appliquées de Rouen  
BP 8, avenue de l'Université, 76800 Saint-Etienne du Rouvray, France

<sup>2</sup>Université Technique de Cluj,  
Str. C. Daicoviciu nr 15, 400020 Cluj - Napoca, Romania  
amoreau@insa-rouen.fr, borza@insa-rouen.fr, marianaarghir@yahoo.com

Identification of dynamic material properties, non-destructive testing and study of vibroacoustic behaviour of different structures impose complex, pointwise and full-field measurements. Among other techniques, optical non-contact techniques are representing today the favourite choice since they do not add any mass to the structure under test. When the range of vibration amplitudes is small, most of these techniques are based on interferometric principles.

In our high-tech digital era, the fast development of computers, laser sources and detectors lead to a continuous improvement of vibration measurement techniques. However, we are still at a stage where painful choices have to be done. The most obvious and difficult of these choices is that between spatial resolution and temporal resolution. Another difficult choice is between space bandwidth product and energetic sensitivity. While the number of pixels of a camera is continuously increasing, the pixel size seems limited at its lower end.

In the field of vibration measurement, the most widely known full-field coherent optical technique is speckle interferometry [1]. Digital holography is also a very promising technique, but for the moment being its applications are mostly in the study of small – microscopic or nanometric – objects. Both techniques are measuring full displacement fields, either static or dynamic. Several researchers proposed solutions [2] aiming at trading the great number of pixels, not always really needed, against speed. They used either linear cameras or random-access CMOS detectors and DSP.

As to the pointwise optical measurements, the instrument of choice is the classical interferometer, mostly known today as "vibrometer". The Doppler vibrometer may be configured to measure either displacements (vibration amplitudes) or speeds. As a step towards full-field techniques, sweeping may allow successive measurements to be done in a relatively small number of points, usually disposed at regularly disposed angular directions. Both vibration amplitude and phase maps may be computed in these points, by using spatial FFT techniques and a reference phase related to the excitation. The spatial FFT processing is computationally efficient but may introduce undesired spatial effects .

The paper presents a comparative study of these representative techniques, as applied at the Mechanics Laboratory of INSA Rouen. The example concerns the free and the forced vibrations of a thick, non-metallic plate used in a study aiming to identify its complex damping.

Fig. 1 shows the graphical interface allowing to implement the procedures proposed in order to characterize the differences between the two amplitude and phase maps.

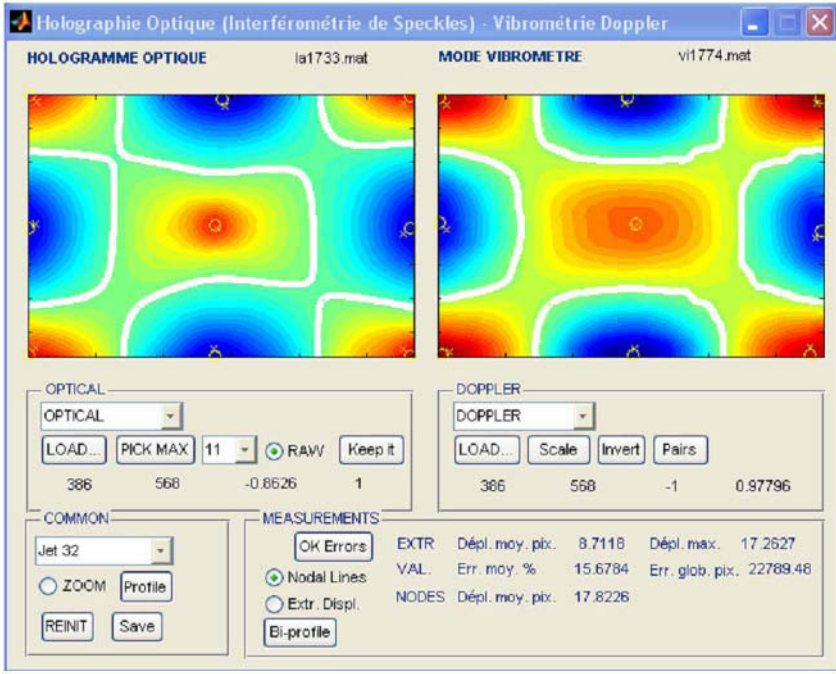


FIGURE 1. Comparison of the (2, 2) mode as measured by speckle interferometry (left) and by vibrometry (right).

Similar procedures are presented in the paper, allowing to use the holographic results in order to validate the numerical model simulation.

## References

1. Lokberg, O. J., *J. Acoust. Soc. Am.*, 1984, vol. **75**(6), pp. 1783-1791
2. Kilpatrick, J. M. et al, 1068, 2000, *Optics Letters*, vol. **25**(15) , 1068-1070

## OPTICAL CONFIGURATIONS FOR ESPI

Amalia Martínez<sup>a</sup>, J.A. Rayas<sup>a</sup> and R. Cordero<sup>b</sup>

<sup>a</sup>Centro de Investigaciones en Óptica, Loma del Bosque 115, Col. Lomas del Campestre, León Gto. C. P. 37150, México

<sup>b</sup>Leibniz Universität Hannover, Herrenhäuser Str. 2, D-30419 Hannover, Germany  
amalia@cio.mx , jrayas@cio.mx , rcordero@ing.puc.cl

It was presented an optical setup that can be switched to get single and double dual illumination, Martínez et. al. [1]. Too it was reported experimental results for a speckle interferometer with three divergent illumination beams where the sources positions give maximum sensitivities for each sensitivity vector components, Martínez et. al. [2]. In this work, we compare both optical systems reported. Experimental results of displacements maps for same object when this is loaded will be presented.

When the propagation vectors of two laser beams forming a speckle interferometer are denoted as  $\hat{e}_1$  and  $\hat{e}_2$ , the sensitivity vector,  $\hat{e}$ , of the speckle interferometer is represented as

$$\hat{e} = \frac{2\pi}{\lambda}(\hat{e}_1 - \hat{e}_2) \quad (1)$$

The sensitivity vector depends of the geometry of the arrangement and on the wavelength of the laser source.

In the double-illumination method, both  $\hat{e}_1$  and  $\hat{e}_2$  correspond to unit vectors that describe the vectorial characteristics of illuminating beams emerging from sources  $S_1$  and  $S_2$ , respectively. In this case the system sensitivity does not depend of the observation direction. In the reference beam method, one vector corresponds to vectorial characteristics of illuminating and the other corresponds to the observation vector. In this case, the system sensitivity depends of the observation direction. An interferogram consisting of a subtraction of two speckle images recorded before after deformation of a test object shows fringes that contour the object deformation. The phase change,  $\Delta\phi$ , arising from the object deformation is related to the three-dimensional displacement vector,  $\vec{d}$ , through sensitivity vector  $\hat{e}$  as

$$\Delta\phi(P) = \vec{d}(P) \cdot \vec{e}(P) \quad (2)$$

where point denotes a scalar dot product. To extract the phase from an interferogram, we use the phase shifting, Kreis [3].

The use of multiple interferometers whose sensitivity vectors are different permits measurements of multiple components displacements. A sensitivity matrix, consisting of three sensitivity vectors that relate the three measured phase maps to the three components of displacement, can be derived. Because the sensitivity matrix is not singular, the inverse sensitivity matrix exists and therefore displacement maps can be calculated from the phase maps. Let us consider the three sensitivity vectors  $e^1(P)$ ,  $e^2(P)$  and  $e^3(P)$ , in which the upper index denote correspondence to each one of the interferometers. In this case  $e^1(P)$  is associated to dual illumination with *x-sensitivity*;  $e^2(P)$  to dual illumination with *y-sensitivity* and  $e^3(P)$  associated to

z-sensitivity. Then, at each point  $P$  we have to solve the system of linear equations to obtain  $d(u,v,w)$ . The solution is

$$\begin{pmatrix} u(P) \\ v(P) \\ w(P) \end{pmatrix} = \begin{pmatrix} e_x^1 & e_y^1 & e_z^1 \\ e_x^2 & e_y^2 & e_z^2 \\ e_x^3 & e_y^3 & e_z^3 \end{pmatrix}^{-1} \cdot \begin{pmatrix} \Delta\phi^1(P) \\ \Delta\phi^2(P) \\ \Delta\phi^3(P) \end{pmatrix} \quad (3)$$

The sensitivity vector components to each case are given by<sup>1</sup>. We have calculated the sensitivity matrix with all the sensitivity vector components.

A second system is used to obtain three sensitivity vectors. The optical system uses illuminating beams to irradiate the object from three directions<sup>2</sup>. Here it provides the phase change undergone by the speckle object wave in response to the object surface deformation, in an in-line reference wave arrangement. This type of arrangement consists in superimposing to the speckle wave diffused by the object surface a smooth reference wave. The latter propagates in the direction of the optical axis of the lens imaging the surface. The phase change is linearly related to the three components of the displacement field and the coefficients depend on the geometry of the set up, i. e. on the directions of the illumination and observation vectors. In order to solve for the all three components, three independent equations are necessary, namely three geometries. The relative sensitivities to the three components are computed to get the displacement vector components and compared with the obtained by the configuration of optical setup that can be switched to get single and double dual illumination designed for 3D deformation, each of them being defined by a single observation along the normal to the object surface and a triplet of three different illumination directions.

## References

1. 1. Martínez A., Rayas J. A., Rodríguez-Vera R. and Puga H. J., *Appl. Opt.*, vol. **43**, 4652-4658, 2004.
2. 2. Martínez A., Rayas J. A. and Cordero R., *Opt. Comm.*, vol. **262**, 8-16, 2006.
3. 3. Kreis T., *Holographic Interferometry*, Akademie Verlag Inc., New York, NY, 1996.

## REDUCTION OF PSEUDO VIBRATIONS IN ROTATIONAL MEASUREMENTS, USING SENSOR ARRAYS

M.L. Jakobsen and S.G. Hanson

Department of Optics and Plasma Research.

Risoe National Laboratory, DK-4000 Roskilde, Denmark.

michael.linde.jakobsen@risoe.dk and steen.hanson@risoe.dk

Angular velocity measurements obtained with optical technologies, using coherent sources, such as laser Doppler velocimetry (LDV) (Halliwell *et al.* [1]) and speckle shearing velocimetry (SSS) (Takai *et al.* [1]), are often contaminated by a noise phenomenon called pseudo vibrations (Rothberg *et al.* [2]). Pseudo vibrations are minor fluctuations appearing in the angular velocity measurements, and caused by laser speckles and their influence through the measurement algorithm. In essence, they appear as the speckle pattern repeats itself for each revolution, and the processing algorithm will repeat the same “errors” not connected to a real variation in the rotational speed but not being distinguishable from a real torsional vibration. Therefore, they appear as a noise contribution, which strongly correlate with the angular position of a rotating target, through the fine structure of its surface. It is often observed in e.g. the power spectrum of angular velocity time series, where it will appear as a comb function with harmonics of the fundamental frequency of the rotating target. Therefore, pseudo vibrations will interfere particularly with any measurements of fluctuations in angular velocity, which correlate to the cycle of the target rotation. In the light of the option of using compact, high-performance sensors at low-cost prices, the prospect of implementing sensor with multiple laser sources or even sensor arrays appears. Therefore, this paper will study these new practical opportunities to reduce speckle-related noise.

A compact, high-performance optical sensor could be based on optical spatial-filtering velocimetry (Jakobsen and Hanson [1]) of the dynamical speckles arising from scattering off a rotating solid object with a non-specular surface. A schematic drawing of the sensor is illustrated in Fig. 1. The speckles are produced when illuminating a non-specular target surface with coherent light. The scattered light propagates through a Fourier-transforming optical arrangement to the sensor inlet (Rose *et al.*<sup>1</sup> []). The sensor for measuring speckle velocity is here based on a lenticular array and implements narrow spatial band-pass filtering of the intensity distribution of the translating speckle patterns. The spatial filter extracts a given spatial frequency in terms of a quasi-sinusoidal intensity distribution. The quasi-sinusoidal spatial intensity distribution is monitored at various phase steps by an arrangement of a couple of photodetector pairs. The photodetector signals have a similar quasi-sinusoidal response as a function of the target angle and allow for simple processing schemes based on e.g. zero-crossing detection. Zero-crossing detection of the frequency of the signals provides real-time measurements of the angular velocity of a rotating target.

Fig. 2. demonstrates the pseudo vibrations. The power spectra of two angular velocity time series, obtained over several cycles of target rotation, are plotted while probing a surface when it is dry and when it is intentionally coated with a thin film of oil. In the first case, the surface will show a clear “finger print” for each cycle in the time signal, and this appears as a detrimental comb function in the power spectra. When coating the surface with a thin film of oil, the speckle patterns do not repeat themselves for each cycle, and the “finger print” of the surface is dramatically reduced. The presentation will discuss other ways to reduce the pseudo vibrations, and quantitative results will be presented.

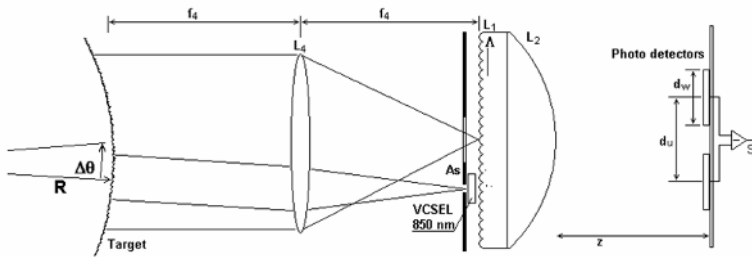


FIGURE 1. A schematic of the sensor design

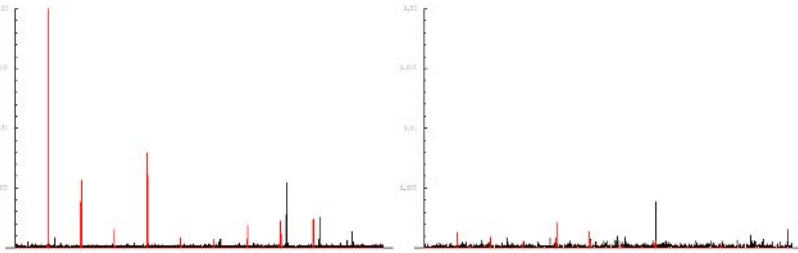


FIGURE 2. The power spectra of two angular velocity time series illustrate the pseudo vibrations. To the left, the surface is dry, while to the right, a thin oil film coats the surface.

## References

1. N. A. Halliwell, C.J.D. Pickering and P.G. Eastwood, "The laser torsional vibrometer: a new instrument", *Journal of Sound and Vibration*, vol. **93**, 588-592 (1984).
2. N. Takai, T. Iwai and T. Asakura, "an effect of curvature of rotating diffuse object on the dynamics of speckle produced in the diffraction field", *Appl. Phys., B*, vol. **26**, 185-192 (1981).
3. S. J. Rothberg, J. R. Baker and N. A Halliwell, "Laser vibrometry: Pseudo vibrations", *Journal of Sound and Vibration*, vol. **135** (3), 516-522 (1989)
4. M. L. Jakobsen and S. G. Hanson, "Micro-lenticular arrays for spatial filter velocimetry on laser speckles from solid surfaces", *Meas. Sci. Tech.*, vol. **15**, 1949-1957 (2004).
5. B. Rose, H. Imam, S. G. Hanson, H. Yura and R. S. Hansen, "Laser-Speckle angular-displacement sensor: theoretical and experimental study", *Applied Optics*, vol. **37**, 2119-2129 (1998).

## CHARACTERISTICS OF OPERATIONAL DISPLACEMENT AND CURVATURE SHAPES AND THEIR EFFECT ON CURVATURE BASED DAMAGE DETECTION ALGORITHMS

Colin P. Ratcliffe and Roger M. Crane

United States Naval Academy, Mechanical Engineering Department, 590 Holloway Road  
Annapolis, Maryland 21402, USA

Naval Surface Warfare Center Carderock Division, Code 655, 9500 MacArthur Boulevard  
West Bethesda, Maryland 20817, USA  
ratcliff@usna.edu, Roger.Crane@navy.mil

Structural damage often results in a localized stiffness change, which affects the dynamic characteristics of the structure. It is well documented that structural damage causes little change to displacement-based mode shapes, Yuen [1]. Therefore, experimental damage detection methods solely based on the analysis of experimentally determined mode shapes, e.g. Liang *et al.* [2] and Chang *et al.* [3], often are not overly sensitive in their location abilities. This is especially the case when damage is located near nodes of displacement. The sensitivity of these procedures is also affected by the errors typically introduced during modal analysis curve fitting.

An alternative approach is to inspect curvature mode shapes. Experimental curvature mode shapes can be obtained by spatially differentiating displacement mode shapes. Curvature and strain are intimately related, and therefore theoretical issues with curvature and strain based methods are often associated. A localized stiffness change causes a feature in an otherwise smooth curvature mode shape, and there is a variety of published methods that look for this feature in order to locate damage, Pandey *et al.* [4] and Ratcliffe [5].

An extension to the modal curvature methods is to omit the need for the modal analysis curve fitting, and to use the entire broadband data sets. Thus, the ‘raw’ data for these methods consists of broadband, frequency-dependant operational displacement or operational curvature shapes. Frequency dependant Operating Deflection Shapes, ODS, are commonly used for visualization of the vibration pattern of a structure under given operating conditions. They are not, though, commonly used for damage identification. There is an increasing interest in using broadband Operational Curvature Shapes, OCS, for damage identification, Ratcliffe [6]. In this category some methods use data obtained at a single frequency which may be at or away from resonance, and some methods use data from an entire broadband spectrum. In this case the data are used irrespective of whether the structure is at resonance or not.

Mode shapes are solely dependent on the structure, and are independent of excitation. Conversely, operating shapes (both displacement and curvature) depend on both the structure and the location of excitation or measurement. Whereas displacement and curvature mode shapes are both continuous and continuously differentiable, the work reported here shows that even for well behaved, simple structures, operational curvature shapes are continuous, but they are not always continuously differentiable, as demonstrated in Fig. 1. The consequence is that algorithms that look for “unusual” features in operational curvature shapes may incorrectly identify these theoretically expected features as damage.

The work presented in this paper inspects the theoretical behavior of a beam with particular regard to the development of frequency and excitation position dependant displacement and curvature operational shapes. The analytical solution is also used to demonstrate the effects of discontinuities such as thickness or material changes. The theoretical effect of a non-continuously differentiable curvature shape on the performance of a curvature-based damage detection



algorithm is presented. Experimental results from a full sized composite structure show that the features generated by the theoretical issues presented in this paper are often more significant than the features generated by real damage. A real-world solution to this problem is presented and discussed.

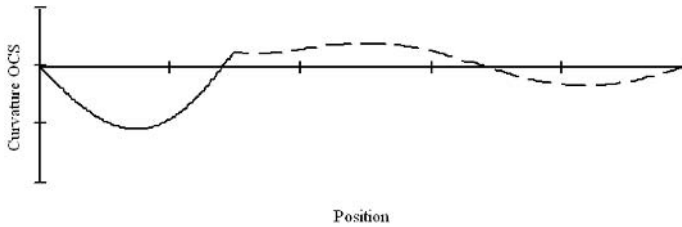


FIGURE 1. An example of a continuous, but not continuously differentiable, operational curvature shape.

## References

1. Yuen, M.M.F., *Journal of Sound and Vibration*, vol. **103**, 301-310, 1995
2. Liang Z, Lee G.C. and Kong F., In *proceedings of the 15th International Modal Analysis Conference, Society of Experimental Mechanics* 1997, vol. **1**, 308-312.
3. Chang K.C., Shen Z, and Lee, G.C., In *proceedings of the Symposium of Structural Engineering, Natural Hazards and Mitigation*, American Society of Civil Engineers, 1997, 1083-1088.
4. Pandey, A.K., Biswas, M. and Samman, M.M., *Journal of Sound and Vibration*, vol. **145** (2), 321-332, 1991
5. Ratcliffe, C.P., *Journal of Sound and Vibration*, vol. **204** (3), 505-517, 1997
6. Ratcliffe, C.P., *Journal of Vibrations and Acoustics*, vol. **122** (3), 324-329, 2000

## BIOMIMETIC GUIDED STRUCTURAL HEALTH MONITORING FOR CIVIL AIRCRAFT

Eddie O'Brien  
Aircraft Technical Solutions Ltd  
46 Downs Cote Drive Bristol. BS9 3TR. United Kingdom  
eddie.obrien@blueyonder.co.uk

A requirement that allows and enables the use of Damage Tolerant principles in the design and operation of Civil Aircraft is a strict regime of inspection and maintenance that ensures the operational safety from the structural point of view, Schmidt [1].

Currently the inspection programme is undertaken largely on a visual basis assisted by a growing number instruments of varying degrees of sophistication. Certain safeguards are built into the inspection procedure whereby all fatigue damages in areas designed by damage tolerant principles are detected and either repaired or monitored for later repair. The manual nature of the inspection and maintenance procedures mean that they are inevitably time consuming and expensive. The drive for cost reduction and improved aircraft availability has led to the demand for more automated forms of inspection that more than meet the existing requirements.

There appears to be two main approaches to Structural Health Monitoring for application to Civil Aircraft

- 1 Advanced Non-Destructive testing (NDT) in which current NDT techniques and equipment are enhanced to ensure finding all the required defects and reduce operator time.
- 2 A new approach that starts with the fracture event caused by fatigue and works back to a remote monitoring method of detection and location that will provide 'directed inspection' and maintenance.

This second approach is the subject of this paper guided by some aspects of biomimetics which uses good design ideas inspired by biology and nature in general, Bath [2].

Civil Aircraft and increasingly Military Aircraft are designed to minimum weight solutions that meet the Damage tolerant criteria, however each individual aircraft in a fleet is designed to a loading envelope that covers all possibilities of operation within the whole fleet. This implies some over-design just which will cover some loading actions that an individual aircraft may never actually see in service. This approach is a necessity for safety reasons, however the manual inspection regime is specified on the basis of the envelope design loading rather than the loading actually experienced by the individual aircraft. Differences in operational loading come from a multitude of sources such as variation in pilots, missions, weather conditions, runway roughness, actual airframe materials, environment etc, etc.

The biomimetic approach is used to give guidance toward an inspection procedure that is commensurate with the operational experience of each individual aircraft that allows reduced costs and flexibility in maintenance and also maximises aircraft availability.

The theory of inventive problem solving TRIZ [3] would indicate that best measurements are those made directly as possible. In the case of Structural Health Monitoring the fatigue damage that must be found by inspection to comply with the Damage Tolerant rules is revealed by 'cracks'. The development of a fatigue damage sensor is guided by biomimetic model in that like the human body the aircraft structure needs a nervous system in which the sensor must be appropriate to the phenomenon being detected and monitored.

In the case of the human nervous sensory system there Chemoreceptors, Mechanoreceptors, Nociceptors, Photoreceptors and Thermoreceptors which detect and transmit data related to Taste, Smell, Touch, Feel, Location, Pain, Vision, Temperature, Danger (too hot/cold) etc. These sensors undertake specific tasks with the resulting data often being combined in the brain. From the biomimetic pattern the choice of sensor to measure specific phenomena is critical to successful monitoring. Within the Damage Tolerant rules Fatigue Damage is what needs to be monitored – this is evidenced in the structure by cracking at the post-nucleation stage of the fatigue life progression. It is this same phenomenon that is required to be found by the current assisted manual inspection technique so when successfully done the Damage Tolerant regulations would be satisfied.

Piezo-electric sensors are one of the most powerful and reliable sensors of structural displacement. During the growth progress of a crack as each striation is formed the strain energy is changed into fracture energy as the partially embrittled plastic zone ahead of the crack is ruptured. This event is quite explosive in nature in which the energy is converted into fracture with an accompanying stress wave or acoustic emission that emanates from the crack tip and is eventually dissipated as heat in the structure. On the Structural Health Monitoring System developed by Airbus UK piezo-electric sensors are attached to the surface of a fatigue sensitive part whereby the stress wave is detected and its source determined by triangulating the time of flight of the wave from source to the sensors.

The sensitivity of this piezo-electric sensors is very high with stress waves of 10 picometres amplitude being easily detected during calibration trials.

By arranging an array of sensors in an aircraft structure in a pattern that reflects the distribution of the fatigue sensitivity of the parts – a Global Structural Health Monitoring System is constructed. The separation of non crack noise sources has been solved by the use of a selection procedure that only acknowledges signals that are repeated regularly from the same location. This actually replicates the physical features of fatigue crack initiation and growth.

This system has been in operation on Major Fatigue Tests for a number of years and a Lockheed Orion and an A340-600 have systems that are operational in flight,(4).

## References

1. Schmidt, H.J., Schmidt-Brandecker, B., Tober, G., Design of Modern Aircraft Structure and the Role of NDI. <http://www.ndt.net/article/ecndt98/aero/001/001.htm>. undated.
1. Bath, Uni. About Biomimetics, <http://www.bath.ac.uk/mech-eng/biomimetics/>. undated.
1. TRIZ, Theory of Inventive Problem Solving, [en.wikipedia.org/wiki/TRIZ](http://en.wikipedia.org/wiki/TRIZ) -51k - 6 Sep. 2006.
1. Recent Advances in Experimental Mechanics. In Honor of Isaac M. Daniel -Gdoutos, EE (Ed.) 2002, 844 p., Hardcover ISBN: 1-4020-0683-7 - Springer.

## IN-SITU HEALTH MONITORING OF OBJECTS CONSISTING OF VISCO-ELASTIC MATERIALS.

Karl-Hans Laermann  
Bergische Universität Wuppertal  
Pauluskirchstraße 7, D-42285 Wuppertal, Germany  
laermann@uni-wuppertal.de

Experimental methods enable in-situ measuring deformations of any kind of technical products and structural objects. The measured data enable drawing conclusions on the actual state of objects and provide reliable knowledge on the actual internal parameters like the strength of materials, on the internal stress state as well as on the changes of the parameters over time, caused e.g. by aging, fatigue and environmental influences. Especially in case of visco-elastic response of material it is inalienable sometimes to dispose on reliable information on the characteristic parameters and their changes over time in order to assess the functionality, reliability and safety of a structure. To observe the parameter changes and their effects on the object responses during the life-time the course of deformations can be pursued by measurements. However the observed phenomena and measured data do not meet generally the finally wanted information on the parameters. Therefore mathematical / numerical methods are to apply for solving the now existing inverse problems. Following it will be described how the information on the actual internal parameters like the relaxation moduli can be determined as functions of time with reference to a plate-in-bending.

Based on Boltzmann's principle the relation between the stress state and the strain state is described in the time space according to Nowacki [1] by a Volterra's integral equation of the 2<sup>nd</sup> kind. The measurements yield the data of the strain state, which are to separate in the volume strain and the strain deviator. As the measurements are performed in discrete time intervals the metered data are discrete data and not available as functions unless they are expanded in a proper series. Therefore the integral equation must be transformed into a finite difference summation equation.

The following considerations refer to the shear-elastic plate theory of the first order, Altenbach et al. [2] because this theory models plate problems more realistic and the equilibrium conditions yield two equations with the unknown parameters, the relaxation bulk modulus  $K(t)$  and the relaxation shear modulus  $G(t)$

$$G(t_n) \cdot \Sigma_{\alpha 0}^* + K(t_n) \cdot \bar{\Sigma}_{\alpha 0} = \sum [G(t_{n-v}) \cdot \Delta_{\alpha v}^* + K(t_{n-v}) \cdot \bar{\Delta}_{\alpha v}] + G(0^+) \cdot \Delta_{\alpha 1}^* + K(0^+) \cdot \bar{\Delta}_{\alpha 1} \quad (1)$$

$K(0^+)$  and  $G(0^+)$  denote the initial values of these parameters at time  $t = 0$ . The expressions  $\Sigma$  and  $\Delta$  depend on the strain state derived from the measured deflection surface and on Poisson's ratio  $\mu$ , which can be approximated in an iterative process.

As an example of application a clamped plate has been chosen, dimensions and loading are shown in Figure 1. The specimen was made of epoxy resin Araldite *F* with hardener *HY951* and plastiziser Araldite *CY208*. By means of electronic speckle pattern interferometry (*ESPI*), the surface of deflection has been measured in time intervals  $\Delta t$ , starting at time  $t(0^+) = 0$  proceeding till  $t_E = 1000$  seconds. For data recording and processing the program *ISTRA* [3] has been used yielding the digital data  $u_3$  in the nodes of an evaluation grid. These data have been subjected to a statistical process of smoothing and adjustment to obtain an approximation function  $u_3(x_1, x_2)$  enabling the calculation of the derivatives of the 2<sup>nd</sup> and 3<sup>rd</sup> order.

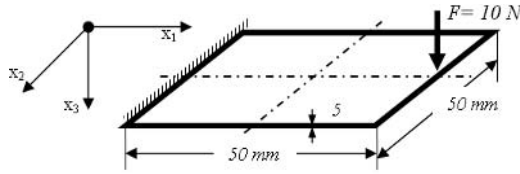


FIGURE 1. Specimen of a clamped plate

Poisson's ratio has been found by the iteration process to  $\mu = 0.40$ . With the now given input data the solution of eq.s (2) yields the characteristic parameters  $K(t)$ ,  $G(t)$  (Fig. 2).

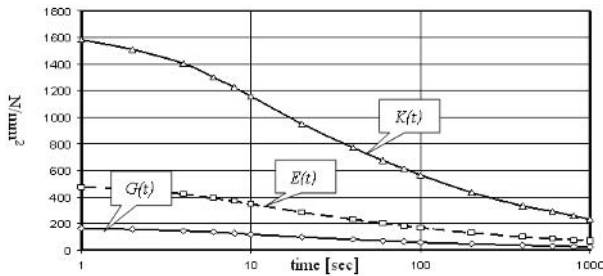


FIGURE 2. Evolution of the relaxation parameters

The preceding contemplations are based on the presumption the measurements to start at the time of initial loading. However the more interesting case is to consider, that the monitoring process begins some time after the initial loading and no information on the history of the relaxation process is available. The principle how to proceed in this case is shown in Fig. 3.

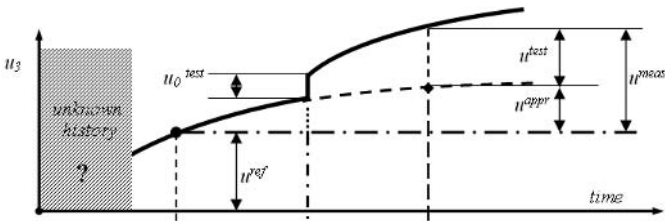


FIGURE 3. Determination of deflection  $u_3(t)$  after applying test-load.

**References**

1. Nowacki. W., *Theorie des Kriechens*, Franz Deuticke, Wien, Austria, 1965.
2. Altenbach, H., Altenbach, J. and Naumenko, K., *Ebene Flächentragwerke*, Springer, Berlin, Germany, 1998.
3. ISTR 3D – *Benutzerhandbuch*, Etemeyer AG, Ulm, 1998.

## EXPERIMENTAL SAFETY EVALUATION OF ROOFS

Marc Gutermann and Klaus Steffens

Hochschule Bremen, Institut für Experimentelle Statik, Neustadtwall 30,

D-28199 Bremen, Germany

ifes@hs-bremen.de

Ingenieurgesellschaft mbH, Neustadtwall 30, D-28199 Bremen, Germany

info@psi-bremen.de

In January 2006 the roof of the German ice-skating rink in Bad Reichenhall near Munich collapsed and killed 15 persons (Fig. 1). Later investigations showed that heavy snow fall as well as massive deficiencies in the construction of the gluelam girders had lead to the disaster, which started a national discussion about the structural safety of existing buildings.



FIGURE 1. Collapse of the German ice-skating rink in Bad Reichenhall (Photo: ZDF)

Structures are planned for a defined use and limited lifetime. When damages occur or the service loads shall be increased due to changed customer's requirements, the serviceability and load carrying safety must be proofed again. If a calculation is not sufficient an experimental approach can be an economical alternative to a conventional strengthening. An experimental safety evaluation yields a better result as computed methods as a rule since a regular erected structure has load carrying reserves, which can be proofed only by experiment:

- 1 The effective material properties are better than the allowed computed values
- 2 The structure has to be simplified for calculation (solvable!) and contains reserves
- 3 An experiment can proof the structural safety with partial reduced safety factors since imponderables are reduced due to the object-related verification (DAfStb [1], Gutermann [2])

This article shall show some examples (Figs 2 - 5) how calculation and experiment can complement each other in analysing the load capacity of roofs, although a computed proof had failed (Steffens [3]).



FIGURE 2. Truss of square-shaped timber

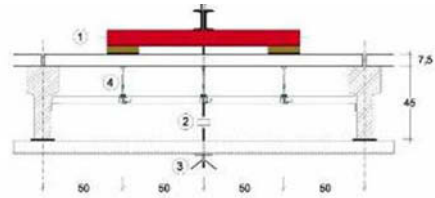


FIGURE 3. Light-weight concrete slabs, Berlin

FIGURE 4. Prestressed precast girders  
made of high-alumina cement

FIGURE 5. Roof of a football stadium, Koblenz.

## References

1. DAFStb (Ed.), Richtlinie für Belastungsversuche an Betonbauwerken, Beuth, Berlin, Germany Sept. 2000
2. Gutermann, M., An article on experimental assessment of structural safety of solid bridges. In *Proceedings of ICEM12- 12th International Conference on Experimental Mechanics*. 29. August – 2. September, 2004 Politecnico di Bari, Italy
3. Steffens, K., Practical Building Examples; In: *Monitoring and Assessment of Structures*, Spon Press, Juli 2001, S. 138-165

## DETERMINTAION OF LOCATION AND SIZE OF A THROUGH-THICKNESS PART-WIDTH CRACK IN CANTILEVER BEAMS

L. Kannappan, K. Shankar and A.G. Sreenatha  
University of New South Wales, Australian Defence Force Academy,  
School of Aerospace, Civil and Mechanical Engineering, ADFA, Northcott drive, Australia  
l.kannappan@adfa.edu.au

With advancements in sensor technology and structural health monitoring systems, the application of modal response measurements for online damage detection and assessment appears more promising than ever. This paper examines the use of natural frequency measurements of the structure for detection of cracks. A method to assess the crack location as well as crack size in elastic beams with through thickness-crack is formulated. Here, crack is modelled as a torsional spring whose stiffness is proportional to the size of the crack. Changes in modal frequencies depend on both location and size of crack. With three or more measured natural frequencies, the location and size of the crack are determined. The theory is first validated with frequency data generated by Finite Element Modelling (FEM) of through-thickness, partial-width cracks in cantilever beams. Experimental Modal Analysis (EMA) is performed on beams with simulated through thickness partial width cracks and the measured frequency changes are used to determine the damage location and size. Good agreement between predicted and actual location of crack is obtained for experimental frequency data.

Cracks are modelled as spring with stiffness,  $k_r$ , and incorporated in the Euler-Bernoulli beam vibration theory. With two boundary conditions at each end of the beam and two more boundary conditions before and after the crack location, a characteristic equation (8x8 matrix) was derived by Ostachowicz and Krawczuk [1], Rizos *et. al.* [2] and Liang *et. al.*[3]. [1] formulated a method to find the crack length of edge cracks in beams using the stress intensity factor (SIF) and change in elastic deformation energy of the crack. Employing a similar method, the length of through-thickness partial-width crack, in beams is determined.

In this study, the SIF derived by Zehnder and Hui [4] is used for determining the size of crack. A finite width correction factor, obtained from Erdogan and Boduroglu[5], is also included in the formulation.

### Theory for determining crack size

If  $K_I$  is the SIF,  $E$  is the Young's modulus and  $A$  is the area of the crack, then, the change in elastic deformation energy of the crack, given by Atluri [6], is

$$\Delta M = \frac{1}{E} \int_0^A K_I^2 dA \quad (1)$$

The SIF of an infinite plate in bending as given by [4]

$$K_I = \frac{6M}{t^2} \sqrt{b} \quad (2)$$

where,  $M$  is the applied bending moment,  $t$  is thickness of the beam and  $2b$  is the crack length

After incorporating Eqn.(2) in Eqn.(1), the spring stiffness is obtained as

$$K_s = \frac{Et^3}{18 + \gamma^2} \quad (3)$$



Alternately, if  $K_s$  is derived from stress intensity factor equations given by [5], then spring stiffness is obtained as

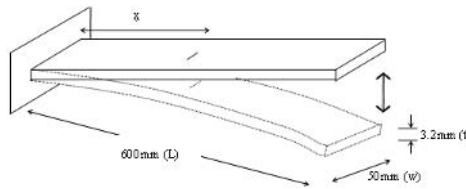
$$K_s = \frac{Et^3}{36 + \gamma^2} f(\gamma) \quad (4)$$

where  $f(\gamma)$  is obtained from the finite width correction factor

$f(\gamma)$  are obtained for different beam thicknesses since the SIF for a plate in bending changes with thickness[5].

## Experiments

Rectangular slots 0.2mm wide and 20 mm long were induced in the beam using wire cut EDM process to simulate crack. The distance from the fixed end to the centre of the damage is changed. EMA is done on the beam in fixed-free boundary condition as in Fig. 1. The error between the experimentally measured natural frequencies and that obtained from FEA are found to be less than 0.5%. Using the experimental frequencies and above said theory, the maximum error in locating the crack is 3% and the maximum error in finding the crack size is 10%.



## References

1. Ostachowicz, W.M. and M. Krawczuk, *Analysis of the effect of cracks on the natural frequencies of a cantilever beam*. Journal of Sound and Vibration, 1991. vol. **150** (2): p. 191.
2. Rizos, P.F., N. Aspragathos, and A.D. Dimarogonas, *Identification of crack location and magnitude in a cantilever beam from the vibration modes*. Journal of Sound and Vibration, 1990. vol. **138** (3): p. 381.
3. Liang, R.Y., J.L. Hu, and F.K. Choy, *A Theoretical Study of Crack-Induced Eigenfrequency Changes on Beam Structures*. Journal of Engineering Mechanics, 1992. vol. **118** (2): p. 384-396.
4. Alan Zehnder and C. Hui, *A theory for the fracture of thin plates subjected to bending and twisting moments*. International Journal of fracture, 1993. vol. **61**: p. 211-229.
5. Boduroglu, H. and F. Erdogan, *Internal and edge cracks in plate of finite width under bending*. Journal of Applied Mechanics, 1983, vol. **50**: p. 620-629.
6. Atluri, S.N., *Computational Methods in Mechanics of Fracture*, vol. **2**. 1986: Elsevier science publishers, Netherlands.

## MONITORING LIFE EXPENDITURE OF POWER STATION ENGINEERING PLANT

Andrew Morris<sup>1</sup>, John Dear<sup>2</sup>, Miltiadis Kourmpetis<sup>2</sup>, Alexander Fergusson<sup>2</sup> and Amit Puri<sup>2</sup>

<sup>1</sup> Group Head Boiler Integrity, E.ON UK, Power Technology  
Ratcliffe-on-Soar, Nottingham NG11 0EE, United Kingdom

<sup>2</sup> Department of Mechanical Engineering, Imperial College London  
SW7 2AZ, United Kingdom

andy.p.morris@eon-uk.com, j.dear@imperial.ac.uk, m.kourmpertis@imperial.ac.uk,  
alexander.fergusson@imperial.ac.uk, amit.puri@imperial.ac.uk

The life of steam pipes in power stations very much depends upon the material's steady state creep rate. A problem is monitoring the steady state creep rate as access to these pipes in power stations is difficult as the pipes are heavily lagged and the network of pipes are in compact installations. Essential is that monitoring sensors are of a very rugged design well able to endure the demanding conditions related to the environment of high pressure steam pipes. It has been necessary to devise a method that can provide creep data for remnant life assessment of pipes when a power generating plant is closed down for periodic maintenance. This is to use gauges developed by E.ON UK, the movement of which is measured by a special-to-purpose optical system. The gauges are located on pipes, bends and other locations most susceptible to early creep strain failure. Both circumferential and axial strain rates are monitored to provide for analysis to identify when pipes are approaching their reliable end-of-life point. This provides for planned replacement of pipes as part of cost effective management of power-stations. The E.ON UK ARCMAC gauge system for measuring strain has been developed in the light of experience of its use to achieve high confidence ratings in the data obtained. This creep strain monitoring system provides data that can be used to underwrite life extension of power stations, many of which are now in operation beyond 225,000 hours.

In co-operation with the Mechanical Engineering Department of Imperial College London, further developments of the ARCMAC system are in progress. This includes the use of Digital Image correlation (DIC) to study the variations in creep strain on pipework adjacent to the ARCMAC gauges. This is particularly useful, for example, when monitoring welds and other localised features on the pipe network. This presentation reports on this research activity. Part of this study has been to validate the combined ARCMAC/DIC system by using laboratory specimens prepared with hidden defects and other features for clarity and sensitivity in the detection of these defects.

A related study is for monitoring the onset of fatigue in wind turbine blades. This requires monitoring when the blades are in operation and the transmission of these data to nearby monitoring and data-recording stations. Also, there is interest in similar life monitoring of other power generation plant being considered for installation.

This paper presents the development of the combination of two monitoring methods that are currently being further developed [1]. Both methods operate on the principle of capturing two digital images of a 'sensor' at different points in time, subsequent analysis of these images results in an estimate of creep strain rate, which is used in remnant life assessments. Precision optics, a CCD camera and light source system are used to capture both ARCMAC and DIC data. Fig. 1 shows an example of the installation of a biaxial ARCMAC gauge from which biaxial strain measurements can be made. Fig. 2 shows an example of a DIC strain plot showing a sub-surface defect.

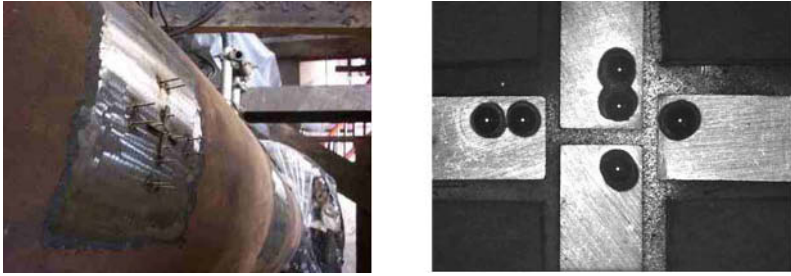


FIGURE 1. Biaxial ARCMAC gauge on extrados of steam pipe with recorded image.

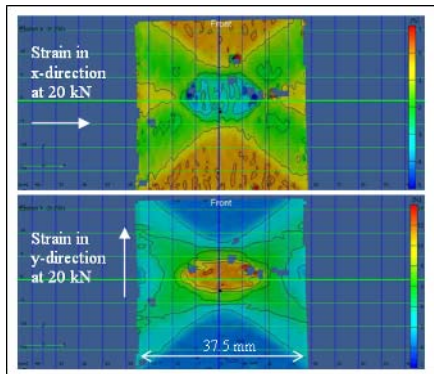


FIGURE 2. Biaxial ARCMAC on extrados of steam pipe.

## References

1. Morris, A. Dear, J. and Kourmpetis, M. "High Temperature Steam Pipelines – Development of the ARCMAC Creep Monitoring System", *Strain*, vol. **42**, 2006, 181-185.

## CONDITION MONITORING OF INDUCTION MOTORS FOR VERTICAL PUMPS WITH THE CURRENT AND VIBRATION SIGNATURE ANALYSIS.

Young-Shin Lee and Yeon-Whan Kim

Department of Mechanical Design Engineering, Chungnam National University,

Director of BK21 Mechatronics Group

220 Gung-Dong, Yuseong, Daejeon, 305-764, Korea

Korea Electric Power Research Institute,

Munji-Dong, Yuseong, Daejeon, 305-380, Korea

leeys@cnu.ac.kr

Induction motors are the workhorse of modern industry because of their versatility and robustness. The diagnosis of mechanical load and power transmission system failures is usually carried out through mechanical signals such as vibration signatures, acoustic emissions, motor speed envelope. The motor faults including mechanical rotor unbalances, broken rotor bar, bearing failure and eccentricities problems are reflected in electric, electromagnetic and mechanical quantities. The recent research has been directed toward electrical monitoring of the motor with emphasis on inspecting the stator current of the motor. The stator current spectrum has been widely used for fault detection of induction motor. The current signature analysis of motor is the useful technique to assess on machinery health condition monitoring. This paper describes the motor condition monitoring by the current signatures paralleled with vibration signatures analysis of induction motors. Condition monitoring on the roller bearing and the journal bearing for large vertical pumps in power plant is conducted to investigate for motor fault detection and diagnosis.

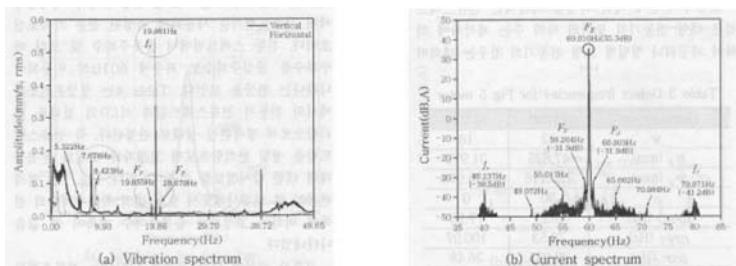
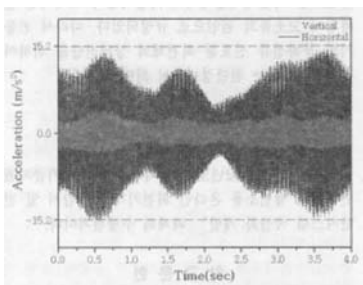


FIGURE 1. Frequency pattern of spectra in induction large motor with journal bearings

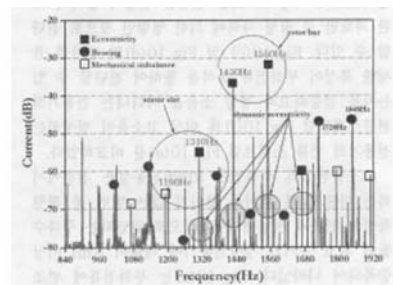
### References

1. KEPRI, "Development of Localization for On-line Condition Monitoring and Diagnostic System in Power plant", 2<sup>nd</sup> Midterm Report, KEPRI, pp. 70~96, 2004.
2. Song, M.-H. Kang, E.-S. Jeong, C.-H. Chow, M.-Y. and Ayhan, B., "Mean Absolute Difference Approach for Induction Motor Broken Rotor Bar Fault Detection," Symposium on Diagnostics for Electric Machines, pp. 4~18, 2004.
3. Berry J. E., "Comparison of Motor Current Analysis and Vibration Analysis in Detecting Rotor Bar and Air Gap Eccentricity Problems in Induction Motors," Technical Associates of Charlotte, Inc, 1996.

4. Stack J. R., "Fault Classification and Fault Signature Production For Rolling Element Bearings in Electric Machines," Symposium on Diagnostics for Electric Machines, pp. 172~176, 2004.
5. Chung, B.-H. and Shin, D.C., "A Study on Detection of Broken Rotor Bars in Induction Motors Using Current Signature Analysis," Transactions of the Korean Society for Noise and Vibration Engineering, vol. 12 (4), ISSN1598-2785, pp. 287~293, 2002.
6. Ayhan, B., Chow, M.-Y., Trussell, H. J., Song, M.-H., "Statistical Analysis on a Case Study of Load Effect on PSD Technique for Induction Motor Broken Rotor Bar Fault Detection," SDEMPED (Symposium on Diagnostics for Electric Machine, Power Electronics and Drive), pp. 119~123, 2003.



(a) Fault vibration waves



(b) Fault current

FIGURE 2. Load modulation of induction large motor system with journal bearings

## UNBIASED EXPERIMENTAL REFLECTION METHOD FOR THE ULTRASONIC CHARACTERIZATION OF MATERIALS

D. A. Sotiropoulos  
Department of Engineering Sciences  
Technical University of Crete  
GR-73100, Chania, Greece  
das@mechanics.tuc.gr

For the ultrasonic evaluation and characterization of bulk properties of various materials and structures such as concrete and cement-based materials as well as the ultrasonic characterization of the structural integrity of bi-material bonds, the reflection of body ultrasonic waves has been widely used as an experimental tool, witnessed by the extensive publication of articles in diverse scientific journals. In these experimental techniques, the structure under investigation is in contact with another medium/material as for example with water, glass or air. This is exemplified by recent publications which include, but are not limited to, the works of Sun et al [1], Ozturk et al [2] and Daniel [3].

The body waves generated in experimental reflection studies, strike the surface of the structure under investigation in various angles usually at normal incidence. The key issue that one faces is to conduct the experiment in such a way as to be unbiased to the angle of incidence. In other words, to generate body waves at such an angle of incidence as to produce the same results independent of which medium contains the incident body wave. For an isotropic bi-material interface when both longitudinal and shear waves are incident, the proposition of Ditre and Lakhtakia [4] for incidence at a generalized Brewster angle is a sound one, in the sense that it establishes an experimental guideline for the unbiased ultrasonic characterization of structural integrity.

However, such a Brewster angle does not always exist for any bi-material combination. The work of Avdelas and Sotiropoulos [5] proved the fact that for the aforementioned materials, the experiment as well as the result are unbiased for any angle of incidence so long as the recorded reflection coefficients are combined in the specific fashion  $R=R_{pp}R_{ss}-R_{sp}R_{ps}$ , with  $p$  and  $s$  denoting the longitudinal and shear waves, respectively. The vanishing of this, the reflectivity, results in wave incidence at the generalized Brewster angle. The reflectivity,  $R$ , is in fact an inherent structural integrity characteristic of the bi-material interface.

However, most experimental techniques in the literature propose investigations that use, in the case of macroscopically isotropic materials, only one kind of body wave, either longitudinal or shear. Therefore, the initial question posed above still remains as to what is the angle of incidence of a single body wave that results in an unbiased experiment as well as in an unbiased characterization of the structural integrity ultrasonically. Furthermore, what would be the angle(s) of incidence for experiments involving anisotropic materials? These questions are answered by the present study with reference to specific experimental configurations and the proposition of a method.

In the present paper, an unbiased experimental method for the ultrasonic characterization of materials is proposed. First, the method is proposed for a single bulk wave incidence, either longitudinal or shear, for a single macroscopically isotropic structure in contact with air. The optimal angle of incidence is found for which an unbiased characterization of the structural integrity of the material is achieved ultrasonically. Then the issue of the presence of water in contact with the structure under investigation is encompassed in this study and the method is extended for this case to determine the angle of incidence for an unbiased experimental

investigation. Results for this particular case for an isotropic material were presented by Sotiropoulos [6].

The experimental method proposed in the present paper is extended for the ultrasonic characterization of anisotropic materials as well. Particular emphasis is paid to the cases where the material is either in contact with air or with water. The multiplicity of body waves present at multiple angles in these cases, requires special attention and more involved experimental set ups.

The relation of the angle(s) of incidence, found in the proposed experimental method, to a Brewster angle concept is established. Results for the proposed experimental method are also presented for different materials and structures. Striking results are obtained when the incident and reflected waves form a golden triangle.

Finally, the effect of the ratio of the bulk material parameters of an isotropic material obeying the golden ratio is examined, in so far as the angle of wave incidence is concerned, for the proposed experimental method. Interesting results are found in relation to the golden triangle reflection and the Brewster angle.

## References

1. Sun, Z., Ye, G., Voigt, T., Shah, S. P. and van Breugel, K., International Symposium: *Advances in Concrete through Science and Engineering*, Evanston, Illinois, USA, 2004
2. Ozturk, T., Kroggel, O., Grubl, P., and Popovics, J. S., *NDT & E International*, vol. **39**, 258-263, 2006
3. Daniel, I. M., *31<sup>st</sup> International SAMPE Technical Conference*, Chicago, Illinois, USA, 1999
4. Ditri, J. J., and Lakhtakia, A., *J. Acoust. Soc. Am.*, vol. **94**, 576-579, 1993
5. Avdelas, G. and Sotiropoulos, D. A., *J. Acoust. Soc. Am.*, vol. **96**, 3126-3131, 1994
6. Sotiropoulos, D. A., *J. Sound & Vibration*, vol. **185**, 501-506, 1995

## FATIGUE CRACK DETECTION BY ACOUSTIC EMISSION MONITORING IN THE COURSE OF LABORATORY STRENGTH TEST

Jiri Behal

Aeronautical Research and Test Institute  
Beranových 130, Prague, Czech Republic  
behal.jr@vzlu.cz

Experimental tasks are important for improving designer knowledge and choosing smaller scatter factor of proposed structure, decreasing its weight and increasing reliability. An optimization of design is the key tool especially in aircraft industry. The Aeronautical Research and Test Institute is a scientific and technological base located in Prague. There are several laboratories such as wind tunnels, flight test facilities and strength testing laboratory. In the Experimental Strength department, the full-scale aircraft frames are loaded during simulation of service condition. Appropriate service maintenance for critical point is established and physical phenomena of inspection techniques are studied too.

Aluminium became an essential metal in aircraft industry. Although the integral structures using composites are validated, the most planes are made of metal today. Significant fraction of airframe structure consists of stiffened panels. The main loads are transferred through beam elements of the spars, Fig. 1. Because of inspection reliability, the periodic inspections by tradition techniques, e.g. visual, eddy current, ultrasound, are supported by acoustic emission monitoring.

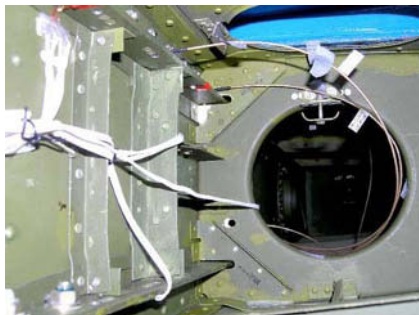


FIGURE 1. Structure of aircraft frame.

Acoustic emission method takes a part in modern range of non-destructive testing applications and it appears to be perspective for next research in an aircraft industry. The acoustic emission monitoring and appropriate analyses of experimental data are objects of research tasks today. The aim of this research is to formulate methodology, according which will be possible to reliably evaluate if the material cracking is present or not. The study is derived on the base of laboratory experiments, where the service conditions are simulated on the aircraft frame and its models.

Draft of the experiment is illustrated in the Figs. 2-4. Crack growth in early stage of propagating as well as acoustic wave dispersion are observed and documented. Common and characteristic features should be recognized for reliable identification of emission source.



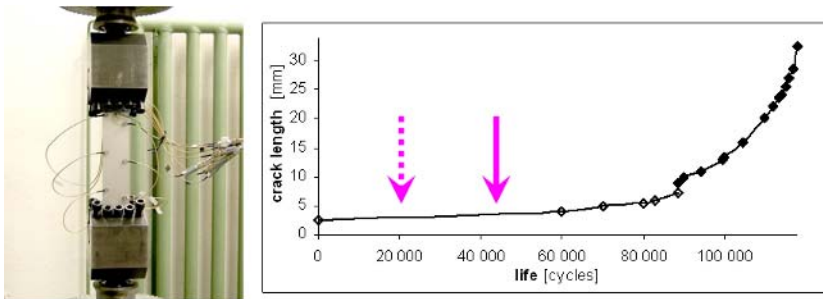


FIGURE 2. Technological sample and crack growth curve.

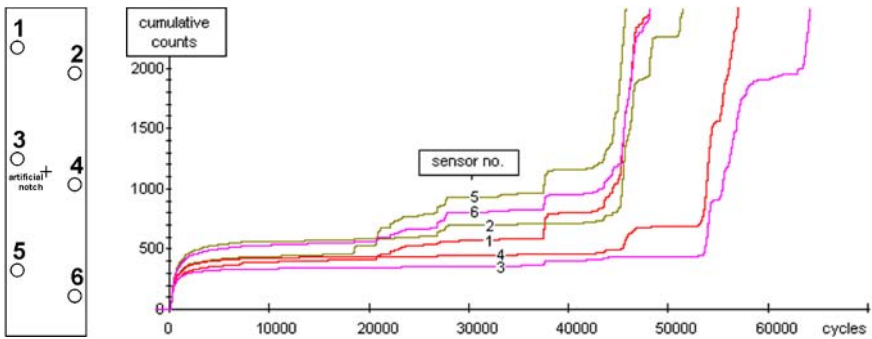


FIGURE 3. Cumulative counts of acoustic emission events.

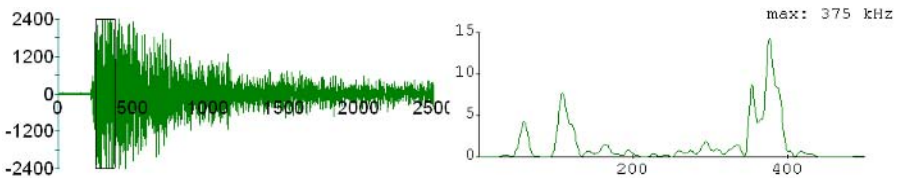


FIGURE 4. Analyses of acoustic emission events in frequency domain.

## RESIDUAL STRESS MEASUREMENT USING A MINIATURISED DEEP HOLE DRILLING METHOD

X. Ficquet, D. J. Smith and C. E. Truman

Department of Mechanical Engineering, University of Bristol  
Queen's Building, University Walk  
Bristol, BS8 1TR, United Kingdom  
C.E.Truman@bristol.ac.uk

One of the significant advantages of the deep hole drilling (DHD) technique over others is that being a semi-invasive technique the experiment may be conducted 'on-site', allowing a component or structure to be withdrawn for testing and subsequent repair. This paper presents the details and recent developments of the deep hole drilling technique and then goes on to present recent research directed towards reducing the overall size of the existing measurement equipment. Using our existing experimental arrangement, which has been extensively developed over recent years [1-4], it was possible to undertake residual stress measurements to depths in excess of 500mm, although this deep through-thickness capability meant that the rig had an overall length of about one meter, which limited its use in confined spaces. It was decided to miniaturise the machine to allow residual stress measurements to be made in environments that were hitherto not amenable to such measurements, e.g. on the inside of a pipe. The trade-off to the miniaturisation process was a reduced measurement depth capability of approximately 50mm. In addition to permitting residual stress measurements to be made in confined spaces, the miniaturisation process also provides improved transportability which, in turn, means that measurements made be made more readily away from the laboratory. The paper will begin by describing in detail the new, miniaturised deep hole drilling system and then go on to use the rig to make a residual stress measurement in a stainless steel component.

The validation component considered in this paper originated as part of the NET (Neutron Evaluation Techniques) European network. Four nominally identical base-plates were machined to the dimensions shown in Fig. 1 (180mmx120mmx17mm) from a single piece of solution heat treated AISI Type 316L austenitic stainless steel plate of nominal dimensions 600mmx150mmx50mm. The base plates were then re-solution heat treated in air to eliminate any machining residual stresses. A single weld bead of nominal length 60mm was deposited along the centre-line of each plate parallel to the longest edge using an automated Tungsten inert gas (TIG) process. During welding, the plates were held horizontally across the 120mm dimension by lightly clamping in a vice. This weld geometry produces a strongly three-dimensional residual stress distribution, with similar characteristics to a weld repair in a compact portable specimen which is amenable to measurement using diverse techniques. The single weld pass is relatively straightforward to model numerically. However, because the bead is deposited onto a relatively thin plate, the predicted stresses are very sensitive to key modelling assumptions such as total heat input and thermal transient time history, making measurements even more necessary.

This specimen had two principal attractions when viewed as a validation specimen for the new DHD rig. Firstly, a previous DHD measurement had been performed using the existing DHD rig (at the position labeled DHD1 in Fig. 1). Secondly, an abundance of experimental and numerical data was available from many research laboratories across Europe for comparison. The paper will concentrate on the application of the DHD procedure to location DHD2 in Fig. 1 (the stop end of the weld) and will present the measurement results and their comparison to other measurements of residual stress at the same spatial location.

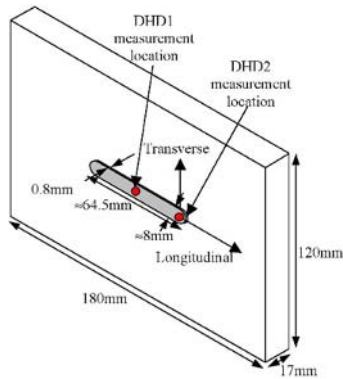


FIGURE 1. Dimensions of the NET specimen A2.1

The results also permit a comparison to be made between the through-thickness residual stress distributions at weld mid-length and at the stop end of the weld. The comparison supports the hypothesis from numerical models that the residual stresses are greatest at the stop end of the weld, a result which has clear implications when viewed in the context of structural integrity assessments or repair welds.

## References

1. Leggatt, R. H., Smith, D. J., Smith, S. D. and Faure, F., *J. Strain Anal.*, vol. **31**, 177-186, 1996
2. Bouchard, P. J., Holt, P. and Smith, D. J., *Proceedings of ASME-PVP Conf.*, vol. **347**, 77-82, 1997
3. George, D., Kingston, E. and Smith, D. J., *J. Strain Anal.*, vol. **37**(2), 125-139, 2002
4. Stefanescu, D., Truman, C. E. and Smith, D. J., *J. Strain Anal.*, vol. **39**(5), 483-497, 2004

## NEUTRON DIFFRACTION PERFORMANCE BASED ON MULTIPLE REFLECTION MONOCHROMATOR FOR HIGH-RESOLUTION NEUTRON RADIOGRAPHY

Pavel Mikula and Miroslav Vrana  
Nuclear Physics Institute and Research Centre Rez Ltd.  
250 68 Rez, Czech Republic  
mikula@ujf.cas.cz

The effects of multiple Bragg reflections in single crystal can be observed when more than one set of planes are simultaneously operative for a given wavelength i.e. when more than two reciprocal lattice points are at the Ewald sphere (see e.g. Chang [1]). Multiple reflection effects can result in reducing the intensity of a strong primary reflection or increasing the intensity of a weak primary reflection. The extreme case is the effect of simulation of forbidden primary reflection (often called as Renninger or *Umweganregung* effect) as first observed Renninger [2] with X-rays and Moon and Shull [3] with neutrons. Using a bent perfect crystal, the multiple reflection effect can be considered as a two step process when primary reflection represented by the lattice planes ( $h_1k_1l_1$ ) is simulated by successive reflections realized on the lattice planes ( $h_2k_2l_2$ ) and ( $h_3k_3l_3$ ) which are mutually in dispersive diffraction geometry (Fig. 1). However, it is a common view that dispersive neutron diffraction settings are not convenient for a practical use in an experiment because of low luminosity of a scattering instrument. In fact, the luminosity corresponds to the volume of the phase space element of the monochromatized beam represented by the wavelength spread  $\Delta\lambda$  and the divergence  $\Delta\theta$ . On the other hand, the dispersive double-crystal reflections can provide very high  $\lambda$ - and  $\theta$ -resolution making  $\Delta\lambda$  and  $\Delta\theta$  very small without use of any collimators. In relation to the value of the bending radius, the obtained doubly reflected beam has, however, a narrow band-width  $\Delta\lambda/\lambda$  of  $10^{-4}$  -  $10^{-3}$  and  $\Delta\theta$ -collimation of the order of minute of arc. It is clear that in comparison with the conventional single reflection monochromators the monochromatic neutron current is lower proportionally to a smaller  $\Delta\lambda$  and  $\Delta\theta$  spread. Recent experimental studies of Mikula *et al.* [4-6] proved the possibility of using the multiple reflection neutron monochromator for high or ultra-high resolution monochromatization in powder diffractometry and residual stress/strain measurements. However, very high collimation of the monochromatic beam can be used in special cases for high-resolution neutron radiography, namely in the cases when a position sensitive detection technique cannot be sufficiently close to the tested irradiated sample volume. In our contribution we present results of the first tests of neutron radiography experiments with the highly collimated monochromatic beam obtained by the multiple reflection monochromator. For our test we used the double-reflection process based on simulation of 222 reflection by the pair of  $111/331$  reflections at  $\lambda = 0.2348$  nm which was realized in a cylindrically bent Si-crystal set for diffraction in symmetric transmission geometry at  $\theta = 48.526^\circ$ [6].

This research has been supported by the projects AV0Z10480505, MSM2672244501 and GA-CR 202/06/0601.

### References

1. Chang, Shih-Lin, *Multiple Diffraction of X-rays in Crystals*, Springer Verlag, Berlin, 1984.
2. Renninger, M., *Zeitschrift für Kristallogr.*, vol. **113**, 99-103, 1960.

3. Moon, R.M. and Shull, C.G., *Acta Crystallographica*, vol. **17**, 805-812, 1964.
4. Mikula, P., Vrana, M. and Wagner, V., *Physica B*, vol. **350**, e667-e670, 2004.
5. Mikula et al., In *Proceeding 12th International Conference on Experimental Mechanics*, Bari, Italy, edited by C. Pappalettere, McGraw-Hill, 2004, CD-ROM - paper 038.
6. Mikula, P., Vrana, M. and Wagner, V., *Zeitschrift für Kristallogr. Suppl.* **23**, 199-204, 2006.

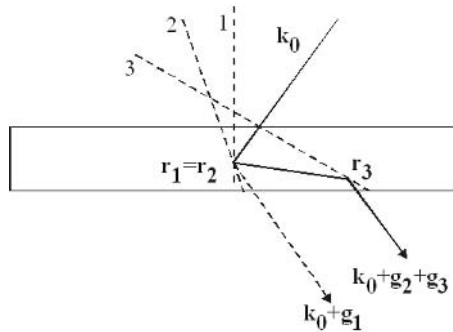


FIGURE 1. Schematic diagram of a two-step multiple Bragg reflection of neutron of the wave factor  $k_0$  simulating a weak of forbidden reflection. The number 1, 2 and 3 correspond to the primary, secondary and tertiary reflection planes and  $g_1$ ,  $g_2$  and  $g_3$  are the corresponding scattering vectors, respectively.

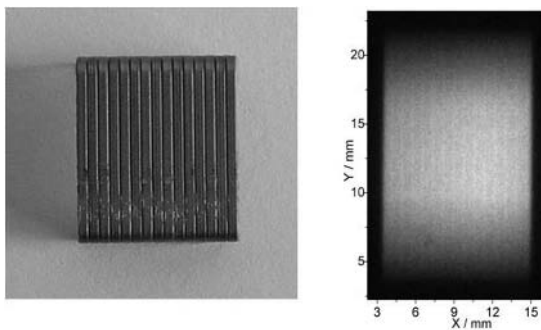


FIGURE 2. Example of the radiography image of the office staples 24/6 taken with the image plate at the distance of 70 cm from the sample.

## A MODIFIED THREE POINT BEND SPECIMEN

Kjell Eriksson

Department of Solid Mechanics

Luleå University of Technology, SE 971 87 Luleå, Sweden

kjell.eriksson@ltu.se

Fracture toughness testing is today used in several countries in integrity assessment work of structures of older steels with unknown toughness properties, the majority erected more than half a century ago. The most common type of test specimen employed is the three-point-bend specimen, which is plane-parallel and of constant thickness. Many typical profiles in older structures, such as angle sections in beams and girders, have however slightly tapered sides, seen in cross section. Samples taken from such profiles are presently machined to produce a plane-parallel shape and it is not uncommon to remove all the original surfaces of the sample. The cross sectional thickness of a fully machined specimen is therefore, in practice, only 60-70% of that of the original sample. In older and inhomogeneous steels an unfairly low toughness might then be obtained, as the toughness of the material near the surface often has been found to be superior.

The aim of the present project is to modify the standard three-point bend specimen, as given e.g. in ASTM E-1820 [1], so as to better accommodate steel samples with tapered sides. The modified specimen will allow a more reliable effective toughness to be determined since the full sample thickness can be used and in particular the critical surface features will be preserved. The cross section of the modified specimen, inscribed in a typical tapered profile, is shown in Fig. 1.

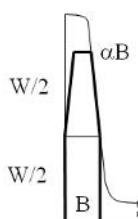


FIGURE 1. Cross section of modified three-point-bend specimen.  $W$  is specimen high,  $B$  is specimen thickness of the lower half, and  $\alpha B$  is thickness at the top of the specimen

The project comprises development, calibration and testing of the modified three-point-bend specimen, including derivation and verification of expressions allowing calculation of fracture toughness from experiment for both linear and non-linear behaviour, in short, to determine the stress intensity factor  $K_I$  and the  $J$ -integral for the modified specimen as functions of relevant parameters.

The calibration work will be both analytical and numerical. The first part of the project, which is reported here, is analytical and aimed at obtaining a first and rough estimate of the order of influence of the modified geometry on crack tip parameters. To this end, the method by Kienzler and Herrmann [2] to obtain approximations of stress intensity factors in cracked beams, has been used. These authors have shown that very simple and close approximations can be obtained with

elementary bending theory and estimations of the strain energy release as a crack is widened. In short, the stress intensity factor is obtained through

$$K_I = \left[ -\frac{k E}{B} \frac{\partial U}{\partial h} \right]_{h=0}^{1/2} \quad (1)$$

where  $k$  is a dimensionless factor of proportionality to be determined,  $E$  Young's modulus,  $B$  specimen thickness,  $U$  strain energy and  $h$  half the width of the crack. First, a value of  $k$  has been obtained for the standard three-point-bend specimen by including both bending and shear force energy in  $U$  and comparing the result with  $K_I$  as given in [1]. A close fit in the crack length range  $0.5 \leq a/W \leq 0.6$ , where  $a$  is crack length, allows  $k = 1.32$ , which is the value obtained by Bazant [3] for pure bending of a single edge notched beam of constant thickness. With this value of  $k$  and  $U$  including bending and shear force energy,  $K_I$  has been calculated with Eq. (1) for the modified specimen with various taper angles. In Fig. 2 is shown a) the very close approximation of the geometry function of  $K_I$  obtained with the method in [2] compared to the present standard [1] and b) normalised geometry functions for the modified specimen type with taper in the range  $0.5 \leq \alpha \leq 1$ , or between an anticipated maximum taper, corresponding to the same line load intensity along the loading devices on both sides of the specimen, and a plane specimen. The influence of tapered sides is found to be small and even negligible in practice where other uncertainties may introduce errors with greater influence than the taper.

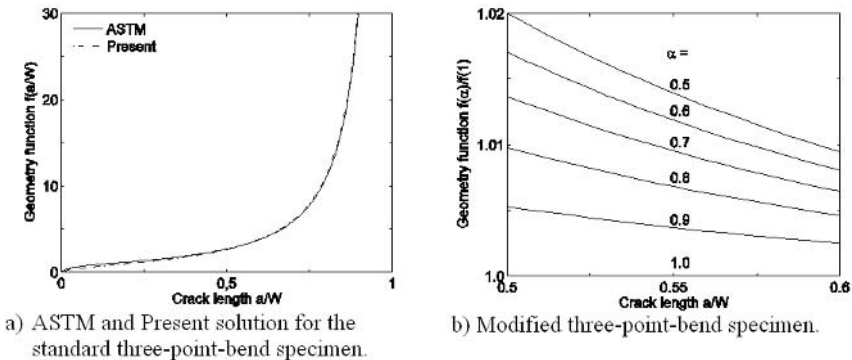


FIGURE 2. Geometry functions of the stress intensity factor for standard and modified three-point-bend specimen.

## References

1. ASTM E-1820-01. Standard Test Method for Measurement of Fracture Toughness. General Book of ASTM Standards, Sect. 3, ASTM, Philadelphia 2001.
2. Kienzler, R. and Herrmann, G., *Acta Mech.*, vol. **62**, 37-46, 1986.
3. Bazant, Z.P., *Engng. Fract. Mech.*, vol. **36**, 523-525, 1990.

## EXPERIMENTAL STUDIES ON WRINKLING BEHAVIORS OF GOSSAMER SPACE STRUCTURES

Changuo Wang and Xingwen Du

Harbin Institute of Technology

Center for composite materials and structures, HIT, Harbin, China, 150080

wangcg@hit.edu.cn

Ultra-large and ultra-lightweight gossamer space structure has received the widest attention due to its small packaging volume and low launching cost. Wrinkles are a common deformation status and a main failure mode of such structures. Experimental test is a main part of wrinkling analysis on gossamer space structures. The contact test can't be used to accurately determine the wrinkling behaviors because of the characteristics of lightweight and flexibility. Non-contact photogrammetry has been successfully applied to the test of deformation of gossamer space structures<sup>[1,2]</sup>. Pappa<sup>[3]</sup> did the test on wrinkle deformation based on the dot-projecting photogrammetry, the out-of-plane wrinkle amplitude was obtained. By now, the accurate test on the small amplitude wrinkle in small scale structures is a key problem of wrinkling experiment.

In this paper, a novel non-contact Dot-Printing Photogrammetry (DPP) based on the technology of the printed-dot targets associated with Tension Wrinkling (TW) tests are used to obtain the out-of-plane wrinkle deformation and the rules of wrinkling occurrence and development. A specimen with printed-dot targets is plotted in Fig. 1. And the test instrument of TW test is shown in Fig. 2. The experimental result on out-of-plane wrinkle deformation is plotted in Fig. 3. The obvious wrinkle wave crest and hollow can be observed from Fig. 3. The plots of tension-amplitude and tension-wavelength are plotted in Fig. 4 and 5, respectively.

The wrinkling mechanisms corresponding to the deformation phase are studied by associating the characteristic curve and experimental results of key nodes. The obvious bifurcation of the in-plane displacement corresponds to the occurrence of the wrinkle, and the critical wrinkling load can be determined at this bifurcation point. Five deformation phases can be obtained from Fig. 6: a) in-plane deformation, oa; b) critical deformation, ab; c) break wrinkling deformation, bc; d) increasing deformation, cd; e) stable deformation, de. The experimental results corresponding to key nodes are plotted in Fig. 7. The key node b corresponds to the occurrence of wrinkle. Wrinkle are the local buckling of structure, and it is formed due to the bifurcation of in-plane displacement. Increasing with the load, the degree, region, amplitude and numbers of wrinkle are increasing, reversely the wavelength.

Nonlinear buckling finite element method associated with ANSYS shell63 element is chosen to simulate the wrinkles. The numerical prediction results of out-of-plane wrinkling deformation are shown in Fig. 8. And the comparison between prediction and experiment test is plotted in Fig. 9. Good agreement can be found in the Fig. 9.

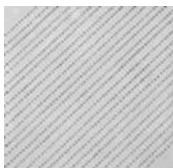


FIG. 1. specimen with printed-dot targets    FIG. 2. TW test instrument



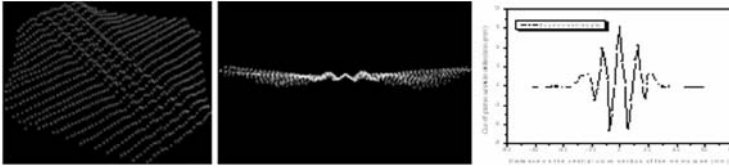


FIG. 3. experimental results

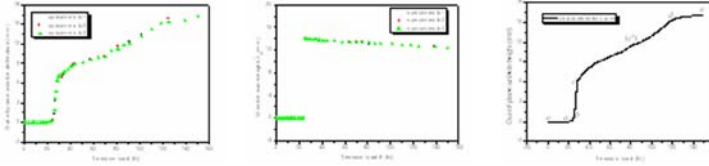
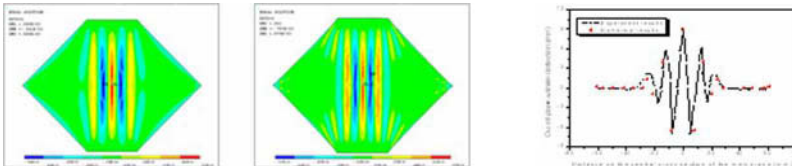


FIG. 4. tension-amplitude curve FIG. 5. tension-wavelength curve FIG. 6. characteristic curve



a) key node o b) key node a c) key node b d) key node c e) key node d f) key node e

FIG. 7. Experimental results corresponding to key nodes of characteristic curve



a) tension is 28.56N b) tension is 43.76N

FIG. 8. Results of wrinkling prediction FIG. 9. Comparison of prediction and experiment

[Chang, Shih-Lin, Multiple Diffraction of X-rays in Crystals, Springer Verlag, Berlin, 1984.] is a reference to a report, [R. S. Pappa, T. W. Jones, and J. T. Black, et al. Photogrammetry Methodology Development for Gossamer Space Structures. Sound and Vibration, 2002, vol. 36(8):12~21] to a journal article, [] to a report.

References

1. L. R. Giersch, and R. Pathfinder. Photogrammetry Research for Ultra-Lightweight and Inflatable Space Structures, NASA CR-2001-211244, November, 2001
2. R. S. Pappa, T. W. Jones, and J. T. Black, et al. Photogrammetry Methodology Development for Gossamer Space Structures. Sound and Vibration, 2002, vol. 36(8):12~21
3. R. S. Pappa, J. T. Black and J. R. Blandino. Photogrammetric Measurement of Gossamer Paccraft Membrane Wrinkling, NASA 2003-SEM-RSP

## A MOMENTUM TRANSFER MEASUREMENT EXPERIMENT BETWEEN CONTACTING BODIES IN THE PRESENCE OF ADHESION UNDER NEAR-ZERO GRAVITY CONDITIONS

M. Benedetti<sup>1</sup>, D. Bortoluzzi<sup>2</sup> and M. De Cecco<sup>2</sup>

<sup>1</sup>Department of Materials Engineering and Industrial Technologies,  
University of Trento, Via Mesiano 77, 38050 Trento, Italy  
matteo.benedetti@ing.unitn.it

<sup>2</sup>Department of Mechanical and Structural Engineering,  
University of Trento, Via Mesiano 77, 38050 Trento, Italy  
daniele.bortoluzzi@ing.unitn.it

The present paper presents a ground-based experiment aimed at measuring the momentum transfer between contacting bodies in the presence of adhesion under near-zero gravity conditions. The measurement of small impulses is necessary in various fields of science and engineering. For instance, in space propulsion studies, the exact knowledge of the impulse imparted by the thrusters to an orbiting satellite is needed for orbit maintenance, repositioning and attitude control. In the applications mentioned, the measured impulse is originated by a non-contact force, that may be electro-magnetic, or inertial (accelerated ions or gas molecules). The advantage thereof resides in the fact that this kind of forces, although acting between two bodies, is not affected by the way such bodies are constrained. Conversely, an application is here presented where the measurement of impulse is concerned between contacting bodies.

In space environment, the in-orbit precise release of bodies implies the contact with some kind of caging devices, that involves the sudden rupture of adhesive forces with consequent transfer of momentum. The breaking of adhesive junctions between contacting bodies, although of slight order of magnitude (from nano- up to milliNewtons), can be promoted in space applications neither by environmental factors, like the gravity field, nor surface contaminants caused by exposure to the atmosphere, nor acoustic noise propagated by the air, nor inertia forces due to ground micro-seismic movement [1]. The unavoidable momentum transferred to the released body may result in too high residual velocities as compared to the required release conditions. A meaningful example of these issues is given by the scientific space mission LISA (Laser Interferometer Space Antenna) [2]. Aim of this ESA NASA joint mission is the first in-flight revealing of gravitational waves, which will be detected by means of laser interferometers arms formed among three orbiting satellites. The gravitational waves sensing elements, constituting the end-mirrors of the interferometer arms, will be cubic masses located within the satellites. During the experiment, the test masses will be set in free flight. In contrast, during launch, the test masses need to be firmly secured to their housings in order to avoid shaking and thus damage. The release of the test masses for the experiment constitutes a mission potential single-point failure, because it must rely on a limited force and torque authority supplied by a capacitive actuation system and on a limited acceleration of the caging device. The residual velocity of the test mass must be less than 5  $\mu\text{m/s}$ , otherwise the capacitive actuation will not be able to catch up the test mass. It is now clear that the exact measurement of the momentum imparted to the test mass due to adhesive interactions plays a crucial role for a successful release.

Accordingly, the experiment is basically aimed at measuring the transferred momentum between two suspended adhered bodies through the detection of the free oscillations of one of the two consequent to a sudden retraction of the other one. Although any adhesive phenomenon arising from the preloading force between TM and finger may be progressively reduced by



## ON FIELD MEASUREMENT OF FORCES AND DEFORMATIONS AT THE REAR PART OF A MOTORCYCLE AND STRUCTURAL OPTIMIZATION

G. Olmi, A. Freddi and D. Croccolo

DIEM – Department of Mechanical Engineering – Engineering Faculty – University of Bologna  
 Viale del Risorgimento, 2 – 40136 Bologna – Italy  
 giorgio.olmi@mail.ing.unibo.it

The present work is about the analysis of the asymmetric displacement behaviour of the rear part of a motorcycle. Stylistic reasons led to the design of a vehicle with only one suspension located at the left side. Some preliminary tests performed on a prototype emphasized that asymmetric design implies also an asymmetric performance: relative displacement between the frame and the fork is different on the two sides. Such performance is particularly evident when route obstacles are overcome and is shown in the scheme in Fig. 1. Differences between left and right side displacements of the fork and the frame are referenced as  $\Delta_f$  and  $\Delta_t$ . The object of this work was to estimate and minimize their sum  $\Delta (= \Delta_f + \Delta_t)$ .

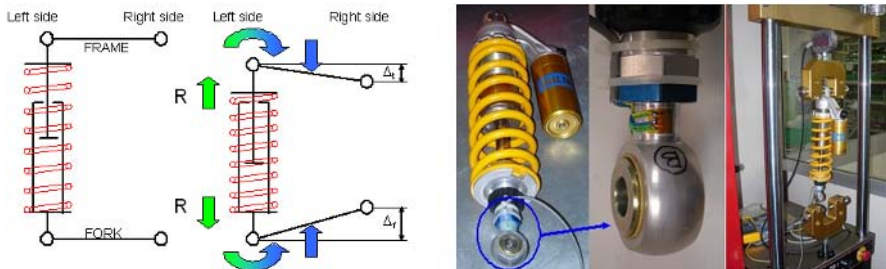


FIGURE 1. A scheme of motorbike rear side. FIGURE 2. Strain gage rosettes application and calibration

The first step consisted in the measurement of loads transmitted between the suspension and the frame and the suspension and the fork. For this purpose an area of the suspension next to fork connection was equipped by two two-grid ( $0^\circ/90^\circ$ ) strain gage rosettes (the use of strain gages for on field tests is suggested by many authors, e.g. Ladda *et al.* or Tu [1, 2]). A full Wheatstone bridge connection was applied for axial force measurement. The measuring device was calibrated (Fig. 2) on a testing machine by subjecting the suspension to compressive load cycles. A very linear calibration curve was derived ( $R^2 = 0.99$ ).

After calibration, tests on the field were conducted. A circuit was set up with seven obstacles on a straight stretch (Fig. 3). The instrumented suspension was mounted on a motorbike prototype, moreover also two potentiometers were assembled on both vehicle sides. The driver performed three passages on the obstacles at three different speeds (40, 50 and 60 km/h) for a total number of nine passages. Strain gage rosettes and potentiometers contextually measured loads on the suspension and deformations on both sides. Trends of force and of  $\Delta$  were related and compared, by plotting diagrams as shown in Fig. 4. The force is indicated with negative values, with reference

to suspension compression. At the first impact with the obstacle, force module rapidly increases up to a maximum. Then, after a drop-kick, the load on the suspension suddenly decreases. Positive values in the diagram indicate the suspension becomes slightly in tension. Then the force trend is inverted and the suspension is again subjected to compression. The described trend is repeated for seven times, as seven are the obstacles and it is interesting to observe that  $\Delta$  distribution appears to be qualitatively mirrored with respect to force's. When load module on the suspension has a maximum value, also  $\Delta$  has its maximum value, with the same trend also for minimum values. This experimental campaign and comparison between force and  $\Delta$  trends can be regarded as an improvement of experiments by Olmi *et al.* in [3], where force and displacement measurements had not been contextual.



FIGURE 3. Passage on seven obstacles.

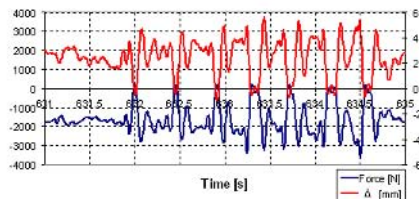


FIGURE 4. Force and  $\Delta$  plotted together

Aiming to structural optimization, FEM models (I-DEAS V11) of the frame and the fork were set up to investigate bending displacements of components at the rear side. Such models were particularly accurate, by applying shell elements and considering carter and hinges real stiffness. The numerical model was integrated by experimental results: the numerical value of the force transmitted by the suspension to the fork and to the frame was derived by experimentation.  $\Delta_f$  and  $\Delta_r$  were calculated for different values of experimental forces, coming to the evaluation of the total term  $\Delta$ . For validation purposes numerical results were compared to experimental ones related to contextually measured forces. Differences were below 10%, which led to the validation of the numerical model, with particular reference to meshing elements, constraining and loading systems. By comparing  $\Delta_f$  and  $\Delta_r$ , it results that their sum  $\Delta$  is strongly dependent (80%) on the fork bending displacements. It implies that a significant structural optimization can be achieved, but modifying the fork's design. A simplified FEM model helped in a qualitative analysis with the aim to individuate the fork modified version with the lowest value of  $\Delta_f$ . Then rigorous calculations were conducted by the previously validated model. The fork design was modified, so that motorbike stylistic line was not altered and asymmetric behaviour (with particular reference to term  $\Delta$ ) was strongly reduced.

## References

1. V. Ladda, J.M. Zschel, *MTB*, vol. **15** (3), 1979
2. J.F. Tu, *Int. J. Math. Tools Manufact.*, vol. **36** (2), 203-216, 1996
3. G. Olmi, A. Freddi, D. Croccolo, G. Ferrazzo, In *Proceedings of the XXXV AIAS National Conference*, edited by D. Amodio, Ancona, 2006

## BALLISTIC IMPACT FACILITY - CONSIDERATIONS AND EXPERIENCES

Peter H. Bull and Jørgen A. Kepler  
Aalborg University  
Pontoppidanstraede 101, DK 9220 Aalborg East  
Denmark  
peb@ime.aau.dk

A facility for testing of ballistic impact has been designed and developed. The goal was to develop a facility which was relatively easy to use and modify, as the requirements for the testing equipment changed with different research projects, e.g. students projects [1]. The setup consisted of a compressed air gun with an exchangeable barrel, a speed trap for measuring the incident velocity and a kinetic pendulum which both served as a means to measure the residual energy of the projectile and to catch the projectile from further travel. The aim of this paper was to cover some of the experiences encountered during the design and development high velocity impact test equipment.

The main equipment was the compressed air gun, Kepler [2]. The gun was fixed to the roof in the gun chamber, figure 1. It was built up in a modular way in order to relatively easily allow for modifications as new needs for testing changed. Thus the gun was designed to use exchangeable barrels. At the time of writing barrels for three different projectile diameters were used, 10 mm, 20 mm and 50 mm. A scuba dive compressor was used to feed compressed air with pressures up to 20 MPa into a pressure chamber at the rear end of the gun. With 20 MPa pressure and the 10 mm calibre barrel it was possible to accelerate projectiles up to 680 m/s.



FIGURE 1. Compressed air gun with pressure chamber in the foreground, a box for a high speed camera and the rig for the kinematic pendulum can be seen in the background.

The gun chamber where the gun was mounted was located in a basement under a 2 m thick concrete floor. The walls and roof were clad with 25 cm thick timber which was intended to slow down or stop possible ricochets. The gun chamber was closed off with a double door at the pressure chamber end of the gun. The door was constructed from the same timber that was used to clad the walls and roof.

In the receiving end there was a kinematic pendulum similar to the one used by Robbins [3] and also described by Johnson [4]. It served a double duty as it was both used to measure the

residual energy of a penetrating projectile and it was also stopped the projectile from further travel. A displacement transducer was used to measure the travel of the pendulum. From that displacement the vertical travel could be calculated and used to calculate the residual energy of a projectile.



FIGURE 2. Rig for mounting test specimens and kinematic pendulum, with a box for mounting high speed camera to the left.

The rig that held the pendulum, figure 2, was also used for fixtures for test specimens. The rig was manufactured from 80 mm square cross section steel tubes and was fixed to the concrete roof. Currently two different fixtures have been used, one which could simulate fixed or simply supported boundary conditions, and one four point bending rig which was used to pre stress test specimens.

## References

1. Christensen, E.P. and Hurup, A., *Analyse og design af ballistiske paneler til lætvægtsarmoring (Analysis and design of ballistic panels for light weight armour)* in Danish, Masters Thesis, Institute of Mechanical Engineering, Aalborg University, 2005.
2. Kepler, J.A., *Localized impact on sandwich structures – an experimental study*, PhD Thesis, Special Report No. 46, Institute of Mechanical Engineering, Aalborg University, 2001.
3. Robbins, B., *New Principles of Gunnery*, F. Wingrave, London, 1805.
4. Johnson, W., *Journal of Impact Engineering*, vol. 4 (4), 205 – 219, 1986.

## MEASUREMENT OF MOMENT REDISTRIBUTION EFFECTS IN REINFORCED CONCRETE BEAMS

R.H. Scott, R.T. Whittle and A.R. Azizi

School of Engineering, Durham University, South Road, Durham DH1 3LE, United Kingdom

Arup Research and Development, 13 Fitzroy Street, London W1T 4BQ, United Kingdom

Crown Agents, Banda, Aceh, Indonesia

richard.scott@durham.ac.uk, robin.whittle@arup.com, abdulrahman.azizi@yahoo.co.uk

Normal practice is to use a linear elastic analysis for calculating the bending moment and shear force distributions in a reinforced concrete structure. This has the virtue of simplicity as well as permitting results from a series of analyses to be combined using the principle of superposition. It is endorsed by major design codes such as BS8110 [1], EC2 [2] and ACI 318 [3]. The assumption of linear elastic behaviour is reasonable at low levels of loading but it becomes increasingly invalid at higher loads due to cracking and the development of plastic deformations. Once an element cracks the behaviour becomes non-linear but it is still reasonable to assume that the tension reinforcement and the concrete in compression both behave elastically up to yield of the reinforcement.

Design codes permit an elastic analysis to be used at the Ultimate Limit State (ULS) but acknowledge the non-linear behaviour by allowing design engineers to redistribute moments from one part of the structure to another subject to maintaining the rules of static equilibrium. The maximum permissible amount of moment redistribution is linked to the ductility of the reinforcement at the ULS.

Implicit in the current use of moment redistribution is the assumption that sections possess sufficient ductility for the requisite plastic deformations to occur. Design codes achieve this by specifying rules which ensure that the tension steel must have yielded and this leads to the question of whether an upper strain limit should be specified in order to avoid rupturing the reinforcement but, to date, this has not been the case. Consequently, designers have effectively worked on the assumption that the reinforcement will be able to develop whatever level of strain is actually required by a specified neutral axis depth and that failure of a section would always be initiated by crushing of the concrete in compression.

This view was challenged in 1987 by the work of Eligehausen and Langer [4] who demonstrated that reinforcement strain at the ULS could be the controlling parameter in the more lightly reinforced types of members, such as slabs. This raised the question of what upper limit to moment redistribution should be permitted in design codes and whether more stringent limitations should be imposed on the level of reinforcement strains developed at the ULS.

The authors have conducted an investigation which aimed to explore the nature of moment redistribution as load is increased on a structure and thus provide some design guidance on the issues outlined above. To do this a series of two-span reinforced concrete beams was tested to investigate moment transfer from the central support into the adjacent spans. A particular feature of the experimental programme was the use of internally strain gauged reinforcing bars to obtain very detailed data concerning the relationship between level of redistribution and associated reinforcement strains.

The reinforcement was internally strain gauged to avoid degradation of the bond characteristic between the reinforcement and the surrounding concrete. Each strain gauged bar was formed by



machining two standard rebars to a half round and then milling a longitudinal central slot the full length of each half bar which was 4 mm wide and 2 mm deep. Electric resistance strain gauges were then installed in the slot and their wiring led along the slot and out of the ends of the bars. The two half bars were then glued together to give the appearance of a "normal" solid bar. Typically, strain gauges had a 3 mm gauge length, were mounted at 12.5 mm centres, and were wired with a three wire system with constant current energisation to minimise the effects of lead wire resistance. Up to 100 gauges could be accommodated.

The strain gauged bars gave very detailed information concerning the relationship between moment redistribution and bar strains. They demonstrated conclusively that significant levels of moment redistribution were developed at the Serviceability Limit State (SLS) when the reinforcement was behaving elastically, even in beams which exhibited a brittle failure mode by failing in shear. The *total* amount of redistribution was shown to be a combination of this *elastic* redistribution plus the redistribution caused by the post yield behaviour of the reinforcement (termed *plastic* redistribution). Thus the contribution of plastic redistribution, which is dependent on reinforcement ductility, was shown to be smaller than has previously been believed to be the case and this has significant consequences for practical design.

These conclusions will be presented in greater detail in the final paper together with full details of the strain gauged bars which proved to be very important tools in the successful implementation of the research programme.

## References

1. BS8110: Structural Use of Concrete Part 1: 1997: Code of Practice for Design and Construction, *British Standards Institution*, London
2. BS EN 1992-1-1:2004 Eurocode 2: Design of Concrete Structures. Part 1-1: General Rules and Rules for Buildings, *British Standards Institution*, London
3. ACI 318: Building Code Requirements for Structural Concrete, *American Concrete Institute*, 2005
4. Eligehausen R. & Langer P., Rotation Capacity of Plastic Hinges and Allowable Degree of Moment Redistribution, Stuttgart, 1987, (Report)

## MECHANICAL PROPERTY MEASUREMENT OF FLEXIBLE MULTI-LAYERED MATERIALS USING POSTBUCKLING BEHAVIOR

Atsumi Ohtsuki

Department of Mechanical Engineering, Meijo University  
1-501 Shiogamaguchi, Tempaku-ku, Nagoya, 468-8502, Japan  
ohtsuki@ccmfs.meijo-u.ac.jp

In application of flexible materials it is very important to evaluate mechanical properties of these materials in both analytical and technological interests. This report deals with an innovative method (: *Compression Column Method*) under large deformations of a flexible multi-layered specimen. Exact analytical solutions based on the non-linear large deformation theory are derived in terms of elliptic integrals. By just measuring the applied load and a vertical displacement and/or a deflection angle, each Young's modulus can be easily obtained for thin and long multi-layered flexible materials. Measurements were carried out on a two-layered material (PVC: a high-polymer material, 0.515mm thick and SUS: a steel material, 0.100mm thick). In the meantime, the *Circular Ring Method* [1], [2], the *Cantilever Method* [3] and the *Compression Column Method* [4] have already been developed and reported for single-layered thin/slender beam/column specimens.

A typical illustration of a load-deflection shape is given in Fig. 1 for a multi-layered material subjected to axial compressive forces. A cross section of two-layered material is shown in Fig. 2.

The basic equation of large deformation (: postbuckling behavior) is derived as follows.

$$\frac{d^2\theta}{d\zeta^2} + \gamma \cdot \sin \theta = 0, \text{ where, } \zeta = s/L, \gamma = PL^2 / \sum_{i=1}^n (E_i I_i) \quad (1)$$

Denoting the half length of a specimen by  $L$  and taking into the conditions  $\zeta_B (=s_B/L) = l$ ,  $\eta_B = \delta/L$ ,  $\xi_B = (L - \lambda/2)/L$ , the maximum non-dimensional arc length  $\zeta_B$ , the maximum non-dimensional vertical displacement  $\eta_B$  and the maximum non-dimensional horizontal displacement  $\xi_B$  are obtained as follows.

$$\zeta_B = 1 = \left(1/\sqrt{\gamma}\right) \cdot F(k, \pi/2), \text{ (where } \kappa = \sqrt{(1 - \cos \theta_B)/2} \text{)} \quad (2)$$

$$\eta_B = \delta/L = \left(2k/\sqrt{\gamma}\right) \cdot \{1 - \cos(\pi/2)\} = 2k/\sqrt{\gamma} \quad (3)$$

$$\xi_B = (L - \lambda/2)/L = \left(1/\sqrt{\gamma}\right) \cdot \{2E(k, \pi/2) - F(k, \pi/2)\} \quad (4)$$

The functions  $F(k, \pi/2)$ ,  $E(k, \pi/2)$  are Legendre-Jacobi's complete elliptic integrals of the first and second kinds, respectively.

Equations (2)-(4) are fundamental formulas based on the non-linear large deformation theory. Therefore, it is possible to calculate each Young's modulus  $E_i$  from the following simultaneous equation (5) or equation (6).

$$\sum_{i=1}^n (E_i I_i) - PL^2/\gamma = 0 \quad (5) \quad \sum_{i=1}^n (E_i I_i) - PL^2 \cdot \{\eta_B / 2 \sin(\theta_B/2)\}^2 = 0 \quad (6)$$

$$\text{where, } I_i = \frac{bh_i^3}{12} + bh_i \left( \bar{y} - \frac{h_i}{2} - \sum_{k=1}^i h_{k-1} \right)^2, \quad (S_i)_z = \frac{bh_i^2}{2} + bh_i \left( \sum_{k=1}^i h_{k-1} \right),$$

$$\bar{y} = \frac{\sum_{i=1}^n E_i (S_i)_z}{\sum_{i=1}^n (E_i A_i)}$$

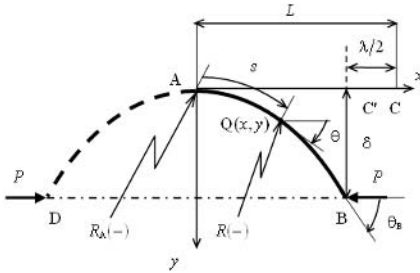


FIGURE 1. Schematic configuration of multi-layered column subjected to axial compressive forces at both hinged supports.

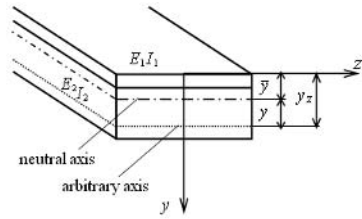


FIGURE 2. Illustration of cross-section of two-layered material.

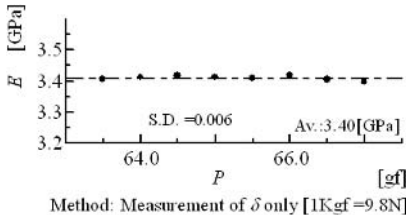


FIGURE 4. Young's modulus (SUS: a steel material).

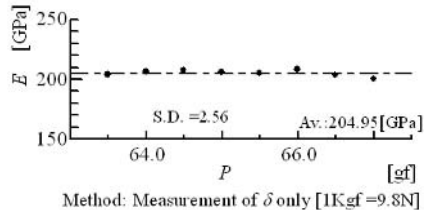


FIGURE 3. Young's modulus (PVC: a polymer material).

Several experiments were carried out using a two-layered material (PVC+SUS). Theoretical and experimental results clarify that the new method is suitable for measuring each Young's modulus of flexible multi-layered materials. Based on the assessments the proposed method can be further applied to multi-layered thin sheets and multi-layered fiber materials.

**References**

1. A.Ohtsuki and H.Takada, *Transactions of Japan Society for Spring Research*, No.47, pp.27-31, 2002.
2. A.Ohtsuki, *Proceedings of the 2005 SEM Annual Conference & Exposition on Experimental and Applied Mechanics*, Section 72, pp.113(1)-113(8) [CD-ROM], 2005
3. A.Ohtsuki, *Proceedings of the 4th International Conference on Advances in Experimental Mechanics*, vols. 3-4, pp.53-58, 2005.
4. A.Ohtsuki, *Fourth International Conference on Thin-Walled Structures*, pp.233-240, 2004.

## FRICTION COEFFICIENTS DEFINITION IN COMPRESSION-FIT COUPLINGS APPLYING THE DOE METHOD

Dario Croccolo, Rossano Cuppini and Nicolò Vincenzi  
DIEM – University of Bologna  
Viale Risorgimento , 2 – 40136 -Bologna – Italy  
dario.croccolo@mail.ing.unibo.it

The design of the fork-pin compression-fit couplings of front motorbike suspensions is uncertain mainly because of the poor knowledge of the mean coupling pressure  $p$ , due to the not symmetric geometry of the fork, and of the first friction coefficient  $\mu_{II}$ . The axial releasing force  $F_{II} = \mu_{II} p \cdot A$ , which is the fundamental design parameter, indeed depends on the mentioned two factors, usually unknown. In this paper is presented a generalized methodology which is useful to calculate the  $\mu_{II}$  parameter concerning the fork-pin couplings of the front motorbike suspensions. The present production is differentiated by the different material of the two elements in contact, the fork and the pin. The possible combinations are: the fork and the pin in steel, the fork in aluminium and the pin in steel and the fork and the pin in aluminium. In previous works two mathematical models have been defined: the first (Croccolo *et al* [1]) is useful to calculate the mean contact pressure  $p$  in every fork-pin coupling by introducing an overall mathematical function, which is able to correct the theoretical formulas valid only for axial-symmetric elements [2]; the second (Croccolo and Reggiani [3]) is useful to calculate the first friction coefficient  $\mu_{II}$ , as a function of the production and assembly specifications, in couplings with both the fork and the pin in steel. The fundamental goal of this work is to define a mathematical model useful to calculate the first friction coefficients  $\mu_{II}$  for the other two combinations of couplings, aluminium-steel and aluminium-aluminium. The second goal is to update an innovative software (Fork Design©), realized by the authors in Visual Basic® programming language, which is useful to perform the design and the verification of the all fork-pin couplings. The mathematical model for  $\mu_{II}$  has been defined through FEM analyses, performed with Ansys 9.0® and applying the Design Of Experiment (DOE) method. The value of the mean coupling pressure  $p$  was previously calculated combining the FEM analyses and the values provided by some strain gauges applied on the forks, so the only unknown parameter in  $F_{II} = \mu_{II} p \cdot A$  is the friction coefficient  $\mu_{II}$ . The DOE method was applied in order to plan the experiment for the friction coefficient definition. According to the production and assembly specifications, three factors have been considered: the resting time, the presence of humidity, and the presence of protecting oil. Two factor levels have been investigated, high and low, which are the presence or the absence of the factor itself during the single test. Therefore a DOE 2<sup>3</sup> was obtained with eight point repeated three times (24 total tests) for each couple of different materials. The first friction coefficient  $\mu_{II}$  was calculated by dividing the axial releasing force  $F_{II}$  (provided by the press machine during the fork-pin coupling tests), by the  $p$  and the  $A$  parameters (calculated with the FEM analysis and by the coupling geometry). Finally, the ANalysis Of VAriance (ANOVA) was applied to the results in order to establish which factors, or which factors combination, were significant to the definition of  $\mu_{II}$ . Therefore the new two mathematical models for the new two combination of materials of the first friction coefficient  $\mu_{II}$  have been defined and reported in (1) and in (2); their response surfaces are plotted in Figs 1 and 2.

$$\mu_{II\_Al-St} = 0.468 - 0.381 \cdot Oil + 0.174 \cdot H_2O \cdot Oil + 0.14 \cdot Oil \cdot Time \quad (1)$$

$$\mu_{II\_Al-Al} = 0.259 - 0.197333 \cdot Oil \quad (2)$$

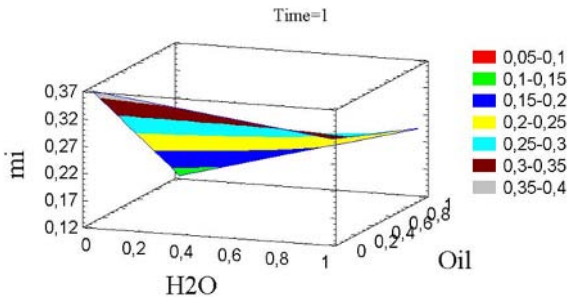


FIGURE 1. The response surface for  $\mu_{II}$  in the case of aluminium-steel coupling

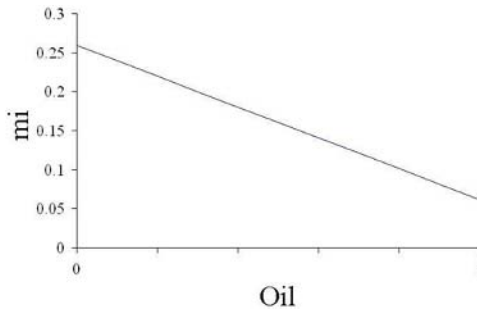


FIGURE 2. The linear response for  $\mu_{II}$  in the case of aluminium-aluminium coupling

The first fundamental result of this work is the definition of the analytical models of the first friction coefficients  $\mu_{II}$  for two different kind of couplings: fork in aluminium and pin in steel, fork and pin both in aluminium. The second result is the updating of an original software Fork Design©, realized by the authors and containing the formulas of the first friction coefficients which is able to design and verify the fork-pin couplings of front motorbike suspensions.

## References

1. Croccolo, D., Cuppini R., and Vincenzi N., *International Design Conference – Design 2006* Dubrovnik - Croatia, May 15 - 18, 2006
2. Niemann Winter, *Elementi di macchine*, Vol. I, EST-SPRINGER (1983)
3. Croccolo, D., Reggiani, S., *Modello di calcolo del coefficiente di attrito in accoppiamenti stabili*, *Organi di trasmissione – Tecniche Nuove*, Gennaio 2002 – pp. 46-55.

## RESIDUAL STRESSES OF WELDED STRUCTURES AND THEIR EFFECT ON THE DYNAMIC BEHAVIOUR

Joeran Ritzke, Peter Nikolay, Andreas Hanke and Guenther Schlottmann  
 University of Rostock  
 Chair of Technical Mechanics/Dynamics of Machinery  
 Albert-Einstein-Str. 2, D-18059 Rostock  
 IMAWIS GmbH  
 Alter Holzhafen 19, D-23966 Wismar, Germany  
 joeran.ritzke@uni-rostock.de, peter.nikolay@imawis.de

The vibration behaviour of local ship structures is highly influenced by residual stresses and predeformations. Measurements have shown that differences of up to 50% in natural frequencies due to welding stresses are possible (Hanke [1]). Uncertainties of this magnitude contain a high risk regarding the estimation of the vibration behaviour during operation of the ship. This implies an economic threat in case of failure to fulfil contracts and therefore an improvement of the prediction of local vibration behaviour is needed.

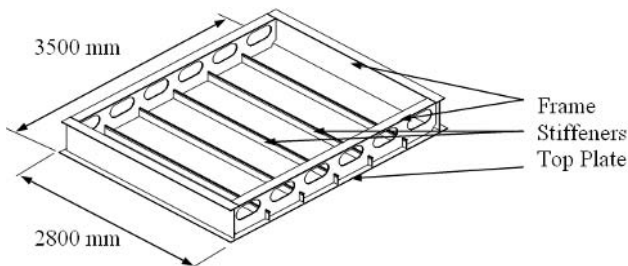


FIGURE 1. Drawing of the ship deck

A detailed thermal finite element modelling of the welding stresses is possible, but leads to high computational costs and depends highly on the assumed parameters. Therefore a simplified model for the influence of welding stresses to modal parameters is aimed. For this purpose, an inherent strain model, similar to that of Ueda [2], is used. The parameters of this model are gained by a model updating using the natural frequencies and mode shapes of welded structures.

In this paper, the experimental investigations necessary to validate the model and to gain the residual stresses of the ship deck as well as the natural frequencies and the mode shapes are presented. A broad experimental investigation of several ship decks, built by different shipyards, was worn out. The geometry of the investigated panel was chosen similar to typical superstructure decks (Figure 1: Drawing of the ship deck1). To account for the bandwidth of usual production techniques, different weld processes with varying energy input per unit length (ranging from 4 to 11 kJ/m) were used. Furthermore, one structure was laser welded to evaluate a welding technique that is uncommon for shipyard use.

Several strain gauges were applied double-sided to the top plate of the panels before assembly. A strain measurement was supplemented during production, allowing the evaluation of residual stresses due to welding (Figure 2: Maximum compression stresses at the measured points2). The strain measurement is accompanied by a residual stress measurement using the hole drilling

method. In contrast to the shipyard measurements, the overall residual stresses including residual stresses due to rolling are evaluated. The investigation was accomplished by a measurement of the top plate deformation using photogrammetry. For this purpose, the deformation of the top plate was measured at each production stage of the structure, i.e. top plate before welding, top plate after welding of the stiffeners and after welding of the frame.

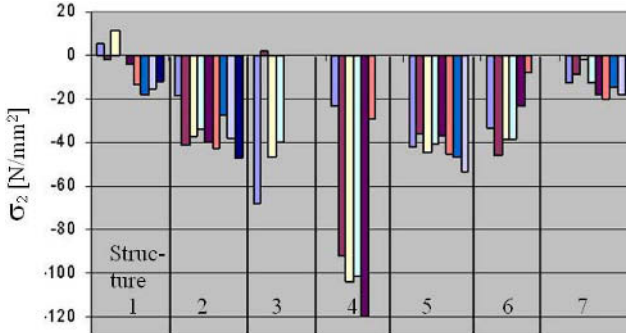


FIGURE 2. Maximum compression stresses at the measured points

The natural frequencies and mode shapes of the decks (table 1) were gained by an experimental modal analysis. Due to the complicated mode shapes, arising from compression stresses between the stiffeners, a high spatial resolution of measurement points was necessary. A further modal analysis was applied to a stress relieved structure. The results of the measurement are compared with numerical results from a finite element computation.

TABLE 1. Comparison of natural frequencies and MAC-values of selected modes

Mode (meas.)	FEA Nr.	f <sub>meas</sub> /Hz	f <sub>FEA</sub> /Hz	ΔE%	MAC/%
1	1	10,7	9,8	-8	99
3	3	22,7	29,7	31	42
4	2	24,1	25,8	7	53
8	6	31,1	35,5	14	73

It is aimed to use the parameters gained by updating for the improved prediction of local vibration behaviour on ship yards. While the computational effort is insignificant higher, the risk of missing vibration amplitudes bound by contract is lower. This helps to avoid cost intensive subsequent changes of the mechanical design to improve the dynamic behaviour.

**References**

1. Hanke, A. and Schlottmann, G., *Model Updating of Ship Decks loaded with Welding Stresses*, In Proceedings of ISMA 2006, edited by P. Sas and M. De Munck, Leuven, 2006, 2579-2592.
2. Ueda, Y. and Yuan, M. G., *Prediction of residual stresses in butt-welded plates using inherent straines*, ASME J. of Engineering Materials and Technology, 417-423, 1993

## AN EXPERIMENTAL TECHNIQUE TO EVALUATE THE STRENGTH OF ADHESIVE BONDS IN MULTIAXIAL LOADING

Lorenzo Peroni and Massimiliano Avalle  
 Dipartimento di Meccanica, Politecnico di Torino,  
 Corso Duca degli Abruzzi 24, 10129 Torino, Italy  
 lorenzo.peroni@polito.it, massimiliano.avalle@polito.it

The need for a continuously improved vehicle deals with some contradictory requirements. One goal is to reduce gas emission and pollution that would induce reduction of the mass of the cars. Another, ever more demanding, necessity is to improve car crash safety that, on the contrary, benefits from greater mass. The body weight reduction and the use of lightweight materials will result in large cost reductions for the car manufacturers, due to reduction of the material and manufacturing costs, and improved design flexibility.

There are several ways to get weight reduction; mainly structural design optimization and the use of lightweight materials. However, the use of lightweight materials (aluminium, composites, plastics and their combinations) introduces many new problems. Among these there are the joining methodology to be use, to substitute the classical spot-welds used for steel bodies.

There is, therefore, a need for the definition of new joining techniques and knowledge of their behaviour for design purposes. Spot-weld joining can be substituted by some point fastening methods, mainly mechanical, such as screwing, riveting, and clinching, or by surface joining, mainly achieved with adhesive bonding. Adhesives have many advantages over the other methods since they have the widest range of combining possibilities, introduce damping (they help improving NVH behaviour), and act as sealants.

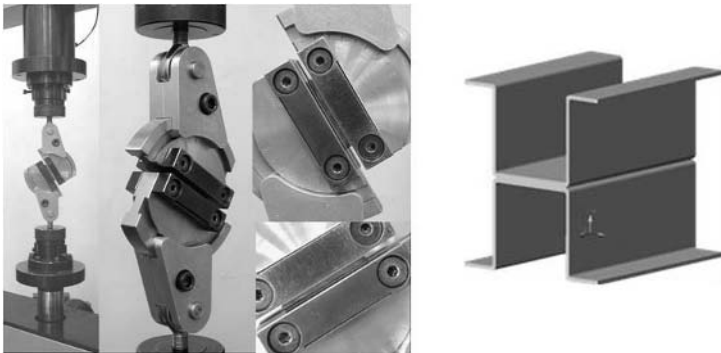


FIGURE 1. New KS2 specimen loaded at different angles, from  $0^\circ$  (shear) to  $90^\circ$  (tensile/peeling) when loading adhesively bonded samples;

However, to introduce bonding in the design practice it is necessary to have complete information on the joint behaviour, not only mechanical. Aim of the present work is to present a testing methodology to characterize the static and dynamic strength of bonding as well for other joining techniques (the method can be used also for fatigue testing). The advantage of these testing



method is to be able to load the same specimen in different loading conditions (ranging from pure shear to tensile) simply by changing the loading orientation. The specimen (called KS2) consists of two C shaped half shells joined in the middle, as it is visible in fig. 1. In this same figure, the loading device that allows for variable loading is shown. Load-stroke curves for each experimental test are obtained, and can be used to obtain the joint strength in different loading combinations. The results can be collected and represented in the form of limit failure curves, as shown in Fig. 2.

Results from different type of adhesive are analysed and discussed, together with the development of a simple failure criterion for this type of joint.

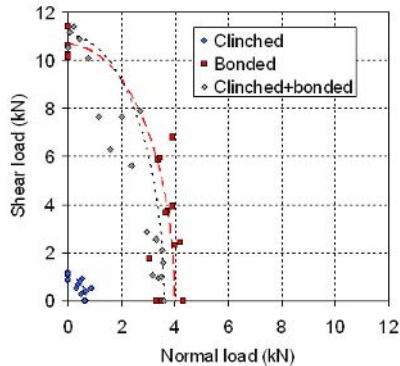


FIGURE 2. Failure limit curves for bonded, clinched and hybrid joints

## References

1. B. Chang, Y. Shi, S. Dong, *J. of Materials Processing Technology*, vol. **87**, 1999, pp. 230-236.
2. B. Chang, Y. Shi, L. Lu, *J. of Materials Processing Technology*, vol. **108**, 2001, pp. 307-313.
3. Blarasin, B. Atzori, P. Filippa, G. Gastaldi, *Design fatigue data for joining steel sheets in the automotive industry*, SAE paper 900742, 1990.
4. S.H. Lin, J. Pan, T. Tyan, P. Prasad, *Failure modelling of spot welds under complex combined loading conditions for crash applications*, SAE paper 2002-01-2032.
5. S.-H. Lin, J. Pan, S. Wu, T. Tyan, P. Wung, *Spot weld failure loads under combined mode loading condition*, SAE paper 2001-01-0428.
6. S. Zhang, *Recent development in analysis and testing of spot welds*, SAE paper 2001-01-0432.

## STUDY OF THE SUBSTITUTION OF LIMESTONE FILLER WITH POZZOLANIC ADDITIVES IN MORTARS

M. Katsioti<sup>1</sup>, D. Gkanis<sup>1</sup>, P. Pipilikaki<sup>1</sup>, A. Sakellariou<sup>2</sup>, A. Papathanasiou<sup>2</sup>, Ch. Teas<sup>3</sup>  
and E. Haniotakis<sup>3</sup>

<sup>1</sup> School of Chemical Engineering, NTUA,  
9 Heroon Polytechniou St., 157 73 Athens, Greece

<sup>2</sup> Public Power Corporation/ Testing Research and Standards Center

<sup>3</sup> Cement Company S.A.  
katsioti@central.ntua.gr

In this work several specimens of mortars were produced with the addition of 5% fly ash and 5% perlite and their mechanical properties and porosity were tested and compared to those of mortars with no additives (reference sample).

Specifically, the influence that these additives have on the elastic modulus and porosity of the mortars was studied. Mortar samples of 40x40x160mm were prepared at a water/solid ratio of 0,15 using one portion of cement I 42,5R and three portions of sand according to EN 196-1. The specimens were cured in a moist atmosphere for 28 days and 90 days at 20°C and 95% relative humidity.

The following measurements were made: a) chemical, mineralogical and granulometric analysis of additives, b) normal plasticity water, c) compressive and bending strength at 28 days and 90 days, d) adhesion, e) air content, f) specific gravity of mortar, g) dispersion, h) porosity and pore size distribution of mortar were investigated by mercury porosimetry, i) the morphological character of different mortar was measured by scanning electron microscopy (SEM). Finally, the Young's modulus of elasticity was measured in cylindrical specimens sized 50/100mm (diameter/height) according to ASTM C 469 – 02 Standard.

The results of the present study indicated a differentiation in the microstructure of the mortars that can be contributed to the use of different additives, such as fly ash and perlite. The value of the elastic modulus is related to the ratio of compressive to bending strength and more specifically, with the increase of the value of the ratio, the value of the Young's modulus of elasticity increases. The development of the microstructure represents a major parameter to improve existing mortars and to formulate new mortars.

### References

1. A.Boumiz, C.Vernet and F. Cohen Tenoudji, Mechanical Properties of Cement Pastes and Mortars at Early Ages, *Advanced Cement Based Materials.*, vol.3 (1996), 94-106
2. J.C Nadeau, Water-cement ratio gradients in mortars and corresponding effective elastic properties, *Cement & Concrete Research*, vol. 32 (2002) 481-490
3. F.Blanco, M.P. Garcia, J.Ayala, G.Mayoral, M.A.Garcia, The effect of mechanically and chemically activated fly ashes on mortar properties, *Fuel*, vol. 85 (2006) 2018-2026
4. C.C Yang, Effect of the transition zone on the elastic moduli of mortar, *Cement & Concrete Research*, vol. 28 (1998) 727-736

- 
5. Oral Buyukozturk and Brian Hearing , Crack propagation in concrete composites influenced by interface fracture parameters, *International journal of Solids Structures*, vol. **35** (1998) 4055-4066
  6. G.Ramesh, E.D. Sotelino and W.F. Chen , Effect of the transition zone on elastic moduli of concrete materials, *Cement & Concrete Research*, vol. **26** (1996) 611-622
  7. A.Boumiz,D.Sorrentino,C.Vernet and F. Cohen Tenoudji, Modelling the development of the elastic Moduli as function of the hydration degree of cement pastes and mortars, *Proceedings 13 of the 2<sup>nd</sup> RILEM Workshop*, RILEM, Dijon, France
  8. K.K. Sideris, P. Manita, K.Sideris , Estimation of ultimate modulus of elasticity and Poisson ratio of normal concrete, *Cement & Concrete Composites*, vol. **26** (2004) 623-631

## A TESTING TECHNIQUE OF CONFINED COMPRESSION FOR CONCRETE AT HIGH RATES OF STRAIN

P. Forquin<sup>1</sup>, F. Gatuingt<sup>2</sup> and G. Gary<sup>3</sup>

<sup>1</sup> Laboratoire de Physique et de Mécanique des matériaux, Université Paul Verlaine de Metz, 57045 Metz, France, pascal.forquin@univ-metz.fr

<sup>2</sup> Laboratoire de Mécanique et Technologie, E.N.S. de Cachan, 61 av. du Pt Wilson, 94235 Cachan, France, Fabrice.Gatuingt@lmt.ens-cachan.fr

<sup>3</sup> Laboratoire de Mécanique des Solides, Ecole Polytechnique, 91128 Palaiseau, France Gary@lms.polytechnique.fr

The compaction of concrete associated with a volume decrease over 10% occurs under high pressures. Such situations are found in military applications (blast loading, penetrating projectile) or in studies for the safety of buildings (power plants) regarding an accidental internal loading or external loading (plane crash). In such situations, a compressive loading develops within the concrete target with high pressure-levels (up to 1000 MPa) and high strain-rates (up to few hundred of  $s^{-1}$ ).

To characterise the behaviour of concrete specimens under such loading, one may perform 1D-strain compression test. A cylindrical specimen (diameter: 30 mm, length: 40 mm in this study) is embedded in an instrumented steel confinement ring (Fig. 1b, outer diameter: 65 mm, length: 45 mm in this study) and compressed using 2 cylindrical plugs (Fig. 1a). This experimental device was already used in quasi-static conditions with a larger ring that was supposed to behave in the elastic regime [1, 2]. In the present work, this technique was extended to the dynamic range using a SHPB device [3] to produce an axial loading and to measure axial forces and displacements (Fig. 1c).

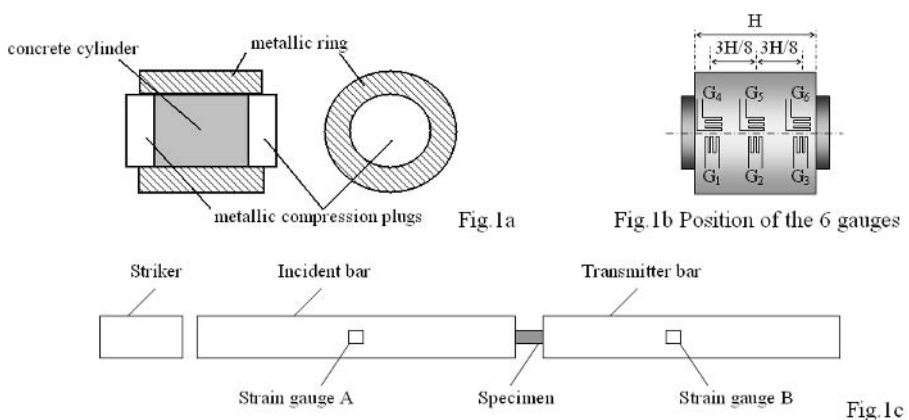


FIGURE 1. 1D-strain compression device.

Moreover, a new method of analysis was used to process the experimental data. In particular, numerical simulations of the cell loaded by an internal pressure were carried out using the finite

elements computer code Abaqus-Implicit. So, a relation is built between the pressure applied by the concrete to the inner surface of the cell and the external hoop strain measured by gauge  $G_5$  (Fig. 1b) taking account of the shortening of the specimen and the elasto-plastic behaviour of the cell. The state of average stresses and strains within the specimen is deduced at any time of loading. It allows deducing the variation of deviatoric stress versus pressure and the spherical law (evolution of pressure versus volumetric strain). The proposed method is validated by several numerical simulations of tests involving a set of 4 different concrete-like behaviours and different friction coefficients between the cell and the specimen.

Three 1D-strain compression tests were performed and processed (Fig. 2) with the MB50 high-performance concrete [4]. It appears that the deviatoric and spherical behaviours are almost independent of the strain rate in the observed range of strain rates ( $80\text{--}221\text{ s}^{-1}$ ). The deviatoric strength is seen to increase regularly with the hydrostatic pressure to reach 950 MPa under a pressure of 900 MPa (test  $221\text{ s}^{-1}$ , Fig. 2). Considering the spherical behaviour, an almost constant dynamic modulus of compressibility (around 5 to 6 GPa) is observed with the three 1D-strain compression tests up to a pressure of 900 MPa.

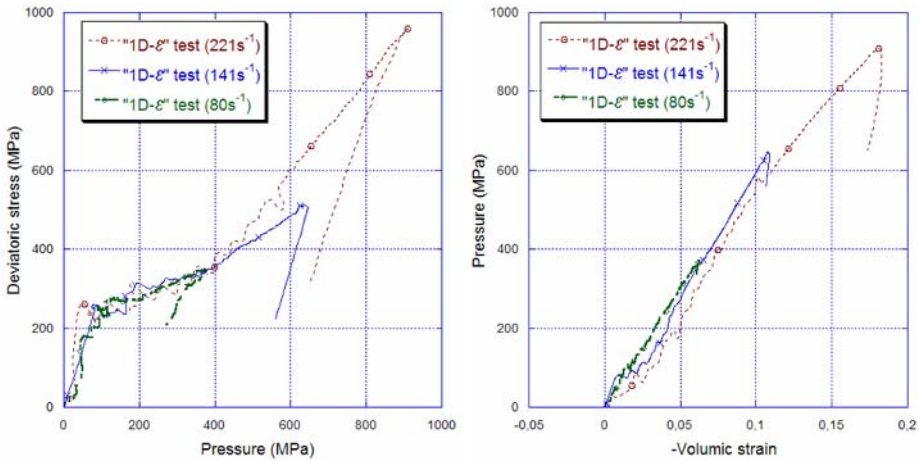


FIGURE 2. Behaviour of MB50 concrete deduced from three 1D-strain compression tests.

## References

1. Burlion, N., *PhD thesis*, Ecole Normale Supérieure de Cachan, 1997.
2. Burlion, N., Pijaudier-Cabot, G. and Dahan, N., *Int. J. Numer. Anal. Meth. Geomec.*, vol. **25**, 467-1486, 2001.
3. Kolsky, H., In *Proceedings of the Physical Society London*, vol. **B62**, 676-700, 1949.
4. Toutlemonde, F., *PhD thesis*, Ecole Nationale des Ponts et Chaussées, 1994.

## A WAVELET-BASED SYSTEM FOR STRUCTURAL HEALTH MONITORING OF AERONAUTIC STRUCTURES

I. Dimino and V. Quaranta  
CIRA, The Italian Aerospace Research Center  
Via Maiorise, 81043 Capua (CE), Italy  
i.dimino@cira.it, v.quaranta@cira.it

Structural Health Monitoring is an important requirement to ensure the safety of structures, contributing to optimize inspection and regular maintenance strategies and monitoring the actual life consumption of each individual aircraft starting from the evaluation of the real loads.

The characteristic and the entity of fatigue cracks, due to high cycle fatigue of aircraft components, depend on the aircraft maneuver, weather conditions and flight parameters. During the aircraft mission, configurations and environments can change frequently and the application of cyclical excitations with different load spectra can lead to a various life consumption. Since fatigue cracks are one of the leading causes of component failure in aircraft, structural health monitoring has received considerable attention in recent years.

The main purpose of this paper is to present a new system for structural health monitoring which employs physical parameters, extracted from the operative condition of the structure, in order to represent in exhaustive way the state condition of the structure by means of its mass and stiffness properties. An artificial neural network coupled with wavelet multi-resolution analysis is utilized for damage detection purposes by processing the structure dynamics monitored by a group of dedicated sensors. The system has been developed in order to constantly interact with the structure and check, in real time, the physical properties during the operative conditions, when the structure is subjected to the real load conditions, in actual boundary conditions. This kind of methodology is based on output only measurements and avoids the uncertainty associated with the modelled governing laws in modal analysis. Classical structural health monitoring algorithms, in fact, utilize vibration measurements to relate change in structural dynamics, in terms of modal parameters, to damage occurrence. But, in some applications, modal characteristics can be insensitive to localized damages due to the large size of structures. Besides, Fourier Transform, typically used for analyzing structural dynamics, does not allow keeping time information, often important for monitoring the damage growth. The uncertainty associated with the modelling of boundary conditions in structural models is another constraint that limits the reliability of such typology of algorithm based on modal-based damage detection.

In this paper, a system, based on a wavelet decomposition of the structural dynamic responses, due to a defined excitation path, and on a neural network classifier, is presented. The system is trained to recognize and detect the existence of different damages, simulated by the changing of the mass properties of the structure, within the structure. The recognition algorithm foresees the wavelet decomposition of the dynamic responses, measured by sensors mounted on the structure, to extract the system feature vectors. Such parameters, representative of the structural health conditions, contribute to derive the input parameters of the artificial neural network. The system employs forced responses, measured for different state conditions, to train the classifier module to identify the damage origin and location. At the end of the training process, the system is able to guarantee the "real-time monitored state" based damage identification and localization. The training and validation of the system has been carried out by means of a dedicated experimental campaign. The reference structure has been an aeronautical panel subjected to a shock testing in order to excite several modes in the frequency range of interest.

The present paper proposes a new diagnosis method for structural health monitoring that employs an integrated system for structural health monitoring of intelligent structures.

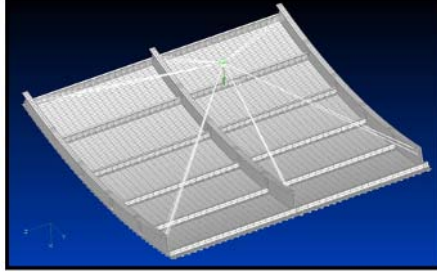


FIGURE 1. FE model of the reference structure.

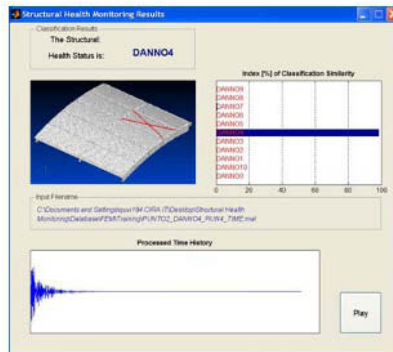


FIGURE 2. Structural Health Monitoring System.

## HOMOGENEOUS ADMINISTRATION OF EXPERIMENTS IN MATERIAL SCIENCE FOR CONFIGURATION, MONITORING AND ANALYSIS

Ferdinand Ferber<sup>1</sup>, Thorsten Hampel<sup>2</sup>, Franz-Barthold Gockel<sup>1</sup>, Thorsten Pawlak<sup>2</sup>  
and Rolf Mahnken<sup>1</sup>

<sup>1</sup> Lehrstuhl für Technische Mechanik (LTM)

<sup>2</sup> Informatik und Gesellschaft (HNI)

University of Paderborn, Warburger Straße 100, D-33098 Paderborn, Germany

ferdinand.ferber@ltm.uni-paderborn.de

In this paper, experimental techniques and studies of deformation and failure arising in thermomechanically loaded specimens as a result of cyclic thermal shock will be given. The deformation is measured by the 3D-digitalisation method. Surface damage and crack initiation are localised by the eddy current method. Because of these problems it seems reasonable to analyze damage in materials by means of state-of-the-art continuum mechanics and experimentally methods [1-4].

As material test ever so often are running lots of cycles the time for a whole test run often lasts several days [5]. This not only needs a high grade of automation, in fact the user interaction must be kept as reduced and as simple as possible. Furthermore the configuration, the monitoring and the analysis of a test run would be best operated from only one system to reduce media-discontinuity. We would like to show how concepts of virtual knowledge spaces [6] can lead to higher productivity for material testing. In short virtual knowledge spaces offer object oriented document management. Access can be archived web based or through rich client applications. Mapping the units of a material test scenario to objects, whether they are force ramps, temperature curves or measurement results, all could be managed in virtual knowledge spaces. This leads to a homogenous administration of the test which is besides location-independent. Furthermore using the existing mechanisms of virtual knowledge spaces for documentation and publishing the need of additional systems is obsolete.

A virtual knowledge space can contain arbitrary interaction objects (research materials, representations of experiments, real machines etc.), which are editable synchronous or asynchronously. A room also enclosed editing and communication functions, thus reducing media discrepancies between researchers. Rooms, once created, are managed in self administration. Due to the concept of views, a virtual knowledge space can be explored in different ways: At times it is displayed as a simple web page, at other times as an electronic whiteboard or even as a structured learning flow graph. This enables a combination of innovative forms of media supported cooperation (e.g. cooperative, discourse oriented, knowledge structured) with a long lasting administration of knowledge repositories (virtual library) and learning objects.

*opensTeam* offers a completely open source based framework and infrastructure to connect existing university services and create a specifically tailored cooperation and even *e-learning* platform. Based on existing standard technologies, a multitude of interfaces and templates can be used and integrated into existing infrastructures according to preferences and available development capacities. Since spring of 2006 *opensTeam* is part of the Sage-Debian-Linux-Distribution.

In Fig. 1 the platform for validation of material simulation and the functions of experimental modules is given.



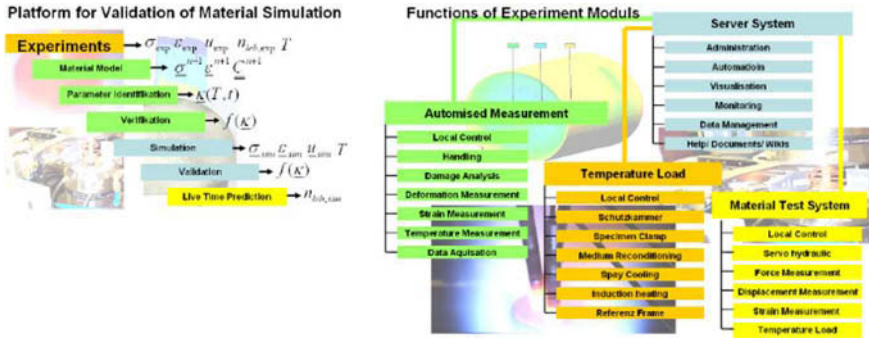


FIGURE 1. The platform for validation of material simulation and the functions of experimental modules.

## References

1. Ferber, F.; Herrmann, K., In *Proceedings of the 9th International Conference on Experimental Mechanics*, edited by V. Askegaard, Aaby Tryk, Copenhagen, Denmark, vol. **1**, 1990, 395-404.
2. Ferber, F., Hinz, O., Herrmann, K.P., In *Proceedings of the 10th International Conference on Experimental Mechanics*, Recent Advances in Experimental Mechanics, edited by J.F. Silva Gomes et al., A.A. Balkema, Rotterdam, vol. **1**, 1994, 217-222.
3. Ferber, F; Herrmann, K.P., In *Proceedings of the 11th International Conference on Experimental Mechanics*, edited by I.M. Allison, A.A. Batkema, Rotterdam, vol. **2**, 1998, 1237- 242.
4. Linnenbrock, K.; Ferber, F and Herrmann, K.P., In *Proceedings of the 11th International Conference on Experimental Mechanics*, edited by I.M. Allison, A.A. Batkema, Rotterdam, vol. **2**, 1998, 1157- 1172.
5. Gockel, F.-B., Mahnken, R., In *Proceedings of the Sixth International Congress on Thermal Stresses*, edited by Franz Ziegler, Vienna, Austria, vol. **2**, 2005, 569-572
6. Merckens, L., Hampel, T. and Ferber, F., In *Proceedings of the World Conference on Educational Multimedia, Hypermedia and Telecommunications*, vol. **2004**, Issue. 1, 2004, 5148-5153

## MATERIAL SIMULATION AND DAMAGE ANALYSIS AT THERMAL SHOCK CONDITIONS

Franz-Barthold Gockel and Rolf Mahnken  
 Chair of Engineering Mechanics (LTM), University of Paderborn,  
 Warburger Str. 100, D-33098 Paderborn, Germany  
 franz-barthold.gockel@LTM.upb.uni-paderborn.de

Thermal shock is an extreme form of thermo-mechanical loading. This detailed investigation close to reality is necessary in industrial engineering in order to get a good prediction of life expectancy for high quality and safety relevant machine components. This paper addresses on experimental investigations of deformation and damage at thermal shocked cylinders. Additionally the parameters for the Chaboche model are identified on the basis of uniaxial cyclic experiments.

### Introduction and experiments

Many modern components and structures in industrial engineering are subjected to thermo-mechanical loading. Within the interaction of analytical, experimental and numerical investigations, basic data are required which characterize the grade of thermal shock loading [1, 2]. This paper gives an overview of thermal shock experimental deformation and damage analysis and parameter identification to utilize this knowledge for finite element simulations.

The tested material is a heat resistant austenitic stainless steel X15CrNiSi20-12, which is used in many high temperature applications. After the application of 500 thermal shock cycles the cylindrical specimen was measured by a 3D-digitalisation. This measurement technique enables a full surface analysis, as shown in Fig. 1a), of the plastic deformation. In addition a damage analysis of the specimens surface has been done by the eddy current method, which makes use of impedance changes in materials effected by cracks and structure changes. Fig. 1b) shows an example of a typical crack signal. For the illustration of the location and degree of damage the signals of the damage analysis are projected to the digital specimen surface as presented in Fig. 1c).

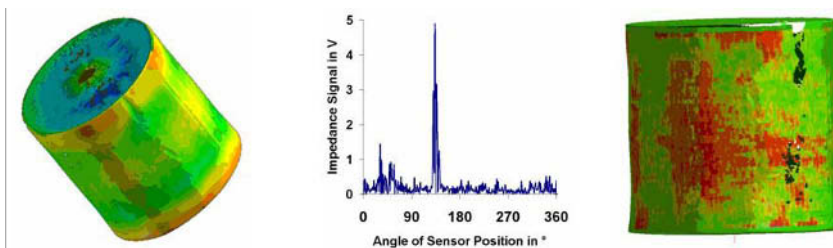


FIGURE 1 a) Deformation after 500 thermal shocks, b) eddy current signal with crack peek, c) eddy current signal projected onto the digital specimen surface

### Uniaxial experiments and parameter identification

To find out the required material properties for the use in material simulations, uniaxial cyclic tests have been done. In the corresponding cyclic stress strain diagram, Fig. 2a) the hysteresis loops show significant temperature dependency. In the experiments different constant temperatures

between 20°C and 900°C and strain rates of 2%/min and 20%/min are realised. A closer examination of the hysteresis loops show hardening and softening effects. These experimental data are the basis for the identification of the eight material parameters and model verification of the Chaboche model [3, 4].

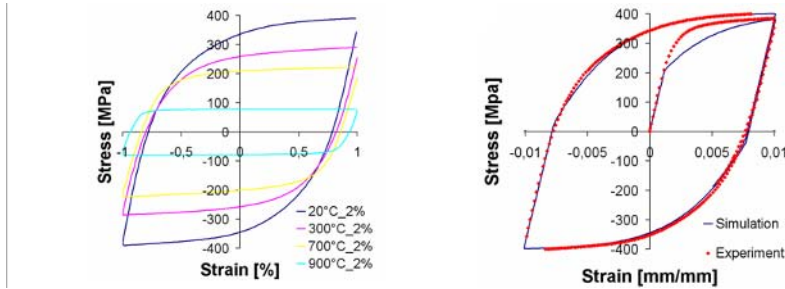


FIGURE 2 Uniaxial tension and compression test: a) Hysteresis loops of the uniaxial tension and compression experiment b) Verification of the Chaboche model, second loop at 20°C

### Measurement of the plastic deformation by the 3D-digitalisation method.

Crack propagation and surface damage is localised by the eddy current method.

Parameter identification was made for the Chaboche model by the use of uniaxial experimental cyclic strain stress data at different temperatures.

Future work will concentrate on finite element simulation of thermal shock by application and extension to damage of the Chaboche material law [5].

### References

1. Dour, G., Medjedoub, F., Leroux, S., Diaconu, G. and Rezai-Aria, F., Normalized Thermal Stresses Analysis to Design a Thermal Fatigue Experiment, *Journal of Thermal Stresses*, vol. **28**, no. 1, 2005.
2. Paffumi, E., Nilsson, K. F., Taylor, N. G., Hurst, R. C. and Bache, M. R., Thermal Fatigue Included by Cyclic Down-Shocks on 316L Model Pipe Components, *Proceedings of the 5<sup>th</sup> international Congress on Thermal Stresses and Related Topics*, TS2003, 8-11 June 2003, Blacksburg, VA.
3. Mahnken, R.: Identification of material parameters for constitutive equations, *In.: Vol. 2 of Encyclopedia of Computational Mechanics*, Eds. E. Stein, de Borst, Hughes, Wiley, 2004
4. Schneidt, A., Identifikation und Optimierung der Materialparameter des hitzebeständigen Edelstahl 1.4828 am Chaboche-Modell, *Student thesis, LTM, University of Paderborn*, 2006.
5. Mahnken, R.: Theoretical, numerical and identification aspects of a new model class for ductile damage, *Int. J. Plast.*, vol. **18**, 801-831 (2002)

## GRIDS REFORMATION FOR EFFECTIVE STRAIN MEASUREMENT OF FORMING TITANIUM TAILOR-WELDED BLANKS AT ELEVATED TEMPERATURES

C. P. Lai<sup>1,a</sup>, L.C. Chan<sup>1,b</sup> and C.L. Chow<sup>2,c</sup>

<sup>1</sup>Department of Industrial and Systems Engineering, the Hong Kong Polytechnic University, Hung Hom, Kowloon, Hong Kong, P.R. China

<sup>2</sup>Department of Mechanical Engineering, University of Michigan-Dearborn, 4901, Evergreen Road, Dearborn, Michigan, USA

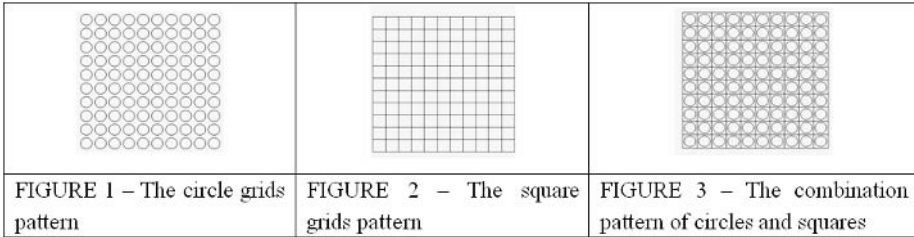
<sup>a</sup>ise.cplai@polyu.edu.hk, <sup>b</sup>mflcchan@inet.polyu.edu.hk, <sup>c</sup>clchow@engin.umd.umich.edu

Titanium and its alloy are widely used in the automobile and aircraft industries because of a variety of advantages: good corrosion resistance, light in weight and high strength [1]. However, use of the titanium and its alloy has been highly selective due to its high cost. Titanium tailor-welded blanks (Ti-TWBs) are expected to be one of the candidate materials to address this issue. In fact, forming both titanium alloy and titanium tailor-welded blanks (Ti-TWBs) at room temperature is very difficult due to their specific characteristics: potential embrittlement, low workability, and high springback effect [2]. To overcome these shortcomings, Ti-TWBs have been recommended to form at elevated temperatures not less than 150°C [2-3]. However, the investigation on the effective strain measurement for forming Ti-TWBs at elevated temperatures is still quite limited.

Many forming processes yield large deformation of stamped components. Accurate measurement of large deformation poses an experimental challenge. Past investigators have found the grid method to be an effective way in strain analysis [4-7]. According to the ASTM standard [8], the grid size of 2.5mm circle diameter or square to measure is recommended for the measurement of large strains. Meanwhile, square grids have been used to measure the strains of non-homogeneous deformation by some investigators [5]. On the other hand, the recommended grid size has been reported to affect the strain gradient measurement due to large grid distortion [9]. Therefore, fine grids such as  $\phi$ 0.4mm or 0.4mm $\times$ 0.4mm have been adopted to measure the sharp strain gradients often found close to the crack region [4], although the method is fairly time consuming [10]. Therefore, the development of an effective strain measurement method to circumvent the aforementioned shortcomings is called for.

In this investigation, a grid reformation for strain measurement is proposed to measure the strain distributions of the deformed Ti-TWBs at elevated temperatures. Titanium alloy (Ti-6Al-4V) test specimens of 0.7mm and 1.0mm thicknesses as well as their different combinations (i.e. 0.7mm/0.7mm, 0.7mm/1.0mm and 1.0mm/1.0mm) with widths of 20mm, 90mm and 110mm are prepared. In order to examine the welding quality of Ti-TWBs, the tensile test under various temperatures is carried out. The Swift Forming Test device with heating elements and temperature control device are developed [11]. In the meantime, titanium base metal in thickness of 0.7mm and 1.0mm is used to determine an optimum grid pattern. Three types of grid patterns, i.e. circle (0.8mm diameter), square (1.0mm) and combination, are laser-marked on the surface of titanium base metal specimen. The patterns of grids are shown in Figures 1 to 3. The forming limit diagrams (FLD) of titanium base metal have been constructed using the three grid patterns. According to the FLDs of titanium base metal, it is found that data reduction analysis of major and minor strains deformation is found to be more accurate using the combination pattern. Subsequently, all Ti-TWBs specimens have been laser-marked with grids of the combination pattern, 1.0mm squares and 0.8mm diameter circle, on their surfaces to measure the major and minor strain distributions at different temperatures (i.e. room temperature, 300°C and 550°C). Then, a comparative study of the

FLDs of Ti-TWBs and titanium base metal at elevated temperatures is carried out to validate the test results. Finally, the investigation reveals that the grid reformation can significantly enhance the efficiency of strain measurement on the formability of Ti-TWBs at elevated temperatures. By using this technique, the effective strain measurement has been achieved.



## Reference

1. F. K. Chen, K. H. Chiu, “Stamping formability of pure titanium sheets”, *Journal of Materials Processing Technology*, vol. **170** (2005), 181 - 186
2. *Metals Handbooks*, “Forming and Forging”, Volume 14 (2001), American Society for Metals
3. C. H. Cheng, L. C. Chan, C. L. Chow and C. P. Lai, “Formability of Ti-TWBs at Elevated Temperatures”, *SAE Technical Papers* (2006), 2006-01-0353
4. Y. C. Leung, L. C. Chan, C. Y. Tang and T.C. Lee, “An Effective Process of Strain Measurement for Severe and Localized Plastic Deformation”, *International Journal of Machine Tools & Manufacture*, vol. **44** (2004), 669 - 676
5. J. W. Dally, “Experimental Stress Analysis”, McGraw-Hill, New York, 1991
6. W. B. Lee and X. Y. Wen, “A Dislocation-model of limit strain prediction in Aluminum Sheet Metals under Biaxial Deformation”, *International Journal of Damage Mechanics*, vol. **9** (2000), 286 - 301
7. L. C. Chan, C. H. Cheng, M. Jie and C. L. Chow, “Damage-based Formability Analysis for TWBs”, *International Journal of Damage Mechanics*, vol. **14** (2005), 83 - 96
8. “Standard Test Method for Determining Forming Limit Curves”, *ASTM Standard*, E-2218 (2002)
9. Z. Marciniak, J. L. Duncan and S. J. Hu, “Mechanics of Sheet Metal Forming”, Butterworth Heinemann (2002)
10. C. C. Wang, J. Lee, L. W. Chen and H. Y. Lai, “A New Method for Circular Grid Analysis in the Sheet Metal Forming Test”, *Experimental Mechanics*, vol. **40** (2002), 190 - 196
11. C. P. Lai, L. C. Chan and C. L. Chow, “Effects of Tooling Temperatures on Formability of Titanium Tailor-welded Blanks at Elevated Temperatures”, *Journal of Materials Processing Technology* (2006), *In-press*

## EXPERIMENTAL STUDY OF OPTIMAL PROCESS PARAMETERS FOR DEFORMATION WELDING OF DISSIMILAR METALS

T.F. Kong<sup>1</sup>, L.C. Chan<sup>2</sup> and T.C. Lee<sup>3</sup>

Department of Industrial and Systems Engineering, The Hong Kong Polytechnic University  
Hung Hom, Kowloon, Hong Kong, People's Republic of China

<sup>1</sup> ise.tfkong@polyu.edu.hk, <sup>2</sup> mflcchan@inet.polyu.edu.hk, <sup>3</sup> mftclee@inet.polyu.edu.hk

The market trends of automobile, aerospace and marine are towards greater demand on light, strong, economical, and corrosion-resistant parts and components. However, no single metal or alloy can perfectly satisfy all these requirements. This has led to the rapid growth in interest of joining dissimilar metals. For example, inexpensive materials can be conserved to combine with high-strength, high-toughness, light-weight, or excellent corrosion-resistant materials. Solid-state welding is particularly suitable for producing such dissimilar-metal joints because the melting of base metals is nearly avoided, the metals being joined can retain their original properties with less effect on heat-affected zone, and the metallurgical damage of the joints can be minimized. Diffusion bonding has been developed for many years among the solid-state welding processes. Since its processing time is very long (from minutes to hours) and the specific work environment such as a vacuum, inert gas, or reducing atmosphere is required, this process has not been widely accepted and implemented in the industry. Deformation welding is another solid-state welding process. It is similar to the diffusion bonding in which both processes require the application of heat and pressure. Comparing to the diffusion bonding, the processing time of deformation welding is relatively short (within seconds) and the requirements of working conditions are less stringent. However, most literatures on joining dissimilar metals tend to use of diffusion bonding, the previous publications of deformation welding of dissimilar metals are very rare as most studies are focusing on joining similar metals. Hence, deformation welding of dissimilar metals is immature for the industrial applications and the optimal process parameters such as welding temperature, amount of deformation, and contact time are difficult to be determined precisely.

In order to solve the above problems, this paper experimentally studies the optimal process parameters such as welding temperature, amount of deformation, and contact time for deformation welding of dissimilar metals such as aluminium alloy with austenitic stainless steel or aluminium alloy with commercially pure titanium. The process is intensively optimized by the Taguchi method to result in the highest quality of weld. The bimetallic specimens were pairs of cylindrical rods with the diameter of 8 mm. The ends of the rods were pushed against each other with sufficient force provided by a 160-ton hydraulic press. An induction coil was used to wind around the specimen and to heat it immediately to welding temperatures. Fig. 1 illustrates the experimental setup of the deformation welding. The welding temperatures chosen in the tests were  $0.7 T_m$ ,  $0.8 T_m$ , and  $0.9 T_m$ , where  $T_m$  was the melting point of the lower-melting-point specimen in Kelvin degree. The amounts of deformation were the reductions of rod heights of 4 %, 8 %, and 12 %. The contact times were 10 seconds, 20 seconds, and 30 seconds. A uniaxial-tensile test and a bending test eventually used to examine the quality of joints. The typical flash or collar resulting from the deformation welding was removed from each specimen prior to tensile tests and bending tests in order to prevent it from influencing the results of tests.

The dissimilar metals were properly welded to form rigid joints. The preliminarily result showed that the increases of welding temperature, and amount of deformation could improve the tensile properties of the specimens, and therefore a stronger bimetallic joint was achieved. The influence of the contact time was relatively less significant for the process because the joints

obtained in 10 seconds were no much different from those obtained in 20 seconds, and 30 seconds. The optimization was carried out by Taguchi method to obtain the optimal process parameters which satisfied the given requirements of the joint in terms of higher tensile strengths, and expected fracture locations. The high-quality joints (according to the standard: AWS WIT-T) of dissimilar metals have been successfully obtained by deformation welding with a short processing time. Therefore, engineers are able to gain better knowledge of how to produce high-quality joints of dissimilar metals using deformation welding.

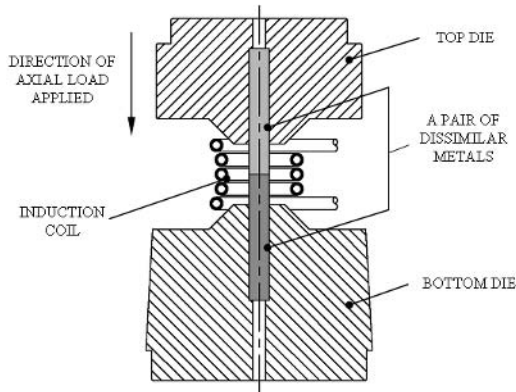


FIGURE 1. The experimental illustration of deformation welding.

## MECHANICAL BEHAVIOUR OF UDIMET 720LI SUPERALLOY

S. Chiozzi, V. Dattoma and R. Nobile

Università degli Studi di Lecce, Dipartimento di Ingegneria dell'Innovazione

Via per Arnesano, 73100 Lecce, Italy

samanta.chiozzi@unile.it , vito.dattoma@unile.it , riccardo.nobile@unile.it

Superalloys are the most diffused material for aeronautical and aerospace applications, mainly for turbines and compressors production, because of their excellent resistance at high temperature. Among them, polycrystalline superalloy Udimet 720Li is an interesting candidate for turbine disc application, due to its high temperature strength, good corrosion resistance and excellent workability [1, 2].

This alloy has been developed starting from Udimet 720 which has excellent stress corrosion and high temperature resistance, but which was found to be prone to sigma formation. Therefore, Li (Low Interstitial) version has been developed to minimize this problem. The main difference between Udimet 720 and Udimet 720Li consists in lower levels of carbon, chromium and boron [3, 4]. The alloy chemical composition is reported in Table 1.

TABLE 1. Chemical composition (wt%).

Al	B	C	Co	Cr	Mo	Ti	W	Zr	Ni
2.25	0.01	0.01	14.0	15.5	2.75	4.75	1.00	0.025	bal

The aim of the present work is to study the static tensile strength of Udimet 720Li superalloy at room and working temperature.

Slow strain rate tests have been performed on smoothed and notched ( $k_t \approx 3.5$ ) cylindrical specimens (Fig. 1), in order to evaluate material ductility and notch sensitivity.



FIGURE 1. Tested specimens.

Tests have been performed at two different working temperature (650°C and 700°C), which covered all possible high temperature alloy employments. This test plan is inserted in an extensive research project carried out in collaboration with Avio S.p.A., in which creep and high temperature low cycle fatigue tests are planned also.



Material is provide by Avio S.p.A., which is also responsible for heat treatments, according to ASM standards for aeronautical components.

Moreover, a microstructural analysis has been performed through Scanning Electron Microscope (SEM) to analyze fracture surfaces and crack nucleation points, evidencing alloy brittle behaviour and possible heat treatments modifications in order to obtain better results at working temperature.

## References

1. Marchionni, M., Osinkolu, G.A. and Onofrio, G., *International Journal of Fatigue*, vol. **24**, 1261-1267, 2002.
2. Onofrio, G., Osinkolu, G.A. and Marchionni, M., *International Journal of Fatigue*, vol. **23**, 887-895, 2001.
3. Goto, M. and Knowles, D.M., *Engineering Fracture Mechanics*, vol. **60**, 1-18, 1998.
4. Na, Y.S., Park, N.K. and Reed, R.C., *Scripta Mater.*, vol. **43**, 585-590, 2000.

## SOLID PHASE CHANGE OBSERVATION USING DIGITAL IMAGE CORRELATION

S. Valance<sup>a,1</sup>, M. Coret<sup>a,1</sup>, J. Réthoré<sup>b,1</sup> and R. de Borst<sup>a,2</sup>

<sup>a</sup> Lamcos (UMR/CNRS 5514), <sup>b</sup> TU Delft, The Netherlands

<sup>a</sup> bât. Coulomb / av. Einstein / 69621 Villeurbanne (F), <sup>b</sup> Kluyverweg / 2629 HS Delft (NL)

<sup>1</sup> {stephane.valance; michel.coret}@insa-lyon.fr, <sup>2</sup> {j.rethore; r.deborst}@TUDelft.nl

This study focus on solid phase change in maraging steel on cooling and on heating, e.g. austenitic and martensitic transformation. It has been shown by Coret [1] that TRIP simulation under complex load scenario is not achievable with actual analytic homogenisation methods. To improve mechanical simulation of solid phase change in steels, it has been decide to study the real deformation happening in such a phase change, with or without a mechanical load.

To achieve that goal, we design a micro tension experiment. The sample is put in a box where we can impose a low argon vacuum in order to remove oxidation on the surface of the test sample. The sample can then be heated by Joule effect due to an enhanced resistivity of the interest's zone produce by a thinning section of the sample.

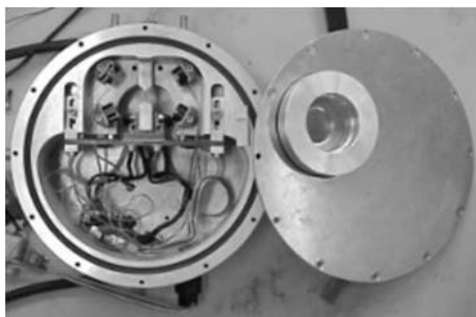


FIGURE 1: Low vacuum box with test sample

During heating and cooling, a digital camera enables observation of the surface of the test sample. An appropriate optical mount, i.e. a bellows in association with close up lenses, gives a magnification of almost five times while keeping a sufficient enlargement and depth of field.

After experiment, we obtain the displacement field using digital image correlation. This displacement field is used to identify the front of phase change. Indeed, a phase change corresponds to a density jump on the interface. A weak discontinuity in the displacement field follows from this jump. Then, identifying a weak discontinuity in the displacement field enable to find the front of phase change.

Finally this result are integrate in an X-FEM [2] code for simulation of multi-phase elasto-plastic mechanical problem. We could then compute material forces [3] which would enable a complete characterisation of the phase front change velocity and initiation condition.

**References**

1. Coret, M., Calloch, S., and Combescure, A., *Eur. J. Mech. A/Solids*, 823–842, 2004
2. Moës, N., Dolbow, J., and Belytschko, T., *Int. J. Numer. Meth. Engng.*, vol. **46**, 131–150, 1999
3. Maugin, G.A., *J. Elas.*, vol. **71**, 81–103, 2003

## EFFECTS OF APPLIED STRESS ON THE SHAPE MEMORY BEHAVIOUR OF NITI WIRES

A. Falvo, F. Furgiuele and C. Maletta  
Dep. of Mechanical Engineering, University of Calabria  
P. Bucci 44C 87030 Arcavacata di Rende (CS), Italy  
Email: carmine.maletta@unical.it

Shape Memory Alloys (SMAs), in particular Nickel-Titanium (NiTi) alloys, are being used in an increasing number of engineering applications due to their special functional properties, namely shape memory effect (SME) and superelastic effect (SE). These properties, which allow large stresses and strains recovery, are due to a thermoelastic phase transformation, between martensite (M) and austenite (A), which is characterized by a hysteretic behaviour. In particular the phase transformation can be induced by a thermal load between the phase transformation temperatures (SME) or by an applied stress (SE). Two-way shape memory effect (TWSME) is another particular property since the material is able to remember a geometrical shape at high temperature, above austenite finish temperature ( $A_f$ ), and another shape at low temperature, below martensite finish temperature ( $M_f$ ) [1]. This functional property can be developed in NiTi alloys by various thermo-mechanical treatments, the so-called training.

As well known, when the dimensions of the component are relatively small, NiTi alloys show very high power/weight ratio, with respect to other types of actuators, due to their capability to recover large strains under high values of applied stresses [2]. However, when increasing the dimensions of the component, the use of these materials is not suitable as a consequence of the high energy required for the activation of the phase transformation. The main drawback of NiTi actuators consists in its high thermal inertia [3], which limits the transformation frequency, and therefore its practical use in many applications. This limitation can be partially overcome by using NiTi wires, with small diameter, because they demonstrate fast cooling rates thanks to their large surface-to-volume ratio. Furthermore, the thermal energy, required in the phase transformation, can be easily supplied by an electric current. For this reasons, NiTi wires are the most useful shape to realize actuators in many application fields such as shape and vibration control, micro electro-mechanical systems, surgical devices and instrumentations and many others [1].

A characteristic which must be taken into account when using these alloys, is the hysteretic behaviour, which characterizes the phase transformation and, consequently, the functional properties. The hysteretic behaviour is influenced by temperature and stress loading history of the material as well as the operating conditions. Among the various affecting factors, the influence of external stress is an important topic to be analyzed, in order to understand the capability of the material to produce work. Furthermore, the applied stress influences the martensite stabilization [4] and the long term performance of the NiTi actuators [4].

In the present work the shape memory behaviour of NiTi wires, in terms of both SME and TWSME, under different constrain conditions is investigated. In particular, the SME, or better the capability of the material to recover its original shape after a mechanical deformation, is investigated under several values of applied stress. Furthermore, after a proper thermomechanical training, the TWSME and its hysteretic behaviour, strain versus temperature, is analysed under different applied stress. As an example, in Fig. 1 the measured hysteresis loops, two way strain versus temperature, in the case of stress free condition, together with those obtained by two fixed values of tensile stress, 50 and 100 MPa, are shown. As expected, the figure clearly show an

increase of the TWSME when increasing the applied stress, together with an increase in the transformation temperatures.

Finally, the thermal stability of the TWSME is investigated by repeated thermal cycles, between the phase transformation temperatures, in order to understand the long term performances of NiTi actuators.

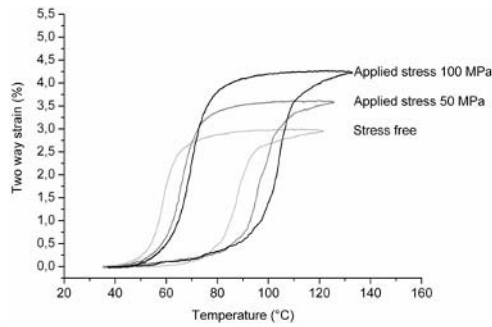


FIGURE 1: Hysteresis loops strain versus temperature at different applied stress

## Reference

1. Schwartz, M., *Encyclopedia of Smart Materials*. John Wiley & Sons, Canada, USA, 2002.
2. Potapov, P.L. and da Silva, E.P., *In Proceedings of ACTUATOR 2000, 7th Int. Conf. On New Actuators*, 2000, Bremen, Germany, 156.
3. Meier, H. and Oelschlager, L., *In Proceedings of SMST Conference on Shape Memory and Superelastic Technologies*, 2003, Pacific Grove USA.
4. Otsuka, K. and Ren, X., *Progress in Materials Science*. vol. **50**, 2005, 511–678.

## STUDY ON MICRO-DAMAGE OF AL ALLOY WELDED JOINT IN AEROSPACE THERMAL CYCLING CONDITION

Cheng Jin<sup>a</sup>, Jitai Niu<sup>b</sup> and Shiyu He

School of Materials Science and Engineering, Harbin Institute of Technology  
Harbin 150001, P.R.China

<sup>a</sup>jincheng@126.com, <sup>b</sup>jtn@hit.edu.cn

Aluminum alloy is one of the most important construction materials, due to its high specific strength, good corrosion resistance property and good weldability. It has been used in almost every branch of transportation industry [1]. Especially, in aerospace industries its light weight, good corrosion resistant properties, and no low temperature point for brittleness transformation make it be widely used in weight sensitive and cryogenic construction [2].

Because of the different microstructure and mechanical performance between the welded joint and base materials, the welded joints often become the weakest part in the whole welded structures. Their performance evolution and failure behavior determine the serve life of the whole welded structures.

The aerospace industry currently uses an amount of tungsten inert gas (TIG) welding technology to join aluminum alloy structures. When the space vehicles travelling in earth orbit during the period of serving in aerospace, some construction material will subject to the space cyclic thermal load as well as the working load [3,4]. That will cause the performances deterioration and material microstructure damage [5,6]. Many works had been done with respect to the damage of composites induced by thermal cycling [7-9]. However, few literatures have been found to investigate the aluminum alloy welded joint performance in aerospace thermal cycling condition.

In order to evaluate the long-life reliability and guarantee the safety of the welded structure under services, it is essential to determine its damage mechanisms and the law of its performance deterioration. This paper focuses on the mechanical performance deterioration of 5000 serial aluminum alloy butt-welded plate under simulated aerospace thermal cycling condition.

A typical composition of the parent aluminum alloy 5A06 sheet used in this study is presented in Table 1. The sheets with 3mm thickness were butt-welded by TIG welding using the same filler wire material.

Table 1. Compositions of 5A06 aluminum alloy

Mg	Mn	Si	Fe	Zn	Cu	Ti	Al	Other
5.8-6.8	0.5-0.8	0.4	0.4	0.2	0.1	0.02-0.1	Bal.	0.1

Carefully X-ray non-destructive detections were carried out on these welded specimens. The specimens with any detectable defects were eliminated to ensure the results consistency in the following tests.

Thermal cycling tests were conducted using a homemade machine. The test parameters were pre-programmed and put into the supervisory control computer. Several welded joint specimens as well as base alloy specimens were put into the thermal isolation cavity of the machine. During the test, an external 70MPa tensile load was applied on the specimens. The specimens were heated using current heat effect and cooled by spraying liquid nitrogen into the test cavity. By means of a thermocouple fixed on the specimen, the temperature is controlled. The cycling temperature range is  $-100\sim 100$  and the cyclic period is 90 minutes.

Monotonic tension test of the specimens were conducted both before and after the thermal cycling test, in order to determine the damage induced by thermal cycling. The fracture surface was observed by scanning electron microscopy (SEM) and EDS to analysis the damage and fracture mechanism.

Results show that thermal cycling condition can induced more severe damage in welded joint than that in base 5A06 aluminum alloy. The particles formed in welding heat-affected zone are the source of local damage in thermal cycling condition. The thermal mismatch stress and external stress can cause debonding between the particles and base alloy. Micro voids nucleation and evolution of the around the particles cause the mechanical properties deterioration of the welded joint.

This damage evolution process was analyzed both theoretical and by FEM numerical simulation.

## References

1. Jeom Kee Paik, , Sjoerd van der Veen, Alexandre Duran and Matthew Collette, *Thin-walled Structures*, vol. **43**, 1550, 2005
2. Tetsumi Yuri, Toshio Ogata, Masahiro Saito and Yoshiaki Hirayama, *Cryogenics*, vol. **41**, 475, 2001
3. C. SivaKumar, S.M.Mayanna, K.N.Mahendra, A.K. Sharma and R. Uma Rani, *Applied Surface Science*, vol. **151**, 280, 1999
4. Jun-Yen Uan, Chi-Yuan Cho, Zhi-Ming Chen and Jun-Kai Lin, *Materials Science and Engineering A*, vol. **419**, 98, 2006
5. Jitai Niu, Wei Guo, Yongling Guo and Qingchang Meng, *Key Engineering Materials*, vol. **297-300**, 2843, 2005
6. Hongbin GENG, Song HE, Dezhang YANG, *Journal of Materials Science & Technology*, vol. **19** Suppl.1, 205, 2003
7. Chuwei Zhou, Wei Yang, Daining Fang, *Journal of Engineering Materials and Technology*, vol. **122**, 203-208, 2000
8. Hui Mei, Laifei Cheng, Litong Zhang, *Scripta Materialia*, vol. **54**, 163-168, 2006
9. C. Badini, M. La Vecchia, A. Giurcanu, J. Wenhui, *Journal of Materials Science*, vol. **32**, 921-930, 1997

## DEVELOPMENT OF A COMPRESSION TOOL FOR POLYMERIC MATERIALS

M. Jerabek<sup>1</sup>, R. Steinberger<sup>1</sup> and Z. Major<sup>2</sup>

<sup>1</sup> Polymer Competence Center Leoben GmbH, Parkstrasse 11, 8700 Leoben, Austria

<sup>2</sup> Institute of Materials Science and Testing of Plastics, University of Leoben, Franz-Josef-Strasse 18, 8700 Leoben, Austria  
jerabek@pccl.at

Besides the time and temperature dependent behaviour of polymeric materials the influence of pressure is of crucial importance. While tensile test is frequently used to determine material parameters, only little research has been conducted in the compression regime. Furthermore, the knowledge of the compression behaviour is of prime practical and theoretical importance for a number of engineering applications (i.e., contact problems, tribology). Hence, the objective of this research work was to develop and implement a compression tool on which different configurations can be mounted and tested on polymers.

In order to figure out the sensitivity of the material behaviour on hydrostatic pressure different compression configurations are necessary. Therefore in this study we applied and further developed uniaxial, plane strain and confined compression setups. Thus it is possible to vary the pressure in a wide range up to values where plastic deformation of the material practically vanishes. To ensure stable testing conditions during the whole test a specially designed compression tool was developed, which can be seen in Fig. 1. One of the problem to get reliable compression data is wobbling of the testing machine, which results in an error in the force transmission upon the specimen. For this purpose four aligning bars in the compression tool were used (Fig. 1) to guide the upper and lower compression plate. In the paper a detailed description of the configurations and their geometries will be given.

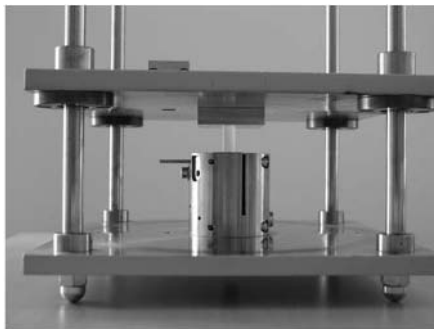


FIGURE 1. Compression tool with the setup for the uniaxial compression test mounted. The four aligning bars at each corner can be seen.

In order to evaluate the compression data one has to distinguish between the small strain and large strain behaviour. The influence of pressure on the yield stress has been widely investigated, e.g. Quinson et al. [1] or Sauer [2], whereas only little research has been conducted on the trend of



the whole stress – strain curve and in particular on the modulus values obtained via different testing methods. However, in this paper the whole stress – strain curves for different configurations will be compared and discussed in terms of true stress vs. true strain. Furthermore, the influence of inhomogeneous deformation beyond the yield strain will be shown. To this end a video camera was applied to accurately determine the lateral deformation.

In the tensile test the material behaviour can be investigated up to final failure of the material with concurrent determination of the tensile modulus. This is also true for compression testing but demands a different procedure how to calculate the compression modulus. In this paper an evaluation method will be explained that accounts for initial effects. Therefore, instead of taking a specific interval for the calculation of the modulus the derivative of the stress – strain curve was calculated and the highest values were assumed to correspond to the material modulus. These values can then be compared to tensile test results, as it can be seen in Fig. 2 for three different strain rates, denoted by  $v_1$ ,  $v_2$  and  $v_3$ . It is obvious that the positive pressure in compression compared to the tensile regime results in an increase in the modulus values. This means, that not only the yield stress is dependent on pressure but also the whole stress – strain curve from the origin is shifted to higher stress values.

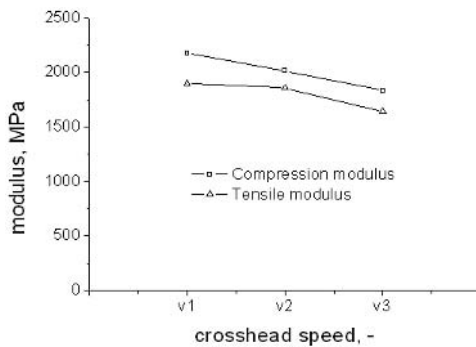


FIGURE 2. Tensile and compression modulus plotted vs. crosshead speed.

## References

1. Quinson, R., Perez, J., Rink, M. and Pavan, A., *J. Mater. Sci.*, vol. **32**, 1371-1379, 1997.
2. Sauer, J. A., *Polym. Engng. Sci.*, vol. **17**, 150-164, 1977.

## APPLICATION OF FULL-FIELD STRAIN AND TEMPERATURE MEASUREMENT AND ANALYSIS FOR POLYMER TESTING

Z. Major<sup>2</sup>, R. Steinberger<sup>1</sup>, Ch. Feichter<sup>1</sup>, M. Jerabek<sup>1</sup> and R.W. Lang<sup>1,2</sup>

<sup>1</sup> Polymer Competence Center Leoben GmbH

<sup>2</sup> Institute of Materials Science and Testing of Plastics  
University of Leoben, A-8700 Leoben, Austria  
zoltan.major@notes.unileoben.ac.at

Recently, full field optical techniques are increasingly appreciated as deformation, strain and stress analysis tools. These new techniques offer high potential in the fields of material and component testing. On the laboratory test specimen level such non-contact methods may provide more accurate strain information over a large deformation range, as an important aspect in testing plastics and elastomers. Applying such systems several local effects associated with the contact methods may also be avoided. Moreover, the verification of numerical simulation of components exposed to mechanical loads requires proper test methods which provide both informations on global deformations as well as local deformations and strains along with their distribution. Furthermore, elastomer and thermoplastic test specimens and components may reveal temperature increase under complex loading conditions. While the high rate monotonic loading is associated with the adiabatic type heating, especially in the post yield deformation regime, due to the viscoelastic loss high frequency cyclic loading causes hysteretic type heating in the linear and non-linear viscoelastic deformation range. Hence, the main objective of this paper is to verify the applicability of non-contact full-field strain and temperature analysis methods to polymer testing.

In the first part of the paper the deformation and strain behavior of elastomer and thermoplastic test specimens over a wide loading rate range are investigated by an image correlation test system (Aramis, GOM, Braunschweig, D). The 2D or 3D image correlation photogrammetry is substantially more robust and has a greater dynamic range than other techniques such as laser speckle interferometry (ESPI) or the conventional Moire interferometry. Based on these features the image correlation method can effectively be used to determine deformations and strains both on a local or global scale and up to high deformations and up to high deformation rates.

The main applications of the non-contact, full-field strain analysis in the material testing are: (1) Simultaneous measurements of the longitudinal and transverse strains and to derive the general Poisson's ratio over a wide deformation range; (2) Determination of the true stress-strain relationship in the post-yield deformation regime (Fig. 1) and (3) Characterization of the local crack tip deformation behaviour in different test fracture specimen configurations (Fig. 2). Based on above methods more adequate material laws can be derived and used in numerical simulations.

Due to their low heat conductivity polymeric materials reveal a significant temperature increase at relatively low loading rates. This internal heating may assist micro-structural changes during the deformation process. A high speed thermography system was used (Orion MWIR from Cedic Infrared Systems (Croissy-Beaubourg, F) to measure the local and global temperature changes in the specimens (3). The camera has a focal plane array detector with 320x240 pixels which is sensitive in the wavelength range between 3 and 5  $\mu\text{m}$ . The results of the thermography measurements are illustrated in several examples;

1. The adiabatic heating was measured on tensile test specimens over a loading rate range from  $10^{-3}$  to 5 m/s for several engineering thermoplastics (PP, PC and PEEK).

2. The adiabatic heating was measured in the plastic zone of fracture specimens.
3. The hysteretic heating was measured during elastomer fatigue tests both in the vicinity of the crack tip and in the remaining specimen ligament.

Summarizing of above results, the non-contact full-field strain and temperature measurement and analysis provided novel, unique information's about the material behaviour and may successfully be used to determine more adequate material laws.

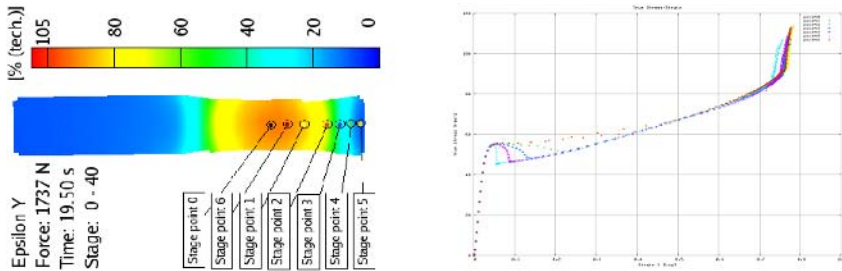


FIGURE 1. Strain distribution in an tensile specimen after the yield point and true-stress-strain curves derived in different cross-sections of the test specimen.

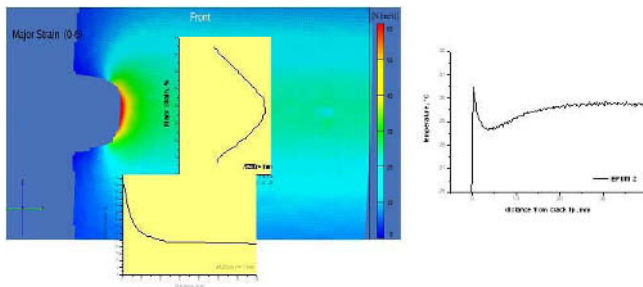


FIGURE 2. Strain and temperature distribution around the blunted crack-tip of an elastomer fatigue test specimen.

#### Acknowledgments

This project were performed at the Polymer Competence Center Leoben GmbH within the  $K_{plus}$ -programme of the Austrian Ministry of Traffic, Innovation and Technology. The funding within this programme by the Governments of Austria, Styria and Upper Austria is gratefully acknowledged

#### References:

1. Dowling, N.E., Mechanics of materials, Prentice Hall, 1999.
2. E. Parsons, M. C. Boyce and D. M. Parks, Polymer, vol. 45, Issue 8, April 2004, 2665-2684.
3. Steinberger et al., Damage characterization during fatigue testing by thermography, 2004

## ASSESSING LIFETIME OF POLYOLEFINS FOR WATER AND GAS DISTRIBUTION SYSTEMS

James Atteck<sup>1</sup>, John Dear<sup>1</sup>, Jean-Louis Costa<sup>2</sup>, Aurélien Carin<sup>2</sup> and Jean-Pierre Michel<sup>2</sup>

<sup>1</sup> Department of Mechanical Engineering, Imperial College London  
SW7 2AZ, United Kingdom

<sup>2</sup>Ineos Polyolefins, B-1120 Brussels, Belgium

james.atteck@imperial.ac.uk; j.dear@imperial.ac.uk; Jean-Louis.Costa@innovene.com;  
Aurelien.Carin@innovene.com; Jean-Pierre.Michel@innovene.com

Continuing improvement in the properties of polyolefins is contributing to the increased use of these materials. This is particularly so for pipes and other components of water and gas distribution networks. Important are reliable lifespan assessments of pipes and components of these networks that are subjected to demanding operational, environmental and disturbance stresses. There is the problem that after installation, under busy streets of towns, cities and other thoroughfares, subsequent access can be costly and disruptive to many transport and other services. Of much interest here is in research directed at improving the rugged durability and life of distribution pipes. This requires, for example, identifying ageing and other failure mechanisms in pipe materials and their causes. One important factor in assessing the lifetime to be expected of new polyethylene materials, for water and gas distribution networks, is their degree of propensity to initiation of brittle failure. New generations of resins are now being developed to have much improved resistance to the onset of brittle failure. Hence, required are appropriately discriminating laboratory assessments able to compare the properties of a wide range of new and existing materials, as to their resistance to brittle failure. This is to complement the use of the standard Full Notch Creep Test (FNCT) techniques that were developed by Fleissner [1] and investigated, for example, by Ting, Williams and Ivankovic [2].

The foremost aim of this research study is to develop evaluation techniques able to obtain and compare an increasing wide range of stress crack resistance data for the new and existing polyethylene materials.

The identified research objectives:

1. To devise a method to achieve well-controlled brittle failures in polyethylene pipe materials that have very high stress crack resistance. If possible, to provide evaluation conditions for brittle failure to occur within a 500-hour evaluation period. This is for repeat assessment of the method and its potential for subsequent use for quality control of material manufacture.
2. To provide a method for researching a wide range of new and existing materials as to their brittle failure characteristics. This is from the initial onset of brittle failure and its subsequent development.
3. To develop the method to include, for example, providing for researching the effects of varying the dimensions of internal and external layers of multi-layered structures and the different properties of the materials in these layers.

This study is related to researching the fracture surfaces of the different materials as they are formed from the first stage of crack initiation up to limiting conditions. Important is that the forces applied to the material to propagate the crack are well isolated from crack initiation forces. Also, it is important to identify the different propagation features generated by the crack in different materials. For this, AFM and SEM are two of the methods that be used for these studies. These

fracture surface data, as related to the micro-structural features of the material, are very informative to the interests of this research. An important research outcome, related to this study, would be improved information identifying causes of early pipe failure for different operational and environmental stress conditions in water and gas pipes.

Fig. 1 shows the FNCT loading geometry with an example of a fracture surface formed. In this case, the pre-notching introduced with a razor blade is equal depth on all four sides and the sample has failed in a brittle way at constant stress in hot water at 80°C. Different types of notch configuration are being researched as to their effect on the time to failure in polyethylene.

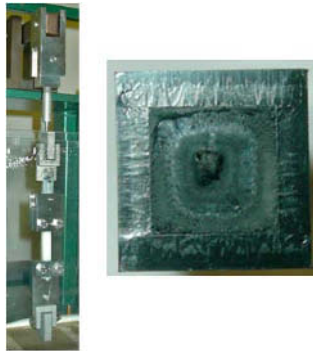


FIGURE 1. FNCT loading geometry and example of fracture surface for polyethylene.

## References

1. Fleissner, M. "Experience With a Full Notch Creep Test in Determining the Stress Crack Performance of Polyethylenes", *Polymer Engineering and Science*, vol. **42**, 330-340, 1998.
2. Ting, S.K.M., Williams, J.G. and Ivankovic, A. "Characterization of the Fracture Behaviour of Polyethylene using Measured Cohesive Curves. I: Effects of Constraint and Rate", *Polymer Engineering and Science*, vol. **46**, 763-777, 2006.

## EXPERIMENTAL CALIBRATION OF COMPUTATIONAL CONSTANTS FOR HOLE DRILLING METHOD

O.Weinberg<sup>a</sup>, J.Václavík<sup>a</sup>, J.Jankovec<sup>a</sup>, P.Jaroš<sup>b</sup> and S.Holý<sup>c</sup>

<sup>a</sup>ŠKODA VÝZKUM s.r.o., Dynamic testing laboratory, Tylova 57, 316 00 Pilsen, Czech Republic

<sup>b</sup>Techlab s.r.o., Sokolovská 207, 190 00 Praha 9, Czech Republic

<sup>c</sup>Technical University in Prague, Mechanical Faculty, Institute of Mechanics,  
Technická 4, 166 07 Praha 6, Czech Republic

otakar.weinberg@skoda.cz, techlab@czn.cz stanislav.holy@fs.cvut.cz

The hole drilling strain-gage method measures residual stresses near the surface of the material. The method involves attaching strain gage rosette to the surface, drilling a hole in the vicinity of the gages and measuring the relieved strains. The measured strains are then related to relieved principal stresses through a series of equations using dimensionless constants  $a$ ,  $b$ . This method is a basic of ASTM E837 [1] standard for residual stress measurement, which involves the constants  $a$ ,  $b$  obtained by FEA calculations. In presented work, the experimental set-up is described for calibration of these constants for uniform stress field; their verification on non-uniform linear stress field and given results of measurements is discussed. The constants are derived using proposed method for several strain gage rosettes and are compared with those, obtained using FEA model and those, given in ASTM standard. One example of using the hole drilling method for uniform and non-uniform stress field is given to show the limits of ASTM standard. As an alternative, the results evaluated from integral method [1] and one own developed method are presented and discussed, focused especially on separation of surface machining stresses.

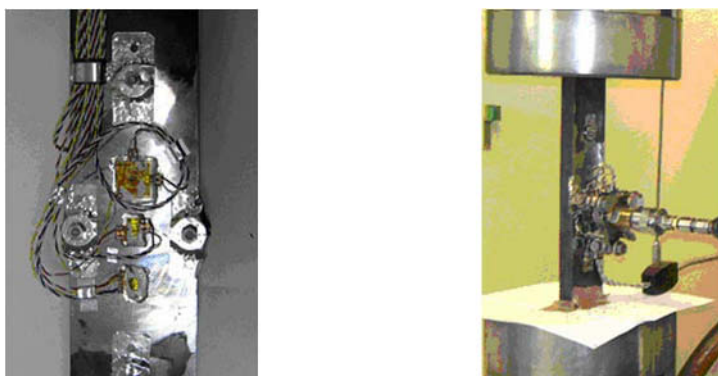


FIGURE 1. Photo of experimental set-up for uniaxial loading

The experimental calibration was performed by a uniaxial loading method. The specimen of cross section  $77 \times 24$  mm and length of 25 mm was stepwise loaded in the hydraulic testing machine. Removing of the particular layers was made using standard hole-drilling device without removing the specimen from the loading machine. Coefficient for several rosette types from HBM and MM Vishay were tested. Two rosettes of each type were drilled on one sample, one in the unloaded, the other in loaded state and the results were compared.

## FE analysis

FE model was created using COSMOS/M. A square plate with dimensions  $150 \times 150 \times 100$  mm with appropriate boundary conditions was considered. The number of elements in one layer was 7152 (type SOLID). Strain gauges were simulated using  $3 \times 9$  elements of type TRUSS3D.

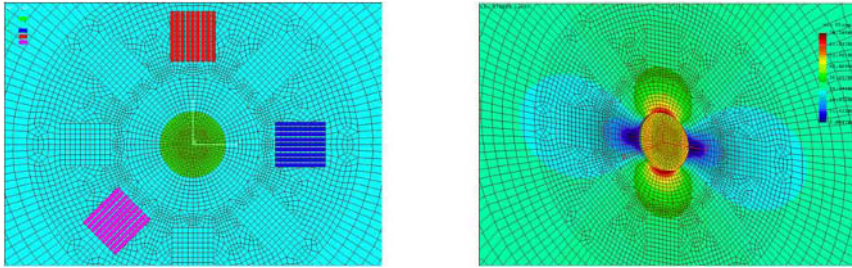


FIGURE 2. Example of FEA meshes and stress distribution after first layer removal

## Conclusion

The aim of the method was to state the calibration constants for special rosette, drilling device and kind of drilling. The both proposed procedures for uniaxial and bending tests should serve for prepared round-robin measurements.

**Acknowledgement:** The paper was created in the framework of the GA R 101/05/2523 and MPO FT-TA2-019 project; the authors thank both organizations for the support in the project solving.

## References

1. ASTM E 837-01 *Standard Test Method for Hole-Drilling Strain Gage Method*, American Society for Testing and Materials, 2002.

## METHODS FOR SITTING POSTURE EVALUATION: STATIC POSTURE AND APPLICATIONS

S. Scena and R. Steindler

Department of Mechanics and Aeronautics, University of Rome “La Sapienza”

Via Eudossiana 18, 00184 Roma, Italy

scenas@tin.it, roberto.steindler@uniroma1.it

Pressure sores (PS) are frequent in subjects with spinal cord injury and thus wheelchair-bound [Injury fact book of the Center for Disease Control and Prevention (CDC). National Center for Injury Prevention and Control, 2001-2002]. The dominant clinical approach for minimizing PS is that of getting the patients used to change their posture frequently [Merbitz, C. T., King, R. B., Bleiberg, J., Grip, J. C., 1985, Wheelchair push-ups: measuring pressure relief frequency, Arch Phys Med Rehabil, vol. 66, pp. 433-438.], for instance using their arms. Experimental data of the best time interval to perform these changes are not exhaustive, and useful informations can be obtained studying the spontaneous kinematic behavior of healthy subjects during long time sitting posture.

To this aim, in the Department of Mechanics and Aeronautics (DMA), Rome University “La Sapienza”, two different investigation methods were developed, using respectively a pressure map sensor [Z. Del Prete L. Monteleone, R. Steindler, A novel pressure array sensor based on contact resistance variation: metrological properties, 2001 Review of Scientific Instruments, vol. 72 no 2, pp.1548-1553], and a potentiometer-based device. The pressure map sensor, arranged on a chair (Fig. 1a), allows pelvis displacement acquisitions, in particular the partial or total rising of one or both buttocks; moreover, for each pelvis map acquired, it is possible to calculate the coordinates of the Centre of Pressure (COP) and then to determine their trends in the frontal plane and in the sagittal plane. The potentiometer-based device is formed by two angular potentiometer (Figs 1b and 1c), and it allows trunk rotation measurements at the basis of the spine in the sagittal and in the frontal planes.

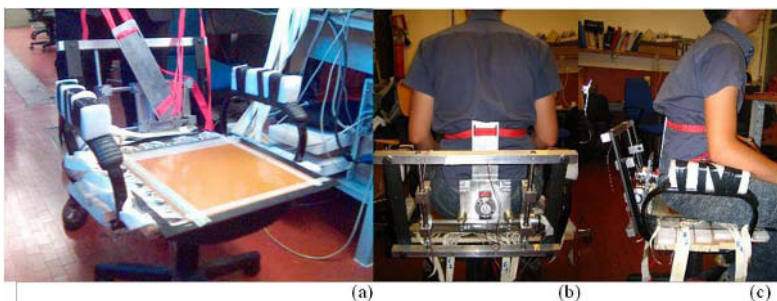


FIGURE 1. The chair with the p-map sensor and the potentiometer-based device

In this paper it is shown how the two device outputs have been correlated to obtain a complete survey of the sitting posture: 10 healthy volunteers, DMA students, were asked to sit on the chair; by means of a couple of belts, each student's trunk was joined to a rectangular plate connected to the mobile elements of the potentiometers. Each student performed an established protocol of



trunk displacements lasting 250 seconds (sampling frequency 8 Hz). For each performance the time trends of the COP were obtained, and then compared to the potentiometer data; from the comparison, a linear relationship between the COP displacements and the measured rotations was found:

$$COP_x = K_\theta \theta + COP_{x,mean} \quad (1)$$

$$COP_y = K_\varphi \varphi + COP_{y,mean} \quad (2)$$

$COP_x$  and  $COP_y$  are the COP coordinates,  $\theta$  is the medio-lateral trunk rotation and  $\varphi$  is the antero-posterior rotation. The values of  $K$  and  $K$  obtained are shown in table 1.

TABLE 1. Established protocol results.

K [cm/rad]	K [cm/rad]	$K^{-1}$ [deg/cm]	$K^{-1}$ [deg/cm]
36.5±8.5	6.4±1.5	1.8±0.4	10.0±2.7

The equation (1) is valid only for medio-lateral for rotations between  $\pm 10^\circ$  from vertical position, while these rotations can reach greater values. The equation (2) is valid for any anterior-posterior rotation.

Then long time sitting posture tests performed using the same devices: 10 new healthy volunteers, again DMA students, were asked to sit on the chair for 60 minutes; the greatest values of the COP displacements in the frontal plane were  $5.2 \pm 2.4$  cm (trunk rotations about  $10^\circ$ ), while the greatest values of the COP displacements in the sagittal plane were  $3.0 \pm 1.4$  cm (trunk rotations about  $30^\circ$ ). There was a postural change every  $7.7 \pm 6.7$  minutes in the frontal plane and every  $5.7 \pm 2.7$  minutes in the sagittal plane.

Experimental data showed good agreement with the literature data, in particular with the Tel Aviv University data [Linder-Ganz, E., Scheinowitz, M., Yizhar, Z., Margulies, S.S., Gefen, A. Frequency and Extent of Spontaneous Motion to Relief Tissue Loads in Normal Individuals Seated in a Wheelchair, 2005 Summer Bioengineering Conference of the ASME Bioengineering Division, Vail, Colorado, USA, June 22-June 26, 2005.].

## References

1. Injury fact book of the Center for Disease Control and Prevention (CDC). National Center for Injury Prevention and Control, 2001-2002
2. Merbitz, C. T., King, R. B., Bleiberg, J., Grip, J. C., 1985, *Wheelchair push-ups: measuring pressure relief frequency*, Arch Phys Med Rehabil, vol. **66**, pp. 433-438.
3. Z. Del Prete L. Monteleone, R. Steindler, *A novel pressure array sensor based on contact resistance variation: metrological properties*, 2001 Review of Scientific Instruments, vol. **72** no 2, pp.1548-1553
4. Linder-Ganz, E., Scheinowitz, M., Yizhar, Z., Margulies, S.S., Gefen, A. *Frequency and Extent of Spontaneous Motion to Relief Tissue Loads in Normal Individuals Seated in a Wheelchair*, 2005 Summer Bioengineering Conference of the ASME Bioengineering Division, Vail, Colorado, USA, June 22-June 26, 2005.

## CORRECT PREDICTION OF THE VIBRATION BEHAVIOR OF THE HIGH POWER ULTRASONIC TRANSDUCERS BY FEM SIMULATION

Abbas Pak and Amir Abdullah  
Ph.D Student of Manufacturing Engineering.

<sup>1</sup> Manufacturing Group, School of Engineering, Tarbiat Modarres University, Tehran, Iran,

<sup>2</sup> Associate Professor of Mechanical Engineering in Advanced Manufacturing Technologies.  
a\_pak@modares.ac.ir amirah@aut.ac.ir

High power ultrasound is nowadays used in a wide variety of applications ranging from medical devices, ultrasonic cleaning, ultrasonic welding and machining to sonochemistry [1]. Since Prof. Langevin developed the first sandwich ultrasonic transducer by embedding piezoelectric rings between two metals and employed it for high intensity vibration, there have been great efforts in modeling and formulating such transducers [2-5]. Of all proposed methods, Mason's has been found the best in design and analysis of PZT transducers. He has offered the Equivalent Circuit Method (ECM) [1&2]. Finite Element Method (FEM) is the most reliable one for analyzing the ultrasonic transducers [6-14]. By using the analytical method the dimensions of high power ultrasonic transducer components were estimated by assuming a certain resonant frequency and a certain power. Then, the finite element analysis provided by commercial ANSYS was employed for 2D, ¼ 3D and full 3D FEM analysis to observe the vibration behavior of the transducer and to find the validity of the analytical method. The FEM analysis was performed under two separate statuses of electrical conditions. In the first case which is commonly called the "resonance" condition, a constant voltage of zero was applied at all electrical contacts of ceramic disks. This is a condition of "short-circuit" where all voltage potentials are connected to common ground. In the second case, called "anti-resonance", only one of the negative poles or the positive poles of the piezo-ceramic disks were connected to zero voltage of common ground and the other poles were left free without any connection. This represents an "open-circuit" condition.

This paper presents a study of three types of finite element analyses of high power ultrasonic transducers by using the finite element commercial software called ANSYS. The transducer geometry is treated as a 2D axisymmetric model, 3D quart and full 3D model. For all of the simulations the modeled transducer is used in modal analysis and harmonic solutions to understand its mechanical behavior and its natural frequency. In the meantime, a comparison is made between each type of modeling. Finally, the simulation and experimental results are compared. The comparison of simulations results with experimental data allows the parameters of FEM models to be iteratively adjusted and optimized and it can be choosing best modeling type.

The analyzed transducer was composed of six PZT-5A piezo-ceramic rings, a steel cylinder-shaped back mass (St 304) and Aluminum (Al 7075-T6) stepped front mass (See figures 1 & 2). The bolt material was from steel. By knowing the thickness of the specimens, the following sound velocities were obtained by a simple calculation. The material properties of the components are shown in tables 1 and 2.

The dimensions of the transducer components were calculated such that the resonance frequency of the transducer to be 22 KHz.

The transducer was modeled by employing 2D, ¼ 3D and full 3D models to simulate its mechanical behavior by FEM modal analysis and to determine its natural frequency by harmonic analysis. As a conclusion, at the end, a comparison was made between each type of modeling.

Table 1-Material properties of Aluminum matching [15]

Standard Code	AL 7075-T6
Sound Velocity (m/s)	6210
Tut (MPa)	572
Modulus of elasticity ( $\frac{N}{m^2}$ )	$7.7 \times 10^{10}$
Density ( $\frac{Kg}{m^3}$ )	2823

Table 2- Material properties of Steel backing [15]

Standard Code	St 304
Sound Velocity (m/s)	5720
Tut (MPa)	505
Modulus of elasticity ( $\frac{N}{m^2}$ )	$20.7 \times 10^{10}$
Density ( $\frac{Kg}{m^3}$ )	7868

For the transducer design discussed in this report, PZT-5A was chosen as piezoelectric material. PZT-5A was an appropriate choice for this application because it can generate high power similar to PZT-4, but with much lower dielectric losses and greater resistance to depolarization [16].

## References

1. R. Frederick, "Ultrasonic Engineering," John Wiley & Sons, Inc., New York, 1965.
2. P. Langevin, French Patent No. 502913 (29.51920); 505703 (5.8.1920); 575435 (30.7.1924).
3. W.P. Mason, "Electromechanical Transducers and Wave Filters", D. Van Nostrand, New York, 1942.
4. R. Krimholtz, D.A. Leedom, G.L. Mattaei, "New equivalent circuits for elementary piezoelectric transducer" Electron. Lett., vol. 6 (1970), 398-399.
5. M. Redwood, "Experiments with the electrical analog of a piezoelectric transducer", J. Acoust. Soc. Am. vol. 36 (10) (1964), 1872-1880.
6. Kagawa, Y., Yamabuchi, T., "Finite Element Simulation of a Composite Piezoelectric Ultrasonic Transducer" IEEE Transactions on Sonics and Ultrasonics, vol. 26, Issue 2, Mar 1979, 81 - 87.
7. Jan Kocbach, "Finite Element Modeling of Ultrasonic Piezoelectric Transducers- Influence of geometry and material parameters on vibration, response functions and radiated field" Doctoral dissertation, University of Bergen, Department of Physics, September, 2000.
8. Jian S. Wang and Dale F. Ostergaard, "A Finite Element-Electric Circuit Coupled Simulation Method for Piezoelectric Transducer" IEEE Ultrasonics Symposium, Proceedings, vol. 2, 17-20 Oct. 1999, 1105 - 1108
9. Patrick M. Cunningham, "Use of the Finite Element Method in Ultrasonic Applications" Ultrasonic Industry Association Symposium, June 2000.
10. Mercedes C. Reaves and Lucas G. Horta."Test case for modeling and validation of structures with piezoelectric actuators" NASA Langley research center Hampton, Virginia, 2001.
11. Iula, A., Cerro, D., Pappalardo, M. and Lamberti, N., "3D finite element analysis of the Langevin transducer" IEEE Symposium on Ultrasonics, vol. 2, 5-8 Oct. 2003, 1663 - 1667.
12. Antonio Iula, Fernando Vazquez, Massimo Pappalardo and Juan A. Gallego, "Finite element three-dimensional analysis of the vibrational behaviour of the Langevin-type transducer" Ultrasonics, vol. 40, Issues 1-8, May 2002, 513-517.
13. David, H. Johnson, "Simulation of an ultrasonic piezoelectric transducer" Penn State-Erie and Dharmendra Pal, Cybersonics, Inc. USA, 2003.
14. Moreno, E., Acevedo, P., Fuentes, M., Sotomayor, A., Borroto, L. Villafuerte, M.E. and Leija, L., "Design and construction of a bolt-clamped Langevin transducer" 2nd International Conference on Electrical and Electronics Engineering, 7-9 Sept. 2005 Page(s):393 - 395.
15. <http://www.matweb.com>
16. "Piezoelectric Technology Data for Designers," Morgan Matroc Inc., Electro Ceramics Division.

## THE INFLUENCE OF THE INSERTION TORQUE ON THE PULL-OUT FORCE OF PEDICLE SCREWS

P. Chatzistergos<sup>1</sup>, E. Magnissalis<sup>2</sup> and S.K. Kourkoulis<sup>1</sup>

<sup>1</sup> Department of Mechanics, National Technical University of Athens, Zografou Campus, Athens, Greece.

<sup>2</sup> First Orthopaedic Department of University of Athens, Greece.  
stakkour@central.ntua.gr

The fixation and stabilization of certain segments of the human spine is strongly indicated for the treatment of numerous pathological situations of the spine, such as spondylolytic and degenerative spondylolisthesis, trauma and tumor. One of the most commonly used spinal instrumentation tools for this purpose is the pedicle screw. In spite of the constant improvement of both the spinal instrumentation systems and the surgical techniques, there is still no foolproof method for the fixation and stabilization of the spine. One of the most serious problems encountered, particularly in osteoporotic patients, is the loss of the surgical construction stability as a result of screw loosening which leads, gradually or abruptly, to the pull-out of the screws from the vertebra.

One of the parameters that are used for the quantification of the capability of a pedicle screw to maintain the stability of the surgical construction is the pull-out strength, namely the value of the parallel to the longitudinal axis of the screw force that is required to pull the screw out of the bone, without macroscopic failure or fracture of neither the screw nor the bone. Although this is a rather simple load case it helps enlightening some controversial points concerning the mechanical behavior of the vertebral bone - pedicle screw system, and in addition it permits the parametrical study of the influence of various factors on the final value of the pull-out force. It is reported in modern literature that the pull-out force of a pedicle screw is influenced by the geometry of the screw, the mechanical properties of the vertebral bone, the technique of insertion and the insertion torque. Controversial reports can be found in the modern literature for the influence of the insertion torque on the pull-out strength of the pedicle screw- vertebral bone system. Daftari et al. [1] studied pedicle screws inserted into synthetic bone and calf vertebra. The authors report that high insertion torque correlates with a higher screw pull-out force. To the same conclusion came, also, Zdeblick et al. [2] after testing pedicle screws implanted into cadaveric vertebrae and subjected to a complex pull-out load (combination of axial pull-out and cephalocaudal toggling). On the other hand Kwok et al. [3] indicate that the pull-out force cannot be predicted reliably from the insertion torque, although there are strong correlations for certain screw types. Finally the study of Inceoglu et al. [4] concluded that there is no significant correlation between pull-out force and insertion torque, at least for the screws tested.

In this context the present study is focused on the detailed parametric study of the influence of the insertion torque on the pull-out force of pedicle screws and is carried out both experimentally and numerically. For the experimental approach pedicle screws of different designs but of the same, more or less, length were placed into blocks of synthetic bone and subjected to pure pull-out loads until failure, using a stiff servohydraulic loading frame and a home-made system of grips permitting the alignment of the axis of the screw with the loading direction (Fig. 1). During the insertion of every screw the insertion torque was measured. For every screw design several tests were conducted for different values of the insertion torque and the pull-out force was measured.

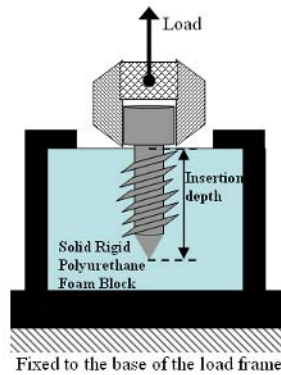


FIGURE 1. Schematic of the test apparatus that was used.

The experimental data obtained were used for the calibration of a Finite Element model of the pedicle screw - synthetic bone system (Fig. 2). The numerical analysis was focused mainly to the investigation of the significance of the “pretension” between the constituent parts of the system and on the development of an accurate and reliable way to simulate it numerically.

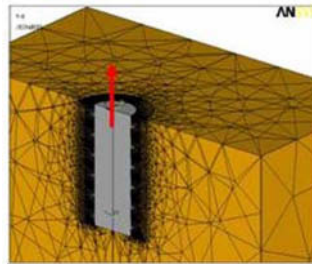


FIGURE 2. The FE model of the system pedicle screw-synthetic bone.

Although additional tests are required before final conclusions are drawn the analysis of the results indicated that the existence or not of a direct relationship between the insertion torque and the pull-out force depends among others on the type of the screw, i.e. conical or cylindrical. In addition, it was observed that the overall design of the screw, namely the shape and the inclination of its threads as well as its pitch cannot be ignored. It is emphasized however, that definite conclusions cannot be drawn before calibration tests are carried out with cadaveric vertebrae instead of synthetic ones since the artificial homogeneity of the latter ones may be misleading.

## References

1. Daftari, T. K., Horton, W. C. and Hutton, W. C., *J Spinal Disord*, vol. **7**, 139-145, 1994.
2. Zdeblick, T. A., Kunz, D. N., Cooke, M. E. and McCabe, R., *Spine*, vol. **18**, 1673-1976, 1993.
3. Kwok, A. W. L., Finkelstein, J. A., Woodside, T., Hearn, T. C. and Hu, R. W., *Spine*, vol. **21**, 2429-2434, 1996
4. Inceoglu, S., Ferrara, L. and McLain, R. F., *The Spine Journal*, vol. **4**, 513-518, 2004.

## **C. SPECIAL SYMPOSIA/SESSIONS**

## SPECIFIC FRACTURE ENERGY DETERMINATION OF DAM CONCRETE BY LARGE-SCALE SIZE EFFECT TESTS

Amirreze Ghaemmaghami and Mohsen Ghaemian

Department of Civil Engineering Sharif University of Technology, Tehran, Iran

ghaemmaghami@mehr.sharif.edu, ghaemmaghami@mehr.sharif.edu

The specific fracture energy of dam concrete is a basic material characteristic needed for the prediction of concrete dam behavior. Data on fracture properties of dam concrete are quite limited to date. A series of tests was carried out based on the size effect law [1] due to a number of geometrically similar notched specimens of various sizes. Experimental tests include three-point bending tests. The specimens were of square cross section with a span to depth ratio of 2/5. Three different specimens, according to RIELM recommendations [2], with depth of 200, 400 and 800mm were considered for the purpose of testing.

Concrete mixtures are provided from the Caroon 3 dam project site using river gravel or commonly crushed stones from quarries. To compare the fracture properties of dam concrete with normal concrete five types of concrete mixes of 65, 50, 40, 30 and 20mm maximum aggregate size were considered. Mix and strength properties are shown in table (1).

TABLE 1. Mix and strength properties

Concrete Mix	M.S.A. (mm)	$f'_c$ (MPa)	$f'_t$ (MPa)	$E_c$ (MPa)
1	65	31.9	2.7	26726
2	50	33.7	3.7	27470
3	40	38.1	4.2	29208
4	30	40.5	4.4	30114
5	20	42.7	4.7	30912

For all mixes, value of relative notch depth of 0.2 is used. Experimental results show that aggregate size has an important effect on specific fracture energy values of dam concrete. According to specific fracture energy definition based on size effect, the specific fracture energy of concrete mixes of 65, 50, 40, 30 and 20mm M.S.A. are 178, 129, 88, 79 and 72 N/m, respectively. To compare the results, the deviations of the specific fracture energy and effective length values obtained in this study from previous prediction formulae [3] are shown in Fig. 1.

This indicates that the high specific fracture energy of dam concrete is the result of the nature, size and properties of its aggregate. The difference between specific fracture energy of normal and dam concrete should be noticed in nonlinear analysis of concrete dams.

The high deviations of the results of this study from previously developed prediction formulae suggests that different formulae may need to be developed for predicting the fracture properties of dam concrete. Because of the high sensitivity of concrete dams to fracture and size effect, a test program should be conducted to estimate the acceptable values of specific fracture energy used in nonlinear numerical analyses in each case study.

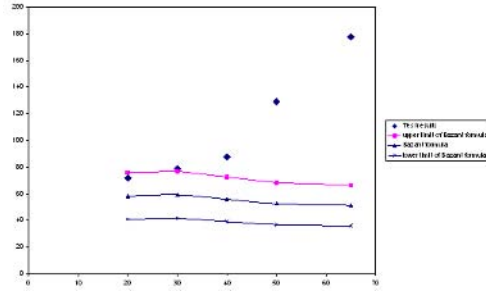


FIGURE 1. Deviations of test results from previous prediction formula for specific fracture energy

## References

1. Bazant, Z.P.(2000), "Size Effects," *Solid and Structures*, vol. **37**, 165-205
2. RIELM committee TC 89-FMT. "Size Effect Method for Determining Fracture Energy and Process Zone Size of Concrete", (RIELM Recommendations). *Material and Structures*. vol. **23**, 461-465
3. Bazant, Z.P., Becq-Giraudon, E.(2002), "Statistical Prediction of Fracture Parameters of Concrete and Implications for Choice of Testing Standard,," *Cement and Concrete Research*, vol. **32**, 529-556



## AUTOGENOUS AND ISOTHERMAL RESTRAINED SHRINKAGE OF HYDRATING CEMENT PASTES - EXPERIMENTAL STUDY

Arnaud Pertue, Pierre Mounanga, Abdelhafid Khelidj and Denis Fournol  
GeM UMR CNRS 6183 - Research Institute on Civil Engineering and Mechanics  
IUT de Saint-Nazaire, 58, rue Michel Ange, BP 420, F-44606 Saint-Nazaire, France  
Arnaud.pertue@univ-nantes.fr, Pierre.mounanga@univ-nantes.fr,  
Abdelhafid.khelidj@univ-nantes.fr, Denis.fournol@univ-nantes.fr

Numerous studies have been carried out to characterize the autogenous shrinkage of cement-based materials in free conditions at early and very early age. But the results obtained are not sufficient to understand the autogenous volume variations of concrete in realistic structural conditions. Indeed, the analysis of such deformations requires investigating the cementitious system's behaviour in restrained conditions, when the internal stresses generated can lead to the premature cracking of the material.

This study focuses on the influence of the curing temperature on the early age cracking of cement-based materials in restrained and autogenous conditions. The test method used is the "ring test", largely described in the literature (Grysbowski and Shah [1], Weiss [2] for example). This method was firstly developed to study the cracking of mortars and concretes due to drying. In the present research work, water evaporation is prevented during the whole test duration and each ring test apparatus is equipped with a peripheral water circulation system, which enables to control the temperature of the specimen investigated (Fig. 1).



FIGURE 1. General view of the experimental device

The peripheral water circulation is ensured by a network of copper tubes connected to a thermostated bath, which makes it possible to maintain the sample in quasi-isothermal conditions.

The test procedure begins with the casting of the freshly mixed cement-based material around a central metal ring. The deformations of the metal ring due to the cement paste's shrinkage are then measured by strain gauges stuck on the internal annulus surface and are automatically

recorded by the data logging system. The test stops at the appearance of the first transversal crack, caused by the internal stresses generated by the autogenous shrinkage.

The experimental program of the study consists in applying three different curing temperatures (10; 20 and 40°C) to cement pastes prepared with three types of cement (CEM I, CEM II and CEM III) and two water-to-cement ratios (W/C=0.3 and 0.4). Moreover, in order to study the effect of the ring restriction degree, three different metals (steel, brass and stainless steel) are used for the central ring. Then two comparisons are carried out: the evolution of the deformations at various temperatures as a function of time and as function of hydration degree. This latter is obtained using the NIST's program, CEMHYD3D [3].

Numerical simulations are also carried out in order to compare the measured cracking age with the one computed through the model developed by Turcry et al. [4]. These calculations are based on the material characteristics (hydration degree and autogenous shrinkage evolutions) and the ring geometry.

The results obtained show that the curing temperature directly influences the age of the first crack. This phenomenon is linked to the thermoactivation of the hydration process, which causes, according to the temperature applied, an acceleration or a deceleration of the deformations and, consecutively, of the internal stresses. A discussion, taking account of the calculation of the apparent activation energy is undertaken in order to quantify more finely the effect of temperature on the prevented deformation of cement-based materials.

## References

1. Grzybowski, M. and Shah, P., *ACI Material Journal*, vol. **87**, 138-148, 1990.
2. Weiss, W.J., PhD Thesis, Evanston, Illinois, 1999.
3. Bentz, D.P., *CEMHYD3D: A Three-Dimensional Cement Hydration and Microstructure Development Modelling Package Version 2.0.*, 2000.
4. Turcry, P., Loukili, A., Haidar, K., Pijaudier-Cabot, G., Berlarbi, A., *J. Mat. in Civ. Engrg.*, vol. **18** (1), 46-54, 2006.

## EXPLORING THE MECHANICAL DESIGN OF WOOD AT THE MICRO- AND NANOSCALE

I. Burgert

Max Planck Institute of Colloids and Interfaces, Department of Biomaterials  
Research Campus Golm, 14424 Potsdam, Germany  
ingo.burgert@mpikg.mpg.de

Wood is known for its excellent mechanical properties with respect to the low density. Its mechanical behaviour can be described by means of an orthotropic elasto-plastic material model [1]. The wood structure expresses a compromise between strengthening and stiffening on one hand and the demands of water transport inside the stem of the tree on the other hand [2,3].

A key feature of wood is its organization into several hierarchical levels. According to Speck *et al.* [4] five levels of hierarchy can be distinguished in wood. The integral level of the entire trunk, the macroscopic level of tissue structures, the microscopic level of cell structure, the ultrastructural level of cell wall organisation and the biochemical level of cell wall polymer assembly. The strong interdependencies between the various levels are of crucial relevance. Slight changes of parameters at one level propagate inevitably into the other levels, influencing the mechanical and structural properties. Hence, macroscopic properties of wood mainly originate from its cell wall organization [5] making particularly the nano- and microscale important for mechanical studies. At these levels of hierarchy, wood shows a wide variety of variable parameters such as cell shape, thickness and arrangement of cell wall layers, the orientation of cellulose microfibrils within cell walls, and in the chemical composition of individual cell wall layers. These aspects are tremendously important according to the objectives and challenges of basic and applied research on wood.

In terms of utilization of wood as a building material, researchers as well as engineers deal mainly with the macroscopic behaviour of the material. Efforts in this field intend to make macroscopic properties of wood better predictable. However, all kinds of changes of growth conditions find their expression in the cambial activity of trees and the differentiation of cells. The high spatial resolution in micro-mechanical investigations can help to elucidate the influence of various regulating factors on the macroscopic properties of wood. Thus a better understanding of wood demands micro-mechanical investigations at its tissue and fibre level.

In this respect, the perception of micro-mechanical studies on wood changed in the last decades. While in the past micro-mechanical examinations were mostly seen as being far from the utilization aspects of wood, nowadays it is widely accepted that micro-mechanics are required to better understand its macroscopic behaviour. However, it will demand greater efforts in developing highly sophisticated micro-mechanical testing setups to gain better insight into the mechanical relevance of cell wall polymers and their interaction. By achieving this objective, the field of micromechanics may become an indispensable mediator between polymer sciences and applied wood research.

The micromechanical testing approaches discussed in this paper aim to provide a high spatial resolution of the structure without disrupting the integrity of plant tissues, cells, or the polymer composite of the cell walls. A powerful strategy to gain access to the mechanical design of wood at the cell and cell wall level are *in situ* methods which simultaneously combine monitoring of mechanical loading and structural deformation. By watching materials deform, we can more precisely and directly detect structure–property relationships at the nano- and microstructural levels. Several approaches for simultaneous examinations have been used in the last decade. In

micromechanical tests combined with scanning electron microscopy, deformation and fracture events at the microscale have been observed during sample straining [6]. In a wet (environmental) mode, specimens can be both tested under moist conditions and examined without conductive coating. This combination is of particular advantage in microfracture studies of wood when new surfaces are created in the deformation process [7,8]. The organization and mechanical interaction of cell wall polymers can be studied by combining micromechanical tests with nanostructural characterization. The interaction between cellulose and hemicelluloses has been successfully measured by dynamic Fourier transform infrared (FT-IR) spectroscopy [9]. In this paper the nano-deformation of cellulose upon mechanical loading is studied by means of X-ray diffraction [10] and Raman microscopy [11]. Results indicate general principles of deformation mechanisms at the cell wall level which result in two important mechanical properties, high stiffness and high toughness [12], making wood particularly well-suited for utilization as a building material.

## References

1. Mackenzie-Helnwein, P., Eberhardsteiner, J. and Mang, H.A., *Holzforschung*, vol. **59**, 311-321, 2005
2. Niklas, K. J., *Plant biomechanics*, Chicago Univ. Press, Chicago, USA, 1992.
3. Booker, R. E. and Sell, J., *Holz als Roh- und Werkstoff*, vol. **56**, 1-8, 1998.
4. Speck, T., Rowe, N. and Spatz, H.-C., *Technische Biologie und Bionik 3 -BIONA-report*, vol. **10**, 101-131, 1996
5. Salmén, L., In *Proceedings of the Third Plant Biomechanics Conference*, edited by H.-C. Spatz and T. Speck, George Thieme Verlag, Stuttgart, 2000, 452-462.
6. Bodner J., Gröll, G. and Schlag, M., *Holzforschung*, vol. **51**, 487-490, 1997.
7. Frühmann, K., Burgert, I., Tschegg, E. K. and Stanzl-Tschegg, S. E., *Holzforschung*, vol. **57**, 326-332, 2003.
8. Mott, L., Shaler, S., Groom, L. and Liang, B.-H., *Tappi*, vol. **78**, 143-148, 1995.
9. Akerholm, M. and Salmén, L., *Polymer*, vol. **42**, 963-969, 2001
10. Keckes, J., Burgert, I., Frühmann, K., Müller, M., Kölln, K., Hamilton, M., Burghammer, M., Roth, S.V., Stanzl-Tschegg, S.E. and Fratzl, P., *Nature Materials*, vol. **2**, 810-814, 2003.
11. Gierlinger, N., Schwanninger, M., Reinecke, A. and Burgert, I., *Biomacromolecules*, vol. **7**, 2077-2081, 2006.
12. Fratzl, P., Burgert, I. and Gupta, H.S., *Phys. Chem. Chem. Phys.*, vol. **6**, 5575-5579, 2004.

## WOOD ADHESIVE BONDLINES BY NANOINDENTATION

Johannes Konnerth<sup>1</sup>, Andreas Jäger<sup>2</sup>, Josef Eberhardsteiner<sup>2</sup>, Ulrich Müller<sup>1,3</sup>  
and Wolfgang Gindl<sup>1</sup>

<sup>1</sup>Institute of Wood Science and Technology, Department of Material Sciences and Process Engineering, BOKU-University of Natural Resources and Applied Life Sciences, Vienna, Austria

<sup>2</sup>Institute for Mechanics of Materials and Structures - Vienna University of Technology, Vienna, Austria

<sup>3</sup>Wood Kplus - Competence Center for Wood Composites and Wood Chemistry, Linz, Austria  
johannes.konnerth@boku.ac.at

The mechanical properties of both the adhesive and interphase cell walls in wood adhesive bonds were determined by nanoindentation. Seven different polymers used frequently as adhesives and/or matrix polymers in wood, wood composites, and natural fibre reinforced composites were studied by nanoindentation (Konnerth et. al [1]) and compared with results from previous uniaxial tensile tests (Konnerth et. al [2]). It was shown that the elastic modulus, the hardness, the creep factor, and the elastic-, plastic-, and viscoelastic work of indentation of the seven different polymers is essentially the same regardless whether the polymers were tested in the form of pure films or in-situ, i.e. in an adhesive bond line with spruce wood. An excellent correlation was found between the elastic modulus measured by tensile tests and the elastic modulus measured by nanoindentation. In spite of the good correlation, the elastic modulus measured by nanoindentation is significantly higher than the elastic modulus measured by tensile tests.

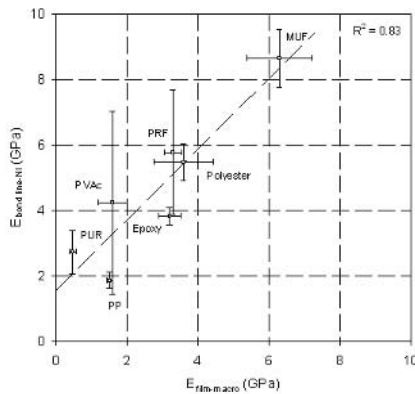


FIGURE 1. Comparison of the reduced elastic modulus from nanoindentation of pure polymer films and polymers in adhesive bond lines (error bars correspond to standard deviation).

Furthermore the elastic properties of wood cell walls in the interphase region of four different adhesive bonds were determined (Konnerth and Gindl [3]). In comparison with reference cell walls unaffected by adhesive, interphase cell walls from melamine-urea-formaldehyde (MUF) and phenol-resorcinol-formaldehyde (PRF) adhesive bonds showed improved hardness and reduced creep, and in the case of MUF also an improved elastic modulus. By contrast, cell walls from the

interphase region in polyvinylacetate (PVAc) and one-component polyurethane (PUR) bonds showed more creep, but lower elastic modulus and hardness than the reference. Considering the different cell-wall penetration behaviour of the adhesive polymers studied here, it is concluded that damage and loss of elastic modulus to surface cells occurring during the machining of wood is recovered in MUF and PRF bond lines, whereas damage of cell walls persists in PVAc and PUR bond lines.

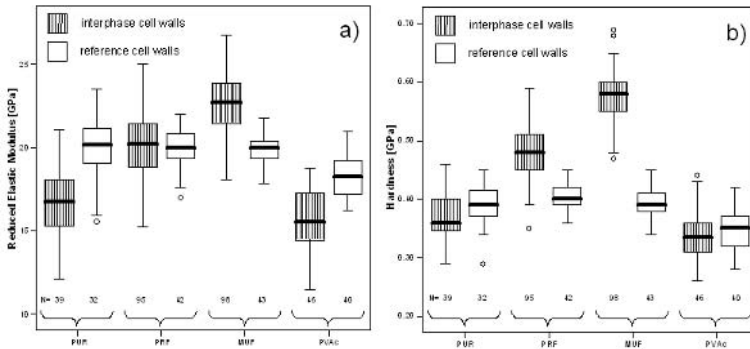


FIGURE 2. – Reduced elastic modulus a) and Hardness b) from nanoindentation of interphase cell walls with adhesive contact compared to reference cell walls distant from the bond line (PUR = one-component polyurethane, PRF = phenol-resorcinol-formaldehyde, MUF = melamine-urea-formaldehyde, PVAc = polyvinylacetate, N = number of indents).

## References

1. Konnerth, J., Jäger, A., Eberhardsteiner, J., Müller, U., Gindl, W., *Journal of Applied Polymer Science*, Elastic properties of adhesive polymers, II. Polymer films and bond lines by means of Nanoindentation vol. **102** (2), 1234-1239, 2006
2. Konnerth, J., Gindl, W., Müller, U. *Journal of Applied Polymer Science*, Elastic properties of adhesive polymers, Part I: polymer films by means of electronic speckle pattern interferometry, in print, 2006
3. Konnerth, J., and Gindl, W., *Holzforschung*, Mechanical characterisation of wood-adhesive interphase cell walls by nanoindentation, vol. **60**, 429-433, 2006

### 3D SHAPE MEASUREMENT AT DIFFERENT LENGTH SCALES USING SPECKLE AND GAP EFFECT

Fu-Pen Chiang and Gunes Uzer  
Dept. of Mechanical Engineering  
Stony Brook University  
Stony Brook, NY 11794-2300, USA  
Fu-Pen.Chiang@sunysb.edu

There is a need to measure height of an object at the micro/nanoscales. The electron speckle method [1] can measure in-plane distance and strain of an object but it cannot be applied to measuring height. In this paper. We propose a method of height measurement using speckle and the gap effect [2-4] to measure height, thus the 3D shape of an object. This technique can be applied to objects of various sizes ranging from meters to microns depending on whether the recording system used is an ordinary macro camera, a optical microscope or a scanning electron microscope. The gap effect is the result of optical perspective. That is: an object appears to be larger when it is closer to the recording camera. This effect gives rise to fictitious strain  $\varepsilon$ . The gap equation [2]  $\varepsilon = \Delta Z / Z$  where  $Z$  is the original distance from the object to camera lens predicts such a phenomenon as shown in Fig. 1. Thus by obtaining the fictitious strain using the speckle photography technique and knowing  $Z$ , the 3D shape, i.e. the variations of  $Z$  can be calculated.

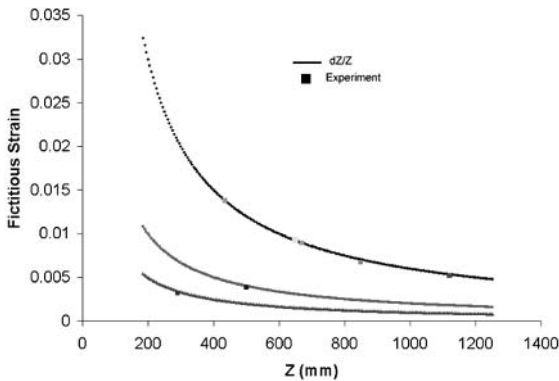


FIGURE 1. Comparison of experimental results and theoretical prediction of the gap effect

**References**

1. Chiang, F.P., *International conference on full-field measurement techniques and their applications in experimental solid mechanics*, Clermont-Ferrand, France, July 10-12 2006
2. Cesar A. Sciammarella, Chiang FP., *ZAMP*, vol. **19**, 326, 1968
3. Chiang FP, A. Asundi, *Applied Optics*, vol. **21** (13), 2167-2169, 1982
4. Chiang FP, A. Asundi, *Applied Optics*, vol. **21**, 1887-1888, 1982



## INDENTATION HARDNESS AND YIELD STRESS CORRELATIONS IN POLYMERS

Thomas Koch and Sabine Seidler

Vienna University of Technology, Institute of Materials Science and Technology

Favoritenstraße 9-11, A-1040 Vienna, Austria

tkoch@mail.zserv.tuwien.ac.at, sseidler@mail.zserv.tuwien.ac.at

Control and prediction of the mechanical behaviour of polymers on the basis of structure-property correlations play an important role in polymer science and engineering. Within this context, microhardness is a powerful tool with high sensitivity to structural changes. On the other hand, information on the relationship between microhardness and other mechanical parameters such as yield stress, E modulus and toughness is of great practical importance both from the point of view of testing and for understanding macroscopic materials behaviour.

Experimentally discovered empirical relationships enable efficient quality assurance for materials and components. However, it must be noted that these empirical correlations are only valid within particular classes of materials. An estimation of macroscopic yield stress is known by the hardness testing of nearly full plastically deformable metallic materials using the Tabor equation [1]. Based on the fundamental ideas by Tabor [1], there exist a few works in which hardness values vs. yield stresses of polymers are plotted [2, 3]. The relationships are linear but the slopes are different due to different testing conditions and methods of evaluation. Additionally, the loading direction has to be considered. In [4] it was reported for polyethylene materials that there is a ratio of hardness to yield stress of about 3 for tensile and of about 2 for compression loading. This difference can be ascribed to a hydrostatic component during compression.

In the presented work tensile ( $\sigma_y$ ) and compression yield stresses ( $\sigma_{cy}$ ) of different thermoplastic polymers, which cover a wide range of stiffness, strength and micromechanical behaviour, were compared with their indentation hardness ( $H_{IT}$ ) and Martens hardness (HM) values. Under tensile loading conditions the results can be divided in two groups, depending on the micromechanical behaviour. An approximately linear correlation between hardness and yield stress can be proved in polymers that are showing shear dominated deformation behaviour. The correlation becomes non-linear in polymers showing clear crazing or voiding (Fig. 1).

Under compression loading the deformation behaviour of all investigated polymers is dominated by shear processes. Therefore the ratios of hardness values to compression yield stresses do not scatter so strong as in the case of tensile loading (Fig. 2). Nevertheless the scatter is also relatively large especially due to the problems in compression yield stress determination on polymers which does not show a distinct yield point.

As a third aspect the testing velocity has to be considered. In viscoelastic materials, testing velocity has a strong influence on both level of the characteristic values and micromechanical behaviour.

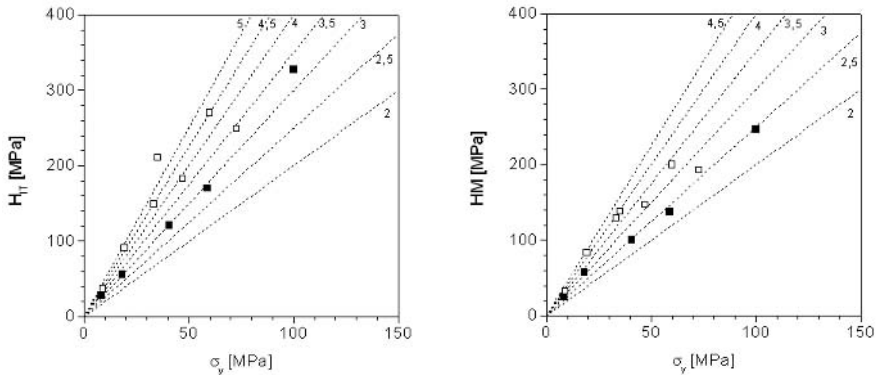


FIGURE 1. Indentation hardness  $H_{IT}$  and Martens hardness HM vs. tensile yield stress; full symbols: no crazing or stress whitening visible, open symbols: crazing or stress whitening visible.

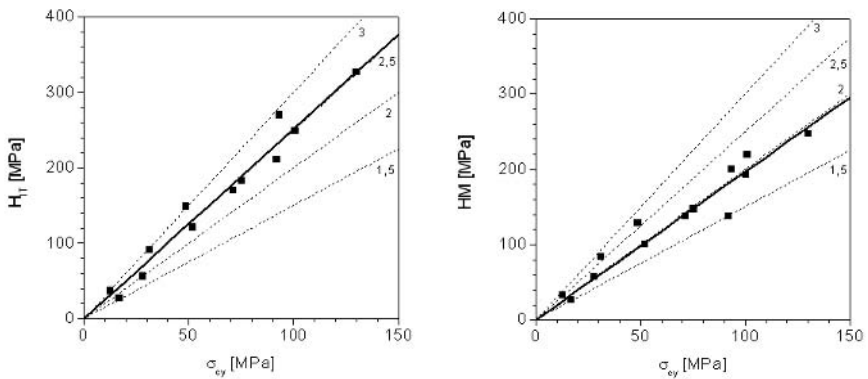


FIGURE 2. Indentation hardness  $H_{IT}$  and Martens hardness HM vs. compression yield stress.

## References

1. Tabor, D., *The Hardness of Metals*, Clarendon Press, Oxford, UK, 1951.
2. May, M.et.al., *Plaste Kautschuk*, vol. **30**, 149-153, 1983
3. Weiler, W., *Härteprüfung an Metallen und Kunststoffen*, Expert verlag, Ehningen, Germany, 1990.
4. Flores, A. et.al, *Polymer*, vol. **41**, 5431-5435, 2000

## ADVANCED TEST METHODS FOR EXPERIMENTAL CHARACTERIZATION OF ASPHALT CONCRETE

Ronald Blab, Michael Wistuba, Markus Spiegl and Karl Kappl  
Institute for Road Construction and Maintenance,  
Vienna University of Technology, Austria  
rblab@istu.tuwien.ac.at

As roads are subjected to high traffic loads due to the strong growth in heavy vehicle traffic, new trends in the automobile and tyre industries, and higher maximum axle loads limits, the traditional binder and asphalt mix tests are often inadequate today for a reliable prediction of the engineering properties and in-service performance of so called flexible road pavements constructed of different hot mix asphalt (HMA) layers. The problem facing designers of flexible road pavements is the need to fully characterise the complex thermo-rheological properties of asphalt on the one hand while on the other hand also providing a realistic simulation of the traffic- and climate-induced stresses to which pavement structures are exposed over their design lives of 20 to 30 years.

Since its foundation in July 2002 the scientific objectives and activities of the Christian Doppler laboratory for performance-based optimization of flexible road pavements have been focused, on the one hand, on the setup and implementation of performance-based test methods for bituminous materials on the basis of effective mechanical characteristics. For that purpose new testing equipment to address key performance characteristics of asphalt has been developed in cooperation with two engineering construction companies and installed at the laboratory. These test methods are now used, in a next step, for specifying the mix properties within an advanced type testing procedure required to meet customised quality standards for materials defined in tender documents as well as for mix design.

On the other hand in parallel to findings from binder and HMA testing research, enhanced modelling methods are being developed on the basis of an innovative multi-scale model for asphalt mixtures allowing a reliable prediction of in-service performance. The objective of this multi-scale model for asphalt mixtures is to enable the simulation of load-induced stresses and mechanogenic effects on the road structure in combination with performance-based tests and thus improved forecasts of the in-service performance of flexible pavements over their entire service lives.

The key performance characteristics of hot mix asphalts (HMA) used for trafficked pavements include during

- the production process: miscibility and workability, as well as compaction and binder aging (@  $T > 100^{\circ}\text{C}$ );
- the service life: permanent deformation (rutting) resistance (@  $30^{\circ} < T < 80^{\circ}\text{C}$ ), fatigue (@  $T < 30^{\circ}\text{C}$ ) and low temperature cracking (@  $T < 0^{\circ}\text{C}$ ), as well as binder aging.

For the optimization process within the mix design of a multi-composed material such as HMA, three different modes can be distinguished:

- 1 variation of mixture characteristics (e.g., binder/aggregate-ratio),
- 2 change of constituents used (e.g., different bitumen or filler type), and
- 3 admixture of additives (e.g., polymers to modify the bitumen).

To allow such an optimization process, influence parameters on the considered performance characteristic were identified, e.g., temperature, time of loading or load-ing characteristics etc., on the basis of literature studies and international expert talks. In consequence, potential key material properties for bitumen, mastic, mortar and as-phalt mixes were selected, e.g., the complex shear modulus  $G^*$  and phase lag  $\phi$  for bitumen and mastic stiffness or the complex modulus  $E^*$  for asphalt stiffness, that are recognized to be applicable as optimization parameter for mix design and performance prediction.

Based on the identified influence parameters and the key material properties appropriate performance-based test methods were selected for each scale of material observation. For rheological binder and mastic tests the laboratory of the institute has been well equipped. With regard to the asphalt scale a major effort was to specify, to order and to install the new test equipment in the lab in the first year. The new equipment comprises

- opposite rotation pug mill to mix HMA
- costume produced segment roller compactor
- special designed electromechanical testing machine for low temperature testing
- servo-hydraulic dynamic testing machine for stiffness and fatigue tests including a self developed and manufactured four-point-bending (4PBT) test element
- servo-hydraulic dynamic testing machine with two independent controlled servo-channels with a special designed triaxial load cell

A laboratory concept and machine layout was developed to most efficiently mix, compact, cut or drill asphalt specimens for different performance-based test methods and purposes. For each machine comprehensive functional tests were necessary to finally ensure the compliance of all demanded machine specifications.

## AUTOGENOUS SHRINKAGE AND CREEP OF EARLY-AGE CEMENT-BASED MATERIALS: MULTISCALE MODELING WITH EXPERIMENTAL IDENTIFICATION AND VERIFICATION

Christian Pichler and Roman Lackner

University Assistant, Institute for Mechanics of Materials and Structures,  
Vienna University of Technology, Karlsplatz 13/202, A-1040 Vienna, Austria.  
University Professor, FG Computational Mechanics, Technical University of Munich,  
Arcisstraße 21, D-80333 Munich, Germany  
Christian.Pichler@tuwien.ac.at, Lackner@bv.tum.de

Concrete is a porous medium gaining its strength and stiffness in the course of the hydration process, i.e., the chemical reaction between anhydrous cement and water. Multiscale models enable the modeling of the hydration process [1] by consideration of finer scales of observation and the respective physical/chemical processes at these scales. In this paper, the spectrum of multiscale modeling of cement-based materials, starting from material characterization by state-of-the-art experimental methods, development of homogenization schemes for determination of macroscopic material behavior, and finally the incorporation of the multiscale model into the design process of concrete structures is presented. Unlike material models formulated at the macroscopic scale of observation, multiscale models allow the explicit link of complex macroscopic behavior to its respective origin at finer scales of observation with a sound physical/chemical basis of the employed constitutive laws at these scales. Recently developed experimental methods for material characterization at finer scales of observation, e.g., nanoindentation, are combined with analytical and numerical methods for (i) interpretation of experimental data [4] and (ii) upscaling towards the macroscopic scale. Whereas an upscaling scheme for elastic properties of early-age cement-based materials has recently been proposed in [1], a homogenization scheme for

- autogenous shrinkage [3], and
- viscoelastic properties

of early-age cement-based materials is presented in this paper. Classical homogenization schemes, e.g. the Mori-Tanaka scheme [2], for upscaling of elastic properties are specialized in order to account for

- the loading of the microstructure comprising the effect of capillary depression in the liquid material phase and swelling phenomena resulting from crystallization pressure and
- viscoelastic material behavior of calcium-silicate-hydrates (CSH).

Moreover, experimental results are presented:

- When performed at finer scales, experiments give access to intrinsic material behavior of the constituents of cement-based materials. Nanoindentation tests were performed to identify finer-scale creep-properties of CSH.
- Macroscopic tests allow to verify the proposed homogenization methods. Uniaxial shrinkage and creep tests were conducted/reviewed from the open literature.

Finally, the material properties obtained from multiscale modeling are incorporated in the macroscopic simulation of shotcrete tunnel linings. These simulations provide access to the level of loading of tunnel linings, considering the characteristics of the employed shotcrete mixture.

**References**

1. O. Bernard, F.-J. Ulm, and E. Lemarchand. A multiscale micromechanics-hydration model for the early-age elastic properties of cement-based materials. *Cement and Concrete Research*, vol. **33**, 1293–1309, 2003.
2. T. Mori and K. Tanaka. Average stress in matrix and average elastic energy of materials with misfitting inclusions. *Acta Metallurgica*, vol. **21**, 571–574, 1973.
3. Ch. Pichler, R. Lackner, and H. A. Mang. A multiscale micromechanics model for the autogenous-shrinkage deformation of early-age cement-based materials. *Engineering Fracture Mechanics*, vol. **74**, 34–58, 2007.
4. Ch. Pichler, R. Lackner, and F.-J. Ulm. Scaling relations for viscoelastic-cohesive indentation – identification of material properties from instrumented indentation. In G. Meschke, R. de Borst, H.A. Mang, and N. Bicanic, editors, *Computational Modelling of Concrete Structures – Proceedings of EURO-C 2006*, pages 191–202, Mayrhofen, Austria, 2006. Taylor and Francis Group, London.

## FINER-SCALE EXTRACTION OF VISCOELASTIC PROPERTIES FROM MATERIALS EXHIBITING ELASTIC, VISCOUS, AND PLASTIC MATERIAL BEHAVIOR

Andreas Jager<sup>1</sup>, Christian Pichler<sup>1</sup>, Thomas Niederkofler<sup>1</sup> and Roman Lackner<sup>1,2</sup>

<sup>1</sup>Institute for Mechanics of Materials and Structures, Vienna University of Technology  
Karlsplatz 13, A-1040 Vienna, Austria

<sup>2</sup>FG Computational Mechanics, Technical University of Munich  
Arcisstr. 21, D-80333 Munich, Germany

Andreas.Jaeger@tuwien.ac.at, Lackner@bv.tum.de

Recent progress in both finer-scale experimentation (atomic force microscopy, nanoindentation (NI), ...) and theoretical and numerical upscaling schemes provides the basis for the development of so-called multiscale models, taking finer scales of observation into account. Hereby, chemical, physical, and mechanical processes taking place at finer scales can be considered and their effect on the macroscopic material performance is obtained via appropriate upscaling schemes. The success of multiscale models is strongly linked to the proper identification of material properties at finer scales, serving as input for the upscaling schemes.

The focus of this presentation is on the extraction of viscoelastic material parameters by means of the NI technique. During NI measurements, a tip with defined shape penetrates the specimen surface with the indentation load  $P$  [N] and the penetration  $h$  [m] recorded as a function of time. Commonly, each indent consists of a loading, holding, and unloading phase (see Fig. 1(a)). In the 1990s, Oliver and Pharr [1] developed a method for the identification of elastic material properties from materials showing elastic and plastic material response. According to [1], Young's modulus  $E$  is obtained from the relation between the measured initial slope of the unloading curve  $S=dP/dh|_{h=h_{max}}$  and the indentation modulus  $M=E/(1-\nu^2)$ , reading

$$S = \frac{2}{\sqrt{\pi}} M \sqrt{A_c}, \quad (1)$$

where  $A_c$  [m<sup>2</sup>] is the horizontal projection of the contact area, and  $\nu$  is Poisson's ratio.

Parameter identification of materials exhibiting elastic and time-dependent behavior requires back-calculation of the parameters from the holding phase of the measured indentation-depth history. Hereby, the experimental data are compared with the respective analytical solution for the mathematical problem of a rigid indenter penetrating a viscoelastic medium (see, e.g., Cheng et al. [2], Vandamme and Ulm [3], and Jager et al. [4]), giving access to the viscoelastic material properties.

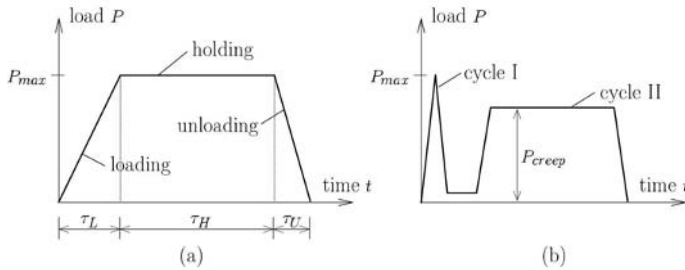


FIGURE 1. Load history for (a) conventional creep test and (b) double-indentation test

Recent results from the back-calculation of viscoelastic properties of bitumen [5], applying the back-analysis scheme proposed in [4], showed that the identified parameters strongly depend on the maximum applied load. This effect was attributed to plastic deformations occurring during the loading phase of the NI test. As a remedy, the following two techniques are presented allowing us to consider plastic deformations during back-analysis of viscous properties for materials exhibiting elastic, viscous, and plastic behavior:

- 1 In order to avoid the development of plastic deformations, spherical tips may be used instead of sharp pyramidal indenters.
- 2 On the other hand, the material may be pre-loaded within the so-called double-indentation technique (see also Zhang et al. [6]). Hereby, the load history is characterized by two load cycles (see Fig. 1(b)). Whereas the first cycle (pre-loading) leads to plastic deformations, the second cycle, showing only viscoelastic deformation is used for back-calculation of viscoelastic properties. The required analytical solution for the penetration of a tip into the imprint resulting from the first load cycle is based on the concept of "effective indenters" proposed by Pharr and Bolshakov [7].

Finally, the experimentally-identified viscoelastic parameters, using a spherical tip and applying the double-indentation technique, are verified by means of finite element calculations.

## References

1. Oliver, W.C. and Pharr, G.M., *Journal of Materials Research*, vol. **7** (6), 1564-1583, 1992.
2. Cheng, L., Xia, X., Scriven, L.E., and Gerberich, W.W., *Mechanics of Materials*, vol. **37**, 213-226, 2005.
3. Vandamme, M. and Ulm, F.-J., *International Journal of Solids and Structures*, vol. **43** (10), 3142-3165, 2006.
4. Jager, A., Lackner, R. and Eberhardsteiner, J., *Meccanica*, in print, 2006.
5. Jager, A., Lackner, R., and Stangl, K., *International Journal of Materials Research*, submitted for publication, 2006.
6. Zhang, C.Y., Zhang, Y.W., Zeng, K.Y., and Shen, L., *Journal of Materials Research*, vol. **20** (6), 1597-1605, 2005.
7. Pharr, G.M., and Bolshakov, A., *Journal of Materials Research*, vol. **17**, 2660-2671, 2002.



## ULTRASONIC CHARACTERIZATION OF POROUS BIOMATERIALS ACROSS DIFFERENT FREQUENCIES

Christoph Kohlhauser<sup>1</sup>, Christian Hellmich<sup>1</sup>, Chiara Vitale-Brovarone<sup>2</sup>, Aldo Boccaccini<sup>3</sup>,  
Dirk Godlinski<sup>4</sup> and Josef Eberhardsteiner<sup>1</sup>

<sup>1</sup>Institute for Mechanics of Materials and Structures

Vienna University of Technology (TU Wien), Karlsplatz 13/202, 1040 Vienna, Austria

<sup>2</sup>Department for Materials Science and Chemical Engineering

Politecnico di Torino, Corso Duca degli Abruzzi 24, 10129 Torino, Italy

<sup>3</sup>Department of Materials and Centre for Tissue Engineering and Regenerative Medicine

Imperial College London, Exhibition Road, London, SW7 2AZ, United Kingdom

<sup>4</sup>Fraunhofer Institute for Manufacturing Technology and Applied Materials Research

Wiener Straße 12, 28359 Bremen, Germany

Christoph.Kohlhauser@tuwien.ac.at

Mechanical testing is the most common experimental technique to determine stiffness and strength of materials. In case of porous materials, especially such with very high porosity, the determination of material strength and stiffness may be strongly biased by inelastic deformations within the microstructure of such materials.

Ultrasound waves propagating in a medium generate very small strain rates and thus enable the direct determination of elastic stiffness coefficients of very porous materials [1]. Another benefit of using ultrasound for stiffness measurement is the possibility of measuring all elastic stiffness tensor components of anisotropic materials on a single sample, reducing the complexity of specimen preparation.

Using ultrasonic waves to measure elastic stiffness tensor components is not a new method. In physics material science such waves were used to determine material properties of single crystal and polycrystalline materials [2]. Several experimental techniques, industrial applications, and theoretical derivations were sophisticated for geotechnical problems and composite materials [3, 4]. In the eighties of the last century extensive measurements on bone and some data for wood were published [5, 6].

At the Vienna University of Technology (TU Wien), we have recently tested several isotropic biomaterials, such as porous titanium [7], Bioglass<sup>®</sup> scaffolds [8] and glass-ceramic composites [9] and other bone replacement materials, with ultrasound frequencies from 100 kHz to 20 MHz, aiming at characterization of the materials at different observation scales. Ultrasonic transducers for different frequencies are depicted in Fig. 1. We also performed measurements on wood which is considered to be of orthorhombic symmetry.

All these materials have in common the strong scattering and absorption effects of the ultrasound beam due to their porous nature. Experimental difficulties involving the characterization of these materials were the coupling of the ultrasonic transducers to the specimen, handling of small and brittle materials and enabling accurate measurements of the time of flight of highly attenuated wave form signals.

The influence of the specimen geometry at different frequencies was an important factor for the interpretation of measured values. Bar and bulk wave propagation were considered in the theoretical evaluation. The influence of the size of inhomogeneities, i.e. pores in proportion to the

wavelength at different frequencies and wave velocities, is given in terms of multiscale homogenization theory [10].



FIGURE 1. Ultrasonic transducers.

**Acknowledgement:** This work was supported in part by the EU Network of Excellence project Knowledge-based Multicomponent Materials for Durable and Safe Performance (KMM-NoE) under the contract no. NMP3-CT-2004-502243.

## References

1. Carcione, J. M., *Wave fields in real media: wave propagation in anisotropic, anelastic and porous media*. Handbook of geophysical exploration, vol. **31**. Pergamon, Elsevier Science Ltd., Oxford, United Kingdom, 1<sup>st</sup> edition, 2001.
2. Hearmon, R.F.S., *Reviews of Modern Physics*, vol. **18**, 409-440, 1946.
3. Markham, M.F., *Composites*, vol. **1**, 145-149, 1970.
4. Helbig, K., *Foundations of Anisotropy for Exploration Seismics*. Handbook of geophysical exploration, vol. **22**. Pergamon, Elsevier Science Ltd., Oxford, United Kingdom, 1<sup>st</sup> edition, 1994.
5. Ashman, R.B., Cowin, S.C., Van Buskirk, W.C. and Rice, J.C., *Journal of Biomechanics*, vol. **17**, 349-361, 1984.
6. Bucur, V. and Archer, R.R., *Wood Science and Technology*, vol. **18**, 255-265, 1984.
7. Thelen, S., Barthelat, F. and Brinson, L.C., *Journal of Biomedical Materials Research*, vol. **69A**, 601-610, 2004.
8. Chen Q.Z., Thompson I.D., and Boccaccini A.R., *Biomaterials*, vol. **27**, 2414-2425, 2006.
9. Vitale-Brovarone C., Verne E., Bosetti M., Appendino P. and Cannas M., *Journal of Materials Science: Materials in Medicine*, vol. **16**, 909-917, 2005.
10. Hellmich, C., In CISM Vol. 480 *Applied Micromechanics of Porous Materials*, edited by Dormieux, L. and Ulm F.J., Springer, Wien-New York, Udine, Italy, 2005, 289-331.

## EXAMINATION OF THE OPTIMAL FREQUENCY OF THE CYCLIC LOAD IN THE INVERSE ANALYSES OF THE HEAT CONDUCTION OF INFRARED THERMOGRAPHY

Kenji Machida<sup>a</sup>, Shohei Miyagawa<sup>b</sup> and Koich Hayafune<sup>c</sup>

Department of Mechanical Engineering, Tokyo University of Science  
2641 Yamazaki, Noda-shi, Chiba, 278-8510, Japan

<sup>a</sup>mac@rs.noda.tus.ac.jp, <sup>b</sup>j7505647@ed.noda.tus.ac.jp, <sup>c</sup>j7506651@ed.noda.tus.ac.jp

Infrared stress image analyses came to be used in a broad field as non-contact and the quantitative stress-analysis method by improvement in an infrared thermography technique in recent years. What can be measured by the infrared thermography is only the sum of the principal stresses, and cannot measure each stress component directly. Since evaluating each stress component is indispensable in order to evaluate the strength and the safety of the structure, the technique of principal stress separation of estimating individual stress components from the sum of the principal stresses has been studied. However, it became clear to have the influence by heat conduction on an infrared stress image in recent years. The temperature images were acquired by the superposition of the temperature field in about 100 cycles of the fixed amplitude of a cyclic load. Therefore, it is considered that those were obtained in a steady state. Then, the influence of heat conduction was investigated by the experiment which changed materials and a cyclic-load frequency. The optimum frequency of cyclic load for exact principal stress separation was examined about the viscoelastic material in which a frequency influences measurement greatly, and several kinds of metals in which heat conductivity differs greatly.

### Experiment

The configuration of the specimen is shown in Fig. 1. Width and height are 60 mm and 100 mm, respectively. Material is a rolled steel for general structures (SS400), an aluminum alloy (A2017), a copper alloy (C1100), and an acrylic resin. Width, height and a crack length are 60 mm, 100 mm and 30 mm, respectively. The thickness of the specimen of metal and an acrylic resin are 3mm and 10 mm, respectively. The experiment was conducted at the room temperature. The frequency of the cyclic load of metals is 1, 5, 10, 15, 20 and 25 Hz, and that of an acrylic resin is 4-10 Hz.

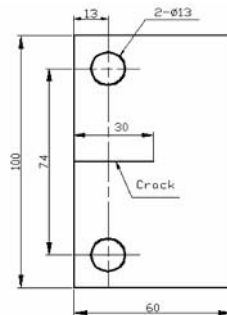


FIGURE 1. Specimen configuration.

**Results and Discussions**

Figure 2 shows the variation of  $\sigma_y$  (normal stress in the y direction) with distance from the crack tip of metals and an acrylic resin. As shown in Fig. 2 (a)(b)(c), in metallic materials,  $y$  approaches the result of a finite element method gradually as a frequency becomes high, and it is mostly in agreement with the result of a finite element method above 10-15Hz. In nonsteady-heat-conduction inverse analysis, the sum of the principal stresses obtained in the experiment is changed into the temperature amplitude. In the low frequency whose temperature field is uniform, since the temperature gradient of the initial temperature amplitude is very low, exact analyses cannot be performed. In a metallic material such as SS400, A2017, and C1100, it can be said that 15Hz or more is the optimum frequency for exact principal stress separation. As can be seen in Fig.2 (d), it is considered that 6 to 8 Hz is the optimum frequency of an acrylic resin.

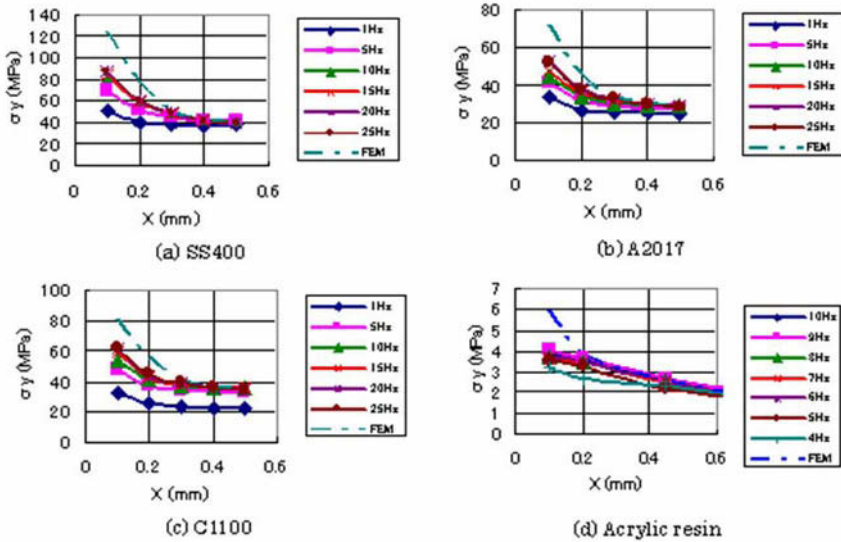


FIGURE 2. Variation of  $\sigma_y$  with distance from the crack tip depending on the frequency of the cyclic load.

**Conclusions**

1. 15Hz or more is recommended to the optimum frequency of the cyclic load in heat-conduction inverse analysis in the metallic material of SS400, A2017, and C1100.
2. As for the optimum frequency of the cyclic load in heat-conduction inverse analysis, 6 to 8 Hz is recommended in an acrylic resin used as a viscoelastic material.

## FORMATION BEHAVIOR OF SHAPE RECOVERY FORCE IN TINI FIBER REINFORCED SMART COMPOSITE

Keitaro Yamashita and Akira Shimamoto  
Saitama Institute of Technology  
1690 Fusaiji Fukaya Saitama 369-0293 Japan  
yamashi@sit.ac.jp, shimamo@sit.ac.jp

The shape recovery force is generated by joule heating it to the shape-memory alloy (SMA) wire which pre-strain of several % of the burial in the resin matrix, and the development of smart composite materials which achieve intellectual effects of the spread obstruction of the crack and the self-restoration, etc. is advanced. Authors try to measure the displacement of the composite material when Joule heating it, and to evaluate the shape recovery force from the amount of shrinkage, and have obtained quantitative information on the relations etc. between the structure of the composite material and the heating condition, etc. [1,2]. However, because many of calories generated from SMA by Joule heating are spent on the heating of the matrix, the reverse-transformation temperature arrival time of SMA is delayed under the low temperature environment. Therefore, because the thermal expansion of the matrix is superior, evaluating the formation behavior of the shape recovery force from the displacement measurement of the composite material becomes difficult. Then, it was tried to evaluate the behavior of the shape recovery force in the smart composite material which reversely transformed SMA by Joule heating in this research by measuring the change in the electrical resistance which related closely to phase transformation of SMA in a wide-ranging operation environment.

SMA used for this research is the TiNi type of 0.4mm in the diameter. The reverse-transformation temperatures are  $A_s$ : 36.1 °C,  $A_f$ : 55.3 °C, and have intermediate R phase transformation at about 40°C. The relation between the shape recovery force and the electrical resistance generated in the SMA fiber fixed to pre-strain of 6% was evaluated first. Because a mechanical characteristic of SMA with pre-strain changed greatly at the temperature before and after the reverse-transformation, the stress change by an ambient temperature was removed and only the shape recovery force generated by Joule heating evaluated. Fig. 1(a) is a change at the time of the shape recovery force and the electrical resistance of the SMA fiber when joule heating it in the measurement environment of 2°C. When the current is increased from D.C.1A to 3A, the generation of the shape recovery force shifts to the shorter side, and reaches the maximum value of about 350MPa by 1sec. On the other hand, the maximum point of the shape recovery force makes the electrical resistance minimum. If a dynamic change in the electrical resistance is measured, it is suggested to be able to monitor the generation behavior of the shape recovery force by Joule heating because this minimum point of the electrical resistance corresponds to reverse-transformation finish temperature  $A_f$  of SMA. Fig. 1 (b) is a correlation of the electrical resistance and the shape recovery force. The electrical resistance has an excellent correlation with the shape recovery force.

The size of the test piece of smart composite materials evaluated by this research is  $W20 \times D5 \times L130$  (mm), and seven SMA fibers are buried in the polycarbonate resin in pre-strain of 6%. Fig. 2(a) shows the relation between Joule heating ( $I=2.5A$ ) time and electrical resistance from -60 to 80°C in ambient temperature. The maximum point of the electrical resistance which relates by becoming the low temperature to R phase transformation appears sharply and it moves to longer time. The maximum point of the shape recovery force is predictable in the composite material test piece according to the evaluation result of the SMA single fiber when formed at time  $t_2$  of a

minimum point after peak point  $t_1$  of the electrical resistance is passed. The  $t_1$  and  $t_2$  show the straight line relationship to the ambient temperature as Fig. 2 (b). After 10-20sec, the maximum value of the shape recovery force is formed with electric resistance peak arrival time  $t_1$ . For instance, to gain the maximum shape recovery force, the electrical resistance needs the heating time of  $t_2=20$ sec under an ambient temperature of  $0^\circ\text{C}$  though  $t_1=5$ sec makes it the maximum.

It has been understood to be able to monitor the progress of heating by Joule heating of smart composite materials and the formation behaviour of the shape recovery force from the above-mentioned result by measuring a dynamic electrical resistance.

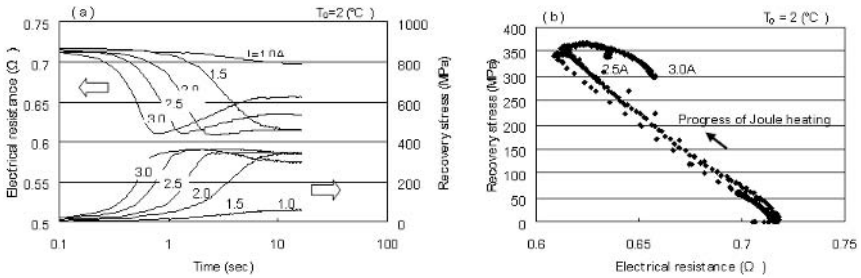


FIGURE 1. Change of shape recovery force and electrical resistance of SMA single fiber

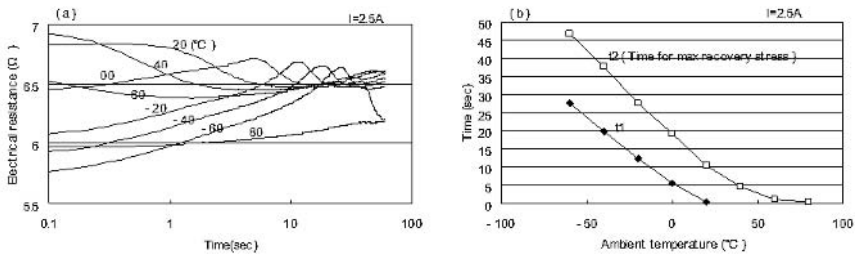


FIGURE 2. Change of electrical resistance of SMA fiber reinforced smart composite

**References**

1. K.Yamashita and A.Shimamoto, *Mater.Trans.*, vol. **45**, 1646-1652, 2004
2. K.Yamashita and A.Shimamoto, *Proc.of SPIE* , vol. **5761**, 429-439, 2005

## EFFECTS OF BIAxIAL STRESS CONDITION FOR FATIGUE PROPERTIES OF TITANIUM

Yasumi Itoh<sup>a, b</sup>, Akira Shimamoto<sup>b</sup>, Do Yeon Hwang<sup>b</sup>, Tetsuya Nemoto<sup>a</sup> and Hiroyuki Matuura<sup>a</sup>

<sup>a</sup>National Institute for Longevity Sciences, NCGG  
36-3, Gengo, Morioka, Obu, Aichi, 474-8522, Japan

<sup>b</sup>Saitama Institute of Technology  
1690 Fusaiji, Fukaya, Saitama, 369-0293, Japan

<sup>a</sup>yito@nils.go.jp, <sup>b</sup>shimamot@sit.ac.jp

According to linear fracture mechanics the crack growth rate is controlled by the stress intensity factor, so the non-singular stress has no effect on the growth rate. While several experimental data by Kitagawa et al. [1] and Liu et al. [2] more or less support this principle, some data indicate that the non-singular stress does influence the crack growth rate. Authors [3-5] already investigated the fatigue crack progress behavior of the magnesium alloy under biaxial stress. As a result, it was suggested that existence of a stress parallel to a crack affects crack progress velocity in AZ31B. In this research, fatigue crack propagation tests of Titanium were conducted under conditions of biaxial loading in order to investigate the effect of non-singular stress cycling. It is because the crystal structure of titanium is the same as magnesium. As a result, we clarified effects of biaxial stress condition for fatigue properties of Titanium.

### Experimental Procedure

Pure Titanium plates used for this research are 2.5mm thickness. The dimension and form of a specimen are shown in Fig. 1. We made  $Y$ -axis of the specimen as the rolling direction. The fatigue tester used for this experiment was the biaxial, electrically operated, oil-pressure servo tension-compression fatigue tester. In the fatigue crack propagation tests, as shown in Fig. 2, we put the stress,  $\sigma_x^0$  on  $X$ -axis and  $\sigma_y^0$  ( $= 45.72$  MPa) on  $Y$ -axis. The experiment was conducted on condition of the load stress ratio  $R_B = \sigma_x^0 / \sigma_y^0 = 0, 0.25, 0.5, 0.75$  and  $1.0$ . We put stress with sinusoidal in shape, with the stress ratio of  $\sigma_{y, \min}^0 / \sigma_{y, \max}^0 = 0$ , and the cycle speed of 10Hz.

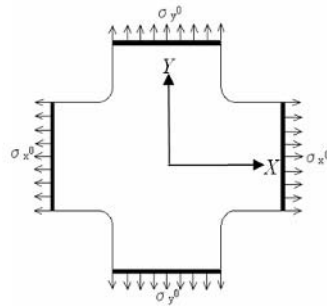
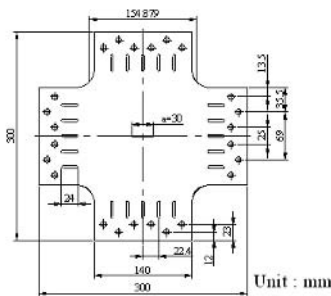


FIGURE 1. Shape and dimension of specimen. FIGURE 2. Stress condition of specimen.

## Experimental Results

Fig. 3(a) shows the relationship between the half crack length and the number of load cycles obtained from fatigue tests. The relationship between the half crack length and the number of load cycles of magnesium alloy [3] is shown in Fig. 3(b) for comparison.

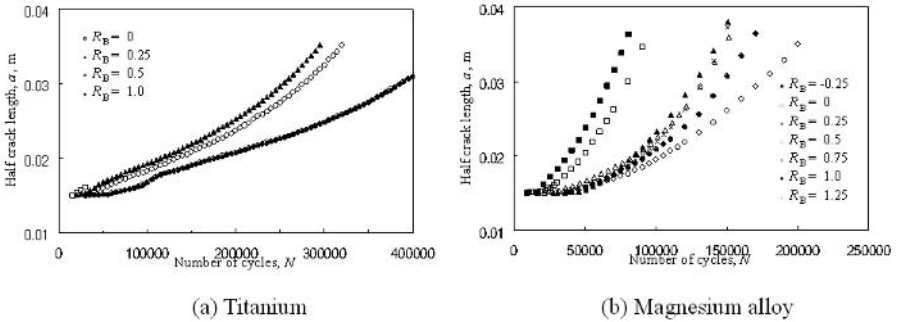


FIGURE 3. Relation between crack length and number of cycle

## Conclusions

The following knowledge was acquired as a result of examining fatigue crack generation and progress process of titanium under various biaxial load stress ratios.

1. In order that stress of  $Y$  directions might decrease with the increase in load of  $X$  directions, it was observed that fatigue crack growth becomes slow.
2. As for magnesium alloy, when a biaxial load ratio was 0.5, fatigue crack growth became slow, but such a phenomenon was not observed by titanium.
3. It is a future subject to clarify the cause of a difference of the biaxial fatigue characteristics of magnesium alloy and titanium.

## Acknowledgments

This work was supported by High-Tech Research Center of Saitama Institute of Technology.

## References

1. H. Kitagawa, R. Yuuki and K. Tohgo, *Fatigue of Engineering Materials and Structures*, vol. **2**, 195-206, 1979
2. A. F. Liu, J. E. Allison, D. F. Dittner and J. R. Yamane, *ASTM STP*, vol. **677**, 5-22, 1979
3. Y. Itoh and A. Shimamoto, *Key Engineering Materials*, vols. **270-273**, 1246-1253, 2004
4. Y. Itoh and A. Shimamoto, *Materials Science Forum*, vols. **488-489**, 859-864, 2005
5. Y. Itoh and A. Shimamoto, *Key Engineering Materials*, vols. **297-300**, 1559-1564, 2005
6. Y. Itoh and A. Shimamoto, *Key Engineering Materials*, vols. **321-323**, 599-602, 2006



## AN APPLICATION OF IMAGE-PROCESSING TO STRESS MEASUREMENT BY COPPER PLATING FOIL (ON THE EFFECT OF FREQUENCY, STRESS RATIO AND STRESS WAVEFORM)

Masakatsu Sugiura<sup>1</sup>, Ryuji Ozeki<sup>2</sup> and Masaichiro Seika<sup>3</sup>

<sup>1</sup>Professor, Department of Mechanical Engineering,  
Daido Institute of Technology, Nagoya, Japan,

<sup>2</sup>Graduate Student, Department of Mechanical Engineering,  
Daido Institute of Technology, Nagoya, Japan

<sup>3</sup>Emeritus Professor, Nagoya University, Nagoya, Japan  
msugiura@daido-it.ac.jp

### 1. Introduction

Strain gauges made of copper plating foil are devised for measuring the elastic surface stress of machine parts in operation. The elastic stress is measured by observing slip bands in the bonded foil. Calibration studied by cyclic tension test with various frequencies, various stress ratios and different stress waveforms are performed on round steel bars with copper plating foil. It is verified that the relation between the threshold stress for the first appearance of slip bands and the number of cycles are not affected by the stress ratios and stress waveforms, but the frequency. Using a computer image-processing system, the density of slip bands in a microscopic image of the bonded foil is analyzed automatically and quantitatively.

In order to examine the accuracy of this method, the peak stresses in grooved shafts under cyclic tension test are obtained using the present method. The results are compared with those derived from the design formulas by Roark and Young.

### 2. Experimental Procedures

#### 2-1 .Testing Machine and Test Specimens

A hydraulic servo type cyclic tension fatigue testing machine(98 kN) was used for cyclic tension tests with a constant load amplitude.

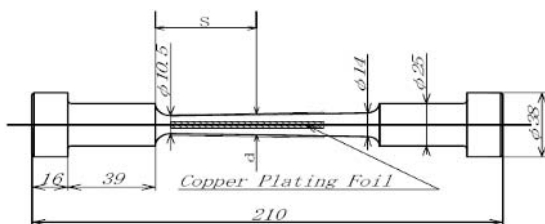


FIGURE 1. Tapered calibration specimen (Dimensions in mm)

Using drawn rods carbon steel annealed after heating at 900°C for one hour, tapered calibration specimens shown in Figure 1.

#### 2-2. Copper Plating Foil and Its Adhesion

A Stainless-steel plate polished by buffing was coated with a copper plating, and a sheet of plating foil about 10  $\mu\text{m}$ -thick was made by stripping the deposited layer from the stainless-steel

plate. The copper plating foil was cut into a number of small rectangular pieces to make foil gauges. Four pieces of the rectangular foil were used for the calibration specimen (Fig.1).

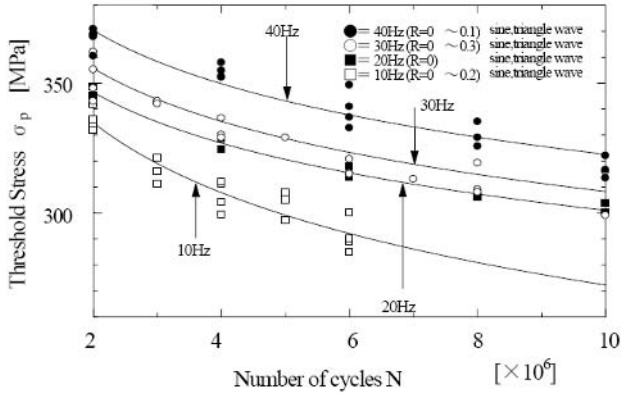


FIGURE 2. Threshold stress  $\sigma_p$  versus number of cycles N for various frequencies various stress ratios and different stress waveforms

### 2-3. Measurement of Threshold Stress

The threshold stress  $\sigma_p$  (Fig. 2) for the first appearance of slip bands in the foil gage was measured using the tapered calibration specimen with rectangular foil to cyclic tension with various frequencies, various stress ratios (R) and different stress waveforms. Slip bands were observed with an optical microscope at a magnification of 100 times. When slip bands in the bonded foil began to appear at the position of the distance S (Fig. 1) under a constant load amplitude W and specified number of cycles N, the threshold stress  $\sigma_p$  in cyclic tension were calculated by the following formulas

$$\sigma_p = 4W / \pi d^2 \quad (1)$$

### 2-4. Image-processing System

The density of slip bands in a microscopic image was obtained by the ratio of the region of slip bands, f pixels, to the whole region of the image, F pixels by image-processing system, which is denoted by the slip bands density r (%) as  $r = (f / F) \times 100$  (%).

## 3. Conclusions

It was found that an application of the computer image-processing to the observation of slip bands in copper plating foil is very useful for improving practical usage of the copper plating foil strain gage.

## References

1. Roark, R. J and W.C. Young., Formulas for Stress and Strain, 5<sup>th</sup> ed., New York, McGraw-Hill, 1975.599.
2. M. Sugiura, A. Arakawa, Y. Aoyama and M. Seika., In Proceeding of International Conference on advanced Technology in Experimental Mechanics, ATEM'03, Nagoya, Japan, 2003, CD-ROM.

## FABRICATION OF CU NANOWIRE AT THE INTENDED POSITION BY UTILIZING STRESS MIGRATION

F. Yamaya, N. Settsu and M. Saka

Department of Nanomechanics, Graduate School of Engineering, Tohoku University  
Aoba 6-6-01, Aramaki, Aoba-ku, Sendai 980-8579, Japan  
saka@ism.mech.tohoku.ac.jp

A technique based on a phenomenon caused by electromigration has been proposed to fabricate metallic nanowires[1,2]. On the other hand, a foundation of fabricating metallic nanowires by utilizing effective collection of the atoms caused by stress migration, which was a phenomenon of atomic diffusion due to the gradient of hydrostatic stress as the driving force, was proposed[3]. The stress migration diffused the atoms towards a position where negative hydrostatic stress with lower absolute value was distributed. At the position, the absolute value was increased because of the local accumulation of the diffused atoms. After that, the collected atoms were discharged by releasing the compressive stress induced. As a result of the phenomenon, metallic nanowire was formed.

In the present research, fabrication of Cu nanowire at the intended position by this phenomenon is studied. First of all, the position where the Cu nanowire is formed is examined by analysis. The physical model of the analysis is developed as shown in Fig. 1, and the mechanical properties of the materials, used for the analysis, are shown in Table 1. Thermal stress is generated in a Cu thin film as a result of the difference in thermal expansion coefficients of Cu and Ta. The temperature of the physical model is raised from 293 to 613K to generate the gradient of the hydrostatic stress.

As a result of the analysis, the hydrostatic stress distribution generated at the top surface of the Cu thin film is shown in Fig. 2(a). It is confirmed that negative hydrostatic stress with lower absolute value is distributed along the line which is at a distance of approximately  $0.5\mu\text{m}$  from the boundary between the Cu and Ta thin films. In addition, the hydrostatic stress distribution, generated at the end of the Cu film, is shown in Fig. 2(b). It is verified that hydrostatic stress, generated at the neighborhood of the corner in the Cu film, is the highest. Therefore, it is considered that the Cu atoms are diffused to the neighborhood of the corner by the stress migration, and then a large amount of Cu atom can be collected there. The result of the analysis suggests that Cu nanowire may be at the neighborhood of the corner in the Cu film.

TABLE 1. Material properties.

Material	Young's modulus / GPa	Poisson's ratio	Thermal expansion coefficient / $\times 10^{-6}\text{K}^{-1}$
Copper	110	0.34	16.2
Tantalum	186	0.34	6.6
Silicon dioxide	180	0.28	4.15
Silicon	163	0.28	4.15

Next, the result of the present analysis was verified experimentally. As a manufacture of a sample, Cu thin films were deposited on a Ta layer by electron beam evaporation and then a Ta layer used as a passivation layer was deposited on them by sputtering. A Si wafer covered with

300nm of SiO<sub>2</sub> was used as a substrate. The temperature of the sample was raised from 293 to 613K for 10 h and then thermal stress was generated in the Cu thin film.

As a result of raising the temperature of the sample, it was confirmed by FE-SEM observation that there were some hillocks at the corner as shown in Fig. 3(a). The formation of the hillocks was not seen in places other than the corner of the Cu thin film. Therefore, it was confirmed that a large amount of Cu atom was collected at the intended position. Moreover, the Cu nanowire product from the hillocks is shown in Fig. 3(b). The Cu nanowire whose diameter and length were 20nm, 2.5μm respectively was fabricated at the intended position.

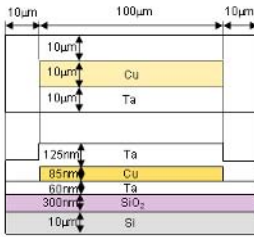


FIGURE 1. Physical model of the analysis.

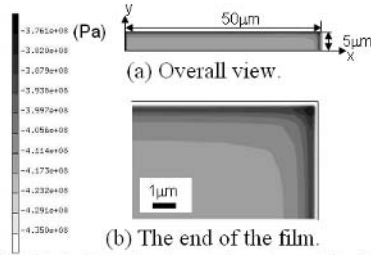
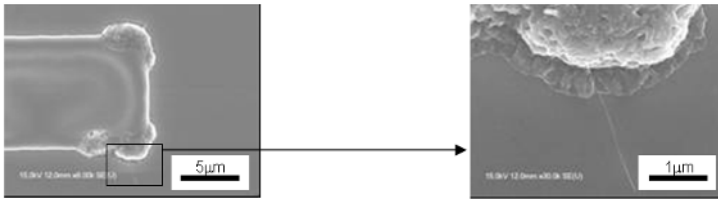


FIGURE 2. The hydrostatic stress distribution generated at the top surface of the Cu thin film.



(a) Hillocks at the corner (intended position). (b) Cu nanowire generated from the hillock.

FIGURE 3. FE-SEM observation of hillocks and nanowire.

**Acknowledgment**

This work was partly supported by Grant-in-Aid for Scientific Research (S) 18106003, “The Exploration of the frontiers of Mechanical Science Based on Nanotechnology”.

**References**

1. M. Saka and R. Ueda, *J. Mater. Res.*, vol. **20**, 2712-2718, 2005.
2. M. Saka and R. Nakanishi, *Mater. Lett.*, vol. **60**, 2129-2131, 2006.
3. F. Yamaya and M. Saka, Proc.2006 Annual Meeting of the JSME/MMD, 673-674, 2006 (in Japanese).

## NUMERICAL AND EXPERIMENTAL STUDY OF BENDING BEHAVIOR OF THIN WALLED BEAMS FILLED WITH METALLIC FOAMS.

Gustavo José Cazzola<sup>1</sup>, Francisco Aparicio Izquierdo<sup>2</sup> and Teresa Vicente Corral<sup>3</sup>

<sup>1</sup> National Technological University

Hipólito Irigoyen 288- General Pacheco- Buenos Aires – Argentina

<sup>2</sup> INSIA-UPM (University Institute for Automotive Research–Politechnic University of Madrid)

Ctra. de Valencia, km,7 28031, Madrid, Spain

<sup>3</sup>INSIA-UPM

gcazzola@frgp.utn.edu.ar, faparicio@insia.upm.es, teresa.vicente@upm.es

The purpose of this work is to know the behavior of big rotation of thin walled beams filled with metallic foam under bending loads. Potential applications of filled sections with metallic foam are to improve vehicles passive safety, for example to the improvement of the coaches structures' energy absorption capability under lateral rollover. The filling acts as a slowdown of the collapse by beams wall buckling; consequently, more energy can be absorbed.

The lateral resistance of the vehicle structures is conditioned by the bending resistance and plastic behavior of the beams used. The mentioned profiles are low thickness ones to obtain high inertias with low weight, which behavior is conditioned to the fold formation at the compression flange characterized by a moment-rotation response that displays as a basic parameters: the maximum resistant moment and the negative slope of decreasing resistance based on the plastic rotation. This fact is in opposition to the previous one: different construction with beams of low thickness being due therefore to reach solutions that keep a difficult balance between resistance and weight. This behavior had been studied by several investigators within whom it is possible to mention Dr. Andrés García Thesis, professor of the Polytechnic University of Madrid.

Recent developments in the cost-benefit relation from the metallic cellular materials of low density processes of production, such as the metallic foam, position them like an alternative of special interest for the application like elements with high energy absorption capabilities reinforcing structures. The filling with metallic foam can be more efficient in terms of optimization of weight than to increase the thickness of the structural beams.

The application of metallic is beginning to be used in some zones of the tourism vehicles' structures, being totally novel any attempt of application in structures of coaches and buses.

Based on previously exposed, Advanced Pore Morphology (APM) foams has been used in this study, developed by Fraunhofer for Institute Manufacturing and Advanced Materials, like material of stuffed for profiles of bodies of buses.

IFAM has developed and patented the process of powder-metallurgy for the foamed metals FOAMINAL®. In contrast to FOAMINAL® process the general concept of technology APM is to separate the process in two parts:

1. Foam expansion
2. Foam conformed in parts

The parts of foam with porous morphology consist on metallic foam elements of small volume which are expanded production volume /mass. When united with others in a separated process elements they form foam APM.

The objective of this paper is to analyze the crushing behaviour of thin –walled beams in the deep bending collapse mode. The strengthening method with aluminium foam is compared to the conventional one of increasing the wall thickness. The effectiveness of the lightweight core is assessed by examining the ratio of energy absorption to the beam weight.

The numerical models and tests presented in this work were made in the facilities of the University Institute for Automobile Research (INSIA) of the Polytechnic University of Madrid.

## EVALUATION OF OFF-AXIS WOOD COMPRESSION STRENGTH

Nilson Tadeu Mascia, Elias Antonio Nicolas and Rodrigo Todeschini  
 School of Civil Engineering, Architecture and Urbanism-State University of Campinas  
 Caixa postal 6021-Unicamp-Campinas-SP-Brazil  
 nilson@fec.unicamp.br, eliasnic@fec.unicamp.br, ditodes@yahoo.com.br

This research focuses on the study of anisotropic material failure criteria, specifically Tsai-Wu tensor failure criterion, Tsai and Wu [1], with theoretical and experimental applications for wood.

This criterion is mathematically written by:

$$F_1 \cdot \sigma_1 + F_2 \cdot \sigma_2 + F_{11} \cdot \sigma_1^2 + F_{22} \cdot \sigma_2^2 + 2F_{12} \cdot \sigma_1 \cdot \sigma_2 + F_{44} \cdot \sigma_4^2 = 1 \quad (1)$$

where:  $\sigma_1, \sigma_2$  are the normal stress,  $\sigma_4$  is the shear stress,  $F_1 = \frac{1}{f_{t1}} - \frac{1}{f_{c1}}$ ,  $F_2 = \frac{1}{f_{t2}} - \frac{1}{f_{c2}}$ ,  $F_{44} = \frac{1}{f_v^2}$ ,  $F_{11} = \frac{1}{f_{t1} \cdot f_{c1}}$ ,  $F_{22} = \frac{1}{f_{t2} \cdot f_{c2}}$  with  $f_t$ : tension strength,  $f_c$ : compression strength,  $f_v$ : shear strength and  $F_{12} < \pm \sqrt{F_{11} \cdot F_{22}}$ . The strength coefficient  $F_{12}$  is the interaction coefficient, which is obtained by biaxial test, Wu [2] and Mullner *et al.* [3].

For materials as wood, when applying a compression or tension load, in an inclined direction of a small angle in relation to its grain, a great reduction of the strength occurs. This reduction is related directly to the wood anisotropic nature. Hence, it is necessary to use a criterion of strength that considers the wood anisotropic behavior and the asymmetry of strength, or either, different compression and tension strengths in one same direction.

Due to the complexity of the phenomena of wood rupture and its composites, the predictions using failure theories had still not been developed completely. Consequently, empirical methods are used, which under some circumstances are reasonable accurate.

Hankinson's formula is one of these methods and it has been applied frequently for wood, particularly in the compression in directions inclined in relation to grain. According to Liu [4] Bodig and Jayne [5], Hankinson's formula is well adjusted to predict the off-axis wood strength under compression or tension being written by:

$$\sigma_\theta = \frac{f_0 \cdot f_{90}}{f_0 \cdot \text{sen}^n \theta + f_{90} \cdot \text{cos}^n \theta} \quad (2)$$

$\sigma_\theta$ : off-axis strength;  $f_0$ : parallel strength;  $f_{90}$ : perpendicular strength;  $\theta$ : grain angle;  
 $n$ : constant.

This present research had been carried through compression tests in wood specimens (5cmx5cmx15cm), of the Brazilian species *Goupia glabra*, in the directions inclined in relation to grain (0°, 15°, 30°, 45°, 60°, 75° and 90°), having as main purpose to compare the results of tests with the values obtained through Hankinson's formula and the Tsai-Wu criterion. Observe to use this criterion by considering Equation 1, it was necessary to perform tension, shear and biaxial tests too (Fig. 1).

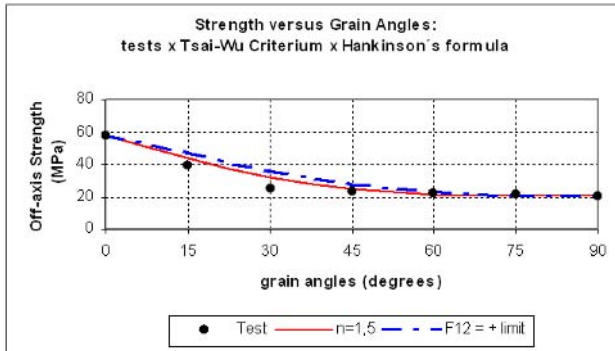


FIGURE 1. Experimental results: plotting and fitting.

In general, the most important conclusions that were drawn can be summarized as follows: the prediction of Tsai-Wu criterion was close of Hankinson's formula and the compression tests results too; Tsai-Wu criterion presents good results, facility in utilizing when comparing to other criteria due to especially its tensor form, and can be applied to evaluation wood strength and other anisotropic materials; Hankinson's formula is more practical and even empirical presented the fitting next to the values obtained in compression tests.

## References

1. Tsai, S. W., Wu, E. M. A general theory of strength for anisotropic materials. *Journal of Composite Materials*, n. 1, vol. 5, 58-80, 1971.
2. Wu, E. M. Phenomenological anisotropic failure criterion. *Mechanis of Composite Materials*, vol. 2, 353-431, 1974.
3. Mullner, H. W., Eberhardsteiner, J., Helnwein, P. M. *Constitutive modelling of clear spruce wood under biaxial loading by means of an orthotropic single-surface model under consideration of hardening and softening mechanics*. Institute for Strength of Materials, Vienna University of Technology. Vienna. Austria, 2004.
4. Liu, J. Y. Evaluation of the tensor polynomial strength theory for wood. *Journal of Composite Material*, vol. 18, 216-22, 1984.
5. Bodig, J. ; Jayne, B. A. *Mechanics of wood and wood composites*. Krieger Publishing Company, Florida, 1982.



## MECHANICAL CHARACTERISTICS OF SPECTACLES

H. Kaneko<sup>1</sup>, S. Kakunai<sup>1</sup>, M. Morita<sup>2</sup> and J. Nishimura<sup>3</sup>

<sup>1</sup> University of Hyogo, Graduate School of Engineering,  
Mechanical and System Engineering, Himeji, Hyogo, Japan

<sup>2</sup> Formerly: University of Hyogo, Himeji, Hyogo, Japan

<sup>3</sup> Paris Miki Inc, Okayama, Japan

<sup>1</sup> 2167 Shosha, Himeji, Hyogo, 671-2201, Japan  
kakunai@eng.u-hyogo.ac.jp

In order to wear spectacles comfortably, the lens power should be optimized and the spectacles should be secured at an appropriate position on the head so as to minimize any sensation of discomfort. For smooth fitting, the frame must be designed by taking in account the mechanical characteristics. However, the design and manufacture of spectacle frames often rely on the experience of engineers. This is partly because spectacle frames have complex forms and complex materials. Measuring and analysis technologies are currently making remarkable progress and consequently they can now be applied to industrial products comparatively easily[1-3]. In this study, we investigated the mechanical characteristics of three types of spectacles that are on the market: a titanium frame of a full-rim model that is popular because of its good lens protection, a gum-metal frame made from a recently developed material, and a rimless frame in which each lens is secured using two screws that allows very flexible lens design.

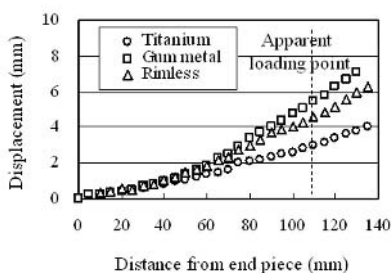


FIGURE 1. Comparison of temple displacement when a 160-mN load is applied

The deformation behaviors of the spectacle frames were investigated by performing optical 3D profile measurements. We employed the light sectioning method, which scans the object using a laser beam. The displacement distribution was obtained by profile measurement before and after deformation under a load. The experimental load was set to about 160 mN so that the temples were extended by 5 mm outward. Figure 1 shows the displacement of the temple of each frame. The temple shows two-step displacement distribution where the displacement gradient becomes great at about 40 to 50 mm from the end piece. Figure 2 shows the front lens displacement of each frame in the out-of-plane direction. The two full-rim types exhibit almost the same displacement curves, but the rimless frame type shows the greatest displacement. The rimless type is lightweight and fashionable but may not be sufficiently strong.

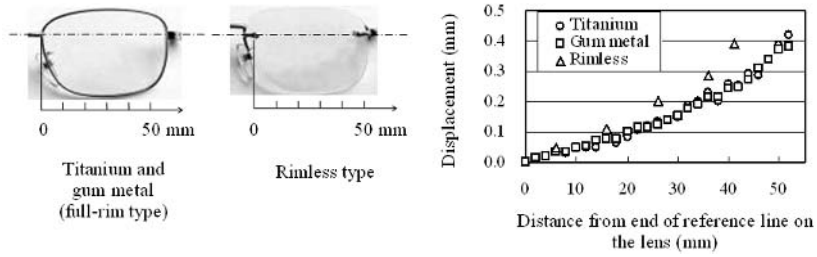


FIGURE 2. Front displacement when load is applied to the temple

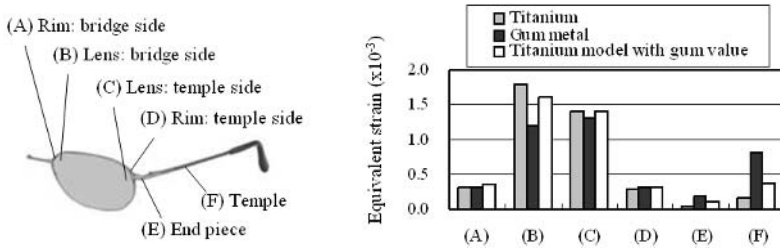


FIGURE 3. Comparison of equivalent strain

We then conducted finite element method (FEM) analysis to investigate the mechanical characteristics of spectacles. Spectacle frames were produced using optical 3D profile measurements and computer-aided design (CAD) software. Figure 3 compares the strain at each section of a full-rim frame for the titanium model, the gum metal model and the titanium model with gum metal properties. The gum metal model had a large strain in the temple section (F) but a small strain in the lens sections (B) and (C). By contrast, the titanium model with gum metal properties had a small strain in the temple section (F) but a very large strain in the lens sections (B) and (C). From these results, we can estimate that the gum metal frames have flexible temples and the end pieces connected to rims are designed to suppress lens strain.

Meanwhile, for the rimless model, the load applied to the temple produced a very large regional stress in the vicinity of the screws. To prevent damage from these areas, it would be useful to design an end piece structure that does not convey temple load easily or to utilize materials like gum metal.

**References**

1. Tsuji, K., *Scientific Manufacturing of Glasses*, Publishing of glasses optics, Tokyo, Japan, 1996.
2. Kouchi M. and Mochimaru M., *Digital Human Modeling Conference 2002*, 69-80, 2002.
3. Kakunai S. et al., *Appl. Optics*, vol. 38, 2824-2829, 1999.

## RUPTURE OF BOTTLENECK SEAL OF LIQUID PACKAGING BAGS

Akira Shimamoto<sup>1</sup>, Hiroyuki Aoki<sup>2</sup> and Katsunori Futase<sup>3</sup>

<sup>1</sup> Advanced Science Laboratory, Saitama Institute of Technology  
1690 Fusaiji, Fukaya, Saitama 369-0293, Japan

<sup>2,3</sup> Taisei Lamick Co., Ltd.

873-1 Shimo-Ohsaki, Minamisaitama, Saitama 349-0293, Japan

<sup>1</sup> shimamot@sit.ac.jp, <sup>2</sup> aoki@lamick.co.jp, <sup>3</sup> tlk-k-k@mua.biglobe.ne.jp

The shapes and types of containers for foods, drugs and medicines, and cosmetics and detergent refills are diverse: glass bottles, cans, PET bottles and laminate-film liquid packaging bags are examples.

In recent years, to increase the ease of pouring out the contents of laminate-film liquid packaging bags, the shape of the heat seal has been changed from a flat seal to a bottleneck seal. However, the large number of bottleneck seal ruptures of liquid packaging bags due to impact load during the transport, loading and unloading of packaged products has been a problem. In our previous study, we investigated impact tensile strength in the heat-sealed area of a laminate film; however, the effects of the bottleneck seal shape and heat-sealed area width on impact tensile strength and rupture occurrence have not yet been clarified.

In this study, experiments were carried out to clarify the effects of the flat and bottleneck seal shapes, as well as heat-sealed area width, on impact tensile strength and bag rupture occurrence. The following two films were used: (1) a multilayered laminate film with barrier characteristics against oxygen and water vapor, which is frequently used for liquid packaging bags owing to its high efficacy in food quality preservation, and (2) a multilayered laminate film without barrier characteristics. On the basis of the results obtained, we established, for the first time, a new standard regarding bottleneck seal shape and heat-sealed area width.

The samples used in this study include 1) the multilayered laminate film NY/XA-S without barrier characteristics against oxygen and water vapor, 2) the multilayered laminate film NY/AE-PET/XA-S with barrier characteristics and 3) the multilayered laminate film NY/AL/XA-S with barrier characteristics (Fig. 1).

We used a rotary impact tensile apparatus for impact tensile tests and developed a new apparatus for bag rupture tests, referring to a falling-weight impact tensile apparatus. The experiments were conducted using the apparatuses developed.

To clarify the effects of impact tensile speed and bottleneck seal shape on the impact tensile strengths of the three films, i.e., NY/XA-S, NY/AE-PET/XA-S and NY/AL/XA-S, impact tensile strength was measured at four impact tensile speeds ( $V = 1.20, 1.40, 1.60$  and  $1.98$  m/s) for five heat-sealed area radii ( $r = 5, 7.5, 15, 20$  mm and  $\infty$  (flat seal)) used as a parameter of bottleneck seal shape. An example of the results is shown in Fig. 2.

As shown in Fig. 2, impact tensile strength decreases as impact tensile speed increases. In particular, the impact tensile strength at  $V = 1.98$  m/s is found to decrease by 21.9% for NY/AE-PET/XA-S, 34.0% for NY/XA-S and 27.8% for NY/AL/XA-S compared with those at  $V = 1.20$  m/s. In addition, it was confirmed that impact tensile strength decreases with increasing impact tensile speed regardless of heat-sealed area radius ( $r = 5, 7.5, 15, 20$  mm and  $\infty$  (flat seal)). When the heat-sealed area radius is 15 mm or larger, impact tensile strength does not increase with heat-seal area radius; impact tensile strength is comparable to that obtained with a flat seal.

Finally, bag rupture experiments were carried out for the heat-sealed area radii of 15 mm and  $\infty$  (flat seal), and for the five heat-sealed area widths (0.30, 0.50, 1.20, 2.00, 10.00 mm), to examine the effect of heat-sealed area width on impact rupture strength. An example of the results is shown in Fig. 3.

When the heat-sealed area width is 1.20 mm or larger, impact rupture strength remains constant. The highest rupture strength comparable to that of a flat seal is obtained.

On the basis of the results obtained, a heat-sealed area width as large as 10.00-15.00 mm is not necessary; the heat-sealed area width of 1.20 mm or larger is adequate for obtaining sufficient impact tensile strength and sufficient impact rupture strength. We established, for the first time, a new standard for heat-sealed area width, considering both the conservation of resources by reducing sealing width and the reduction in the number of ruptures.

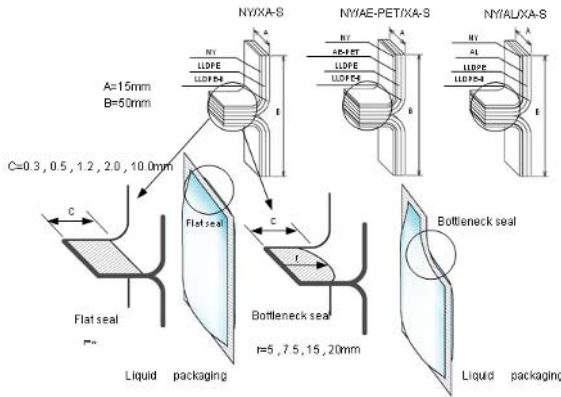


FIGURE 1 Specimens

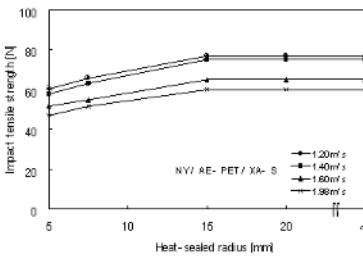


FIGURE 2 Relationship between impact tensile strength and heat-sealed radius

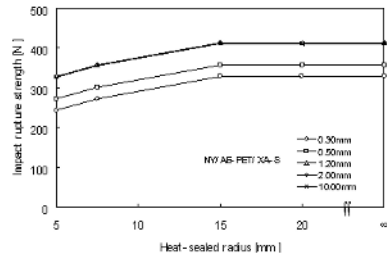


FIGURE 3 Relationship between impact rupture strength and heat-sealed radius

References

1. Aoki H., Shimamoto A., Futase K. and Kamada Y., *Journal of the Japanese Society for Non-Destructive Inspection*, vol. 55, 340-344, 2006

## CRACK INHIBITION EFFECT OF TiNi FIBER REINFORCED CFRP COMPOSITE

Doyeon Hwang and Akira Shimamoto  
Advanced Science Laboratory, Saitama Institute of Technology  
1690 Fusaiji, Fukaya, Saitama 369-0293, Japan  
hwang@sit.ac.jp, shimamot@sit.ac.jp

Recently, the TiNi fiber reinforced composite has attracted much attention as an intelligent material. Moreover, the complex material which makes the best use of the strengthening the fiber is a fiber reinforced composite. Especially, fiber reinforced plastics (FRP) has been used in practical engineering widely at present.

In this study, the TiNi fiber reinforced CFRP (Carbon Fiber Reinforced Plastic, P3052S-17, 8131 TORECA, Toray Co. Ltd.) composites were developed. Various levels of prestrain  $\varepsilon = 0, 1, 3,$  and  $5\%$  were applied to the embedded TiNi fiber and angles of CFRP layer  $0, 45^\circ$  and  $90^\circ$ . The thin layer of photoelastic material was coated on the surface of the specimen, and then the specimens were processed with a pre-crack on one side. (Fig. 1) Tensile tests under constant load were carried out for the specimens made of this composite. The reduction effect of the stress concentration, enhancement of mechanical properties and resistance of deformation of the TiNi fiber reinforced CFRP composites were investigated, and action of the crack closure due to the shape memory effect was studied by using the reflection photoelasticity method.

The testers used for this experiment is Tensiron/RTM-1T tensile device with an isothermal bath, and a reflection photoelastic device. We caused the stress concentration at the crack tip so that the 5 or 6th photoelastic fringe order appeared. Subsequently, we heated the entire specimen in eight steps in the isothermal bath. The stages of ambient temperature are 20, 30, 40, 50, 60, 70, 80, and  $90^\circ\text{C}$ . This way we caused the shape memory reverse transformation above the  $A_f$  temperature. The changes in  $K_I$  value at the crack tip due to the heating shrinkage of the TiNi fiber is observed from the changing photoelastic fringe pattern at the crack tip part. We sequentially take a picture of the photoelastic fringe pattern with CCD (charge-coupled device) camera. They are analyzed by a personal computer according to the temperature change. One of the problems with this method is that the photoelastic fringe order decreases as the compressive force is generated above the reverse transformation temperature ( $A_f$ ). This may cause the inaccurate measure of the stress intensity factor. To solve this problem, we employ the technique of fringe doubling and sharpening was employed. As calculating the stress intensity factor  $K_I$  value from the photoelastic fringe patterns, we measure the distance  $r_m$  and the angle  $\theta_m$  from the crack tip to the furthest point on the fringe. Then, we plug the values in Eq. 1.

$$K_I = \frac{n\sqrt{2\pi t_m}}{\alpha \sin \theta_m} \left[ 1 + \left( \frac{2}{3 \tan \theta_m} \right)^2 \right]^{-0.5} \left[ 1 + \frac{2 \tan(3\theta_m / 2)}{3 \tan \theta_m} \right] \quad (1)$$

Where  $n$  is fringe order,  $t$  is specimen thickness, and  $\alpha$  is a photoelastic sensibility, respectively. To minimize the error, we use the range of  $\theta_m$  where  $73.5^\circ < \theta_m < 134^\circ$ . For the same reason, we calculate  $K_I$  values from 2 or 3 fringe loops. Then, we estimate the mean  $K_I$  value from them. We calculate  $\alpha$  that is a photoelastic sensibility from the Eq. 2. We substitute  $\alpha$  and  $t$  that is thickness of the coating sheet into the Eq. 1 to calculate the stress intensity factor by the photoelastic coating method.

$$\alpha = 1 / \left( \frac{\lambda}{K} \frac{E}{1 + \nu} \right) \tag{2}$$

In the Eq. 2,  $\lambda$  is light wavelength (white light,  $0.577\mu\text{m}$ ),  $K$  is a strain optical coefficient,  $E$  is the Young's modulus, and  $\nu$  is Poisson's ratio according to the coating sheet, respectively.

Stress intensity factor  $K$  value was determined by using reflection photoelasticity to examine the crack closure effect of the TiNi fiber reinforced CFRP composites. The result was confirmed that the crack closure effect improved greatly.

The shape memory effect and thermal expansion behavior of the matrix caused by temperature increasing examined the fracture resistance improvement effect by the decrease of stress intensity factor  $K$  value. It was confirmed that the effect of crack closure is attributed to the compressive stress field in the matrix due to shrinkage of the TiNi fibers above austenitic finishing temperature ( $A_f$ ).

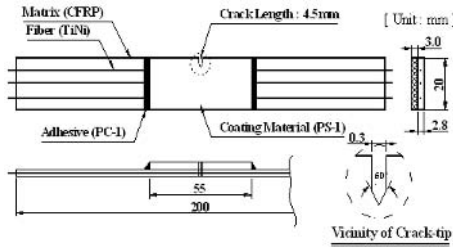


FIGURE 1 Dimension of SMA TiNi /CFRP composite

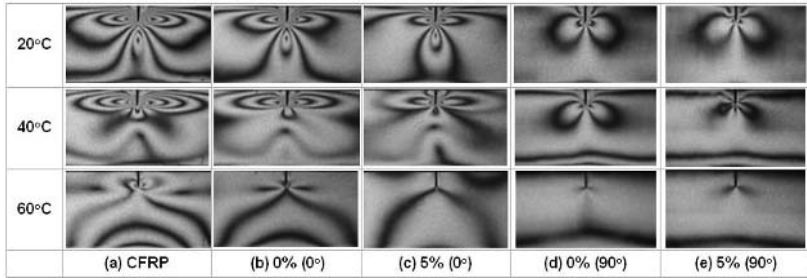


FIGURE 2 Fringe pattern of different temperature at the prestrain and layer angle (Dark field)

**References**

1. Yamada, Y., Taya, M. and Watanabe, R., *Matl. Trans., JIM*, vol. **34-3**, 254-260, 1993.
2. Shimamoto, A. and Taya, M., *JSME Journal*, vol. **63-605**, 26-31, 1997.

## DAMAGE INSPECTION AND EVALUATION IN THE WHOLE VIEW FIELD USING LASER

Akira Kato and Tin Aung Moe  
Dept. Mechanical Engineering, Chubu University  
Kasugai, Aichi 487-8501, Japan  
katoa@isc.chubu.ac.jp

We have investigated methods to evaluate fatigue damage of steels without contact using laser. In the earlier stage of fatigue, slipbands are produced on a metal surface and the slipband density increases with progress of fatigue damage. Diffusion pattern of the reflected laser light from the specimen surface changes due to surface change. Using this method, we are able to detect fatigue damage based on diffusion pattern change due to surface property change caused by slipbands. We developed a fatigue sensor using a spot beam of a He-Ne laser. We tried to evaluate fatigue damage at a point of a steel specimen observing diffusion pattern reflected by a spot beam and made fatigue life estimation observing diffusion pattern change during fatigue. The method is found to be effective for fatigue damage evaluation and estimation of fatigue life. The method is applicable for pointwise observation at fatigue damaged zone, Kato [1]. It is necessary to find first a position that fatigue damage starts to occur in a machine structure, however. In the present study, we investigated methods to observe fatigue damage in the whole view field. We tried to make both detection of fatigue damaged zone and evaluation of fatigue by this method.

Two kinds of optical setups were used. One is that collimate beam of a laser illuminates the specimen surface and observe the speckle pattern formed on the specimen surface and the other is that slit beam illuminates the specimen and diffusion pattern by the reflected light is observed formed on a screen placed in front of the specimen and observation in whole view area was made scanning the slit beam on the specimen surface. The method of the slit beam is illustrated in Fig. 1 and the optical setup is shown in Fig. 2. Fatigue tests were made using mild steel. Test specimen is a plate with edge notches at both sides shown in Fig. 1. Diffusion pattern was observed during fatigue loading. Figure 3 shows the superimposed image of the diffusion patterns by the slit beam at seven different locations on the specimen surface at the number of loading cycles  $N = 3 \times 10^4$  and  $15 \times 10^4$ . Figure 3 (a) shows the speckle pattern on the surface. Dark part of the image is the fatigue damaged zone. Fatigue damaged zone broadens with increase of the number of loading cycles. Figure 3 (b) shows that image of the reflected light from slit beam at each position of the scanning. The image shows clearly that the light intensity decreases at the position where fatigue damage occurred and the area where the light intensity decreases broadens with increase of  $N$ . These images show that the fatigue damaged zone is clearly visualized by this method.

Figure 4 shows gray level distribution of diffusion patterns at fatigue damaged zone at different numbers of loading cycles  $N$ . The distribution shows that gray level at the center decreases and gray level distribution broadens with increase of  $N$ . This shows that gray level distribution at the fatigue damaged zone changes with progress of fatigue damage. It will be possible to evaluate fatigue damage by the observation of gray level distribution of the diffusion pattern of laser at fatigue damaged zone.

The method described in this study has many aspects in fatigue damage inspection. It is useful to visualize fatigue damage in materials as light intensity distribution of diffusion pattern and fatigue damaged zone can be detectable from the image as shown in Fig. 3. It will also be possible to evaluate fatigue damage by observing the light intensity distribution of the diffusion pattern in the fatigue damaged zone.

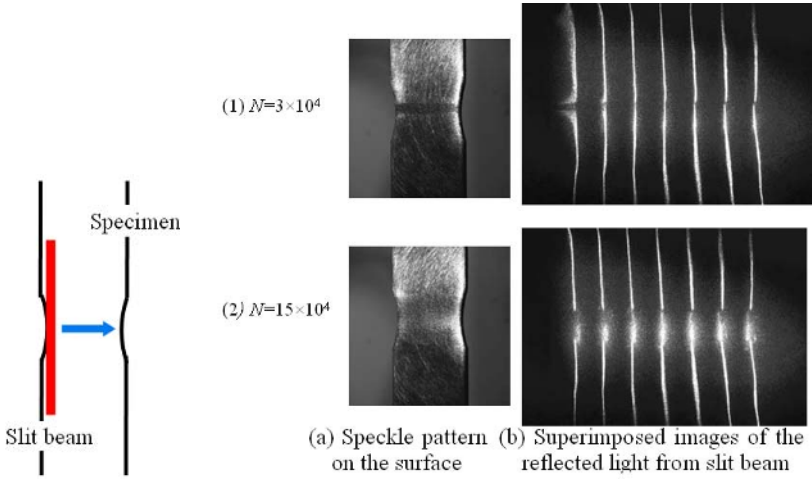


FIGURE 1.

FIGURE 3.

FIGURE 1. Fatigue damage inspection by laser beam scanning (mild steel)

FIGURE 3. Fatigue damage inspection by reflected light from slit beam

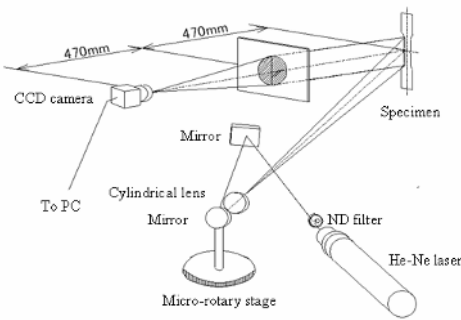


FIGURE 2.

FIGURE 2. Optical setup for slit beam

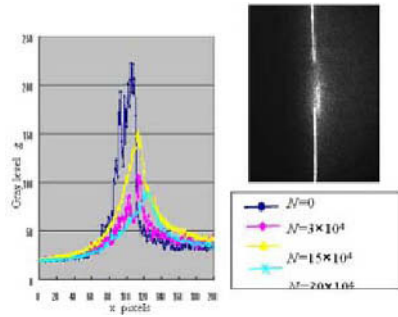


FIGURE 4.

FIGURE 4. Change in light intensity distribution depending on fatigue damage

**References**

1. Kato A., Detection of Fatigue Damage in Steels Using Laser Speckle, *Optics and Lasers in Engineering*, vol. 33, 323-333, 2000



## BEHAVIORS OF YOUNG'S MODULUS BY CONSTRICTION OF REINFORCED SMART TINI-FIBER COMPOSITE

Teruko Aoki and Akira Shimamoto  
 Oita National College of Technology  
 1666 Maki, Oita-shi, Oita, 870-0512, Japan  
 Advanced Science Laboratory Saitama Institute Technology  
 1690 Fusaiji, Okabe, Saitama, 369-0293, Japan  
 aoki@oita-ct.ac.jp, shimamot@sit.ac.jp

Recently, Shape Memory Alloy (SMA) has been researched and developed as one of the most valuable and feasible materials because of its high performance comparable to those of living organisms in such points as perception, judgment and respond and so on.

Previously, the present authors proposed a design concept[1] of composite materials imbedded by SMA fiber, which can restore itself and strengthen on the high temperature side by generating compressive stress inside the matrix by using shape recovery/restoration effects caused by reverse transformation on the high temperature side by applying instant electric current to the imbedded SMA fiber.

In this research, TiNi-fiber-reinforced /epoxy-resin composite materials were made, based on the above design concept. Using specimen models, assuming structure-members to be able to decrease the excessive member stress caused by attack from earthquakes or sudden accidents, the central part was experimented in vibration tests. The variations of Young's modulus of TiNi-fiber accompanied by contraction under electric heating, fiber volume-fraction and pre-strain volume were measured and evaluated. The specimen's Young's modulus  $E$  was obtained by the equation (1) by measuring resonance frequency when the imbedded TiNi fiber was applied by electric current.

$$E_i = n_i^2 \left( \frac{2\pi\ell^2}{\lambda_i^2} \right) \frac{\gamma A}{I g} \quad (i = 1, 2, 3 \dots \dots) \quad (1)$$

Here,  $n_i$  is character frequency of  $i$ -th-order,  $l$  is the lengths of the specimen,  $\gamma$  is weight volume ratio,  $A$  is the cross section area of the specimen,  $I$  is the cross section of the geometrical moment of inertia and  $g$  is the gravitational acceleration.  $\lambda_i$  is the value obtained by numerical analysis method from characteristic equation of vibration. Each Young's modulus was calculated by the resonance frequencies of the first, second and third order, respectively, and the average value was set to be Young's modulus  $E$ . The results are shown in Fig.1 and Fig. 2.

Fig. 1 shows the relationship between the pre-strain value and Young's modulus, and Fig. 2 shows the relationship between applied current and Young's modulus. As is seen from Fig.1, the Young's modulus increases in accordance with the increase of pre-strain value, fiber volume fraction, and constriction of SMA. However, from Fig. 2, the following can be observed: in the case of pre-strain value 0%, the Young's modulus is constant, despite the increase of the applied

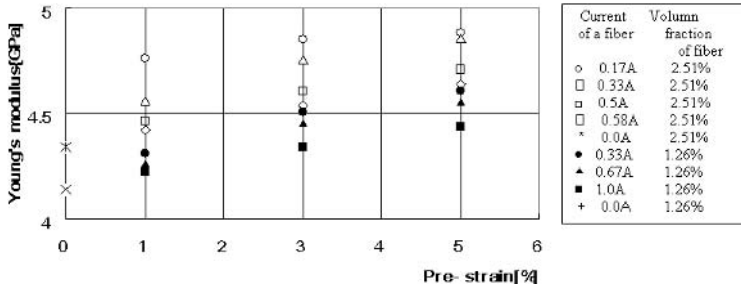


FIGURE 1. Relationship between pre-strain and Young's modulus

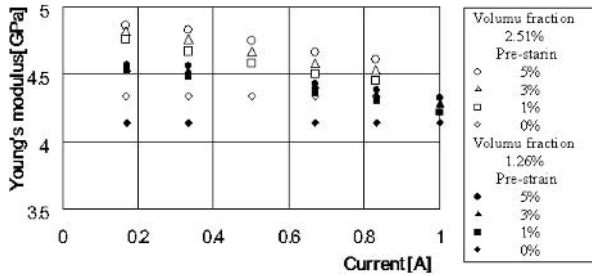


FIGURE 2. Relationship between current and Young's modulus

current: in the case of pre-strain 5% and volume fraction 2.51%, the Young's modulus lies 4, 8 ~ 4, 6 between 0, 17A ~ 0, 83 of applied current values: and in the case of volume fraction 1.26%, the values are found to be slightly lowered 4, 6 ~ 4, 3. It has already reported that the Young's modulus of composite matrix decreases in accordance with the rise of temperature[2]. The Young's modulus E of SMA can be described as follows.

$$E = V_m E_m + V_f E_f \tag{2}$$

Here,  $V_m$ : Volume fraction of Matrix,  $E_m$ : Young's Modulus of Matrix,  $V_f$ : Volume fraction of SMA-fiber:  $E_f$ : Young's modulus of SMA-fiber

As equation (2) shows, the Young's modulus of SMA can be obtained by the matrix, the Young's modulus of imbedded fiber into the matrix and volume fraction. But, in the case of pre-strain of TiNi fiber 0%, the Young's modulus lowers despite the increase of the applied current value, which can be considered to be the influence of  $V_m$  and  $E_m$  of the matrix. From the results, it is confirmed that the Young's Modulus of TiNi fiber reinforced composite materials can be obtained by the applied current.

**References**

1. Shimamoto, A. and Taya, M, *JSME(A)* **67**, 654, 2001.
2. Ishida, M, Teshima, N and Takahashi, S, *Proceeding of APCSMS*, edited by GAO Zhen-Tong, International Academic Publishers , China, 1996

## EVALUATION OF MIXED-MODE THERMAL STRESS INTENSITY FACTOR AT VARIOUS TEMPERATURES

Masahiro Suetsugu<sup>1</sup>, Kouichi Sekino<sup>2</sup>, Takashi Nishinohara<sup>3</sup> and Koji Shimizu<sup>4</sup>

<sup>1</sup> Suzuka National College of Technology, Shiroko, Suzuka, Mie 510-0294, Japan

<sup>2</sup> Japan Power Engineering and Inspection Corporation

<sup>3</sup> Graduate School of Eng., Kanto Gakuin University (Present; Marui Industrial Co., Ltd.)

<sup>4</sup> Kanto Gakuin University  
suetsugu@mech.suzuka-ct.ac.jp

We attempted to evaluate the mixed-mode thermal stress-intensity factors by using the method of caustics at high temperatures and at low temperatures. The following results are obtained in this study.

- Theoretical caustic patterns are calculated in various cases mentioned below.
  - The ratio of  $K_I$  and  $K_{II}$
  - The combination of signs of plus-minus of  $K_I$  and  $K_{II}$
  - The optical properties of materials
  - The optical system using for the experiment
- Configuration of the specimen is shown in Fig. 1. Bottom edge of the notched plate of glass is heated to 673K. Example of caustic patterns is shown in Fig. 2. These caustic patterns are obtained by using a convergent light system, therefore, the sign of  $K_I$  should be negative. On the other hand, caustic patterns similar to shown in Fig. 2 are obtained by using a parallel light system in case of the natural crack, therefore, the sign of  $K_I$  in this condition is positive.

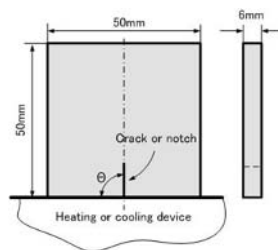


FIGURE 1. Configuration of the specimen of glass plate.

- Caustic patterns observed from the heated glass plate with an inclined notch are shown in Fig. 3. In comparison between the caustic pattern at  $t=5s$  and that one at  $t=180s$ , the direction of aberration of asymmetric caustic pattern is opposite each other. This means that the sign of  $K_{II}$  varies from positive to negative with time  $t$ .

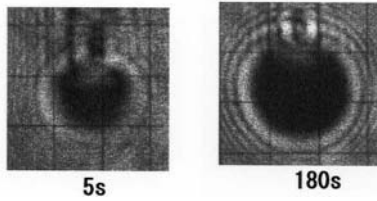


FIGURE 2. Example of caustic patterns for glass plate with a notch at 673K by convergent light



FIGURE 3. Example of caustic patterns for glass plate with an inclined notch at 673K by convergent light ( $\theta = 45^\circ$ )

4. Caustic patterns at low temperatures,  $T=233\text{K}$  and  $T=123\text{K}$ , are obtained from the cooled glass plates same as shown in Fig. 1. In these low temperature conditions, whether a notch or a natural crack, the sign of  $K_I$  is positive.
5. Crack is propagated from an initial notch or a crack in some temperature conditions. The values of  $K$  at the moment of crack initiation are shown in Table 1. The values of  $K_c$  shown in Table 1 are almost the same as static fracture toughness of the material.

TABLE 1. Fracture toughness values of glass at various temperatures

	$K_c/\text{MPam}^{1/2}$
$T=473\text{K}$ , natural crack	0.70
$T=123\text{K}$ , natural crack	0.90
$T=123\text{K}$ , notch	1.35

6. The direction of crack propagation is in accordance with the theory of  $\sigma_{max}$  at high temperatures and at low temperatures. However, the crack propagation direction is abruptly varies right after the initiation of crack propagation at low temperatures. We revealed that this phenomenon is caused by the existence of compressive stress in the specimen by FEM analysis.

## STRESS ANALYSIS OF AN UNPRESSURIZED ELASTOMERIC O-RING SEAL INTO A GROOVE BY PHOTOELASTIC EXPERIMENTAL HYBRID METHOD

Jeonghwan Nam<sup>1</sup>, Jaisug Hawong<sup>1</sup>, O.-Sung Kwon<sup>2</sup>, Songling Han<sup>2</sup> and Gun Kwon<sup>2</sup>

<sup>1</sup> School of Mechanical Engineering, Yeungnam Univ.,

<sup>2</sup> Graduate School of Mechanical Engineering, Yeungnam Univ.,

214-1 Daedong Gyeongsan, Gyeongbuk (712-749) Korea

jhnam2@ynu.ac.kr, jshawong@ynu.ac.kr, kwon0123@korea.com,

hansongling2005@hotmail.com, gunbbang80kg@nate.com

In this research, contact stresses of O-ring with uniform deformation in upper and lower direction are analyzed by photoelastic experimental hybrid method.

The O-ring is made from rubber and is used to sealing of the high pressure vessel.

The compressive deformation ratios of O-ring are 10% and 20%. Stress components ( $\sigma_{xx}$ ,  $\sigma_{yy}$ ,  $\tau_{xy}$ ) of O-ring under uniform deformation obtained from the photoelastic experimental hybrid method are almost identical to those from Hertz's theory. Therefore, stress freezing method and photoelastic experimental hybrid method are effectively applied to the stress analysis of O-ring made from rubber that under uniform deformation. The loading device developed in this research is used to produce the uniform deformation of O-ring for stress freezing.

Using the photoelastic experimental hybrid methods, isochromatic fringe patterns by photoelastic experiment and using the Hertz solution, the internal stress components and the contact stresses are obtained. And then they are compared each other. We can confirm the internal stress fields of O-Ring under each uniform contractive ratio by developed photoelastic experimental hybrid method. Stress distributions at the upper contact surface of O-ring are almost identical to those from the lower contact surface of O-ring.

Maximum of  $\sigma_{yy}$  and  $\tau_{xy}$  are occurred at the center of contact length. However, maximum of  $\sigma_{xx}$  is occurred at the right side moved from the center of contact surface length by little.

The maximum of  $\sigma_{xx}$  is greater than that of  $\sigma_{yy}$  by little.

The maximum of  $\sigma_{xx}$  and  $\sigma_{yy}$  are increased by similar ratio in accordance with the squeeze deformation ratio increasing.

In this research, we measured the contact length (upper, lower and right side) of O-ring under uniform deformation using stress freezing method.

As shown in Fig. 1 and Fig. 2, the contact stress  $\sigma_{yy}$  of upper side under uniform deformation are compared between Hertz solution and photoelastic experimental hybrid method.

Fig. 3 shows the internal stress field  $\sigma_{yy}$  for upper side and lower side under 10% uniform deformation using photoelastic experimental hybrid method which developed in this research.

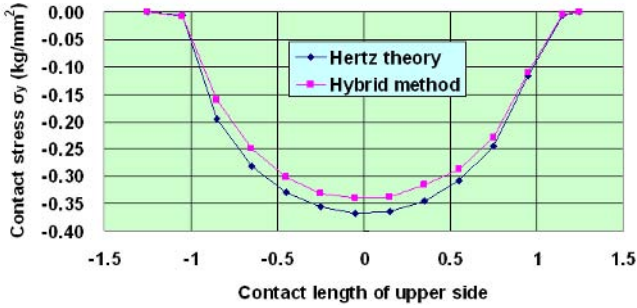


FIGURE 1. Stress component ( $\sigma_{yy}$ ) under 10% uniform deformation at the upper side

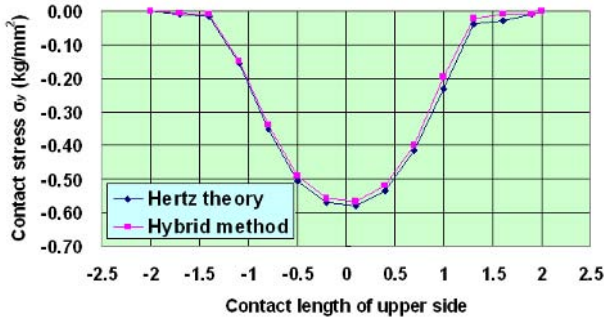


FIGURE 2. Stress component ( $\sigma_{yy}$ ) under 20% uniform deformation at the upper side

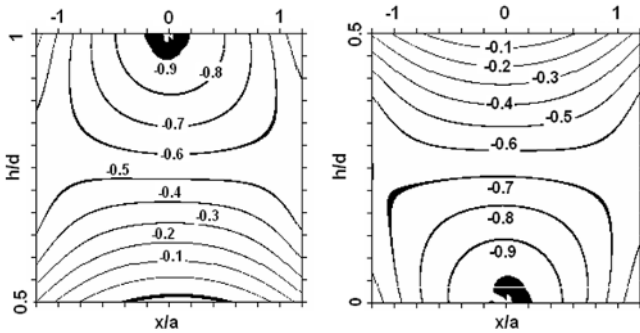


FIGURE 3. Internal stress field using photoelastic experimental hybrid method (10% uniform deformation)

## EVALUATION IN SKIN BY HIERARCHICAL SEPARATION VISCOELASTICITY MEASUREMENT BY RHEOMETER

Tetsuya Nemoto<sup>1</sup>, Zenzo Isogai<sup>2</sup>, Kazuharu Koide<sup>2</sup>, Yasumi Itoh<sup>2</sup>,  
Hroyuki Matsuura<sup>2</sup> and Akira Shimamoto<sup>3</sup>

<sup>1</sup>National Institute for Longevity Sciences,  
6-3 Gengo, Morioka, Obu, 474-8522 Aichi, Japan

<sup>2</sup>National Institute for Longevity Sciences, NCGG

<sup>3</sup>Saitama Institute of Technology  
nemo@nils.go.jp

The engineering of human tissue represents a major technique in clinical medicine [1]. Material evaluation of skin is important as preventive medicine. Decubitus originates in pressure and the rub [2-4]. However, shearing in the skin has exerted the influences on the sore pressures most [5]. This paper examines one demand of crucial importance, namely the real time in vivo monitoring of the shearing characteristics skin tissue. Rheometer is a technology developed to measure viscoelasticity of solid and liquid. To measure viscoelasticity of the skin in the noninvasive with this device, we remodeled it. It is ideal for the continuous monitoring of tissues in vivo.

Fig. 1 shows the rheometer used by this research. This measuring instrument machine is AR550 made by TA Instruments, and the angular velocity is 100rad/s, and the situs perversus resolution ability is 0.62 $\mu$ rad.

The photograph under measurement is shown in Fig. 2. The photograph of Fig. 2 is in the measurement status of the ramus-palmaris-nervi-ulnaris palmar upper part. It was performed as follows so that the disk of a probe and operation of the skin might be in agreement. A probe disk and the skin attached the fixed jig on the measurement stage so that it might become isofacies.



FIGURE 1. Three point bend specimen.

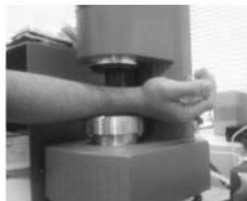


FIGURE 2. Photograph at viscoelasticity determination of forearm part

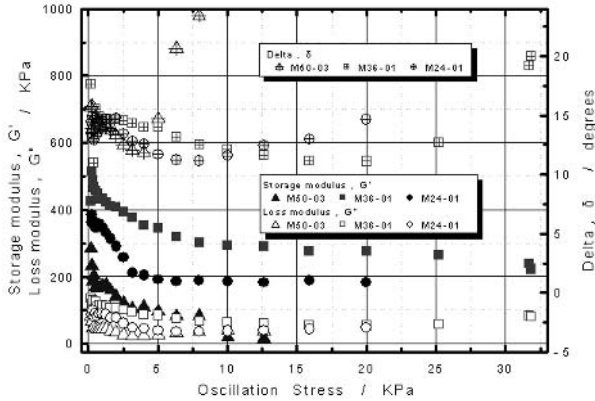


FIGURE 3. Viscoelasticity determination result of a male forearm part

The viscoelasticity determination result of the forearm palmar part of 24 years old, 36 years old, and 50 years old male is shown in Fig. 3. M24-01 is 24 years old, M36-01 is 36 years old, and M50-03 is 50 years old. Moreover, all measurement persons are men. As for the phase angle delta, a big change was not seen although storage modulus  $G'$  and loss modulus  $G''$  changed with measurement conditions, such as a measured region and forcing power, a lot during measurement. Here, when its attention is paid to delta, in M50-03, it understands that agitation of the skin becomes large and it is impossible to follow to displacement near the amplitude stress 10KPa. However, in M36-01 and M24-01, most agitation was not seen (20KPa or more), but was understood that displacement of a probe and the skin is almost the same. Moreover, change was not accepted in the range until a phase progresses with the increase in stress in all the measurement results of whose were about 13 degrees in 5KPa or less, however M50-03 and a phase angle results in 20KPa in M36-01 and M24-01.

## References

1. Ghosh Peter and Guidolin Diego, *Semin Arthritis Rheum*, vol. **32**, No.1, 10-37, 2002.
2. Powell, Courtney A; Smiley, Beth L; Mills, John; Vandenburg and Herman H, *Am J Physiol Cell Physiol*, vol. **283**, No.5, C1557-1565, 2002.
3. Xisto Debora G, Farias Luciana L, Ferreira Halina C, Picanco Miguel R, Amitrano Daniel, Lapa E Silva Jose R, Negri Elnara M, Mauad Thais, Carnielli Denise, Silva Luiz Fernando F, Capelozzi Vera L, Faffe Debora S, Zin Walter A and Rocco Patricia R M, *Am J Respir Crit Care Med*, vol. **171**, No.8, 829-837, 2005.
4. Pathak A P, Silver-Thorn M B, Thierfelder C A and Prieto T E, *IEEE Trans Rehabil Eng*, vol. **6**, No.1, 12-20, 1998.
5. Galbraith J A, Thibault L E and Matteson D R, *J Biomech Eng* vol. **115**, No.1, 13-22, 1993.



## A NEW METHOD FOR INVESTIGATING THE MECHANICAL PROPERTIES OF TWIN WALLS

Haika Drezner and Doron Shilo

Department of Mechanical Engineering, Israel Institute of Technology

Department of Mechanical Engineering, Technion, Haifa 32000, Israel

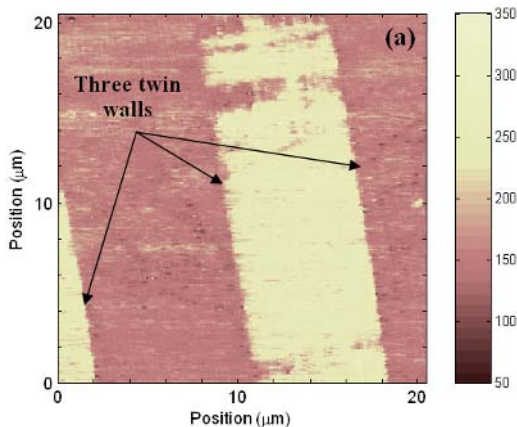
haika@tx.technion.ac.il

The microstructural twin pattern and its kinetics are responsible for the electro/thermo mechanical response of a broad class of active materials including ferroelectrics and shape memory alloys. These, in turn, are governed by the properties of twin walls that separate between different twin variants/domains.

Despite the important role of twin walls, their structure and properties are still ambiguous as they can be quite narrow, in the nanometer scale, in many materials of interest. In particular, the spatial changes of mechanical properties in a vicinity of individual twin walls have not been explored yet.

We present a new method for investigating the mechanical properties of a twin wall with nano-scale resolution. The method is based on a modulus mapping technique, implemented by means of a hybrid nanoindentation and force modulation instrument, which has been developed by Syed Asif *et al.* [1,2]. Recently, Ganor and Shilo [3] introduced a procedure for finding the experimental parameters that provide an optimal modulus contrast and demonstrated the technique's capability to resolve between regions with elastic moduli as close as 5%. We apply this procedure to study the changes of elastic moduli, with nm-scale resolution, in a close vicinity of individual twin walls in BaTiO<sub>3</sub> and PbTiO<sub>3</sub> crystals.

An example for modulus mapping taken from BaTiO<sub>3</sub> single crystal is represented in Fig. 1. The image exhibits a very clear contrast, which reveals three twin walls separating between domains with an in-plane and an out-of-plane orientation. Mappings of both the storage and loss moduli taken from a close vicinity of individual twin walls will be presented and twin wall properties will be discussed.



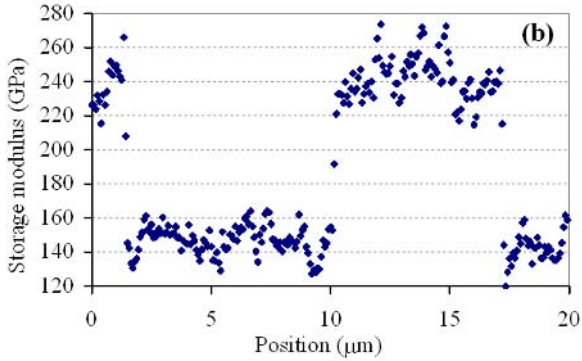


FIGURE 1. (a) Storage modulus maps taken from a BaTiO<sub>3</sub> single crystal at frequency of 780 Hz.  
(b) Storage modulus cross section taken from one of the 256 line scans composing Fig. 1(a)..

### References

1. Syed Asif, S. A., Wahl, K. J., and Colton, R. J., *Rev. Sci. Instrum.* vol. **70**, 2408, 1999.
2. Syed Asif, S. A., Wahl, K. J., Colton, R. J., and Warren, O. L., *J. Appl. Phys.* vol. **90**, 1192, 2001.
3. Ganor, Y., and Shilo, D., *Appl. Phys. Lett.* vol. **88**, 2006.

## OPTO - MECHNAICAL RELIABILITY STUDIES OF ALN DRIVEN CANTILEVERS

A. Andrei<sup>1</sup>, K. Krupa<sup>1</sup>, L. Nieradko<sup>1</sup>, C. Gorecki<sup>1</sup>, L. Hirsinger<sup>2</sup>, P. Delobelle<sup>2</sup>, J. Kacperski<sup>3</sup>  
and M. Jozwik<sup>3</sup>

<sup>1</sup>Department of Optics LOPMD, FEMTO-ST, 16 Route de Gray 25030 Besancon, France  
alexandru.andrei@femto-st.fr, kkrupa@univ-fcomte.fr, lukasz.nieradko@femto-st.fr,  
christophe.gorecki@univ-fcomte.fr

<sup>2</sup>Department of Applied Mechanics LMARC, FEMTO-ST, 24 Chemin de l'Epitaphe 25000  
Besancon, France  
lhirsing@univ-fcomte.fr, patrick.delobelle@univ-fcomte.fr

<sup>3</sup>Institute of Micromechanics and Photonics, Warsaw Univ. of Technology,  
8 Sw. A. Boboli St., 02-525 Warsaw, Poland  
j.kacperski@mchtr.pw.edu.pl, jozwik@mchtr.pw.edu.pl

MicroElectroMechanical Systems (MEMS) represent an extraordinary technology that promises to transform whole industries and drive the next technological revolution. These devices can replace bulky actuators and sensors with micrometer scale equivalents that can be produced in large quantities by silicon micromachining. MEMS improved functionalities and potential capabilities have brought in range many different application fields, including optical communications, medicine, guidance and navigation systems, RF devices, weapons systems, biological and chemical agent detection, and data storage. Because the field of commercial MEMS is still in its infancy, there is nevertheless an important issue for new MEMS which still requires advanced research, i.e. MEMS reliability.

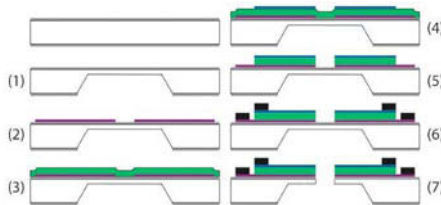


FIGURE 1. Technological process flow chart.

The goal of this study was the investigation of multilayer cantilevers, operating as MEMS actuators. The transducer material is a promising material for MEMS/MOEMS applications : aluminium nitride (AlN) [1]. The AlN driven microbeams were fabricated on 380- $\mu\text{m}$  thick, 3'' (100) oriented Si wafers. The process flow is shown in Fig. 1. After realizing a 15  $\mu\text{m}$  thick Si membrane by KOH etch of bottom side of the wafer (step 1), on the top side are successively deposited three thin layers : two CrNi PVD metal layers (150 nm at step 2 and 350 nm at step 4) that have between them the AlN film. The 1  $\mu\text{m}$  of AlN has been deposited (step 3) in a pulsed reactive DC sputtering machine. The top CrNi electrode patterned at step 4, has been used as a hard mask during AlN and silicon etching (steps 5 and 7). The last RIE step removed the silicon which was not protected by the CrNi hard mask, transforming the initial Si membranes into an array of free standing cantilevers. They had a constant width of 50  $\mu\text{m}$  and variable lengths from

200  $\mu\text{m}$  up to 900  $\mu\text{m}$ . The final device has been diced and connected to the package. Prior the fabrication of the devices, a series of test structures has been realized. They allowed the measurement of the stress in the films and the influence of the bottom electrode nature over the stress in the AlN film. Nano-indentation tests were performed on the AlN films of the test structures using a nanoindenter IIS (Nano-Instruments) with a Berkovich tip. The study was conducted following the continuous contact stiffness measurement procedure [2] with a frequency of 45 Hz and an indenter vibration amplitude of 1 nm during the penetration on the tip into the sample. It allowed the determination of the  $M\langle hkl \rangle$  modulus for AlN deposited on Pt and CrNi electrodes.

The technological process of cantilevers fabrication has an influence on the flatness and initial shape of microstructures. The deposition and etch of multiple thin layer on an initially straight Si introduces internal compressive stress and generates bending. In order to investigate the initial parameters and long term stability, the behaviour of the cantilevers has been studied by interferometry. The measurement system was a multifunctional interferometric platform dedicated MEMS/MOEMS testing [3]. It gives the possibility to combine the capabilities of interferometry methods to find static (e.g., initial shape as shown in Fig. 2, static out-of-plan displacements) and dynamic parameters of samples (e.g., resonance frequencies and amplitude distributions in vibration modes).

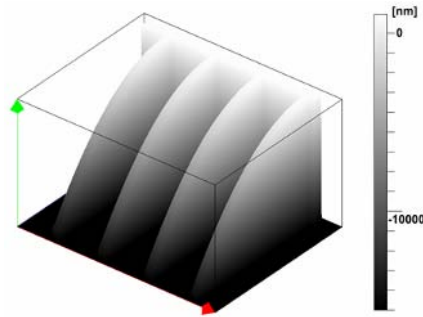


FIGURE 2. The initial deflection of 700m long cantilevers.

## References

1. Ruffieux D., Dubois M.A. and de Rooij N.F., In *Proceedings of the 13th Annual International Micro Electro Mechanical Systems Conference*, IEEE, Miyazaki, 2000, 662-667.
2. Oliver W.C. and Pharr G.M., *J. Mater. Res.*, vol. 7, 1992, 1564-1583.
3. Gorecki C., Jozwik M. and Salbut L., *J. Microlith., Microfab., Microsyst.* vol. 4, 2005, 041402.

## INSTABILITIES IN NANOSTRUCTURED MATERIALS

K.T. Ramesh<sup>1</sup>, S.P. Joshi<sup>1</sup> and B.E. Schuster<sup>2</sup>

<sup>1</sup>Department of Mechanical Engineering  
The Johns Hopkins University  
Baltimore, MD 21218, USA

<sup>2</sup>Army Research Laboratory  
Aberdeen Proving Ground, MD 21005, USA  
ramesh@jhu.edu

We present results on (a) relatively new “nano-micro” composites that are consciously developed by controlling structure at two different length scales, and (b) on metallic glasses (which may be viewed as an extreme case of “nanostructure”).

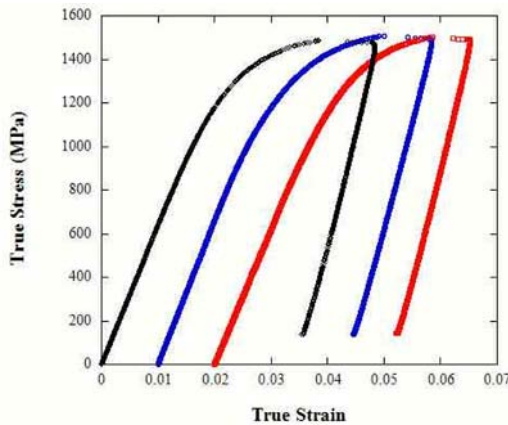


FIGURE 1. Stress-strain curves obtained from nanocrystalline nickel in microcompression.

Microcompression experiments (with specimens 20  $\mu\text{m}$  in diameter and 40  $\mu\text{m}$  tall) are described that provide the first measurements of the response of a nanostructured nickel (grain size 20 nm) to significant plastic strains [1]. At larger length scales, we describe results obtained on a nano-micro composite in compression at both low and high strain rates, and discuss shearing instabilities in nanomaterials [2].

### References

1. Schuster, B.E., et al., *Microcompression of Nanocrystalline Nickel*. Applied Physics Letters, 2006. **88**(103112).
2. Jia, D., K.T. Ramesh, and E. Ma, *Effects of Nanocrystalline and Ultrafine Grain Sizes on Constitutive Behavior and Shear Bands in Iron*. Acta Materialia, 2003. **51**(12): p. 3495-3509.

## USE OF INSTRUMENTED MICROINDENTATION TO DETERMINE THE GLOBAL MECHANICAL BEHAVIOR OF NANOCRYSTALLISED COPPER SAMPLES

L. Waltz<sup>a</sup>, B. Guelorget<sup>a</sup>, D. Retraint<sup>a,\*</sup>, A. Roos<sup>a</sup> and J. Lu<sup>a, b</sup>

<sup>a</sup> Institut Charles Delaunay, FRE CNRS 2848, LASMIS, University of Technology of Troyes, 10000 Troyes, France

<sup>b</sup> Department of Mechanical Engineering, Hong Kong Polytechnic University, Hung Hom Kowloon, Hong Kong

\*delphine.retraint@utt.fr

The excellent corrosion properties of copper justify its use in a large number of industrial applications, in spite of its low strength in the traditional state. To overcome this problem and to enhance the mechanical behavior of this material, the Surface Mechanical Attrition Treatment (SMAT) seems to be well-adapted [1]. As shown in several previous works, SMA-Treatment induces a grain refinement up to the nanometer scale in the top surface layer of the treated sample, through severe plastic deformation performed at high strain rate. While the grain size of the untreated material is in the micrometer scale, nanograins are generated beneath the treated surface. Between this nanocrystallised layer and the bulk of the sample, a transition layer is also present which is characterised by a grain size gradient: the grain size grows from the nanometer to the micrometer scale as the depth below the treated surface increases. The treated metal can thus be seen as a multilayered material. All these microstructural changes lead to strong modifications of the plastic properties of the samples subjected to SMAT [2] [3]. In the last years, several methods have been proposed to determine the Young's modulus, the yield stress and the strain hardening coefficient using microindentation tests. More recently, Cao and Lu [4] [5] developed a new inverse method to extract plastic properties of metallic materials based on instrumented spherical indentation.

The aim of the present work is the use of instrumented sharp and spherical microindentation tests to determine the mechanical properties of the nanocrystallised and the transition layers. To this end, indentation tests were performed on the cross-section of samples subjected to SMAT, from the top surface to the bulk of the samples (Fig. 1).

A first task has been carried out on the determination of the evolution of the Young's modulus and the microhardness along the cross-section using 500 nm deep sharp indentations.

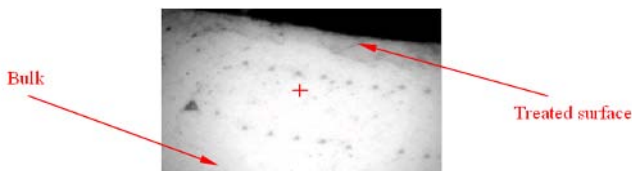


FIGURE 1. Measurement points along the cross-section of a copper sample subjected to SMAT using a Berkovich indenter.

Accordingly to this, spherical microindentations were performed in the different sub-layers of the sample. The maximum indentation depth was 820 nm, i.e.  $1/10^{\text{th}}$  h the tip radius, measured by SEM imaging. Afterwards, the yield stress as well as the hardening coefficient was determined for each sub-layer, using the inverse method developed by Cao and Lu [5].

Finally, the experimental results were implemented in the Zebulon finite element model code in order to simulate the global mechanical response of the samples. The simulated results are in good agreement with the experimental data and show the enhanced mechanical properties of the copper subjected to SMAT.

## References

1. Tao, N.R., Sui, M.L., Lu, J, and Lu, K, *Acta Metallurgica*, vol. **11**, 443-440, 1999.
2. Roland, T., Rehrant, D., Lu, K., Lu, J., *Materials Science Forum*, edited by Trans Tech Publications, Switzerland,, 625-630, 2005.
3. Chen, X.H., Lu, J., Lu, L., Lu K., *Scripta Materialia*, vol. **52**, 1039-1044, 2005.
4. Cao, Y.P., Lu, J., *Journal of Mechanics and Physics of Solids*, vol. **53**, 49-62, 2005.
5. Cao, Y.P., Lu, J., *Acta Materialia*, vol. **52**, 4023-4032, 2004.

## FATIGUE CHARACTERISTICS OF NANO-STRUCTURED TOOL STEEL UNDER LOAD VARIATION BY ULTRASONIC COLD FORGING TREATMENT

Chang-Min Suh<sup>1</sup>, Gil-Ho Song<sup>2</sup>, Min-Ho Kim<sup>1</sup> and Young-Shik Pyoun<sup>3</sup>

<sup>1</sup> School of Mechanical Engineering, Kyungpook National University

<sup>2</sup> Technical Research Center, POSCO

<sup>3</sup> Dept. of Mechanical and Control Engineering, SunMoon University

<sup>1</sup> 1370, Sankyuk-dong, Bukgu, Daegu, Korea 702-701

<sup>1</sup>cmsuh@knu.ac.kr, <sup>2</sup>ghsong@posco.co.kr, <sup>3</sup>pyoun@sunmoon.ac.kr

### Introduction

Recently, the use of high strength steels (HSS) for automotive applications has been drastically increased not only to enhance the safety and durability of vehicles, but also lighten the weight for a high degree of fuel efficiency. In the side trimming operation in the production of HSS and mild steel, knife breakage and burr frequently occur. In addition, such breakage and bad quality of strip cutting face are affected by yield as well as by reduced productivity and reliability on production line [1-5]. This study examined the variation of mechanical properties of nano-structured surface by ultrasonic cold forged tool steel (SKD-61). Same ultrasonic cold forging treatment (UCFT) process was applied to produce the trimming knife. Their effectiveness and reliability of the UCFT were successfully verified through the field test by trimming process in cold rolling line of POSCO.

### Experiments and UCFT

UCFT uses ultrasonic vibratory energy as a source, and tens of thousand times per second are struck on the material surface as constant pressure is applied. These strikes cause severe plastic deformation to surface layers and induce a nano-scale crystal structure. The UCF device consists of several components such as the ultrasonic generator; generating electric ultrasonic frequency, the air compressor; pushing ultrasonic generator unit with constant pressure, the piezo-transducer ( $\text{Pb}(\text{Zr},\text{Ti})\text{O}_3$ ), the booster; amplifying the ultrasonic vibration, the horn; transmitting the ultrasonic vibration and ball tip (tungsten carbide). To verify the feasibility of the UCFT, various experiments were carried out with a tool steel SKD-61, which is the material of the trimming knife used in the cold rolling mill. Specimens were fabricated using the UCF device. 20 kHz of frequency was applied to the ball tip, and the applied static force was 100 N.

### Results and Discussion

Fatigue tests were conducted using Ono type rotary bending machine (H5, Shimadzu Co.) at 3400 rpm of revolution at room temperature, and the specimens were prepared under the JIS Z2274 standard. The fatigue characteristics of smooth specimen, before and after the UCFT, are shown in Fig. 1. The  $10^7$  cycles fatigue limit before the UCFT was 719 MPa, whereas that after the UCFT was 899 MPa, which represent a 25% increase. SEM micrograph of the fracture surface of surface-originating fracture was observed in SKD61 raw material; before the UCF treated smooth specimen. At surface-originating crack site we easily observed an inclusion; its size was about 20  $\mu\text{m}$ . This inclusion is analyzed by EDS and contains Fe 94.51%, Cr 4.86% and V 0.63%. SEM micrographs of interior-originating fracture, fish-eye crack was observed in case of the UCFT



smooth specimen. A fish-eye contains an inclusion is analyzed by EDS and contains Fe 94.63%, Cr 5.37%. From these SEM observations, surface-originating fracture occurred at raw material while interior-originating fracture, fish-eye crack, occurred after the UCFT because of nano structured modification by severe plastic deformation and compressive residual stress in case of the smooth specimen.

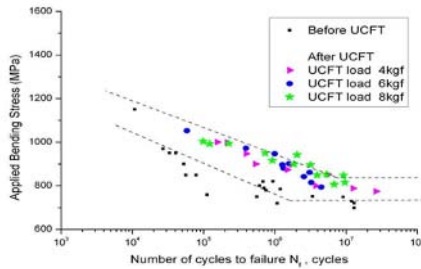


FIGURE 1. S-N curves of smooth specimen before and after the UCFT

## Conclusion

The grain size of SKD61 surface treated by ultrasonic cold-forging treatment (UCFT) becomes very fine to nano-scale crystal and nano-scale structure is observed till certain depth. The surface hardness of SKD61 is increased up to 37% and the compressive residual stress becomes -811 MPa to a 150  $\mu\text{m}$  depth after the UCFT. Fatigue limit of  $10^7$  cycles of SKD61 is increased by 25% after the UCFT at the smooth specimen. Interior-originating fracture, fish-eye crack, occurs after the UCFT because of nano structured modification by surface plastic deformation and compressive residual stress in case of smooth specimen. UCFT improves the mechanical properties effectively and is becoming a practical method to improve the service life of the trimming knives. Productivity and reliability of cold rolling process have improved more than 2 times by the application of the UCFT trimming knives.

## References

1. Hwang, S. Y., 2000, "Improvement of Mechanical Properties of Knife for Tandem Cold Rolling", RIST report
2. Pyoun, Y. S., Han, C. H and Azuma, N, 2001, "Development of an Automated Super Surface Finishing System for the 3D Sculptured Surface of Model and Dies using Ultrasonic Micro Burnishing Technology", Processing of the 32nd ISR

## GAUSSIAN DECOMPOSITION OF NON-STATIONARY RANDOM VEHICLE VIBRATIONS

Vincent Rouillard  
Victoria University  
PO BOX 14428 MCMC, Victoria, Australia  
Vincent.Rouillard@vu.edu.au

This paper addresses some of the deficiencies and limitations of current methods used for synthesising random vehicle vibrations. When wheeled vehicles traverse irregular surfaces, the interaction between the vehicle and the terrain give rise to a dynamic process that produces complex forces and motions within the vehicle. Because pavement surface irregularities are generally random in nature, the resulting vehicle vibrations are also random. Furthermore, the levels of the resulting vibrations are not solely dependent on the pavement roughness but are also a function of vehicle type, payload and vehicle speed. The effect of these parameters tends to make the complex mechanical interactions between the vehicle and pavement surface difficult to characterise and predict. It is therefore widely acknowledged that the analysis and simulation of road-related vehicle vibrations demand some level of sophistication.

Although vibrations generated by road vehicles have been thoroughly studied on numerous occasions, because of their inherent complexity, variability and unpredictability there does not exist a definitive method to predict, analyse or synthesize them. There have been, however, a number of attempts in characterising some aspects of the process. By far the most common approach is to compute the average Power Spectral Density (PSD) of the vibrations. The technique is useful in many ways, such as identifying prevalent frequencies and the overall (RMS) vibration level, and is still widely used today to characterise ride quality. One major drawback of the average PSD is that it effectively describes the average energy level (in this case acceleration) for each frequency band within the spectrum. It does not contain information on time-variant parameters such as possible variations in amplitude or frequency or the time at which these variations occur. Furthermore, the temporal averaging process inherent to the PSD cannot separate the effects of transients within the signal. This is of no consequence if the process is both Gaussian and stationary. In such cases the nature of the signal is well defined by the normal distribution and its higher-order moments. However, as it has repeatedly been shown, road vehicle vibrations can often be significantly non-stationary mainly due to variations in pavement roughness and vehicle speed [1][2]. In such cases the average PSD fails to fully and accurately describe the process.

Charles [3] was one among many to recognize that there existed problems relating to the interpretation of vertical vibration data from road vehicles for use to generate laboratory test specifications. He observed that wheeled vehicle vibrations are “unlikely to be stationary” due to variations in road surface quality and vehicle speed. He also showed that the statistical distribution of vehicle vibrations is more likely to contain large amplitude peaks than a true Gaussian process.

Charles [3], who studied a variety of road types, stated: “even for a good classified road, whole range of surface irregularities may be encountered”. He acknowledged that there exist difficulties associated with distinguishing shocks from vehicle vibrations. He also suggested that the analysis method for characterising non-stationary vehicle vibrations should include the identification of stationary sections using the “RMS time histogram (sic)” (presumably meaning time history), the examination of vibration severity in terms of RMS and peak amplitude as a function of vehicle speed and verification of the normality of the data by computing the amplitude

probability analysis. The non-stationary and non Gaussian nature of road vehicle vibrations has been confirmed in more recent studies [4].

As the importance and significance of optimising protective packaging designs intensifies the need for closer and more accurate monitoring and understanding of hazards in the distribution environment increases.

The paper deals with the development of a technique for decomposing non-stationary random vibration signals into constituent Gaussian elements [4]. It aims at testing a hypothesis that non-stationary road vehicle vibrations can be modelled statistically as a sequence of Gaussian processes with varying standard deviations and durations or segment lengths. These variations in the standard deviation are manifested in the time domain by fluctuations in the overall amplitude of the signal resulting in Probability Density estimates that exhibit highly non-Gaussian characteristics. The paper shows how non-stationary road vehicle vibration signals can, in general, be systematically decomposed into these independent random Gaussian elements by means of a numerical adaptive curve-fitting procedure. The paper describes the development of the algorithm which is designed to automatically extract the parameters of each constituent Gaussian process, namely the RMS level and the Vibration Dose. The validity of the Random Gaussian Sequence Decomposition (RGSD) method was tested using a large set of road vehicle vibration records and was found to be capable of successfully extract the Gaussian estimates as well as the corresponding Vibration Doses. Validation is achieved by comparing the sum of these Gaussian estimates against the PDF of the original vibration record. All validation cases presented here show that the RGSD algorithm is very successful in breaking-down non-stationary random vibration records into their constituent Gaussian processes. The results from the Random Gaussian Sequence Decomposition (RGSD) method are important in that they yield a series of normal random processes which are completely characterized by the second-order statistic (the root-mean-square for zero-mean processes). This is very significant in that it affords great simplicity for the synthesis of normal random vibrations.

## References

1. Richards, D.P. *Environmental Engineering*, Dec. 1990, 23-26.
2. Rouillard, V. & Sek, In *Proceedings of the Institution of Mechanical Engineers.*, vol. **215**, Part D, 1069-1075, 2001
3. Charles, D. *Journal of the Institute of Environmental Sciences*, UK. 37-42, Jan-Feb 1993
4. Rouillard, V. *On the laboratory synthesis of road vehicle vibrations*. PhD thesis, Monash University, Australia (to be published).

## ON THE STATISTICAL DISTRIBUTION OF SEGMENT LENGTHS OF ROAD VEHICLES NON-STATIONARY VIBRATIONS

Vincent Rouillard  
Victoria University  
PO BOX 14428 MCMC, Victoria, Australia  
Vincent.Rouillard@vu.edu.au

This paper addresses an important limitation of current methods used for synthesising random vehicle vibrations. It is self-evident that vehicle vibrations are caused, in the main, by uneven pavement surfaces. These have been found to be random in nature which, in turn, cause the vehicle vibrations to be random. Variations in pavement roughness and fluctuations in the vehicle's speed within a particular journey combine to produce variations in the overall energy levels of the vehicle vibrations. These variations make the process highly non-stationary [1, 2] and introduce a level of complexity that cannot be adequately dealt with using conventional methods that are used for Gaussian and stationary processes. The most commonly-used technique for laboratory simulation of transport vibrations has been in place for some years. The method assumes that the vibrations produced by wheeled vehicles can be approximated by a zero-mean, normally-distributed (Gaussian) random process. In addition, the overall root-mean-square (rms) level of the process is often assumed to be constant thus implying stationarity. It has been shown that vibration synthesis at a constant rms level fail to accurately reproduce the fluctuations in vibration levels that occur naturally during road transportation realizations [2]. Most laboratories make use of a random vibration controller (RVC) which uses a feedback loop to synthesize and control random signals according to a PSD function. When non-stationarity is acknowledged, vibrations are synthesized at various rms levels for pre-determined durations. However, the length an sequence of each constant rms synthesized segment is not known. This is the outstanding issue addressed by this paper [3].

One important aspect pertaining to the synthesis of non-stationary random vibrations is the issue of signal segmentation. If the hypothesis that the process can be modelled statistically as a sequence of segments, each belonging to a family of Gaussian process with varying standard deviations, then there must exist identifiable boundaries (change-points) at which the transition from one segment to another occurs. The detection of such change-points should make it possible to determine the segment lengths and their relationship with the segment standard deviation as well as their statistical characteristics. Segmentation is critical when considered in the context of synthesis. This will determine the statistical parameters upon which the length and sequence of each Gaussian segment will be synthesized. Change-point detection is a process that emerged out of a need to identify real changes in random processes such as economic indicators and the monitoring and control of quality in manufacturing process. Techniques range from cumulative sum (cum-sum) schemes first proposed by Page [4,5,6] and further developed by Hinkley [7] and Pettitt [8] to Singular-Spectrum Analysis [9]. The cumulative sum techniques are primarily geared toward detecting significant deviations in the mean of random processes. The procedure is greatly enhanced by including a bootstrapping algorithm which is used to provide an estimate in the significance of the change-point. Bootstrapping effectively rearranges the sequence, or order, of the sample in a random fashion a number of times while re-evaluating the sample (in this case using the cum-sum algorithm). This gives a basis for determining whether the change is truly significant or merely apparent. In this paper, a change-point detection algorithm, based on the cum-sum / bootstrapping techniques was developed and applied to the instantaneous magnitude of the vibration signals. The arguments for this approach rely on the fact that level type non-

stationarities in random signals are well manifested through changes in the instantaneous magnitude as computed by the Hilbert Transform.

This paper presents the development of a change-point detection algorithm that was used to determine the length of stationary segments within a large number of typical non-stationary random vibration records. These include measured vibration records as well as numerically generated records based on measured pavement profiles. The statistical distribution of segment lengths for each vibration record was computed with the aim at identifying similarities and trends for the development of an overall statistical model for segment lengths to be used for synthesis purposes. One outcome of note was that the shape of the segment length distributions computed from a wide range of vibration records are generally comparable and exhibit an asymptotic like decrease in probability of occurrence as the segment length increases. This behaviour was found to be best modelled with a hyperbolic function in the form

$$p(s) = C / \sinh(ks) = C \operatorname{csc} h(ks) \quad (1)$$

to represent the probability density function of the segment lengths, where  $C$  and  $k$  are empirical constants obtained by a non-linear least squares regression method. The paper reveals that this model was found to adequately describe the statistical characteristics of segment length for both measured and simulated vibration records. These results find significance in the synthesis of non-stationary random vibrations when the segment length distribution function can be used to statistically determine both the duration and sequence of each stationary segment.

## References

1. Richards, D.P. *Environmental Engineering*, Dec. 1990, 23-26.
2. Rouillard, V. & Sek, In *Proceedings of the Institution of Mechanical Engineers*, vol. **215**, Part D, 1069-1075, 2001
3. Rouillard, V. *On the laboratory synthesis of road vehicle vibrations*. PhD thesis, Monash University, Australia (to be published).
4. Page, E.S. (1954) *Biometrika*, vol. **41**, No.1,2, pp 100 – 115.
5. Page, E.S. (1955) *Biometrika*, vol. **42**, No. 3,4, pp 523 - 527.
6. Page, E.S. (1957) vol. **44**, No. 1,2, pp 248 - 252.
7. Hinkley, D.V. (1971) *Biometrika*, vol. **58**, No. 3, pp 509 – 523.
8. Pettitt, A.N. (1980) *A Simple Cumulative Sum Type Statistic for the Change-Point Problem with Zero-One Observations*. *Biometrika*, vol. **67**, No. 1, pp 74 - 84.
9. Moskvina, V. (2001) *Application of the Singular Spectrum Analysis for Change-Point Detection in Time Series*. PhD Dissertation, School of Mathematics, Cardiff University, UK.

## THE STATISTICAL DISTRIBUTION OF THE ROOT MEAN SQUARE OF ROAD VEHICLE VIBRATION

M.A. Garcia-Romeu-Martinez and V. Rouillard  
ITENE, Instituto Tecnológico del Embalaje, Transporte y Logística  
Polígono Industrial D'Obradors, C/Soguers 2, 46110 Godella – Valencia, Spain  
Victoria University, Melbourne Australia  
PO Box 14428 MCMC, Melbourne 8001, Australia  
mgarciaromeu@itene.com, Vincent.rouillard@vu.edu.au

In order to develop optimum packaging it is important that packaging engineers know the expected mechanical hazards that packages will observe during shipping and handling. This information allows them to engineer the right amount of protective packaging needed. To help designers to reduce cost, either by avoiding wasting packaging materials by over-packaging or avoiding damage by under-packaging, test methods to simulate the shipment of the packaged goods in the laboratory need to be based on actual measured vibrations.

Vibrations that occur in vehicles during transportation are complex and play a significant role in the level of damage experienced by products during shipment. Vehicle vibrations are random and their character and level is dependent on the type of vehicle, suspension type, payload, vehicle speed and road condition. Because of these variabilities, it is not always possible to represent transport vibrations with a simple function such as the power spectral density (PSD) function. With the advent of sophisticated vibration recorders in the past decade, packaging engineers have been able to measure and analyze increasing volumes of vibrations that occur in commercial shipments. Recently, numerous studies have been undertaken with the aim of measuring and evaluating the vibrations in various distribution environments around the globe and using particular vehicle types to enable packaging engineers to develop packaging solutions to meet world-wide distribution challenges [1, 2, 3, 4]. The main purpose of these exercises is to generate effective laboratory test schedules for evaluating the performance of package systems when subjected to vehicle vibrations during distribution.

This paper present the initial results of a study was aimed at measuring and developing simulation methods for road transport. The study quantifies vibration characteristics in trucks as a function of speed, payload, and suspension type. The shipments were instrumented with vibration data recorders to measure the vibration levels and , in some cases, a Global Position System to measure the truck speed and location. Over ten different vehicles with a variety of suspension types, payloads and road surface types were studied with high-capacity vibration recorders mounted at various locations on the vehicles.

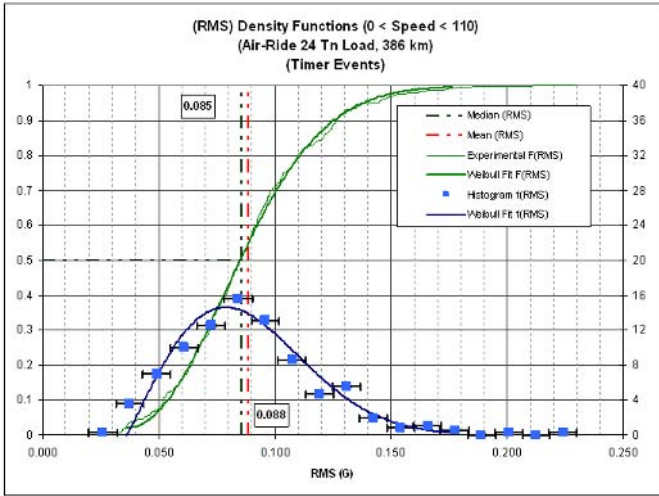
The measured data was subjected to a range of statistically analyses that include the PSD and the statistical distribution of the (moving) root-mean-square (RMS) level. Limitations relating to the computation of the moving RMS with respect to window width are discussed and examined [5].

The paper focuses on the development of a model for characterising the probability density of the moving RMS of the vibrations for various vehicle types, payloads and sensor location. A model, based on the three-parameter Weibull distribution, includes an additional parameter ( $x_0$ ) which accounts a shift in the distribution for the overall RMS level.

$$\rho \cdot \frac{\varphi}{x - x_o} \cdot \left( \frac{x - x_o}{\alpha - x_o} \right)^\varphi \cdot e^{-\left( \frac{x - x_o}{\alpha - x_o} \right)^\varphi}$$

Where x is the moving RMS and alpha, gamma and rho are the Weibull parameters.

The model was subject to validation tests against a number of vibration samples and were found to offer good agreement as shown in Figure 1 which shows a typical example.



**References**

1. Singh S.P, Joneson E. and Singh J. *Journal of Packaging Technology and Science* Published online (Early view)
2. Singh, S. P. and J. Marcondes, *Journal of Testing and Evaluation*, vol. **20**, No. 6, 466-469, 1992.
3. Pierce, C., S. P. Singh and G. Burgess. *Journal of Packaging Technology and Science*, vol. **5**, 11-15, 1992.
4. Singh S. P., J. Antle and G. Burgess, *Journal of Packaging Technology and Science*, vol. **5**, 71-75, 1992.
5. Rouillard, V, Sek, M.A. & Perry, T. *Journal of Transportation Engineering*, vol. **122** (3), 241-245.

## FULL 3D STRAIN MEASUREMENT BY DIGITAL VOLUME CORRELATION FROM X-RAY COMPUTED AND OPTICAL SCANNING TOMOGRAPHIC IMAGES

A. Germaneau, P. Doumalin and J.C. Dupré

Laboratoire de Mécanique des Solides, CNRS, UMR 6610, Université de Poitiers  
SP2MI Bd Marie et Pierre Curie, Téléport 2, 86960 Futuroscope Chasseneuil, France  
germaneau@lms.univ-poitiers.fr, doumalin@lms.univ-poitiers.fr, dupre@lms.univ-poitiers.fr

Currently, the determination of mechanical data fields during a loading is generally performed by non-contact optical techniques like mark tracking or Digital Image Correlation techniques. However, these methods are only surface measurement techniques and even if we add the measurement of out-plan displacements, we can't calculate all the three-dimensional strain components. To obtain the full 3D strain tensor, DIC techniques [1] have been extended to Digital Volume Correlation (DVC) [2,3,4,5]. So we are able to investigate 3D mechanical phenomena in the core of materials or structures without hypothesis nor using numerical simulation. DVC allows the measurement of 3D displacement by considering a 3D material transformation which can be assimilated at a pure translation or at a translation combined with a local gradient. This technique needs volume images which contain a 3D random distribution of grey levels. In order to obtain a subvoxel accuracy, a trilinear interpolation of the grey levels is used and the final positions are calculated with an optimization of a correlation coefficient. In this study, we present 3D measurements made by images from X-ray computed tomography and optical scanning tomography. In order to define the fields of application of both techniques, we show their performances and we evaluate their measurement uncertainty.

### DVC and X-Ray Computed Tomography

Up to the present, DVC technique has principally applied on 3D images generated by X-ray computed tomography (CT) [2,3,5]. The distribution of grey levels is due to local differences of density and so is given by the microstructure of the material of the studied specimen. X-rays are well adapted to study materials with a native heterogeneous microstructure like tissues and organs as applications in medicine or biology but also enable the observation of other heterogeneous materials like for example ceramics or geomaterials... However, all the materials do not present, by X-ray CT, a natural local contrast sufficient to use DVC. Then it is necessary to include some markers, small dense particles, during the making of the material. X-ray CT requires a heavy device, like a medical or laboratory tomography device or a synchrotron radiation device. In this study, volume images are generated by micro-Computed Tomography. To evaluate the measurement uncertainty of this technique and to have images with a good quality, we work with silicone specimens which contain copper particles having a size going from 50 $\mu\text{m}$  to 150 $\mu\text{m}$ .

### DVC and Optical Scanning Tomography

Recently, we have developed an optical technique to generate volume images by optical slicing in transparent materials containing particles [4]. A plane laser beam scans the specimen and 2D images of the scattered light involved by particles are successively recorded at each position of the beam in order to constitute a volume (Fig. 1). The random distribution of the grey levels within the volume image is given by the scattered light phenomenon. We have shown [4] that a good quality of images can be obtained with specimens made in epoxy resin or in polyurethane by including particles of polyamide with a size of approximately 150 $\mu\text{m}$ . DVC from optical scanning tomography, which needs a simple experimental device and allows a quick recording of volume



images of specimens made by an easy cast elaboration, seems to be well adapted for the study of strain concentration in structures.

## Experiments

First for both techniques, we have evaluated the displacement measurement uncertainty by imposing several subvoxel displacements at the specimens between several states. In assuming that the displacements are homogenous in the whole specimen, we determine gaps between imposed and measured displacement. Then, we calculate the standard deviation giving the uncertainty. Fig. 2 shows for example the standard deviation values obtained by both techniques. To evaluate the strain measurement uncertainty, we have to impose a strain value on the specimen. For that, we have developed an experimental setup made in an X-ray transparent material (PMMA) allowing us to make a tensile test on the specimen inside the micro-CT system. So, we can make similar tests by using X-ray micro-CT device and optical scanning tomography device. These different tests allow us to improve the knowledge of these 3D full field measurement techniques in order to make material and structure studies.

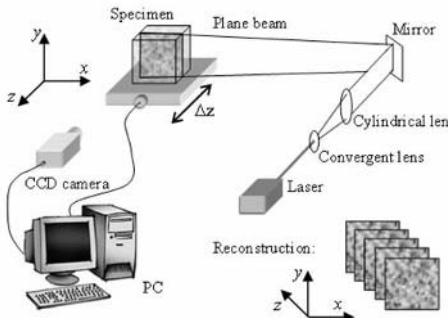


FIGURE 1: Optical scanning tomography

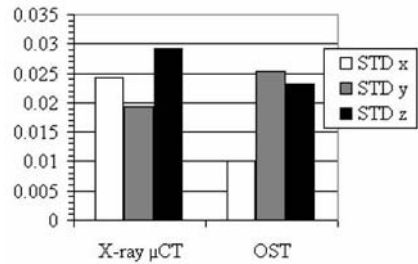


FIGURE 2: Standard deviation on the displacements obtained by X-ray micro-CT and by optical scanning tomography (OST)

## References

1. Bruck, H.A., Mc Neill, S.R., Sutton, M.A. and Peters, W.H., *Exp. Mech.*, vol. **29**, 261-267, 1989.
2. Bay, B.K., Smith, T.S., Fyrhie, D.P. and Saad, M., *Exp. Mech.*, vol. **39**, 217-226, 1999.
3. Verhulp, E., Van Rietbergen, B. and Huiskes, R., *J. of Biomech.*, vol. **37**, 1313-1320, 2004.
4. Germaneau, A., Doumalin, P. and Dupré, J.C., In *Proceedings of Photomechanics 2006*, edited by M. Grédiac and J. Huntley, Clermont-Ferrand, France, 2006.
5. Bornert, M., Doumalin, P. and Maire, E., In *Proceedings of ICEM 12*, edited by C. Pappalettere, Bari, Italy, McGraw-Hill, 445-446, 2004.

## CRACK TIP GROWTH MEASUREMENT USING DIGITAL IMAGE CORRELATION

Phillip L. Reu, Brendan R. Rogillio and Gerald W. Wellman  
Sandia National Laboratories  
P.O. Box 5800, Albuquerque, NM 87185-1070, USA  
plreu@sandia.gov

We present the results of sub-surface crack-length measurements in an aluminium sample that are inferred from surface strains calculated using digital image correlation (DIC). DIC is a photometric technique that uses a calibrated stereo camera system to calculate the 3D shape and motion of an imaged scene [1,2]. Image correlation has already proven itself to be useful for crack tip investigation due to the ability to obtain a relatively dense set of strain measurements in a region of interest. Traditionally, this has been accomplished using 2D-DIC techniques that require only a single camera [3], however, the more complex geometry of the current experiment required 3D information to correctly map the crack-tip strains onto the curved surface. This complex sample geometry was carefully constructed to maintain a stable strain field in order to produce crack growth at rates easily captured with high-resolution digital cameras operating with a 4-Hz frame rate (see Fig. 1). A preliminary experiment was conducted where the crack growth was halted and x-ray methods were used to find the sub-surface crack-tip location. The sub-surface crack location corresponded to a surface strain of 10%. This value was then used for tracking the crack extension as the specimen failed. The three samples tested showed excellent agreement. The crack length and applied load versus sample extension (measured with a linear variable differential transformer) for a single sample is shown in Fig. 2. Also shown are images of the strain field at assorted times during the test. The theoretical “peanut” shaped crack-tip strain predicted by the plane stress Tresca criterion is evident in the measured strain field.

Details on the experimental setup and procedure are presented and highlight some of the strengths and difficulties in using DIC in a laboratory environment. This includes information regarding setup of the high-resolution 4-Megapixel cameras, calibration, specimen preparation and use of image correlation software for analyzing the resulting images.

Sandia is a multiprogram laboratory operated by Sandia Corporation, a Lockheed Martin Company, for the United States Department of Energy’s National Nuclear Security Administration under contract No. DE-AC04-94AL85000.

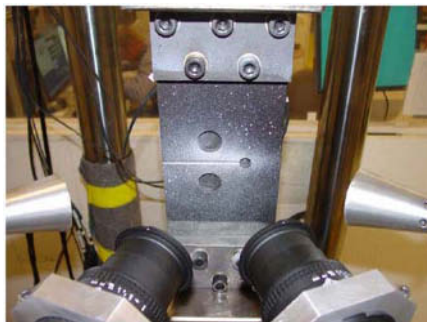


FIGURE 1. Specimen in load frame showing basic geometry of the specimen and DIC camera arrangement.

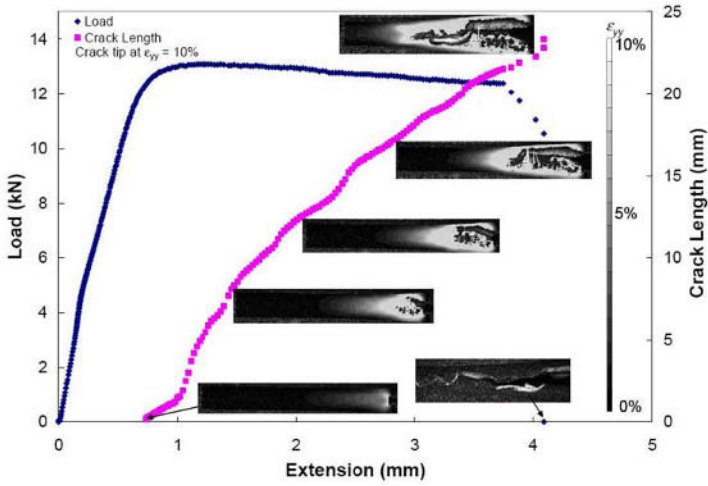


FIGURE 2. Crack growth results for an aluminium sample. The grayscale corresponds to the strain contours for the DIC results.

## References

1. Cheng, P., M.A. Sutton, H.W. Schreier, and S.R. McNeill, *Experimental Mechanics*, vol. **42**, 344-352, 2002
2. Garcia, D., J. Orteu, M. Devy, In *5<sup>th</sup> Fall Workshop on Vision, Modeling, and Visualization 2000*, IEEE Signal Processing Society, Saarbrücken, Germany, 2000
3. Han, G., M.A. Sutton, Y.J. Chao, *Experimental Mechanics*, vol. **34**, 125-140, 1994

## STUDY ON DEFROMATION OF A MICRO BEAM USING INTERFEROMETRY

W. Sun<sup>1, 2, a</sup>, X.-Y. He<sup>1, b</sup>, M. Li<sup>2, c</sup> and Y. Fu<sup>2, d</sup>

<sup>1</sup> Department of Engineering Mechanics, Southeast University,  
Sipailou st, Nanjing 210096, P R China

<sup>2</sup> Department of Mechanical Engineering, National University of Singapore,  
10 Kent Ridge Crescent, Singapore 119260  
a Pnancysun@seu.edu.cn, PbP mmhxy@seu.edu.cn,  
Pc Plimingzhou@nus.edu.cn, PdP mpefuy@nus.edu.cn

MEMS (Micro Electro-Mechanical Systems) is a rapidly growing field building upon the existing silicon processing infrastructure and techniques to create micro-scale devices or systems [1]. However, the progress of the MEMS depends on the state-of-the-art test and measurement methodologies to inspect the deformation of the microcomponents for further understanding of their mechanical properties, which will push the design to its extreme. Among the existing optical techniques, interferometry is still widely used due to its capability of performing accurate measurements on microcomponents with surface deformation ranging from less than 0.1nm to several hundreds of microns. In this paper an optical Michelson interferometry technique is developed for testing deformation and corresponding mechanical parameters of a surface micromachined beam under applied voltage (both AC and DC source). A long distance microscope with the CCD camera or high-speed camera is utilized to capture the interference fringe pattern that results from recombination of two beams reflected from the optical mirror in the Mirau objective and the micro-beam.

There are many widely used ways to process the resulted interference fringe patterns, including skeletonization & fringe tracking, phase measurement methods and so on. Major limitations of the conventional fringe counting analysis exist in the correct location of bright and dark fringe peaks especially in noisy fringes and the densities of the fringes [2]. Recently, there has been much interest in demodulation of fringe patterns using phase measurement methods, such as Fourier transform profilometry, phase stepping, digital phase locked loop, and direct phase detection, all of that significantly improved the resolution, accuracy, and repeatability in the fringe analysis technologies [3]. Since dynamic deformations are involved in this paper, phase stepping which requires multiple images is not available. For single-image based technique, Fourier transform are commonly used. In some cases it is quite difficult to select a proper bandpass filtering window. Lately, Wavelet analysis has become an effective tool in optical interferometry, in particular its application in phase retrieval using one fringe pattern; speckle noise reduction; and flow detection.

In this paper, wavelet analysis is employed to extract phase from the experimental fringe patterns, which give a better solution with noise reduction and without deficiency for filter window choice as in Fourier transform. Phase extraction is performed by computing the phase at a wavelet ridge:

$$\varphi(b) = \tan^{-1} \left\{ \frac{\text{Im}[W_S(a_{rb}, b)]}{\text{Re}[W_S(a_{rb}, b)]} \right\} \quad (1)$$

where Im and Re are respectively the imaginary and real part of a complex wavelet coefficients.  $a_{rb}$  is a scaling on the ridge[4]. Obviously, phase unwrapping cannot be avoided. To overcome the problem of phase ambiguity, carrier technique is frequently used on an initial interferogram. The basic principle of the technique is to introduce a known set of linear carrier fringes. Within defined

limits, this results in a simple fringe pattern (with monotonically increasing or decreasing fringe order) which enables straightforward determination of the phase. Due to the limited image resolution, interference range, defocus of the image in micron range and fringes of high density, it is quite difficult to introduce enough carrier fringes so that the resultant fringes are directed at the same orientation. In our case, a limited linear carrier is introduced by a slight tilt of the substrate, which cannot be absolutely avoided in the actual experimental conditions. The detailed procedures of phase extraction are as follows: firstly, unwrap phase from one end of the beam to the other ends over the entire span; secondly, identify the point which introduces phase ambiguity (in this case, the point is corresponding to the inflexion point on the unwrapped phase curve); thirdly, reflect the phase values starting from this point; finally, subtract the phase introduced by the carrier fringe. Since we obtained the final unwrapped phase map, profile of the specimen can be easily converted by multiplying by  $\lambda / 4\pi$ . Both simulation and experimental tests are conducted to validate the feasibility of this practical method.

This paper is focused on the investigation of a micro beam under applied voltage using the proposed phase extraction method. Both static and dynamic tests are performed by applying a dc and ac voltage across the beam, respectively. Deflections of the beam under different loading conditions are obtained. Furthermore, corresponding mechanical properties of the micro-beam are also determined, including residual stress, Young's modulus, resonant frequency and Q-factor. The experimental results show that the proposed technique is relatively simple and accurate, and is a potential method for the evaluation of mechanical properties of micro components.

## References

1. Cornelilus, T. Leondes, *MEMS/NEMS Handbook Techniques and Applications*, Springer, Los Angeles, USA, 2005.
2. Quan, C. , Shang H.M., Bryanston-cross P.J., *Opt. Laser Technol.*, vol. **28**, 7-13, 1996.
3. Gary, L. Cloud, *Optical Methods of Engineering Analysis*, Cambridge University Press, USA, 1995.
4. Tay, C.J., Quan, C, Fu, Y. and Huang Y.H., *App. Opt.*, vol. **43**, 4164-4171, 2004.

### 3D SURFACE ELASTIC-PLASTIC STRAIN MAPPING IN HEMMING, BENDING, AND INDENTATION TESTS

Wei Tong

Department of Mechanical Engineering, Southern Methodist University  
3101 Dyer Street, 200G Embrey Building, Dallas, TX 75275 USA  
wtong@smu.edu

To measure the surface deformation of an initially flat object undergoing three-dimensional rigid body motion and deformation by digital image correlation technique (see Tong [1-3] and Tong et al. [4-5]), one needs to have at least two images of the object at two different viewing angles before and after the deformation. While a dual-camera stereo imaging system commonly used in machine vision is a natural choice for such measurements, there are many practical applications when such a dual-camera stereo imaging system is not feasible. Here we present a 3D surface strain mapping technique based on digital image correlation using mostly a single camera imaging system for several applications, including hemming of automotive sheet metals, three-point and four-point bending tests, and indentation test with cylindrical or spherical indenters.

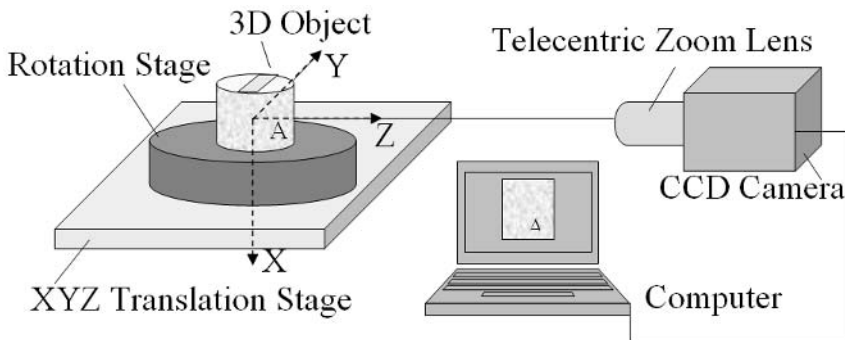


FIGURE 1. Single camera imaging system for 3D surface deformation mapping [1].

One experimental configuration for measuring the surface deformation of an object with a curved surface is shown in Fig. 1. It consists of a combined rotation and translation specimen stage, a telecentric zoom lens, a CCD digital camera, and a computer (for acquiring digital images from the camera and for image processing and data analysis). It is assumed that the optical axis of the imaging system is parallel with the Z-axis of the specimen stage and a flat object with its surface aligned with the XY-plane on the specimen stage is imaged digitally. The intercepting point between the XY-plane and the optical axis defines the origin of the physical coordinate system ( $X=Y=Z=0$ ). It is not necessary that the optical axis should intercept the axis of the rotation stage (but the rotation axis should be parallel with the X-axis of the physical coordinate system and lies within the XY-plane). Such an experimental set-up is ideal for off-line measurements and it has been used successfully for measuring the *total cumulative* strains of thin sheet metals after hemming or bending operations [1] and is readily extended to indentation tests after unloading.

When there is a need to monitor the evolution of the deformation field or to measure the elastic strains (so the unloading step is not allowed) during a bend test or an indentation test, one would have to perform the on-line real-time measurements (i.e., acquiring a sequence of images) during the test. One of the possible experimental configurations is given here (see Fig. 2). To facilitate the in-situ image acquisition, the bend apex region is set to remain more or less stationary while the loading pins on the sides are moving (Fig. 2a). The camera 1 (mounted to a stand fixed to the lab floor) is used to measure the deformed sample that initially lies in the XY plane and remains in focus after some out-of-plane motion due to bending while the camera 2 (also mounted to a stand fixed to the lab floor) is used to monitor at the same time the bent shape of the sample from the side view (Fig. 2b).

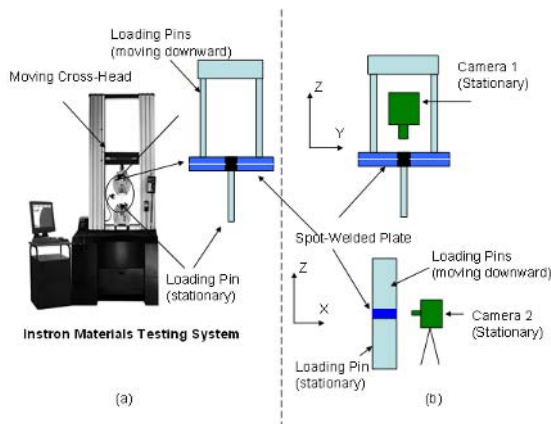


FIGURE 2. Experimental set-up for bending tests: (a) schematic of the bend test; (b) image acquisition by camera 1 and camera 2 during the test.

Results of experiments using both types of setups along with some practical issues will be presented to demonstrate the feasibility, reliability and accuracy of the 3D surface plastic deformation measurements using digital image correlation techniques.

## References

1. Tong, W., *Exp. Mech.*, vol. **44**, 502-511, 2004.
2. Tong, W., *Exp. Tech.*, vol. **28**, 63-67, 2004.
3. Tong, W., *Strain*, vol. **41**, 167-175, 2005.
4. Tong, W., H. Tao, N. Zhang, and L.G. Hector, *Scripta Mater.*, vol. **53**, 87-92, 2005.
5. Tong, W., H. Tao, X. Jiang, N. Zhang, M. Marya, L.G. Hector, and X.Q. Gayden, *Metall. Mater. Trans. A*, vol. **36**, 2651-2669, 2005.

## PROJECTED FRINGE PATTERN ANALYSIS BY THE FOURIER METHOD: APPLICATION TO VIBRATION STUDIES

R. Rodriguez-Vera, C. Meneses-Fabian, J.A. Rayas, and F. Mendoza-Santoyo  
Centro de Investigaciones en Optica  
Loma del Bosque 115, Col. Lomas del Campestre, León, Mexico  
rarove@cio.mx

This presentation introduces a new technique of fringe analysis based on the Fourier method, Takeda, *et al.* [1] and is applied to vibration study of a free-end cantilever beam. When a Ronchi ruling is projected on a homogenous cantilever, which is subjected to harmonic vibration, its behaviour can be considered as a time-varying interference pattern that contains a constant carrier frequency in the horizontal direction, as shown in Fig. 1. Our method considers that the integration time of the CCD camera is smaller than the temporal vibration period. Actually, this integration is 1/800 of a second. Then, under this condition any captured frame of the projected fringe pattern can be modelled as

$$I_k(x, y) = a(x, y) + b(x, y) \cos [\phi_k(x, y) + 2\pi\mu_0 x], \quad (1)$$

where the subscript  $k$ , is a positive integer that indicated the  $k$ -th captured pattern  $I_k(x, y) = I(x, y, t_k)$  by the CCD camera at instant  $t = t_k$ . Note that the term  $2\pi\mu_0 x$  is not always bigger than  $a(x, y)$ ,  $b(x, y)$ , and  $\phi_k(x, y)$  because the pattern of Eq. (1) does not have a monotonous comporting, but it depends of the natural mode present on the cantilever.

The expression (1) can be written in a more convenient way as

$$I_k(x, y) = a(x, y) + c_k(x, y) \exp(i2\pi\mu_0 x) + c_k^*(x, y) \exp(-i2\pi\mu_0 x), \quad (2)$$

where  $i$  is the imaginary unit given by  $\sqrt{-1}$ , the symbol  $*$  denotes complex conjugated of  $c_k(x, y)$ , which is given by

$$c_k(x, y) = \frac{1}{2} b(x, y) \exp[i\phi_k(x, y)], \quad (3)$$

Using the Fourier method principle, and with the idea of phase extraction introduced by Kreis [2], the term  $c_k(x, y) \exp(i2\pi\mu_0 x)$  can be separated of  $I_k(x, y)$ . Then, considering this fact, we propose, for two consecutive patterns,  $k$  and  $k+1$ , to calculate the quotient  $\Delta c_k(x, y) = c_{k+1}(x, y) \exp(i2\pi\mu_0 x) / c_k(x, y) \exp(i2\pi\mu_0 x)$ , then

$$\Delta c_k(x, y) = \exp[i\Delta\phi_k(x, y)], \quad (4)$$

eliminating, in this way, the modulation intensity and the carrier frequency terms. As a result, a complex exponential function relative to phase difference,  $\Delta\phi_k(x, y) = \phi_{k+1}(x, y) - \phi_k(x, y)$  of the pattern  $k+1$  and the pattern  $k$ , is obtained.

Note that, if we chose the term  $c_k(x, y) \exp(i2\pi\mu_0 x)$  instead of the term  $c_k(x, y)$ , as is usually used in the Fourier-transform method, facilitates remove possible ambiguity when locating the filtering component in the centre of coordinates. This is, due to implicitly removing the carrier frequency. Also, with this operation is possible eliminate other problems as the non linearity of



detector and the non uniformity illumination. Then, the phase difference can be calculated choosing the imaginary part of the logarithm of the expression (4). That is

$$\Delta \phi_k(x, y) = \text{Im} \{ \log [\Delta c_k(x, y)] \}, \tag{5}$$

Eq. (5) shows the principal value wrapped between 0 and  $2\pi$  radians. Although, it should be possible chose properly, without losing of generality, the Ronchi ruling period, angles  $\alpha$  and  $\beta$ , such that Eq. (5) be minor or equal to  $2\pi$  radians. Then it can be considered as the equivalent measure to the spatial form of the vibration mode without necessity of the unwrapping phase. Some vibration shape modes obtained experimentally are show in Fig. 2.

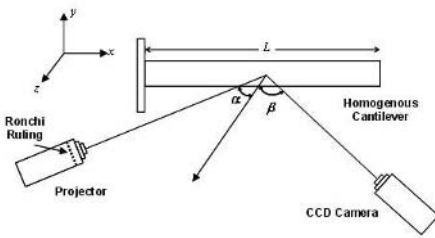


FIGURE 1. Experimental setup.

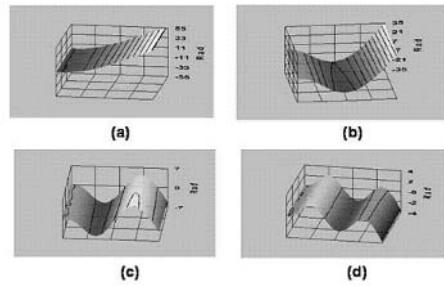


FIGURE 2. Experimental shape modes of a free-end cantilever beam: (a) First, (b) Second, (c) Third, and (d) Fourth, modes.

**References**

1. M. Takeda, H. Ina, and S. Kobayashi, *J. Opt. Soc. Am.*, vol. **72**, 156-160, 1982.
2. T. Kreis, *J. Opt. Soc. Am. A*, vol. **3**, 847-855, 1986.

## ANTIPLANE PROBLEM OF CRACK ARREST FOR A CRACKED PIEZOELECTRIC PLATE

R.R. Bhargava and Namita Saxena

Department of Mathematics

Indian Institute of Technology, Roorkee, India

rajrbfma@iitr.ernet.in, mitandma@iitr.ernet.in

Some of the recent work done in anti-plane problems are: Chen et al. [1] investigated the crack problems for nonhomogenous materials under anti-plane shear loading using a displacement-based formulation. Wang [2] studied the behavior of a mode III crack in functionally graded piezoelectric materials investigating materials that are weakened by a single crack or a series of collinear cracks. Under the permeable crack assumption Li and Tang [3] analyzed electro-elastic problems of an interface anti-plane shear crack in a layered piezoelectric plate. Bhargava and Saxena [4] solved the anti-plane problem of crack arrest for a piezoelectric ceramic weakened by a crack when developed plastic zones are subjected to variable stress.

The problem investigated in the present paper is of a poled infinite piezoelectric ceramic plate occupying the  $xy$ -plane. The plate is poled in  $z$ -direction perpendicular to  $xy$ -plane.

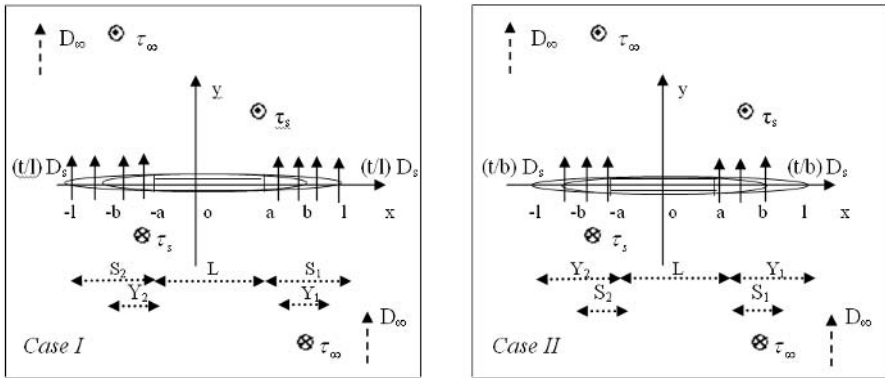


FIGURE 1. Schematic representation of problems

The plate is weakened by a hairline straight crack,  $L$ , from  $(-a, 0)$  to  $(a, 0)$ . The infinite boundary of the plate is subjected to uniform constant anti-plane stress  $\sigma_{yz} = \tau_\infty$  at infinity and in-plane uniform electric displacement  $D_y = D_\infty$  such that the crack yields both mechanically and electrically. Consequently a plastic zone and a saturation zone protrude ahead of each tip of the crack. Two cases are investigated:

**Case I:** Saturation zone length exceeds the plastic zone length.

**Case II:** Plastic zone length is bigger than that of the saturation zone.

To arrest the crack from further opening, the rims of each developed plastic zone are subjected yield point shear stress,  $\sigma_{yz} = \tau_s$  and in-plane normal, cohesive electric displacement

$D_y = (t/l)D_s$  is applied on the rims of developed saturation zones. Here,  $t$  refers to point on any of the saturation zones. In both cases, a mathematical model is obtained using linear piezoelectric theory. The Fourier integral transform method is employed to obtain the desired potentials and closed form expressions are obtained to determine the length of yield zone and saturation zone in each case.

**Case I:** Plastic zone length  $b-a$  and saturation zone length  $l-a$  along  $x$ -axis are determined using

$$\frac{b}{a} = \sec \left\{ \frac{\pi}{2} \frac{G_{11}\tau_\infty + G_{12}D_\infty}{G_{11}\tau_s} \right\}; \quad \frac{l}{a} = \frac{2D_s}{\sqrt{4D_s^2 - \pi^2 D_\infty^2}}$$

$$\text{where } G = [G_{ij}] = \frac{1}{2} \begin{pmatrix} c_{44} & e_{15} \\ e_{15} & -\epsilon_{11} \end{pmatrix}^{-1}$$

**Case II:** similarly, plastic zone length  $l-a$  and saturation zone length  $b-a$  are obtained from

$$\frac{l}{a} = \sec \left\{ \frac{\pi}{2} \frac{\tau_\infty}{\tau_s} \right\}; \quad \frac{b}{a} = \sec \left\{ \frac{\pi}{2} \frac{G_{21}\tau_\infty + G_{22}D_\infty}{G_{21}\tau_s} \right\}$$

In each case analytic expressions for the crack opening displacement, crack opening potential drop and energy release rate have been derived. A case study for them is presented in graphical form with respect to the affecting parameters viz. material constants, crack length, plastic zone length, saturation zone length and the loads applied at infinity for a specific ceramic.

## References

1. Chen, Y. S., Paulino, G.H., and Fannjiang, A.C., *Int. J. Solids and Struct.*, vol. **33**, 2989-3005, 2001.
2. Wang, B.L., *Mech. Research Comm.*, vol. **30**, 151-159, 2003.
3. Li, X.F. and Tang, G.T., *European J. Mech. A/Solids*, vol. **22**, 231-242, 2003.
4. Bhargava, R.R., and Saxena, Namita, *Sadhna*, vol. **31**, 213-226, 2006.

## ELECTRIC-FIELD INDUCED FATIGUE CRACK GROWTH IN FERROELECTRIC SINGLE CRYSTALS

F. Fang, W. Yang, F.C. Zhang, R.H. Wen

Failure Mechanics Laboratory, School of Aerospace, Tsinghua University

Beijing 100084, China

fangf@mail.tsinghua.edu.cn, yw-dem@mail.tsinghua.edu.cn

As one important class of the functional materials, ferroelectrics have been widely used as sensors, actuators, and transducers in smart structures. However, due to a strong electro-mechanical coupling, ferroelectrics suffer rather high stress under cyclic electric field. The low fracture toughness (lower than  $1\text{MPa}\cdot\sqrt{m}$ ) and large switching strain render the reliability issue a bottleneck for the performance against crack propagation of ferroelectrics in smart structures. The importance for the reliability of ferroelectric materials gives a strong impetus for the studies on the crack propagation and the underlying mechanisms [1-9]. As fatigue crack growth in ferroelectric ceramics is often related with the grain boundary effects, a systematic study using single crystals is warranted for a better understanding of the electric-field-induced fatigue crack growth and its close relationship with the  $90^\circ$  domain switching.

In this study, in-situ observation of electrically induced fatigue crack growth and  $90^\circ$  domain switching were carried out for ferroelectric single crystals of  $\text{BaTiO}_3$  and PMN-PT under alternating electric field. Substantial crack growth was found for PMN-PT 62/38 and  $\text{BaTiO}_3$  single crystals both below and above  $E_c$ . It was observed that crack propagation behavior is a repeated process of progressive but small increments followed by a sudden increase in the crack length. When there is a sudden increase in the crack length, crack bifurcation or branching always occurs, as shown in Fig. 1.

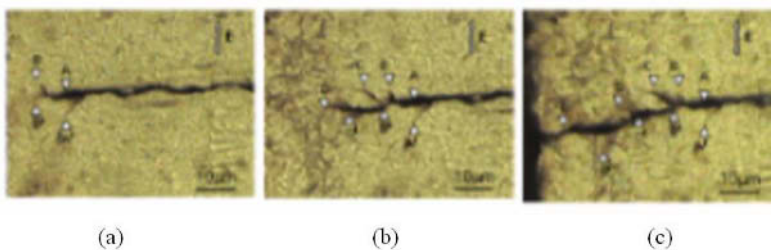


FIGURE 1. Crack morphologies for the PMN-PT 62/38 single crystal electrically cycled at a field magnitude of  $234\text{V/mm}$  ( $0.78E_c$ ) for cycle numbers (a) 300, (b) 1700, and (c) 5200. The arrows indicate the directions of applied cyclic electric field.

Direct evidence of the crack propagation accompanied with the forward movement of  $90^\circ$  domain boundaries was found, as shown in Fig. 2 [10].

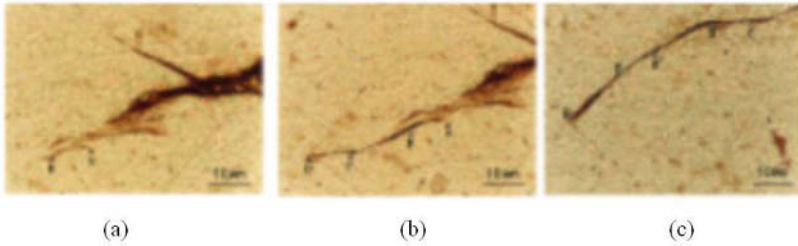


FIGURE 2. The transmission polarized optical micrographs of crack patterns for BaTiO<sub>3</sub> single crystal electrically cycled at a field of 600V/mm (3.3E<sub>c</sub>) for (a) 0, (b) 7000, and (c) 45000 cycles.

Significant orientational effect was found for BaTiO<sub>3</sub> single crystals. For poled [001]-oriented BaTiO<sub>3</sub> single crystal, the applied cyclic electric field is perpendicular to the poling direction. Electric field-induced fatigue crack tends to propagate perpendicular to the applied electric field or in 45° directions, but not in the direction parallel to the cyclic electric field, before the global domain switching takes place. At the same time, cracks that initiated from the electrode/crystal interface grow rapidly along the domain boundary. For poled [100]-oriented BaTiO<sub>3</sub> single crystal, the applied electric field is parallel to the poling direction. The cracks induced by Vickers indentation remains stationary under a cyclic electric field below the coercive field, but start to extend when the cyclic field causes global domain switching. The crack slightly propagates along its original crack direction, and then arrests. When the electric field increases further, the indented cracks remain unchanged while cracks emanating from the electrode propagate rapidly within the single crystal.

It was suggested that the crack morphology, the electric boundary condition along the crack faces, as well as the stresses induced by 90° domain switching play important roles in the observed crack propagation behavior.

## References

1. Yang W., *Mechatronic Reliability*, Tsinghua University Press, Beijing China and Springer, Berlin Germany, 2002.
2. Cao H. C., Evans A. G., *J. Am. Ceram. Soc.*, vol. **77**, 1783-1786, 1994.
3. Schneider G. A., and Heyer V., *J. Eur. Ceram. Soc.*, vol. **19**, 1299-1306, 1999.
4. Lynch C. S., Yang W., Collier L., Suo Z., McMeeking R. M., *Ferroelectrics*, vol. **166**, 11-30 (1995).
5. Shieh J., Huber J. E., and Fleck N. A., *J. Eu. Ceram. Soc.*, vol. **26**, 95-109, 2006.
6. Nuffer J., Lupascu D. C., Glazounov A., Kleebe H., and Roedel J., *J. Europ. Ceram. Soc.*, vol. **22**, 2133-2142, 2002.
7. Fang F., Yang W. and Zhu T., *J. Mater. Res.*, vol. **14**, 2940-2944, 1999.
8. Yang W., Zhu T., *J. Mech. Phys. Solids*, vol. **46**, 291-311, 1998.
9. Zhu T. and Yang W., *Acta Materialia*, vol. **41**, 4695-4702, 1997.
10. Fang F., Yang W., Zhang F. C., and Luo H. S., *J. Am. Ceram. Soc.*, vol. **88**, 2491-2497, 2005.

## INTEGRITY OF PIEZO-COMPOSITE BEAMS UNDER HIGH CYCLIC ELECTRO-MECHANICAL LOADS – EXPERIMENTAL RESULTS

Lucy Edery-Azulay and Haim Abramovich  
Faculty of Aerospace Engineering, Technion  
I.I.T., Haifa 32000, Israel

lucy@aerodyne.technion.ac.il; haim@aerodyne.technion.ac.il;

One key issue in the study of the structural integrity of smart structures is the research of high cyclic electro-mechanical (E/M) loading. To truly understand the integrity of smart structures, investigation must include active sensors/actuators embedded or bonded as a part of smart structure, and to be loaded in a combined electro-mechanical cyclic loads as the way they will be used in real applications. A better understanding of the effects of cyclic E/M loading is necessary to characterize the lifetime behavior of active ceramic components.

The present research is a part of a comprehensive<sup>1</sup> experimental study dealing with the structural integrity of smart structures. A composite laminate made of graphite-epoxy with a quasi-isotropic lay-up was used as a host structure for all the specimens. Two commercially available piezoelectric patches (PZT-5H, lead zirconate titanate) were used: ACX patches from QP15N Cymer Inc. U.S.A. and PIC255 from PI Ceramics, Germany. The first part of the present study investigates the behaviour of piezo-laminated beams with embedded or surface bonded patches, subjected to axial tension/compression loads. Seven different specimens (numbered as AX-EM) with embedded piezoceramic patches and another two specimens (numbered as AX-SM) with four piezoceramic patches bonded to the surface of each host structure (one pair of ACX and one pair of PIC-255 patches) were tested. Figs. 1(a-b) illustrate schematically both embedded and surface bonded axially loaded specimens.

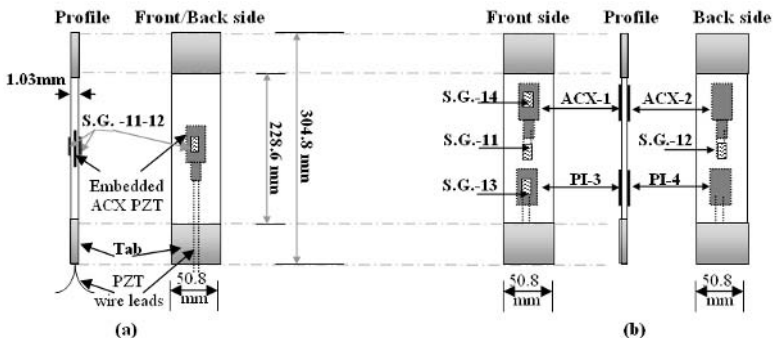


FIGURE 1- Schematic description of the two specimens. (a). Embedded piezoelectric actuators, (b). Surface bonded piezoelectric actuators

The second part of the present study investigates the behaviour of seven specimens (numbered as BEN1-7) with four piezoelectric patches, one pair of ACX and one pair of PIC-255, bonded on each side of the host structure. These specimens were subjected to bending cyclic loads using four-

point bending setup tests. Figs. 2(a-b) present a schematic drawing of the four-point bending test setup and its realization using the MTS loading machine.

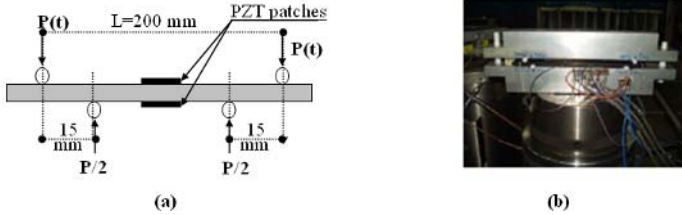


FIGURE 2. Four-point bending setup test. (a) Schematic illustration, (b) - Test setup

The aim of the present research is to examine the changes in the piezoceramic sensing capabilities as a piezo-laminated structure is undergoing an increasing number of electro-mechanical load cycles. These two types of integrated loads, called Electro-Mechanical (E/M) loads can be applied in-phase (both loads cause either tension or compression) or out-of-phase (one load causes tension while the other causes compression and vice versa).

The degradation in the sensing abilities of the piezoelectric patches for an increasing number of E/M load cycles was monitored and recorded. Fig. 3 shows typical degradation results for patches subjected to E/M cyclic load in an out-of-phase configuration, tensile/compression and bending.

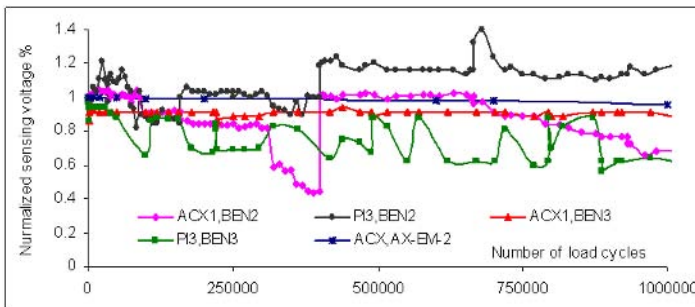


FIGURE 3. Typical degradation results for patches subjected to an out-of-phase E/M cyclic load

It is expected that the main impact of the present research will be its capability to predict the structural integrity of a given smart structure as a function of its use, yielding a balanced design with an enhanced survivability and a higher confidence in the usage of piezoelectric patches.

<sup>1</sup> Yet, in general, structural life prediction involves analyzing data gathered from a large number of tests. The present review does not pretend to cover the whole spectrum of experiment that have to be done.

## M-INTEGRAL FOR PIEZOELECTRIC CERAMICS USING THE EXACT BOUNDARY CONDITIONS ON CRACK SURFACES

Yael Motola and Leslie Banks-Sills

The Dreszer Fracture Mechanics Laboratory,  
Department of Solid Mechanics, Materials and Systems, Faculty of Engineering,  
Tel Aviv University, Ramat Aviv 69978, Israel  
ymotola@eng.tau.ac.il, banks@eng.tau.ac.il

As a result of their wide use in the form of sensors and actuators, much interest has been focused on the reliability and failure behavior of piezoelectric materials. This leads to the need to develop techniques for predicting crack growth under monotonic and fatigue loading (both mechanical and electric). To this end, accurate methods are required for calculating stress and electric flux density intensity factors in these materials. The solution is affected by the mechanical and electrical coupling, as well as material anisotropy in its poled state.

In this study, a conservative integral is derived for calculating the intensity factors associated with piezoelectric material for an impermeable crack, as well as for the exact boundary conditions proposed by Landis [1]. This is an extension of the  $M$ -integral or interaction energy integral for mode separation in mechanical problems. In addition, the method of displacement extrapolation is extended for this application as a check on results obtained with the conservative integral. The crack is assumed along the  $x$ -axis in the  $xy$  – plane. Poling is at an arbitrary angle with respect to the crack plane with poling within the  $z = 0$  plane. These methods were extended in this study in order to calibrate specimens for carrying out fracture tests in piezoelectric materials.

There are three approaches in the literature for describing the boundary conditions on the crack faces for piezoelectric materials, i.e. impermeable, permeable and semi-permeable crack models. With the impermeable crack assumption, the permittivity of the gap is taken to be zero. This implies that the normal component of the electric flux density must vanish. In contrast, with the permeable model, the crack is assumed not to perturb the electric field directly so that both the electric potential and normal electric flux density are continuous across the crack faces. Semi-permeable boundary conditions were proposed by Hao and Shen [2], in which the electric permeability in the crack gap is accounted for. In each of these three models, it is assumed that the crack faces are traction free. Landis [1] proposed a new set of boundary conditions that consists of additional closing tractions; these conditions are called the exact boundary conditions and will be used here in order to derive an  $M$ -integral. It should be noted that so far, the  $M$ -integral has not been derived using the exact boundary conditions.

To obtain the  $M$ -integral, use is made of the relation between the energy release rate and the  $J$ -integral. The former is given by

$$\mathcal{G} = \frac{1}{2} \mathbf{k}^T \mathbf{L}^{-1} \mathbf{k} \quad (1)$$

where  $\mathbf{k}$  is the intensity factor vector, namely  $\mathbf{k}^T = [K_{II}, K_I, K_{III}, K_{IV}]$ , and  $\mathbf{L}$  is one of the Barnett-Lothe tensors. The path independent  $J$ -integral which is given by



$$\begin{aligned}
 J &\equiv \lim_{r \rightarrow 0} \oint_{C_3} (hn_1 - T_i u_{i,1} + D_i n_i E_1) ds \\
 &= \oint_{C_1} (hn_1 - T_i u_{i,1} + D_i n_i E_1) ds + \int_{C_2} (\sigma_{i2} u_{i,1} - D_2 E_1) dx_1 + \int_{C_4} (\sigma_{i2} u_{i,1} - D_2 E_1) dx_1 \quad (2)
 \end{aligned}$$

where  $C_3$  is an infinitesimal circle of radius  $r$  surrounding the crack tip,  $C_1$  is an arbitrary path surrounding the crack tip, beginning at the lower crack face and terminating at the upper crack face,  $C_2$  and  $C_4$  are paths along the upper and lower crack faces. In eq. (2),  $h$  is the electric enthalpy density given by  $h = C_{ijks} \varepsilon_{ij} \varepsilon_{ks} - \kappa_{ij} E_i E_j / 2 - e_{sij} E_s \varepsilon_{ij}$ ,  $n_i$  is the unit outward normal to the paths,  $T_i = \sigma_{ij} n_j$  is the traction,  $u_i$  and  $D_i$  are the displacement and electric flux density fields, and  $E_1$  is the electric field in the  $x$ -direction. It should be noted that for the impermeable crack assumption, the expressions along  $C_2$  and  $C_4$  are zero (see Suo, et al. [3]).

To obtain the  $M$ -integral, two equilibrium solutions are assumed and superposed; this is possible since the material behaves linearly. Thus, the expressions for the stress, strain, displacement, electric fields, the electric flux density and the intensity factors are written as a combination of two solutions. The first solution is the sought after solution; the fields are obtained by means of a finite element calculation. The second solution consists of four auxiliary solutions which are derived from the first term of the asymptotic solution. By the usual manipulation, two expressions for the  $M$ -integral are derived and equated.

Several problems are analyzed by means of the finite element method with the program ANSYS [4]. Eight noded quadrilateral coupled field elements are employed. Quarter-point elements are used at the crack tip, so that the square-root singularity is well modeled. In order to accurately calculate the stress and electric fields at the crack tip, the mesh density is increased in that region.

Several benchmark problems are examined to demonstrate the accuracy of the method. Numerical difficulties encountered resulting from multiplication of large and small numbers is solved by normalizing the variables. Since an analytical solution exists, a finite length crack in an infinite body is also considered. In addition, a four point bend specimen subjected to both an applied load and an electric field is presented for a crack at an angle to the poling direction. It is seen that neglecting the piezoelectric effect in calculating stress intensity factors may lead to errors. Finally, results obtained by means of the impermeable and exact boundary conditions are compared.

## References

1. Landis, C.M., *Int J Solids Struct*, vol. **41**, 6291-6315, 2004.
2. Hao, T.-H. and Shen, Z.-Y., *Engng Fract Mech*, vol. **47**, 793-802, 1994.
3. Suo, Z., Kuo, C.-M., Barnett, D.M. and Willis, J.R., *J Mech Phys Solids*, vol. **40**, 739-765, 1992.
4. ANSYS, Release 8.1, Ansys, Inc., Canonsburg, Pennsylvania, 2004.

## FAILURE PZT THIN FILMS IN MEMS

D.F. Bahr, D.J. Morris, M.C. Robinson, A.L. Olson, C.D. Richards and R.F. Richards  
Mechanical and Materials Engineering, Washington State University  
PO Box 642920, Pullman WA 99164-2920, USA  
dbahr@wsu.edu

Many microelectromechanical systems (MEMS) are based on polysilicon films used for electrostatic actuation. However, piezoelectric films, such as lead zirconate titanate (PZT), can provide the ability to generate high forces at lower strains as actuators [1] or for use in energy conversion applications, bringing a different set of challenges regarding processing and reliability in mechanical applications. These often are used in the form of thin PZT membranes [2], and so this structure is of particular interest for piezoelectric MEMS, among the many possible geometries for this type of material [3]. In this presentation, failure mechanisms in PZT MEMS will be described for both processing requirements and during service.

During processing the stresses that often develop are due to thermal expansion mismatch between the PZT film and substrate, leading to tensile stresses on the order of 100's of MPa and subsequent film cracking and delamination. The thickness, electrode materials, and underlying adhesion layers impact the cracking and demonstrate that fracture in these cases is due to total elastic strain energy generated during cooling from high temperature annealing processes. Typical failures due to fracture during processing are shown in Fig. 1.

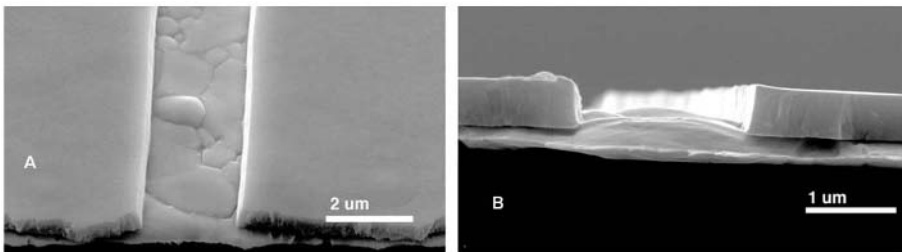


FIGURE 1. Through thickness cracking in PZT films during processing, Robinson *et. al.* [4]

During service, thin membranes and cantilevers are often stressed to large deflections, where elastic strains on the order of 0.2% are reached. The failure mechanism in this case tends to be related to tensile bending stresses, rather than membrane stresses. In very thin membrane structures, which are common in MEMS; this balance between bending and stretching can be used to accentuate the electromechanical coupling of thin PZT films if operated such that regions of the film in bending are utilized in compression and not tension. Using pressure – deflection curves measured from bulge testing these structures it is possible to measure both residual stresses, overall compliance, and fracture and failure strains. A bulge testing system has been developed using a laser vibrometer for deflection measurements to allow both static (Fig. 2) and dynamic measurements of deflection during bulge testing. The pressure deflection tests can be fit using the pressure,  $p$ , to deflect a pre-stressed membrane

$$p = Cw + Dw^3 \quad (1)$$

where C and D are constants related to stress and elastic modulus respectively, and w is the deflection at the midpoint of the membrane.

Microscopy of failed PZT films, along with electrical output from the films, will be presented to demonstrate the failure mechanisms in service. Fatigue testing using electrical actuation of the PZT film will be compared directly to that from mechanical forcing mechanisms to demonstrate fatigue behavior in excess of over a billion cycles under operating conditions.

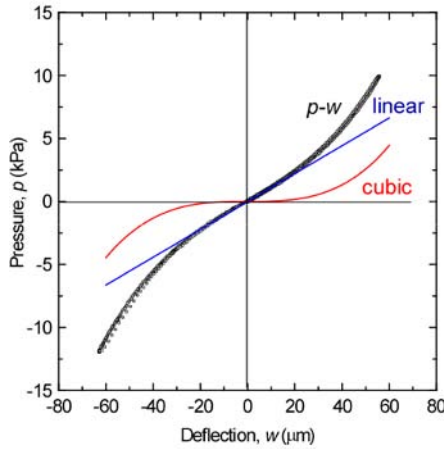


FIGURE 2. Pressure deflection relationship for 2  $\mu\text{m}$  PZT film on a 1  $\mu\text{m}$  Si membrane showing data (black) with eq. 1 deconvolved into the respective linear and cubic terms.

## References

1. Murali, P., Kholkin, A., Kohli, M., Maeder, T., *Sensors and Actuators A*, vol. **53**, 398-404, 1996.
2. Hong, E., Krishnaswamy, S.V., Freidhoff, C.B., Trolrier-McKinstry, S., *Sensors and Actuators A*, vol. **119**, 521-527, 2005.
3. Polla, D.L., Francis, L.F., *Annual Review of Materials Science*, vol. **28**, 563-597, 1998.
4. Robinson, M.C., Morris, D.J., Hayenga, P.D., Cho, J., Richards, C.D., Richards, R.F., Bahr, D.F., *Applied Physics A*, vol. **85**, 135-140, 2006.

## CHARGE-FREE ZONE MODEL FOR FAILURE OF CONDUCTIVE CRACKS IN PIEZOELECTRIC CERAMICS UNDER ELECTRICAL AND/OR MECHANICAL LOADING

Tong-Yi Zhang

Department of Mechanical Engineering

Hong Kong University of Science and Technology

Clear Water Bay, Kowloon, Hong Kong, China

mezhangt@ust.hk

In the present presentation, we report the success of applying the concepts of fracture mechanics to the failure of electrically conductive cracks in dielectric and piezoelectric ceramics. In industrial practice, internal electrodes have widely been adopted in electronic and electromechanical devices made of dielectric and piezoelectric ceramics. These embedded electrodes may naturally function as pre-conductive cracks or notches if Young's modulus of the electrode is much smaller than Young's modulus of the ceramics. In addition, dielectric breakdown and partial discharge may convert an originally electrically insulating crack to an electrically conductive crack. To ensure that the electric field inside the conductive crack remains zero, electric charges in the conductive crack surfaces rearrange themselves to produce an induced field that has the same magnitude as the applied one but with an opposite sign. As a result, the charges in the upper and lower crack surfaces near the crack tip have the same sign. Charges with the same sign repel each other and have a tendency to propagate the crack. The  $J$ -integral for a conductive crack in a dielectric material under purely electric loading is similar to the  $J$ -integral for a conventional crack under purely mechanical loading. It is therefore of practical importance and academic significance to apply the concepts of fracture mechanics to the failure of conductive cracks in dielectric and piezoelectric ceramics. Experimental results have confirmed that purely electric loading can fracture conductive cracks in poled and depoled lead zirconate titanate ceramics [1, 2]. The concepts of fracture mechanics can successfully be applied to the failure of conductive cracks under purely electric loading.

To understand the experimentally observed failure behaviors of conductive cracks in dielectric and piezoelectric ceramics under electric and/or mechanical loading, Zhang et al. [3, 4] proposed the Charge-Free Zone (CFZ) model by analogy to the Dislocation-Free Zone (DFZ). The CFZ model treats dielectric and piezoelectric ceramics as mechanically brittle and electrically ductile. The CFZ model is a two-dimensional model, in which charges are treated as line charges per unit length. Under applied electric loading, the high electric field at a conductive crack tip has the tendency to emit charges from the tip, while there are image forces acting on the charges, which are against the charge emission. Therefore, there must be a charge-free zone in front of the crack tip in order to emit charges continuously from the crack tip. These emitted charges are entrapped in a strip in front of the crack tip. The entrapped charges partially shield the crack tip from the applied electrical field and the local electric intensity factor has a non-zero value. Consequently there is a non-zero local electric energy release rate, which contributes to the driving force to propagate the conductive crack. By using the local energy release rate as the failure criterion [4], the CFZ model gives the following failure formula:

$$\left( \frac{K_{\sigma,C}^a}{K_{\sigma,C}^o} \right)^2 + \eta \left( \frac{K_{\sigma,C}^a}{K_{\sigma,C}^o} \right) \left( \frac{K_{E,C}^a}{K_{E,C}^o} \right) + \left( \frac{K_{E,C}^a}{K_{E,C}^o} \right)^2 = 1 \quad (1)$$

where  $K_{\sigma,C}^o$  (or  $K_{E,C}^o$ ) is the mechanical (or electrical) fracture toughness under purely mechanical (or electrical) loading,  $K_{\sigma,C}^a$  (or  $K_{E,C}^a$ ) is the critical stress (or electric) intensity factor under combined mechanical and electrical loading, and  $\eta$  is called the coupling factor. Mathematically, Eq. (1) has the form of  $x^2 + \eta xy + y^2 = 1$  with  $x = K_{\sigma,C}^a / K_{\sigma,C}^o$  and  $y = K_{E,C}^a / K_{E,C}^o$ , which can be expressed in the form of an ellipse,  $\hat{x}^2/[2/(2+\eta)] + (\hat{y}^2/[2/(2-\eta)] = 1)$ , where the  $(\hat{x}, \hat{y})$  coordinates are established by rotating  $45^\circ$  counterclockwise from the  $x$ -axis of the  $(x, y)$  coordinate system. The absolute value of  $\eta$  is less than two and thus Eq. (1) indeed describes an ellipse in terms of the normalized applied intensity factors. For dielectric materials with zero piezoelectric constants, the coupling factor is zero and Eq. (1) reduces to the failure criterion for conductive cracks in the dielectric materials [3]. The merit of the CFZ model, similar to the DFZ model, lies in the ability to directly apply the Griffith criterion to link the local energy release rate to the fracture toughness in a purely brittle manner. As a result, the CFZ model provides an explicit failure criterion for predicting the failure behavior of conductive cracks in dielectric and piezoelectric ceramics under electrical and/or mechanical loading. The advantage of applying such a failure criterion lies in the ability to predict the critical electric field and the critical mechanical load at which a dielectric or piezoelectric ceramic material containing a conductive crack or an internal electrode fails under electrical and/or mechanical loading. The critical electric field and the critical mechanical load are functions of the crack size or the length of the electrode, while both the electrical fracture toughness and the mechanical fracture toughness are material properties. Thus, one can predict the critical electric field and the critical mechanical load when the sample geometry and the electrical fracture toughness and the mechanical fracture toughness are available.

### Acknowledgements:

This work was supported by a RGC grant from the Hong Kong Research Grants Council, HKSAR, China.

### References:

1. Fu, R., Qian, C.F., and Zhang, T.Y., *Appl. Phys. Lett.*, vol. **76**, 126-128, 2000.
2. Wang, T. and Zhang, T.Y., *Appl. Phys. Lett.*, vol. **79**, 4198-4200, 2001.
3. Zhang, T.Y., Wang, T., and Zhao, M.H., *Acta Mater.*, vol. **51**, 4881-4895, 2003.
4. Zhang, T.Y., Zhao, M.H., Liu, G., *Acta Mater.*, vol. **52**, 2013–2024, 2004.
5. Zhang, T.Y., Liu, G., and Wang, Y., *Acta Mater.*, vol. **52**, 2025–2035, 2004.

## FRACTURE MECHANICS FOR ELECTROACTIVE MATERIALS

Robert M. McMeeking  
Department of Mechanical Engineering  
University of California, Santa Barbara, California 93106, USA  
rmcm@engineering.ucsb.edu

Electroactive materials include piezoelectrics, ferroelectrics and electroactive polymers. In the simplest form, this class of materials also includes isotropic dielectrics where there is minimal coupling between the mechanics and electrostatics. Indeed, electroactive polymers can be isotropic. Then they derive their useful properties of electrically stimulated actuation from their low mechanical stiffness. In such materials, large actuation strains occur when electric fields are applied. In the presentation, a consistent energetic formulation of boundary value problems for electroactive materials is formulated, including the electrostatic stress. This step is important because a correct energy balance for fracture mechanics can only be achieved after the proper formulation is obtained. The energy release rate for cracks in electroactive materials is then calculated and the J-integral for these systems obtained. The results are specialized to simple isotropic dielectrics, electroactive polymers, piezoelectrics and ferroelectrics. Fracture models are then considered for each type of material, including brittle failure concepts for simple dielectrics and piezoelectrics, switching zone effects in ferroelectrics and energy balance models for electroactive polymers. The outcome is a comprehensive and consistent fracture mechanics for electroactive materials. However, experiments on the fracture mechanics of electroactive materials are difficult for a variety of reasons, including the great sensitivity of the electrostatics of such materials to changes of shape, so that small crack openings cause large effects on the capacitance of the specimen being tested. In addition, free charge in the air has a very big effect on the electrostatic condition of specimens with cracks, and this makes it difficult to determine the physical nature of the electrical boundary conditions on the crack boundary, since free charge is easily attracted to the crack surfaces. Another difficulty is that very large electric fields can be generated readily inside the crack gap, so that electrical breakdown can occur. Electrical breakdown involves a flux of energy as charge is transmitted from one location with a given potential to another at a different potential. Thus electric discharge can disrupt the energy balance that is fundamental to the understanding of fracture mechanics. However, electric breakdown is difficult to detect in fracture experiments, and is seldom monitored. An additional difficulty is that instrumentation for electroactive material fracture mechanics is tricky, since it is difficult to establish a common datum for capacitance. Furthermore, leakage currents cause complications in the measurements, whether due to spurious features such as conducting paths extrinsic to the material such as on its surface, or intrinsic effects such as caused by the semi-conducting nature of many materials. This complex situation will be assessed and the state-of-the-art in this area summarized. Essential directions for future research will be recommended with the aim of resolving some of these challenging issues.

## FRACTURE IN PIEZOELECTRIC CERAMICS AND PZT/ELECTRODE INTERFACES

H. Jelitto<sup>1</sup>, F. Felten<sup>1</sup>, G.A. Schneider<sup>1</sup>, C. Häusler<sup>2</sup> and H. Balke<sup>2</sup>

<sup>1</sup> Hamburg University of Technology, Institute of Advanced Ceramics,  
Denickestraße 15, D-21073 Hamburg, Germany

<sup>2</sup> Technische Universität Dresden, Institut für Festkörpermechanik,  
D-01062 Dresden, Germany  
h.jelitto@tu-harburg.de

The fracture behavior of piezoelectric ceramic (PZT) as well as metal/PZT interfaces under mechanical and electric loading is examined in four and three point bending under conditions of controlled crack growth (see Fig. 1). The experiments are performed in a custom made very stiff testing machine. A special modulation technique, i.e. a small signal compliance method, allows in situ determination of the mechanical compliance  $C_m$ , the capacitance  $C_e$ , and the piezoelectric compliance  $C_p$  as a function of the crack length. By calculating the derivatives of these generalized compliances with respect to the crack surface area we get the total linear energy release rate.

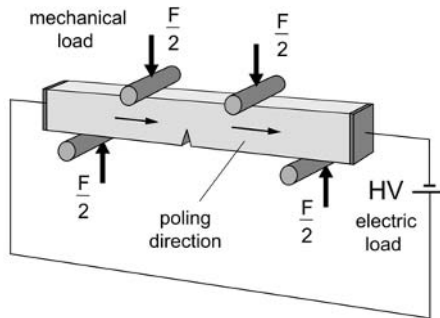


FIGURE 1. Schematic four point bending set-up.

The energy release rate is given in eq. (1) representing a generalized Irwin-Kies-Relation (Z. Suo [1]). The superscript ' $V$ ' stands for constant voltage and ' $F$ ' for constant force. We have

$$G_{tot} = \frac{F^2}{2} \frac{\partial C_m^V}{\partial A} + \frac{V^2}{2} \frac{\partial C_e^F}{\partial A} + FV \frac{\partial C_p}{\partial A} \quad (1)$$

$$\text{with } C_e^F = \left( \frac{\partial Q}{\partial V} \right)_F, \quad C_m^V = \left( \frac{\partial \Delta}{\partial F} \right)_V, \quad \text{and } C_p = \left( \frac{\partial Q}{\partial F} \right)_V = \left( \frac{\partial \Delta}{\partial V} \right)_F \quad (2)$$

Scrutinizing the modulation technique and the results we found that the small displacement modulation with an amplitude of about 30 nm yields pure linear elastic response of the material. Thus, we measure solely the intrinsic toughness due to the creation of new crack surface. It follows that the linear elastic energy is separated from inelastic and other dissipative processes.

This method was applied for ferroelectric bulk material (PZT PIC151) as well as for metal ceramic interfaces in commercial piezoelectric actuators. In the case of PZT bulk material measurements with insulating and conducting cracks were performed. The effect of an external electric field is quite different. In the case of the insulating crack an electric field of 500 V/mm yields a toughness change of the order of 10 %. This is much less than theoretically predicted for an impermeable crack, implying that the interior of the crack is highly permeable to electric fields. In the case of a conducting crack (see also Heyer et al. [2]), realized with a NaCl-solution in the crack interior, the effect of a corresponding electric field is of the order of 100 %. For example, with the appropriate field direction the crack grows by its own without any mechanical loading, which is in agreement with theoretical predictions.

For PZT bulk material as well as for metal ceramic interfaces in multilayer actuators the experimental data are compared with FEM-calculations, taking into account the piezoelectric coupling and the layout of the inner metal electrodes of the actuators. Technically it is more difficult to achieve stable crack growth in metal ceramic interfaces than in PZT-bulk material. The fracture toughness was measured for different poling configurations.

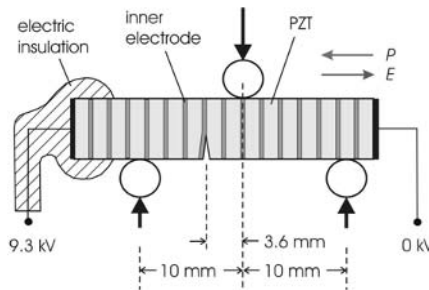


FIGURE 2. Schematic 3-point-bending arrangement of a multilayer actuator specimen for mixed mode loading and external electric field  $E$  ( $P$  = polarization).

In order to investigate mixed mode loading we performed an experiment in symmetric three point bending with stable crack growth. The notch is shifted away from the middle position between the lower support rollers (see Fig. 2), which yields a combination of the stress intensity factors  $K_I$  and  $K_{II}$ . During the measurement the crack does not bend off but stays in the interface. Thus, a new method is presented which allows for the determination of the total linear energy release rate including the mechanical, the electric and the piezoelectric contribution. A paper [3] has been submitted and two others are in preparation.

## References

1. Suo, Z., *ASME 1991*, AD-vol. **24**/AMD-vol. **123**, 1-6
2. Heyer, V., Schneider, G.A., Balke, H., Drescher, J., and Bahr, H.-A., *Acta Mater.*, vol. **46**(18), 6615-6622, 1998
3. Jelitto, H., Felten, F., Swain M.V., and Schneider G.A., *J. Appl. Mech.*, submitted



## VIBRATION PHASE BASED ORDERING OF VIBRATION PATTERNS ACQUIRED WITH A SHEARING SPECKLE INTERFEROMETER AND PULSED ILLUMINATION

Peter A.A.M. Somers and Nandini Bhattacharya  
Optics Research Group, Delft University of Technology  
Lorentzweg 1, NL-2628 CJ Delft, The Netherlands  
P.A.A.M.Somers@TNW.TUdelft.nl;  
N.Bhattacharya@TNW.TUdelft.nl

Harmonic vibrations of diffusely reflecting objects can be visualized using interferometric methods such as holography or speckle interferometry. The vibrating object can be illuminated by a CW laser or a pulse laser. When using a CW laser and exposing the holographic medium or CCD camera for a period that is relatively long compared to the vibration period, time average interferograms are obtained, while phase information is lost. When a pulse laser is used two exposures with appropriate timing can be made to obtain correlation fringes after subtraction.

Full temporal characterisation of the vibration pattern requires additional measures in order to obtain quantitative data from different vibration phase values. For this purpose a stroboscopic approach can be used, either employing pulsed illumination or synchronized camera exposure. In both cases precise external control of laser source and camera is required.

For the acquisition of vibration patterns with a phase stepped speckle interferometer several processes requiring synchronization are involved: object vibration, image acquisition, phase stepping, and illumination when a pulse laser is used. In many cases object vibration is considered to be the master process: the other processes are synchronized to the vibration frequency. Pulse lasers that provide sufficient power are not always easy to synchronize to external events. For our experiments a flash lamp pumped Nd:YAG pulse laser was available that could not be triggered externally, but did provide access to synchronization pulses. Using those, a set-up has been developed in which the pulsed illumination was the master process. Image acquisition was controlled by the synchronization pulses provided by the pulse laser. As a consequence, vibration patterns were acquired in random order. In order to be able to put the randomly acquired vibration patterns in the right order an additional measurement of vibration phase at the moment of acquisition was taken. After sorting the series of speckle interferograms using the vibration phase as the sorting key, the data could be processed sequentially to produce phase difference and unwrapped accumulated phase difference distributions for all measured values of the vibration phase. Since the interferometer was a two-channel system, Somers [1-2], that allowed simultaneous acquisition of two  $\pi/2$  phase stepped interferograms, there was no need for synchronization of the phase stepping process.

Vibration frequency is considered to be an independent variable while sampling frequency is governed by pulse repetition rate, which is also independent in the present set-up. Although the laser could not be synchronized as a slave process, it was possible to slightly change its pulse repetition rate in order to avoid the vibration frequency to be a multiple of the sampling frequency, a condition that also has to be met for stroboscopic systems. With proper settings an even distribution of samples over the vibration period can be obtained. In practice, where sampling and vibration frequencies differed by one or two orders, it appeared to be very hard to achieve settings for which an unacceptable distribution of samples over the vibration period was obtained.

A general purpose counting board and some custom electronics for pulse shaping were used to implement measuring of elapsed time between two input pulses: vibration sync and laser sync. The

difference represents vibration phase, which was used to sort speckle interferograms that were acquired on laser sync. After sorting, the interferograms were processed using temporal phase unwrapping, Huntley [3], allowing accumulation of phase differences to represent unwrapped phase at any instance of the vibration phase. In Fig. 1a the accumulated phase difference distribution over the positive part of the vibration is presented, Fig. 1b shows the negative portion. Since the interferometer is of the shearing type spatial derivatives of the out of plane displacement are shown. Shear is in vertical direction.

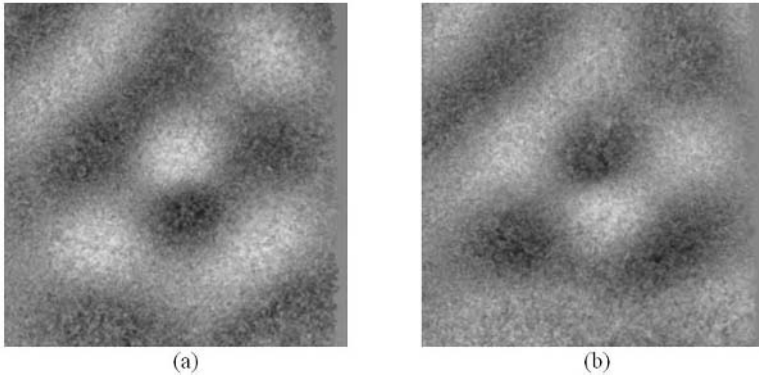


FIGURE 1. Spatial derivatives of accumulated phase difference distributions of a plate vibrating at 900 Hz, acquired with a pulse repetition rate of 10 Hz. (a) during the positive part of the vibration, (b) during the negative part. Shear is vertical.

### References

1. Somers, P.A.A.M. and Bhattacharya, N., in *Proceedings of SPIE conference "Optical Metrology 2005"*, SPIE vol. **5856**, edited by W. Osten, C. Gorecki and E. Novak, SPIE, Bellingham, 2005, 664-673.
2. Somers, P.A.A.M. and Bhattacharya, N., *Journal of Optics A: Pure and Applied Optics*, No. 7, S385-S391, 2005.
3. Huntley, J.M. and Saldner, H., *Applied Optics* vol. **32**, No. 17, 3047-3052, 1993.

## RECENT DEVELOPMENTS OF SPECKLE PATTERN INTERFEROMETER FOR BONE STRAIN MEASUREMENT

L.X. Yang and H. Yokota

Optical Laboratory, Department of Mechanical Engineering, Oakland University, Rochester, Michigan 48309, USA

Departments of Anatomy and Cell Biology, and Biomedical Engineering  
Indiana University Purdue University Indianapolis, Indianapolis, Indiana 46202, USA  
yang2@oakland.edu

For over 100 years load-driven bone remodeling has been investigated [1]. Many animal and clinical studies support that mechanical loads strengthen bone and reduction in loading due to long-term bed rest, cast immobilization or microgravity in space induces bone loss and mineral changes [2, 3]. Despite these outcomes, the mechanisms underlying load-induced bone remodeling are not well understood. The current hypothesis is that bone remodeling is mediated by interstitial fluid flow in porous bone matrix, and load-driven strain stimulates fluid flow [4]. In order to examine the quantitative relationship between bone deformation and interstitial fluid flow, the precise strain measurement is indispensable.

Although strains in bone are commonly measured using strain gauges, there are several limitations in the current measurements. First, a strain gauge must be attached to a site of strain measurement, but it is often difficult to glue it to non-flat bone surfaces. Second, the size and the number of gauges on a bone sample limit spatial resolution of strain measurements. The present resolution is in the order of 1 mm, which does not allow us to evaluate the precise strain distribution in the lacunocanicular networks in bone. Third, any strain gauge can hardly provide the 3D strain distribution including in-plane and out-of-plane components. In order to improve current strain measurements with strain gauges, digital speckle pattern interferometry (ESPI) will be employed in this studies.

DSPI is a well-established method for measuring 3D-deformations and thus 3D-strains, DSPI can be considered an electronic version of holographic interferometry that uses a CCD camera instead of photographic film to acquire electronic fringe images. First, a laser is split into two illuminating beams (an object beam and a reference beam). The object beam is then directed to the surface of the sample and its reflecting beam is combined with the reference beam. The phase difference between the reflecting beam and the reference beam is indirectly recorded through intensity of an interference pattern named as a speckle interferogram. Alteration in the phase difference before and after the mechanical loading to bone is analyzed, and the amount of deformation and the distribution of strains in the loaded sample are determined.

So far, DSPI technique has been used to measure bone strains [5-7], but most of the results published have not considered any significant contour change, which will not allow one to derive accurate strain distributions because of complex surface contours inherent to biological samples. This paper presents recent developments for bone strain measurement by Digital Speckle Pattern Interferometer: First, we develop a custom-made piezoelectric loading device as well as a DSPI-based force calibration system. A integrated DSPI system including a mechanical loading system will be presented; Second, both of contour and deformation have been measured by a single DSPI system so that the true strain distributions on the bone surface have been determined quantitatively. We determined high-resolution three-dimensional strains on the mouse femur in response to two loading modalities: an axial loading modality (ALM) and a knee loading modality (KLM). Fig. 1 shows 3D-deformation distributions induced by a KLM load.

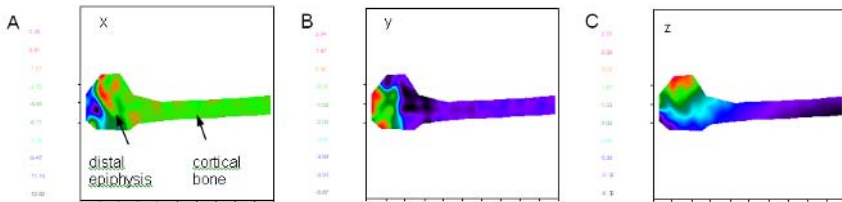


FIGURE 1. 3D deformations measured with DSPI system in response to a load of 0.5 N. The load was applied to the distal epiphysis along the y-axis (direction perpendicular to the femoral shaft). The deformations were illustrated with a color code in (A), (B) and (C) in the x, y, and z directions, respectively. The color pattern indicates the complex pattern of deformation in the distal epiphysis and the spots of altered deformations in the cortical bone.

The results presented above are related to a fresh bone, but not a bone with a completely wet surface. In order to measure bone *vivo ex* (with a wet surface), a special hydrophilic polymer coating has been developed to suppress movements of water molecules on the surface. Different attempts have been made and results will be presented.

## Summary

1. C.H. Turner, *Bone* 23, 399 (1998).
2. G. Carmeliet, L. Vico, and R. Bouillon, *Critical Rev. Eukaryotic Gene Expression*, vol. **11**, 131 (2001).
3. P.J. Ehrlich, and L.E. Lanyon, *Osteoporos. Int.*, vol. **13**, 688 (2002).
4. M.L. Knothe Tate, R. Steck, M.R. Forwood, and P. Niederer, *J. Exp. Biol.* 203, 2737 (2000).
5. J.F. Orr and J.C. Shelton, *Optical Measurement Methods in Biomechanics*, Chapman and Hill, London (1996), Chapter 4: *Holographic interferometry*, edited by J.R. Tyrer and J.C. Shelton, Chapter 5: *Speckle techniques*, edited by J.D. Briers, and Chapter 6: *Electronic speckle pattern interferometry*, edited by Tyrer.
6. M. Su, P. Samala, H. Jiang, S. Liu, L.X. Yang, and H. Yokota, Measurement of bone strain using electronic speckle pattern interferometry, *J Holography and Speckle*, vol. 2, No. 1: pp. 34-39 (2005).

## INVESTIGATION OF THE THERMAL DEFORMATION OF ELECTRONIC PACKAGES WITH ELECTRONIC SPECKLE PATTERN INTERFEROMETRY

Hans Reinhard Schubach  
Dantec Dynamics GmbH  
Kässbohrer Str. 18, 89077 Ulm, Germany  
Reinhard.schubach@dantecdynamics.com

Electronic components are used in the automotive, communication, aerospace and other industries. Miniaturization, higher package density and accelerated development processes have a great impact on the reliability of components. Rapid changes of ambient temperature or internal production of heat may occur during operation. This may create high thermal stresses due to the mismatch of the thermal expansion coefficients of the different materials in electronic components. Nowadays, a big amount of the car recalls by the manufacturers are due to electronic malfunctions.

The thermal expansion is very important for the durability of electronic components. Joining of different materials exposed to variations of temperature generates the strain mismatch which can be locally strong. These strains might cause cracks which initiate malfunctions.

Strain mismatch occurs by the following process:

- During the production process (soldering conditions, heat production during curing, ...)
- During the operation due to local production of heat (Resistant losses, microprocessors, diode laser, ...) and during the change of ambient temperature

On the other side simulations (FEM, ...) are used in the electronic industry, but the material parameters (coefficient of thermal expansion, young's modulus, ...) have to be known. A validation of results is necessary. In some cases simulations are not possible, than the measurement precise deformation is necessary.

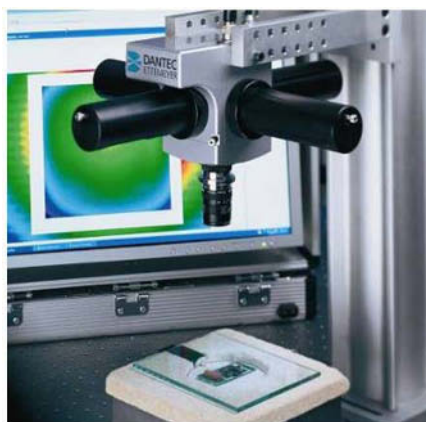


FIGURE 1. Three points bend specimen.

The 3D electronic speckle interferometry [1], [2] is a very powerful tool to investigate the thermal expansion of electronic components. Due to the full field measuring technique combined with a high resolution the determination of critical areas and hot spots in electronic components is very easy. Fig. 1 shows the experimental setup of the EPSI measuring system. The capability of this measuring technique will be shown on various examples (see Fig. 2).

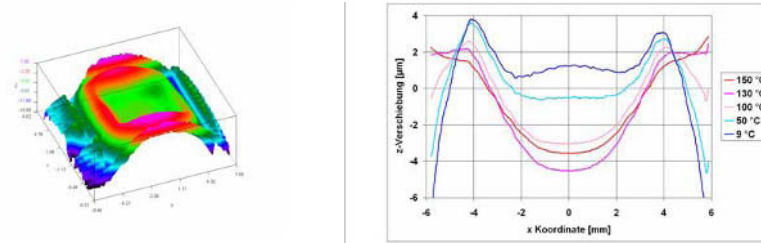


FIGURE 2. Deformation of a Ball Grid Array after cooling from 180°C down to 9°C.

## References

1. Kreis, Th., *Handbook of Holographic Interferometry*, Springer Weinheim 2005
2. Maas, A. A. M., *Phase shifting speckle interferometry*, Delft 1991, 13ff

## ONE-SHOT DIGITAL HOLOGRAPHY USING POLARIZATION IMAGING WITH A PIXELATED MICRO-RETARDER ARRAY

S. Yoneyama<sup>1</sup>, N. Mizuhara<sup>1</sup>, K. Tabata<sup>1</sup>, T. Nomura<sup>2</sup> and H. Kikuta<sup>1</sup>

<sup>1</sup>Department of Mechanical Engineering, Osaka Prefecture University  
1-1 Gakuen-cho, Sakai, Osaka 599-8531, Japan

<sup>2</sup>Department of Opto-Mechatronics, Wakayama University  
930 Sakaedani, Wakayama 640-8510, Japan  
yoneyama@me.osakafu-u.ac.jp

Digital holography is becoming popular technique in the fields not only of experimental mechanics but of optical information processing [1-4]. Phase-shifting technique is usually used for obtaining reconstructed images efficiently and accurately. However, the phase-shifting technique requires more than three images for a fully complex fields. That is, the current phase-shifting method has the disadvantage of a time lag during phase-shifting and acquisition between phase steps. This means that the current techniques cannot be applied to time-variant problems such as mechanics of vibrating objects or time-dependent materials. Recently, some techniques have been proposed for reducing images for phase-shifting digital holography [5,6]. However, it is not yet possible to record phase-stepped images simultaneously in a single frame.

This paper presents a new instantaneous phase-shifting technique for digital holography using a CCD camera that equips a pixelated micro-retarder array. An optical setup of polarization interferometry using a Twyman-Green type interferometer with two retarders is constructed to record a hologram. Light emerging from the interferometer is recorded using a CCD camera that has the micro-retarder array on the CCD plane. This micro-retarder array has four different principal directions. That is, an image obtained by the CCD camera contains four types of information corresponding to four different optical axes of the retarder. The four images separated from the image recorded by the CCD camera are reconstructed using gray level interpolation. Then, the reconstructed image is obtainable from the separated images using Fresnel diffraction integral.

Figure 1 portrays a CCD camera configuration with a pixelated micro-retarder array [7,8]. Many sets of four ( $2 \times 2$ ) micro-retarders with uniform retardation values, whose fast axes subtend four different angles, form the large array on the polarizer and the CCD, as shown in this figure. The size of a single micro-retarder is equivalent to a single pixel of the CCD. The micro-retarder position is aligned with the CCD sensors. A single CCD sensor detects the intensity of light that passes through a single retarder with a specific angle of the fast axis. Then, the four light intensity distributions corresponding to the four retarders are obtained as a single image. Spatial resolution of each light intensity distribution is reduced to one-fourth of the CCD's resolution. In addition, the spatial positions of the four light intensity distributions do not mutually correspond. Therefore, light intensities other than the angle of the retarder at the point are determined from light intensities at the neighboring points using interpolation such as bilinear or bicubic interpolation methods. This study employs a bilinear interpolation method. Then, the four light intensity distributions whose respective sizes are equivalent to the CCD are obtained by a single exposure. The four light intensity distributions are therefore phase-stepped images, similar to those obtained in other phase-shifting methods.

Figure 2 shows microscopic photographs of the part of the pixelated micro-retarder array that is produced using a micro-fabrication technology [9]. A 10-mm-thick polarizer is placed on the CCD with  $640 \times 480$  pixel resolution and  $7.4 \mu\text{m} \times 7.4 \mu\text{m}$  pixel size. For the retarder shown in

this figure, the subwavelength structure with a period of 300 nm is made of  $\text{TiO}_2$  on a silica substrate. The grating thickness is  $1.03 \mu\text{m}$  and the single retarder area is  $7.4 \mu\text{m} \times 7.4 \mu\text{m}$ . The phase retardation of the retarder is controllable by the groove depth and the duty cycle of the grating. The optical axis coincides with the grating direction. The optimized combination [10] of the retarders with the retardation of 2.30 rad, whose fast axes make angles of  $\pm 0.264$  rad and  $\pm 0.902$  rad with the optical axis of the polarizer, for polarimetry is used for designing the micro-retarder array in this study.

It is emphasized that this method is applicable to time-variant problems because multiple exposures are unnecessary for sufficient data acquisition.

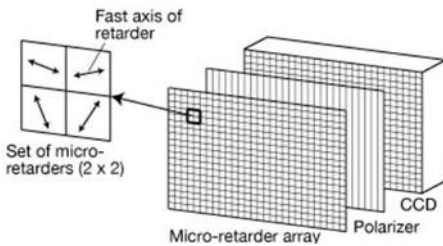


FIGURE 1. Configuration of the micro-retarder array

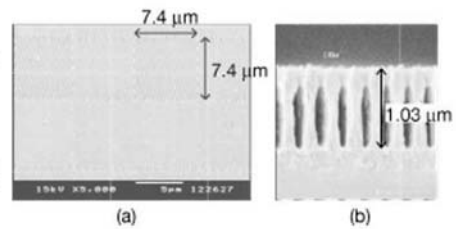


FIGURE 2. Microscopic photographs of the micro-retarder array: (a) top view; (b) cross-section

## References

1. Yamaguchi, I. and Zhang, T., *Opt. Lett.*, vol. **22**, 1268–1270, 1997.
2. Takao, S., Yoneyama, S., and Takashi, M., *Opt. Lasers Eng.*, vol. **38**, 233–244, 2002.
3. Xu, L., Peng, X., Guo, Z., Miao, J., and Asundi, A., *Opt. Express*, vol. **24**, 2444–2452, 2005.
4. Morimoto, Y., Nomura, T., Fujigaki, M., Yoneyama, S., and Takahashi, I., *Exp. Mech.*, vol. **45**, 65–70, 2005.
5. Nomura, T., Murata, S., Nitani, E., and Numata, T., *Appl. Opt.*, vol. **45**, 4873–4877, 2006.
6. Awatsuji, Y., Sasada, M., Fujii, A., and Kubota, T., *Appl. Opt.*, vol. **45**, 968–974, 2006.
7. Yoneyama, S., Kikuta, H., and Moriwaki, K., *Exp. Mech.*, vol. **46**, 451–456, 2005.
8. Yoneyama, S., Kikuta, H., and Moriwaki, K., *Opt. Eng.*, vol. **45**, 083604, 2006.
9. Kikuta, H., Toyoda, H., and Yu, W., *Opt. Rev.*, vol. **10**, 63–73, 2003.
10. Sabatke, D.S., Descour, M.R., Dereniak, E.L., Sweatt, W.G., Kemme, S.A. and Phipps, G.S., *Opt. Lett.*, vol. **25**, 802–804, 2000.



## EXPLOSIVE EMBOSsing OF HOLOGRAPHIC STRUCTURES: COMPUTATIONAL SIMULATION OF PROCEDURAL INFLUENCES TO THE RECONSTRUCTED HOLOGRAM

T. Scholz<sup>1</sup>, A. Kraft<sup>1</sup>, E. Reithmeier<sup>1</sup> and G. Helferich<sup>2</sup>

<sup>1</sup> Institut für Mess- und Regelungstechnik IMR, Universität Hannover  
Nienburger Straße 17, D-30167 Hannover, Germany

<sup>2</sup> Fraunhofer-Institut für Chemische Technologie ICT  
Joseph-von-Fraunhofer-Straße 7, D-76327 Pfinztal (Berghausen), Germany  
till.scholz@imr.uni-hannover.de, arne.kraft@imr.uni-hannover.de,  
sekretariat@imr.uni-hannover.de, guenter.helferich@ict.fraunhofer.de

Nowadays, the moulding of holographic structures is a relatively complex process: First a master-hologram has to be created in a very soft, possibly even near-liquid, medium. These however are too soft to be of interest for industrial structuring. Further stabilizing of the structures present in the master-hologram requires galvanic processing, which is both energy- and time-intensive as well as environmentally questionable, due to hazardous residues from the galvanic baths. As the medium used is usually relatively soft and hence not really dimensionally stable under stress as found in industrial processes, the mastershims resulting from the first galvanic process are themselves duplicated by further galvanic processing to produce numerable and most importantly interchangeable daughter-shims. In contrast to this laborious process, explosive embossing requires moderate energy- and minimal time-resources, while not producing any hazardous waste. Additionally, the process of explosive embossing enables the use of relatively soft materials to structure hard materials, such as steel. Moreover, it also addresses the issue of forgery-immunity, as the original masterstructure is destroyed in the process, which is schematically displayed in Fig. 1.

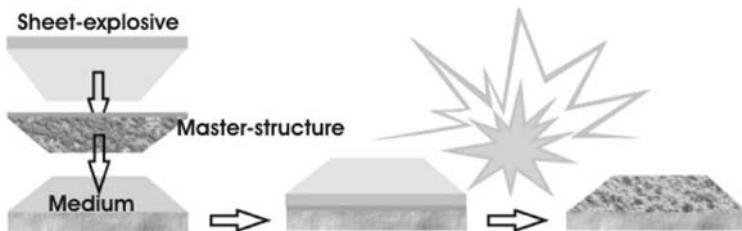


FIGURE 1: Schematic of the process of explosive embossing. (Source: Fraunhofer ICT)

The process of explosive embossing will probably introduce some deviations into the final nanostructure, hence it is important to determine the transfer-function as accurately as possible in order to be able to adjust the masterstructure in such a way, that any possible deviations from the optimum case are minimized. In order to determine said transfer-function we envisioned a computer-program to digitally analyze the differences between the holographic results yielded by the masterstructure and its explosive-embossing-result.



FIGURE 2: An example of a blast-embossed macro-structure (Source: Fraunhofer ICT)

Fig. 2 shows an exemplary result of explosive embossing of macrostructures. The masterstructures used were proper plant-leaves and the medium was steel; a fact which should impress the large variety of possible combinations of materials, which can be used for explosive embossing.

The “Institut für Mess- und Regelungstechnik” (Numerical simulations and experimental verification) and the Fraunhofer Institute for Chemical Technology (explosive embossing) are currently presiding over a project of the Federal Ministry of Education and Research (BMBF), which includes the following partners: Kugler GmbH, Georg Neumann GmbH, topac GmbH, Firma Rieger and Holo-Support.

We wish to thank the Federal Ministry of Education and Research (BMBF) and the German Aerospace Center (DLR) as project executing organisation for funding this project.

## References

1. Helferich, G.; Keicher, T. (*Einprägsam. Sprengprägen zur schnellen Erzeugung von Werkzeug-Oberflächenstrukturen.*) In: *mo-metalloberfläche*, 7/2001, Hanser-Verlag, 55. Jahrgang, 40-41, 2001
2. Helferich, G., Ziegler, L., Keicher, T., Elsner, P., *Explosive Structuring for High-Speed Generation of Mold Surface Structures*. SAE 2002, Detroit, USA, March 04-07, 2002

**CONTOURING OF DIFFUSED OBJECTS BY USING DIGITAL HOLOGRAPHY**

Chandra Shakher, Dalip Singh Mehta, Md. Mossaraf Hossain and Gyanendra Sheoran  
Laser Applications and Holography Laboratory  
Instrument Design Development Center  
Indian Institute of Technology, Delhi  
New-Delhi-110016, India  
cshakher@hotmail.com, cshakher2001@yahoo.co.in, cshakher@iddc.iitd.ernet.in

Three dimensional shape measurements by non-contact optical methods have been extensively studied because of its importance in automated manufacturing, quality control of components, robotics and modeling application. Several optical surface contouring methods interferometry, light scattering, speckle photography, moiré, Talbot interferometry and holography etc. have been developed [1-11]. Optical surface contouring method using interferometry fulfills the condition of non-contacting and whole field measurement of surface shape with high resolution. Fizeau and Twyman-Green interferometers can be used only for continuous mirror surfaces, on the other hand low coherence interferometry [12] and wavelength scanning interferometry, which are applicable for stepped and diffusely reflecting surfaces on the other [13]. These methods are not suitable for small and complicated components as MEMS and others. Digital Holography can be combine interferometry with the image formation of 3D object by a computer and is also be endowed with a function of microscopy which suits to the surface contouring of complicated structures like MEMS. Nowadays, with the availability of new generation of high-speed microprocessors, high-resolution opto-electronic sensors and liquid crystal display systems, digital holography became feasible, where holograms are recorded using opto-electronic sensors and the digitized holographic data are processed numerically to reconstruct the images using computer programs which makes the entire process faster, reliable and almost in real time. Digital holographic interferometry, which is fast and robust as compared to conventional holographic interferometry, can be easily adopted in industrial environment by using proper instrumentation. In Digital holographic interferometry, a “digital double exposure hologram” is formed by addition of two digital holograms corresponding to two different stages of the object can be numerically reconstructed to give the intensity interferograms superimposed on the image of the object [14-20]. Using digital holographic process, the individual phases of two numerically reconstructed wavefronts corresponding to two different states of the object are calculated and can be compared to yield the desired interference phase [20]. Contour generation is the formation of image of an object on which contours of constant elevation with respect to some plane are superimposed. Such an image and contour maps can be easily interpreted and provides full field display of three-dimensional surface shapes. Several methods for contouring have been investigated by using conventional holography, by using the refractive index variation, changing the wavelength, varied illumination direction and light-in-flight recording. In digital holography, contouring by light-in-flight measurement and by varying the direction of object illumination/phase shifting digital holography is reported.

In this paper, we present a method of contouring for diffused objects by using lens less Fourier transform digital holographic interferometry and dual index immersion method. The method exploits “digital double exposure holography” to obtain the intensity interferograms. The desired interference phase map corresponding to these interferogram are calculated by modulo 2 subtraction of the phases obtain from the individual holograms recorded with different refractive indices pairs of the alcohol-distilled water solutions. This method may find important application for measuring various sized defects in mechanical parts and complicated diffused objects. Because of poor resolution and limited aperture of the opto-electronic sensors, the minimum value of depth

contour interval obtained in this method is limited. With the advancement of sensor technology, in near future, this method may be of greater utility.

## References

1. Rastogi, P.K., Editor. *Optical measurement techniques and applications*, artech House, Inc. Boston. London, 1997.
2. Sirohi, R.S., Chau, F.S., *Holographic interferometry, Speckle metrology, Optical methods of measurement*, 10<sup>th</sup> edition, Marcel Dekker, Inc. 1999.
3. Gasvik, K.J., *Optical metrology*, 3<sup>rd</sup> edition, John Wiley and sons, Ltd., 2002.
4. Idesawa, M., Yatagai, T., Soma, T., *Appl. Opt.*, vol. **16**, 2152-2161, 1977
5. Choi, Y.B., Kim, S.W., *Opt. Eng.*, vol. **37**, 1005-1010, 1998
6. Mirza, S., Shakher, C., *Opt. Eng.*, vol. **44**(1), 13601-13606, 2005
7. Hildebrand, B.P., Haines, K.A., *J. Opt. Soc. Amer.*, vol. **57**, 155-162, 1967
8. Verner, J.R., *Appl. Opt.*, vol. **10**, 212-213, 1991
9. Adams, M., Kreis, T., Juptner, W., *Proc SPIE Opt inspection and micro-measurements II* 1997, vol. **3098**, 234-40.
10. Kreis, T., Juptner, W., Geldmacher, J., *Proc of SPIE, Laser interferometry IX: Techniques and analysis* 1998, **3478**, 45-54.
11. Nilsson, B., Carlsson, T.E., *Appl. Opt.*, vol. **37**, 7954–7959, 1998
12. Dresel, D., Hausler, G., Venzke, H., *Appl. Opt.*, vol. **31**, 919-925, 1991
13. Takeda, M., Yamamoto, H., *Appl. Opt.*, vol. **34**, 7829-7837, 1994
14. Takeda, M., Ina, H., Kobayashi, S., *J. Opt. Soc. Am.*, vol. **72**, 156-60, 1982
15. Kreis T., *J. Opt. Soc. Am. A.*, vol. **3**, 847-55, 1986
16. Pedrini, G., Froening, Ph., Fessler, H., Tiziani, H., *Opt. Laser Technol.*, vol.**29**,505–511, 1997
17. Yamaguchi, I., Ohta, S., Kato, J.I., *Opt. Laser Technol.*, vol. **36**, 417-428, 2001
18. Pedrini, G., Tiziani, H., *Opt. Laser Technol.*, vol. **29**, 249–256, 1997
19. Hossain, M.M., Mehta, D.S., Shakher, C., *Opt. Eng.*, (to be appear in 2006).
20. Schnars, U., *J. Opt. Soc. Am. A.*, vol. **11**(7), 2011-2015, 1994

## NONLINEAR BULK ELASTIC WAVES IN LAYERED SOLID WAVEGUIDES

I.V. Semenova, G.V. Dreiden and A.M. Samsonov  
 A.F.Ioffe Physical Technical Institute  
 26, Polytekhnicheskaya, St.Petersburg, 194021, Russia  
 Irina.Semen@mail.ioffe.ru

Layered structures, e.g., various thin film coatings or adhesively bonded components, are increasingly used in modern technologies, from aerospace industry to microelectronics. It is well known that the integrity of layered structures is determined by the quality of their interfaces. Indeed, an abrupt change in material properties at the interface and different deformation behaviour under loading can result in considerable stress concentrations near interfaces and lead to delamination and cracking. These destructive processes not only affect the functionality of structures but can also cause their complete failure. That is why it becomes important both to learn wave processes that can develop in such structures and be a potential source of excessive loads, and to elaborate reliable methods for structure quality testing and delamination detection.

Bulk strain soliton is a nonlinear long quasistationary localized strain wave that can be formed in a solid waveguide (having certain elastic and geometrical characteristics) from an initial pulse (also having certain parameters) (see [1-3] for our previous results on theoretical and experimental research on the generation and succeeding propagation of bulk strain solitary waves in various polymeric waveguides). Being formed the soliton propagates then along the homogeneous wave guide with almost no changes of amplitude, shape and velocity (see Figure 1 for the holographic interferogram of a strain soliton in a uniform PMMA bar).

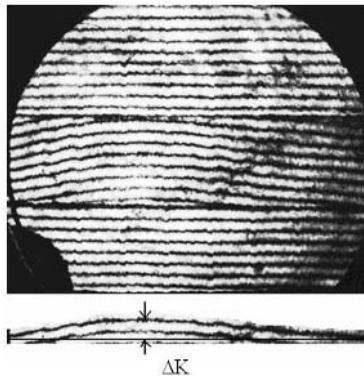


FIGURE 1. Holographic interferogram of a strain soliton in the PMMA bar at the distance 350-400 mm from its input. Wave moves from left to right. Fringe shift, representing the wave, is shown below the interferogram.

Bulk strain solitary waves being occasionally generated and propagating along a layered waveguide, may cause delamination and cracks at the interface. For this reason soliton recording and determination of its parameters is important for further prediction of material 'resistance' and stability. On the other hand these elastic waves can be used as a tool to detect inhomogeneities in

layered structures. In particular, for the initial velocity of the strain soliton, its amplitude and shape given, it is possible to determine the characteristics of damaged area via the variations of soliton features. The latter can be potentially used for NDT of layered structures, using bulk nonlinear solitary elastic waves.

The glue layer in adhesively bonded structures can be positioned along, across or at a slant to the soliton propagation direction. To begin with in our experiments only two first cases are considered. The soliton propagation through a perpendicularly oriented bonding layer can be considered as a head-on impact of soliton on the interface. In our experiments with layered wave guides we use a complex rod/bar structure (see Figure 2), in which soliton is initially formed in a uniform part (rod) and then enters a layered part (bar, made of 2 or 3 longitudinal layers glued together) through a transverse bonding layer.

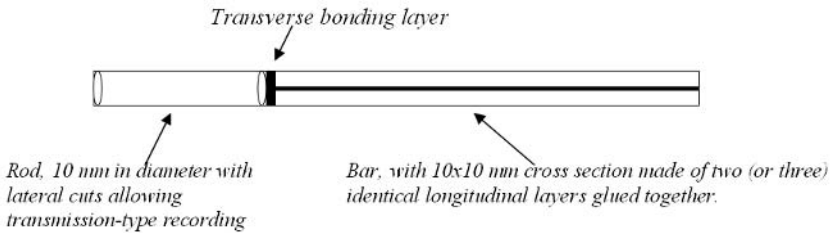


FIGURE 2. Schematic of a layered waveguide used in experiments

In this paper we present experimental results on the evolution of a formed strain soliton in layered bars shown in Fig. 2, made of PMMA.

## References

1. G.V.Dreiden et al., *Techn.Phys.Lett.*, vol. **21** (6), 415-417, 1995.
2. A.M. Samsonov et al., *Physical Review B*, vol. **57** (10), 5778-5787, 1998.
3. G.V.Dreiden et al., *Techn.Phys.*, vol. **46** (5), 505-511, 2001.
4. I.V.Semenova, G.V.Dreiden, and A.M.Samsonov. *Proc. SPIE*, vol. **5144**, 521-532; 2003.
5. I.V.Semenova, G.V.Dreiden, and A.M.Samsonov. *Proc. SPIE*, vol. **5880**, 32-39; 2005.

## EFFECTS OF WINDOW SIZE ON ACCURACY AND SPATIAL RESOLUTION IN WINDOWED PHASE-SHIFTING DIGITAL HOLOGRAPHIC INTERFEROMETRY

Yoshiharu Morimoto<sup>1</sup>, Toru Matui<sup>1</sup>, Motoharu Fujigaki<sup>1</sup> and Norikazu Kawagishi<sup>2</sup>

<sup>1</sup>Faculty of Systems Engineering, Wakayama University

<sup>2</sup>Graduate School of Systems Engineering, Wakayama University

Sakaedani, Wakayama 640-8510, Japan

morimoto@wakayama-u.ac.jp, matui@sys.wakayama-u.ac.jp, fujigaki@sys.wakayama-u.ac.jp, s062009@sys.wakayama-u.ac.jp

In phase-shifting digital holography, a hologram is usually recorded on a CCD sensor instead of a photographic plate. The complex amplitude of the object is analyzed from the phase-shifted holograms obtained by shifting the phase of the reference beam. The reconstructed image can be calculated from the complex amplitudes of the hologram [1].

In phase-shifting digital holographic interferometry[2] for measuring a displacement distribution of an object, displacement at each point is obtained from the phase-difference between the reconstructed images analyzed by digital holograms recorded before and after deformation[3-5]. Small displacement of a cantilever is analyzed by using Twyman-Green type holographic interferometry. Figure 1(a) shows the analyzed phase distribution. Figure 2(a) shows the displacement distribution along the centerline. The standard deviation of the errors from the theoretical displacement is 16.4nm.

Holograms and reconstructed images have speckle noise and they provide large errors in the calculation of displacement analysis. In order to reduce the effect of speckle noise, the authors proposed a novel method using many windowed holograms [4,5].

In holography, any part of a hologram has the optical information of the whole reconstructed image. By using the feature of hologram, the hologram is divided into several parts by superposing many different windows. The phase-difference values at the same reconstructed point obtained from any other different part of the hologram should be the same. If there is speckle noise, the phase-difference with higher intensity at a reconstructed point is more reliable than that with lower intensity. Therefore, the phase-difference at the same point is calculated by averaging the phase-differences obtained from all the windowed holograms by considering the weight of the intensity. It provided the displacement distribution with high-resolution. Figure 1(b) shows the analyzed phase-difference distribution obtained from 16 windowed holograms. Figure 2(b) shows the displacement distribution along the centerline. The standard deviation of the errors from the theoretical displacement is 1.95nm. The effect of the number  $n$  of the windowed holograms and the weight, i.e., the  $m$ -th power of the absolute amplitude of the complex amplitude of the reconstructed object on accuracy is checked. When the number of windows is 1024, the standard deviation is 0.67 nm.

When this method is applied to flat plate movement, the best standard deviation of the errors is 88 picometer when  $n=1024$  and  $m=2$ .

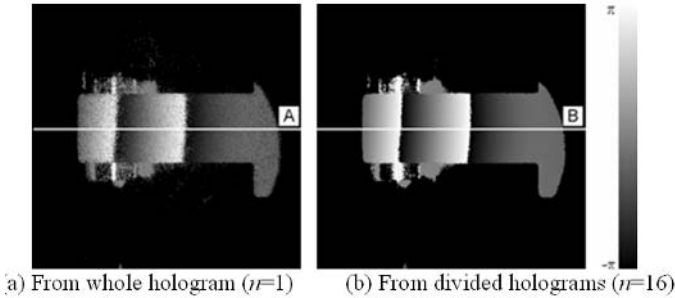


FIGURE 1 Phase-difference distributions obtained by digital holographic interferometry

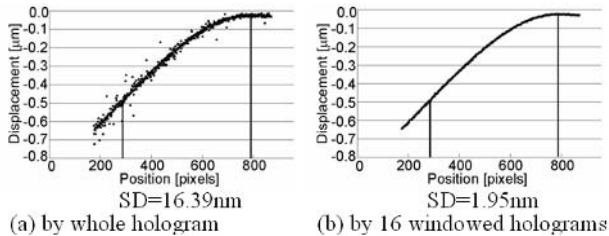


FIGURE 2 Displacement distribution along lines A and B shown in Fig.1

The resolution becomes better when the number of windows becomes larger. However, the spatial resolution becomes low when the number of windows becomes larger. The relationship among the number of windows, the size of windows, the resolution and the spatial resolution is studied.

## References

1. U. Schnars and W. Jüptner, *Digital Holography*, Springer, (2005).
2. I. Yamaguchi and T. Zhang, "Phase-shifting digital holography", *Opt. Lett.*, vol. **22**(16), pp.1268-1270 (1997).
3. Morimoto, Y., Nomura, T., Fujigaki, M. Yoneyama S. and Takahashi, I., Deformation Measurement by Phase-shifting Digital Holography, *Experimental Mechanics*, 2005, vol. **45**(1), 65-70.
4. Fujigaki, M., Matui, T., Morimoto, Y., Kita, T., Nakatani, M. and Kitagawa, A., Development of Real-Time Displacement Measurement System Using Phase-Shifting Digital Holography, *Proceedings of the 5th International Conference on Mechanics of Time Dependent Materials (MTDM05)*, 160-163,(2005).
5. Morimoto, Y., Matui, T., Fujigaki, M. and Kawagishi, N., Effect of Weight in Averaging of Phases on Accuracy in Windowed Digital Holographic Interferometry for Pico-meter Displacement Measurement, *Proc. of SPIE*, vol. **6049**, 60490D(CD-ROM)(2005).



## IDENTIFICATION OF SPECIMEN POSITION AND ORIENTATION USING STANDARD DEVIATION OF INTENSITY IN PHASE-SHIFTING DIGITAL HOLOGRAPHY

Motoharu Fujigaki, Youhei Ashimura, Toru Matui and Yoshiharu Morimoto  
 Faculty of Systems Engineering, Wakayama University  
 Sakaedani 930, Wakayama, Japan  
 fujigaki@sys.wakayama-u.ac.jp

Phase-shifting digital holography was proposed by Yamaguchi et. al[1, 2]. It is a valuable method to measure the displacement distribution and the strain distribution of an object surface[4, 5, 6, 7].

The complex amplitude distribution of an object surface is obtained as the complex amplitude distribution at a distance of reconstructed length. If there are optical components such as a lens on the optical path, it is difficult to measure the reconstructed length. We discovered that the standard deviation of the intensity on the reconstructed image becomes maximum value when reconstructed length is same as optical length. Figure 1(a) shows a relationship between reconstructed length and standard deviation. In this case, the object is a flat plate. Figure 1(b) shows the neighborhood of local maximum of Fig. 1(a).

In this paper, the method to identify the position and the orientation of a specimen using standard deviation of intensity distribution is proposed.

Table 1 shows a result of an experiment of displacement measurement of a flat plate. The plate was moved to the  $z$ -direction. The result shows the displacement measurement was performed with small errors.

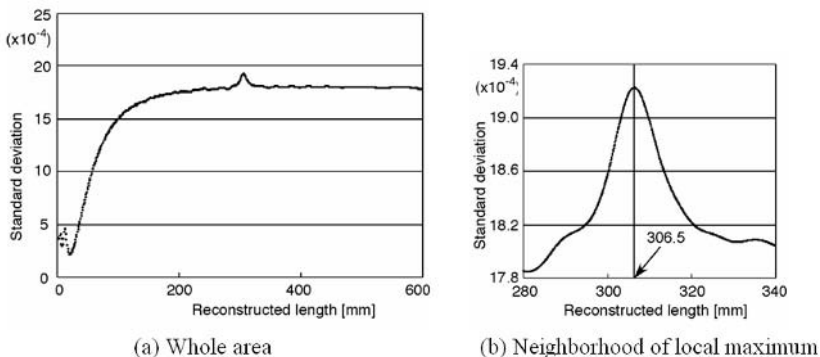


FIGURE 1. Relationship between reconstructed length and standard deviation

Figure 2 shows a result of identification of orientation. The specimen was tilted to 15 degrees and it was moved by 5 mm and 10 mm along  $z$ -direction. The analyzed area was 300 x 300 pixels and the area was moved from left to right at intervals of 10 pixels. At each analyzed area, local maximum value of standard deviation was obtained. The result orientation was 14, 10 and 13 degrees at the case of the position 0, 5 and 10 mm, respectively.

TABLE 1. Result of displacement measurement

Given displacement	Reconstructed length	Measured displacement	Error [mm]
-20.0	286.0	-20.5	-0.5
-15.0	291.3	-15.2	-0.2
-10.0	295.9	-10.6	-0.6
-5.0	301.4	-5.1	-0.1
0.0	306.5	0.0	0.0
5.0	311.5	5.0	0.0
10.0	316.7	10.2	0.2
15.0	321.6	15.1	0.1
20.0	326.8	20.3	0.3

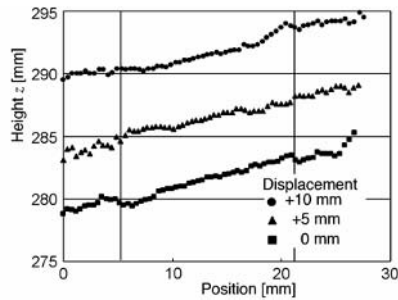


FIGURE 2. Result of identification of orientation

## References

1. Yamaguchi, I. and Zhang, T., Phase-shifting Digital Holography, *Opt. Lett.*, vol. **22**-16, 1268-1270, 1997.
2. Zhang, T. and Yamaguchi, I., Three-dimensional Microscopy with Phase-shifting Digital Holography, *Opt. Lett.*, vol. **23**-15, 1221-1223, 1998.
3. Morimoto, Y., Nomura, T., Fujigaki, M., Yoneyama, S. and Takahashi, I., Deformation Measurement by Phase-shifting Digital Holography, *Experimental Mechanics*, vol. **45**-1, 65-70, 2005.
4. Okazawa, S., Morimoto, Y., Fujigaki, M. and Matsui, T., Simultaneous Measurement of Out-of-Plane and In-Plane Displacements by Phase-Shifting Digital Holographic Interferometry, *Advances in Experimental Mechanics*, BSSM, 223-228, 2005.
5. Morimoto, Y., Nomura, T., Fujigaki, M. and Takahashi, I., Reduction of Speckle Noise Effect by Divided Holograms in Phase-shifting Digital Holography, *Proc. of 12th International Conference on Experimental Mechanics(ICEM12)*, 554-555, 2004.
6. Morimoto, Y., Matsui, T., Fujigaki, M. and Kawagishi, N., Accurate Displacement Measurement by Windowed Holograms in Digital Holographic Interferometry, *Proc. of 2005 SEM Annual Conference & Exposition on Experimental Mechanics*, SEM, CD-ROM, 2005.

## REFLECTION HOLOGRAM INTERFEROMETRY AS UNIQUE TOOL IN THE COURSE OF RESIDUAL STRESSES DETERMINATION

V.S. Pisarev and V.V. Balalov

Ph. D., Head Scientist, Central Aero-Hydrodynamic Institute (TsAGI),  
140180 Zhukovsky Moscow reg., Russia

Ph. D., Professor, Moscow State University of Service Industries,  
141200 Cherkizovo Moscow reg., Russia  
pisarev@tsagi.ru, balalov@pues.ru

A problem of experimental determination of residual stresses is of great importance in many fields of modern engineering. A wide variety of experimental techniques is based on drilling small hole for releasing residual stress energy. Implementing coherent optics techniques such as holographic and speckle interferometry for deriving local deformation parameters gives us the maximum possible sensitivity of the hole drilling method with respect to residual stresses determination. At first, this is attributed to a high sensitivity of measurement techniques used to in-plane components of strain-induced displacements. Second, a high quality of interference fringe patterns that is especially inherent in reflection hologram interferometry allows us to obtain required deformation parameters at the nearest proximity of small hole of diameter 1-3 mm. Thus a combination of the hole drilling method with optical interferometric measurements represents by itself “the least destructive technique” from all others destructive methods of residual stress determination.

Unique capabilities of reflection holographic interferometry to residual stresses determination in plane structures, when through or blind probe holes are drilled, are described in a set of previous works [1-8]. Among these capabilities recognising principal strain directions at a stage of reconstruction of fringe patterns, which are recorded by reflection hologram, is of great metrological importance. This is attributed to the fact that double exposure hologram, which is recorded at the probe hole proximity, carries the most possible information volume in a sense of residual stresses determination comparing with any others optical interferometric techniques of whole-field nature. That is why reflection hologram interferometry can be effectively used for metrological justification of any interferometric or traditional techniques, which are combined with probe hole drilling for a transformation of residual stress energy release into measurable mechanical parameters.

The main difficulty to be overcome for reliable determination of residual stress components consists of constructing a correct transition model. Such a model rigorously depends on a type of residual stress field of interest, which has to be considered as unknown before experiment. It is shown how whole-field information that is resulted from holographic interferometric measurements can be effectively used for a reliable choice of the transition model.

The presentation includes theoretical principals inherent in the developed non-traditional approach as well as a set of examples of its implementing for a determination of residual stress fields in plane and curved structures connected by welding of different technology. Special attention is paid to questions, which are related to a reliable transition from measured deformation parameters to required residual stress values. Traditional approaches to solving this problem, which follow from preliminary prescribing a type of residual stress state, are discussed as well as original way based on a formulation and solution of specific inverse problem. The presentation includes a wide set of obtained results. Estimation of errors, which are inherent in an analysis of some typical distributions of residual stress components near welded joints of plates and tubes, are presented and discussed in detail.

**References**

1. Pisarev V.S., Balalov V.V., Aistov V.S., Bondarenko M.M., Yustus M.G., *Optics & Lasers in Engineering*, vol. **36**(6), 551-597, 2001.
2. Pisarev V.S., Balalov V.V., Aistov V.S., Bondarenko M.M., Chumak S.V., Grigoriev V.D., Yustus M.G., *Optics & Lasers in Engineering*, vol. **41**(2), 353-410, 2004.
3. Pisarev V.S., Balalov V.V., *Optics & Lasers in Engineering*, vol. **41**(2), 411-462, 2004.
4. Pisarev V.S., V.V. Balalov V.V., Bondarenko M.M., *Optics & Lasers in Engineering*, vol. **42**(6), 673-702, 2004.
5. Pisarev V.S., V.D. Grigoriev V.D., Balalov V.V., Chumak S.V., *Optics & Lasers in Engineering*, vol. **42**(6), 703-726, 2004.
6. Pisarev V.S., Bondarenko M.M., Chernov A.V., Vinogradova A.N., *International Journal of Mechanical Sciences*, vol. **47**(9), 1350-1376, 2005.
7. Pisarev V.S., Balalov V.V., Avdiushkin E.V., Gudnin N.V., Chernov A.V., Vinogradova A.N., *Journal of Holography and Speckle*, vol. **2** (2), 41-56, 2005.
8. Pisarev V.S., Apalkov A.A., Odintsev I.N., Bondarenko M.M., *Journal of Holography and Speckle*, vol. **2** (2), 57-71, 2005.

## COMPENSATION SPECKLE PATTERN INTERFEROMETRY IN MATERIAL TESTING TECHNIQUES

I.N. Odintsev and V.S. Pisarev

Ph. D, Senior Scientist, Russian Academy of Science,  
Blagonravov Mechanical Engineering Research Institute,  
101990 Moscow, Russia

Ph. D., Head Scientist, Central Aero-Hydrodynamic Institute (TsAGI),  
140180 Zhukovsky Moscow reg., Russia  
INO54@mail.ru, pisarev@tsagi.ru

The main advantage of implementing optical interferometric methods in experimental mechanics comparing with traditional approaches resides in a whole-field character of the measurement procedure. This fact is of great importance in the field of high-precision material testing. First, an availability of interferometric fringe patterns, which are obtained as a mechanical response of the specimen under study on external loading, allows us to estimate a degree of correspondence between real deformation state and a model used for converting initial experimental parameters into required values of elastic constants. Second, whole-field data may be used for increasing measurement accuracy on a base of least square method.

Practical realisation of whole-field approaches to material testing is often restricted by a complex configuration of interferometric fringe patterns to be interpreted for deriving required information. This difficulty can be overcome on a base of the compensation principal. An essence of this principal consists of modifying optical phase difference, which is caused by real deformation of the object surface, by means of introducing artificial phase field of known form. A superposition of two optical phase fields, which can be controlled in real time, eventually gives interferometric fringe patterns of reference type such as straight lines, regular circles, etc. These fringe patterns can be reliably interpreted in terms of required mechanical parameters without complex mathematical evaluation.

Compensation technique has been successfully implemented in the course of bending testing of thin plates having rectangular form. Directions and values of principal curvatures are reliably measured by means of compensation holographic and compensation speckle interferometry [1,2]. Such information allows us highly accurate determination of elastic constants of both isotropic and anisotropic materials. But in the latter case three differently oriented specimens in a form of rectangular plate have to be used for obtaining a complete set of elastic constants [2]. Main disadvantage of this approach follows from the fact that different parameters are measured over different areas of initial sheet of composite material.

Further progress in this direction has to be based on creating a technique that would be capable of deriving complete set of anisotropic elastic constants proceeding from testing a single specimen. This presentation includes a description of such technique, which is based on testing thin circular disk subjected to four-point anticlastic bending and uniformly distributed loading. The main part of initial experimental information is obtained by multiple-step procedure. For performing the first step a specimen is mounted in loading device with directions of anisotropy axes in general case do not coincide with axes of laboratory co-ordinate system. These axes are directed along two orthogonal lines passing through two pairs of points where forces of the same sign are applied. Measurement results, which are obtained by compensation speckle pattern interferometry, include two values of principal curvature related to disk bending and a value of the angle between directions of principal curvature and axes of laboratory co-ordinate system. After completing the

first step a specimen is rotated by known angle and the second measurement step is performed. A number of measurement steps must be not less than four. For deriving all required anisotropic elastic constants the above-mentioned results have to be completed with data describing deflection field of the same disk loaded by uniform pressure. These data are also obtained on a base of compensation technique. It is shown how the results of the above-mentioned measurements can be used for deriving required elastic constants of anisotropic material. A description of experimental equipment including optimal design of loading device as well as the results of testing various composite materials by different approaches are also presented.

## References

1. Shchepinov V.P., Pisarev V.S., Novikov S.A., Balalov V.V., Odintsev I.N., Bondarenko M.M., *Strain and Stress Analysis by Holographic and Speckle Interferometry*, John Wiley, Chichester, 1996.
2. Odintsev I.N., Apalkov A.A., Pisarev V.S. In *Interferometry '99: Applications*, edited by W. Juptner, K. Patorski, Proceedings of SPIE, 1999, vol. **3745**, 355-364.

## FAST TRANSFORMS FOR DIGITAL HOLOGRAPHY

L. Yaroslavsky

Dept. of Interdisciplinary Studies, Faculty of Engineering, Tel Aviv University,  
Tel Aviv 69978, Israel  
yaro@eng.tau.ac.il

In digital reconstruction of holograms, holograms are first sampled by CCD or CMOS photosensitive cameras and the array of numbers obtained is then subjected in computer to digital transformations that imitate wave back propagation from the camera to the object plane. As a result, samples of the object wave front amplitude are obtained. For reconstruction of holograms recorded in far diffraction zone, integral Fourier Transform has to be implemented numerically. For holograms recorded in near diffraction zone, numerical implementation of integral Fresnel Transform and Kirchhoff-Rayleigh-Sommerfeld Transform are required. Accuracy and computational complexity of these implementations are of primary importance for digital holography. The process of numerical reconstruction of the object wave front from samples of its hologram can be treated as sampling the object wave front. As signal sampling is a linear transformation, it is fully specified by its point-spread function. Therefore, metrological characterization of the process of numerical reconstruction of holograms requires determination of its point spread function. The paper addresses these problems. Specifically,

(i) Different versions of discrete representations of the diffraction integral transforms are introduced that correspond to different geometries of hologram and reconstructed image sampling and are oriented toward the use of Fast Fourier Transform algorithm:

$$\text{Canonical Discrete Fourier Transform (DFT): } \alpha_r = \frac{1}{\sqrt{N}} \sum_{k=0}^{N-1} a_k \exp\left(i2\pi \frac{kr}{N}\right);$$

$$\text{Scaled Shifted DFT: } \alpha_r^\sigma = \frac{1}{\sqrt{\sigma N}} \sum_{k=0}^{N-1} a_k \exp\left(i2\pi \frac{\tilde{k}\tilde{r}}{\sigma N}\right);$$

$$\text{Rotated DFT: } \alpha_{r,s}^\theta = \frac{1}{\sigma N} \sum_{k=0}^{N-1} \sum_{l=0}^{N-1} a_{k,l} \exp\left[i2\pi \left( \frac{\tilde{k} \cos \theta + \tilde{l} \sin \theta}{N} \tilde{r} - \frac{\tilde{k} \sin \theta - \tilde{l} \cos \theta}{N} \tilde{s} \right)\right];$$

$$\text{Canonical Discrete Fresnel Transform (DFrT): } \alpha_r = \frac{1}{\sqrt{N}} \sum_{k=0}^{N-1} a_k \exp\left[i\pi \frac{(k\mu - r/\mu)^2}{N}\right];$$

$$\text{Focal plane invariant DFrT: } \alpha_r^{\left(\mu, \frac{N}{2\mu}\right)} = \frac{1}{\sqrt{N}} \sum_{k=0}^{N-1} a_k \exp\left\{-i\pi \frac{[k\mu - (r - N/2)/\mu]^2}{N}\right\};$$

$$\text{Scaled Shifted DFrT: } \alpha_r^{(\mu,w)} = \frac{1}{\sqrt{\sigma N}} \sum_{k=0}^{N-1} a_k \exp\left[-i\pi \frac{(k\mu - r/\mu + w)^2}{\sigma N}\right];$$

$$\text{Partial DFrT: } \tilde{\alpha}_r^{(\mu,w)} = \frac{1}{\sqrt{N}} \sum_{k=0}^{N-1} a_k \exp\left(-i\pi \frac{k^2 \mu^2}{N}\right) \exp\left[i2\pi \frac{k(r - w\mu)}{N}\right];$$

Convolutional DFrT:  $\alpha_r = \sum_{k=0}^{N-1} a_k \text{frincd}^*(N; \mu^2; k - r + w);$

Discrete Kirchhoff-Rayleigh-Sommerfeld transform:

$$\alpha_r = \sum_{k=0}^{N-1} a_k \frac{\exp \left[ i2\pi \frac{\tilde{z}^2 \sqrt{1 + (\tilde{k} - \tilde{r})^2 / \tilde{z}^2}}{\mu^2 N} \right]}{1 + (\tilde{k} - \tilde{r})^2 / \tilde{z}^2},$$

where  $N$  is the number of samples,  $\mathbf{k}, \mathbf{r}$  are sample indices in signal and transform domains, respectively,  $\{\tilde{k} = k + u\}, \{\tilde{r} = r + v\}, \mathbf{u}, \mathbf{v}$  are shifts of signal and its transform sampling grids with respect to corresponding signal and its transform coordinate systems,  $\sigma$  is a sampling scale parameter,  $\theta$  is rotation angle of the sampling grid with respect to signal coordinate system,  $\mu^2 = \lambda Z / N \Delta f^2, w = u / \mu - v \mu, \lambda$  is wave length,  $Z$  is the distance between the object and its hologram,  $\Delta f$  is hologram sensor's camera pitch,

$$\text{frincd}(N; q; x) = \frac{1}{N} \sum_{r=0}^{N-1} \exp \left( i\pi \frac{qr^2}{N} \right) \exp \left( -i2\pi \frac{xr}{N} \right)$$

(ii) Fast computational algorithms for holographic transforms are reviewed;

(iii) Point spread functions of different hologram reconstruction algorithms are derived that explicitly show how the reconstruction results depend on the holographic set-ups and photographic camera physical parameters such as object-to-camera distance, radiation wave length, camera size, pitch, fill factor and alike.



## NULL TEST IN SPECKLE LIGHT BY COMPARATIVE DIGITAL HOLOGRAPHY

Wolfgang Osten, Giancarlo Pedrini, Xavier Schwab and Thorsten Baumbach<sup>1</sup>

Institut für Technische Optik

Universität Stuttgart

70569 Stuttgart, Pfaffenwaldring 9

<sup>1</sup> a&a technologies GmbH Bremen

osten@ito.uni-stuttgart.de

Modern production requires effective methods for inspection and quality control at the production place. Outsourcing and globalization result often in large distances between co-operating enterprises. This may cause serious problems with respect to the just-in-time exchange of information and the response to possible violations of quality standards. Consequently, new challenges arise for optical measurement techniques especially in the field of shape control, such as

- the inspection of parts where the master and the sample are not at the same place,
- the maintenance of calibration tools at different places or
- the matching of samples produced at different places.

A basic requirement for the solution of these tasks is the availability of the 3D information of the objects to be compared.

In this paper we describe the progress in Comparative Digital Holography CDH [1]. This technique allows for the direct comparison of the shape or the deformation of two nominally identical objects having different microstructures. The procedure does not require that both samples are located at the same place. In contrast to well known incoherent techniques based on inverse fringe projection this new approach prefers a coherent mask that is used for the coherent illumination of the sample object. Consequently, interferometric sensitivity is assured in the measurement process. The coherent mask is created by Digital Holography to enable the instant access to the complete optical information of the master object at any wanted place. The transmission of the digital master hologram to any place can be done via digital telecommunication networks. At the place of comparison the master hologram has to be reconstructed by a spatial light modulator SLM such as a liquid crystal display or a digital micro mirror device. Using the conjugated wavefront the sample object is illuminated by the coherent image of the master object. This delivers the basis for making Comparative Digital Holography which leads to an interferogram that indicates only the difference in shape or deformation between master and sample.

### Comparative Digital Holography

Comparative Digital Holography uses the advantages of Digital Holography:

- the direct access to the phase of the involved wave fronts,
- the inherent possibility of independent storage and reconstruction of all wave fronts,
- the possibility to compensate rigid body motions digitally with regard to a compensation of errors in the calibration between master and sample, and
- the flexible and efficient reconstruction of the master holograms with a SLM.

The schematic setup for CDH is shown in Fig. 1. The digital holograms of the master object are recorded at location A, Fig. 1a. The transmission to location B can be done via a data network (e.g. the internet). At location B the holograms are fed into a LCD-modulator. A laser reads out the holograms and reconstructs the conjugated wave front of the master object. This wave front illuminates the test object from the direction of observation during recording the master object. The observation of the test object is accomplished from the direction where the master object has been illuminated. It is essential that the separate storage and recording of all states of the objects is automatically delivered by Digital Holography. Therefore an additional reference wave for the separate coding of the respective holograms is not necessary.

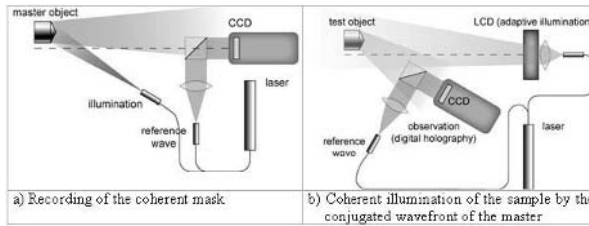


FIGURE 1. Schematic setup for Comparative Digital Holography

### Example: Shape Comparison

Here we show an example for comparative shape measurement by the two-wavelength method [2]. The objects under test are two macroscopically identical step pyramids with a conical shape, figure 2. One of the two pyramids has a deviation in the step parallelism of approximately one degree. With a ring diameter of 10.5mm this comes up to a maximum height difference of about 183 $\mu$ m.

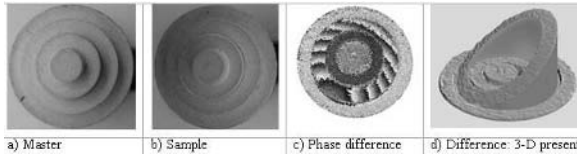


FIGURE 2. Comparative measurement of 2 step pyramids

For the experiment a synthetic wave length of  $\Lambda = 86 \mu\text{m}$  was generated by two single exposures with  $\lambda_1 = 580\text{nm}$  and  $\lambda_2 = 585\text{nm}$ . Taking the set-up geometry into account, we have an effective wave length  $\Lambda_{\text{eff}}$  of  $35\mu\text{m}$ . The reconstructed image of the contour difference (fig. 2c) originates not from the numerical difference between the two interference phases but from the optical generation of the difference between the two involved objects. The indicated difference phase corresponds to the difference of the height deflections between master and sample. The maximum height difference here is  $227\mu\text{m}$ . The deviation to the theoretical value is most likely introduced by production inaccuracies. Also in the result a small curvature in the difference can be seen.

### References

1. 1. Osten, W.; Baumbach, Th.; Jüptner, W., *Optics Letters*, vol. **27** (2002) 20, 1764-1766
2. 2. Baumbach, Th.; Osten, W.; von Kopylow, C.; Jüptner, W., *Applied Optics*, vol. **45** (2006) 5, 925-934

### 3D PULSED DIGITAL HOLOGRAPHY FOR THE SIMULTANEOUS ACQUISITION OF VIBRATION DISPLACEMENTS

Fernando Mendoza Santoyo , Carlos Perez Lopez , Tonatiuh Saucedo and Ramon Rodriguez Vera  
Centro de Investigaciones en Optica, A.C., Loma del Bosque 115,  
Colonia Lomas del Campestre, Leon, Guanajuato, Mexico 37150  
fmendoza@cio.mx, cperezl@cio.mx, tsaucedo@cio.mx, rarove@cio.mx

Non contact full field optical techniques such as speckle and holographic interferometry are being developed in order to apply them to the study of displacements, crack detection or any other type of defects that are in areas hidden within an object, superficially or within its walls. Both techniques have been well received in the past as a solution to 3D measure static and dynamic events from object areas easily imaged and in many types of environmental conditions. A drawback to date has been the gaining of access to hidden areas, mainly because the imaging device, e.g., an endoscope, did not have enough image resolution and thus both techniques did not render significant results, Ref. 1. Besides, the interferogram analysis for speckle and holography had to be done using data stored on photographic and holographic films, respectively, Ref. 1-3. Good quality image endoscopes and high resolution CCD sensors appeared recently, making it possible to design systems capable of obtaining out-of-plane displacements, Refs. 4-6. Non endoscopic pulsed speckle and digital holographic interferometric systems have been used in the past to measure displacements along all three perpendicular coordinate axes  $X$ ,  $Y$  and  $Z$ . The optical set up relied on the object surface being illuminated from three diverging sources located at three arbitrary, but known, positions, Ref. 7. The majority of those systems acquire the information sequentially, meaning that the experiment has to be repeated several times. There are however, occasions in which the experiment cannot be repeated and then a system was designed to simultaneously acquire in a single CCD frame the three orthogonal displacement components, Ref. 8, from the easily seen surface of a harmonically vibrating object.

The aim of the research work reported here was to design a pulsed digital holography system that incorporates a high image quality rigid endoscope that carries on it three multi mode optical fibers used to illuminate and hence simultaneously interrogate in 3D hidden object areas. A rigid endoscope as compared to a flexible one has higher image resolution since the former uses a lens arrangement and the latter a bundle of optical fibers. The imaging system resolution together with the CCD camera parameters such as pixel number and size and dynamic range, give digital holography the possibility to obtain good quality data that can be Fourier processed the main key feature of the technique. A conventional set up for digital holography, i.e, one that does not use an endoscope, has better resolution but cannot observe hidden areas. Results from the three orthogonal displacements  $X$ ,  $Y$  and  $Z$  are presented from the inner surface of a metallic cylinder subjected to harmonic vibrations. These three components may be individually studied and combined to get useful information as the tangential and normal, to the surface, object displacements.

---

**References**

1. D. Hadbawnik, "Holographische endoskopie," *Optik*, vol. **45**, 21-38 (1976).
2. H. I. Bjelkhagen, M. D. Friedman and M. Epstein, "Holographic high resolution endoscopy through optical fiber," *Proc. Laser Inst. Am.*, vol. **64**, 94-103 (1988).
3. M. Yonemura, T. Nishisaka, and H. Machida, "Endoscopic hologram interferometry using fiber optics," *Appl. Opt.*, vol. **20**, 1664-1667 (1981).
4. B. Kemper, D. Dirksen, W. Avenhaus, A. Merker, and G. Von Bally, "Endoscopic double pulse electronic speckle pattern interferometer for technical and medical intracavity inspection," *Appl. Opt.*, vol. **39**, 3899- 3905 (1999).
5. G. Pedrini, S. Schedin, and H. J. Tiziani, "Use of endoscopes in pulsed digital holographic interferometry," in *optical Measurement System for Industrial Inspection II: Applications in productions Engineering*, R. Holfling, W. Jupter and M. Kujawinska, eds. *Proc. SPIE 4399*, 1-8 (2001).
6. O. Coquoz, R. Conde, R. Taleblou, and C. Depeursinge, "Performance of endoscopy holography with a multicore optical fiber," *Appl. Opt.*, vol. **34**, 7186-7193 (1995).
7. C. M. Vest, "Holography Interferometry," (Wyle, New York, 1979).
8. S. Schedin, G. Pedrini, H. J. Tiziani, and F. Mendoza Santoyo, "Simultaneous three-dimensional dynamic deformation measurement with pulsed digital holography," *Appl. Opt.*, vol. **38**, 7056-7062 (1999).

## DIGITAL HOLOGRAPHIC INTERFEROMETERS CAMERAS FOR REMOTE MONITORING AND MEASUREMENTS OF MECHANICAL PARTS

Aneta Michalkiewicz and Malgorzata Kujawinska  
 Institute of Micromechanics and Photonics, Warsaw University of Technology  
 8 Sw. A. Boboli Str, 02-525 Warsaw, Poland  
 a.michalkiewicz@mchtr.pw.edu.pl, m.kujawinska@mchtr.pw.edu.pl

Fast growing technology and requirements for testing of different types of materials and devices require new methods and systems for investigation of their parameters. Main interesting quantities are: shape, roughness, local materials constants and displacements of elements under load. One of many techniques for analysis of different types of elements is holography and holographic interferometry and in particular their digital versions. They allow remote monitoring and measurement of different parameters in the same setup. At the moment we observe fast development of holographic systems for microelements and microregion studies. Those systems with compact design and “black box” measurement approach should allow fast and accurate measurement performed directly at the element and often in outdoor environment.

Digital holography provides a way to record and restore amplitude and phase of investigated object [1]. It allows, using amplitude information, distant monitoring of object and remote optoelectronic reconstruction. Proper manipulation of phase could provide information about shape of an object and its out-of-plane and in-plane displacement during loading [2]. The scheme of proposed system is shown in figure 1. It consists of DHI head, controlling/illumination module and reconstruction module. For remote monitoring the optoelectronic reconstruction of digital holograms (transferred via internet) by means of LCOS spatial light modulator is proposed. Due to fibre optics light delivery system the DHI head is able to work in a distance from its electronic/processing part and it allows direct access to all mechanical parts of machinery. The DHI head can be hand-held or can be mounted directly at a machine.

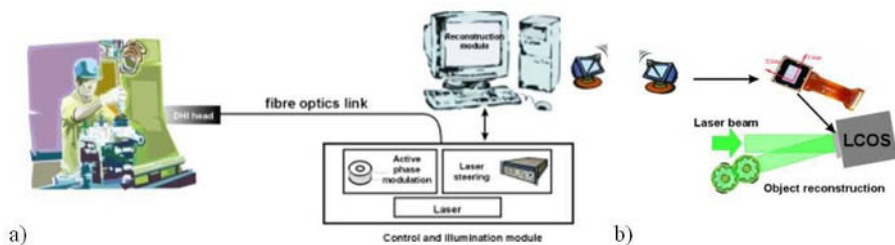


FIGURE 1. Scheme of DHI system for mechanical parts monitoring a) measurement module, b) optoelectronic reconstruction module.

In the paper we propose two versions of holocameras: one for out-of-plane/shape and the second for in-plane displacement measurement. Both cameras can measure fast changes of object by short exposure holography. A first system uses a 532 nm pigtailed laser, it consists of one illumination and one reference beam and dimensions of the measurement head are: diameter-50mm, length- 110 mm (Fig. 2a). The second system has 4 illumination and one reference beams,

uses 1064 nm laser and provides information about an arbitrary displacement vector distribution at the region of interest (Fig. 2b).

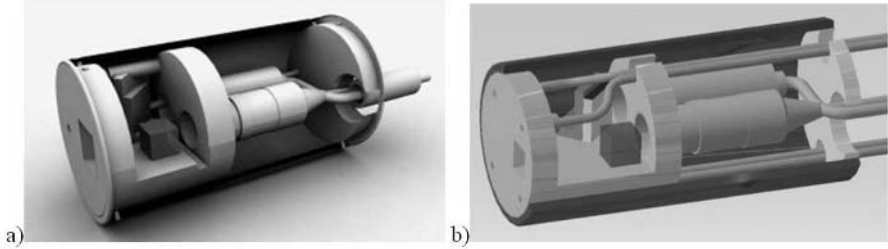


FIGURE 2. Holographic interferometer heads for a) out-of-plane displacement and shape determination, b) arbitrary vector displacement determination.

The exemplary results of a transistor subjected to thermal load are shown in figure 3. A series of digital holograms captured with video rate 5 frames/s during heating of the transistor was stored. The result of out-of-plane displacement measurements in the form of phase  $\text{mod}2\pi$  (Fig.3b) and horizontal crosssections A-A obtained for 3 sequential states of element ( $t= 0\text{ s}, 3\text{ s}, 6\text{ s}$ ) are presented in Fig. 3c.

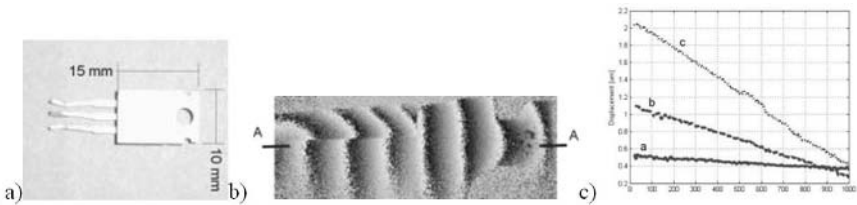


FIGURE 3. Measurement of transistor under thermal load a) image of the object, b) phase  $\text{mod}2\pi$  map, c) profile A-A of out-of-plane displacement maps for object after 0.5 s, 3s and 6s.

The utility of the systems has been proven by many other measurements performed directly at the microregions of machinery. In the paper we also discuss the advantages, challenges and opportunities that exist in the field of digital holography application for experimental mechanics.

## References:

1. Kreis, T., *Holographic Interferometry*, Akademie Verlag, Berlin, Germany, 1996
2. Michalkiewicz, A., et al. *Phase manipulation and optoelectronic reconstruction of digital holograms by means of LCOS spatial light modulator* Proc. SPIE vol. **5776**, 144-152, 2005
3. Kujawska, M., *Optical metrology: from micromasurements to multimedia*. In: Proceedings of the Symposium on Photonics Technologies for 7th Framework Program, Wroclaw, Poland, 2006

### 3-D MICRO-STRUCTURE MEASUREMENT METHOD BASED ON SHADOW MOIRÉ USING SCANNING

Yasuhiko Arai and Shunsuke Yokozeki  
 Department of Engineering, Faculty of Engineering, Kansai University,  
 3-3-35, Yamate-cho, Suita, Osaka 564-8680  
 Jyouko Applied Optics Laboratory,  
 2-32-1 Izumigaoka, Munakata, Fukuoka 811-4142, Japan  
 aria@kansai-u.ac.jp

The novel precise three dimensional shape measurement method using SEM and moiré topography has been proposed. The possibility for measurement of wave length order by this method has been discussed using the results (Fig. 1) of experiments for confirming the principle of this idea. In the experiments, the method with high resolution power based on the new measurement method is also proposed by employing the fringe scanning technology for the shadow moiré. The optical system (Fig. 2) is constructed with SEM using backscattering electrons, the grating holder which can shift the position of the grating, and the grating of which the pitch is 120 micro meter. Results (Figures 3 and 4) using a bearing ball as a sample show that the high resolution measurement around one macro meter can be obtained by introducing the fringe scanning method to the new measurement.

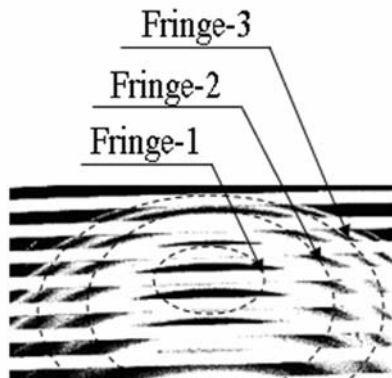


FIGURE 1. Moiré fringes on sphere surfaces

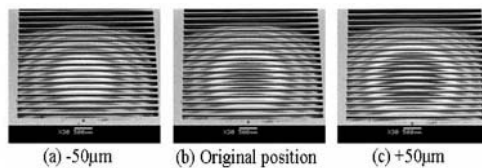


FIGURE 3. Moiré fringes at different positions of grating

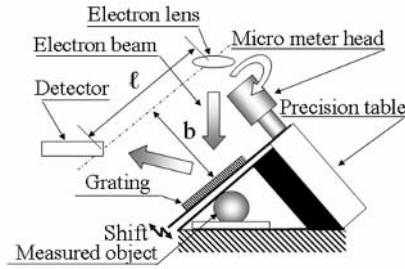


FIGURE 2. Grating holder for shifting grating

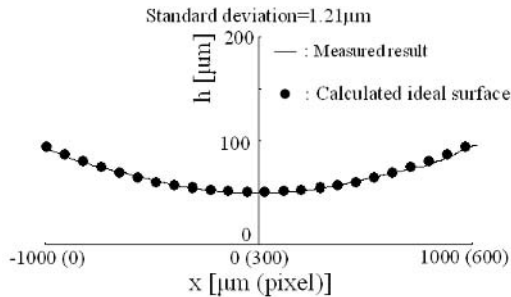


FIGURE 4. Measured result of ball with fringe scanning method

## References

1. J. I. Goldstein, *Scanning Electron Microscopy and X-Ray Microanalysis*, Plenum press, New York, 1981.
2. L. Reimer, *Transmission Electron Microscopy*, Springer-Verlag, Berlin Heidelberg 1984
3. D. M. Meadows, *Appl. Opt.*, vol. **9** (4), 942-947, 1970.
4. H. Takasaki, *Appl. Opt.*, vol. **9** (6), 1467-1472, 1970.
5. D. Malacara, *Optical shop testing, 2ed*, John Wiley & Sons, New York, 1992.
6. T. Suganuma, *J. Electron Microscopy*, vol. **34**, 328-337, 1985.
7. D. Malacara, *Optical shop testing, 2ed*, John Wiley & Sons, New York, 1992.
8. Y. Arai, S. Yokozeki, and Tomoharu Yamada, *Appl. Opt.*, vol. **34** (22), 4877-4882, 1995.
9. Y. Arai and S. Yokozeki, *Appl. Opt.*, vol. **38** (16), 3503-3507, 1999.
10. E. O. Doebelin, *Measurement systems 4th-ed*, McGraw-Hill International Editions, New York, 1990.



## MEASUREMENT OF SURFACE SHAPE AND POSITIONS BY PHASE-SHIFTING DIGITAL HOLOGRAPHY

I. Yamaguchi, T. Ida and M. Yokota  
 Department of Electronic Engineering, Gunma University  
 Tenjincho 1-5-1, Kiryu, Gunma 376-8515, Japan  
 ichiyama@el.gunma-u.ac.jp

Phase-shifting digital holography is applied to measure shape and positions of rough surfaces from the phase and modulus of the product of the reconstructed complex amplitudes corresponding to dual wavelengths. The sensitivity of the position is one hundredth of focal depth and that for surface shape proved to be a few tens of micrometers. Theory and experimental results are presented.

By digital holography we can measure shape and deformation of diffusely reflecting surfaces quantitatively. Surface shape can be measured from the difference of the reconstructed phase recorded before and after changes of incident angle or wavelength. Sensitivities of these methods are proportional to the changes of wavelength or incident angle. If we employ phase-shifting digital holography (Yamaguchi [1]), the size of the object can be extended substantially because we can use an in-line setup to eliminate zero-order and conjugate image. Phase-shifting digital holography also provides directly 3-d distribution of complex amplitude without any filtering procedure. This paper presents methods for measurement of not only surface shape but also its distance from a CCD by using phase-shifting digital holography. Complex amplitudes on the object surface are reconstructed and their conjugate product is calculated. The shape is derived from the phase of the product, while the position of points on the surface is obtained from the reconstruction distance where the product becomes maximum. The principle for distance measurement corresponds to finding the position of the highest fringe contrast in conventional holographic interferometry. In this paper we present both theory and experiment for this method aiming at diffusely reflecting surface. Roles of speckle displacement in the above method is also indicated.

In the coordinate system shown in Fig. 1 we can reconstruct 3-dimensional distribution of the complex amplitude  $U_a(x,z)$  and  $U_b(x,z)$  corresponding to the wavelength  $\lambda$  and  $\lambda+\Delta\lambda$ , represented here in 2-dimensional coordinate. Since the conjugate product  $U_a(x,z)U_b^*(x,z)$  exhibits fluctuations associated with speckle, we need to average the product spatially on  $x$  to yield the coherence factor  $\langle U_a(x,z)U_b^*(x,z) \rangle$ . In theoretical analysis this averaging is replaced by an average over a statistical ensemble of microscopic structure of a rough surface. In numerical reconstruction we carry out averaging over a moving matrix. According to a theory based on linear transmission of complex amplitude the product is represented by

$$\frac{\langle U_a(x,z)U_b^*(x,z) \rangle}{\sqrt{I_{oa}I_{ob}}} = \left| \int P^*(s)P \left[ s \left( 1 + \frac{\Delta k}{k} \right) + A_s \right] \exp \left( i\Delta k \frac{s^2 z}{2L^2} \right) \exp \left( ik \frac{szA_s}{L^2} \right) ds \right| \quad (1)$$

where  $P(s)$  is represents the aperture of CCD,  $k=2\pi/\lambda$ , and  $\Delta k = -2\pi\Delta\lambda/\lambda^2$  the change in wave number corresponding to wavelength shift, and

$$A_x = -\frac{Lz}{L+z} \frac{\Delta k}{k} [\alpha(\cos \theta_s + 1) + \sin \theta_s] \quad (2)$$

the speckle displacement caused by wavelength shift at the CCD plane (Yamaguchi et al[2]). In Eq.(2)  $\theta_s$  is the incident angle of object illumination and  $\alpha$  is the surface slope.

We employed the setup shown in Fig. 2 (Yamaguchi et al[3]). We used a laser of wavelength  $\lambda=657$  nm and output power of 30 mW. Its wavelength shift of  $0.508\pm 0.0038$  nm was provided by mode-hop of the laser diode subject to change of injection current between 55 mA and 59 mA. Three in-line holograms were recorded by a CCD having pixels of  $512\times 512$  with phase-shift of  $\pi/2$  before and after the wavelength shift. The contour sensitivity is  $424 \mu\text{m}$ . Figure 3 represents a cross-section of the phase difference representing shape of a plate tilted by 30 degrees and positioned at a distance of  $L=325$  mm. The peak position of the coherence factor is also plotted which shows remarkable fluctuations. The width of the fluctuation amounts to 10 mm that is much larger than the focal depth of the reconstructed image equal to 1.57 mm. It should be noticed, however, that we need to mark no target such as point or line on the surface.

In conclusion we have developed a new digital holographic technique which can determine distance and shape of diffusely reflecting surfaces without any marking. It uses a single optical setup and computer processing on the complex amplitude reconstructed in 3-d space. This method uses both the amplitude and phase of the coherence function. So the method may be extended to measure position, shape, and deformation of a diffusely reflecting object.

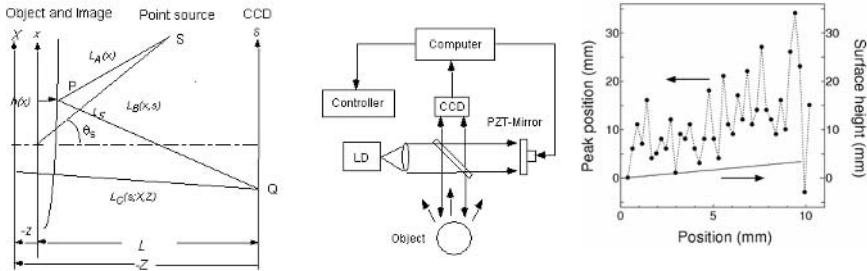


FIGURE 1. Coordinate system. FIGURE 2. Experimental setup. FIGURE 3. Experimental results.

**References**

1. Yamaguchi, I., In *Digital Holography and Three-Dimensional Display*, edited by T.-C. Poon, Jones, Springer, New York, Germany, 2006.
2. Yamaguchi, I. et al., *Holography and Speckle*, vol. 4, 2006 (in print).
3. Yamaguchi, I. et al., *Appl. Opt.*, vol. 45, 7610-7616, 2006.

## TERAHERTZ DIGITAL HOLOGRAPHY

Yan Zhang and Weihui Zhou  
Department of Physics, Capital Normal University  
Xisanhuan Beilu 105, Beijing 100037 China  
yzhang@mail.cnu.edu

Recent years, Terahertz (THz) radiation which occupied an extremely large portion of the electromagnetic spectrum between the microwave and infrared has drawn much attention and interest, since the rapid advances in the femtosecond pulsed laser technology and the rich physical and chemical processes that occur in this region. In past decade, various THz image techniques have been proposed. The THz imaging system based on the CCD camera has also been used to study the property of the object. The THz field distribution passing through the object can be displayed on the computer screen in real-time[1]. Three dimensional (3D) T-ray imaging has also been demonstrated[2]. However, all of these technologies are based on the focus plane imaging, the diffraction and dispersion of the THz in the free space have not been considered. Since the wavelength of the THz radiation is quite longer than the visible light, the diffraction effect is more serious. Therefore, in order to resolve the exact information about the object, the diffraction and propagation characteristics of THz radiation should be taken into account[3,4]. The image reconstruction is necessary.

In this work, the digital holography technology is combined with the THz imaging technology to achieve exact information of the original object. The basic idea of the THz digital holography is as follows: The CCD camera is used to record the time domain waveform of the two-dimensional distribution of the THz field after it passes through or is reflected from the object, then the reconstruction algorithm is used to reconstruct the field just after the object, thus the exact information about the object can be extracted from the reconstructed time domain waveform. In the reconstruction, the frequency component of the THz pulse is drawn by using the Fourier transform, then the Angle Spectrum theory is used to retrieve the original distribution for each component, at last the Fourier transform is used again to get the time domain waveform. Thus many pieces of information about the object such as absorption spectrum, index distribution can be achieved. Since the CCD records all of the information, such as phase information, of the field in the time domain waveform, it can also be called digital holography.

The computer simulation is presented here to show the basic idea of the THz digital holography. The evolution pattern of a pulsed plane THz beam at  $z=50\text{cm}$  after passing through a sample with capital letters "CNU" is shown in Fig. 1. It can be seen that due to the diffraction and propagation, the evolution pattern obtained on the observation plane cannot reveal the real information of the picture. Only for the time of  $t=0.00\text{s}$ . Therefore, it is necessary to reconstruct the original field distribution in the incident plane. By using the method of reconstruction, the reconstructed images are shown in Fig. 2. The original sample has been well reconstructed and the sharp boundary can be clearly seen. This simulation demonstrates the THz digital holography well. The experimental result will also be presented in the talk to exhibit the validity of the proposed method.

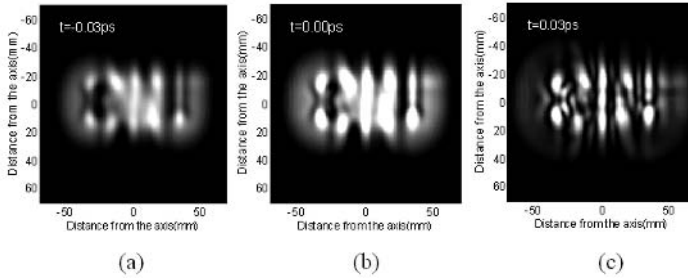


FIGURE 1. The evolution image of the capital letters CNU in the observation plane, (a)-(c) corresponds to the times  $t = -0.03, 0.00$ , and  $0.03$ ps, respectively.

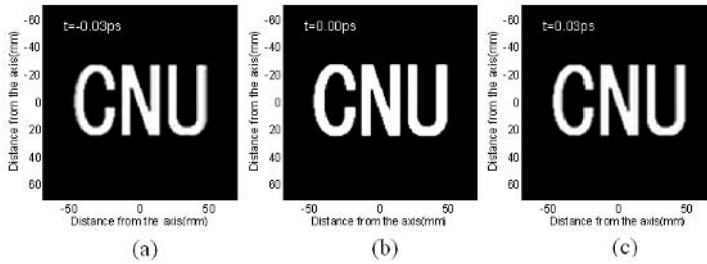


FIGURE 2. Reconstructed image of the capital letters CNU, (a)-(c) corresponds to times  $t = -0.03, 0.00$ , and  $0.03$ ps, respectively.

## References

1. Wang S. H., Ferguson B., Zhang C. L. and Zhang X. C., *Acta Phys. Sin.*, vol. **52**, 120, 2003
2. Wang S., Ferguson B., Abbott D. and Zhang X.C., *J. Biol. Phys.*, vol. **29**, 247–256, 2003
3. Lefrançois M. and Pereira S. F., *Opt. Express*, vol. **11**, 1114, 2003
4. Kaplan A. E., *J. Opt. Soc. Am. B.*, vol. **15**, 951, 1999

## THE THREE-DIMENSIONAL DISPLACEMENT MEASUREMENT OF SANDWICH CIRCULAR PLATES WITH A SINGLE FULLY-POTTED INSERT USING ELECTRONIC SPECKLE PATTERN INTERFEROMETRY

Song-Jeng Huang and Hung-Jen Yeh

Department of Mechanical Engineering, National Chung Cheng University

168 University Rd., Ming-Hsiung, Chia-Yi, 621, Taiwan, ROC

ime\_hsj@ccu.edu.tw, yehdidi@giga.net.tw

This study presents the construction and operation of an electronic speckle pattern interferometry (ESPI) applied to sandwich plates with inserts[1]. Proposed ESPI is a full-field and non-destructive testing that can measure tiny out-of-plane and in-plane displacement in the elastic region[2-4]. The experimental construction is to integrate out-of-plane and in-plane measurement into one optical system, to measure the three-dimensional displacement of the sandwich plates. The experimental result indicates that the displacement of the sandwich plate will decrease as the core thickness is increasing (Fig. 1). The result also indicates that the displacement will decrease as the diameter of insert is increasing, but the strength estimated to be increasing (Fig. 2). For validation purpose, the analytical and FEM analysis were introduced to compare with the result of ESPI measurements. Comparison between the results of ESPI, FEM and analytical revealed a convincing agreement.

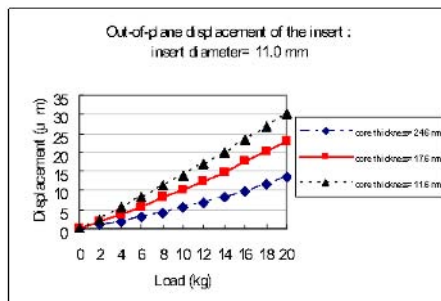


FIGURE 1. Out-of-plan displacement with changing core thickness, using ESPI

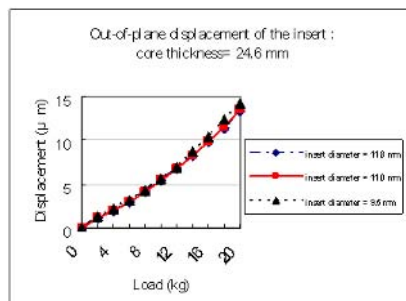


FIGURE 2. Out-of-plan displacement with changing insert diameter, using ESPI

**References**

1. Thomsen, T., *Compos. Struct.*, vol. **40**, 159-174, 1998.
2. Thomsen, T. and Rits, W., *Compos. P. B.*, vol. **29B**, 795-807, 1998.
3. Butters, J.N. and Leendertz, J.A., *Opt Laser Techno*, vol. **3**, 26-30, 1971.
4. Huang, S.J., Lin, H.L., *J. Mech.*, vol. **20**(4), 273-276, 2004.

## MECHANICAL CHARACTERISTICS DETERMINATION OF MATERIALS AND COVERS BY MEANS OF MICRO- AND NANO- STM-HARDNESS METER WITH SEMI-CONDUCTOR DIAMOND PYRAMIDS

V.A. Andruschenko, A.A. Bondarenko, V.N. Nikitenko and V.V.Meleshko  
 Department of Theoretical and Applied Mechanics,  
 Kiev National Taras Shevchenko University  
 Volodymirska, 64, Kiev, Ukraine, 01033  
 andron@univ.kiev.ua, aabondarenko@univ.kiev.ua, nivini@univ.kiev.ua,  
 meleshko@univ.kiev.ua

The paper addresses the results of investigation of a compact device that combining and interconnecting static, dynamic and resonance tests of specimens. At present, the acoustics resonance methods for elastic constants determination are the most precise, especially for high-Q materials.

Our method utilizes square or circular plates as the specimens. In the case of directional property investigation square plate is cut from the circular one after preliminary resonance trials. High-Q piezoelectric and piezoceramic (PZT type ceramics) materials are selected for tests. Investigations of elastic vibration spectrums for both substrate layers and layers with films are carrying out using either piezoeffect (an excitation by means of electrodes) or diamond sputtering indenters gripping square or circular plate (Fig.1). Diamond indenters are identical and joint with special sensors for excitation and receiving vibrations of plates.

The main attention in the paper is paid to describing a complicated structure of the frequency spectrum for square plates in comparison with spectrum for circular ones. It is demonstrated how to choose resonant frequencies, which will can used for calculations of elastic characteristics with the help of worked out software support. Description of experimental base-scheme, necessary equipment and sequence of operations are presented below.

The minimal requirements for experiments  $\nabla$  measurement specimens: circular and (or) square plates, with 1 – 3 mm of thickness and size 10 – 30 mm (see Fig. 1).

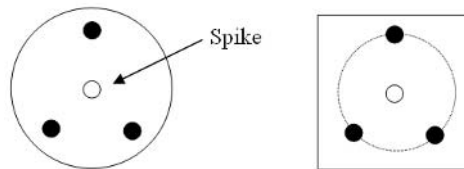


FIGURE 1. Circular and square plates with spike point.

Test  $\nabla$  materials: SiO<sub>2</sub> (piezo- and poly-), Si (single-crystal and polycrystal), SiC (silicon carbide), TiN (titanium nitride), BaTiO<sub>3</sub> (piezoceramics).

Sequence of operations:

1. The resonance spectrum is determined by actuating the specimen (i.e. substrate layer) before being estimating the elastic modulus, sound speed, and the quality factor (integral characteristics of the substrate layer's material).
2. The same procedure is applied to the specimen with superimposed film. We estimate the elastic modulus, sound velocity, and the quality factor (integral characteristics of the film coating).
3. The micro-hardness is determined (i.e. local characteristics of the interesting area of the surface) in several points through the diagram: indenter's loading - indenter's displacement. The signal of acoustic emission is registered on the hysteresis characteristic (loading-unloading) simultaneously.

The final result of the gear's measuring: physic-mechanical characteristics of the materials under test :

1. elastic modulus;
2. quality factor(dissipation);
3. anisotropy factor of elastic properties;
4. sound speed (longitudinal waves, shear waves, Rayleigh's waves);
5. micro-hardness (minimal and maximal) subject to the depth of indentation;
6. value of the pressure limit before plastic deformation initiation (determined by AE signal);
7. The same characteristics but into the range of temperature when changing of phase;

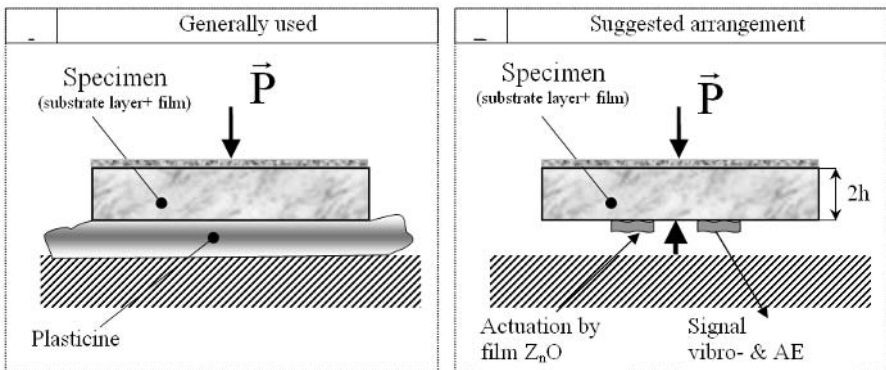


FIGURE 2. The base scheme of the experiment (add-on device).

The essential particularity of the suggested methods – one specimen, in one time, by one researcher, on one portable hardware system and in accordance with uniform technology.



## A NEW INSTRUMENT FOR TENSILE TESTINGS OF THIN FREE STANDING FILMS AT HIGH STRAIN RATES

Eran Ben-David, David Elata, Daniel Rittel, and Doron Shilo  
 Department of Mechanical Engineering, Israel Institute of Technology  
 Department of Mechanical Engineering, Technion, Haifa 32000, Israel  
 shilo@tx.technion.ac.il

The design of more reliable and sophisticated Micro Electro Mechanical Systems (MEMS) relies on the knowledge, understanding, and ability to control their mechanical response. In recent years, enormous progress has been made in developing new measurement techniques for studying the mechanical response of  $\mu\text{m}$  and sub- $\mu\text{m}$  scale specimens (e.g. Kraft and Volkert [1] and Srikar and Spearing [2]). However, there is still a lack of knowledge and testing techniques regarding the response of MEMS structures to mechanical shocks, which can appear during fabrication, deployment, or operation.

We present an instrument for testing the mechanical response of thin free standing films under uniaxial tensile stress at high strain rates of up to  $2 \times 10^3 \text{ sec}^{-1}$ . The freestanding specimen (Fig. 1) is produced by MEMS fabrication techniques on a chip that also includes springs to protect the specimen and aluminum grating lines for measuring the displacement. One side of the chip is pulled by a piezoelectric translation stage (Fig. 2), which allows controlling the displacement with a nanometric resolution and applying high velocities and accelerations. The specimen displacement is monitored by an optical encoder device that measure the displacement of the aluminum grating located on the chip close to the specimen (Fig. 2). This device has an accuracy of about 10 nm and sampling rates of up to 10 MHz. The load is determined by measuring the charge on a piezoelectric shear plate, which is connected to the pin that holds the chip. This allows measuring forces with a sensitivity of about 1  $\mu\text{N}$  and sampling rates as high as 10 MHz.

The new instrument is applied for studying the response of thin aluminum films with thickness of 0.5-1  $\mu\text{m}$ , width that varies between 5 to 50  $\mu\text{m}$ , and length of 150  $\mu\text{m}$ . The mechanical response of these specimens is measured at different strain rates and is compared to measurement done by nanoindentation.

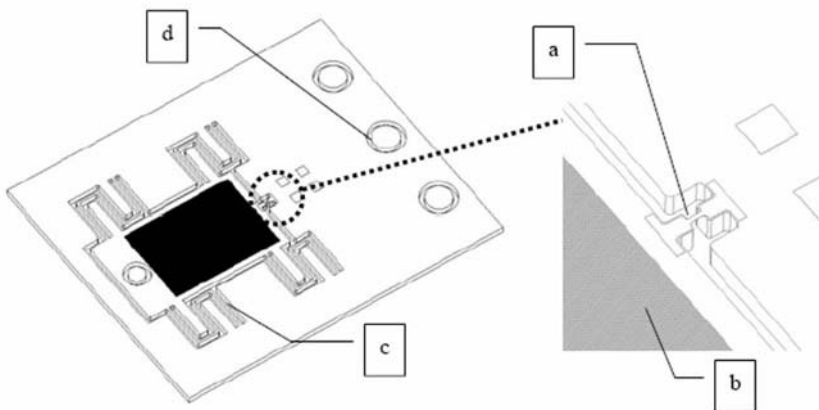


FIGURE 1. Schematic diagram of the chip. (a) - Thin aluminum film, (b) - encoder grating lines, (c) - Si springs, and (d) - holes for gripping.

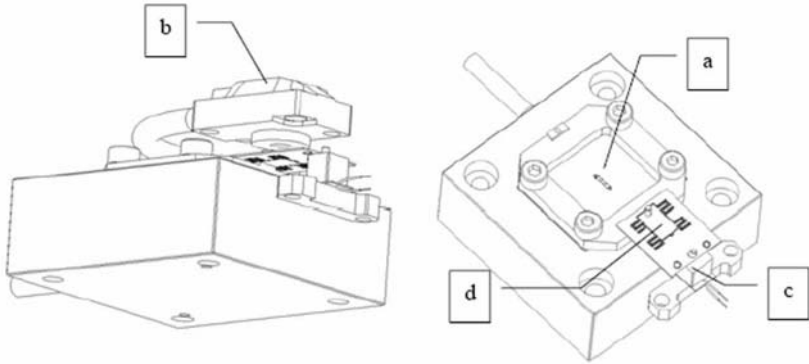


FIGURE 2. Schematic diagram of the tensile test instrument. (a) - Piezoelectric translation stage, (b) - optical encoder, (c) - piezoelectric force sensor, and (d) – micro chip.

### References

1. Kraft, O. and Volkert, C. A., *Adv. Eng. Mater.* vol. 3, 99-110, 2001.
2. Srikar, V. T. and Spearing, S. M., *Experimental Mechanics* vol. 43, 238-247, 2003.

## NANOCHARACTERIZATION OF GOLD/ GOLD CONTACT SURFACE FAILURE IN MEMS CONTACT SWITCHES

M. Al-Haik<sup>1</sup>, H. Sumali<sup>2</sup>, S. Trinkle<sup>1</sup> and J.M. Redmond<sup>2</sup>

<sup>1</sup>Department of Mechanical Engineering  
University of New Mexico,  
Albuquerque, NM 87131, USA

<sup>2</sup>Applied Mechanics Development Department  
Sandia National Laboratories  
Albuquerque, NM 87185, USA  
alhaik@unm.edu

Switching components have been viewed as a great application opportunity for micro electro-mechanical systems (MEMS). For competitive products, reliability problems must be resolved. The study presented in this paper is a basic step toward the understanding of the failure of gold/gold contact switches. This involves the interrelationship among surface conditions, hardness, adventitious insulating layers, fatigue cycling and the operational environment [1]. These elements provide the guidelines and assessment of contact wear, deformation, surface fatigue and adhesion characteristics of MEMS contact switches. In this study, gold micro contacts are investigated and characterized through atomic force microscopy, nanoindentation, nanoscratch, and nanofatigue tests using the state-of-the-art NanoTest characterization system.

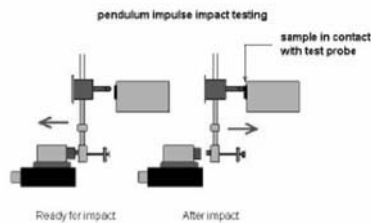


FIGURE 1. NanoTest system on impact phase.

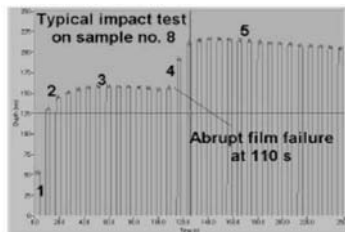


FIGURE 2. Impact failure of 100 nm DLC films on Silicon. 1 = initial contact; 2 = plastic deformation; 3 = fatigue (slow crack growth) 4 = fast crack propagation and material removal 5 = further slow crack growth

The NanoTest system is a fully flexible nano-mechanical property measurement system. It is capable of measuring hardness, modulus, toughness, adhesion and many other properties of thin films and other surfaces. Load ranges can be from sub-mN to 500mN and samples environments and impacting conditions can be set-up to closely replicate conditions that these materials actually see in-use. The instrument consist of a pendulum impulse system( Fig.1) allowing the quantification of total energy delivered to the contact point prior to any observable coating/adhesion failure event. The impulse method is very useful for low cycle fatigue and allows the durability (toughness) of the material to be assessed as well as its mode of failure

An important challenge in the reliability of MEMS is to understand contact failure [2,3]. In many cases, impacts between contacting surfaces increase the contact resistance so much that it is out of specifications after only a few thousand cycles. A major cause of contact failure is surface damage due to mechanical impact, asperity welding and ripping off, and chemical reactions. A nano-level understanding of how contacting surfaces evolve with repeated impacts is therefore crucial to understanding how electrical resistance in micro contacts changes with time. An example of Impact failure detection using the Nano test system is illustrated in Fig. 2.

Another important challenge in assuring the reliability of MEMS contact switches is to determine relevant mechanical properties of the MEMS component, such as elastic and plastic tensile properties, fatigue properties and so on. In many cases, the sizes of MEMS devices are such that their mechanical properties are not same as those for the bulk materials, as mechanical properties in micro-scale depend on the size and fabrication process. The smallest dimension of the MEMS comprises merely a few grains of the gold. Therefore, evaluation of mechanical properties is a challenging problem for the design of MEMS devices. Figure 3 (a) illustrates an array of load-controlled indentations for a titanium nitride coating. The data of the load-depth curves; Fig. 3. (b) are used to calculate both the modulus and hardness of the coating material as shown in Fig. 3. (c).

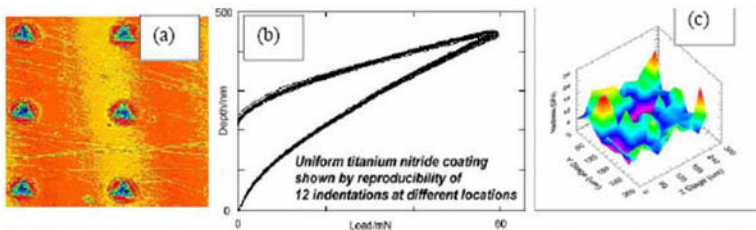


FIGURE 3. a) NanoTest Berkovich tip indentations on a Titanium nitride coating, (b) the depth-load curves, (c) the variation of the hardness over different points on the coating.

Mechanical property measurements and surface nano-characterization results will be presented in the full paper. The comprehensive nano characterization approach could provide valuable insight into failure mechanisms at the micro scale and therefore enhance the ability to design micro devices.

Part of this work was performed at Sandia. Sandia is a multi-program laboratory operated by Sandia Corporation, a Lockheed Martin Company, for the United States Department of Energy's National Nuclear Security Administration under Contract DE-AC04-94AL85000.

## References

1. L. Kogut and K. Komvopoulos, *J. Appl. Phys.*, vol. **95**(2), 2004, 576–585.
2. R.M. Kwiatkowski et al., *Proc. 50th IEEE Holm Conf. on Electr. Contacts*, 160-167.
3. S. Majumder et al., *Sensors and Actuators, A: Physical*, vol. **93**(1), 2001, 19-26.

## MEASURING NATURAL FREQUENCY AND NON-LINEAR DAMPING ON OSCILLATING MICRO PLATES

Hartono Sumali  
 Sandia National Laboratories  
 MS 1070, PO Box 5800, Albuquerque, NM 87185, USA  
 hsumali@sandia.gov

In MEMS, squeezed-film damping determines the dynamics of plates moving a few microns above the substrate, especially around resonance. Squeeze film damping is important in MEMS accelerometers, radio-frequency (RF) MEMS switches, MEMS gyroscopes, etc. Models have been developed by other researchers [1-3] and used widely for designing MEMS devices. However, experimental validation of the models has not kept up with the accuracy of the recent models. This paper presents a method for measuring squeeze film damping forces in MEMS, and validation of a model. The measurements were done on MEMS plates suspended by folded springs (Fig. 1). The substrate (base) was shaken with a piezoelectric transducer. The plate vibrated as a result, especially at the resonant frequency. The velocities of the suspended plate and of the substrate were measured with a laser Doppler vibrometer and a microscope (Fig. 2). Time-domain and frequency-domain methods are used to calculate the damping ratio from measured velocities. To achieve a wide range of squeeze numbers, the experiment was repeated under several different pressures. The measurement was also repeated on an array of plates. A few commonly used squeeze film damping models are compared with the experimental results.

Three models were used to predict the linearized non-dimensional damping ratios of the array of micro plates. Blech's model [1] has been used extensively. The newer Veijola's model [3] takes into account the inertia of the gas. Andrews et al.'s model [2] is the low-squeeze-number limit of Blech's model. Figure 3 shows a comparison among the three models, and typical damping ratios from measurement as a function of squeeze number.

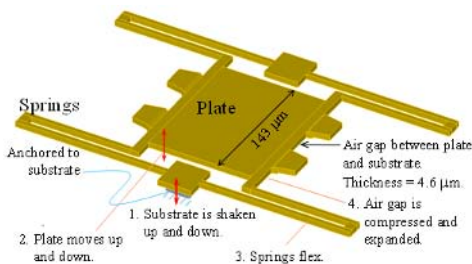


FIGURE 1. Micro plate suspended by four folded-beam springs. Oscillation of the plate expands and squeezes the air layer between the plate and the substrate.

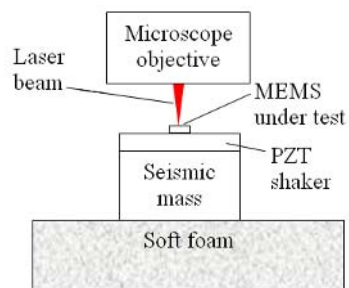


FIGURE 2. Experiment Setup.

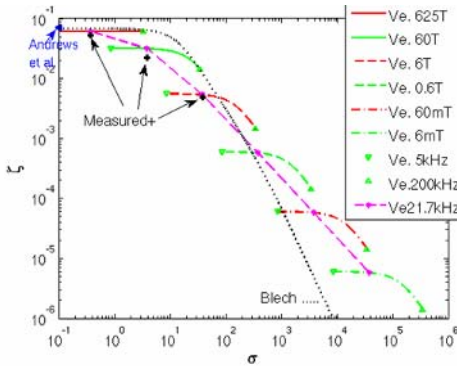


FIGURE 3. Damping ratio  $\zeta$  versus squeeze number  $\sigma$ .  $\blacktriangle$  Marks Andrews et al.'s model;  $\cdots$  Marks Blech's model;  $+$ 's Mark Measurement from test structure whose natural frequency was 21.7kHz. Different pressures and frequencies for Veijola's model (Ve.) are marked by the legends in the inset.

Figure 4 shows the damping ratios from the three models compared with measurement results from the array of micro plates.

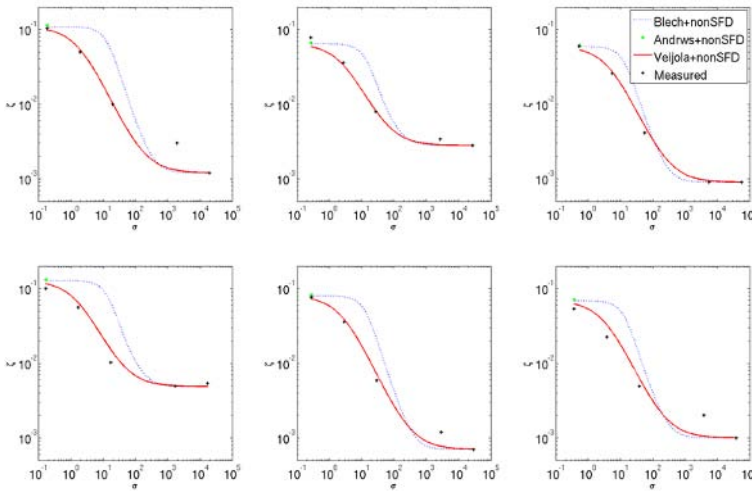


FIGURE 4. Damping ratio versus squeeze number: Comparison among Blech's, Andrews et al.'s, and Veijola's models, and measured data on a 2x3 array of micro plates. NonSFD denotes damping not caused by squeezed film.

**References**

1. Blech, J.J., *Journal of Lubrication Technology*, vol. **105**, 615-620, 1983.
2. Andrews, M., Harris, I., and Turner, G., *Sensors and Actuators A*, vol. **36**, 79-87, 1993.
3. Veijola, T., *Journal of Micromechanics and Microengineering*, vol. **14**, 1109-1118, 2004.

## BIOLOGICALLY INSPIRED MECHANICS OF WAVY SURFACE ADHESION

Pradeep R. Guduru  
 Division of Engineering, Brown University  
 182 Hope St, Providence, RI 02912, USA  
 Pradeep\_Guduru@Brown.edu

Inspired by the attachment ability of insects with smooth pads to vertical walls and ceilings, the mechanics of detachment of a rigid solid from an elastic wavy surface has been analyzed for the axisymmetric case of a sphere and the plane strain case of a cylinder [1]. Due to the qualitative similarities, the discussion was limited to the axisymmetric case only. The load-displacement curve for a sphere indenting a wavy flat surface is shown in Fig. 1, in which the load  $P$  is normalized with the JKR pull-off force  $P_{JKR}$  and the approach displacement  $h$  is normalized with the waviness amplitude  $\lambda$ .

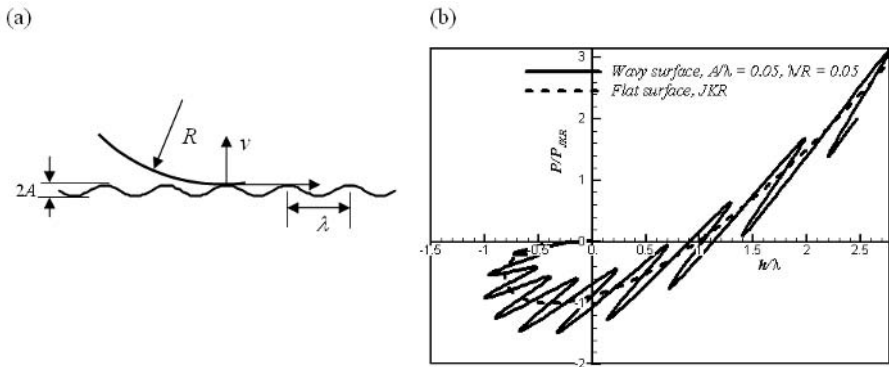


FIGURE 1. (a) The geometry of the problem. A sphere (or cylinder) of radius  $R$  contacts an elastic half space with a single wavelength cosine surface. (b) The force-deflection curve for wavy surface adhesion (solid curve), superposed on top of the classical JKR curve (dashed). The presence of waviness modifies the JKR result such that there is an increase in pull-off force due to the oscillations of the force-deflection curve.

It is shown that the surface waviness makes the detachment process proceed in alternating stable and unstable segments and each unstable jump dissipates mechanical energy, as illustrated in Fig. 2a. As a result, the external work and the peak force required to separate a wavy interface are higher than the corresponding values for a flat interface; i.e., waviness causes interface toughening as well as strengthening. A systematic experimental investigation is also presented which examines the above theoretical analysis, by measuring adhesion between a “rigid” wavy punch and a soft “elastic” material. The observed increase in adhesion due to waviness closely agrees with the theoretical predictions within the experimental and material uncertainties, as shown in Fig. 2b. The experiments not only validate the theory, but also demonstrate that adhesion of a soft material can be substantially enhanced by topographic optimization alone, without modifying the surface chemistry [2].

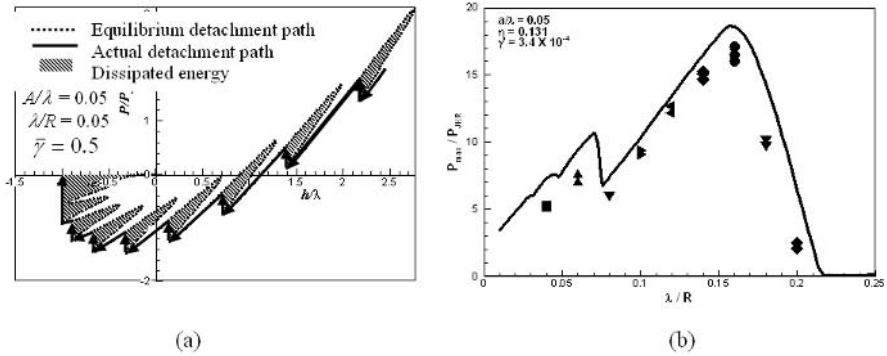


FIGURE 2. (a) Energy dissipation due to unstable detachment of a sphere from an axisymmetric wavy surface. Dashed curve is the equilibrium path and the solid line is the actual path followed in displacement controlled loading. Each vertical solid line segment represents an unstable jump during which the crack advances spontaneously to the next available stable position. The hatched area adjoining each unstable segment is the mechanical energy dissipated during that crack jump. (b) Summary of experimental data on adhesion force as a function of wavelength: comparison between the experimental measurements (symbols) and theoretical predictions (solid lines). Experimental results capture not only the magnitude of the predictions, but also features such as the local maxima.

## References

1. Guduru, P.R. *J. Mech. Phys. Solids*, to appear, 2007.
2. Guduru, P.R. and C. Bull. *J. Mech. Phys. Solids*, to appear, 2007.



---

**EMBEDDED SENSORS IN RUBBER AND OTHER POLYMER COMPONENTS**

Keith Harmeyer, Michael A. Holland and Gary Krutz  
Purdue University Agricultural and Biological Engineering  
225 S University Street  
West Lafayette, IN 47907  
mholland@purdue.edu, kharmeyer@purdue.edu, krutz@purdue.edu

Many rubber or other polymer components are susceptible to catastrophic failure or are critical to the performance of the products that they make up. Because of this it is beneficial to be able to monitor or sense structural failures or a performance drop in these components. In the past this has been difficult to accomplish as polymer components often have complex shapes or are assembled in places that are difficult to access with a typical sensor. Current sensor technologies are often too expensive or are impractical to manufacture.

Micro-scale electronic sensors have been developed at Purdue University to indicate multiple types of failures in rubber and other polymer materials. Failure modes that are detected include: wear, loss of adhesion, excessive compression or expansion, overheating, fractures or breaks, changes in material properties, leakage of fluids and others.

The rubber/polymer structural sensors are integral to the product they are made of. The component itself can be used as the sensor by utilizing conductive mixtures of rubber or other polymer materials. Carbon-polymer composites can achieve conductivities on the order of  $10 (\Omega\text{-cm})^{-1}$ , Sichel [1]. Research has been done to identify optimal mixtures for the best conductivity while retaining the necessary material properties for particular applications. This makes the sensor more robust and decreases the total number of parts, which enables the manufacturing process to be more efficient.

The rubber/polymer sensors use LCR measurements to monitor changes in the structure that may be critical to the performance of the components. Finite Element analysis of a multi-layer system at various loading situations was conducted and confirmed the principles of the sensor. Preliminary testing has proven to be effective at sensing impending failures and performance drops in the range of 100-600 cycles before failure (Fig. 1). Changes in the electrical properties are on the magnitude of 300%. This high sensitivity limits the number of erroneous signals given by the sensor. The electronic signal can be used to indicate a problem to an operator or may be input as a control parameter to a product.

Electronic components for the sensor can be contained on micro-scale circuitry. Signal collection and conditioning consists of a relatively simple circuit design and includes minimal components. However, circuitry is build to be durable for severe manufacture and operating conditions. In some applications the circuitry must be able to endure the curing process that polymer materials typically go through. These processes can exceed temperatures of 150°C (300°F), Baranwal and Stephens [2]. Some applications may require remote sensing, in which a radio frequency transmitter and receiver can be used to transmit the signal.

There is a broad range of applications that can be served by this technology. Components that are most suited include products that are susceptible to wear, fracture or separation of bonded surfaces. Tests have been completed successfully for multiple applications. These prototypes were able to sense pending structural failure several minutes (hundreds of cycles) prior to catastrophic failure.

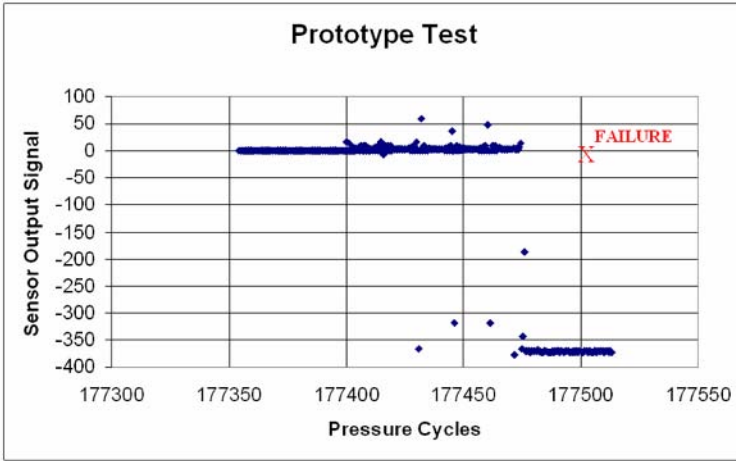


FIGURE 1. Prototype testing results.

Several different methods of sensing failures or anomalies have been analyzed. Different methods may be optimal depending on the application, material properties and common failure mode. Two US patents have been filed and proprietary research is being conducted for particular applications.

## References

1. Sichel, E.K. *Carbon Black-Polymer Composites, The Physics of Electrically Conducting Composites*, Marcel Dekker Inc, New York, 1982.
2. Baranwal, K.C. and Stephens, H.L. *Basic Elastomer Technology*, The Rubber Division, American Chemical Society, Baltimore, 2001.

## EVALUATION OF FINITE ELEMENT BASED CORRECTION OF LAYER REMOVAL DURING XRD MEASUREMENTS FOR GEOMETRIES AND STRESS DISTRIBUTIONS OF INTEREST IN AIRCRAFT ENGINES

Yogesh K. Potdar<sup>1</sup>, Karthick Chandraseker<sup>2</sup>, Robert McClain<sup>3</sup>, Mike Hartle<sup>3</sup>, Paul Domas<sup>4</sup>  
and Rohinton Irani<sup>1</sup>

<sup>1</sup>Mechanical Engineer (GE Global Research), <sup>2</sup>Research Intern (GE Global Research), <sup>3</sup>Sr. Staff Engineer and <sup>4</sup>Consulting Engineer (GE-Aviation)

<sup>1</sup>One Research Circle, K1-3C2B, Niskayuna, NY 12309, USA

<sup>1</sup>potdar@research.ge.com

X-Ray diffraction has evolved as one of the most practical methods to measure surface residual stresses. The method is regularly used to measure sub-surface stresses by removing thin surface layers by electro-polishing. When such layer removal is performed, the measured stress needs to be corrected for the stress relaxation and redistribution that occurs because of layer removal. The underlying principles of mechanics for this method are described by Francois et.al. [1]. Most standards on XRD measurements (e.g. SAE HS-784 [2]) cite analytical solutions derived and published in 1958 by Moore and Evans [3] as a recommended correction for simple geometries. We have extended these corrections by developing and implementing analytical solution for internal holes – a geometry of interest in aircraft engine applications.

Further, when the geometry is not simple and/or only a portion of material is removed instead of a full layer, these analytical solutions are not valid. Finite element based correction methodology has been previously published by Hornbach et. al. [4] and Lambda Research [5]. It has been claimed that only geometry dependent correction factors can be developed for typical stress distributions of interest. It is not obvious if and how sensitive these corrections are to the choice of material properties and stress levels as well as gradients. In this work, we will evaluate this assumption and demonstrate that while the concept works very well with linear elastic finite element analysis, the correction matrix is sensitive to material model, and qualitative and quantitative nature of residual stress distribution.

It will be shown that more rigorous transfer functions can be developed for a particular class of problems – that depend on geometry, material property and stress distribution. We will show results for such corrections on specimens with split sleeve cold expanded (SSCE) holes and a flat plate with different levels of shot-peening. It will be demonstrated that given the asymmetric stress distribution along the circumference of the holes and the large depth of high compressive stresses in case of SSCE processes, the correction procedure must account for plasticity. In the case of shot-peening alone, since the corrections are small relative to the magnitude of stresses, a simpler approach with linear analysis may suffice.

For the case of a flat plate with multiple alternatively peened zones, it is shown that removing sufficiently small regions of material from a particular shot-peened region does not disturb residual stresses over the rest of the plate and thus an efficient testing plan can be developed that enables testing of various shot-peening conditions with minimal number of specimens.

Finally, we will also discuss and demonstrate the feasibility of developing enhanced tools that employ only a small number of FE analysis results as basis functions to calculate corrections to any given stress profile in specimens of the same material and geometry.

**References**

1. Francois, M., Convert, F., Lu, J. et. al., Handbook of Measurement of Residual Stresses, Society of Experimental Mechanics, Inc., Ed. Jian Lu, 71-132, 1996
2. SAE International, Residual Stress Measurement by X-Ray Diffraction, HS-784, 77-84, 2003
3. Moore, M.G. and Evans, W.P., SAE Transactions, vol. **66**, 340-345, 1958
4. Hornbach, D.J., Prevey, P.S., and Mason, P.W., In *Proceedings of the First International Conference on Induction Hardened Gears and Critical Components*, Indianapolis, IN, Gear Research Institute, 69-76, 1995
5. Lambda Research, Diffraction Notes, No.17, 1996

## STRESS ANALYSIS OF LASER MARKED LOW CARBON STEEL

Z. Kalincsak<sup>1</sup>, L. Balogh<sup>2</sup>, L. Borbas<sup>3</sup> and J. Takacs<sup>1</sup>

<sup>1</sup> Dep. of Vehicle Manufac. and Rep., BUTE, H-1111 Bertalan L. 2., Budapest, Hungary

<sup>2</sup> Dep. of Material Physics, Lorand Eotvos University,  
H-1117, Pazmany Peter setany 1/a., Budapest, Hungary

<sup>3</sup> Dep. of Vehicle Parts and Drives, BUTE, H-1111 Bertalan L. 2., Budapest, Hungary

<sup>4</sup> Dep. of Vehicle Manufac. and Rep., BUTE, H-1111 Bertalan L. 2., Budapest, Hungary  
kalincsak@kgtt.bme.hu, levente@metal.elte.hu, borbas@kge.bme.hu, takacs@kgtt.bme.hu

Laser marking on steel surfaces is considered to apply to create local phase transformations and/or local stress level change in order to produce bar codes on low carbon steel surfaces. The local phase transformations caused by the rapid heating and cooling process combined with the stress accumulations within the heat affected zones [1]. The stress, generated by the marking procedure ("marking stress") has of a primary importance from the point of view of reading out. This kind of codes can be widely applied in the production logistics. The investigated materials are cold rolled low carbon steel sheets (typical car body sheets with 0.1 % C content). In this paper the working principle of this stress detection as well as some technical details will be described.

Previously, the photostress analysis and the Moire effect were applied for the detection of these local stresses. However the resolution of these methods was not able to reveal the changes in the stressed state of the investigated specimen [2]. Local micro-stress analysis of the laser scribed zone was carried out within X-ray diffraction using CoK $\alpha$  radiation. The diffraction was measured two positions, in the base material (1. measuring position) and in the laser treated zone (2. meas. pos.). The applied measuring arrangement and the specimen can be seen in Fig. 1.

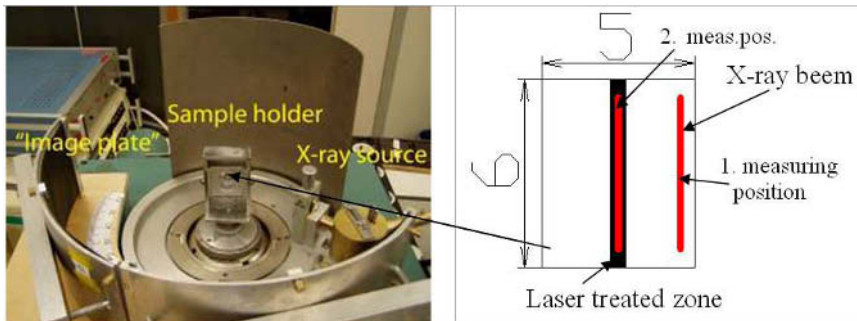


FIGURE 1. Measuring arrangement and the applied specimen.

The reflections were recorded in "image plate" used Debye-Scherrer method. Fig. 2. shows the Debye-Scherrer rings of (310) reflection in the base material and the laser treated part. The intensity distribution in base material is homogenous, hints to the material contains fine grain structure. Contrary, the intensity distribution of laser treated part is inhomogeneous influence of roughened average grain structure.

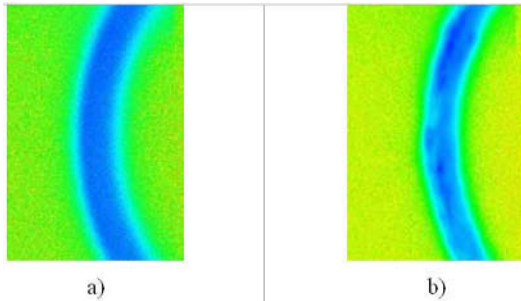


FIGURE 2. Debye-Scherrer rings of (310) reflection, a) base material, b) laser treated part

Williamson-Hall method was used by qualitative evaluation [3,4]. The decreasing of full width of high maximum hints to the decreasing the density of dislocations and the level of inner micro stress [5]. The types of dislocations were also changed. In the base material dominant the screw dislocation contrary in the laser treated zone significant the edge dislocation.

## References

1. Z. Kalincsak, J. Takacs, G. Vertesy, A. Gasparics: The optimisation of laser marking signals for eddy current detecting of marks, *Laser Assisted Net Shape Engineering 4*, Erlangen, 2004. September 21-24., pp. 535-544 in Volume 1.
2. Z. Kalincsak, J. Takacs, L. Borbas: Local stress detection in low carbon steels by using fotostress analysys, *Advanced Manufacturing and Repair Technologies in Vehicle Industry*, Balatonfured, May 17-19, 2004, pp. 174-178.
3. Balogh Levente: *Nanokristalyos rez termikus stabilitasa*, Diplomamunka ELTE TTK Altalanos Fizika Tanszek, 2004.
4. T. Ungar, J. Gubicza, G. Ribarik, A. Borbely: Crystallite size distribution and dislocation structure deterined by diffraction profile analysis: principle and practical application to cubic and hexagonal crystals, *J. of Applied Crystallography*, vol. **34**, 2001.
5. Schultz, Jerold M.: *Az anyagvizsgalat diffrakcios modszerei*, Muszaki konyvkiado, Budapest, 1987.

## INVESTIGATION OF RESIDUAL STRESSES DEVELOPEMENT IN A SINGLE FIBRE COMPOSITE WITH FBG SENSOR

F. Colpo<sup>1</sup>, D. Karalekas<sup>2</sup> and J. Botsis<sup>1</sup>

<sup>1</sup> Ecole Polytechnique Fédérale de Lausanne EPFL, CH-1015, Switzerland

<sup>2</sup> University of Piraeus, Piraeus, GR-185 34, Greece

fabiano.colpo@epfl.ch, dkara@unipi.gr, john.botsis@epfl.ch

A combined experimental and numerical study was undertaken to improve understanding of the development of residual strains in thermoset polymer matrix composites due to subsequent thermal post-curing treatment. In the present work, long Bragg grating sensor was used to measure the complete strain distribution built-up along a fibre embedded in epoxy cylinders and post-cured at various temperatures. The optical glass fibre was centrally located within the epoxy, thus acting as reinforcement and as a sensor providing relatively non-invasive strain and stress measurements. Such residual stresses are due to volume shrinkage of the epoxy resin during curing and post-curing treatment and by the mismatch between the elastic and thermal properties of the two constituents.

Each tested cylindrical specimen, having an outer diameter of 8 mm and length of 40 mm, was prepared by using a mixture of DER 330, DER 732 Dow Epoxy resins and a DEH 26 curing agent. The resulted epoxy system was initially poured into a specially designed mould and then left to cure at room temperature for 24h. The initial liquid mixture reacts to give a highly cross-linked structure. Afterwards, the cylindrical specimens were removed from the mould and post cured sequentially in an air conventional oven at 60, 100 and 110 °C for 9 hours each time. All specimens contained a standard optical fibre, centrally located along the cylinder's axial direction, of 0.125 mm in diameter. The optical fibre was equipped with a FBG of 24 mm in length. The grating was located in such a way that 20 mm of its total length remained inside the specimen and the rest 5 mm in the outside. A novel optical low-coherence reflectometer (OLCR) apparatus, previously designed at EPFL, was used to directly reconstruct the strain distribution from the FBG complex impulse response measurements [1, 2, 3] without any assumption on the strain profile.

From the obtained measurements, plotted in Fig. 1, the cylindrical specimen experienced substantial non-uniform compressive strains due to epoxy's consolidation during curing and further thermal post-curing treatment. It is seen that a maximum strain of -700 micro-strains is recorded close to the centre of the specimen right after curing at room temperature. However, the magnitude of the obtained strains increases considerably when the specimen is thermally post-cured at higher temperatures, 60 and 100 °C respectively. Any additional post-curing at temperatures close to the glass transmission temperature of the epoxy (~115 °C) did not lead to any strain increase.

An axisymmetric finite element (FE) model, based on an equivalent thermo-elastic approach, was used to determine the residual stresses in the thermally treated cylindrical specimens. In the performed analysis the specimen was modelled as a cylindrical fibre-reinforced composite consisted of two concentric cylinders. The simulated strain at 100 °C post-curing is plotted in Fig. 1, while the corresponding stresses on the plane  $z = 0$  are shown in Fig. 2. It is seen that numerical results are in good agreement with the ones obtained experimentally.

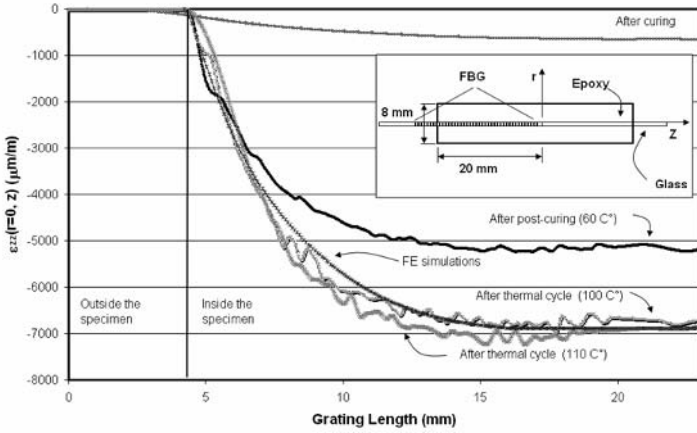


FIGURE 1. Measured and simulated (at 100 °C) axial strain distributions along the grating length (before and after thermal post-curing).

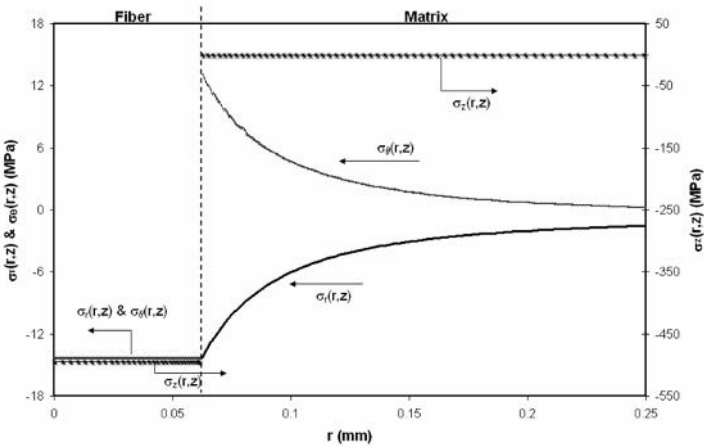


FIGURE 2. Axial and transversal strain evolutions in the plane  $z=0$ .

**References**

1. Giaccari P. et al., *Smart Materials and Structures*, vol. **14**, 127-136, 2005.
2. Colpo et al., *Composites Part A: Applied Science and Manufacturing*, vol. **37**, 652-661, 2006.
3. Colpo F., *Ph.D. Thesis*, n° 3533, EPFL, 2006.



## VALIDATION SPECIMEN FOR CONTOUR METHOD EXTENSION TO MULTIPLE RESIDUAL STRESS COMPONENTS

P. Pagliaro<sup>a</sup>, M.B. Prime<sup>b</sup>, B. Zuccarello<sup>a</sup>, B. Clausen<sup>b</sup> and T.R. Watkins<sup>c</sup>

<sup>a</sup> Dipartimento di Meccanica, Università degli Studi di Palermo, Viale delle Scienze, 90128 Palermo, pagliaro@dima.unipa.it, zuccarello@dima.unipa.it

<sup>b</sup> Los Alamos National Laboratory, Los Alamos, NM 87545, USA

<sup>c</sup> High Temperature Materials Laboratory, Materials Science and Technology Division, Oak Ridge National Laboratory, Oak Ridge, TN 37831, USA  
prime@lanl.gov, clausen@lanl.gov

A new theoretical development of the contour method [1], that allow the user to measure the three normal residual stress components on cross sections of a generic mechanical part, is presented. To validate such a theoretical development, a residual stress test specimen was properly designed, fabricated and then tested with different experimental techniques.

In the classical approach of the contour method [1,2], the analysed specimen is carefully cut in two along a plane using a wire EDM machine. Residual stresses relax as free surface is created by the cut. After cutting, the contours of the two opposing surfaces created by the cut are measured using a CMM machine or by laser scanning. Assuming that the contours are caused by elastic relaxation of the residual stresses, a straightforward finite element calculation, in which the opposite averaged contour is applied as boundary conditions to the FE model, permits to reveal the original residual stresses component  $\sigma_x^{(A)}$  normal to the cut surface (see Fig. 1).

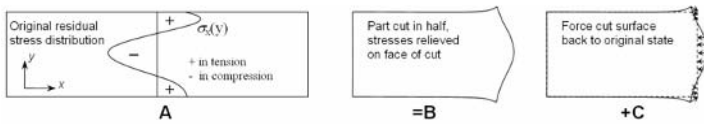


FIGURE 1. Contour method approach. Bueckner's superposition principle.

This is based on Bueckner's superposition principle: the original residual stress component  $\sigma_x^{(A)}$  is given by the simple summation of the stress components of steps B and C of Fig. 1, i.e:

$$\sigma_x^{(A)} = \sigma_x^{(B)} + \sigma_x^{(C)} \quad (= \sigma_x^{(C)} \text{ on cut plane}) \quad (1)$$

The new theoretical development should allow the contour method to measure all three stress components on the cut plane. The same finite element calculation that determines the  $\sigma_x^{(C)}$  in the cut plane, also determines how much two stress components in the plane of the cut,  $\sigma_y^{(C)}$ ,  $\sigma_z^{(C)}$  and  $\tau_{yz}^{(C)}$  were changed by the relaxation from the cut. After the surface is cut, the post-relaxation in-plane stresses ( $\sigma_y^{(B)}$ ,  $\sigma_z^{(B)}$  and  $\tau_{yz}^{(B)}$ ) can be measured by a surface technique after electrochemical removal of material affected by the cut. A simple summation with the results of

the finite element calculation (Eq.1) then provides the original components  $\sigma_y^{(A)}$ ,  $\sigma_z^{(A)}$  and  $\tau_{yz}^{(A)}$  of the residual stress on the cut plane:

$$\sigma_i^{(A)} = \sigma_i^{(B)} + \sigma_i^{(C)} \quad (i = y, z, yz) \quad (2)$$

A test specimen was chosen to provide a residual stress distribution particularly well suited to testing the new theory. The test specimen was carefully designed by means of an extensive set of finite element simulations. As a result, a 60-mm diameter and 10-mm thick plate of 316L stainless steel will be locally plastically compressed through the thickness of a 15 mm diameter region in the centre of the plate. This provides a stress distribution like a shrink-fit ring and plug (a real ring and plug would fall apart during contour method cutting). In the compressed region, the radial and hoop stresses are nearly equal in compression. In the outer region, the radial stresses are still compressive but the hoop stresses are tensile. Fig. 2 shows preliminary FEM results of the residual stress field produced by the compression. This unique biaxial stress state is ideal for testing the theory and also to test the accuracy of different residual stress measurement methods, because of the variation of the stresses along the radial direction and through the thickness.

The compression process and resulting residual stresses will be FEM simulated based on measured constitutive behaviour of the source material and load-displacement data taken during the compression. The 316L stainless steel and the plate thickness were chosen for their suitability for neutron and x-ray diffraction measurements, which will be part of the measurement and validation process.

A series of experimental tests will be used to validate the new contour method theory. For an independent stress measurement, the stresses were measured using neutron diffraction at the Los Alamos Neutron Science Center (LANSCE). A conventional contour method experiment will be a diametrical cut on the specimen to measure  $\sigma_\theta$  (hoop stress). The extension of the contour method will be tested by measuring the in-plane stresses on the cut surface (radial and axial stresses) using X-ray diffraction and subsequently hole-drilling. Combining the contour method results with the surface stress measurements, the result of the new approach will be compared with the neutron diffraction measurements and the FEM prediction. Fig. 2 shows the FEM residual stress prediction and the neutron diffraction measurement along the centre line of the disk.

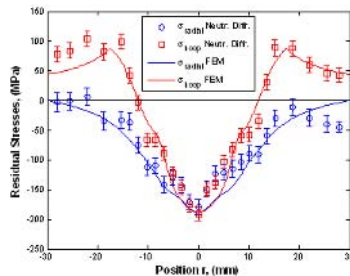


FIGURE 2. Comparison between neutron diffraction measurement and FE prediction of radial and hoop residual stresses on the centre line of the specimen.

## References

1. Prime, M. B., *J. of Eng. Mat. and Tech.*, vol. **123**(2), 162-168, 2001.
2. Prime, M. B., Sebring, R. J., Edwards, J. M., Hughes, D. J., and Webster, P. J., *Experimental Mechanics*, vol. **44**(2), 176-184, 2004.

## DEVELOPMENT AND UNCERTAINTY ANALYSIS OF A SONIC CONTROLLED DRILLING UNIT ON RESIDUAL STRESSES MEASUREMENT BY THE HOLE DRILLING METHOD

A. Albertazzi Jr.<sup>1</sup>, M.R. Viotti<sup>1</sup> and W.A. Kapp<sup>2</sup>

(1) Federal University of Santa Catarina

(2) LACTEC

Cx Postal 5053

Florianópolis, SC, Brazil – CEP 40 040-970

albertazzi@labmetro.ufsc.br

The hole drilling method is widely used in laboratory and non-laboratory applications for residual stresses measurement. A small blind hole is drilled on the material where the residual stresses have to be determined, producing a local stress relaxation. The radial strain field around the drilled hole is measured and correlated to the residual stresses value by an appropriate mathematical model. The radial strain field is normally sampled by a special three-element strain gauge rosette.

The authors' group developed an alternative way of sampling the measurement data. A radial in-plane sensitive electronic speckle pattern interferometer was developed and is used for residual stresses measurement.<sup>[1, 2]</sup> Conical mirrors are used to promote a double illuminated area on the material surface that produces radial in-plane sensitivity. Figure 1 shows the basic configuration of the ESPI interferometer used for residual stresses measurement.

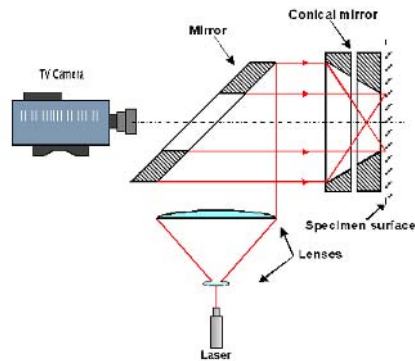


FIGURE 1 – Basic configuration of the radial in-plane interferometer used for residual stresses measurement.

The drilling process is very critical on the residual stresses measurement uncertainty. It is usually done with an ultra high speed drilling unit driven by a pneumatic turbine. To avoid the introduction of new residual stresses due to the drilling process, the cutting tool is typically an inverted cone shaped milling tool as the ones regularly used by dentists. The cutting process has a very strong influence on the measurement uncertainty. Particularly the drilling advance speed is critical. A constant drilling advance speed is not the best choice due to localized material inhomogeneities.

This paper presents a sonic approach to optimize the cutting process. The idea is to sample the cutting air turbine sound by a microphone and continuously determine its fundamental frequency. The drilling sound frequency is used in a closed loop to control the drilling advance speed. For example, if the cutting tool reaches a harder layer of material, the rotation speed is naturally reduced, what lower the frequency of the produced sound. In this case, the drilling advance speed must be diminished. This approach imitates the human behavior of a well trained technician, but in a more accurate and predictable way.

This paper evaluates the effects of this new approach on the residual stresses measurement results. A 3 m long annealed specimen is loaded in a well controlled way to mechanically simulate a reference residual stresses field. Several tests are performed with different control parameters and the dispersion and deviation of the results are compared and critically discussed. Finally the improvements of the developed approach on the residual stresses measurement uncertainty are presented.

## References

1. Armando Albertazzi G. Jr., Cesar Kanda, Maikon R. Borges, Frank Hrebabetzky, "*Radial in-plane interferometer for ESPI measurement*", Proc. SPIE vol. **4101**, 83-94, Laser Interferometry X: Techniques and Analysis; Malgorzata Kujawinska, Ryszard J. Pryputniewicz, Mitsuo Takeda; Eds., 2000
2. Armando Albertazzi G. Jr., Celso L. Veiga, Daniel P. Willemann, "*Evaluation of the optical rosette for translation, stresses, and stress gradient measurement*", Proc. SPIE Vol. 5144, p. 533-544, Optical Measurement Systems for Industrial Inspection III; Wolfgang Osten, Malgorzata Kujawinska, Katherine Creath; Eds., 2003

## STRAIN AND TEMPERATURE DISCRIMINATION AND MEASUREMENT USING SUPERIMPOSED FIBER BRAGG GRATING SENSOR

M. Demirel<sup>1,2</sup>, L. Robert<sup>1</sup>, J. Molimard<sup>2</sup>, A. Vautrin<sup>2</sup> and J.-J. Orteu<sup>1</sup>

<sup>1</sup> Ecole des mines d'Albi Carmaux, CROMeP, 81013 Albi Cedex 9, France

<sup>2</sup> Ecole des Mines de Saint Etienne, Centre SMS, 42000 Saint-Étienne, France  
demirel@emse.fr

This paper presents a contribution to the joint *in-situ* measurement of strain and temperature by using Fiber Bragg Gratings (FBG) sensor. FBG's are particularly suited to measuring strain and temperature in smart structures, e.g. for composite laminate materials *in-situ* measurements [Botsis, J., Humbert, L., Colpo, F. and Giaccari, P., Opt. Las. Eng., vol. 43, 491-510, 2005.]. Advantages are weakly intrusive characteristics, linearity, high sensitivities and multiplexability. One of the problems in using FBG is the discrimination of temperature and strain responses. In this work, we detail our solution which is based on two superimposed FBGs. An application will be presented in which the sensor is embedded in carbon/epoxy composite coupons submitted to both mechanical and thermal solicitations.

When an optical fibre is submitted to axial tension or temperature change, the spectrum presents a peak (light reflected by grating) who shifts linearly with the amplitude of the solicitation. Measurement with FBG is simply based on the peak shift measurement. The wavelength shift can be expressed after differentiation as:

$$\Delta\lambda_B = K_\varepsilon \varepsilon + K_T T \quad (1)$$

where  $K_\varepsilon$  and  $K_T$  are respectively the strain and temperature sensitivities.

Eq. (1) shows that two wavelength shifts are necessary to discriminate the  $\varepsilon$  and  $T$  variables. Several arrangements have been proposed in the literature to obtain a second shift information [Zhao, Y. and Liao, Y., Opt. Las. Eng., vol. 41, 1-18, 2004.]. Temperature and strain were determined after inverting the following system (supposed to be well conditioned):

$$\begin{pmatrix} \Delta\lambda_{B1} \\ \Delta\lambda_{B2} \end{pmatrix} = \begin{pmatrix} K_{1T} & K_{1\varepsilon} \\ K_{2T} & K_{2\varepsilon} \end{pmatrix} \begin{pmatrix} T \\ \varepsilon \end{pmatrix} \quad (2)$$

Xu et al. [M. G. Xu, M.G., Electronics Letters, vol. 30-13, 1085-1087, 1994.] demonstrate that it is possible to discriminate (T,  $\varepsilon$ ) using two superimposed FBGs at 850 nm and 1300 nm. Their system needs two interrogation devices and two broadband sources. Our proposed solution consists in considerably reducing the gap around 100 nm between the two Bragg wavelengths and using particular shape of FBG spectra with different depths and bandwidths. The optical treatment thus could be simplified, and the shape difference may produce a better conditioning system (Eq. (2)). Superimposed FBGs are photo-written by using Lloyd mirrors interferometer bench developed at the TSI laboratory (Saint-Etienne, France). The Bragg wavelength for the first FBG is around  $\lambda_B^{\text{FBG1}}=1489$  nm, and around  $\lambda_B^{\text{FBG2}}=1565$  nm for the second one. Recall that FBGs are localized at the same spatial place that insured a 3 mm spatial resolution.

Thermal and strain calibration of FBG sensors can be performed in two situations: (i) the sensor is kept free and calibration is done using a specific calibration bench, or (ii) the optical fibre is glued on a plate specimen that could be submitted to tensile test.

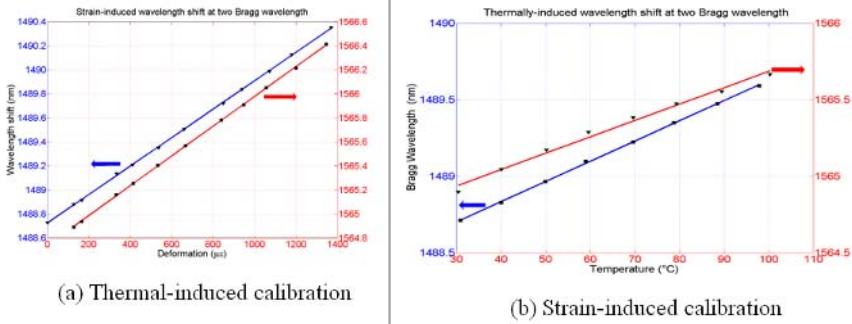


FIGURE 1. Thermal-induced and strain-induced calibration of two FBG sensors

Figure 1 presents typical calibration curves for a superimposed FBG sensor glued on a carbon/epoxy composite coupon. Thermal-induced calibration (Fig. 1(a)) is done by using an oven and a thermocouple. Strain-induced calibration (Fig. 1(b)) is done during the tensile test of the specimen, using a mechanical testing machine and two electrical gages for the strain measurements. Finally, the measured values of the sensitivities matrix components write as follows:

$$\lambda_B^{T,FBG1} = 13,21 (\pm 0.1).T + 1488,304.10^3 (\pm 12,99) \text{ pm}/^\circ\text{C}$$

$$\lambda_B^{T,FBG2} = 10,70 (\pm 0.4).T + 1564,614.10^3 (\pm 54,53) \text{ pm}/^\circ\text{C}$$

$$\lambda_B^{\varepsilon,FBG1} = 1,183(\pm 5.10^{-3}).\varepsilon + 1488,726.10^3 (\pm 14,82) \text{ pm}/\mu\varepsilon$$

$$\lambda_B^{\varepsilon,FBG2} = 1,239(\pm 5.10^{-3}).\varepsilon + 1564,740.10^3 (\pm 13,42) \text{ pm}/\mu\varepsilon$$

After inversion of the sensitivity matrix in order to calculate strain and temperature errors, one finds typically  $\delta\varepsilon=10 \mu\varepsilon$  and  $\delta T=1^\circ\text{C}$ . Calibration using free sensor and a specific calibration bench is in progress, as well as the study of the influence of the width between the two peaks of each FBGs and the shape of the spectra on the measurement resolution of the superimposed FBG sensors. The well-designed superimposed FBG sensor will be embedded in a UD carbon/epoxy prepreg specimen ( $250 \times 25 \times 4 \text{ mm}^3$ ) and used to measure the longitudinal strain and the temperature simultaneously during the matrix curing and the tensile tests in the  $20^\circ\text{C}$ - $180^\circ\text{C}$  temperature range.

## References

1. Botsis, J., Humbert, L., Colpo, F. and Giaccari, P., *Opt. Las. Eng.*, vol. **43**, 491-510, 2005.
2. Zhao, Y. and Liao, Y., *Opt. Las. Eng.*, vol. **41**, 1-18, 2004.
3. M. G. Xu, M.G., *Electronics Letters*, vol. **30**-13, 1085-1087, 1994.

## MONITORING OF LRI PROCESS BY OPTICAL FIBRE BRAGG GRATINGS

S. Vacher<sup>1</sup>, J. Molimard<sup>1</sup>, A. Vautrin<sup>1</sup>, H. Gagnaire<sup>2</sup> and P. Henrat<sup>3</sup>

<sup>1</sup> ENSM.SE, 158, Cours Fauriel 42023 Saint-Étienne Cedex 2, France

<sup>2</sup> LTSI / UMR CNRS 5516 - Université Jean Monnet - Saint-Étienne, France

<sup>3</sup> HEXCEL Reinforcements, Z.I. les Nappes, 38630 Les Avenières, Cedex, France  
vautrin@emse.fr

Fibre reinforced/polymer matrix composites are now widespread in industrial sectors such as aerospace, automotive and civil engineering. Moreover, they tend to be more and more used in structural applications, therefore the quality and reliability of these materials on the long term should be carefully checked. Residual stress due to the manufacturing process is one of the most critical phenomena. In service life, it may generate ply-cracking, ply-delamination, drop of fracture toughness and fatigue strength of composite structures. Finally, quality of the product should be assessed and monitored along the process to reduce the number of rejected components since cost of components tend to increase due to their complexity. It is now established that optical fibre based sensors are good candidates to set up efficient methods to follow the parameters conditioning the product properties, since optical fibres can sustain harsh conditions and be located both within the component and mould.

The paper presents an experimental analysis showing that those types of sensors could be used to assess residual manufacturing stresses in Liquid Resin Infusion process, which is a promising technique to produce complex or large structural parts [1].

Resin Film Infusion (RFI) is first introduced. It is a cost effective process to manufacture complex shaped large composite structures. A semi-cured resin film is melt and transversely infused through the thickness of a dry fibrous preform under prescribed temperature and pressure histories. For a given polymer matrix, mould filling by LRI is faster than other liquid composite-moulding processes such as RTM, since the resin infusion distance is shorter. The resin film is set below the preform in the mould then a mechanical compaction results in the melt resin flow through the preform. However, it is more difficult to make the resin infuse into upright sections, such as stiffeners for instance, because the proper pressure of volumes is usually hard to achieve without any specially designed compaction device. The mould filling is further assisted by vacuum to reduce the air voids remaining in the part.

Optical Fibre Bragg Grating sensors (OFBG) are then briefly described. They have highly attractive features which make them well suited to the measurement of temperature and strains. Those types of sensors are immune to electromagnetic interference and ground loops, light weight and have small dimensions. Furthermore, no connecting wires are required to connect sensors to demodulation systems. The fibres can be either embedded into the composite part or into the mould to assess the response of the structure to processing or hygrothermal changes.

The calibration procedure is presented and the particular case of a  $[0_6/90_3]_S$  carbon / RTM6 epoxy laminate manufactured by LRI is analyzed. An OFBG is embedded into the mid-plane of the 90 degrees dry unidirectional carbon layers NC2<sup>®</sup> in the mould before the resin infuses the preform, the direction of the sensor being is that of the unidirectional fibres of the ply [1].

After the resin infusion and curing at 180°C, the laminate cooling from the curing to the ambient temperature results in two reflected peaks proving that accidental birefringence effect

takes place, due to the shear strain within the optical fibre cross-section. The directions of principal strain and principal refraction indices are along the width and the thickness of the laminate.

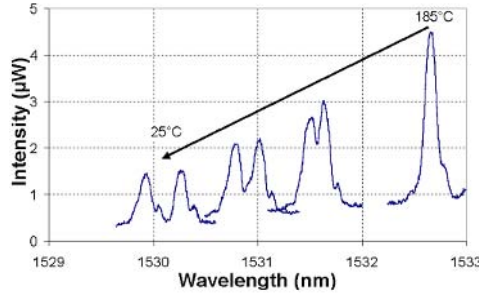


FIGURE 1. accidental birefringence effect during the cooling phase.

The horizontal displacement of each peak is a linear function of both the temperature and the stress within the fibre. It is easy to show that the difference leads to maximum shear strain within the fibre cross-section:

$$\frac{\Delta\lambda_{B,p}}{\lambda_B} - \frac{\Delta\lambda_{B,q}}{\lambda_B} = \frac{n_e^2}{2} (p_{12} - p_{11})(\varepsilon_2 - \varepsilon_3)$$

The relative displacement is due to the fact that  $\varepsilon_2$  is different from  $\varepsilon_3$ , direction 1 is the fibre direction, 2 and 3 two orthogonal axes in the cross-section along width and thickness respectively,  $p_{11}$  and  $p_{12}$  are photoelastic constants. Then, in the final part the mechanical analysis of the problem is performed. The problem of the determination of the principal strains along axes 1, 2 and 3 is considered. A two-step approach is necessary, firstly, the mechanical modelling of the local stresses and strains due the OFBG when the medium is subjected to a given state of stress far from the fibre (i.e. at three times the fibre radius), secondly, the modelling of the relationship between the strains and the displacements of the two reflected Bragg peaks.

First step is solved analytically by using the solution of Lekhnitskii [2], assuming the fibre cross-section to an inclusion surrounded by unidirectional composite. Second step is simply based on the photomechanical relationship between peak displacement and strains. Finally, a set of two equations is finally obtained for three unknowns. Assuming that a laminate ply is mainly in plane stress, the normal stress in the out-of-plane direction is set to 0; therefore the system can be solved, leading to the residual laminate strains  $\varepsilon_2$  and  $\varepsilon_3$ .

Comparison is done with approximations given by the Classical Laminated Plate Theory is showed that the experimental approach is consistent. Possible improvements are discussed to move towards a routine technique.

**References**

1. S. Vacher, J. Molimard, H. Gagnaire, A. Vautrin, ‘Monitoring of the RFI Process by Fibre Bragg Gratings, Euromech 453, December, 1 – 3 2003, Saint-Étienne, France.
2. S. Lekhnitskii, ‘Theory of Elasticity of an Anisotropic Body’, Moscow, MIR Publishers, 1977.



## EXTENSION OF THE GRID METHOD TO LARGE DISPLACEMENTS

J. Molimard<sup>1</sup>, K. Zhani<sup>1,2</sup>, C. Desrayaud<sup>1</sup> and M. Darrieulat<sup>1</sup>

<sup>1</sup> Centre de Sciences des Matériaux des Structures,  
ENSM-SE, 158 Cours Fauriel, 42023 Saint Etienne, France

<sup>2</sup> Laboratoire de Mécanique des Matériaux Hétérogènes,  
Faculté des Sciences et Techniques de Tanger, BP 416, Maroco  
molimard@emse.fr, k\_zhani@hotmail.com, cdesray@emse.fr, darrieulat@emse.fr

The Grid Method is used from the beginning of the nineties. This method is based on the well-known Moiré effect: the surface is encoded with a periodic pattern. The variations of this pattern are analysed through a phase either using global Fast Fourier Transform, or a local approach, for example with wavelet transform. This method is efficient for small displacements: typically, its resolution is 1/100 of the grid step i.e. 5/100 pixels. The classical phase subtraction is performed at the same geometrical point, which means that a small displacement assumption is necessary. If large displacements are achieved, the image correlation technique is of great interest because it provides a result in the initial frame of reference. For small displacements, the technique becomes difficult to implement, and sub-pixel interpolation with larger correlation windows have to be used. More generally, the typical spatial resolution for image correlation (8 to 64 pixels) appears to be larger than the spatial resolution for grid method (from 4 to 17 pixels). Thus, this latter could in principle retrieve more localized phenomena. Even if basically, these two methods use different patterns (periodic or random), it is possible to decode the information with either of the numerical strategies: wavelet transform on a random pattern [1]; image correlation on periodic pattern [2]. In this second case, many different maxima appear in the correlation map, and the selection of the right one is made by the user himself, considering external knowledge. Nevertheless, this solution is widely spread among the metallurgists community at a microscopic scale. In this particular case, the surface is marked with a periodic pattern for very practical reasons. Then, the situation is the following: displacements are large, but the pattern is periodic. Instead of using the image correlation technique, we propose here to extend the use of the grid method to large displacements. The expected result is firstly an easier way to extract the information and secondly results of better metrological qualities.

The adopted strategy consists in an iterative algorithm: in a first step, the small displacements assumption is kept. It leads to an approximation of displacements in the deformed frame of reference. Displacements are estimated in the initial frame of reference, then the initial image is numerically deformed with the estimated displacement. In the second step, the difference between this first estimation and the mechanical deformation is calculated. This displacement, expressed in the initial frame of reference can be added to the first one, and the initial image is numerically deformed once again. The process ends when the numerical and the mechanical transformations are close enough, i.e. when the remaining displacement is within the noise level. A complete metrological study will be described. In particular, resolution and spatial resolution will be addressed. The reader should retain that these properties are directly given by the last iteration.

Lastly, the method has been applied to single crystals of aluminium compressed in channel-die [4] at room temperature. The channel-die ensures plane strain compression, in conditions close to the transformation undergone by metals in the rolled sheets. All the more, it has vertical walls against which the lateral faces of the test-piece remain plane, which facilitates all sorts of observations. One lateral side of the test-piece (Al-Mn Goss oriented crystal) has been covered with a pre-inked grid with steps of 100  $\mu\text{m}$ . Initially, it was 10.44 mm high, 8.21 mm long and 7

mm thick. It has been investigated with a total field view of  $11 \times 10 \text{ mm}^2$  ( $773 \times 695 \text{ pixels}^2$ ). The test-piece, whose width is constant, was deformed by steps of  $E = \ln(h_0/h) = 0.15$  in which  $h_0$  is the initial height and  $h$  the current one. This allows taking photographs of the sample when it is taken out of the channel-die. Displacements results can be presented without any filtering process. In this case, the resolution is at its worst:  $1 \text{ }\mu\text{m}$  ( $0.07 \text{ pixels}$ ) and the mean spatial resolution is at its best:  $195 \text{ }\mu\text{m}$  ( $13.7 \text{ pixels}$ ). But in order to obtain Green-Lagrange strains, it is better to use a low-pass filter before deriving with a least-square approach. Thus, it has been possible to calculate the resolution ( $0,8 \%$  or  $0.07 \text{ pixels}$ ) and the spatial resolution ( $457 \text{ }\mu\text{m}$  i.e.  $32 \text{ pixels}$ ) on strain. Figure 1 shows the strains undergone during the first step of deformation. The compression is far from homogeneous at the mesoscopic scale, even at this early stage. The map of the compressive component  $\varepsilon_{yy}$  shows the classical strain cross, the map of the shear strain  $\varepsilon_{xy}$  shows two shear bands initiating at the corners of the sample with a characteristic slant of about  $35^\circ$ . Such features become clearly visible at higher deformation. One result of the present analysis is that it shows that the heterogeneities are present from the very start.

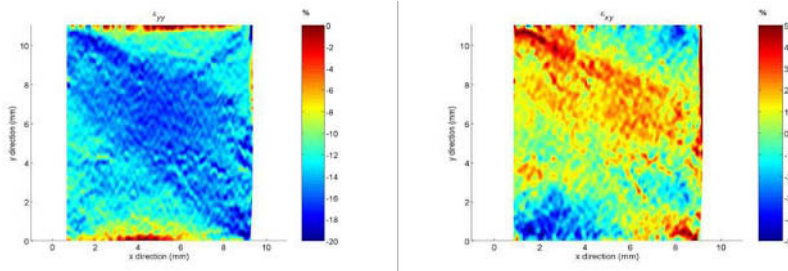


FIGURE 1.  $\varepsilon_{yy}$  and  $\varepsilon_{xy}$  for a 15 % compression test

## References

1. Molimard, J., Vautrin, A., in *Proceedings of the CMOI/MTOI Conference, Nov. 2005, Marseille, France*, edited by P. Smigielski, 2005, 89-90.
2. Doumalin, P., Bornert, M., in *Proceedings of Interferometry in Speckle Light, Theory and Applications*, edited by P. Jacquot and J.M. Fournier, Springer, Lausanne, 2000, 67-74.
3. Molimard, J., Vautrin, A., in *Proceedings of the CMOI/MTOI Conference, Nov. 2005, Marseille, France*, edited by P. Smigielski, 2005, 2-3.
4. Maurice C., Piot D., Klöcker H., Driver J., *Metall. Mater. Trans. A*, 2005, 1039-1047.

## TIME-DEPENDENT BEHAVIOR OF ROPES UNDER IMPACT LOADING

A. Nikonov, M. Udov, B. Zupani, U. Florjani, B.S. von Bernstorff<sup>1</sup> and I. Emri  
Center for Experimental Mechanics, University of Ljubljana,  
Cesta na Brdo 85, Ljubljana, Slovenia, igor.emri@fs.uni-lj.si

<sup>1</sup>BASF Aktiengesellschaft, Ludwigshafen, Germany

Climbing ropes are designed to secure a climber. They are designed to stretch under high load so as to absorb the shock force. This protects the climber by reducing fall forces. Ropes should have good mechanical properties, such as high breaking strength, large elongation at rupture and good elastic recovery [1].

The UIAA (Union Internationale des Associations d'Alpinisme) has established standard testing procedures to measure, among other things, how a rope reacts to severe falls [2]. Ropes are drop tested with a standardized weight and procedure simulating a climber fall. This tells us how many of these hypothetical falls the rope can withstand before it ruptures. Virtually all the ropes on the market can withstand the minimum number of test falls, while some are rated to a much higher number. The second thing the standard drop test measures is the amount of force which is transmitted to the falling climber.

The standard says little about the durability of the rope, which is more difficult to define or assess with a simplified procedures. Ropes are produced from polyamide fibers, which exhibit viscoelastic behavior. Thus durability in this case does not mean just failure of the rope, but rather deterioration of its time-dependent response when exposed to an impact force. The experiments prescribed by the UIAA standard are not geared to analyze the time-dependent deformation process of the rope, which causes structural changes in the material and consequently affects its durability. Time-dependent response of the rope also governs the evolution of all physical quantities that are responsible for the safety of a climber, e.g., first derivative of climber (de)acceleration.

We developed an experimental-analytical methodology, based on a simple non-standard falling weight experiment, which allows examination of the time-dependent elasto-visco-plastic behavior of ropes exposed to arbitrary falling weight loading conditions. Namely, we solve equation of motion by numerical integration of time-dependent force signal. Doing that from a single response of the rope, which is exposed to impact loading, we can calculate important mechanical properties of ropes, such as maximum impact force; maximum deformation (elongation); elastic, viscoelastic, viscoplastic, and plastic parts of rope deformation; stored, retrieved, and dissipated energy; stiffness of the rope; derivative of the (de)acceleration; force impulse. To estimate the accuracy of the calculated properties we perform the parametric error analysis for all calculated mechanical properties.

Three different commercial manufacturers were selected for comparative analysis of the mechanical behavior of climbing ropes, which were denoted as A, B, and C. The ropes were exposed to the same loading conditions. The lengths of all tested ropes were 4 m, mass of the weight was 40 kg. Time interval between two neighboring falls was 5 minutes. Calculated mechanical properties of all three types of ropes were then compared using the methodology presented above.

The impact force and maximum deformation of all three ropes are shown in Fig. 1.

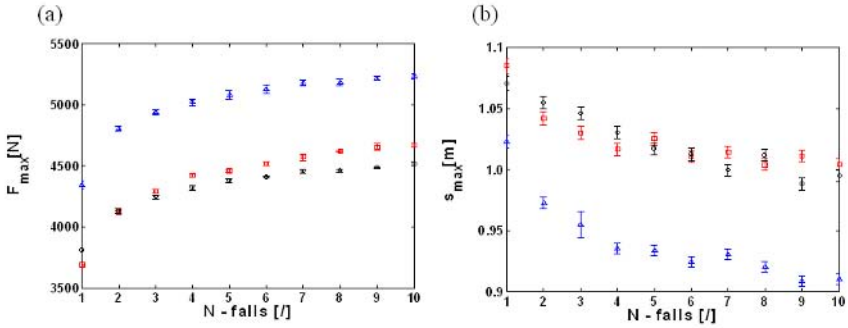


FIGURE 1. Impact force (a) and maximum deformation of the rope (b) as functions of number of loadings:  $\square$  - rope A,  $\triangle$  - rope B,  $\circ$  - rope C.

The obtained results indicate that ropes behave differently under the same loading conditions. The impact force increases with each following loading of the rope. However, deformation of the rope decreases with each following loading. Similarly, the first derivative of (de)acceleration, stiffness of the rope, stored, dissipated and retrieved energy, as functions of number of loadings were analyzed.

This work provides a foundation for the development of new methodology for testing and analyzing time-dependent mechanical properties of climbing ropes. This knowledge could be used in development of the new generation of ropes with pre-determined (mechanical) properties.

## References

1. Jenkins, M., *Materials in Sports Equipment*, Woodhead Publ. Ltd., Cambridge, 2003.
2. <http://www.uiaa.ch/web.test/visual/Safety/UIAA101DynamicRopes07-2004.pdf>

## MATERIAL PROPERTIES OF MIXTURES

Samo Kralj

Faculty of Natural Sciences and Mathematics, University of Maribor, Slovenia

and Jožef Stefan Institute, Ljubljana, Slovenia

Address: Faculty of Natural Sciences and Mathematics, Koroška 160, 2000 Maribor, Slovenia

samo.kralj@uni-mb.si

In recent years we face an increasing interest in material properties of mixtures. Of particular interest are mixtures displaying behaviour that neither of the pure constituents exhibit. In some cases such behaviour hinges on simple physical concepts, giving rise to universal macroscopic responses (i.e. independent of microscopic details).

In this contribution we consider a chemical inert mixture in which one component (A) exhibits a continuous symmetry breaking phase transition at  $T=T_c$  on lowering the temperature  $T$ . The phase transition can be either of the 1<sup>st</sup> or 2<sup>nd</sup> order. The resulting low temperature phase is described in terms of the hydrodynamic order parameter and Goldstone (also called Gauge) continuum field. The other component (B) exhibits non-critical behaviour and is coupled to the first one only via a short range interaction at the A-B interface. The interaction couples both to the order parameter and the Goldstone field, giving rise to the so called wetting and anchoring (or pinning) phenomena, respectively [1]. We will demonstrate the following phenomena. (i) B-induced distortions in the Goldstone field can strongly depress  $T_c$ . (ii) For strong enough wetting potential or B-induced disorder the critical behaviour of A can be replaced by a non-critical gradual evolution of ordering on varying  $T$ . (iii) The coupling between A and B can give rise to an additional structural transition (Griffiths-like phase). (iv) In some cases the coupling between A and B triggers glassy behaviour. (v) Surface interaction often dominate the phase behaviour, randomness the domain structure, and finite size effects the specific heat singularity (in case of 2<sup>nd</sup> order phase transition) of A. (vi) If B also exhibits critical behaviour, then the specific coupling interaction term can give rise to the master-slave type behaviour. We show that this mechanism can be used to achieve A-driven and controlled patterning of the B component. In particular, the last phenomenon can be used for the controlled assembling of nano-particles.

To demonstrate these universal phenomena we chose various liquid crystal (LC) phases [1] as the component A. As the component B we use either nano-particles [2], Controlled porous glass [3] or aerogel porous matrices [4]. We chose LCs because of their i) experimental accessibility and relatively easy preparation of samples, and because ii) they possess various phases&structures exhibiting almost all physical phenomena. Consequently, they represent an ideal testing ground not only for condensed matter, but even for cosmology and particle physics [5]. We focus mainly on the isotropic-nematic ( $I-N$ ) and nematic-smectic A ( $N-SmA$ ) LC phase transitions. We chose these transitions, because they exhibit 1<sup>st</sup> ( $I-N$ ) and 2<sup>nd</sup> ( $N-SmA$ ) critical behaviour, and continuous symmetry breaking in the orientational ( $I-N$ ) and translational ( $N-SmA$ ) ordering. We have used different candidates for the component B in order to distinguish among surface wetting, surface anchoring, randomness and finite size effects.

As experimental tools we use x-ray scattering [6], dielectric [7], NMR [5], and high precision calorimetry [2,3]. To explain the observed phenomena we use Landau-Ginzburg and Landau-de Gennes type phenomenological approaches [1]. The orientational ordering is described in terms of the nematic tensor order parameter  $Q$  and the smectic layers with the smectic translation complex order parameter  $\psi$ . We consider simplest symmetry allowed interface coupling terms, that can trigger qualitative changes in systems of interest as control parameters (i.e. temperature, a typical

geometrical length scale, surface interaction strength) are varied. The phase behaviour is calculated via minimization of the resulting free energy  $F$ , expressed in terms of the continuum fields. In order to give insight into some phenomenological terms in  $F$  we use a simple semi-microscopic approach.

Our results show that all chosen candidates for B [2-4] depress the transition temperatures of the  $I-N$  and  $N-SmA$  phase transition. For large enough surface to volume ratio of the LC component phase the  $I-N$  and  $N-SmA$  transitions cease to exist [6,7] and are replaced by gradual evolution of ordering. In some cases the  $I-N$  transition exhibits double peak specific heat appearance, that might signal the onset of intermediate Griffiths-like phase [8]. In systems exhibiting large enough geometrically induced disorder hysteresis phenomena [4] and non-Arrhenius type relaxation [7] is observed, suggesting glassy behaviour. The specific heat jump at the 2<sup>nd</sup> order  $N-SmA$  phase transition in almost all samples obeys finite size scaling hypothesis [3] with respect to the characteristic geometric length of the system. We further show, that a mixture of LC and anisotropic nano-particles exhibits slave-master behaviour regarding phase transition behaviour (i.e. one component strongly influences another, while the reverse influence is negligible). This phenomenon could be used for future all-carbon nano-tube based microelectronics. Namely, a LC phase&structure can serve as a structural driving force to construct different patterns in nano-tube arrangements. Afterwards the liquid LC phase could be removed (e.g. via soaking), leaving behind a pure nano-tube pattern.

## References

1. de Gennes, P.G. and Prost, J., *The Physics of Liquid Crystals*, Oxford University Press, Oxford, 1993.
2. Cordoyiannis, G., Kralj, S., Nounesis, G., Žumer, S. and Kutnjak, Z., *Phys. Rev. E*, vol. **73**, 031707-1-4, 2006.
3. Kutnjak, Z., Kralj, S., Lahajnar, G. and Žumer, S., *Phys. Rev. E*, vol. **70**, 51703-1-11, 2004.
4. Kralj, S., Zidanšek, A., Lahajnar, G., Muševič, I., Žumer, S., Blinc, R. and Pintar, M.M., *Phys. Rev. E*, vol. **53**, 3629-3638, 1996.
5. Digal, S., Ray, R. and Srivastava, A.M., *Phys. Rev. Lett.*, vol. **83**, 5030-5033, 2002.
6. Kralj, S., Zidanšek, A., Lahajnar, G., Žumer, S. and Blinc, R., *Phys. Rev. E*, vol. **62**, 718-725, 2000.
7. Kutnjak, Z., Kralj, S. and Žumer, S., *Phys. Rev. E*, vol. **66**, 041702-1-8, 2002.
8. Mercury, F., Paoloni, S., Zammit, U. and Marinelli, M., *Phys. Rev. Lett.*, vol. **94**, 247801-1-4, 2005.

**COLLOIDAL EMULSIONS**

Gennady Maksimochkin<sup>1</sup>, Sergey Pasechnik<sup>1</sup>, Mitja Slavinec<sup>2</sup>, Milan Svetec<sup>2</sup> and Samo Kralj<sup>2</sup>

<sup>1</sup> Moscow State University of Instrument Engineering and Computer Sciences, Moscow, Russia

<sup>2</sup> Faculty of Natural Sciences and Mathematics, University of Maribor, Slovenia  
Faculty of Natural Sciences and Mathematics, Koroška 160, 2000 Maribor, Slovenia  
mitja.slavinec@uni-mb.si

Colloidal emulsions are dispersions of liquid droplets [1]. They can be used for detailed studies of fundamental processes of broad relevance, such as crystallization and glass formation. In addition they are also of great technological importance. They are essential ingredient of several applications, ranging from paints to drugs. In case of attractive interactions among the particles phase separation can take place. To prevent it, attractive interactions have to be counterbalanced.

Most studies so far studies cases of liquid-liquid dispersions. However, recently focus has shifted to cases, where various liquid crystal (LC) phases [2] are also included. These phases are typical representatives of soft matter systems, i.e. are extremely susceptible to perturbations. In addition they are characterized by orientational and/or translational long or quasi long range order. The LC phases are obtained via symmetry breaking phase transitions. Consequently a structure within a given phase is characterised by the so called Gauge field. The interaction of this field with the other phase in the liquid-LC mixture can give rise to delicate long-range interactions within the system [3].

In our contribution we consider acoustic properties of emulsions consisting of (i) liquid crystal droplets in isotropic fluid and (ii) isotropic droplets in LC matrix. The LC matrix [3] exhibits in addition to liquid behavior also orientational anisotropy below the clearing point  $T_c$ . Above it LC enters an ordinary liquid (the so called isotropic) phase. We focused on temperature intervals where the LC phase was either isotropic (I) or nematic (N). The latter is characterized by orientational long range order. We study these systems by means of an ultrasound absorption coefficient ( $\alpha$ ) and sound velocity measurements. We demonstrate that this method is useful for the study of critical properties of the LC component [4]. The emulsions were prepared using intensive ultrasound.

In the case (i) we used the nematic mixture H96 as LC and water as isotropic fluid. In the pure H96 the isotropic-nematic phase transition takes place at  $T_c=345.3$  K. This LC was chosen because its acoustic impedance is comparable to that of water. Consequently, the scattering of acoustic waves is relatively small. N96 has wide temperature stability of the nematic phase and is chemically stable when contacted with water. It is also stable in acoustic fields that we used in experiments. In addition densities of N96 and water are comparable, what enables stability of the system.

We prepared two different samples. In the first one the main diameter  $d$  was picked at  $d=0.8$   $\mu\text{m}$  and in the other one at  $d=4.6$   $\mu\text{m}$ . We henceforth refer to these cases as the submicrometer and supramicrometer sample, respectively. The distribution of diameters was probed using microphotometrical technique and photocorrelation spectroscopy. We observed the critical increasing of  $\alpha$  in the vicinity of a clearing point  $T_c$  in both samples. Substantial deviations from the bulk behaviour were observed only in the submicrometer sample. We observed the increasing depression of phase transition temperatures  $T_c$  with decreasing  $d$ . We further observed that dispersions with large enough ( $d > \mu\text{m}$ ) LC droplets were relatively more stable with respect to samples with submicron sized droplets.

We also studied (ii) emulsions with small droplets of isotropic liquids (silicon oil) in liquid crystal matrix. For LC we used the nematic mixture ZhK440 (97.3 %) and the polymethylsiloxane silicone oil (2.7 %). Acoustic response was studied at the frequency 0.7 MHz. The structure of the system was monitored using polarized microscope connected with CCD camera. The emulsion was studied across the isotropic-nematic LC transition. The silicon oil droplet sizes were picked at around  $d=4 \mu\text{m}$ . We found that critical properties were different in emulsions in comparison to the pure LC sample. Also in this sample we observed the depression of the I-N phase transition temperature.

In order to explain the observed results we used simple Landau-de Gennes phenomenological approach [2]. We take into account the bulk condensation, elastic and LC-isotropic fluid interface wetting and anchoring free energy contribution [5,6]. In it the nematic orientational ordering was described with the uniaxial order parameter, describing the degree of nematic ordering, and the nematic director field, that gives the information on local symmetry breaking direction. In order to estimate the regime where dispersions are stable we used Flory-Huggins approach [7]. We derive the expression for the depression of the clearing point  $T_c$  for the samples i) and ii). We further show that the stability of dispersions of supramicron sized LC droplets can be explained using topological arguments.

## References

1. Poon, W., Pusey, P., and Lekkerkerker, H., *Physics World*, April, 27, 1996.
2. de Gennes, P.G. and Prost, J., *The Physics of Liquid Crystals*, Oxford University Press, Oxford, 1993.
3. Poulin, P., Stark, H., Lubensky, T.C., Weitz, D.A., *Science*, vol. **275**, 1770-1773, 1997.
4. Maksimochkin, G.I., and Pasechnik, S.V., *Proc. 13<sup>th</sup> Session. Russian Acoust. Soc.*, Moscow vol. **1**, 178-181, 2003.
5. Kralj, S., and Žumer, S., *Phys. Rev. A*, vol. **45**, 2461-2470, 1992.
6. Kralj, S., Žumer, S., and Allender, D.W., *Phys. Rev. A*, vol. **43**, 2943-2952, 1991.
7. Popa-Nita, V., and Kralj, S., *Phys. Rev. E*, vol. **73**, 041705-1-8, 2006.



## AN AUTOMATED PHASE UNWRAPPING ALGORITHM FOR ISOCLINIC PARAMETER IN PHASE-SHIFTING PHOTOELASTICITY

Pichet Pinit and Eisaku Umezaki

Graduate Student, Nippon Institute of Technology

4-1 Gakuendai, Miyashiro, Saitama 345-8501, Japan

Department of Mechanical Engineering, Nippon Institute of Technology

4-1 Gakuendai, Miyashiro, Saitama 345-8501, Japan

ipichet@yahoo.com, umezaki@nit.ac.jp

This paper presents an automated phase unwrapping algorithm for unwrapping the isoclinic parameter in the true phase interval  $(-\pi)/2$  to  $\pi/2$ . This unwrapping algorithm is combined with the four-step colour phase shifting technique. A dark-field plane polariscope system coupled with a white light source is used for recording photoelastic fringes. The phase unwrapping is designed incorporating the existence of the isotropic point.

When the specimen is properly place in the dark-field plane polariscope and then loaded by a force, the general equation of the irradiance  $I$  with generic orientations  $m$  of the transmission axes of the Polaroid's in a crossed fashion coming out of a digital camera is given by Ramesh [1],

$$I_{m,i} = I_{\text{mod},i} \sin^2 2(\theta - \beta_m) + I_{b,i} \quad (1)$$

where  $I_{\text{mod},i} = \frac{1}{\Delta\lambda_i} \int_{\lambda_1}^{\lambda_2} F_i I_{p,i} \sin^2(\delta_i/2) d\lambda_i$  (the modulated irradiance),  $i$  denotes the primary wavelengths R, G, and B of the white light.  $\lambda_1$  and  $\lambda_2$  are the lower and upper limits of the spectrum acquired by the associated filter of the camera,  $F_i$  is the spectral response of the camera filters,  $I_{p,i}$  is the irradiance coming out of the polarizer,  $\delta_i$  is the fractional retardation,  $\theta$  is the isoclinic angle,  $\beta_m$  is the induced phase shift angle and  $I_{b,i}$  is the background irradiance.

Making elaborate manipulation to Eq. 1 with the trigonometric identity  $\sin^2(\alpha/2) = (1 - \cos \alpha)/2$  and applying the four-step phase shifting method such that the induced phase shift angle  $\beta_1=0$ ,  $\beta_2=+\pi/8$ ,  $\beta_3=+\pi/4$  and  $\beta_4=+3\pi/8$ , yield the equation for determining the isoclinic parameter as

$$\theta_w = \pi/8 - 0.25 \arctan \left( (I_1^s - I_3^s / I_2^s - I_4^s) \right), \quad \theta_w \in (-\pi/4, +\pi/4] \quad (2)$$

where  $w$  denotes that  $\theta$  is wrapped value,  $(-\pi/4, +\pi/4]$  represents  $-\pi/4 < \theta_w \leq +\pi/4$  and

$$I_m^s = I_R^s + I_G^s + I_B^s \quad (3)$$

Before using Eq. 2, the summed value in Eq. 3 should be normalized by a factor such that the summation does not exceed the maximum grey level used as done by Pinit and Umezaki [2]. Further, the modulated irradiance as shown in Eq. 4 is used in the unwrapping algorithm as a quality index of the pixel.

$$I_{\text{mod}}^s = \sqrt{(I_1^s - I_3^s)^2 + (I_2^s - I_4^s)^2} \quad (4)$$

The unwrapping starts by expanding the wrapped phase interval obtained from Eq. 2 to others wrapped phase intervals. Next, define the binary image representing the valid region of the unwrapped phase by an intersection between those expanded phase intervals. Create another binary image using to represent the location of the isotropic point found by a detecting algorithm.

The region around the isotropic point is expanded with a certain size of a mask kernel. Then, perform the intersection between these two binary images to get the first valid region of the unwrapped phase. Applying the connected component labelling algorithm to the resultant binary image yields the largest valid region of the unwrapped phase and it is used as the starting region.

First, to validate the performance of the algorithm, it is applied to unwrap the simulated wrapped phase data of the circular disk under compressive load and the result is shown in Fig. 1(a). It is obviously seen that the algorithm provides good continuous unwrapped phase map of the isoclinic parameter in the true phase interval. In case of experimental phase map, it is shown in Fig. 1(b) and the algorithm provides satisfactory phase map and this is because of the effect of the isochromatic parameter. Figure 2 shows the continuous phase map of the circular disk under three radial loads. It is clearly seen that there is the isotropic point locating near the center of the model. It can be safely conclude that the proposed algorithm has ability for unwrapping the wrapped phase data with or without the isotropic point.

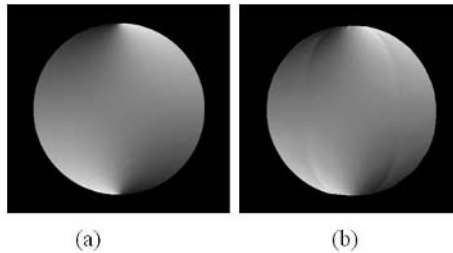


FIGURE 1. Continuous unwrapped phase map of the circular disk under compression: (a) simulated result and (b) experimental result.

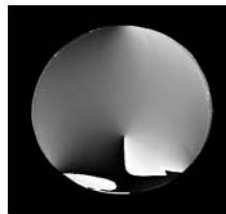


FIGURE 2. Continuous unwrapped phase map of the circular disk under three radial loads.

## References

1. Ramesh, K., *Digital Photoelasticity: Advanced Techniques and Applications*, Springer, Berlin, Germany, 2000.
2. Pinit, P., Umezaki, E., *Opt. Rev.*, vol. **12**, 228-232, 2005

## PHASE UNWRAPPING FOR ABSOLUTE FRINGE ORDER IN PHOTOELASTICITY

Pichet Pinit<sup>1</sup>, Yudai Nomura<sup>2</sup> and Eisaku Umezaki<sup>3</sup>

<sup>1,2</sup>Graduate Student, Nippon Institute of Technology  
4-1 Gakuendai, Miyashiro, Saitama 345-8501, Japan

<sup>3</sup>Department of Mechanical Engineering, Nippon Institute of Technology  
4-1 Gakuendai, Miyashiro, Saitama 345-8501, Japan

<sup>1</sup>ipichet@yahoo.com, umezaki@nit.ac.jp

A phase unwrapping (PU) algorithm for processing fractional fringes photoelastically obtained using an arccosine operator is presented. The PU algorithm works with three primary wavelengths RGB of white light source. The three fractional fringe values at a point are used to generate a plane. One point in the fringe fields is automatically chosen to be the seed point. A set of selected fringe values from fringe candidates is chosen and adjusted with certain conditions. The circular disk under compression demonstrates the performance of the proposed PU algorithm.

Intensity equations of the dark- and bright-field plane polariscope coming out of a colour digital camera are given by [1],

$$I_{m,i} = I_{\text{mod},i} \sin^2 2(\theta - \beta_m) + I_{b,i} \quad (1)$$

$$I'_{m,i} = F_i I_{p,i} - I_{\text{mod},i} \sin^2 2(\theta - \beta_m) + I_{b,i} \quad (2)$$

where  $I_{\text{mod},i} = \frac{1}{\Delta\lambda_i} \int_{\lambda_1}^{\lambda_2} F_i I_{p,i} \sin^2(\delta_i/2) d\lambda_i$  (the modulated irradiance),  $i$  denotes the primary wavelengths R, G, and B of the white light.  $\lambda_1$  and  $\lambda_2$  are the lower and upper limits of the spectrum acquired by the associated filter of the camera,  $F_i$  is the spectral response of the camera filters,  $I_{p,i}$  is the irradiance coming out of the polarizer,  $\delta_i$  is the fractional retardation,  $\theta$  is the isoclinic angle,  $\beta_m$  is the induced phase shift angle and  $I_{b,i}$  is the background irradiance.

Making elaborate manipulation to Eqs. 1 and 2 with the trigonometric identity  $\sin^2(\alpha/2) = (1 - \cos \alpha)/2$  and applying the four-step phase shifting method such that the induced phase shift angle  $\beta_1=0$ ,  $\beta_2=+\pi/8$ ,  $\beta_3=+\pi/4$  and  $\beta_4=+3\pi/8$ , yield the equation for determining the fractional fringe as

$$N_i^f = \frac{1}{2\pi} \arccos \left( 1 - \frac{2I_{\text{mod},i}}{F_i I_{p,i}} \right), \quad 0.0 \leq N_i^f \leq 0.5 \quad (3)$$

where  $F_i I_{p,i} = I_{1,i} + I'_{1,i} - 2I_{b,i}$ ,  $I_{\text{mod},i} = \{ [I_{1,i} - I_{3,i}]^2 + [I_{2,i} - I_{4,i}]^2 \}^{1/2}$ ,  $I_{b,i} = I_{B,i} - (1/2)I_{\text{mod},i}$  and  $I_{B,i} = (1/4)\{I_{1,i} + I_{2,i} + I_{3,i} + I_{4,i}\}$ . Then, for the absolute fringe order, we can write

$$N_i^u = N_{\text{int}} \pm N_i^f \quad (4)$$

where  $N_i^u$  is the absolute fringe order.

The unwrapping starts by finding the seed point with conditions:  $N_R^f < N_G^f < N_B^f$  and  $r^2 \leq r_{pre}^2$  where  $r_{pre}^2$  and  $r^2$  are the coefficient determinations of linear regression set by the user and determined by the fitted straight line through  $N_R^f$ ,  $N_G^f$ ,  $N_B^f$  and zero value. Then, recalculate the

absolute fringe orders from the fitted line and use them to generate the plane. After that, adjust this plane to be parallel to the reference plane generated from theoretical value of the absolute fringe order using the orthogonal projection.

The seed point (also plane) is used as a central pixel of 8-neighbor window to unwrap all wrapped pixel in this window. The absolute fringe candidates are generated using Eq. 4. One combination of the fringe candidates that satisfies  $N_R^u < N_G^u < N_B^u$  and provides minimum error  $\varepsilon = \left| N_R^u f_{\sigma,R} - N_G^u f_{\sigma,G} \right| + \left| N_G^u f_{\sigma,G} - N_B^u f_{\sigma,B} \right| + \left| N_B^u f_{\sigma,B} - N_R^u f_{\sigma,R} \right|$  is, then, selected. Use these selected fringe values to generate their plane and adjust this plane to be parallel to the plane at the central pixel and then, reassign for that pixel the absolute fringe orders from the adjusted plane.

To examine the performance of the PU algorithm, it was applied to unwrap the simulated wrapped phase data of the circular disk subjected to a diametrically compressive load. The colour fractional fringes ( $N_R^f$ ,  $N_G^f$  and  $N_B^f$ ) obtained from Eq. 3 is shown in Fig. 1(a). Figure 1(b) shows the colour absolute fringe order map ( $N_R^u$ ,  $N_G^u$  and  $N_B^u$ ) with  $N_B^u \approx 14.0$  fringe. The absolute fringe order values at the disk centre are nearly equal to the theoretical values [2] ( $N_R^u = 2.0766$ ,  $N_G^u = 2.3234$  and  $N_B^u = 2.9083$  fringe)

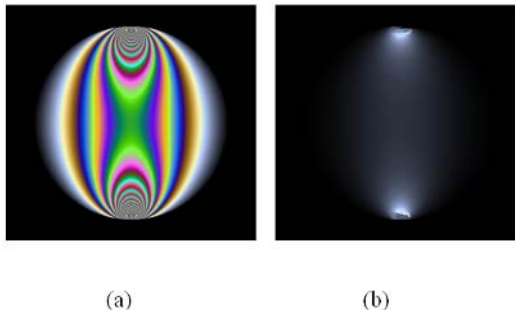


FIGURE 1. (a) colour fractional fringe phase map (b) colour absolute fringe order map with ( $N_G^u$ ).

## References

1. Ramesh, K., *Digital Photoelasticity: Advanced Techniques and Applications*, Springer, Berlin, Germany, 2000.
2. Forcht, M.M., *Photoelasticity*, Vol. 2, John Wiley & Sons, New York, 1967.

## A NEW AUTOMATED MEASURING INSTRUMENT FOR MINUTE PHOTOELASTICITY

Kenji Gomi, Kensuke Ichinose and Yasushi Niitsu  
 Department of Mechanical Engineering, Tokyo Denki University,  
 2-2 Kanda Nishiki-cho, Chiyoda-ku, Tokyo, Japan, 101-8457  
 kenji@cck.dendai.ac.jp

This paper introduces the principles and execution of a new technique for minute birefringence measurements based on simple polarimetry. The technique requires only three stepped photoelastic images although conventional phase-stepping methods require four images, Hobbs *et al.* [1]. Fig. 1 is the schematic drawing and photograph of the instrument based on the new technique. This instrument enables the simultaneous measurement of the optical retardation and the angular orientation of birefringence without any rotating optical element using simple polarimetry.

To verify the new technique experimentally, a precise crystal wave plate of having  $10.0 \pm 4.7$  nanometers in retardation was used as a specimen. The measurements of the retardation with standard deviation were found to be  $10.1 \pm 0.467$  nanometers, which agreed well and narrowed the deviation in spite of low-level amount of retardation. To estimate the measurements accuracy of the angular orientation of the birefringence, the angular position of the rotation stage for the specimen was rotated intermittently  $10.0$  degrees at a time during the experiment. As a result, the measured offsets of the angular orientation were found to be  $10.0 \pm 0.792$  degrees with standard deviation as shown in Table 1. It is concluded that the new technique is effective for minute birefringence measurements.

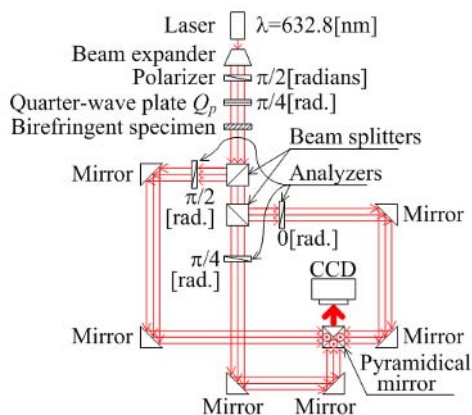


FIGURE 1. The design specification of the automated birefringence-measuring instrument.

Table 1 The comparison of the precise estimation by the specimen provider by thickness, with the measured average retardation with standard deviation using the new technique based on a simple polarimetry. To measure the angular orientation of the birefringence of the specimen, the specimen was rotated intermittently 10 degrees at a time in the experimental sequence.

Estimation of retardation by the specimen provider using its thickness with tolerance, nm	79.1±3.5	10.0±4.7
Average of measured retardation with standard deviation before correction, nm	77.6± <u>3.24</u>	10.5± <u>2.62</u>
↓ (Decreasing rate of s.d.)	(19.4%) ↓	(57.6%) ↓
After correction, nm	77.5± <u>2.61</u>	10.3± <u>1.11</u>
Average offset of measured angles with standard deviation before correction, degree	10.1± <u>1.23</u>	10.1± <u>4.31</u>
↓ (Decreasing rate of s.d.)	(26.3%) ↓	(29.2%) ↓
After correction, degree	10.0± <u>0.906</u>	10.0± <u>3.05</u>
Number of the measurements	110	111

**References**

1. Hobbs, J. W. *et al.*, *Experimental Mechanics*, vol. 43(4), 403-409, 2003.

## EFFECT OF UV ILLUMINATION WAVELENGTHS ON STRESS AND TEMPERATURE IN CURING PROCESS OF UV CURING RESIN

Eisaku Umezaki and Masahito Abe

Department of Mechanical Engineering, Nippon Institute of Technology

4-1 Gakuendai, Miyashiro, Saitama 345-8501, Japan

Graduate Student, Nippon Institute of Technology

4-1 Gakuendai, Miyashiro, Saitama 345-8501, Japan

omezaki@nit.ac.jp, m1021107@mstu.nit.ac.jp

Stress and temperature in the curing process of UV curing resin illuminated at different UV wavelengths were measured using a system that can simultaneously measure stress and temperature in structures in time series. The system consists of a photoelastic apparatus for measuring stress (GFP2100), a thermographic apparatus (Radiance HS) and a beam splitter, which can reflect infrared light and transmit visible light [1].

The specimens consist of a glass bar, glass plates, a potassium bromide (KBr) plate, cellophane tapes and UV curing resin in liquid form. The KBr plate can transmit infrared light. The liquid resin was poured into a cavity (3 mm thick, 2 mm high and 76 mm wide). The specimens were placed on the stage such that the KBr plate would turn to the direction of the beam splitter, and then were illuminated at different wavelengths in the ranges of  $\lambda_{r1}=220\text{-}325$  nm and  $\lambda_{r2}=325\text{-}385$  nm with light intensity,  $E$ , of 8 W/cm<sup>2</sup> for 300 s. The light of these wavelength ranges was obtained from a mercury lamp combined with four kinds of filters. The photoelastic fringe images and thermal images were captured at intervals of 5 and 0.5 s, respectively. The isochromatic fringes and principal stress directions were obtained from the photoelastic fringe images.

Figures 1 and 2 show isochromatic fringes for UV illumination durations,  $t$ , of 10 and 30 s at  $\lambda_{r1}$  and  $\lambda_{r2}$ , as examples, respectively. Figure 3 shows temperature distributions with time at the center of the cavity at  $\lambda_{r1}$  and  $\lambda_{r2}$ , as examples. In Figs. 1 and 2, the shape of the UV curing resin in the specimen is denoted by broken lines.

The order of the isochromatics generated in the cured UV resin for  $t=10$  s at  $\lambda_{r1}$  shown in Fig. 1 was higher than that at  $\lambda_{r2}$  shown Fig. 2. However, the order for  $t=30$  s at  $\lambda_{r2}$  was approximately equal to that at  $\lambda_{r1}$ . The thermal images indicate that the curing of the resin started from the upper part of the resin and proceeded downward. The temperature generated in the curing UV resin at  $\lambda_{r2}$  was higher than that at  $\lambda_{r1}$  and indicated a more rapid variation than that at  $\lambda_{r1}$ .

The above results indicated that stress and temperature during the curing of the UV curing resin illuminated with the UV rays were affected by the UV wavelengths of the rays. It was inferred that this is due to the dependence on the amount of heat generated in the curing resin on the UV ray absorptivity of the initiator contained in the resin and the UV ray transmissivity of the resin.

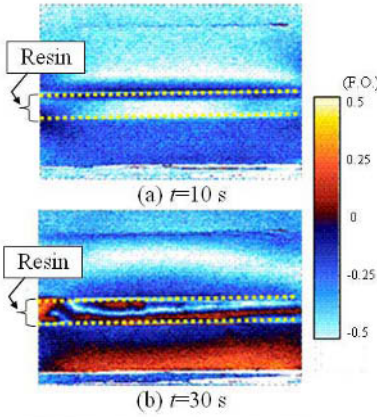


FIGURE 1. Isochromatic fringes for  $\lambda_1=230\text{-}325\text{ nm}$ .

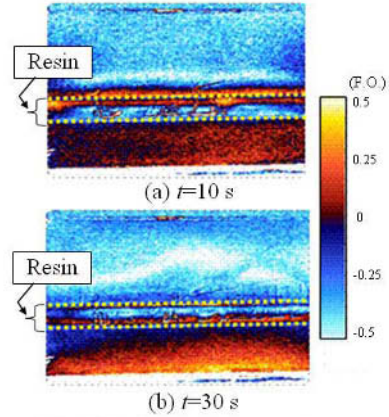
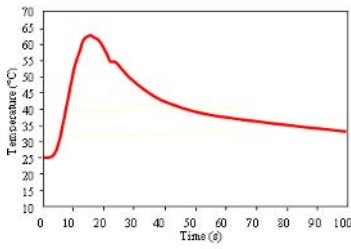
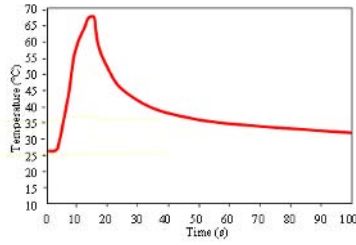


FIGURE 2. Isochromatic fringes for  $\lambda_2=325\text{-}385\text{ nm}$ .



(a)  $\lambda_1=230\text{-}325\text{ nm}$



(b)  $\lambda_2=325\text{-}385\text{ nm}$

FIGURE 3. Variation of temperature with time.

References

1. Umezaki, E. and Abe, M., *Key Engineering Materials*, vol. **326-328**, 163-166, 2006.



## MEASUREMENT OF STRESS AND TEMPERATURE IN CURING PROCESS OF EPOXY ADHESIVES

Eisaku Umezaki and Kazuya Iwanaga

Department of Mechanical Engineering, Nippon Institute of Technology

4-1 Gakuendai, Miyashiro, Saitama 345-8501, Japan

Undergraduate Student, Nippon Institute of Technology

4-1 Gakuendai, Miyashiro, Saitama 345-8501, Japan

omezaki@nit.ac.jp, m1031136@mstu.nit.ac.jp

This study deals with stress and temperature in the curing process of epoxy adhesives measured using a system that can simultaneously measure stress and temperature in structures in time series.

The system consists of a photoelastic apparatus for measuring stress (GFP2100), a thermographic apparatus (Radiance HS) and a beam splitter, which can reflect infrared light and transmit visible light [1]. The specimens consist of two epoxy resin plates (3 mm thick, 26 mm wide and 76 mm long) and adhesive. The adhesive was prepared by mixing epoxy as the base resin with polythiol as the hardener, then applied on an area of 26 mm x 26 mm of one end of one epoxy resin plate. Thereafter, one end of the other epoxy resin plate was overlapped over area of 26 mm x 26 mm in the opposite direction to the epoxy plate on which adhesive was applied. The thickness of the adhesive was about 1 mm. Immediately after the specimens, both ends of which were fixed between steel blocks, were put on the stage, the photoelastic fringe and thermal images were captured at intervals of 1 min and 10 s, respectively.

Figures 1, 2 and 3 show isochromatic fringes, principal stress directions and thermal images for durations,  $t$ , of 1, 10 and 20 min after mixing, as examples, respectively.

The order of the isochromatics generated in the curing adhesive shown in Fig. 1 increased with time up to about  $t=10$  min. In particular, the order of the isochromatic at the under side of the adhesive was higher than those at other parts. The direction of one principal stress of the curing adhesive was toward the center of the area of the adhesive and the direction of other principal stress was concentric up to about  $t=10$  min. After about  $t=10$  min, the order of the isochromatics of the adhesive decreased with time, and the direction of the principal stress became indistinct. The thermal images shown in Fig. 3 indicate that the curing of the resin started from the under side of the area of the adhesive, and proceeded circumferentially. The temperature of the adhesive increased up to about  $t=10$  min, and then decreased with time.

The results show that the curing of the area where the adhesive was applied was not uniform and the residual stress in the adhesive after curing was low.

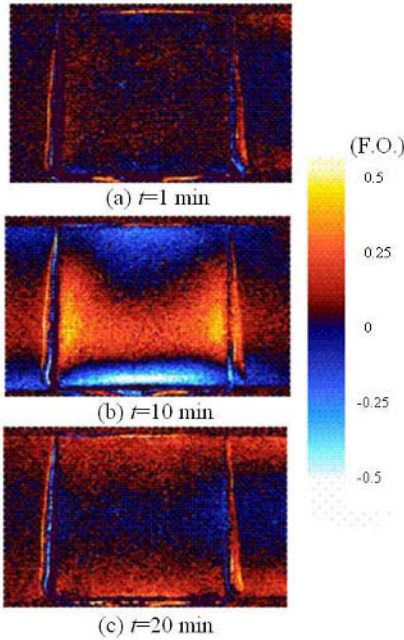


FIGURE 1. Isochromatic fringes.

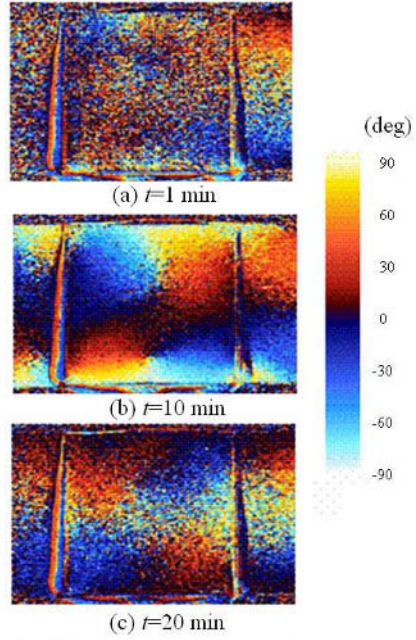


FIGURE 2. Principal stress directions.

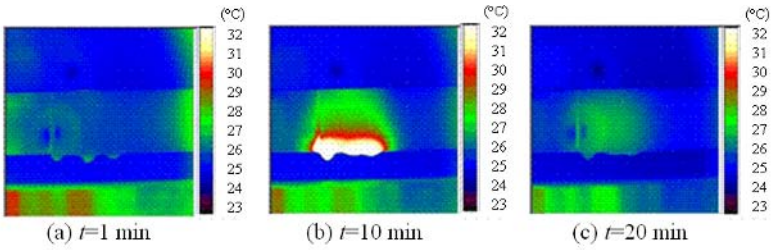


FIGURE 3. Thermal images.

**References**

1. Umezaki, E. and Abe, M., Key Engineering Materials, vol. 326-328, 163-166, 2006.

## IDENTIFICATION OF STRAIN-RATE SENSITIVITY WITH THE VIRTUAL FIELDS METHOD

Stéphane Avril<sup>a</sup>, Fabrice Pierron<sup>a</sup>, Junhui Yan<sup>b</sup> and Michael A. Sutton<sup>b</sup>

<sup>a</sup> LMPF, ENSAM, Rue Saint Dominique, BP508, 51006 Châlons en Champagne, FRANCE

<sup>b</sup> Department of Mechanical Engineering, University of South Carolina,  
Columbia, SC 29208, USA  
Stephane.avril@chalons.ensam.fr

The experimental identification of parameters governing the elasto-visco-plastic constitutive behavior of materials is a key issue which usually relies on performing simple mechanical tests for which a closed-form solution for the corresponding equivalent mechanical problem is available. These tests, such as tension or compression on prismatic specimens or torsion on thin tubes, usually lead to uniform states of stress and strain and therefore, the identification can be performed from a few strain data obtained through strain gages or extensometers. However, in order to fully characterize the material behavior, multi-axial tests are often necessary, requiring costly testing machines and difficult specimen design to obtain uniform stress states in some area of the specimen. Moreover, the models describing the elasto-plastic or visco-plastic behavior of materials are governed by several parameters which cannot be directly determined from these experiments in all cases.

As suggested by Meuwissen et al. [1], an alternative is to perform tests leading to non uniform stress states, with the idea of retrieving more parameters from one test. It has already been shown that non uniform stress distribution can be handled by carrying out full-field measurements across the specimen and by processing them using an appropriate inverse methodology. Among these methodologies, the virtual fields method (VFM) is interesting because it is at the same time light and robust, as proved by Grédiac and Pierron [2] and then by Pannier et al. [3].

Nevertheless, in all the studies which have been mentioned previously, the strain-rate was never a concern. It was low enough (about  $10^{-4} \text{ s}^{-1}$ ) in order to provide quasi-static conditions during the test. The purpose of this study is to investigate what occurs at higher strain-rates (in the range  $1 - 10 \text{ s}^{-1}$ ).

For this purpose, a tensile test has been specially designed to give rise to heterogeneous stress fields across a thin steel bar having a waisted shape (Fig. 1). Displacement fields are measured over a given surface of the specimen (denoted  $S$  in Fig. 1) by the digital image correlation (DIC) technique with the help of the VIC-2D software [4]. Images are grabbed using two high-speed cameras (5000 frames per second) mounted back-to-back in order to provide measurements on both the specimen faces. The strain-rate distribution is then deduced from the displacement fields, showing a very sharp localization at the center of the specimen 7 ms after the beginning of the test (Fig. 1), just at the onset of the plastic behavior. Because of this localization, it is essential to take into account the dependence of the yield stress to the strain rate in the model used for the identification. Therefore, the final identification with the VFM provided the five constitutive parameters driving the constitutive equations of the tested material: Poisson's ratio, Young's modulus, the initial yield stress, the hardening modulus along with the strain-rate sensitivity. It must be underlined that the strain rate sensitivity of the yield stress was identified over a range of 1 to  $10 \text{ s}^{-1}$  with just one test. This illustrates the power of heterogeneous tests.

Other similar tests are currently underway for validating this new procedure.

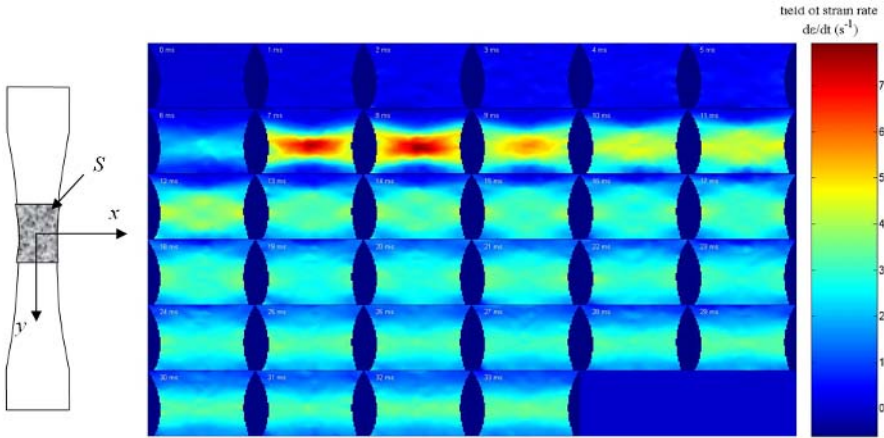


FIGURE 1. Schematic view of the tensile specimen along with strain-rates distribution across surface  $S$  imaged at 1000 Hz during the 33 first milliseconds of the test.

## References

1. Meuwissen, M.H.H., Oomens, C.W.J., Baaijens, F.P.T., Petterson, R., and Janssen, J.D. *J. Mater. Process Tech.*, vol. **75**, 204–211, 1998.
2. Grédiac, M. and Pierron, F. *Int. J. Plast.*, vol. **22**, 602-627, 2006.
3. Pannier, Y., Avril, S., Rotinat, R., and Pierron, F. *Exp. Mech.*, in press, 2006.
4. [www.correlatedsolutions.com](http://www.correlatedsolutions.com).

## IDENTIFICATION OF 3-D HETEROGENEOUS MODULUS DISTRIBUTION WITH THE VIRTUAL FIELDS METHOD

Stéphane Avril<sup>a</sup>, Jonathan M. Huntley<sup>b</sup>, Fabrice Pierron<sup>a</sup> and Derek D. Steele<sup>b</sup>

<sup>a</sup> LMPF, ENSAM, Rue Saint Dominique, BP508, 51006 Châlons en Champagne, FRANCE

<sup>b</sup> Wolfson School of Mechanical and Manufacturing Engineering, Loughborough University, Loughborough, Leicestershire, LE11 3TU, United Kingdom

<sup>c</sup> Departments of Radiology and Biomedical Engineering, University of Michigan Medical Center, 3315 Kresge III, Ann Arbor, MI 48109-0553, USA

Stephane.avril@chalons.ensam.fr

In this study, we present the first extension of the virtual fields method [1, 2] to the identification of heterogeneous stiffness properties from 3-D bulk full-field measurements. Two main issues are addressed: 1. the identification of the stiffness ratio between two different media in a heterogeneous solid, 2. the identification of stiffness heterogeneities buried in a heterogeneous solid.

The approach is tested on experimental full-field data obtained within the framework of a biomedical application. Indeed, in medicine, the accurate characterization of stiffness properties inside the human body is essential in order to detect tumours and diagnose disease. Thanks to ultrasound and magnetic resonance imaging (MRI), it is possible to measure displacement fields inside many human tissues. Phase contrast MRI is used in this study through a dedicated sequence called “stimulated echo MRI” [3].

The application is the characterization of a stiff spherical inclusion buried within a lower modulus material (Fig. 1). The specimen, known as a phantom, is not made of real tissues but of silicone gel, mimicking a tumour inside the human body. It has a parallelepipedic shape and is loaded in uni-axial compression. The MRI scanner provides 3D arrays of all three displacement components across the phantom. These displacement fields are first interpolated using a basis of piecewise trilinear functions, and then processed through the virtual fields method [2]. The virtual fields are expanded using the same basis of piecewise trilinear functions. The modulus is assumed to be piecewise constant. A large system of equations is deduced, involving the modulus values of all the elements of the predefined mesh (111000 unknowns). This system of equation is solved by the conjugate gradient method.

Results concerning the ratio between the modulus of the inclusion and the modulus of the surrounding material are in close agreement with the reference. Results concerning the calculated modulus distribution through the whole investigated volume are also quite promising (Fig. 2). However, the field of the identified modulus is rather scattered. This is explained by the fact that the approach is ultimately based on a second order differentiation of the data, which amplifies the noise in the data. A study is currently underway for reducing this effect.

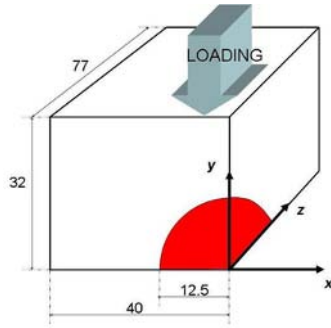


FIGURE 1. Schematic view of an eighth of the specimen.

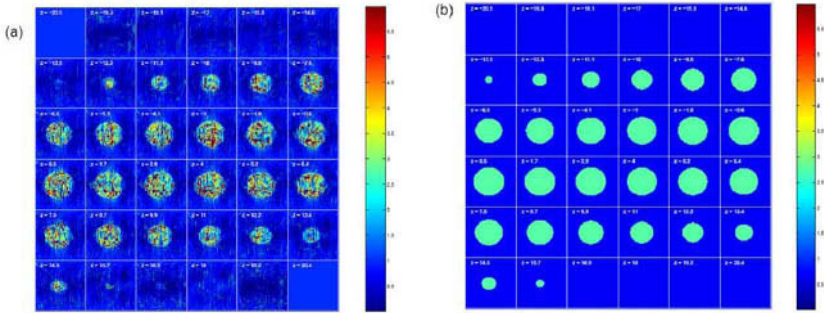


FIGURE 2. (a) Identified modulus distribution across different cross sections of the phantom. (b) Reference modulus distribution across the same cross sections.

**References**

1. Grédiac, M. *C.R. Mécanique*, vol. **309**, 1-5, 1989.
2. Avril, S., Grédiac, M., and Pierron, F. *Comp. Mech.*, vol. **34**(6), 439-452, 2004.
3. Steele, D.D., Chenevert, T.L., Skovodora, A.R. and Emelianov, S.Y. *Phys. Med. Biol.*, vol. **45**, 1633-1648, 2000.

## IDENTIFICATION FROM MULTI-PHYSICS FULL-FIELD MEASUREMENTS AT THE MICROMETER SCALE: THE ELECTRO-ELASTIC COUPLING

F. Amiot<sup>1</sup>, F. Hild<sup>2</sup>, F. Kanoufi<sup>3</sup> and J.P. Roger<sup>4</sup>

<sup>1</sup> MIC-NanoDTU, TU. Denmark,

Oersteds Plads, DTU Building 345 east DK-2800 Kgs. Lyngby, Denmark

<sup>2</sup> LMT-Cachan / ENS Cachan / CNRS UMR-8535 / Université Paris VI, France

<sup>3</sup> LECA / ESPCI / CNRS UMR-7121, France

<sup>4</sup> LOP / ESPCI / CNRS UPR-A0005 / Université Paris VI, France

<sup>1</sup> fabien.amiot@mic.dtu.dk

We use metal coated micro-cantilevers as transducers from their electrochemical environment (Lavrik *et al.* [1]). Using the metallic layer of these cantilevers as a working electrode allows one to modify the electrochemical state of the cantilever surface. Since the mechanical behaviour of micrometer scale objects is significantly surface-driven, this environment modification induces a bending of the cantilever (Raiteri and Butt [2]). However, if the existence of this surface coupled phenomena has been demonstrated, the modelling of the connection between the electrochemical state of an interface and the induced deformation remains an open issue. Since one of the main difficulty is to ensure a uniform and well defined loading at the micrometer scale, it is thought that increasing the experimental information content may lead to a significant improvement of modelling, provided the redundancy of the measured quantity is sufficient. This statement is at the origin of the development of identification techniques based on full-field measurements in solids mechanics.

The electrocapillarity effect is implemented by using a gold-coated silica cantilever introduced in a potassium chloride solution and varying the surface electric potential in the double-layer (*i.e.* reversible transformations) region. The considered experiments are carried out in a home-made fluid-cell, which allows for in-situ optical monitoring. The cyclic voltammetry results (Fig. 1a) prove that the system under scrutiny does not experience any (irreversible) chemical reaction. Using a full-field interferometric measurement set-up (Amiot and Roger [3]) to monitor the objects then provides an optical phase map  $\phi$  (see Fig. 1b), which is found to originate both in electrochemical and mechanical effects

$$\phi = \phi_{mec} + \phi_{ec} \quad (1)$$

The scaling of the electrochemically induced phase with respect to the surface charge density is modelled according to Gouy-Chapman-Stern theory, whereas the relationship between the mechanical effect and the surface charge density  $\sigma_m$  is under scrutiny. The sensitivity of the electrochemically-induced phase to  $\sigma_m$  is evaluated using results on electrode-electrolyte interface (Stedman [4]) and an ellipsometric calibration, which yield

$$\frac{\partial \phi_{ec}}{\partial \sigma_m} \simeq -2.7 \times 10^{-4} \text{rad m}^2 / \text{C} \quad (2)$$

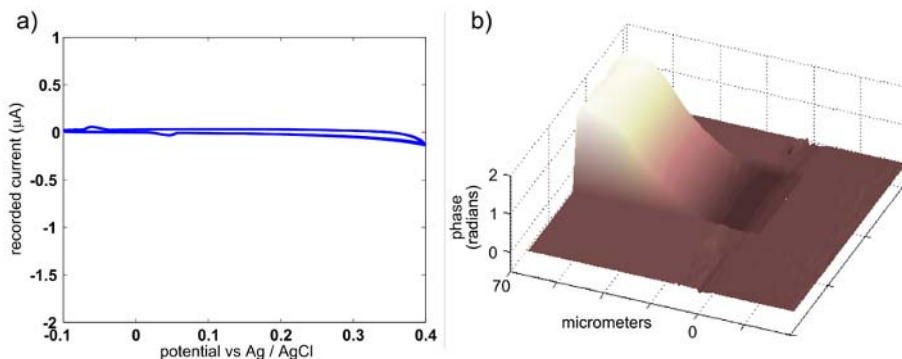


FIGURE 1. a) Cyclic voltammety of the micro-cantilevers array in a  $10^{-2}$ M KCl solution. Number of cycles: 3; scan rate: 2 mV/s; starting potential -0.1 V vs. Ag/AgCl. b) Typical phase map measured during cyclic voltammety.

Assuming the linear relationship (2), the electrochemical ( $\phi_{el}$ ) and mechanical ( $\phi_{mec}$ ) contributions to the measured optical phase ( $\phi$ ) are decoupled. The identification problem turns then to retrieve from the optical phase map, which then yields information on both the surface electrical state and the cantilever bending:

- the spatial distribution of the surface charge density;
- the constitutive relation between the local surface charge density and the apparent mechanical effect on the cantilever.

A suitable identification technique is then proposed to build a modelling of the electro-elastic coupling and to characterize the localization of the electrocapillarity effects.

The surface charge density is found to be heterogeneous and highly localized at the end of the cantilever (sharp tip effect of the electric field) and a power-law dependence of the surface shear-stress with respect to surface charge density is identified, thus yielding the identification of the equations governing of the electro-elastic coupling from multi-physics full-field measurements.

## References

1. Lavrik, N.V., Sepaniak, M.J., Datskos, P.G., Cantilever transducers as a platform for chemical and biological sensors, *Review of Scientific Instruments*, vol. **75**(7), 2229-2253, 2004.
2. Raiteri, R., Butt, H.J., Measuring electrochemically induced surface stress with an atomic force microscope, *J. Phys. Chem.*, vol. **99**, 15728-15732, 1995.
3. Amiot, F., Roger, J.P., Nomarski imaging interferometry to measure the displacement field of micro-electro-mechanical systems, *Appl. Optics*, vol. **45**(30), 7800-7810, 2006.
4. Stedman, M., Reflectance and ellipsometry of Metal/Electrolyte Interfaces, *Trans. Faraday Soc.*, pp. 64-71, 1970.



## DETERMINATION OF THE ELONGATIONAL PROPERTIES OF POLYMERS USING A MIXED NUMERICAL-EXPERIMENTAL METHOD

L. Robert, S. Hmida-Maamar, V. Velay and F. Schmidt  
 Research Centre on Tools, Materials and Processes (CROMeP)  
 Ecole des Mines d'Albi-Carmaux, 81013 ALBI Cedex 9, France  
 {laurent.robert,hmidahmi,vincent.velay,fabrice.schmidt}@enstimac.fr

The biaxial properties of materials such as rubbers or polymers are often difficult to identify, and generally a simple isotropic behaviour derived from classical 1D tensile test is considered. However, biaxial properties are useful for the simulation of plastic-processing operations such as blow moulding [1] or thermoforming. As previously reported, the rheological behaviour and the mechanical properties of rubbers and polymers can be obtained by using a bubble inflation rheometer [2-4], or multi-axial tensile test [5]. In this work, experimental data provided by optical measurements on tensile tests and bubble inflation tests are coupled with Finite Element Method simulations for identifying the rheological behaviour. This work is actually based on natural rubber and will be extend to thermoplastic (PP and PET) materials.

A bubble inflation rheometer has been developed in the laboratory. It allows to blow under controlled pressure rubber or thermoplastic membranes [2]: a circular membrane, clamped at the rim, is inflated by applying air pressure to its bottom face (see Fig. 1, left). In the case of thermoplastic, a heating step is necessary before applying the pressure. The heating can be performed by air convection, by conduction (heating cartridge at the rim) and by IR radiation.

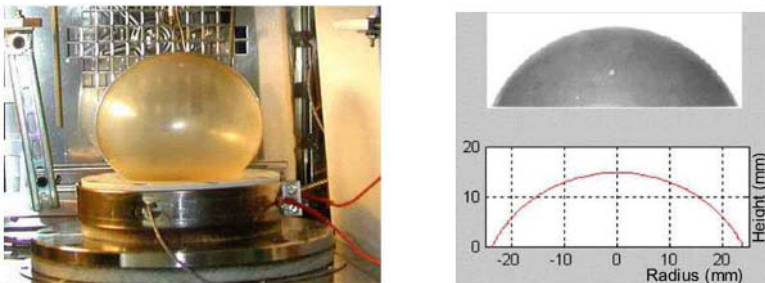


FIGURE 1. Bubble inflation rheometer (detail, left) and shape contour extraction (right).

Two experimental optical techniques based on non-contact measurement by CCD cameras have been developed for in situ measurements: (i) images acquisition of the 2D projection of the bubble is done during the inflation process, giving shape contours versus inflated pressure (see Fig. 1, right); (ii) Digital Image Stereo-Correlation (DISC) [6] is applied using a calibrated stereo rig in order to obtain the three-dimensional description of the strain fields on the surface of the bubble. To perform DISC directly on the rubber bubble, several difficulties are to be solved (large level of deformation, semi-transparent aspect of the materials, lighting, etc.).

In addition, tensile tests have been performed using DISC due to the high level of strain. Tensile test performed on standard specimen give, on the one hand, the stress/strain curve. On the

other hand, open hole tensile tests are performed on drilled specimen, putting in evidence non-homogeneous strain fields measured by the optical full field method.

The Mooney-Rivling hyperelastic behaviour has been chosen for its simplicity (2 parameters) and because it is representative of natural rubbers behaviour, at least for reasonable stretch ratio  $\lambda$  (no strain hardening). Fitting of the 1D stress/strain curve gives a set of parameters using eq. (1), numerical values obtained are  $C_{10} = 0.136$  MPa and  $C_{01} = 0.097$  MPa.

$$\frac{F}{S_0} = 2C_{10} \left( \lambda - \frac{1}{\lambda^2} \right) + 2C_{01} \left( 1 - \frac{1}{\lambda^3} \right) \quad (1)$$

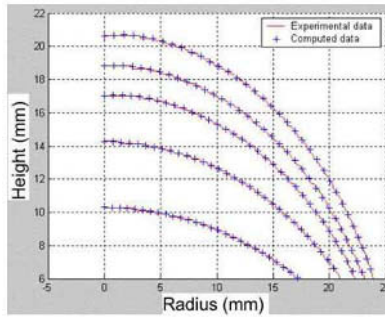


FIGURE 2. Experimental and numerical shape contours after optimization.

Then identification of the Mooney Rivling coefficients based on experimental shape contours using a Finite Element Model Updated (FEMU) procedure is performed using Abaqus<sup>®</sup>. The cost function to minimise is defined as the norm (least squares sense) between experimental and numerical bubble shapes, and a Sequential Quadratic Programming (SQP) optimisation algorithm has been used. Results show that the Mooney-Rivling behaviour seems to be correct for small stretch ratio (< 200%) (see Fig. 2).

The second identification approach is based on a FEMU procedure using full field measurements by DISC (Vic-3D<sup>®</sup>) during the open hole tensile test. Boundary conditions, cost function and preliminary results of the identification will be presented. Parameters values resulting from the identification based on the heterogeneous displacement field will be compared with those identified from the contour extractions and discussed.

## References

1. Rosato, D.V. and Rosato, A.V., *Blow molding handbook*, 2<sup>nd</sup> ed. Hanser, Munich, 2003.
2. Reuge, N., Schmidt, F.M., Lemaoult, Y., Rachik, M. and Abbe, F., *Polym. Eng. Sci.*, Vol. **41**-3, 522-531, 2001.
3. Li, Y., Nemes, J.A. and Derdouri, A.A., *Polym. Eng. Sci.*, vol. **41**-8, 1399-1412, 2001.
4. Jones, A., Shaw, J. and Wineman, A., *Exp. Mech.* vol **46**-5, 579-587, 2006.
5. Chevalier, L. and Marco, Y., *Polym. Eng. Sci.*, vol. **42**-2, 280-298, 2002.
6. Garcia, D., Orteu, J.-J. and Penazzi, L., *J. Mat. Proc. Tech.*, vol. **125**, 736-742, 2002.

## THERMOMECHANICAL BEHAVIOUR PREDICTION OF GLASS WOOL BY USING FULL-FIELD MEASUREMENTS

Jean-Francois Witz, Stéphane Roux and François Hild  
LMT-Cachan, ENS Cachan / CNRS-UMR 8535 / Université Paris 6  
61 avenue du Président Wilson, F-94235 Cachan Cedex, France  
{witz,roux,hild}@lmt.ens-cachan.fr

Mineral wool is a cellular solid made of fibres with micrometric diameter and millimetric or centimetric length. The fibres are entangled to form a very loose mat (with a mass density of a few  $\text{kg/m}^3$ ). A binder sprayed on the fibres, and cured in an oven, freezes the arrangement of the fibres and provides some elasticity to the product. As such, this gives a very good insulating material, with however poor mechanical performances. For applications that are more demanding on the mechanical side, the fibre mat is processed before the curing stage to produce a structure endowing the material with a stronger mechanical strength (to compression, tearing, or shear). This step is called “crimping”. The mechanical stiffness and strength are enhanced due to a more isotropic fibre orientation. The aim of the present study is to relate the thermomechanical behaviour of a crimped glass wool product and its initial texture. There is a duality between the mechanical and thermal behaviour. For applications that are more demanding on the thermal side, the lighter and non-crimped products are used.

To characterise the texture of a finished product, a digital image analysis has been developed (Bergonnier *et al.* [1]). Through the analysis of the autocorrelation function of small zones, it provides, from a textured product image, a local anisotropy field, i.e., the dominant orientation and its associated amplitude.

For the mechanical part, Digital Image Correlation (based on a Q4 code, Besnard *et al.* [2]) is used to measure the displacement field of mineral wool samples subjected to uniaxial compression tests. A linear elastic and anisotropic Finite Element code has been designed to compute the mechanical response of the material as a function of the initial texture of a mineral wool sample and the loading. Based on the initial texture field, and the experimental measured displacement, the local elastic properties are estimated via an inverse identification procedure. The latter procedure is shown to account for the main features of the displacement heterogeneities. Moreover, even though the approach is simply linear elastic (and anisotropic), the observed strain concentrations correlate well with the localisation bands that develop in experiments. This observation suggests that the ultimate mechanical strength may be estimated using this approach.

The temperature field of mineral wool samples subjected to a stationary uniaxial heat flux is obtained by using a middle wave Infrared camera. A Finite Element code has been implemented in order to compute the thermal steady state response of the material as a function of the initial texture of a mineral wool sample and the loading. Based on the initial texture field, and the experimental measured temperature, the anisotropic conductivity properties are estimated via an inverse identification procedure.

### References

1. Bergonnier, S., Hild, F. and Roux, S., *J. of Pattern Recognition*, in press, 2006.
2. Besnard, G., Hild, F. and Roux, S., *Exp. Mech.*, in press, 2006.

## MODELING OF ADSORPTION-INDUCED MECHANICAL LOADING ON MICROCANTILEVERS USING FULL-FIELD MEASUREMENTS

Nicolas Garraud<sup>1,2</sup>, Fabien Amiot<sup>3</sup>, François Hild<sup>1</sup>, Jean Paul Roger<sup>2</sup>

<sup>1</sup> Laboratoire de Mécanique et Technologie, ENS Cachan, CNRS-UMR 8535, Université Paris 6  
61 Avenue du Président Wilson, F-94235 Cachan, France

<sup>2</sup> Laboratoire d'Optique Physique, ESPCI Paris, CNRS-UPR A0005, Université Paris 6  
10 Rue Vauquelin, F-75231 Paris CEDEX 05, France

<sup>3</sup> Department of Micro and Nanotechnology NanoDTU, Technical University of Denmark  
Oerstedts Plads, DTU Building 345 east DK-2800 Kgs. Lyngby, Denmark  
garraud@lmt.ens-cachan.fr

The present study deals with micro-mechanical-systems and their interactions with their environment. Because of their high surface/volume ratio, the mechanical behaviour of the microcantilevers used in this study is driven by surface phenomena. We focus here on the mechanical effect induced by the adsorption of decane-thiol molecules onto a gold surface (Berger *et al.* [1]). The displacement fields are measured in-situ during the adsorption thanks to a Nomarski imaging interferometer, presented in the first part. The adsorption experiments are then described, as well as the identification procedure used to model the resulting mechanical loading.

### Interferometric set-up

The used cantilever is a silica beam ( $70 \times 20 \times 0.77 \mu\text{m}$ ) covered with a thin gold layer (50 nm). A shear-interferometer (Amiot and Roger [2]), described in Fig. 1, is used.

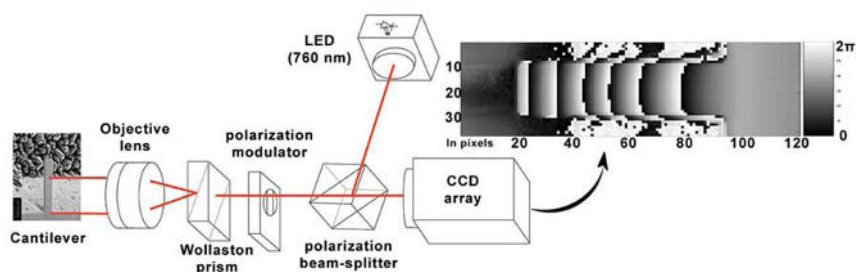


FIGURE 1. Schematic view of interferometric imaging set-up and measured phase map.

A monochromatic light beam is split into two coherent beams with a small angle between each other. After reflection on the cantilever, the two beams are recombined, and the interference figure is recorded on a CCD array. By comparing topographies before and after loading, out-of-plane displacement fields along the beam surface are obtained.

### Decanethiols adsorption and loading modeling

We used neutral molecules of decanethiol whose chemical formula is  $\text{CH}_3-(\text{CH}_2)_9-\text{SH}$ . The gold surface is electrochemically cleaned while varying its potential in a KCl solution (concentration of  $10^{-2} \text{ mol.l}^{-1}$ ), until a stable voltammogram is obtained. The experiments are

performed at a controlled temperature of 22 °C. The beam is observed in a solution composed of KCl ( $10^{-2} \text{ mol.l}^{-1}$ ), 1% of ethanol, and decane-thiol molecules that must be adsorbed ( $7 \times 10^{-8} \text{ mol.l}^{-1}$ ). The upper gold surface tends to increase in order to support the adsorption of molecules, which is thermodynamically favourable. The resulting effect is a downward bending of the cantilever.

Assuming a uniform stiffness along the beam, a model of the mechanical loading induced by the decane-thiol adsorption is built. Several displacement fields, linked to different loading modellings, are derived to derive a basis of statically admissible fields. The first deformed shape is written by considering a uniform pressure  $p$  along the beam

$$Y_p = \frac{p \cdot b}{24EI} (6L^2x^2 - 4Lx^3 + x^4) \tag{1}$$

where  $EI$  is the bending stiffness,  $b$  and  $L$  the cantilever width and length. Assuming a continuous film of molecules, the second one is derived from distributed shear-stress  $\tau_s$

$$Y_s = \frac{\tau_s \cdot \delta \cdot b}{6EI} (3Lx^2 - x^3) \tag{2}$$

where  $\delta$  is the distance to the neutral axis. The last one is determined by assuming that adsorption occurs in a heterogeneous manner, by small islands inducing a shear-stress  $\tau_{loc}$

$$Y_{loc} = \frac{\tau_{loc} \cdot D_{loc} \cdot \delta \cdot b}{16EI} x^2 \tag{3}$$

where the islands characteristic length is  $D_{loc}$ . The measured displacement field  $Y_{mes}$  is then projected onto the above described statically admissible basis, thus yielding least squares error indicators (Fig. 2), which are used to assess the modelling quality.

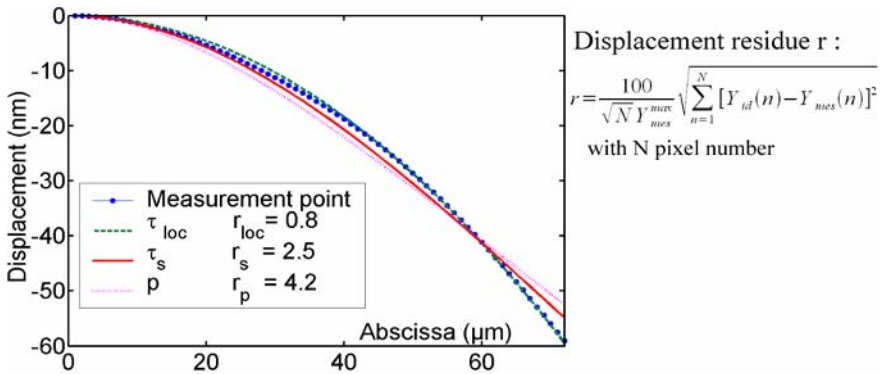


FIGURE 2. Loading model identification.

**References**

1. Berger, R., Delamar, E., Lang, H.P., Gerber, C., Gimzewski, J.K., Meyer, E., Guntherodt, H.J., *Appl. Physics A*, vol. **66**, S55-S59, 1998
2. Amiot, F., Roger, J.P., *Appl. Optics*, vol. **45**(30), 7800-7810, 2006

## ON THE IMAGE CORRELATION MEASUREMENT OF DISPLACEMENT FIELDS WITH STRONG STRAIN GRADIENTS OR DISCONTINUITIES

Wei Tong and Hang Yao

Department of Mechanical Engineering, Southern Methodist University  
3101 Dyer Street, 200G Embrey Building, Dallas, TX 75275, USA  
wtong@smu.edu, hyao@smu.edu

Digital image correlation (DIC) based full-field deformation measurement technique has been successfully used to map both nominally homogenous and non-homogenous deformation fields [1-5]. Among the key parameters in a digital image correlation analysis are grid point selection, subset size and shape, local mapping function for the subset, and the image correlation criterion and its optimization solution algorithm used. In particular, the affine deformation mapping function (equivalent to the assumption that the subset deforms uniformly) is most commonly used. For a given deformation field with a very high strain gradient (such as the strain field around a sharp crack tip [1] and the boundary region across a shear band or tensile deformation band due to certain material softening behaviour [4]), such a choice of the local mapping function for a given subset is questionable. Furthermore, the common use of a uniform grid point set with subset centred at each grid point would also not be proper to achieve the optimum balance between the spatial resolution and accuracy of displacement field measurements. Several novel digital image correlation analysis methods are presented here to specifically address the above mentioned issues.

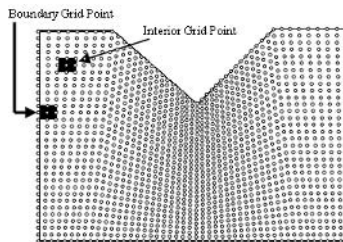


FIGURE 1. Adaptive gridding of a notched specimen [1].

For measuring a deformation field with high strain gradients such as around a notch tip as shown in Fig. 1, it is proposed that an adaptive grid point set is used (similar to the finite element meshing with more dense grid points around the notch tip region). The subset for each interior grid point will be centered but the subset for the boundary grid point (such as the ones on the free surface of the notch region) will be properly offset (Fig.1) so the image pixels outside the specimen boundary will not be considered. Such an adaptive grid point set has been successfully used to extract the notch tip displacement field and a growing crack tip displacement field (with an additional procedure of the so-called backward image correlation) [1]. The remaining issues are how to define the grid point set, subset size and shape, and local mapping functions optimally to achieve the highest spatial resolution and accuracy of the local displacements within the limit of the system and image noises.

When a localized deformation band with a uniform strain existing a sample, it is found that the extracted displacement field and strain field are not accurate when they are obtained by the digital image correlation analysis of a uniform grid point set over the entire sample region, see Fig.2. The original deformation band of a width 100 pixels (from  $X_1=250$  to 350 pixels) is distorted and the sharp transition in strain or displacement gradient  $U_{11}$  across the deformation band boundaries ( $X_1=250$  and  $X_1=350$ ) is greatly smeared and the strain distribution is of a bell-like shape. It is found that when one limits the region of interest (ROI) in the digital image correlation analysis to the deformation band region, the band strain distribution is nearly uniform instead of a bell-like shape. In actual applications, one has to locate the deformation band region adaptively and iteratively without any prior knowledge.

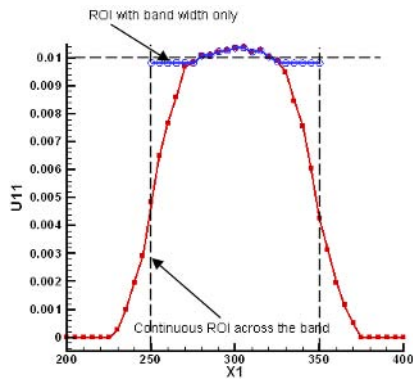


FIGURE 2. Effect of the DIC's ROI on the strain distribution of a deformation band.

## References

1. Tong, W., *Exp. Tech.*, vol. **28**, 63-67, 2004.
2. Tong, W., *Exp. Mech.*, vol. **44**, 502-511, 2004.
3. Tong, W., *Strain*, vol. **41**, 167-175, 2005.
4. Tong, W., H. Tao, N. Zhang, and L.G. Hector, *Scripta Mater.*, vol. **53**, 87-92, 2005.
5. Tong, W., H. Tao, X. Jiang, N. Zhang, M. Marya, L.G. Hector, and X.Q. Gayden, *Metall. Mater. Trans. A*, vol. **36**, 2651-2669, 2005.

## IDENTIFICATION OF THE LOCAL STIFFNESS REDUCTION OF DAMAGED COMPOSITE PLATES USING FULL-FIELD MEASUREMENTS

J.-H. Kim<sup>a</sup>, F. Pierron<sup>a</sup> and M. Wisnom<sup>b</sup>

<sup>a</sup>: LMPF, ENSAM, Rue St Dominique, BP 508, 51000 Châlons en Champagne, France

<sup>b</sup>: Advanced Composites Centre for Innovation and Science, University of Bristol  
Queen's Building, University Walk, BS8 1TR Bristol, United Kingdom

jin.kim@chalons.ensam.fr – fabrice.pierron@chalons.ensam.fr – m.wisnom@bristol.ac.uk

Composite panels are prone to delamination damage caused by impact or manufacturing process. This results in a local loss of stiffness in the panel where the delamination has occurred. The present study aims at taking advantage of full-field measurements and inverse identification procedures to solve this problem. A deflectometry technique [1] is employed to perform full-field slope measurements. The curvatures are then obtained from the slopes by numerical differentiation. The deflectometry setup is shown in Fig. 1.

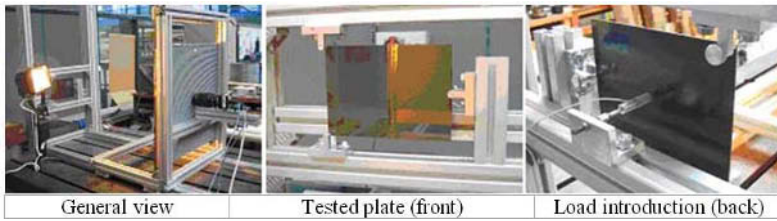


FIGURE 1. Deflectometry set-up.

The Virtual Field Method (VFM) [2-3] is used to process curvatures for the identification of the local loss of stiffness. Due to the reduction of stiffness in a local area on the laminate, the bending stiffnesses are different from those of the undamaged material. Thus, the VFM should be adapted to the case of a local stiffness reduction.

$$\tilde{D} = D^0 \{1 + p(x/L, y/W)\} \quad (1)$$

where  $\tilde{D}$  is the bending stiffness tensor of the damaged area,  $D^0$  that of the undamaged area and  $p$  is a polynomial function. The virtual fields method was adapted to identify the coefficients of the polynomial provided that the undamaged stiffnesses are known.

The case considered here is a rectangular composite panel containing a local damage characterized by a stiffness reduction coefficient as shown in Fig. 2.a. In order to validate the identification procedure, the first step was to use numerically simulated curvature data from an FE model. Fig. 2.b shows the plot of the stiffness reduction map for a 30% nominal stiffness reduction. On the plot, the red colour indicates no stiffness reduction (*i.e.*, no damage) and the blue, a reduction of stiffness (damage), with the magnitude of the stiffness reduction on the colour bar. It is clear that the method picks up the location of the damage and also provides a fairly good estimate of the stiffness reduction.



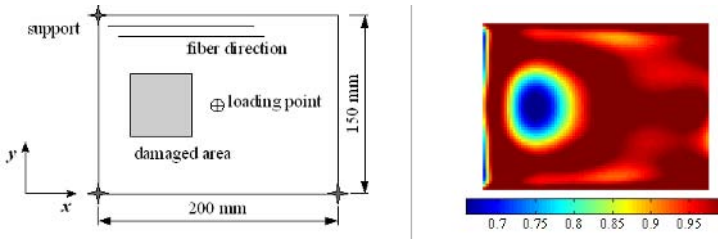


FIGURE 2. (a) Damaged plate dimensions and test configuration (b) The stiffness reduction identified from the simulated curvature maps (8<sup>th</sup> order polynomial function).

For the initial experiment, a unidirectional T300/914 carbon epoxy laminate plate with artificial damage was fabricated. To create the artificial isotropic damage, a 50x50 mm<sup>2</sup> size FEP release film was inserted into the interface between 2<sup>nd</sup> and 3<sup>rd</sup> lamina during fabrication of the laminate. After curing, the 1<sup>st</sup> and 2<sup>nd</sup> lamina over the film were taken off to represent a delamination effect. The first result of local stiffness reduction detection on the damaged plate is shown in Fig. 3.a. It can be seen that the result from experiment is similar to the one obtained from simulated measurements.

However, in practice, anisotropic damage is likely to occur, so additional experiments have been performed for other types of damage. The results are presented in Fig. .b (delamination) and 3c (fibre cut). The results are promising. The paper will present more extensive comments.

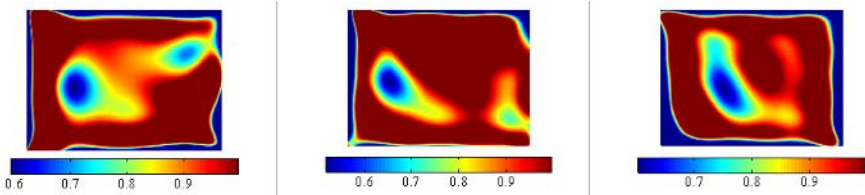


FIGURE 3. Identification of the stiffness reduction with experiment (a) Isotropic damage (b) Anisotropic damage (delamination only) (c) Anisotropic damage (fibre cut only).

**References**

1. Avril S., Grédiac, M., Pierron F. and Surrel Y., In *Proceedings of Xth SEM International Congress on Experimental Mechanics*, Costa Mesa, USA, 2004.
2. Grédiac M., Toussaint E. and Pierron F., *International Journal of Solids and Structures*, vol. **39**, 2691-2705, 2002.
3. Grédiac M., Toussaint E. and Pierron F., *International Journal of Solids and Structures*, vol. **40**, 2401-2419, 2003.

## AN ATTEMPT TO IDENTIFY HILL'S YIELD CRITERION PARAMETERS USING STRAIN FIELD MEASURED BY DIC TECHNIQUE

H. Haddadi and S. Belhabib  
CNRS-LPMTM, Université Paris 13 – Institut Galilée  
99, av. J.-B. Clément, 93430 Villetaneuse, France  
haddadi@Lpmtm.univ-paris13.fr

The identification of material parameters is very important in order to achieve more realistic prediction of the material behaviour by numerical simulations. An alternative method consists in the exploitation of the strain field measured on a non standard specimen. We have shown in previous studies the improvement brought by the exploitation of the strain field to the quality of the identification of the hardening material parameters [1,2]. The aim of this work is to improve the identification of Hill's yield criterion parameters using full-field measurements of strain, force-displacement and  $r$ - $\alpha$  curves.

The application concerns dual-phase steel used in the automobile industry. This material is assumed to have standard rate independent elasto-plastic behaviour. The elasticity is linear and isotropic. The yield criterion of plasticity used is the Hill'48 [4]. It is given by:

$$F(\sigma, \varepsilon^p) = \bar{\sigma} - Y(\varepsilon^p) = 0 \quad (1)$$

$$\text{where } \bar{\sigma}^2 = F(\sigma_{yy} - \sigma_{zz})^2 + G(\sigma_{zz} - \sigma_{xx})^2 + H(\sigma_{xx} - \sigma_{yy})^2 + 2L\sigma_{yz}^2 + 2M\sigma_{zx}^2 + 2N\sigma_{xy}^2 \quad (2)$$

$\bar{\sigma}$  is the equivalent stress of Hill,  $\sigma_{ij}$  denotes the components of the stress tensor of Cauchy in the orthotropic axes and  $\varepsilon^p$  is the equivalent plastic strain.

The work-hardening is assumed to be isotropic. Its evolution is explicitly given by a Swift law :

$$Y(\varepsilon^p) = Y_0 \left( 1 + \frac{\varepsilon^p}{\varepsilon_0} \right)^n \quad (3)$$

The parameters to be identified are F, G, N for the yield criterion, and  $Y_0$ ,  $\varepsilon_0$ , n for the hardening Swift law. Notice that  $G+H=1$ , this is obtained by imposing the equality between the measured yield limit for a uniaxial traction along the rolling direction and the equivalent stress given by Hill's yield criterion for the same direction. We assume also that  $L=M=1.5$ . These laws were implemented in an FE code called EPIM3D [5]. The measurement of the strain field is performed using the software 7D [6].

The identification strategy consists in the minimization of the total cost-function  $\Phi$  given by the following expression:

$$\Phi(\mathbf{P}) = (1 - \beta_1 - \beta_2)\Phi_F(\mathbf{P}) + \beta_1\Phi_\varepsilon(\mathbf{P}) + \beta_2\Phi_r(\mathbf{P}) \quad (4)$$

where  $\Phi_F$ ,  $\Phi_\varepsilon$  and  $\Phi_r$  represent a least square difference between the measured and the simulated total force, strain field and Hill's coefficient of anisotropy  $r(\alpha)$  respectively,  $\beta_1$  and  $\beta_2$  are weighting coefficients, so that  $\beta_1 + \beta_2 < 1$ , and  $\mathbf{P} = \{F, G, N, Y_0, \varepsilon_0, n\}$  is the parameters set to identify.

First results show that it is possible to obtain a good agreement between numerical and experimental values of strain fields, force-displacement and  $r$ - $\alpha$  curves.

### References

1. Haddadi, H., Belhabib, S., Gaspérini, M., Vacher, P., In *Photomechanics 2006*, Edited by M. Grédiac and J. Huntley, Clermont Ferrand – France, 2006.
2. Haddadi, H., Belhabib, S., Gaspérini, M., In Proc. *8<sup>th</sup> European Mechanics of Materials Conference*, Edited by O. Allix, Y. Berthaud, F. Hild and G. Maier, Cachan – France, 2005.
3. Haddadi, H., Bouvier, S., Levée, P., J. Phys. IV, vol. **11**, 329-337, 2001.
4. Hill, R., Proc. Roy. Soc. A, vol. **193**, 281-297, 1948.
5. Menezes, L. F., *PhD thesis*, University of Coimbra - University Paris 13, 1994.
6. Vacher, P., Dumoulin, S., Morestin, F., Mguil-Touchal, S., In Proc. *Instn. Mech. Engrs., 213 Part C ImechE*, 811-817, 1999.

## EFFECT OF ALUMINUM FOAM AND FOAM DENSITY ON THE ENERGY ABSORPTION CAPACITY OF 3D “S” SPACE FRAMES

Roselita Fragoudakis and Anil Saigal  
 Graduate Student, Department of Mechanical Engineering  
 Tufts University, Medford, MA 02155, USA  
 Professor, Department of Mechanical Engineering  
 Tufts University, Medford, MA 02155, USA  
 roselita.fragoudakis@tufts.edu, anil.saigal@tufts.edu

Passenger safety during front collision depends to a great extent on the capability of the car's front space frame structures to absorb energy generated during the crash, while deforming the least possible, Han and Yamazaki [1], and Cheon and Meguid [2].

Finite element analysis (FEA) models of 3D S-shape extruded aluminum frames were developed using the FEA simulation software ABAQUS/CAE and were evaluated for their crashing behavior when loaded axially.

All models investigated possess an aluminum frame, 45° curvature angles and a square cross-section. All models were loaded identically. One of the models tested was hollow inside, while the others were reinforced with aluminum foams of different properties (density and modulus of elasticity). Table 1 lists the properties of the aluminum foams used in this investigation.

The aluminum frame with foam 10.8/40/L with the highest relative density (10.8%) and 40 cpi (cells per inch of foam), tested longitudinally to the direction of solidification revealed a structure (SSF-1-45-45-1) that can sustain great compression with the least deformation. Figure 1 shows deformed plots of typical empty and aluminum reinforced 'S' space frame structures.

TABLE 1. Properties of Aluminum foam, Nieh *et al.* [3].

Structure	Foam	Modulus of Elasticity / MPa	Density / kg.m <sup>-3</sup>
SSF-1-45-45-1	10.8/40/L	752	299
SSF-1-45-45-4	4.8/40/L	110	133

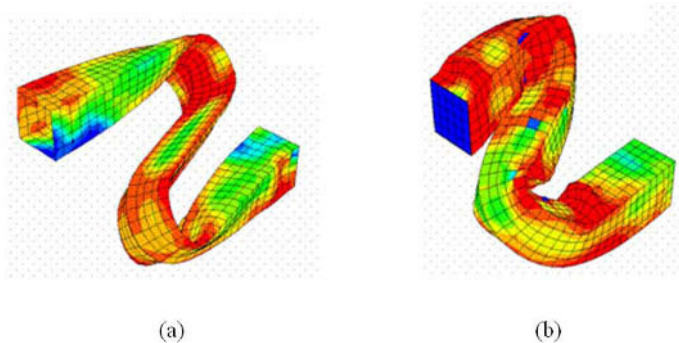


FIGURE 1. Deformed contour plots of (a) empty (SS-1-45-45) and (b) aluminum foam reinforced (SSF-1-45-45-1) structures.

TABLE 2. Energy Absorbed and Specific Energy Absorption as a function of Aluminum Foam Reinforcement.

Structure	Foam	Mass / kg	Force / N	Energy / J	SEA / J.g <sup>-1</sup>
SSF-1-45-45-1	10.8/40/L	2.84	38987	8405	2.96
SSF-1-45-45-4	4.8/40/L	1.93	32014	5391	2.79
SS-1-45-45	EMPTY	1.20	16068	1675	1.40

Table 2 shows the estimated peak force, energy absorbed and specific energy absorption for different structures. Based on this study, it can be concluded that aluminum foam is an efficient energy absorber, but higher density foam does not increase the Specific Energy Absorption of the structure much as compared to lower density foam due to the overall increased mass. In addition, the increase in total energy absorption due to aluminum foam reinforcement is accompanied by an undesirable significant increase in the peak force.

## References

1. Han J. and Yamazaki K., *International Journal of Vehicle Design*, vol. **31** (1), 72-85, 2003.
2. Cheon S.S. and Meguid S.A., *International Journal of Automotive Technology*, vol. **5** (1), 47-53, 2004.
3. Nieh T.G., Higashi K. and Wadsworth J., "Effect of cell morphology on the compressive properties of open-cell aluminum foams", *Materials Science and Engineering*, vol. **A283**, 105-110, 2000.

## HIGH STRAIN-RATE COMPRESSIVE CHARACTERISTICS OF A UNIDIRECTIONAL CARBON/EPOXY LAMINATED COMPOSITE: EFFECT OF LOADING DIRECTIONS

T. Yokoyama<sup>1</sup>, K. Nakai<sup>2</sup> and T. Odamura<sup>2</sup>

<sup>1</sup>Department of Mechanical Engineering  
Okayama University of Science  
Ridai-Cho, Okayama 700-0005, Japan

<sup>2</sup>Department of Mechanical Engineering  
Okayama University of Science  
1-1 Ridai-Cho, Okayama 700-0005, Japan  
yokoyama@mech.ous.ac.jp

Composite material exhibits superior mechanical properties such as high specific stiffness and strength over metallic materials and, hence, are increasing used in various industries. In many practical situations, the composite structures are often subjected to impact loading. Therefore, it is required to characterize the mechanical properties of composite materials at high rates of strain.

In the present work, the compressive stress-strain properties of a unidirectional carbon/epoxy (T700/2521) laminated composite in the three material directions were determined using a conventional split Hopkinson pressure bar. To avoid uncertainties related to size effects, the specimens in all the tests had the same geometry, i.e., cube specimen of nominal size 10mm. High strain-rate compression tests on the unidirectional carbon/epoxy laminated composite were performed in three material directions or 1(in- plane longitudinal), 2(in-plane transverse) and 3 (through-thickness) directions. Low strain-rate compression tests were carried out in a Instron testing machine. The specimens in the 1 direction showed higher strain rate effects than the specimens in the 2 and 3 directions. In the low strain-rate tests, cube specimens were observed to fail by axial splitting. In the 2 and 3 directions, cube specimens were split into two parts along a direction which was about 45 degree from the specimen axis. In the high strain-rate tests, specimens in each of the 1, 2 and 3 directions invariably failed in almost the same way as was their counterparts in low strain-rate tests.

Table 1. Type of reinforcing fiber and matrix resin used in unidirectional carbon/epoxy laminated composite

	Unidirectional carbon/epoxy
Fiber	T700(Torayca)
Matrix resin	Epoxy#2521
Fiber volume ratio $V_f$	0.65

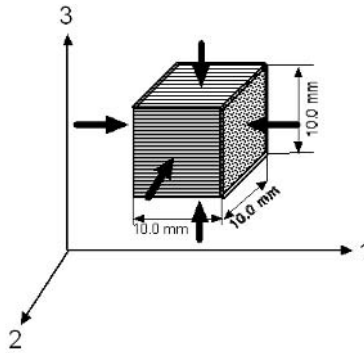


FIGURE 1. Cube specimen, and 1, 2 and 3 loading direction

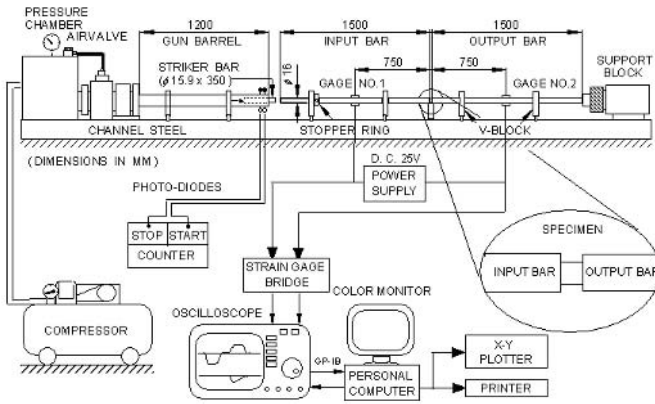


FIGURE 2. Schematic diagram of conventional split Hopkinson pressure bar

## DETERMINATION OF VERTICAL CHARACTERISTICS OF RAIL VEHICLE SUSPENSIONS BY DROP TEST ON THE TRACK

J. Chvojan<sup>a</sup>, R. Mayer<sup>b</sup>, P. Polach<sup>a</sup> and J. Vaclavik<sup>a</sup>

<sup>a</sup> SKODA VYZKUM s.r.o., Dynamic testing laboratory, Tylova 57, 316 00 Pilsen, Czech

<sup>b</sup> Sciotech office, Department of Engineering, University of Reading, RG6 6AY, Republic,  
jan.chvojan@skoda.cz, rayner@sciotech.demon.co.uk

The environmental impact of the vehicle designates the lifetime cost of the maintaining the infrastructure and the environment. One of principal objectives of EUREKA Footprint project is to develop the measurement techniques for measurement of this impact and to relate it to economic costs. The vehicle footprint is especially a function of suspension system quality. To be classified as "rail-friendly" the suspension must isolate the wagon from rail unevenness so that the dynamic wheel loading is minimized. The main factors, influenced dynamic loading is unsprung and sprung masses of the vehicle, sprung mass frequency and sprung mass damping ratio. Purpose of this article is an easy test method proposal for determination the dynamic characteristics of the suspension with full scale wagons on the track by crossing an artificial bump. The EC Drop test directive for road vehicles was adopted for this test.

Presented work goes out from tests, performed on shaker rig [1]. Here, the drop test was simulated using hydraulic actuator and optimum drop height has been determined to be 10 to 15 mm, just enabling the suspension to raise the oscillation with several peaks. Following procedure is proposed for the track drop test. Three artificial wedge shaped bumps of the height 10 mm, 15 mm and 20 mm are step by step placed on to each rail in front of the wagon and fixed to the rail (Fig. 1). The wagon is then draped over these bumps with three known velocities. Each bump over crossing is three times repeated for statistical purposes.



FIGURE 1. Wagon instrumentation and test performance

Following instrumentation is used on the wagon and track. Accelerometers are placed above each wheel of crossing axle on sprung and unsprung masses, total amount are 4 pieces. Two displacement transducers, connecting unsprung and sprung masses at each wheel of crossing axle may be used as an option. Deformation sensor is attached to both rails bottom just under the wedge end; the rails can be alternatively strain gauged at these positions.



### Suspension characteristics determination from drop test

Natural frequency and sprung mass damping is determined directly from sampled acceleration or displacement. The mean value of the logarithmic damping decrement  $\bar{\delta}$ , the critical damping ratio  $\bar{\xi}$  and suspension natural frequency  $f_o$  are usually calculated from all  $n+1$  peaks, having values  $q_i$  and observed at time  $t_i$ , which can be read out from the chart using following relation

$$\bar{\delta} = \frac{1}{n} \cdot \ln \frac{q_i}{q_{i+n}}, \quad \bar{\xi} = \frac{\bar{\delta}}{2\pi}, \quad f_o = \frac{\sqrt{1+\bar{\xi}^2}}{\sum T_{di}} = \frac{\sqrt{1+\bar{\xi}^2}}{(t_{i+n} - t_i)} \quad (1)$$

Dynamic load coefficient DLC is defined as the ratio of the real operation RMS dynamic wheel force  $s_F$  to the mean wheel force  $\bar{F}$  according following equation

$$DLC = \frac{s_F}{\bar{F}} \quad (2)$$

This coefficient is estimated indirectly from rail deformation dynamic peaks  $\varepsilon_{vi}$  measured at particular crossings of the bumps at given velocities  $v_i$  and the static deformation value  $\varepsilon_{v0}$  obtained at standing wagon at the bump according following equations

$$DLC = \frac{K(\varepsilon_{v1}, \varepsilon_{v2}, \varepsilon_{v3})}{\varepsilon_{v0}} \quad (3)$$

Coefficient  $K$  is obtained on the base of calculation using multibody software package **alaska**. The derivation of this coefficient is based on comparison of bump force peak and the force time history, obtained from representative truck. The verification of this procedure was performed using forces, measured at shaker rig test during truck simulations [1].

### Conclusion

Further works are planed for estimation the vehicle dynamic characteristics using measuring station without using any artificial bump and for relating the dynamic loading coefficient to economic costs in order to justify the basis for usage charging. The authors thank the Eureka Unit, Czech Republic for financial support of this project, which is led under internal notification OE 197, OE and the Department of Trade and Industry, UK.

### References

1. Chvojan, J., Cherruault, J.-Y., Kotas, M., Rayner, M., V?clav?k, J., Dynamic investigations on freight wagon suspensions, Proceedings of 12th international conference ICEM 12, Bari, 2004.

## DYNAMIC EFFECTS ON MECHANICAL CHARACTERISTICS OF COMPOSITE PLATES SUBMITTED TO IMPACT TESTS

G. Belingardi, M.P. Cavatorta and D.S. Paolino  
 Mechanics Department - Politecnico di Torino  
 Corso Duca degli Abruzzi 24 – Torino - Italy  
 giovanni.belingardi@polito.it

The present work deals with the behaviour of composite material plates submitted to impact loading conditions. The considered composite material consists of long fibers in polymeric resin. Different stacking sequences and different plate thickness are considered. Impact tests are performed according to the ASTM 3029 standard using our instrumented free-fall drop dart testing machine, that allows to acquire the dart load and the dart velocity histories.

The testing machine is equipped with a load cell for the force measurement and a optoelectronic device for the impact velocity measurement. Signals from the transducers are acquired with a NI board installed in a PC. Then the signals are accurately elaborated in order to get the values of the dart acceleration, velocity and displacement. Finally the history of deformation energy is calculated. Results are presented in terms of load-displacement (Fig. 1) and energy-displacement (Fig. 2) diagrams.

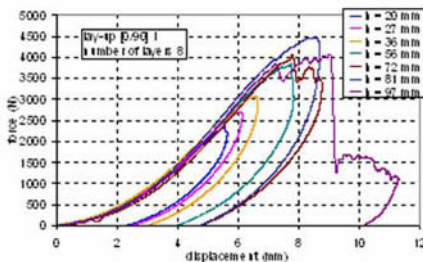


FIGURE 1. – Force displacement diagram

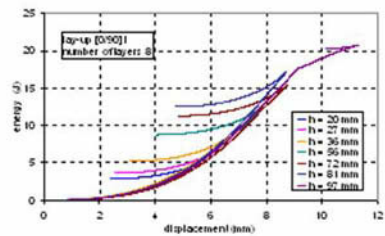


FIGURE 2. - Energy displacement diagram

The strain-rate sensitivity of the material is analysed with respect to some characteristic quantity such as the First Damage Threshold, the initial stiffness, the Maximum Load. Figure 3 shows, for example the dependency of the initial bending stiffness of the impacted plates on the impact velocity. The experimental methodology is aimed to characterise the energy absorption capability of the plates. In this perspective experimental data are analysed by means of the damage index, that establish a meaningful relation between the impact energy and the energy dissipated by the impacted material.

The index recently defined by the authors results to be more effective than the damage index previously defined by Belingardi and Vadori, particularly in the case of thick laminate when, penetration and perforation events are well distinguished.

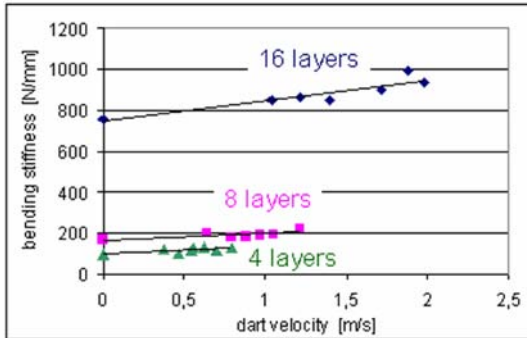


FIGURE 3. - Dependency of the initial stiffness of the impacted plates on the impact velocity

## References

1. Belingardi, G., Grasso, F. and Vadori, R., 1998, "Energy absorption and damage degree in impact testing of composite materials", Proceedings XI ICEM (Int. Conf. Experimental Mechanics), Oxford (UK), pp. 279-285.
2. Belingardi, G., and Vadori, R., 2002, "Low velocity impact tests of laminate glass-fiber-epoxy matrix composite materials plates", Int. J. of Impact Engineering, vol. **27**, 213-229.
3. Caprino, G., Lopresto V., Scarponi, C. and Briotti, G., 1999, "Influence of material thickness on the response of carbon-fabric/epoxy panels to low velocity impacts", Composite Science and Technology, vol. **59**, 2279-2286.
4. Liu, D., Raju, B.B. and Dang, X., 1998, "Size effect on impact response of composite laminates". International Journal of Impact Engineering, vol. **21**, 837-854.
5. ASTM D3029 – "Standard Test Method for Impact Resistance of Rigid Plastic Sheeting or Parts by means of a Tup (Falling Weight)". American Society for Testing Materials (1982).
6. Sutherland, L.S. and Guedes Soares, C., 1999, "Effects of laminate thickness and reinforcement type on the impact behaviour of e-glass/polyester laminates", Composites Science and Technology, vol. **59**, 2243-2260.
7. Belingardi, G., Cavatorta, M.P. and Paolino, D.S., 2006, "Comparative response in repeated impact tests of hand lay-up and vacuum infusion glass reinforced composites". 8<sup>th</sup> Biennial ASME Conference on Engineering Systems Design and Analysis, July 4-7 2006.
8. Belingardi, G., Cavatorta, M.P. and Paolino, D.S., 2006, "A new damage index to monitor the range of the penetration process in thick laminates", submitted to Composites Science and Technology

## A METHOD TO MEASURE CRACK OPENING DISPLACEMENT OF FAST PROPAGATING CRACK IN ARALDITE B

Shinichi Suzuki and Kazuya Iwanaga

Department of Mechanical Engineering, Toyohashi University of Technology  
Hibarigaoka 1-1, Tempaku-cho, Toyohashi, Aichi, 441-8580, Japan  
Shinichi@mech.tut.ac.jp

When a brittle material breaks under external force, a fast propagating crack often appears whose speed is more than 200m/s. The fast propagating crack bifurcates into two cracks if the crack speed is high enough (Suzuki et al. [1]). Bifurcation is a characteristic feature of fast propagating cracks, accordingly, many researchers have studied it theoretically and experimentally. But the mechanism of bifurcation is not fully understood yet.

One of the most important problems to figure out the mechanism of rapid crack bifurcation is the continuity of energy release rate at bifurcation. The area of crack surface with the unit length extension of the crack after bifurcation is twice as large as that before bifurcation. Hence the energy release rate immediately after bifurcation becomes discontinuously twice as large as that before bifurcation, if the crack speed after bifurcation is the same as that before bifurcation. On the other hand, if the energy release rate is continuous at bifurcation, the crack speed must decrease discontinuously at the bifurcation. But, it was impossible to measure the energy release rate just after bifurcation, because strong interaction occurs between the near-tip stress fields around the two branch crack tips since the distance between the two crack tips is very short.

Suzuki and Sakaue [2] recently proposed a method to measure the energy release rate of fast propagating cracks after bifurcation. If the bifurcation angle  $\theta$  is small and the lengths of the branch cracks are short (see Fig. 1), the crack can be thought to be a single crack, and the *COD* of the mother crack is proportional to the square root of the distance from the crack tip. Such conditions are approximately satisfied just after crack bifurcation. Consequently, the energy release rate of the crack just after bifurcation can be obtained by measuring the *CODs* of the mother crack with the formula of *COD* for a single crack. They measured the energy release rate of fast propagating cracks in PMMA, and obtained the result that both of energy release rate and crack speed are continuous at bifurcation.

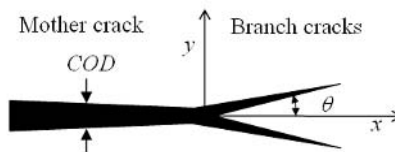


FIGURE 1. Bifurcated crack.

Suzuki et al. [3] applied the method of *COD* to the cracks in Araldite B. But, the corner of a crack surface and the specimen surface is chipped off in the case of fast propagating cracks in Araldite B (Fig. 2). As the result, it is often difficult to measure *CODs* from microscopic photographs of the fast propagating cracks.

The present paper shows a method to measure *CODs* even in the region where *CODs* are difficult to be measured directly from the microscopic photographs. The procedure is as follows.

- 1 High-speed holographic microscopy [1], [2] is applied to take microscopic photographs of fast propagating cracks in Araldite B.
- 2 From the photographs *COD* and *D* in Fig.2 are measured in the region where both of *COD* and *D* can be measured. The sum of the width of the defect,  $\delta_1 + \delta_2$ , and its mean value,  $\overline{\delta_1 + \delta_2}$ , is obtained from the measured *COD* and *D*.
- 3 The *COD* in the region where *COD* can't be measured directly from the microscopic photographs is approximately obtained by measuring *D* and by subtracting  $\overline{\delta_1 + \delta_2}$  from *D*.

The results of the *COD* measurement described above have good measurement accuracy. It is shown that the measured *COD* is proportional to the square root of the distance from the crack tip, not only in the case of single cracks but also in the case of mother cracks after bifurcation.

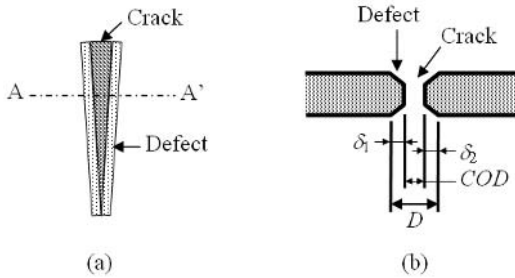


FIGURE 2. (a) Fast propagating crack with defect in Araldite B, (b) the cross section of the specimen along A-A' in (a).

## References

1. Suzuki, S., Inayama, A. and Arai, N., In *Proceedings of the 11<sup>th</sup> International Conference on Experimental Mechanics*, edited by L. M. Allison, Balkema, Rotterdam, 1998, 583-588.
2. Suzuki, S. and Sakaue, K., *JSME International Journal*, series A, vol. **48**(3), 264-273, 2004.
3. Suzuki, S., Sakaue, K. and Iwanaga, K., *J. Mech. Phys. Solids*, (Submitting).

## EXPERIMENTAL INVESTIGATION OF THE STATIC BEHAVIOUR OF A HOLE DRILLED STEEL PLATE REINFORCED WITH A COMPOSITE PATCH

Nicholas G. Tsouvalis and Lazaros S. Mirisiotis  
National Technical University of Athens  
School of Naval Architecture and Marine Engineering  
Shipbuilding Technology Laboratory, Division of Marine Structures  
Heroon Polytechniou 9, GR-157 73 Zografos, Greece  
tsouv@deslab.ntua.gr

There are many circumstances in a steel marine structure, when the need arises for local reinforcements or repairs. This need can be the consequence of requirements for higher load-carrying capacity of the structure, which can in turn be the result of either a problematic initial design or an improper manufacturing procedure or a change in the operational conditions. An additional very common reason for local repairs is the existence of local defects in the steel structure, like cracks, plastic deformations or corrosion. The basic objective of these local reinforcements and/or repairs is the increase of the structure's residual strength or the elongation of its operational life in cyclic loading. The use of composite materials patching is a very attractive alternative to the traditional reinforcement or repair methods (i.e. bolted doubler plates, welding), overcoming many of their limitations and disadvantages and being in many cases the only practically and economically feasible solution. Although there is a plethora of literature references dealing with composite patch reinforcements in aluminum aircraft structures, the reported composite patch applications in steel marine structures are very few, like those of Grabovac [1] and the QinetiQ team [2,3].

The aim of this paper is to investigate experimentally the efficiency of a carbon/epoxy composite patch for reinforcing a steel plate having a hole. The hole acts as a severe defect in the steel plate, resulting in the development of high stress concentrations. The geometry of the specimens is schematically shown in Fig. 1. The 4 mm thick steel plate has a 14 mm diameter central hole and is reinforced on one side by a 3.7 mm thick carbon/epoxy composite patch, having tapered ends in the longitudinal direction. The specimens are loaded in static tension.

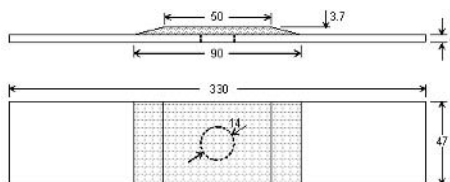


FIGURE 1. Geometry of the specimens tested.

Among the basic objectives of this work was to use low cost, easy to find composite materials and apply a conventional manufacturing method, that could be easily followed in the harsh marine environment of a ship by a non expert personnel. Thus, the patch is made of 12 layers of carbon epoxy twill 2x2 160 g/m<sup>2</sup> fabric, laminated directly on the steel plate using a common epoxy resin and the hand lay-up method. The steel is ordinary marine grade with an elevated yield stress of

348 MPa. Material characterization tests were performed in standard carbon/ epoxy coupons, resulting in a fiber ratio of 47.4%, a tensile modulus of 41.51 GPa and a tensile strength of 478 MPa. Thus, the resulting stiffness ratio of the patched specimens is equal to 0.2.

The main parameter investigated in the experimental program was the steel surface preparation method before laminating the patch. Thus, four different methods were studied, namely the use of a simple wire brush (WB), the use of blasting with aluminum oxide grit No. 60-80 (BAO), blasting with 1.2 mm diameter steel shots (BSS) and blasting with Nickel slags (BNS). Two similar specimens were tested for each case, plus reference hole drilled unpatched specimens (REF). Two sets of tests were performed, involving 6 specimens each. The first set was displacement controlled tests and involved two reference, two WB and two BAO specimens. The second set was force controlled tests and involved two reference, two BSS and two BNS specimens. Strains were measured at two locations on the steel plate, next to the hole and near the loaded edge and on the external surface of the carbon/epoxy patch.

In all cases the first failure appeared at the resin adhesive layer between the patch and the plate, when steel strains near the hole reached a value between 14500 and 17000  $\mu\epsilon$ , that is well into steel plasticity. As shown in Fig. 2, patched specimens exhibited a considerable increase of the applied load required for yielding, varying between 27 and 48%, whereas there is no clear effect of the surface preparation method on the results.

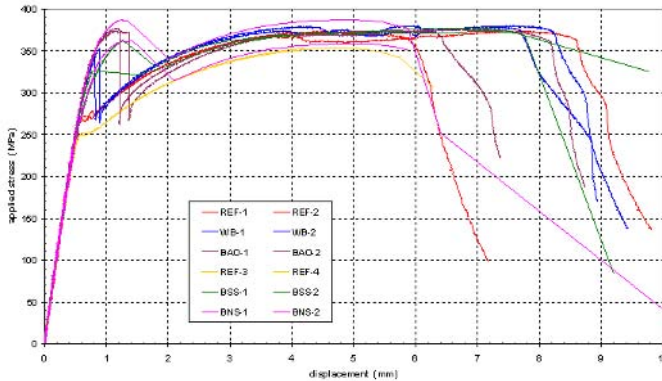


FIGURE 2. Applied stress versus longitudinal displacement for all specimens tested.

## References

1. Grabovac, I., *Composites Part A*, vol. **34**, 847-854, 2003.
2. Dalzel-Job, J., Sumpter, J.D.G. and Livingstone, F., In *Proceedings of Advanced Marine Materials: Technology and Applications*, RINA Conference, London, 2003.
3. Turton, T.J., Dalzel-Job, J. and Livingstone, F., *Composites Part A*, vol. **36**, 1066-1072, 2005.

## ITALIAN DESIGN GUIDELINES FOR THE STRUCTURAL STRENGTHENING WITH FRP MATERIALS

Luigi Ascione and Luciano Feo  
Department of Civil Engineering, University of Salerno  
Via Ponte Don Melillo, 84084 – Fisciano (SA), Italy  
l.ascione@unisa.it, l.feo@unisa.it

It is a common feeling, among those involved in research and design activities in the field of strengthening with fibre-reinforced composites, that Italy is getting a worldwide reputation, both for the value of its contribution in improving the knowledge in this field, as well as for the presence of a peculiar and important building heritage. This includes those of historical and architectural relevance as well as more recent masonry, reinforced concrete, prestressed concrete, timber and metallic structures. Most of the latter structures are now over 30 years old and in need of urgent structural remedial works.

The main international initiatives for the identification of design guidelines to address these needs are well known. It is worth mentioning the Japanese (JSCE – 1997 [1]), the American (ACI 440 – 2000 [2]) as well as the European guidelines (FIP-CEB – 2001[3]). All the aforementioned documents deal with structures made of reinforced concrete.

Both the scientific interest for the innovative use of fibre-reinforced polymers (FRP) in structural applications, as well as the peculiarity that the Italian building heritage, has attracted the attention of many researchers working in the fields of Structural Mechanics, Construction, Structural Strengthening, and Seismic Engineering. They have started a number of scientific programs funded by the most important Italian Research Centres, particularly by the Italian Ministry for University and Research (MUR) and the Italian National Research Council (CNR).

The CNR, through its Advisory Committee on Technical Recommendations for Constructions has promoted, both in the academic and industrial level, a special initiative of a number of professors of Structural Mechanics and Structural Analysis and Design involved in research activities on FRP.

The professors are: Luigi Ascione, Andrea Benedetti, Edoardo Cosenza, Angelo Di Tommaso, Ciro Faella, Luciano Feo, Antonio Grimaldi, Antonio La Tegola, Raimondo Luciano, Franco Maceri, Gaetano Manfredi, Giorgio Monti, Antonio Nanni, Renato Sante Olivito, Luciano Rosati, Elio Sacco, Marco Savoia, Enrico Spacone.

Nearly all the professors and researchers involved in this emerging and promising research field have taken part in this initiative, as well as the technical managers of major manufacturing and installation firms specialized in the strengthening with composites.

After less than two years of working activity, a series of guidelines for the design and construction of externally bonded FRP systems for strengthening existing structures, were issued by the CNR.

These documents are also conceived with an informative and educational spirit, which is crucial for the dissemination, in the professional sphere, of the mechanical and technological knowledge needed for an aware and competent use of such materials. They have also been prepared for informative and explanatory purposes to promote the mechanical and technological knowledge of FRP materials to professional and designers.



The documents are:

- CNR-DT 200/2004: Guide for the Design and Construction of Externally Bonded FRP Systems for Strengthening Existing Structures: materials, RC structures, prestressed RC structures, masonry structures;
- CNR-DT 201/2005: Guide for the Design and Construction of Externally Bonded FRP Systems for Strengthening Existing Timber Structures;
- CNR-DT 202/2005: Guide for the Design and Construction of Externally Bonded FRP Systems for Strengthening Existing Metallic Structures.

The aim of this paper is to contribute to their diffusion within the international scientific community, with particular attention to the one dedicated to RC structures.

## References

1. JSCE, Recommendation for design and construction of concrete structures using continuous fiber reinforcing materials, (1997).
2. ACI Committee 440, Guide for the design and construction of concrete reinforced with FRP bars, (2000).
3. CEB-FIP, Externally bonded FRP reinforcement for RC structures, (2001).
4. CNR-DT 200/2004, Guide for the Design and Construction of Externally Bonded FRP Systems for Strengthening Existing Structures: materials, RC structures, prestressed RC structures, masonry structures, (2004).
5. CNR-DT 201/2005, Guide for the Design and Construction of Externally Bonded FRP Systems for Strengthening Existing Timber Structures, (2005).
6. CNR-DT 202/2005, Guide for the Design and Construction of Externally Bonded FRP Systems for Strengthening Existing Metallic Structures, (2005).

Further references can be found in the bibliographies of the above mentioned CNR Documents, available on line:

7. [http://www.cnr.it/sitocnr/IICNR/Attivita/NormazioneeCertificazione/DT200\\_2004.html](http://www.cnr.it/sitocnr/IICNR/Attivita/NormazioneeCertificazione/DT200_2004.html).
8. [http://www.cnr.it/sitocnr/IICNR/Attivita/NormazioneeCertificazione/DT201\\_2005.html](http://www.cnr.it/sitocnr/IICNR/Attivita/NormazioneeCertificazione/DT201_2005.html).
9. [http://www.cnr.it/sitocnr/IICNR/Attivita/NormazioneeCertificazione/DT202\\_2005.html](http://www.cnr.it/sitocnr/IICNR/Attivita/NormazioneeCertificazione/DT202_2005.html)

## LABORATORY TESTS AND MECHANICAL MODELS FOR THE VALIDATION OF FRP REINFORCEMENT OF MASONRY STRUCTURES

Alessandro Baratta, Ileana Corbi and Ottavia Corbi  
Dept. Structural Mechanics, University of Naples Federico II  
Via Claudio 21, 80125 Napoli, Italy  
alessandro.baratta@unina.it, ileana.corbi@unina.it, ottavia.corbi@unina.it

A big spread out of researches linked to the adoption of composite materials, and, in particular, of Fibre Reinforced Polymers (FRPs), can be recorded in the field of rehabilitation and strengthening of the monumental heritage, usually made of masonry material: typical applications are structural adaptation or improvement of historical constructions for seismic purposes, structural reinforcement of masonry constructions, either for repairing already formed cracks or for preventing the formation of unilateral hinges that can result in the activation of collapse mechanisms in masonry patterns such as arches and vaults, or for reducing the stress in masonry panels, thus, increasing the loading capacity of the wall.

In the paper, in order to evaluate the benefits induced on traditional masonry structural typologies, such as arches or walls, by the application of carbon fibre strips, experimental tests are developed; all of these tests have been realized at the Laboratory of Materials and Structural Testing of the University of Naples "Federico II".

In details, on one side one considers models of masonry arches and, on the other side, laboratory prototypes of symmetrical masonry panels, made of tuff bricks, are analysed, with a central hole covered by a steel architrave.

Each typology is subject to its own weight and to a varying horizontal force, and many loading cycles are produced for the unconsolidated and consolidated case.

The adopted consolidation technique basically consists, as regards to portal arches, of gluing some FRP strips at strategic positions of the arcade, and, as concerns masonry walls, of enveloping the lower part of the masonry structure with mono-directional FRP strips.

Results are really encouraging, showing how a proper choice of the reinforcement can produce an high increase of the loading capacity of the structure.

### References

1. Heyman J.: The stone skeleton. *Journal of Solids and Structures*, vol. **2**, 269-279, 1966.
2. Baratta, A.: Structural Analysis of Masonry Buildings. In "Seismic Risk of Historic Centers. A Preliminary Approach to the Naples Case", A. Baratta and T. Colletta Eds., La Città del Sole B.C., Napoli, 76-122, 1996. ISBN88-86521-36-7.
3. Baratta A.: Il Materiale Non Reagente a Trazione Come Modello per il Calcolo delle Tensioni nelle Pareti Murarie. *Journal of "Restauro"*, vol. **75/76**, 53-77, 1984.
4. Baratta A., Corbi O.: No-Tension Masonry Model for FRP Reinforcement Assessment. In "Computer Methods in Structural Masonry", T.G.Hughes and G.N.Pande Ed.s, Computers & Geotechnics LTD 2001, Swansea. ISBN 0 9510380 2 8.
5. Baratta A., Corbi O.: Masonry Arches Refurbishment by Fibers Reinforced Polymers. *Proc. 3<sup>rd</sup> International Conference on Arch Bridges*, Parigi, 2001.

- 
6. El-Badry M.: Advanced Composite Materials Bridges and Structures. *Proc. 2<sup>nd</sup> Int. Conf. Advanced Composite Materials in Bridges and Structures*, Montréal, 1996.
  7. Traintafillou T.C.: Innovative Strengthening of Masonry Monuments with Composites. *Proc. 2<sup>nd</sup> Int. Conf. Advanced Composite Materials in Bridges and Structures*, Montréal, 1996.
  8. Schwegler G.: Masonry Construction Strengthened with Fiber Composites in Seismically Endangered Zones. *Proc. 10<sup>th</sup> Eur. Conf. Earthquake Engineering*, Vienna, 1994.

## ADHESION PROBLEMS BETWEEN FRP REINFORCEMENT AND MASONRY SUPPORT IN EXISTING BUILDING STRENGTHENING

Silvia Briccoli Bati, Luisa Rovero and Ugo Tonietti  
Dipartimento di Costruzioni, Università di Firenze, Italy  
Piazza Brunelleschi 6 - Firenze  
bricc@dicos.unifi.it, luisa.rovero@unifi.it, ugo.tonietti@unifi.it

The technique of bonding with composite materials having a polymeric matrix reinforced with long carbon fibers (CFRP) has become very widespread in the consolidation of masonry structural elements.

While on the one hand the potentials offered by this new technique, understood above all as an anti-seismic defense, are evident, on the other there are still aspects to be clarified. The correct use of composite materials as reinforcement for masonry structures is subordinated, in fact, to a knowledge of the mechanical behavior of the reinforced masonry system, with particular reference to the collapse modes that emerge due to a detachment of the reinforcement from the masonry support, since in this case the failure mechanism is a brittle one and should therefore be avoided.

The key factor characterizing the mechanical behavior of the CFRP masonry reinforcement is, therefore, the bond strength, i.e. the maximum load that can be transferred from the masonry to the composite material in order to avoid brittle collapse due to a loss of bonding.

In the literature, many research projects of an experimental and theoretical nature exist that study the bond between CFRP reinforcement and structural elements made of concrete. As far as the literature on masonry is concerned, there are many fewer experimental results available, and the theoretical models proposed are derived from ones determined from experimentation on concrete. The existing studies on masonry structural elements reinforced with CFRP have pointed out that the collapse mode is almost always determined by de-bonding of a thin layer of brick adjacent to the masonry-to-adhesive interface. This observation emphasizes the fact that the bonding capacity must thus depend significantly also on the resistance of the support.

Another important aspect revealed by these experiments is that an effective bond length exists beyond which no increase the collapse load.

In this paper, we report the results of an extensive experimental investigation aimed at studying the strength of the brick-CFRP bonding, using shear test on brick reinforced with CFRP (Carbon Fiber Reinforced Polymer) of varying dimensions.

The results made it possible to point out the influence played by the dimensions of the reinforcement sheet on the collapse load, ultimate slip, quality of the load-displacement diagram, and collapse modes. Lastly, identification of the local strains along the reinforcement sheet enabled us to formulate hypotheses regarding the local bond-slip relationship and then on the transfer mode of the stresses from the reinforcement to the brick.

### References

1. R.N. Swamy, R. Jones, A. Charif. *Shear adhesion properties of epoxy resin adhesives. Adhesion between polymers and concrete*, H.R. Sasse, ed., RILEM, Paris, 741-755, 1986.
2. D.J. Oehlers, J.P. Moran. Premature failure of externally plated reinforced concrete beams, *J Struct Div Am Soc Civil Engr.*, vol. **116(4)**, 978-995, 1990.

3. D.J. Oehlers, J.P. Moran, Premature failure of externally plated reinforced concrete beams, *J. Struct. Engrg.*, vol. **116(4)**, 978-995, 1990.
4. M.J. Chajes, W.W.Jr. Finch, T.F. Januszka, T.A.Jr. Thomson. Bond and force transfer of composite material plates bonded to concrete, *J. ACI Struct.*, vol. **93(2)**, 295-303, 1996.
5. B. Täljsten. Strengthening of concrete prisms using the plate-bonding technique, *Int J Fracture*, vol. **82**, 253-266, 1996.
6. L. Bizindavji, KW. Neale. Transfer lengths and bond strength for composites bonded to concrete, *J. Compos Construct*, vol. **3(4)**, 153-160, 1999.
7. MS. Mohamed Ali, DJ. Oehlers, MA. Bradford. Shear peeling of steel plates bonded to the tension faces of RC beams, *J Struct Eng ASCE*, vol. **127(12)**, 1453-1460, 2001.
8. L. De Lorenzis, B. Miller, A. Nanni Bond of fiber-reinforced polymer laminates to concrete, *ACI Mater J.*, vol. **98(3)**, 256-264, 2001.
9. JF. Chen, JG. Teng. Anchorage strength models for FRP and steel plates bonded to concrete, *J Struct Eng, ASCE*, vol. **127(7)**, 784-791, 2001.
10. ZS. Wu, H. Yuan, H. Niu. Stress transfer and fracture propagation in different kinds of adhesive joints, *J. Eng Mech. ASCE*. vol. **128(5)**, 562-573, 2002.
11. ST. Smith, JG. Teng. FRP-strengthened RC beams-I: review of debonding strength models, *Eng Struct.*, vol. **24(4)**, 385-395, 2002.
12. ST. Smith, JG. Teng. FRP-strengthened RC beams-II: assessment of debonding strength models, *Eng Struct.*, vol. **24(4)**, 397-417, 2002.
13. J. Yao, J.G. Teng, J.F. Chen. Experimental study on FRP-to-concrete bonded joints, *J. Composites. Part B: engineering, Elsevier*, vol. **XX**, 1-15, 2004.
14. H. Yuan, J.G. Teng, R. Seracino, Z.S. Wu, J. Yao. Full-range behavior of FRP-to-concrete bonded joints, *Eng Struct.*, vol. **26(59)**, 553-564, 2004.
15. A. Avorio, A. Borri. Problemi di collegamento tra Materiali FRP e strutture murarie [in Italian]. *Proceeding of national conference mechanics of masonry structures strengthened with FRP material*. Italy, Venezia, 2000.
16. M.A. Aiello, S.M. Sciolti. Bond analysis of masonry structures strengthened with CFRP sheets, *J. Construction and Building Materials, Elsevier*, vol. **20**, 90-100, 2006.
17. T. C. Triantafillou. Strengthening of masonry structures using epoxy-bonded FRP laminates, *J. Compos. for Constr., ASCE*, vol. **2(2)**, 96-104, 1998.
18. M. R. Valluzzi, M. Valdemarca, C. Modena. Behavior of Brick Masonry Vaults Strengthened by FRP Laminates, *J. Compos. for Constr. ASCE*, vol. **5(3)**, 163-169, 2001.
19. S. Briccoli Bati, L. Rovero. Experimental validation of a proposed numerical model for the FRP consolidation of masonry arches. *Proc. of III International Seminar on Structural Analysis of Historical Constructions*. Guimarães, Portugal, 2001.
20. S. Briccoli Bati, T. Rotunno, L. Rovero, U. Toniatti. Innovative techniques and materials for the reinforcement of historical buildings. *Proc. of IC-SGECT'04*, Mansoura, Egypt, 2004.

## QUALITY CONTROL AND MONITORING OF FRP APPLICATIONS TO MASONRY STRUCTURES

Renato S. Olivito and Francesca A. Zuccarello  
Department of Structural Engineering – University of Calabria  
Via Pietro Bucci, cubo 39B – 87036 Rende (CS), Italy  
rs.olivito@unical.it, francesca\_zuccarello@hotmail.com

During the last few decades, fibre-reinforced composite materials (FRP) have been utilised in many civil engineering applications. Their use in strengthening and restoring interventions on existing structures is greatly increasing due to their considerable strength/weight ratio and excellent corrosion resistance, as a consequence of the fact that conservation and restoration of the built heritage of past generations is becoming a key issue.

For this reason, huge scientific researches have been made by national and international engineering community for the safeguard of historical buildings. These have led to several research projects; in particular, CNR DT 200/2004 technical recommendations [1] for the design and construction of strengthening techniques with FRP systems have been published in Italy to provide an aid to designers interested in the field of composite materials and to avoid their incorrect application.

The Guidelines handle with different types of FRP applications to masonry and reinforced concrete structures and take into account quality control and monitoring phases that should follow a strengthening intervention. In fact, several aspects affect the effectiveness of FRP systems: above all, surface preparation and FRP installation are the most important ones. Moreover, once FRP strengthening has been carried out, monitoring by non-destructive or semi-destructive tests should be performed to assure the intervention quality and effectiveness (see Ascione *et al.* [2] and Bastianini *et al.*[3] for instance).

In the present work, semi-destructive and non-destructive techniques have been conducted for the quality control and monitoring of FRP applications to masonry structures, according to CNR DT 200/2004 Guidelines. Different types of FRP fabrics have been adopted: carbon fiber and glass fiber fabrics.

In particular, both pull-off tests and shear tearing tests have been performed on real brick and natural stone masonry buildings for the assessment of the properties of the restored surface and the quality of bond between FRP and masonry substrate, respectively. The test procedure is the following: after the substrate preparation by means of removal and reconstruction of any deteriorated masonry zone, cleaning of the surface and removal of possible vegetation plant or similar, and the execution of tests on the homogeneity of the structure to be strengthened, FRP fabric can be applied. Then, pull-off tests can be carried out attaching a steel plate to the FRP and pulling it off by means of an ad hoc device, as shown in Fig. 1.

Shear tearing tests may be carried out when it is possible to pull a portion of the FRP system in its plane close to an edge detached from the substrate.

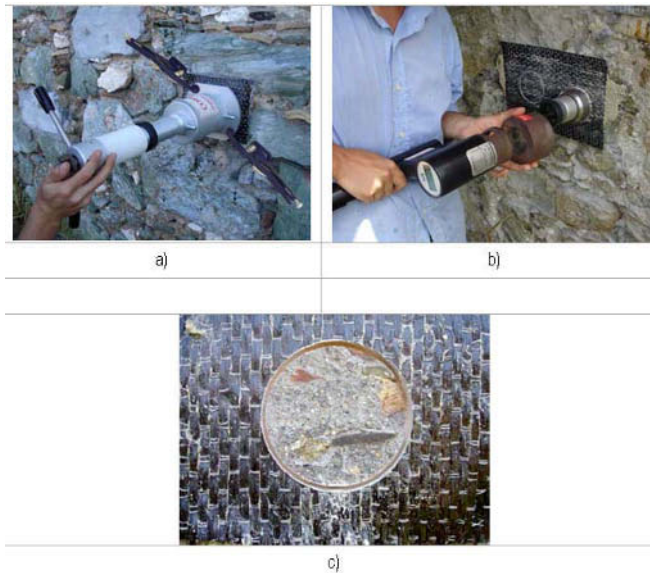


FIGURE 1. Pull-off test on a masonry building: a) FRP and substrate cutting; b) steel plate adhesion on FRP system; c) test result.

The semi-destructive test results were useful for the experimental validation of procedures, methods and theoretical relationships suggested in [1].

Moreover, non-destructive tests have been carried out to characterize the uniformity of FRP application by means of thermographic tests. These tests have been conducted on brick masonry macro-elements at University of Calabria and on real masonry structures, with the aim of detecting defects on the strengthening interventions used for the above mentioned semi-destructive tests. Artificial heating of the specimens has been used to obtain a uniform heating distribution on their surface, without reaching the glass transition temperature of FRP system. From the tests, thermographic pictures have been obtained, in some cases indicating the presence of air bubbles below the fabric or irregular substrate surface.

## References

1. CNR DT 200/2004, *Guide for the Design and Construction of Externally Bonded FRP Systems for Strengthening Existing Structures*, Rome, CNR July 13<sup>th</sup>, 2004.
2. Ascione, F., Feo, L., Olivito, R.S., Poggi, C., In *Proceedings of National Italian Conference "Ambiente e Processi Tecnologici – La certificazione di Qualità dei materiali e dei prodotti da costruzione"* (in italian), Naples, 20th April 2005.
3. Bastianini, F., Olivito, R.S., Pascale, G., Prota, A., *L'Edilizia*, vol. **139**, 66-71, 2005.

## EXPERIMENTAL INVESTIGATION ON DEBONDING BETWEEN MASONRY AND FRP

Christian Carloni<sup>a</sup>, Kolluru V. Subramaniam<sup>b</sup> and Lucio Nobile<sup>c</sup>

<sup>a,c</sup> DISTART, University of Bologna, Viale Risorgimento 2, 40136 Bologna, Italy

<sup>b</sup> Dept. Civil Engineering, The City College of the City University of New York (CUNY), New York, NY 10031, USA

<sup>a</sup> christian.carloni@mail.ing.unibo.it, <sup>b</sup> ksubram@ce.engr.cuny.cuny.edu,

<sup>c</sup> lucio.nobile@mail.ing.unibo.it

The increasing use of carbon fiber reinforced polymer (CFRP) sheets for strengthening existing reinforced concrete beams has generated considerable research interest in understanding the debonding mechanism of failure in such systems. Less attention has been paid on the application of the FRP technology to masonry structures and specifically in the case of restoration of historical monuments and buildings. Since this technique is, in many cases, not invasive, easy to apply and free from corrosion, its application has been extended to preserve historical buildings.

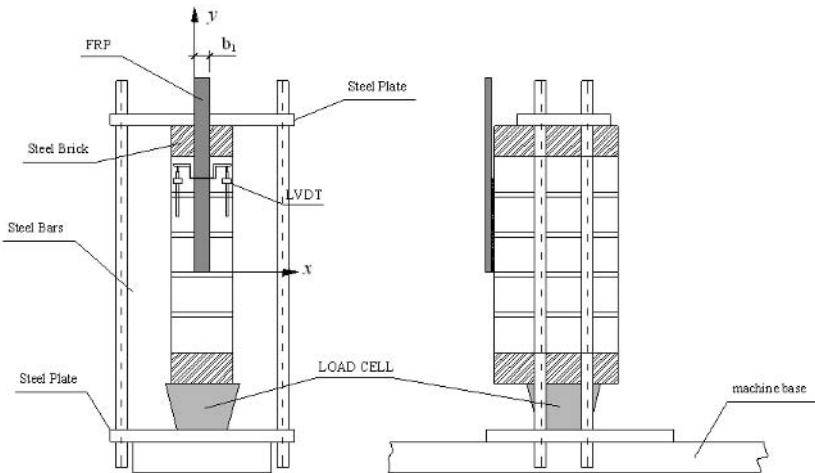


FIGURE 1. Test setup

The effectiveness of such strengthening depends upon the load transfer from FRP composite to the substrate. Shear debonding is usually caused by a crack that forms and then propagates at the interface between the adherents [1-7]. Referring to masonry, the shear debonding has not been studied completely and the effect of the mortar joints can be further investigated [8].

In this paper, an experimental investigation into the shear debonding of FRP sheets from masonry blocks is reported. The FRP sheet was bonded in the center on one side of the masonry specimen. Direct shear tests were used using the classical pull-push configuration. In a typical test, the tensile load is applied to the FRP composite, while the masonry is restrained against



movement. The masonry specimen consisted of five bricks and 4 mortar joints. Previously, shear tests has been carried out on mortar blocks and bricks and the cohesive laws [9,10] have been obtained, respectively. After that, the shear test has been carried out on masonry. Masonry specimens were first preloaded in compression and maintained in compression by means of two steel plates. The compression load has been monitored through a cell load inserted between the steel plates up to the shear test. The system, consisting of masonry specimen, steel plates and load cell, was then bolted to the machine base. Prior to running the shear test, the creep has been studied to evaluate the compression load. The FRP strip was bonded after the specimen has prestressed. During each test, spatially continuous measurements of the surface displacements on the FRP and concrete are obtained using an optical technique known as digital image correlation [11]. The load carrying capacity is related to the compression in masonry. The strain along the FRP length has been analysed. It shows a drop corresponding to the mortar joint. The length of the stress transfer zone is derived and compared to the one obtained with FRP/concrete interface debonding. Moreover, a simple model to be taken into account for the effect of the mortar joints, based on the experimental results, is proposed.

## References

1. Wu, Z., Matsuzaki, T. and Tanabe, K., *Japan Concrete Institute*, 1:319-326, 1997.
2. Buyukozturk, O., Gunes and O., Karaca, E., *Construction and Building Materials*, vol. **18**, 9-19, 2004.
3. Leung, C.K.Y., *Journal of Materials in Civil Engineering, ASCE*, vol. **13**(2), 106-113, 2001.
4. Meier, U., Deuring, Meier, H. and Schuregler, G., In *Proceedings 1st International Conference on Advanced Composite Materials in Bridges and Structures, The Canadian Society for Civil Engineering*, Montreal (Canada), 1992, 243-251.
5. Triantafillou, T.C and Pelvris, N., *Material and Structures*, Paris, vol. **25**(149), 201-211, 1992.
6. Buyukozturk, O. and Hearing, B., *Journal of Composites for Construction*, vol. **2**(3), 138-144, 1998.
7. Teng, J.G., Smith, S.T., Yao, J. and Chen J.F., *Construction and Building Materials*, vol. **17**, 447-462, 2003.
8. Aiello, M.A. and Sciolti, S.M., *Construction and Building Materials*, vol. **20**, 90-100, 2006.
9. Carloni, C., Ali-Ahmad, M. and Subramaniam, K., In *Proceedings of the 7th International Conference on Mesomechanics, Montreal*, August 1-4, 2005, 37-42.
10. Ali-Ahmad, M., Subramaniam, K.V., and Ghosn, M.. *Journal of Engineering Mechanics, ASCE*, vol. **132**, 914-923, 2006.
11. Sutton, M.A., Wolters, W.J., Peters, W.H., Ranson, W.F., and McNeill, S.R., *Image and vision Computing*, vol. **1**, 133-139, 1983.

## FRP WIDTH EFFECT ON SHEAR DEBONDING FROM CONCRETE

Kolluru V. Subramaniam<sup>a</sup>, Christian Carloni<sup>b</sup> and Lucio Nobile<sup>c</sup>

<sup>a</sup> Dept. Civil Engineering, The City College of the City University of New York (CUNY), New York, NY 10031, USA

<sup>b,c</sup> DISTART, University of Bologna, Viale Risorgimento 2, 40136 Bologna, Italy

<sup>a</sup> ksubram@ce.engr.cuny.cuny.edu, <sup>b</sup> christian.carloni@mail.ing.unibo.it,

<sup>c</sup> lucio.nobile@mail.ing.unibo.it

Fiber reinforced polymer (FRP) sheets have been extensively used for increasing the stiffness and load carrying capacity of existing concrete structures. The FRP sheets are basically used as supplementary tensile reinforcement. Tensile stresses are produced in the FRP due to stresses transferred through the interfacial bond between the concrete and the FRP.

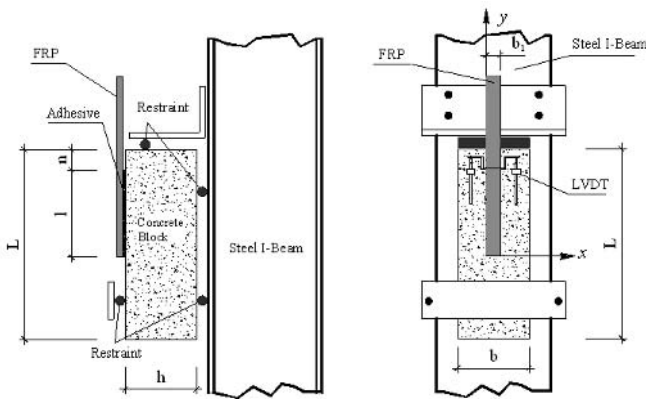


FIGURE 1. Test setup

When the FRP bridges a crack in the concrete, the sharp discontinuity at the edge of the crack introduces a stress concentration along the FRP-concrete interface. The high stresses and stress gradients result in the initiation of debonding in the vicinity of the crack [1,2,3]. Debonding has been shown to be produced by an interface crack which initiates and propagates in the interface region comprising of the surface layer of concrete where the epoxy impregnates the concrete. The debonding mechanism has been shown to be one of the most important causes of inefficiency of the repair and considerable attention has been paid to this problem [2,4,5,6,7]. It is generally acknowledged that the geometric variables such as the length and the width of the FRP laminate sheet have a significant influence on the debonding load [8,9,10,11,12]. It has been shown that the ultimate nominal stress for debonding increases with an increase in the bonded length, up to a critical bond length. An increase in the bonded length beyond the critical bond length does not produce any increase in the ultimate stress. Less attention has been paid to the scaling in the ultimate load with the width of the FRP [10,11,12].

An experimental investigation into the influence of the width of the FRP sheet on the load carrying capacity of a given FRP-concrete interface is reported in this paper. The load carrying capacity refers to the nominal stress in the FRP at debonding. The primary focus of this study is to understand the dependence of the load-carrying capacity on the FRP laminate width. Direct shear tests (Fig. 1) were performed using FRP composite sheets of varying widths attached to concrete blocks. A fixed bond length which is greater than the critical bond length was used for all specimens. The contribution of the two factors, the boundary effect and the restraint from the surrounding concrete, was studied from the measured strain distribution. It is shown that a region of constant width associated with high shear strains is found at the edge of the FRP sheet during the entire debonding process. The presence of the edge effect primarily contributes to the observed increase in the load carrying capacity with an increase in the width of the FRP.

## References

1. Wu, Z., Matsuzaki, T. and Tanabe, K., *Japan Concrete Institute*, 1:319-326, 1997.
2. Buyukozturk, O., Gunes and O., Karaca, E., *Construction and Building Materials*, vol. **18**, 9-19, 2004.
3. Leung, C.K.Y., *Journal of Materials in Civil Engineering, ASCE*, vol. **13**(2), 106-113, 2001.
4. Meier, U., Deuring, Meier, H. and Schuregler, G., In *Proceedings 1st International Conference on Advanced Composite Materials in Bridges and Structures, The Canadian Society for Civil Engineering*, Montreal (Canada), 1992, 243-251.
5. Triantafillou, T.C and Pelvis, N., *Material and Structures*, Paris, vol. **25**(149), 201-211, 1992.
6. Buyukozturk, O. and Hearing, B., *Journal of Composites for Construction*, vol. **2**(3), 138-144, 1998.
7. Teng, J.G., Smith, S.T., Yao, J. and Chen J.F., *Construction and Building Materials*, vol. **17**, 447-462, 2003.
8. Lu, X.Z., Teng, J.G., Ye, L.P., and Jiang, J.J., *Engineering Structures*, vol. **27**, 920-937, 2005.
9. Taljsten, B., *International Journal of Adhesion and Adhesives*, vol. **17**(4), 319-327, 1997.
10. Ueda, T., Sato, Y., and Asano, Y., In *Proceedings, 4th Int. Symposium on Fiber Reinforced Polymer for Reinforced Concrete Structures, American Concrete Institute (SP-188)*, Detroit, Mich., 1999, 407-416.
11. Kamel, A. S., Elwi, A.A. and Cheng, R.J., *Emirates Journal for Engineering Research*, vol. **9**(2), 71-76, 2004.
12. Carloni, C., Ali-Ahmad, M. and Subramaniam, K., In *Proceedings of the 7th International Conference on Mesomechanics, Montreal*, August 1-4, 2005, 37-42.

## ADVANCED COMPOSITES FOR RETROFIT OF HISTORICAL MASONRY STRUCTURES: DYNAMIC TESTS AND COMPARATIVE ASSESSMENT

Gaetano Manfredi and Andrea Prota  
Dept. of Structural Analysis and Design, University of Naples Federico II  
Via Claudio, 21 – 80125 – Naples, Italy  
gamanfre@unina.it; aprota@unina.it

Within the framework of project TE.M.P.E.S. two 1:2 scaled models of the typical tuff masonry buildings have been constructed and tested on the seismic simulation shaking table located in the structural laboratory of CESI, Bergamo, Italy. The two as-built prototypes were tested and damaged at increasing intensity level up to a significant damage was observed, after they were repaired by means of two different techniques based on innovative materials. According to the scaling rules, the prototypes have been constructed with plane dimensions of 2.60 m x 2.85 m; they were characterised by two stories with total height of 3.20 m. Thickness of the three-leaf walls was equal to 0.30 m. The three-leaf type of masonry is typical of many structures in Europe and in the Mediterranean area, and is locally known as “a sacco”; it is characterised by two external layers of masonry blocks (0.10 m thick) and an inner core (0.10 m thick) made of chopped tuff mixed to mortar. FIGURE 1. View of the three-leaf (“a sacco”) walls during construction and as-built prototype1 shows a three-leaf wall during construction. Each of the two weak walls of the prototype were characterized by two 0.70 m x 1.20 m doors at first storey and two 0.70 m x 0.70 m windows at second storey, while the other two perpendicular walls had one 0.70 m x 0.70 m window at each storey (Fig. 1). The two wooden floors were realised by 0.10 m x 0.15 m wooden beams on which a wooden ply was nailed. For one of the two models, a 0.30 m x 0.20 m Reinforced Concrete (RC) riddle was designed at both levels in order to assure an effective connection between the four sides. This detail was not realized in the second model for which the connection of the four sides was assured by means of composite bars.



FIGURE 1. View of the three-leaf (“a sacco”) walls during construction and as-built prototype

In order to perform a fast repair, typically needed for a building that has been damaged by an earthquake and occupants safety has to be immediately assured with respect to risks related to potential aftershocks, the selected technique was based on the use of Glass FRP laminates. A view of the GFRP repaired model is shown in Fig. 2. The second model was repaired using a system based on a GFRP grid bonded with a cementitious mortar. The advantages of this system can be

summarized as follows: matrix less sensitive to fire and high temperature compared to epoxy resin; matrix compatible with a humid substrate typical of natural masonry; lower cost compared to epoxy bonded FRP; possibility to compensate irregular substrate by varying the thickness of the first layer of mortar. FIGURE 2. Prototypes repaired with GFRP laminates (right) and GFRP grid bonded with cementitious mortar (left) shows the second prototype during installation of the GFRP grid bonded with cementitious matrix.



FIGURE 2. Prototypes repaired with GFRP laminates (right) and GFRP grid bonded with cementitious mortar (left)

The paper summarizes the main outcomes of the dynamic tests performed on both prototypes discussing the influence of each retrofit solution on the behavior of the models in terms of damage, energy dissipation, strength and displacements. A comparative analysis between the tested techniques is proposed with the aim of supporting the structural engineer in a wise selection of the most appropriate technique based on original conditions of the structure, outcomes of the structural assessment and objectives of the retrofit intervention.

## APPLICATIONS OF THE EMPIRICAL MODE DECOMPOSITION METHOD IN SPECKLE METROLOGY

María B. Bernini<sup>1</sup>, Gustavo E. Galizzi<sup>2</sup>, Alejandro Federico<sup>3</sup> and Guillermo H. Kaufmann<sup>4</sup>

<sup>1</sup>Instituto de Física Rosario (CONICET – UNR)

Blvd. 27 de Febrero 210 bis, S2000EZP Rosario, Argentina

<sup>2</sup>Instituto de Física Rosario (CONICET – UNR)

Blvd. 27 de Febrero 210 bis, S2000EZP Rosario, Argentina

<sup>3</sup>Electrónica e Informática, Instituto Nacional de Tecnología Industrial

P.O. Box B1650WAB, B1650KNA San Martín, Argentina

<sup>4</sup>Instituto de Física Rosario (CONICET – UNR)

Blvd. 27 de Febrero 210 bis, S2000EZP Rosario, Argentina

guille@ifir.edu.ar

In the last decade, Huang *et al.* [1] presented a non-linear method called Empirical Mode Decomposition (EMD) for adaptively representing a non-stationary signal as a sum of zero-mean well-behaved fast and slow oscillation empirical modes, which are known as Intrinsic Mode Functions (IMFs). An IMF is a function that satisfies two conditions: (1) in the whole data set, the number of extrema and the number of zero crossings must be either equal or differ at most by one; (2) at any point, the mean values of the envelopes defined by the local maxima and minima are zero. This decomposition is carried out through a sifting algorithm that generates a fully data-driven method, so that no basis functions are fixed in the analysis process. Therefore, the frequency discrimination does not correspond to a predetermined sub-band filtering and the mode selection corresponds to an automatic and adaptive filtering. Consequently, the evaluation of the performance of the EMD method in a given field must be analysed by means of numerical analysis. In addition, the sifting process facilitates the application of the Hilbert transform to each IMF, so that it can be associated to an instantaneous amplitude and frequency obtained by means of the implementation of its analytic signal.

This paper shows the application of the EMD method to the reduction of speckle noise in digital speckle pattern interferometry (DSPI) fringes and to the analysis of the activity of dynamic speckle.

The removal of speckle noise in DSPI is a complex problem which has generated an active area of research. Various methods have been applied to reduce speckle noise, although they were only partially successful. We propose a novel denoising approach based on the EMD method, consisting in the one-dimensional decomposition of the DSPI image along four different directions and the manipulation of the obtained fast oscillation modes. Then, the resulting images are averaged to compute the final filtered fringe pattern. The effectiveness and limitations of the presented EMD-based denoising technique are evaluated using computer simulated DSPI images presenting different fringe densities and average speckle sizes. To quantify the performance of this novel approach to remove speckle noise, two figures of merit were calculated: the image fidelity that quantifies how good image details are preserved after noise removal and the speckle index that evaluates the local smoothness of the filtered fringe patterns. These results are compared with those obtained using a wavelet-based noise reduction approach. Additionally, the application of the EMD method to smooth experimental DSPI fringe patterns is also presented.

Dynamic speckle is the phenomenon generated by the interference between the coherent optical fields from a large numbers of scattering centres that present some type of activity [4]. This

phenomenon can be due to the random movement of the scattering centres and also to other more complex phenomena present in the sample. As these phenomena are quite difficult to be characterised, the evaluation of the speckle activity can be used as a useful approach to understand the processes produced in the sample. Dynamic speckle can be used to study several industrial processes such as steel corrosion and paint drying, as well as some biological phenomena such as fruit bruising and seed viability. Using an appropriate optical setup with very low experimental complexity, it is possible to segment the regions of the sample that present different speckle activities by processing the intensity of the scattered light [5].

In this work, the EMD method was used to analyse temporal sequences of dynamic speckle patterns recorded from a fruit bruising experiment in order to find different activity levels of the sample and also to characterise them in the time–frequency plane. The EMD method was applied to the intensity signal along the time axis for each pixel of the sequence of dynamic speckle patterns. Thus, each IMF is a 3D array where two coordinates are associated with the analysed pixel of the speckle pattern and the third coordinate corresponds to the temporal axis. The analysis of the whole data sequence for each pixel allows the segmentation of areas with different activity levels. Additionally, the analysis of the intensity signal corresponding to pixels from regions with different activities depicts the dissimilar temporal dependence of the speckle activity in those areas. These results are compared with those obtained through the application of frequency filter banks [6].

## References

1. Huang, N. E., Shen, Z., Long, S. R., Wu, M. C., Shih, H. H., Zheng, Q., Yen, N. C., Tung, C. C. and Liu, H. H., *Proc. Roy. Soc. London A*, vol. **454**, 903-995, 1998.
2. Davila, A., Kaufmann, G. H. and Kerr, D., *J. Mod. Opt.*, vol. **42**, 1795-1804, 1995.
3. Federico, A. and Kaufmann, G., H., *Opt. Eng.*, vol. **40**, 2598-2604, 2001.
4. Aizu, Y. and Asakura, T., *Opt. Laser Technol.*, vol **23**, 205-219, 1991.
5. Pajuelo, M., Baldwin, G., Rabal, H., Cap, N., Arizaga, R. and Trivi, M., *Opt. Laser Eng.*, vol. **40**, 13-24, 2003.
6. Sendra, G. H., Arizaga, R., Rabal, H. and Trivi, M., *Opt. Lett.*, vol **30**, 1641-1644, 2005.

## FLAW DETECTION ENHANCEMENT IN LOCKIN TEMPORAL SPECKLE INTERFEROMETRY USING THERMAL WAVES

A.E. Dolinko and G.H. Kaufmann

Instituto de Física Rosario (UNR-CONICET)

Blvd. 27 de Febrero 210 bis, S2000EZP Rosario, Argentina

dolinko@ifir.edu.ar, guille@ifir.edu.ar

The detection of internal defects using digital speckle pattern interferometry (TSPI) combined with thermal loading has generated great interest in the field of non-destructive testing. Recently, Kaufmann *et al* have shown that the technique called temporal speckle pattern interferometry can be used to visualise time-dependent deformations generated by long thermal waves [1,2]. By testing thin aluminium plates containing flat-bottomed holes with different depths, it was demonstrated that the use in TPSI of thermal waves rather than unmodulated heating improves the defect detectability.

In the present work, flawed aluminium specimens were stressed using a periodically modulated heat source that locally heated its surface at a frequency of approximately 0.2 Hz. Simultaneously, a set of several hundreds of speckle interferograms were continuously recorded by means of a digital camera at a rate of 100 Hz with temporal phase shifting carried out by a Pockels cell synchronized with it. Temporal phase unwrapping through the whole sequences of frames enabled the determination of out of plane absolute displacement maps as a function of time.

The specimens used in the experiments were circular aluminium plates clamped along their edges. In each specimen, four defects were milled in the form of flat-bottomed slots with different depths. The back surface of each specimen was painted black to increase thermal absorbtivity and was heated with an IR lamp. The radiation emitted by the lamp passed through a rotating chopper driven by a variable speed motor to modulate the heat received by the specimen.

A lockin approach based in a modification of the technique proposed by Gerhard and Busse [3] was implemented. It consists basically in the modulation of the heat source along time following a triangular waveform. This modulation will be manifested in the measured displacements along time. The method is based in the calculation of the Fourier transform of the temporal history of each pixel. Afterwards, the complex value of each resonant mode of the resulting spectrum was selected and these values were added up.

It was demonstrated that as a consequence of the application of this approach, the detectability of flaws in metal plates was enhanced. The hypothesis behind this method is that the plate behaves like a low pass filter for the thermal wave travelling along the plate thickness. A defect can be considered as a region where the transfer function of the filter varies. Considering the whole set of modes, from the fundamental to the highest frequency mode measurable, it is possible to obtain a better characterization of the response of the plate to the thermal wave.

In order to quantify the quality of the detection achieved by this approach, a coefficient which allows to compare the level of detectability in the phase images that were generated using different methods was utilised. This coefficient ranges from 1 to 10, where a value of 1 corresponds to null detection and 10 for the maximum detectability. It is shown that the application of the lockin approach produces a value of this coefficient which is approximately two times higher than the one determined when it is not used. Fig. 1(a) shows the phase image obtained using the lockin method, where the defects are indicated by 1, 2, 3 and 4. The corresponding contour plot for the image shown in Fig. 1(a) is displayed in Fig. 1(b).



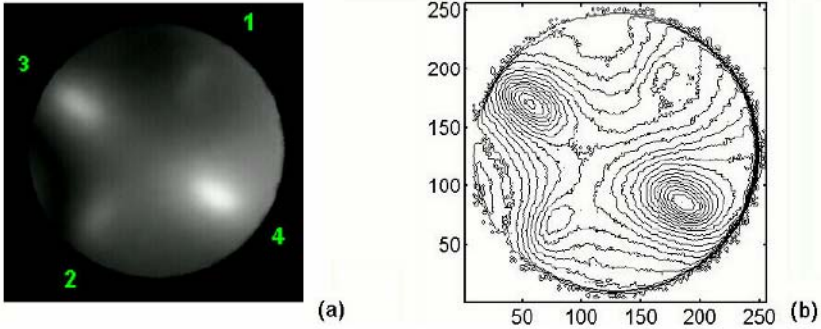


FIGURE 1. (a) Phase image obtained with the lockin method. (b) Contour plot corresponding to the same image.

Hidden flaws imaged by means of the lockin method appear to be more selectively detected in comparison to the images extracted from the displacement fields generated by the thermal waves measured directly. In addition, the resulting images have a constant background and the magnitude of the intensity of the displayed defects agrees quite well with their depths.

## References

1. Kaufmann, G.H., *Opt. Eng.*, vol. **42**, 2010-2014, 2003.
2. Kaufmann, G.H., Viotti, M.R. and Galizzi, G.E., *J. Holography Speckle*, vol. **1**, 1-5, 2005.
3. Gerhard, H. and Busse, G., In *Advances in Signal Processing for Nondestructive Evaluation of Materials V*, edited by X. Maldague, E. du CAO, Québec, 2006, 57-67.

## THE SPATIAL STRUCTURES OF PSEUDOPHASE SINGULARITIES IN THE ANALYTIC SIGNAL REPRESENTATION OF A SPECKLE PATTERN AND THEIR APPLICATION TO BIOLOGICAL KINEMATIC ANALYSIS

Wei Wang<sup>1</sup>, Yu Qiao<sup>2</sup>, Reika Ishijima<sup>1</sup>, Tomoaki Yokozeki<sup>1</sup>, Daigo Honda<sup>1</sup>, Akihiro Matsuda<sup>1</sup>,  
Steen G. Hanson<sup>3</sup> and Mitsuo Takeda<sup>1</sup>

<sup>1</sup> Department of Information and Communication Engineering, The University of Electro-Communications, 1-5-1, Chofugaoka, Chofu, Tokyo, 182-8585, Japan.

<sup>2</sup> Department of Information Management Science, The University of Electro-Communications

<sup>3</sup> Optics and Plasma Research Department, Risoe National Laboratory, Denmark.  
weiwang@ice.ucc.ac.jp

Over the past decades, optical vortices or phase singularities have come to attract more and more attentions in the fields of applications such as optical metrology and photon manipulation. Recently, we proposed a new technique of micro-displacement measurement, called *Optical Vortex Metrology* (OVM) [1-2]. The key idea of this technique is to make use of the phase singularities in the pseudophase information of the complex analytic signal obtained from partial Hilbert transform, Riesz transform or Laguerre-Gauss transform of speckle patterns. Although we have experimentally demonstrated the validity of the proposed OVM in displacement measurement with both large dynamic range and high spatial resolution, the application of the proposed technique was restricted because the distortions of the morphology for the phase singularities stemming from speckle decorrelation enhance the difficulty in the unique search and identification of the registered marker phase singularity for calculation of their coordinate difference. In this paper, we propose a new technique that substantially improves the OVM technique in its ability of uniquely identifying the matching phase singularities under large distortions. In addition to the information about the location and the core structures of the phase singularities, we also detect the spatial structures of a group of the pseudophase singularities. This spatial structure can serve as a “constellation” that uniquely characterizes the mutual position relation between the individual phase singularities, and can be used for the purpose of the unique identification of a cluster of the phase singularities. Experimental results have been demonstrated that support the proposed principle.

Instead of directly correlating the raw speckle intensity distribution  $I(x, y)$  used in conventional speckle metrology, we first generate the complex signal representation  $\tilde{I}(x, y)$  by a Laguerre-Gauss filtering [2], and detect the positions and the core structures of the pseudophase singularities through the interpolated real and imaginary parts of  $\tilde{I}$ . When observed with focus on the object surface, the movement of the phase singularity constellation can be directly related to the movement of the object surface. The schematic diagram for the proposed technique based on the phase singularity constellation has been shown in Fig. 1. After identifying corresponding phase singularities before and after displacement making use of their spatial configuration and core structures as fingerprints, we can decompose the complicated movement of an object into translation  $(\Delta x, \Delta y)$ , rotation  $\phi$  and scaling  $\alpha$  by tracing the movements of the phase singularities.

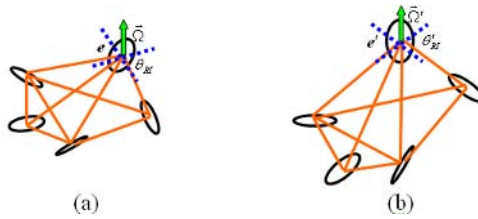


FIGURE 1. Schematic diagram for the proposed technique based on the constellation of pseudophase singularities. (a) Before movement; (b) After movement.

Experiments have been conducted to demonstrate the validity of the proposed principle. We recorded the swimming of a fish by a fast camera (FASTCAM-NET) the frame rate 30 frames per second. For every sequential two frames, we generated the complex signals by Laguerre-Gauss filtering, retrieved the pseudophase information, and analyzed the fish movement based on the phase singularity constellation. Figs 2(a)-(d) show the examples of the recorded fish movements and the corresponding phase singularities. As shown in Fig. 2(e) for fish swimming decomposition, the translation has a typical periodical movement with average frequency around 5 hertz, which was introduced by fish fin to provide the internal force. Meanwhile, a large rotation and a slight depth change in the water can also be observed for this fish. Therefore, figure 2 demonstrate the validity of the proposed technique for biological kinematic analysis.

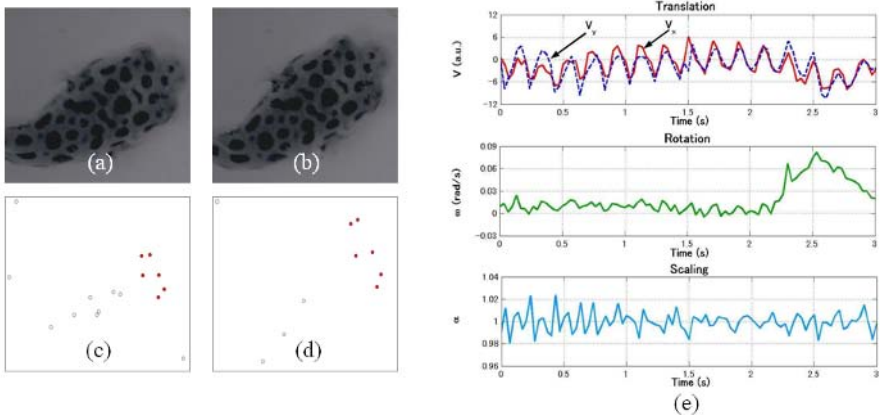


FIGURE 2. Recorded fish movements, the corresponding phase singularities and movement decomposition. (a),(c): Before movement; (b),(d) After movement.

## References

1. Wang, W., Yokozeki, T., Ishijima, R., Wada, A., Miyamoto, Y., Hanson, S. G. and Takeda, M., *Opt. Express*, vol. **14**, 120-127, 2006.
2. Wang, W., Yokozeki, T., Ishijima, R., Hanson, S. G. and Takeda, M., In *Proc. of SPIE*, Vol. 6292, edited by K. Creath, J. Schmit, 2006, 62920X-1:8.

## A NEW FAMILY OF SPECKLE INTERFEROMETERS

Luigi Bruno, Andrea Poggialini and Orlando Russo  
 Department of Mechanical Engineering – University of Calabria  
 Via P. Bucci CUBO 44C – 87036 Arcavacata di Rende (CS), Italy  
 bruno@unical.it - poggialini@unical.it - orlando.russo@gmail.com

Despite the variety of speckle interferometric setups dedicated to the detection of mechanical deformations which have been reported in the literature since the early 70's, sometimes with various misleading acronyms, the operating principle of speckle interferometry has been till now essentially applied by two basically different approaches.

The first one utilizes an external reference beam (Ennos *et al.* [1]), smooth or speckled, which is superimposed to the speckle pattern generated by the object surface and focused by the imaging system on a spatial light sensor device (at the present state of the art: a CCD or a CMOS sensor). The external reference beam can actually be superimposed to the object beam by a beam-splitter located between the lens and the light sensor or, alternatively, between the object and the lens (see Fig. 1). Alternatively it can also be fed by a mirror (a prism or an optical fibre – renouncing to a portion of the aperture of the focusing system). In any case, when assembling an externally referenced speckle interferometer, the most important thing is to ensure that both the imaging wavefront and the reference wavefront possess the same average curvature. The component of displacement detected by this family of speckle interferometer is exactly the same of that one given by holographic interferometry, that is the component along the bisector of the angle between the illumination and the observation directions.

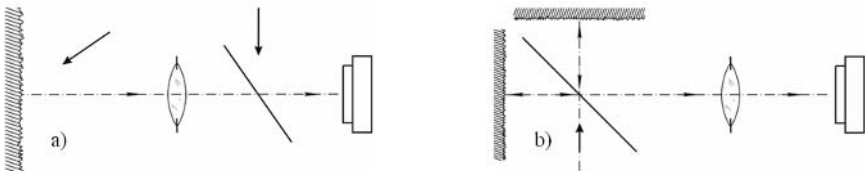


FIGURE 1. Interferometer with external reference beam obtained by a beam-splitter located between the lens and a) the light sensor, b) the object.

The second approach permits to develop self-referenced speckle interferometers which do not require the feeding of an external reference beam. The two families of speckle interferometers following this approach and which have been till now reported in the scientific literature, rely, essentially on the “double-illumination” (Leendertz [2]) and the “double-image” (Hung [3]) principle (see Fig. 2).

The double-illumination speckle interferometers detect the component of displacement lying on the plane defined by the two illuminating directions and normal to their bisector, with no dependency from the observation direction. This family of speckle interferometers is mainly devoted to the detection of in-plane or near in-plane displacement components; for the detection of in plane components it is required that the illuminating directions form equal angles with the normal to the object surface (preferably coinciding with the observation direction). The sensitivity

depends on the incident angle of the illuminating directions and it is exactly the same as it can be achieved by moiré interferometry when adopting the same setup governing angles.

The double-image speckle interferometers actually perform an optical (and thus approximated) differentiation of the component of displacement along the bisector of the illumination and observation directions (the same component detected by holographic interferometry). The approximation (and the sensitivity) depends on the amount of shear applied between the two images of the object. This family of speckle interferometers is mainly devoted to the detection of the rotations of the normal to the object surface; for the detection of rotations (that is the derivative of the out of plane displacement components) it is required that the illumination and observation directions form equal angles with the normal to the object surface.

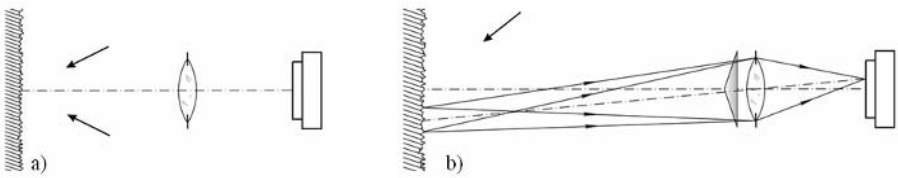


FIGURE 2. Self-referenced interferometer based on a) double-illumination and b) double-image principle.

These two families of speckle interferometers, compared with the externally referenced family, permit to assemble more simple and compact devices but none of them is capable of furnishing directly the out-of-plane component of displacement. Both of them can anyway assure, in a simple way, quite low optical path differences for the whole inspected area, thus permitting to utilize low-coherence diode lasers.

The present paper reports a completely new family of speckle interferometers which rely on a quite different operating principle. This family of speckle interferometers is capable of detecting the same component of displacement of that one given by holographic interferometry, that is the component along the bisector of the angle identified by the illumination and the observation directions, but with no need of an external reference beam. The only requisite actually necessary to the well functioning of the speckle interferometer, is that only a portion of the illuminated area undergoes a sensible deformation. The operating principle of this new type of speckle interferometer can be indifferently implemented by adopting a Michelson or a Mach-Zender configuration. By using the proper optic components the interferometer can also be balanced so to make feasible the utilization of a short coherence diode lasers. Alternatively a single diffractive element (i.e. a grating or a spatial light modulator) on line with the focusing lens can be used.

## References

1. Ennos, A.E., Burch, J.M., Archbold, E. and Taylor, P.A., *Nature*, vol. **222**, 263-265, 1969.
2. Leendertz, J.A., *J. Phys E: Sci. Instrum.*, vol. **3**, 214-218, 1970.
3. Hung, Y.Y., *J. Nondestructive Testing*, vol. **8** (2), 55-67, 1989.

## ANALYSIS OF DSPI FRINGE PATTERNS ISSUED FROM TRANSITORY MECHANICAL LOADINGS

V. Valle<sup>1</sup>, E. Robin<sup>2</sup> and F. Brémand<sup>1a</sup>

<sup>1</sup>LMS, UMR 6610, SP2MI, Bd P&M Curie, BP30179, 86962 FUTUROSCOPE Cedex, France

<sup>2</sup>LARMAUR, FRE-CNRS 2717, PPT - Bât 10B - Camp Beaulieu, 35042 Rennes Cedex, France  
valle@lms.univ-poitiers.fr, robin@lms.univ-poitiers.fr, bremand@lms.univ-poitiers.fr

The aim of this paper concerns the development of a phase demodulation technique from a single fringe pattern, which is applied in the case of a DSPI measurement method used during transitory mechanical loadings. Actually, DSPI method is employed for the measurement in dynamics for repetitive mechanical loading, because the extraction of the measured parameter is obtained with the help of a phase shifting (or phase stepping) technique which necessitates a minimum of 3 shifted fringe patterns of the same loading state [1]. This is achieved by storing the images of each phase shift at a same loading value but at different cycle of it.

During a transitory dynamic event, we can not use a phase shifting technique because the mechanical parameters involve according to the time. This problem can be avoided with the development of specific algorithms which can extract the mechanical information with the help of only one fringe pattern [2, 3, 4, 5]. In this way, we presented two algorithms, the MPC [4] (Modulated Phase Correlation) and the pMPC [5] (polynomial Modulated Phase Correlation). These algorithms allow us to extract the phase  $\phi$  from a single fringe pattern  $I$  (eq.1) obtained, for example, by shadow moiré, photoelasticity or interferometry [6]. These processes are based on the use of the virtual fringe pattern  $F_i$  (eq.2) which locally approaches the real fringes morphology.

$$I(x, y) = A(x, y)\cos[\phi(x, y)] + B(x, y) \quad (1)$$

$$F_i(\xi_i, \gamma_i) = A_i \cdot \cos\left(\frac{2\pi}{p_i} \cos(\alpha_i)(x_i + \xi_i) + \frac{2\pi}{p_i} \sin(\alpha_i)(y_i + \gamma_i) + \varphi_i\right) + B_i \quad (2)$$

$$\psi_i(A_i, B_i, \alpha_i, p_i, \varphi_i) = \iint_{L_i} (F_i(\xi_i, \gamma_i) - I(x_i + \xi_i, y_i + \gamma_i))^2 d\xi_i d\gamma_i \quad (3)$$

The similarity degree  $\psi_i$  between real and virtual fringe patterns is estimated by digital correlation technique (eq.3). When the best similarity is obtained, we suppose that the virtual phase function  $\varphi_i$  is very near of the real phase function  $\phi$ . After this demodulation process, we have to unwrap the phase to calculate the mechanical parameter. One particularity of these algorithms is their little sensitivity to noise and this is why they are well adapted to analyse DSPI fringe patterns.

So, we propose, for the first time, to use the MPC or the pMPC algorithms in order to extract mechanical information in dynamic from a single interferogram obtained by digital speckle pattern interferometry. This interferogram is calculated by subtracting the intensities of a speckle image at the initial state with a speckle image at each state of the dynamic event.

We have made experimental tests of impact loading on different specimens. For example, we propose to perform a relief measurement during an impact loading. The tested material is a textile, and we dispose of a high speed camera (PHOTRON Cam) having a frame rate equal to 6000 frames per second and a 1,5 watt laser (Argon) with a wavelength  $\lambda = 514$  nm.

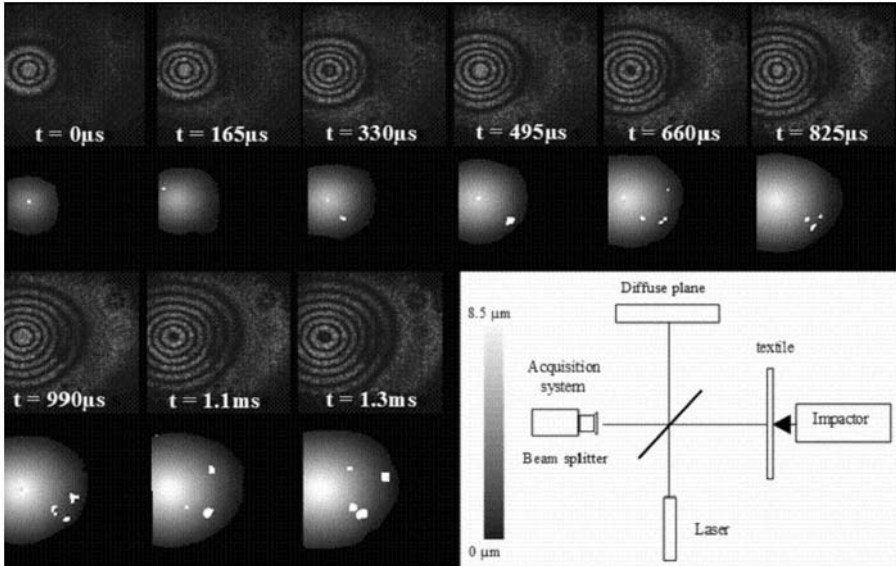


FIGURE 1. Relief measurement field calculated from DSPI fringe pattern.

In figure 1, we can see the DSPI fringe pattern calculated from the acquired speckle pattern images, and the results of the relief extraction. We show the efficiency of the proposed algorithms and we discuss about their accuracies.

## References

1. Creath K., Proceedings of SPIE - The International Society for Optical Engineering, vol **556**, 337-346, (1985).
2. Takeda M., Hideki I., Kobayashi S., *J. of OSA*, vol. **72** (1), 156-160, 1982.
3. Servin M., Marroquin J. L. and Cuevas F. J., *Opt. Eng.*, vol. **33**, 3709-3714, 1994.
4. Robin E. and Valle V., *J. of Applied Optics*, vol. **43**, 4355-4361, 2004.
5. Robin E., Valle V. and Brémand F. *J. of Applied Optics*, vol. **44**, 7261-7269, 2005.
6. Hedan S., Valle V. and Cottion M. *J de Physique IV*, vol. **134**, 597-601, 2006.

## MULTIFUNCTIONAL ENCODING SYSTEM FOR ASSESSMENT OF MOVABLE CULTURAL HERITAGE

V. Tornari<sup>1</sup>, E. Bernikola<sup>1</sup>, W. Osten<sup>2</sup>, R.M. Grooves<sup>2</sup>, G. Marc<sup>3</sup>, G.M. Hustinx<sup>4</sup>, E Kouloumpi<sup>5</sup>  
and S. Hackney<sup>6</sup>

<sup>1</sup> Foundation for Research and Technology-Hellas (FORTH), Institute of Electronic Structure and Laser (IESL), Vassilika Vouton-Voutes, 71110 Heraklion, Crete, Greece.

<sup>2</sup> ITO Institut für Technische Optik, Universität Stuttgart, Pfaffenwaldring 9, 70569 Stuttgart, Germany

<sup>3</sup> Centre Spatial de Liège, Liege Science Park, 4031, Angleur Liege

<sup>4</sup> OPTRION, Spatiopôle – Rue des Chasseurs Ardennais, B-4031 Liege

<sup>5</sup> Conservation Department, National Gallery – Alexandros Soutzos Museum, 1 Michalacopoulou Street, 11601, Athens, Greece

<sup>6</sup> Conservation Department, Tate, Millbank, London SW1P 4RG, UK.  
vivitor@iesl.forth.gr

Nowadays safety, ethical, economical and security issues as well as the increase demand for loaning of art objects for exhibitions in transit, are forcing the Conservation Community to undertake strong initiatives and actions against various types of mistreatment, damage or fraud, during transportation of movable Cultural Heritage. Therefore the interest directs to the development of innovative methodologies and instrumentation to respond to critical aspects of increased importance in cultural heritage preservation, among which to secure proper treatment, to assess probable damage and to fight fraud actions in transportation are of prior consideration.

Europe's works of art, such as paintings and sculptures, are the lifeblood of Europe's cultural heritage. Museums put them on display and, increasingly, loan them out to other institutions. However, exhibiting art and moving it from place to place causes problems. Repeated handling, the need for conservation treatments and exposure to sudden environmental and climatic changes can all take their toll on old and delicate objects. Art in transit is also under threat from mishandling and fraud. Conservators need to monitor the condition of artwork in a way that responds to these issues.

The MULTIENCODE aims to create a new way of monitoring the condition of artworks by using the latest holographic technology. It will produce innovative methods and tools which will allow conservators to assess the conservation state of an object and the need for any treatment; illustrate any new damage; monitor the impact of transport; and confirm a piece's originality. An object would be scanned and its distinct features encoded holographically before being digitally archived. The coded data can then be easily compared with past and future entries to assess changes to the object.

It is proposed the development of a novel *Impact Assessment Procedure* by exploiting and providing to the conservation community the holographic technology advances and innovative tools for a highly secure encoding-decoding system of objects' features required in many critical aspects for sustainable preservation of movable artworks.

It may apply in many functional and strategic decision-makings in museums operation, from routine seasonal examination of conservation state, to periodic assessment of conservation treatments and materials compatibility, to deterioration control and definition of early-induced



damage, to continuous monitoring of transportation impact, to direct confirmation of originality and control of maintenance for any art object in transit, etc.

The effective proposed method relies on the original coded extraction of distinct features from the artwork under conservation, transportation and loan that characterizes the state of conservation of the artwork and its originality. The coding and decoding of such characteristic features can be performed holographically before and after have been optically and numerically transformed for digital archiving. The object features or the archived coded data forming the signatures of the object can be compared at any later time to provide indication of induced alterations. The project advances the state of the art elaborating in synergy with existing methods and practices and concludes with specific novel instrumentation and standards for universal application and worldwide exploitation.

The proposed method advances the state of the art elaborating in synergy with existing methods and practices and concludes with specific novel instrumentation and standards for universal application and worldwide exploitation. It would enable us to make further progress on our previous research into the deterioration of objects through handling, transport and environmental conditions.

The laser holography method will allow to identify minute cracks, voids and discontinuities in works of art. The intention is to create an initial hologram of an object followed by a second hologram at a later date and then superimpose the two wave forms to observe the interference fringes resulting from any very small relative movement of parts of the object.

## References

1. V. Tornari, V. Zafiroopoulos, A. Bonarou, N. A. Vainos and C. Fotakis, “*Modern technology in artwork conservation: A laser based approach for process control and evaluation*”, *Journal of Optics and Lasers in Engineering*, vol. **34**, (2000), pp 309-326.
2. V. Tornari, A. Bonarou, E. Esposito, W. Osten, M. Kalms, N. Smyrnakis, S. Stasinopoulos, “*Laser based systems for the structural diagnostic of artworks: an application to XVII century Byzantine icons*”, *SPIE 2001*, vol. **4402**, Munich Conference, June 18-22, 2001.

## IDENTIFICATION OF SOME ACOUSTIC NOISE SOURCES IN CARS BY SPECKLE INTERFEROMETRY

Dan Borza

Institut National des Sciences Appliquées de Rouen  
BP 8, avenue de l'Université, 76800 Saint-Etienne du Rouvray, France  
borza@insa-rouen.fr

Acoustic noise reduction is an important subject of research and development efforts for car manufacturers. Some of the most important sources of noise are investigated by different techniques, mostly acoustical, like acoustical holography. Tires and their interaction with the road and with the surrounding car structures are one of these noise sources. So does the motor and the associated components. The conditions in which the noise is produced are extremely varied. Some of the parameters involved are speed, road properties, tire model and pressure, developed power, environment, brakes, different mechanical and acoustical properties of assemblies, individual components, outer panels of the car body, and so on.

There are at least three different points of view describing the major disturbances produced by noise: the comfort and the security of the driver and other occupants of the vehicle, the effects on persons and buildings situated close to the street where the vehicle is passing by, and -last but not least- the dissuading effects noise might have on a potential buyer of a new car.

Speckle interferometry [1] is a fine tool able to help understand and identify some noise sources and thus bring assistance to acoustical techniques widely used in this field. The most important characteristics of speckle interferometry are related to its high sensitivity, non-contact and full-field measuring capabilities.

An example of noise source which is related to the comfort of the driver and which might dissuade a potential buyer of a car is the noise which may be produced by closing a car door. As well the inner door panel vibrations (Fig. 1) as the outer panel may contribute to this noise.

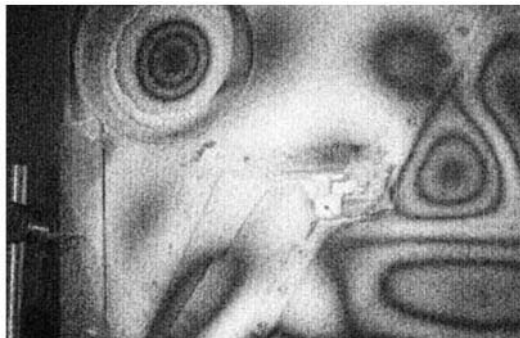


FIGURE 1. Vibration mode of an interior door panel.

Another example, related only to the comfort of the driver is the acoustical behaviour of the elastic, rubber joint placed between the door and the car body. One of its essential roles is to

achieve a good acoustical isolation between the vehicle occupants and the world outside the vehicle. At some higher speeds, this acoustical behaviour of the joint is suddenly worsening. An investigation by speckle interferometry revealed that at some frequencies, the joint may have resonancies, as shown in Fig. 2. The vibration modes at these frequencies are so that the full contact between joint and car body is lost, and a direct noise propagation from outside the vehicle to the interior becomes possible.

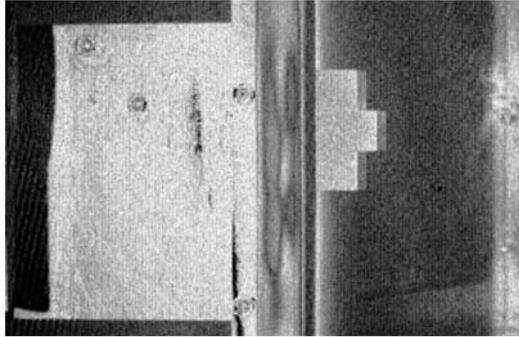


FIGURE 2. Vibration mode of a rubber joint between door and car body.

Other less known examples of noise sources, related to all the factors previously mentioned, have been investigated and some results are presented in the full paper.

From the point of view of the metrological optical technique being used, the paper discusses some enhancements in the time-average speckle interferometry for vibration measurement. These enhancements concern as well the contrast as the spatial resolution of interferometric fringe patterns and may be applied, with small variations, to the different coherent techniques - TV-holography, digital holography and also shearography and in-plane speckle interferometry.

## References

1. Pryputniewicz, R. J. and Stetson, K. A., Proc. SPIE, vol. **1162**, 456-467, 1989

## PHASE EXTRACTION IN DYNAMIC SPECKLE INTERFEROMETRY BY EMPIRICAL MODE DECOMPOSITION

Antonio Baldi<sup>a</sup>, Sébastien Equis<sup>b</sup> and Pierre Jacquot<sup>b</sup>

<sup>a</sup>Dipartimento di Ingegneria Meccanica, Università degli Studi di Cagliari,  
Piazza d'Armi, 09123 Cagliari, Italy

<sup>b</sup>Nanophotonics and Metrology Laboratory, Swiss Federal Institute of Technology Lausanne  
EPFL-STI-NAM, Station 11, CH-1015 Lausanne, Switzerland  
baldi@iris.unica.it, sebastien.equis@epfl.ch, pierre.jacquot@epfl.ch

In many respects, speckle interferometry techniques are now considered as mature tools in the experimental mechanics circles. These techniques have enlarged considerably the field of optical metrology, featuring nanometric sensitivities in whole-field measurements of profile, shape, and deformation of mechanical rough surfaces. Nonetheless, the phase extraction of speckle interferometry patterns is still computationally intensive, preventing a more widespread use of this technique especially in dynamic experiments. A promising approach lies in the temporal analysis of the pixel signals of photodetector arrays. The basic idea is to extract the instantaneous frequency (IF) of these signals, in order to obtain, *in fine*, the phase, i.e. the quantity of interest. A pioneering work has been done in this direction in [1] by using the ridge tracking method of Delprat *et al* [2] applied to the Morlet wavelet transform (MT).

Instantaneous frequency is actually a sensitive concept [3-5]. In 1946, Gabor gave a well-known method to build an analytical signal from a zero-mean real-valued signal by means of the Hilbert Transform (HT), so as to extract the phase from this complex valued signal. But there are restrictive conditions in a meaningful use of this technique for real-world signals (spectra of the amplitude and of the phase well separated [6], signal locally centered and monocomponent). Since we are dealing with mean, amplitude and frequency modulated signals, an efficient tool is missing to make them amenable to Hilbert phase extraction methods.

Huang *et al* proposed in [7] a new method, the Empirical Mode Decomposition (EMD), likely to satisfy this need, which decomposes any real-valued signal into Intrinsic Modes Functions (IMF). As the decomposition functions are built a posteriori, they can be thought to be best adapted to the signal, leading to a sparser representation and to the expectation that the useful information can be extracted from few relevant modes, ideally the first one in our case. This paper shows how the EMD is able to put interferometric temporal pixel signals into a shape suitable for a subsequent easy phase extraction.

In this paper, after having reminded the basics of EMD, we implement, discuss and test it, using first pure mathematical signals with a known amount of noise, and then, simulated [8] and experimental interferometric signals. The important conclusion is that the phase of the 1<sup>st</sup> IMF is a correct determination of the phase of the signal, so that we naturally focus our analyses on this mode only. At the post-processing stage, we compare the results given by, *i*) the HT, *ii*) the maximum MT amplitude ridge, and *iii*) the ridge extraction [1] algorithms (see Fig. 1 for a noisy mathematical signal). Finally, we assess their respective reliability and variance, especially for simulated interferometric signals for which the amount of displacement is known.

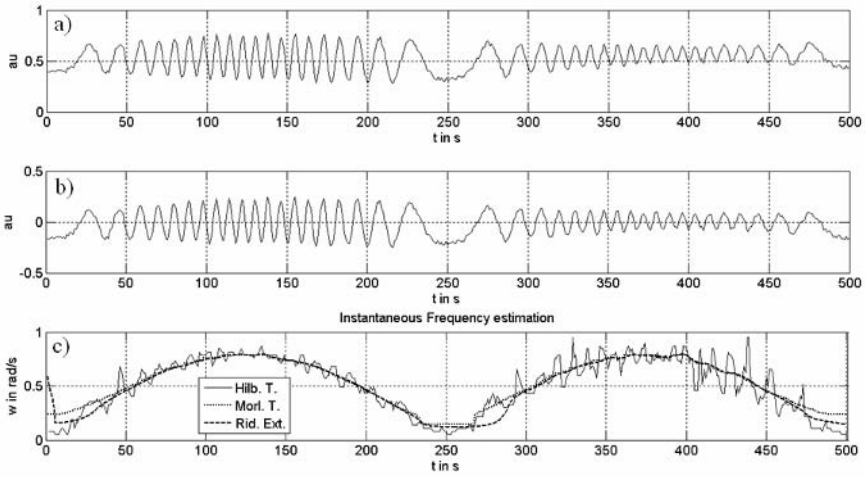


FIGURE 1. a) Original mathematical signal; b) 1<sup>st</sup> mode; c) IF extraction from the 1<sup>st</sup> mode with HT, maximum MT amplitude and ridge extraction algorithms.

The series of tests performed using a variety of input signals lead us to conclude that EMD is certainly an interesting method, worth to be added to the set of existing ones for processing dynamic speckle interferometry signals.

## References

1. X. Colonna de Lega, *EPFL thesis*, N° 1666, 1997.
2. N. Delprat et al, *IEEE Trans on Inf. Th.*, vol. **38**, 644-664, 1992.
3. L. Mandel, *Amer. J. Phys.*, vol. **45**, 840-846, 1974.
4. B. Boashash, *Proc. IEEE*, vol. **80**, 520-568, 1992.
5. P.J. Loughlin, B. Tacer, *J. Acoust. Soc. Am.*, vol. **100**, 1594-1601, 1996.
6. E. Bedrosian, *Proc. IEEE*, vol. **51**, 868-869, 1963.
7. Norden E. Huang et al, *Proc. R. Soc. Lond. A*, vol. **454**, 903-995, 1998.
8. S. Equis, P. Jacquot, *Proc. SPIE*, vol. **6841**, International Conference Speckle06, 2006.

## ANALYTIC PROCESSING OF EXPERIMENTAL DATA BY A B-SPLINE FITTING

Luigi Bruno

Department of Mechanical Engineering – University of Calabria  
Via P. Bucci CUBO 44C – 87036 Arcavacata di Rende (CS), Italy  
bruno@unical.it

Among the main advantages of interferometric techniques, the possibility to carry out full-field measurements is certainly one of the most appealing. When interferometric techniques, like photoelasticity [1], moiré interferometry [2], speckle interferometry [3] or digital holography [4] are applied, the experimental data typically consist of fringe patterns which represent the contour map of a particular quantity. If a real full-field approach is desired it is necessary the application of a phase-shifting procedure [5,6], in order to obtain the phase maps by means of a number of fringe patterns. Actually the phase maps provide point-wise measurements, although an unwrapping procedure becomes necessary in order to remove the phase jumps always present when the optical path difference exceeds one wavelength.

Aside from the drawbacks (many of which are nowadays overtaken) that arise by unwrapping a phase map particularly noisy [7], a residual noise on the measurements is still present. The entity and the origin of this noise is strictly dependent on the type of technique and on the operative experimental conditions.

Many are the attempts available in the scientific literature to smooth the noise either in the space domain or in the spatial frequency domain [8-10], but, as it is shown in the papers dealing with these approaches, it is not possible to obtain a smooth distribution of the phase without fluctuations.

The only way to obtain a smooth phase distribution consists in using an approach based on a fitting operation [11]. By this approach, very popular in the field of reverse engineering [12-13], it is necessary to define an analytical expression based on a number of parameters which must be evaluated by a proper optimization procedure.

If a reliable analytical model is available for the problem under investigation the fitting can be carried out with high probability of success, otherwise the choice of the analytical model becomes a very crucial step of the whole fitting procedure.

A typical analytical model is based on the use of polynomial functions which are particularly easy to manage and allow to obtain always a system of linear equations. On the other hand the need of higher modeling capability brings to increase the order of the polynomial and it implies unwanted fluctuations of the model, which does not follow the physical nature of the phenomena represented by the phase maps. The use of particular polynomial functions, like orthogonal Legendre or Zernike [14] polynomials, can improve the performance of the polynomial fitting, but the instabilities can be only lowered or shifted outside the domain of interest, not removed. Further improvements can be obtained by adopting different functions or nonlinear models [15] that lead to the use of particular solving algorithms. Finally it is important to say that, although most of mono-dimensional fitting is straightforward, when we handle interferometric data the problem becomes bi-dimensional with consequent increase of the calculation complexity.

The present paper reports a bi-dimensional fitting procedure based on the use of B-spline functions [16] applicable to differently shaped domains. According to this model a number of piecewise polynomial functions are defined and their existence is limited to a portion of the total

domain. The number of the functions and the order of the polynomials can be chosen independently from each other; in this way a complex phase map can be fitted simply by increasing the number of functions without increasing the order of polynomials. The advantages of this approach are the linearity of the model to be optimized, the local control and the possibility to keep low the order of polynomial functions involved in the definition of the model. On the other hand the piecewise formulation implies a more complex mathematical model to be implemented, although it is easily achievable by the actual software environments like MatLab or Mathematica. Moreover the application of the procedure to a non rectangular domain requires a space transformation consisting of further mathematical manipulations.

## References

1. Frocht, M.M., *Photoelasticity Vol. I*, John Wiley and Sons, New York, 1941.
2. Post, D., Han, B. and Ifju, P., *High sensitivity moiré*, Springer Verlag, Berlin, 1997.
3. Erf, R.K., *Speckle metrology*, Academic Press, New York, 1978.
4. Schnars, U. and Jueptner, W., *Digital holography*, Springer, Berlin, 2005.
5. Creath, K., "Temporal phase measurement methods" in *Interferogram analysis*, Robinson D.W. & Reid G.T. ed, Institute of Physics Publishing, Bath, Great Britain, 1993.
6. Kujawinska, M., "Spatial phase measurement methods" in *Interferogram analysis*, Robinson D.W. & Reid G.T. ed, Institute of Physics Publishing, Bath, Great Britain, 1993.
7. Ghiglia, D.C. and Pritt, M.D., *Two-dimensional phase unwrapping*, John Wiley & Sons, New York, 1998.
8. Aebischer, H.A. and Waldner, S., *Optics Communications*, vol. **162**(4-6), 205-210, 1999.
9. Huang, M.J., He, Z.N. and Lee, F.Z., *Measurement*, vol. **36**(1), 93-100, 2004.
10. Kemao, Q., Hock Soon, S. and Asundi, A., *Opt. Las. Technology*, vol. **35**(8), 649-654, 2003.
11. Novak, J. and Miks, A., *Optics and Lasers in Engineering*, vol. **44**(1), 40-51, 2005.
12. Bajaj, C.L. and Xu, G., *Journal of Symbolic Computation*, **23**(2-3), 315-333, 1997.
13. Juttler, B. and Felis, A., *Advances in Computational Mathematics*, vol. **17**(1), 135-152, 2002.
14. Furgiuele, F., Muzzupappa, M. and Pagnotta, L., *Exper. Mech.*, vol. **37**(3), 285-291, 1997.
15. Bates, D.M. and Watts, D.G., *Nonlinear regression analysis and its applications*, John Wiley & Sons, New York, 1988.
16. Anand, V.B., *Computer graphics and geometric modeling for engineers*, John Wiley & Sons, New York, 1993.

## ESPI-MEASUREMENT OF STRAIN COMPONENTS ON A CFRP-REINFORCED BENDING BEAM

Erwin Hack and Ann Schumacher  
Laboratory for Electronics/Metrology  
Laboratory for Structural Analysis  
EMPA, Ueberlandstrasse 129, CH-8600 Dübendorf, Switzerland  
erwin.hack@empa.ch, ann.schumacher@empa.ch

Reinforcement of structural elements using adhesively bonded carbon-fibre reinforced polymers (CFRP) is a well-advanced strengthening method. In particular, concrete or steel beams are strengthened with CFRP plates. Due to the stress concentration at the end of the plate debonding can often be expected. We describe a laboratory experiment to assess the stress transfer at the end of a CFRP plate, with a special focus on shear and normal stresses. A small-scale, 1.2 m long steel I-beam with 120 mm width was reinforced. The beam was loaded with manually controlled hydraulic jacks in a four-point bending arrangement. In order to allow interferometric measurements, the experiment was performed on a vibration isolated optical table in a temperature stabilized laboratory.

Digital speckle pattern interferometry (DSPI) was used to measure the 3D-deformation field in the area of interest. A standard four-frame phase-stepping algorithm with sequential acquisition of three illumination directions was applied. The phase maps of the displacement components for the three illumination directions were transformed to Cartesian coordinates ( $u$ ,  $v$ ,  $w$ ) using the sensitivity matrix. The sensitivity matrix was calculated from the geometry of the experimental set-up. In order to assess its variations, it was calculated on a grid of  $11 \times 11$  points across the field of view. The sensitivity matrix components vary less than 1%, and could therefore be assumed constant.

The rigid body motion of the specimen due to the loading forces caused complete speckle decorrelation. This was of course expected in view of the small area of interest measured in the experiment. Hence, an evaluation method that regains the speckle correlation by image shifting had to be used to measure the displacement fields. More details are found in Hack and Schumacher [1]. After each major load step, a series of data was taken with additional small load increments. This procedure guarantees that at least one pair of well-correlated speckle patterns is found for each of the major load steps after an appropriate shift of the images by an integral number of pixels. The image pair with the best correlation was chosen for subsequent analysis, which consisted in adding of the major load steps to the total load, and strain evaluation. Shear strain was evaluated by image shearing of the  $u$ - and  $v$ - displacement field. A preliminary result is given in Fig. 1.

A Finite Element Analysis (FEA) of the strengthened beam was conducted using the commercial finite element code ABAQUS. For symmetry reasons, only half of the beam was simulated. In order to accurately capture the stress concentrations at the plate end, submodeling with a fine mesh was carried out for the area of interest [2].

For quantitative analysis and comparison to results from FEA interpolating the in-plane displacement data along selected lines and numerically differentiating it will be presented. Different fitting strategies were used to average out the noise, among which is a set of cubic splines within intervals along each line. The polynomial coefficients of the splines were calculated according to a least squares criterion under the boundary condition of continuity of first and second derivatives of the resulting fit line at the interval borders. The strain values were then calculated



numerically from the fit lines. An uncertainty estimation will be given based on the comparison of different fit strategies. The standard uncertainty in the strain values from the DSPI evaluation can be estimated to be  $20 \times 10^{-6}$ .

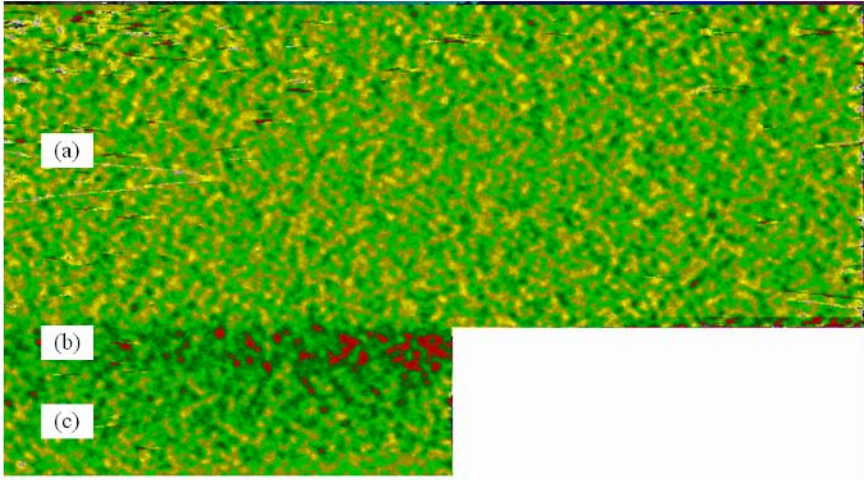


FIGURE 1. Shear strain near the edge of the CFRP reinforcing plate (preliminary result). Steel beam (a), adhesive (b) and CFRP reinforcing plate (c). Field of view is  $16 \times 11 \text{ mm}^2$ .

## References

1. Hack, E. and Schumacher, A., *Opt. Las. Eng.*, 2007 (in press)
2. Coronado C.A. and Lopez M.M., *Cement and Concrete Composites*, vol. 28, 102-114, 2006

## MARTENSITE AND REVERSE TRANSFORMATION DURING TWO-DIRECTION SIMPLE SHEAR OF NITI SMA

S.P. Gadaj<sup>1</sup>, W.K. Nowacki<sup>1</sup>, E.A. Pieczyska<sup>1</sup> and J. Luckner<sup>2</sup>

<sup>1</sup> Institute of Fundamental Technological Research, Warsaw, Poland

<sup>2</sup> Department of Mechanical Engineering, AICHI Institute of Technology, Japan  
epiecz@ippt.gov.pl

The investigations of the quasistatic two-sides simple shear of NiTi shape memory alloy (SMA) have been carried out. The goal of this study was obtaining the mechanical and thermal characteristics during the shear process. By comparison of them the processes of martensite and reverse transformations during the shear process can be analyzed.

The experiments were performed on specimens of NiTi SMA of the constitution Ni55.85wt%Ti, characterized by  $A_f$  temperature of 283 K. The flat specimens of dimensions 27 mm  $\times$  30 mm  $\times$  0.5 mm were cut from the NiTi sheet by electro-erosion technique. They were placed in a specially designed grip, transforming the compression into a simple shear process. The grip was fitted in the testing machine. The mobile part of the grip was moved up, returned and next moved down and returned again. The process of shear takes place on one shear zone of the specimen, 30 mm length and 3 mm width. The measurements were carried out at room temperature of about 295K; so the NiTi SMA demonstrates a complete loop of pseudoelasticity during the test.

An infrared camera was used in order to register the temperature distribution on the specimen surface and to find its temperature changes. A mean temperature of the shear zone was calculated over an area of dimension 1 mm  $\times$  20 mm, located in the central part of the specimen. The stress and the temperature vs. strain curves obtained during one cycle of the shear deformation are presented in Fig. 1a, while some examples of the shear zones thermograms are shown in Figs. 1b and 1c.

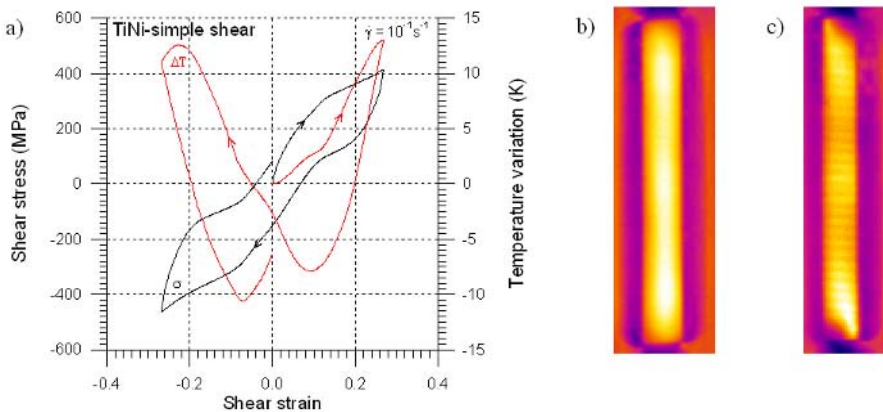


FIGURE 1. a) Stress and temperature vs. strain, b) thermogram of the shear zone at strain rate of  $10^{-1} \text{ s}^{-1}$  and c) thermogram of the shear zone at strain rate of  $0.8 \times 10^{-1} \text{ s}^{-1}$

Shape of stress-strain loops during the two-direction of the simple shear process is similar to each other (Fig. 1a) but they are rather different from those obtained during tension tests [1]. The average specimen temperature increases during loading in both sides of the shear, while the martensite transformation takes place; and decreases during unloading, while the reverse transformation occurs.

During the former tension test of TiNi SMA [1,2,3], the temperature distributions registered during loading and unloading were inhomogeneous in the ranges of martensite and reverse transformations which demonstrate that both the transformations occurred in inhomogeneous way, via subsequent bands of new phase, similar to Lüders bands.

Inhomogeneous distributions of temperature are also seen during simple shear test (Figs. 1b, c), especially at higher rate of shear. It is pointed out that both martensite and reverse transformations during simple shear are also heterogeneous. This phenomenon is not so visible as during tension test due to the huge impact of the heat exchange with the solid grips.

Stress-strain and temperature-strain relations obtained during 20 cycles of the two-sides simple shear tests are presented in Fig. 2.

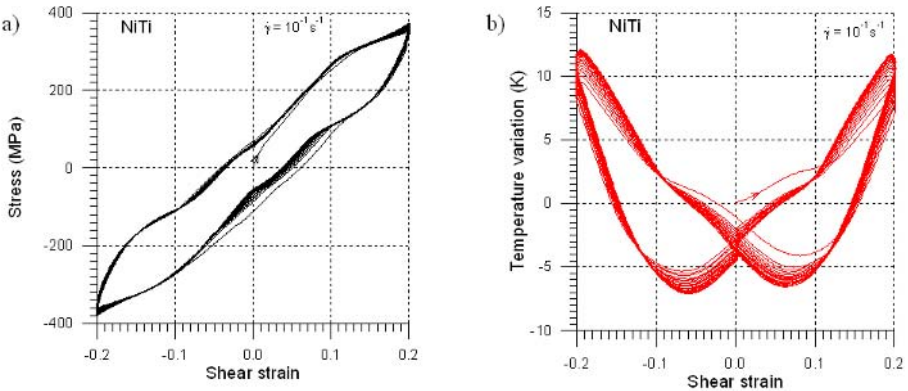


FIGURE 2. Stress-strain a) and temperature vs. strain b) relations obtained during 20 cycles of two-direction of simple shear tests

From the second cycle, both stress-strain as well as temperature-strain loops during the two-direction of the simple shear test are almost symmetric. In the subsequent cycles of deformation, the differences between the stress-strain hysteresis loops are getting smaller (Fig. 2a). Maximal stresses in the both side of these loops increase a little as the result of increase of the average temperature of the shear zone (see Fig. 2b).

Temperature changes of the shear zone during martensite and reverse transformation are not symmetric in the both branches of loading. It results from a heat exchange with the heavy grips holding the NiTi SMA specimen.

**Acknowledgement:** The research has been partially carried out with the support of Polish Grant No. 4T08A06024, the JSPS Grants: No.13650104 (C), Post-doc P04774, Joint Research of JSPS and PAS: No. 6612.

### References

1. S.P. Gadaj, W.K. Nowacki, E.A. Piecyszka and H. Tobushi (2005). Temperature measurement as a new technique applied to the phase transformation study in a TiNi shape memory alloy subjected to tension, *Archives of Metallurgy and Materials*, vol. **50**, 3, 661-674.
2. E.A. Piecyszka, S.P. Gadaj, W.K. Nowacki and H. Tobushi (2004) Thermomechanical Investigations of Martensite and Reverse Transformations in TiNi Shape Memory Alloy, *Bull. Pol. Ac.: Tech.*, vol. **3**, 165-171.
3. J.A. Shaw and S. Kyriakides (1997). On the nucleation and propagation of phase transformation fronts in a TiNi Alloy, *Acta Mater.*, vol. **45**, 2, 683-700.

## TRANSFORMATION INDUCED EFFECTS IN TINI SHAPE MEMORY ALLOY SUBJECTED TO TENSION

E.A. Pieczyska<sup>1</sup>, S.P. Gadaj<sup>1</sup>, W.K. Nowacki<sup>1</sup> and H. Tobushi<sup>2</sup>

<sup>1</sup> Institute of Fundamental Technological Research PAS,  
Swietokrzyska Street 21, 00-049 Warsaw, Poland  
Phone: 48 228261281 ext. 260; FAX: 48 228268911

<sup>2</sup>Department of Mechanical Engineering, AICHI Institute of Technology,  
1247 Yachigusa, Yakusa-cho, Toyota 470-0392, Japan  
epiecz@ippt.gov.pl

Transformation induced effects in shape memory alloy (SMA) subjected to tension test at room temperature are investigated. The experiments were carried out on belt type specimens TiNi SMA of the constitution Ti-55.3wt%Ni, sizes 160x10x0.4 mm and  $A_f$  temperature 283 K. The loading was realized on high quality testing machine, which enables to obtain the stress-strain characteristics with high accuracy. Smart infrared camera was used to register the temperature distribution on the specimen surface and to find its temperature changes with the accuracy up to 0.05K.

Recent study show that during superelastic deformation of TiNi SMA, the phase transformations can be accompanied by unstable mechanical behavior and localized Lüders-like transformation, resulting in propagating of phase transformation fronts. The bands of the new phase were characterized by the angle of inclination with the direction of tension of 48° and the variation in temperature of about 8 K. They were followed by the next generation of the bands inclined at the same angle but in the opposite direction [1, 2, 4, 5].

Some effects of the localized phase transformation during stress relaxation for not temperature-controlled test, i.e. carried out in room conditions were investigated in [1, 2]. A large stress drops, caused by the developing transformations, were observed there in both the course of loading and unloading, while for the temperature controlled conditions, in the unloading branch the stress increased under constant strain, due to the stress recovery [3].

Objective of the current work is study of terms of nucleation, developing as well as vanishing of the martensitic and reverse phase transformations. In particular the onset and evolution of the phase transformation fronts under specific conditions is analyzed. The goal is to demonstrate that thermomechanical couplings do work during the stress-induced phase transformations. To this end, a specimen of TiNi SMA has been subjected to a particular program of tension test with a constant stress rate of 12.5 MPa/s. Namely, the specimen is loading till strain value of 1.6mm was achieved. The mechanical characteristic is registered and the specimen surface is observed by infrared camera. When the martensite transformation has been found to be advanced and bands of the localized heterogeneous phase transformation accompanied by no-uniform temperature distribution occur, the stress has been programmed to decrease by about 5% (0.5 MPa/s) in order to affect, i.e., to stop the phase transformation (Fig. 1a, b). It works, since the temperature decreases and the temperature distribution observed by infrared camera started to be more uniform. Next the specimen was loading again till the strain limit of 8%. During unloading, the reverse transformation occurs in typical, for shape memory alloys, way.

For the subsequent test, the specimen is loading till 8% until the martensite transformation was completed. During unloading, when the reverse transformation was already advanced, the stress has been programmed to increase, respectively, in order to affect the reverse transformation and

stop it. However, it was not realized, since it was very difficult to control the testing machine in this way.

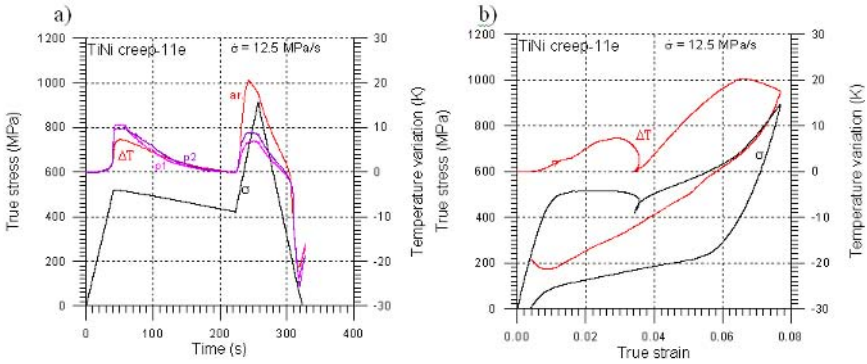


Figure 1. Stress  $\sigma$  and temperature change a) vs. time during particular program of tension test of TiNi SMA; p1 – Temperature change  $\Delta T$  at point of 1-st transition band, p2 – point at minimum temperature, T- average temperature, b)  $\sigma$  and  $\Delta T$  vs. strain

Figures 1a, b present stress  $\sigma$  and temperature  $\Delta T$  vs. time and vs. strain curves obtained for the test above described. The temperature was measured as an average from the chosen area, or from the points chosen on the specimen surface.

During investigation of transformation-induced creep-like effects against the phase transformation direction, induced in the branch of loading, the thermomechanical coupling work and the phase transformation was stopped.

During investigation of transformation-induced creep-like effects against the phase transformation direction, induced in the branch of unloading, the reverse transformation has been still developed, however the transformation process was slower. The rate of stress change was too small. The proper one is really difficult to realize on the testing machine.

**Acknowledgement:** Authors wish to extend their thanks to Prof. B. Raniecki from IFTR (Poland) and Prof. S. Miyazaki from Tsukuba University (Japan) for fruitful discussions and scientific advice.

## References

1. E.A. Pieczyska, S.P. Gadaj, W.K. Nowacki and H. Tobushi, Phase-transformation front development and transformation-induced stress relaxation effects in TiNi shape memory alloy; Proc. ICIM705 Tokyo (2005), pp. 163-166.
2. E. A. Pieczyska, S. P. Gadaj, W. K. Nowacki and H. Tobushi, Transformation induced stress relaxation during superelastic behavior of TiNi SMA, Int. J. Applied Electromagnetic & Mechanics, Special Issue on "The International Symposium on Shape Memory Materials for Smart Systems", 21 (2005), pp. 1-6.
3. R. Matsui, H. Tobushi and T. Ikawa, Transformation-induced creep and stress relaxation of TiNi shape memory alloy, Proc. Instn. Mech. Engrs., J.Materials:Design and Applications, 218, Part L (2004), 343-353.
4. E. Pieczyska, H. Tobushi, S. Gadaj and W. K. Nowacki, Superelastic deformation based on phase transformation bands in TiNi SMA, Mater. Trans., vol. 47 (2006), pp. 1-7.
5. A. Pieczyska, S. P. Gadaj, W. K. Nowacki and H. Tobushi, Phase transformation front evolution for stress- and strain-controlled tests in TiNi shape memory alloy, Experimental Mechanics, vol. 46(4) (2006), pp. 531-542.

## FROM THERMOMECHANICAL HEAT SOURCE RECONSTRUCTION TO THE VALIDATION OF MECHANICAL BEHAVIOR'S LAWS

N. Renault, S. Andre and C. Cunat  
 LEMTA – UMR CNRS 7563  
 2, av. de la forêt de Haye – BP160  
 F-54504 Vandoeuvre Cedex, France

Norbert.Renault@ensem.inpl-nancy.fr , Stephane.Andre@ensem.inpl-nancy.fr

The development of thermal imaging in the past 25 years lead the mechanical sciences community to use this tool in order to analyze the thermal effects accompanying deformation processes of materials. At first, it allows to check some qualitative effects observed previously when thermocouples were embedded in the specimens. The discussions were relying on a qualitative analysis of the temperature behavior associated to each thermomechanical behavior (thermoelasticity, viscoplasticity, damage...). Then it appears clearly that some source reconstruction was unavoidable as temperature is not an intrinsic variable to describe the internal thermal processes : it depends on heat exchanges with the surroundings i.e. the external dissipation or entropy flux to use the appropriate language of thermodynamics of irreversible processes. Until now, very limited observed thermomechanical behaviors have been properly reproduced with a consequentially model. But some attempts have been done that illustrates all the benefits ones could retrieve from such achievement [Chrysochoos, 1992,2000]

In this paper, we first present two distinct methods for a 2D heat source reconstruction. The first one relies on the minimization of a functional involving both a constrained optimization criteria and a regularizing approach in the sense of Tikhonov. It corresponds to a refinement of the methods initially proposed by Wong and Kirby (1990). It leads to a very easy algorithm to implement. The second one relies on a spectral decomposition of the temperature variable that results from an integral transform in space of the heat diffusion operator and lead to a convolution formulation in time. Some regularization is achieved using the future time approach of Beck (1961). These two methods have been applied both on simulated signals (stemming from FEM calculations) and on experimental signals. These latter have been obtained in the case of a tensile test at constant deformation rate, which is maybe the most difficult case to handle for such an objective. It will be shown that the two methods compare well and their respective advantages or disadvantages will be clearly stated. Figure 1 shows the thermomechanical power density reconstructed from a tensile test performed on HDPE. This thermal power involve both (i) the thermoelastic effect easily spotted at short deformations and accompanied by a heat sink effect, (ii) thermomechanical couplings between state and internal variables, that are generally interpreted as latent internal energy of deformation, and (iii) the pure dissipative component corresponding to the irreversible conversion of the input mechanical power into heat. Unlike measurements performed by deformation calorimeter, these three components are present in the source term that is reconstructed.

The challenge is then to account for this experimental characterization of thermomechanical couplings in a theoretical framework ensuring the construction of well-behaved (or thermodynamically consistent) behavior's law. We will demonstrate in the paper that an original approach called DNLR for Dynamics of Non Linear Relaxations [Cunat, 2001], which is based on all universal axioms [Callen, 1966] applied to thermodynamics of irreversible processes, allows very clearly the modeling of thermomechanical behaviors. A set of coupled equations based on the dual variables ( $s$ -entropy,  $T$ -temperature), ( $\sigma$ -stress,  $\varepsilon$ -strain) and the dissipative dual variables ( $A$ -affinities,  $z$ -internal variables) is able to perfectly explain some interesting features observed

experimentally. One of them, the entropic character of stress relaxation, as evident on figure 1 below, is perfectly reproduced by the model (solid line). The theoretical stress-strain curve does not perfectly fit with the data as a result of the use of a Mooney-Rivlin description of the relaxed state. This will be modified for the full paper.

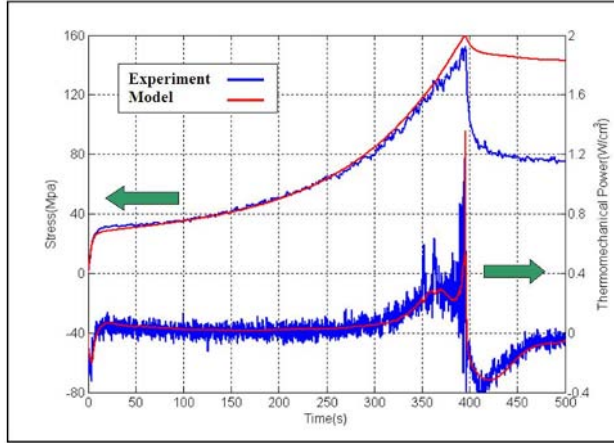


FIGURE 1. Experimental and theoretical validation on two signals : true stress-strain curve and evolution of the involved calorific power during a tensile test at rate  $\dot{\epsilon} = 10^{-2} s^{-1}$ .

## References

1. Chrysochoos, A. and Belmahjoub, F., *Archives of Mechanics*, vol. **44**, 1, 55-68, 1992
2. Chrysochoos, A. and Louche, H., *Int. J. Eng. Science*, vol. **38**, 1759-1788, 2000
3. Wong, A.K., and Kirby, G.C., *Eng. Fracture Mechanics*, vol. **37**, 3, 493-504, 1990.
4. Beck, J.V., *AVCO Corp. Res.*, Tech. Report RAD-TR-7-60-38, March30, 1961.
5. Cunaat, C., *Mechanics of Time-Dependent Materials*, vol. **5**, 39-65, 2001.
6. Callen, H.B., In *Thermodynamics*, John Wiley & Sons, 1966.

## THE INFLUENCE OF TEMPERATURE AND PRE-AGING ON THE LOW CYCLE FATIGUE BEHAVIOUR OF NICKEL COATINGS (NI 200/201)

Hubert Koberl, Heinz Leitner and Wilfried Eichlseder  
 Chair of Mechanical Engineering, University of Leoben, Leoben, Austria  
 Franz-Josef-Strasse 18, 8700 Leoben, Austria  
 Hubert.Koeberl@mu-leoben.at

Nickels are generally used for thermal barrier coatings, with their function of extending fatigue life. Nevertheless the thermal cyclic loading often takes place in the low cycle fatigue (LCF) region [1], become the process are driven by cyclic plasticity. Therefore it is necessary to study the low cycle fatigue behaviour of Ni 200/201, as shown in Fig. 1, according to Manson-Coffin-Basquin law [2, 4].

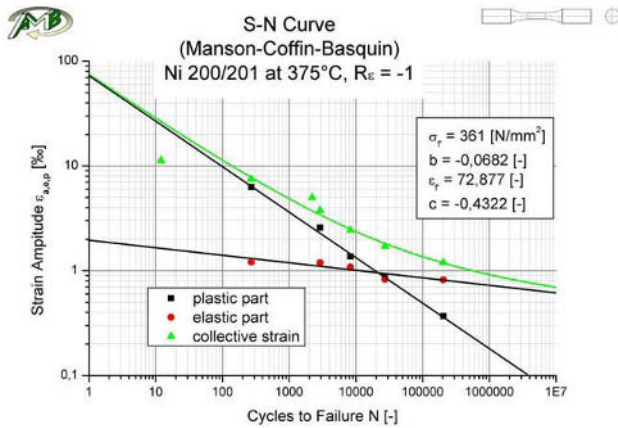


FIGURE 1. Strain S-N Curve at 375 °C

For thermal barrier coating, studies of the influences of temperature including pre-aging and oxidation are a basic feeding. In the recent research the regions and the limits of the thermal application of Nickel are described in the manor of strain based S-N curves at different temperatures and varying pre-aging steps. So the lifetime of these coatings can be very strong affected by the temperature behaviour, described by nodal temperatures as well as their gradient. The second influence of thermal loaded Nickel coatings is the oxidation at high temperatures. The oxidation results in an embrittlement of the surface. The brittleness is also reflected in the lifetime behaviour. Optimised Nickel service conditions lead to a significant increase in service life which reduces the recoating costs.

The tests were performed strain controlled with a servo-hydraulic test rig at a strain rate of 1 % per second. For temperature application, an inductive coil is used. The result in Fig. 2 shows a high influence of the temperature and the pre aging on the cycle behaviour of nickel, which gets more important with lower strain amplitudes. As second investigation a comparison between LCF and TMF behaviour was done.



For example, at 2 ‰ strain amplitude and 25 °C nickel tolerates over 50.000 cycles to failure, but at 575 °C about 10.000 cycles, which is a factor of 5 in lifetime. But at strain amplitudes of 1 ‰ the sustained cycles decrease rapidly from about 3.000.000 at 25 °C to about 100.000 at 575 °C, which is a factor of 30 in lifetime.

Comparing 25 °C and 375 °C, the influence of temperature still exists, but the difference in the lifetime behaviour is not as seriously as above. At 2 ‰ the lifetime factor is about 3 (more than 20.000 cycles at 375 °C), and at 1 ‰ the factor is 6 (more than 500.000 cycles at 375 °C).

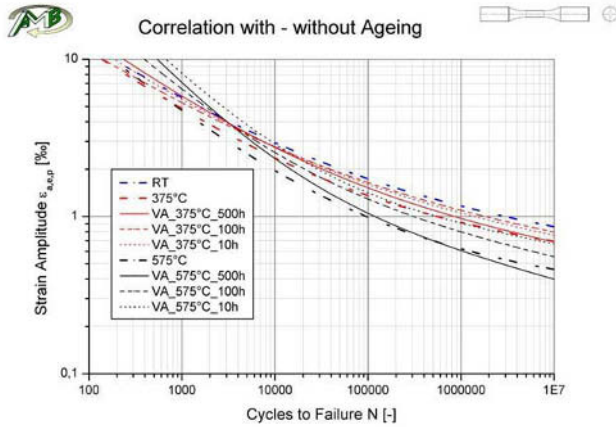


FIGURE 2. Correlation with and without ageing

## References

1. T.R. Lee, C.P. Chang, P.W. Kao.: The tensile behaviour and deformation microstructure of cryo-rolled and annealed pure nickel, Material Science and Engineering, 2005
2. S.S. Manson.: Behaviour of materials under cyclic stress, NACA TN 2933, 1953
3. S. Mrowec, Z. Grezik, B. Rajchel, A. Gil, J. Dabek.: The influence of aliovalent impurities on the oxidation kinetics of nickel at high temperatures, Journal of Physics and Chemistry of Solids, 2005
4. L.F. Jr. Coffin.: A study of the effects of cyclic stresses on a ductile metal, Trans ASME, 1954

## GEOMETRIC SCALE EFFECT IN DYNAMIC TENSION TESTS, A NUMERICAL ANALYSIS

R. Cheriguene<sup>1</sup>, A. Rusinek<sup>1</sup>, R. Zaera<sup>2</sup> and J.R. Klepaczko<sup>1</sup>

<sup>1</sup>Laboratory of Physics and Mechanics of Materials, UMR-CNRS 7554  
Ile du Saulcy; 57045 Metz Cedex, France

<sup>2</sup>Department of Continuum Mechanics and Structural Analysis, University Carlos III of Madrid  
Avda. de la Universidad, 30; 28911 Leganés, Madrid, Spain  
rusinek@univ-metz.fr

Many specimen designs are nowadays used in dynamic tension tests, Fig. 1. However, no normalization so far has been attempted. It is clear that using different specimen geometries for the same type of equipment may generate some differences in final results. Those effects are only due to specimen geometry, for example [1] and [2]. An optimisation of any specimen design by reduction of strain gradients due to shape and elasto-plastic waves is necessary, but it insufficient to resolve the problem. Moreover, to be able to reach strains up to 0.5, for example using experimental set-ups like Hopkinson bars, that are characterized by small specimen net displacements, the specimen initial length have to be reduced, and consequently, a reduction of lateral dimension is also necessary retain the uniaxial stress. Such small dimensions substantially perturb the determination of real material behavior. In this paper a systematic analytical and numerical study of short and long specimens loaded in impact tension were performed to analyse the differences caused by specific geometries are presented.

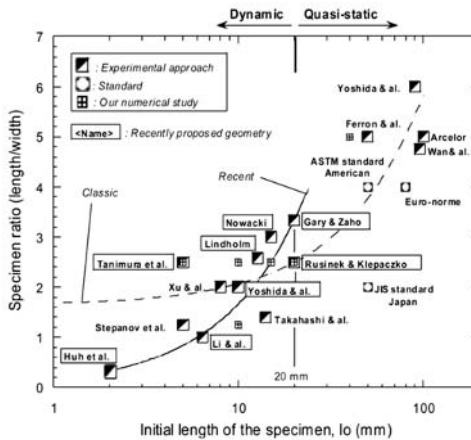


FIGURE 1. Some specimen geometries used to study behavior of sheet steel in tension impact and quasi-static tests.

### Numerical simulation

In order to analyze the effect of temperature and high strain rate on the flow stress, we use a semi-phenomenological constitutive relation developed for thermo-visco-plastic modelling[3]. The finite element code ABAQUS/Explicit has been used to simulate six specimens of mild steel ES.

Their initial length  $l_0$  varies from 5 to 100 mm. The left hand side of the specimen is embedded and the right side is submitted to a constant impact velocity  $V_0$  from 10 to 100 m/s, Fig. 2. In order to compare all geometries studied in the range of strain rates varying from  $10^{-2}s^{-1}$  to  $10^3s^{-1}$  the 3D simulations have been performed with the thermo-visco-plastic constitutive relation coupled with an original validated thermo-visco-plastic algorithm using a VUMAT subroutine allowing the implementation of this kind of constitutive relation [4] and [5].

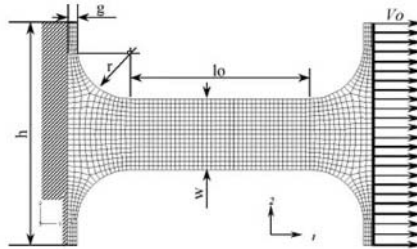


FIGURE 2. Initial and boundary conditions, specimen dimensions and representative mesh used during the 3D numerical simulations with ABAQUS/Explicit.

Recently, a complementary experimental und numerical study using the same approach has been performed for the following high strength steels DP and TRIP, [7].

## References

1. G.H. Staab and A. Gilat, *Exp Mech*, vol. **X**, 232-235, 1991.
2. H. Huh, W.J. Kang and S.S. Han, *Exp Mech*, vol. **42**, 8-17, 2002.
3. A. Rusinek and J.R. Klepaczko, *Int J Plast*, vol. **17**, 87-115, 2001.
4. R. Zaera, Fernandez-Saez J., *Int J of Solids and Structures*, vol. **43**, 1594-1612, 2006.
5. A. Rusinek, R. Zaera, J.R. Klepaczko and R. Cheriguene, *Acta Materialia*, vol. **53**, 5387-5400, 2005.
6. Tanimura S, Mimura K., *In Proceedings of the 4th international symposium on impact engineering*, edited by S. Tanimura & K. Hokamoto, Impact Eng Application, Japan, 2001, 57-64.
7. P. Larour, A. Rusinek, J.R. Klepaczko and W. Bleck, *Int Steel Research*, vol. **X** (2006),(in press).

## EFFECT OF A QUASI-STATIC PRESTRAIN ON SUBSEQUENT DYNAMIC TENSILE CURVES

L. Durrenberger<sup>1</sup>, A. Rusinek<sup>1</sup>, A. Molinari<sup>1</sup> and D. Cornette<sup>2</sup>

<sup>1</sup> Laboratory of Physics and Mechanics of Materials, UMR CNRS 75-54, University of Metz, Ile du Saulcy, 57045 Metz cedex, France

<sup>2</sup> Arcelor Research, Voie Romaine, BP 30320, F-57283 Maizières les Metz, France  
durrenberger@lpmm.univ-metz.fr

Ecological and safety preoccupations require the application of Ultra High Strength Steels in the automotive industry. Thanks to the very high mechanical characteristics of these steels, the safety performance is improved without increasing car weight. During the manufacturing of crash structure, an evolution of the microstructure is observed. It has been shown in [1] that the prestrain process generates a phase transformation which increases the crash response of a crash-box structure.

The non-prestrained material is generally used to explore the strain rate dependence of the flow stress. In this study, dynamic tensile loading have been carried out with two automotive steels after two quasi-static prestrain levels. The prestrain has been performed using sheet steels with dimensions 350\*460mm. The tensile specimens were then machined using the previous sheet steel only in the homogenous strain zone [1]. All the tests were performed at 90° of the rolling direction. At the end of the quasi-static process, the strain tensor is the following,

$$\overset{=}{\varepsilon} = \varepsilon \begin{pmatrix} 1 & 0 & 0 \\ 0 & -0.435 & 0 \\ 0 & 0 & -0.565 \end{pmatrix} \quad (1)$$

The two considered materials are a bake hardening steel BH260 and a TRIP800 steel. Klepaczko *et al* [2,3] have already shown that the effect of a jump of strain rates on the flow stress depends of the microstructure of the material. Because the specimens are unloading during the two loadings, strain rate history effects may be here studied. Von-Mises equivalent plastic strains  $\varepsilon_{eq} = \sqrt{2/3 \times \varepsilon_{ij}^p \varepsilon_{ij}^p}$  are used to compare the behaviour before and after the prestrain process. It is shown that a dynamic tensile loading after an initial quasi-static deformation leads to substantial decrease of the flow stress compared to the initial dynamic loading curve for TRIP steel, Fig. 1a. Conversely, a dynamic tensile loading after an initial quasi-static deformation leads to substantial increase of the flow stress compared to the initial dynamic loading curve for a BH260 steel, Fig. 1.b.

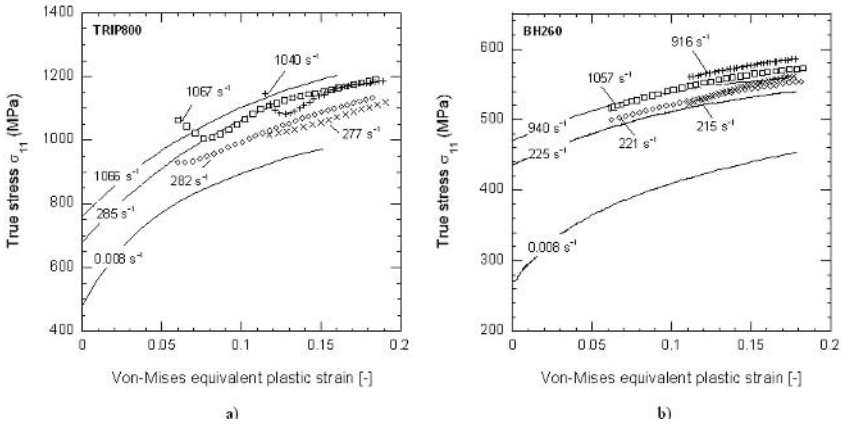


FIGURE 1. Strain rate history effect a) for the TRIP800 steel b) for the BH260 steel

The evolution of the dislocation density, which is strain and strain rate dependant, governs the evolution of the flow stress in the BH260 steel. In TRIP steel the behaviour is more complex, because the chemical composition, the initial austenite volume fraction and the strain path will affect the evolution of the flow stress.

## References

1. Durrenberger, L., Even, D., Molinari, A., Rusinek, A., 2006. Influence of the strain path on crash properties of a crash-box structure by experimental and numerical approaches. *Journal de Physique IV*, DYMAT Congress, Dijon 2006, France.
2. Klepaczko, J.R., Frantz, R.A., Duffy, J., 1977. History effects in polycrystalline FCC metals subjected to rapid changes in strain rate and temperature. *Rozprawy inzynierskie, Engineering transactions*, vol. **25**(1), 3-22.
3. Klepaczko, J.R., Duffy, J., 1982. History effects in polycrystalline BCC metals and steel subjected to rapid changes in strain rate and temperature. *Arch. Mech.*, vol. **34**, Warszawa. pp. 419-436.

## SELF-HEALING OF A SINGLE FIBER-REINFORCED POLYMER MATRIX COMPOSITE

Eyassu Woldeesenbet and Rochelle Williams  
Mechanical Engineering, Louisiana State University  
2508 CEBA, Baton Rouge, LA 70803, USA  
woldesen@me.lsu.edu

Excellent mechanical properties such as high strength, low specific weight, and impact and corrosion resistance, as well as advanced manufacturing methods and tailor ability of the lay-up make fiber-reinforced polymer matrix composites attractive candidates for use in many performance oriented structures. However, their use is limited due to the difficulty of damage detection and repairs, and lack of extended fatigue resistance. Healing of materials, such as glass, polymers, and concrete, has been investigated [1-3]. In these investigations, the healing process involved human intervention and thus the materials were not able to self-cure. There has been only a limited amount of research in self-healing of composite materials. Two of these suggest the inclusion of tubes in a brittle matrix material for self-repair of cracks in polymers and corrosion damage in concrete [4,5]. A more recent development at University of Illinois, Urbana-Champaign, which attracted a considerable amount of attention, was the incorporation of microcapsules that contained a polymer precursor into the matrix material of a composite [6]. The polymer precursor was contained in microcapsules and embedded into the matrix. The matrix contained randomly dispersed catalyst that was supposed to react with the precursor flowing through any crack formed due to damage and initiate polymerization. The polymer was then supposed to bond the crack face closed. The investigators overcame several challenges in developing microcapsules that were weak enough to be ruptured by a crack but strong enough not to break during manufacture of the composite system. The researchers have shown that it was possible to recover up to 75% of the maximum tensile strength of the virgin composites.

This paper presents the experimental results of self-healing single fiber-reinforced polymer (FRP) matrix composites. The idea for this work is inspired by natural living systems that initiate an autonomic healing process in response to damage. The initial development of self-healing composites involves the placing of a healing agent within a hollow fiber. A catalyst is then placed on the outer surface of the hollow fiber to avoid untimely polymerization. When a crack reaches the hollow fiber (Fig. 1), the healing agent fills and heals the crack after the filled hollow fibers partially or fully fracture allowing the healing agent to polymerize when it comes in contact with the catalyst (Fig. 2). Preliminary experiments show that self-healing is achieved in a single fiber test with high degree of restoration of the original tensile strength. This work will be extended to include a combination of hollow fibers, solid fibers, resin, a healing agent and a catalyst, that will be carefully assembled to develop functional self-healing fiber-reinforced polymer matrix composites. Further development of autonomic/self-healing fiber reinforced composites and associated advancement in the methods of self-healing mechanism will include the ability of localized healing and high healing efficiency when large scale composite systems with multiple fibers are involved.

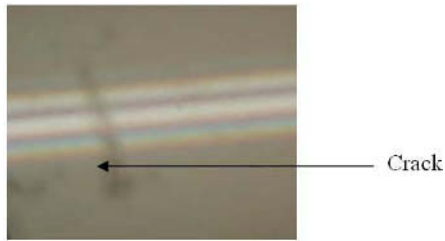


FIGURE 1. Initial crack placed on hollow glass fibers.

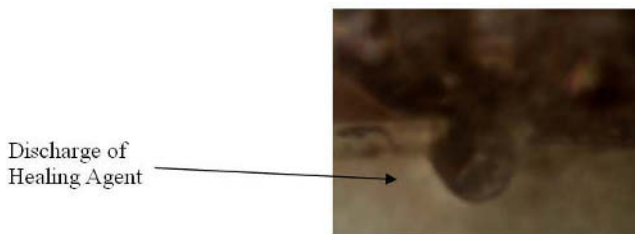


FIGURE 2. Release of healing agent through crack in hollow glass fiber.

## References

1. Stavrinidis, B. and Holloway, D.G., "Crack Healing in Glass," *Journal of the American Ceramic Society*, vol. **53**, 486-489, 1970.
2. Edvardsen, C., "Water permeability and Autogeneous Healing of Cracks in Concrete," *ACI Materials Journal*, vol. **96**, 448-454, 1999.
3. Wool, R.P. and O'Conner, K.M., "A Theory of Crack Healing in Polymers," *Journal of Applied Physics*, vol. **52**, 5953-5963, 1982.
4. Motuku, M., Vaidya, U.K. and Janowski, G.M., "Parametric Studies on Self-Repairing Approaches for Resin Infusion Composites Subjected to Low Velocity Impact," *Smart Materials and Structures*, vol. **8**, 623-638, 1999.
5. Dry, C., "Procedures Developed for Self-Repair of Polymeric Matrix Composite Materials," *Composite Structures*, vol. **35**, 263-269, 1996.
6. White, S.R., Sottos, N.R., Geubelle, P.H., Moore, J.S., Kessler, M.R., Sriram, S.R., Brown, E.N. and Viswanathan, S., "Autonomic Healing of Polymer Composites," *Nature*, vol. **409**, 794-797, 2001.

## MONITORING AND ANALYSIS OF DAMAGE DEVELOPMENT IN PIPELINES DUE TO EXPLOITATION LOADINGS

Zbigniew L. Kowalewski<sup>1,2</sup>, Tadeusz Skibiski<sup>3</sup>, Jacek Szelazek<sup>1</sup> and Sawomir Mackiewicz<sup>1</sup>

<sup>1</sup> Institute of Fundamental Technological Research

ul. witokrzyska 21, 00-049 Warsaw, Poland

zkowalew@ippt.gov.pl, jszela@ippt.gov.pl, smackiew@ippt.gov.pl

<sup>2</sup> Institute of Motor Transportation, ul. Jagiellońska 80, Warsaw, Poland

zbigniew.kowalewski@its.waw.pl

<sup>3</sup> Institute of Power Engineering, ul. Augustówka 5, 02-981 Warsaw, Poland

tadeusz.skibinski@ien.com.pl

Damage development due to creep under uniaxial tension at elevated temperatures is assessed using destructive and non-destructive methods in steels (A336, 40HNMA) and aluminium alloy. The results obtained using two different destructive methods for assessments of damage development are critically discussed. As the non-destructive method of damage development evaluation the ultrasonic investigations were applied.

In the first destructive method applied the specimens after different amounts of creep prestraining were stretched up to failure and variations of the selected tension parameters were taken into account for damage identification. In the second one, a damage degree was evaluated by studying variations of an initial yield locus position in the stress space and by determination of the yield loci dimensions. In this case variations of mechanical properties of copper and aluminium alloy are compared for the materials after both the plastic deformation due to monotonic loading at room temperature and the creep deformation due to constant load at elevated temperature.

The ultrasonic investigations were selected as the non-destructive method of damage development evaluation. In the case of this method the elasto-acoustic coefficient and acoustic birefringence coefficient were used to identify damage development in the tested materials. In order to get more thorough understanding of the phenomena associated with an influence of deformation history on mechanical properties of materials the paper considers two types of deformation processes: deformation due to creep and deformation due to plastic flow caused by the monotonically increasing load.

Uniaxial tension creep tests were carried out on two kinds of steel commonly used on elements working at elevated temperatures i.e. A336 and 40HNMA using plane specimens. Tests for A336 were conducted under stress level equal to 425 MPa, and temperature - 698 K, whereas for 40HNMA under 250 MPa at 773K. In order to assess a damage development during the process of creep the tests for A336 steel were interrupted for a range of the selected time periods 50h, 75h, 100h, 128h, 171h which correspond to the increasing amounts of creep strain equal to 1.72%, 1.98%, 2.57%, 5.5%, 7.0%, respectively. In the case of 40HNMA the tests were interrupted after 100h (0.34%), 360h (1%), 452h (1.1%), 550h (1.2%) and 988h (6.5%). The same magnitudes of deformation were applied to prestrain specimens by means of plastic flow at room temperature. After each prestraining test a damage of specimen was assessed using the non-destructive methods. In the next step of experimental procedure, the same specimens were mounted on the hydraulic servo-controlled MTS testing machine and then stretched until the failure was achieved. Variations of the basic mechanical properties of both steels, i.e. Young's modulus, conventional yield point, ultimate tensile strength and elongation, due to deformation achieved by prior creep or plastic flow were determined. It was observed for both materials that Young's modulus is almost not sensitive



on the magnitude of creep and plastic deformations. Contrary to the Young's modulus the other considered tension test parameters, especially the conventional yield point and the ultimate tensile strength, exhibit clear dependence on the level of prestraining. Taking into account the results for A336 steel we can conclude that assessments of creep damage development only on the basis of mechanical parameters determined from the standard tension tests for the material subjected to various amounts of creep prestraining do not allow to evaluate accurately whether some exploitation elements can further work safely or should be exchanged to protect a construction against the premature failure. However, in the case of 40HNMA steel such tests well described damage due to creep.

Ultrasonic wave velocity and attenuation are acoustic parameters most often used to assess material damage due to creep or fatigue. Results of investigations show that attenuation of ultrasonic waves is in practice stable until the last creep or fatigue stages. It was also observed that velocity changes due to creep or fatigue are small, and therefore, application of velocity measurement for damage evaluation in industrial conditions is very difficult. In this work, to evaluate damage progress in steels the elastoacoustic coefficient and acoustic birefringence  $B$  were applied instead of velocity and attenuation measurements. Specimens were subjected to creep or plastic deformations according to program presented earlier.

Elastoacoustic coefficient is the measure of elastoacoustic effect and describes ultrasonic wave velocity changes due to stress variation. Value of depends on material grade, mode of ultrasonic wave and correlation between ultrasonic wave propagation, polarization and stress directions. The highest value of is observed for longitudinal wave propagated along the stress. It was shown that this parameter is sensitive on prior creep deformation in case of A336 steel, for 40HNMA steel, however, it was completely not sensitive.

Acoustic birefringence  $B$  is a measure of material acoustic anisotropy. It is based on the velocity difference of two shear waves polarized in perpendicular directions. In the specimen subjected to creep the shear waves propagated in the specimen thickness direction and were polarized along its axis and in the perpendicular direction. The results show that acoustic birefringence can be an indicator of material degradation and can help to localize the regions where material properties are changed due to creep.

A good correlation of mechanical and ultrasonic parameters identifying creep damage is observed for 40HNMA steel.

## EXPERIMENTAL INVESTIGATION OF STRESS CONCENTRATIONS CAUSED BY INSERTS IN SANDWICH PANELS

Nicholas G. Tsouvalis and Maria J. Kollarini  
 National Technical University of Athens  
 School of Naval Architecture and Marine Engineering  
 Shipbuilding Technology Laboratory, Division of Marine Structures  
 Heron Polytechniou 9, GR-15773 Zografos, Greece  
 tsouv@deslab.ntua.gr

The high stiffness-to-weight and strength-to-weight ratios, which are the basic advantages of composite sandwich materials, are continuously improving during the last years, allowing the use of these materials in an always broadening range of engineering applications. Thus, joining and functional requirements for these materials are becoming much more demanding. Among the most difficult loading conditions a sandwich structure can carry, is the application of transverse concentrated loads, against which sandwich materials are by default sensitive. The local implantation of small high stiffness reinforcing inserts (i.e. wooden or metallic) in the core of the sandwich during manufacture is a quite common solution to the above problem. These inserts, however, have as a result an abrupt change in the material stiffness, thus leading in high local bending stresses in the sandwich skins, as well as in high local normal and shear stresses in the core of the sandwich. Several efforts to calculate these stress concentrations have recently been presented in the literature, being both analytical and numerical and including comparisons to relevant experimental measurements, like the works by Bozhevolnaya *et al.* [1], Bozhevolnaya and Lyckegaard [2], Thomsen *et al.* [3] and Tsouvalis and Kollarini [4].

The aim of the present paper is to investigate experimentally the magnitude that these stress concentrations can reach, as well as to test different inserts' geometries in an effort to compare various insert design concepts. Thus, eight sandwich beam specimens have been tested in 3-points bending, corresponding to four different geometries (2 specimens per case). The notation of the various geometric and material magnitudes used is shown in Fig. 1. Specimens with no insert were first tested, followed by specimens having a central butt insert (angle equals zero), a central scarf insert with  $\theta = 60^\circ$  and a central scarf insert with  $\theta = 45^\circ$ . The dimensions of the beam specimens are 340 mm length, 62 mm width, 25 mm core thickness,  $t_c$ , and approximately 2.7 mm skin thickness,  $t_f$ .

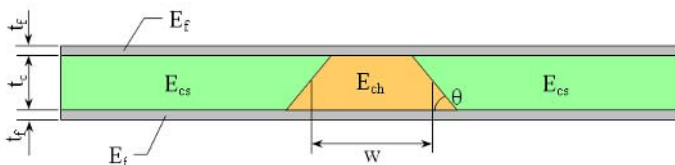


FIGURE 1. Geometric and material definitions.

Typical marine composite materials were used for manufacturing the test specimens. Hence, the normal core is Klegecell R 45, whereas the stiffer insert is made of Airex C70.130. After the

connection of the normal core to the insert, the assembly was properly grooved, since the sandwich panel was manufactured using the Vacuum Infusion method. Both skins are identical, comprising of three layers of combined Mat-Woven Roving and one MAT layer of glass reinforcement, whereas a low viscosity polyester resin was used for the infusion ( $W_f = 58\%$ ).

The material characterization of the glass/polyester skins was done by performing tensile and bending tests in standard specimens cut from a test plate specially infused for this purpose, keeping infusion conditions same to those followed for the sandwich plate.

The sandwich specimens were tested in 3-points bending. The magnitudes measured during the tests are central deflection and strains at 15 separate locations of the sandwich skins, both on the upper and on the lower surface of the specimen. Local strains in the vicinity of the insert-core junction were measured with the aid of small special purpose chain-gages.

In all cases, shear failure appeared in the normal core, close to the central insert. Comparative results are given for all insert geometries tested, as for example those in Fig. 2, which shows the load-deflection curves for the specimens tested. In the linear part of the response, strain concentration factors up to 4 were measured by the chain-gages at the insert-core junctions.

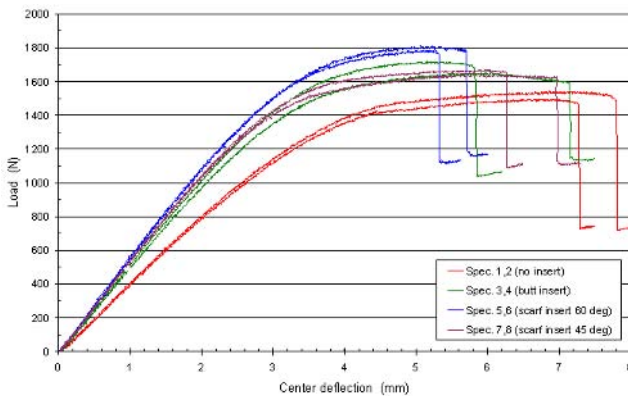


FIGURE 2. Load-deflection curves for specimens having inserts with various geometries.

## References

1. Bozhevolnaya, E., Lyckegaard, A. and Thomsen, O.T., *Appl Compos Mat*, vol. **12**, 135-147, 2005
2. Bozhevolnaya, E. and Lyckegaard, A., *Compos Struct*, vol. **73**, 24-32, 2006
3. Thomsen, O.T., Bozhevolnaya, E. and Lyckegaard, A., *Compos Part A: Appl Sci & Manuf*, vol. **36**, 1397-1411, 2005
4. Tsouvalis, N.G. and Kollarini, M.J., In *Proceedings of the 12<sup>th</sup> European Conference on Composite Materials*, Biarritz, France, 2006.

## ON THE PROGRESSIVE COLLAPSE OF MICRO LATTICE STRUCTURES

R.A.W. Mines, S. McKown, W. Cantwell, W. Brooks and C.J. Sutcliffe  
Department of Engineering, University of Liverpool,  
Liverpool, L69 3GH, United Kingdom  
r.mines@liv.ac.uk

Foam and honeycomb materials have been used for many years as cores in sandwich construction. Foam materials range from polymeric materials (Divinycell, Rohacell), through metals (Alporas aluminium foam), to graphite. Similarly, materials for honeycomb can be aluminium (Hexcel) or aramid (Hexcel). The main design variable for these cellular materials is density, but in general the microstructures of these materials are restricted to one, or a few, geometries. More recently, rapid prototyping manufacturing processes, such as selective laser melting, have been developed that allows the realisation of metallic open cellular lattice structures with resolution of 50 micro meters [1]. This process allows the tailoring of cellular architectures.

Usually sandwich construction is used in lightweight transport applications. This means that the design of such construction is driven by a variety of application issues, e.g. fatigue, in plane buckling of skins, local loading (connectors), foreign object impact etc. The application of interest here is foreign object impact. In such a case, the core is subject to multi axial stresses and can suffer progressive damage.

A number micro lattice geometries, manufactured in stainless steel by selective laser melting, are discussed. Fig. 1 gives two examples.

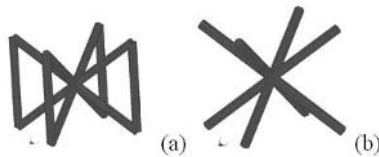


FIGURE 1. Two micro lattice geometries: (a) bcc,z and (b) bcc

Blocks of cellular material of dimension 25mm cubed were manufactured using the selective laser melting method [1]. The blocks were then subject to a number of loading conditions. In the uni-axial compression test, the blocks were placed between two platens in an Instron 50kN servo hydraulic machine and force and deformation recorded. Also, photos were taken of the progressive collapse of the cellular structures. In the shear case, the blocks were bonded to aluminium blocks that were then mounted an Arcan Rig. This rig allows various combinations of tension and shear. Fig. 2 shows the progressive collapse for compression loading for the selected micro lattice structures.

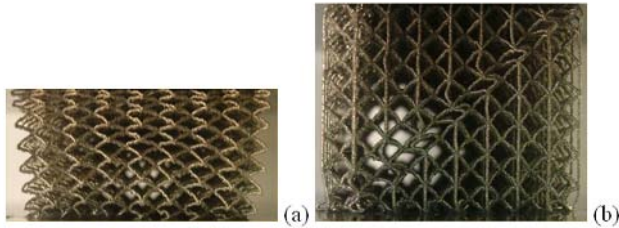


FIGURE 2. Progressive collapse of micro lattice structures: (a) bcc and (b) bcc,z

As far as global stress strain data is concerned, engineering stress strain data was derived for all tests. Data was typical of cellular materials, giving an elastic region ( $E_1, G_1$ ) a progressive collapse regime ( $\sigma, \tau$ ) and a densification regime.

It is shown that the Young's modulus for bcc,z is five times the modulus for bcc. This shows the effect of the vertical struts. The factor on the crush strength is 2.5. Figure 2 shows a change in failure mode. No localisation occurs for the case of no vertical struts. However, for the shear case the position is reversed, and the bcc lattice shows localisation.

Another cellular structure discussed is Alporas foam (as a benchmark), and this can be modelled as a truncated octahedron lattice structure. Finally, a  $f_2fcc,z$  structure is discussed. In this way, the progressive crush behaviours of various micro lattice structures are discussed under compression and shear loading. The aim is to make progress in understanding the many collapse mechanisms for these micro lattice materials.

## Reference

1. Santorinaios, M., Brooks, W., Sutcliffe, C.J., Mines, R.A.W., *WIT Transactions on the Built Environment*, vol. 85, 481-491, 2006

## QUASI-STATIC TESTING OF NEW PEEL STOPPER DESIGN FOR SANDWICH STRUCTURES

J. Jakobsen, E. Bozhevolnaya and O.T. Thomsen  
Department of Mechanical Engineering, Aalborg University  
Pontoppidanstraede 105, 9220 Aalborg, Denmark  
jja@ime.aau.dk , eb@ime.aau.dk , and ott@ime.aau.dk

A sandwich material is a layered assembly made of two thin strong face sheets separated by and bonded to a compliant lightweight core. This provides a lightweight structural element with very high bending stiffness and very high strength. Such structural sandwich elements, which may possess other desirable features such as high thermal insulation, high internal damping, high corrosion resistance, low maintenance costs, etc., are well suited for applications in the aerospace, marine, automotive, sustainable energy industries as well as in civil engineering. However, sandwich structures are sensitive to failure due to delamination between the face sheets and the core, for instance due to impact or fatigue damages. Such delaminations may start without prior warning, propagate very fast and eventually lead to a complete failure of the sandwich structure.

Initiation and propagation of cracks in sandwich structures are in focus of many previous and ongoing studies. Burman and Zenkert studied the fatigue behaviour of initial damaged and undamaged sandwich structures loaded in four point bending [1,2]. They found that fatigue may start in the core and continue as a face/core delamination. Carlsson *et al* studied the influences from face/core debonds on the crack developments in sandwich panels under compressive loads [3-6]. They found that the debonded area propagated as a face/core delamination when the load reached the buckling/instability level of the sandwich panel. Furthermore Bozhevolnaya *et al* studied the influences of core junctions on the structural response [7-11]. They found that the fatigue life was very dependant on the shape of the particular internal core junctions, and face/core delamination was commonly observed as the failure mode.

In this paper a specially designed peel stopper will be presented. The proposed peel stopper appears as a sub-structural component, which has to be embedded into the core of the sandwich element during its manufacturing (see Figure). The peel stopper works by activating an internal mechanism that prevents the propagation of delamination beyond the peel stopper boundaries, and thus restricts damage to a limited area where the delamination/peeling was initiated. When delamination/peeling is locally confined to the allowable and a priori predicted damage areas, the structural integrity of the sandwich is preserved, and the development of global failure/collapse may efficiently be prevented.

Three configurations of sandwich beams were manufactured and tested in 3 point bending under quasi-static load conditions. The first configuration had not been furnished with the peel stopper. The second configuration had an insert of the same material and of equal weight as the implemented peel stopper. The third configuration had the peel stoppers embedded. High-speed video recordings were performed during loading of the specimens up to failure, and post mortem inspections were subsequently conducted. The results of the tests showed that only the specimens with peel stoppers were able to arrest the crack propagation, thus ensuring that the material behind the peel stoppers remained intact and undamaged.

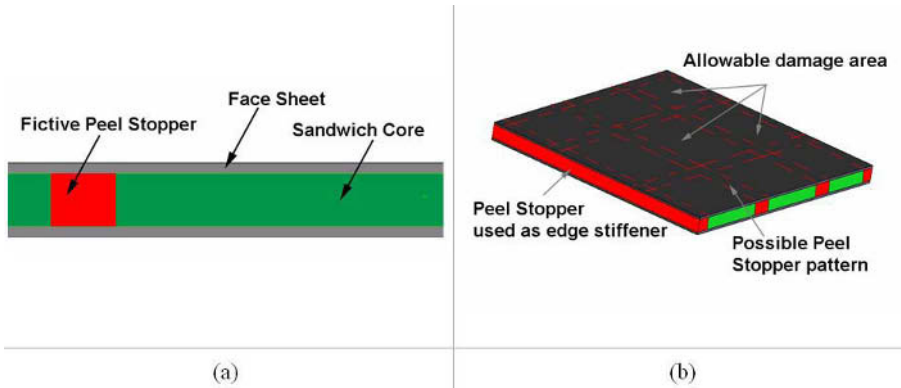


FIGURE 1. Peel stopper concept. (a) Cross-section of peel stopper embedded in core material. (b) Illustration of possible implementation of the peel stoppers into a sandwich panel.

## References

1. Burman, M. & Zenkert, D., *Int J Fatigue*, vol. **19**(7), 551-561, 1997
2. Burman, M. & Zenkert, D., *Int J Fatigue*, vol. **19**(7), 563-578, 1997
3. Avilés, F. & Carlsson, L., *J. Sandw. Struct. Mater.*, vol. **8**(1), 7-31, 2006
4. Carlsson, L.; Matteson, R.; Aviles, F. & Loup, D., *Compos. Sci. Technol.*, vol. **65** (15-16), 2612-2621, 2005
5. Mahfuz, H.; Islam, S.; Saha, M.; Carlsson, L. & Jeelani, S., *Appl Compos Mater*, vol. **12**(2), 73-91, 2005
6. Vadakke, V. & Carlsson, L., *J. Sandw. Struct. Mater.*, vol. **6**(4), 327-342, 2004
7. Bozhevolnaya, E. & Lyckegeard, A., *Compos. Struct.*, vol. **73**(1), 24-32, 2006
8. Bozhevolnaya, E. & Thomsen, O., *Compos. Struct.*, vol. **70**(1), 1-11, 2005
9. Bozhevolnaya, E. & Thomsen, O., *Compos. Struct.*, vol. **70**(1), 12-23, 2005
10. Lyckegeard, A.; Bozhevolnaya, E. & Thomsen, O., *J. Sandw. Struct. Mater.*, vol. **8**(5), 423-435, (2006)
11. Thomsen, O.; Bozhevolnaya, E. & Lyckegeard, A., *Compos Part A Appl Sci Manuf*, vol. **36**(10), 1397-1411, 2005
12. Grenestedt, J., *Compos. Sci. Technol.*, vol. **61**(11), 1555-1559, 2001
13. Wonderly, C. & Grenestedt, J., *J Compos Mater*, vol. **38**(10), 805-831, 2004

## OPTIMIZATION OF SURFACE DAMPING TREATMENTS FOR VIBRATION CONTROL OF MARINE STRUCTURE

Ramji Koon<sup>1</sup>, Ganesh Kumar. PVS<sup>2</sup> and S. Ranganath<sup>3</sup>

<sup>1</sup> Professor, Mechanical Engineering Department, A.U. College of Engineering, Andhra University, Visakhapatnam – 530 003, Andhra Pradesh, India

<sup>2</sup> Additional Director and Scientist F, NSTL, Vidyanagar, Visakhapatnam-530 027, A.P., India

<sup>3</sup> Assistant Professor, Raghu Engineering College, Dakamarri, JNTU, Vizianagaram, A.P., India  
ramjidme@yahoo.co.in

Dynamic excitation results in vibration of machinery and the support structures. Structural damping treatment i.e. Free layer damping (FLD) and Constrained layer damping (CLD) are passive control methods that consist of sandwiched metal and viscoelastic layer combinations which help to reduce vibration [1]. This paper presents the studies carried out on modeling of free layer damping and constrained layer damping. Modeling of FLD and CLD was carried out using Ross Kerwin and Ungar (RKU) analysis discussed by Paul J. Macioco [2]. The loss factor is calculated by using Hermann Oberst and Alfred Schommer [3] approach with help of RKU equations. Parametric studies have also been carried out by varying constrained layer thickness to obtain optimal loss factor. The Oberst beam technique, Hermann Oberst and Alfred Schommer approach [3] have been used to measure the experimental damping.

This paper utilizes the finite element analysis methodology to model the beam structure and validate results obtained from RKU analysis for Mild Steel (MS), CLD and FLD beams and Marine Structure. Modal analysis for the above structures with and without damping was carried out using ANSYS software. From the results, based on the principle of maximum strain energy, suitable locations for partial application of CLD and FLD were obtained. The MS and CLD, FLD treated test specimens have been modeled in ANSYS with Shell 63 and Shell 99 respectively and the required material properties are shown in Table 1. Modal analysis has been carried out to find out the natural frequencies of the specimen to validate with experimental results. The response of the MS, CLD, FLD beams and Marine structure were measured using FFT analyzer and the frequency response of FLD is shown in Fig. 1. The values obtained through ANSYS and experiment are comparable for the above said cases and thus validating the experiment.

From the results, it can be observed that treatment of MS bar with CLD and FLD has reduced the vibration response levels. However, it is seen that CLD is giving better performance as compared to FLD. CLD has a limitation in its degraded performance on vertical surfaces and FLD is found to be useful for vertical surfaces. When weight is a constraint, FLD can be more useful. Finally, CLD treatment was applied on the base frame of the marine equipment and a flat plate below Shock and Vibration mounts connecting to foundation. The viscoelastic layer is joined to the plate of the vibrating surface by means of an adhesive, and this layer is further constrained by a metallic layer. The relative vibration response (Amplitude) for the case of with and without CLD is also shown in Fig. 2.

The studies were also carried out for uncoated and coated beams (CLD & FLD). Inferences have been drawn from the results on the effectiveness of various damping configurations. The efficacy of partial coverage for vibration mitigation has also been brought out by a Finite Element analysis study. This paper also presents as case study, a typical application to marine structures.



Table 1. Material Properties.

Name of the Material	Young's Modulus (N/m <sup>2</sup> )	Poisson Ratio	Density (kg/m <sup>3</sup> )	Damping
Mild Steel	2.0E11	0.33	7850	0.002
Viscoelastic material	1125.0E6	0.49	1200	0.75



FIGURE 1. Response spectrum of FLD beam (test specimen 1)

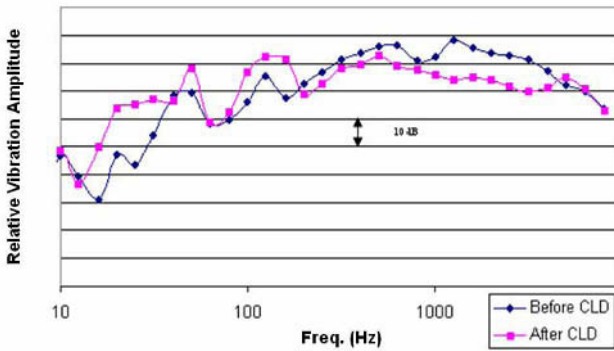


FIGURE 2. Relative vibration amplitude response for CLD Marine Structure

**References**

1. Crandall S.H., The Role of Damping in Vibration Theory, *Journal of Sound and Vibration*, vol. 11(1), 3-18, 1970.
2. Paul J.Macioco., Design for Damping Performance of Laminated Metals, *Appliance Manufacturer*, February 2002.
3. Hermann Oberst and Alfred Schommer., Acoustical Fatigue in Aerospace Structures, *Syracuse University Press*, Syracuse, N.Y, 1965.

## MEASURING MIXED MODE COHESIVE LAWS FOR INTERFACES IN SANDWICH STRUCTURES

Christian Lundsgaard-Larsen<sup>1</sup>, Christian Berggreen<sup>1</sup> and Bent F. Sørensen<sup>2</sup>

<sup>1</sup>Department of Mechanical Engineering,  
Technical University of Denmark  
DK-2800 Kgs. Lyngby, Denmark

<sup>2</sup>Materials Research Department,  
Risø National Laboratory  
DK-4000 Roskilde, Denmark  
cl@mek.dtu.dk

The purpose of this work is to establish a test procedure that allows fracture mechanics characterization of interface cracking in sandwich structures. This often entails large scale fiber bridging, which increases the size of the process zone beyond a point where linear elastic fracture mechanics (LEFM) is applicable. Instead of assigning the fracture processes to a single point at the crack tip (as in LEFM) the fracture process zone is represented by a cohesive zone in which the traction separation law (cohesive law) needs to be determined. The cohesive law can be measured, either indirect by modeling experiments and fitting parameters until numerical and experimental results coincide, Li *et al.* [1], or by direct measurement by e.g. the J integral approach, Sørensen and Kirkegaard [2]. In this study mixed mode cohesive laws are measured directly by relating the J integral to the normal and tangential opening of the initial crack tip. The test method is based on a double cantilever beam (DCB) specimen loaded by uneven bending moments, see Fig. 1. The test is conducted under displacement control in a tensile test machine, and the moment ratio is kept constant throughout one test. By varying the moment ratio the crack opening can be varied from pure normal opening to pure tangential crack surface displacements. A detailed description of the test method can be found in [2].

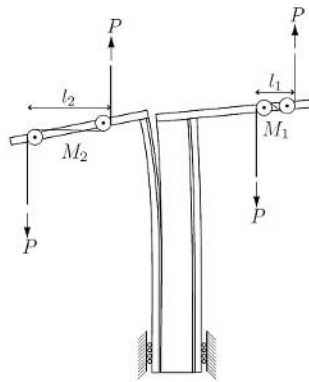


FIGURE 1. DCB sandwich specimen loaded by uneven bending moments.

The J integral is derived in closed form for the DCB sandwich specimen as function of specimen geometry, elastic properties and applied moments. The opening in the normal and tangential directions of the pre-crack tip is obtained using digital photogrammetry. By using stereo cameras and a speckled pattern painted on the specimen the system software tracks full field 3D displacements of the specimen surface, from which the openings are achieved. The cohesive stresses in the normal and tangential direction are obtained by differentiating the measured fracture toughness (equal to J) with respect to the normal and tangential openings. This is written as

$$\sigma_n(\delta_n^*, \delta_t^*) = \frac{\partial J(\delta_n^*, \delta_t^*)}{\partial \delta_n^*} \quad \sigma_t(\delta_n^*, \delta_t^*) = \frac{\partial J(\delta_n^*, \delta_t^*)}{\partial \delta_t^*} \quad (1)$$

The measured J value as function of pre-crack tip normal opening,  $\delta_n^*$ , is plotted for one specimen on Fig. 2 (left). The data points are fitted by splines, and the measured and fitted date are represented by full and dashed lines respectively. The cohesive law plotted in Fig. 2 (right) is obtained by differentiating the fitted fracture toughness with respect to the crack normal opening  $\delta_n^*$ .

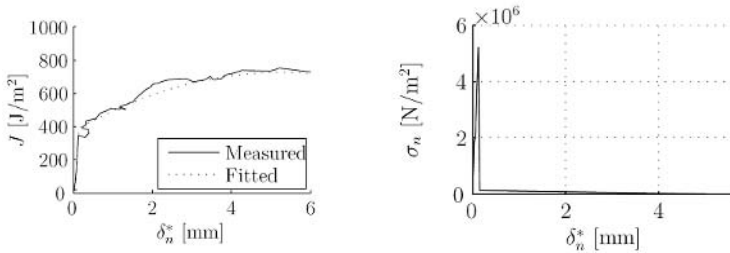


FIGURE 2. Measured and fitted J as function of crack normal opening (left) and derived cohesive law (right).

In Fig. 2 (left) initially J increases rapidly from 0 to 400 J/m<sup>2</sup> with a crack opening  $\delta_n^*$  of only 0.15 mm. Hereafter the crack propagates with slowly increasing fracture toughness from 400 to 740 J/m<sup>2</sup>. The fracture resistance (equal to J) increases since large scale fiber bridging is developing behind the crack tip. The obtained cohesive law shown in Fig. 2 (right) indicates two separate fracture processes. Initially as the material separates the stress increases rapidly to 5.2 MPa and then drops to 0.13 MPa, which corresponds to separation of the interface. As the crack propagates bridging fibers are formed in the crack wake and the cohesive stress decreases from 0.13 MPa to 0 as the crack opens from 0.15 to 5.7 mm.

## References

1. Li, S., Thouless, M.D., Waas, A.M., Schroeder, J.A. and Zavattieri, P.D., *Composites Science and Technology*, vol. **65**, 281-293, 2005
2. Sorensen, B.F. and Kirkegaard, P., *Engineering Fracture Mechanics*, vol. **73**, 2642-2661, 2006

## TESTING OF SANDWICH CORE MATERIALS AND SANDWICH PANELS SUBJECTED TO SLAMMING LOADS

Carl-Johan Lindholm  
Engineer - Technical Services, DIAB  
Box 201, SE-312 22 Laholm, Sweden  
carl-johan.lindholm@se.diabgroup.com

The present paper reports on proceedings in research of sandwich panels subjected to impact loads. The main objective with the research project is to find and validate methods to design sandwich structures subjected to localized- and impact loads.

The first part of the paper presents an experimental study on how the behaviour of foam core material changes with increasing strain rate. Two densities of Divinycell H grade have been tested at four different strain rates. The material was tested in tension with modified Amsler pendulum impact machine, se Fig. 1.

In the second part sandwich beams and panels have been tested in order to evaluate how different core material perform under a slamming load. Core materials used in sandwich structure have very different ductility or elongation at break. They range from stiff and strong but very brittle materials such as end-grain balsa and honeycombs to very ductile PVC and SAN based foam cores. Some marine classification societies give opportunity to design with lower safety factors for more ductile core materials. A trend in the industry is therefore to produce and use these more ductile cores. It is of interest to evaluate how much better a more “ductile” core is than a “brittle” one. A range of different core material has been tested, in beams and panels, at different load rates from quasi-static to “slamming” type loads.

The beam testing was made according to ASTM C393 with the DNV Dynamic test (DNV HSLC Pt.2 Ch.4 Sec.2 D300) specifying a particular stress based loading rate (65 MPa/s). The panel testing was done in a unique Servo-hydraulic Slam Test System (SSTS) machine. To provide greater control of the water impact event than provided by traditional drop tests the SSTS utilises a high speed (up to 10m/s) computer controlled closed loop feedback servo-hydraulic system.



FIGURE 1. Test setup for strain rate testing. The raised pendulum connects with the stiff carbon fiber rod when vertical, bringing the rod and one end of the specimen with it. The other end of the specimen is locked in a small aluminum fork connected directly to the load cell. The laser keeps track of the pendulum position and the pendulum speed can be calculated.

## ASSESSMENT OF HYGROTHERMAL AGEING AND DAMAGE IN SANDWICH FOAM USING TSA.

E. Lembessis, J.M. Dulieu-Barton, R.A. Sheno  
Fluid Structure Interactions Group  
School of Engineering Sciences, University of Southampton,  
Southampton, SO17 1BJ, United Kingdom  
elli@soton.ac.uk

This work deals with the experimental measurement and characterisation of damage to PVC closed-cell sandwich core foams. The damage to the foam is introduced in the form of moisture effects after immersion in a controlled hygrothermal environment and later, by the insertion of a crack. The non contact technique of Thermoelastic Stress Analysis (TSA) is detailed by Dulieu-Barton and Stanley [1], is used to assess and evaluate the effects of these damage conditions upon the foam. The TSA system used in this work is the ‘Silver’ model manufactured by Cedip Infrared Systems and comprises of a 320x240 array of infra-red detectors to register the thermal changes in a material subjected to an excitation. One advantage of the TSA technique is the option of a zoom lens attachment which permits the transformation from a full-field to a high resolution assessment of localised effects in individual foam cells. TSA thus provides the scope for validating theoretical models presented in the literature for foam cell behaviour under load.

This work is motivated by the challenges faced by designers in the marine industry which commonly seeks to integrate different foam types and densities within the same sandwich structure, while enduring variable loading forces and environmental conditions for the duration of the service life of the structure. Recent trends in marine design philosophy favour linear foams for use in areas subject to localized impact loading, and may further optimize the structure by reducing the design safety factors of the core in deference to the good mechanical properties exhibited by linear foams under test conditions. This work seeks to examine the severity of influence environmental conditions have upon the behavior of a sandwich core. Progressive ageing of the foam core is simplified for laboratory conditions and the moisture uptake accelerated by immersing the foam specimens in distilled water held at 60°C. Gravimetric data for both linear and cross-linked foams is collected for a range of densities manufactured by Airex© R63.50., R63.80, R63.140., C70.55, C70.75, C70.90, C70.130., C70.200, and C71.75ET, a foam designed to withstand elevated temperatures. Predictably higher density foams are found to be more resilient to moisture uptake. However, linear foams are significantly more sensitive to hygrothermal ageing than cross-linked foams as is the foam suitable for use at elevated temperatures. Ageing results in changes in fracture toughness for modes I and II while all materials exhibit increased brittleness. The resulting change in material behavior due to ageing, is assessed using TSA for two structural foams R63.140 and C70.130.

The foam test specimens are shown in Fig. 1 as mounted in a CTS-type rig adapted to accommodate larger specimens so that TSA could be performed. The rig can be rotated within the test machine so as to allow the mode mixity to vary by increments between pure mode I and mode II. The specimen is subject to a mean tensile strain, and dynamically excited with a sine wave amplitude cycle. The aged and the unaged foam specimens may then be used to calibrate the received thermoelastic signal. Mechanical damage in the form of a ‘crack’ is then introduced and the subsequent interaction between crack-tip and foam cell wall as shown in Fig. 2, may then be analyzed using TSA.

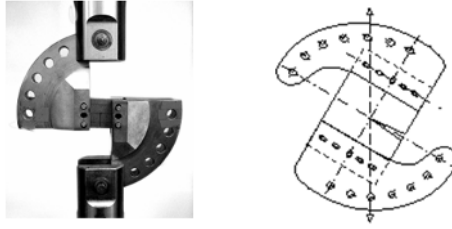


FIGURE 1. Initial CTS-type rig (left), and diagram of adapted CTS rig (right) to show lines of force pass through center of specimen and crack-tip (shown exaggerated), as it is rotated by increments of 10°, 30°, 45°, 60°, 80° between modes I and II.

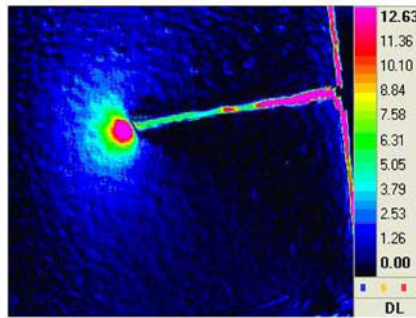


FIGURE 2. TSA Image of a mixed-mode crack-tip in an unaged specimen

The sensitivity of the technique provides the potential to quantitatively explore the behaviour of foam and damage on both a global and cellular level with the promise to validate and refine models of structural behaviour [2], while the flexibility and portability of the equipment provides the potential for in-situ examination of a marine hull.

## References

1. Dulieu-Barton, J.M., Stanley, P., *J. of Strain Analysis*, vol. **33**, no.2., 93-104, 1998
2. Gibson, L. Ashby, M. *Cellular Solids-Structure and Properties*, Cambridge Press, Second Edition, 1997

## ALUMINUM/FOAM SANDWICH BEAMS IN THREE-POINT BENDING

E.E. Gdoutos and D.A. Zacharopoulos  
School of Engineering, Democritus University of Thrace  
Vasilissis Sofias 12, GR-671 00, Xanthi, Greece  
egdoutos@civil.duth.gr

Sandwich construction is of particular interest and widely used, because the concept is very suitable and amenable to the development of lightweight structures with high in-plane and flexural stiffness [1-13]. Sandwich panels consist typically of two thin face sheets (or facings, or skins) and a lightweight thicker core. Commonly used materials for facings are composite laminates and metals, while cores are made of metallic and non-metallic honeycombs, cellular foams, balsa wood and trusses. The facings carry almost all of the bending and in-plane loads, while the core helps to stabilize the facings and defines the flexural stiffness and out-of-plane shear and compressive behavior.

In the present work a thorough study of the nonlinear load-deflection behavior of aluminum/foam sandwich beams under three-point bending was undertaken. The beams were made of aluminum facings and a PVC closed-cell (Divinycell) core. Four types of core material H60, H80, H100, and H250Kg/m<sup>3</sup> with densities 60, 80, 100 and 250 Kg/m<sup>3</sup> respectively, were used. The thickness of the facings and core were 1 mm and 25.4 mm, respectively. A host of spans were tested. The uniaxial tensile, compressive, and shear stress-strain curves of the facings and core materials were obtained. It was found that aluminum exhibits an elastic-plastic stress-strain behavior in uniaxial tension and compression, while the shear stress-strain curve of the core material presents an initial linear part followed by a nonlinear part with gradually decreasing shear modulus up to fracture. Experimental results of three-point bend sandwich specimens reveal that the load-deflection curves are composed of an initial linear part followed by a nonlinear behavior up to fracture. The extent of the nonlinear part depends on the length and configuration of the sandwich beam.

A nonlinear mechanics of materials analysis was used to predict the experimental results. To account for large deflection effects the finite deformation solution of a three-point bend made of a monolithic material was used. In the nonlinear range an incremental procedure was applied. For this reason, the bending and shear stress components were first calculated for each loading step and the stress-strain curves in tension or compression of the facings and in shear of the core were used to obtain the corresponding tensile, compressive and shear moduli of the two materials. The beam deflection increment was then calculated from elementary beam theory as the sum of bending and shear contributions.

The experimental results were in good agreement with theoretical predictions. For the beam spans studied it was shown that the load-deflection nonlinearity is mainly attributed to the nonlinear behavior of the core material, whereas the effects of the facings nonlinearity and the relatively large deflections of the beam are small. Furthermore, a thorough study of the combined effect of specimen dimensions and material properties of the facings and core on the nonlinear load-deflection behavior of the composite sandwich beams was conducted. The shear contribution to the beam deflection was calculated and compared with the corresponding bending contribution of the facings for various beam spans and foam core materials.



**References**

1. Daniel, I. M., Gdoutos, E. E., Wang, K.-A. and Abot, J. L., 2001, *International Journal of Damage Mechanics*, vol. **11**, 309-334, 2002.
2. Gdoutos, E.E., Daniel I.M. and Wang, K.-A., *Proceedings of the 6th Greek National Congress on Mechanics*, edited by E.C. Aifantis and A.N. Kounadis, July 19-21, 2001, Thessaloniki, Greece, pp. 320-326, 2001.
3. Daniel, I.M., Gdoutos, E.E and Wang, K.-A., *Proceedings of the Second Greek National Conference on Composite Materials, HELLAS-COMP 2001*, Patras, Greece, 6-9 June 2001, 2001.
4. Daniel, I.M., Gdoutos, E.E., Abot, J.L. and Wang, K.-A., *ASME International Mechanical Engineering Congress and Exposition*, New York, November 11-16, 2001, in *Contemporary Research in Engineering Mechanics*, edited by G.A. Kardomateas and V. Birman, AD-Vol. **65**, AMD-Vol. **249**, pp. 293-303, 2001.
5. Gdoutos, E.E., Daniel, I.M., Abot, J.L and Wang, K.-A., *Proceedings of ASME International Mechanical Engineering Congress and Exposition*, New York, November 11-16, 2001.
6. Gdoutos, E.E., Daniel, I.M. and Wang, K.-A., *Experimental Mechanics*, vol. **42**, 426-431, 2002.
7. Daniel, I.M., Gdoutos, E.E and Wang, K.-A., *Advanced Composites Letters*, vol. **11**, 49-57, 2002.
8. Abot, J.L., Daniel, I.M., and Gdoutos, E.E., *Proceedings of the 14th European Conference on Fracture*, Cracow, September 8-13, 2002, edited by A. Neimitz et al, Vol. I, pp. 13-19, 2002.
9. Abot, J.L., Daniel, I.M. and E.E. Gdoutos, *Journal of Sandwich Structures and Materials*, vol. **4**, 157-173, 2002.
10. Gdoutos, E.E., Daniel, I.M. and Wang, K.-A., *Mechanics of Materials*, vol. **35**, 511-522, 2003.
11. Daniel, I.M., Gdoutos, E.E., Abot, J.L. and Wang, K.-A. in *Recent Advances in Composite Materials*, edited by E.E. Gdoutos and Z.P. Marioli-Riga, Kluwer Academic Publishers, pp. 279-290, 2003.
12. Daniel, I.M., Gdoutos, E.E. and Abot, J.L., *Proceedings of the 2003 SEM Annual Conference*, June 2-4, 2003, Charlotte, North Carolina, 2003.
13. Gdoutos, E. E., Daniel, I. M. and Wang, K.-A., *Composites, Part A*, vol. **33**, 163-176, 2002.

## RESEARCHING THE PROCESSES LEADING TO THE FAILURE OF COMPOSITE SANDWICH STRUCTURES

Alexander Fergusson, Amit Puri, John Dear and Andrew Morris<sup>2</sup>

Department of Mechanical Engineering, Imperial College London, SW7 2AZ, UK

<sup>2</sup> Group Head Boiler Integrity, E.ON UK, Power Technology

Ratcliffe-on-Soar, Nottingham NG11 0EE, United Kingdom

alexander.fergusson@imperial.ac.uk; amit.puri@imperial.ac.uk;

j.dear@imperial.ac.uk & y.p.morris@eon-uk.com

There is much interest in reducing the propensity for onset of failure processes in composite sandwich materials. Already, composite sandwich materials are increasingly finding new applications and this will be more so if their propensity to failure can be reduced. Initial onset of a failure can sometimes be attributed to inherent shortcomings in the design and manufacture of the composite sandwich panels. Mostly, other failures can be attributed to the way the sandwich panels are used in the structure. The interest in this study is to simulate loading conditions that can be generated in composite sandwich panels when employed in different engineering structures and to investigate causes for failure processes to be initiated in these materials. The aims of the research reported on in this paper were:

- To study the development and distribution of strain in composite sandwich panels when subjected to four-point flexure and the failure processes as they occur.
- To relate the onset of failure processes in producing delamination and other types of failure.
- To develop the use of DIC and other methods to assist in evaluating the integrity of different types of composite sandwich structure and also for in-service monitoring of these panels.

The experimental method used for this study was four-point flexure as this provided well for a constant bending moment between the two central rollers. It was important to have a central region of the specimen subjected to constant flexural loading so that the effect of defects on flexure in sandwich panels could be examined consistently. Testing was performed to appropriate standards [1]. Also, four-point loading allowed for observation of the area of the panels between the central two rollers using Digital Image Correlation (DIC) [2] as well as other methods. The composite panels studied included those produced by the RIFT method [3] as this low cost method is becoming very attractive for some applications as an alternative to autoclaved pre-preg materials.

Composite sandwich materials are susceptible to different damage and defects depending on their design, manufacture and use in structures. Also, the causes for the damage are many. Damage in wind turbine blades, for example, can occur from events such as dropped tools during maintenance, or debris impacting during periods of high wind as well as long service fatigue. Once initiated, damage can develop into delaminations, core disbands and cracks at lower stress levels. The resulting damage is often invisible to the naked eye and is mostly on the interior facings of the composite skins. Inflicted damage to composite sandwich components by events such as mentioned above can also develop existing manufactured defects. These manufactured defects and shortcomings can take the form of resin dry spots, skin-core disbands and such features. Whilst the cause and nature of defects are wide ranging, their effect can be similar. Namely, these often well-hidden defects can locally reduce the stiffness of these structures and can be detrimental, to different degrees, to the functional integrity of the component. Fig. 1 shows one example of DIC

analysis of a foam core between the two central rollers of the four-point bend loading geometry [3-5]. In this case, Aluminium tabs were used to reduce core crush immediately beneath the rollers. Strain gauges were attached to upper and lower skins of the sandwich panel for comparison with the DIC results.

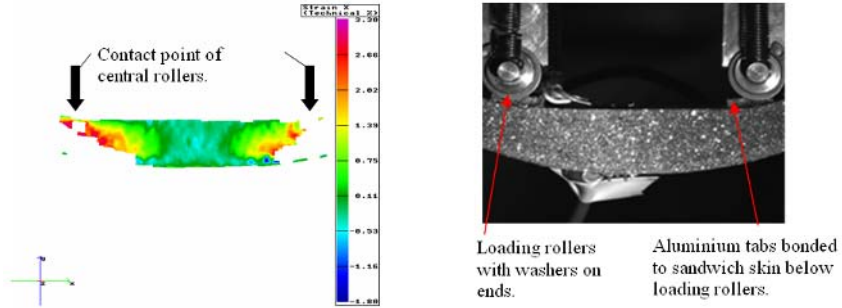


FIGURE 1. DIC of the foam core of a sandwich panel in four-point bend loading.

## References

1. ASTM Standard Test Method for flexural properties of sandwich constructions. C393, 1994.
2. <http://www.gom.com> Deformation measurement system developed by GOM mbH in Germany.
3. Fergusson, A. Resin infusion of composite sandwich structures for skis and snowboards. *MSc Dissertation*, Imperial College London, 2005.
4. Puri, A. Digital image correlation applied to wind turbine structures. *MEng Final Year Project*, Imperial College London, 2006.
5. Robinson, R. Flexural behaviour of composite sandwich panels. *MSc Dissertation*, Imperial College London, 2006.

## IMPACT ENERGY ABSORPTION IN NOVEL, LIGHTWEIGHT SANDWICH PANELS WITH METALLIC FIBRE CORES

J. Dean<sup>1</sup>, P.M. Brown<sup>2</sup> and T.W. Clyne<sup>1</sup>

<sup>1</sup> University of Cambridge, Department of Materials Science and Metallurgy, Pembroke Street, Cambridge, UK, CB2 3QZ

<sup>2</sup> Defence Science and Technology Laboratories, Porton Down, United Kingdom  
jd362@cam.ac.uk

Novel, stainless steel sandwich panels incorporating bonded networks of metallic fibres in the core were penetrated at low ballistic velocities. The sandwich panels (approximately 1.5 – 2 mm thick), were impacted by hardened, spherical steel projectiles. Incident and emergent velocities were measured and the absorbed energies calculated. Impact tests were also conducted on isolated face and core material to ascertain their respective contribution to the overall absorbed energy. The sum of the absorbed energies from the face and core materials was found to differ from the energy absorbed by the sandwich panels. This suggests that some synergy between the face and core material exists, which contributes in some way to the overall absorbed energy.

3-D simulations were conducted using the finite element code, ABAQUS/Explicit. Suitable faceplate material models were first developed (see Fig. 1), which successfully captured the combined effects of plasticity, fracture and rate dependence using a phenomenological ductile failure model available in ABAQUS. Experimental faceplate data is shown to be in good agreement with predictions. Additionally, the effect of faceplate separation distance on absorbed energy was investigated. The results indicate that an optimal separation distance exists.

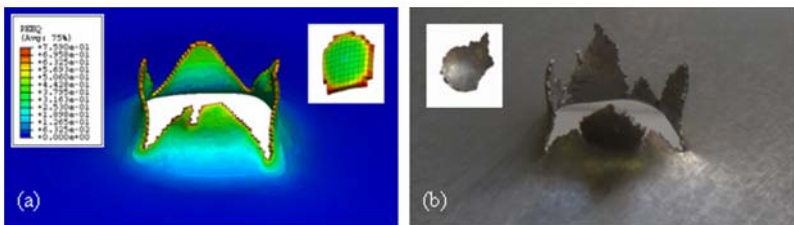


FIGURE 1. (a) Equivalent plastic strain contours for a stainless steel faceplate impacted at 218 m s<sup>-1</sup> and (b) a comparison with experiment.

Finally, the predictions obtained from sandwich panel simulations were found to be in excellent qualitative agreement with experiment (both petalling and plugging phenomena were successfully modelled – see Fig. 2). Encouragingly, the sandwich panel model adequately captured the observed experimental trends and is, therefore, considered a capable tool for rapid optimisation.



FIGURE 2: (a) Equivalent plastic strain contours for a sandwich panel impacted at  $235 \text{ m s}^{-1}$  and (b) a photograph showing the equivalent experimental result.

## DYNAMIC MODULUS OF SYNTACTIC FOAM CORE - A NON DESTRUCTIVE APPROACH

Eyassu Woldesenbet and Phani Mylavarapu  
Mechanical Engineering, Louisiana State University  
2508 CEBA, Baton Rouge, LA 70803, USA  
woldesen@me.lsu.edu

Sandwich composites are a special class of composite materials which are widely used because of their high specific strength and bending stiffness. Lower density of these materials makes them well suited for marine and aerospace applications. Developments in aviation posed requirement of lightweight, high strength and highly damage tolerant materials. Sandwich structured composites, fulfilling these requirements became the first choice for many applications including structural components for ground transport and marine vessels. The use of cores such as closed cell structured foam in sandwich structures gives some distinct advantages over open cell structured foams and cores [1]. The specific compressive strength of close cell structured foams is much higher and absorbs less moisture than open cell structured foam.

Syntactic foams are hollow particle filled core materials that have recently emerged as attractive material for use in applications requiring low weight, low moisture absorption and high insulation properties. Quasi- static and dynamic properties of these syntactic foams are very important as these materials are used in various important structural applications in aerospace and marine industry [2-3]. Even though various destructive techniques such as quasi-static compression and split Hopkinson pressure bar apparatus are used as tools to find quasi-static and dynamic modulus, there is a need for characterizing these materials non-destructively.

Several Non Destructive techniques such as Ultrasound are used in the industry to check for quality in these materials [4]. Although Ultrasonic imaging can be used for a variety of materials, it is difficult to use this technique for porous materials and foams due to high attenuation of ultrasonic waves in air. The ultrasonic equipment used in this research is shown in Fig. 1. The present study focuses on the prediction of dynamic modulus using ultrasonic testing in various types of solid and hollow particle reinforced syntactic foams. The volume fractions in the particulate composites are varied from 10-60%. Longitudinal and shear wave velocities are used for calculating the dynamic modulus using the time of arrival of reflections from the sample. Effect of longitudinal attenuation behavior along with longitudinal and shear wave velocities on the varying density and volume fraction of syntactic foams is also discussed. The Pulse Echo method [5] is used for the ultrasonic characterization of these materials.

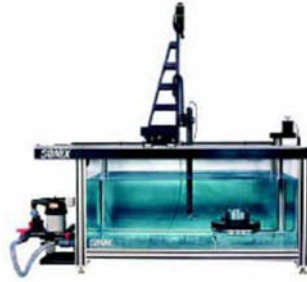


FIGURE 1. Ultrasonic Equipment used in the research.

### References

1. Vinson J.R., *The Behavior of Sandwich Structures of Isotropic and Composite Materials*. Lancaster: Technomic, 1999.
2. Gupta N, Woldesenbet. E., and Mensah. P., *Composites A: Appl Sci and Manuf*, vol. **35**(1), 103-111, 2004.
3. Woldesenbet E., Nikhil Gupta and Jadhav A., *Journal of Materials Science*, vol. **40**, no.15, 4009-4017, 2005.
4. Krautkramer H., and Krautkramer J, *Ultrasonic Testing of Materials*, Springer Verlag, New York, 1969.
5. Tattersall H G., *J. Phys. D: Appl. Phys.*, vol. **6**, 819-832, 1973.

## THERMAL AND MECHANICAL RESPONSE OF SANDWICH PANELS IN FIRE

P.A. Cutter<sup>1</sup>, R.A. Shenoi<sup>1</sup> and H. Phillips<sup>2</sup>

<sup>1</sup>University of Southampton, Highfield, Southampton, SO17 1BJ, United Kingdom

<sup>2</sup>Royal National Lifeboat Institution, Poole, Dorset, BH15 1HZ, United Kingdom  
p.a.cutter@soton.ac.uk, r.a.shenoi@soton.ac.uk, hphillips@rnli.org.uk

A major factor preventing further widespread use of polymeric sandwich materials is their behaviour in fire. The fire aboard the RNoN composite mine hunter “Orkla” in 2002 [1] did much to harbour the belief that sandwich materials are not safe to be used in structures where there is a risk of fire. One of the main factors leading to the eventual loss of the vessel was the collapse of the composite sandwich wheelhouse. The ability to be able to predict changes in strength of such structures when subjected to fire would be a valuable asset to designers and operators in the future.

The Royal National Lifeboat Institution (RNLI) is a registered charity that provides 24-hour lifeboat search and rescue cover up to 100 nautical miles off the coast of the United Kingdom and the Republic of Ireland. The RNLI is responsible for the design, build and operation of over 300 lifeboats ranging in size from 5m to 17m in length. The largest lifeboat in the RNLI’s fleet is the Severn Class lifeboat (Fig. 1). which is, like the majority of the all-weather fleet, constructed from advanced composites including sandwich materials. This research is being conducted as part of the RNLI’s general safety assessment of these composite lifeboats and is being entirely funded by the RNLI at the University of Southampton. The FTP Code [2] stipulates the requirements for materials to be used in maritime structures with regards to fire safety. This covers the many aspects of material response to fire including the heat transfer through and strength of, decks and bulkheads exposed to fire. This does not however provide a cost effective method of trialing different materials or an assessment of the overall structural response in fire.



FIGURE 1. RNLI Severn class lifeboat in service.

Davies *et al.* [3] provides an overview of the current state of knowledge in the testing and numerical modelling of polymeric materials when subjected to fire. The work has concentrated on the heat transfer through and degradation of single skin polymer composites subjected to fire as well as assessments of the strength during and after fire. There is however lacking a detailed study on the performance of sandwich structures in fire.

At the University of Southampton a test rig has been developed by Cutter *et al.* [4] in which it is possible to test the strength of composite materials in fire (Fig. 2). Panels of dimensions 200 mm × 200 mm up to 100mm thick can be subjected to a heat source on one side from a propane fired burner, which can follow a specific temperature-time curve up to 900°C. A detachable loading



module has also been built which fixes onto the furnace in order to apply out-of plane loads to the panels. The unit has been designed to be portable and is housed in a laboratory fume cupboard. The system provides a much more economic method for determining the performance of sandwich materials in fire than was previously available.



FIGURE 2. Fire testing apparatus.

The work at the University of Southampton aims to provide an assessment of the risks posed by fire aboard a lifeboat. These are being evaluated through the use of the apparatus described above and through the development of numerical models. The research has been split up into 4 stages in order that each aspect of the response of sandwich materials in fire is understood independently. The first stage involves the testing of sandwich panels exposed to intense fire sources so as to characterise the heat transfer through the materials and the degradation of the core material. Fig. 3 shows the result of such a test on a specimen from a deck constructed from sandwich. Small scale testing has also taken place to characterise the effects of heating on core materials using thermal decomposition apparatus to obtain transition temperatures. The second stage requires the strength of the heated panels to be tested after different exposure times and intensities. Using simple models related to the thickness of char material formed in the panels it is possible to predict the changes in strength of these materials. The third stage relates to the combined thermal and mechanical testing of sandwich panels exposed to fire. These results will then be used to verify finite element models predicting the changes in strength of the test panels. The final stage of the work involves the scaling of these results to a full size sandwich deck.

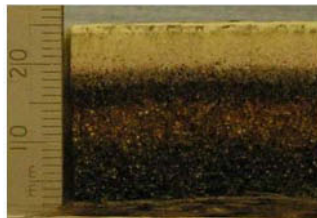


FIGURE 3. Cross section through Severn class deck sandwich panel after exposure to fire. The thickness of the distinct layers shown is used to predict the strength of the sandwich.

## References

1. RNoN, "The fire on board the HNoMS Orkla 19th November 2002," Technical Expert Group Norwegian Defence Logistics Organisation 2003.
2. IMO, FTP Code- International Code for Application of Fire Test procedures: IMO, 1998.
3. Davies, J.M., Wang, Y.C., and Wong, P.M.H., "Polymer composites in fire", *Composites Part A: Applied Science and Manufacturing*, vol. 37, 1131-1141, 2006.
4. Cutter, P. A., Gillitt, A. W., Hilmanson, G., and Mitsotakis, N., "Development of a Method for Assessing the Strength of Composite Materials in Fire," MEng Group Design Project Report, School of Engineering Sciences, Ship Science, University of Southampton, 2004.

## TENSILE AND FLEXURAL PROPERTIES OF SOLID-STATE MICROCELLULAR ABS PANELS

Krishna Nadella and Vipin Kumar  
 Department of Mechanical Engineering  
 Box 352600, University of Washington  
 Seattle, WA 98195-2600, USA  
 krivenk@u.washington.edu, vkumar@u.washington.edu

Microcellular foams refer to thermoplastic foams with cells of the order of 10  $\mu\text{m}$  in size. Typically these foams are rigid, closed-cell structures. The microcellular process was invented at Massachusetts Institute of Technology in early eighties [1, 2], in response to a challenge by food and film packaging industries to reduce the amount of polymer used in thin-walled articles. Thus was born the idea to create microcellular foam, where we could have, for example, 100 bubbles across 1 mm thickness, and expect to have a reasonable strength for the intended applications. An early review of the subject appeared in 1993 [3]. A more recent account of microcellular foams can be found in the Handbook on Polymer Foams, 2003 [4].

We have adopted the original microcellular process to produce thick, flat panels that could be used as part of a panel system for housing construction, for example. This is achieved in a Constrained Foaming process illustrated in Fig. 1. The foaming step is conducted inside the platens of a heated press, where metal shims maintain a gap equal to the desired panel thickness. The constrained foaming process has been used for producing microcellular ABS panels with densities as low as 10% of solid ABS [5, 6]. A unique aspect of the solid-state microcellular process is that a solid skin of desired thickness that is integral to the foam core can be created [7]. Since skin-core structures can be directly produced in the solid-state process, these panels may be suitable for use in certain applications, such as structural foams, without further modification. On the other hand, the smooth polymer skin makes these foams ideal as core materials for lamination with stiff outer sheets of higher stiffness.

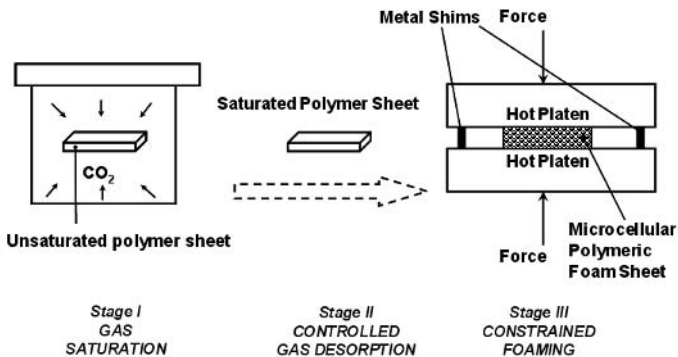


FIGURE 1. Constrained foaming process for microcellular thermoplastic panels.

This research is motivated by the potential of microcellular panels as novel core materials in sandwich construction. We report on the ABS core properties in tension and flexure. Microcellular ABS panels with densities in range of 20%-80% of solid density, were produced using CO<sub>2</sub> as the physical blowing agent. Following this, the integral skin on each of the panels was machined off via a milling operation. This was done in order to test the mechanical properties of only the cellular cores of these panels. Once the skin was removed, the panels were further machined and sanded into tensile and bending test samples. The sample preparation and testing was conducted according to ASTM D638 for tensile and ASTM D790 for flexural property characterization. It was found that tensile and flexural behavior of the microcellular ABS panels is described quite well by the Gibson-Ashby cubic cell model [8].

## References

1. Martini J., Waldman F. A., and Suh N. P., *Proceedings of SPE ANTEC 1982*, San Francisco, CA, USA, pp. 674, 1982
2. Martini J., Waldman F. A., and Suh N. P., *US Patent 4473665*, 1984
3. Kumar V., *Progress in Rubber and Plastics Technology*, vol. **9**, No. 1, pp. 54, 1993
4. Kumar V., and Nadella K., *Chapter on Microcellular Foams in Handbook on Polymer Foams*, David Eaves, Ed., RAPRA, UK, 2003
5. Nadella K., Kumar V., and Li W., *Cellular Polymers*, vol. **24**, No. 2, pp. 71-90, 2005
6. Nadella K., Kumar, V., and Li, W., *ABT 2002-Proceedings of the International Conference on Advances in Building Technology*, Vol. I, Hong Kong, Dec 4-6, pp. 121-128, 2002
7. Kumar V. and Weller J. E., *Polymer Engineering and Science*, vol. **34**, pp. 169-173, 1994
8. Gibson L. J., and Ashby M. F., *Cellular Solids: Structures and Properties*, 2<sup>nd</sup> Ed., Cambridge University Press, Cambridge 1997

## MIXED PROBLEM FOR FREE RADIAL VIBRATIONS OF A CLOSED SPHERICAL SANDWICH SHELL

V. Polyakov and R. Chatys

Latvian University, Institute of Polymer Mechanics

23 Aizkraukles, LV-1006, Riga, Latvia

Technical University, Al. 1000-lecia Pastwa Polskiego 7, Kielce, Poland

polyakov@pmi.lv, chatys@tu.kielce.pl

There are many publications devoted to model definition of wave-mechanical process in sandwich plates and shells (see, for example, [1-3]), but the problem of modeling the transverse waves in normal cross-section of sandwich plates and shells is still actual. Free vibrations across the thickness of a spherical shell are studied. In the beginning the closed-form solution of the one-dimensional along a radius wave problem was specified for the homogeneous elastic sphere with a central cavity. The solution was used in the problem setting for a joint vibration of three spherical layers. With the aim in view the approximate version of vibration has been assumed. The version was based on the assumption of stiff and thin layers bordering the soft and thick core. The elastic reactions of the thin face layers were taken as the boundary conditions enabling three layers wave motion to be reduced to the unique core vibratory motion under mixed boundary conditions. The wave problem of the soft core was deduced by the method of separation of variables [4]. The transcendental equation for the certain problem of free vibration was derived. A specific distinction of the frequency analysis unlike to the wave pattern analysis of radial vibrations of bottled gas [5] was demonstrated.

It is convenient to present the eigenfrequency equation through its tie-up with the eigenvalue equation:

$$\operatorname{tg} \xi = \frac{a_3 \xi^3 + \xi}{b_4 \xi^4 + b_2 \xi^2 + 1} \quad (1)$$

$$\omega_k = \frac{\xi_k}{2\pi(R_3 - R_2)} \left[ \frac{E(1-\nu)}{\rho(1+\nu)(1-2\nu)} \right]^{1/2}, \quad k = 1, 2, \dots \quad (2)$$

where the second term in the latter formulae (in parentheses) represents the velocity of core acoustic waves. The difference  $R_3 - R_2$  denotes the thickness of a core whereas the boundary surfaces of face layers are  $r = R_1$  and  $r = R_4$ , at that  $R_1 < R_2 < R_3 < R_4$ . The coefficients  $a_3$ ,  $b_2$ ,  $b_4$  in the upper equation depend on all radii and the elastic constants of three spherical layers. The case of a homogeneous sphere results in degeneracy of eigenvalues dependent on the Poisson coefficients only when the two-sided boundary surfaces are free.

TABLE 1. Parameters of the sandwich three-layer sphere.

Layer	$R_1 = 100 \text{ mm}$	$E, \text{ GPa}$	$\nu$	$\rho, \text{ kg/m}^3$
$R_4 - R_3$	5	10	0.30	—
$R_3 - R_2$	30	0.04	0.40	119
$R_2 - R_1$	5	10	0.30	—

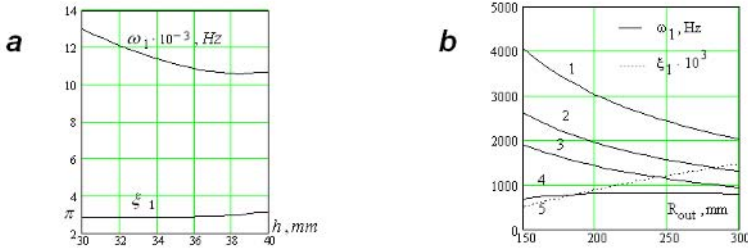


FIGURE 1. Variation of the reference frequency  $\omega_1, \text{ Hz}$  and matching eigenvalue  $\xi_1$  for radial vibrations of a three layer spherical shell against the filler thickness  $h = R_3 - R_2$  (a) and the one of a solid sphere (b) versus outer radius  $R_{out}$  with the clamp surface 1, free surfaces: 2 ( $\nu = 0, 4$ ), 3 ( $\nu = 0, 3$ ) and with a spherical cavity of radius  $R_{im} = 50 \text{ mm} - 4$ .

## References

1. Hohe J. and Librescu L., A nonlinear theory for doubly curved anisotropic sandwich shells with transversely compressible core. - International Journal of Solids and Structures, 40: 1059-1088, 2003.
2. Kadyrov S. and Skvortsov V.. Dynamic transient response of shallow sandwich panel subjected to pressure field. Sandwich Structures 7: Advancing with Sandwich Structures and Materials. Ed. by O.T. Thomsen, E. Bozhevolnaya and A. Lyckegeard, Springer, Netherlands, 2005, 519-526.
3. Sorokin, S. V., Analysis of wave propagation in sandwich plates with and without heavy fluid loadind. - Journal of Sound and Vibration, vol. 36, pp.1039-1062, 2004.
4. Sneddon J. N. and Berry D. S., The Classical Theory of Elasticity, Springer-Verlag, Berlin-Gottingen-Heidelberg, 1958.
5. Koshlakov, N., Gliner, E. and Smirnov, M., *Mathematical Physics Equations in Partial Derivatives*, Ed., Higher School, Moscow, 1970 (in Russian).

## FINITE ELEMENT FOR SANDWICH PANELS BASED ON ANALYTICAL SOLUTION OF CONSTITUTIVE EQUATIONS

Markus Linke and Hans-Gunther Reimerdes  
RWTH Aachen University  
Department of Aerospace and Lightweight Structures  
Wüllnerstr. 7, D-52062 Aachen, Germany  
hg\_reim@ilb.rwth-aachen.de

Sandwich structures with low strength honeycomb or foam cores are being used due to their high bending stiffness to weight ratio in many structural applications. Because of their high flexibility, the deformation field of these core materials show a nonlinear pattern in the through-thickness direction as well as in the core in-plane which can affect significantly the local as well as the global structural behaviour of sandwich panels.

In principle, commercial finite element programs enable a computation of the nonlinear deformation pattern in the sandwich core if a detailed idealisation is used in the through-thickness direction of the sandwich, in particular, in the core. However, the application of standard finite elements during the analysis of the above mentioned sandwich structures results in a very high computational effort not only during the design of large sandwich structures but also in early design stages. Fast finite elements for the analysis of sandwich structures accounting for the nonlinear deformation pattern in low strength cores are consequently preferable.

In order to represent this core behaviour appropriately for the static and stability analysis of sandwich plates, a finite element is developed using a three-layer sandwich model (cp. Fig. 1). The face sheets are modelled as plate elements based on the Reissner-Mindlin theory considering transverse shear strains according to an MITC4-plate element (Mixed Interpolation of Tensorial Components with 4 element nodes according to Bathe *et al.* [1]). The core displacement field is developed based on the solution of the underlying differential equations of the core in the through-thickness direction and the assumed displacement field of the face sheets as boundary conditions. The differential equations are set up using a specific three-dimensional material law that neglects the in-plane core stiffnesses according to Bansemir [2] (cp. also Frostig *et al.* [3]). As a result, the core displacement pattern is computed leading to in-plane core deformations  $u_c$  and  $v_c$  which are cubic functions and to an out-of-plane deflection  $w_c$  which is a quadratic function of the transverse direction (cp. similar approach according to Oskooei and Hansen [4]). Based on the interpolation functions the linear and geometric stiffness matrix for static and stability problems are derived. The geometric stiffness matrix is set up by considering geometric nonlinearities in the  $v$ . Kàrmàn sense in the face sheets and the core.

Static and stability analyses based on the proposed element formulation are performed by integrating it in the finite element (FE-)program NASTRAN (MSC.Software Corporation, USA). The results are compared to the ones of computations carried out by the FE-program MARC (MSC.Software Corporation, USA) which are based on a detailed discretisation of the face sheets as well as the core. The aim of this investigation is to demonstrate the capabilities of the presented element formulation as well as the limits of the underlying theory and its simplifications.

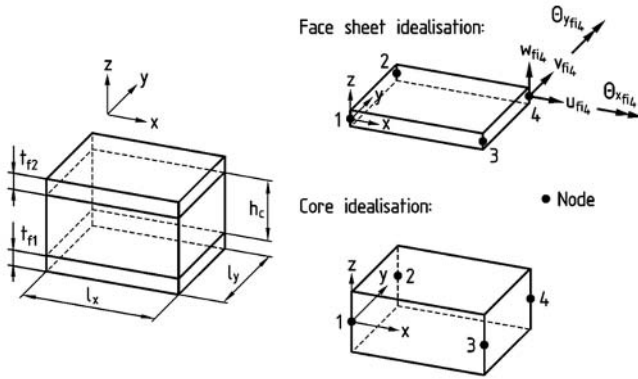


FIGURE 1. Three-Layer-Model and corresponding element nodes

## References

1. Bathe, K.J., Bucelem, M.L. and Brezzi, F., *Engineering Computations*, vol. 7, 291-302, 1990.
2. Bansemir, H., Ein Beitrag zur Biegetheorie von Sandwichplatten und Plattenstreifen sowie zur Krafterleitung in versteifte orthotrope Scheiben, PhD thesis (in German), Technische Universität München, Germany, 1973.
3. Frostig, Y., Baruch, M., Vilnay, O. and Sheinman I., *Journal of Engineering Mechanics*, vol. 118(5), 1026-1043, 1992.
4. Oskooei, S. and Hansen, J.S., *AIAA Journal*, vol. 38(3), 525-533, 2000.

## IMPACT DAMAGE IN SANDWICH COMPOSITE STRUCTURES FROM GAS GUN TESTS

Nathalie Toso-Pentecote and Alastair Johnson  
German Aerospace Center (DLR)  
Institute of Structures and Design  
Pfaffenwaldring 38-40, 70569 Stuttgart, Germany  
nathalie.pentecote@dlr.de, alastair.johnson@dlr.de

The paper studies the High Velocity Impact (HVI) response of aircraft structures by means of gas gun impact tests and post-test NDE evaluation. The scope of the activity comprises structural components such as stringer stiffened composite panels and a range of composite sandwich structures, with projectiles such as ice, synthetic birds, runway debris and tyre/rim debris. The tests and simulations are used to support concept design, and certification phases of new aircraft structures based on carbon fibre composites. To perform these tests DLR has installed and commissioned a new gas gun test facility comprising three different barrels having calibres of 200mm, 60mm, and 32/25mm. The guns fire into a steel target chamber where the test structures are mounted. Impact damage to structures is characterised by a number of NDE techniques, including ultrasonic C-scan, lock-in thermography, X-ray and computer tomography (CT).

The paper describes recent progress on damage assessment in aircraft sandwich structures subjected to foreign object impacts from both hard and soft impactors. A gas gun impact test programme was carried out on twin-walled composite panels under a range of impact conditions. Attention is focussed on novel composite sandwich panels with energy absorbing cores. These are non-standard sandwich structures, in which a main load-bearing composite laminate is protected from impact damage by an energy absorbing core and a second cover laminate. The core materials considered include folded composite plate structures (foldcore) developed in IFB, University of Stuttgart, which are now being investigated by Airbus in new twin-walled shell concept structures for future transport aircraft (Kupke *et al.* [1], Mudra and Hachenberg [2]). High velocity impacts from steel impactors and deformable, soft body impactors such as ice and rubber are a critical design load for such sandwich structures, since the thin brittle outer skin is susceptible to impact damage. Of particular interest is to determine the impact damage threshold in the inner load-bearing laminate for impacts on the cover laminate, as impactor type and impact energy is varied. To study this a gas gun impact test programme was carried out at the DLR on twin-walled composite panels with projectiles such as steel cubes, ice balls and tyre rubber fragments at impact velocities in the range 50 – 220 m/s. A wide range of failure modes have been observed, ranging from rebound from the outer skin, outer skin damage, core penetration, inner skin damage and inner skin penetration. Without suitable NDE methods it was not possible to quantify the impact damage, particularly in the case of non-visible damage such as shell delaminations. Through the NDE methods applied here, X-ray, lock-in thermography, ultrasonic A- and C-scans (Aoki *et al.* [3]), it was possible to ascertain the presence and nature of the impact damage. Furthermore, in many cases the internal structure and damage in the twin-walled composite structures could be quantified.

Results from a series of HVI tests on two foldcore sandwich composite curved shells will be presented in detail. Two impact scenarios relevant to fuselage upper and lower panel structures are described. One of these is the hail impact scenario which includes hail on ground with hailstones up to 60 mm in diameter and velocities 30 – 50 m/s, and hail in flight with small 20 mm diameter ice balls at impact velocities up to 180 m/s. The second is hard runway debris, simulated by steel cubes or balls typically 10 mm in size at impact speeds in the range 50 – 100 m/s. Fig. 1 shows the



visible damage after a hail impact under  $60^\circ$ , the extent of the damage in the foldcore using X-ray and the thermography picture detecting a slight damage in the inner skin. The aim of the test programme was to determine the critical energies and velocities for a given projectile and test panel causing first damage on the outer skin, perforation of the outer skin, first damage on the inner skin and finally the complete perforation of the sandwich panel. These damage thresholds will be presented for two foldcore panels, one with a thin outer CFRP skin  $\sim 0.9$  mm, and one with a more conventional balanced sandwich panel with  $\sim 2$  mm outer CFRP skin. The role of skin and core properties and thicknesses on the critical damage thresholds will be discussed in detail.

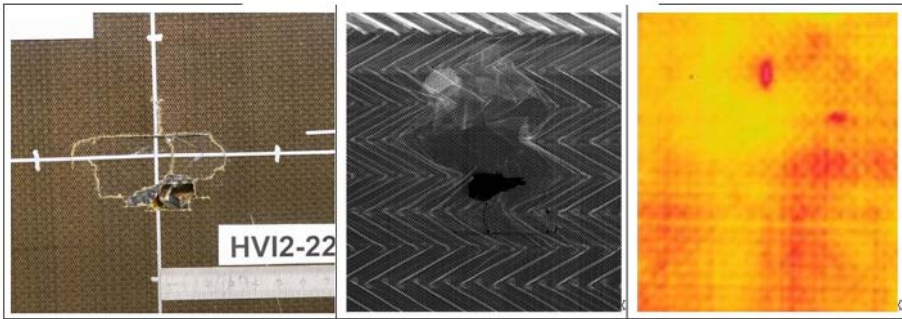


FIGURE 1. Visible damage after hail impact (173 m/s, 11g) under  $60^\circ$  on a sandwich panel with a foldcore, corresponding radiography and lock-in thermography (inner skin) pictures.

## References

1. Kupke, M., Rückert, C., Dolzinski, W.-D., Kolax, M., Der CFK-Rumpf - Ergebnisse aus Bauweisenkonzeption und Wissenserwerb, *Deutscher Luft- und Raumfahrtkongress 2002*, DGLR-JT2002-062, 2002.
2. Mudra, C., Hachenberg, D., Alternative sandwich core structures – Efficient investigation of application potential using FE modeling, *SAMPE Europe*, Paris, 2004.
3. Aoki, R.M., Eberle K., Drechsler K., Wagner, H. et al., NDE assessment of long fibre reinforced GFRP and CFRP, In *Damage and its Evolution in Fiber Composite Materials: Simulation and Non-destructive Evaluation*, G. Busse, B. Kröplin (eds), to be published, 2006.

## EFFECTS OF MISSING CELLS ON THE COMPRESSIVE BEHAVIOR OF CLOSED-CELL AL FOAM

I. Jeon<sup>a</sup>, Y. Yamada<sup>b</sup>, T. Yamada<sup>b</sup>, K. Katou<sup>b</sup>, T. Sonoda<sup>b</sup> and T. Asahina<sup>b</sup>

<sup>a</sup>School of Mechanical Systems Engineering, Chonnam National University  
300 Yongbong-dong, Buk-gu, Gwangju, 500-757, South Korea

<sup>b</sup>Materials Research Institute for Sustainable Development,  
National Institute of Advanced Industrial Science and Technology(AIST),  
Shimoshidami, Moriyama-ku, Nagoya, 463-8560, Japan  
i\_jeon@chonnam.ac.kr

Cellular material has lately attracted considerable attention for the lightweight components of transportation applications [1]. The mechanical properties of the material that are the elastic stiffness and peak stress, i.e., the stress at the first peak of the stress-strain curve should be important parameters for designing those components. Because the processing defects in the cellular structures are known for affecting on the mechanical properties, many researchers have investigated for the effects of the defects.

The numerical study using 2-D honeycomb structures for the influence of geometrical imperfections, i.e., missing cells, fractured cell walls, rigid inclusions, cell-wall waviness, etc. on the mechanical properties of the honeycomb structure has been carried out to provide the guideline for improving the properties of the commercial metallic foams [2, 3]. Among the imperfections, missing cells show a large influence on both the elastic modulus and the yield strength of 2-D cellular structures. Only a few experimental results, however, about the effect of imperfections, i.e., cell wall curvatures and cell wall microstructures of actual cellular solids have been reported up to present [4, 5].

In this research, a simple experimental approach is attempted to analyze the effects of missing cells, which are generally found in the closed-cell Al foam and should be expected to reduce the mechanical performance seriously [2, 3], on the compressive deformation. Considering the volume fraction of the missing cells, different size of specimens are fabricated using EDM (Electrical Discharge Machine) such as  $50 \times 50 \times 50 \text{mm}^3$ ,  $15 \times 15 \times 15 \text{mm}^3$  and  $10 \times 10 \times 10 \text{mm}^3$  (see Fig. 1). The missing cells in the fabricated specimens are carefully investigated through the density measurement and the surface observation. Then two specimen groups that include or do not include the missing cells are arranged and tested separately to compare the results with each other.

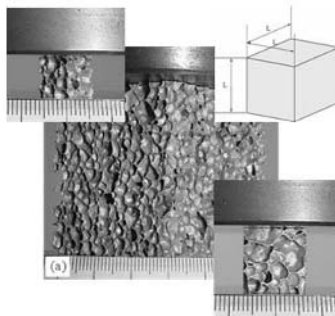


FIGURE 1. Fabricated specimens

**References**

1. J. Banhart, *Prog. Mater. Sci.*, vol. **46**, 559-632, 2001.
2. C. Chen, T.J. Lu, N.A. Fleck, *J. Mech. Phys. Solids*, vol. **47**, 2235-2272, 1999.
3. C. Chen, T.J. Lu, N.A. Fleck, *Int. J. Mech. Sci.*, Vol. **43**, 487-504, 2001.
4. E. Andrews, W. Sanders, L.J. Gibson, *Mat. Sci. Eng. A*, vol. **270**, 113-124, 1997.
5. A.E. Markaki, T.W. Clyne, *Acta Mater.*, vol. **49**, 1677-1686, 2001.

## FAILURE BEHAVIOUR INVESTIGATION OF METALLIC OPEN LATTICE CELLULAR STRUCTURES

G.N. Labeas and M.M. Sunaric  
Department of Mechanical Engineering and Aeronautics  
University of Patras  
Laboratory of Technology and Strength of Materials (LTSM)  
Panepistimioupolis, Rion 265 00, Greece  
labeas@mech.upatras.gr, msunaric@mech.upatras.gr

Sandwich structures made of metallic or plastic core and composite skins have attracted the attention of the engineering industry since many years. Cellular structures are sandwich structures, characterized by the construction of their core, which is made up of an interconnected network of solid struts or plates. The applications of cellular structures are widespread. Thermal insulation, packaging, structural, buoyancy and many other engineering sectors are the most common fields for the utilization of cellular structures [1]. The usual design parameters of cellular sandwich structures are the relative density and the elastic specific stiffness and strength [2]. The mechanical behaviour of sandwich structures is dependent on both the mechanical properties of the cellular core and the composite skins.

The cellular core behaviour is dependent on the cell geometry and cell size. The present work focuses on the failure behaviour of metallic open lattice cellular cores. This behaviour is considered to be one of the keys to the successful development of improved sandwich structures with tailored properties. The failure behaviour is analysed by means of modelling and FE simulation of cellular cores. Due to the high difference of size scale between the cell structure constitutes (which is usually of the order of a few millimetres) and the entire sandwich cellular structure, the ordinary numerical analysis methodologies lead to very large models, requiring high computing power for their solution. In contrary, alternative and multiscale modelling strategies are preferable, based on very detailed unit cell models for determining the cellular metallic core properties in terms of material properties, cell geometry and cell size. Two different cell geometries have been investigated, as presented in Fig. 1, namely the 'bcc-h' cell with density of 994kg/m<sup>3</sup> and the 'bcc,z-h' cell having a higher density of 1258kg/m<sup>3</sup> [3]. The size of the examined cells varies from 1.25mm to 2.5mm. The unit cell structure, which consists of vertical members with diagonal cross members, is constructed using the selective laser melting technique with Stainless steel 316L from Sandvik [4] as powder material.

The cellular structure simulations deal with predicting the elasticity modulus and failure of the structure in axial compression. The beam element type BEAM4 is used in ANSYS finite element code to model the unit cell. By multiplying the unit cell in three dimensions the cellular structure is generated. The loading situation is approximated by applying force on the nodes at the top surface of the structure and by constraining vertical translation to the nodes at the bottom surface of the structure. The final deformation state is approximated in the geometrically and materially non-linear static numerical analysis. The material non-linear data of the 316L stainless steel material, used in the present analysis, is part of a testing campaign performed by the University of Liverpool. The numerically calculated stress-strain curves are compared in Fig. 2 to the respective experimental compression stress-strain data by McKown and Mines [4]. A good correlation is obtained between experimental and numerical results.

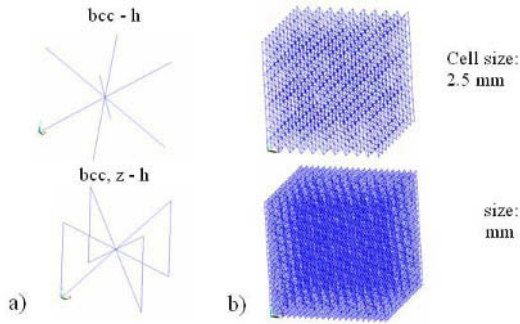


FIGURE 1. a) Unit cells used in the cellular cores and b) analyzed core structures of cell sizes of 2.5mm and 1.25mm

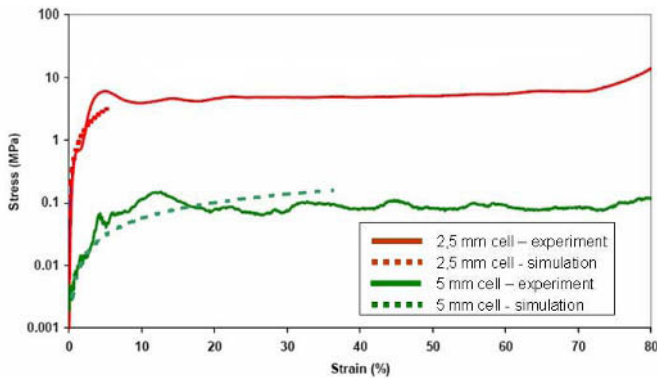


FIGURE 2. Stress vs. strain for two cellular cores analyzed

## References

1. Gibson, L. J. and Ashby, M. F., *Cellular solids*, Cambridge Solid State Science Series, Cambridge University Press, Cambridge, United Kingdom, 1997.
2. Zenkert, D.A., *Introduction to Sandwich Construction*, EMAS Publishers, 2000.
3. Mines, R.A.W, McKown, S., Cantwell, W., Brooks, W. and Sutcliffe, C. J., *On the Progressive Collapse of Micro Lattice Structures*, 13<sup>th</sup> International Conference on Experimental Mechanics, Alexandroupolis, Greece, 2007.
4. McKown, S and Mines, R.A.W., *Impact behaviour of metal foam cored sandwich beams*, 16<sup>th</sup> European Conference on Fracture , Alexandroupolis, Greece, Paper No. 254, July 2006.

## SMART MESHING OF IMPERFECT STRUCTURES FOR THE IMPROVED PREDICTION OF BUCKLING AND POSTBUCKLING BEHAVIOUR

Carol A. Featherston

Cardiff School of Engineering, Cardiff University  
Queens Buildings, The Parade, Cardiff, CF24 3AA, United Kingdom  
FeatherstonCA@cardiff.ac.uk

It is generally accepted, that the buckling loads and postbuckling behaviour of many engineering components are substantially impaired by the existence of small initial geometric imperfections such as deviations in shape, eccentricities and local indentations. These imperfections can lead to large discrepancies between predicted and actual failure loads, which can result in catastrophic failure unless large safety factors are applied, resulting in non-optimised structures. In industries such as the aerospace industry, which rely on the use of minimum weight structures, this inability to accurately model the effects of such imperfections acts to reduce the industry's competitiveness.

Extensive work therefore has been based on modelling imperfections, allowing their effects to be assessed. This has been summarised in reviews eg Simitsev [1], and collated by several researchers to form imperfection data banks (Arbocz [2]). Results have been obtained using a variety of techniques, all of which involve some degree of approximation.

Initial work to develop a general theory of buckling and postbuckling which incorporated sensitivity to imperfections was carried out by Koiter [3] and Arbocz [4] among others. This work was however, limited to a small range of load and boundary conditions. Since then, with the increasing sophistication of numerical analysis software combined with high powered computers, it has become possible to model the buckling and postbuckling behaviour of shells under complex load and boundary conditions whilst incorporating the effects of imperfections and other nonlinearities. Nevertheless, difficulties still arise due to the need to model these imperfections, and convert numerical buckling loads into a design load for a particular structure. Several approaches have been considered.

Two main types of approach exist. The first is based on a linear elastic bifurcation buckling analysis and applies reduction factors to bifurcation loads to account for geometric imperfections (Samuelson and Eggwertz [5]). The alternative to this approach is to carry out a fully non-linear analysis with geometric imperfections, plasticity and large deflections accurately modelled. This requires the amplitude and form of the imperfection to be decided. The most accurate method is to base any analysis on actual imperfections. Work has therefore been carried out to measure real imperfections using contact techniques and then model these imperfections (Singer and Abromovich [15]).

In most cases detailed information on actual imperfections in a structure is not available and is uneconomical to obtain. In such cases researchers such as Speicher and Saal [6] have recommended that imperfections whose form is based on the first bifurcation or eigenmode be used. Most commercially available finite element codes recommend a similar approach, setting the maximum amplitude of the imperfection equal to that anticipated in the component itself. However since these models represent a worst case scenario, the use of this limit in design calculations will result in the component being over-engineered.

This paper presents a technique which overcomes these difficulties by using fast, accurate optical shape measurement methods to create finite element models representative of real structures, which can be analysed to predict their buckling and postbuckling behaviour. The method is based on the use of image correlation to provide geometric data on components in the

form of a 3-D co-ordinate cloud. Software has been developed to allow this shape data to be converted directly into a mesh suitable for finite element analysis. Mesh density is adapted according to the geometry of the component to give a finer mesh in areas with high curvature e.g. imperfections, and a coarser one in the remainder of the component. This results in an efficient mesh which can be analysed using non-linear finite element techniques to accurately predict their behaviour whilst minimising processing time.

The technique is validated by comparing the results with those obtained from experiments on a series of curved panels. These specimens have been selected as representative of some of the structures commonly found in aerospace applications which are relatively sensitive to imperfections (Fig. 1). The specimens have aspect ratios varying from 1:1 to 2:1, and a range of different radii of curvature are assessed, since this is one of the main factors affecting the imperfection sensitivity of the specimens. Each specimen is subjected to a combination of compression and shear, which is again representative of the loading conditions commonly found in the aerospace industry (Fig. 2). Prior to testing, each specimen is measured using image correlation software and the data processed to provide an associated finite element mesh. The specimens are then tested whilst a fully nonlinear finite element analysis based on the mesh derived is carried out using the finite element analysis code ABAQUS/Standard. The results are then compared.

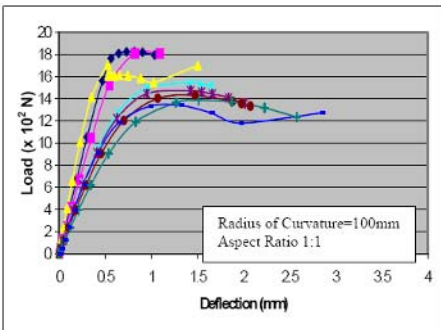


FIGURE 1. Imperfection sensitivity of a panel

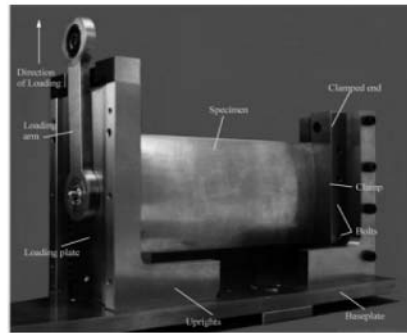


FIGURE 2. Typical test set-up

## References

1. Simitses, G. J., *Applied Mechanics Review*, vol. **39** (10), 1517-1524, 1986.
2. Arbocz, J., *Buckling of Shells*, edited by E. Ramm, Springer-Verlag, Berlin, Germany, 1982.
3. Koiter, W.T., *On the stability of elastic equilibrium*, PhD Thesis, University of Delft, 1945.
4. Arbocz, J., *Thin-Shell Structures*, edited by Y.C. Fung and E.E. Sechler, Prentice-Hall, Inc., Englewood Cliffs, USA, 1974.
5. Samuelson, L. and Eggwertz, S., *Shell stability handbook*, Elsevier Applied Science, London, 1992.
6. Speicher, G. and Saal, H., *Buckling of Shell Structures, on Land, In the Sea, and in the Air*, edited by J.F. Julien, Elsevier Applied Science, London, 1991.
7. Singer, J. and Abromovich, H., *Thin-Walled Structures*, vol. **23** (14), 1995.

## CYCLIC BUCKLING TESTS OF CFRP BOXES UNDER COMPRESSION AND TORSION

Chiara Bisagni and Potito Cordisco  
Department of Aerospace Engineering, Politecnico di Milano  
Via La Masa 34, 20156 Milano, Italy  
chiara.bisagni@polimi.it, cordisco@aero.polimi.it

Carbon fiber reinforced plastic (CFRP) stiffened structures exhibit several advantages over those constructed from metallic materials, particularly in terms of their high specific mechanical properties. Whereas nowadays the applications of CFRP structures are becoming more and more both in aeronautical and mechanical industries, their efficient use is restricted by the limited availability of buckling design criteria, mainly due to uncertainties related to the behaviour of these structures under repeated cyclic buckling, Singer *et al.* [1]. This paper presents some results obtained during an European research project, COCOMAT (Improved MATERIAL Exploitation at Safe Design of COMposite Airframe Structures by Accurate Simulation of Collapse) on stringer stiffened composite panels subjected to cyclic buckling, Degenhardt *et al.* [2]. Presented results are part of an investigation carried out for understanding what happens to the post-buckling field of such a structure after that the buckling load is reached thousands of times.

The considered boxes are manufactured by Agusta-Westland and are tested at the Department of Aerospace Engineering of Politecnico di Milano. Each of the boxes consists of four curved panels, with a curvature radius of 1500 mm, and a height of 700 mm. Two panels are 700 mm width, while the other two are about 280 mm. They present L-shaped stringer stiffeners, which are bonded to the skin. The all boxes are made in unidirectional and fabric carbon composite material. Two views of a box are shown in Fig. 1.

The testing machine is able to apply both static loads using a position control mode, based on five stepping motors, and cyclic loads, by a hydraulic cylinder controlled by a servo-valve (Fig. 2). The tests are performed under axial compression, torsion and combined axial compression and torsion, Bisagni and Cordisco [3-4].

At first, the local buckling of the skins, the behaviour in post-buckling under combined loading, and the collapse under torsion are investigated. The boxes are tested until the post-buckling field, measuring the load-shortening curve and the torque-rotation curve, by means of a load cell and LVDTs.

The boxes are instrumented with strain gauges. In particular, strain gauges are attached on three sides of the boxes, both internally and externally. On the fourth side, the strain gauges are attached only internally, so to leave it free in order to be scanned by a laser based scanning system. This system allows to measure one panel of the box and so to monitor the behaviour during the tests.

Finally the boxes are tested under cyclic buckling, with load blocks of five hundreds of cycles. After each block, the test is stopped so to allow taking measurements in the post-buckling field. In particular the torque-rotation curve, the strains and the deformation of the panel with the laser system are measured. In this way it is possible to investigate the effect of cyclic buckling in terms of changes in the global response of the specimen, strain measurements and post-buckling deformations.



The behaviour of the CFRP boxes is deeply investigated, so to demonstrate that they can safely work in the post-buckling field even if during their operative life the buckling load is reached thousands of times.



FIGURE 1. CFRP box.

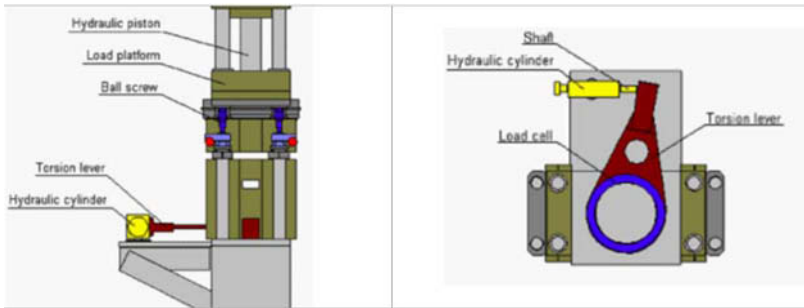


FIGURE 2. Test facility for cyclic buckling.

### Acknowledgements

This work is supported by the European Commission, Competitive and Sustainable Growth Programme, Contract No. AST3-CT-2003-502723, project COCOMAT. The information in this paper is provided as is and no guarantee or warranty is given that the information is fit for any particular purpose. The user thereof uses the information at its sole risk and liability.

### References

1. Singer J., Arboz J., Weller T., *Buckling experiments – experimental methods in buckling of thin walled structures*, vol. 2, John Wiley and Sons, New York, USA, 2002.
2. Degenhardt R., Rolfes R., Zimmermann R., Rohwer K., “Improved material exploitation at safe design of composite airframe structures by accurate simulation of collapse”, *Proceedings of International Conference on Buckling and Postbuckling Behavior of Composite Laminated Shell Structures*, Eilat, Israel, 2004.
3. Bisagni C., Cordisco P., “Testing of stiffened composite cylindrical shells in the postbuckling range until failure”, *AIAA Journal*, vol. 42 (9), 1806-1817, 2004.
4. Bisagni C., Cordisco P., “An experimental investigation into the buckling and post-buckling of CFRP shells under combined axial and torsion loading”, *Composite Structures*, vol. 60, 391-402, 2003.

## FLOOR DYNAMICS FOR TRUSS SYSTEM WITH LIGHT GAUGE STEEL AND CONCRETE

S.E. Lee

Research Institute of Industrial Science & Technology  
79-5 Young-chun Dongtan Hwasung Kyunggido R. of Korea  
leese@rist.re.kr

The vibration of a structure has more influence if the structure is lighter and more flexible, and also if its damping ratio is smaller. Problems related to vibration of structures are very unpredictable due to the fact that the structure itself is composed of various materials and that the environmental vibration applied on the structure is irregular.

Evaluation of the vibrational influence on buildings range from serious vibration, which has great impact on the safety of the structure, to micro vibration. Due to the fact that steel Framed house is a structure which uses light and flexible materials, its vibration properties should be subjected to scrutinized evaluation.

Through this research, results of vibration measurement in 3 type of floor composed with single channel, truss channel and truss B-type channel and floor dynamic simulation of 50pyung-type steel Framed house are presented (Fig. 1). Therefore, it would be possible to predict floor vibration of steel Framed house by making a comparative analysis of such results.

### Floor Dynamic Simulation

A floor dynamic simulation was carried on the 2nd floor of Pohang's model steel Framed house to compare with measurement results. Programs used for dynamic analysis were SAP2000. And the elements used were 4-joint plate element, 3-joint plate element, 2-joint beam element, while MPC(Multi-Point Constraint) was used for joining the plate elements with the beam elements. Boundary conditions for this simulation were ; simple support for 4 sides of the slab and substitution of the interior partition walls into spring.

### Floor vibration measurement

The following tests were carried out for 3 type of floor (3.6x4.8m) composed with single channel, truss channel and truss B-type channel.

- Micro vibration measurement of walking load
- Impact test of jumping load (1 adult person)
- Experimental modal analysis



FIGURE 1. Type of Floor Panel for test

Table. 3 type with 2 end connection of Floor Panel for test

Floor Type	Member	h/spacing (mm)	Method of end connection	Topping
Single	300JL16	300/600	-	Deckplate / Concrete 70mm
C_Truss1	90SL12	300/600	Squared End	Deckplate/Concrete 70mm
C_Truss2	90SL12	300/600	Extended End	Deckplate/ Concrete 70mm
B_Truss1	100PRY08	300/600	Squared End	Deckplate/ Concrete 70mm
B_Truss2	100PRY08	300/600	Extended End	Deckplate/ Concrete 70mm

### References

1. AISI, *Specification for the Design of the cold Formed Steel Members* , 1996
2. J. Mills and R. LaBoube, *Self-drilling Screw Joints for Cold-Formed Channel Portal Frames*, 2002
3. Y.B Kwon, G.D Kim and I.S Song, *Structural Behavior of Cold-Formed PRY Section*, KSSC vol. **14-2**, pp 357-364

## LOCAL BUCKLING AND POSTBUCKLING BEHAVIOUR OF THIN-WALLED SHELLS (TEST DATA & THEORY)

G.D. Gavrylenko

S.P. Timoshenko Institute of Mechanics, Ukrainian Academy of Sciences, Kiev,  
Nesterova str. 3, 03057 Kiev, Ukraine  
gavr@inmech.kiev.ua

**Experimental Procedure and Test Specimens.** The experimental results fully belong to Prof. Krasovskii [1] Was investigated the behavior of circular cylindrical shells at all stages of deformation in the area of artificial initial local dents that trigger the process of the loss of stability. Other perturbing factors were minimized, wherever possible.

All specimens were manufactured from the same material (X18N9n steel sheet) using the same technique (contact spot welding with one longitudinal weld) and tested with the fulfillment of unified requirements to the observations and measurements made.

Prior to testing, the shells were dented with spherical segments to produce a local dent of certain dimensions, whose depth was controlled by the pressure force.

Initial imperfections were measured at a load of approximately 0.1% of the critical one. Subsequent measurements were made step-by-step at various load levels. The loads, at which the last measurement was made, were as high as 80 to 90% of the critical one. The mean values of the relative critical loads in axial compression  $\bar{P} = N_{cr} / N_{cl}$  (where  $N_{cr}$  and  $N_{cl}$  are the respective actual and classical values of the critical load in a smooth shell) for specimens with  $r/t = 150$  (○, ●), 260 (△, ▲) and 360 (◇, ◆) were 0.83, 0.72, and 0.60, respectively.

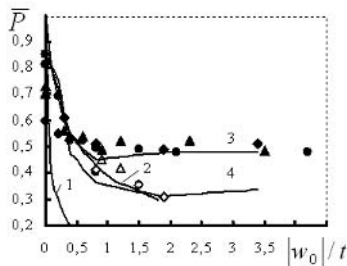


FIGURE 1. Experimental & theoretical relations  $\bar{P} = f(|w_0|/t)$

Fig. 1 presents the relationships  $\bar{P} = f(|w_0|/t)$  for specimens of various thickness with small shallow dents. In this figure, solid symbols correspond to the overall buckling and open symbols to the local buckling.

Note that the attempt to use the Koiter approach [2] for assessing the critical load by considering a single dent as an axisymmetrical regular deflection results in a considerable underestimation of the load-carrying capacity of an imperfect shell (curve 1 in Fig. 1). At the same time a rather good agreement with the experimental data is observed when the calculation is

made by the formula derived as a result of the asymptotic analysis of the nonlinear functional of the total potential energy of an elastic cylinder with a localized dent [3]. Curve 2 in Fig. 1 corresponds to this calculation.

**Theoretical Predictions of Buckling Loads & Comparison with the Test Observations.** Based upon a Donnell-type nonlinear theory of shells, theoretical modelling of this problem is realized by using a finite difference method (FDM) [4]. This modelling allows incorporation of the effects of nonuniform pre and post-buckling nonlinearities, including the effects of arbitrary initial geometric imperfections, and has been extended to handle isotropic, as well as orthotropic continuous and discrete rib-reinforced shells.

Fig.1 shows typical comparisons between test observations and predictions from the FDM. The full analyze of theoretical and experimental dependencies is given in Fig.1 for isotropic shell having  $\ell/r = 2$ ,  $r = 143$  mm,  $r/t = 360$ . The finite difference mesh used had  $71 \times 230$  divisions in the axial and circumferential directions respectively, and  $14 \times 22$  divisions covering the area of the local dent imperfection.

The upper line (3) represents the maximum loads on the load deflection plots at which a general buckling occurs. The lower line (4) indicates the load at which a local buckle is initiated in the region of the dent imperfection.

Buckling loads are normalized with respect to the classical axial critical load  $p_{c1}$  for the perfect cylinder, and are shown as functions of the amplitude of the local dent imperfections,  $w_o$ , normalized in terms of the shell thickness,  $t$ .

Theoretical local dents in centre of shell surface are taken as a single lobe of the form

$$f_o = -\frac{w_o}{t} \sin \frac{\pi x}{\ell_1} \sum_{n=1,3} \sin \frac{n\pi y}{\ell_2}, \quad (1)$$

with wavelengths  $(\ell_1, \ell_2)$  chosen to model as closely as possible the local dents of the test specimen. The values of buckling load will be estimated with using of expression (1) and  $n=1,3,5$ .

A row of test shells with  $w_o/t = 0,817$  and  $1,95$  had both as local buckling load determining the beginning of process loss stability so general buckling load, when load – carrying capacity may be lost in full.

In the case where  $150 \leq r/t \leq 360$  a good agreement between the calculated and experimental values of the critical loads values is also reached.

## References

1. Gavrylenko, G. D., Krasovskii, V. L., *J. Strength of Materials*, vol. **36**, no. 3, 260 – 268, 2004.
2. Koiter, W.T., *Proc. Koninkl. Nederl. Acad. Wet.*, vol. **B 66**, no. 5, 265 – 279, 1963.
3. Grishchak, V.Z. *Strength and Life of Structures [in Russian]*, Naukova Dumka, Kiev, 1980.
4. Gavrylenko, G. D., *Stability of ribbed shells of incomplete form*, Inst. of Mathematics of NAS of Ukraine, Kiev, Ukraine, 1999.

## INITIAL SKIN BUCKLING AND MODE-JUMPING IN INTEGRALLY STIFFENED METALLIC PANELS

Adrian Murphy, Damian Quinn and Mark Price  
School of Mechanical and Aerospace Engineering  
Queen's University Belfast, Northern Ireland  
a.murphy@qub.ac.uk, dquinn14@qub.ac.uk and m.price@qub.ac.uk

Stiffened panels dominate aircraft structure with their design potential for high strength with low weight. This characteristic is due to the use of high strength materials and the stable post-buckling response of stiffened panels to compression and shear loading. By permitting the skin between stiffeners to buckle in service at defined percentages of the panel ultimate load, panel strength-to-weight ratio is maximised. Advances in strength and damage tolerant characteristics of available aerospace materials offers opportunities for increased working and limit stresses. To fully exploit material improvements as weight savings on aircraft primary structures, it is desirable to enhance the buckling stability of stiffened panels. To further increase structural efficiency of integrally machined stiffened panels it is plausible to vary the skin thickness between stiffeners to increase the skin stability without increasing material volume, Murphy *et al.* [1]. Additionally, considering the issues surrounding the damage tolerance of integrally stiffened panels, local skin profiling may be designed to retard fatigue crack growth, improving the damage tolerance characteristics of the structure, Farley *et al.* [2] and Ehrström *et al.* [3]. As static strength performance gains are achieved by changing the initial form and magnitude of skin buckling, experimental capture of skin deformation behaviour under test is required to validate local profiling analysis and optimisation tools. The work presented in this paper documents the experimental programme undertaken to validate strength analysis tools by capturing initial skin buckling behaviour and post-buckle mode-jumping of integrally machined stiffened panels with local skin profiling.

A series of four panel specimens with varying local skin profiles were designed, manufactured and tested. Specimen design was constrained to representative aerospace material, machining technology, panel loading intensities and buckling to post-buckling strength ratios. In addition, the skin local profiling was designed to act as integrated crack retarders, improving the damage tolerant characteristics of the structure. All specimens were designed to have an equal length, breadth and a cross-sectional area within 1.25% of a baseline design which had no skin profiling (constant skin thickness). Each specimen was integrally machined from single 50 mm thick billets of 2024-T351. Once machined each specimen was marked and strain gauged in preparation for test. Gauges were located to assist in the determination of initial skin buckling behaviour. Two calibrated displacement transducers, one either side of the specimen, were used to measure specimen end-shortening. The specimens were tested in a 250 kN capacity hydraulic, displacement-controlled compression-testing machine. The specimen was loaded monotonically at a rate of 10 kN per minute until specimen failure occurred. Deflection and strain data were recorded automatically at 4-second intervals. Additional specimens were tested to assess experimental repeatability. As a key goal of the physical tests was the assessment and potential validation of local profiling analysis and optimisation tools, a non-contact Digital Image Correlation system was used to measure specimen skin out-of-plane deformation during testing.

The paper documents the experimental testing of the specimens focusing on the initial skin buckling and post-buckling behaviour. Fig. 1 presents typical specimen experimental results, illustrating a specimen load versus end-shortening curve with additional skin out-of-plane buckling deformation data superimposed. All but one of the specimens exhibited skin wave formation which changed within the post-buckling range. The paper also details the analysis tools examined to

predict specimen behaviour and the correlation between the predicted skin behaviour and the experimental data. The paper highlights the required analysis fidelity to accurately predict initial skin buckling and post-buckling skin behaviour. Finally, the paper concludes by assessing the potential for local skin profiling on integrally machined stiffened panels discussing the potential performance gains and application issues.

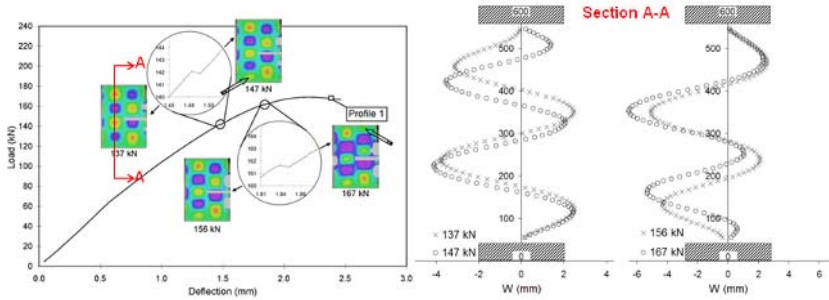


FIGURE 1. Typical specimen experimental results.

## References

1. Farley, G. L., Newman, J. A., and James, M. A., *In Proceedings of the 45<sup>th</sup> AIAA/ASME/ASCE/AHS/ASC Structures, Structural Dynamics & Materials Conference*, 19-22 April 2004, Palm Springs, California, AIAA 2004-1924.
2. Ehrström, J-C., Van der Veen, S., Arsène, S. and Muzzolini, R., *In Proceedings of ICAF*, 6-10 June 2005, Hamburg.
3. Murphy, A., Quinn, D., Mawhinney, P., Ozakça, M., and van der Veen, S., *In Proceedings of the 47<sup>th</sup> AIAA/ASME/ASCE/AHS/ASC Structures, Structural Dynamics, and Materials Conference*, 1-4 May 2006, Newport, Rhode Island, AIAA-2006-1944.

## BUCKLING DESIGN OPTIMISATION OF FIBRE REINFORCED POLYMER SHELLS USING LOWER BOUND POST-BUCKLING CAPACITIES

Hongtao Wang and James G. A. Croll  
Department of Civil and Environmental Engineering  
University College London, WC1 E 6BT, England  
j.croll@ucl.ac.uk

For optimum design of thin shells constructed from advanced composites it is arguably even more important than for metallic shells to take account of the reductions in elastic load carrying capacities that result from the effects of initial imperfections. Relative to other construction materials, the typically low elastic stiffness to strength ratios of composites will mean that elastic nonlinearities are likely to play a considerably greater role in determining the buckling behaviour. This paper will outline an approach for which an extension of classical critical load analysis allows the provision of lower bounds to the imperfection sensitive buckling loads of composite shells. Its simplicity and its basis within direct physical interpretations of shell buckling behaviour will be demonstrated to make this approach a powerful tool for making rationally based design decisions with potential for optimisation of the use of materials.

The so called “reduced stiffness method” (RSM) is based upon an analysis of the various energy contributions that are developed within the classical critical modes. These energy contributions control the shells initial resistance to buckling. This energy breakdown allows identification of the energy terms providing the crucial roles in resisting buckling in the various possible modes. Through simple physical reasoning it is possible to identify those initially stabilising energy terms that are lost during the, imperfection controlled, nonlinear post buckling behaviour. An analysis of critical loads, from which these “at risk” energy terms have been removed, then enables specification of lower bounds to the imperfection sensitive buckling in each of the possible buckling modes. Comparisons with extensive programmes of past physical experimental research, will demonstrate the reliability of the lower bounds for wide classes of both stiffened and unstiffened metal shells. Theoretical confirmation of the predictions of the RSM will be illustrated by comparisons with carefully controlled parametric studies, undertaken for both metal and composite shells, making use of validated nonlinear numerical experiments.

By virtue of its explicit form and analytical simplicity, the paper will then show how the RSM offers scope for identifying appropriate strategies to predict the likely effects of variations of the many shell material and geometric parameters that govern the safe resistance to buckling. This will show, *inter alia*, that the modes exhibiting the most severe reductions in imperfection sensitive buckling loads are commonly quite different from the modes that give rise to the lowest classical critical loads. It will be shown that design optimisation based upon consideration of just the classical critical loads can be very misleading in terms of what is the most appropriate choice of optimising parameters. Furthermore, even making allowance for the reductions in buckling loads, due to post-buckling nonlinearities in the modes associated with the lowest of the classical critical loads, can also be equally misleading in terms of predicting the safe load carrying capacities. As a tool for guiding appropriate combinations of parameters to affect enhanced, or even “optimum”, buckling capacities the RSM approach will be demonstrated to have considerable advantages over many of the currently available alternative means used for trying to improve design performance. Case studies will illustrate this design potential.



## METALLURGICAL REASONS OF SCATTERING OF TOUGHNESS IN THE WELDED JOINTS OF THE CONSTRUCTION STEELS

E. Bayraktar<sup>1</sup>, D. Kaplan<sup>2</sup> and J.P. Chevalier<sup>3</sup>

<sup>1</sup>Supmeca/LISMMA-Paris, School of Mechanical and Manufacturing Engineering, France

<sup>2</sup>ARCELOR Group, Paris-France

<sup>3</sup>Chair of Industrial Materials, CNAM, case 321, 292 rue Saint Martin, 75141 Paris 03 -France  
bayraktar@supmeca.fr

The compositions of steels for the metallic construction have made the object regular improvements in both of metallurgical and manufacturing aspects, in particular at the request of the users who realize these products by welding process, efficiently to separate the responsibilities of the steel maker and welding designer for increasing the reliability of the welded structures. A considerable attention is rewarded to the properties of the fusion zone (weld bead) or the Heat Affected Zone (HAZ), just in the vicinity of the fusion line.

The dispersive nature of the results of toughness which affects these zones is well-known. The most common idea says that this situation is generally related to certain geometrical parameters (difficulty of central positioning of the notch, thermal gradient thus microstructural changement, etc.). However, even in the weld bead in monopass welding (where the above factors are not discussed), sometimes, an important scattering can be seen in toughness.

The objective of this study thus was to search the factors which explain qualitatively and quantitatively this scattering. The study was then undertaken on different microstructures (bainite and ferrite-pearlite) and a variety of inclusion populations, some characteristics of HAZ or weld bead in submerged arc welding (SAW). Starting from impact tests, carried out in the field lower than the fragile - ductile transition, the scattering of the results in toughness have been determined by taking the standard deviation calculated on the all of the test specimens. In certain cases, tensile tests on the notched axisymmetric specimens, accompanied by a study of the local fracture approach, allowed an estimate of the critical cleavage stresses of and scattering.

The distribution in the face of the selected microstructural parameters (ferrite grains, pearlite small islands, bainite packages) was carried out by metallographic examination. The standard deviations corresponding to these laws of distribution thus are able to be measured.

After that a real comparison were made between mechanical scattering and these factors of metallurgical scattering. In first approach, any metallurgical parameter allows explaining alone the dispersion of toughness. If the fracture theory of Griffith is considered, a multi-parameters approach (i.e. a combination of the various metallurgical parameters signed above) permit to report the variations of mechanical scattering. In the case of ferrite-pearlite structures, this parameter, assigned "D", depends on the number of ferrite grains and pearlite islands of the big sizes (> 20 $\mu$ m), as well as a great number of inclusions of which the size is higher than 1 $\mu$ m. In the case of the bainite structures, this one is a function of the bainite packages of big size (> 20 $\mu$ m), as well as large inclusions.

A special care was given to the observation of the fracture surfaces and the nickel plated transverse sections for better understanding the role of the inclusion on the toughness (Fig. 1). All of the observations show, without doubt, the harmful role of inclusions, that it is in the weld bead and also in the HAZ.

All of these results thus make it possible to suggest improvement paths to reduce the native scattering in toughness in the welded joints.

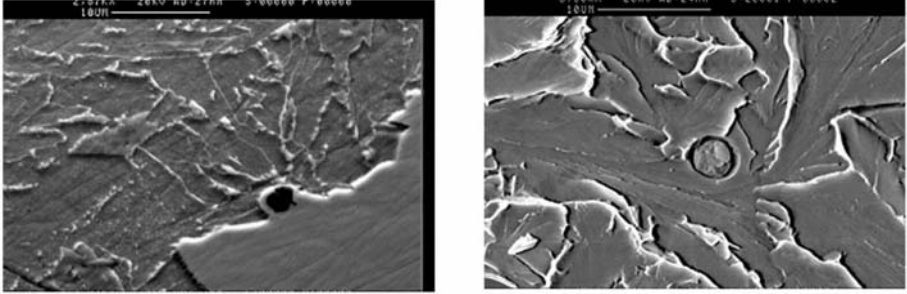


FIGURE 1. Example of fracture initiation from a large ( $\approx 3\mu\text{m}$ ) Ti (Al) oxide inclusion Steel A-J-R (Ti-O Steel) CGHAZ, Charpy V-Specimen, cleavage fracture KV (-80) = 6 J.

### References

1. Bayraktar E., Kaplan D., Buirette C. and Grumbach M., *J. of Mater. Proc. Technology*, vol. **145**, I, 27-39, 2004
2. Kluken A. Ø., GrØng O. and Hjelen J., *Mater. Sci and Technology*, vol. **4**, 649-654, 1988

## STUDY OF A SUBSTITUTION TEST FOR EXPLOSION TESTS ON SUBMARINES HULLS

Thierry Millot and Aude Menegazzi  
DCN/CESMAN, DCN Propulsion, 44620 La Montagne  
DGA/SPN/PFN/MN, 8 Blvd Victor Paris 15eme, France  
thierry.millot@dcn.fr, aude.menegazzi@dga.defense.gouv.fr

Knowledge about the failure of metallic materials and their welded assemblies has been the subject of numerous studies resulting in steady progress being made since the middle of the twentieth century. By failure, we mean the brittle fracture resulting from a defect and not the conventional exceeding of the ultimate strength of the material.

The defects in question result in cracks and may come from various sources:

- Manufacture (particularly in welded joints)
- Fatigue
- Stress corrosion cracking

Under certain loading conditions, these cracks may lead to the brittle fracture of the structure. Where the structure is of a sensitive nature, or the failure would lead to serious consequences, a safety strategy must be put in place for the materials and assemblies regarding the brittle fracture problem. This strategy must be both sure but also economically justifiable. Depending upon requirement, each industry (nuclear, offshore, aeronautics, naval, etc.) has developed or chosen specific tests which meet these requirements as closely as possible. Consequently, there are a large number of failure tests, both standardized and otherwise. Furthermore, depending on the objective, (design, qualification, approval, procurement), the tests used are not necessarily the same.

In the naval domain, and more particularly in the case of armed submarines, the structural test most generally used is the BET (Bulge Explosion Test) and ECST (Explosion Crack Starter Test), Pellini and Srawley [1]. This is used to approve a material or a welding process as regards the risk of brittle fracture in the event of underwater explosion. BET testing includes several closely-related test variants which are still relatively empirical and which have remained indispensable since the end of the 50's for showing the suitability of use of a material or assembly in severe dynamic stress situations, MIL-STD-2149A [2].

The cost constraints associated with carrying out explosion tests have forced DCN and DGA to attempt to validate a substitution test. As the idea of a dynamic fracture mechanic crack stop type test is attractive, it is this approach which has been explored in a collaboration between DCN and the Département Mécanique du Solide et de l'Endommagement (*Mechanics of Solids and Damage department*) at ONERA in Lille. This new test is called "SIFT" (Simplified Impact Fracture Toughness), Sumpter [3] or "Drop Weight J test".

The experimental equipment requires:

- A high loading speed
- High potential energy
- An ability to absorb the residual energy

The idea was to use the ONERA crash tower at Lille as a basis and to create equipment able to take test samples after temperature setting, stress them by dynamic three points bending, carry out test condition validation measurements and lastly absorb the residual energy.

The SIFT test specimens were taken through a welded joint of 80 HLES ( $Rp0.2 > 700$  MPa) submarine hull steel. Given the mechanical nature of the test failure, an initial crack was produced by fatigue on each of the test specimens. The SIFT results were compared with the ECST results and numerically simulated.

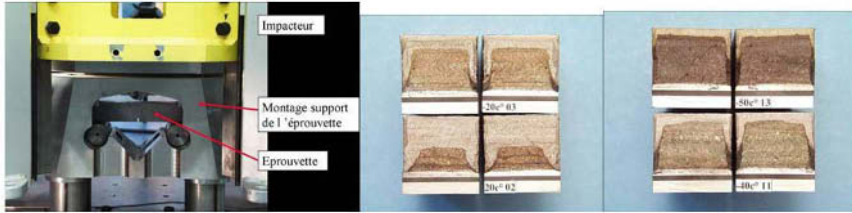


FIGURE 1. View of the assembly and specimens after test.

Development carried out on the "SIFT" (Simplified Impact Fracture Toughness) test, the correlations with the results from other types of mechanical tests of dynamic failure as well as the use of numerical simulations give us good reason to hope that a replacement will soon be found for the explosion tests. Before the change can take place however, "SIFT – explosion test" correlations must be made using other grades of steel with differing characteristics to be certain that the SIFT results are relevant in all cases.

## References

1. W .S. PELLINI, J.E. SRAWLEY (US Naval Research Laboratory) "Procedures for the evaluation of fracture toughness of pressure vessel materials" 08/06/1961
2. MIL-STD-2149A(SH) 1990 "Standard procedure for explosion bulge testing of ferrous and non ferrous metallic materials and weldments".
3. J.D.G. SUMPTER ECF 12 (Fracture from defects) "Simplified Fracture Toughness measurement by drop weight loading"

## HIGH STRAIN RATE RELOADING COMPRESSION TESTING OF A CLOSED-CELL ALUMINUM FOAM

Alper Tasdemirci<sup>a</sup>, Mustafa Güden<sup>a</sup> and Ian W. Hall<sup>b</sup>

<sup>a</sup>Department of Mechanical Engineering, Izmir Institute of Technology

<sup>a</sup>Gülbağçe Köyü, Urla, Izmir, Turkey 35430

<sup>b</sup>Department of Mechanical Engineering, University of Delaware

<sup>b</sup>Newark, DE 19716, USA

alpertasdemirci@iyte.edu.tr

Aluminum (Al) closed-cell foams are materials of increasing importance because they have good energy absorption capabilities combined with good thermal and acoustic properties. They can convert much of the impact energy into plastic energy and absorb more energy than bulk metals at relatively low stresses. When used as filling materials in tubes, they increase total energy absorption over the sum of the energy absorbed by foam alone and tube alone [1]. In designing with metallic foams as energy absorbing fillers, mechanical properties are needed for strain rates corresponding to those created by impact events. Quasi-static mechanical behavior of metallic foams has been fairly extensively studied, but data concerning high strain rate mechanical behavior of these materials are, however, rather sparse [2,3]. This study was initiated, therefore, to study and model the high strain rate mechanical behavior of an Al foam produced by foaming of powder compacts and to compare it with quasi-static behavior and, hence, determine any effect on energy absorbing capacity.

High strain rate tests ( $10^2$ – $10^3$  s<sup>-1</sup>) were performed using a Split Hopkinson Pressure Bar (SHPB) apparatus equipped with aluminum bars 3.53 m long and 19mm in diameter. The samples are compressed by accelerating the striker bar from a gas chamber so that it impacts the incident bar. The resulting elastic wave travels down the incident bar to the specimen/bar interface where part of the wave is reflected and part continues through the sample and into the transmitter bar. The incident, transmitted and reflected waves are measured by strain gages on the bars. Experiments were performed in which many reflections of the waves were recorded. The raw data from such an experiment are presented in Fig. 1. The figure shows that the magnitudes of the incident and reflected waves diminish and that of the transmitted wave increases with each successive passage. In each successive passage, the foam sample reloaded and the strain rate in each loading was very similar, allowing the application reloading tests in a single SHPB testing and hence loading the foam sample to relatively large strains at a constant strain rate.

To observe how the specimen (foam) underwent deformation during SHPB testing and to compare the experimental data and numerical simulation results, a high speed camera Ultra 8, was used to record the SHPB tests. The deformation process (or fracture process) was observed by photographing the specimen sequentially in predetermined short time intervals (of the order of few microsec) using the high speed camera. With the Ultra 8 high speed camera used for the present study, a maximum of eight frames can be photographed in the speed range of 500 to 100 million frames per second. In the time domain, this implies that the interframe time can be varied between 10 nsec to 1 msec. The camera can be synchronized with the incident bar strain-gage or can be delayed to photograph the events of interest only. Fig. 2 shows the high speed camera record of the dynamic deformation process of the Aluminum foam sample during the SHPB experiment. The first image was taken before the loading pulse reached the specimen. The next four images were taken at 400 microsec intervals after the arrival of the incident pulse at the specimen. The bar on

the left is the incident bar, which moves toward the right during loading. The bar on the right is the transmission bar. Finally, a three-dimensional SHPB finite element model using the commercial explicit finite element code LS-DYNA 970 was used to study stress wave propagation in aluminum foams. Numerical simulations were carried out using the MAT\_HONEYCOMB material model of LS-DYNA 970 for aluminum foam.

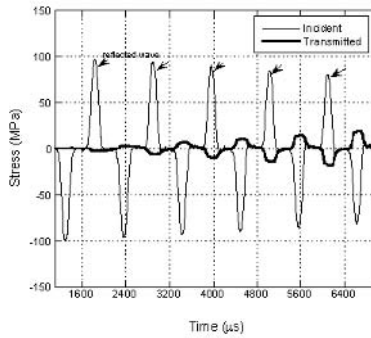


FIGURE 1. Incident, reflected and transmitted waves in a typical SHPB testing.

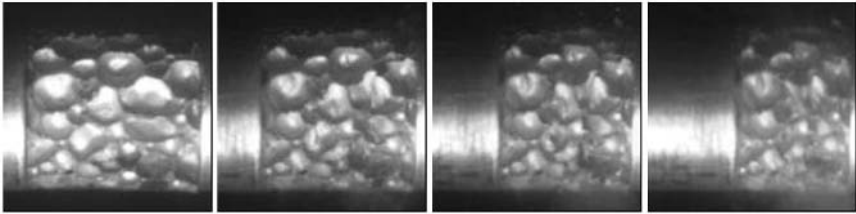


FIGURE 2. The high speed camera record of the dynamic deformation of a foam sample.

## References

1. Seitzberger, M., Rammerstorfer F.G., Degischer HP, et al., *Acta Mechanica*, vol. **125** (1-4), 93-105, 1997
2. Mukai T., Kanahashi H., Miyoshi T., et al, *Scripta Materiala*, vol. **40**, 921-927, 1999
3. Han F.S., Zhu Z.G., Gao J.C., *Met. Mat. Trans. A.*, vol. **29** (10), 2497-2502, 1998

## QUASI-STATIC AXIAL CRUSHING BEHAVIOR OF ALUMINUM CLOSED CELL FOAM-FILLED MULTI-PACKED ALUMINUM AND COMPOSITE/ALUMINUM HYBRID TUBES

Mustafa Guden, Halit Kavi and Sinan Yuksel  
Department of Mechanical Engineering, Izmir Institute of Technology,  
Gulbahce Koyu, Urla, Izmir, Turkey 35430  
mustafaguden@iyte.edu.tr

The light-weight foam filling of metallic columnar structures increases the Specific Absorbed Energy (SAE) values of foam-filled tubes over those of empty counterparts when appropriate tube geometry, tube wall-foam filler bonding and foam density are chosen [1-6]. Foam filling usually results in an interaction between tube wall and foam filler, increasing the average crushing loads of filled-tube over the sum of the crushing loads of foam (alone) and tube (alone). Despite the many experimental investigations conducted to understand the crushing behavior of foam-filled single metal and empty composite tubes, the crushing behavior of empty and foam-filled multi-packed and hybrid (metal/composite) tubes have not been investigated as much. In this study, the quasi-static crushing behavior of empty and Al foam-filled single and two multi-tube designs, hexagonal (Fig.1 (a)) and square packing (Fig. 1(b)) and empty and foam-filled hybrid tubes (Fig. 1(c)) were investigated.

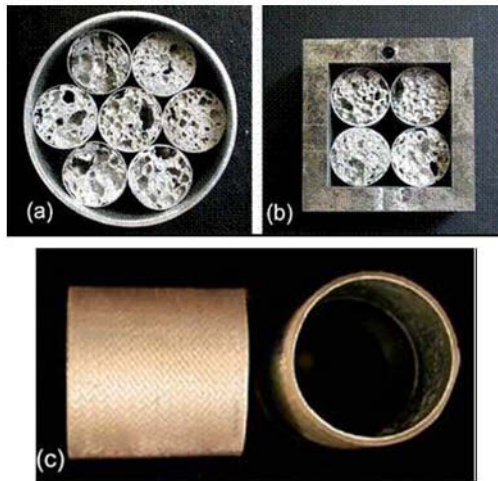


FIGURE 1. Foam filled (a) hexagonal and (b) square packed multi tubes and (c) empty hybrid composite/aluminum tubes.

The effects of foam filling in single metal tubes were (a) to increase the average crushing load over that of the tube (alone) + foam (alone) and (b) to decrease the fold length. The strengthening coefficient of foam filling in single tubes was extracted to be 1.65. Similar to single empty tubes, the foam filling shifted the deformation mode of empty tubes from diamond to concertina mode in multi-tube designs. The effect of multiple tube packing was seen as the increased crushing and

average crushing load values over the sum of the average crushing loads of the equal number of single empty and foam-filled tubes. The increase in the average crushing loads of multi-tube designs over the single tubes was attributed to the constraint effects and frictional forces between tubes and tubes and outer tube walls. The foam density was further found to increase the interaction effects in multi-tube designs. Although foam filling in single and multi tubes resulted in higher energy absorption than the sum of the energy absorptions of the tube(s) and foam(s), it was not effective in increasing the SAE values over the empty single tube and empty multi-tube designs. At similar foam filler densities multi-tube designs were however energetically more effective than Al foam-filled single tubes for both hexagonal and cubic packed designs.

Two crushing modes, progressive and catastrophic, were observed in the testing of empty E-glass woven fabric composite and empty hybrid tubes. The progressive crushing mode resulted in higher crushing loads, hence higher SAEs. In empty hybrid tubes, the deformation mode of Al tube was found to be a more complex form of the diamond mode of deformation, leading to higher SAE values than the sum of the SAEs of empty composite tube and empty metal tube. The increased load and SAE values of hybrid tubes were attributed to the interaction between composite tube and Al tube. The foam filling of the composite tubes was found to be ineffective in increasing foam-filled tube crushing loads over the sum of the crushing loads of empty composite and foam in the progressive crushing region. However, the foam filling induced a more stable tube crushing trigger and progression. In the foam-filled hybrid tubes, the composite tube failed by axial splitting due the resistance imposed by the foam filler to the metal tube inward folding; therefore, foam filling was ineffective in increasing crushing loads; hence, SAE values over those of empty composite tube + empty Al tube + foam.

## References

1. Santosa, S., Wierzbicki, T., *Comp. Struc.*, vol. **68**, 343-367, 1998.
2. Kavi, H. Toksoy, A.K., Guden, M., *Mater. & Design*, vol. **27**, 263-269, 2006.
3. Toksoy, A.K., Tanoglu, M., Guden, M., Hall, I.W., *J. Mater. Sci.*, vol. **39**, 1503-1506, 2004.
4. Reid, S.R., Reddy, T.Y., Gray, M.D., *Inter. J. Mech. Sci.*, vol. **28**(5), 295-322, 1986.
5. Reddy, T.Y., Wall, R.J., *Inter. J. Impact Eng.*, vol. **7**(2), 151-166, 1988.
6. Seitzberger, M., Rammerstorfer, F.G., Gradinger, R., Degischer, H.P., Blaimschein, M., Walch, C., *Inter. J. Solids Struc.*, vol. **37**, 4125-4147, 2000.



## CALIBRATION OF DUCTILE FRACTURE PROPERTIES OF TWO CAST ALUMINUM ALLOYS

Hiroyuki Mae<sup>1</sup>, Xiaoqing Teng<sup>2</sup>, Yuanli Bai<sup>2</sup> and Tomasz Wierzbicki<sup>2</sup>

<sup>1</sup> Honda R&D Co., Ltd. \*\* Massachusetts Institute of Technology

<sup>2</sup> 4630 Shimotakanezawa, Haga-machi, Haga-gun, Tochigi 321-3393, Japan  
hiroyuki\_mae@n.t.rd.honda.co.jp

To numerically predict crack formation and growth of aluminum cast components under accidentally loading, it is necessary to characterize fracture properties at the macroscopic level. In this study, ductile fracture loci formulated in the space of the effective plastic strain to fracture and the stress triaxiality for two cast aluminum alloys were obtained using combined experimental numerical approaches. A total of twelve tests were conducted including six tensile tests on notched and un-notched round bars and six biaxial loading tests on flat butterfly specimens in each material. The round bars were tested on a conventional kinematically controlled loading frame and the objective of these tests was to determine experimentally the true stress-strain curves from the above two types of materials. The butterfly specimens were tested in a uniquely designed Universal Biaxial Testing Device (UBTD) and in each case the displacement to fracture was recorded. The butterfly specimens were tested with five different orientations with respect to the longitudinal axis of the testing machine. Each orientation provides different an average stress triaxiality ranging from  $-1/3$  to  $+1/3$ . Because of the limited number of specimens, only one test was run for each configuration except the shear test (zero stress triaxiality) in which two specimens were tested. Detailed finite element models were developed for all the specimens. In the case of the butterfly specimens, approximately 40,000 solid elements were used. From the results of numerical simulations and the experimentally found displacement to fracture, 2-D fracture envelopes were determined for two materials. The fracture envelope was constructed in the space of the equivalent plastic strain to fracture and the stress triaxiality. It was found that the material ductility is decreasing sharply with the stress triaxiality. However, for shear and combined shear/compression the ductility of the cast aluminum alloy is quite high. The obtained fracture loci cover a wide range of stress triaxiality and thus it be applicable to various loading cases.

Figure 1 illustrates a butterfly specimens mounted in the UBTD with the orientation angle 10 degree. By suitably changing the orientation of the specimen with respect to the loading direction, different stress states would develop from pure tension, combined tension and shear, pure shear, combined compression and shear, all the way to pure compression. A detailed description of the UBTD can be referred to the paper [1]. The butterfly specimens have a complex, double curvature geometry in the gauge section such that cracks would initiate in the central region in most of the loading cases. A detailed discussion on the development of this type of specimens could be found in Ref. [2].

All the test points were plotted on the graph with the stress triaxiality as an independent variable and the equivalent fracture strain as the ordinate. Without resorting to the damage accumulation rule, the average value of the stress triaxiality is defined here

$$\left( \frac{\sigma_h}{\bar{\sigma}} \right)_{ave} = \frac{1}{\epsilon_f} \int_0^{\epsilon_f} \frac{\sigma_h}{\bar{\sigma}} d\bar{\epsilon}_{pl} \quad (1)$$

The results for two cast aluminium alloys are shown in Fig. 2. There is a very strong dependence of the material ductility of two cast aluminium alloys of the magnitude of the stress

triaxiality. The material made by sand molding shows less material ductility than that made by metal molding. It is investigated that the microstructure of the materials has a strong effect on the material ductility.

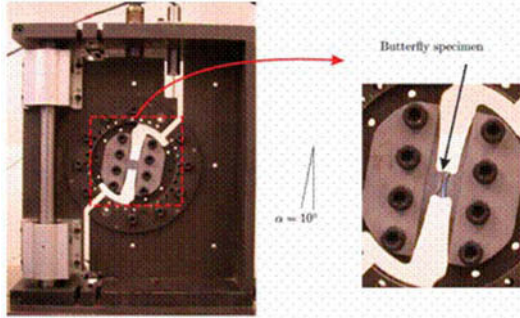


FIGURE 1. A butterfly specimen with the orientation angle 10 degree in the UBTD.

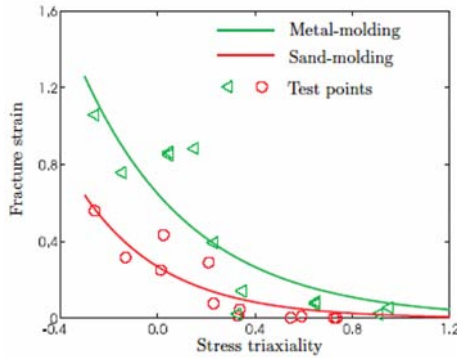


FIGURE 2. Comparison of fracture loci between the metal and sand moldings.

## References

1. Mohr, D., Doyoyo, M., *Journal of Applied Mechanics*, vol. **71**, 375-385, 2004.
2. Bao, Y., Bai, Y., Wierzbicki, T., *Technical Report*, No. 135, Impact and Crashworthiness Lab, MIT, Cambridge, MA, 2005.

## STATE OF THE ART OF IMPACT TENSILE TEST (ITT): ITS HISTORICAL DEVELOPMENT AS A SIMULATED CRASH TEST OF INDUSTRIAL MATERIALS

E. Bayraktar<sup>1</sup>, D. Kaplan<sup>2</sup> and M. Grumbach<sup>2</sup>

<sup>1</sup>Supmeca -Paris (EA2336), School of Mechanical and Manufacturing Engineering, France

<sup>2</sup>ARCELOR Group, Paris, France

bayraktar@supmeca.fr; dominique.kaplan@arcelor.com; marc.grumbach@wanadoo.fr

History of Brittle Fractures had begun with French scientist Georges Charpy who has developed firstly pendulum impact testing at the beginning of the 20th century. Very useful scientific works had been carried out by Charpy's team at the laboratory of "CNAM-Paris, Arts et Métiers from 1904" (formerly Ecole arts et Manufactures) in order to determine the amount of energy absorbed by a material during fracture, which is a measure of a given material's toughness.

Essentially, much experimental evidence had been gathered by the 1920/1930s which showed that high strain rates applied at temperatures close to or somewhat below room temperature in the presence of notches were more likely to result in brittle or sudden failure. This problem was identified in a number of catastrophic failures in ferritic steel structures and whilst the science of fracture mechanics increasingly allows a rigorous approach to designing against brittle fracture in steel structures, the Charpy test remains as a well recognized method of specifying steel quality. Empirical correlations have been shown between Charpy value and service performance.

After the mid 1950s, welding techniques were improved and Charpy testing became an essential part of steel specification. Among them, a number of examples of brittle failure were registered such as Liberty Ship in 1943, Plate Girder Bridge in 1951, Post Office Building in 1954. Today, the literature review shows that starting from the earliest Charpy' test machine development work, researchers are interested in designing equipment capable of measuring both the energy expended in fracturing the specimen, and the force-deflection and energy-deflection curves. However, all of these evolutions are mainly for the thicker steels and any of them do not replace the real crash test simulations and these types of the tests show many dispersion at the level of ductile/brittle transition zone.

At the mid 1970s, French scientists Marc Grumbach & Germain Sanz have imagined and fully described the principle of the impact tensile test -"ITT" at IRSID-Paris Research Laboratory. This was a revolution in this domain. In its initial conception, this test was designed for base metal testing of cylindrical and plate specimens of which thicknesses were 5mm.

At the mid 1990s, French scientists Emin Bayraktar and Dominique Kaplan in Paris have developed the technique of Grumbach and applied with success for testing of welded sheet materials of which thicknesses vary between 0.7 and 5mm. This addresses either to continuous welding (LASER, GTAW...) or to discontinuous processes (resistance spot welding). Energy level of this technique was extended up to 450 Jules [1]. The research works carried out by Dominique Kaplan's research team allowed developing this technique in industrial scale in order to approach to the real crash test conditions. This test is based on the use of a two-body tensile specimen (in small size and real big size), which includes a smooth part and a section with stress-concentration. This specimen is mounted in a special device (Figure 1a) and the whole set is brought to the desired testing temperature. Afterwards, this set is rapidly placed in a pendulum device where special housing has been arranged and fractured. A double hammer is instrumented with strain gages allowing deriving (force-displacement) curve during fracture.

Recently (~2000), an industrial machine installed at the research laboratory in Paris (SOLLAC-Arcelor Auto) allows testing the thin welded specimens (TWB-Tailored Welded Blanks) up to the energy levels of 750 Jules (Figure 1b).

It needs more development of this test for the technological reasons. Why?

On one hand, some very simple static tests (chisel test, peeling, shear or cross tensile tests for spot welds, Erichsen tests for LASER welds) are useful for materials and joining conditions screening. However, these tests do not give real indication on the behaviour of the welds in the case of dynamic loading.

On the other hand, some crash tests, performed on almost “full scale” specimens are of course more representative. Nevertheless, they are more complicate, and in some cases not fully adapted to evaluate rapidly the influence of welding conditions on the mechanical properties.

At an intermediate level, some dynamic compression tests of pillars (“hat square column”, see for example) seem more satisfactory. But this kind of test seems more interesting for testing overall geometry, weld disposition, base metal properties, rather than for evaluating intrinsic weld quality. This is why it is felt that another “intermediate” dynamic testing, adapted to the characterisation of continuous or discontinuous welds, is needed.

This paper reports the early history of instrumented impact testing, and concentrates on the recent results of experiments and numerical modelling obtained on the different welded steel grades by means of the new developed machine as a comparative study in two aspects;

1. State of the art concerning joining techniques for automotive industry
2. State of the art concerning dynamic testing of high strength welds for automotive industry

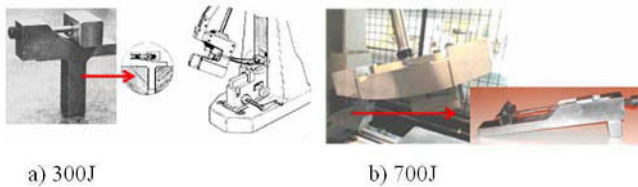


FIGURE 1. Impact tensile pendulum developed by Grumbach & Sanz in 1972 a) and new impact tensile device developed at the beginning of 2000 b)

## References

1. Grumbach M., Sanz G., *Revue de Métallurgie*, vol. 2, 145-164, 1972.
2. Bayraktar E., Kaplan D. and Grumbach M., *J. of Mater. Proc. Technology*, vol. 145, I, 27-39, 2004.
3. Bayraktar E., Kaplan D., Hugel D. and Jansen J.P., *J. of Mater. Proc. Technology*, vol. 147, II, 155-162, 2004.
4. Bayraktar E., Kaplan D. and Grumbach M., *J. of Mater. Proc. Technology*, vol. 153, 80-86, 2004.

## EXPERIMENTAL AND NUMERICAL ANALYSIS OF CIRCULAR TUBE SYSTEMS UNDER QUASI-STATIC AND DYNAMIC LOADING.

Edmund Morris<sup>1</sup>, A.G. Olabi<sup>1</sup>, M.S.J. Hashmi<sup>1</sup> and M.D. Gilchrist<sup>2</sup>

<sup>1</sup> School of Mechanical and Manufacturing Engineering, Dublin City University, Glasnevin, Dublin 9, Ireland

<sup>2</sup> School of Electrical, Electronic and Mechanical Engineering, University College Dublin, Belfield, Dublin 4, Ireland  
abdul.olabi@dcu.ie

In the study of impact attenuation devices, rings/tubes have received a large amount of research due to their adaptability, i.e. they are low in cost and are readily available for selection in the design process. They also exhibit desirable force-deflection responses which is important in the design of energy absorbing devices. The function of such a device is to bring a moving mass to a controlled stop and ideally cause the occupant ride down deceleration to be within acceptable limits so as to avoid injuries or to protect delicate structures.

In this work, the quasi-static and dynamic analysis of nested circular tube energy absorbers was examined using experimental and numerical techniques. Although these devices are usually exposed to much higher velocities, it is common to analyse the quasi-static response first, since the same pre-dominant geometrical effects will also occur under dynamic loading conditions.

In this investigation, quasi-static tests were performed via a Universal Instron machine with an applied velocity of 3-5mm/min whilst dynamic tests were performed with velocities ranging between 5m/s and 7 m/s. The various nested tube systems consisted of one standard and one optimised design. Their crushing behaviour and energy absorption capabilities were obtained and analysed both experimentally and numerically.

**KEYWORDS:** Energy absorbers, lateral crushing, nested system.

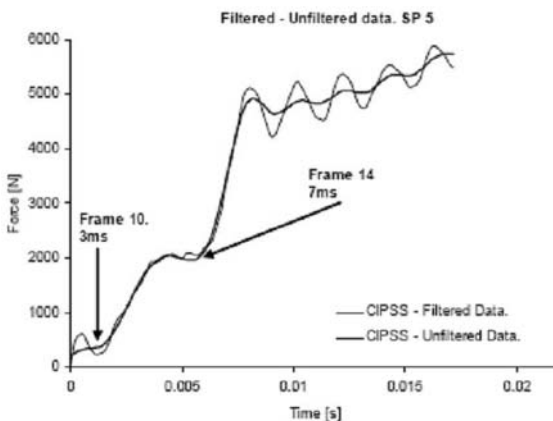


FIGURE 1. Sample five of a CIPSS in its filtered and unfiltered state.

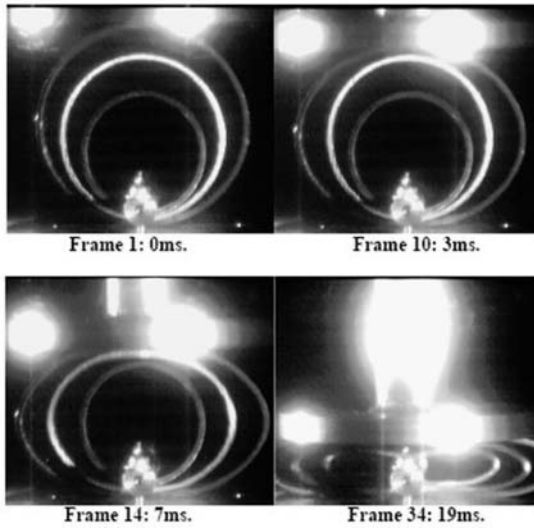


FIGURE 2. Dynamic displacement evolution of a CIPSS.

## References

1. Burton, R.H., Craig, J.M., "An Investigation into the Energy Absorbing Properties of Metal Tubes Loaded in the Transverse Direction. "1963, BSc (Eng) Report, University of Bristol, England.
2. DeRuntz, J. A., Hodge, P. G., "Crushing of a Tube between Rigid Plates." Transactions of ASME, Journal of Applied Mechanics., 1963, vol. **30**, 391-395.
3. Redwood, R. G., "Discussion of Ref. 2." Transactions of ASME, Journal of Applied Mechanics., 1964, vol. **31**, 357-358.
4. Reid, S. R., Reddy, T. Y., "Effect of Strain Hardening on the Lateral Compression of Tubes between Rigid Plates. " Int J of Solids and Structures, 1978, vol. **14** (3), 213-225.
5. Avalue, M., Goglio, L., "Static Lateral Compression of Aluminium Tubes: Strain Gauge Measurements and Discussion of Theoretical Models." Journal of Strain Analysis., 1997, vol. **32**(5), 335-343.
6. Reddy, T., Reid, S., "On Obtaining Material Properties from the Ring Compression Test." Nuclear Engineering and Design, 1979, vol. **52**, 257-263.

### 3D MECHANICAL ANALYSIS OF AXIALLY LOADED CFRP CONFINED CONCRETE COLUMNS

Youliang Chen<sup>1,2</sup>, Ping Zheng<sup>2</sup>, Jing Ni<sup>2</sup>, Lequn Chang<sup>2</sup> and Feng Yang<sup>2</sup>

<sup>1</sup>College of Urban Construction and Environmental Engineering, University of Shanghai for Science and Technology, 516 Jungong Road, 200093 Shanghai, PR China

<sup>2</sup>Department of Civil Engineering, Shanghai University,  
149 Yanchang Road, 200072 Shanghai, PR China  
ballackchang@163.com

The behaviour of CFRP confined concrete column under axial compressive force and the longitudinal constraint mechanism of specimen on different CFRP wrapped ways were studied by tests of three CFRP confined concrete columns and one reference concrete column and by three-dimensional nonlinear FEM (finite element method) analysis. The result indicated that when the axial compressive stress is large than 0.8~0.9 times of peak stress, the lateral expansion deformation of concrete increases rapidly. The longitudinal strain-circumferential strain relationship curve is in linear convergence. There exists strain concentration of the strap wrapped specimens in the place where no CFRP is wrapped. Based on the distribution of the lateral tensile strains  $\varepsilon_F$  along the longitudinal axis at different relative stress levels of CFRP confined concrete columns, the whole procedure of axially loaded experiment of specimens can be divided into three phases: elastic stage, elastic-plastic stage, plastic stage.

CFRP wrapping of existing circular concrete columns has been proven to be an effective retrofitting technique. There have already existed many researches on the behaviour of axial compressive concrete columns, which are wrapped with CFRP. Most researches lay emphasis on the experimental approaches, and experimental parameter is the quantity of CFRP used in the reinforced concrete columns.

In this study, a group of concrete columns confined with CFRP have been tested under axial static compressive loading and the model for three-dimensional nonlinear FEM (finite element method) analysis is established. The computed stress-strain curves of CFRP confined concrete column under axial load indicate good agreement with experimental results. The confinement effect of the core concrete with different types of CFPR jacket has been analyzed, and the transverse confinement mechanism of CFPR confined concrete specimens has been studied.

In this study, three CFRP confined concrete columns and one reference concrete column have been tested. In this test, the carbon fibber sheet is cut into straps with 12mm in width and 25mm in length and is painted with resin on both sides. We make one group of three specimens, and make experiments for material properties after 7 days natural maintenance. The measured objects are the tensile strength  $f_F$ , the elastic modulus  $E_F$  and the ultimate tensile strain  $\varepsilon_F$  of carbon fibber sheet. The specimens on the ZWICK-Z020 high-low material test machine are tested under tensile loading with continuously increasing loading (the speed of loading is 1mm/min). The stress-strain curve of CFRP composites obtained from the measurement is shown in Fig. 1. The material properties of carbon fibber sheet and resin are supplied by the factory.

The experiments are executed on 100t computer governed electronic experimental equipment. The location of 4 longitudinal and circumferential strain gauges for specimen C4 is shown in Fig. 2, and it is the same for another 3 specimens. The displacement in the middle of the specimen is recorded by the equipment automatically. The loading is governed by displacement, and the speed of loading is 1mm/min.

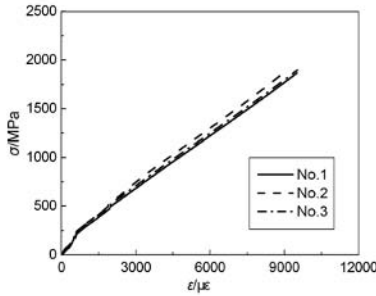


FIGURE 1. Stress-strain relationship curve of CFRP tensile experiment

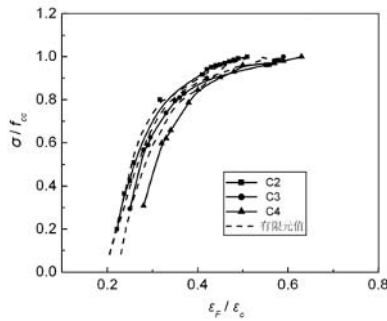


FIGURE 2.  $\sigma/f_{cc}-\varepsilon_F/\varepsilon_c$  response curve about the lateral swell deformation of concrete

**Reference**

1. Toutanji, H., and Saafi, M. (2002). "Stress-strain behaviour of concrete columns confined with hybrid composite materials." *Mater. Struct.*, vol. **35**, 338–347.
2. Li, Y., Lin, C., and Sung, Y. (2003). "A constitutive model for concrete confined with carbon fiber reinforced plastics." *Mechanics of Materials*, vol. **35**, 603–619.
3. L. P. Ye, K. Zhang, S. H. Zhao, and P. Feng. (2003). "Experimental study on seismic strengthening of RC columns with wrapped CFRP sheets." *Construction and Building Materials*, vol. **17**, 499–506.
4. Wu, G., and LÜ, Z. (2003). "Study on the stress-stain relationship of FRP confined concrete circular column without a strain-softening response." *Architecture and Structure*, vol. **24** (25), 1-9.
5. Li, J., Qiang, J., and Jiang, J. (2004). "Axial compressive loading test of FS confined concrete column and nonlinear finite element analysis." *Architecture and Structure*.
6. Yu, Q. (2000). "Calculation of bearing capacity and strength of FRP confined concrete columns." *Ind. Constr.*, vol. **30** (10), 31-34.



## CONCEPTION AND CONSTRUCTION OF AN IMPACT MACHINE (100KJ) FOR FRONTAL AND SKEW SHOCKS

Etienne Pecquet<sup>1</sup>, Jérôme Tchuindjang<sup>2</sup> and Serge Cescotto<sup>1</sup>

<sup>1</sup>Department ArGENCo – Solids, Structures and Fluids Mechanics – University of Liège

<sup>2</sup>Department A&M – Metallurgy and Materials Science – University of Liège

<sup>1&2</sup>Bât. B52/3 – 1, Chemin des Chevreuils – B-4000 Liège, Belgium

Etienne.Pecquet@ulg.ac.be, J.Tchuindjang@ulg.ac.be, Serge.Cescotto@ulg.ac.be

The conception and the construction of an impact machine are financed by the *Communauté Française de Belgique*. This is performed in a fundamental research that deals on metallic macro foams. These products are obtained assembling together pieces of metal with big voices between pieces. Then, energy dissipation can be obtained by plastic deformations. The products can imply direct re-use of metal like old soft drink cans, wires, ... allowing energy saving in comparison with return to the electric furnace. Low cost products are searched for applications in road safety and in civil engineering.

Often, to characterize products in dynamic or impact loading, especially for road safety products, two opposite tests exist: tests on small specimen and with relatively low energy absorption or complete crash tests that are very expensive. Here, the goal is developing a machine between these two situations. So, this machine will allow to best developments of products and then saving money by reducing missed tests in real scales.

The global concept consists in using the height of the laboratory to create the kinetic energy. So, a big slide (400mm in width maintained by a beam HEB300) is constructed on which the mass moves from the top to the cellar of the laboratory. Figure 1 gives a schematic view of the slide. Geometry is also studied to obtain horizontal shocks like in road crashes.

The maximum impact load of this equipment is about 700kg. Because of the 15m in height of the laboratory, the maximum theoretical speed is given by equation 1. The maximum energy available is given by equation 2.

$$V = \sqrt{2 \cdot g \cdot H} = 17,1 \text{ m/s} \approx 60 \text{ km/h} \quad (1)$$

$$E = m \cdot g \cdot H = 100 \text{ kJ} \quad (2)$$

These performances should be a little bit reduced by frictions. Normally, these ones will be small because of metallic punctual contacts only. Mass and impact speed can be chosen freely because mass can be easily adapted and dropped from each height.

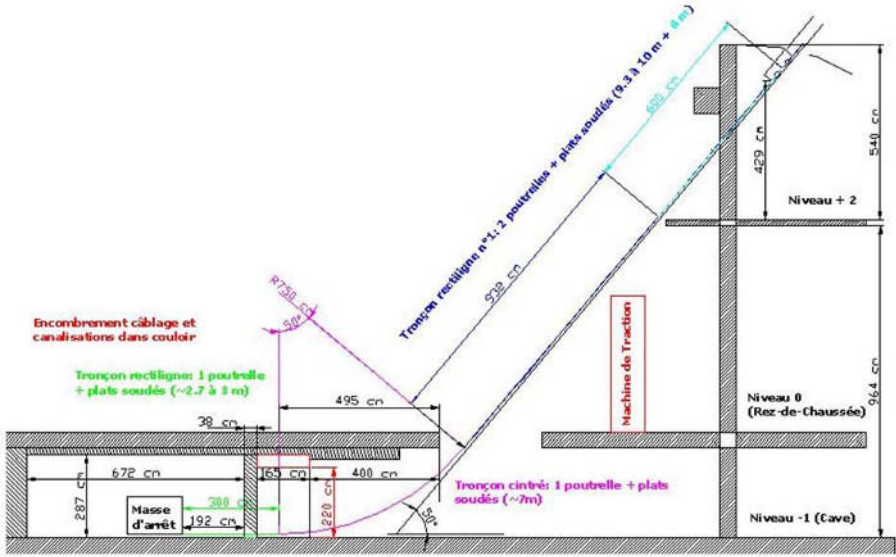


FIGURE 1. Schematic view of the slide.

The impact mass is a wagon only putted on the slide. Many shapes and materials can be mounted on this wagon. The maximum front area of the wagon is 1,60m in width and 1m in height. A second wagon, fixed behind the first one, allows, by ball bearings all around the slide, to maintain the right trajectory.

When the impact mass comes in the cellar, both wagons are disconnected and the guide wagon is stopped by dampers. Then, the impact mass can crush the specimen choosing freely its trajectory as well during crushing as during the rebound.

In the cellar, the testing zone is a large metallic horizontal floor measuring 6x6,5m. On it, eight metallic slabs, each one with a mass of three tons, are placed as we want to maintain the specimen to crush. Because of the important modularity of this floor, the great interest of this machine is the availability to do skew shocks.

So, many products for road safety can be tested : bumpers in frontal or skew shocks, safety barriers, ends of these barriers, whole types of shock absorbers, ... Especially concerning safety barriers in metal, as well the cable effect in the barrier as the rebound of the mass after the shock can be examined.

For measurements, the main part will be done with high speed cameras. In addition, force sensors, displacement sensors, accelerometers or other techniques can be added.

## INFLUENCE OF PRECIPITATION ON THE GRAIN GROWTH DURING THE WELDING OF INTERSTITIAL FREE (IFS) STEELS

E. Bayraktar<sup>1</sup>, D. Kaplan<sup>2</sup> and J.P. Chevalier<sup>3</sup>

<sup>1</sup>Supmeca/LISMMA-Paris, School of Mechanical and Manufacturing Engineering, France

<sup>2</sup>ARCELOR Group, Paris-France

<sup>3</sup>Chair of Industrial Materials, CNAM, case 321, 292 rue Saint Martin, 75141 Paris 03 -France,  
bayraktar@supmeca.fr

Abnormal grain-growth in the Heat Affected Zone (HAZ) during the welding of Interstitial Free (IF) steels has been reported in our previous study [1]. This phenomenon takes place in certain IF steels at a given distance from the fusion line and related to regions where the maximum attained temperature is slightly over  $\alpha \rightarrow \gamma$  transformation temperature,  $Ac_3$ .

In fact, the phenomenon of abnormal grain growth was primarily interpreted in relation to the thermal gradient, which must constitute the “driving force of it”. However, it is natural to feel that the abnormal grain growth can occur only if its development is completed easily within a matrix of great purity and/or very low precipitates. In bear of this claim, one observes indeed a contrary that the phenomenon of abnormal grain growth does not occur during the welding of steel grades, of which carbon contains is slightly larger than that of IFS (example:  $C > 15-20 \times 10^{-3} \%$ ), and under the same conditions of very intense thermal gradient (resistance spot welding - RSW, GTAW, LASER welding, etc...). Thus, this stage of the research requires understanding the private role and/or the effect of each precipitate individually on this phenomenon, in order to answer the following questions:

- What is the initial state of precipitation of the various grades of IFS examined here?
- How this state of precipitation can be modified during the welding and in which condition play a role on the phenomenon of abnormal grain growth?

Many direct observations have been carried out by the researchers on the IFS grades [1-9] but many of them were under the hot deformation (rolling) conditions and only a few studies were published related to the real welding operations. First, for the sake of the simplicity, the state of precipitation was estimated by means of calculations of products of solubility. After then, for each grade, the evolution of the state of the precipitate fraction volume in HAZ of was determined as a function of the temperature reached during welding operation.

In a general way, the state of precipitation in equilibrium can be estimated by the product of solubility:

$$\text{Log } (\%M) (\%C, N) = A - B/T$$

where:

M and C are the percentages (wt % or at %) of the elements liable to form the compound,

A and B are coefficients used in this calculation and T is the solution temperature (in Kelvin).

By detailing the various grades of IFS studied here, the precipitates were taken into account separately for each grade such as IF-Ti, IF-TiNb, IF-TiB, etc. in this analysis.

The objective of this study thus was to search the factors (steel grades and welding conditions) which make clear the role of each precipitate qualitatively on the abnormal grain growth phenomenon. A typical study was then undertaken on TIG (GTAW) and the Resistance spot

welding (RSW) of the different grades of IFS and a special application was given on the grade of IF-TiNb.

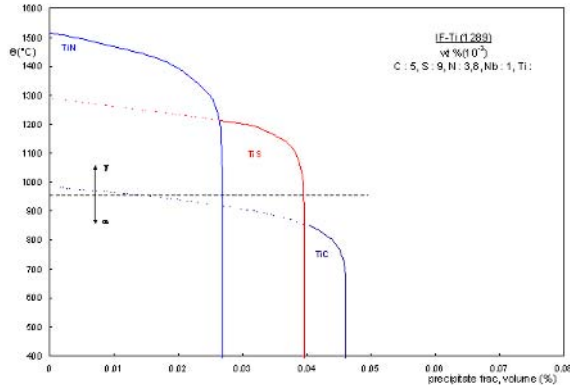


FIGURE 1. Example of calculation of the evolution of the state of the precipitate fraction volume in HAZ of a grade of IFS (IF-Ti) as a function of the temperature reached during welding operation.

## References

1. Foley R.P., Matlock D.K. and Krauss G., *42<sup>nd</sup> MWSP Conf. Proc.*, ISS, vol. **38**, 55-468, 2000
2. Takshi H. and Abiko K., *Mater. Trans., JIM*, vol. **41** (1), 116-121, 2000
3. Bayraktar E., *Final research report, IRSID (ARCELOR research) IRSID/MPM*, vol. **99**, 20152/1, 2002
4. Craven A. J., K. HE, Garvie A. J. and Baker T. N., *Acta Mater.*, vol. **48**, 3869-3880, 2000
5. Strid J. and Esterling K. E., *Acta Metall.*, vol. **33** (11), 2057-2074, 1985
6. Abiko K. Takaki S., Yokota T. and Satoh S., *Mater. Trans., JIM*, vol. **41** (1), 102-108, 2000
7. Fekete J.R., Strugala D.C. and Yao Z., *JOM*, 17-21, **January**, 1992

## ANALYSIS OF MECHANICAL BEHAVIOUR OF SPOTWELD AND FSW METALLIC ASSEMBLIES UNDER QUASI-STATIC AND DYNAMIC LOADINGS

J. Fabis<sup>a</sup>, S. Blanchard<sup>a</sup>, B. Langrand<sup>a</sup> and E. Markiewicz<sup>b</sup>

<sup>a</sup> Department of Solid and Damage Mechanics, ONERA-Lille, 5, boulevard Paul Painlevé, F-59045 Lille Cedex, France

<sup>b</sup> LAMIH, University of Valenciennes, Le Mont-Houy, 59313 Valenciennes Cedex 9, France  
mahelle@onera.fr; markiewicz@univ-valenciennes.fr; fabis@onera.fr

When subjecting a metallic structure to an impact or a crash loading, two kinds of fracture can be seen to appear jointly : rupture initiated in the sheet and rupture located in the joint areas. Depending on the type of transportation mean and materials used for the design of the vehicles, structures can be assembled either by rivets, spotwelds, weld beads and, more recently, Friction Stir Welded joints. To prevent the failure of these joints, which can lead to a complete and particularly brutal structural dismantlement, their mechanical behaviour must be studied under quasi-static and transient dynamic loadings.

The frame of the presented work concerns the analysis of the response of a welded joints under quasi-static and dynamic loadings, to determine the load velocity influence on its behaviour, to understand how and where the failure starts and propagates in the assembly, and also propose relevant experimental data to use for F.E. simulations. Results will be helpful in further works to improve the efficiency of behavioural and failure models for large shell-based crashworthiness or vulnerability FE models. The results of three studies will be presented :

1. **Original quasi-static and dynamic “ARCAN type test” protocol and specimens**, which make it possible to mix loading directions and to control the boundary conditions around spotwelds, have been developed and performed under quasi-static and dynamic loadings (5mm/mn to 1m/s). Four tensile/shear ratio were chosen to characterise the spotweld behaviour (0°, 30°, 60°, 90°) (Fig. 1a). A new device was also developed to test spotwelds in tensile direction on a Split Hopkinson Pressure Bar (Fig. 1b). This device uses SHPB in a non-direct tensile testing configuration and a velocity of 13 m/s is reached,



FIGURE 1. Shape of failed spotweld after tensile test

2. The behaviour and rupture of friction stir welded joints under quasi-static loadings is also presented. FSW joint is typically composed of continuously changing material zones and the strength of some of them may be reduced compared to base material. To better understand the various material and structural behaviours which lead to damage and

rupture of this kind of FSW assembly (heterogeneous by nature), the authors analyse the elastic and plastic (location) strain fields using the **stereo digital image correlation** technique under medium velocity rates. However, a fundamental objective is to characterise main “material states” that compose the FSW joint in order to perform numerical analyses (e.g. 3D solid FE analyses of more or less complex specimens or 3D shell full-scale complex structure). solution that may be interesting to investigate is based on the use of strain field measurement on FSW ARCAN specimen (Fig. 2),

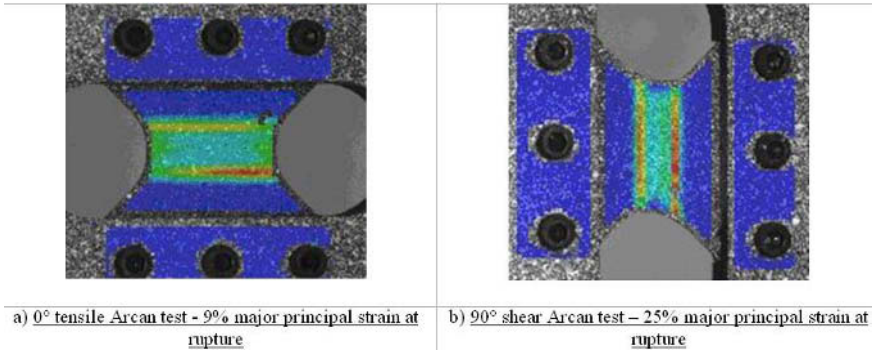


FIGURE 2. DIC analysis of Arcan type test on FSW specimen

3. Very interesting results mixing the DIC capability and dynamic loadings on a spoltweld joint, to understand how and where the failure starts and propagates in the assembly are presented. Cross tensile tests, peeling tests and tensile/shear tests have been performed on an high speed hydraulic jack in a range of velocities from 5mm/mn to 1m/s. Load-displacement responses, energy-displacement reponses, failure mechanisms and topographies were obtained. The strain distribution around the spotweld and the shape of the specimen were measured using a 3-D digital imaging correlation system (Fig. 3).

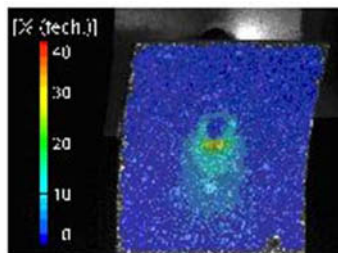


FIGURE 3. Strain field measurement on single lap Tensile/shear specimen under dynamic loading

General conclusions will be drawn from the different studies in terms of applicability of these experimental techniques and outlooks will be presented in terms of improvements, intrinsic limitations, and new Research paths.

## TESTING AND MODELING OF MOISTURE DIFFUSION INTO ALUMINUM PARTICLE FILLED EPOXY ADHESIVE

Ramazan Kahraman and Mamdouh Al-Harathi

Department of Chemical Engineering

King Fahd University of Petroleum & Minerals, Dhahran 31261, Saudi Arabia

kahraman@kfupm.edu.sa

Moisture and aggressive ion ingress into bonded joints are primary causes of adhesive degradation. In this study, moisture diffusion behavior of aluminum powder filled epoxy adhesive was investigated through utilizing fluid immersion tests under complete immersion in distilled water and salt solutions with varying NaCl concentration. Aluminum powder is used in the adhesive for the purpose of improvement of its thermal properties, as demanded in a variety of industrial applications.

The epoxy adhesive used in this investigation is a two-part epoxy obtained from Lord Corporation. The adhesive is prepared by mixing equal volumes of the resin and hardener parts. The mixed adhesive cures fully in 24-48 hours at room temperature. The aluminum powder used for filling the epoxy adhesive was obtained from Allied Britannia Limited. The Al particles were spherical with size smaller than 50 m in diameter. The adhesive sheets (30 ' 30 ' 1 mm<sup>3</sup>) for the moisture diffusion tests were molded between wax covered metal sheets. Four different aluminum filler contents (0, 10, 25 and 50 wt%) were studied. Three pieces of each particular adhesive were immersed in a solution for several months at room temperature. Five test solutions were used in the investigation: distilled water and sodium chloride solutions at 100 ppm, 1000 ppm, 0.5 M and 1.0 M concentrations. The test specimens were suspended/immersed in the test fluids without making contact with each other. The containers were covered with aluminum foil to prevent moisture evaporation. At various time intervals, test specimens were removed from the fluid, extra surface water dried with clean tissue and the specimens weighed by an analytical balance.

Mass diffusivity for each specimen was determined by two methods, one using the diffusion data at early times (away from the saturation point) and the other using the data at large times (close to the saturation point). In Method 1 (by use of Equation 1 [1]),  $M_t/M_\infty$  (where  $M_t$  and  $M_\infty$  are the amounts of moisture intake in time,  $t$ , and at saturation, respectively) is plotted against  $4(t/\pi^2)^{1/2}$  (where  $l$  is the thickness of the adhesive sheet) and the apparent diffusivity,  $D$ , is determined from the initial slope of the plot (slope is  $D^{1/2}$ ). In Method 2 (by use of Equation 2 [1]),  $\ln(1-M_t/M_\infty)$  is plotted against  $\pi^2 t/l^2$  and the diffusivity is determined from the slope of the straight line at large times (slope is  $-D$ ).

$$\frac{M_t}{M_\infty} = 4 \left( \frac{Dt}{\pi l^2} \right)^{1/2} \quad (1)$$

$$\frac{M_t}{M_\infty} = 1 - \frac{8}{\pi^2} e^{-\frac{D\pi^2 t}{l^2}} \quad (2)$$

It took about a year for the 1-mm thick specimens to reach saturation. Qualitatively, similar results were obtained in both methods. The results did not show a significant trend for the effect of aluminum filler content on the apparent moisture diffusivity in epoxy adhesive specimens with some scattering in data. On the other hand the effect on diffusivity by the salt concentration of the

test solution was significant. The rate of diffusion was faster in the test solutions with high salt content (0.5 M and 1 M salt solutions) than in those with low or no salt content (distilled water, 100 ppm and 1000 ppm salt solutions). Diffusivity values ranged from about  $3 \cdot 10^{-10}$  cm<sup>2</sup>/s in distilled water to about  $1 \cdot 10^{-9}$  cm<sup>2</sup>/s in 1 M NaCl solution. It is believed that concentrated salt solutions somehow enhance the formation of microcavities in adhesive materials [2], thereby increasing the rate of moisture diffusion.

Quantitatively, however, the results of the two methods were different, the apparent diffusivity values obtained through Method 1 (at early times) were about twice those obtained through Method 2 (at large times). It is clear that diffusivity is concentration dependent and it decreases with diffusant concentration. Hence, it can be stated that constant diffusivity assumption might lead to error in quantifying moisture diffusion in epoxy systems.

A diffusion model was then developed by considering concentration dependency of the diffusivity using the following relation

$$D = \frac{D_o}{1 + \lambda Q} \quad (3)$$

where  $D$  is the diffusivity,  $D_o$  is the corrected diffusivity,  $\lambda$  is a parameter and  $Q$  is the dimensionless concentration (concentration divided by the concentration at the surface). Corrected diffusivity is concentration independent. The model developed was applied for the diffusion tests in distilled water. A good agreement was observed between the resultant Fickian model solved numerically and the experimental data. Corrected diffusivity values ranged from about  $6.7 \times 10^{-10}$  to  $8.0 \times 10^{-10}$  cm<sup>2</sup>/s. Similar to the results of the previous two methods, the results did not show a significant trend for the effect of aluminum filler content on diffusivity in epoxy adhesive specimens with some scattering in data.

### Acknowledgments

This study has been partly funded by King Fahd University of Petroleum & Minerals under Project # SAB-2001/08.

### References

1. Crank, J. and Park, G.S., Editors, "Diffusion in Polymers", Academic Press, London, 1968.
2. Tai, R. C. L. and Szklarska-Smialowska, Z., "The Microhardness Change and Delamination of Automotive Epoxy Adhesives in Distilled Water and NaCl Solutions", *Journal of Materials Science*, vol. **28**, 6205-6210 (1993).



## JOINING AND MECHANICAL STRENGTH OF SELF-PIERCING RIVETED STRUCTURE – NUMERICAL MODELING AND EXPERIMENTAL VALIDATION

S. Fayolle, P.O. Bouchard and K. Mocellin  
CEMEF – Ecole des Mines de Paris  
BP 207, 06904 Sophia-Antipolis Cedex, France  
Sebastien.fayolle@ensmp.fr

To decrease the weight of new cars, aluminium alloys are progressively replacing steels in parts of the “body-in-white”. However, the use of aluminium alloys requires sometimes new joining techniques to replace classical welding-points. Self-piercing riveting (SPR) or clinching are two of these relatively new joining techniques in which joining comes from the materials plastic deformation. In this study, we focus on the numerical modelling of self-piercing riveting and its experimental validation.

Various studies are dealing with the numerical simulation of riveting, Abe *et al.* [1], Porcaro *et al.* [2]. The originality of our approach, initially presented in Bouchard *et al.* [3], is the use of damage in the modelling of material behaviours (sheets and rivet). Throughout this paper, we will show the importance of taking damage into account.

In order to achieve the numerical analysis of SPR process, we use the finite element software FORGE 2005®. This software deals with the finite deformation of elastic-(visco)-plastic materials. Damage modelling is based on the Lemaitre damage model [4] and we use the kill-element technique to model the fracture of the upper sheet. This technique consists in deleting the elements within damage have reached a critical value.

To determine the parameters of the isotropic hardening and of the damage law, we use an inverse analysis. The methodology is based on an evolutionary algorithm. Due to the number of parameters, we perform for each part two different mechanical tests to valid the identified parameters. Details are given in the article.

In this paper, we use a 2D axisymmetric configuration to model the SPR process. When the computation is done, we validate the riveting process simulation thanks to the experimental load-displacement curves and the geometrical cuts of the samples.

The second aim of this paper is to present the ability of our model to simulate the mechanical strength of the joined specimen under static loading (tensile, shear and mixed solicitations). With FORGE 2005®, it is possible to export mechanical fields from a 2D axisymmetric mesh to a 3D mesh. The creation of the 3D sample is achieved in many steps using the final geometries of the SPR process. First, a 3D geometry is extrapolated from the 2D geometry. Then a new mesh is generated and the mechanical fields (residual stresses, damage, ...) are transported using an interpolation technique. To finish, the 3D circular meshes are cut to have a rectangular numerical specimen closest to geometry of the experimental.

As in Langrand *et al.* [5], the experimental data are obtained thanks to an ARCAN test illustrated in Fig. 1a. This specific device enables to mix and control tensile and shear loadings on a riveted cross-shaped specimen (Fig. 1b). The experimental campaign and the ARCAN test are detailed in this paper.

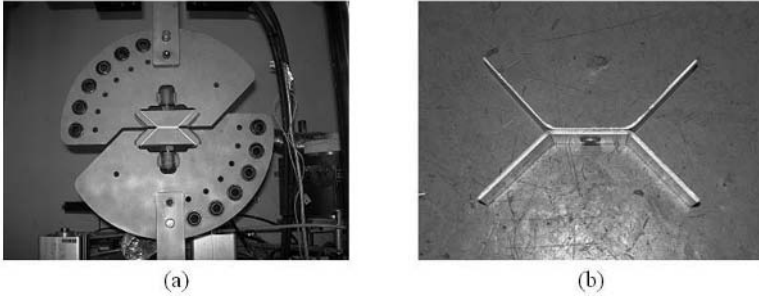


FIGURE 1. (a) ARCAN test, (b) ARCAN test specimen.

Comparisons between the experiments and numerical simulations are done on the load-displacement curves for three different angular positions ( $0^\circ$ ,  $45^\circ$ ,  $90^\circ$ ) and on the failure mode. The simulations show good agreements with experiments, which validates our developments.

In the future, such a tool can be used to improved SPR mechanical strength by optimizing the geometries of rivets or SPR tools.

## References

1. Abe, Y., Kato, T. and Mori, K., *Journal of Materials Processing Technology*, vol. **177**, 417-421, 2006.
2. Porcaro, R., Hanssen, A.G., Langseth, M. and Aalberg, A., *Journal of Materials Processing Technology*, vol. **171**, 10-20, 2006.
3. Bouchard, P.O., Fayolle, S. and Mocellin, K., In *Proceedings of the Eight International Conference on Computational Structures technology*, Las Palmas de Gran Canaria, Spain, 2006, 657-658.
4. Lemaitre, J., *A course on damage mechanics*, Springer-Verlag, 1996.
5. Langrand, B., Deletombe, E., Markiewicz, E. and Drazéć, P., *Finite Elements in Analysis and Design*, vol. **38**, 21-44, 2001.

## A COMPARATIVE STUDY ON LASER WELDED JOINTS: MECHANICAL AND METALLURGICAL ASPECTS

E. Bayraktar<sup>1</sup>, D. Kaplan<sup>2</sup> and B.S. Yilbas<sup>3</sup>

<sup>1</sup>Supmecca -Paris (EA2336), School of Mechanical and Manufacturing Engineering, France

<sup>2</sup>ARCELOR Group, Paris, France

<sup>3</sup>King Fahd University of Petroleum & Minerals, Box 1913, Dhahran 31261, S. Arabia  
bsyilbas@kfupm.edu.sa; bayraktar@supmecca.fr

In order to satisfy the requirements of productivity and quality, the welding processes of thin sheets assemblies or Tailored Welded Blanks (TWB) have given many successful advantages in manufacturing engineering. The LASER process of welding in particular makes it possible to joint sheet steels in thickness and grade identical or different in many industrial applications (car industry, pipe lines, tubes...). Additionally, Interstitial Free (IF) steels with very low C and N contents have been successfully developed in order to perform specific or complex deep drawing operations in the automotive industry. Major developments of TWB by means of LASER welding in this area have also occurred. Certain grades of IF steel are particularly suitable for deep drawing operations due to high “r” values (Lankford ratio) [1-2].

However, because of the thinness of the weld bead and important hardness gradient, determination of “toughness” (definition of a criterion of the « ductile/brittle » transition during the impact test) of the welded connection (weld bead and Heat Affected Zone) confirm very delicate in LASER welding.

From the conventional bending or tensile tests, it is difficult to direct the evolution of the welding conditions or the composition towards an optimal solution. Widely held of the brittle fracture tests were developed in order to characterize relatively thick specimens of which thickness higher than 10 mm. In order to study the mechanical and metallurgical behaviours of the welded sheets, it is quasi impossible to carry out the notched deflection tests in thin specimens because of the deformation of the specimens.

The main objective of this paper was to make a comparative study for the toughness characterization of the thin sheet assemblies, base metal or welded by LASER. For that a procedure of test specifically adapted was developed for welded thin sheets (t<4mm).

In this study, we considered different steel grades such as two grades of the FE360BFN steel (t = 4mm) and a grade of the Interstitial Free Steel (IF-Ti, t = 0.8mm), HR 60 (t=2.5mm) welded by LASER (Table 1).

Table 1. Tensile properties of the steel grades

Type	LD			TD		
	$\sigma_y$ (MPa)	UTS (MPa)	A (%)	$\sigma_y$ (MPa)	UTS (MPa)	A (%)
FE360BFN (4mm)	282	412	37			
IF-Ti (0.8mm)	175	339	41	186	346	41
FE360BFN (10mm)	279	417	33			
HR60 (2.5mm)	558	634	18	555	630	16

Welding power energy varied from 2 to 5.2 KW with the welding speeds going from 2 to 7 m/min. The morphology of the welded zone made it possible to evaluate a value of the thermal yielding-efficiency of LASER welding process going from 5% to 15% (Figure 1). Structural examination allowed to estimate the speed of solidification about  $10^5$  (C/s). The temperature of ductile-brittle transition from the base metal and LASER molten metal were measured by impact tensile test (ITT) developed in IRSID.

The test showed that an increase the speed of welding, or a reduction of the specimen thickness, lead to a fall in the temperature of transition (Figure 2). In conclusion, the development of these experimental results (mechanical and metallurgical) opens the way of the detail studies to evaluate the influence of the welding conditions or the chemical compositions on the properties of the welded joints LASER.

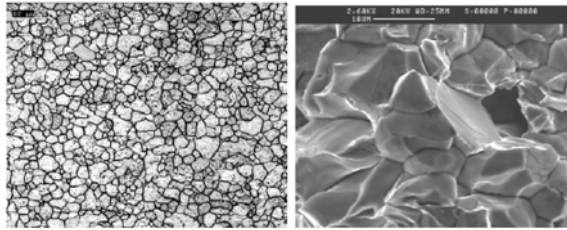


FIGURE 1. Microstructure of IF-Ti, right and its fracture surface (intergranular) after ITT test, left

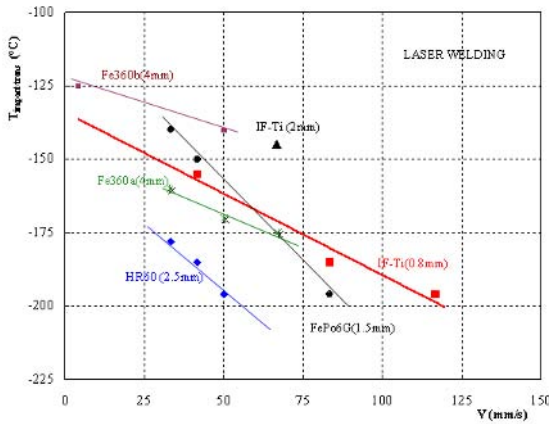


FIGURE 2. Effect of welding speed on the Impact ductile/brittle transition values

**References**

1. Bayraktar E., Kaplan D., Buirette C. and Grumbach M., *J. of Mater. Proc. Technology*, vol. **145**, I, 27-39, 2004
2. Zeng D., Liu S., Makam V., and Zweng F., *SAE technical paper series 2002-01-0639* SAE World Congress Detroit, 2002

## CARBURIZATION BEHAVIOR OF HAYNES-214 IN ETHANE-HYDROGEN GAS MIXTURES

I.M. Allam

King Fahd University of Petroleum & Minerals,  
Dhahran 31261, Saudi Arabia  
allam@kfupm.edu.sa

The Nickel Based alloy HAYNES 214 has been known for its excellent resistance to carburization at elevated temperatures. This was primarily attributed to the formation of an impervious surface layer of  $Al_2O_3$  which effectively blocks the carbon pick-up during exposure. The behavior of this alloy has been investigated in methane –hydrogen gas mixtures over a wide range of temperature with carbon activities ranging from 0.23 to 12.45. The results show that the formation of continuous protective  $Al_2O_3$  surface layer is limited only to exposures at extreme temperatures (1100 °C).

At lower temperatures, a fine dispersion of Lamellar  $Al_2O_3$  forms within the sub-surface zone of the exposed alloy. The morphology of this dispersion-containing layer and the size and distribution of the  $Al_2O_3$  particle is strongly dependent on the exposure temperature and also on the duration of exposure.

The concentration of Aluminum in the alloy, and the oxygen partial pressure in the exposure environment play important roles in determining the morphology of the dispersion and its transformation from dispersed particles at lower exposure temperatures to an effective barrier layer at elevated temperatures. At relatively low exposure temperature, the relatively low concentration of aluminum in the alloy along with the low oxygen partial pressure in the gas phase mitigate the transition from internal to external oxidation of Aluminum, while exposure at very high temperature promote this transition and allow the formation of protective  $Al_2O_3$  scale, thus enhancing its effectiveness as a barrier layer.

**Key words:** HAYNES 214, Carburization,  $Al_2O_3$

### References

1. Nickel J., Shuaib A. N. and I. Allam M., Transactions of the ASME, Journal of Tribology, vol. **19**, 1972, 47-61.
2. M. Allam, "The effect of NaCl concentration on the low temperature hot corrosion behaviour of IN-738 and MAR-M-509," Proceedings on the 35<sup>th</sup> Annual Technical Meeting, Eds. Society of Engineering Science, Washington State University, Pullman, WA, USA, 1998, 27-30.

## ISOTHERMAL CRYSTALLIZATION KINETICS OF POLY(3-HYDROXYBUTYRATE)/LAYERED DOUBLE HYDROXIDE NANOCOMPOSITES

Tzong-Ming Wu<sup>1</sup>, Sung-Fu Hsu<sup>1</sup> and Chien-Shiun Liao<sup>2</sup>

<sup>1</sup> Department of Materials Science and Engineering, National Chung Hsing University  
250 Kuo Kuang Road, Taichung, Taiwan 402

<sup>2</sup> Department of Chemical Engineering, Yuan-Ze University  
135 Yuan-Tung Road, Chung-Li, Taoyuan, Taiwan 320  
tmwu@dragon.nchu.edu.tw

The biodegradable polymers, poly(3-hydroxybutyrate) (PHB), have attracted more attention due to its renewable resources, thermoplastic and outstanding physical and mechanical properties close to those of isotactic polypropylene [1]. A new promising class of inorganic layered material, layered double hydroxides (LDH), has been considered as emerging host-guest materials [2]. PHB/LDH nanocomposites were prepared by mixing PHB and PEOPA-modified LDH (PMLDH) in chloroform solution [3]. Both X-ray diffraction data and TEM micrographs of PHB/PMLDH nanocomposites indicate that the PEOPA-modified LDHs are randomly dispersed and exfoliated into the PHB matrix. In this study, the effect of PMLDH on the isothermal crystallization behavior of PHB was investigated using a differential scanning calorimeter and polarized optical microscopy. Mechanical properties of the fabricated nanocomposites measured by dynamic mechanical analysis (DMA) show significant improvements in the storage modulus when compared to that of neat PHB.

In isothermal crystallization kinetics, the values of activation energy  $\Delta E_a$ , equilibrium melting temperature  $T_m^0$  and surface free energy  $\sigma\sigma_c$  for PHB and PHB/PMLDH nanocomposites are summarized in TABLE 1. The results of PHB/PMLDH nanocomposites show that the addition of 2 wt % PMLDH into PHB induced more heterogeneous nucleation in the crystallization significantly increased the crystallization rate and reduced their activation energy. By adding more PMLDH into the PHB probably causes more steric hindrance of the diffusion of PHB, reducing the transportation ability of polymer chains during crystallization, thus increasing the activation energy. The value of  $T_m^0$  for PHB/PMLDH nanocomposites decreased with increasing PMLDH content, and this result suggested that the crystalline structures of PHB/PMLDH nanocomposites was less perfect than that of the PHB. It is probably due to the presence of more heterogeneous nucleation induced by PMLDH and more restriction of PHB polymer chains to pack between layered double hydroxides, leading to less perfect crystal that caused the  $T_m^0$  shifted to lower temperatures. The analysis of kinetic data using a modified Lauritzen-Hoffman equation indicates that PHB has the highest values of product of the lateral and folding surface free energy  $\sigma\sigma_c$ . These results suggest that the incorporation of PMLDH into PHB probably induces heterogeneous nucleation of PHB crystallization and then decreases the surface energy barrier for PHB crystallization.

TABLE 1. Values of  $E_a$ ,  $T_m^0$  and  $\sigma\sigma_e$  for PHB and PHB/PMLDH nanocomposites.

	PHB	2 wt % PHB/ PMLDH	5 wt % PHB/ PMLDH
$\Delta E_a$ (kJ/mol)	-165.6	-183.1	-167.4
$T_m^0$ (°C)	190.9	190.1	188.4
$\sigma\sigma_e$ (erg <sup>2</sup> cm <sup>-4</sup> )	1190.4	1069.8	906.7
$\sigma_e$ (erg cm <sup>-2</sup> )	41.6	37.4	31.7

The results of dynamic storage modulus  $G'$  of neat PHB matrix and PHB/PMLDH nanocomposites over a temperature range of -50 to 100 °C are listed in TABLE 2. These results indicate the reinforcement effects of PHB/PMLDH nanocomposite are predominated by the presence of PMLDH and better interaction between the PEOPA-modified LDH and PHB. But the addition of more PMLDH into PHB, the PHB/PMLDH nanocomposites containing more organic PEOPA molecules with low mechanical properties may reduce the storage modulus of nanocomposites.

TABLE 2. Dynamic mechanical properties.

	$G'$ (MPa)	
	- 50	25
PHB	1600	700
2 wt % PHB/PMLDH	3000	1450
5 wt % PHB/PMLDH	2020	890

## Reference

1. Chen, C.; Fei, B.; Peng, S.; Zhuang, Y.; Dong, L.; Feng, Z. *Europ. Polym. J.*, vol. **38**, 1663-1670, 2002.
2. Rives, V.; Ulibarri, M. A. *Coord. Chem. Rev.*, vol. **181**, 61-120, 1999.
3. Liao, C. S.; Ye, W. B. *J. Polym. Res.*, vol. **10**, 241-246, 2003.

## THERMAL PROPERTIES OF SILK/POLY(LACTIC ACID) BIO-COMPOSITE

Hoi-Yan Cheung and Kin-Tak Lau

Department of Mechanical Engineering, The Hong Kong Polytechnic University,  
Kowloon, Hong Kong SAR  
mmktlau@polyu.edu.hk

Due to the fast development on bio-technologies, it is now possible for doctors to use patients' cells to repair orthopedic defects. In order to support the three-dimensional tissue formation, implants made by biocompatible and bioresorbable polymers and composite materials, for providing temporary support of damaged body and cell structures have been developed. The major concern in developing implants for different surgical and orthopedic operations is the selection of suitable biomaterials. Potential materials that have been proven with experimental data on their validity for biomedical applications are metal, ceramics, polymers and the combinations of these materials (composites). For metallic materials and ceramics, they have contributed to lists of medical applications, particularly in orthopedic tissue replacements. However, there are three major limitations, they are (i) not biodegradable except biodegradable bio-ceramics, (ii) poor processability, and (iii) necessity of second surgical operation induces extra pain for the patients. Therefore, biocompatible and biodegradable polymers have shown a tremendous promise in providing more viable alternatives for tissue engineering applications.

Basically, there are four types of polymeric materials used for clinical applications; they are (i) natural polymers, (ii) synthetic polymers, (iii) hydrogels and (iv) composites. Many natural polymers found in living organisms of known biocompatibility can be used to replace or regenerate native tissue structures and allows positive cell interactions with surrounding tissues. Conversely, synthetic polymers are formed through controllable chemical processes to achieve desirable material and chemical properties for a wide range of bio-medical applications. Hydrogels are primarily composed of fluid that swells the polymer network to form a biphasic construct. Although the hydrogels can be synthesized, they are always formed naturally. Composite materials are attractive as they combine material properties in ways not found in nature. Such materials often result in lightweight structures having tailored properties for specific applications. Broadly defined, bio-composites are composite materials made from natural/bio-fiber and non-biodegradable polymers like PE and epoxies or biopolymers like PLA and PGA [1].

One of the notable synthetic bio-polymers, poly(lactic acid) (PLA), which is an alpha polyester used widely in medical applications and it has been approved by FDA for implantation in human body. PLA is a highly versatile biopolymer derived from renewable resources like starch or sugar-based materials such as corns [2]. Most work in literatures on fully resorbable bio-composites has done with the use of PLA. The reason is that PLAs possess two major characteristics that make them an attractive bioabsorbable material: (i) they can be degraded inside the body in a controllable rate, and (ii) if crystallization of PLA is prevented, their degradation products are nontoxic, biocompatible, and can be easily metabolized [3]. Bio-composites from natural/bio-fiber and PLA have useful properties for environmental and biomedical applications. For reinforcements of bio-composites, spider and silkworm silks, are animal-based natural/bio-fibers that have been well recognized as high strength animal silks that can be resorbed by human body. Combining these silks with biodegradable polymers can produce a moderate strength and durable biocompatible and bio-resorbable polymer-based composite for potential bio-medical and orthopedic applications [4].



This study will be mainly focused on the biomaterials that can be used as implants in human body, therefore, thermal properties and stability of the biomaterials will be an essential consideration. In this study, natural/bio-fiber reinforced biodegradable polymeric bio-composite, silkworm silk/PLA will be formed and comparison will be made between this type of bio-composite and pure PLA-polymer according to their thermal properties in order to estimate for further development of clinical applications. For thermal property tests, differential scanning calorimetry (DSC), thermogravimetric analysis (TGA) and dynamic mechanical analysis (DMA) will be used for investigating glass transition, melting and decomposition temperatures, thermal stability, and dynamic loss modulus, dynamic loss modulus and  $\tan(\delta)$  as a function of temperature and frequency of the silk/PLA bio-composite respectively.

**Keywords:** Bio-composites, Silk fibers, Poly(lactic acid), Thermal properties

### References:

1. Mohanty A.K., Misra M., Drzal L.T., Selke S.E., Harte B.R. and Hinrichsen G.. Natural fibers, biopolymers, and biocomposites: an introduction. In Mohanty A.K., Misra M. and Drzal L.T. (ed), Natural fibers, biopolymers, and biocomposites. CRC Press, FL, 2005.
2. Sun X.S.. Plastics derived from starch and poly(lactic acids). In Wool R.P. and Sun X.S. (ed), Bio-based polymers and composites. Elsevier Academic Press, UK, 2005.
3. Berger S.A., Goldsmith W. and Lewis E.R. (ed), Introduction to bioengineering. Oxford University Press, Oxford, 1996.
4. Lee S.M., Cho D.H., Park W.H., Lee S.G., Han S.O. and Drzal L.T.. Novel silk/poly(butylenes succinate) biocomposites: the effect of short fiber content on their mechanical and thermal properties, *Comp. Sci and Tech.* 2005, vol. **65**, 647-657

## CRYSTALLIZATION KINETICS AND THERMAL BEHAVIOR OF PCL/MULTI-WALLED CARBON NANOTUBES COMPOSITES

Erh-Chiang Chen and Tzong-Ming Wu

Department of Materials Science and Engineering, National Chung Hsing University  
250 Kuo Kuang Road, Taichung 402, Taiwan  
d9266001@mail.nchu.edu.tw

In this work, Poly(-caprolactone) (PCL)/multi-walled carbon nanotube (MWNT) composites were prepared via the ultrasonically mixing of PCL and non-functionalized MWNT in a tetrahydrofuran solution. The fabricated PCL/MWNT composites show MWNT is well dispersed into PCL matrix. Differential scanning calorimetry (DSC), thermogravimetry analysis (TGA), polarized optical microscopy (POM), and X-ray diffraction methods have been used to study the crystallization kinetics, thermal behavior and crystalline structure of PCL/MWNT composites.

According to our early researches [1-3], the Avrami model can be used to study the isothermal kinetics of organic/inorganic nanocomposites. Therefore, we can apply the same model for PCL/MWNT system. Several isothermal crystallization parameters of the PCL and PCL/MWNT composites can be determined from this model, such as  $t_{1/2}$ ,  $n$  and  $k$  values, which were listed in table 1.

Figure 1 shows the Arrhenius plots of  $1/n (\ln k)$  versus  $1/T_c$  for PCL and PCL/MWNT composites. In this plots, the activation energies of the PCL and PCL/MWNT composites can be obtained from the slopes of the best-fitting lines. Figure 2 shows the thermal behavior data of pure PCL and PCL/MWNT composites. From these curves, we know that the addition of small amount MWNT into PCL matrix can enhance the thermal properties as compare to pure PCL.

The isothermal kinetics DSC data shows that the activation energy ( $\Delta E$ ) of PCL drastically increased with presence of 0.25 wt% MWNTs in PCL/MWNT composites and then decreased with increasing MWNTs content. The result indicates that the addition of MWNTs into PCL were reduced the polymer chains mobility (higher  $\Delta E$ ) at a fewer MWNTs content and then induced more significantly heterogeneous nucleation at higher MWNTs content (lower  $\Delta E$ ) during crystallization processes. The detail of isothermal kinetics parameters such as the crystallization half-time ( $t_{1/2}$ ), Avrami exponent nucleation constant ( $n$ ), crystallization rate constant ( $k$ ) and lateral and fold surface energies ( $\sigma\sigma_e$ ), as well as the activation energy were discussed. In this study, the thermal melting and degradation behaviors can be also discussed.

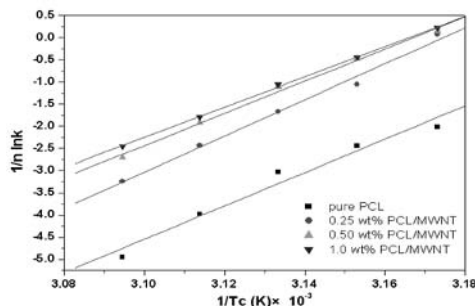


FIGURE 1. Arrhenius plots of  $1/n (\ln k)$  versus  $1/T_c$  for PCL and PCL/MWNT composites.

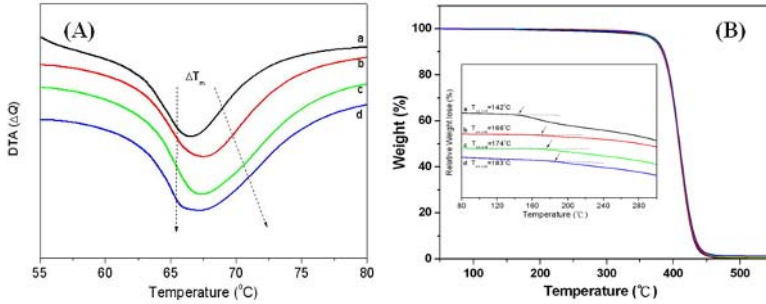


FIGURE 2. The thermal behavior of (A) DTA curves and (B) TGA curves of the a. pure PCL, b. 0.25 wt%, c. 0.5 wt% and d. 1.0wt% PCL/MWNT composites.

Table 1. Values of  $t_{1/2}$ ,  $k$ , and  $n$  at Various  $T_c$  for PCL and PCL/MWNT composites

	$T_c$ (°C)	42	44	46	48	50
PCL	$t_{1/2}$ (min)	6.51	10.13	17.97	46.74	125.23
	$n$	2.52	2.72	2.76	2.86	2.48
	$k$	6.20E-03	1.30E-03	2.30E-04	1.20E-05	4.60E-06
0.25 wt% PCL/MWNT	$t_{1/2}$ (min)	0.83	2.49	4.74	10.07	22.72
	$n$	2.37	2.52	2.67	2.55	2.49
	$k$	1.20E+00	7.00E-02	1.20E-02	2.00E-03	3.10E-04
0.5 wt% PCL/MWNT	$t_{1/2}$ (min)	0.78	1.45	2.73	6.09	13.26
	$n$	2.78	2.63	2.54	2.57	2.27
	$k$	1.50E+00	2.90E-01	5.90E-02	7.30E-03	2.10E-03
1.0 wt% PCL/MWNT	$t_{1/2}$ (min)	0.72	1.39	2.54	5.33	10.24
	$n$	2.55	2.54	2.49	2.42	2.19
	$k$	1.80E+00	3.30E-01	7.30E-02	1.30E-02	4.70E-03

## References

1. Wu, T.M., Hsu, S.F., Chien, C.F. and Wu, J.Y., *Polym. Eng. Sci.*, vol. **44**, 2288-2297, 2004
2. Wu, T.M., Lien, Y.S. and Hsu, S.F., *J. Appl. Polym. Sci.*, vol. **94**, 2196-2204, 2004
3. Wu, T.M. Chen, E.C., *J. Polym. Sci., Part B: Polym. Phys.*, vol. **44**, 598-606, 2006

## PREPARATION AND CHARACTERIZATION OF NEW BIODEGRADABLE MATERIALS: POLY(LACTIC ACID)/LAYERED DOUBLE HYDROXIDES NANOCOMPOSITES

Ming-Feng Chiang and Tzong-Ming Wu

Department of Materials Science and Engineering, National Chung Hsing University  
250 Kuo Kuang Road, Taichung 402, Taiwan  
bmw740li.tw@gmail.com

Over the past decade, significant attention has been focused on polymer/clay nanocomposites due to their superiority properties, such as excellent physical and mechanical properties compared to those of neat polymer [1]. Poly(lactic acid) (PLA), one of the ecological materials, has been widely studied because its renewable resources, biodegradable and biocompatible quality [2]. Layered double hydroxides (LDHs) containing anionic interface possess smaller gallery than montmorillonite (MMT) due to their stronger electrostatic interaction between hydroxylate layers [3]. Although a lot of studies have been made on PLA/MMT nanocomposites [4], PLA/LDHs nanocomposites have never been studied. In this article, we have synthesized LDHs with different Mg/Al molar ratio and then mixed PLA with the surface modification of LDHs by PLA-COOH.

Fig. 1 reveals the XRD results of LDHs with various Mg/Al molar ratio. These results indicate the (003) diffraction peak slight shifts to lower angle by raising the molar ratio of Mg/Al, which is probably due to the decrease of the electrostatic interaction between positive hydroxylate layers and negative interlayers anions as increasing Mg/Al molar ratio. The TEM micrograph of neat LDHs synthesized using the molar ratio of Mg/Al = 2/1 (21LDHs) is presented in Fig. 2. From this date, it reveals that a part of LDHs exist in the form of stacked layered structure. This phenomenon can be attributed to the electrostatic force occurred between positive hydroxide sheets and interlayer anion species. Fig. 3 shows the XRD data of pure 21LDHs and organically-modified LDHs by PLA-COOH with various treated times. It is obvious that diffraction peak of LDHs at  $2\theta = 11.24^\circ$  (trace a in Fig. 3), corresponding to the (003) plane of a layered structure, shifts to lower angle after modified by PLA-COOH. Moreover, the XRD profile must be noted that small diffraction peak was observed at  $2\theta = 6.42^\circ$  when 21LDHs was modified by PLA-COOH for 6 hours (trace b in Fig. 3), and the intensity of this diffraction peak gradually increase with increasing reaction times. According to Bragg's equation ( $2d\sin\theta = \lambda$ ), we found the interlayer distance of LDHs increases from 0.78 nm to 1.42nm as reaction times achieve at 48 hours (Fig. 3, trace f). This result indicates that molecular chain of PLA-COOH probably intercalated into the interlayer of LDHs, causing the increase in the interlayer distance between hydroxides. In addition, it is noteworthy that (009) diffraction peak of 21LDHs disappear dramatically when PLA-COOH react to LDH. The phenomenon is probably reasonable as original layered structure of LDHs was changed after treated with PLA-COOH.

Both X-ray diffraction (XRD) data and transition electron microscopy (TEM) image of PLA/LDH nanocomposites indicate that polymer chain intercalated into the gallery of LDH. In addition to these, the morphology and chemical properties of PLA/LDH nanocomposites were measured by field-emission scanning electron microscopy (FE-SEM) and Fourier transform infrared (FTIR). More experimental results of PLA/LDH nanocomposites will be discussed in the report.

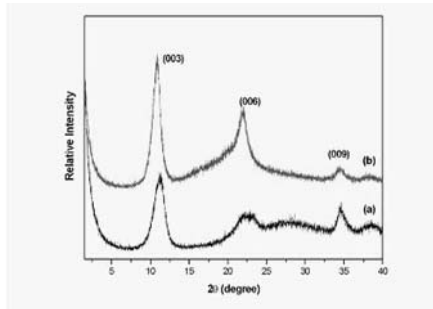


FIGURE 1. The XRD pattern of diffraction Mg/Al molar ratio (a)2:1LDHs and (b)3:1LDHs

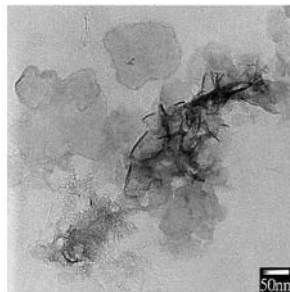


FIGURE 2. TEM micrograph of LDHs (Mg/Al ratio=2)

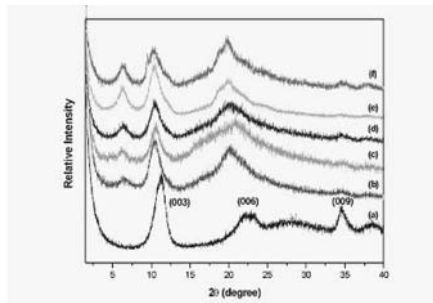


FIGURE 3. The XRD pattern of (a)2:1LDHs and P-2:1LDHs for different reaction times, (b)6h, (c)12h, (d)24h, (e)36h, (f)48h

## References

1. Giselle, S., Humberto, J., Riza, K., Sonke, S., Kathleen, A.C., *Chem. Mater.*, vol. **15**, 838-848, 2003
2. Vahik, K., Darrin, J.P., *Chem. Mater.*, vol. **15**, 4317-4324, 2003
3. Shane, O., Dermot, O., Gordon, S., *Chem. Comm.*, 1506-1507, 2002
4. Wu, T.M., Chiang, M.F., *Polym. Eng. Sci.*, vol. **45**, 1615-1621, 2005

## ISOTHERMAL CRYSTALLIZATION KINETICS OF POLY(LACTIC ACID)/ MONTMORILLONITE NANOCOMPOSITES

Mei-Jan Chu and Tzong-Ming Wu

Department of Materials Science and Engineering, National Chung Hsing University  
250 Kuo Kuang Road, Taichung 402, Taiwan  
evin0603.tw@yahoo.com.tw

Poly(lactic acid)(PLA) is a linear aliphatic thermoplastic polyester, produced from renewable resources, and is readily biodegradable through hydrolytic and enzymatic pathways [1]. The mechanical properties and degradation rates of PLA depend on their morphology and crystallinity. In recent years, a lot of studies have been focused on the crystallization behavior of PLA, especially the effects of undercooling and the addition of inorganic filler acted as nucleating agent. In this report, PLA/montmorillonite (MMT) nanocomposites were prepared by mixed PLA with commercial organically-modified MMT, such is, Cloisite 30B, through melt blending process. The isothermal crystallization kinetics and crystalline structure of PLA/MMT nanocomposites were investigated using the differential scanning calorimeter (DSC), polarized optical microscopy (POM), and X-Ray diffraction (XRD).

From the isothermal crystallization data, the values of Avrami exponent ( $n$ ) and crystallization rate ( $k$ ) can be determined using the Avrami equation and then the activation energy can be obtained through the Arrhenius plot of  $1/n \ln k$  against  $1/T$ . All data of PLA and PLA/MMT nanocomposites are listed in Table 1. From above data, it is necessary to point out that the crystallization rate of PLA and PLA/MMT nanocomposites can be divided into two categories and is strongly dependent on their crystallization temperatures. The crystallization rate of PLA is increasing as increasing  $T_c$  from 85°C to 110°C and then decreased as increasing  $T_c$  from 110°C to 125°C. Similar behaviors are also obtained for PLA/MMT composites. The activation energy of PLA/MMT nanocomposites is increased with the addition of MMT, which may be due to the steric hindrance to reduce the transportation ability of polymer chains during crystallization processes.

Figure 1 shows the DSC thermal traces of PLA and PLA/MMT nanocomposites. Multiple melting peaks are observed in both system and are also consistent with above crystallization data. Figure 2 indicates the XRD data of PLA and PLA/MMT nanocomposites. All data illustrate the PLA and PLA/MMT nanocomposites contain only one crystalline form.

### References

1. Tsuji, H., Ikada, Y., *J Appl. Polym. Sci.*, Vol. **67**, 405, 1998
2. Ke, T.N., Sun, X.Z., *J Appl. Polym. Sci.*, Vol. **89**, 1203-1210, 2003
3. Tadakazu M., Toru M., *Polymer*, Vol. **39**, 5515-5521, 1998
4. Cartier L., Okihara T., Ikada Y., Tsuji H., Puiggali J., Lotz B., *Polymer*, Vol. **41**, 8909-8919, 2000

Table1: Values of active energy, Ea, k and n at various isothermal crystallization temperatures (Tc)

Tc	PLA				3wt% PLA/MMT nanocomposite			
	n	k	t <sub>1/2</sub>	Ea	n	k	t <sub>1/2</sub>	Ea
85	3.25	0.00018	12.78	72.1	3.63	0.00043	7.69	90.4
90	3.07	0.00033	12.15		3.23	0.00191	6.19	
95	2.92	0.00121	8.81		3.07	0.00592	4.73	
100	2.94	0.00145	8.15		3.05	0.00859	4.23	
105	2.81	0.00267	7.20		3.04	0.01140	3.86	
110	3.28	0.00335	5.10	-239	2.96	0.00428	5.56	-194.7
115	2.98	0.00120	8.45		2.76	0.00271	7.49	
120	2.62	0.00047	16.2		2.81	0.00151	8.88	
125	2.64	0.00020	21.95		2.82	0.00063	11.9	
							9	

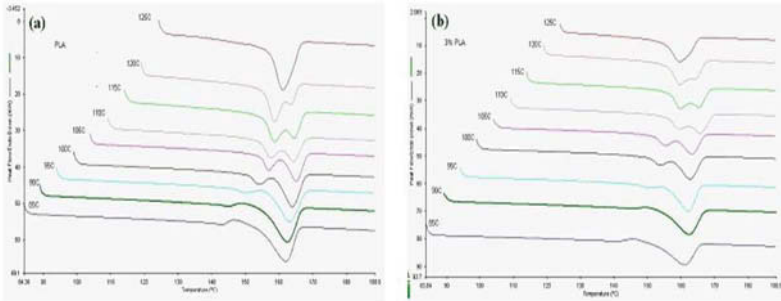


FIGURE 1. DSC trace of (a) PLA, (b) 3wt% PLA/MMT nanocomposite at various isothermal temperature crystallization.

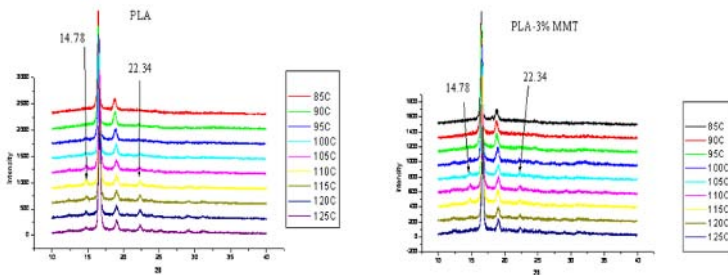


FIGURE 2. The XRD patterns of (a) neat PLA and (b)3 wt % PLA/MMT nanocomposite

## SYNTHESIS AND CHARACTERIZATION OF SOL GEL DERIVED SILICON SUBSTITUTED POROUS HYDROXYAPATITE SCAFFOLDS - EFFECT OF SILICON LEVEL ON THE *IN VITRO* BIOCOMPATIBILITY OF SI-HAP

A. Balamurugan, J.H.G. Rocha, S. Kannan, A. Rebelo, J.M.G. Ventura and J.M.F. Ferreira  
Department of Ceramics and Glass Engineering, University of Aveiro, CICECO, 3810-193  
Aveiro, Portugal  
jmf@cv.ua.pt

Ceramics based on calcium phosphates are known to be perspective materials for biomedical applications. Noticeable attention has been paid to hydroxyapatite  $\text{Ca}_{10}(\text{PO}_4)_6(\text{OH})_2$  due to its affinity to a bone mineral, Hench *et al* [1]. It was recognised recently that Si- substituted HAP is a highly promising material in sense of bioactivity improvement, Patel *et al* [2]. In the frame of distinct research activity structured around this subject, some important problems are to be solved: (a) solubility of Si in the HAP lattice; (b) rationalization of Si effect on the sintering of HAP; (c) *in vitro* biocompatibility of the Si-HAP. The present work is focused on the sol gel synthesis of Si-HAP with  $\text{Ca}_{10}(\text{Si}_x\text{PO}_4)_{6-x}(\text{OH})_{2-x}$  ( $x=0.56$ ) nominal composition and evaluation of the effect of Si on HAP ceramics. The limit of Si solubility in HAP lattice was estimated to be not higher than  $x=0.56$ . The incorporation of Si influences the initial stages of sintering. The effect of Si on sintering behaviour can be viewed in terms of its segregation to grain boundaries, the phenomenon arising from lattice instability of Si-HAP due to the charge compensation in the course of aliovalent substitution, LeGeros [3]. The *in vitro* biocompatibility of the Si substituted HAP was tested on human osteoblasts. The cells were cultured on hydroxyapatite, and Si-substituted hydroxyapatite (Si-HAP) discs. However, an increase of the silicon content from 0.8 to 1.6 wt % leads to the polymerization of the silicate species at the surface. The *in vitro* bioactivity assays showed that the formation of an apatite-like layer onto the surface of silicon-containing substrates is strongly enhanced as compared with pure silicon-free hydroxyapatite, Jarcho [4]. The samples containing monomeric silicate species showed higher *in vitro* bioactivity than that of silicon-rich sample containing polymeric silicate species, Carlisle [5]. The influence of these substrates on cell behaviour *in vitro* was assessed by measuring total protein in the cell lysate and the production of several phenotypic markers: collagen type I (COL I), alkaline phosphatase (ALP), osteocalcin (OC), and the formation of bone mineral. There was a significantly higher production of ALP on Si-HAP at day 7 following which, the addition of hydrocortisone promoted the differentiation of cells. Mineral deposits were visualized on the surface of the materials at day 21. These deposits coincided with the areas of high cell density. At day 28, a larger number of deposits were observed (Fig. 1). No difference in the pattern or timing of mineralization was seen between the materials.



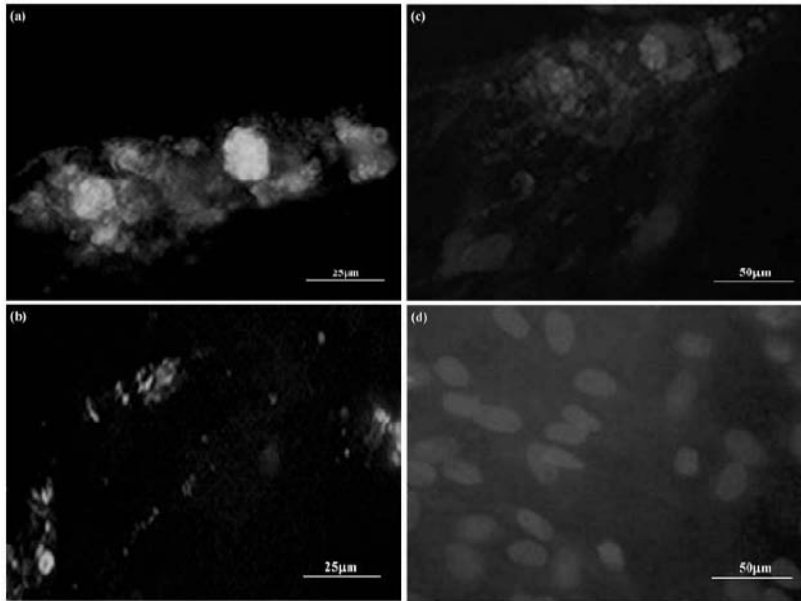


FIGURE 1. Mineral deposits labelled with tetracycline on the surface of (a) 0.8 wt % Si-HAP and (b) 1.6 wt % Si-HAP after 28 days: cell nuclei stained with DAPI. Mineral deposits on the surface of (c) 0.8 wt % Si-HAP and (d) 1.6 wt % Si-HAP.

## References

1. Hench L, Splinter R, Allen W, Greenlee T. *J Biomed Mater Res*, vol. **2**, 117-141, 1972
2. Patel N, Best S, Gibson IR, Hing K, Damien E, Bonfield W. *J Mater Sci Mater Med.*, vol. **13**, 1199-1206, 2002
3. LeGeros RZ. *Nature*, vol. **206**, 403-404, 1965
4. Jarcho M. *Clin Orthop*, vol. **157**, 259-278, 1981
5. Carlisle E. *Silicon Biochemistry*. New York: Wiley; 1986

## DESIGNING INTELLIGENT POLYMERIC SCAFFOLDS FOR TISSUE ENGINEERING: BLENDING AND CO-ELECTROSPINNING SYNTHETIC AND NATURAL POLYMERS

Peter I. Lelkes<sup>1</sup>, Mengyan Li<sup>1</sup>, Anat Perets<sup>1</sup>, Mark J. Mondrinos<sup>1</sup>, Yi Guo<sup>2</sup>, Xuesi Chen<sup>3</sup>, Alan G. MacDiarmid<sup>4</sup>, Frank K. Ko<sup>5</sup>, Christine M. Finck<sup>6</sup> and Yen Wei<sup>2</sup>

<sup>1</sup> School of Biomedical Engineering, Science, and Health Systems, Drexel University, Philadelphia, Pennsylvania, USA

<sup>2</sup> Department of Chemistry, Drexel University, Philadelphia, Pennsylvania USA

<sup>3</sup> Chinese Academy of Sciences, Changchun Institute of Applied Chemistry, Changchun, P.R. China

<sup>4</sup> Department of Chemistry, University of Pennsylvania, Philadelphia, Pennsylvania, USA

<sup>5</sup> Department of Materials Science Engineering, College of Engineering, Drexel University, Philadelphia, Pennsylvania, PA, USA

<sup>6</sup> St. Christopher's Hospital for Children, Philadelphia, Pennsylvania, PA, USA  
pil22@drexel.edu

There is a growing interest in blending natural and synthetic polymers as biomaterials for generating complex fibrous scaffolds for tissue engineering purposes. In this talk we will report on co-electrospinning binary and tertiary blends of gelatin (denatured collagen) with either a conductive polymer, polyaniline (PANi), or with a mixture of polylactic acid / polyglycolic acid, and elastin (PGE) Finally, we will demonstrate the usefulness of elastin- based fibrous scaffolds for pulmonary tissue engineering

As a first example, we evaluated the potential usefulness of co-electrospun gelatin and PANi for tissue engineering purposes (Li et al., 2006a) . Conductive polymers have been considered for diverse biomedical applications (Bidez et al., 2006). Co-electrospun PANi-gelatin fibers were characterized by scanning electron microscopy (SEM), atomic force microscopy (AFM), electrical conductivity measurement, Differential Scanning Calorimetry (DSC), and mechanical tensile testing. For blends containing less than 5 % PANi in total weight, uniform fibers were obtained with no evidence for phase segregation. Our data further indicate that with increasing the amount of PANi (from 0 to ~5 % w/w), the average fiber size was reduced from 803±121 nm to 61 ±13 nm ( $p < 0.01$ ) and the tensile modulus increased from 499±207 MPa to 1384 ±105 MPa ( $p < 0.05$ ). To test the usefulness of PANi-gelatin blends as a fibrous matrix for supporting cell growth, H9c2 rat cardiac myoblast cultures were evaluated in terms of cell proliferation and morphology. Our results indicate that all PANi-gelatin blend fibers supported H9c2 cell attachment and proliferation to a similar degree as the control tissue culture-treated plastic (TCP). Depending on the concentrations of PANi (fiber sizes), the cells initially displayed different morphologies substrates, but after 1 week all cultures reached confluence of similar densities and morphology.

As a second example for generation of novel biomaterials, we report on co-electrospinning tertiary blends of poly-(lactide-co-glycolide) (PLGA), gelatin, and elastin (PGE) which yield composite scaffolds with physicochemical properties suitable for tissue engineering applications (Li et al., 2006b). Fibrous scaffolds were co-electrospun from a blend of a synthetic biodegradable polymer (poly-(lactic-co-glycolic acid), PLGA, 10% solution) and two natural proteins, gelatin (denatured collagen, 8% solution) and -elastin (20% solution) at ratios of 3:1:2 and 2:2:2 (v/v/v). The resulting PLGA-gelatin-elastin (PGE) fibers were homogeneous in appearance with an average diameter of 380 ± 80 nm, which was considerably smaller than fibers made under identical

conditions from the starting materials (PLGA:  $780 \pm 200\text{nm}$ ; gelatin:  $447 \pm 123\text{nm}$ ; elastin:  $1060 \pm 170\text{nm}$ ). Upon hydration, PGE fibers swelled to an average fiber diameter of  $963 \pm 132\text{ nm}$ , but did not disintegrate. Importantly, PGE scaffolds were stable in an aqueous environment without crosslinking and were more elastic than those made of pure elastin fibers. In order to investigate the cytocompatibility of PGE, we cultured H9c2 rat cardiac myoblasts and rat bone marrow stromal cells (BMSCs) on fibrous PGE scaffolds. We found that myoblasts grew equally as well or slightly better on the scaffolds than on tissue-culture plastic. Microscopic evaluation confirmed that myoblasts reached confluence on the scaffold surfaces while simultaneously growing into the scaffolds. Histological characterization of the PGE constructs indicated that BMSCs penetrated into the center of scaffolds and began proliferating shortly after seeding. Our results suggest that fibrous scaffolds made of PGE and similar biomimetic blends of natural and synthetic polymers may be useful for engineering soft tissues, such as heart, lung and blood vessels.

Finally, we will describe a comparison of synthetic and natural scaffolds for application in pulmonary tissue engineering. The ability to generate functional pulmonary tissue *in vitro* would be invaluable in treating pulmonary disease states such as neonatal pulmonary hypoplasia (Mondrinos et al, 2006). An elastic scaffold that provides mechanical support and facilitates proper differentiation state will be essential to achieving this goal. Elastin is a major component of the fibrous extracellular matrix of the lung, providing the compliance required to sustain respiratory movements. Previously we have optimized the parameters for electrospinning elastin and other synthetic and natural polymers and demonstrated the efficacy of fibrous elastin scaffolds for 3-D cell culture (Li et al., 2005a). To test the ability of these matrices to support growth and tissue-specific differentiation of cultured lung cells, micro/nanofiber scaffolds (made of either PLLA, PLGA or elastin) were seeded with primary murine fetal pulmonary cells isolated by enzymatic digestion of embryonic day 17 lungs. Analysis of cell proliferation, using the Alamar Blue assay, demonstrated the superiority of these substrates compared to culture on/in Matrigel. Immunohistochemical staining for cytokeratin (epithelial marker) revealed a unique morphology of pulmonary epithelial cells, with the cells extending numerous processes to interact with elastin fibers and displaying a migratory phenotype. More importantly, for up to 7 days of *in vitro* culture these substrates supported the differentiation of alveolar type II cells, on elastin scaffolds, but not on the purely synthetic substrates, as evidenced by RT-PCR analysis for surfactant protein C gene expression. Taken together these data suggest that the incorporation of fibrous elastin in a composite scaffold may be beneficial for lung tissue engineering.

#### Acknowledgments:

This work is supported by grants-in-aid from the Nanotechnology Institute of Southeast Pennsylvania (NTI, supporting ML and MG, with PIL, as PIs), NASA (NAG 2-1436, NNJ04HC81G-01, and NCC9-130, to PIL) and NIH (1R21EB003520-01A2 to CMF and PIL). MJM was supported, in part, through a grant from NSF (Grant no. DMI-0300405). We gratefully acknowledge NSF Award (BES-0216343) for the environmental scanning electron microscope (ESEM).

#### References:

1. Bidez, P.R., Wei, Y., MacDiarmid, A.G., and Lelkes, P.I. (2006) Polyaniline, an electroactive polymer, supports adhesion and proliferation of cardiac myoblasts, *Journal of Biomaterials Science. Polymer Edition*, vol. **17**, 199-212.
2. Li, M., Mondrinos, M.J., Yang, Y., Gandhi, M.R., Ko, F.K., Yang, G., Weiss, A.S., and Lelkes, P.I. (2005a) Electrospun Protein Fibers as Matrices for Tissue Engineering, *Biomaterials*, vol. **26**, 5999-6008.
3. Li, M., Guo, Y., Wei, Y., MacDiarmid, A.G., and Lelkes, P.I. (2006a) Electrospinning polyaniline-contained gelatin nanofibers for tissue engineering applications. *Biomaterials*, vol. **27**, 2705-2715.
4. Li, M., Mondrinos, M.J., Gandhi, M.R., Ko, F.K. Chen, X., and Lelkes, Peter I. (2006b) Electrospun Blends of Natural and Synthetic Polymer as Tissue Engineering Scaffolds, *Journal of Biomedical Materials Research*, in press.
5. Mondrinos, M.J., Koutzaki, S., Jiwanmall, E., Li, M. DeChadaverian, J.P., Lelkes, P.I. and Finck, C.M. (2005) Engineering 3-D Pulmonary Tissue Constructs, *Tissue Eng.* 2006 Apr., vol. **12**(4), 717-28.

## THE EVALUATION OF GRAIN BOUNDARY DIFFUSION COEFFICIENT OF IRON IONS IN WÜSTITE

Yasushi Sasaki<sup>1</sup>, Manabu Iguch<sup>2</sup> and Mitsutaka Hino<sup>1</sup>

<sup>1</sup> Graduate School of Engineering, Tohoku University, Sendai, 9810-8579, Japan

<sup>2</sup> Graduate School of Engineering, Hokkaido University, Sapporo, 060-8628, Japan  
yaz@material.tohoku.ac.jp, gaku@eng.hokudai.ac.jp, takahino@material.tohoku.ac.jp

In this study, the effect of grain boundary diffusion on the iron nuclei formation during wüstite reduction process was investigated. Combined with the measurement of width of the iron nucleation dominant zone from grain boundaries with time and a grain boundary diffusion model, the grain boundary diffusion coefficient of  $\text{Fe}^{2+}$  ion in wüstite at 1073K has been evaluated.

Dense polycrystalline wüstite samples (5x5x2 mm) equilibrated with 50%CO-CO<sub>2</sub> gas mixture for 432ks were reduced at 1073 K using 75%CO-CO<sub>2</sub> to produce iron nuclei on the wüstite surface. The surface morphology of surface was observed with time by FE-SEM. The orientation of surface grains in the wüstite specimens was measured by electron backscattering diffraction (EBSD) technique [1]. The number of formed iron nuclei near grain boundaries was found to be significantly larger than that away from grain boundaries.

The dominant effect of the grain boundary on the iron nucleation was found on all of grains with different grain orientations. Since the supersaturation of  $\text{Fe}^{2+}$  concentration on the wüstite surface is required to produce iron nuclei, there must be some mechanisms to enhance  $\text{Fe}^{2+}$  surface concentration in the area near grain boundaries than that away from grain boundaries. The surface area near the grain boundary is convenient for grain boundary diffusion processes. Those grain boundary diffusion rate are well known to be significantly faster than the bulk diffusion rate. Thus, it is expected that the flows of  $\text{Fe}^{2+}$  ions to the surface layer near the grain boundary area are dominantly driven by the grain boundary diffusions. Namely, the prevalence of the iron nucleation process near grain boundaries can be due to the fast transport process of  $\text{Fe}^{2+}$  ions by the grain boundary diffusion.

The models of enhanced diffusion along an isolated grain boundary have been studied by many researchers [2-7]. As a first step, the approximate solution obtained by Fisher [7] is used in the present study and is

$$\frac{c}{c_0} = \exp(-\pi^{1/4} \eta \beta^{-1/2}) \operatorname{erfc}\left(\frac{1}{2} \xi\right) \quad (1)$$

where  $\eta = \frac{y}{(Dt)^{1/2}}$ ,  $\xi = \frac{x - \delta/2}{(Dt)^{1/2}}$  and a parameter  $\beta = \frac{D'}{D} \frac{\delta/2}{(Dt)^{1/2}}$ ,  $c_0$  and  $c$  denote the initial concentration and that at particular time,  $y$  is the depth from the surface,  $x$  is the distance on the surface from the boundary,  $D'$  and  $D$  are the diffusion coefficient of boundary and bulk respectively,  $t$  is the diffusion time and  $\delta$  is the grain boundary width. The grain boundary concentration contour is schematically illustrated in Fig. 1.

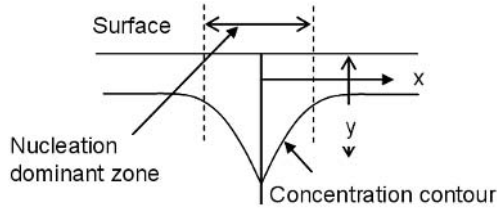


FIGURE 1. Typical shape of grain boundary concentration contour

Grain boundary diffusion coefficient is evaluated by adjusting the value of  $D'$  for fitting the horizontal area of the grain boundary concentration contours for the width of iron nuclei non-dominant area. The evaluated  $D'/D$  ratio can be more than 750. The bulk diffusion coefficient of wüstite is about  $1 \times 10^{-8} \text{ cm}^2/\text{sec}$  at 1073K [8]. Thus the grain boundary diffusion coefficient of wüstite must be more than  $7.5 \times 10^{-6} \text{ cm}^2/\text{sec}$  at 1073K.

## References

1. Wright, S. I., Adams, B. L. and Kunz, K., *Met. Trans.*, 1993, vol. **24A**, 819-831.
2. Preis, W. and Sitte, W., *J. Appl. Phys.*, vol. **97**, 93504-935014, 2005
3. Chung, Yong-Chae, Wuensch, B. J., *J. Appl. Phys.*, vol. **79**, 8323-8329, 1996.
4. Gilmer, G. H. and Farrell, H. H., *J. Appl. Phys.*, vol. **47**, 3792-3798, 1976.
5. Levine, H. S. and MacCallum, *J. Appl. Phys.*, vol. **31**, 595-599, 1960.
6. Le Claire, A. D., *Brit. J. Appl. Phys.*, vol. **14**, 351-356, 1963.
7. Fisher, J. C., *J. Appl. Phys.*, vol. **22**, 74-77, 1960.
8. Himmel, L., Mehl, R. F. and Birchenell, C. E., *Trans AIME*, vol. **197**, 827, 1953.

## WET ETCHING RATE IN THE CAVITY OF PRINTED CIRCUIT BOARD

Katsutoshi Matsumoto, Daiki Takahashi, Kazutoshi Matsumura, Takaharu Suzuki  
and Shoji Taniguchi

Tohoku University, Aoba-yama6-6-02, Sendai, Japan  
kmatsu@material.tohoku.ac.jp

Recently, integration of LSI and IC has been developed dramatically because of miniaturization of electronics. So, the wet etching of copper foil plays an important role in the ultra-fine processing technology. In order to produce finer circuits efficiently, kinetics on the etching rate of copper foil in aqueous solutions must be clarified under turbulent flow condition.

In our previous studies [1]-[3], a mechanism of wet etching of copper was studied using an agitation vessel. In this study, in addition to that, spray nozzle is used to make clear the mechanism of wet etching of copper in ferric chloride solution.

Firstly, the etching rate of plate-shaped copper is measured to confirm the rate limiting step. Etching rate is obtained by the specimens' weight loss after the experiment. The effects of flow rate and solution's temperature on the etching rate are investigated. From the results of dissolution of copper plate, it is found that the liquid mass transfer process is mainly the rate limiting step of wet etching.

Secondly, line-patterned copper specimens are etched by spray experiment to study the cavity formation. The specimen is prepared from TAB segment, which has line openings with various widths on the photoresist film. After the experiment, the cross-section of specimen is observed under microscope to measure the quantity of dissolved copper.

In the case of line-patterned copper specimens, the mean etching rate of copper during  $t=0$  to  $t$  was calculated using the following equation:

$$-r = \frac{\rho_{Cu} S}{\{(L_0 - L)/2\} M_{Cu} t}$$

where  $L_0$  is the line spacing,  $L$  is the peripheral length of the cavity,  $S$  is the cross-sectional area of cavity,  $\rho$  and  $M$  are density and atomic weight of copper.

Figure 1 shows the change in etching rate with time at various line spacing. From this figure, it is clear that etching rate decreased with time and is found to decrease with decreasing line spacing. Furthermore, a mass-transfer model of wet etching for printed circuit boards has been developed and discussed.

In conclusion, it is found that this model is almost reliable to evaluate the cavity formation for the fine pattern etching. However, the calculated cavity shape appears to be inconsistent with the observed one in the case of wide line spacing. It seems that this deviation is caused by the effect of bulk convection.

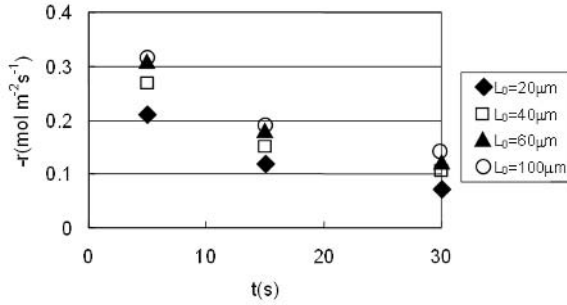


Fig.1 Change in the etching rate with time ( $q=1.67 \times 10^{-5} \text{m}^3 \text{s}^{-1}$   $\text{FeCl}_3$  solution).

## References

1. Matsumoto, K., Arai, H., Taniguchi, S. and Kikuchi, A., In *Proceeding of the 38th Annual Conference of Metallurgist*, Quebec, Canada, 1999, 183-191.
2. Matsumoto, K., Arai, H., Taniguchi, S. and Kikuchi, A., *J. Japan Inst. Electronics Packaging*, vol. 5, 35-41, 2001.
3. Matsumoto, K., Funahashi, S. and Taniguchi, S., In *Proceeding of the 36th International Symposium on Microelectronics*, Boston, USA, 2003, 345-350.

## EXPERIMENTAL DETERMINATION OF PREFORM PERMEABILITY VARIATION WITH POROSITY FOR WOVEN FIBERGLASS AND CARBON MATS

Hossein Golestanian

Mechanical Engineering Department, University of Shahrekord  
Shahrekord, Kilometer 2 of Saman Rd., Iran  
golestanian@eng.sku.ac.ir

Fiber bed permeability is an important parameter in the design of manufacturing processes in composite industries. This parameter must be determined experimentally for every liquid injection process prior to process/tool design. For example, in Resin Transfer Molding (RTM) resin flow behavior determines the integrity of the manufactured composite part. Resin Transfer Molding (RTM) is a process which involves transfer of resin into an enclosed mold containing previously positioned reinforcement preforms. This process can be employed to manufacture large and complicated composite parts. Typical examples of products that are produced with RTM include fiberglass boats, swimming pools, bathtubs, and parts in automotive and aircraft industries [1, 2]. Proper planning of the process requires determination of the injection port position, injection pressure, and injection time [1, 3]. These process parameters could be determined only when the fiber bed permeability is known.

This paper presents the results of experimental investigation on fiber bed permeability variation with porosity for woven carbon and fiberglass mats. Resin flow experiments were performed using a rectangular cavity loaded with different fiber volume fractions. RL 440 epoxy resin was used as the working fluid in the experiments. Several layers of plain-weave fiberglass and carbon fiber mats were used as reinforcements. The effects of reinforcement type and porosity on fiber bed permeability were investigated. Permeability of woven mats showed large degrees of anisotropy. That is, resin flow front followed an elliptical pattern in these mats. Thus an analysis based on anisotropic fiber preform was performed on the experimental measurements in each case. The analysis procedure is long, thus it is not presented in this abstract. In all cases preform permeability increased nonlinearly with fiber bed porosity (Figs 1 and 2). As porosity increases above a certain value, permeability increases sharply. This indicates that there is a lot of space between the weave of the fiber mats, thus resin flow becomes faster at large porosity values. Also, fiber bed permeability of fiberglass mats was several times higher than carbon fiber mats at the same preform porosity. The results of this investigation could be employed in the manufacturing process optimization in liquid composite molding.

### References

1. Golestanian, H., "Modeling of Process Induced Residual Stresses and Resin Flow Behavior in Resin Transfer Molded Composites with Woven Fiber Mats," Ph.D. thesis, University of Missouri-Columbia, MO, 1997.
2. Lim, S.T. and Lee, W. II, *J. Composites Science and Technology*, vol. **60**, 961-975, 2000.
3. Babu, B.Z. and Pillai, K.M., *In Proceedings of SAMPE Conference*, Long Beach, CA, 2002.



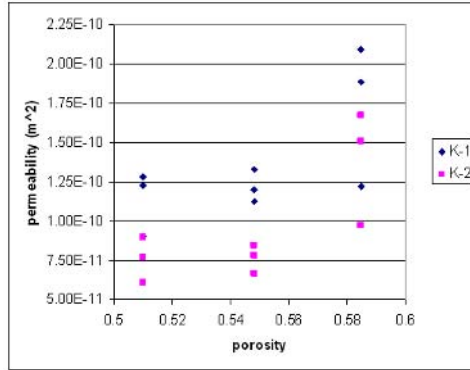


FIGURE 1. Variation of preform permeability with porosity for woven fiberglass mats.

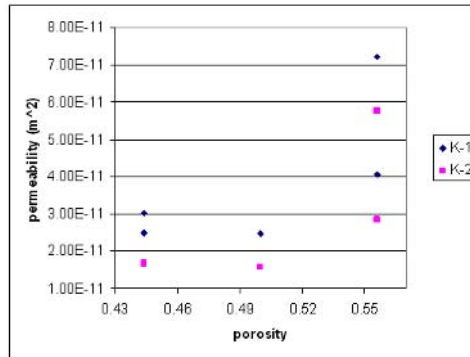


FIGURE 2. Variation of preform permeability with porosity for woven carbon mats.

## SWIRLING JET MIXING OF A BATH COVERED WITH A TOP SLAG LAYER

M. Iguchi<sup>1</sup>, Y. Sasaki<sup>2</sup>, D. Iguchi<sup>1</sup> and T. Ohmi<sup>1</sup>

<sup>1</sup> Graduate School of Engineering, Hokkaido University,  
North 13, West 8, Kita-ku, Sapporo, 060-8628 Japan

<sup>2</sup> Graduate School of Engineering, Tohoku University,  
02 Aza-aoba, Aramaki, Aoba-ku, Sendai, 980-8579, Japan  
gaku@eng.hokudai.ac.jp

Mixing of a bath by gas injection is widely used in many engineering fields. In particular, molten iron and steel baths are commonly agitated by Ar gas injection for homogenizing temperature and components and for removing non-metallic inclusions and impurities from molten steel<sup>1)</sup>. In recent years it also finds its applications to parlor wastewater and sludge treatments<sup>2)</sup>.

When gas is injected through a single-hole centric bottom nozzle under a subsonic condition, the gas disintegrates successively into many bubbles at the nozzle exit and then they rise in the bath while entraining the surrounding liquid behind their wakes. As a result, a bubbling jet is formed above the nozzle.

The bubbling jet did not always rise straight upwards, but rotated around the centerline of the bath under specific conditions. Two types of swirl motions appeared depending on the bath depth: the shallow-water wave type and deep-water wave type<sup>3)</sup>. The former appeared for an aspect ratio,  $H_L/D$ , smaller than approximately 0.3 and the latter appeared for an aspect ratio,  $H_L/D$ , between approximately 0.3 and unity. Here,  $H_L$  and  $D$  denote the bath depth and bath diameter of the reactor, respectively. These swirl motions were caused by bath surface oscillations associated with the impingement of bubbling jet onto the bath surface. The direction of the swirl motion was not uniquely decided because the vessel was not large enough to be affected by the Coriolis force.

Splashing of molten steel became frequent with  $Q_g$ . As the splashing of molten steel is dangerous, practical application of the swirl motion of a bubbling jet is not acceptable to the steelmaking industry. Accordingly, the commonly used reactors in the steelmaking industry are designed to operate for  $H_L/D < 0.3$  (converters) and  $H_L/D > 1.0$  (ladles).

The swirl motion of the deep-water wave type however has high mixing ability compared to a bubbling jet rising straight upwards. The swirl motion therefore was applied to wastewater and sludge treatments because the splashing of water is not dangerous at all.

In this study we focus on the deep-water wave type swirl motion. The period of the swirl motion,  $T_s$ , hardly depended on the gas flow rate, whereas the amplitude,  $A$ , of the swirl motion increased with an increase in the gas flow rate,  $Q_g$ . Accordingly, the bath agitation becomes strong with an increase in the gas flow rate. The period was satisfactorily approximated by the following analytical solution for the period of the rotary sloshing caused by oscillating a cylindrical bath in the vertical or horizontal direction. This is because the swirl motion and the rotary sloshing are the most stable motion of liquid contained in the cylindrical vessel.

$$T_s = 2\pi / \omega_1 \quad (1)$$

$$\omega_1 = [(2g\lambda_1/D) \cdot \tanh(2\lambda_1 H_L/D)]^{1/2} \quad (2)$$

$$\lambda_1 = 1.84 \quad (3)$$

where  $\omega_1$  is the angular frequency and  $g$  is the acceleration due to gravity.

In practical applications the starting time and damping time of swirl motion are of essential importance. The period from the start of liquid injection to the moment at which a swirl motion became steady is named the starting time. The damping time is defined as the period from the stoppage of gas injection to the moment at which the amplitude becomes less than 0.5mm. Empirical equations were proposed for the amplitude, starting time and damping time. In addition, the occurrence condition of the swirl motion was clarified.

Swirl motions similar to those mentioned above occurred when a liquid or a mixture of gas and liquid was injected into a bath through a centric bottom nozzle<sup>4)</sup>. The two types of swirl motions also appeared under these injection conditions. The occurrence mechanisms of the swirl motions of a liquid jet and a gas-liquid two-phase jet were the same as that of a bubbling jet. In this water model study the basic characteristics of the deep-water wave type swirl motions of a bubbling jet, a gas-liquid two-phase jet, and a liquid jet were experimentally investigated.

## References

1. Mori, K. and Sano, M., *Tetsu-to-Hagane*, vol. **67**, 1981, 672-695.
2. Ilegbusi, O. J., Iguchi, M. and Wahnsiedler, W., *Mathematical and Physical Modeling of Materials Processing Operations*, Chapman & Hall/CRC, Boca Raton, USA, 1999.
3. Iguchi, M., Hosohara, S., Koga, T., Yamaguchi, R. and Morita, Z., *ISIJ International*, vol. **33**, 1993, 1037-1044.
4. Yoshida, J., Iguchi, D., Shitara, M. and Iguchi, M., *ISIJ International*, vol. **43**, 2003, 1890-1896.

## DISSOLUTION BEHAVIOR OF ELEMENTS IN STEELMAKING SLAG INTO SEAWATER

Takahiro Miki and Mitsutaka Hino

Department of Metallurgy, Graduate School of Engineering, Tohoku University,  
Aoba-yama 6-6-02, Aoba-ku, Sendai 980-8579, Japan  
miki@material.tohoku.ac.jp, takahino@material.tohoku.ac.jp

Inorganic minerals such as C, O, N, Si, P, and Fe are necessary for the phytoplankton multiplication. It has been reported by Nakamura *et al.* [1] that some kinds of phytoplankton can grow quite rapidly once Fe, Si, P and N are supplied into seawater in the adequate proportion. One of the best candidates as a source of such minerals for the phytoplankton multiplication is steelmaking slag because of its cheap cost, sufficient quantity (15 million ton per year in Japan), adequate mineral concentration and its ionic nature (steelmaking slags basically consists of  $\text{Fe}_2\text{O}_3$ ,  $\text{CaO}$ ,  $\text{SiO}_2$  and  $\text{P}_2\text{O}_5$ ). On the other hand, steelmaking companies are now seeking new technologies to reduce the amount of steelmaking slag and to reuse the slag as new valuable resources [2]. If such technologies are successfully developed, we will be able to regard steelmaking slag as a new ecomaterial.

This paper will deal with our findings on the morphology of the precipitated phases in steelmaking slags during cooling period, the dissolution behavior of some elements from steelmaking slags and pure substances such as  $4\text{CaO}\cdot\text{P}_2\text{O}_5$  (8.5mass%P),  $3\text{CaO}\cdot\text{P}_2\text{O}_5$  (10.0mass%P) and  $2\text{CaO}\cdot\text{SiO}_2\text{-}3\text{CaO}\cdot\text{P}_2\text{O}_5$  (2.8mass%P) solid solution phase into artificial seawater, and the solubilities of Si, P and Fe in seawater.

Relation between phosphorus contents in steelmaking slags or pure substances and final phosphorus contents into artificial seawater after the dissolution experiment is shown in Fig. 1. It seemed that there was no clear correlation between phosphorus contents in steelmaking slags or pure substances and final phosphorus contents in artificial seawater. This phenomenon is due to the difference of stability of precipitated phase in steelmaking slag and the kind of phosphorus ion in seawater.

In order to understand the dissolution limits of minerals into seawater and to estimate the best conditions for slag addition to seawater, stability diagram of silicon, phosphorus, and iron have been determined. The content of objective element in seawater and pH were the variables, while concentration of all the other elements such as Ca, Mg, Cl and so on were fixed according to those in natural seawater[3]. Stability diagram of phosphorus in seawater at 298K is presented in Fig. 2 as a typical example. Curves in the stability diagrams are the solubility limits of each phases. Substances in square bracket are the possible stable solid phases which are considered in the steelmaking slags. Possible dissolved kinds of ions in seawater are represented in parenthesis.

Solid circle shows the concentration in natural seawater. Since the phosphorus content in seawater is higher than the solubility limit at  $2\text{CaO}\cdot\text{P}_2\text{O}_5$  or  $3\text{CaO}\cdot\text{P}_2\text{O}_5$  saturation, phosphorus can not dissolve from steelmaking slags containing these phases. However, phosphorus concentration equilibrated with  $4\text{CaO}\cdot\text{P}_2\text{O}_5$  phase is higher than that in natural seawater. Hence, phosphorus can dissolve into seawater if  $4\text{CaO}\cdot\text{P}_2\text{O}_5$  phase could be present in steelmaking slag. Phosphorus effectively dissolved from  $4\text{CaO}\cdot\text{P}_2\text{O}_5$  according to the result of dissolution experiment of phosphorus from pure substances. This is in accordance with the stability diagram of phosphorus in seawater.

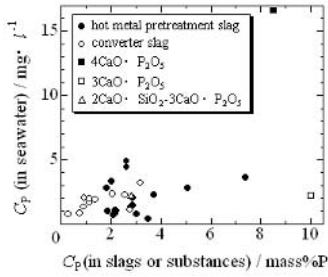


FIGURE 1. Relation between phosphorus contents in steelmaking slags or pure substances, and final phosphorus contents into artificial seawater after dissolution experiment.

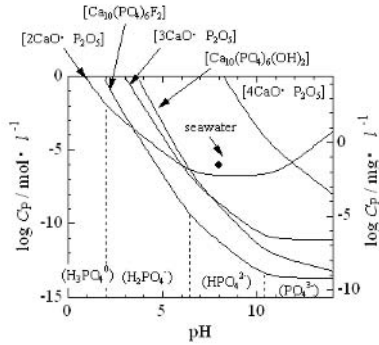


FIGURE 2. Stability diagram of P in seawater at 298K.

**References**

1. Y. Nakamura, A. Taniguchi, S. Okada and M. Tokuda: *ISIJ Intern.*, vol. **38**, 390, 1998.
2. *Final Report of the Research group on Minimization of Steelmaking Slag as an Industrial Waste* (The Iron and Steel Institute of Japan, Tokyo, Japan 1999)
3. K. K. Turekian: *Handbook of Geochemistry*, ed. by K. H. Wedepoh, Springer-Verlag, Berlin, 1969, p. 309

## EXPERIMENTAL STUDY OF THE STRESS RELIEF IN PATCHED ALUMINIUM SPECIMENS

Marie-Pierre Moutrille, Xavier Balandraud and Michel Grédiac

Laboratoire de Mécanique et Ingénierie (LaMI)

Blaise Pascal University (UBP), French Institute for Advanced Mechanics (IFMA)

Campus de Clermont-Ferrand / Les Cézeaux, BP 265

F-63175 Aubière, France

Didier Baptiste, Katell Derrien

Laboratoire d'Ingénierie des Matériaux LIM, UMR CNRS 8006

ENSAM Paris, 75013 Paris, France

moutrille@ifma.fr

Composite patches are often used to reinforce or to repair damaged structures, especially aeronautical components [1]. The mechanical properties of the bonded joint between metallic substrate and composite patch clearly influence the quality of the reinforcement. So the objective of this work is to study in detail the mechanical response of such a joint.

The response in terms of strains, displacements and stresses of an adhesive bonded joint and particularly the stress transfer between substrate and adherent has been intensively studied in the literature. For instance, many theoretical and numerical mechanical models are available [2] [3]. The load transfer from the substrate to adherent induces shear stress concentrations in the adhesive near the free edges, along the so-called “transfer length”. To the knowledge of the authors, this shear stress concentration has only seldom been experimentally studied whereas many theoretical or numerical studies on this topic are available in the literature. This lack of experimental data has recently led the present authors to use Digital Image Correlation (DIC) to measure shear strain fields in the adhesive along the transfer length [4].

The aim of the present work is to complete these first results with the experimental evidence of the normal stress decrease in the aluminium substrate since this decrease reveals the actual relief of the substrate. Temperature variations measured with an infrared camera are used for this purpose.

According to the principles of thermodynamics, a relationship exists between temperature and stress. This relation is given by heat diffusion equation under the assumption of adiabatic conditions:

$$\Delta T = - \frac{\alpha T}{\rho C_p} (\Delta \sigma) \quad (1)$$

where  $\rho$  is the density,  $\alpha$  is coefficient of thermal expansion,  $C_p$  is the heat capacity at constant pressure,  $T$  is the ambient temperature, and  $\sigma$  the sum of the principal stresses.

Specimens are made in 2024-T3 aluminium plates reinforced with carbon epoxy unidirectional composite. The adhesive is a structural epoxy resin. These specimens are subjected to a cyclic tensile loading at a sufficient level of frequency to insure adiabatic conditions. The temperature field is captured during the test by an infrared CEDIP camera which features a focal plane array of 320×240 pixels. The thermal resolution of the camera is about 20 mK.

For each pixel, the temperature variation amplitude at the loading frequency is obtained using Discret Fourier Transformation. Figure 1 shows an example of temperature amplitude map in the specimen. Within the framework of thermoelasticity, it is then possible to deduce the stress relief due to patch reinforcement.

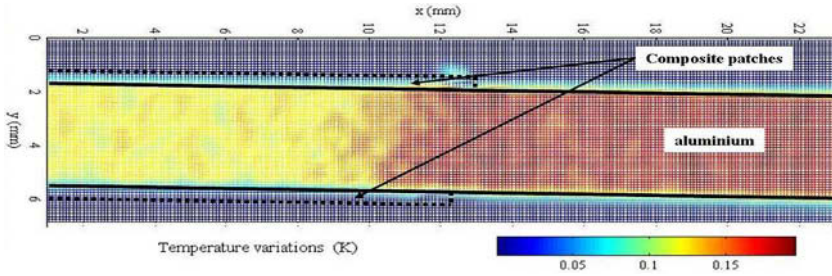


FIGURE 1. Field of temperature variation in the aluminum

The testing device and the experimental results will be presented in the paper, with a special emphasis on the comparison between the shear strain distribution given by various theoretical models and the present temperature fields which are connected to the stress relief in the substrate. The present results will also be compared to the shear strain field distribution in the glue measured in Ref. [4].

## References

1. Baker, A.A., "Bonded composite repair of fatigue-cracked primary aircraft structure", *Composite structure*, vol. **47**, 431-443, 1999
2. Tsai M.Y., Morton J., An evaluation of analytical and numerical solutions to the single-lap joint, *International Journal of Solids and Structures*, vol. **31**, 2537-2563, 1994.
3. Tsai M.Y., Oplinger D. W., Morton J., Improved theoretical solutions for adhesive lap joints, *International Journal of Solids and Structures*, vol. **35** (12), 1163-1185, 1998
4. Mountrille M-P., Derrien K., Baptiste D., Grédiac M., Balandraud X., Through thickness strain field measurement in an adhesive joint between composite and aluminium, *12<sup>th</sup> European Conference on Composite Materials*, Biarritz, France, 2006

## STRESS SEPARATION USING THERMOELASTIC DATA

Eann A. Patterson and Robert E. Rowlands  
Department of Mechanical Engineering  
Michigan State University  
East Lansing, Michigan  
Department of Mechanical Engineering  
University of Wisconsin, Madison, Wisconsin, USA  
eann@egr.msu.edu, rowlands@engr.wisc.edu

Stress analysis of engineering artifacts and structures is a routine and essential component of the design process that is often performed using computation tools. Such tools require verification using experimental data and for complex structures the stress analysis must be validated via experiment. In addition to its applicability for assessing the reliability of other solutions, thermoplastic stress analysis (TSA) can be used to analyze cases for which other methods are difficult not feasible. The technique is based on the small temperature changes that occur when a material is subject to a time-varying strain. In thermoelastic stress analysis, it is common practice to employ cyclic loading and to measure the resultant temperature changes using an infrared sensor or camera. For an isotropic material under plane stress, the relationship between the principal stresses,  $\sigma_p$  and  $\sigma_q$ , and the signal generated by the sensor,  $S^*$  can be simplified to

$$S^* = K (\Delta\sigma_p + \Delta\sigma_q) \quad (1)$$

where  $K$  is the thermoelastic coefficient. Equation (1) suggests neither a state of pure shear stress nor static stresses produces any thermoelastic response for an isotropic material. Interpretation of thermoelastic stress analysis signals can therefore require some insight based on the loading and geometry of the component being analyzed. For zero mean stresses, Eq. (1) provides isopachic information and therefore locates the center of Mohr's circle. If there is non-zero proportional cyclic loading about some mean stress, TSA provides only the change in isopachic stress. Under orthotropy,  $S^*$  depends on a linear combination of the changes in normal stresses in the directions of material symmetry. Thermoelastic stress analysis methods have been developed to smooth measured temperature data, formulate approaches for three-dimensional components and to obtain individual components of stress (or strain) in isotropic and orthotropic composite materials. This paper reviews these methods, provides an update on progress and highlights the areas where further research is needed.

There are two fundamental approaches that can be taken to separating or deconvoluting the stress or strain data from thermoelastic stress analysis: employing theory of elasticity via compatibility and, or equilibrium; and by integration in a hybrid experimental approach, most commonly using photoelasticity. Recognizing many of these approaches benefit from the use of a process to smooth the data as a precursor, some attention will be paid to this process. Separated stresses can also be obtained at single points using various types of strain gauges.

The use of equilibrium or compatibility conditions usually involves the use of a differencing technique seeded from a traction free boundary and, or the use of sophisticated functions to describe the stress distribution away from the boundary. Progress in digital technology and inexpensive computational power has allowed increasingly sophisticated techniques to be developed in order to address the underlying issue associated with the propagation of errors in these iterative techniques. These are reviewed and compared in the paper.



Hybrid methods involve the integration of two or more techniques in order to yield more or better quality information than is available from the sole use of a technique. Hybridizing experimental and computational techniques as well multiple experimental techniques has been utilized to obtain the individual components of strain (or stress) from thermoelastic data.. Perhaps the simplest approach is integrating thermoelasticity, which provides the sum of the principal stresses, with photoelasticity from which the direction and difference of the principal stresses is readily obtained. The addition and subtraction of the isopachic fringe data from thermoelasticity and the isochromatic fringe data from photoelasticity produces the maximum and minimum principal stress with suitable pre-processing, whilst the isoclinic fringe data from photoelasticity gives their orientation. This operation can be performed following separate experiments employing the two techniques independently. However more recently, the realization that photoelastic coatings can act as strain witnesses in both thermoelasticity and photoelasticity has enabled simultaneous application of the two techniques with at least one specialist instrument designed for this purpose.

Finally, the authors speculate on the future of the subject and the directions open to future research.

## EVIDENCE OF VISCOELASTIC AND ELASTO-PLASTIC DISSIPATION IN METALS BY MEASUREMENTS OF THE THERMAL ENERGY RELEASE IN CYCLIC TENSILE TESTS

F. Maquin and F. Pierron

LMPF, ENSAM, Rue St Dominique, BP 508, 51000 Châlons en Champagne, France  
 francois.maquin@chalons.ensam.fr, fabrice.pierron@chalons.ensam.fr

The use of temperature as a marker of material damage is not a new idea [1,2]. More recently, the availability of high performance infrared cameras has given a new impulse to this topic. For instance, a number of authors have claimed to be able to determine the fatigue limit of metals by using temperature measurements [3-5]. However, this method does not rely on firm physical grounds and the results are sometimes difficult to interpret. The idea of this work is to explore the heat released during the very first cycles of a cyclic in-plane loading test of some metallic materials. To do so, a very fine experimental procedure has been devised. It is based on the measurement of temperature fields at the surface of a plane specimen. From this information, a data processing technique has been set up in order to calculate the heat sources using the heat diffusion equation, as proposed by Chrysochoos and his team in a series of studies [5,7, for instance]. The experimental set-up is shown on Fig. 1.

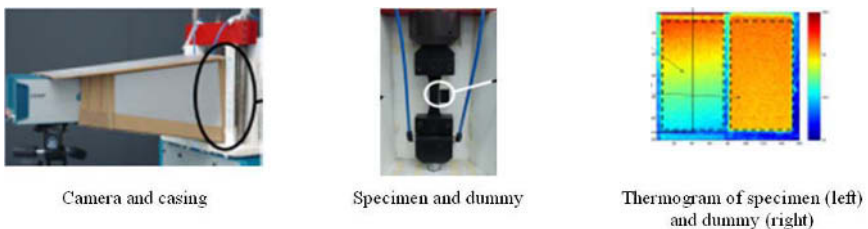


FIGURE 1. Experimental set-up

Several series of tests have been performed on a low carbon steel material. The tensile stress strain curve of this material is given in Fig. 2. The cyclic tests consisted in 30 to 60 cycles at 15 Hz with stress ratios  $R$  of 0.1 and -1. For each test, the total energy released during the test was calculated and reported. Fig. 3 shows the energy dissipated in the different tests for  $R=0.1$ . It can be seen that below 60 MPa, the heat generated is below the detection threshold. Then, between 60 and 110 MPa, significant amounts of heat are dissipated which levels vary linearly with the stress level. Then, above 110 MPa, a new change of dissipation regime is detected with much higher levels of heat. It is interesting to note that 110 MPa is also the onset of the non linearity of the stress strain curve (Fig. 2). It was thought that 110 MPa was the limit between viscoelastic internal friction effects and microplasticity effects. To support this assumption, Fig. 4 shows the heat dissipated for the specimens tested at  $R=-1$ . It can be seen that the heat is much larger for a given stress level (high stress levels could not be reached because of specimen buckling). But if the energy is plotted against strain rate (Fig. 5), then the points coincide up to 110 MPa at  $R=0.1$ . Even more interesting is the fact that these points can be fitted by a quadratic curve, confirming the fact

that these effects are viscoelastic. These results are highly promising to explore how the activation of these mechanisms can be correlated to fatigue performance.

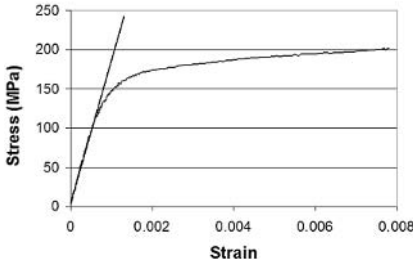


FIGURE 2. Stress-strain curve

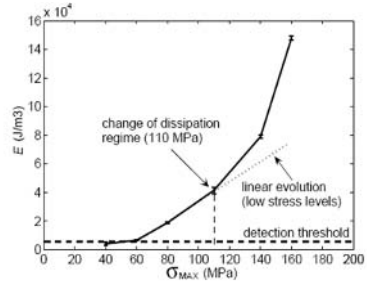


FIGURE 3. Heat dissipated, R=0.1

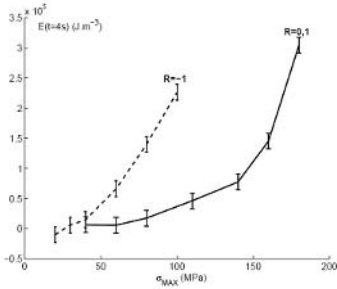


FIGURE 4. Stress-strain curve

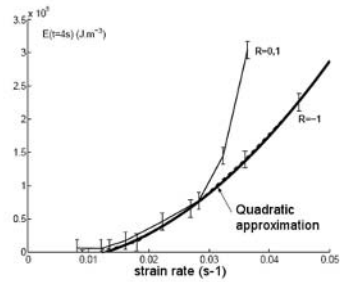


FIGURE 5. Stress-strain curve

**References**

1. Moore, H.F. and Kommers, J.B., *Chem. and Met. Eng.*, vol. **25**, no. 25, 1141-1144, 1921.
2. Harry, R., Joubert, F. and Gooma, A., *J. of Eng. Mat. and Tech. (ASME)*, vol. **103**, no. 1, 71-76, 1981.
3. Luong, M.P., *Mechanics of Materials*, vol. **28**, 155-163, 1998.
4. La Rosa, G. and Risitano, A., *Int. J. of Fatigue*, vol. **22**, 65-73, 2000.
5. Boulanger, T., Chrysochoos, A., Mabru, C. and Galtier A., *Int. J. of Fatigue*, vol. **26**, 221-229, 2004.
6. Curà, F., Curti, G. and Essana, R., *Int. J. of Fatigue*, vol. **27**, 453-459, 2005.
7. Louche, H. and Chrysochoos, A., *Mat. Sci. and Eng. A*, vol. **307**, no. 1-2, 15-22, 2001.

## THERMOELASTIC INVESTIGATION OF CRACK PATHS

R.A. Tomlinson<sup>1</sup>, J.R. Yates<sup>2</sup> and M. Zanganeh<sup>3</sup>

Department of Mechanical Engineering, The University of Sheffield, United Kingdom

<sup>1</sup>r.a.tomlinson@sheffield.ac.uk, <sup>2</sup>j.yates@sheffield.ac.uk, <sup>3</sup>m.zanganeh@sheffield.ac.uk

Traditionally fracture mechanics is mostly concerned with the opening mode of crack growth. Stability and crack path problems are relatively well understood in this case and it is expected that a crack grows in its own plane. However, cracks may exist in different orientations and moreover more than one crack may be found in a structure. The growth of these cracks even under uniaxial tensile loading may not be so easily predicted. The direction of crack initiation under different loading conditions, the path that a crack extends after initiation, directional stability even under pure mode I loading and interaction of cracks with each other, are problems that are not still fully understood, despite the extensive amount of research undertaken in these areas. Having greater knowledge of these problems will be helpful in crack arrest problems, safety issues and many other problems that exist in industrial applications.

In this work, the interaction of cracks and corresponding paths are investigated experimentally and numerically in five sets of double edge cracked specimens with different vertical offsets. Due to the great potential of the thermoelastic stress analysis (TSA) technique in fatigue and fracture applications, i.e. the non contacting feature, ability to yield full field data and working under cyclic load, this method is used as the experimental technique. The range of the mixed mode stress intensity factor and the moving crack tip position are determined from TSA signals using the genetic algorithm and the downhill simplex method embedded in the FATCAT software [1].

In conjunction with the experiments the finite element method, FRANC2DL package [2], is also used to find the stress intensity factors and the crack paths. The maximum tangential stress criterion, minimum strain energy density criterion and maximum energy release rate criterion are used as the crack path prediction criteria. Additionally, different methods for calculating stress intensity factors are used for one of the specimens. Because of the relatively good agreement between the FE results for that specimen, the maximum tangential stress criterion and J integral are used for determining the crack path and stress intensity factors respectively for the remaining specimens in numerical simulations.

The experimental and the FE results are qualitatively and quantitatively compared. It is observed that despite the agreement between experimental results and theoretical predictions in some cases, it can not be stated that the elastic stress field is the only controlling parameter for the fatigue crack direction. It is suggested that seeking a way to measure the plastic strain field directly would give further insight into the trajectory of fatigue cracks and further work in this area is underway.

N.B. Figures too large to be uploaded, therefore not included. Version with Figures sent to session Chair.

### References

1. Diaz, F.A., *Development of a methodology for thermoelastic investigation of the effective stress intensity factor*, PhD thesis, The University of Sheffield, UK, 2004.
2. James, M. and Swenson, D., <http://www.mne.ksu.edu/~franc2d>.

## A NEW MOTION COMPENSATION TECHNIQUE FOR INFRARED STRESS MEASUREMENT USING DIGITAL IMAGE CORRELATION

Takahide Sakagami, Naoki Yamaguchi and Shiro Kubo  
Dept. of Mechanical Engineering, Graduate School of Engineering, Osaka University,  
2-1, Yamadaoka, Suita, Osaka 565-0871 Japan  
Takashi Nishimura  
JFE Steel Corporation, 1, Kawasakidori, Mizushima, Kurashiki 712-8511 Japan  
sakagami@mech.eng.osaka-u.ac.jp

A new technique was developed for motion compensation in thermoelastic stress measurement by the infrared thermography. Two different techniques for motion compensation are proposed in this study. One technique uses only infrared images, and the other technique uses visible images for motion analysis as well as infrared images for stress analysis. The feasibility of the proposed motion compensation techniques was demonstrated by experimental studies.

### Motion Compensation Techniques in Infrared Stress Measurement

Displacement sometimes causes an experimental error in infrared stress measurement, when a large deformation or a steep stress change is observed in the field of view (FOV). Thus motion compensation techniques, such as optical techniques with moving mirrors or lens, or computational techniques by the post data processing based on the movements of characteristic points in infrared images, have been developed and have been installed to the commercially available stress analysis systems. However, it is not possible to conduct full field motion compensation. In this study, two full field motion compensation techniques are proposed based on the digital image correlation method.

In this study, two different motion compensation techniques are proposed. One technique uses only infrared images. Brindled pattern with different infrared emissivities was installed on the test sample for the motion analysis. Infrared images of the brindled pattern were taken under the same loading condition as the thermoelastic stress measurement. Displacements and deformations on the test sample were analyzed by the digital image correlation method based on the information of the movement of the brindled pattern. Automatic motion compensation was conducted in the subsequent thermoelastic stress measurement based on the results of displacement measurement. It is noteworthy that experiment can be carried out in one time if emissivity correction is accurately conducted in the thermoelastic stress measurement even for objects with the brindled emissivity pattern.

The other motion compensation technique uses both visible images and infrared images instead of using the brindled emissivity pattern. Sequential visible images are taken by a digital video camera whose FOVs and framing times are completely synchronized with those of infrared images. Full field displacement measurements are conducted in every captured frame by the digital image correlation method using visible images, then the motion compensation of the infrared images were carried out based on this displacement data.

### Experimental Results

Experimental results obtained by the proposed motion compensation technique using the brindled emissivity pattern are shown below. Configurations of the employed specimen with a circular hole and the brindled pattern on it are shown in Fig. 1. Feasibility of the full field motion compensation was investigated in the thermoelastic stress analysis as well as in the  $2f$  lock-in analysis for local plasticity identification [1]. Motion compensation results can not be shown due

to the lack of space, but it was found that accurate full field displacement data were obtained by the digital image correlations using brindled pattern. Experimental results without motion compensation obtained under elastic loading condition and under local plasticity loading condition are shown in Figs. 2 and 3, respectively. It is found that distributions of lock-in values are very noisy in all cases, and strong edge effects are found at the hole edge. Experimental results with motion compensation are shown in Figs. 4 and 5. It is found in these figures that edge effects almost disappear and low noise lock-in images are obtained. Especially correct distribution of  $2f$  lock-in values indicating local plasticity can not be obtained until using motion compensation technique.

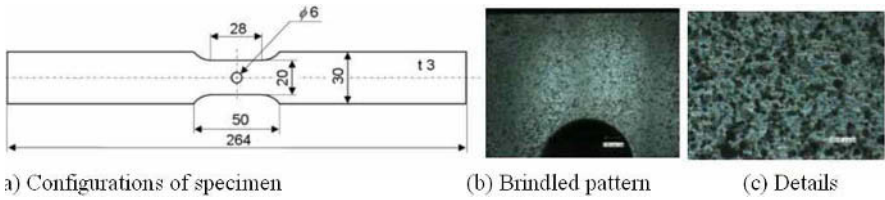


FIGURE 1. Test specimen and brindled pattern drawn by black and gray dots.

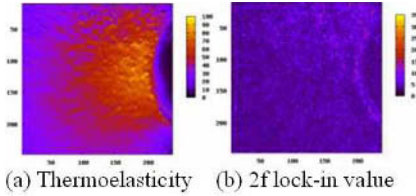


FIG. 2. Lock-in processing under elastic condition without motion compensation.

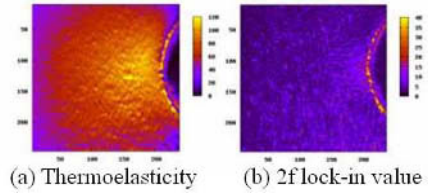


FIG. 3. Lock-in processing under local plasticity condition without motion compensation.

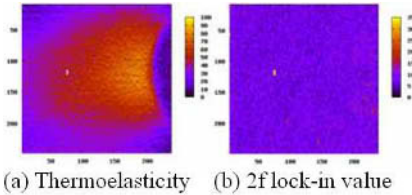


FIG. 4. Lock-in processing under elastic condition with motion compensation.

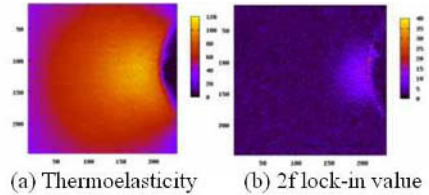


FIG. 5. Lock-in processing under local plasticity condition with motion compensation.

**References**

1. T.Sakagami, S.Kubo, et al., Identification of plastic-zone based on double frequency lock-in thermographic temperature measurement, Proc. of 11th Int. Conf. on Fracture, Turin, 2005.

## THERMOELASTIC INVESTIGATION OF DAMAGE EVOLUTION IN SMALL STAINLESS STEEL PIPEWORK

S. Quinn<sup>1,a</sup>, P.J. Tatum<sup>2,b</sup>, J.M. Dulieu-Barton<sup>1,c</sup> and J. Eaton-Evans<sup>1,d</sup>

<sup>1</sup> School of Engineering Sciences University of Southampton  
Highfield, Southampton, SO17 1BJ, United Kingdom

<sup>2</sup> Reading Berkshire, RG7 4PR, United Kingdom

<sup>a</sup>s.quinn@soton.ac.uk, <sup>b</sup>ptatum@awe.co.uk, <sup>c</sup>janice@ship.soton.ac.uk, <sup>d</sup>jeee103@soton.ac.uk

In this work thermoelastic stress analysis (TSA) is used to reveal information about the damage evolution process in small stainless steel pipework. TSA is a well-established stress analysis technique, see Dulieu-Barton and Stanley [1], based on the measurement of the small temperature change developed in a material as a result of elastic cyclic loading. The temperature change is directly proportional to the change in the sum of the principal surface stresses ( $\Delta(\sigma_1 + \sigma_2)$ ), see Stanley and Chan [2]. This relationship is usually sufficient for linear elastic, homogeneous problems, where the assumption is made that the temperature change is adiabatic.

However, TSA has also been successfully used to detect and evaluate subsurface damage and flaws by Sathon and Dulieu-Barton [3], by considering information from thermoelastic data for a range of loading frequencies. In this work damage, in the form of semi-circular notches, was introduced into a flat aluminium plate and thermoelastic data was gathered from the undamaged side of the plate. Damage increases the stress gradient in a component and can lead to non-adiabatic behaviour. This non-adiabatic behaviour can be used to reveal the sub surface stresses, by considering the phase information from the thermoelastic signal [3]. In Ref. [3] different damage severities were considered and flaws only a quarter the way through the thickness of the 5.3 mm thick plate were revealed by the thermoelastic data. This illustrates the promise of TSA to assess subsurface damage and in the current work this is tested for a real industrial problem.

The pipes under consideration were of cylindrical section and have an outside diameter of 3.175 mm and an inside diameter of 1.753 mm, i.e. a wall thickness of 0.711 mm. On assembly in service the material, 304L quarter hardened stainless steel (UNS S30400), is cold worked by bending around a former. During the product life cycle, maintenance is performed that requires the pipes to be straightened and then bent back to the original shape. To model this operation six specimens, with different deformation histories, of the stainless steel cylindrical section have been deformed to shape around a former identical to that used in the assembly process. The bent shape is illustrated in Fig. 1, along with the loading arrangement. The specimens were loaded in bending by applying cyclic compression through the loading blocks shown in Fig. 1. Only one loading block is shown, for clarity, the details are mirrored about the horizontal centreline. A loading pip was machined in the centre of two flat loading platens and the specimen was loaded in compression through the use of two 5 mm diameter ball bearings.

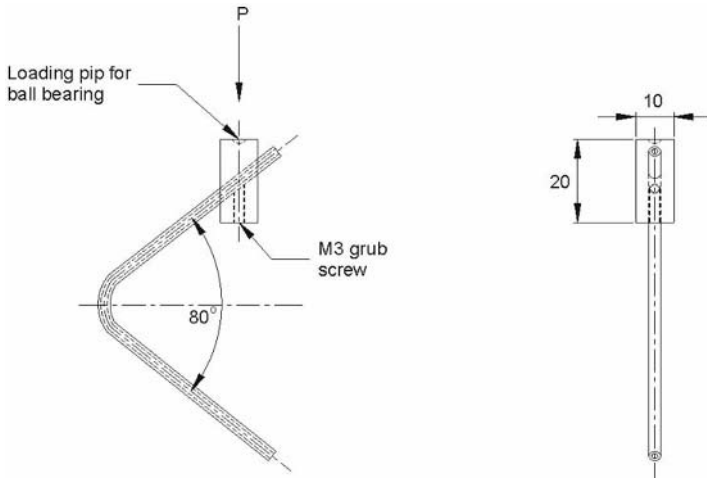


FIGURE 1. Schematic diagram of the loading arrangement for the deformed pipe tests.

Previous work, Quinn *et al.* [4], identified that failure of these pipe is instigated at the inside of the outer surface of the pipe. This is obviously not optically accessible and so the techniques developed in [3] have been adopted to reveal information about the damage evolution process at this inner surface under fatigue conditions. The most damaged pipe, subjected to 6 bending and straightening cycles, was inspected at various loading frequencies to reveal the presence of any subsurface flaws. This pipe was then subjected to a series of damaging fatigue cycles and re-inspected using TSA. By repeating this process information about the damage evolution has been revealed.

## References

1. Dulieu-Barton, J.M. and Stanley, P., *J. of Strain Analysis*, vol. **33**, 93-104, 1998.
2. Stanley, P. and Chan, W. K., *J. of Strain Analysis*, vol. **20**, 129-137, 1985.
3. Sathon, N. and Dulieu-Barton, *Key Eng. Matls.*, vols. **293 – 294**, 279-286, 2005.
4. Quinn, S., Tatum, P.J., Dulieu-Barton, J.M. and Eaton-Evans, J., In *Proceedings of SEM Annual Conference and Exposition on Experimental and Applied Mechanics*, Saint Louis, 2006, Paper Reference 288 [10pp on CD].



## COMBINING THERMOELASTIC AND STRESS FUNCTION DATA TO EVALUATE INDIVIDUAL STRESSES AROUND A NEAR-EDGE HOLE

S.-J. Lin<sup>1,a</sup>, S. Quinn<sup>2,b</sup>, D.R. Matthys<sup>3,c</sup>, I.M. Kincaid<sup>1,d</sup>, B.R. Boyce<sup>4,e</sup> and R.E. Rowlands<sup>1,f</sup>

<sup>1</sup>University of Wisconsin, Madison, WI, USA

<sup>2</sup>University of Southampton, Southampton, United Kingdom

<sup>3</sup>Marquette University, Milwaukee, WI, USA

<sup>4</sup>Stress Photonics Inc., Madison, WI, USA

<sup>a</sup>jliun@cae.wisc.edu, <sup>b</sup>s.quinn@soton.ac.uk, <sup>c</sup>don.matthys@marquette.edu, <sup>d</sup>ikincaid@wisc.edu,

<sup>e</sup>bboyce@stressphotonics.com, <sup>f</sup>rowlands@enr.wisc.edu

The individual stresses are determined on and near the edge of a hole immediately beneath but close to a concentrated edge load in an approximate half-plane. Experimental thermoelastic data is combined with Airy's stress functions to achieve this. Two approaches are utilized, both involving a series representation of the stress function. Coefficients of the respective stress functions are evaluated from measured temperature information. One of the stress functions utilizes real variables and the traction-free conditions on the hole boundary are satisfied by imposing  $\sigma_r = \tau_{r\theta} = 0$  on the edge of the hole for all values of the angle  $\theta$ , see Lin *et. al.* [1, 2]. This advantageously enables one to reduce the number of coefficients in the stress function series. The second concept, which employs a complex variable representation of the stress function and mapping techniques, satisfies the traction-free conditions on the edge of the hole by analytic continuation. Although the second approach is very effective it tends to be most convenient for evaluating stresses on, and reasonably close to, the edge of a geometric discontinuity. Moreover, since it also only provides stresses throughout a finite region and along only a portion of the entire edge of the hole, the scheme has to be repeated to determine stresses around the entire hole. On the other hand, the real variable representation of the stress function enables the individual components on and near the entire hole boundary to be evaluated in a single operation. Both methods simultaneously smooth the measured input data, satisfy the traction-free boundary conditions, and evaluate individual stresses on, and in the neighborhood of, the edge of the hole.

A review of the theory, developments and application of Thermoelastic Stress Analysis (TSA) has been provided by Dulieu-Barton and Stanley [2], and one of the topics covered is stress separation. Fig. 1 is a thermoelastic stress analysis (TSA) image of the measured temperature information. Individual stresses have been determined from this experimental data by utilizing the real variable stress function approach. Fig. 2 shows where the TSA data was selected. The TSA-determined hoop stress  $\sigma_{\theta\theta}$  on the edge of the hole is shown in Fig. 3 (a) and the TSA-determined shear stress  $\sigma_{r\theta}$  at locations away from the hole is shown in Fig. 3 (b). These experimentally determined stresses agree well with those predicted using ANSYS.

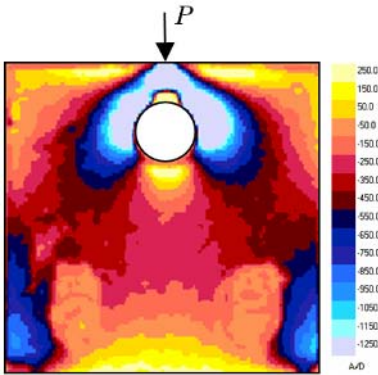


FIGURE 1. TSA image of circularly perforated edge-loaded plate.

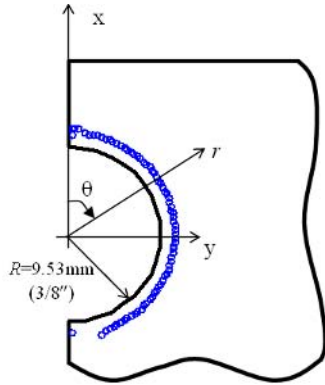
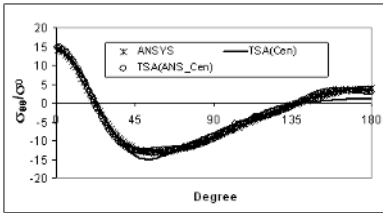
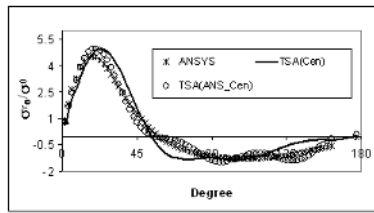


FIGURE 2. Selected data locations away from the hole.



(a)



(b)

FIGURE 3. Normalized stresses. (a) hoop stress  $\sigma_{\theta\theta}$  on the boundary of the hole (b) shear stress  $\sigma_{r\theta}$  for locations shown in Fig. 2.

**References**

1. Lin, S.-J., Matthys, D.R. and Rowlands, R.E., Accepted for *ASME IMECE Conference*, Chicago, November 2006, Paper Reference 14885.
2. Dulieu-Barton, J.M. and Stanley, P., *J. of Strain Analysis*, vol. **33**, 93-104, 1998.

## THERMOELASTIC STRESS ANALYSIS OF SANDWICH STRUCTURES WITH CORE JUNCTIONS

M. Johannes<sup>1</sup>, J. M. Dulieu-Barton<sup>2</sup>, E. Bozhevolnaya<sup>1</sup> and O.T. Thomsen<sup>1</sup>

<sup>1</sup> Department of Mechanical Engineering, Aalborg University  
Pontoppidanstræde 101, 9220 Aalborg East, Denmark

<sup>2</sup> School of Engineering Sciences, Fluid Structure Interactions Group,  
University of Southampton, United Kingdom  
maj@ime.aau.dk

A sandwich structure is a layered composite element with two relatively thin and strong outer layers, known as the face sheets, and a relatively thick and lightweight inner layer, known as the core. The sandwich assembly is formed by adhesively bonding the face sheets to the core. A sandwich structure has favourable specific strength and stiffness properties and can outperform that of structurally equivalent monolithic structures for most load cases. Sandwich constructions have thus gained an important role in lightweight construction and are being used in many applications such as ship and aircraft structures.

Difficulties arise when local effects disturb the uniform distribution of stresses in the components of the sandwich structure. These local effects occur due to discontinuities in the structure such as changes of geometry or material properties, or when localised external loads are applied. It is generally well-known that in the vicinity of sub-structures in sandwich panels, e.g. local to joints or inserts, stress concentrations are present. These may initiate local failure processes which lead to global failure of the whole sandwich structure [1].

In the case of local effects that are caused by the mismatch of the elastic properties of the adjoining materials at core junctions, there is a local bending of the face sheets and local tension/compression of the core. This is accompanied by a rise of the in-plane stresses in the sandwich faces and a variation of the shear and through-the-thickness stresses in the adjacent cores. The effect of the discontinuities on the stress distribution has been analytically and numerically modelled for the linear elastic range and the predicted face deformations have been verified experimentally by taking local strain measurements [2-5]. With respect to the failure behaviour, however, it is considered that the influence of non-linear behaviour of the constituent materials and the high stress gradients close to the junction are important factors [6-7]. There is a difficulty in establishing an appropriate criterion for assessing the role of the stresses in the initiation of failure. These issues are particularly important when non-continuous cellular polymeric materials are used as sandwich cores. In the current paper more detailed experimental data on the stress/strain state close to the core junctions are obtained, so that the local effects governing the failure behaviour of the sandwich can be classified in more detail.

The present investigation focuses on obtaining experimental data from sandwich structures with core junctions using means of thermoelastic stress analysis (TSA) [8]. The structures considered are sandwich beams with sections of different core materials representing typical sandwich sub-structures used in maritime and aeronautic applications, e.g. polymer foam cores of different densities and solid metal or plastic inserts. A diagram of a sandwich beam with core junctions and the loading conditions used for the TSA investigations is shown in Fig. 1.

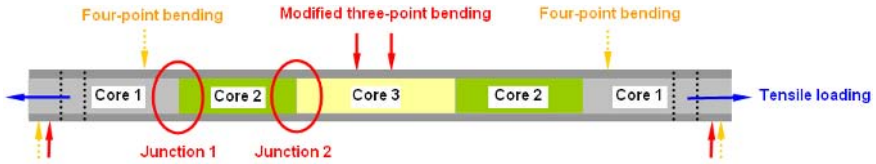


FIGURE 1. Specimen design for TSA investigations.

To obtain quantitative data from the TSA calibration measurements for all beam constituents have been carried out. The sandwich specimens are subjected to a cyclic loading, as this is essential when using the TSA method. Several combinations of cores are tested for different loading conditions and the stress field around the core junctions is investigated with the TSA-method. The feasibility and accuracy of the method for this specific application is analysed. Particular issues associated with the complex thermoelastic behaviour of the sandwich constituent materials are considered, as well as questions regarding the possible spatial or 'stress' resolution of the TSA method in this context.

## References

1. Zenkert, D., *An Introduction to Sandwich Construction*, EMAS, London, 1997.
2. Bozhevolnaya, E., Thomsen, O. T., Kildegaard, A., Skvortsov V., *Composites Part B: Engineering*, vol. **34**, 509-517, 2003.
3. Bozhevolnaya, E., Thomsen, O.T., *Composite Structures*, vol. **70**, 1-11, 2005.
4. Bozhevolnaya, E., Thomsen, O.T., *Composite Structures*, vol. **70**, 12-23, 2005.
5. Bozhevolnaya, E., Lyckegaard, A., *Composite Structures*, vol. **73**, 24-32, 2006.
6. Lyckegaard, A., Bozhevolnaya, E., Thomsen, O.T., In *Proceedings of the 16th European Conference on Fracture (ECF-16)*, 2006, 557-558.
7. Johannes, M., Bozhevolnaya, E., Thomsen, O.T., In *Proceedings of the 12th European Conference on Composite Materials (ECCM-12)*, 2006, 565-566.
8. Dulieu-Barton, J., Stanley, P., *Journal of Strain Analysis for Engineering Design*, vol. **33**, 93-104, 1998.

## PROGRESS IN THE DEVELOPMENT OF A THERMOELASTIC GAUGE FOR STRESS SEPARATION

P. Stanley<sup>1</sup>, T. S. Phan<sup>2</sup> and J.M. Dulieu-Barton<sup>2,a</sup>

<sup>1</sup> University of Manchester

School of Mechanical, Aeronautical and Civil Engineering,  
Simon Building, Oxford Road, Manchester, M13 9PL, United Kingdom

<sup>2</sup> University of Southampton,

School of Engineering Sciences  
Highfield, Southampton, SO17 1BJ, United Kingdom

<sup>a</sup>janice@ship.soton.ac.uk

The thermoelastic stress analysis (TSA) technique, described by Dulieu-Barton and Stanley in [1], uses an infrared detector for the measurement of the temperature variations on the surface of a cyclically loaded body as the basis for the quantitative determination of the surface stresses. It is a highly sensitive, non-contact technique and is proving an invaluable asset in the fields of stress analysis and related studies. However, the received signal is proportional to the sum of the principal surface stress changes and not to *one* specific stress change. The possibility of determining *individual* stress values from the stress sum data (referred to as "stress separation") by using a supplementary signal from a "coupon" of another material bonded to the stressed surface is under consideration. Recent theoretical and experimental work on this topic is described in this conference paper.

The possibility that the bonded coupon might significantly reinforce the stressed body (referred to as the "specimen" or 'substrate'), thereby modifying the surface stresses, has been explored both analytically and numerically. Following a detailed analysis, an approximate expression has been developed for the reinforcing effect of a bonded coupon (derived as the relative reduction in the coupon strain) in terms of the thickness and elastic moduli of the coupon, bond and specimen materials. In addition the effects of possible difference in the Poisson's ratios of the coupon and specimen have been studied numerically. As a result of this work it has been shown that in a wide range of possible applications the reinforcing effect can be considered unimportant.

A further practical consideration, central to the viability of the TSA technique, is that the response of both the specimen and the coupon to the cyclic temperature change should be adiabatic. The consequences of this requirement for the specimen are well understood and simply impose a lower limit on the frequency of the temperature cycle. For the coupon, however, the effect is more complicated and it is necessary to ensure that any heat conduction from the specimen into the coupon is negligible since this would significantly modify the thermoelastic signal from the coupon. This effect has been studied analytically and the necessary conditions for adiabatic behaviour have been established. The importance of the insulating effect of the adhesive layer between the coupon and the specimen has been shown.

Experimental work has included the study of a circular disc specimen under diametral compression with a bonded orthotropic coupon at the centre of the disc. The disc is tested in a succession of orientations so as to vary systematically the angle between the principal material axes of the coupon and the principal stress directions in the specimen. The TSA equipment used throughout was the Deltatherm system. The variation in the coupon signal with disc orientation provides a convenient means of assessing the suitability of the coupon material for use as a stress separation device. The work is continuing.

The overall progress to date in this important topic will be reviewed and future plans outlined.

**Key Words**

Thermoelastic stress analysis, bonded coupon gauge, stress separation

**Reference**

1. Dulieu-Barton, J.M. and Stanley, P., *J. of Strain Analysis*, vol. **33**, 93-104, 1998.

## THERMOELASTIC STRESS ANALYSIS BY MEANS OF A STANDARD THERMOCAMERA AND A 2D-FFT BASED LOCK-IN TECHNIQUE

G. Pitarresi, L. D'Acquisto, F. Lo Nigro and A.M. Siddiolo

Dipartimento di Meccanica, Università degli Studi di Palermo, Viale delle Scienze, 90128, Italy

pitarresi@dima.unipa.it, siddiolo@dima.unipa.it, dacquisto@dima.unipa.it

The thermoelastic effect in a generic orthotropic body under adiabatic and linear elastic stress conditions induces small and reversible temperature changes that can be correlated with the stress field by means of linear relationships. Infrared techniques are mainly used to measure temperature changes on the component surface [1], while adiabatic conditions are generally achieved by applying cyclic loads above a threshold frequency. The resolution resulting from implementing a Thermoelastic Stress Analysis (TSA) technique is a combination of the infrared acquiring system resolution and of the signal post-processing procedure. State of the art infrared detectors have NETD (Noise Equivalent Temperature Difference) values ranging between 0.1 and 0.01 K. In order to further enhance the resolution and to filter out noisy components affecting the small temperature changes induced by the thermoelastic effect, the most employed signal processing technique is a lock-in analysis. This results in a narrow-band filter where the components of the measured signal at frequencies different from a reference one are identified and rejected. If the reference frequency is the loading frequency, the harmonic filtered is the one carrying the amplitude and phase information of the thermoelastic signal.

One of the reasons which has slowed down the more widespread adoption of TSA based techniques is the significant cost of infrared differential thermocameras available in the market, generally comprising a high resolution thermocamera and an analogical or digital lock-in amplifier specifically designed to measure the thermoelastic signal. While thermographic systems are now available at ever cheaper prices, the purpose of this work is to set up a system able to perform TSA by using a standard average performances infrared thermocamera and a custom developed lock-in algorithm in order to achieve a resolution sufficient for investigating many key aspects of TSA.

The experimental set-up presented in this work employs a Varioscanner 3022 thermocamera by Jenoptik, acquiring the temperature field upon unidirectional GRP tensile coupons. Measured data are digitalised at 16 bit and exported in a 8 bit bitmap format in MATLAB<sup>®</sup> where they are further processed and filtered by means of a lock-in algorithm developed *ad hoc*. The thermocamera employs a single MCT detector with a resolution of 0.12 K, scanning each horizontal line (up to 360 pixels) at high frequency, while the vertical scanner builds up a complete image frame (up to 240 lines) at about 1 Hz. Each acquired row in a frame can be referred to the same line in the object (vertical scanner off) or to lines shifted vertically by the internal camera mirrors, with a maximum object field of view of 20° vertical by 30° horizontal. With the vertical scanner off, i.e. in the single-line acquiring mode, whatever the stress field in the object, the signal from each scanned point is sampled at a frequency of 240 Hz, resulting in a Nyquist frequency sufficient for sampling the signal in most applications (cyclic loading frequencies generally lower than 20Hz). The uniform stress field in the analysed unidirectional GRP tensile coupons, loaded with sinusoidal loads along the fibres direction, produces a set of horizontal thermoelastic fringes in the space domain (vertical scanner on). Similar results on steel samples have been obtained in [2], by using a higher resolution thermocamera with a similar single-detector scanning mode. In the single-line acquiring mode analogous fringe patterns can be obtained versus time, although they are collected in a two-dimensional frame for visualisation purposes. Fringe images acquired in this way are shown in Fig. 1a-b. Even if the fringe structure is barely visible in Fig. 1b, it was effectively processed by the developed lock-in procedure. The proposed algorithm is based upon

an extensive use of the 2D-FFT; custom procedures have been also developed to reduce the edge effects at the domain borders and to further enhance the capabilities of standard lock-in analyses. The GRP composite coupons have been chosen for their high thermoelastic constant (enhanced by the presence of the polyester resin) and their linear elastic behaviour (all samples tested have a marked linear behaviour, at least up to 400 MPa, with Young modules ranging between 25 GPa, for laminates manufactured by hand lay-up, and 45 GPa, for laminates consolidated with a vacuum bag).

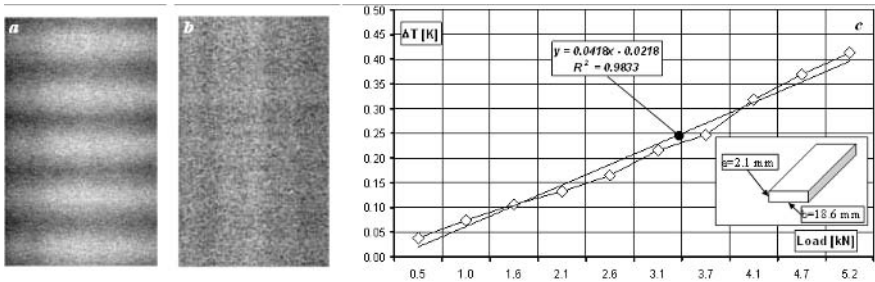


FIGURE 1. 2D representation of a single line scan. Average load 6 kN, Freq. 6 Hz, load amplitude of a) 5 kN and b) 0.5 kN; c) Measured  $\Delta T$  vs applied load amplitude.

Initial tests have proved the effectiveness of the proposed methodology. In fig. 1c results regarding measurements on the coupon whose images were partially displayed in fig. 1a-b are presented. The registered linear trend ensures about the goodness of the lock-in procedure adopted. A number of issues are at the moment under investigation with the proposed experimental set-up: analysis of the resolution limits of the lock-in procedure, analysis of the influence of hysteretic heating by monitoring the absolute temperature with thermocouples, influence of the average load and cycling frequency on the acquired filtered results, influence of motion due to large displacements in the coupon samples, analysis of stress gradients by testing coupons with central holes, analysis of GRP samples with different fibre volume fractions.

## References

1. Dulieu-Barton, J.M. and Stanley, P., *J. Strain Analysis*, vol. **33** (2), 93-104, 1998.
2. Audenino, A.L., Crupi, V. and Zanetti, E.M., *Exp Tech*, vol. **28**, 23-28, 2004.



## ENERGY ANALYSIS OF STEEL SUBJECTED TO HIGH CYCLE FATIGUE

A. Chrysochoos, B. Berthel, A. Galtier<sup>2</sup>, F. Latourte, S. Pagano and B. Wattrisse  
 Lab. of Mechanics and Civil Engineering, CC 048, P. E. Bataillon, 34095 Montpellier, France  
<sup>2</sup> Arcelor Research SA, Voie Romaine BP 30320, 57283 Maizières-lès-Metz, France  
 chryso@lmgc.univ-montp2.fr

During the high cycle fatigue of a steel specimen, the stress states remain traditionally within the mesoscopic elastic domain of the material. However, slight energy dissipation due to the irreversible evolution of the microstructure is observed during the multiplicity of cycles performed at important loading frequencies. This dissipation is then superimposed with the classical thermoelastic coupling sources due to the thermal expansion of the crystalline network.

This paper presents a method to locally estimate the different terms of the energy balance. The method involves two quantitative imaging techniques.

On the one hand, Digital Image Correlation (DIC) provides displacement fields and after derivation, fields of strain  $\varepsilon$  and strain-rate  $\dot{\varepsilon}$ . A variational method, associated with an energy functional, is used both to identify the field of elastic parameters and to determine the stress pattern  $\sigma$  [1-2]. The knowledge of stress and strain-rate fields allows then constructing a pattern of deformation energy.

On the other hand, Infrared Thermography (IRT) provides thermal images which are used to estimate separately the distributions of thermoelastic source amplitudes  $\Delta s_{\text{the}}$  and intensities of intrinsic dissipation  $\bar{d}_1$ . The image processing uses a local linear expression of the heat diffusion equation [3-4].

### Energy balance construction

The fatigue tests were carried out by imposing a series of loading blocks on thin, flat specimens. Each block consisted of  $2 \cdot 10^4$  cycles performed at constant loading frequency  $f_L$ , constant load ratio  $R_\sigma$ , and constant stress range  $\Delta\sigma$ . At the end of each loading block, the thermal equilibrium was awaited before the start of the next block. The temperature variations  $\theta = T - T_0$  remaining small ( $|\theta| < 10$  K,  $T_0 \approx 293$  K) throughout the tests, we then neglected their influence on the microstructural state (no auto-annealing) and on the strain fields. In this framework, the deformation energy rate was approximated by a purely elastic one:

$$\sigma : \dot{\varepsilon} = E^{-1} : \sigma : \dot{\sigma} + \lambda \operatorname{tr} \sigma \dot{\theta} \approx E^{-1} : \sigma : \dot{\sigma} \quad (1)$$

where  $E$  is the elastic rigidity tensor and  $\lambda$  the isotropic thermal expansion coefficient.

To estimate  $\sigma : \dot{\varepsilon}$ , we proceeded as follows. During a test, the in-plane displacement field  $u$  is measured (by DIC) on the surface of the specimen. The load applied at its boundary is known. Noting  $E$  and the rigidity and the stress tensor respectively, the couple  $(E, \sigma)$  is then one solution of the identification problem if it satisfies the local equilibrium equations, the constitutive equations and the global equilibrium. We associated to this problem the energy functional  $F$  defined by [5]:

$$F(\tau, B) = \frac{1}{2} \int_{\Omega} (\tau - B : \varepsilon(u)) : B^{-1} : (\tau - B : \varepsilon(u)) \, d\Omega \quad (2)$$

where the stress field  $\tau$  is statically admissible, and where the compliance tensor  $B$  is supposed to be symmetrical, non negative and definite. The functional  $F(\tau, B)$  is convex and positive, and null if

and only if the couple  $(\tau, B)$  satisfies the constitutive equation. Therefore the identification is performed by numerically minimizing the functional  $F(\tau, B)$ . A minimisation over the first and second variable gives the stress field solution and the field of elastic parameters, respectively.

In the same framework and under several supplementary hypotheses [3-4], the local heat equation was written in the following simplified form:

$$\rho C \left( \frac{\partial \theta}{\partial t} + \frac{\theta}{\tau_{th}} \right) - k \Delta_{x,y} \theta = d_1 + s_{the} \quad (3)$$

where  $\rho$  is the mass density,  $C$  the specific heat,  $\tau_{th}$  a time constant characterizing the heat losses perpendicular to the surface of the specimen,  $k$  the isotropic conduction coefficient,  $\Delta_{x,y} \theta$  the Laplacian term corresponding to the in-plane losses. We underline that the left-hand side of equation (3) is a differential operator applied to  $\theta$ . To estimate the heat sources, a local least-squares fitting of thermal data was chosen. The local approximation function has the following form:

$$\theta^{app}(x, y, t) = \underbrace{p_1(x, y)t + p_2(x, y)}_{\text{"instantaneous" drift}} + \underbrace{p_3(x, y) \cos(2\pi f_L t) + p_4(x, y) \sin(2\pi f_L t)}_{\text{periodic response}} \quad (4)$$

The trigonometric time functions describe the periodic part of the thermoelastic effects (with a possible phase shift) while the linear part takes into account transient effects due to heat losses, dissipative heating and possible drifts of the equilibrium temperature. The functions  $p_i(x, y)$ ,  $i=1, \dots, 4$ , are second order polynomials of the in-plane coordinates  $x$  and  $y$ . The identification of the best fitting functions allowed us, for each approximation zone, to compute the amplitudes of the thermoelastic source and the mean intensity of the dissipation per cycle.

## References

1. Latourte, F., Chrysochoos, A., Geymonat, G., Pagano, S., Wattrisse, B., *In Proceedings of the 8<sup>th</sup> Euromech Mecamat Conference*, edited by Allix, O., et al., Cachan, 2005, 155-163.
2. Latourte, F., Chrysochoos, A., Geymonat, G., Pagano, S., Wattrisse, B., *In Proceedings of the 2005 SEM Annual Conference & Exposition on Experimental and Applied Mechanics*, edited by Archie T., et al., Portland, 2005, 349-356
3. Chrysochoos, A., Louche, H., *International Journal of Engineering Sciences*, vol. **38**, 1759-1788, 2005.
4. Boulanger, T., Chrysochoos, A., Mabru, C., Galtier, A., *International Journal of Fatigue*, vol. **26**, 221-229, 2004.
5. Geymonat, G., Hild, F., Pagano, S., *C.R. Mécanique S.* vol. **330**, 403-408, 2002.

## THE EFFECT OF CRACK-TIP INTERACTIONS ON THE CURVE-FITTING OF MIXED-MODE ISOPACHICS

G. Isaac, A. Spencer, K. Worden and J. M. Dulieu-Barton<sup>1</sup>

Department of Mechanical Engineering  
University of Sheffield

Mappin Street, Sheffield S1 3JD  
School of Engineering, Ship Science  
University of Southampton  
Highfield, Southampton SO17 1BJ

<sup>1</sup> janice@ship.soton.ac.uk

Thermoelastic Stress Analysis (TSA) is a full-field technique for experimental stress analysis that has proved to be extremely effective for studying stress fields in the vicinity of crack-tips. An understanding of such fields is vital to the development of effective diagnosis and prognosis algorithms for Non-Destructive Testing (NDT) and Structural Health Monitoring (SHM). The key to crack-tip studies using TSA is the observation that the stress-sum contours (isopachics) in the vicinity of the tip take the form of a simple curve - the cardioid. This was exploited in [1] in order to estimate the Stress Intensity Factors (SIFs) for crack-tips in mode 1 and mixed-mode opening. The analysis [1] made use of the cardioid nature of the isopachics by deriving expressions for the SIFs in terms of the cardioid area and the positions of certain tangents to the curve.

Recent work by the authors has allowed the estimation of crack-tip Stress Intensity Factors (SIFs) by curve-fitting a cardioid form to measured isopachics from Thermoelastic Stress Analysis (TSA). Both Genetic Algorithms (GAs) [2] and Differential Evolution (DE) [3] proved successful for the actual parameter estimation, but some of the curve-fits indicated that the cardioid form was inappropriate for the base model.

A possible explanation for the poor curve-fit is that the cardioid form is only theoretically suitable for an *isolated* crack-tip stress field, as derived from the Westergaard equations. The effect of the other crack-tip in a central crack has been neglected from previous analyses. Further work has [4] considered a mode 1 central crack, placed in a plate, which therefore had two interacting crack-tips. Figure 1 shows the analytically derived stress sum field around both an isolated mode 1 crack and a twin crack-tip. The curves for an isolated crack-tip are shown as solid lines - these curves are true cardioids. The curves for the twin crack-tip case are shown as dashed lines. It is clear that these curves are not cardioids, although the level of distortion is quite small for the inner curves.

The object of the current paper is to determine numerically, the stress field for a mixed-mode crack system and to quantify the effect of any interactions on the curve-fitting procedure and compare with experimental data for a 30° crack.

### References

1. Dulieu-Barton, J.M., Fulton M.C. and Stanley, P. "The analysis of thermoelastic isopachic data from crack-tip stress fields", *Fatigue and Fracture of Engineering Materials and Structures*, 2000, vol. **23**, 301-313.
2. Dulieu-Barton, J.M. and Worden, K. "Genetic identification of crack-tip parameters using thermoelastic isopachics" *J. Measurement Science and Technology*, 2003, vol. **14**, 176-183.

3. Dureau-Barton, J.M. and Worden, K. "Identification of crack-tip parameters using thermoelastic isopachics and differential evolution", *Key Engineering Materials*, vol. **245-246**, 2003, 77-86.
4. Worden, K. Spencer, A.B. and Dureau-Barton, J.M., "The effect of crack-tip interactions on the curve-fitting of isopachics", *Applied Mechanics and Materials*, vol. **1-2**, 2004, 121-126.

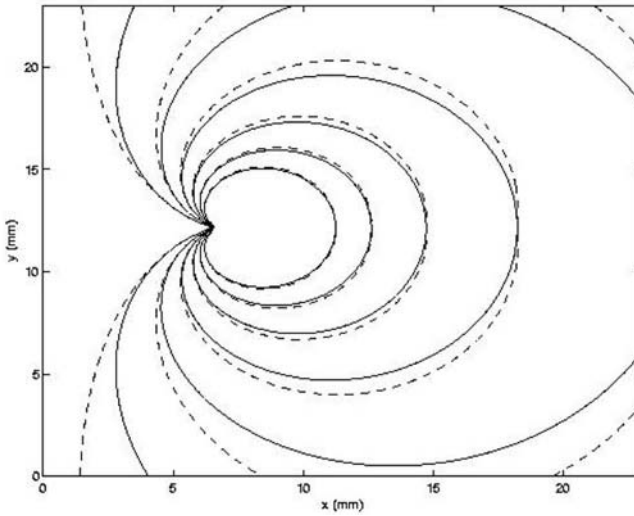


FIGURE 1. Isopachics in the neighbourhood of an isolated (solid line) and twin (dashed line) mode I crack tip

## A NOVEL EXPERIMENTAL PROCEDURE FOR STRESS SEPARATION ON COMPOSITE COMPONENTS

D. Modugno, G. Vitale, U. Galietti and C. Pappalettere  
Mechanical and Management Engineering, Politecnico di Bari  
Viale Japigia 182, Bari, Italy  
d.modugno@poliba.it

The aim of the present work is to develop a complete experimental procedure, involving both photoelastic and thermoelastic techniques, suited for industrial application. Similar works from literature [1-3] are often based on hybrid experimental-numerical techniques. These methods however have difficulties in modelling and discretize the wide variety of composite materials.

The present work shows a complete experimental procedure applied on an aeronautical component. Automated reflective photoelasticity has been used in order to get full field data of the difference of principal strains and their orientation.

Thermoelastic signal has been acquired by using a differential infrared camera, DeltaTherm 1560 by Stressphotonics. The surface investigated is covered with birefringent coating for both photoelastic and thermoelastic data acquisition so that the coating actually behaves as a witness of the strain field on the specimen, as shown in literature [4-6].

The load is applied to the component one time, acquiring simultaneously both Photo and Thermoelastic data, with no need of the typical cyclic loading. The isotropy of the coating allows to obtain a full field map of principal strains which can be easily calibrated by means of one of the techniques described in literature. This innovative procedure allows to get strain field on the component without passing through the knowledge of the constitutive equations of the material.

A matching algorithm [7] has been developed in order to uniform experimental data format and field of view, so to perfectly superimpose them. Experimental data from a composite aeronautical component are reported as example in Fig. 1.

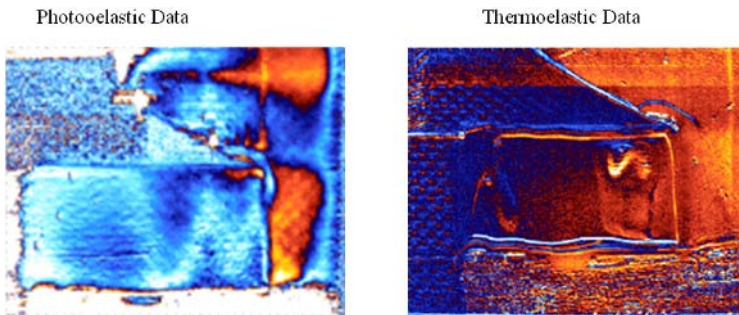


FIGURE 1. Experimental raw data on a composite component

---

**References**

1. E.A. Patterson and Z.F. Wang, Simultaneous observation of phase-stepped images for automated photoelasticity. *Journal of Strain Analysis*, vol. **33**, 1–15, 1998
2. B. Fiedler and K. Schulte, Photoelastic analysis of fibre-reinforced model composite materials. *Compos Sci Technol*, vol. **57**, 859–867, 1997
3. S. Lutze, Confocal laser scanning photoelasticity: improvement of precision for quantitative photoelastic studies on model composite materials. *Scanning*, vol. **23**, 273–278, 2001
4. Stanley, P., Chan, W.K., "Quantitative stress analysis by means of the thermoelastic effect", *Journal of Strain Analysis*, vol. **20** (3), 129-137, 1985
5. Potter, R.T., Greaves, L.J., The application of thermoelastic stress analysis technique to fibre composites, *Proceedings of the Conference on Optical and Opto-electronic Applied Science and Engineering*, SPIE, vol. **817**, 134-146, 1988.
6. Lin, S.T., Rowlands, R.E., Thermoelastic Stress Analysis of Orthotropic Materials", *Experimental Mechanics*, vol. **35**, 257-265, 1995.
7. Galietti, U., Modugno, D., Pappalettere, C., Vitale, G., Stress separation on a composite component Thermo and Photoelastic techniques, *Proceedings of Photomechanics 2006*, 2006

## COMBINED THERMOELASTIC AND THERMOGRAPHIC DATA FOR THE EVALUATION OF CRACK GROWTH IN INDUSTRIAL COMPONENTS

F. Carofiglio, U. Galietti, D. Modugno and C.Pappalettere  
Mechanical and Management Engineering, Politecnico di Bari  
Viale Japigia 182, Bari, Italy  
f.carofiglio@poliba.it

The application of infrared thermography as a non-destructive method to detect the occurrence of damage and to investigate the fatigue process of materials has become popular and has been widely investigated in literature. Thermography has clearly shown to be a powerful tool for the characterization of structural material properties such as fatigue limit. Many previous works from literature have gone into the relation between the damage in the material and the temperature arising as result of internal energy dissipation.

On the other hand, thermoelastic stress analysis has become in the last years a well established technique for the determination of the stress field in mechanical components, even with an high geometrical complexity.

The present work starts from the observation that damage in the material results both in a change in superficial temperature and in a change of the stress field. A differential infrared camera, DeltaTherm 1560 by Stressphotonics, has been used to acquire both thermographic and thermoelastic data from industrial mechanical components subjected to a fatigue cyclic load.

Infrared signal from the samples has been acquired with a time gap of few minutes, in order to have a continuous monitoring of the crack growth in the sample under investigation until the occurrence of the failure. A comparison of thermographic and thermoelastic data shows that the change in temperature field is strictly related with the change in the pattern of the stresses distribution due to the evolution of the damage in the material.

Aim of this work is to develop a method to evaluate the crack evolution in fatigue tests. Experimental data are provided from welded joints.

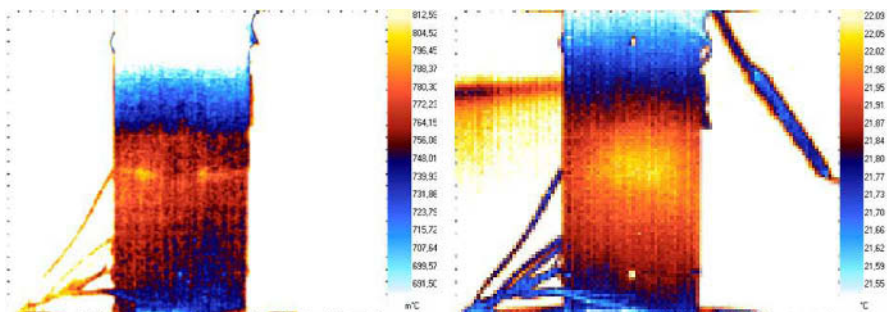


FIGURE 1. Difference between temperature at the beginning and at the end of the test (on the left). Thermographic image of a welded joint just before the occurrence of the failure (on the right).

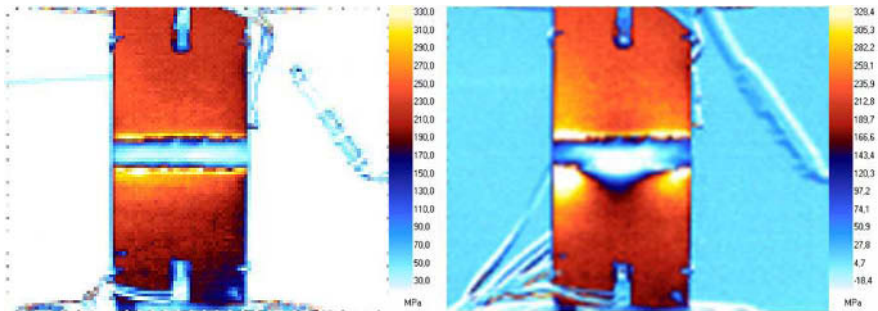


FIGURE 2. Thermoelastic image of a welded joint, (on the left) at the beginning of the test, (on the right) just before the occurrence of the failure.

## REFERENCES

1. M. P. Luong, "Fatigue limit evaluation of metals using an infrared thermographic technique", *Mechanics of Materials*, vol. **28**, 1998, pp. 155-163.
2. G. La Rosa, A. Risitano, "Thermographic methodology for rapid determination of the fatigue limit of materials and mechanical components", *International Journal of Fatigue*, vol. **22**(1), 2000, pp. 65-73.
3. J.C. Krapez, D. Pacou and G. Gardette, "Lock-in thermography and fatigue limit of metals". *Quantitative infrared thermography 5: QIRT'2000*.
4. A. Chrysochoos, H. Louche, "An infrared image processing to analyse the calorific effects accompanying strain localisation", *International Journal of Engineering Science*, pp. 1759-1788, vol. **38** (2000).
5. A.E. Morabito, "Analisi termomeccanica degli effetti termoelastici e dissipative associati al comportamento a fatica della lega di alluminio 2024 T3", PHD thesis, Università degli Studi di Lecce, 2003, in Italian.
6. Stanley, P., Chan, W.K., "Quantitative stress analysis by means of the thermoelastic effect", *Journal of Strain Analysis*, vol. **20** (3), 1985, pp. 129-137.
7. Maldague, X.P.V., "Theory and practice of infrared technology for nondestructive testing", 2001 John Wiley & Sons Inc., ISBN 0-471-18/190-0.
8. Harwood, N., Cummings, W.M., "Thermoelastic Stress Analysis", Adam Hilger IOP Publishing.



## THERMOMECHANICAL ANALYSIS OF THE YIELD BEHAVIOUR OF A SEMICRYSTALLINE POLYMER

Jean-Michel Muracciole, Bertrand Wattrisse and André Chrysochoos  
Mechanics and Civil Engineering Laboratory, Montpellier II University, France  
muraccio@lmgc.univ-montp2.fr

The cold drawing of semi crystalline polymer has been observed in the early 1930s by Carothers and Hill [1]. Ever since, various attempts were made to explain this phenomenon in terms of crystallinity modification. This behaviour, usually related to a rearrangement of the crystallites, depends on the nature of the stretched materials. In some materials, during necking, part of chains in crystalline blocks are unfolded and transfer into amorphous phase with more or less orientation (see Peterlin and Olf [2], Gent *et al.* [3]). In other polymers, Strauch and Schara [4] exhibit realignment of crystallite. Other authors, Waddon and J., Karttunen [5], emphasize solid-solid phase transition. Nevertheless, everyone agree that a local rise of temperature occurs in the neck shoulders.

To perform energy balance during such local phenomena, we combine the evolution of thermal fields obtained by InfraRed Thermography (IRT) and kinematic fields given by Digital Image Correlation (DIC). The DIC techniques give access to the measurement of displacement and deformation fields while the thermal images allow the estimation of the distribution of heat sources induced by the deformation process.

An electronic system was designed to simultaneously record those speckle and infrared images. Tracking the observed material surface elements and monitoring their temperature evolution allow us to construct local energy balances, even if localization mechanisms are revealed at the observation scale associated with the lens of the camera. Applications to steel and polymer were already carried out for quasi-static loadings [6].

In what follows, we illustrate the capabilities of the developed experimental approach by considering, at first, monotonic tension tests on Polyamide samples. For this kind of material the necking zone spreads out during the test. Using thermal and kinematic data, we construct the Lagrangian representation of temperature maps. Figure 1 corresponds to space-time charts with the abscissa axis representing the time and the ordinate axis being the loading sample axis (in the deformed configuration: Figure 1.a., or in the reference configuration: Figure 1.b.). In these Figures, the evolution of the longitudinal profiles of temperature variations  $\theta$  during the loading are plotted on a "colormap". We can notice two hot spots which indicate the existence of two competing necking zones, the upper one spreading along the specimen axis.

The paths of four material surface elements (MSE) named  $A$ ,  $B$ ,  $C$  and  $D$  were plotted in Figure 1. Naturally, in the Lagrangian configuration the MSE paths remain horizontal. The MSE  $A$  is associated with the inception of the necking.  $B$  corresponds to the location reached by the lower necking lip at the end of the monotonic loading. At the end of the monotonic loading,  $A$  is thus located in the middle of the necked zone. As shown in Figure 1,  $D$  has been chosen in the middle of a second localization zone. Finally,  $C$  is set between  $B$  and  $D$ , in a region not yet reached by the necking.

We show that the heat transfers by matter transport are not negligible in the neck shoulders. Then, we analyse the thermomechanical coupling effects that appear during cyclic loadings of the necked specimen around a given tension state.

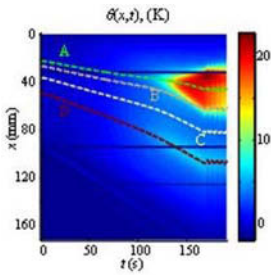


FIGURE 1.a. Eulerian space-time evolution of the temperature variation

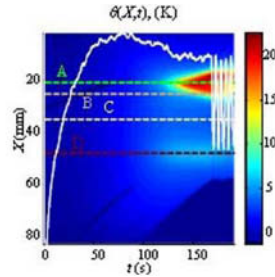


FIGURE 1.b. Lagrangian space-time evolution of the temperature variation

The Figure 2 illustrates the heat sources evolution during the loading cycles for the 4 MSEs. This curve also represents the evolution of the nominal stress applied to the sample. The oscillating part of the responses can be associated with coupling mechanisms rather in phase with the loading as observed in the case of materials in a rubbery state. A method based on the integration of the equilibrium equation is used to compute the local stress distribution in the neck shoulders in order to perform the thermomechanical analysis of the material behaviour.

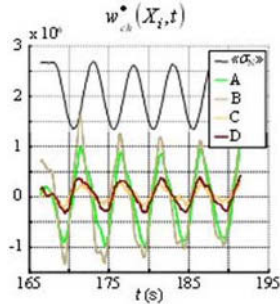


FIGURE 2. Heat sources evolution during the cyclic loading.

## References

1. Carothers, W. H., Hill, J. W., *J. of Amer. Chem. Soc.*, vol. **54**, 1579-1587, 1932.
2. Peterlin, A., Olf, H.G., *J. Polym. Sci A*, vol. **2**, 4, 587-598, 1966.
3. Gent, A.N., Jeong, J., *Polym. Eng. Sci.*, vol. **26**, 285-289, 1986.
4. Strauch, V., Schara, M., *Polym.*, vol. **26**, 3435-3438, 1995.
5. Waddon, A. J., Karttunen, N. R., *Polym.*, vol. **42**, 2039-2044, 2001.
6. Wattrisse B., Muracciole J.-M., Chrysochoos A., *Int. J. of Therm. Sci.*, vol **41**, 5, 422-427, 2001.

## THERMAL EFFECTS IN VISCOELASTIC MATERIALS

A. Hussain<sup>1</sup>, R. J. Greene<sup>2</sup> and R. A. Tomlinson<sup>3</sup>

University of Sheffield

Department of Mechanical Engineering

Sheffield, United Kingdom

<sup>1</sup>a.hussain@sheffield.ac.uk, <sup>2</sup>r.j.greene@sheffield.ac.uk, <sup>3</sup>r.a.tomlinson@sheffield.ac.uk

The science of thermoelasticity is a study of the coupling phenomenon between thermal energy and mechanical deformation in elastic materials. The non-contacting investigation of the thermoelastic effect using infrared technology was first reported in 1967 by Belgen [1,2]. This technology has developed to a stage where highly sensitive array detectors are now widely used for thermoelastic stress analysis (TSA) and a variety of thermographic and thermal NDE studies[3]. Array systems such as the DeltaTherm system may be used to obtain full-field maps of the minute differential temperature on the surface of a component due to the thermoelastic effect. In addition, these systems are also capable of providing static thermal images of the absolute temperature of the component at the time the image is captured.

The majority of research using TSA has involved metals and composite materials, although the early work on the thermoelastic effect can be traced back to J. Gough who experimented with rubber in 1805 [4]. While most solids heat up in compression and cool down in tension, some rubbers behave in the opposite way. Little research using TSA has been performed on such viscoelastic materials. However the advanced technologies now available offer the opportunity to study in detail both the temperature and thermoelastic effects of such materials.

In the present study, the thermal and thermoelastic effects in rubber were investigated with the aid of the DeltaTherm system. Tensile specimens of four different types of rubber were cyclically loaded and both the static and differential temperatures were obtained at a range of loads and frequencies. The rapidly changing absolute temperatures corresponding to load fluctuations were captured using the 'movie' mode, a special built-in feature in DeltaVision software. The specimen heating and cooling were observed during increasing and decreasing loads respectively. The viscoelastic heating over time may also be observed. Figure 1 shows that the generation of heat and the steady state temperature depend on the driving frequencies and the mean and amplitude of the cyclic loads.

Previous studies have shown that the second harmonic of the reference signal may be used to investigate the mean stress effect in thermoelasticity. However this signal is very low in metals making measurement difficult [5]. Preliminary measurements on our rubber samples have shown signals of comparable magnitudes using the first and second harmonic frequencies. This information will therefore be used in understanding the relationship between thermal and thermoelastic effects in viscoelastic materials.

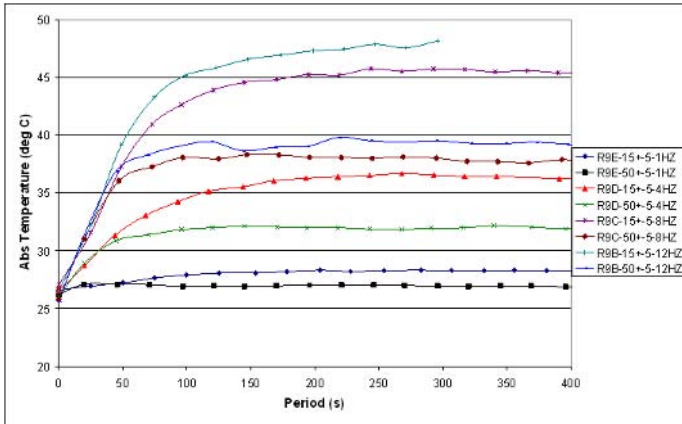


FIGURE 1. Viscoelastic heating over time for various driving frequencies and the mean and amplitude of cyclic loads

## References

1. Belgen, M. H., Structural stress measurements with an infrared radiometer, *ISA Transactions*, 1967, vol. 6, p. 49-53.
2. Belgen, M. H., Infrared radiometric stress instrumentation application range study, *NASA Contractor Report: CR-1067*, 1968.
3. Lesniak, J. R. and Boyce, B. R., A high-speed differential thermographic camera, *Proceeding of the Society of Experimental Mechanics Spring Conference*, 1994, Baltimore.
4. Harwood, N., Cummings, W. M., and MacKenzie, A. K., An introduction to thermoelastic stress analysis, *Thermoelastic Stress Analysis*, Harwood, N. and Cummings, W. M., eds., 1991, Adam Higler. p. 1-34.
5. Gyekenyesi, A. L. and Baaklini, G. Y., Quantifying residual stresses by means of thermoelastic stress analysis, In *Proceedings of the International Conference on Stress Nondestructive Evaluation of Aging Materials and Composites IV*, Proceedings of SPIE, 2003, vol. 3993, p. 78-91.

## THERMOELASTIC STRESS ANALYSIS OF INHOMOGENOUS COMPOSITE MATERIALS

R.K. Fruhmann<sup>a</sup>, J.M. Dulieu-Barton<sup>b</sup> and S. Quinn<sup>c</sup>  
 School of Engineering Sciences, University of Southampton  
 Highfield, Southampton, SO17 1BJ, United Kingdom

<sup>a</sup>rkf@soton.ac.uk, <sup>b</sup>janice@ship.soton.ac.uk, <sup>c</sup>s.quinn@soton.ac.uk

In this work a study of how the inherent heterogeneity of a typical woven composite material influences the evaluation of the stress field using the thermoelastic effect is presented. The problem of heterogeneity has recently been examined by Pittarresi *et. al.* [1] at the macroscopic scale, using the resin layer at the surface to act as a strain witness.

In this paper the effect of individual rovings is considered. This is made possible using high resolution lenses and motion compensation techniques. The thermoelastic stress analysis system used in this work is the Silver 480M manufactured by Cedip Infrared Systems. The infra-red detector array is a cryogenically cooled 320 x 256 InSb array which is radiometrically calibrated. The calibration has the advantage that the surface temperature of the specimen is measured directly. This is important in composite materials, where viscoelastic and frictional heating can be an issue, and so these effects can be separated from those due to thermoelasticity [2].

Tensile specimens of 370 x 26 x 3.2 mm are used in this study. They are made of glass fibre reinforced epoxy composite consisting of five plies of woven roving and four plies of chopped strand mat. These are arranged in a symmetrical lay up with one ply of woven roving on the surface and a stack of three woven plies in the centre.

The woven surface is treated as a patchwork of unidirectional fibre bundles arranged orthogonally, as depicted in Fig. 1. Due to the heterogeneity, the stress field will vary throughout the specimen. The strain however will be uniform throughout the material. Hence the equation of thermoelastic effect as presented by Dulieu-Barton and Stanley [3] is rewritten in terms of strain.

$$\Delta T = - \frac{T}{\rho C_p} \left( \{ \Delta \alpha \}^T [Q] [T]^{-T} \{ \Delta \epsilon \} \right) \quad (1)$$

The material constants ( $\alpha$  and  $Q$ ) are expressed in the directions of the principal material axes on the specimen surface while the strain ( $\epsilon$ ) is that in the direction of the loading axes.  $T$  is a transformation matrix which relates the two coordinate systems. For the case where the material and loading axes are aligned ( $\theta = 0^\circ$ ) we can write

$$\Delta T = \frac{-T}{\rho C_p} \left[ (\alpha_{11} Q_{11} + \alpha_{22} Q_{12}) \Delta \epsilon_L + (\alpha_{11} Q_{12} + \alpha_{22} Q_{22}) \Delta \epsilon_T \right] \quad (2)$$

As the strain is uniform across the specimen, it is apparent from equation (2) that variations in the observed thermoelastic response are due to a combination of the material stiffness and thermal coefficients of expansion in the two orthogonal material directions.

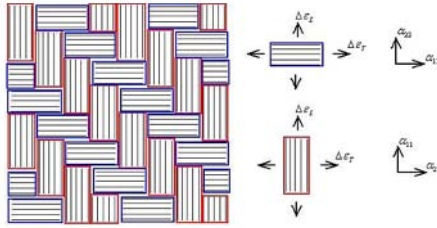


FIGURE 1. Break down of the weave pattern into unidirectional elements.

In the cross-sectional view the individual woven lamina of the specimen are clearly visible when motion compensation has been applied. An advantage when compared with the frontal view is that the two material components (glass and epoxy) are both exposed on the surface. Therefore there is no attenuation and dissipation of the thermoelastic response through a surface layer. However, differences in the emissivity from the two constituent materials must now be accounted for. The image in Fig. 2 was taken of a sample coated with one thin layer of matt black paint. Despite the paint coating, it clearly shows the three plies of woven material in the centre of the specimen as well the two surface plies.

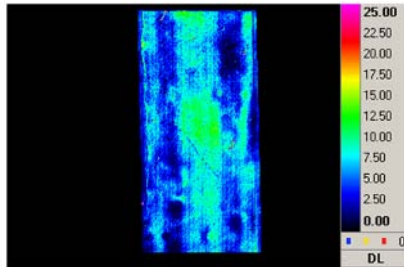


FIGURE 2. Cross-sectional view of a [WR1 CSM2 WR1 1/2]S specimen under a cyclic load of 5kN amplitude at 15Hz

### Acknowledgements

The authors would like to thank AWE plc for providing the thermoelastic stress analysis equipment used in this study.

### References

1. Pittarresi, G., Found, M.S. and Patterson, E.A., *Composites Science and Technology*, vol. **65**, 269-280, 2005.
2. Dulieu-Barton, J.M., Emery, T.R., Quinn, S. and Cunningham, P.R, *Measurement Science and Technology*, vol. **17**, 1627-1637, 2006.
3. Dulieu-Barton, J.M. and Stanley, P., *J. of Strain Analysis*, vol. **33**, 93-104, 1998.

## OPTIMIZATION OF THE FSW PROCESS FOR ALUMINUM ALLOYS AA5083 BY THE GREY-BASED TAGUCHI METHOD

Thaiping Chen<sup>\*a,b</sup>, Chi-Hui Chien<sup>b</sup>, Wei-Bang Lin<sup>c</sup> and Yuh J. Chao<sup>d</sup>

<sup>a</sup> Department of Electrical Engineering,

Fortune Institute of Technology, Kaohsiung 83160, Taiwan

<sup>b</sup> Department of Mechanical and Electro-Mechanical Engineering,

National Sun Yat-Sen University, Kaohsiung 80424, Taiwan

<sup>c</sup> Department of Mechanical Engineering, Chinese Military Academy, Kaohsiung 83059, Taiwan.

<sup>d</sup> Department of Mechanical Engineering, University of South Carolina,

Columbia, SC 29208, USA

taiping@center.fotech.edu.tw, chchien@mail.nsysu.edu.tw, linwb@mail.cma.edu.tw,  
chao@enr.sc.edu

Friction Stir Welding (FSW), invented by W.M. Thomas et al. [1], can produce superior mechanical properties in the weld zone. The purpose of this paper is to find the optimum operating conditions of FSW process for two plates of aluminum alloy AA5083 welded in butt joint. In the FSW procedure, there were four major controllable four-level factors, i.e., the tool rotation speed, transverse speed (feed rate), tool tilt angle with respect to the workpiece surface and pin tool length, as shown in Table 1.

Table 1 Process parameters and their levels

Symbol	Process parameter	unit	Level 1	Level 2	Level 3	Level 4
A	Rotation speed	rpm	550	1100	1250	1800
B	Transverse speed	mm/min	53	90	143	180
C	Tool tilted angle	degree	1	2	3	4
D	Pin tool length	mm	2.5	2.7	2.9	3.1

In order to achieve the aim of the multiple-response process of robustness, the grey-based Taguchi method is proposed. A grey relational grade (grg) obtained Y. S. Tarn et al. [2], from the grey relational analysis is used as the performance characteristic in the Taguchi method. Analysis of variance (ANOVA) is the statistic method used to interpret these experimental data assigned to the L16 (44) orthogonal arrays, grey relational grade and its order, as shown in Table 2. Taguchi technique with ANOVA is used to find out the significant variables (factors), at least 95% confidence, for the ultimate tensile strength and elongation rate, as shown in Table 3 and Table 4 respectively, measuring with the grey relational grade performance.

Table 2 Experimental results for uncontrol factors

Trial no.	Tensile strength (MPa)					Elongation rate (%)				
	No. 1	No. 2	No. 3	Grg	Order(Grg)	No. 1	No. 2	No. 3	Grg	Order(Grg)
1	282.8	290	287.3	0.64	5	16.8	16.15	15.52	0.57	5
2	272.4	278.9	264.4	0.59	7	10.91	13.98	13.05	0.49	9
3	270.9	274.7	253.6	0.58	8	10.7	12.38	11.94	0.47	10
4	211.1	225.9	209	0.44	11	8.48	7.23	7.62	0.38	14
5	336.4	326.9	317.7	0.82	2	19.63	19.52	21	0.67	2
6	169.8	163.8	147.9	0.33	16	6.08	5.8	5.42	0.33	16
7	186.9	180.1	182.3	0.37	15	7.9	7.76	9.2	0.39	13
8	213.2	226.9	211.3	0.44	10	9.19	9.17	9.74	0.41	12
9	319.9	300.8	298.9	0.72	4	15.73	16.41	16.35	0.57	6
10	327.9	329.3	292	0.77	3	18.1	19.86	15.94	0.62	3
11	187.3	195.5	202.4	0.40	12	9.33	7.1	11.77	0.42	11
12	190.7	194.9	182.7	0.39	13	6.63	7.04	7.71	0.36	15
13	203.7	178.2	185.5	0.39	14	15.71	12.27	12.62	0.51	7
14	290.9	265.8	258.6	0.59	6	14.15	12.78	12.47	0.50	8
15	266.1	223.6	221.4	0.50	9	17.55	16.76	17.64	0.60	4
16	354.4	359.5	364.4	1.00	1	29.77	30.32	30.14	1.00	1

Grg: grey relational grade

Table 3 ANOVA summary of tensile strength in grey relational grade

Source	SS	DOF	MS	F	Critical value	Contribution(%)
A	0.03	3	0.01	2.93	9.28	4.00%
B	0.07	3	0.02	5.91	9.28	10.17%
C	0.03	3	0.01	2.24	9.28	2.57%
D	0.29	3	0.10	25.52	9.28	50.80%
ERROR	0.13	35	0.00			32.46%
Total	0.54	47				100.00%

Table 4 ANOVA summary of elongation rate in grey relational grade

Source	SS	DOF	MS	F	Critical value	Contribution(%)
A	0.10	3	0.03	14.00	9.28	23.20%
B	0.03	3	0.01	4.53	9.28	6.30%
C	0.03	3	0.01	3.88	9.28	5.14%
D	0.16	3	0.05	21.96	9.28	37.40%
ERROR	0.08	35	0.00			27.96%
Total	0.40	47				100.00%

**References**

1. Thomas, W.M., Nicholas, E.D., Need ham, J.C., Murch, M., Templesmith, G. P. and Dawes, C.J., GB Patent Application No. 91259788 (Dec. 1991).
2. Targ, Y.S., Juang, S.C. and Chang C.H., J Mater. Processing Technol. vol. **128**, 1-6, 2002.



## THE EFFECTS OF DIFFERENT CRANIAL SIZE ON MECHANICAL PROPERTIES OF CRANIAL SUTURE IN RAT AND SAME-AGED MICE

Chi-Hui Chien<sup>1,\*</sup>, Yii-Der Wu<sup>1</sup> and Yuh J. Chao<sup>2</sup>

<sup>1</sup>Department of Mechanical and Electro-Mechanical Engineering,  
National Sun Yat-Sen University, Kaohsiung, Taiwan 804, R.O.C.

<sup>2</sup>Department of Mechanical Engineering, University of South Carolina,  
300 Main Street, Columbia, SC 29208, USA

\*chchien@mail.nsysu.edu.tw

“Cranial suture” is the soft tissue connecting the cranial bones forming the skull of mammals and is responsible for regulating the growth of cranial bones. Abnormal growth of brain/skull in infants results in craniostyostosis. Furthermore, the frequency of head injuries among humans has inspired numerous investigations of the mechanical properties of cranium. This work focused on the mechanical characteristics of the cranial suture in Lewis rat and C57BL/6 mice, where the cranial size in rat is larger than in mice (listed in Table 1).

Mechanical properties of cranial sutures in mammalian skulls have been studied by Jaslow [1]. He showed that sutures were not as strong in bending as bone. The load-displacement characteristics of Neonatal rat cranial sutures have been studied by McLaughlin et al. [2]. Their study provides data regarding the basic mechanical behavior of neonatal cranial sutures in mammalian system. Infant skull and suture properties have been studied by Margulies and Thibault [3]. They have shown that the elastic modulus and the rupture modulus of infant cranial bone and suture increase significantly with loading rate but do not approach adult values. And the energy absorbed to failure in each of the pediatric tissues does not change significantly with loading rate.

The objective of this study was to determine the mechanical properties of cranial sutures in different mammals. Ten sagittal sutures were harvested from 4-month-old female rats and mice. The specimens, kept moist, were mounted fresh and distracted at 15 m/sec until rupture. Load-displacement curves were constructed.

Using the slope of the linear region BC from the stress-strain curve (as shown in Fig. 1), the Young’s modulus,  $E$ , of the sample is written by [4,5]

$$E = \frac{\Delta \sigma}{\Delta \varepsilon} \quad (1)$$

where  $E$  is the slope of BC section from the stress-strain curve shown in Fig. 1,  $\Delta \sigma$  and  $\Delta \varepsilon$  are the stress level and strain from B to C, respectively.

If one assumes the elastic response until fracture, the maximum stress or the fracture strength,  $\sigma_c$  can then be calculated by

$$\sigma_c = \frac{P_{max}}{A} \quad (2)$$

where  $P_{max}$  is the maximum load from the test and  $A$  is the cross-sectional area.

The area under the complete load-displacement curve yields the total energy to break the sample. And, the area under the curve from A to D gives the energy to fracture (initiation).

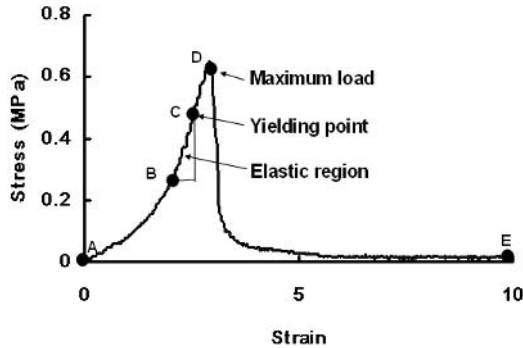


FIGURE 1. A typical stress-strain curve of suture specimen in C57BL/6 mice.

The geometric size, Young’s modulus, fracture strength and fracture energy were calculated and listed in Table 1. Moreover, the effect of different type of build and mechanical behaviors of cranial sutures under tensile loading were also discussed in the study. The results show difference between the two groups with higher values from rat. In conclusion, it shows the higher mechanical properties occurred mainly on the large type of build in our mammal system.

TABLE 1. Size and mechanical properties of cranial sutures from Lewis rat and C57BL/6 mice

Material	Cranial width/mm	Cranial length/mm	Cranial depth/mm	Young’s modulus/MPa	Fracture energy/Joule	Fracture strength/MPa
Rat	~13.5	~23.5	~1.7	2.35 ± 0.86	0.00154 ± 0.00047	2.00 ± 0.77
Mice	~10.0	~15.0	~0.6	0.58 ± 0.22	0.00010 ± 0.00007	0.62 ± 0.05

**References**

1. Jaslow, C.R., *J. Biomech.*, vol. **23**, 313-321, 1990.
2. McLaughlin, E., Zhang, Y., Pashley, D., Borke, J. and Yu, J., *Cleft Palate-Cran. J.*, vol. **37**, 590-595, 2000.
3. Margulies, S.S. and Thibault, K.L., *J. Biomech. Eng-T ASEM*, vol. **122**, 364-371, 2000.
4. Timoshenko, S.P. and Goodier, J.N., *Theory of Elasticity*, McGraw-Hill, New York, 1951.
5. Fung, Y.C., *Biomechanics: Mechanical Properties of Living Tissues*, Springer-Verlag, New York, 1993.

## VALIDATION OF MECHANICAL PROPERTIES OF SINGLE CRYSTAL SILICON BY ATOMIC-LEVEL NUMERICAL MODEL

Chun-Te Lin, Chan-Yen Chou and Kuo Ning Chiang  
 Department of Power Mechanical Engineering, National Tsing Hua University  
 101, Sec. 2, Kuang-Fu Rd., HsinChu Taiwan 300  
 knchiang@pme.nthu.edu.tw

In this research, an atomistic-continuum mechanics (ACM) based on the finite element method (FEM) is applied to investigate the elastic constant of the nanoscale single crystal silicon in different crystallography planes of (100), (110), and (111) under uniaxial tensile loading and modal analysis.

The ACM transfers an originally discrete atomic structure into an equilibrium continuum model by atomistic-continuum transfer elements. The mean positions of each atom of the metallic elements can be treated as the positions which achieve the minimum total energy. All interatomic forces, which are described by the empirical potential function, can be transferred into atomic springs to form the lattice structure. The spring network models were also widely utilized in finite element method based nanostructure studies [1-3]. The ACM model simplifies the complexities of interaction forces among atoms, while the calculation accuracy is still acceptable and the computational time is affordable. Therefore, two atomic-level virtual experiments are performed based on the ACM model. Besides, all results are validated with bulk properties with good agreements.

After the atomic-level models are constructed, the tensile static loading and modal analysis are conducted separately. The elastic  $E$  could be calculated by equation (1) in tensile loading test and by equation (2) in modal analysis. The results are shown in Fig. 1 and Table 1.

$$E_t = \frac{\sigma}{\varepsilon} = \frac{F_{total}}{A_e \cdot \varepsilon} \quad (1)$$

where  $F_{total}$  is the total reaction force,  $\varepsilon$  represents the applied tensile strain loading, and  $A_e$  represents the equivalent area in the ACM model.

$$E = \frac{12 \rho L^4 \left[ \frac{2 \pi f_1}{(1.875)^2} \right]^2}{t^2} \quad (2)$$

where  $\rho$  is the density,  $L$  represents the length, and  $f_1$  represents the first oscillation frequency of the ACM model.

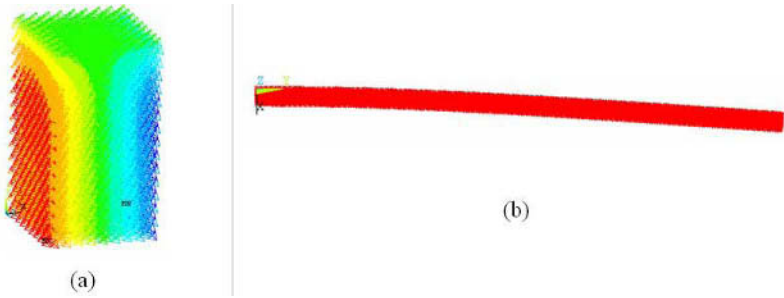


FIGURE 1(a): Displacement distribution of tensile static testing. 1(b): First mode shape in modal analysis.

TABLE 1. Calculation results comparison. The bulk value are obtained from Sato et al. [4]

Crystallography planes	Tensile testing results (GPa)	Modal analysis results (GPa)	Bulk Value (GPa)
Plane (100)	121.8	128.7	125
Plane (110)	153	154.7	140
Plane (111)	174.6	179.8	180

## References

1. K. N. Chiang, C. Y. Chou, and C. J. Wu, and C. A. Yuan, Appl. Phys. Lett., vol. **88**, 171904, 2006.
2. K. N. Chiang, C. H. Chang and C. T. Peng, Appl. Phys. Lett, vol. **87**, 191901, 2005.
3. Andrei A. Gusev, Phys. Rev. Lett. 93, 034302, 2004.
4. K. Sato, T. Yoshioka, T. Ando, M. Ahilida, and T. Kawabata, Sensor & Actuator A, vol. **70**, 148-152, 1998.

## STRAIN MEASUREMENT OF NICKEL THIN FILM BY A DIGITAL IMAGE CORRELATION METHOD

Shun-Fa Hwang<sup>1</sup>, Jhih-Te Horn and Hou-Jiun Wang

Department of Mechanical Engineering, National Yunlin University of Science and Technology  
123 University Road, Sec. 3, Douliu, Taiwan 640, R.O.C.

<sup>1</sup>hwangsf@yuntech.edu.tw

Digital image correlation (DIC) is a whole-field and non-contact deformation measuring method. It could provide deformation information of a specimen by processing two digital images that are captured before and after the deformation. In 1982 Peters and Ranson [1] first employed digital image correlation for displacement and strain measurement under the assumption that there is a one-to-one correspondence on the intensity pattern of surface images before and after deformation. Chu et al. [2] utilized a cross-correlation coefficient as an objective function and measured the rigid body translation, rigid body rotation, and uniaxial uniform strain. Initially, the searching method was a coarse-fine iterative technique, in which the searching range was progressively reduced until the stop criterion was satisfied. Newton-Raphson method was later applied to search the six deformation components [3].

Instead of Newton-Raphson method, a hybrid genetic algorithm [4] is used in digital image correlation in this work to release the limitation on the searched parameter range. In addition to the conventional single region for strain searching, a double region is proposed to calculate the strain of the specimen. This method is used to measure the strain of nickel thin film during micro tensile testing, and its mechanical properties are obtained.

If a subset is arbitrary chosen from the image taken before a deformation increment and a reference point  $(x_0, y_0)$  as well as a nearby point  $(x, y)$  is selected from this subset, the position  $(x', y')$  of the nearby point after the deformation increment could be described as

$$x' - x = u + \frac{\partial u}{\partial x} dx + \frac{\partial u}{\partial y} dy \quad (1)$$

$$y' - y = v + \frac{\partial v}{\partial x} dx + \frac{\partial v}{\partial y} dy \quad (2)$$

where  $(u, v)$  are the displacements of the reference point, and  $(dx, dy)$  are the position differences of the reference point and the nearby point before deformation. The nickel specimen and the subsets are shown in Fig. 1 and it was fabricated by MEMS technology with electroplation.

The Ni specimen with 12m thickness was tested under 1 m/sec crosshead rate. Two subsets are selected and denoted as y[320]x[200] and y[280]x[200]. The y-directional strains measured by both the grip displacement and digital image correlation with respect to the y-directional stresses are compared in Fig. 2. In addition, two subsets that are denoted as double region are selected on the top and bottom of the gauge section of the specimen. Instead of calculating the strains from each subset, the distance between these two subsets are calculated before and after the deformation by digital image correlation. Then, the y-directional strains are calculated from the change of the distance. The results are denoted as double region in Fig. 2. It is very surprising that the strains obtained by the grip displacement of MTS are significantly larger than those obtained by digital image correlation. The curve of the double region is about the average of the two curves obtained

from single region. From these results, one could say that the large strains obtained by MTS are not correct. The possible reason might be that in addition to the gauge section, the end sections of the specimen may be extended without the protection from the silicon wafer because they may be separated under extension. As for the variation of the strains obtained by digital image correlation with single region, this may result from the variation of the method because the strains are the derivatives of the displacement and they are not so sensitive as the displacements during the searching process. In addition, the variation between the two curves obtained from single region may be caused by the nonuniform deformation at different regions.

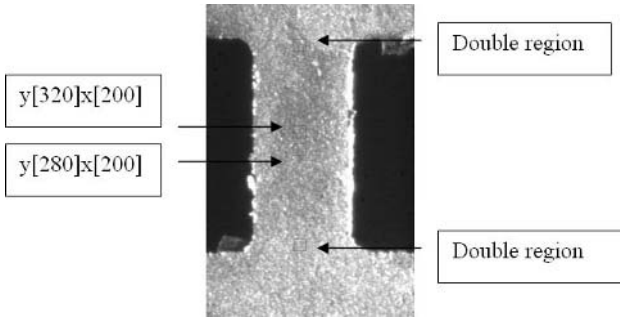


FIGURE 1. The specimen and the subsets.

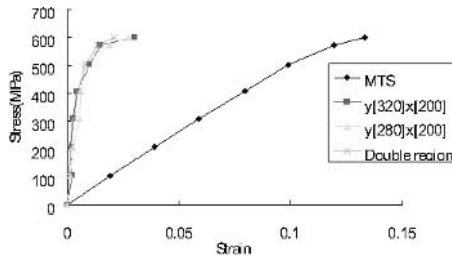


FIGURE 2. Stress-strain curves

## Reference

1. Peters, W.H., Ranson, W.F. *Opt Eng*, vol. **21**, 427-31, 1982.
2. Chu, T.C., Peters, W.H., Sutton, M.A., McNeil, S.R., *Image Vis Comput*, vol. **25**, 232-45, 1985.
3. Bruck, H.A., McNeill, S.R., Sutton, M.A., Peters, W.H., *Exp Mech*, vol. **29**, 261-7, 1989.
4. Hwang, S.F., He, R.S., *Adv Eng Soft*, vol. **37**, 406-18, 2006.

## THE EFFECTS OF INTERNAL STRESSRS IN BGA NI LAYER ON THE STRENGTH OF SN/AG/CU SOLDER JOINT

Chi-Hui Chien<sup>a</sup>, Chi-Chao Tseng<sup>a,b</sup> and Thaiping Chen<sup>a,c</sup>

<sup>a</sup> Department of Mechanical and Electro-Mechanical Engineering  
National Sun Yat-Sen University, Kaohsiung 80424, Taiwan

<sup>b</sup>BGA R&D Group, ASE GROUP, Kaohsiung 80424, Taiwan

<sup>c</sup> Department of Electrical Engineering, Fortune Institute of Technology  
Kaohsiung 84241, Taiwan

chchien@mail.nsysu.edu.tw, CJ\_Tseng@aseglobal.com, taiping@center.fjtc.edu.tw

Due to the consideration of environmental protection policy, all electronic products are requested to be lead free. In package field, solder ball is also requested to be lead free and currently the most popular type of solder ball is the Sn/Ag/Cu solder[1]. Sn/Ag/Cu solder has higher melting point and narrower control window of re-flow profile than eutectic solder ( Sn/Pb )[2], therefore the strength of solder joint of Sn/Ag/Cu solder has risk to be worse than Sn/Pb Solder .

In this study, the effects of internal stresses in BGA Ni layer on the strength of Sn/Ag/Cu solder joint are investigated. The drop test and peel off test are adopted in testing the strength according to the standard of JEDEC.

For package assembly to be tested, the Sn/Ag(4)/Cu(0.5) solder balls are chosen and the 260 of IR Re-flow profile was adopted in ball mount process. The specifications of the PCB board to be tested are 1.0 mm board thickness, 8 layers, OSP metal finish and 0.43 mm opening size. The specifications for substrate structure to be tested are 0.26 mm board thickness,  $30 \pm 10 \mu\text{m}$  solder resist thickness,  $300 \pm 50 \mu\text{m}$  ball opening,  $5 \sim 10 \mu\text{m}$  Ni thickness and  $0.5 \sim 1.0 \mu\text{m}$  Au thickness.

The tensile internal stresses in the Ni layer are obtained by adjusting the current density corresponding to Ni plating and use additive “saccharin“ to obtain the compressive internal stresses. The values of internal stresses in Ni layer are measured by spiral contractometer.

The peak acceleration of drop test is 1500G with 0.5 ms pulse duration and the failure criterion is 1000ohm detected. According to the definition of “JEDEC Standard “ , the result is pass when there is no failure occurs after 30 drops .

Figure 1 shows the drop test results corresponding to different internal stresses in the Ni layer and are described with Weibull analysis. It can be seen that the compressive internal stresses in the Ni layer have worse effects on the joint strength than tensile internal stresses can affect. The failure modes are analyzed also and the results are shown in Figure 2.

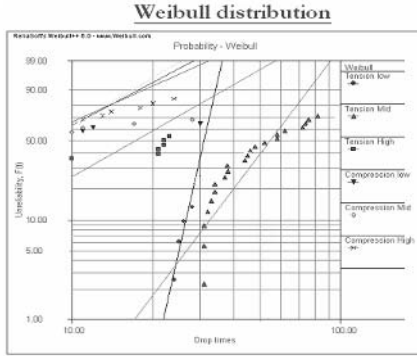


FIGURE 1. The drop test results corresponding to different internal stresses in the Ni layer.

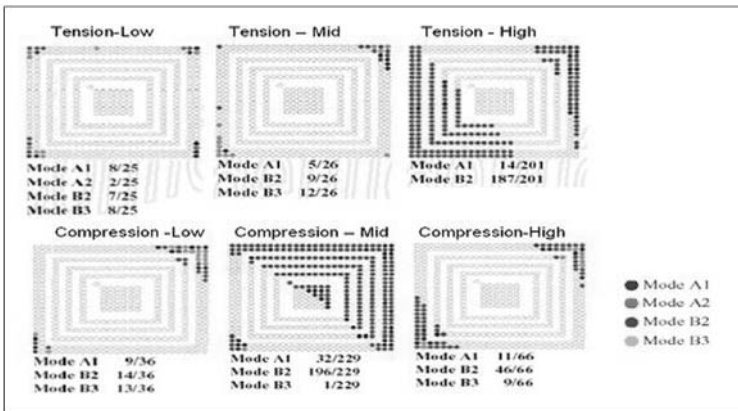


FIGURE 2. Failure modes subjected to the peel off test.

## References

1. Karl J. Puttlitz and Kathleen A. Stalter, "Handbook of Lead-Free Solder Technology for Microelectronic Assemblies. 5. Market, Product, and Corporate Policy Trends," IBM Corporation , 149-165(2004).
2. Karl J. Puttlitz and Kathleen A. Stalter, "Handbook of Lead-Free Solder Technology for Microelectronic Assemblies. 8. Sn-Ag and Sn-Ag-X Solders and Properties," IBM Corporation , 239-280(2004).



## NOVEL APPLICATIONS OF EXPERIMENTAL MECHANICS ON THE DESIGN OF ULTRASONIC HORNS

Wei-Chung Wang, Ying-Huang Tsai and Chun-Yao Ni  
Department of Power Mechanical Engineering  
National Tsing Hua University  
Hsinchu, Taiwan 30013, R.O.C.  
wawang@pme.nthu.edu.tw

In recent years, ultrasonic wave has been widely employed in many industrial applications. The ultrasonic horn is the key component of ultrasonic equipment. Because of its complicated geometry, exact solutions cannot be easily obtained for the ultrasonic horn. Numerical technique such as finite element method (FEM) can be used; however, the validity of its results must be verified. Methods of experimental mechanics thus become indispensable not only for solving problems but also for verification purpose. In this paper, two novel applications of experimental mechanics on the design of two ultrasonic horns, i.e. horn I and horn II, for ultrasonic welding and flip-chip bonding are reported.

Transmitted photoelasticity was adopted in the design of horn I for ultrasonic welding. In the photoelastic experiment, the horn itself was simulated as a plate with dimensions 95.1mm x 30mm x 6mm. Those dimensions were selected from a commercially available ultrasonic horn. The photoelastic material used is PSM-1 (Measurements Group Co.). The ultrasonic wave was impinged on the right end of the specimen (Fig. 1). Within about 0.1 seconds after the ultrasonic struck the specimen, fringe pattern caused by standing wave only (Fig. 1(a)) was obtained. In 2006, the first two authors proposed the complete theory and calibration procedures of time-averaged photoelasticity to analyze the state of stress of Fig. 1(a). The highest order of fringe 5 occurs near the center of the right and central parts of the fringe pattern. To investigate the ultrasonic wave generated thermal stress in the ultrasonic horn, the power of the ultrasonic equipment was shut down 7 seconds after the ultrasonic wave struck the specimen. The fringe pattern caused by the thermal stress only is shown in Fig. 1(b). The highest order of fringe 2 occurs at points G and H.

To achieve best quality of flip-chip bonding, an ultrasonic horn must possess two features: (1) the resonant mode of the horn should be purely longitudinal; (2) the degree of coplanarity must be as high as possible. Based on the one-dimensional longitudinal wave equation of a uniform bar, an initial length of the horn II was obtained. This initial length was then used in the FEM calculations. SKD-11 was selected as the material of the horn II. By considering the aforementioned two features and other factors (e.g. stress concentration, accommodation of the tightening screw, etc); a series of modifications of the design of the horn II was performed. Final dimensions of the horn II were then obtained. Both the amplitude-fluctuation electronic speckle pattern interferometry (AF-ESPI) and laser Doppler vibrometer were used to verify the correctness of the FEM results. Both fringe patterns shown in Fig. 2 were obtained by an AF-ESPI in-plane setup. Fringes depicted in Fig. 2(a) are nearly perpendicular and they are parallel to each other, i.e. the displacement is almost purely longitudinal. As to the end face of the ultrasonic horn, no fringes are present, i.e. no in-plane displacements. In other words, the degree of coplanarity is very high. A laser Doppler vibrometer was used to measure the out-of-plane displacement along a diameter of the end face. As shown in Fig. 3, the largest and smallest displacements along a diameter of the end face are 3.873m and 3.735m, respectively. The difference 0.138m between the largest and smallest displacements is much lower than the 2m required by industry.

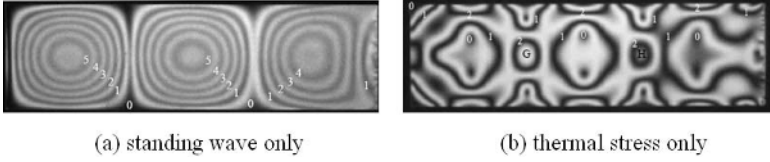


FIGURE 1. Photoelastic fringe patterns of horn I

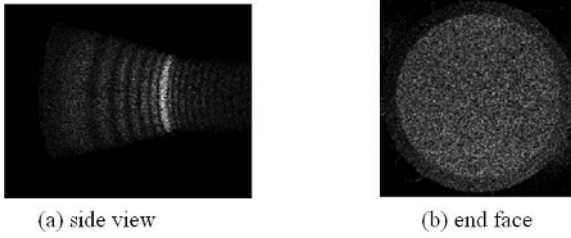


FIGURE 2. AF-ESPI fringe patterns of horn II

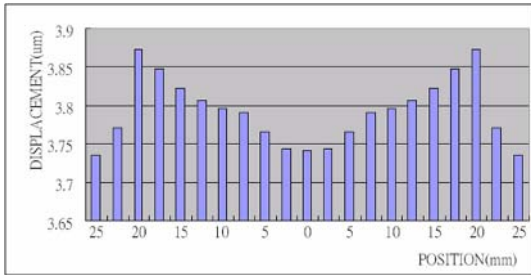


FIGURE 3. Displacement distribution on the end face

## THE OUT-OF-PLANE STRAINS MEASUREMENT IN SANDWICH PLATES WITH SINGLE FULLY-POTTED INSERT BY USING DIGITAL SPECKLE PATTERN SHEAROGRAPHY

Song-Jeng Huang and Yu-Tan Lin

Department of Mechanical Engineering, National Chung Cheng University

168 University Rd., Ming-Hsiung, Chia-Yi, 621, Taiwan, R.O.C

<sup>1</sup>ime\_hsj@ccu.edu.tw, <sup>2</sup>cruise2955@yahoo.com.tw

The construction and operation of digital speckle pattern shearography (DSPS) applied to sandwich plates with single fully-potted insert has been presented in this paper (refer Figs. 1 and 2). Proposed DSPS has advantages of full-field and non-destructive testing [1-4] that can measure tiny out-of-plane strain in the elastic region without wasting specimen. For validation purpose, the analytical solution analysis (ASA) [5] was conducted. By comparing the results of DSPS and ASA strain fields throughout the sandwich surface that a convincing agreement is revealed (see Tables 1-2), thus showing successfully the full-field strains of the single fully-inserted sandwich plates.

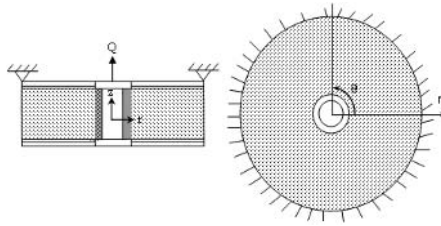


FIGURE 1. Sandwich plate with single fully-potted insert

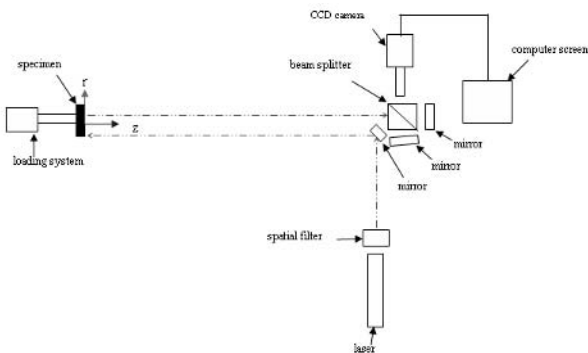


FIGURE 2. DSPS experimental setup for out-of-plane strain measurements.

Table 1. Comparison of out-of-plane strain between DSPTS and ASA as specimen is loaded up to 2kg.

Loaded up to 2kg	r, mm	Fringe order	$\frac{\partial w}{\partial r}$ DSPTS	$\frac{\partial w}{\partial r}$ ASA	error
	-15.3	1	$3.48 \times 10^{-4}$	$3.04 \times 10^{-4}$	
-5.5	0.5	$1.71 \times 10^{-4}$	$1.77 \times 10^{-4}$	3	
0	0	0	0	0	
5.6	-0.5	$-1.7 \times 10^{-4}$	$-1.76 \times 10^{-4}$	3	
15.5	-1	$-3.53 \times 10^{-4}$	$-3.07 \times 10^{-4}$	15	

Table 2. Comparison of out-of-plane strain between DSPTS and ASA as specimen is loaded up to 4kg.

Loaded up to 4kg	r, mm	Fringe order	$\frac{\partial w}{\partial r}$ DSPTS	$\frac{\partial w}{\partial r}$ ASA	error
	-23.9	1	$3.84 \times 10^{-4}$	$4.28 \times 10^{-4}$	
-19.7	1.5	$5.33 \times 10^{-4}$	$5.73 \times 10^{-4}$	7	
-15.1	2	$7.01 \times 10^{-4}$	$6.2 \times 10^{-4}$	13	
-11.2	1.5	$5.42 \times 10^{-4}$	$6.12 \times 10^{-4}$	11	
-6.5	1	$3.58 \times 10^{-4}$	$3.95 \times 10^{-4}$	9	
-3.8	0.5	$2.02 \times 10^{-4}$	$2.28 \times 10^{-4}$	11	
0	0	0	0	0	
3.3	-0.5	$-1.75 \times 10^{-4}$	$-1.82 \times 10^{-4}$	4	
6.3	-1	$-3.63 \times 10^{-4}$	$-3.89 \times 10^{-4}$	7	
9.1	-1.5	$-5.27 \times 10^{-4}$	$-5.43 \times 10^{-4}$	3	
15.8	-2	$-6.86 \times 10^{-4}$	$-6.11 \times 10^{-4}$	12	
19.9	-1.5	$-5.34 \times 10^{-4}$	$-5.75 \times 10^{-4}$	7	
25.4	-1	$-3.55 \times 10^{-4}$	$-3.74 \times 10^{-4}$	5	

**References**

1. Thomsen, T., *J. Compos. Struct.*, vol. **40**, 159-174, 1998.
2. Thomsen, T. and Rits, W., *Compos. P. B*, vol. **29B**, 795-807, 1998.
3. Steinchen, W., Kupfer, G., Mackel, P. and Vossing, F., *Measur.*, vol. **26**, 79-90, 1999.
4. Huang, S.J., Lin, H.L., *J. Mech.*, vol. **20**, no. 4, 273-276, 2004.
5. Huang, S.J., Chiu, L.W., Kao, M.T., In *Proceedings of the 2004 AASRC (Aeronautical and Astronautical Society of the Republic of China) / CCAS Joint Conference*, Taichung, Taiwan, 2004.

## AN EXPERIMENTAL STUDY ON THE ELASTIC-PLASTIC FRACTURE IN A DUCTILE MATERIAL UNDER MIXED MODE LOADING

Peng-Fei Luo and Ching-Hsiung Wang

Department of Mechanical Engineering

Chung Hua University

No. 707, Sec. 2, Wu Fu Rd., Shin Chu 30012, Taiwan, R.O.C.

luo@chu.edu.tw

A stereo vision [1,2] is used to measure the crack tip parameters (such as J integral[3], plastic mixity [4], and elastic mixity [4]) of mixed mode fracture specimens, and to study the applicability of the Shih's plane strain solution [4,5] to the mixed mode crack tip fields. The fracture specimen used in the paper is a compact tension shear (CTS) specimen made of 2024-O aluminum. To conduct mixed mode fracture experiments at the loading angles of  $75^\circ$  and  $45^\circ$ , a special loading device is used [6,7]. Fig. 1 shows the experimental setup for the loading angle of  $75^\circ$ .

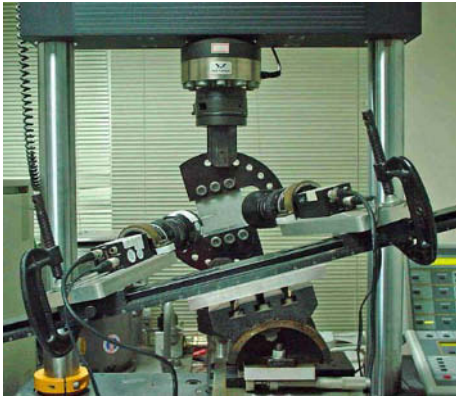


FIG. 1. Experimental setup (Loading angle =  $75^\circ$ )

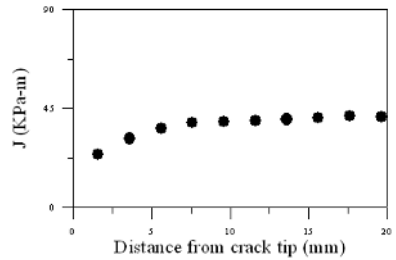


FIG. 2. distribution of J integral at 23,400 N (Loading angle =  $45^\circ$ )

The in-plane strain and stress fields near the mixed mode crack tip are determined using the deformation field measured by the stereo vision. Then the J integral along rectangular contours surrounding the mixed mode crack tip can be evaluated. Fig. 2 presents the computed J integral plotted against distance measured from the crack tip to the path of the line integral. It can be seen that the computed J integral values approach constant after  $r/h > 0.5$ .

In the paper the in-plane strains determined experimentally at several points near the crack tip are compared with the values calculated using Shih's plane strain solution. Figs. 3 and 4 show the comparison of the experiment data and the calculated values at the loading angles of  $75^\circ$  and  $45^\circ$ , respectively. It is found that the measured values follow the trends of the Shih's plane strain solution. It is also noted that the location of the points indicated in Figs. 3 and 4 is beyond the region ( $r/h < 0.5$ ) where the three dimensional effects exist. The elastic mixity evaluated using the measured crack tip stress fields are close to those obtained from analytical solution. However the evaluated plastic mixity deviates from the analytical solution.

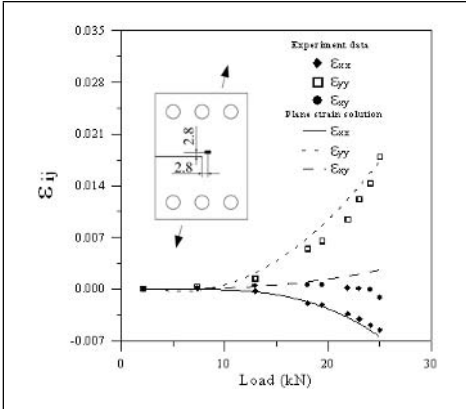


FIG. 3. Comparison of the experimental and numerical results at the loading angle of  $75^\circ$

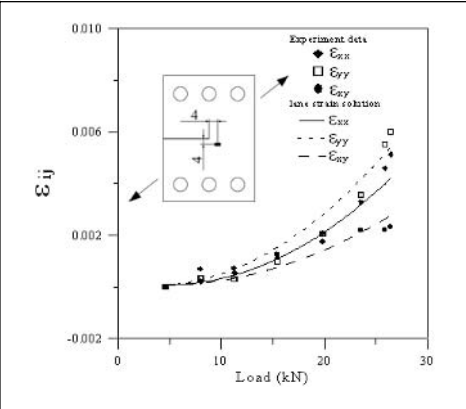


FIG. 4. Comparison of the experimental and numerical results at the loading angle of  $45^\circ$

**References**

1. Luo, P.F., Chao, Y.J., Sutton, M.A. and Peters, W.H., *Experimental Mechanics*, vol. **33** (2), 123-132, 1993.
2. Luo, P. F., Chao, Y.J. and Sutton, M.A., "*Optical Engineering*", vol. **33** (3), 981-990, 1994.
3. Rice, J.R., *ASME Journal of Applied Mechanics*, vol. **35**, 368-379, 1968.
4. Shih, C.F., *Fracture Analysis*, ASTM STP560, American Society for Testing and Materials, 187-210, 1974.
5. Symington, M., Shih, C.F. and Ortiz, M., *Tables of Plane Strain Mixed-Mode Plastic Crack Tip Fields*, Material Research Laboratory, Brown University, Rhode Island, 1988.
6. Richard, A., *International Journal of Fracture*, vol. **22**, R55-58, 1983.
7. Pawliska, P., Richard, H.A. and Kenning, J., *International Journal of Fracture*, vol. **47**, R43-R47 (1991).

## MECHANICAL CHARACTERIZATION OF KMPR™ BY NANO-INDENTATION FOR MEMS APPLICATIONS

Kuang-Shun Ou, Hong-Yi Yan and Kuo-Shen Chen  
Department of Mechanical Engineering  
National Cheng-Kung University  
Tainan, Taiwan, 70101, R.O.C.  
kschen@mail.ncku.edu.tw

The ability to create high-aspect ratio structures (HARS) are extremely important for many MEMS sensors and actuators applications such as gyros, accelerometers, and pumps. Traditionally, HARS are fabricated using LIGA [1] and ICP techniques. However, the expensive and the consuming LIGA process is usually unaffordable and the silicon ICP process usually suffers from poor sidewall quality. As a result, the UV based LIGA-Like process becomes a competitive fabrication process for creating HARS in polymeric materials. During the past decade, with the negative photosensitive resin, SU-8, UV LIGA-Like process has successfully demonstrated its capability in shaping HARS. However, SU-8 needs stringent temperature and time control in baking cycle to avoid cracking and potentially, the reliability of the fabricated structure become a concern. Recently, a new negative photosensitive resin, called KMPR™ [2], has been reported to have better characteristics in fabrication and it does not require tight baking control. It has the potential to replace SU-8 in the future. However, to our best knowledge, its mechanical properties are not yet reported and this represents a gap for related MEMS design. The purpose of this paper is therefore to provide specific material properties, namely hardness and elastic modulus of KMPR after different thermal treatments via nano-indentation [3] for MEMS design.

The processing parameters of KMPR are listed in Table 1. Test structures are fabricated via spin-coating and the associated baking processes. Finally, a thermal treatment period (ranged from 100 - 180°C, period = 100 minutes) is performed using an oven. After finishing specimen preparation, as schematically shown in Figure 1, an MTS nanoindenter with Berkovich indenter is employed to carry out the material properties measurement. A typical set of nanoindentation test data of KMPR with no thermal treatment is shown in Figure 2. The hardness and the elastic modulus can be extracted from the curvature and the unload slope of these curves, respectively. A summary on the obtained hardness and modulus is shown in Figure 3. In Figure 3(a), the elastic modulus of KMPR increases with the indenting depth from 6 to 7.5 GPa. On the other hand, the hardness exhibits the different tendency shown in Figure 3(b). In addition, the effect of thermal treatment temperature is also observed. In general, the elastic modulus of KMPR decreases with heat treatment temperature. On the other hand, a higher heat treatment temperature would increase the hardness. Meanwhile, by SEM inspection, there are no visible cracks propagated from the Berkovich impression. This implies that the fracture toughness of KMPR should be sufficient to resist fracture. With the test data reported in this work, MEMS engineers should be able to adjust their fabrication parameter for structural design optimization of KMPR HARS.

TABLE 1. The processes parameters of KMPR

Spin speed	Soft bake	Expose energy	Post exposure bake
4000rpm (film thickness =20μm )	Step I: 65°C, 5min Step II: 95°C, 20min	365nm, 400 mJ	Step I: 65°C, 2min Step II: 95°C, 5min

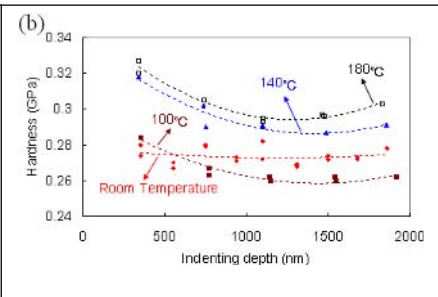
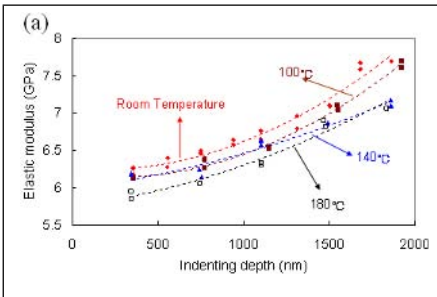
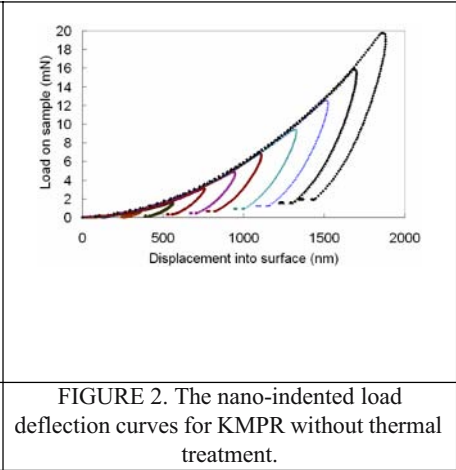
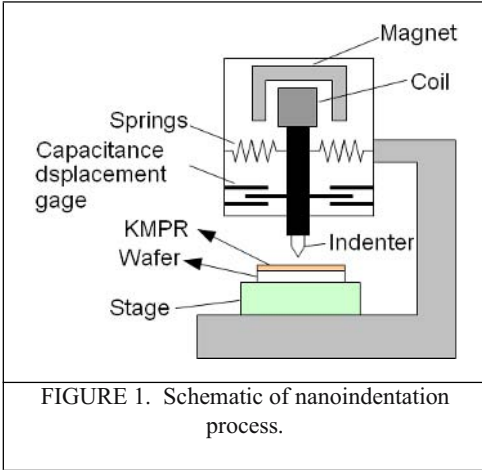


FIGURE 3. Mechanical properties of KMPR obtained by nanoindentation at different thermal treatment temperature (a) elastic modulus and (b) hardness.

**References**

1. Becker, E. W. et al. *Microelectronic Engineering*, vol. 4, no. 1, 35~56, 1986.
2. MicroChem Corp.1254 Chestnut Street Newton, MA 02464.
3. Oliver, W. C. and Pharr, G. M., *J. Mater. Res.* vol. 7, 1564, 1992.

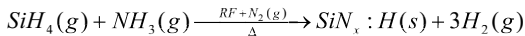


## MECHANICAL PROPERTIES MEASUREMENT OF PECVD SILICON NITRIDE AFTER RAPID THERMAL ANNEALING USING NANOINDENTATION TECHNIQUE

Hong-Yi Yan, Kuang-Shun Ou and Kuo-Shen Chen  
 Department of Mechanical Engineering  
 National Cheng-Kung University  
 Tainan, Taiwan, 70101, R.O.C.  
 kschen@mail.ncku.edu.tw

PECVD silicon nitrides have been widely used in MEMS and IC devices as a mask or barrier material. The mechanical properties of PECVD nitride subjected to thermal processing are traditionally important information for the device integrity and performance [1]. This paper explores the thermo-mechanical behaviour of PECVD nitride films after rapid thermal annealing (RTA) at 200 - 800°C using nanoindentation techniques. Major issues to be measured or observed are: residual stress, elastic modulus, hardness, and film cracking.

The experimental flow is shown in Figure 1. 5000Å PECVD nitrides were deposited on 4-inch silicon wafers using a Nano-Architect Research/BR-2000LL PECVD system at temperature between 250 and 400°C and a pressure of 5 Torr following the following formula:



After deposition, the wafers were die-sawed into square dies (10 mm × 10 mm). The initial curvatures were then inspected via a TENCOR INSTRUI/MA-1450 Profilometer. After inspection, specimens were then experienced rapid thermal annealing process using an Annealsys/AS-One 100 RTA system at temperatures of 200, 400, 600, and 800°C and with an annealing period of 60 seconds. After the RTA process, the curvatures of the corresponding specimens were measured again to evaluate the residual stress generation. Meanwhile, the elastic modulus, as well as the hardness, of the nitride specimens was also characterized by a MTS Nano Indenter XP nanoindenter using a Berkovich indenter head [2].

Figure 2 shows a typical specimen profile before and after RTA at 600°C. The increased curvature implies that residual tensile stress was generated during RTA process. The amount of residual stress generation can be estimated by converting the effective specimen curvature using Stoney's formula as 540MPa [3]. A typical set of nanoindentation data is shown in Figure 3 and it indicates that the hardness increases with the RTA temperature. A more comprehensive nanoindentation study results are shown in Figures 4 and 5 and those results suggest that the hardness and stiffness increase with the RTA temperature and the maximum indentation load. The maximum indentation load dependent hardness and elastic modulus is believed to be caused by the substrate effect. Finally, by SEM inspection, it was found that cracks would be generated for these nitrides after 600 and 800°C thermal processing. This suggested that the stress intensity factor at these temperatures might exceed the fracture toughness of the material. By the results obtained, it is possible to maintain structural integrity and improve fabrication performance in related applications.

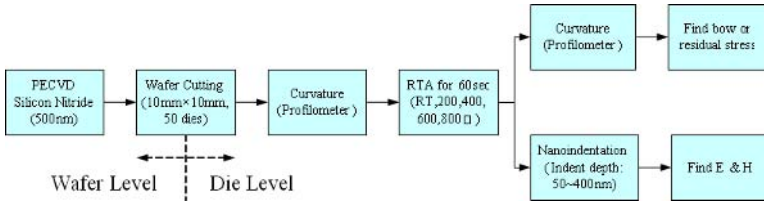


FIGURE 1. The experimental flow

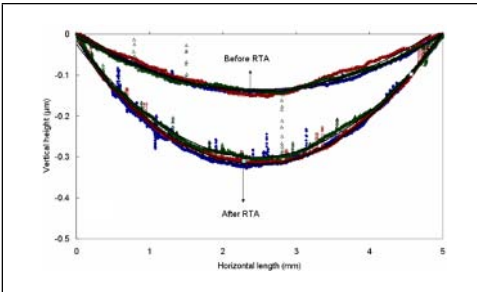


FIGURE 2. Surface profile of nitrides before and after RTA at 600°C

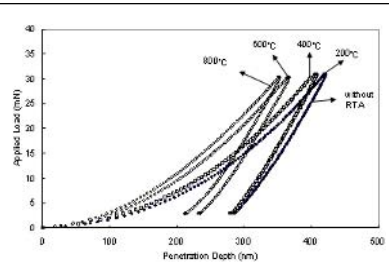


FIGURE 3. Load-deformation curves of nitride after different RTA processing

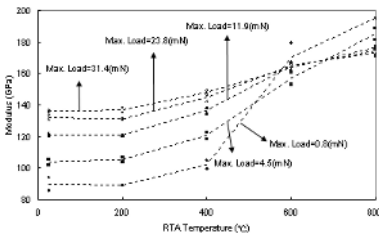


FIGURE 4. Modulus-RTA temperature curves at different Max Loads

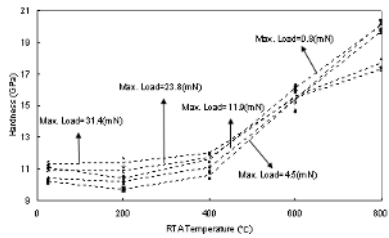


FIGURE 5. Hardness-RTA temperature curves at different Max Loads

**References**

1. Chen, K-S, Zhang, X. and Lin, S-Y, *Thin Solid Films*, vol. **434**, 190, 2003.
2. Oliver, W. C. and Pharr, G. M., *J. Mater. Res.*, vol. **7**, 1564, 1992.
3. Stoney, G. G., *Proc. R. Soc. London, A*. vol. **82**, 172, 1909.

## NOVEL PHASE UNWRAPPING ALGORITHM FOR RETRIEVING ESPI MAP WITH REAL PHYSICAL DISCONTINUITY

M.J. Huang and J.K. Liou  
Prof. and Chair of Mechanical Engineering, National Chung Hsing University  
250, Kuo-Kuang Road, Taichung, Taiwan, R.O.C.  
mjhuang@dragon.nchu.edu.tw

This paper aims to provide an effective and distortion-free approach for the phase unwrapping of digital speckle pattern interferometry (ESPI) map with real physical discontinuities. ESPI is a powerful measurement tool for industry. However, due to the speckle noise, its unwrapping job is quite difficult, especially, when treating ESPI map obtained from the deformation field of an object with certain degree of tear. The minimum  $L^p$  norm method proposed by Ghiglia and Romero [1] can treat the aforementioned problem with acceptable accuracy. However, the time needed is long. Therefore, a novel method with a hybrid of regional algorithm proposed by Gierloff [2], branch cut method proposed by Goldstein *et al.* [3] and parallel unwrapping method with region-referenced algorithm proposed by Huang and He [4] is presented herein. With this newly developed algorithm, quite noisy map coupled with real physical discontinuities can also be retrieved accurately and efficiently.

As it has been stated above, noisy speckle noise and real physical discontinuity should be circumvented simultaneously under treating ESPI map with real discontinuity. Therefore, a powerful and simple noise-immune algorithm with parallel pixels checking [4], which is designed to bypass the speckle noise induced inconsistencies (, basically exist in forms of either fringe interruptions or extra fringe pieces) is used to generate fringes shifting first. Usually, by several times of fringes shifting, the  $2\pi$  ambiguities of most isolated jumps can be successfully eliminated with a wrapped map with much clearer fringes left for further regional phase unwrapping. These phenomena have been studied and published by Huang and Lai [5]. Since the wrapped map is with real physical discontinuities, thus the physical shear should further be located and set as barriers to avoid any crossing among them. After that, regional phase unwrapping [2] can be easily applied further on and the phase retrieval job can be done with ease and correctness.

With the aid of the noise-immune algorithm [4] and image processing techniques, the breaking point of each fringe contour can be located. Further defining each fringe's shifting direction can help the successful barrier generation and the final regional 2 phase ambiguities eliminating.

The proposed algorithm is practically applied to a wrapped map obtained from ESPI experiment for out-of-plane deformation detection of a centrally loaded plate clamped along its four boundaries. The sample plate is with a break-through tear from its center up to the top center point of the upper edge. Therefore, the out of plane deformation of the torn plate is in a rotational phase distribution, which has been proven to be able to be unwrapped by the proposed algorithm herein. The experimental result of the wrapped map is shown in Fig. 1. (Since the size restriction of abstract file should be less than 200KB, therefore all the other figures, including the fringe-shifting ensemble, the fringe thinning results, the shear barrier, and the unwrapped result are deleted.)

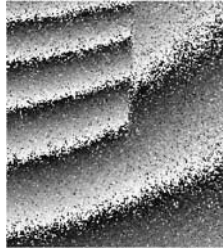


FIGURE 1. ESPI wrapped phase map with real physical discontinuity.

### References

1. Ghiglia D.C. and Romero L.A., *J. Opt. Soc. Am. A*, vol. **13**, 1999-2013, 1996
2. Gierloff J.J., *SPIE*, vol. **818**, 2-9, 1987
3. Goldstein R.M., Zebker H.A. and Werner C., *Radio Sci.* vol. **23**, 713-720, 1988
4. Huang M.J. and He Z.N., *Opt. Com.*, vol. **203**, 225-241, 2002
5. Huang M.J. and Lai C.J., *Opt. Eng.*, vol. **41**, 1373-1386, 2002

## WAVELENGTH SHIFT DETERMINATION USING A COMMON-PATH INTERFEROMETER

Shyh-Tsong Lin and Cheng-Chung Chang

Professor and graduate student, Department of Electro-optical Engineering, National Taipei University of Technology, Taipei 10608, Taiwan, R.O.C.  
f10402@ntut.edu.tw and s4658002@ntut.edu.tw

The wavelength scanning techniques are widely accepted in the systems adopted for measuring object parameters [1-6] in the past years and thus become more and more important. In general, the parameters to be determined are functions of the wavelength shift of the light source incident into the measurement system, the measurement resolutions thus highly depend on how small the wavelength shift can be detected. This reminds the researchers of developing the schemes for measuring the wavelength shift.

The wavelength shift of a beam can be determined by the use of a spectrometer [7], a system with a detection module whose intensity response is proportional to the wavelength [8], a system with a wavelength tracing grating [9], or an unequal-path [10] or a common-path interferometer [11]. In which, the unequal-path one gives high measurement resolution and the common-path one provides high measurement stability. To enhance an interferometer so it possesses both the properties of high measurement resolution and stability, a feedback control system [12] is built into the unequal-path interferometer to eliminate the environment disturbances.

A novel interferometer is thus proposed. It is composed of a polarizer with transmission axis at  $45^\circ$ , a calcite prism with optical axis at  $0^\circ$ , a quarter-wave plate with slow axis at  $45^\circ$ , an analyzer and a chopper rotated co-axially, and two photo-detectors  $D_m$  and  $D_r$ . A laser beam is first separated into a measurement beam and a reference beam; the measurement beam passes through the polarizer, calcite prism, quarter-wave plate, and analyzer to generate an interference signal  $I_m$  on detector  $D_m$ ; the reference beam passes through the chopper to generate a TTL signal  $I_r$  on the detector  $D_r$ ; both these two signals are delivered to a phase meter where the phase difference between these two signals is extracted. As the wavelength of the laser beam is shifted by  $\Delta\lambda$ , the increment of the phase difference is

$$\phi = 2\pi \cdot \Delta n \cdot d \frac{\Delta\lambda}{\lambda^2} \quad (1)$$

where  $\Delta n$  is the birefringence of calcite crystal,  $d$  is the thickness of the calcite prism, and  $\lambda$  is the wavelength.

The above derivation shows that the wavelength shift can be determined as the increment of the phase difference is obtained. Besides, the interferometer is an unequal- and common-path one. The interferometer can thus provide high resolution and high stability detections of wavelength shift.

In this paper, a setup developed to accomplish the interferometer is also described, and the experimental results of using this setup to determine the wavelength shift of a laser source and the wavelength shift of the light reflected from a loaded fibre-optic Bragg grating are finally presented. The results agree the validity and applicability of the interferometer.

**References**

1. H. Kikuta, K. Iwata, and R. Nagata, *Appl. opt.*, vol. **25**, 2976-2980, 1986.
2. T. Zhang and M. Yonemura, *Appl. opt.*, vol. **35**, 5650-5656, 1996.
3. Y. Otani, A. Tanahashi, and T. Yoshizawa, *Opt. Eng.*, vol. 35, 1070-1073, 1996.
4. A. Yamamoto and I. Yamaguchi, *Opt. laser technol.*, vol. **32**, 261-266, 2000.
5. S. H. Lu, C. I. Chiueh, and C. C. Lee, *Appl. opt.*, vol. **41**, 5866-5871, 2002.
6. G. Coppola, P. Ferraro, M. Iodice, and S. D. Nicola, *Appl. opt.*, vol. **42**, 3882-3887, 2003.
7. D. C. O'Shea, *Spectrometers*, Chap. 9 in *Elements of Modern Optical Design*, John Wiley and Sons, 1985.
8. S. M. Melle, K. Liu, and R. M. Measures, *IEEE photonics technol. lett.*, vol. **4**, 516-518, 1992.
9. D. A. Jackson and A. B. Lobo Ribeiro, *Opt. lett.*, vol. **18**, 1192-1194, 1993.
10. A. D. Kersey, T. A. Berkoff and W.W. Morey, *Opt. lett.*, vol. **18**, 72-74, 1993.
11. K. H. Chen, C. C. Hsu, and D. C. Su, *Opt. commun.*, vol. **209**, 167-172, 2002.
12. Y. N. Ning, W. J. Shi, K. T. V. Grattan, A. W. Palmer, and B. T. Meggitt, *Opt. commun.*, vol. **138**, 27-30, 1997.

## ON THE THERMAL DISSIPATION OF THE BOARD-LEVEL ELECTRONIC PACKAGING

Hsien-Chie Cheng<sup>1</sup>, Wen-Hwa Chen<sup>2</sup> and Hwa-Fa Cheng<sup>2</sup>

<sup>1</sup>Dept. of Aerospace and Systems Engineering, Feng Chia University  
100, Wenhwa Rd., Seatwen, Taichung, Taiwan 40724, R.O.C.

<sup>2</sup>Dept. of Power Mechanical Engineering, National Tsing Hua University  
101, Section 2 Kuang Fu Road, Hsinchu, Taiwan 30013, R. O. C.  
hccheng@fcu.edu.tw, whchen@pme.nthu.edu.tw

Nowadays, thermal management for semiconductor devices has become critical. A poor thermal management and design in a high power electronic device may result in a significant chip junction temperature and considerable temperature gradient among components within a package. Mulgaonker et al.[1] indicated that in a typical design guideline, the temperature of chips could not exceed 105°C and that of PCB should be less than 90°C. Thus, the main objective of this work is to study the heat dissipation mechanism of the board-level Plastic Ball Grid Array (PBGA) electronic packaging (Fig. 1(a)) in a steady state under a natural convection environment based on JEDEC specification [2-5]. To achieve the goal, theoretical characterization that integrates a detailed three-dimensional finite element modeling technique (Ellison[6]) is proposed. The validity of the proposed theoretical characterization is confirmed in terms of chip junction temperature as well as junction-to-ambient (J/A) thermal resistance through an effective infrared(IR)-thermography-based thermal characterization technique (Fig. 1(b)) and thermal test die measurement (Chen et al.[7]). To perform surface temperature measurement (Fig. 2(a)) using an IR thermometer, the black paint coating is applied on the surface of packages so as to calibrate the surface radiation. The associated emissivity is approximately assessed using a simple calibration experiment, and besides, an appropriate thickness of the coating is determined. Moreover, to demonstrate the accuracy of the thermal test die measurement, the uncertainty analysis is also performed. Based on the validated theoretical model, the influences of various design parameters of the PCB structure on the thermal performance are studied.

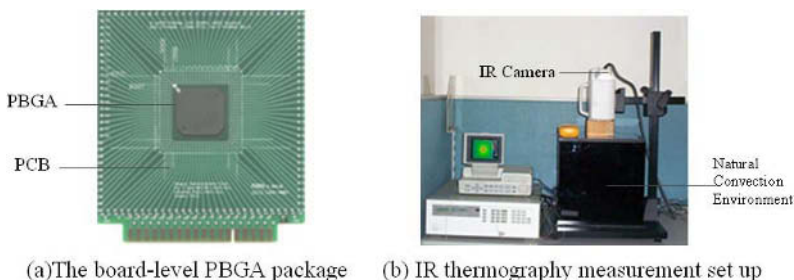


FIGURE 1. Test vehicle and experimental set up

Results show that the proposed theoretical model turns out to be very effective in predicting the thermal performance of the board-level PBGA packages (Fig. 2). In addition, the worst possible uncertainty in the measured power, based on the specific power supply, is about 0.005

watt (w) and that in the chip junction temperature measurement is about 0.78°C. In order to reduce the chip junction temperature so as to better the packages' board-level thermal performance, reducing the in-plane and out-of-plane thermal resistances of the PCB can be very essential and effective since it serves as heatsink of the PBGA package.

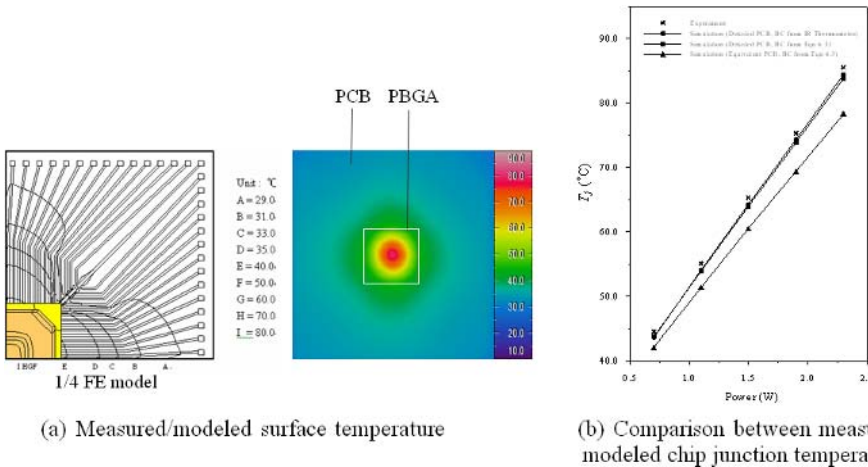


FIGURE 2. Test vehicle and experimental set up.

**References**

1. Mulgaonker, S., Chambers, B., Mahalingam, M., Ganesan, G., Hause, V. and Berg, H., 1994, *IEEE Transaction on Components, Packaging, and Manufacturing Technology-Part A*, vol. 17, No. 4, pp. 573-581.
2. JEDEC Standard EIA/JESD51, *Methodology for the Thermal Measurement of Component packages (Single Semiconductor Device)*, 1995.
3. JEDEC Standard EIA/JESD51-1, *Integrated Circuits Thermal Measurement Method - Electrical Test Method (Single Semiconductor Device)*, 1995.
4. JEDEC Standard EIA/JESD51-2, *Integrated Circuits Thermal Test Method Environmental Conditions - Natural Convection (Still Air)*, 1995.
5. JEDEC Standard EIA/JESD51-9, *Test Boards for Area Array Surface Mount Package Thermal Measurements*, 1995.
6. Ellison, G.N., *Thermal Computations for Electronic Equipment*, R.E. Krieger Publishing Company, Mala-Bar, Florida, 1989.
7. Chen, W.H., Cheng, H.C., and Shen, H.A., *IEEE Transactions on Components and Packaging Technologies*, vol. 26, No. 1, March, 2003.



## USE OF DIGITAL IMAGE CORRELATION TECHNIQUE TO MEASURE DENTAL COMPOSITE SHRINKAGE

Shu-Fen Chuang<sup>1</sup>, Terry Yuan-Fang Chen<sup>2</sup> and Chih-Han Chang<sup>3</sup>

<sup>1</sup> Institute of Oral Medicine

<sup>2</sup> Department of Mechanical Engineering

<sup>3</sup> Institute of Biomedical Engineering

National Cheng Kung University

Tainan, Taiwan 70101, R.O.C.

ctyf@mail.ncku.edu.tw

Resin-based composites have become widely used in dental restorative materials. Although they exhibit advantages as tooth-color appearance and enough strength, the polymerization shrinkage is criticized as their inherent defect. Clinically, shrinkage leads to post-restorative consequences such as distortion of restorations, the bonded tooth deflection and even microfracture in a weakened tooth [1, 2]. A method to identify the shrinkage direction and amount is necessary in evaluating these materials.

Digital image correlation (DIC) is an application based on the comparison of two characterized images. With a sequence of analyzing gray-value distributions, establishing the correlation, and utilizing interpolation functions to obtain subpixel accuracy, the displacement of a specific point can be identified [3]. The objective of the present study was to apply the DIC to examine the polymerization shrinkage of a composite material and the displacement of surrounded tooth.

A stainless steel cube with a rectangular slot was used as a simulated cavity. The composite was placed into the slot. One side of the composite was sprayed with a white powder to create a characteristic pattern. The reference image was captured and digitized by an image acquisition system which was assembled with an optical microscope and a high-resolution CCD camera. Following irradiation under quartz-tungsten halogen lamp, the deformed image was captured and the images were analyzed by a DIC program.

Eight intact extracted human molars were used for the composite polymerization in real teeth. A transverse cavity, with 4 mm deep and 2 mm wide, was prepared on the occlusal surface. The cavity surfaces were treated with resin adhesive then filled with dental composite. The speckle pattern was generated on the restoration. The images of unpolymerized composite and post-polymerized images at 1 min, 5min and 10 min after light curing were recorded by the camera.

Using a 50 x 50 pixels sub-image, the deformation on the top surface of the composite in the slot of the steel cube was determined. It was found that the displacement component along the y-direction of all the measured points was greater than that along the x-direction except at two attached ends. The largest y-direction displacement was 54  $\mu$ m. In the real teeth, these movements on the boundaries of the composites at different time were also measured. The correlation coefficients obtained between the pre-cured and post-cured images were greater than 99% in all cases. The amount of deformation ( $\mu$ m) of different points at different time on the occlusal surface is investigated. The 10 min post-cured image was found to have the greatest amount of deformation, which indicated that the deformation continued after light irradiation. In addition, the greatest deformation was on the free surfaces, and the least on the gingival wall.

A novel application of DIC to measure dental composite shrinkage is presented. Using this technique, the displacement of specific location can be identified and the overall profile of

polymerization shrinkage can be described. This technique can be extended to evaluate different composite materials and also for the improvement of restorative techniques.

### References

1. Tantbirojn, D., Versluis, A., Pintado, M.R., DeLong, R., and Douglas, W.H., *Dent Mater*, vol. **20**, 535-42, 2004.
2. Kanca, J III., and Suh, B.I., *Am J Dent*, vol. **12**, 107-12, 1999.
3. Bruck, H. A., McNeil, S. R., Sutton, M. A. and Peters, W. H. *Exp Mech*, vol. **29**, 261-7, 1989.

## THE FLEXIBLE 3-DIMENSIONAL LOAD MEASUREMENT SENSOR USING THE ELASTIC SPHERE

Noboru Nakayama, Jianhui Qiu, Tetsuo Kumazawa and Kenji Torii  
Akita Prefectural University

84-4 Tsuchiya-Ebinokuchi, Yurihonjo, Akita/ 015-0055, Japan  
Graduate school of Akita Prefectural University

84-4 Tsuchiya-Ebinokuchi, Yurihonjo, Akita/ 015-0055, Japan  
nakayama@akita-pu.ac.jp, qiu@akita-pu.ac.jp, kumazawa@akita-pu.ac.jp  
m08a014@akita-pu.ac.jp

A product is manufactured by the robot at a factory. The present robot's surface (especially robot arm part) is a metal. Therefore, it is dangerous if human contacts a robot. Since it is certain to use a robot for medical treatment or welfare in the near future, a possibility that a work robot and a human will contact becomes high. When a robot and human being will live together in the near future, it is necessary to develop the sensor which carries out flexible modification. Although the 2-dimensional distribution load measuring method using flexible material is proposed, the sensor which can detect load in three dimensions is not developed [1]-[2].

The purpose of this research is developing the flexible 3-dimensional load measurement sensor using the elastic sphere.

Figure 1 shows the principle of load measurement of the developed sensor. The developed sensor consists of a skin layer, an elastic sphere, and a load measurement layer. The load can be divided into the normal load  $P$  and the shearing load  $W$  as shown in Figure 1. If the normal load  $P$  loads to a sensor, an elastic sphere will change. Therefore, an increase of the normal load  $P$  increases the contact surface product  $A_C$  of an elastic sphere and a load measurement layer. That is, the normal load  $P$  is measured by measuring the contact area  $A_C$ . If the shearing load  $W$  loads to a sensor, the spherical center is moved from a datum point (center). Therefore, an increase of the shearing load  $W$  increases the  $X$  (the distance from a datum point). That is, the shearing load  $W$  can be measured for by measuring  $X$ . The load measurement layer has the microswitch in the position of - shown in Fig.1. A microswitch will be turned on if a load measurement layer contacts an elastic sphere by load.

The material of the elastic sphere is natural rubber, and silicone oil (120ml) was poured into the elastic sphere. The diameter of an elastic sphere was 60mm.

The sensor was loaded by the normal load  $P$  or the shearing load  $W$ , and the contact area  $A_C$  and the  $X$  (the distance from a datum point) were measured.

Figure 2 shows the relationship between the normal load  $P$  and the contact area  $A_C$ . The contact area  $A_C$  is increasing as the normal load  $P$  increases.

Figure 3 shows the relationship between the shearing load  $W$  and the  $X$  ( $P=10N$ ).  $X$  (the distance from a datum point) is increasing with the increase in the shearing load  $W$ .

In this research, the new sensor was developed using these principles. The following conclusions were obtained.

1. The normal load and the contact area of an elastic sphere and a load measurement layer are proportionality.
2. The shearing load and the distance from a datum point are proportionally.

From the above result, the flexible 3-dimensional load measurement sensor using the elastic sphere has been developed.

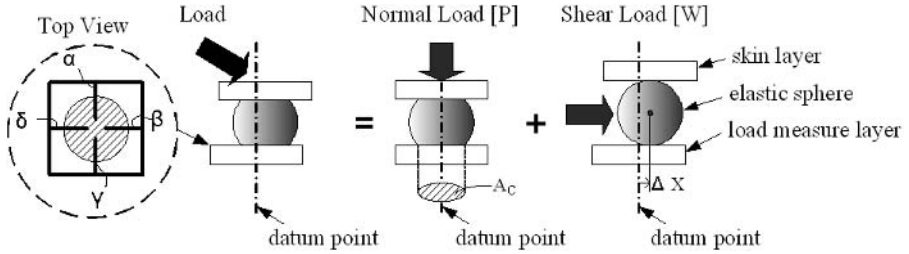


FIGURE 1. The principle of load measurement of the developed sensor

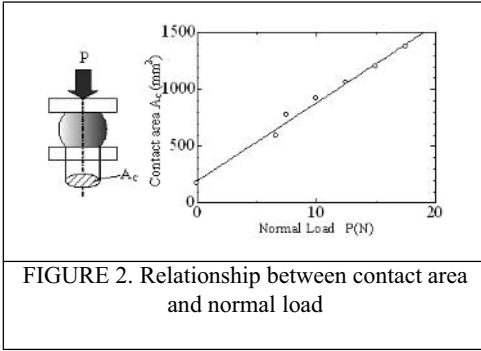


FIGURE 2. Relationship between contact area and normal load

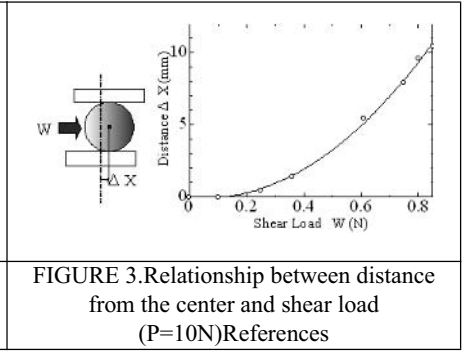


FIGURE 3. Relationship between distance from the center and shear load (P=10N)References

**References**

1. R.Tajima et al., Advanced Robotics, Vol. 16, No. 4, 381-397, 2002.
2. Jonathan.E, et al., J. Micromech. Microeng. Vol. 13, 359-366, 2003.

## IN-PLANE RESIDUAL STRESS ANALYSIS COMBINING HOLE-DRILLING AND MOIRÉ INTERFEROMETRY

J.N. Aoh, C.Y. Huang and J.Y. Lee

Department of Mechanical Engineering, National Chung Cheng University  
Minhsiung, Chiayi, 621, Taiwan, R.O.C.  
imejna@ccu.edu.tw

Residual stress measurement combining hole-drilling method and moiré interferometry has been developed to improve accuracy of stress measurement and has opened a new area for novel stress measurement technique [1, 2]. Validation of the technique under uni-axial loading in a previous work [3] has established the relationship between moiré patterns and the associated stress magnitude. Based on this preliminary work, a biaxial loading frame shown in Fig. 1 was developed to apply a biaxial state of loading on the test specimen, on which both the hole-drilling and moiré interferometry were then conducted. A four-beam interferometry optics and a hole-drilling set-up were integrated with the biaxial loading frame into a system, shown in Fig. 2 with which a known biaxial stress state can be applied to the specimen. The corresponding fringe patterns obtained from the moiré interferometry after hole-drilling were obtained to correlate with the corresponding stress state. This provides a quantitative data base for the relationship between in-plane residual stress and the moiré fringe pattern. Specimen grating with a frequency of 1200 lines/mm was applied to specimens made of 6061-T6 aluminum alloy (3mm × 50mm × 50mm). The milling guide was moved on a motorized precision stage at the speed of 1.25m/sec. The successive drilled hole depths were 0.3 to 1.2mm with 1.6mm in diameter.

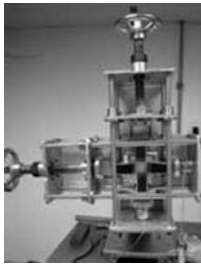


FIGURE 1. The bi-axial loading frame with specimen set-up.

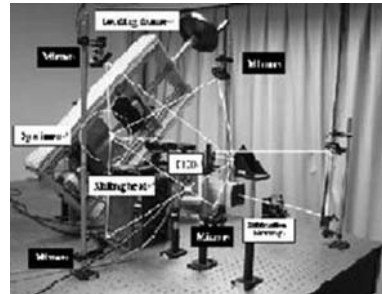


FIGURE 2. Four-beam Moiré interferometry and hole-drilling set-up integrated with loading frame.

Equations were derived for the relationship between displacement  $u$ ,  $v$  at the in-plane stress state around the hole. Also the relationship between  $u$ ,  $v$  and the fringe geometry can be explicitly obtained. Eq. (1) is the expression for  $u$ -field. Similar equation was also derived for  $v$ -field. With these equations, the experimental results can be compared with the analytical ones.

$$u = \frac{(1+\nu)}{2E} \left[ \frac{R(\sigma + \sigma)}{\sqrt{x+y}} - \frac{R(\sigma - \sigma)}{(x+y)^2} \frac{x-y}{x+y} \cos 2\theta + \frac{R(\sigma - \sigma)}{(x+y)^2} \frac{2xy}{x+y} \sin 2\theta + \frac{4R(\sigma - \sigma)}{\sqrt{x+y}(1+\nu)} \frac{x-y}{x+y} \cos 2\theta - \frac{4R(\sigma - \sigma)}{\sqrt{x+y}(1+\nu)} \frac{2xy}{x+y} \sin 2\theta \right] \frac{x}{\sqrt{x+y}} - \frac{(1+\nu)}{2E} \left[ -\frac{R(\sigma - \sigma)}{(x+y)^2} \frac{2xy}{x+y} \cos 2\theta - \frac{R(\sigma - \sigma)}{(x+y)^2} \frac{x-y}{x+y} \sin 2\theta + \frac{2R(\nu-1)(\sigma - \sigma)}{\sqrt{x+y}(1+\nu)} \frac{2xy}{x+y} \cos 2\theta + \frac{2R(\nu-1)(\sigma - \sigma)}{\sqrt{x+y}(1+\nu)} \frac{x-y}{x+y} \sin 2\theta \right] \frac{y}{\sqrt{x+y}} \quad (1)$$

Results and discussion

Upon applying the grating on a specimen, the direction of grating may deviate from the specimen axis. Thus the effect of the angle of optical grating on the fringe pattern was studied analytically and experimentally under uni-axial and biaxial state. Fig. 3 shows the development of fringe patterns at different hole depth. Fig. 4 reveals the u-field fringe pattern at hole depth 1.2mm, stress at 52.18MPa and 55MPa and angles of optical grating  $0^0$  and  $55^0$  respectively. The results show a good agreement between prediction contours and experimental fringes. Similar results are obtained for v-field. The effect of polarization angle of the laser beam on the fringe patterns is showed in fig.5. Different polarization angles caused different degrees of contrast while the fringe patterns did not change substantially. The results provide a basic knowledge on the quantitative correlation between fringe date and in-plane residual stress. The experimental setup for biaxial loading has not been developed elsewhere.

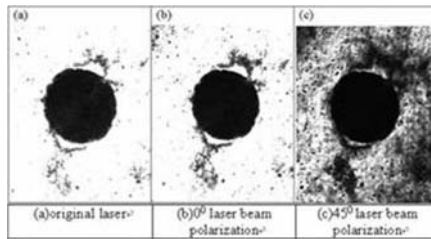
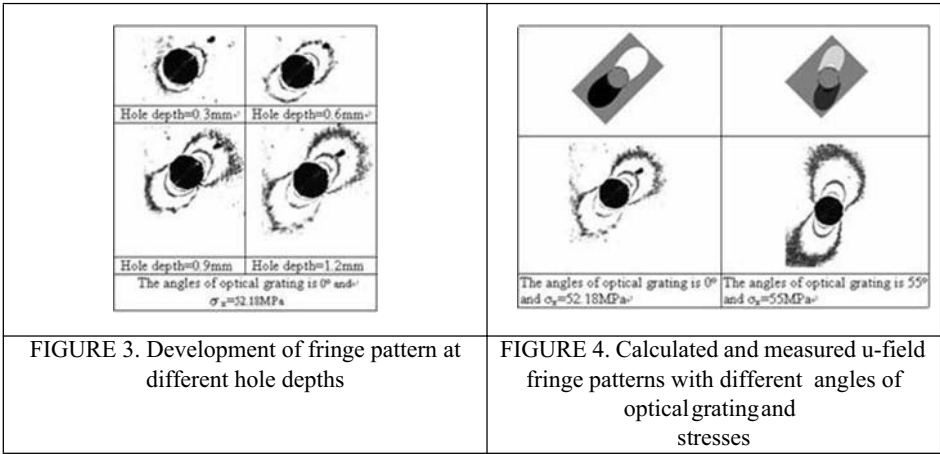


FIGURE 5. Fringe patterns at different laser beam polarization

References

1. Z. Wu, J. Lu, B. Han, *J. Appl. Mech. Trans ASME*, vol. **119**, 1, 1997, pp. 837-843
2. Z. Wu, J. Lu, B. Han, *J. Appl. Mech. Trans ASME*, vol. **119**, 1, 1997, pp. 844-850
3. J.N. Aoh, H.M. Chen, Y.S. Chen, *In Proceedings of ICEM12-12<sup>th</sup> International Conference on Experimental Mechanics, 29 August-2 September, 2004 Politecnico di Bari, Italy*

## THE DEVELOPMENT AND APPLICATION OF MAGNETOPHOEELASTICITY

A. Conway, R. Tomlinson and G. Jewell

University of Sheffield

Department of Mechanical Engineering Sheffield, United Kingdom

University of Sheffield

Department of Electronic and Electrical Engineering Sheffield, United Kingdom

a.conway@sheffield.ac.uk, r.a.tomlinson@sheffield.ac.uk, g.jewell@sheffield.ac.uk

Magnetophotoelasticity was conceived as a viable method of solving the problem of integrated three-dimensional photoelasticity [1]. In particular, the technique allows for the solution of stress distributions that vary along the light path in a manner which produces an integrated optical effect of zero. By placing a three dimensional model in a magnetic field which is parallel to the direction of the incident polarised light, the light experiences a rotation due in part to the birefringence of the model and in part due to an induced Faraday rotation. As a consequence, it becomes possible to measure an optical effect and describe the stress distribution along the light path.

To date, application of the technique has relied upon experimental determination of the characteristic parameters in both the presence and absence of the magnetic field. This information, together with an assumption regarding the form of the stress field, has enabled the stress distribution to be accurately described [1-4].

Perhaps the greatest drawback of the technique is the relatively small Faraday rotation that is achievable under a static magnetic field. Therefore, previous work has dealt with increasing the Faraday rotation in order to reduce the unusually high experimental accuracy which is otherwise needed to obtain the characteristic parameters. Methods have included the use of modelling materials with a high Verdet constant [1], the use of optically active modelling materials in addition to the use of a magnetic field [5], the use of multiple reflections of light through the model [6] and the use of pulsed magnetic fields [3, 4].

The authors will demonstrate that a magnetopolariscope has been constructed that utilises pulsed magnetic fields. The benefits of which are two-fold: a high magnetic field increases the Faraday rotation through a given model and allows intensity data to be collected at a large number of discrete magnetic field strengths simultaneously. Full field intensity images are collected by the use of a high speed video camera intimately linked to the pulse of the magnetic field. Both the concept design and the constructed magnetopolariscope will be discussed.

Furthermore, the authors will describe how the equivalence theorem, expressed in the Mueller calculus, can be used to solve for an unknown stress distribution by using data collected at different field strength values [7-9]. This 'multiple field' technique, despite having been proposed in earlier work, has not yet been utilised to solve for unknown three dimensional stress distributions. The authors' ultimate aim is to use the technique to determine the principal stress difference at a sufficiently large number of discrete points to more accurately describe the stress distribution along the light path. This would enable not only eccentricity in the parabolic form of stress in toughened glass to be determined, but also the presence of membrane stresses and zones of stress concentration.

---

**References**

1. Aben, H. K., *Experimental Mechanics*, vol. **10**, 97-105, 1970.
2. Clarke, G. P., McKenzie, H. W. and Stanley, P., In *Proceedings: Mathematical, Physical and Engineering Sciences*, vol. **455**, 1149-1173, 1999.
3. Gibson, S, Tomlinson, R A, and Jewell, G W, (2006) Full-field pulsed magneto-photoelasticity - A description of the instrument, *Journal of Strain Analysis for Engineering Design*, **41**(2), 161 – 170.
4. Gibson, S, Tomlinson, R A, and Jewell, G W, (2006) Full-field pulsed magneto-photoelasticity – Experimental Implementation, *Journal of Strain Analysis for Engineering Design*, **41**(2), 171 - 182.
5. Aben, H. K., Idnurm, S. J., Klabunovskii, E. I. and Uffert, M. M., *Experimental Mechanics*, vol. **8**, 361-366, 1974.
6. Ainola, L., *Journal of Optics A: Pure and Applied Optics*, vol. **6**, 51-56, 2004.
7. Hurwitz, H. and Jones, R. C., *Journal of the Optical Society of America*, vol. **31**, 7, 493-499, 1941.
8. Theocaris, P. S. and Gdoutos, E. E., In *Proceedings of the 6th International Conference on Experimental Stress Analysis, Sep 18-22, Munich, West Germany*, 1978.
9. Hermanne, A., *Bulletin De La Classe Des Sciences Academie Royale De Belgique*, vol. **58**, 2, 262-291, 1972.



**DETERMINING INDIVIDUAL STRESSES AROUND A NEAR-EDGE HOLE  
SUBJECTED TO AN OFFSET LOAD USING THERMOELASTICITY**

S-J. Lin<sup>1,a</sup>, D.R. Matthys<sup>2,b</sup>, S. Quinn<sup>3,c</sup>, J.P. Davidson<sup>1,d</sup>, B.R. Boyce<sup>4,e</sup> and R.E. Rowlands<sup>1,f</sup>

<sup>1</sup>University of Wisconsin, Madison, WI, USA

<sup>2</sup>Marquette University, Milwaukee, WI, USA

<sup>3</sup>University of Southampton, Southampton, United Kingdom

<sup>4</sup>Stress Photonics Inc., Madison, WI, USA

<sup>a</sup>jiun@cae.wisc.edu, <sup>b</sup>don.matthys@marquette.edu, <sup>c</sup>s.quinn@soton.ac.uk,

<sup>d</sup>jpgdavidson@wisc.edu, <sup>e</sup>bboyce@stressphotonics.com<sup>†</sup> <sup>f</sup>rowlands@engr.wisc.edu

Thermoelastic stress analysis (TSA) is a full-field experimental stress analysis technique, see Dulieu-Barton and Stanley [1], which measures the small temperature change developed in a solid under elastic cyclic loading. For linear elastic, homogeneous materials it is assumed that adiabatic conditions prevail and thus the temperature change is directly proportional to the change in the sum of the principal surface stresses ( $\Delta(\sigma_1 + \sigma_2)$ ). However, engineering analysis frequently rely on a knowledge of the individual stress components, which often requires additional methods to separate the stresses.

This is avoided by synergizing a stress function in real, polar coordinates (see Lin *et. al.* [2]) with experimental TSA data to determine the individual stresses. The particular case considered in this paper is an aluminium plate that contains a near-edge circular hole when the plate is subjected to a concentrated edge load away from the hole, Fig. 1. The coefficients of the series representation of the stress function are evaluated from the thermoelastic data and the least squares method. Imposing the traction-free conditions analytically, rather than discretely, on the edge of the hole enables the number of coefficients that must be retained in the stress function to be significantly reduced, as well as the number of equations involved in the least squares process. Such problems can also be solved using photoelastic isochromatics. However, whereas the latter approach typically necessitates the use of non-linear least squares analysis, TSA only requires linear least squares. TSA, which can be applied to the actual material of interest (no model or coating is needed, other than perhaps a thin layer of paint), also benefits from the availability of contemporary commercial systems capable of providing extensive amounts of data in a matter of minutes.

The complete individual stresses are determined thermoelastically on, and around the edge of the hole. Fig. 2 compares the TSA-evaluated tangential stress (TSA(Offset)) around the edge of the hole with that predicted using ANSYS and the agreement is generally good.

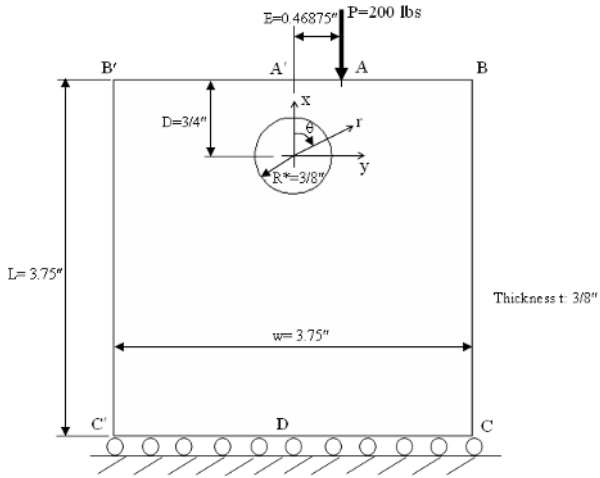


FIGURE 1. Schematic geometry of offset-loaded semi-infinite plate with a near edge hole.

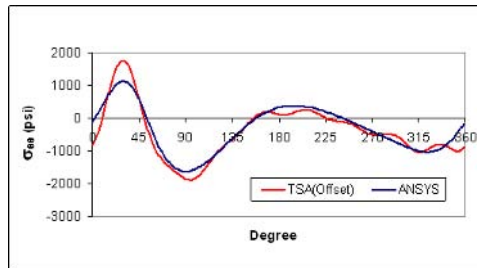


FIGURE 2. Thermoelastically determined tangential stress at the hole rim.

## References

1. Dulieu-Barton, J.M. and Stanley, P., *J. of Strain Analysis*, vol. **33**, 93-104, 1998.
2. Lin, S-J., Matthys, D.R. and Rowlands, R.E., In *Proceedings of SEM Annual Conference and Exposition on Experimental and Applied Mechanics*, Portland, 2005, Paper Reference 186 [9 pp on CD].

## A NEW HETERODYNE POLARISCOPE FOR SEQUENTIAL MEASUREMENTS OF MULTI-PARAMETER IN A MULTIPLE-ORDER WAVEPLATE

Yu-Tsan Jeng and Yu-Lung Lo

National Cheng Kung University, Department of Mechanical Engineering

No. 1, University Road, Tainan City 701, Taiwan, R.O.C.

loyl@mail.ncku.edu.tw

A new heterodyne polariscope with sequential measurements in the complete optical parameters of linear birefringence materials is proposed. In this study, a multiple-order crystalline quartz quarter-waveplate used as a sample is tested by two sequential setups. In the first setup, we use an electro-optic modulator to modulate the circular heterodyne polariscope and then the phase-locked technique is applied to precisely measure the principal axis angle. In the second setup, after removing the first quarter waveplate from the first setup, it comes into a linear heterodyne polariscope, and again we use the phase-locked technique to extract the apparent retardance. Furthermore, tilting the sample and placing a known-thickness material into the second setup, the order, thickness and refractive indices ( $n_e$  and  $n_o$ ) of a multiple-order waveplate are then all determined by using the new proposed algorithm.

The configuration of two optical setups in the proposed sequential measurement method by the phase-locked methodology is shown in Figure 1.

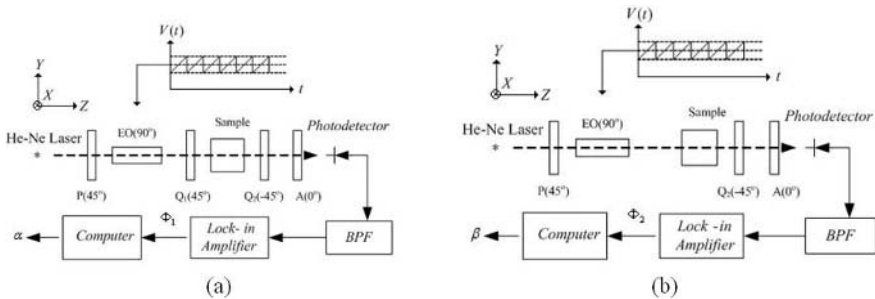


FIGURE 1. Setup in the phase-locked methodology

The configuration in Figure 1(a) is based on the circular polariscope and that in Figure 1(b) based on the linear polariscope. The only difference between them is that the first quarter waveplate is removed in Figure 1(b).

According to the Jones matrix formalism, the detected intensity from the configuration in Figure 1(a) is

$$I_1 = I_{dc} (1 - \sin \beta \sin(\omega t + \frac{\pi}{2} - 2\alpha)) = I_{dc} - R_1 \sin(\omega t + \Phi_1) \quad (1)$$

The intensity expression for e configuration in Figure 1(b) is expressed as

$$I_2 = I_{dc} (1 + \sqrt{(\sin \beta \cos 2\alpha)^2 + (\cos \beta)^2} \sin(\omega t - \tan^{-1}(\cos 2\alpha \tan \beta)))$$

$$= I_{dc} + R_2 \sin(\omega t - \Phi_2) \tag{2}$$

A lock-in amplifier can be employed to lock the ac component of the output intensities,  $I_1$  and  $I_2$ , at the reference frequency  $\omega$  in order to measure the phase terms:  $\Phi_1$  and  $\Phi_2$ . Consequently, the principal axis angle,  $\alpha$ , and the phase retardation,  $\beta$ , of a sample can be determined. The new heterodyne polariscope for sequential measurements is presented. The flow chart of this whole idea is illustrated in Figure 2. Since the birefringence ( $n_e - n_o$ ) of sapphire, quartz, sellaite and wurtzite are ranged from 0.0082 to 0.022, the order of two standard plates made from one of materials will be equal if the thickness difference of two standard plates is within 0.03 mm. It is noticed that the phase retardations of two standard plates,  $\beta_1$  and  $\beta_2$ , can be measured by Figure 1(b) as well. Thus, only the thickness of two standard plates,  $d_1$  and  $d_2$ , should be known in advance. As a result, it enables the sequential measurements in the principal axis angle ( $\alpha$ ), phase retardation ( $\beta$ ), order ( $m$ ), thickness ( $d$ ) and refractive indices ( $n_e$  and  $n_o$ ) of a multiple-order waveplate successfully.

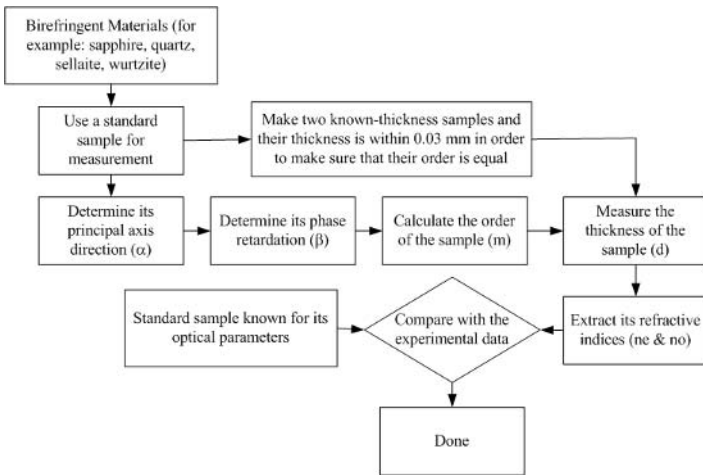


FIGURE 2. Flow chart

In experiments, a multiple-order quarter waveplate made of quartz is chosen for demonstration. There have average absolute errors of  $0.2167^\circ$  and  $0.15\%$  with respect to the principal axis angle and phase retardation that is within the uncertainty range of commercial quarter waveplates. Besides,  $m = 7$ ,  $d = 0.502965$  mm and refractive indices ( $n_e = 1.5553$  and  $n_o = 1.5462$ ) also have a good agreement with the sample data. The precise measurements in different parameters are all limited by the resolution in a lock-in amplifier.

## MEASUREMENTS FOR THE OPTICAL PARAMETERS OF LINEAR BIREFRINGENCE MATERIALS BY USING THERMAL LIGHT POLARIZATION-SENSITIVE OPTICAL COHERENCE TOMOGRAPHY

Yu-Lung Lo<sup>a,\*</sup>, Chia-Chi Liao<sup>a</sup>, and Cheng-Yen Yeh<sup>b</sup>

<sup>a</sup>National Cheng Kung University, Department of Mechanical Engineering

<sup>b</sup>Institute of Micro-Electro-Mechanical System Engineering

No.1, Ta-Hsueh Road, Tainan 701, Taiwan, R.O.C.

loyl@mail.ncku.edu.tw

Optical coherence tomography (OCT) developed by Huang *et al.* [1] is an emerging optical imaging technique that provides micrometer-scale cross-sectional images of tissue structure without invasion. In earlier research, there has been the report of the measurement in the refractive index and thickness issued by Tearney *et al.* [2] by use of OCT, and the result is good for homogeneous material. However, many optical materials have birefringence property in practice, and this conventional OCT does not have the capability to sense the information in the change of the polarization state caused by the birefringence of materials.

The polarization-sensitive optical coherence tomography (PSOCT) developed by Hee *et al.* [3] is a polarimetry-based birefringence measurement technique that uses a light of known polarization state to probe the sample and measures the changes in this state after propagation through the sample. Therefore, the phase retardation can be extracted by the change of the interferometric signal between orthogonal linear polarization modes at the reflective surface in a linear birefringence sample.

In this study, a new PSOCT structure is proposed by modifying the OCT that have been developed earlier as shown in Fig. 1. The new structure combines the polarimetry technique for measurement of the birefringence property and employs the thermal light source for the higher resolution in improving capability of extracting the extraordinary and ordinary refractive indices. Furthermore, the new structure needn't the highly precise scanning stage and stage controller by inserting a fixed beam as the reference signal.

As a result, the POSCT system can measure the thickness, mean refractive index, phase retardation and optical axis orientation of the linear birefringence sample simultaneously. The measured data are in good agreements, and one of the measured results in the optical axis orientation of QWP is shown in Fig. 2. The error could be found due to the dispersion effects from the broadband source used in the new structure. Since the optical axis orientation is obtained, the sample could be rotated at the designated angle, and the QWP in the sample arm is removed to generate the pure linear polarized light which incidents upon the sample. If the polarization state just corresponds to the optical axis of the sample, the measured refractive index would be the extraordinary refractive index. Similarly, the ordinary refractive index also could be measured. This novel polarization-sensitive low coherence interferometry can be used to extract the complete optical parameters from the linear birefringence materials. As the knowledge from author, this is the first instrument that probe into the property of the linear birefringence materials, like as waveplates and could measure all the optical parameters from only one system. It is believed that this novel measuring system could be applied in the opto-electronics industries for highly precise measurements in various optical parameters.

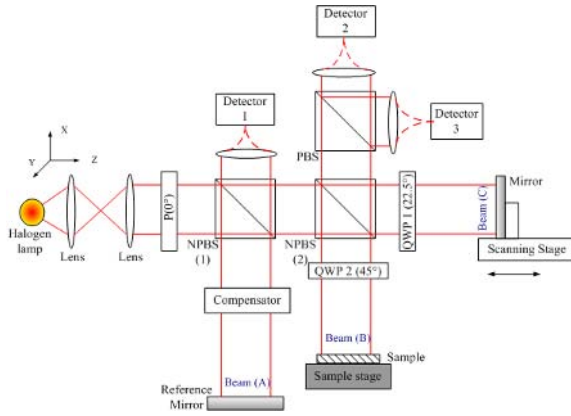


FIGURE 1. Schematic diagram of the new PS-OCT system

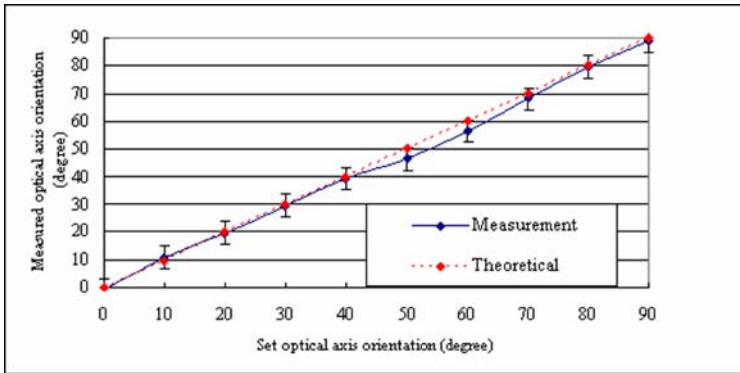


FIGURE 2. Schematic diagram of the new PS-OCT system

References

1. Huang, H. D., Swanson, E. A., Lin, C. P., Schuman, J. S., Sinson, W. G., Chang, W., Hee, M. R., Flotte, T., Gregory, K., Puliafito, C. A., and Fujimoto, J.G., *Science*, vol. **254**, 1178-1181, 1991.
2. G. J. Tearney, M. E. Brezinski, J. F. Southern, B. E. Bouma, M. R. Hee, and J. G. Fujimoto, *Optics Letters*, vol. **20**, 2258-2260, 1995.
3. Hee, M.R., Huang, D., Swanson, E.A., and Fujimoto, J.G., *Journal of the Optical Society of America B*, vol. **9**, 903-908, 1992.

## FULL-FIELD MAPPING OF THE STRESS-INDUCED BIREFRINGENCE ON THE INTERNAL INTERFACES USING A POLARIZED LOW COHERENCE LIGHT INTERFERENCE MICROSCOPE

Jenq-Shyong Chen and Yung-Kuo Huang

Department of Mechanical Engineering, National Chung-Cheng University  
168, University Rd., Ming-Hsiung, Chia-Yi 621, Taiwan, R.O.C.  
imejsc@ccu.edu.tw,

In any semiconductor and optic materials such as ceramic/wafer/polymer/glass, changes in birefringence may, for instance, indicate changes in functionality, structure and stress inside the materials. These devices are usually fabricated by a sequence of planar process to form a multiple layer structure. Manufacturers need to detect and classify the internal interface adhesion properties between layers at many different stages in the construction of the devices. For the reason, we had developed a polarization-sensitive optical coherence microscope (PS-OCM) to inspect the variation of the birefringence of the internal interface of layer structures. The PS-OCM is an extended embodiment of the OCT technology that enables the polarization state of backscattered light to be detected and quantified. By simultaneous detection of interference fringes in two orthogonal polarization states allows determination of the Stokes parameters of light. Comparison of the Stokes parameters of the incident state to that reflected from the sample can yield a depth-resolved map of optical properties such as birefringence and refractive index.

The proposed PS-OCM is based on a Linnik interference microscope. Two important advantages of the Linnik configuration with high NA wide-aperture lens. The reflected light beams of the sample arm and reference arm are combined, interfered and pass through the polarized beam splitter that separated the interfered light into two orthogonal polarization states. Two CCD image sensors are used to detect the light intensity of these two polarization states, named as vertical polarized interference fringe and horizontal polarized interference fringe and polarized interference signal.

Figure 1 shows an example of the birefringence distribution on the top surface of a glass. The stress-induced birefringence variation around a cut groove has been clearly identified and quantified. Figure 2 shows another example that a quarter-wave plate of 1mm thickness is compressed by a load. We had measured the interference components of the two polarized states on the bottom face of the quarter-wave plate. We successfully demonstrated that the PS-OCM can inspect the stress-induced birefringence inside the internal interface of a layered material.

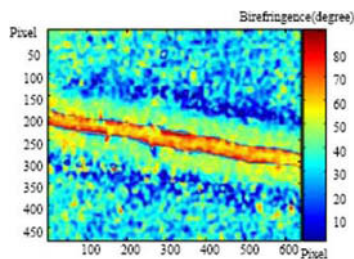


FIGURE 1. The distribution of the birefringence variation on the top surface of a grooved glass

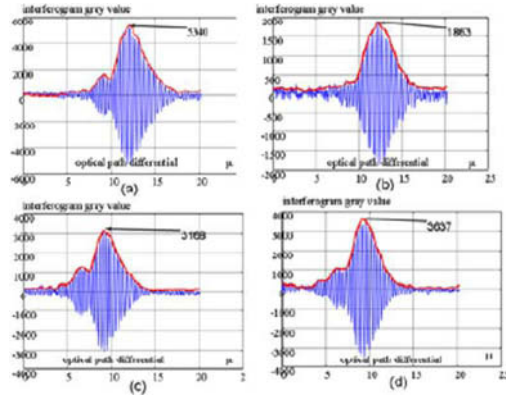


FIGURE 2. The interference on the bottom face of a glass before and after a compressed load, (a) vertical polarized interference before loading, (b) horizontal polarized interference before loading, (c) vertical polarized interference after loading (d) horizontal polarized interference after loading



## DIFFRACTOMETER WITH A MOBILE X-RAY TUBE-DETECTOR SYSTEM

B.S. Roshchin, V.E. Asadchikov, A.V. Buzmakov, I.V. Kozhevnikov and R.A. Senin  
A.V. Shubnikov Institute of Crystallography RAS  
Leninskii prospekt 59, Moscow, 119333 Russia  
ross@ns.crys.ras.ru

The diffractometer with a mobile X-ray tube-detector system [1, 2] was designed to achieve the following objectives:

1. To offer a means for studying the processes of X-ray diffraction and scattering with the sample in a fixed position (this can be done when the X-ray source and the detector are able to rotate independently of one another);
2. To attain the highest possible controllable accuracy of all angular displacements;
3. To allow independent measurements of reflected (or scattered) X-rays from two directions using two different detectors (one of which is a position-sensitive detector and other is a scintillation detector); as a result, it is possible to simultaneously detect X-rays over a wide solid angle.

In the present work, we describe both the design for the diffractometer and its new applications, in which it is the above design features of the instrument that allow the experimental tasks to be performed.

The external appearance of the X-ray diffractometer with a mobile X-ray tube-detector system is shown in Fig. 1.

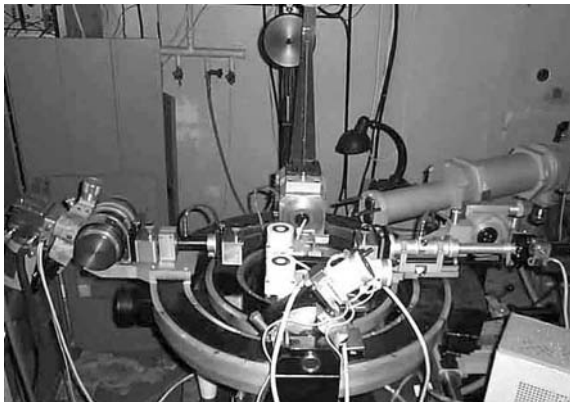


FIGURE 1. External appearance of the diffractometer with a mobile X-ray tube-detector system.

The X-ray and optical part of the diffractometer allows the rotation of the X-ray tube holder through  $90^\circ$ ; the crystal-monochromator through  $45^\circ$ ; the X-ray tube in the plane of ring support 4 from  $-30^\circ$  to  $+30^\circ$ ; the scintillation detector holder in the plane of ring support 5 from  $-30^\circ$  to  $+30^\circ$ ; and the ring supports about the horizontal axis from  $0^\circ$  to  $35^\circ$ . The rotation encoder for the angular supports has an accuracy of  $2''$ . The alignment table can be displaced in the vertical plane

by  $20 \pm 0.05$  mm. The alignment table, together with the sample, can rotate about the vertical axis through angles of 0 to  $360^\circ$  with an accuracy of 1" (this is achieved using the angular movement encoder).

The structure of the instrument and its performance characteristics show that this diffractometer can be applied to study different phenomena ranging from small-angle scattering and X-ray diffraction analysis to tomography. The simultaneous operation of both detectors helps in studying multiwave diffraction. In addition, the instrument can be used successfully to analyze the structure of liquids, surfaces and multilayer structures by the X-ray reflectivity method. In this work we also present the latest results in the framework of VAMAS project "X-ray reflectivity measurements for evaluation of thin films and multilayers thickness", the curves of X-ray reflectivity from water and organic layers on its surface and the tomographic experiments as well.

## References

1. Asadchikov, V.E. *et al. Instruments and Experimental Techniques*, vol. **48** (3), 364–372, 2005.
2. Alautdinov, B.M. *et al. Nauchn. Priborostr.*, vol. **5** (1-2), 95-112, 1995.

## WAVELET BASED FEATURE EXTRACTION FOR ACOUSTIC EMISSION

J. Hensman and K. Worden  
The University of Sheffield

Department of Mechanical Engineering, Mappin St, Sheffield S1 3JD, United Kingdom  
mep04jh@shef.ac.uk

A new feature extraction method for acoustic emission signals is presented. The method works in the time-frequency domain, as compared to the time domain in which features have previously been taken. The new method is directly compared with the old method, showing improved identification of crack events in a box girder bend test.

Time domain based feature extraction of Acoustic Emission (AE) signals has been shown to be successful in separating different types of AE event (Manson et al 2001), by means of dimension reduction and clustering of feature data. More recently, Hamstad et al (2002) showed the applicability of wavelet transforms (WT) to AE signals in order to distinguish the modal structure.

This paper aims to provide the basis of a feature extraction algorithm in the time-frequency (wavelet) domain. These features are dependant on the modal structure of the signal, which is not the case with time domain based features.

The algorithm is based upon the summation of a series of 2-D Gaussians, which form a surface to approximate the WT of the signal. Simulated annealing (Kirkpatrick et al 1983) is used to optimise this function approximation; many of the problems associated with this type of optimisation are eliminated by use of initial conditions close to the final solution.

The heights, widths and positions of the Gaussians are then used as features. They can be dimension reduced and clustered in a similar fashion to time domain based features. This makes a comparison of the two methods elementary.

The method is applied to a set of data from a box girder fatigue test, detailed by Manson et al (2001). The time domain feature extraction is compared with the time-frequency feature extraction, and the results are presented for comparison.

The time-frequency domain based features show tighter clustering for crack events, whilst the time domain features show better linear separability. An amalgamation of the two methods is shown to give the best result.

The pitfalls of this new feature extraction method are discussed, as well as suggestions for their avoidance. Further optimisation of the algorithm and use of different function approximation techniques (in lieu of simulated annealing) are currently under investigation.

**References**

1. Manson G, Worden K, Holford K, and Pullin R. 2001. Visualisation and Dimension Reduction of Acoustic Emission Data for Damage Detection. *Journal of Intelligent Material Systems and Structures*, vol. **12**(8), 529-536.
2. Hamstad MA, O’Gallagher A and Gary J. 2002. A wavelet transform applied to acoustic emission signals: Part 1 Source identification. *Journal of Acoustic Emission*, vol. **20**, 39-61
3. Kirkpatrick S, Gelatt CD and Vecchi MP. 1983. Optimization by simulated annealing. *Journal of Science*, vol. **220**(4598), 671-680.

## EMBEDDED PVDF SENSORS FOR IMPACT AND AE DETECTION IN COMPOSITE STRUCTURES

C. Caneva, I.M. De Rosa and F. Sarasini

Department of Chemical and Materials Engineering, University of Rome "La Sapienza"

Via Eudossiana 18, 00184 Rome, Italy

claudio.caneva@ingchim.ing.uniroma1.it igor.derosa@uniroma1.it fabrizio.sarasini@uniroma1.it

This work focuses on the assessment of the damage due to low-velocity impact on composite laminates. Damage of polymeric composite structures through impact events is perhaps one of the most important aspects of mechanical behaviour which limit the wide applications of these materials and it is critical to the Structural Health Monitoring system (SHM). This kind of damage can occur during assembly or in service.

In composite structures low-energy impact can produce damage which is barely visible and that exists in the form of extensive subsurface matrix cracks, backside fiber failure and delaminations and this can significantly degrade a structure's performance. Because the existence of barely visible impact damage can be a significant safety threat, the capability to have a better understanding of the impact response of composite laminates and of their structural performance is of great utility. To achieve this goal an embedded piezoelectric (PVDF) thin film sensors system (Santulli [1], H.N.Bar *et al.* [2], Caneva *et al.* [3]) for Acoustic Emission (AE) was realized to investigate, in real time, post impact damage in aramid woven fabric reinforced epoxy. AE was used because it shows several advantages over traditional NDT methods, including high sensitivity, on line capability, global monitoring and source location.

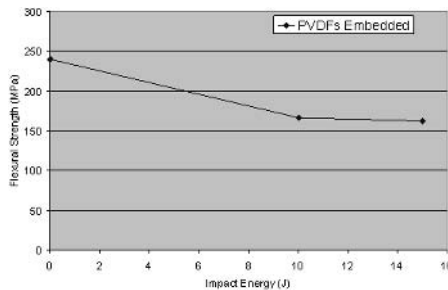


FIGURE 1. Flexural strength at different impact energies: 0, 10 and 15J.

First of all, aramid fiber/epoxy composite specimens with embedded PVDFs previously impacted at different energies, namely 5J, 10J and 15J, were tested using three-point bending tests. The mechanical behaviour of the specimens was investigated in order to assess that these sensors have a negligible effect on the mechanical properties of the impacted laminates. It appears (Fig. 1), from the mechanical tests, that the flexural strength decreases passing from the not impacted specimens to those impacted with the highest energy and that embedding PVDFs (Fig. 2) in the laminates does not affect the structural integrity of the impacted composites, since the mechanical response of specimens with and without PVDF sensors is almost identical.

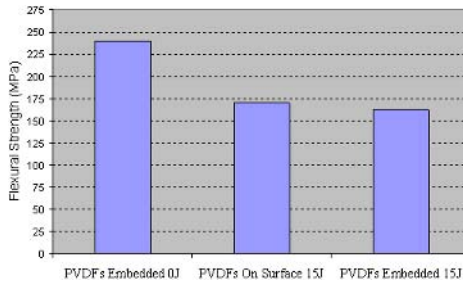


FIGURE 2. Flexural strength for impacted and not impacted specimens.

Moreover, to verify that the PVDF sensors are reliable during the impact loading without experiencing any kind of damage, impacts at energies as high as 20J were performed on the area over the sensor. The lack of damage was assessed by using the Hsu-Nielsen source.

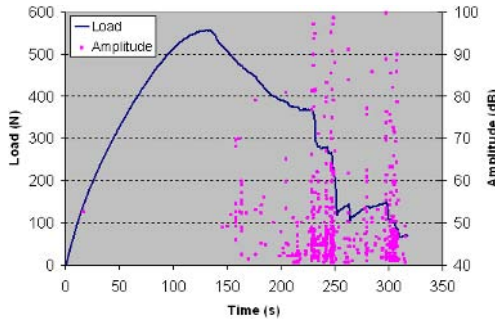


FIGURE 3. Typical flexural load and AE amplitude versus time.

Then, the degree of impact damage, represented by the decrease of mechanical properties has been correlated with the AE activity by means of a parametric analysis of the acoustic emission signals detected during the post impact mechanical tests. In particular, the analysis of the distribution of the AE parameters at different stress levels and impact energies, has been compared with the actual damage formation and progression observed using a Scanning Electron Microscope (SEM). This allowed us to better understand the microscopic fracture processes leading to the final failure of the composites. It was also verified that there is no great difference in the AE detected by the PVDF sensors embedded and by those surface mounted. In conclusion this study showed that the use of Acoustic Emission detected by PVDF sensors has great potential for the on-line detection of the impact damage and, consequently, for the establishment of an effective SHM system based on it.

## References

1. Santulli, C., *J. Mater. Sci. Letters*, vol. **41**, 1255-1260, 2005.
2. Caneva, C., De Rosa, I.M., Sarasini, F., In *Proceedings of the 27<sup>th</sup> European Conference on Acoustic Emission Testing*, Trans Tech Publications, 2006, 337-342.
3. Bar, H.N., Bhat, M.R. and Murthy, C.R.L, *J. Nondestructive Eval.*, vol. **24**, 121-134, 2005.

## ADVANCED LOCATION AND CHARACTERISATION OF DAMAGE IN COMPLEX METALLIC STRUCTURES USING ACOUSTIC EMISSION

Rhys Pullin, Karen M. Holford, Sam L. Evans and Matthew Baxter  
School of Engineering  
Cardiff University, The Parade, Cardiff, CF24 3AA, United Kingdom  
pullinr@cardiff.ac.uk, Holford@cardiff.ac.uk, evanssl6@cardiff.ac.uk

The current commercial approach to acoustic emission source location, called time-of arrival (TOA), requires knowledge of the sensor position and an accurate measure of wavespeed. Furthermore TOA assumes a straight path of propagation between the source and the sensor, which in complex geometries is rarely the case, whilst ambiguities and errors arise due to the minimising of the number of sensors, premature triggering of timing measurements and dispersion of the wave. In previous work [1], a novel solution for AE source location in geometrically complicated structures has been developed. Delta-t mapping source location utilises an artificial source; differences in times of arrival from a number of locations are recorded, to improve source location. The method does not require knowledge of the sensor position or wavespeed. This work however only reported on the results from an artificial source.

In this paper fatigue fractures were grown in two test specimens with complex geometries and monitored using the Delta-t technique (Fig. 1). Specimen 1 was manufactured from 3 mm mild steel plate with a variety of holes to interfere with direct wavepaths from source to sensor, and the specimen was loaded in uniaxial tension from 0.35 – 35 kN until failure. A second investigation was completed to investigate the effect of varying plate thickness on source location. Specimen 2 was manufactured, again from mild steel, and loaded in uniaxial tension from 0.4 - 40 kN until failure. Additional holes were added to this specimen to introduce a stress raiser to ensure failure in the thinnest section which would have the most complicated source to sensor propagation path.

In any investigation, once the position of a source is identified, a method of source characterisation is needed. A common method is to examine the feature data of a signal (amplitude, energy, rise-time, counts etc.), but this can be complex as it is only possible to visualise the data in two or three dimensions, such as amplitude against counts. However using principle component analysis (PCA) data can be observed in a greater number of dimensions and clusters of data with maximum separation can be displayed. With prior knowledge of cluster locations a source characterisation would be possible.

An analysis of the results post failure demonstrated that the technique of delta-t mapping showed approximately 50% improvement in source location over the traditional TOA technique. A PCA of background noise and regions of fracture growth showed distinct separate clusters, allowing a discrimination of non fracture signals to be completed. The two investigations demonstrated that the two techniques can be developed into an appropriate method for on-line source location and characterisation of complex metallic geometries.

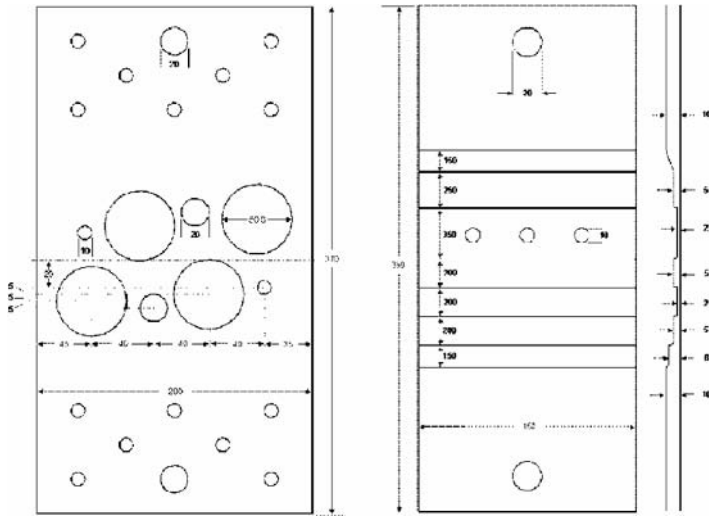


FIGURE 1. Test Specimen.

## References

1. M. G. Baxter, R. Pullin, K. M. Holford and S. L. Evans, "Delta T Source Location for Acoustic Emission". *Mechanical Systems and Signal Processing*, in press.



## CURRENT PRACTICE AND APPLICATIONS OF ACOUSTIC EMISSION

K.M. Holford and R. Pullin  
School of Engineering, Cardiff University  
Queen's Buildings, The Parade, Cardiff, CF24 3AA, United Kingdom  
Holford@cf.ac.uk, PullinR@cf.ac.uk

Acoustic emission (AE) is a technique that is often misunderstood and misrepresented, but is fast emerging as a powerful method in terms of damage assessment and structural health monitoring (SHM). Early pioneers of the technique during the late 1960's through to the early 1980's such as Dunegan, Pollock, Wadley, Scruby, Birchon, Schofield, Beattie, Proctor, Harris and Ono produced outstanding scientific analyses despite the limitation of their equipment and indeed many of today's researchers are revisiting this work. AE is currently experiencing an increase in popularity due to recent advances in high-speed digital waveform-based AE instrumentation which permits vast numbers of AE waveform signals to be digitised and stored for analysis. Coupled with improvements in high fidelity, high sensitivity broadband sensors and the development of advanced PC based signal analysis software; these advances have given rise to recent work that has been directed at an enhanced understanding of AE signal propagation in terms of guided acoustic modes. The approach, more recently designated "Modal Acoustic Emission", offers the potential to depart from the traditional reliance on statistical analysis and significantly improve the structural monitoring capabilities of AE.

Wave analysis has been well-established for many decades; in fact Lamb wave analysis has been exploited by researchers in ultrasonic techniques for over thirty years. Researchers in AE testing, however, have largely ignored applications of Lamb's theory to analysing AE data – probably due to the fact that early AE experiments were conducted on small specimens, where the theory is not applicable. A further reason is that ultrasonic researchers transmit a harmonic wave to select the mode desired for a given plate thickness, while AE researchers work with waves generated by a transient event and therefore such selection is not possible

AE differs from other methods of investigating material deformation and damage processes in three significant respects. Firstly, the energy that is detected originates from the specimen itself, rather than being supplied from an external source. Secondly, it does not take a 'snap shot' of the condition of a specimen, but instead detects the actual dynamic processes associated with the degradation of structural integrity, and thirdly, a sensor located anywhere in the vicinity of an AE source can both detect and locate the resulting emission. The result is a truly powerful monitoring technique that has considerable potential in a variety of applications.

Source characterisation is one of the most challenging areas of AE research, because the signal at the sensor bears very little resemblance to the dynamics of the source event. There are two main approaches to the solution of this problem. The deterministic approach attempts to develop quantitative relationships between source parameters and physical measurements of the transducer signal. In this paper this approach is studied in terms of wave propagation analysis for example in the work of Gorman [1], Gorman and Prosser [2,3], Prosser [4] Prosser *et al* [5], Majji and Satpathi [6] and Dunegan [7] and prediction of received waveforms for example in the work of Wilcox *et al.* [8]. Alternatively, a stochastic approach can be utilised; this uses distribution, rate and correlation analysis of AE feature data from a range of different defect sources in samples of interest to compile empirical correlations with measured source properties and behaviour; this pattern recognition approach can use neural networks and visualisation and clustering techniques is has been explored by a number of researchers including

Holford *et al* [9], Rippengill *et al* [10], Roy *et al* [11] and Ono *et al.* [12]. A combination of both the stochastic and deterministic approaches is also explored in this paper.

Finally, applications of the AE technique from a variety of industries, for example civil, aerospace, offshore and automotive, are presented illustrating the successful application of the technique.

## References

1. Gorman, M.R., *J. Acoustical Society of America*, vol. **90**, 1, 358-364, 1991.
2. Gorman, M.R. and Prosser, W.H., *J. Acoustic Emission*, vol. **9**, 283-288, 1991.
3. Gorman, M.R. and Prosser, W.H. *J. Appl. Mech.*, vol. **63**, 555 – 557, 1996.
4. Prosser, W.H., *J. Acoustic Emission*, vol. **14**, 1-11. 1997.
5. Prosser, W.H., Hamstad, M. A., Gary, J. And O’Gallagher, A., *J. Acoustic Emission.*, vol. **17**, 37 – 47. 1999.
6. Maji, A.K. and Satpathi, D., *Engineering Mechanics*, vol. **1**, 597-600. 1995.
7. Dunegan, H.L., in *Structural Materials Technology NDE Conference*. 1996.
8. Wilcox, P.D., Lee, C. K., Scholey, J. J., Friswell, M.I., Wisnom, M.R. and Drinkwater, B.W., *Advanced Materials Research*, vols **13 – 14**, 69 – 76. 2006.
9. Holford, K.M., Yan T., Carter D.C. and Brandon, J.A., *Journal of Acoustic Emission*, vol **17** 49 – 59, 1999.
10. Rippengill S., Worden K., Holford K.M. and Pullin R. *STRAIN – Journal of the British Society for Strain Measurement*, vol **39**, 31 – 41, 2003.
11. Roy, C., Maslouhi A., Gaucher D. and Piasta Z., in *Canadian Aeronautics and Space Institute Symposium, Montreal*, 224-232, 1988.
12. Ono, K. and Huang Q., in *Progress in AE (vii), Proceedings of 12th International Conference of the Japanese Society for NDI* , 68-78. 1994.

## SIGNAL PROCESSING AND PATTERN RECOGNITION OF AE SIGNATURES

Athanasios A. Anastasopoulos  
Envirocoustics S.A.,  
El. Venizelou 7 & Delfon, GR-144 52 Athens, Greece  
nassos@envirocoustics.gr

The present work, presents the essential elements of signal processing and pattern recognition, as applied to the analysis of AE data from different materials, structures and processes. Signal processing and pattern recognition [1] are extensively used in Acoustic Emission (AE) data evaluation in order to discriminate relevant from non relevant indications, characterize the source of emission and correlate with the associated failure mechanism. The background idea is that each AE source, is characterized by its signature, to be identified during the analysis process.

Signal processing is performed at the waveform level, either by applying digital filtering, Fourier transforms or other processing such as wavelet transform, or by extracting AE features as a mean to describe the shape and content of a detected AE waveform. In either case the aim is to discriminate one type of waveform from another and correlate with different source mechanisms. The basic principles of AE signal processing are presented herein together with a comparison between the waveform based versus features based processing strategies.

The use of histogram analysis and/or two dimensional correlation plots is discussed as conventional AE signature identification process. The respective limitations are discussed and the alternative of multi-dimensional features processing is presented, Fig. 1, as an introduction to the necessity of pattern recognition in AE data analysis. The use of Neural network and pattern recognition techniques on AE feature data, to identify one type of waveform shape from another by analyzing AE features in combination, is discussed. The use of both supervised and unsupervised pattern recognition techniques is presented and representative examples are given.

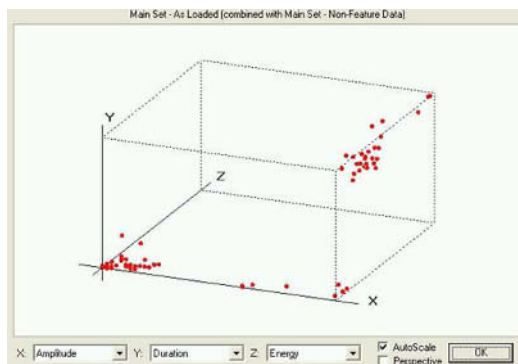


FIGURE 1. AE Data in 3D view. The addition of the 3<sup>rd</sup> dimension enables the understanding of the true data structure compared with 2D correlation plot.

*Supervised Pattern Recognition* [2], involves a learning process and where each new (unknown) set of AE data is processed and classified to previously known classes comparing its features to a data base or using rules derived from the learning process. In this case, the Classifier design is a process of "Learning from Examples" and is called Supervised Pattern Recognition.

*Unsupervised Pattern Recognition* [3], is the process by which AE data are classified in general groups according to their similarity. This process does not require any previous knowledge or data base. Objects are classified into groups by comparing their features and deciding upon their similarity. In the absence of a priori knowledge about recognition problem as it is often the case in acoustic emission, "Unsupervised Pattern Recognition" techniques are employed. In such cases, the number of classes/categories must be estimated as well as a meaningful grouping of the AE data for further use as a training set during the classifier design.

What makes pattern recognition problems hard is that there can be a large degree of variability of inputs that belong in the same class, relative to the differences between patterns in different classes, i.e. data not really separable. The effect of measurement set-up and data quality in both signal processing and recognition algorithms is discussed. In addition to that, in the case of Unsupervised Pattern Recognition, the problem is not uniquely defined and multiple solutions should be expected. Within this framework, the paper discuss in depth the difficulties and limitations of the different pattern recognition techniques.

Demonstrating that Pattern Recognition is not a panacea, the paper shows that the algorithms and respective software offers all the necessary tools for evaluating the complexity of the problem and proceed with classifier design for signatures recognition and concludes with summary of successful applications [3]-[6].

## References

1. Anastasopoulos, A.A., ASNT Handbook, 3<sup>rd</sup> Edition: Vol. 6, Acoustic Emission Testing, chapter 5, Part 2, Technical Editors R. K. Miller & Erik V. K. Hill, ASNT 2005.
2. Anastasopoulos, A. A., Nikolaidis, V. N. and Philippidis, T. P., Neural Computing & Applications, 1999, vol. 8, 53-61.
3. Anastasopoulos, A. A., Philippidis, T. P., J. of Acoustic Emission, vol. 13, Noa 1/2, 1995, 11-21.
4. Tsimogiannis, A., Georgali, B., Anastasopoulos, A.A., J. of Acoustic Emission, vol. 18, 2000, 21-28.
5. Dutton, A. G., et. all, British Journal of NDT Insight, vol. 42, No. 12, 805-808, December 2000.
6. Anastasopoulos, A. A. and Tsimogiannis, A. N., J. of Acoustic Emission, vol. 22, 2004, 59-70.

## INVERSE METHOD FOR PARAMETER DETERMINATION OF BIAXIALLY LOADED CRUCIFORM COMPOSITE SPECIMENS

A. Smits<sup>1</sup>, D. Lecompte<sup>2</sup>, D. Van Hemelrijck<sup>1</sup>, H. Sol<sup>1</sup> and W. Van Paepegem<sup>3</sup>

<sup>1</sup>Vrije Universiteit Brussel (VUB) - Department of Mechanics of Materials and Constructions - Pleinlaan 2 - 1050 Brussels, Belgium

<sup>2</sup>Royal Military Academy (RMA) - Department of Materials and Construction - Av. De la Renaissance 30 - 1000 Brussels, Belgium

<sup>3</sup>Ghent University - Laboratory Soete - Department of Mechanical Construction and Production - Sint-Pietersnieuwstraat 41 - 9000 Ghent, Belgium

Arwen.Smits@vub.ac.be, David.Lecompte@rma.ac.be, dvhemelr@vub.ac.be, hugos@vub.ac.be, Wim.VanPaepegem@ugent.be

This paper presents an inverse method for the identification of the in-plane orthotropic apparent engineering constants of bi-axially loaded composite materials using cruciform specimens. The full field displacements are identified by a digital image correlation technique. From the displacement field a strain field is computed and compared with finite element strain results of the experiment. The apparent engineering constants are unknown parameters in the finite element model. Starting from initial values, these parameters are updated till the computed strain field matches the experimental strain field. In a first stage, global apparent engineering constants were determined. In this stage a more local determination of the engineering constants is studied.

In general, composite laminates are developing multi-axial stress states [1]. However, there is little existing experimental capability to evaluate the multi-axial response of composite materials, even though large demand for such information exists [2]. The most appropriate method for biaxial testing consists of applying in-plane biaxial loads to cruciform specimens. Therefore, a plane biaxial test device has been developed at the Free University of Brussels (Fig. 1).



FIGURE 1. Biaxial cruciform device.

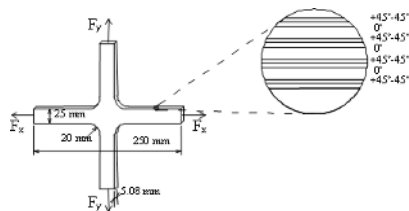
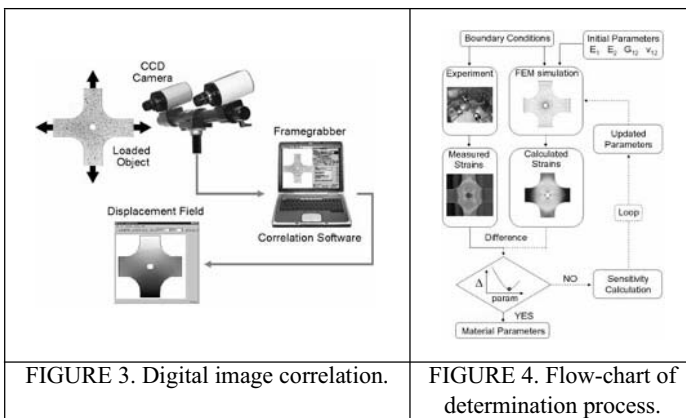


FIGURE 2. Specimen with material lay-up.

This device has four independent servo-hydraulic actuators with a control unit to keep the centre of the specimen still and has a capacity of 100 kN in both directions [3]. The cruciform geometry has a total length 250 mm; the width of the arms is 25 mm and the radius of the corner fillet 20 mm (Fig. 2). The material used is glass fibre reinforced epoxy with a  $[(+45^\circ -45^\circ 0^\circ)_3(+45^\circ -45^\circ)]$ -lay-up. Due to the geometry of the specimens however, the mechanical material parameters cannot be obtained as with standard uni-axially loaded beamlike specimens.

Therefore, an inverse method was used. This method has been developed at the Royal Military Academy (RMA), which integrates an optimization technique, a full-field measurement technique and a finite element method [4]. In this paper, a method is proposed for the more local identification of the in-plane apparent engineering constants  $E_1$ ,  $E_2$ ,  $G_{12}$  and  $\nu_{12}$  of an orthotropic material based on surface measurements. The responses of the system, i.e. the surface displacements are measured with digital image correlation (Fig. 3). Strains are subsequently calculated, based on the measured displacement field. A finite element model of the cruciform specimen serves as numerical counterpart for the experimental set-up. The difference between the experimental and numerical strains (the cost function) is minimized in a least squares sense by updating the values of the engineering constants (Fig. 4). The optimization of the parameters is performed by a Gauss-Newton method.



The obtained material parameters agree well with the values obtained by traditional uni-axial tensile tests for the global parameter identification in the linear elastic range. The extension to more local parameter identification is first performed in the linear elastic range. In the future parameter identification beyond the linear elastic zone will be considered as well as material degradation under fatigue loading.

## References

1. Lin, W.P., Hu, H.T., *Parametric study of failure stresses in fibre reinforced composite laminates subjected to biaxial tensile load*, *J Comp Mater*, vol. **36**(12), 1481-1504, 2002.
2. Boehler J.P., Demmerle S., Koss S., *A new direct biaxial testing machine for anisotropic materials*, *Exp Mech*, vol. **34**(1), 1-9, 1994.
3. Lecompte D., Smits A., Sol H., Vantomme J., Van Hemelrijck D., *Mixed Numerical-Experimental technique for orthotropic parameter identification using biaxial tensile tests on cruciform specimens*, *Int. J. Sol.& Struct.*, In press, 2006.
4. Smits A., Van Hemelrijck D., Philippidis T.P., Cardon A., *Design of a cruciform specimen for biaxial testing of fibre reinforced composite laminates*, *Comp. Sc & Tech.*, vol. **66** (7-8), 964-975, 2006.

## A REVIEW OF BIAXIAL TEST METHODS FOR COMPOSITES

A. Smits<sup>1</sup>, C. Ramault<sup>1</sup>, A. Makris<sup>1</sup>, D. Van Hemelrijck<sup>1</sup>, A. Clarke<sup>2</sup>, C. Williamson<sup>2</sup>, M. Gower<sup>3</sup>,  
R. Shaw<sup>3</sup>, R. Mera<sup>3</sup>, E. Lamkanfi<sup>4</sup> and W. Van Paepegem<sup>4</sup>

<sup>1</sup>Vrije Universiteit Brussel, Mechanics of Materials & Constructions, Brussels, Belgium

<sup>2</sup>QinetiQ, Cody Technology Park, Ively Road,  
Farnborough Hampshire GU 14 OLX, United Kingdom

<sup>3</sup>National Physical Laboratory, Hampton Road Teddington  
Middlesex TW 11 OLW, United Kingdom

<sup>4</sup>Ghent University, Laboratory Soete, Mechanical Construction & Production, Ghent, Belgium  
dvhemelr@vub.ac.be, abclarke@qinetiq.com, michael.gower@npl.co.uk,  
wim.vanpaepegem@ugent.be

This paper will give an overview of the existing biaxial test methods for composite materials from the early beginning till the currently used methods. An evolution in both the biaxial testing capabilities and the applied inspection methods will be shown.

The use of composite materials in aerospace, aviation and automotive industry has increased rapidly in recent years. In general, composite laminates are developing multiaxial stress states [1]. However, there is little existing capability to evaluate the full multiaxial (or even the biaxial) response of composite materials, even though large demand for such information exists [2].

Different experimental techniques and specimens have been used to produce biaxial stress states. These techniques may be classified into two categories [3]: (i) tests using a single loading system and (ii) tests using two or more independent loading systems. In the first category the biaxial stress ratio depends on the specimen geometry or the loading fixture configuration, whereas in the second category it is specified by the applied load magnitude.

Examples of the first category are bending tests on cantilever beams, anticlastic bending tests of rhomboidal shaped composite plates [4] and bulge tests [5]. Anticlastic bending allows the material to be analyzed in the second and fourth quadrants of the two-dimensional stress space. However, each stress ratio requires a specific shape of the plates. In the hydraulic bulge test, pressure is applied to the surface of a round or elliptical flat specimen. A stress gradient appears in the thickness of the specimen [6] and it has been proved that the developing stress fields are non-homogeneous due to the gripping of the specimen's edges. Like the bending method, this technique requires a different specimen's shape for each stress ratio.

Examples of the second category are thin-wall tubes subjected to a combination of tension / compression and torsion or internal / external pressure, and cruciform specimens under in-plane biaxial loading. The technique with the thin-wall tube is the most popular one [7], because it allows tests with any constant load ratio to be performed. However, it presents some inconveniences [8]: (i) radial stress gradients may not be negligible depending on the thickness of the tube, (ii) real construction components in fibre reinforced composite materials are often flat or gently curved and differ a lot from tubular specimens, (iii) thin-wall tubes are not easy to fabricate and (iv) obtaining a perfect alignment and load introduction is not straightforward. The most realistic technique to create biaxial stress states consists of applying in-plane loads along two perpendicular arms of cruciform specimens. Biaxial creep testing machines have been developed using a deadweight lever system where loads are applied by means of ropes which pass over pulleys [9]. The use of hydraulic actuators represents a very versatile technique for the application of the loads. The main differences between the techniques are the use of one actuator per loading

direction or two. For the techniques using one actuator per loading direction [10] the centre of the specimen will move during a test causing side bending of the specimen. Systems with two actuators per loading direction [11] with a close-loop servo control, allow the centre of the specimen standing still. The biaxial test devices used at the Free University of Brussels [12], at Qinetiq [13] and at the National Physical Laboratory are of this type. Various inspection techniques are nowadays applied on the specimens under biaxial stress states e.g. digital image correlation, ESPI, acoustic emission... Also post failure analysis inspection techniques are available e.g. X-ray photography, ultrasonic inspection, fractographic analysis...

To conclude, we can state that the development of the biaxial testing techniques, led to a better understanding of the behaviour of composite materials under biaxial stress states, but that further research in this domain is needed.

## References

1. Lin WP, Hu HT. Parametric study of failure stresses in fibre reinforced composite laminates subjected to biaxial tensile load. *J Comp Mater* 2002; **36**(12), 1481-1504.
2. Boehler JP, Demmerle S, Koss S. A new direct biaxial testing machine for anisotropic materials. *Exp Mech* 1994, vol. **34**(1), 1-9.
3. Zouani A, Bui-Quoc T, Bernard M. A proposed device for biaxial tensile fatigue testing. *Fatigue and Fracture* 1996, ASME PVP-323, vol. **1**, 331-339.
4. Hazell CR, Marin J. A possible specimen for the study of biaxial yielding of materials. *Int. J. Mech. Sci.* 1967, vol. **9**, 57-63.
5. Lukyanov VF, Lyudsmirskii YG, Naprasnikov VV. Testing components of shell structures in the biaxial stress states. *Ind. Lab.-USSR.* 1986, vol. **52**(7), 661-664.
6. Havard DG, Topper TN. Biaxial fatigue of 1018 mild steel at low endurance. *Proc 1<sup>st</sup> Int Conf on pressure vessels Tech ASME*, 1969. p. 1267-1277.
7. Lefebvre D, Chebl C, Thibodeau L, Khazzari E. A high-strain biaxial testing rig for thin-walled tubes under axial load and pressure. *Exp Mech* 2000, vol. **40**(3), 312-320.
8. Dawicke DS, Pollock W.D. Biaxial testing of 2219-T87 aluminum alloy using cruciform specimens. *Nasa Contractor Report 4782.* 1997. p. 1-46.
9. Hayhurst DR. A biaxial tension creep rupture testing machine. *J. Str An* 1973, vol. **8**(2), 119-123.
10. Fessler H, Musson J. A 30ton biaxial testing machine. *J. Strain Analysis* 1969, vol. **4**, 22-26.
11. Shiratori E, Ikegami K. A new biaxial tensile testing machine with flat specimen. *Bul. Tokyo Inst. Of Tech.* 1967, vol. **82**, 105-118.
12. Smits A, Van Hemelrijck D, Philippidis TP, Cardon A. Design of a cruciform specimen for biaxial testing of fibre reinforced composite laminates. *Com Sc & Tech*, vol. **66** (7-8), 2006, 964-975.
13. Williamson C, Cook J, Clarke AB, Investigation into the failure of open and filled holes in CFRP laminates under biaxial loading conditions, *Proc. ECCM 11*, Greece.



## PLASTIC MATERIAL MODEL IDENTIFICATION USING DIC ON BIAxIAL TENSILE TEST

D. Lecompte<sup>1</sup>, S. Cooreman<sup>2</sup>, H. Sol<sup>2</sup>, J. Vantomme<sup>1</sup>, D. Van Hemelrijck<sup>2</sup> and A.M Habraken<sup>3</sup>

<sup>1</sup>Royal Military Academy, Department of Materials and Construction  
Av. De la Renaissance 30, 1000 Brussels, Belgium

<sup>2</sup>Vrije Universiteit Brussel, Mechanics of Materials and Construction  
Pleinlaan 2, 1050 Brussels, Belgium

<sup>3</sup>Université de Liège, Mechanics of Materials and Structures  
Chemin des Chevreuils 1, 4000 Liège, Belgium  
David.lecompte@rma.ac.be

The accuracy of a Finite Element Simulation for plastic deformation strongly depends on the chosen constitutive laws and the value of the material parameters within these laws. The identification of those mechanical parameters can be done based on homogeneous stress and strain fields such as those obtained in uni-axial tensile tests and simple shear tests performed in different plane material directions. Another way to identify plastic material parameters is by inverse modeling of an experiment exhibiting a heterogeneous stress and strain field. Material parameter identification methods, which integrate optimization techniques and numerical methods such as the finite element method (FEM), indeed offer an alternative tool. The most common approach is to determine the optimal estimates of the model parameters by minimizing a selected measure-of-fit between the responses of the system and the model. In the present study a method is proposed for the identification of the initial yield stress, the two parameters of a Swift isotropic hardening law and the four parameters of the Hill48 yield surface, based on the full-field surface measurements of a cruciform specimen subjected to biaxial tensile loading. Experimental forces and strains are in this case compared to the simulated values. A finite element model of the perforated specimen serves as numerical counterpart for the experimental set-up. The difference between the experimental and numerical strains ( $\epsilon_x$ ,  $\epsilon_y$  and  $\epsilon_{xy}$ ) is minimized in a least squares sense by updating the values of the different parameters simultaneously. The sensitivities used to obtain the parameter updates are determined by finite differences, using small parameter perturbations. The optimization routine used, is based on a constrained Newton-type algorithm.

The yield function  $\Phi$  which governs the onset and continuance of plastic deformation is chosen to be represented by the Hill48 yield criterion. This criterion allows the introduction of material anisotropy, which is interesting for sheet specimens, cut out of a cold rolled material. In an orthogonal coordinate system, based on the axes of orthotropy of the material the criterion can be written as:

$$\Phi = H(\sigma_x - \sigma_y)^2 + G(\sigma_x - \sigma_z)^2 + F(\sigma_y - \sigma_z)^2 + 2N\sigma_{xy}^2 + 2M\sigma_{xz}^2 + 2L\sigma_{yz}^2 - 2\sigma_f^2 \quad (1)$$

in which  $\sigma_f$  represents the current flow stress and H, G, F, N and M define the form of the yield surface. The Hill48 quadratic yield criterion is a widely used yield criterion for the simulation of sheet metal material behavior. The plane of the sheet contains the x- and y-axis, while the z-axis is perpendicular to it. Assuming a plane stress situation, the parameters to be identified are F, G, H and N.

A hardening model is needed to represent the evolution of the yield surface during the process of plastic deformation. The type of hardening considered in the present study is a Swift type of isotropic hardening which describes the evolution of the yield surface size:

$$\sigma_f = \sigma_{y0} + K(\epsilon_{eq}^{pl})^n \tag{2}$$

in which  $\sigma_f$  represents the actual flow stress,  $\sigma_{y0}$  is the initial yield stress and  $\epsilon_{eq}^{pl}$  represents the equivalent plastic strain.

The identification problem can be formulated as an optimization problem where the function to be minimized is some error function that expresses the difference between numerical simulation results and experimental data. In the present case the strains are used as output data. Fig. 1 represents the flow-chart of the present inverse modeling problem. This type of parameter identification can also be found in Kajberg [1] and Lecompte [2].

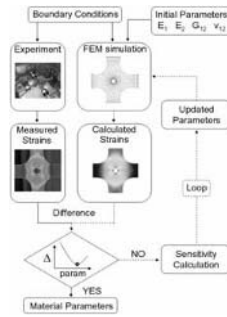


FIGURE 1. Inverse modeling flow chart

It is shown that numerically the biaxial tensile test on the perforated cruciform specimen contains enough information for the Hill48 yield surface to be identified. The parameters of the Swift type of isotropic hardening law can be identified as well, as long as the deformation is important enough.

**References**

1. Kajberg, J. and Lindkvist, G., *I. J. Solids and Structures*, vol **41** (13), 3439-3459, 2004
2. Lecompte, D. et al, *Solids and Structures*, doi:10.1016/j.ijsolstr.2006.06.050

## DEVELOPMENT OF A CRUCIFORM SPECIMEN GEOMETRY FOR THE CHARACTERISATION OF BIAxIAL MATERIAL PERFORMANCE FOR FIBRE REINFORCED PLASTICS

M. Gower, R. Shaw and R. Mera

Engineering and Process Control Division, National Physical Laboratory, Teddington, Middlesex, TW11 0LW, United Kingdom  
 dvhemelr@vub.ac.be

The vast majority of composite components experience multi-axial loading during service life. Existing composite material test standards for generating mechanical design data are predominantly uniaxial in scope, and although several European laboratories are proposing standard methods for multi-axial characterisation, there is currently no standard protocol in place. There are several methods of creating multi-axial loads, including the use of axial forces and pressure (internal/external) using tube specimens, biaxial plate or cruciform type biaxial configurations and full rig systems applying combinations of axial, bending and/or twisting loads. Currently, the biaxially loaded cruciform specimen has been identified as of most interest.

This paper will detail initial experimental tests undertaken to develop a cruciform specimen geometry suitable for the tension-tension biaxial characterisation of quasi-isotropic glass and carbon fibre reinforced plastic materials. The work at the National Physical Laboratory has been undertaken in line with a Versailles Project on Advanced Materials and Standards (VAMAS) initiative that has been set up to coordinate the various initiatives worldwide in order to guide research towards the production of an international standard.

NPL has recently commissioned a multi-axial test facility, that is being used for test method development plus loading of components. The multi-axial strong floor facility set-up consists of a tee-slotted cast iron strong floor, upon which can be mounted up to four hydraulic actuators (axes 1-4), each with a static load capacity of  $\pm 100$  kN, or a dynamic rating of  $\pm 50$  kN. Each of the hydraulic rams has a stroke of  $\pm 50$  mm and can be positioned on the strong floor independently, providing, for example, the flexibility to configure the facility from four single-axis test rigs, to a bi-axial loading arrangement for cruciform test components. Figure 1 shows the set-up as used for biaxial testing of a cruciform specimen geometry.

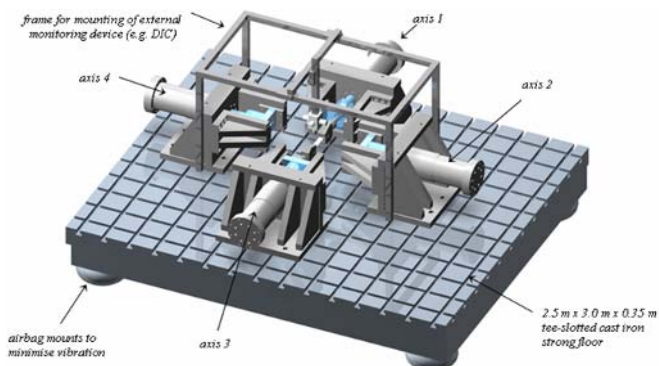


FIGURE 1. – The NPL multi-axial test rig

The initial specimen geometry (Figure 2) has been governed by the size and load capacity of the biaxial test rig and also by the size of panels that can be manufactured at NPL. Specimens have been machined from 300 mm square panels and are of quasi-isotropic lay-up. The thickness of the material tapers from 4 mm in the region of the specimen arms, to 2 mm in a 40 mm diameter circular region in the centre gauge section. Initially the specimen arms have been end-tabbed using  $\pm 45^\circ$  GRP material and mechanical wedge action grips used to grip the specimen

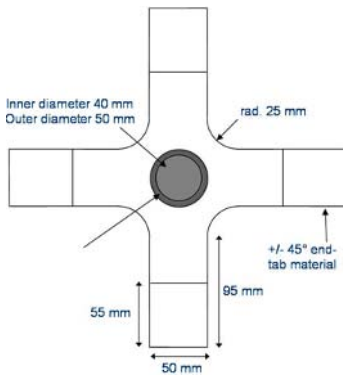


FIGURE 2. Initial coupon geometry

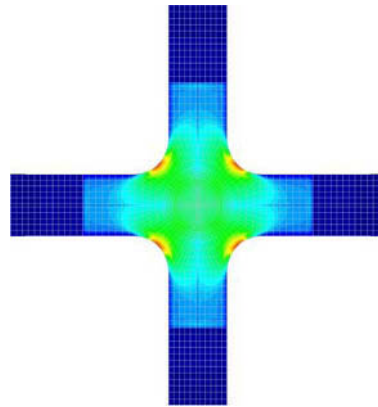


FIGURE 3. Equivalent stress distribution by FEA

The specimen geometry has been modelled using finite element analysis (Figure 3) to investigate the severity of stress concentrations in the radiused regions of the coupon and the uniformity of strain distribution in the centre gauge section. The FEA strain predictions will be compared to full-field strain distributions obtained using digital image correlation (DIC) and strain gauge data from mechanical tests. FEA models will also be used to undertake a parametric study of the effect of; (i) end-tab material, geometry and design, (ii) the shape of the tapered centre gauge section and (iii) the radiused regions. In this way a cruciform coupon geometry suitable for accurate measurement of biaxial material properties will be developed.

### Acknowledgements

This work forms part of the Characterisation of Materials Programme funded by the United Kingdom Department of Trade and Industry (National Measurement System Directorate). The authors would like to express their gratitude to the Industrial Advisory Group, and colleagues Graham Sims, Grant Klimayts and Bruce Duncan whose contributions and advice have made the work possible.

## INVESTIGATION INTO THE FAILURE OF OPEN HOLES IN CFRP LAMINATES UNDER BIAXIAL LOADING CONDITIONS

C. Williamson and J. Thatcher

QinetiQ Ltd.

Bldg A7, Rm 2008, Cody Technology Park,  
Farnborough, Hampshire, GU14 0LX, United Kingdom  
cwilliamson@QinetiQ.com & jethatcher@QinetiQ.com

The use of fibre-reinforced polymer composite materials in the manufacture of structures, from aircraft to racing cars, has increased considerably in recent years. Their specific strength and stiffness permit significant improvements in performance compared to conventional metallic structures. However, the full commercial and strategic benefits of structural composites have not been realised because their failure processes are not fully understood, forcing components to be designed with conservative safety factors. Although a large database has been built up for damage growth, resulting from features such as fastener holes (both filled and open) and impact damage, the vast majority of these results have come from uniaxial tests. Unfortunately, despite the reliance of the certification process on results from uniaxial tests, the majority of structures are very rarely loaded uniaxially in service, and little is known about failure under multiaxial loading conditions.

This paper describes the results from a study which investigated the failure of carbon fibre reinforced plastic (CFRP) laminates with open holes, and how the presence of the hole affected structural strength.

A test method, developed to give valid failure data under multiaxial loading conditions using a planar cruciform specimen, has been used to experimentally determine the failure envelopes and failure mechanisms for open hole specimens under the full spectrum of biaxial loading; that is, tension-tension, tension-compression, compression-tension and compression-compression. Specimens with quasi-isotropic lay-up, manufactured from T300H/914 carbon-fibre/epoxy prepreg, and with thicknesses of 2mm, 3mm, 4mm, and 10mm, were tested. A single hole was drilled through the specimen centres by means of a CNC machine. The hole diameters were 6mm, 10mm, 15mm, 20mm and 25mm. The specimens between 2mm and 4mm thick were tested in a Biaxial machine with four 500kN actuators, whereas the 10mm thick specimens were tested in a larger Biaxial test machine with four 1500kN actuators (Fig. 1).

Good repeatability in specimen failure load was demonstrated. A set of techniques have now been developed that allows the test specimens to be reliably tested to failure loads in excess of 1 MN.

For the majority of specimens, failure was clearly identifiable as either predominately tensile or compressive in nature. However, at biaxial loading ratios of (+1.0: -1.0) and (-1.0: +0.7), both tensile and compressive failure modes were apparent.

The use of the biaxial cruciform test data to develop failure criteria provides a clear example of how an experimental technique, allied to suitable analysis tools, can be used to further our understanding of complex composite structures.



FIGURE 1. 1500kN Biaxial Test Machine

## APPLICATION OF ULTRASONIC PHASED ARRAY FOR NONDESTRUCTIVE DETECTION OF DAMAGE IN BIAXIAL CRUCIFORM

E. Lamkanfi<sup>1</sup>, A. Smits<sup>2</sup>, W. Van Paepegem<sup>1</sup> and D. Van Hemelrijck<sup>2</sup>

<sup>1</sup> Department of Mechanical Construction and Production, Ghent University, Sint-Pietersnieuwstraat 41, B-9000 Ghent, Belgium.

<sup>2</sup> Department of Mechanics of Materials and Construction, Free University of Brussels, Pleinlaan 2, B-1050 Brussels, Belgium.  
 ebrahim.lamkanfi@ugent.be

During the last decades, the use of fibre-reinforced composites has largely increased and currently, these materials are used in almost every industrial sector. Yet, current research shows a number of important shortcomings, both in the experimental and theoretical domain. Standard mechanical tests on uniaxially loaded specimens appear unsatisfactorily for an accurate description of the mechanical behaviour of these materials. A biaxial loading approach should give a better representation. In the past, different techniques were developed for creating a biaxial loading state. Anticlastic bending of thin rhomb plates and tension/torsion of thin-walled tubes are just two out of a series of possible solutions [1-5]. A recent alternative technique is the loading of a cruciform specimen (Fig. 1) along its two orthogonal directions. This shows a lot of advantages compared to the other methods [6-7].

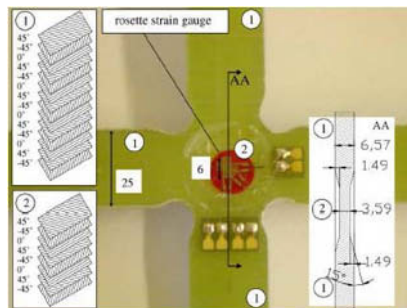


FIGURE 1. A biaxial cruciform with its corresponding stacking sequence.

Another key issue is the detection and monitoring of damage in these materials. From static biaxial tests it appeared that complex stacking sequences can give rise to delaminations starting from the corners of the cruciform and growing to the central zone. To yield accurate information about the initiation and propagation of this damage, the ultrasound phased array technique is used [8-9]. A phased array is a linear one-dimensional array of 64 ultrasound probes that all can be steered individually. By use of a water column or water jet, the measurement can happen without removing the specimen from the biaxial loading set-up. By focusing the ultrasonic beam on a defect at a certain depth, the reflected signal contains valuable information about this fault. It is clear that this ultrasonic technique can also be used to produce C-scans (Fig. 2). As such, an attempt will be made to detect damage in the biaxial specimen after static loading experiments.

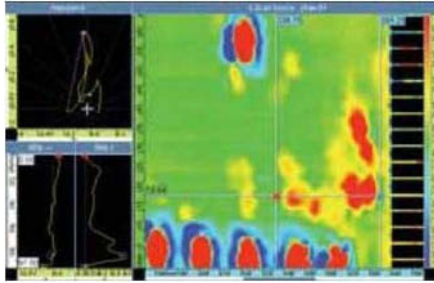


FIGURE 2. C-scan produced with the phased array.

Next to these experiments, some finite element simulations will be conducted to get a better insight in the ultrasonic phenomena such as reflection, transmission and scattering effects of the ultrasonic beam falling onto defects in the biaxial specimen. This numerical method will allow an optimization of the use of the phased array and the prediction of its performance in a real experiment.

## References

1. Zouani A., Bui-Quoc T. and Bernard M., R.P., *Experimental Mechanics*, vol. **39**, 47-61, 1999
2. Boehler J.P., Demmerle S. and Koss S., *Experimental Mechanics*, vol. **34**, 1-9, 1994
3. Lefebvre D., Chebl C., Thibodeau L. and Khazzari E., *Experimental Mechanics*, vol. **23**, 384-392, 1983
4. Andrews J.M.H. and Ellison E.G., *J. Strain Analysis*, vol. **8**, 168-175, 1973
5. Hazell C.R. and Marin J., *Int. J. Mech. Sci.*, vol. **9**, 57-63, 1967
6. Welsh J.S. and Adams D.F., *Experimental Mechanics*, vol. **40**, 312-320, 2000
7. Yu Y., Wan M., Wu X.D. and Zhou X.B., *Journal of Materials Processing Technology*, vol. **123**, 67-70, 2002
8. Mahaut S., Godefroit J.-L., Roy O. and Cattiaux G., *Ultrasonics*, vol. **42**, 791-796, 2004
9. Lhemery A., Calmon P. and Chatillon S., *Ultrasonics*, vol. **40**, 231-236, 2002



## ON THE RESIDUAL STRESS FIELD IN THE ALUMINUM ALLOY FSW JOINTS

V. Dattoma, M. De Giorgi and R. Nobile

Dipartimento di Ingegneria dell'Innovazione, University of Lecce

Via Arnesano – 73100 Lecce, Italy

vito.dattoma@unile.it, marta.degiorgi@unile.it, riccardo.nobile@unile.it

In the last ten years, the aerospace and automotive industries addressed a large attention to a new welding technology, called Friction Stir Welding (FSW), based on a solid-state process. The FSW process presents several advantages, in particular the possibility to weld dissimilar aluminium alloys. As the FSW does not melt the parts being joined, it offers a great potential to produce joints between unweldable aluminium alloys between dissimilar alloys also [1].

Friction Stir Welding is an innovative joining process invented and patented at The Welding Institute (TWI) in the 1991 [2]. FSW uses a rotating (non-consumable) cylindrical tool that consists of a shoulder and a probe. The former is pressed against the surface of the materials being welded, while the probe is forced between the two components by a downward force. The rotation of the tool under this force generates frictional heat, which decreases the resistance to plastic deformation of the material. The softened material then easily moves behind the tool and forms a solid-state weld as the stirred material is consolidated.

This process produces a high quality joints with excellent mechanical properties [3-6].

Since fatigue is the primary cause of 90% of all engineering failures, fatigue performance of FSW joint is one of the most important properties to estimate the failure behaviour of friction stir welded structures.

Furthermore, because residual stresses exert a significant effect on the fatigue properties, so that the crack growth behaviour is generally dominated by residual stress state rather than microstructural changes [7-9], it is of practical importance to investigate the residual stress distribution in the FSW joints. Even if the FSW is a solid-state process where the maximum temperature is lower than the melting point, the rigid clamping used during welding process avoids the contraction of the weld nugget and heat-affected zone during cooling in both longitudinal and transverse directions, originating a residual stress field.

In this work, the residual stress field, due to FSW process, was evaluated on aluminium alloy butt-welded joints. Both similar and dissimilar joints have been considered in 2024-T3 and 6082-T6 aluminium alloy 0.8, 1.5 and 3 mm thick.

The residual stress measurements were carried out by hole-drilling method using the RESTAN automatic system according to ASTM-E837 standard [10]. The rectangular rosettes CEA-062UM-120 were used in the half-bridge configuration to compensate the possible thermal strain. On the 0.8 and 1.5 mm a through hole was executed, on the 3 mm thick joints a blind hole (2 mm depth) was executed. Incremental hole was obtained by a parabolic steps distribution, with an advancing speed of 0.08 mm/min. On the thicker joints, two residual stress measurements were executed also on the root side, on the 2024 and 6082 side at 1 mm away from the weld toe.

To obtain correct measurements, thinner joints, which are significantly warped, were clamped on a workplane. This operation originated bending strain field, which were evaluated before the hole execution according to the thin plate theory in order to correct the stress relaxed by drilling. In this manner, the residual stresses calculated are not affected spurious stress.

For 0.8 and 3mm thick joints, the longitudinal and transversal residual stress distributions were obtained in a transversal section to the weld cord. In the dissimilar joints, the longitudinal residual stress distribution is very similar to the distribution present in the traditional welded joints. It presents, in fact, a tensile region near the weld cord, which is balanced by compressive regions away. On the contrary, other joints present a low compressive stress at the weld toe, which began tensile away.

For 1.5 mm thick joint, the residual stress measurements were executed at the weld toe, where the longitudinal residual stress results maximum, in order to verify the uniformity of residual stress field along the weld cord.

## References

1. Thomas W.M., Nicholas E.D., Needham J.C., Murch M.G., Templesmith P., Dawes C.J., International Patent Application No. PCT/GB92/02203.
2. Sutton M.A., Yang B., Reynolds A.P., Taylor R., *Materials Science and Engineering A*, vol. **323**, 160-166, 2002.
3. R. S. Mishra, Z. Y. Ma, *Materials Science and Engineering R50*, 1-78, 2005.
4. W. M. Thomas, E. D. Nicholas, *Materials & Design*, vol. **18**, 4/6, 269-273, 1997.
5. M. Peel, A. Steuwer, M. Preuss, P.J. Withers, *Acta Materialia* 51, 4791–4801, 2003.
6. A.P. Reynolds, Wei Tang, T. Gnaupel-Herold, H. Prask, *Scripta Materialia* 48, 1289–1294, 2003.
7. M.B. Prime, T. Gnäupel-Herold, J.A. Baumann, R.J. Lederich, D.M. Bowden, R.J. Sebring, *Acta Materialia*, vol. 54, 4013 – 4021, 2006.
8. R. John, K.V. Jata, K. Sadananda, *International Journal of Fatigue*, vol. **25**, 939-948, 2003.
9. L. Fratini, B. Zuccarello, *International Journal of Machine Tools & Manufacture*, vol. **46** 611-619, 2006.
10. ASTM E 837-01, Standard Method for Determining Residual Stress by the Hole-Drilling Strain Gage Method, 2001

## FINE INCREMENT HOLE-DRILLING METHOD FOR RESIDUAL STRESS MEASUREMENT, PROPOSAL OF A CALIBRATING APPARATUS

E. Valentini<sup>a</sup>, M. Benedetti<sup>b</sup>, V. Fontanari<sup>b</sup>, M. Beghini<sup>c</sup>, L. Bertini<sup>c</sup> and C. Santus<sup>c</sup>

<sup>a</sup> SINT Technology s.r.l. Via Giusti, n.229 – 50041 – Calenzano (FI), Italy.

<sup>b</sup> Dipartimento di Ingegneria dei Materiali. Università di Trento.  
Via Mesiano, n.77 – 38050 – Trento, Italy.

<sup>c</sup> Dipartimento di Ingegneria Meccanica Nucleare e della Produzione. Università di Pisa.  
Via Diotisalvi, n.2 – 56126 – Pisa, Italy.  
ciro.santus@ing.unipi.it

Hole drilling is one of the most widely used technique for residual stress measurements, due to its precision and low cost. Standard ASTM E 837 [1] is limited to the uniform distribution of residual stresses, whereas it is well known that residual stresses usually feature high gradient along the depth, particularly if residual stresses are induced by surface treatments such as shot peening. The incremental hole-drilling method can be used to evaluate the not-uniform residual stress distribution as shown by Schajer [2,3]. The strain measurement is repeated at different hole depths to achieve information on the residual stress gradient, from relaxed surface strain. Influence functions for the incremental hole drilling are proposed by Beghini and Bertini [4] by which the relaxed strain can be evaluated analytically if the residual stress distributions are known for any kind of rosette, hole diameter and elastic material. Valentini [5] has developed an apparatus able to produce fine increment hole drilling, by means of a high speed air turbine drill automatically controlled. Valentini *et al.* [6] used the apparatus to experimentally show the effects on residual stresses measurement by the hole drilling such as eccentricity and sequence of increments steps.

In the present paper the procedure for measuring and interpreting variable residual stress by fine increment hole drilling is assessed by a calibrating procedure. The proposed method is based on the possibility to apply and remove a controlled bending stress distribution after each depth increment. The apparatus to perform controlled bending is schematically reported in Fig. 1(a). The bending reference imposed load offers several advantages, in terms of measurement accuracy:

- accidentally ineffective or biased strain gage can be figured out, since expected strain measure is known before drilling;
- hole eccentricity, with respect to the center of strain-gage rosette, is evaluated by applying bending after hole drilling, and eccentricity correction can be performed;
- little confidence on the initial hole drilling position is eliminated;
- Poisson ratio is obtained, with good accuracy, by transversal over longitudinal strain signal ratio, performed before drilling;
- Young modulus of elasticity  $E$  and strain-gage gain  $K$  are not needed to be known with high accuracy before performing the test, indeed strain-gage signals can be directly converted in stresses with reference to the imposed bending.

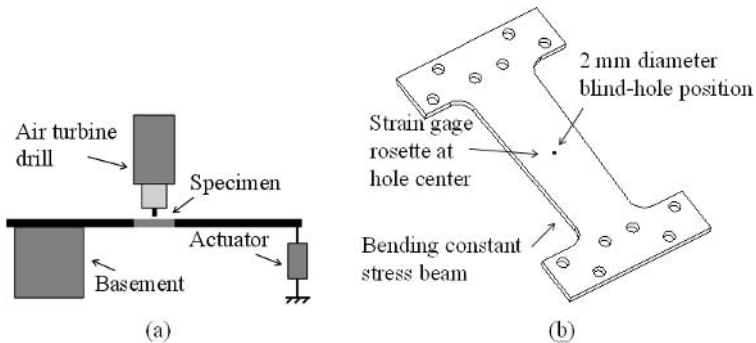


FIGURE 1. (a) Apparatus configuration. (b) Details of the plate specimen.

Bending constant stress specimen configuration, Fig. 1(b), offers no stress gradient as the reference imposed bending is applied.

Tests performed on the aluminium alloy AA 7075-T651 are reported in the paper. Residual stresses were induced through shot peening surface treatment on a 4 mm thickness plate specimen. Comparison to X-ray diffraction residual stress measurements is also provided.

## References

1. AMERICAN SOCIETY FOR TESTING AND MATERIALS, *ASTM E 837 - 95*; Standard Test Method for Determining Residual Stresses by the Hole-Drilling Strain-Gage Method. 1996.
2. G. S. Schajer "Measurement of Non-Uniform Residual Stresses Using the Hole-Drilling Method. Part I - Stress Calculation Procedures" *Journal of Engineering Materials and Technology*, vol. **110**, 1988, 338-343.
3. G. S. Schajer "Measurement of Non-Uniform Residual Stresses Using the Hole-Drilling Method. Part II - Practical Application of the Integral Method" *Journal of Engineering Materials and Technology*, vol. **110**, 1988, 344-349.
4. Beghini M., Bertini L., "Analytical influence functions for variable residual stress measurement by the hole drilling", *Journal of Strain Analysis*, IMechE, vol. **35** No. 2, 2000, 125-135.
5. Valentini E., "An automatic system for measuring non-uniform residual stress by the hole drilling Method", XIII IMEKO World Congress, Torino settembre 1994, 1904-1909.
6. Valentini E., Benincasa A., Baggiani M., Brogelli S., "Evolution of high speed drilling technology for evaluating residual stress by hole drilling", *Proc. XXXIV Convegno Nazionale AIAS*, Milano 14-17 settembre 2005, 1627-1636. (In italian).

## RESIDUAL STRESS ON TITANIUM ALLOY WELDED JOINTS

Caterina Casavola and Carmine Pappalettere  
Politecnico di Bari – Dip. di Ingegneria Meccanica e Gestionale  
Viale Japigia, 182 – 70126 Bari, Italy  
casavola@poliba.it, c.pappalettere@poliba.it

Titanium and its alloys presents an elevated strength/weight ratio, good mechanical properties also to high temperatures, elevated resistance to corrosion and to most part of acids attack. These characteristics makes this material attractive for numerous applications.

Thanks to recent improvements in welding techniques that allow the realization of high quality welded joints, the employ of titanium alloys is spreading in numerous field which range from aerospace to chemical industry. Naval industry, for which the corrosion in the aggressive sea air constitutes a discriminating element in the choice of materials, is weighing possible employs of the titanium. Structural application of titanium alloy are still under study, while some use of titanium sheet as coating of the bottom of the ships against corrosion, instead of the traditional but polluting protective paints, are yet realized.

Economic complications (supplying of titanium is still rather expensive with respect to aluminium or steel) and technological difficulties in welding operations (the risk of contamination of melted bath from atmosphere is high, so skilled workers and specific devices are essentials) exist, but benefits in terms of improvements in mechanical and corrosion strength and in weigh reduction are important aspects which give reasons for this study and are conducive to near future changes in materials choice.

Residual stresses exist in practically all rigid parts as consequence of the “history” of the manufacturing process of the structure. The thermal welding cycle, in addition to modification of the material’s microstructure and local geometry, produces residual stresses in all welded joints [1-2].

Although residual stresses are self-equilibrated systems, their effects on mechanical (and especially fatigue [3]) strength of materials are often relevant and requires to contemplate them in joint design. Residual stresses, superposed to a field of service stress, could produce local overload till reach the yield point of material.

Previous works on steel plates welded by means of electric arc revealed high residual stresses fields in thick plates and large distortion in thin plates. In these cases the effects on fatigue strength of residual stresses and misalignments were analyzed [4-8].

Titanium and its alloys, due to its low thermal conductivity, is suitable for laser arc and electron beam welding which are characterized above all by a limited heat affected zone (HAZ). This should restrict the transformation of titanium in its  $\alpha$ -phase, but do not avoid the development of residual stresses. The role of residual stresses on titanium welded components is not clearly explained. So, whereas on the one hand new industrial application, particularly naval application, push for titanium employs, on the other hand the problem of residual stresses which seems to be greater on material with high mechanical properties [9] represses this, at least till large experimental data and/or reliable prediction model will be available.

The incremental hole drilling method (HDM) has been used in this work to measure residual stresses [10] on welded plates in titanium grade 2 and 5. The plates are 3 and 1.5 mm thick, the welding technique are laser arc and electron beam.

**References**

1. Masubuchi, K., *Analysis of Welded Structures*, Pergamon Press, Oxford, N.York, 1980.
2. The Welding Institute, *Residual Stresses and their Effects*, Abington Hall, Cambridge, 1981.
3. Yong-Bok Lee, Chin-Sung Chung, Young-Keun Park, Ho-Kyung Kim, *Int. J. of Fatigue*, vol. **20**, n.8, 565-573,1998.
4. Casavola C., Pappalettere C., Sallustio V., In *Proceedings of New Trends in Fatigue and Fracture 4 (NT2F4)*, Aleppo (Syria), 2004.
5. Casavola C., Pappalettere C., In *Proceedings of 2004 SEM Annual Conference and Exposition on Experimental and Applied Mechanics*, Costa Mesa (USA), 2004.
6. Casavola C., Nobile R., Pappalettere C., *Revue Internationale d'Ingénierie des Systèmes de Production Mécanique*, vol. **8**, 4-10, 2004.
7. Casavola C., Dattoma V., De Giorgi M., Nobile R., Pappalettere C., In *Proceedings of 4th International Conference on Fracture and Damage Mechanics (FDM)*, Mallorca (Spain), 2005.
8. Pappalettere C., In *Proceedings of The International Conference on the Effects of Fabrication Related Stresses on Product Manufacture and Performance*, Cambridge (UK), 399-411, 1985.
9. *Handbook on Residual stress*, Society for Experimental Mechanics, USA, 2005.
10. ASTM E 837 Standard method for determining residual stresses by the hole-drilling strain gage method, *Annual Book of ASTM Standards*, 2001.

## RESTORING MARBLE FRAGMENTS: THE PULL-OUT PROBLEM

S.K. Kourkoulis<sup>1</sup>, I. Vayas<sup>2</sup>, A. Marinelli<sup>2</sup> and S.-A. Papanicolopoulos<sup>1</sup>

<sup>1</sup>Department of Mechanics, <sup>2</sup>Faculty of Civil Engineering,

National Technical University of Athens, Zografou Campus, GR-157 73, Athens, Greece  
stakkour@central.ntua.gr; amarin@central.ntua.gr

Joining together fragmented structural elements is perhaps the most challenging task during a restoration project. For the monuments of the Acropolis of Athens a pioneering method has been developed already from the early eighties requiring the use of threaded titanium bars and suitable cement mortar [1]. For the complete assessment of the method and the development of innovative connections for the structural integrity of ancient stone temples, in general, it is imperative, among others, to understand the mechanisms leading to the pull-out phenomenon, namely the gradual or abrupt removal of the reinforcing bars from the body of the member. Although the problem is studied by structural engineers long ago, an analytic solution is not yet available and many questions remain still unanswered due to the great number of parameters involved [2]. In this context a combined experimental and numerical analysis is presented here in an effort to study parametrically the various factors affecting the phenomenon.

The experimental part of the study included a series of pure pull-out tests, where the term “pure” indicates that the load is applied along the axis of the reinforcing bar. The specimens were made from Dionysos marble, the material used exclusively for the restoration of the Parthenon Temple. They were prismatic in shape (Fig. 1a) and threaded titanium bars (t) were planted in drilled holes of slightly higher diameter compared to that of the bars (Fig. 1b). The adhesion between the marble (m) and the bar (t) was achieved using a suitable cementitious material (c).

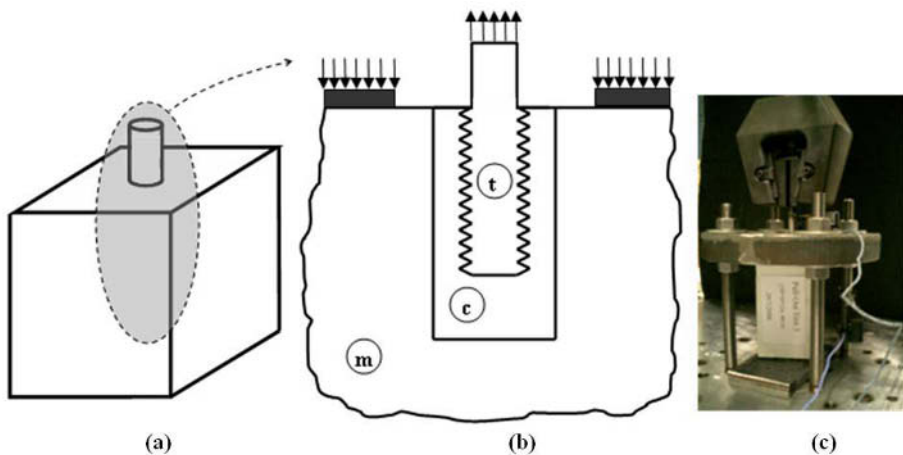


FIGURE 1. Schematic representation of the specimens (a,b) and the pull-out experiments (b,c).

The main criterion adopted for the design of the connections is to avoid completely the failure of marble. The parameters studied included the diameter of the titanium bars, the anchorage length, the thread pitch and the marble prism dimensions. The experimental set-up comprising suitable

supporting and measuring systems was improvised (Fig. 1c), given the absence of a relevant to this particular problem standard. The evaluation of the results was made in terms of the load  $P$  versus the displacement curves derived from the experiments. A typical  $P$ - curve obtained from these experiments is shown in Fig. 2a: It consists of an almost linear initial portion followed by a non-linearly increasing part which ends with an abrupt load drop, equal to about half the peak load attained. From this point on the load decreases smoothly until the whole anchored length is removed from the specimen. All possible performances expected during a pull-out test were observed depending on the specific combination of the parameters: pure pull-out, titanium failure, marble fracture as well as combinations of them.

In order to obtain a deeper insight of the failure mechanisms activated a parametric study was carried out with the aid of a numerical analysis, calibrated on the basis of the experimental results. A 3D model (Fig. 2b) was created using the commercially available code ABAQUS. The model consisted of three parts (threaded bar, mortar, marble). The material properties assigned are the ones obtained from a series of preliminary direct tension tests while the boundary conditions simulated accurately the pull-out tests. It was concluded that in some cases (combinations of parameters) there might be need for revising the current design approach, since the failure mechanism activated first is the fracture of marble, violating thus basic restoration principles.

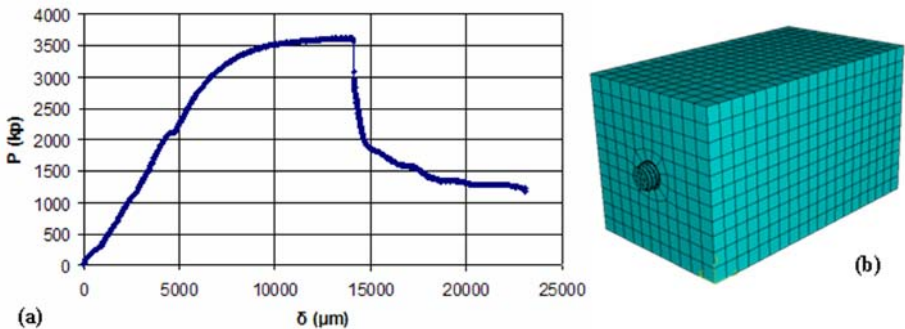


FIGURE 2. A typical force-displacement curve (a). 3D pull-out test model (b).

### Acknowledgements

The present study is part of the scientific project “PROHITECH: Earthquake Protection of Historical Buildings by Reversible Mixed Technologies”, Contract number: INCO-CT-2004-509119, financially supported by EU. The support is gratefully acknowledged.

### References

1. Zambas, C., Ioannidou, M., and Papanikolaou, A., In: *Proceedings of the IIC Congress on Case Studies in the Conservation of Stone and Wall Paintings*, The International Institute for Conservation of Historic and Artistic Works, Bologna, 1986, pp. 138-143.
2. Banholzer, B., Brameshuber, W. and Jung, W., *Cement and Concrete Composites*, vol. **28**, 564-571, 2006.



## TRANSVERSELY ISOTROPIC NATURAL BUILDING STONES UNDER THREE-POINT BENDING

S.K. Kourkoulis

Department of Mechanics, National Technical University of Athens  
5, Heroes of Polytechnion Avenue, Zografou Campus, GR-157 73, Athens, Greece  
stakkour@central.ntua.gr

Three-point bending (3pb) is a very popular test since it is based on a simple experimental procedure and important data about the mechanical behaviour of the material are obtained from it. As long as the length of the beam significantly exceeds the other dimensions and the study is focused at sections far from the central one the classical Bernoulli-Euler theory yields more or less satisfactory results. However, as the central section is approached serious local perturbations of the stress field arise and a detailed elastic solution appears to be indispensable. The situation becomes more complicated if the beam is made from anisotropic material, which is the case of most natural building stones. A general closed form solution of the problem is not available, even for the rather simple case of transversely isotropic materials. In this direction, an attempt is made here to find a solution of the problem, assuming that plane stress conditions prevail.

Consider a simply supported prismatic beam of unit width, length  $2L$  and height  $2c$ , made from a transversely isotropic material (Fig. 1). Assuming that the elastic modulus normal to the isotropy plane is negligible, i.e.  $E_y \rightarrow 0$ , Reissner [1] proved that the displacement field reads as:

$$u = \frac{1}{E_x} \left[ -\frac{x^2}{2} f'(y) + xg(y) + h(y) \right], \quad v = \frac{1}{E_x} \left[ \frac{x^3}{6} f''(y) - \frac{x^2}{2} g'(y) + \frac{E_x}{G} x f(y) + k(y) \right] \quad (1)$$

where  $f$ ,  $g$ ,  $h$  and  $k$  are arbitrary functions,  $E_x$  is the elastic modulus along the length of the beam and  $G$  is the shear modulus. In practice no material exists with  $E_y=0$  and therefore the present theory should be considered as the limiting case for materials with very small  $E_y/E_x$  ratios or an approximation for problems for which the  $\sigma_{yy}$  stress is very small. The boundary conditions are:

$$x = 0 \rightarrow \frac{\partial u}{\partial x} = 0, \quad v = 0, \quad x = L \rightarrow v = C, \quad y = \pm c \rightarrow \tau_{xy} = 0 \quad (2)$$

where  $C$  is an arbitrary constant. After long algebraic manipulations the stress field is obtained as:

$$\sigma_{xx} = -\frac{2xCGe^{-\alpha c} \alpha \sinh(\alpha c)}{L(1+e^{-2\alpha c})}, \quad \tau_{xy} = -\frac{CG}{L} + \frac{2CGe^{-\alpha c} \cosh(\alpha y)}{L(1+e^{-2\alpha c})} \quad (3)$$

The constant  $C$  is determined by equating the external load  $P$  with the force developed by the stress  $\tau_{xy}$  [2]. The predictions of the theoretical analysis were compared to those of an experimental programme with specimens prepared from the natural building stone used by ancient Greeks for the erection of the Zeus Temple at Olympia, i.e. a type of soft rock called conchylites shellstone. It is an inhomogeneous material, of layered structure which imposes to the material a strongly anisotropic character of the transverse type. The mechanical properties of the material, as obtained by Vardoulakis et al. [3], resemble those adopted by Reissner. Series of three-point bending tests were carried out using prismatic specimens cut from recently excavated conchylites blocks parallel to the material layers. It means that the longitudinal axis of the beams coincided

with the strong anisotropy direction, while the y-direction coincided with the weak one, resulting to a ratio of the elasticity moduli equal to  $E_y/E_x \cong 0.04$ .

Specimens with three different length over height ratios, equal to 2, 4 and 6, were tested. The results concerning the deflections are plotted in Fig. 2, together with the respective elastic curves. It can be seen from this figure that the experimental points are sufficiently close to the elastic curves; however they are systematically higher, especially at the central section.

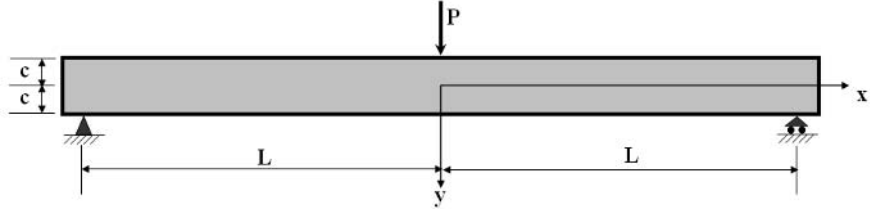


FIGURE 1. The configuration of the problem.

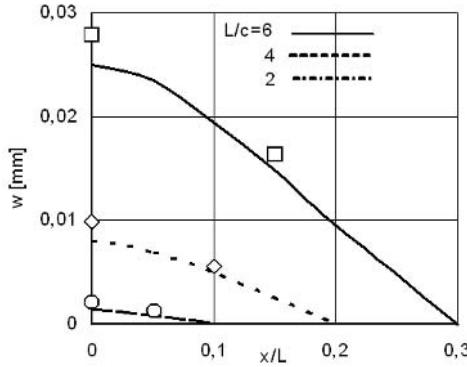


FIGURE 2. The deflection at the mid-section according to the theoretical analysis and the respective experimental results.

The above discrepancies can be justified by taking into account that the theoretical solution disregards the influence of the point load which, especially for short beams, is extremely pronounced [4]. Also the linearity assumption for conchylites is not fully justified experimentally, especially for loads approaching the fracture load. In addition, the assumption that  $E_y \rightarrow 0$  is not absolutely true for the conchylites shellstone, inevitably introducing additional discrepancies (although the values of the transverse stress measured do tend to zero). Summarizing it can be said that the present approach constitutes a first step for understanding the behaviour of transversely isotropic materials under 3PB and yields rather satisfactory results, provided that the assumptions on which it is based are fulfilled.

**References**

1. Reissner, E., *Phil. Mag.*, vol. **30**, 418-429, 1940.
2. Exadaktylos, G.E., Kourkoulis, S.K., *Electronic proceedings of the 4th National Congress on Computational Mechanics, GRACM 2002, Patras, Greece, 2002.*
3. Vardoulakis, I., Kourkoulis, S.K. and Zambas, C., *Proceedings of the 2nd International Symposium on Hard Soils Soft Rocks, Naples, Italy, 911, 1998.*
4. Kourkoulis, S.K., Stavropoulou, M.C., Vardoulakis I., Exadaktylos G.E., *Proceedings of the 9th International Congress on Rock Mechanics, Paris, France, pp. 623-626, 1999.*

## THE BRAZILIAN DISC WITH A CENTRAL NOTCH: A NUMERICAL AND EXPERIMENTAL STUDY

S.K. Kourkoulis and A.D. Levantis

Department of Mechanics, National Technical University of Athens  
Zografou Campus, GR-157 73, Athens, Greece,  
stakkour@central.ntua.gr

The direct tension test in case of rock type materials is, perhaps, the most difficult task of the Experimental Strength of Materials. The main obstacles hard to overcome is the preparation of standardized specimens, the application of the tensile load and the development of parasitic moments, caused by even the slightest non co-axialities and misalignments. A number of solutions have been proposed, however, most of them are time and labor consuming, the stress field is not uniaxial, the dimensions of the specimens may be restricted and the scattering of the results is significant. As a result, simpler tests were introduced, among which the Brazilian test, proposed by Carneiro and Barcellos already from the late forties [1], is the most popular one due to its simplicity.

However and in spite of the intensive research a number of questions remain still unanswered, especially in the case of cracked discs, for which an analytic solution is not available. In this context a numerical analysis is presented here carried out with the aid of the Finite Element Method. The specimens modeled were disc-shaped with diameter equal to 100 mm and thickness equal to 10 mm. The material was considered as isotropic and linearly elastic. The disc is loaded along two symmetric arcs by uniform radial compression. The boundary conditions included a roller along the vertical direction ( $dx=0$ ) while the lowermost point of the disc was fully restrained. A parametric study was conducted including the inclination, the shape (rectangular or elliptic) and the dimensions of the crack and the width of the loading arcs. The numerical analysis is carried out, using the ANSYS 9.0 software. The final model consisted of 50518 elements and 134400 nodes (Figs.1a,b). In Fig. 2a the influence of the loading arc on the stress at the tip of the notch is shown, while the radial variation of the stress components along the axis of symmetry of the notch is plotted in Fig.2b, for an elliptic crack inclined  $60^\circ$  with respect to the load.

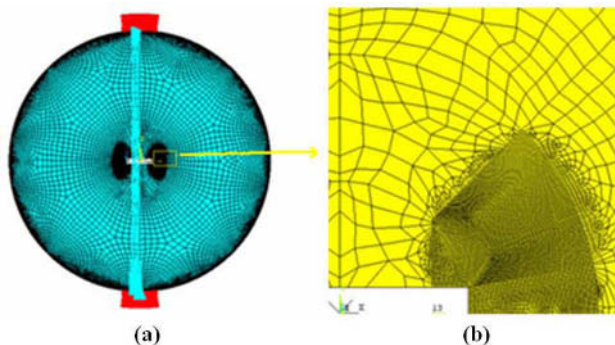


FIGURE 1. (a) An overview of the numerical model. (b) Detailed view around the tip of the notch.

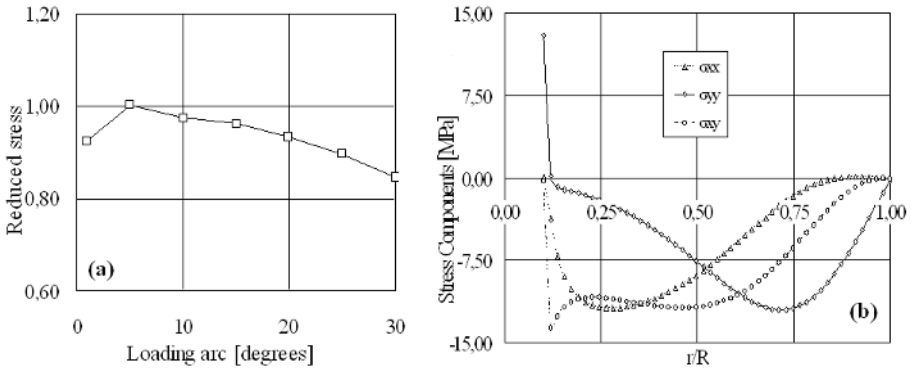


FIGURE 2. The influence of the loading arc on the stress at the tip of the notch (a) and the variation of the stress components along the line of symmetry of the notch (b).

For the validation and the assessment of the model a series of Brazilian tests were carried out with specimens made either from Dionysos marble or from PMMA. The dimensions of the specimens were those of the numerical model. The specimens were loaded using the device suggested by ISRM. The load was applied by a stiff hydraulic loading frame. The strains developed were measured with the aid of a system of strain gauges either along the notch and normal to it (Fig3a) or along an arc encircling the tip of the notch (Fig. 3b). Knowing the strain field components one can estimate the stress field adopting Hooke’s law.

In general the agreement between the numerical and the experimental results is satisfactory. Only for the regions very close to the loading arc, i.e.  $r/R > 0.8$ , and in the immediate vicinity of the tip of the notch, the discrepancies become significant. The maximum deviation does not exceed 20% and it appears at the tip of the notch. The results of the experiments exceed slightly but consistently those of the numerical simulation. Such a behaviour should be expected since the numerical analysis is based on linear elasticity which is not the case, since both Dionysos marble [2] and PMMA exhibit some nonlinearity. In addition the simulation of the uniformly distributed load by the finite element method is achieved by applying a number of concentrated loads on the respective nodes, inevitably causing local stress concentrations which influence the stress distribution.

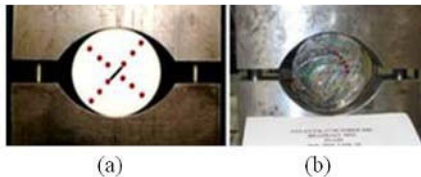


FIGURE 3. The experimental set-up according to the standards suggested by ISRM and the two types of specimens

**References**

1. Carneiro, F. and Barcellos, A., *Bulletin RILEM*, **I(13)**, 97-108, 1953.
2. Vardoulakis, I., Kourkoulis, S.K., Exadaktylos, G.E. and Rosakis, A., *Proc. Interdisciplinary Workshop “The building stone in monuments”*, Athens, Greece, Eds. M. Varti-Mataranga and Y. Katsikis, IGME Publishing, 187-210, 2002.

## THE INFLUENCE OF THE FLUTES ON THE MECHANICAL BEHAVIOUR OF THE ANCIENT GREEK COLUMNS

S.K. Kourkoulis<sup>1</sup>, K.E. Moupagitsoglou<sup>2</sup> and N.L. Nini<sup>3</sup>

<sup>(1)</sup>Department of Mechanics, <sup>(2)</sup>Faculty of Civil Engineering,  
National Technical University of Athens, Zografou Campus, GR-157 73, Athens, Greece

<sup>(3)</sup>Archaeological Museum of Epidauros, GR 210-52, Ligourio, Hellas  
stakkour@central.ntua.gr

It is commonly assumed that the columns in ancient Greek Temples were fluted due to aesthetical reasons only. However, a detailed numerical analysis of the contact between adjacent drums of typical ancient columns revealed that the distribution of stress concentrations along the perimeter of the stone drum during sliding corresponds to the typical fluting present in columns of ancient Greek and Roman architecture [1]. Hence, fluting of the columns might have been a conscious decision, based on previous evidence that such regions were prone to cracking, in order to prevent and control possible material deterioration at the surface. Indeed engineering judgement suggests that the arched shape of the flutes resists surface cracking and acts as reinforcement. Therefore beyond aesthetic advantages it is possible that the flutes influence the mechanical behaviour of the whole column. This could be expected due to the singularities introduced by the imposed abrupt change of the boundary conditions of the specimen, where the friction boundary of the base meets the free boundary of the lateral surface. The combination of compression (due to the friction cone) and extension (the lateral expansion produced by axial compression) makes it a favourable place for crack initiation, i.e. non-homogeneous straining, eventually leading to fracture. In trying to eliminate this effect, apart from minimizing the friction, one should also try to provide support to the free boundary against exfoliation and cracking.

Following the previous line of thought it was decided to check this hypothesis, by studying the mechanical behaviour of a typical column of the Parthenon Temple of the Acropolis of Athens. These columns have 20 flutes the shape of which is accurately described as an arc of an ellipse [2]. The material of them is Pentelik marble, which in a first approximation was considered isotropic with Young's modulus  $E=70$  GPa and Poisson's ratio  $\nu=0.3$ . As a first step the problem was studied numerically with the aid of the Finite Element Method. Three successive drums were considered. The interface between them was modelled with contact and target elements and the coefficient of friction was set equal to 0.7. It was assumed that the lower base of the lower drum is rigidly clamped to the ground. The elements used for the meshing are 3-D tetrahedral elements with 10 nodes and 3 linear degrees of freedom on each node. The final model of a single drum is shown in Fig. 1a. The loading modes included the own weight of the drums, a uniform pressure on the upper surface of the uppermost drum, simulating the weight of the superimposed members, as well as bending and torsional moments. The variation of the equivalent stress in a typical drum under its own weight and bending moment is shown in Fig. 1b.

As a second step an experimental programme was carried out with specimens prepared in accordance to the shape of the drums of the doric column of ancient Greek architecture, with their lateral surface, i.e. the free boundary, fluted. Each specimen had 20 flutes and the proposed configuration was tried for specimens made from Cyprus stone, Alfopetra stone, Kenchreae stone and Dionysos marble. Two cases are compared for each material, one standard (cylindrical) and one fluted. The observed changes, as it is seen in Fig.2a, in which the results for the Cyprus stone are plotted, are striking. The peak strength is reduced by about 30%, the failure strain increases by more than five times and the mode of failure changes from brittle to ductile. The energy density

input (the area under the stress-strain curve) for the fluted specimen is five times that of the standard one, indicating the increased capacity of the so configured specimen to absorb energy.

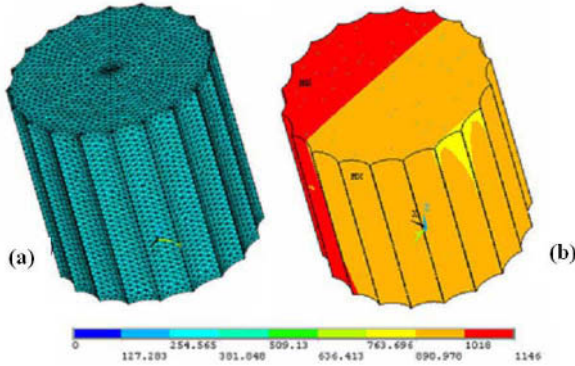


FIGURE 1. (a) The model of typical drum. (b) The variation of the equivalent stress in a typical drum under its own weight and bending moment.

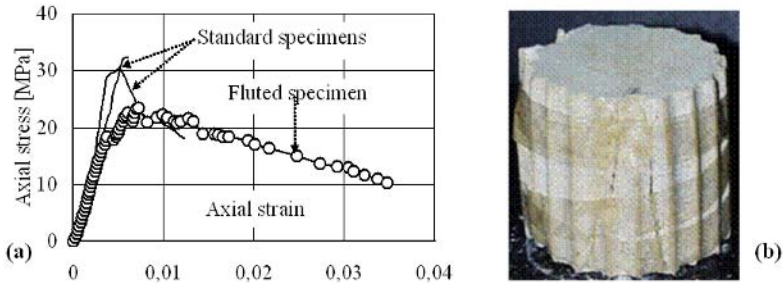


FIGURE 2. (a) Standard vs. fluted specimens for Cyprus stone. (b) A typical fractured specimen.

Concluding it can be said that fluting of the lateral free boundary reduces the peak strength and adds to the stress-strain curve a large strain-softening regime. Finally it is emphasized that fluted specimens did not fail at macrostructural level; cracking was restricted to their lateral surface only.

**References**

1. Ninis, N. L., Kakaliagos, A. K., Mouzakis, H., Karydis, P., *Proceedings of the 5<sup>th</sup> Int. Conf. on Analysis of Discontinuous Deformation*, Beer-Sheva, Israel, Y. H. Hatzor, A. A. Balkema Publishers, The Netherlands, 2002
2. C. Zambas, *The refinements of the columns of the Parthenon*, YSMA, Athens, Hellas, 2002.

## THE SIZE-EFFECT FOR NATURAL BUILDING STONES

S.K. Kourkoulis<sup>1</sup>, E. Ganniari-Papageorgiou<sup>1</sup> and N.L. Ninis<sup>2</sup>

<sup>1</sup>Department of Mechanics, National Technical University of Athens,  
Theocaris Building, GR-157 73 Zografou Campus, Hellas

<sup>2</sup>Archaeological Museum of Epidauros, GR-210-52, Ligorio, Hellas  
stakkour@central.ntua.gr

The dependence of the mechanical properties of natural building stones on the size of the specimens used in the laboratory tests is the object of the present study. The phenomenon, known as size effect, was long ago well known in the engineering community. The dependence of the strength of ropes on their length was known to Leonardo da Vinci already from the beginning of the 16th century. Griffith was the first one who studied thoroughly the variation of the nominal strength of glass fibres with their diameter. Since then the phenomenon was attributed to statistical reasons. The “weakest-link” model and Weibull’s classical statistical size-effect laws were of general acceptance and use. It was only at the early of seventies when experimental results were presented that could not be explained by the statistical analysis and this gave birth to increased interest to the phenomenon. Nowadays two basic approaches are identified: the deterministic energetic theory introduced by Bažant [1] and that of crack fractality introduced by Carpinteri [2].

In the present paper the size effect is studied experimentally for the case of the porous stone of Cefallonia, a natural building stone considered as a candidate substitute of the porous stone of Kenchreae, the material used by ancient Greeks for the erection of the Asklepieion of Epidauros. Series of uniaxial compression tests were carried out using cubic and cylindrical specimens of different sizes and apertures. The basic mechanical properties of the material were determined by appropriate analysis of the test data. The results exhibited clearly the dependence of almost all mechanical properties studied (peak stress, strain at peak stress, modulus of elasticity, elastic strain energy density and total strain energy density) on the dimensions of the specimens. It was also indicated that the kind of dependence is different in the case of the cylinders in comparison to that of the cubes (Figures 1, 2). Indeed it was proved that all mechanical properties of the cubic specimens depend on the size according to a non-monotonous law and the extrema are very clear. On the contrary for the cylinders some of the properties varied according to a non-monotonous law while the variation for other properties was monotonous.

The above described rather peculiar behaviour and the relatively restricted number of apertures tested in this first series rendered the execution of additional tests indispensable demand. In this direction complementary tests were carried out with cylindrical specimens of eight different apertures (height / diameter ratios) ranging from 8 to 2 (Fig. 3). The material used was the porous stone of Alfa of Crete. This is another candidate substitute of the porous stone of Kenchreae of relatively higher compressive strength in comparison to that of the authentic material [3].

It was concluded definitely that at least the peak strength of this stone depends on the size of the specimens according to a non-monotonous law again, with a clear but relatively weaker extremum compared to that of the cubic specimens. In other words a specimen size exists for which the peak strength becomes maximum. Such a conclusion is extremely important for those using these materials in a series of restoration projects: In case the design of a structure is based on data obtained from experiments with specimens of this “optimum” size it is possible that the strength of the structure is overestimated. Finally, the fact that the experiments support a non-monotonous influence of the specimen size on the peak strength is in contrast to the theories mentioned in the introduction and further investigation is necessary.

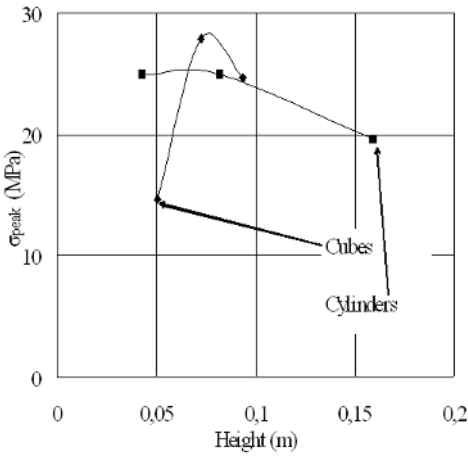


FIGURE 1



FIGURE 3

FIGURE 1. The dependence of the peak stress on the size of the specimens

FIGURE 3. The specimens used for the study of the anomalous behaviour of the size effect.

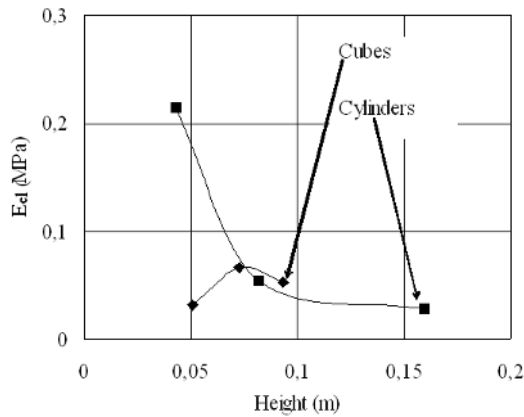


FIGURE 2. The dependence of the elastic strain energy density on the size of the specimens.

**References**

1. Bažant, Z. P., *J. of Engng. Mech*, vol. **110**, 518-535, 1984.
2. Carpinteri, A. and Chiaia, B., *Sdhan*, vol. **27**(4), 425-448, 2002.
3. Ninis, L., Kourkoulis, S. K. and Sakellariou, A., *Proc. of the Interdisciplinary Workshop: The building stone in monuments*, Athens, November 2001, IGME Publishing, Eds. M. Varti-Mataranga and Y. Katsikis, 235-248, 2002.



## EVALUATION OF ACCELERATED WEATHERING EFFECTS ON THE SURFACE OF TWO COLOURED SICILIAN BUILDING STONES

Rizzo Giovanni<sup>a</sup>, Ercoli Laura<sup>b</sup> and Megna Bartolomeo<sup>a</sup>

<sup>a</sup> Dipartimento di Ingegneria Chimica dei Processi e dei Materiali, Università di Palermo

<sup>b</sup> Dipartimento di Ingegneria Strutturale e Geotecnica, Università di Palermo  
Viale delle Scienze 90128 Palermo, Italy

rizzo@dicpm.unipa.it, ercoli@diseg.unipa.it, megna@dicpm.unipa.it

The dark grey *Breccia di Billiemi* and the *Ammonitico Rosso* of Piana degli Albanesi, widely employed outdoor and indoor in monuments in Sicily, undergo significant alteration processes, affecting not only the chromatic aspect but also the state of aggregation.

In a previous paper [1] the effects of accelerated weathering in laboratory was compared with natural ageing in the urban environment. The study included the description of lithofacies, the characterisation by means of petrographic and physical-chemical techniques and accelerated weathering experiments on both lithotypes.

Aim of this paper is to quantify the effect of artificial accelerated weathering procedure. Experimental tests were performed using at least two slabs of each lithotype. The exposed surfaces, 2.5\*10 cm, were polished in order to evidence the degradation effects. Both weight measurements and image analysis [2] of the samples surfaces were performed during accelerated washout and acid etching tests.

The accelerated weathering procedures were also used to evaluate the effect of some commercial products, currently applied to protect stone surfaces against the effects of urban pollution. Infact, acid atmosphere and rain washout can induce a severe decay of the stone, leading to microcracks and colour alteration. The effectiveness of protection was tested by the same methods used to quantify the decay of unprotected samples.

In [1] the different effect of ageing agents on veins and grains was related to the difference in porosity. In this paper such assumption was verified by contact angle measurements on different areas of untreated samples. Furthermore, such measurements were performed also on treated samples during artificial ageing tests, in order to investigate the mechanisms of protective action.

As most of preservatives are organic polymeric materials, such ageing procedures included also UV radiation.

The results of this paper give a contribution to the comprehension of both degradation mechanisms of natural building stones and role of preservatives in protection from aggressive environments. Furthermore a procedure is proposed to evaluate the effectiveness of preservatives, in order to choose suitable products for a durable conservation intervention.

### References

1. Rizzo G., Ercoli L., Megna B., "Natural and Accelerated Weathering of Two Coloured Sicilian Building Stones" in "Fracture and Failure of Natural Building Stones", S.K. Kourkoulis ed., Springer, Dordrecht, The Netherlands, Chapter 5.4, 329-341, 2006.
2. Figueiredo C., Figueiredo P., Pina P., Aires-Barros L., Ramos V., Machaqueiro P., "Texture analysis of images taken from artificially aged stones: a statistical and structural approach", in Aires-Barros L., Zezza F. 6th International Symposium on the Conservation of the

---

Monuments in the Mediterranean Basin. Influence of the environment and defense of the territory on recovery of cultural heritage, Lisbona, 7-10 April 2004, 248-252.

3. Charola A. E. and R. Ware, "Acid Deposition and the Deterioration of Stone: a Brief Review of a Broad Topic", *Natural Stone, Weathering Phenomena, Conservation Strategies and Cases Studies*, Geological Society Special Publication n° 205, 2002, 393-406.
4. P. Di Stefano and A. Mindszenty, "Jurassic Drowning Unconformities: Dissolution Surfaces Capped by Hard-ground in Western Sicily" *Proceedings of the 79th Congresso Nazionale della Società Geologica Italiana*, 1998, vol. B, Offset Studio Palermo ed., 423- 426.
5. M. Fazzuoli, R. Sartori, S. Vannucci, "Rosso Ammonitico e Marne del Sugame (Successione Toscana): Caratterizzazione Mineralogico – Geochimica" *Proceedings of the 79th Congresso Nazionale della Società Geologica Italiana*, 1998, vol. B, Offset Studio Palermo ed., 423- 426.

## THE BOND MECHANISM IN STONE OR BRICK TO GROUT INTERFACES

Elizabeth Vintzileou and Chryssi-Elpida Adami  
National Technical University of Athens- Laboratory of Reinforced Concrete  
5 Iroon Polytechniou str., Zografou, GR-157 73, Greece  
elvintz@central.ntua.gr, adamis@central.ntua.gr

In conservation of historic masonries, grouting is one of the most commonly applied techniques. However, the design of adequate grout mixes, as well as the prediction of the mechanical properties of a grouted masonry is not based on quantified data regarding the bond properties of interfaces. Within the present work, a systematic study of the bond mechanism is carried out in composite grout/substrate specimens. Two types of tripartite (lime-pozzolan-cement) grouts are examined (G2 (cement 30%-lime 35%-metakaolin 35%) and G4 (cement 30%-lime 23%-milos earth 47%)), combined with three substrates (two types of limestone with different porosity (Dionysos marble and travertine) and solid bricks). A cement-based grout, G1 (cement 80%-lime 20%), is used as a reference. The interfaces between grout and substrate are characterized by means of mechanical tests in direct tension and shear. The in-time development of the tensile and shear bond strength is also investigated. Thus, tests were carried out at ages of 28 to 180 days. In case of shear tests, the value of the normal compressive stress,  $\sigma$ , on the interface was considered as an additional parameter. Three values of this parameter were considered, namely: 0.1, 0.3, and 0.6 MPa. Based on a sensible selection of combinations of parameters, 111 and 135 composite specimens were prepared and tested in direct tension (Fig. 1) and shear (Table 1), respectively. In order to correlate the characteristics of the substrates and the obtained strengths of the interfaces, their surfaces were examined and their porosity was measured.

The main conclusions of this study are that (a) the studied tripartite grouts can develop tensile and shear bond strength comparable to Portland cement-based grout, although their mechanical properties are lower than those of the cement grout, (b) the value of the reached bond strength is governed mainly by the substrate characteristics and the binding properties of the grouts (see for example Fig.1, where conclusion (a) is illustrated, whereas it is shown that for the same grout mix, low porosity marble exhibited in general lower bond strength values than the higher porosity travertine). Furthermore, (c) interfaces subjected to shear have presented similar behaviour with interfaces within concrete (see i.a. Tassios and Vintzileou, [1]). In fact, as shown in Table 1, the maximum mobilized shear resistance ( $\tau_u$ ) increases for increasing normal compressive stress on the interface, whereas the friction coefficient  $\mu$  (expressed as the ratio between maximum shear resistance and corresponding shear slip) is decreasing with increasing normal compressive stress. Thus, the beneficial effect of normal compressive stress on the interface was confirmed. Therefore, the results of this project confirm the efficiency of tripartite lime-pozzolan-cement grouts with reduced Portland cement content for repair and strengthening of historic masonries.

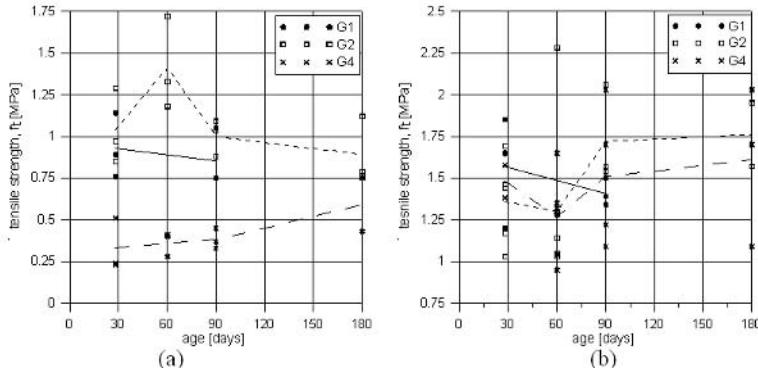


FIGURE 1. In-time development of: (a) marble-to-grout and (b) travertine-to-grout bond tensile strength.

TABLE 1. Summary of shear test results (mean values of two or three specimens per combination of parameters).

days	Substrate type	Ref. No of the grout	$\tau_0$ [MPa]			$\mu_{max}$		
			$\sigma=0.1$ MPa	$\sigma=0.3$ MPa	$\sigma=0.6$ MPa	$\sigma=0.1$ MPa	$\sigma=0.3$ MPa	$\sigma=0.6$ MPa
28	marble	G1		0.47			1.57	
		G2		0.82			2.73	
		G4		0.26			0.87	
	travertine	G1	(*)	1.00	1.14	(*)	3.33	1.90
		G2	1.05	1.10	1.12	10.50	3.67	1.87
		G4	0.66	0.45	0.80	6.60	1.50	1.33
60	travertine	G2		1.37			4.56	
		G4		0.64			2.13	
90	marble	G1		0.61			2.03	
		G2		0.54			1.80	
		G4		0.50			1.67	
	travertine	G1	0.61	0.70	0.88	6.10	2.33	1.47
		G2	0.99	0.93	1.14	9.90	3.10	1.90
		G4	1.02	0.95	1.14	10.20	3.20	1.90
180	travertine	G2		0.86			2.87	
		G4		0.65			2.17	
(*) unreliable test results								

References

1. Tassios, T.P., Vintzileou, E., Concrete-to-concrete friction, *Journal of Structural Engineering ASCE*, vol. **113**, 832-849, 1987.

## MECHANICAL STRENGTH AND WATER CONTENT OF POROUS LIMESTONES

Kevin Beck, Hamidreza Adib-Ramezani and Muzahim Al-Mukhtar

Centre de Recherche sur la Matière Divisée, Université d'Orléans - CNRS-CRMD

1B, rue de la Férollerie 45071 Orléans Cedex 2, France.

beck@cnsr-orleans.fr ; hamidreza.ramezani@cnsr-orleans.fr ; muzahim@cnsr-orleans.fr

Limestones are commonly used as a construction material in many engineering structures. The knowledge of the influence of moisture on the mechanical properties of stones such as compressive strength and tensile strength are important to characterize the suitability of the use of limestones for several engineering purposes. Effects of the environment influence the strength properties and can be useful for the mining industry in the operation of fracturing and extraction of limestones on a cost effective basis. Many properties such as the water content, the degree of saturation and macro and microstructure (porous spaces and textural organisation) influence the mechanical resistance properties of the limestones (Dobereiner [1], Ojo [2], West [3]). So, changes in water content induce changes in mechanical stresses. With cyclic environmental conditions (humidity, rain water, ...), this changes can induce hydromechanical fatigue and can affect the behaviour of the stone. This communication is a part of a research program devoted to understand the geotechnical engineering behaviour of two French porous limestones, namely; white tuffeau and Sébastopol stone.

The first limestone, Tuffeau is largely used in constructions of the castles in the Loire Valley - France. Many elegant and aesthetic frontend sculptures have been constructed using these stones. One of the key advantages of the stone is its relative high ductility property. However, over a period of time these sculptures gradually deteriorate due to the effects of erosion. In some of these sculptures, gullies of a few centimetre thicknesses are typically formed due to problems associated with erosion. The second stone Sébastopol used in the study is selected to provide a comparison of mechanical properties along with Tuffeau. The total porosity value of both the limestones used is similar (near 45%).

The mechanical strengths of the two limestones are tested under various water contents within the stone: from completely dry to completely saturated. Between these two extremes moisture conditions, water content of the stones are controlled using saturated salt solutions, osmotic solutions and tensiometric plates. The water retention curves established for all the range of capillary suction (shown at the Fig. 1) and pore size distributions were also determined for both the limestones. The mechanical resistance properties of the tested limestones are determined by means of compressive and tensile tests for samples with several water content induced by the relative humidity applied (or its equivalent suction). Results are showed at Fig. 2. The mechanical stress strongly decreases when the water content increases. This effect is particularly important for the low water contents.

The differences in the mechanical behaviour (in compression and tension) of the two examined stones which have relatively the same total porosity are explained by their mineralogical composition, pore size distribution and water retention capacity behaviour.

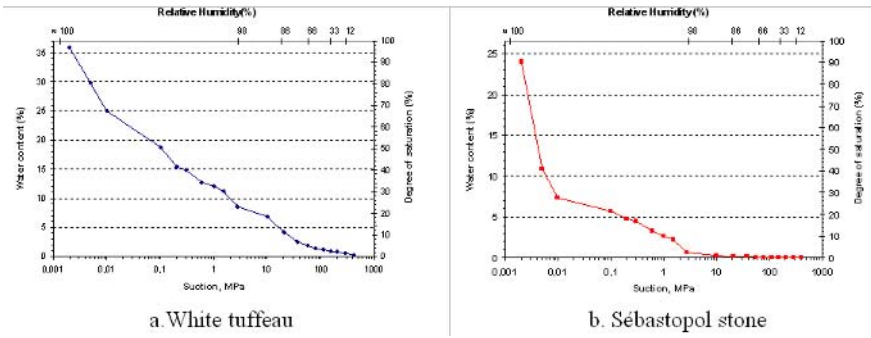


FIGURE 1. Water retention curves for the two studied stones

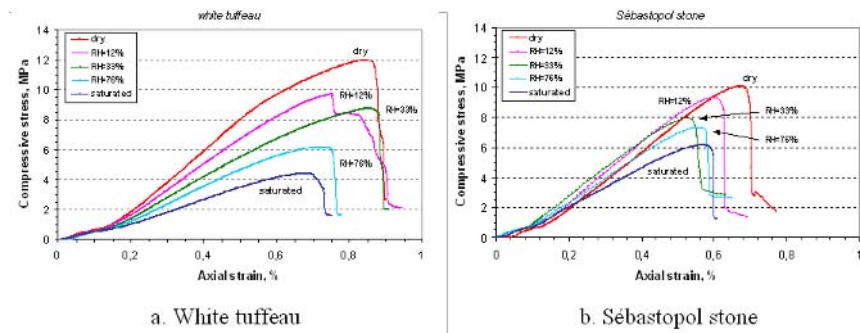


FIGURE 2. Strength/Strain curves for uniaxial compressive strength tests with hydrous state (water content) of the stones

**References**

1. Dobereiner L. & De Freitas M.H., *Géotechnique*, vol. **36**, No. 1, 79-94, 1986.
2. Ojo O. & Brook N. 1990, *Mining science and technologie*, vol. **10**, 145-156, 1990.
3. West G., *Quarterly Journal of Engineering Geology*, vol. **27**, 51-56, 1994.

## CRYSTALLIZATION PRESSURE AND SALT DISTRIBUTION IN TUFFEAU LIMESTONE

Thua-Tri Van, Kévin Beck, Xavier Brunetaud, Muzahim Al-Mukhtar  
 Centre de Recherche sur la Matière Divisée, Université d'Orléans, CNRS-CRMD  
 1B rue de la Férollerie, 45071 Orléans Cedex 2, France  
 thua-tri.van@cnrs-orleans.fr, beck@cnrs-orleans.fr, xavier.brunetaud@univ-orleans.fr,  
 muzahim@cnrs-orleans.fr

Presence of soluble salts in the building limestone's which can originate from different pathways (marine environments, dissolution of the calcite of the stone due to water transfer,...etc) gradually induces textural and mineralogical modifications in the stones. These salts are one of the key contributors towards degradation of monuments due to weathering action (Fig. 1). In this paper, weathering test are carried out on white Tuffeau limestone with high total porosity of 48%. This limestone, extracted from the Lucet quarry in Saint-Cyr-en-Bourg in Maine-et-Loire, France, is largely used in constructions of the castles of Val de Loire.

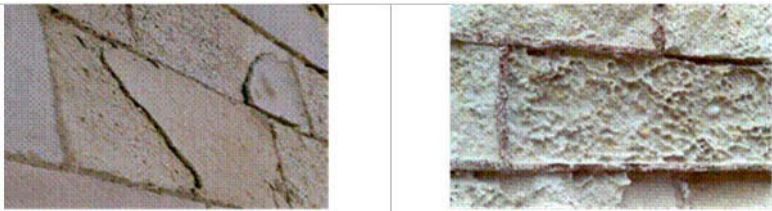


FIGURE 1. Main deterioration forms of white Tuffeau: a) contour scaling (Chaumont castle), b) granular disintegration (Bretagne castle- Nante)

Samples of 25 mm x 25 mm x 50 mm are firstly imbibed with the salt solution of NaCl and  $\text{Na}_2\text{SO}_4 \cdot 10\text{H}_2\text{O}$ . Samples are consecutively subjected to accelerated weathering test in moisture condition controlled, at 20°C. Weathering tests are bases on cycles of relative humidity (RH) from 20% to 98%, each one lasting 2 days.

At the end of cycles, the weight of the sample, the salt distribution (Fig. 3), the residual water content are determined.

During the drying stage, transformation from soluble salt solution to solid crystals induces mechanical stresses which in turn can cause rupture of the stone matrix. Salt crystallization induces pressure in the pores at the micro-scale level and tends to collapse the stone at the macro-scale level.

The tensile stress generated by the precipitation of the salts can be estimated using a homogeneous crystallization pressure,  $P_{ch}$  that can be calculated from local crystallization pressure

$P_c(r)$  in a pore of radius  $r$ , following:

$$P_{ch} \times S_{salt} = \int_{r_{access}^{min}}^{r_{access}^{max}} P_c(r) \times S_p(r) dr \tag{1}$$

Where  $S_{salt} = \int_{r_{access}^{min}}^{r_{access}^{max}} S_p(r) dr$  represents the total surface corresponding to pores where salt can precipitate (between  $r_{access}^{min}$  and  $r_{access}^{max}$ ) and  $S_p(r)$  represents the surface of pores.

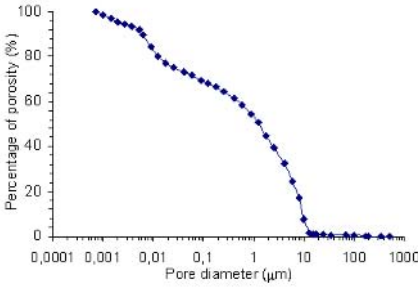


FIGURE 2. Pore- size distribution by MIP and BET

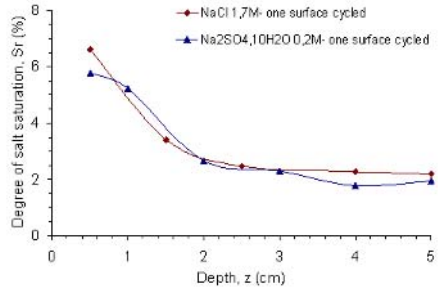


FIGURE 3. Salt distribution of Na<sub>2</sub>SO<sub>4</sub> 10H<sub>2</sub>O and NaCl after 100 cycles of RH (20-98-20)

Using pore-size distribution from mercury intrusion porosimetry (MIP), BET (Fig. 2) and porosity measured by water absorption (Beck *et al.* [1, 2]),  $r_{max}$  can be estimated from volumetric saturation of salt solution during imbibition and  $r_{min}$  can be calculated from the volume of salt after drying stage (Fig. 3).

$P_c(r) = \frac{2\sigma}{r}$  is a first- step estimator of the local crystallization pressure in a pore of radius (r), as suggested by Wellman and Wilson [3], this definition may be subsequently improved.

Weathering level can be estimated basing on the comparison between the calculated tensile stress induced by salt crystallization and the ultimate tensile strength of the Tuffeau matrix.

**References**

1. Beck K, Al-Mukhtar M, Rozenbaum O., Rautureau M, *Build Environ*, vol. **38**, 1151–1162, 2003.
2. Beck K., Al-Mukhtar M., *Int J Restor Build Monum*, vol. **11**(4), 219–226, 2005.
3. Wellman H. W., and Wilson A.T., *Nature*, vol. **205**(4976), 1097– 98, 1965.



## ANALYSIS AND INTERPRETATION OF THE STRUCTURAL FAILURES OF THE ORTHOSTATE BLOCKS OF THE NORTHERN WALL OF THE ATHENS PARTHENON

Eleni-Eva Toumbakari  
Ministry of Culture, Greece  
Polygnotou 10, GR-105 55, Athens, Greece  
elenit@otenet.gr

The major events that affected the structural history of the Parthenon of Athens are the destructive fire of 267 a.D. and the explosion that took place in 1687 a.D. during the siege of Athens by the Venetian fleet. Following the fire, the Parthenon roof collapsed, whereas the marble blocks that were subjected to thermal action were severely cracked or even lost an important portion of their mass. Following the explosion, a big part of the remaining Parthenon collapsed, whereas important damages have been generated in those areas that did not collapse. Of course, other events, such as earthquakes, occasionally occurred during the monument's life, but their effect appears minor in comparison to the aforementioned.

The first restoration of the long walls of the cella was carried out between 1842-1844. During this period, 158 wall blocks were put back in arbitrary order, whereas those surfaces that were damaged by the 267 a.D. fire were completed with the use of solid bricks, which were subsequently removed in 1926-1927. In the following years only minor interventions took place, consisting mainly in conservation measures such as rejoining of the marble fragments in situ with or without the addition of small reinforcement to avoid detaching of marble surface fragments. Within the framework of the recent restoration campaign, the restored building blocks were dismantled in 1992-1993. Purposes of this restoration campaign were (a) to locate the original position of the restored stones, so as they are put back in their initial position, as well as to identify the original position of building blocks that were not used during the previous campaign, and (b) to proceed to the repair and strengthening of the damaged stones as well as to the structural design of the wall to be erected with the use of those blocks. The original position of the marble blocks of the first row of the Northern Wall of the cella (orthostate) was determined following detailed architectural studies (Toganidis [1,2], Toganidis & Matala [3]). The present study is part of the actions undertaken for the structural analysis and design of the restored walls.

The bearing system of the walls of the cella consists in an assembly of marble blocks connected with clamps and dowels. The fact that those structural members are independent to each other, does not imply that they do not interact to each other. This interaction is controlled by their mass and generated friction but also by their connectors. For long, however, the effect of the connectors on the structural pathology was not studied, as it was widely believed that they failed, in limit state situations, before any damage could be generated on the marble blocks. In case failure was observed on the connectors' area, this was attributed to rust of the iron clamps and dowels.

The methodology adopted for the structural analysis and design was first developed for the Parthenon Opisthodomos (Toumbakari [4]), and was subsequently applied at the Orthostate blocks of the N.Walls (Toumbakari [5]). The approach was based on two observations: (a) most of the recorded damages are concentrated in the areas of the connectors, and (b) the state of preservation of the ancient clamps and dowels that were removed from the Opisthodomos during the restoration campaign of 2001-2004 was very good. It has to be mentioned that there are very few original connectors of the Walls that survived, the assumption is however made that they all were of the same quality as those of the Opisthodomos. This assumption is validated by observations made in

other Monuments of the Acropolis as well. It was therefore necessary to record, analyse and interpret the pathology of the Orthostate blocks before proceeding to the design of the appropriate repair measures.

In the paper, first the description of the walls' constructional features is given. Then, the failure areas are identified, together with a description of the configuration of the failure surfaces. On the basis of the study of those elements, five failure modes were detected. The interpretation of the damages was based on the simultaneous consideration of (a) the kinematic restrictions of each block separately, (b) the applied system of deformations / displacements on each structural member and (c) the applied system of deformations / displacements on the wall itself. Moreover, the effect of the marble orthotropy was also considered.

The main conclusion of the study is that the observed structural pathology is related to the presence of the connectors. Available experiments on dowels (Zambas [6]) are in agreement with these conclusions. Further experimental and numerical research is however needed, to describe and verify the action of the connectors.

## References

1. Toganidis, N., *Study for the Restoration of the Parthenon: preliminary study of the long walls of the Parthenon cella*, vol. 2, Min.of Culture, Athens, Greece, 1989 (in Greek).
2. Toganidis, N., *Study for the Restoration of the Parthenon: Study of the long walls of the Parthenon cella*, vol.5, Min.of Culture, Athens, Greece, 1994 (in Greek).
3. Toganidis, N. and Matala, K., *Study for the Restoration of the Parthenon: Study for the Restoration of the Parthenon Northern Wall*, Min.of Culture, Athens, Greece, 2002 (in Greek).
4. Toumbakari, E.-E., *Analysis & interpretation of the structural pathology of the Parthenon Opisthodomos*, unpubl. Report under preparation, YSMA (in Greek).
5. Toumbakari, E.-E., *Documentation of the bearing structure - Analysis & interpretation of the structural pathology – Design of the interventions of the Orthostate blocks of the N.Wall of the Parthenon – Function & behaviour of the connectors*, unpubl. Report, YSMA, 2007 (in Greek).
6. Zambas, K. , *Study for the Restoration of the Parthenon*, vol. 3b, Min.of Culture, Athens, Greece, 1994 (in Greek).

## COMPACTION BANDS IN OEDOMETRIC TESTS ON HIGH POROSITY SOFT ROCKS

Riccardo Castellanza<sup>1</sup>, Eleni Gerolymatou<sup>2</sup> and Roberto Nova<sup>1</sup>

<sup>1</sup>Department of Structural Engineering,  
Milan University of Technology  
p.za L. da Vinci 32, 20133 Milano

<sup>2</sup>National Technical University of Athens, GR-157 73, Athens, Greece

<sup>1</sup> riccardo.castellanza@polimi.it

The paper presents the experimental results obtained in a series of displacement controlled oedometric tests on soft rocks. Four different materials characterized by a high void ratio have been investigated; three natural soft rocks and an artificial one. The materials examined were conchyliaades stone, Puglia calcarenite, pumice stone and gasbeton. In order to be able to monitor also the stress path, a soft oedometer ring was designed and constructed for the measurement of the radial stresses. The observed behaviour is summarized as follows. After an initial phase in which the mechanical response is essentially elastic, a second phase starts, in which bonds are progressively broken so that in the axial strain-stress curve an unload is recorded and a sort of 'curl' appears in the stress path. This means that strain non-homogeneities can occur in the form of compaction bands. In the final part of the test, the axial stress increases exponentially and the stress path comes back to be linear, as the one expected for a cohesionless material. The experimental behaviour is reproduced by means of an elastoplastic strain-hardening/softening constitutive model and the occurrence of compaction bands is theoretically predicted.



FIGURE 1. High porosity soft rocks tested and the Soft Oedometer Apparatus

Volcanic soil, as well as calcareous sands, develop diagenetic bonds in time. These are weak and brittle in nature, so that even moderate pressures, such as those transmitted by a foundation, can break the bonds and cause larger settlements. This kind of bonded soils (Fig. 1) was employed as construction material for buildings that constitute nowadays an important cultural heritage (Greek temples, churches and other monuments). The study of bonded soils under confined compression has therefore some engineering relevance.

In order to investigate the mechanical behaviour of such a material, an oedometer ( $\Phi=37$  mm) with flexible ring (Castellanza and Nova 2004) was put under the loading ram of a triaxial cell (Fig. 1). In this way, it was possible to control vertical displacements and measure the axial load by

means of a load cell. Since the ring is flexible, very small radial strains occur, so that the cinematic conditions are not exactly oedometric, but very close to them. The associated average circumferential stretch of the ring can be measured by three strain gauges with the resolution of about  $1.0 \mu\text{m/m}$ . The ring thickness of  $0.8\text{mm}$  was designed by means of the Mariotte formula for hollow cylinders under uniform pressure for working up to  $6 \text{MPa}$  with a resolution of  $3.5 \text{kPa}$ . The results obtained for 'conchiliades' and gasbeton are shown in Fig.2.

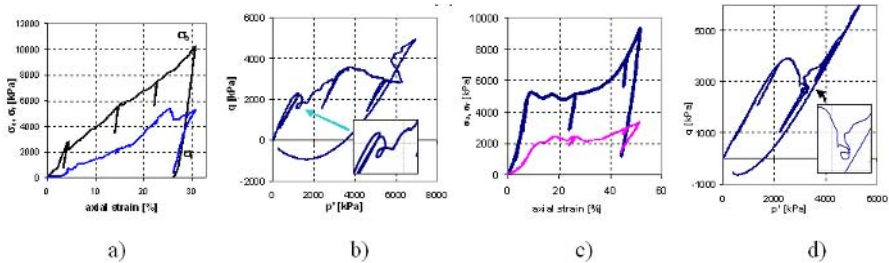


FIGURE 2. Axial - radial stress vs. axial strain and stress path: conchiliades (a,b), gasbeton (c,d)

In Fig.2 it was shown that, after an initial phase in which the stress path is linear, there is a second phase in which the deviator stress increases less than the isotropic pressure and can even temporarily decrease. Such a phase is associated to the progressive deconstruction of the specimen due to the breakage of the bonds. When the bonds are completely broken and the material has been transformed in a granular assembly of cohesionless grains, the stress path comes back to be approximately a straight line as for a virgin granular material. It was further shown that strain non-homogeneities can occur in the form of a compaction bands.

It is interesting to note that soft rocks with different microstructures, as the 'foam type' (GasBeton and Pumice) and the 'bonded grain' (Conchiliades and Calcarenite), exhibit similar mechanical responses when subjected to a displacement controlled oedometric compression test.

A constitutive model able to describe the behaviour of bonded geomaterials, progressively loosing their cementation is presented. It is worth noting that the occurrence of the compaction band was theoretically predicted (Nova et al. 2003) before it could be actually observed in experiments.

## References

1. Castellanza R., Nova R., Oedometric Tests on Artificially Weathered Carbonatic Soft Rocks, *J. Geotechnical and Geoenvironmental Engineering ASCE*, vol. **130**, 7, 728-739, 2004
2. Nova R., Castellanza R., Tamagnini C., A constitutive model for bonded geomaterials subject to mechanical and/or chemical degradation, *Int. J. Num. Anal. Meth. Geomech.*, vol. **27**(9), 705-732, 2003.

# Author Index

## A

Abdullah, A., 481  
Abe, M., 657  
Aben, H., 3, 93  
Abramovich, H., 567  
Abu Bakar, M.A., 97  
Adami, C.-E., 961  
Adib-Ramezani, H., 963  
Ait Alaiwa, A., 339  
Akematsu, Y., 167  
Aktas, E., 119  
Albertazzi Jr., A., 637  
Alfano, M., 267  
Alfaro, M.P.M., 211  
Al-Haik, M., 621  
Al-Harathi, M., 811  
Allam, I.M., 817  
Al-Mukhtar, M., 963, 965  
Alvarez, J.A., 175  
Ambrosio, L., 247  
Amiot, F., 665, 671  
Anastasopoulos, A.A., 929  
Andre, S., 349, 729  
Andrei, A., 539  
Andrianopoulos, N.P., 153, 367  
Andruschenko, V.A., 617  
Angelova, D., 257, 259  
Ansari, F., 171  
Anton, J., 3, 95  
Aoh, J.N., 907  
Aoki, H., 523  
Aoki, T., 529  
Aoki, Y., 227  
Arai, M., 55  
Arai, Y., 609  
Arashnia, O., 319  
Arghir, M., 401  
Arola, D., 91, 331  
Asadchikov, V. E., 919  
Asahina, T., 773  
Ascione, L., 691  
Ashcroft, I.A., 357  
Ashimura, Y., 595  
Ashokan, K., 85  
Atteck, J., 475  
Avalle, M., 447  
Avril, S., 661, 663  
Azizi, A. R., 439

## B

Bae, J.-S., 61  
Baek, S.-K., 391  
Baek, U.B., 255  
Bahr, D.F., 571  
Bai, Y., 797  
Balalov, V.V., 597  
Balamurugan, A., 829  
Balandraud, X., 135, 843  
Baldi, A., 719  
Balke, H., 577  
Balogh, L., 631  
Banks-Sills, L., 569  
Baoning, H., 343  
Baran, D., 147  
Baratta, A., 693  
Baravian, C., 349  
Bartolomeo, M., 959  
Bati, S.B., 695  
Baumbach, T., 603  
Baxter, M., 925  
Bayraktar, E., 789, 799, 807, 815  
Beck, K., 963, 965  
Beghini, M., 945  
Behal, J., 423  
Belhabib, S., 677  
Belingardi, G., 291, 685  
Belmonte, H.M.S., 375  
Ben-David, E., 619  
Benedetti, M., 433, 945  
Berggreen, C., 749  
Bernikola, E., 715  
Bernini, M.B., 705  
Bernstorff, B.S. von, 645  
Berthel, B., 863  
Bertini, L., 945  
Bhargava, R.R., 563  
Bhatt, S., 191  
Bhattacharya, K., 385  
Bhattacharya, N., 579  
Bisagni, C., 779  
Blab, R., 499  
Blanchard, S., 809  
Boccaccini, A., 505  
Bochkareva, L.V., 35  
Boieriu, C., 127  
Bondarenko, A.A., 617  
Borbás, L., 631  
Borst, R. de, 465  
Bortoluzzi, D., 433  
Borza, D., 401, 717  
Bossuyt, S., 279  
Botsis, J., 633  
Bouchard, P.O., 813  
Boulougouris, V.C., 153  
Boyce, B. R., 855, 911  
Bozhevornaya, E., 745, 857  
Bozkurt, S.B., 119  
Branco, C.M., 229  
Brémand, F., 67, 713  
Broggiato, G.B., 305, 353  
Brondsted, P., 235

Brooks, W., 743  
Brown, I.A., 5  
Brown, P.M., 759  
Brunetaud, X., 965  
Brunner, A.J., 141  
Bruno, L., 711, 721  
Bukhanko, A., 315  
Bull, P.H., 287, 437  
Burgert, I., 491  
Buysschaert, F., 387  
Buzmakov, A. V., 919  
Byrne, J., 229

## C

Calloch, S., 389  
Calomfirescu, M., 299  
Camargo, J.A.M. de, 245  
Caneva, C., 923  
Cantwell, W., 743  
Capela, C., 253  
Cappello, F., 117  
Carin, A., 475  
Carloni, C., 699, 701  
Carmona, J.R., 189  
Carofiglio, F., 869  
Carol, I., 197  
Carpio, J., 175  
Casado, J.A., 175  
Casarotto, L., 163, 353  
Casavola, C., 947  
Castellanza, R., 969  
Catalanotti, G., 117  
Cavatorta, M.P., 685  
Cazzola, G.J., 517  
Cecco, D. De., 433  
Cellard, C., 69  
Cescotto, S., 805  
Chabaa, M., 233  
Chalal, H., 307  
Chan, H.L., 51  
Chan, L.C., 317, 459, 461  
Chandraseker, K., 629  
Chang, C.-C., 899  
Chang, C.-H., 903  
Chang, H.-S., 391  
Chang, L., 803  
Chao, Y.J., 877, 879  
Charalambides, M., 107  
Chatys, R., 767  
Chatzistergos, P., 483  
Chelubeev, D.A., 351  
Chen, E.-C., 823  
Chen, F., 325  
Chen, J.-S., 917  
Chen, K.-S., 893, 895  
Chen, T., 877, 885

Chen, T.Y.-F., 903  
 Chen, W.-H., 901  
 Chen, X., 831  
 Chen, Y., 803  
 Cheng, H.-C., 901  
 Cheng, H.-F., 901  
 Cheriguene, R., 733  
 Cheung, H.-Y., 821  
 Chevalier, J.P., 789, 807  
 Chiang, F.-P., 7, 209, 495  
 Chiang, K.N., 881  
 Chiang, M.-F., 825  
 Chien, C.-H., 877, 879, 885  
 Chiozzi, S., 463  
 Chirani, S.A., 389  
 Cho, J., 43  
 Choa, S.-H., 61  
 Chou, C.-Y., 881  
 Chow, C. L., 459  
 Chrysochoos, A., 863, 871  
 Chu, M.-J., 827  
 Chuang, S.-F., 903  
 Chvojan, J., 683  
 Cioffi, M.O.H., 245, 247, 249, 251  
 Cirello, A., 395  
 Clarke, A., 933  
 Claudio, R.A., 75, 229  
 Clausen, B., 635  
 Clyne, T.W., 759  
 Colpo, F., 633  
 Comandini, M., 225  
 Combescure, A., 231  
 Conway, A., 909  
 Cooreman, S., 935  
 Coppieters, S., 279  
 Corbi, I., 693  
 Cordero, R., 403  
 Cordisco, P., 779  
 Coret, M., 231, 465  
 Cornette, D., 735  
 Corral, T.V., 517  
 Cortese, L., 305  
 Costa, J.D., 253  
 Costa, J.-L., 475  
 Costa, M.Y.P., 249  
 Cottron, M., 187  
 Crane, R. M., 407  
 Crequy, S., 181  
 Croccolo, D., 435, 443  
 Croll, J.G.A., 787  
 Cunat, C., 349, 729  
 Cuppini, R., 443  
 Curtu, I., 127  
 Cutter, P.A., 763  
 Cvijovic, Z., 277

**D**

D'Acquisto, L., 359, 861  
 Dai, F., 321

Daniel, I.M., 43  
 Dantal, B., 37  
 Darrieulat, M., 643  
 Darwish, F.A.I., 211  
 Dattoma, V., 463, 943  
 Davidkov, A., 259  
 Davidson, J. P., 911  
 De Rosa, I. M., 923  
 Dean, J., 759  
 Dear, J., 417, 475, 757  
 Delobelle, P., 539  
 Demirel, M., 639  
 Deshpande, V.S., 131  
 Desrayaud, C., 643  
 Dierke, H., 163  
 Dimino, I., 453  
 Djouder, S., 233  
 Dolinko, A.E., 707  
 Domas, P., 629  
 Dontas, I.A., 81  
 Doumalin, P., 67, 89, 553  
 Drdacky, M., 275  
 Dreiden, G.V., 591  
 Drezner, H., 377, 537  
 Droudakis, A.I., 101  
 Du, X., 431  
 Dulieu-Barton, J.M., 5, 753, 853, 857, 859, 865, 875  
 Dupre, J.-C., 67  
 Dupre, J.C., 89, 553  
 Durrenberger, L., 735  
 Dzugan, J., 297

**E**

Eaton-Evans, J., 5, 853  
 Eberhardsteiner, J., 493, 505  
 Edery-Azulay, L., 567  
 Egilmez, O.Ö., 119  
 Eichlseder, W., 125, 183, 731  
 Ekmektzoglou, K.A., 81  
 Elata, D., 619  
 Elnasri, I., 295  
 Eman, J., 195  
 Emri, I., 645  
 Equis, S., 719  
 Errapart, A., 3, 93, 95  
 Espinosa, H.D., 9  
 Euler, E., 309  
 Eum, S., 113  
 Evans, S.L., 313, 925  
 Ezumi, T., 237

**F**

Fabis, J., 809  
 Falvo, A., 467  
 Fang, F., 565  
 Fatemi, A., 173  
 Fayolle, S., 813

Featherston, C.A., 777  
 Federico, A., 705  
 Fedorchenko, D., 315  
 Feichter, Ch., 273, 473  
 Felten, F., 577  
 Feo, L., 691  
 Ferber, F., 455  
 Fergusson, A., 417, 757  
 Ferreira, J.A.M., 253  
 Ferreira, J.M.F., 829  
 Ficquet, X., 425  
 Finck, C.M., 831  
 Fleck, N.A., 131  
 Florjani, U., 645  
 Focke, O., 299  
 Fontanari, V., 945  
 Forquin, P., 451  
 Forsberg, F., 337  
 Fourrestey, G., 205  
 Fournol, D., 489  
 Fragoudakis, R., 679  
 Francois, M., 139, 145, 397, 399  
 Freddi, A., 225, 435  
 Fruhmann, R.K., 875  
 Fu, Y., 557  
 Fujigaki, M., 21, 593, 595  
 Furgiuele, F., 267, 467  
 Futakawa, M., 301  
 Futase, K., 523

**G**

Gadaj, S.P., 725, 727  
 Gagnaire, H., 641  
 Galanis, K.P., 207  
 Galietti, U., 867, 869  
 Galizzi, G.E., 705  
 Galtier, A., 863  
 Ganniari-Papageorgiou, E., 957  
 Ganor, Y., 379  
 Garcia-Romeu, M., 285  
 Garcia-Romeu-Martinez, M.A., 551  
 Garraud, N., 671  
 Gary, G., 451  
 Gatingt, F., 451  
 Gavrylenko, G.D., 783  
 Gazonas, G.A., 11  
 Gdoutos, E.E., 755  
 Geers, M.G.D., 149  
 Germaneau, A., 89, 553  
 Gerolymatou, E., 969  
 Ghaemian, M., 487  
 Ghaemmaghani, A., 487  
 Gharghour, M., 241  
 Ghidossi, P., 181  
 Ghoranneviss, M., 59  
 Giannopoulos, G., 387  
 Gilchrist, M.D., 801

Gindl, W., 493  
 Giorgi, M. De, 943  
 Giovanni, R., 959  
 Girard, Y., 295  
 Gkanis, D., 449  
 Glazov, A.L., 373  
 Glorieux, C., 361  
 Gockel, F.-B., 455, 457  
 Godlinski, D., 505  
 Gogossi, E., 83  
 Goldstein, R.V., 351  
 Golestanian, H., 105, 837  
 Gomes, J.F.S., 369  
 Gomi, K., 655  
 Gope, P.C., 109, 111, 191,  
 193, 213  
 Gorecki, C., 539  
 Gower, M., 933, 937  
 Grediac, M., 13, 135, 843  
 Greene, R. J., 873  
 Grooves, R.M., 715  
 Grumbach, M., 799  
 Gubeljak, N., 277  
 Guden, M., 793, 795  
 Guduru, P.R., 625  
 Guedes, R.M., 369  
 Guelorget, B., 139, 145, 397,  
 543  
 Guo, Y., 831  
 Guochang, L., 99  
 Guster, Ch., 125  
 Gutermann, M., 413  
 Gutierrez-Solana, F., 175

## H

Habibi, M., 59  
 Habraken, A. M., 935  
 Hack, E., 723  
 Hackney, S., 715  
 Haddadi, H., 677  
 Hall, I.W., 793  
 Hampel, T., 455  
 Han, B., 15  
 Han, S., 533  
 Han, Y., 91  
 Haniotakis, E., 449  
 Hanke, A., 445  
 Hanson, S.G., 405, 709  
 Harmeyer, K., 627  
 Hartle, M., 629  
 Hasanifard, S., 215  
 Hashmi, M.S.J., 801  
 Häusler, C., 577  
 Hawong, J., 533  
 Hayafune, K., 507  
 He, S., 469  
 He, X.-Y., 325, 341, 557  
 Hedan, S., 187  
 Helferich, G., 587  
 Hellmich, C., 505

Hemelrijck, D.V., 361, 931,  
 933, 935, 941  
 Hendrick, P., 387  
 Henrat, P., 641  
 Hensman, J., 921  
 Hesser, F., 67  
 Hicher, P.-Y., 339  
 Hild, F., 179, 665, 669, 671  
 Hino, M., 833, 841  
 Hirao, A., 167  
 Hirsinger, L., 539  
 Hlado, V., 147  
 Hmida-Maamar, S., 667  
 Hoefnagels, J.M.P., 149  
 Hoefnagels, J.P.M., 63  
 Holford, K.M., 925, 927  
 Holland, M.A., 627  
 Holt, C.A., 313  
 Holy, S., 477  
 Holy, T., 355  
 Honda, D., 709  
 Hong, D.-P., 143  
 Hong, Y., 143  
 Horn, J.-T., 883  
 Hossain, Md.M., 589  
 Hosseinzadeh, F., 73  
 Hsu, S.-F., 819  
 Huang, C.Y., 907  
 Huang, M. J., 897  
 Huang, S.-J., 615, 889  
 Huang, Y.H., 323  
 Huang, Y.-K., 917  
 Hung, Y.Y., 323  
 Huntley, J.M., 357, 663  
 Hussain, A., 873  
 Hustinx, G.M., 715  
 Hwang, D., 525  
 Hwang, D.Y., 511  
 Hwang, S.-F., 883

## I

Ichinose, K., 655  
 Ida, T., 611  
 Igawa, H., 113  
 Iguch, M., 833  
 Iguchi, D., 839  
 Iguchi, M., 839  
 Ikeda, K., 185  
 Iliopoulos, A.P., 367  
 Inamoto, K., 169  
 Irani, R., 629  
 Isaac, G., 865  
 Ishijima, R., 709  
 Isogai, Z., 535  
 Itoh, Y., 511, 535  
 Iwanaga, K., 659, 687  
 Izquierdo, F.A., 517

## J

Jacquot, P., 17, 719  
 Jager, A., 493, 503  
 Jakobsen, J., 745  
 Jakobsen, M.L., 405  
 Jakubek, J., 355  
 Jakubek, M., 355  
 James, R.D., 379  
 Jankovec, J., 477  
 Jaros, P., 477  
 Jasiski, J., 79  
 Javidi, A., 183  
 Jelitto, H., 577  
 Jeng, Y.-T., 913  
 Jeon, I., 773  
 Jerabek, M., 393, 471, 473  
 Jesson, D.A., 375  
 Jewell, G., 909  
 Jin, C., 469  
 Jirousek, O., 275  
 Johannes, M., 857  
 Johnson, A., 771  
 Joshi, S.P., 541  
 Jozwik, M., 539  
 Jumbo, F., 357  
 Jung, H.-C., 391  
 Jurko, J., 77

## K

Kacperski, J., 333, 539  
 Kageyama, K., 113, 167  
 Kahraman, R., 811  
 Kaizu, K., 185  
 Kakunai, S., 521  
 Kalam, A., 97  
 Kalincsak, Z., 631  
 Kalogiannakis, G., 361  
 Kanai, M., 113  
 Kaneko, H., 521  
 Kang, K.-S., 391  
 Kang, X., 341  
 Kannan, S., 829  
 Kannappan, L., 415  
 Kanoufi, F., 665  
 Kaplan, D., 789, 799, 807,  
 815  
 Kapp, W.A., 637  
 Kappl, K., 499  
 Karalekas, D., 633  
 Kato, A., 527  
 Kato, M., 57  
 Katou, K., 773  
 Katsioti, M., 449  
 Kaufmann, G.H., 705, 707  
 Kavi, H., 795  
 Kawagishi, N., 593  
 Keller, T., 141, 201, 203, 205  
 Kepler, J.A., 287, 437  
 Khelidj, A., 489  
 Khromov, A., 315

Kikuta, H., 585  
 Kim, B.J., 219, 269  
 Kim, H., 49  
 Kim, H.S., 47  
 Kim, J.-H., 675  
 Kim, J.R., 49  
 Kim, K.-S., 391  
 Kim, M.-G., 165  
 Kim, M.-H., 545  
 Kim, S.G., 49  
 Kim, Y.-M., 143  
 Kim, Y.-W., 419  
 Kincaid, I. M., 855  
 Kinoshita, H., 185  
 Kireitseu, M.V., 35  
 Kiric, M., 221  
 Kisel, V.P., 151  
 Kishimoto, S., 321  
 Klepaczko, J.R., 733  
 Ko, F.K., 831  
 Koberl, H., 731  
 Koch, T., 497  
 Kocherov, E., 315  
 Koenig, Ch.R., 299  
 Kohlhauser, C., 505  
 Koide, K., 535  
 Kollarini, M.J., 741  
 Kong, T. F., 461  
 Konnerth, J., 493  
 Konsta-Gdoutos, M.S., 43  
 Koon, R., 747  
 Kopecky, M., 177  
 Korjamins, A., 115  
 Kouloumpi, E., 715  
 Kourkoulis, S.K., 81, 83, 133,  
 483, 949, 951,  
 953, 955, 957  
 Kourmpetis, M., 417  
 Kowalewski, Z.L., 739  
 Kozhevnikov, I. V., 919  
 Kozintsev, V.M., 351  
 Kraft, A., 587  
 Kralj, S., 647, 649  
 Krupa, K., 539  
 Krutz, G., 627  
 Kubo, S., 851  
 Kudiran, N.H., 97  
 Kujawinska, M., 333, 607  
 Kumar, B., 213  
 Kumar, S.M.S., 383  
 Kumar, V., 765  
 Kumar, G. PVS, 747  
 Kumazawa, T., 371, 905  
 Kuwazuru, O., 303  
 Kuzukami, S., 303  
 Kwon, G., 533  
 Kwon, O.-S., 533  
 Kytopoulos, V., 133

**L**

Labeas, G.N., 161, 775  
 Lackner, R., 501, 503  
 Laermann, K.-H., 411  
 Lai, C. P., 459  
 Lamberti, L., 363, 365  
 Lamkanfi, E., 933, 941  
 Lang, R.W., 125, 223, 273,  
 393, 473  
 Langrand, B., 809  
 Latourte, F., 863  
 Lau, K.-T., 821  
 Laura, E., 959  
 Lecompte, D., 279, 931, 935  
 Lederer, K., 223  
 Lee, H.-J., 61  
 Lee, H.M., 255  
 Lee, J.Y., 907  
 Lee, K.B., 47  
 Lee, S.E., 781  
 Lee, S.G., 49  
 Lee, S.J., 49  
 Lee, T.C., 317, 461  
 Lee, Y.J., 47  
 Lee, Y.-S., 419  
 Leguillon, D., 199  
 Leitner, H., 731  
 Lelkes, P.L., 831  
 Lembessis, E., 753  
 Levantis, A.D., 953  
 Lexcelent, C., 389  
 Li, J., 199  
 Li, M., 557, 831  
 Li, Y., 321  
 Liao, C.-C., 915  
 Liao, C.-S., 819  
 Lica, D., 127  
 Lim, B.S., 219, 269  
 Lin, C.-T., 881  
 Lin, S.-J., 855, 911  
 Lin, S.-T., 899  
 Lin, W.-B., 877  
 Lin, Y.-T., 889  
 Lindholm, C.-J., 751  
 Linke, M., 769  
 Liou, J. K., 897  
 Lira, I., 397  
 Little, E.G., 5  
 Liu, L., 323  
 Liu, W.-W., 341  
 Liu, Z., 321  
 Lo, Y.-L., 913, 915  
 Lomov, S., 311  
 Lopes, H.M., 369  
 Lopez, C.P., 605  
 Lu, J., 45, 51, 139, 543  
 Luckner, J., 725  
 Lundsgaard-Larsen, C., 749  
 Luo, M., 331  
 Luo, P.-F., 891  
 Lyoo, W.S., 47, 49

**M**

MacDiarmid, A.G., 831  
 Machida, K., 507  
 Mackiewicz, S., 739  
 Mae, H., 797  
 Magnissalis, E., 483  
 Mahnken, R., 455, 457  
 Main, J.A., 11  
 Major, Z., 223, 273, 393, 471,  
 473  
 Makris, A., 933  
 Maksimochkin, G., 649  
 Maletta, C., 267, 467  
 Manfredi, G., 703  
 Manolopoulos, V.M., 153  
 Mansori, M. El, 181  
 Maquin, F., 847  
 Maras, A., 399  
 Marc, G., 715  
 Marinelli, A., 949  
 Markiewicz, E., 809  
 Markou, I.N., 101  
 Martinet, A., 53  
 Martinez, A., 403  
 Maruschak, P., 147  
 Mascia, N.T., 519  
 Mathur, S., 111  
 Matsuda, A., 709  
 Matsumoto, K., 835  
 Matsumura, K., 835  
 Matsuno, H., 227  
 Matsuura, H., 535  
 Matthys, D. R., 855, 911  
 Matui, T., 21, 593, 595  
 Matuura, H., 511  
 Mayer, R., 683  
 McClain, R., 629  
 McKown, S., 743  
 McMeeking, R.M., 575  
 Mehta, D.S., 589  
 Meleshko, V.V., 617  
 Mendelovich, A., 377  
 Mendoza-Santoyo, F., 561  
 Menegazzi, A., 791  
 Meneses-Fabian, C., 561  
 Mentl, V., 297  
 Mera, R., 933, 937  
 Meraghni, F., 307  
 Merzouki, T., 307  
 Messier, J., 379  
 Metaxa, Z., 43  
 Michalkiewicz, A., 607  
 Michel, J.-P., 475  
 Miki, T., 841  
 Mikula, P., 427  
 Milanese, A.C., 251  
 Millot, T., 791  
 Mines, R.A.W., 19, 743  
 Mini, R., 381  
 Mirisiotis, L.S., 689  
 Miyagawa, S., 507



Mizuhara, N., 585  
 Mkaddem, A., 181  
 Mocellin, K., 813  
 Modugno, D., 867, 869  
 Moe, T.A., 527  
 Mohebbi, H., 375  
 Mohri, N., 167  
 Moita, P.J., 75  
 Molimard, J., 639, 641, 643  
 Molinari, A., 735  
 Mondrinos, M.J., 831  
 Monreal, J., 387  
 Montay, G., 145, 397, 399  
 Montenegro, O.I., 197  
 Moreau, A., 401  
 Morimoto, Y., 21, 593, 595  
 Morita, M., 521  
 Morren, G., 311  
 Morris, A., 417, 757  
 Morris, D.J., 571  
 Morris, E., 801  
 Motola, Y., 569  
 Mounanga, P., 489  
 Moupagitsoglou, K.E., 955  
 Moussy, F., 53  
 Moutrille, M.-P., 843  
 Mueller, D.H., 299  
 Mukhamediev, E.D., 261  
 Mulheron, M.J., 375  
 Mulinari, D.R., 41  
 Muller, U., 493  
 Muracciole, J.-M., 871  
 Muratikov, K.L., 373  
 Murayama, H., 113, 167  
 Murphy, A., 785  
 Mylavarapu, P., 761  
 Mylonas, G.I., 161

## N

Nadella, K., 765  
 Nakai, K., 681  
 Nakasa, K., 57  
 Nakayama, N., 39, 371, 905  
 Nam, J., 533  
 Naoe, T., 301  
 Naranji, R., 59  
 Natarajan, V.D., 97  
 Nazari, A., 331  
 Nemoto, T., 511, 535  
 Neuhauser, H., 163  
 Ni, C.-Y., 887  
 Ni, J., 803  
 Nicolas, E.A., 519  
 Niederkofler, T., 503  
 Nieradko, L., 539  
 Nigro, F. Lo, 861  
 Niitsu, Y., 655  
 Nikitenko, V.N., 617  
 Nikolay, P., 445  
 Nikonov, A., 645

Ninis, N.L., 955, 957  
 Nishimura, J., 521  
 Nishinohara, T., 531  
 Nistea, I., 401  
 Niu, J., 469  
 Nobile, L., 699, 701  
 Nobile, R., 463, 943  
 Noguchi, H., 227  
 Nokkentved, A., 235  
 Nomura, T., 585  
 Nomura, Y., 653  
 Nova, R., 969  
 Nowacki, W.K., 725, 727

## O

O'Brien, E., 409  
 Ochi, Y., 55  
 Oda, Y., 227  
 Odamura, T., 681  
 Odintsev, I.N., 599  
 Oh, C.-S., 61  
 Ohmi, T., 839  
 Ohtsuki, A., 441  
 Olabi, A.G., 801  
 Olier, P., 45  
 Olivito, R.S., 697  
 Olmi, G., 225, 435  
 Olson, A.L., 571  
 Olsson, E., 337  
 Orteu, J.-J., 639  
 Osawa, I., 113  
 Osmond, P., 69  
 Osten, W., 603, 715  
 Ou, K.-S., 893, 895  
 Ozeki, R., 513  
 Ozolins, O., 115  
 Ozturk, H., 313

## P

Paepegem, W.V., 931, 933,  
 941  
 Pagano, S., 863  
 Pagliaro, P., 635  
 Pak, A., 481  
 Pan, B., 321  
 Pandermarakis, Z.G., 217  
 Pant, M., 191  
 Pantelakis, Sp.G., 161  
 Paolino, D.S., 685  
 Papadopoulos, G.A., 271  
 Papanicolopoulos, S.-A., 81,  
 949  
 Papatnasiou, A., 449  
 Papazoglou, V.J., 207  
 Pappalettere, C., 867, 869,  
 947  
 Parker, A., 155, 157  
 Pasechnik, S., 649  
 Pasta, A., 395

Pasta, S., 263  
 Pastor, M.L., 135  
 Patterson, E.A., 845  
 Patofofatto, S., 295  
 Pawlak, T., 455  
 Pecquet, E., 805  
 Pedrini, G., 603  
 Peerlings, R.H.J., 149  
 Perets, A., 831  
 Peroni, L., 291, 447  
 Peroni, M., 291  
 Perrea, D.N., 81  
 Pertue, A., 489  
 Phan, T. S., 859  
 Philip, J., 85  
 Phillips, H., 763  
 Pica, A. La, 359  
 Pichler, C., 501, 503  
 Pieczynska, E.A., 725, 727  
 Pierron, F., 661, 663, 675, 847  
 Pillai, S.A., 85  
 Pinit, P., 651, 653  
 Pinter, G., 125  
 Pipilikaki, P., 449  
 Pisarev, V.S., 597, 599  
 Pitarresi, G., 861  
 Pizele, D., 115  
 Podlesnyh, A.V., 351  
 Poggialini, A., 711  
 Polach, P., 683  
 Polilov, A.N., 121  
 Polyakov, V., 767  
 Popoi, A., 127  
 Popov, A.L., 351  
 Posavljak, S., 65  
 Potdar, Y.K., 629  
 Prete, Z. Del, 353  
 Price, M., 785  
 Prime, M.B., 635  
 Priyadarshini, R.I., 383  
 Protta, A., 703  
 Pullin, R., 925, 927  
 Puri, A., 417, 757  
 Pyoun, Y.-S., 545

## Q

Qiao, Y., 709  
 Qiu, J., 905  
 Qiu, S., 343  
 Quan, C., 327  
 Quaranta, V., 453  
 Quinn, D., 785  
 Quinn, S., 853, 855, 875, 911

## R

Ragulskis, M., 335  
 Rajapakse, Y.D.S., 23  
 Rakin, M., 277  
 Ramault, C., 933

- Ramesh, K., 85  
 Ramesh, K.T., 541  
 Ramesh, M., 87  
 Ramji, M., 87  
 Ranganath, S., 747  
 Rao, C.L., 381, 383  
 Ratcliffe, C. P., 407  
 Ravichandran, G., 385  
 Ray, S.K., 265  
 Rayas, J.A., 403, 561  
 Rebelo, A., 829  
 Recho, N., 199  
 Redmond, J.M., 621  
 Reifsnider, K., 25  
 Reimerdes, H.-G., 769  
 Reithmeier, E., 587  
 Remy, S., 69  
 Renault, N., 349, 729  
 Rethore, J., 179, 465  
 Retraint, D., 45, 69, 543  
 Reu, P.L., 555  
 Reynolds, A.P., 263  
 Rezende, M.C., 247  
 Richards, C.D., 571  
 Richards, R.F., 571  
 Rieger, U., 183  
 Riga, Ch., 133  
 Rittel, D., 619  
 Ritzke, J., 445  
 Robert, J.L., 135  
 Robert, L., 347, 639, 667  
 Robin, E., 713  
 Robinson, M.C., 571  
 Rocha, J.H.G., 829  
 Rodriguez-Vera, R., 561  
 Roger, J.P., 665, 671  
 Rogillio, B.R., 555  
 Roland, T., 45  
 Roos, A., 45, 543  
 Rosenberger, A.H., 209  
 Roshchin, B. S., 919  
 Rosu, D., 129  
 Rouhaud, E., 69, 399  
 Rouillard, V., 155, 157, 285, 547, 549, 551  
 Roux, S., 179, 669  
 Rovero, L., 695  
 Rowlands, R.E., 845, 855, 911  
 Ruiz, G., 189, 281, 283  
 Ruiz, P.D., 357  
 Rusinek, A., 733, 735  
 Russell, B.P., 131  
 Russo, O., 711
- S**  
 Sah, P.L., 109  
 Saidi, K., 313  
 Saigal, A., 37, 679  
 Saiyouri, N., 339  
 Saka, M., 515  
 Sakagami, T., 851  
 Sakai, T., 243  
 Sakellariou, A., 449  
 Samsonov, A.M., 591  
 Santafe, F., 387  
 Santoyo, F.M., 605  
 Santus, C., 945  
 Sarasini, F., 923  
 Sarens, B., 361  
 Sasaki, S., 237  
 Sasaki, Y., 833, 839  
 Sasikala, G., 265  
 Sato, T., 159  
 Saucedo, T., 605  
 Saxena, N., 563  
 Scena, S., 479  
 Schlottmann, G., 445  
 Schmidt, F., 667  
 Schneider, G.A., 577  
 Scholz, T., 587  
 Schubach, H.R., 583  
 Schumacher, A., 723  
 Schuster, B.E., 541  
 Schwab, X., 603  
 Sciammarella, C.A., 27, 363, 365  
 Sciammarella, F.M., 365  
 Scott, R. H., 439  
 Sedmak, A., 221, 277  
 Seidler, S., 497  
 Seika, M., 513  
 Sek, M.A., 155, 157, 285  
 Sekino, K., 531  
 Semenova, I.V., 591  
 Senin, R. A., 919  
 Settsu, N., 515  
 Sezgin, F.E., 119  
 Sfer, D., 197  
 Shakher, C., 589  
 Shamirzaev, S.Kh., 261  
 Shamirzaeva, G.Yu., 261  
 Shang, H., 321  
 Shankar, K., 415  
 Sharma, J.K., 111  
 Sharma, S.P., 213  
 Sharpe, W.N., Jr., 29, 329  
 Shaw, R., 933, 937  
 Shenoi, R.A., 753, 763  
 Sheoran, G., 589  
 Shield, T.W., 379  
 Shilo, D., 377, 379, 385, 537, 619  
 Shimamoto, A., 509, 511, 523, 525, 529, 535  
 Shimizu, I., 71  
 Shimizu, K., 531  
 Shrive, N.G., 313  
 Sicot, O., 399  
 Siddiolo, A. M., 861  
 Siddiolo, A.M., 359  
 Silva, J.D., 75  
 Silva, L.C.P., 41  
 Singh, V.K., 193  
 Sivakumar, S.M., 381  
 Sjodahl, M., 345  
 Skibiski, T., 739  
 Slavinec, M., 649  
 Slizkova, Z., 275  
 Smith, D.J., 73, 425  
 Smith, P.A., 375  
 Smits, A., 931, 933, 941  
 Sol, H., 279, 311, 931, 935  
 Somers, P.A.A.M., 579  
 Song, G.-H., 545  
 Song, Li, 289  
 Sonoda, T., 773  
 Sørensen, B.F., 749  
 Sorkhabi, A.H., 319  
 Sotiropoulos, D. A., 421  
 Sotirpoulou, A.B., 217  
 Spencer, A., 865  
 Spiegl, M., 499  
 Sreenatha, A.G., 415  
 Stanciu, M., 127  
 Stanley, P., 859  
 Stapountzi, O.A., 107  
 Steele, D.D., 663  
 Steffens, K., 413  
 Steinberger, R., 393, 471, 473  
 Steindler, R., 479  
 Subramaniam, K.V., 699, 701  
 Suetsugu, M., 531  
 Sugiura, M., 513  
 Suh, C.-M., 545  
 Sultan, H.S., 103  
 Sumali, H., 621, 623  
 Sun, W., 557  
 Sun, Z.-J., 137  
 Sunaric, M.M., 775  
 Sundin, K.G., 195  
 Sutcliffe, C.J., 743  
 Sutton, M.A., 661  
 Suzuki, S., 687  
 Suzuki, T., 835  
 Svetec, M., 649  
 Swallowe, G.M., 357  
 Szelazek, J., 739  
 Szota, M., 79
- T**  
 Tabata, K., 585  
 Taheri, F., 241  
 Taillard, K., 389  
 Takacs, J., 631  
 Takahashi, D., 835  
 Takahashi, N., 169  
 Takeda, M., 709  
 Takeishi, H., 39  
 Takezoe, S., 57  
 Talati, F., 319  
 Tanaka, N., 301

Tanaka, S., 169  
 Taniguchi, S., 835  
 Tanoglu, M., 119  
 Tardif, N., 231  
 Tasan, C.C., 149  
 Tasdemirci, A., 793  
 Tatar, K., 337  
 Tatous, N.A., 121  
 Tatum, P. J., 853  
 Tay, C.J., 327  
 Tchuindjang, J., 805  
 Teas, Ch., 449  
 Teng, X., 797  
 Teodorescu, H., 129  
 Thatcher, J., 939  
 Thomsen, O.T., 31, 235, 745, 857  
 Tobushi, H., 727  
 Todeschini, R., 519  
 Tokunaga, H., 185  
 Tomlinson, R. A., 849, 873, 909  
 Tong, W., 559, 673  
 Tonietti, U., 695  
 Torii, K., 905  
 Tornari, V., 715  
 Toso-Pentecote, N., 771  
 Touati, M., 233  
 Toumbakari, E.-E., 967  
 Tourneix, M., 397  
 Toyama, H., 55  
 Trinkle, S., 621  
 Trioux, F., 53  
 Truman, C.E., 73, 425  
 Tsai, Y.-H., 887  
 Tseng, C.-C., 885  
 Tsouvalis, N.G., 689, 741  
 Tumino, D., 117  
 Tutsch, R., 163

**U**

Udov, M., 645  
 Ulea, M., 129  
 Umezaki, E., 651, 653, 657, 659  
 Uzawa, K., 113  
 Uzer, G., 209, 495

**V**

Vacher, S., 641  
 Vaclavik, J., 477, 683  
 Vakili-Tahami, F., 319  
 Valach, J., 275, 355  
 Valance, S., 465  
 Valentini, E., 945  
 Valido, A.J., 75  
 Valle, V., 67, 187, 713  
 Vallee, T., 141, 205  
 Van, T.-T., 965

Vantomme, J., 279, 387, 935  
 Vassilopoulos, A.P., 201, 203  
 Vautrin, A., 639, 641  
 Vavrik, D., 275, 355  
 Vayas, I., 949  
 Vaz, M.A., 369  
 Velay, V., 667  
 Ventura, J.M.G., 829  
 Vera, R.R., 605  
 Verleye, B., 311  
 Vial-Edwards, C., 397  
 Viguera-Sancho, A., 69  
 Vincenzi, N., 443  
 Vintzileou, E., 961  
 Viotti, M.R., 637  
 Viso, J.R. Del, 189  
 Vitale, G., 867  
 Vitale-Brovarone, C., 505  
 Vlase, S., 129  
 Vlassak, J.J., 63  
 Voorwald, H.J.C., 245, 247, 249, 251  
 Vrana, M., 427

**W**

Waltz, L., 45, 543  
 Wang, C., 431  
 Wang, C.-H., 891  
 Wang, G.-P., 143  
 Wang, H., 787  
 Wang, H.J., 883  
 Wang, L., 317  
 Wang, L.-L., 137, 289  
 Wang, S.H., 327  
 Wang, W., 709  
 Wang, W.-C., 887  
 Watkins, T.R., 635  
 Wattrisse, B., 863, 871  
 Wei, W., 343  
 Wei, Y., 831  
 Weinberg, O., 477  
 Wellman, G.W., 555  
 Wen, R.H., 565  
 Whittle, R. T., 439  
 Wierzbicki, T., 797  
 Williams, J.G., 107  
 Williams, R., 737  
 Williamson, C., 933, 939  
 Wisnom, M., 675  
 Wistuba, M., 499  
 Witz, J.-F., 669  
 Wollesenbet, E., 737, 761  
 Worden, K., 865, 921  
 Wu, K.-W., 123  
 Wu, T.-M., 819, 823, 825, 827  
 Wu, Y.-D., 879

**X**

Xanthos, T., 81

Xiaoyuan, H., 343  
 Xie, H., 321  
 Xin, H., 343  
 Xing, L., 25  
 Xingwen, D., 99  
 Xu, Z., 171

**Y**

Yadav, R.P., 109  
 Yamada, T., 773  
 Yamada, Y., 773  
 Yamaguchi, I., 611  
 Yamaguchi, N., 851  
 Yamashita, K., 509  
 Yamaya, F., 515  
 Yan, H.-Y., 893, 895  
 Yan, J., 661  
 Yang, F., 803  
 Yang, L.M., 289  
 Yang, L.X., 581  
 Yang, W., 565  
 Yao, H., 673  
 Yaroslavsky, L., 601  
 Yasniy, P., 147  
 Yasuoka, M., 239  
 Yates, J. R., 849  
 Yeh, C.-Y., 915  
 Yeh, H.J., 615  
 Yilbas, B.S., 815  
 Yiu, E.C.Y., 323  
 Yokosuka, H., 169  
 Yokota, H., 581  
 Yokota, M., 611  
 Yokoyama, T., 681  
 Yokozeiki, S., 609  
 Yokozeiki, T., 709  
 Yoneyama, S., 585  
 Yoon, K.B., 255  
 Yordanova, R., 257  
 Yoshikawa, N., 303  
 Young, C., 49  
 Youshan, W., 99  
 Yu, R.C., 281, 283  
 Yuen, B.K.C., 241  
 Yuksel, S., 795

**Z**

Zacharopoulos, D.A., 755  
 Zaera, R., 733  
 Zanganeh, M., 849  
 Zehsaz, M., 215  
 Zhang, D., 91, 331  
 Zhang, F.C., 565  
 Zhang, T.-Y., 573  
 Zhang, X., 281, 283  
 Zhang, Yan, 613  
 Zhang, Ye, 203  
 Zhani, K., 643  
 Zhao, H., 295

Zheng, J., 57  
Zheng, P., 803  
Zhou, W., 613  
Zimmerman, M., 37  
Zografos, G.C., 81  
Zoroufi, M., 173  
Zrilic, M., 277  
Zuccarello, B., 117, 635  
Zuccarello, F.A., 697  
Zupani, B., 645